

AD-A201 474

AFOSR-TR. 88-1259

①

PROCEEDINGS OF THE JOINT INTERNATIONAL
SYMPOSIUM ON

MOLTEN SALTS

Edited By

Gleb Mamantov
Department of Chemistry
University of Tennessee
Knoxville, Tennessee

Milton Blander
Chemical Technology Division
Argonne National Laboratory
Argonne, Illinois

Charles Hussey
Department of Chemistry
University of Mississippi
University, Mississippi

Charmaine Mamantov
Department of Chemistry
University of Tennessee
Knoxville, Tennessee

Marie-Louise Saboungi
Chemical Technology Division
Argonne National Laboratory
Argonne, Illinois

John Wilkes
The Frank J. Seiler
Research Laboratory
U.S. Air Force Academy
Colorado Springs, Colorado



PHYSICAL ELECTROCHEMISTRY AND HIGH TEMPERATURE MATERIALS DIVISIONS

Proceedings Volume 87-7

THE ELECTROCHEMICAL SOCIETY, INC., 10 South Main Street, Pennington, NJ 08534-2896

Approved for public release;
distribution unlimited.

UNCLASSIFIED

SECURITY CLASSIFICATION OF THIS PAGE

REPORT DOCUMENTATION PAGE				Form Approved OMB No. 0704-0188	
1a. REPORT SECURITY CLASSIFICATION UNCLASSIFIED			1b. RESTRICTIVE MARKINGS		
2a. SECURITY CLASSIFICATION AUTHORITY			3. DISTRIBUTION/AVAILABILITY OF REPORT Approved for public release; Distribution is unlimited		
2b. DECLASSIFICATION/DOWNGRADING SCHEDULE			5. MONITORING ORGANIZATION REPORT NUMBER(S) AFOSR-TK-88-1259		
4. PERFORMING ORGANIZATION REPORT NUMBER(S)			7a. NAME OF MONITORING ORGANIZATION AFOSR/NC		
6a. NAME OF PERFORMING ORGANIZATION The Electrochemical Society		6b. OFFICE SYMBOL (if applicable)	7b. ADDRESS (City, State, and ZIP Code) Building 410 Bolling AFB, DC 20332-6448		
6c. ADDRESS (City, State, and ZIP Code) 10 South Main Street Pennington, NJ 08534-2896		9. PROCUREMENT INSTRUMENT IDENTIFICATION NUMBER AFOSR-88-0003			
8a. NAME OF FUNDING/SPONSORING ORGANIZATION AFOSR		8b. OFFICE SYMBOL (if applicable) NC	10. SOURCE OF FUNDING NUMBERS		
8c. ADDRESS (City, State, and ZIP Code) Building 410 Bolling AFB, DC 20332-6448		PROGRAM ELEMENT NO. 61102F	PROJECT NO. 2303	TASK NO. A1	WORK UNIT ACCESSION NO.
11. TITLE (Include Security Classification) Joint International Symposium on Molten Salts 172nd Electrochemical Society National Meeting					
12. PERSONAL AUTHOR(S) Gleb Mamantov et al.; R. L. McCreery and R. M. Wightman					
13a. TYPE OF REPORT Final		13b. TIME COVERED FROM 10-1-87 TO 9-30-88		14. DATE OF REPORT (Year, Month, Day)	
				15. PAGE COUNT 3387	
16. SUPPLEMENTARY NOTATION					
17. COSATI CODES			18. SUBJECT TERMS (Continue on reverse if necessary and identify by block number)		
FIELD	GROUP	SUB-GROUP			
19. ABSTRACT (Continue on reverse if necessary and identify by block number) <p>The Joint International Symposium on Molten Salts was held 18-23 October 1987 in Honolulu, HI. Topics emphasized include fundamentals and applications of room-temperature haloaluminates, molten salt batteries, molten-metal solutions and their application to extractive metallurgy by electrochemical techniques, and nuclear processes utilizing molten salts media. The symposium on Spectroelectrochemistry and Electroanalytical Science was held at the joint meeting of the Electrochemical Societies of the United States and of Japan. The symposium incorporated work directed toward obtaining information about the electrode/solution interface and the adjacent solution, including spectral probes of the electrode surface and diffusion layer and electrochemical methods for analyzing solutions.</p>					
20. DISTRIBUTION/AVAILABILITY OF ABSTRACT <input checked="" type="checkbox"/> UNCLASSIFIED/UNLIMITED <input checked="" type="checkbox"/> SAME AS RPT <input type="checkbox"/> DTIC USERS			21. ABSTRACT SECURITY CLASSIFICATION UNCLASSIFIED		
22a. NAME OF RESPONSIBLE INDIVIDUAL Dr. John S. Wilkes			22b. TELEPHONE (Include Area Code) (719) 472-2655		22c. OFFICE SYMBOL NC

DD Form 1473, JUN 86

Previous editions are obsolete.

SECURITY CLASSIFICATION OF THIS PAGE
UNCLASSIFIED



Accession For	
NTIS CRA&I	<input checked="checked" type="checkbox"/>
DTIC TAB	<input type="checkbox"/>
Unannounced	<input type="checkbox"/>
Justification	
By	
Dist	
Date	
Dist	
Date	
A1	

Copyright 1987

by

The Electrochemical Society, Incorporated

***Papers contained herein may not be
reprinted and may not be digested by pub-
lications other than those of The Electrochemical
Society in excess of 1/6 of the material presented.***

Library of Congress Catalog Number: 87-82356

Printed in the United States of America

PREFACE

The Joint International Symposium on Molten Salts is a joint effort between the Electrochemical Society and the Electrochemical Society of Japan. Since 1976 the Electrochemical Society has sponsored five international symposia on molten salts; the current symposium is the sixth symposium in this series. In 1983 the Molten Salt Committee of the Electrochemical Society of Japan chaired by Professor N. Watanabe sponsored the First International Symposium on Molten Salt Chemistry and Technology; the current symposium is also the second symposium in that series. This collaboration between the two societies has resulted in one of the largest meetings ever devoted to molten salts; 123 papers will be presented at this Symposium of which over 80% are included in the proceedings volume. The presence of many papers from countries other than the U.S. and Japan is a good indicator of the increased interest throughout the world in molten salt chemistry and its applications to areas such as batteries and fuel cells, production of light metals, electrodeposition of refractory metals, synthesis of new materials, thermal energy storage as well as other uses.

I would like to express my appreciation to the Cochairmen of this Symposium, Milton Blander, Hironao Kojima, Zensaku Kozuka, Marie-Louise Saboungi, Nobuatsu Watanabe as well as to the other editors of this volume who, in addition to Drs. Blander and Saboungi, include Drs. Charles Hussey, Charmaine Mamantov and John Wilkes. The timely work by this group of editors is making it possible to provide this volume in time for the Symposium. The assistance of Dr. George Shankle, Robert Walton, Connie Robledo and Renee Thomas is also gratefully acknowledged.

Gleb Mamantov

AIR FORCE OFFICE OF SCIENTIFIC RESEARCH (AFSC) NOTICE OF TRANSMITTAL TO DTIC

**This technical report has been reviewed and is
approved for public release IAW AFR 190-12.**

Distribution is unlimited.

RECEIVED DTIC

Chief, Technical Information Division



Hahn Floer

DEDICATION
PROFESSOR HÅKON FLOOD

The Joint International Symposium on Molten Salts wishes to dedicate this volume to one of the founding fathers of modern molten salt chemistry, professor Håkon Flood, Trondheim, Norway.

Håkon Flood was born September 25, 1905 and graduated from the Norwegian Institute of Technology, Trondheim in 1930, majoring in inorganic chemistry and electrochemistry.

Flood spent the year 1930-1931 in Berlin at the famous institute of Professor Max Volmer. Returning home in 1932, he became a research associate at his alma mater. In 1933 he was granted a leave of absence and returned to Volmer's institute to finish his Doctor's Thesis. The topic was: Tröpfchenbildung in Übersättigten Dämpfen. Prädikat: Mit Auszeichnung bestanden. Håkon Flood was appointed Docent (associate professor) in inorganic chemistry at The Norwegian Institute of Technology in 1935 and held this position until he was appointed full professor in inorganic chemistry at the same university in 1953.

Professor Flood's scientific production in the years following the completion of his studies in Berlin is mainly in the field of phase kinetics. However, in the late thirties he became interested in certain aspects of analytical chemistry and in several papers he made important contributions to the theory of potentiometric titration. In this period Flood also took up the study of vanadium-oxyhalides, a study which was later expanded to a more general study of oxide systems containing vanadium. This work resulted in one of the first papers on semi-conducting nonstoichiometric compounds. During the early forties most of Professor Flood's scientific production was in the field of analytical chemistry. Among his papers from this period are pioneering contributions to paper chromatography.

Later in the forties Professor Flood turned toward the area of research for which he has become best known: High-temperature and molten salt chemistry. In this field he has won widespread international recognition, and he has created what may be called a Norwegian school in the field of the chemistry of molten salts. The first part of Professor Flood's high-temperature chemistry period is mainly devoted to acid-base reactions in oxide systems. In this field he has made contributions to the elucidation and definition of fundamental concepts, which have resulted in text books on inorganic chemistry referring to "The Flood-Lux" concept of acid base reactions in oxide systems. In 1949 The Norwegian Institute of Silicate Chemistry was established through funds granted from The Royal Norwegian Council for Scientific and Industrial Research. In recognition of his achievements in this field of research, Flood was appointed the director of this institute in addition to continuing in his position in inorganic chemistry at The Technical University of Norway. At this time Professor Flood's research facilities were greatly improved and his inspiring leadership attracted a number of students and young scientists to work with him.

A major problem which engaged Flood's group in the following years was the thermodynamics of molten salt mixtures. Some of the early papers on activity-composition relations in molten salt mixtures by Flood and his co-workers are now considered classic contributions to the literature in this field, and a large number of later publications by Flood and his co-workers have served to test and further elucidate some of the theories formulated in the earlier papers.

Professor Flood has also maintained an interest in phase-transition reactions and in the formation of defects in solids. A considerable part of his research work in high temperature chemistry has also been directly related to industrial problems.

Professor Flood's success in creating an internationally-known Norwegian school of molten salt chemistry testifies to his rare combination of intellectual capacity with the inspiring personality which ignites in his students and associates the enthusiasm and scientific curiosity which are so typical of Flood. The stimulating atmosphere in Flood's institute in Trondheim not only has provided an excellent starting point for many young Norwegians who are now engaged in research and teaching in the field of high-temperature chemistry, but has also provided for foreign visitors the kind of surroundings in which they worked happily and productively and from which they emerged with renewed scientific enthusiasm.

TABLE OF CONTENTS

Max Bredig Award Acceptance Speech--Creating A Crystal Ball for Molten Salt Solutions M. Blander	1
A Thermodynamic Database for Multicomponent Molten Salt Solutions A. D. Pelton	12
Quasichemical Model for Silicate Melts A. E. Grau and S. N. Flengas	28
Thermodynamic Properties of the Molten PbO-PbCl ₂ Solutions A. Hacetoglu and S. N. Flengas	52
Condensed and Gaseous Products Chemistry in the Combustion and Gasification of High Sulfur Coal S. Sinha, K. Natesan and M. Blander	72
A Model and Data for Freezing Temperature Lowering of 4 to 7 Component Molten Salt Mixtures H. W. Prengle, Jr. and S. P. Shah	83
Thermodynamics of 1-Methyl-3-Ethylimidazolium Chloride--Aluminum Chloride Mixtures C.J. Dymek, Jr., C. L. Hussey, J. S. Wilkes and H. A. Øye	93
Vaporization of Water from Hydrous Melts and Concentrated Electrolyte Aqueous Solutions S. Deki, M. Fukui, A. Kajinami and Y. Kanaji	105

Thermodynamic Properties of Molten Magnesium Chloride Hydrates in Presence of Potassium Chloride H.-H. Emons, A. Dittrich and W. Voigt	111
Storing Energy at Ambient Temperatures: A Study of the Melting-Freezing Equilibria of $(\text{CaCl}_2, 6\text{H}_2\text{O}) - (\text{K}^+, \text{NH}_4^+)(\text{Cl}^-, \text{NO}_3^-)$ Mixtures J. Guion, A. Jaffrin, M. Laugt and M. Teisseire	130
Theoretical Determination of Exchange Integrals in Salts H. S. Darendelioglu	139
Application of a Modified Lindemann's Melting Formula to Isentropic and Isothermal Compressibilities of Molten Salts at Their Melting Points T. Iida, T. Mizobuchi and Z. Morita	146
Thermodynamic Prediction of Sulfide Capacities in $\text{Na}_2\text{O-SiO}_2$ Melts R. C. Reddy, M. Blander and B. Chen	156
X-Ray Structural Analysis of Molten KF-KX($\text{X}=\text{Cl}, \text{Br}, \text{and I}$) Systems Y. Okamoto, K. Igarashi and J. Mochinaga	165
X-Ray Diffraction Study of Molten $\text{CaCl}_2\text{-KCl}$ System K. Igarashi, Y. Okamoto and J. Mochinaga	...	175
Ab Initio Molecular Orbital Investigation of the Structure of Al_2F_7^- and Al_2Cl_7^- L. A. Curtiss	185

Liquid Dichlorides and Dichloride Monochloride Mixtures M. Rovere and M. P. Tosi 195
Small Angle X-Ray Scattering (SAXS) and PVTX-Behaviour of Fluid K_xKCl_{1-x} Solutions E. Pfeiffer, K. Garbade and W. Freyland 200
Structure and Thermodynamics of Metal-Salt Solutions: the Theoretical Viewpoint G. Chabrier 210
Theoretical Analysis of Collective Modes in Metal-Molten Salt Mixtures and Molten Salt Mixtures G. Chabrier 222
Electronic Conduction in Molten Sodium Chloride G. M. Haarberg, K. S. Osen, J. J. Egan 235
Addition of Molten Salt in Molten Metal. Structure and Dynamics J. F. Jal, C. Matthieu, J. Dupuy, P. Chieux and J.-B. Suck 244
Dynamic Conductivity of Molten $3 KNO_3 \cdot 2 Ca(NO_3)_2$ at Frequencies above 100 MHz K. Funke and J. Hermeling	... 256
Electrical Conductivity of Binary Melts Containing $NbCl_5$, $TaCl_5$ and $NaCl-KCl(1:1)$ N. Sato and M. Nanjo	.. 267
Enrichment of Li-6 by Countercurrent Enrichment of Molten $LiNO_3$ T. Haibara, O. Odawara, I. Okada, M. Nomura and M. Okamoto	... 275

The Chemla Effect in the Mobilities in the Molten ... Binary System NaOH-KOH C.-C. Yang, O. Odawara and I. Okada	285
Prediction of the Occurrence of the Anion Chemla Effect--Self Exchange Velocity in the Molten Binary System Li(Cl, Br) Studied by MD Simulation S. Baluja, A. Endoh and I. Okada	295
Structure Effects on Binary Organic Glass Forming Molten Salt Solution Transport Properties A. M. Elias and M. E. Elias	305
Viscosity Measurements: Molten Ternary Carbonate Eutectic T. Ejima, Y. Sato, T. Yamamura, K. Tamai, M. Hasebe, M. S. Bohn and G. J. Janz	317
Ultrasonic and Hypersonic Spectroscopy of Alkali Nitrate Single and Binary Melts T. Ejima, T. Yamamura and K. Zhu	324
Supercooling Phenomena in Electrolyte-Amide Binary ... Mixtures. Ultrasonic and Dielectric Study Showing the Presence of Polymeric Structures in Supercooled Mixtures: NaCNS, LiNO ₃ , KCNS/CH ₃ CONH ₂ G. Berchiesi, G. Vitali, G. G. Lobbia and R. Plowiec	333
Space Thermal Diffusion Experiment in a Molten AgI-KI Mixture J. Bert, D. Henry, H. Mellon and J. Dupuy	340
A New Infrared Detection System and its Data Processing for the Thermal Conductivity Measurements of Molten Salts H. Ohta and Y. Waseda	353

Generation of Cationic Species in Chloroaluminate	363
Melts: Strategies Based on Protonic Superacid Chemistry	
T. A. O'Donnell	
Influence of the Acido-Basicity and of the Cationic ..	373
Composition on the Chemical Properties in Molten Hydroxides	
P. Claes, G. Peeters and J. Glibert	
Optical Basicities in Some Oxide - Halide Systems ...	382
T. Nakamura, Y. Ueda and T. Yanagase	
Infrared Reflection Spectra of $AlCl_3-MCl_2$...	391
(M= Mg, Ca, Sr, Ba, Mn and Zn) and Oxochloroaluminate Melts	
M.-A. Einarsrud and E. Rytter	
The Chemistry of Water in Ambient-Temperature	406
Chloroaluminate Ionic Liquids: NMR Studies	
T. A. Zawodzinski, Jr. and R. A. Osteryoung	
Ionic Structure and Interactions in 1-Methyl-	414
3-Ethylimidazolium Chloride/ $AlCl_3$ Molten Salts	
K. M. Dieter, C. J. Dymek, Jr., N. E. Heimer, J. W. Rovang and J. S. Wilkes	
Nuclear Spin Relaxation of Cesium-133 in the	424
Molten Lithium Nitrate - Cesium Nitrate System	
Y. Nakamura, J. Funaki and S. Shimokawa	
Spectroscopical Study of Anodic Micro-Plasmas	428
Observed During Anode Effect in Molten LiCl-KCl Mixtures	
J.-P. Bardet, J.-C. Valognes and P. Mergault	

An Electrochemical Approach for the Determination ... of Oxide Impurities in Acidic Alkali Chloroaluminates J.-P. Schoebrechts, P. A. Flowers and G. Mamantov	437
Spectroelectrochemistry in Room Temperature Haloaluminate Ionic Liquids E. H. Ward, P. A. Barnard, I-W. Sun and C. L. Hussey	445
Spectrochemical and Electrochemical Properties of Some Lanthanides and Actinides in Room-Temperature Melt S. P. Sinha	458
Potentiometric Studies of Some Oxyanions in Molten ... Fluorides K. H. Stern	469
Redox Potential of Pb^{2+}/Pb^0 in Borate and Silicate .. Melts M. Shimizu, K. Kawamura and T. Yokokawa	485
An Investigation of the Dissolution of Neodymium in Molten Neodymium Trichloride Q. T. Lu, S. X. Li, R. L. Yu and S. G. Chen	491
The Activity of Lanthana in $NaF-AlF_3-Al_2O_3-La_2O_3$ Melts L. Xuliang and S. Shiyang	498
Electrochemical Studies on Disproportionation Reaction of Titanium and Titanium Ions in $KCl-NaCl$ Molten Salts T. Oki, M. Okido and C. Guang-sen	507

Pulse and A. C. Impedance Studies of the Electro- chemical Systems of Titanium in LiCl-KCl Eutectic Melt at 743 K D. M. Ferry, G. S. Picard and B. L. Tremillon	517
Carbon Anode Reaction and Intercalation Compounds ... in Fluoride Melt N. Watanabe and T. Nakajima	527
Electrochemical and Chemical Intercalation of Fluorine in Graphite in the KF ₂ HF Melt T. Nakajima, T. Ogawa and N. Watanabe	537
Study of CF _x Passivating Layers on Carbon Electrodes in Relation to Fluorine Production M. Chemla and D. Devilliers	546
Kinetic Study of O ²⁻ /1/2O ₂ Electrodes in Molten Salts H. Numata, K.-i. Asako, T. Kawasaki, A. Momma and S. Haruyama	557
Kinetic Study of Hydrogen Oxidation in Molten Alkali Carbonate I. Uchida, T. Nishina and M. Takahashi	571
Behaviour of HF/H ₂ Electrode in a Molten LiF-KF System K. Ema, Y. Ito, T. Takenaka and J. Oishi	581
Gallium Species Electrochemistry in Room Temperature Chloroaluminate Melts S. P. Wicelinski and R. J. Gale	591
On the Initiation of Anode Effect in Chloride Melts U. Erikson and Reidar Tunold	602

Concepts and Realities of Chemical and Electro-	613
Chemical Reactions in Molten Salts	
K. E. Johnson and F. W. Yerhoff	
Evaluation of LiCl-LiBr-KBr Electrolyte for Li-	621
Alloy/Metal Disulfide Cells	
T. D. Kaun	
Overcharge Protection in Li-Alloy/Metal Disulfide ...	631
Cells	
L. Redey	
Molten Salt Electrochemistry for High Temperature ...	637
Thermochemistry and Kinetics of the System Li-Fe-S	
A. Rabenau, B. Schoch and W. Weppner	
A Comparative Study of the Electrochemistry of the ...	647
LiAl Anode in Molten Salt and Organic Media	
Y. S. Fung	
A Novel Inorganic Low Melting Electrolyte for	657
Secondary Aluminum-Nickel Sulfide Batteries	
H. A. Hjuler, S. von Winbush, R. W. Berg	
and N. J. Bjerrum	
Performance of Na/Se(IV) Molten Chloroaluminate	669
Batteries	
Morio Matsunaga and K. Hosokawa	
On the Technological Status of Molten Carbonate	677
Fuel Cells	
N. Q. Minh	

Influence of the Acidity on the Unstableness and the Corrosiveness at High Temperature of Molten Nitrates and Nitrate-Nitrite Mixtures. A Demonstrative Example Showing the Interest of Controlling the Acidity in Molten Salts B. L. Tremillon	689
The Solubilities of Metal Oxides in Fused Na_2SO_4 Solutions Y. S. Zhang and R. A. Rapp	707
Corrosion of Hot-Pressed Silicon Nitride in Alkali Carbonate Melts K. Tajiri, T. Nishio, T. Asahina and M. Kosaka	717
Hot Corrosion of Heat-Resistant Alloys Induced by Molten Fluoride Mixtures M. Kawakami, M. Kawabe, M. Okuyama and K. Ito	723
A Design Principle of Bipolar Electrodes for Electrowinning Cell from Chloride Melts T. Ishikawa, S. Konda and T. Narita	734
A Study of the Electrocatalytic Activity of Doped Carbon Anodes in Cryolite-Alumina Melts L. Yexiang, X. Haiming and L. Longyu	744
Studies of the Anodic Process at SnO_2 -Based Electrodes in Aluminium Electrolysis L. Yexiang and X. Haiming	751
Electric Field is Calculated by Solving Laplace's Equation on a Cylindrical Graphite Anode in Molten NaF and Na_3AlF_6 C. Brunet and P. Mergault	753

The Influence of MgO on the Diffusion of Magnesium Ion in Magnesium Electrolysis Z. Yueqiang and L. Qingfu 758
Disproportionation Reaction in Molten Salts and and Their Application to Surface Coating Treatment T. Oki 765
Electrodeposition of Titanium from Chloride Melts W. Rolland, A. Sterten and J. Thonstad	775
The Synthesis of β -Vanadium Bronze and Vanadyl Phosphate by Molten Salt Electrolysis Y. Kaneko, H. Hashida and H. Kojima 786
Smooth Electrodeposits of Molybdenum from KF-B ₂ O ₃ -Li ₂ MoO ₄ Melt K. Koyama and Y. Hashimoto 795
Electrodeposition of Tungsten and Tungsten Carbide ... from Molten Halide H. Yabe, Y. Ito, K. Ema and J. Oishi	804
Electrodeposition of Tungsten from ZnBr ₂ -NaBr Melts H. Hayashi, N. Hayashi, K. Uno, Z. Takehara and A. Katagiri	814
Electrochemical Reaction of WO ₄ ²⁻ Ion in LiCl-KCl Eutectic Melt Y. Ito, T. Shimada, H. Yabe and J. Oishi	825
Preparation of Neodymium-Iron Master Alloys from Neodymium (III) Salts and Metallic Iron in Molten Chloride - Fluoride Mixtures F. M. Seon	835

Metallothermic Reduction of Nd_2O_3 with Ca in CaCl_2 -NaCl Melts R. A. Sharma and R. N. Seefurth 846
The Study on the Dissolving Loss of Rare Earth Metals in the RECl_3 -KCl- CaF_2 Melt X. Xiuzhi, W. Xujun and C. Yong 858
The Role of Oxide Solubility in the Electrochemical .. Extraction of Rare Earth Elements from Fused Fluorides A. Mitchell and B. Thomas	863
Applications of Molten Salts in Plutonium Processing .. D. F. Bowersox, D. C. Christensen and J. D. Williams	872
Status of Plutonium Purification by Bismuth Solvent .. Anode Electrorefining K. W. Fife, D. F. Bowersox, L. E. McCurry, P. C. Lopez and C. Brown	888
Compact Molten-Salt Fission Power Stations (FUJI- series) and their Developmental Program K. Furukawa, K. Minami, K. Mitachi and Y. Katoh	896
Impact-Fusion Molten-Salt Breeder (IFMSB) Using Shaped-Projectile and Axially Symmetric Mass Driver K. Ikuta and K. Furukawa	906
Submerged Arc Flux Welding with CaF_2 - CaO - SiO_2 Fluxes: Possible Electrochemical Effects on Weld Metal S. Shah, M. Blander and J. E. Indacochea	916

Electrochemical Reactions at the Electrode in Submerged Arc Welding J. H. Kim, R. H. Frost, D. L. Olson and M. Blander 928
A Method for Continuous Monosilane Generation Utilizing Molten Salt Electrolysis K. Seto, N. Dai, K. Kinoshita, N. Saotome, M. Itatsu, H. Suzuki and Y. Yatsurugi 939
Effect of Metal Complex Ion Added into a Molten NH_4F nHF on the Current Efficiency of NF_3 -Formation A. Tasaka, H. Kobayashi, M. Hori and H. Nakayama 949
A Review of the Chemical and Physical Properties of Molten Alkali Nitrate Salts and Their Effect on Materials Used for Solar Central Receivers R. W. Bradshaw and R. W. Carling 959
Molten Salt Chlorination of a Brazilian Titanium Ore .. R. L. Combes, A. J. A. Soirat, M. J. Paixao and J. M. Paixao	970
Catalysis and Reactivity of Electrophilic Reactions .. in Room Temperature Chloroaluminate Molten Salts J. A. Boon, S. W. Lander, Jr., J. A. Levisky, J. L. Pflug, L. M. Skrzynicki-Cooke and J. S. Wilkes	979
The Acylation of Coal and Model Coal Compounds in ... Room Temperature Molten Salts D. S. Newman, T. H. Kinstle and G. Thambo	991
Some Aromatic Reactions Using AlCl_3 -Rich Molten Salts . E. Ota	1002

Spectroscopic and Electrochemical Studies of Molten .. Salt Electrolysis of Aluminum and Magnesium S.-Y. Yoon and D. R. Sadoway	1011
Electrodeposition of Microcrystalline Chromium from Fused Salts T. Vargas, R. Varma and A. Brown	1018
Use of Impedance Measurements for Studying the Effect of Acidity on the Corrosion of Iron in the Molten Equimolar NaNO_3 - NaNO_2 -Mixture G. S. Picard, H. M. Lefebvre and B. L. Tremillon	1028
Author Index 1043	
Subject Index 1046	

MAX BREDIG AWARD ACCEPTANCE SPEECH

CREATING A CRYSTAL BALL FOR MOLTEN SALT SOLUTIONS

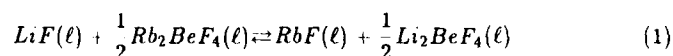
Milton Blander
Argonne National Laboratory
Chemical Technology Division
Materials Science and Technology Program
Argonne, Illinois 60439-4837

The two parts of the title, "Max Bredig Award" and "Molten Salt Chemistry," define the double honor I feel in accepting this award. First, I am honored because it bears the name of Max Bredig. He was a warm and gentle person who influenced me with his definitive scientific views, which emphasized accuracy of measurements as well as caution and precision in the description of results. When we were colleagues at the Oak Ridge National Laboratory (ORNL), about thirty years ago, he encouraged me to examine the concepts of complex ions in order to better define this loosely used term, which was too often a catchall to "explain" the unexplainable. Second, I am honored because the core of my scientific work has been molten salt chemistry and this award lends support to my choice of methods and views, which have proven to be productive and useful in technology.

Over the years, my work has focused on a number of different topics. It would not be possible to discuss them all. Instead, I would like to emphasize two general thoughts that I have often called upon to guide my thinking. The first is that molten salts are relatively simple as a solvent and should be relatively simple to model theoretically. I remember returning home from an interview for a position to do research on molten salts with the reactor group led by Warren Grimes at ORNL. On the flight, I asked myself why I had the feeling that molten salts are difficult, "gunky" materials to study when many of them can be represented by a simple collection of charged spheres. At that point, I decided to accept the position. The second thought, which is implied by the title of my talk, sounds obvious, but is one that is too little followed. It is, that concepts and theories developed to describe molten salts (or any other materials for that matter) should ultimately provide the means for making predictions far beyond the scope of the information used to deduce them. Too many "theories" in the early days of molten salt research could only describe past results, but not predict anything to come. A "crystal ball" was needed to predict future experiments and properties of technological materials. It is not only the complexity or beauty

of concepts and theories which makes them important, it is the ability to use them to make scientifically and technologically useful predictions a priori.

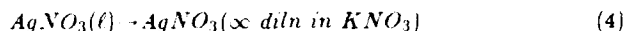
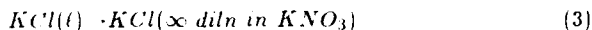
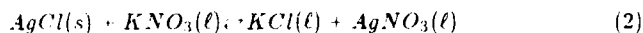
In my early work at ORNL I became intrigued by the properties of a particular class of ternary molten fluoride phase diagrams of interest for nuclear reactors. These contained two alkali fluorides mixed with ZrF_4 , BeF_2 , UF_4 or ThF_4 . Figure 1 exhibits the topology of one of these phase diagrams, that for the LiF - RbF - BeF_2 ¹ system. The liquidus isotherms (which are also isoactivity curves) for LiF are strongly bowed in a manner which clearly indicates strong positive deviations from ideal solution behavior, whereas the RbF liquidus indicates somewhat negative deviations from ideal solution behavior. Thus, in a single system, two different components exhibited opposite deviations from ideal behavior. This property was contrary to common beliefs of solution chemists. A cursory investigation uncovered many systems like this. The closeness of the properties of the LiF - BeF_2 system to those of silicates led to the realization that many important silicate and oxide systems, e.g., CaO - FeO - SiO_2 , behaved in a similar manner. In an extreme case, the positive deviations of FeO were so large in the CaO - FeO - P_2O_5 system that a miscibility gap was present. I was to return to silicates twenty-five years later. The magnitude of the effect seemed to be related to the differences in the stabilities of the compounds such as, Rb_2BeF_4 and Li_2BeF_4 . It became obvious that the controlling factor was the sign and magnitude of the free energy change of the corresponding metathetical reaction, ΔG_1°



which is positive and large. The dissolution of LiF in Rb_2BeF_4 can be defined in terms of reaction (1) and the standard free energies of solution of $RbF(\ell)$ (ΔG_F°) and $\frac{1}{2} Li_2BeF_4(\ell)$ (ΔG_{Li}°) in Rb_2BeF_4 . If ΔG_1° is positive and very large and the values of ΔG_F° and ΔG_{Li}° for the corresponding binary systems are relatively small (which is commonly true), then LiF will have large positive deviations from ideal behavior. Correspondingly, RbF would exhibit negative deviations from ideal behavior. This sort of analysis provided a rationalization of the odd behavior of these systems.

Another observation was that these systems resembled reciprocal systems, which have at least two cations and two anions. For example, we see in Figure 2 that some of the characteristics of the phase diagram for the Li^+ , K^+/F^- , Cl^- reciprocal system² parallel those of the lower portion of the LiF - RbF - BeF_2 system in Figure 1. In fact, the deviations from ideality are so large in the Ag^+ , K^+/NO_3^- , Cl^- reciprocal system that there is a low solubility of $AgCl$ in KNO_3 and a liquid-liquid ternary miscibility gap. For this latter type of system I deduced a simple method for calculating the enthalpy and standard free energy

of solution by consideration of three steps.^{3,4} For solid AgCl in KNO₃, these steps are



Thus, the free energy and enthalpy would be

$$\Delta G_2^\circ + \Delta G_3^\circ + \Delta G_4^\circ = \Delta G_{\text{soln}}^E - RT \ln K_{SP} \quad (5)$$

$$\Delta H_2^\circ + \Delta H_3^\circ + \Delta H_4^\circ = \Delta H_{\text{soln}} \quad (6)$$

where the asterisk (*) denotes a standard value. Equations (3), (4), and (5) provide an exact method for calculating the solubility product. In general, the largest contributions come from the metathetical reaction (Eq. (2)). Steps such as Eqs. (3) and (4) are generally relatively small for insoluble materials such as AgCl.

In 1956 I discovered a key paper by Flood, Førlund, and Grjotheim (FFG),⁵ who had used a simple cycle to deduce an important equation for reciprocal systems. For example, for the Li⁺, K⁺/F⁻, Cl⁻ system, the total excess free energy of mixing (ΔG_m^E) of the three components LiF, KF, and KCl is given by five terms

$$\begin{aligned} \Delta G_m^E = & X_{Li} X_{Cl} \Delta G^\circ + X_{Li} X_K X_F \lambda_F + X_{Li} X_K X_{Cl} \lambda_{Cl} \\ & + X_F X_{Cl} X_{Li} \lambda_{Li} + X_F X_{Cl} X_K \lambda_K \end{aligned} \quad (7)$$

where ΔG° is the standard free energy change for the metathetical reaction $\text{LiF} + \text{KCl} \rightleftharpoons \text{KF} + \text{LiCl}$, and λ_i is a "regular" solution interaction parameter for the binary system containing two salts with the common ion *i*. Equation (7), although inexact, contained within it all the concepts implicit in the exact Eqs. (5) and (6). More important, it showed promise for calculating thermodynamic properties at all concentrations. When calculating the ratios of activities of components, the authors were successful. However, Eq. (7) did not work for the calculation of absolute values of activities of components. They considered the use of quasichemical theory (QCT) to explain discrepancies between the phase diagram for the Li⁺, K⁺/F⁻, Cl⁻ system and that predicted by Eq. (7). For example, Eq. (7) leads to the prediction of a nonexistent miscibility gap and to higher liquidus temperatures than those measured. Flood *et al.* calculated the magnitude of the correction to the total excess free energy of mixing from the QCT and found it to be small. As a consequence, they did not explore the QCT further. After considerable study, we⁶ realized that the phase relations

considered are not controlled by the magnitude of the total excess free energy, but by the magnitude of the first derivatives related to the activity coefficients of a component and to the second derivatives which define an inflection in the free energy of mixing and miscibility gaps. A series expansion of the equations deduced from the QCT led to a term which can be added to Eq. (7) in an *ad hoc* manner

$$\Delta G^E = \Delta G^E \text{ (Eq. 7)} - X_{Li}X_KX_FX_{Cl} \frac{(\Delta G^E)^2}{2ZRT} \quad (8)$$

where Z is a nearest neighbor coordination number. From the empirical combination of the QCT theory and the four binary terms containing λ_i in Eq. (7), one can obtain a useful approximation² for the upper consolute temperature (the temperature below which one has a miscibility gap)

$$5.5T_C = \frac{\Delta G^E}{R} + \frac{\lambda_{A+} + \lambda_{B+} + \lambda_{C-} + \lambda_{D-}}{2R} \quad (9)$$

From Eq. (7), the coefficient of T_C would be 4.0, and the apparent value of T_C would be about 38% higher than that calculated from Eq. (9). Values of T_C calculated from Eq. (9) are consistent with a large number of measurements of miscibility gaps. Up to this point, the equations have been deduced in an *ad hoc* way by combining the QCT (which does not take coulomb interactions into account) with the four binary terms deduced by FFG. As will be discussed later, these results are a natural consequence of the conformal ionic solution theory, which was the first solution theory to specifically take coulomb interactions into account.

In effect, the term expressed in Eq. (8) is a first correction term for non-random mixing of the ions. In dilute solutions, it became obvious that the QCT would provide a means for defining and understanding the thermodynamic properties of one type of "complex ion." Because of the loose usage of this term, I generally referred to these as associated species. A generalization of the QCT⁷ led to expressions for the formation of associated species of A^+ and C^- ions in a solvent BD



where the A^+ and C^- ions on the left-hand side denote ions having only solvent ions as near neighbors. Formation constants for any value of n were deduced. For example, for n = 1 and 2, the formation constants K_{1n} , are

$$K_{11} = Z(\beta_{11} - 1) \quad (11)$$

$$K_{12} = \frac{Z(Z-1)}{2}(\beta_{11}\beta_{12} - 2\beta_{11} + 1) \quad (12)$$

In the above equations, β_{1n} is $\exp(-\Delta A_{1n}/RT)$, where ΔA_{1n} is a specific bond free energy for the n 'th C^- ion bonded to an A^+ ion. These association constants can be defined exactly by the limit of derivatives of activity coefficients at infinite dilution. For example, for a solution of the salts AD ($AgNO_3$) and BC (KCl) in the solvent BD (KNO_3)

$$\lim_{X_{A^+}, X_{C^-} \rightarrow 0} \left(\frac{\partial \ln \gamma_{AD}}{\partial X_{C^-}} \right) = -K_{11} \quad (13)$$

where X_{A^+} is the cation fraction of A^+ and X_{C^-} is the anion fraction of C^- . Equation (13) and analogous equations for other species involving higher derivatives serve to define association or "complexing" constants and provided insights into the meaning of this class of "complex ions." For example, the -1 in parentheses in Eq. (11) leads to unusual properties for K_{11} when β_{11} is not much larger than unity. In addition, when ΔA_{11} is positive (denoting repulsion between A^+ and C^-) and β_{11} is less than unity, one obtains a negative value of K_{11} . This leads to problems in defining the standard free energy of association. These peculiarities are due to the fact that, in an ideal solution, K_{11} is zero even though AC species are formed by random encounters of A^+ and C^- ions and that fewer than this number of AC pairs are formed when ΔA_{11} is positive. An analogous peculiarity is present for virial coefficients of gases (which can be defined as the negative of an association constant) and, indeed, there is a positive second virial coefficient for helium because of the predominance of repulsive forces.

At about the same time, an important experimental technique used to study solubility products of silver halides was reported by Flengas and Rideal.⁸ An adaptation of their technique proved to be ideal for the study of associated species in nitrate melts.⁹ Studies of a large number of melts indicated that the specific bond free energies, ΔA_{1n} , were independent of temperature when the associating ions were spherical. As a consequence, these formation constants at all temperatures can be predicted from measurements at a single temperature. This was true not only in molten salts, but also in metallurgical systems. An extension of the generalized QCT⁷ led to the coordination cluster theory (CCT),¹⁰ which applies to dilute solutions of a solute in ionic or metallic solvents. With the CCT, it was demonstrated that one can use thermodynamic measurements for solutions of oxygen and sulfur in alloys at one temperature to predict them at all other temperatures.

Perhaps the most important development in molten salt solution chemistry was the conformal ionic solution (CIS) theory¹¹ by Reiss and coworkers. This statistical-mechanical perturbation theory uses the most fundamental property of a simple salt; that is, that it is composed of spherical ions which interact

with a spherically symmetric pair potential. In the original paper, only hard sphere ions in a binary salt were considered in deducing an equation for the first polynomial term for excess free energies of mixing of two salts AX and BX

$$\Delta G_m^E = \Gamma(T,V) X_{AX} X_{BX} \left(\frac{d_o}{d_{AX}} - \frac{d_o}{d_{BX}} \right)^2 + \dots \quad (14)$$

where $\Gamma(T,V)$ and d_o are constants and d_i is an interionic distance. It was later shown that the theory was valid for a much more general potential^{12,13} and that the next two higher order terms were proportional to a function of interionic distances. The importance of the CIS theory stems from the fact that it demonstrated that one could represent the excess solution properties of ionic systems by a polynomial similar to that used for nonionic mixtures. The theory provided fundamental support for many of the intuitive ideas which had been developed for molten salt chemistry without specifically including the charge-charge interactions between ions.

Despite its importance, the CIS theory for binary systems could never lead to predictions *a priori* because no ionic pair potential is accurate enough to reliably evaluate the coefficient $\Gamma(T,V)$. This failing concerned me for about a year before I realized that a way around this problem for multicomponent systems is to express the thermodynamic properties of such solutions in term of the properties of the lower order systems without identifying the pair potential. In collaboration with S. J. Yosim, this was done for ternary reciprocal systems,¹³ and it was shown that (for example, in the Li^+ , K^+ , F^- , Cl^- system) the CIS theory led to all the terms in Eq. (7) as well as to a term proportional to $X_{Li} X_K X_F X_{Cl} (\Delta G^E)^2$ similar to that in Eq. (8). The proportionality constant is related to a large number of complex integrals, which have not yet been evaluated. However, because of its similarity to the term deduced from the QCT, we felt it safe to approximate this constant by the same proportionality constant as that in Eq. (8). The equation was used to calculate the phase diagram of the Li^+ , K^+ , F^- , Cl^- system (Figure 3),² which reproduces the features and complex topology of the measurements surprisingly well (Figure 2).

Little was done on this subject until my collaboration with M.-L. Saboungi starting in 1971, which led to some of the most important papers on molten salts in which I have been involved. Our work, which created a major part of the "crystal ball," was concerned with testing and generalizing the CIS theory for various applications and for making predictions *a priori*. The use of the CIS theory for reciprocal systems led to excellent correspondence with measured phase diagrams for simple systems,^{14,15} and empirical extensions of the theory were used to calculate phase diagrams for the more complex charge asymmetric

systems.¹⁶ Of course, in addition to phase diagrams, the theory provides a prediction of all the chemical properties of all the solution components. We also extended the CIS theory for additive ternary systems (A^+ , B^+ , C^+/X^-)¹⁷ to obtain the equation

$$\Delta G_m^E = \sum_{i,j} \sum a_{ij} X_i X_j + \sum_{i \neq j} \sum b_{ij} X_i^2 X_j + \sum_{i < j} \sum c_{ij} X_i^2 X_j^2 + A X_A X_B X_C + \sum_{i \neq j < k} B_i X_i^2 X_j X_k \quad (15)$$

where it was shown that the ternary interaction terms are related to the terms a_{ij} , b_{ij} , c_{ij} by the expressions

$$A = (b_{AB}^{1/3} + b_{AC}^{1/3}) (b_{BA}^{1/3} + b_{BC}^{1/3}) (b_{AC}^{1/3} + b_{BC}^{1/3}) \quad (16)$$

$$B_i = (c_{ij} c_{ik})^{1/2} \quad (17)$$

Thus the properties of the ternary system could be predicted solely from data on the subsidiary binaries. Equation (15) has been empirically extended and used for asymmetrically charged multicomponent systems. Equations (15), (7), and (8) and their empirical extensions have proven to be useful in a number of technologies for making predictions of phase diagrams and of chemical equilibria in molten salts. In addition, even when enough accurate information is not available for prediction, such equations, because of their thermodynamic self-consistency, can aid experimentalists by greatly minimizing the number of measurements necessary to characterize the chemistry and phase relations of any given system. An extension of the equations for ternary reciprocal systems to higher order systems by Saboungi¹⁸ has proven to be important for predictions in complex multicomponent systems.

One class of systems which has proven to be difficult to characterize are the ordered solutions. Examples of such systems are the chloroaluminates, silicates, and fluoroberyllates (e.g., NaCl-AlCl_3 , CaO-SiO_2 , and NaF-BeF_2). These have often been characterized by the formation of complex ions (e.g., AlCl_4^- , SiO_4^{4-} , and BeF_4^{2-}) in basic melts and clusters and chains in acid melts. Our molecular dynamics calculations have been used to characterize some of the structural properties of these ordered or complex ion forming melts.^{19,20} However, theories for such solutions are inadequate for characterizing their thermodynamic properties, which cannot be represented at all by the use of polynomials for the excess free energies. This difficulty arises from the tendency to have "V" shaped enthalpies of mixing and "m" shaped entropies of mixing. In collaboration with Pelton,^{21,22} an empirical extension of quasichemical theory has led to a unique,

but preliminary, method for accurately describing the thermodynamic properties of a number of binary silicates as a function of concentration and temperature using only a small number (3-7) of parameters. More important, we have developed an empirical combining rule that leads to predictions of the solution properties of multicomponent systems from the subsidiary binaries. This rule is (1) consistent with the predictions of the CIS theory in basic solutions and (2) consistent with all available data. Thus, we have developed a method for predicting the properties of such multicomponent solutions *a priori* from data on lower order systems. Much more work on ordered solutions is needed to reduce the empiricism.

In conclusion, because of time and space limitations, I have glossed over many details and ignored work which I feel is important. In particular, I have not discussed my own applications of some of these concepts to submerged arc flux welding²³ and pyrometallurgical chemistry.²⁴ These concepts have also been helpful in understanding the high temperature condensation processes in coal combustion,²⁵ as well as in the formation of meteorites and all other condensed matter in our solar system²⁶. These applications underscore my belief that more "crystal balls" are needed to permit us to predict the properties of scientifically and technologically important materials. The urge for precision and care which Max Bredig displayed is a precursor to creating such "crystal balls."

ACKNOWLEDGMENTS

This work was supported by the U.S. Department of Energy, Division of Materials Sciences, Office of Basic Energy Sciences, under Contract W-31-109-ENG-38. The work described herein has also been supported in the past by the U.S. Atomic Energy Commission (at ORNL) and by the Rockwell International Science Center in Thousand Oaks, California.

REFERENCES

1. R. E. Thoma, Phase Diagrams of Nuclear Reactor Materials, ORNL-2548, Oak Ridge National Laboratory, Oak Ridge, TN (1959).
2. M. Blander and L. E. Topol, *Inorg. Chem.* **8**, 1641 (1966).
3. M. Blander, J. Braunstein, and M. D. Silverman, *J. Am. Chem. Soc.* **85**, 895 (1963).
4. M. Blander and E. B. Luchsinger, *J. Am. Chem. Soc.* **86**, 319 (1964).
5. H. Flood, T. Førland, and K. Grjotheim, *Z. Anorg. Allgem. Chem.* **276**, 189 (1954).
6. M. Blander and J. Braunstein, *Ann. New York Acad. of Sciences* **79**, 838-852 (1960).
7. M. Blander, *J. Chem. Phys.* **34**, 432 (1961).

8. S. N. Flengas and E. K. Rideal, *Proc. Roy. Soc. (London)* **233A**, 443 (1956).
9. M. Blander, "Thermodynamic Properties of Molten Salt Solutions" in *Molten Salt Chemistry*, ed. M. Blander, Interscience, New York pp. 127-237 (1964).
10. M. Blander, M.-L. Saboungi, and P. Cerisier, *Metall. Trans. B* **10B**, 613 (1979); M. Blander and M.-L. Saboungi in *Chemical Metallurgy, a Tribute to Carl Wagner*, ed. N. A. Gokcen, TMS-AIME, Warrendale, PA pp. 223-31 (1981).
11. H. Reiss, J. L. Katz, and O. J. Kleppa, *J. Chem. Phys.* **36**, 144 (1962).
12. M. Blander, *J. Chem. Phys.* **37**, 172-173 (1962).
13. M. Blander and S. J. Yosim, *J. Chem. Phys.* **39** 2610-1616 (1963).
14. M.-L. Saboungi and M. Blander, *High Temp. Sci* **6**, 37-51 (1974).
15. M.-L. Saboungi, H. Schnyders, M. S. Foster, and M. Blander, *J. Phys. Chem.* **78**, 1091-1096 (1974).
16. M.-L. Saboungi and M. Blander, *J. Amer. Ceram. Soc.* **58**, 1-7 (1975).
17. M.-L. Saboungi and M. Blander, *J. Chem. Phys.* **63**, 121-220 (1975).
18. M.-L. Saboungi, *J. Chem. Phys* **73**, 5800-5806 (1980).
19. M.-L. Saboungi, A. Rahman, and M. Blander, *J. Chem. Phys.* **80**, 2141-2150 (1984).
20. M. Blander, M.-L. Saboungi, and A. Rahman, *J. Chem. Phys.* **85**, 3995-4004 (1986).
21. A. D. Pelton and M. Blander, *Metall. Trans. B*, **17B**, 805-815 (1986).
22. M. Blander and A. D. Pelton, *Geochim. et Cosmochim. Acta* **51**, 85-95 (1987).
23. J. E. Indacochea, M. Blander, N. Christensen, and D. L. Olson, *Metall. Trans. B*, **16B**, 237-245 (1985).
24. R. Reddy and M. Blander, *Metall. Trans.*, in press; this volume.
25. S. Sinha, K. Natesan, and M. Blander, this volume.
26. M. Blander, "Non-Equilibrium Effects on the Chemistry of Nebular Condensates: Implications for the Planets and Asteroids" in *Asteroids*, ed. T. Gehrels, University of Arizona Press, Tucson, AZ, pp. 809-821 (1979).

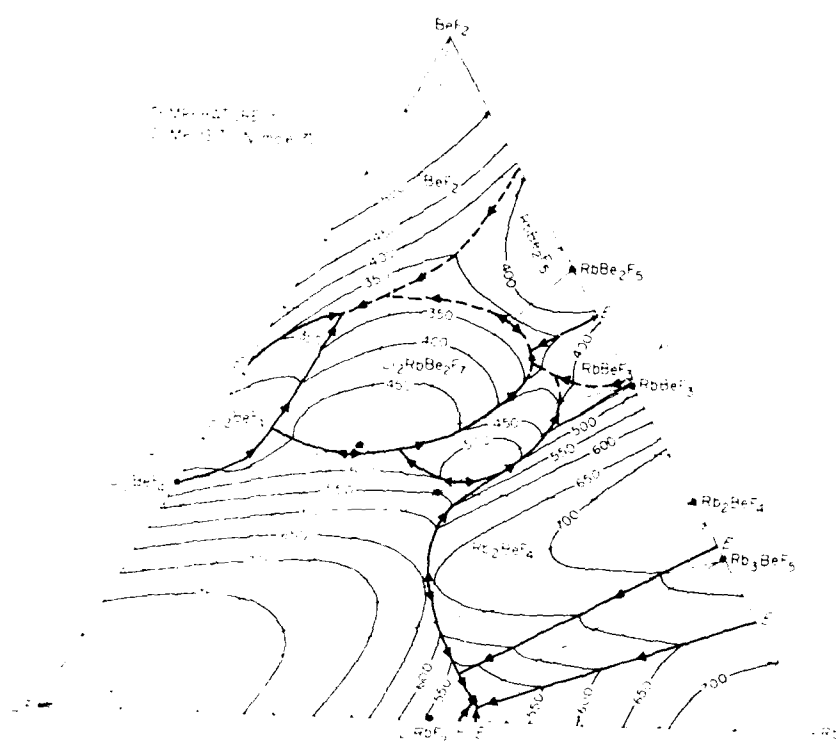


Fig. 1. Measured Phase Diagram of the LiF-RbF-BeF₂ Ternary System.¹

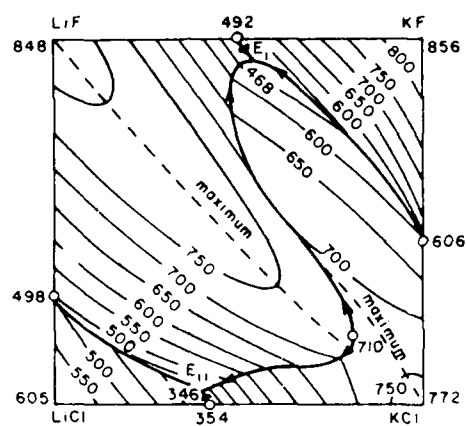


Fig. 2. Measured Phase Diagram of the $\text{Li}^+ \text{K}^+ / \text{F}^- \text{Cl}^-$ Ternary Reciprocal System.²

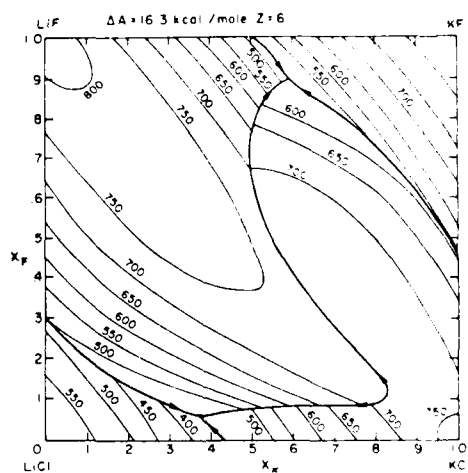


Fig. 3. Phase Diagram of the $\text{Li}^+ \text{K}^+ / \text{F}^- \text{Cl}^-$ Ternary Reciprocal System Calculated from the Conformal Ionic Solution Theory.²

A THERMODYNAMIC DATABASE FOR MULTICOMPONENT MOLTEN SALT SOLUTIONS

Arthur D. PELTON
Centre de Recherche en Calcul Thermochimique
Ecole Polytechnique de Montréal
P.O. Box 6079, Station A, Montreal, Quebec, Canada, H3C 3A7

ABSTRACT

Thermodynamic properties and phase diagrams of over 200 binary and ternary molten salt systems have been critically and systematically evaluated to obtain binary and ternary coefficients of polynomial expansions for the excess thermodynamic properties. An equation is presented which permits the thermodynamic properties of multicomponent molten salt solutions to be calculated from these binary and ternary coefficients which are stored in a computer database. An interactive free-energy minimization program, which permits automatic access to these data as well as to extensive stored data on other compounds and solutions, allows the calculation of complex multiphase equilibria involving multicomponent molten salt solutions. The data base is publicly accessible through the F*A*C*T computer system.

INTRODUCTION

For a great many binary molten salt solutions, simple polynomial expansions in the ionic fractions provide a good representation of the excess Gibbs energy. Least-squares techniques have been developed (1) which permit coefficients of such empirical expansions to be determined by a simultaneous optimization of all available thermodynamic and phase diagram data.

Models have been developed to permit the properties of ternary common-ion (2-4) and reciprocal (5, 6) molten salt solutions to be calculated from the binary coefficients. Empirical ternary coefficients may also be included in these equations.

Saboungi (7) has extended the Conformal Ionic Solution (CIS) Theory to multicomponent molten salt solutions.

In the present article we give a general equation for calculating the Gibbs energy of a multicomponent molten salt solution from binary and ternary coefficients. This equation essentially reduces to that of Saboungi (7) for

reciprocal ternary sub-systems, whereas for common-ion sub-systems it reduces to one of two "geometrical models" (2, 3) commonly used to represent multicomponent Gibbs energies. With this method of calculation, any number of empirical binary or ternary terms can be used in the expansions. The equation is well-suited to use with computer databases. The calculation method has proven to be very successful for a wide variety of simple molten salt solutions.

Many binary and ternary molten salt systems are being systematically evaluated in order to build up a database of binary and ternary coefficients. The data are accessible to users of the F*A*C*T (Facility for the Analysis of Chemical Thermodynamics) computer system (8) along with an extensive database of thermodynamic properties of other compounds and solutions. An interactive free-energy minimization program with automatic data access permits the calculation of complex multiphase equilibria involving multicomponent molten salt solutions.

CALCULATION METHOD

A notation similar, but not identical, to that of Saboungi (7) will be used.

Cations are denoted by A, B, C, ... (or alternatively c, c', c'') and anions by X, Y, Z, ... (or alternatively a, a', a''). Ionic charges are denoted by q_A , q_B , q_X , q_Y , ...

Cationic and anionic site fractions are denoted by X_C and X_A . For example:

$$X_A = n_A / (n_A + n_B + n_C + \dots) \quad [1]$$

$$X_X = n_X / (n_X + n_Y + n_Z + \dots) \quad [2]$$

where n_i is the number of moles of ion i in solution.

Equivalent cationic and anionic fractions are denoted by Y_C and Y_A . For example:

$$Y_A = q_A n_A / (q_A n_A + q_B n_B + \dots) \quad [3]$$

$$Y_X = q_X n_X / (q_X n_X + q_Y n_Y + \dots) \quad [4]$$

All thermodynamic properties in this article are expressed per equivalent of solution. One equivalent of solution contains

$$(\sum_c q_c X_c)^{-1} \text{ moles of cations and } (\sum_a q_a X_a)^{-1} \text{ moles of anions}$$

The Gibbs energy per equivalent of solution may be written as:

$$g = \sum_c \sum_a Y_c Y_a g_{c/a} + \Delta g(\text{ideal}) + g^E \quad [5]$$

where the summation is over all cation-anion pairs and $g_{c/a}$ represents the standard Gibbs energy per equivalent of the neutral salt consisting of cations, c , and anions, a . $\Delta g(\text{ideal})$ is the ideal mixing term, and g^E is the excess Gibbs energy.

Ideal mixing term

The expression for the ideal Gibbs energy of mixing is obtained from the Temkin model. The number of cation and anion sites are always equal to the numbers of cations and anions. All cations and anions mix randomly on their respective sites regardless of their charges. This gives, for the ideal Gibbs energy of mixing per equivalent:

$$\Delta g(\text{ideal})/RT = (\sum_c q_c X_c)^{-1} (\sum_c X_c \ln X_c) + (\sum_a q_a X_a)^{-1} (\sum_a X_a \ln X_a) \quad [6]$$

Binary common-ion systems

In a binary common-anion system A,B/X containing one anion and two cations, the excess Gibbs energy per equivalent is expressed as a polynomial in the equivalent cationic fractions:

$$g^E = \sum_{i=1} \sum_{j=1} \phi_{AB/X}^{ij} Y_A^i Y_B^j \quad [7]$$

where the $\phi_{AB/X}^{ij}$ are constant binary coefficients obtained by fitting experimental data. The corresponding expression for a common-cation binary system A/X,Y is:

$$g^E = \sum_{i=1} \sum_{j=1} \phi_{A/XY}^{ij} Y_X^i Y_Y^j \quad [8]$$

For example, in the system K,Li/CO₃ a least-squares optimization of available phase diagram and thermodynamic data (9) gives, for the liquid solution:

$$g^E = Y_K Y_{Li} [(-13780 + 8.197T) + (-5500 - 2.329T) Y_{Li}] \text{ J/equiv.} \quad [9]$$

That is:

$$\phi_{11}^{KLi/CO_3} = (-13780 + 8.197T) \text{ and } \phi_{12}^{KLi/CO_3} = (-5500 - 2.329T)$$

In this example, the data considered by the least-squares optimization program were calorimetric data for liquid-liquid mixing (10), and the measured phase diagram (11, 12). Gibbs energies of fusion of the components were taken from (13). The resultant optimized equation [9] reproduces the measured phase diagram very well as can be seen in the computer-generated diagram in Fig. 1. The measured enthalpy of mixing (10) is also reproduced very closely by eq [9].

The least-squares optimization technique also gives properties of solid compounds and solutions in the system. In the present example, the Gibbs energy of formation of the compound $KLiCO_3$ from the pure liquid carbonates was given as:

$$\Delta G_{\text{form}} = -89654 + 78.136 T \text{ J/mol} \quad [10]$$

Ternary common-ion systems

For a large number of ternary common-ion molten salt systems, we have had much success in expressing the excess Gibbs energy per equivalent by the following expression first proposed by Kohler (2). For a common-cation system A/X,Y,Z:

$$g^E = (Y_X + Y_Y)^2 g_{A/XY}^E + (Y_Y + Y_Z)^2 g_{A/YZ}^E + (Y_X + Y_Z)^2 g_{A/XZ}^E \quad [11]$$

where g^E is the excess Gibbs energy in the ternary solution at point p in Fig. 2a, and $g_{A/XY}^E$, $g_{A/YZ}^E$ and $g_{A/XZ}^E$ are the excess Gibbs energies in the three binary systems at points z, x and y. The factors $(Y_A + Y_{A'})^2$ in eq [10] are obtained from regular solution theory. Eq [10] is exact if the solution is strictly regular.

If the binary excess Gibbs energies are expressed as polynomials as in eqs [7, 8] then eq. [11] can be written as follows. In eq [12] "ternary terms" have also been added.

$$g^E = \sum_{a>a'} \left[\sum_{i>1} \sum_{j>1} \frac{\phi_{ij}^{A/aa'}}{i!j!} (Y_a + Y_{a'})^2 (Y_a / (Y_a + Y_{a'}))^i (Y_{a'} / (Y_a + Y_{a'}))^j \right] \\ + \sum_{i>1} \sum_{j>1} \sum_{k>1} \frac{\phi_{ijk}^{A/XYZ}}{i!j!k!} Y_X^i Y_Y^j Y_Z^k \quad [12]$$

The $\phi_{A/XYZ}$ are ternary coefficients obtained by fitting experimental ternary data. All the ternary terms become zero in the binary sub-systems. An expression for g^E of a common-anion system A,B,C/X can be written similarly.

As an example, the computer-generated liquidus surface of the K/F,Br,I system is shown in Fig. 3. Binary terms were first obtained by least-squares optimization of all available binary thermodynamic and phase diagram data (14). Application (15) of eq [12] with no ternary terms then gave a calculated ternary liquidus surface which agreed everywhere within 10 with the reported (16) liquidus. This is approximately equal to the experimental error limits. The calculated minimum in the univariant line was 536 C. In order to make this minimum coincident with the measured minimum at 529 C, a small ternary term

$$\phi_{111}^{K/FBrI} Y_F Y_{Br} Y_I = - 6500 Y_F Y_{Br} Y_I \text{ J/equiv.}$$

was included.

In addition to the Kohler equation, a number of other equations may be used for ternary common-ion salt solutions. In the equation proposed by Toop (3), g^E at point p in Fig. 2b is related to the values of g^E in the three binary systems at the points z, y and x by the equation:

$$g^E = (Y_Y / (Y_Y + Y_Z)) g_{A/Y}^E + (Y_Z / (Y_Y + Y_Z)) g_{A/Z}^E + (Y_Y + Y_Z)^2 g_{A/YZ}^E \quad [13]$$

As in the case of the Kohler equation, eq [13] is exact if the solution is strictly regular. If the binary excess Gibbs energies are expressed as polynomials, then eq [13] can be expanded in terms of the binary coefficients and ternary terms can be added as was done in eq [12] for the Kohler equation.

The asymmetric Toop equation (Fig. 2b) is generally more appropriate than the symmetric Kohler equation (Fig. 2a) when one of the three components is chemically different from the other two. For example, in the K/SO₄, F, Cl system one might choose the divalent sulphate as the "asymmetric component" $A_1/q_A X_1/q_X$ in Fig. 2b. However, because eqs [11]

and [13] become identical when the solutions are regular, for a large number of molten salt systems in which the binary g^E functions are well represented by 2- or 3-term polynomials the use of either eq [11] or [13] will give very similar results for the ternary system.

Other "geometric equations", such as the "Muggianu equation" in which g^E in the ternary solution is related to values of g^E in the three binaries at the ends of perpendiculars dropped from the ternary composition point, are discussed by (17).

The CIS Theory (4) also provides a similar equation for calculating g^E in a ternary system from binary parameters. This theory has the advantage over the above-mentioned "geometric equations" of having a sounder theoretical basis.

Again, for most simple molten salt solutions which do not require more than 3 parameters in the binary g^E expansions, all these ternary equations yield very similar and equally good results.

Multicomponent common-cation systems

For a multicomponent common-cation system, $A/X, Y, Z, W, \dots$, the Kohler equation [12] may be extended:

$$g^E = \sum_{a>a'} \left[\sum_i \sum_j \phi_{ij}^{A/aa'} (Y_a + Y_{a'})^2 (Y_a / (Y_a + Y_{a'}))^i (Y_{a'} / (Y_a + Y_{a'}))^j \right] \\ + \sum_{a>a'>a''} \left[\sum_{i>1} \sum_{j>1} \sum_{k>1} \phi_{ijk}^{A/aa'a''} (Y_a + Y_{a'} + Y_{a''})^3 (Y_a / (Y_a + Y_{a'} + Y_{a''}))^i \right. \\ \left. (Y_{a'} / (Y_a + Y_{a'} + Y_{a''}))^j (Y_{a''} / (Y_a + Y_{a'} + Y_{a''}))^k \right] \quad [14]$$

where the first summation is over all binary sub-systems and the second summation is over all ternary sub-systems. Eq [14] permits multicomponent thermodynamic properties to be calculated from binary (and if available, ternary) coefficients. An analogous expression can be written for common-cation systems.

Similar multicomponent versions of the Toop and other ternary equations can also be derived. In particular, we have devised a consistent "multicomponent Kohler/Toop" equation for the case in which some of the ternary sub-systems have been expressed by means of the Kohler

equation while others have been expressed via the Toop equation. Essentially, the method consists in dividing all components into two groups (for example, all divalent salts in one group and all monovalent salts in the other). A ternary sub-system in which all three components are members of the same group is treated by means of the Kohler equation, while a ternary sub-system with two components from one group and one from the other is expressed via the Toop equation. For the sake of brevity, the general expression will not be reproduced here.

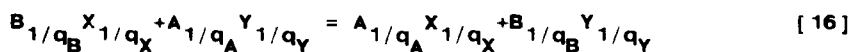
Reciprocal ternary systems A,B/X,Y

For common-ion systems, the terms containing $g_{c/a}$ in eq [5] have no influence upon the activities of the salts in the solution. This is no longer true in the case of a reciprocal ternary system which is defined as one containing two cations and two anions.

Writing eq [5] for the system A,B/X,Y, substituting eq [6] for $\Delta g(\text{ideal})$, and differentiating to obtain the activity of the salt $B_{1/q} Y_{1/q}$ yields:

$$RT \ln a_{B_{1/q} Y_{1/q}} = -Y_A Y_X (g_{B/Y}^0 + g_{A/X}^0 - g_{A/Y}^0 - g_{B/X}^0) + (RT/q_A) \ln X_B \\ + (RT/q_Y) \ln X_Y + g_{B_{1/q} Y_{1/q}}^E \quad [15]$$

The term in parentheses in eq [15] is the Gibbs energy change Δg^{EX} , for the "exchange reaction":



If $\Delta g^{EX} < 0$, then $A_{1/q_A} X_{1/q_X}$ and $B_{1/q_B} Y_{1/q_Y}$ are called the

"stable pair". From eq [15] it is seen that in this case there will be a positive contribution to $RT \ln a_{B_{1/q_B} Y_{1/q_Y}}$

which varies directly with Δg^{EX} . Hence, for the two salts forming the stable pair, positive deviations will be observed. Similarly, for the other two salts which form the unstable pair, negative deviations will be observed. These deviations are generally larger than the deviations resulting from the g^E term.

The composition of a reciprocal ternary system is most conveniently represented on a square as in Fig. 4. The excess Gibbs energy per equivalent may be written by summing the excess Gibbs energies of the four binaries, each weighted by the appropriate ionic fraction, and including reciprocal ternary terms:

$$\begin{aligned}
g^E = & Y_X \sum_{i=1} \sum_{j=1} \phi_{AB/X}^{AB/X} Y_A^i Y_B^j + Y_Y \sum_{i=1} \sum_{j=1} \phi_{AB/Y}^{AB/Y} Y_A^i Y_B^j \\
& + Y_A \sum_{i=1} \sum_{j=1} \phi_{A/XY}^{A/XY} Y_X^i Y_Y^j + Y_B \sum_{i=1} \sum_{j=1} \phi_{B/XY}^{B/XY} Y_X^i Y_Y^j \\
& + \sum_{i=1} \sum_{j=1} \sum_{k=1} \sum_{l=1} \phi_{AB/XY}^{AB/XY} Y_A^i Y_B^j Y_X^k Y_Y^l \quad [17]
\end{aligned}$$

The CIS theory (5, 6) predicts this expression for g^E with one reciprocal ternary term $\phi_{AB/XY}^{AB/XY}$ which is usually denoted by Λ . Since the formation of a reciprocal ternary solution involves changes in the number of cation-anion pairs, whereas the formation of a common-ion ternary solution involves only changes in the number of second-nearest-neighbor cation-cation or anion-anion pairs, it is expected that non-random mixing effects will be greater in the former, and consequently the importance of ternary terms will be greater. The first term in a Taylor expansion of an expression resulting from simple quasichemical theory (18) gives the following approximate expression for Λ resulting from non-random effects:

$$\Lambda \approx -(\Delta g^{EX})^2 / 2ZRT \quad [18]$$

where Z is a coordination number.

If no experimental reciprocal ternary data are available, then Λ can be approximated by eq [18]. If data are available, then Λ and other reciprocal ternary terms if warranted, can be considered as adjustable parameters.

As an example, the computer-generated liquidus surface for the Na,K/F,Cl system is compared with the reported phase diagram (19) in Fig. 4. Binary terms were first obtained by least-squares optimization of binary data. Δg^{EX} was obtained from tabulations (13) of data for the pure salts, and Λ was estimated from eq [18]. Agreement between the calculated and reported diagrams is good. Positive deviations along the "stable diagonal" between the stable pair, NaF and KCl, are clearly seen in Fig. 4, while negative deviations for NaCl and KF are also evident. Calculated reciprocal ternary phase diagrams are very sensitive to the value of Δg^{EX} .

In general, we have found that good calculations of reciprocal ternary phase diagrams can be obtained as long as Δg^{EX} is not too large. As Δg^{EX} becomes larger, the tendency to non-randomness becomes greater, and a simple $\Delta g(\text{ideal})$ term with a polynomial correction term no longer provides a sufficient description. We are currently working on a model involving a more complete application of the quasichemical theory to reciprocal salt solutions. As a rule of thumb, we have found that if Δg^{EX} is so large that a miscibility gap appears along the stable diagonal, then the simple model can no longer be expected to provide a quantitatively correct description.

General multicomponent system

We can now combine the above equations into one general equation for the Gibbs energy per equivalent of a multicomponent molten salt solution involving binary terms as well as common-ion and reciprocal ternary terms:

$$\begin{aligned}
 g = & \sum_c \sum_a Y_c Y_a g_{c/a} + RT \left[\left(\sum_c X_c \right)^{-1} \left(\sum_c X_c \ln X_c \right) + \left(\sum_a X_a \right)^{-1} \left(\sum_a X_a \ln X_a \right) \right] \\
 & + \sum_a Y_a \left[\sum_{c>c'} \left(\sum_{i=1} \sum_{j=1} \phi_{ij}^{cc'/a} Y_c Y_{c'} (Y_c + Y_{c'})^{2-i-j} \right) \right. \\
 & \left. + \sum_{i=1} \sum_{j=1} \sum_{k=1} \phi_{ijk}^{cc'c''/a} Y_c Y_{c'} Y_{c''} (Y_c + Y_{c'} + Y_{c''})^{3-i-j-k} \right] \\
 & + \sum_c Y_c \left[\sum_{a>a'} \left(\sum_{i=1} \sum_{j=1} \phi_{ij}^{c/aa'} Y_a Y_{a'} (Y_a + Y_{a'})^{2-i-j} \right) \right. \\
 & \left. + \sum_{i=1} \sum_{j=1} \sum_{k=1} \phi_{ijk}^{c/aa'a''} Y_a Y_{a'} Y_{a''} (Y_a + Y_{a'} + Y_{a''})^{3-i-j-k} \right] \\
 & + \sum_{c>c'} \sum_{a>a'} \left(\sum_{i=1} \sum_{j=1} \sum_{k=1} \sum_{l=1} \phi_{ijkl}^{cc'/aa'} Y_c Y_{c'} Y_a Y_{a'} \right) \quad [19]
 \end{aligned}$$

Eq [19] incorporates the Kohler equation [14] for the multicomponent common-ion systems. The more general expression incorporating the Kohler/Toop formalism mentioned above is actually used in our database but, for the sake of brevity, will not be reproduced here.

Expressions for the partial Gibbs energies of all neutral salts have been derived from eq [19]. Again, because of space restrictions, these will not be reproduced here but will be reported elsewhere.

DATABASE DEVELOPMENT

Least-squares optimizations have been systematically performed for all common-ion binary systems involving the alkali halides AX (A - Li, Na, K, Rb, Cs; X - F, Cl, Br, I) (14) as well as for all binary common-ion systems involving the cations (Li, Na, K) and the anions (F, Cl, NO₃, OH, CO₃, SO₄) (9) for a total of 124 binary systems. Exhaustive literature surveys of all thermodynamic and phase diagram data were performed. The optimizations provided the binary parameters of eqs [6, 7] for all binary liquid phases as well as expressions for the thermodynamic properties of all solid phases. This work was supported by the American Ceramic Society. All evaluations are scheduled to appear in "Phase Diagrams for Ceramists". Many other binary salt systems have similarly been evaluated (20).

The 60 common-ion ternary systems involving the alkali halides have been systematically evaluated (15). For the approximately 40 systems for which ternary liquidus surfaces have been reported, eq [12] with no ternary terms reproduced the liquidus surface within experimental error limits in nearly every case. One small ternary term, O_{111} , was included in 8 systems for which the liquidus measurements were very accurate. The other common-ion and reciprocal ternary systems involving the 124 binary systems mentioned above are being systematically evaluated. Results are invariably very good for the common-ion systems and are also very good for the reciprocal systems as long as ΔG^{EX} is not so large as to provoke liquid immiscibility. Many other ternary systems have also been evaluated (20).

All evaluated binary, ternary and reciprocal ternary coefficients are being stored in a computer database which forms part of the F*A*C*T (Facility for the Analysis of Chemical Thermodynamics) on-line computer system (8). The data are accessible along with data on several thousand inorganic compounds and other solutions. Thermodynamic

properties of multicomponent salt solutions are calculated from the binary and ternary coefficients via eq [19] (extended to include the more general Kohler/Toop formalism). An interactive free-energy minimization program known as EQUILIB permits users of F*A*C*T to access all the data automatically and to perform complex multiphase, multicomponent equilibrium calculations for a wide variety of constraints. The EQUILIB program is based upon the SOLGASMIX program of G. Eriksson (21).

SAMPLE CALCULATION

A sample calculation using the program EQUILIB is shown in Tables I and II. Interactive input and output are shown for a calculation involving a gas/molten salt equilibrium similar to that encountered in a carbonate fuel cell.

In Table I, the reactants are entered as a gas phase consisting of 9.8 mol CO, 7.5 mol CO₂, etc. along with a small amount of Li₂CO₃, K₂CO₃ and Na₂CO₃ which will form the molten salt phase. The reactants are to be equilibrated at 973 K at a pressure of 10 atm.

The "possible products" are then listed. These are simply all compounds and solutions containing the input elements for which there are data in the F*A*C*T database. In Table I the list has been abbreviated, but we see that there are data for 289 pure compounds as well as for the multicomponent salt solution Li,Na,K/OH,SO₄,CO₃. The user has chosen to consider species 1 to 120 (all gaseous species) the molten salt solution (species 290-298) as well as species 243, 268, 281 which are the solid carbonates.

Data are then automatically retrieved from the databases. The calculated equilibrium compositions are shown in the output of Table II. There are 85.697 moles of gas phase formed containing 41.727% H₂, 37.732% H₂O, etc. The amounts of volatile Li- and K-containing gaseous species such as KOH(H₂O), LiOH(H₂O), KOH and LiOH can be read from this output. (There were actually 120 species in the calculated gas phase. The output list in Table II has been shortened.) There are also 0.22375 moles of a molten salt solution formed whose composition can be read from the output listing. It can be seen how much hydroxide and sulfate enters the molten salt phase. Finally, we see that zero moles of the solid carbonates precipitate.

ACKNOWLEDGEMENTS

This work was carried out over several years in collaboration with C.W. Bale, W.T. Thompson, G. Eriksson and J. Sangster. Financial support from the Natural Sciences and Engineering Research Council of Canada and from the American Ceramic Society is gratefully acknowledged.

REFERENCES

1. C.W. Bale and A.D. Pelton, Met. Trans., **14B**, 77 (1983).
2. F. Kohler, Mh. Chem., **91**, 738 (1960).
3. N.J. Olson and G.W. Toop, TMS-AIME, **236**, 590 (1966).
4. H. Reiss and O.J. Kleppa, J. Phys. Chem., **36**, 144 (1962); M. Blander and S.J. Yosim, J. Chem. Phys., **39**, 2610 (1963); M.-L. Saboungi and P. Cerisier, J. Electrochem. Soc., **121**, 1258 (1974); M.-L. Saboungi and M. Blander, J. Chem. Phys., **63**, 212 (1975); M. Blander and M.-L. Saboungi, "Molten Salts", pp 93-106, The Electrochemical Society, Inc. (1976).
5. M. Blander and S.J. Yosim, J. Chem. Phys., **39**, 2610 (1963).
6. M.-L. Saboungi and M. Blander, J. Am. Ceram. Soc., **58**, 1 (1975).
7. M.-L. Saboungi, J. Chem. Phys., **73**, 5800 (1980).
8. F*A*C*T (Facility for the Analysis of Chemical Thermodynamics) Users' Instruction Manual, by W.T. Thompson, C.W. Bale and A.D. Pelton, 500 pages, 2nd edition (1985).
9. J. Sangster, Y. Dessureault and A.D. Pelton, to appear in "Phase Diagrams for Ceramists", vol. 7.
10. B.K. Andersen and O.J. Kleppa, Acta Chem. Scand., **A30**, 751 (1976).
11. M. Rolin and J. Recapel, Bull. Soc. Chim. Fr., 2104 (1964).
12. G.J. Janz and M. Lorenz, J. Chem. Eng. Data, **6**, 321 (1961).
13. I. Barin, O. Knacke and O. Kubaschewski, "Thermochemical Properties of Inorganic Substances" (and supplement), Springer-Verlag, N.Y. (1973, 1977).
14. J. Sangster and A.D. Pelton, J. Phys. Chem. Ref. Data, in press; also to appear in "Phase Diagrams for Ceramists", vol. 7.
15. J. Sangster and A.D. Pelton, to appear in "Phase Diagrams for Ceramists", vol. 7.
16. N.S. Domborskaya, Izv. Sekl. Fiz. Khim. Anal., **20**, 124 (1950).

17. M. Hillert, Calphad J., 4, 1 (1980).
18. M. Blander and J. Braunstein, Ann. N.Y. Acad. Sci., 79, 838 (1960).
19. V.D. Polyakov, Izv. Sektora Fiz.-Khim. Analiza Inst. Obshch. Neorgan. Khim. Akad. Nauk SSSR, 13, 308 (1940).
20. A.D. Pelton, "Computer Modeling of Phase Diagrams", ed. L.H. Bennett, 19, Met. Soc. AIME Conf. Proc., Warrendale, PA (1986).
21. G. Eriksson, Chemica Scripta, 8, 100 (1975).

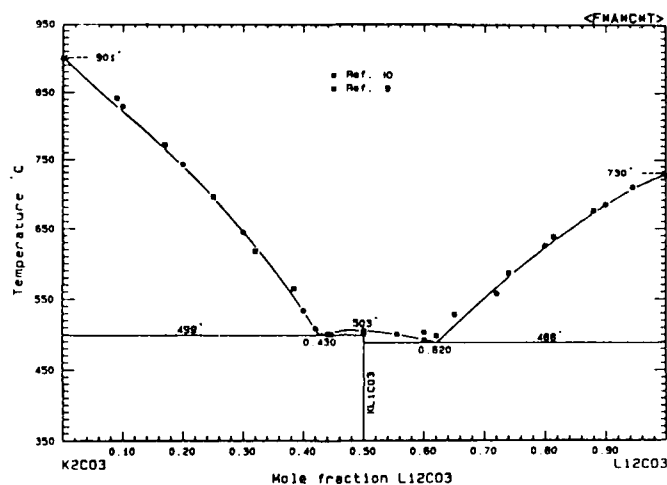


Fig. 1: K,Li/CO₃ Phase Diagram Calculated from Eqs [9, 10]. Points are experimental.

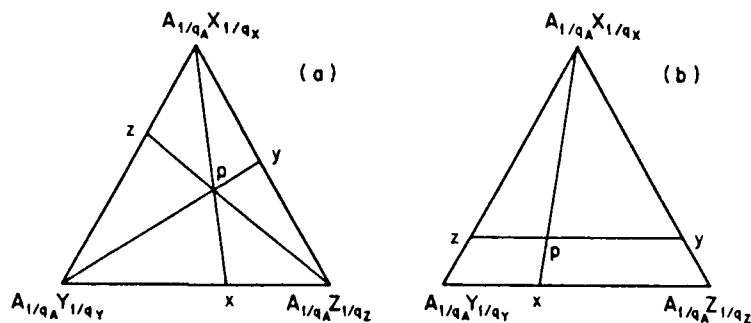


Fig. 2: Common-Ion Ternary Systems Illustrating the Geometrical Relationships Involved in (a) the Symmetric Kohler Eq. [11] and (b) the Asymmetric Toop Eq. [13].

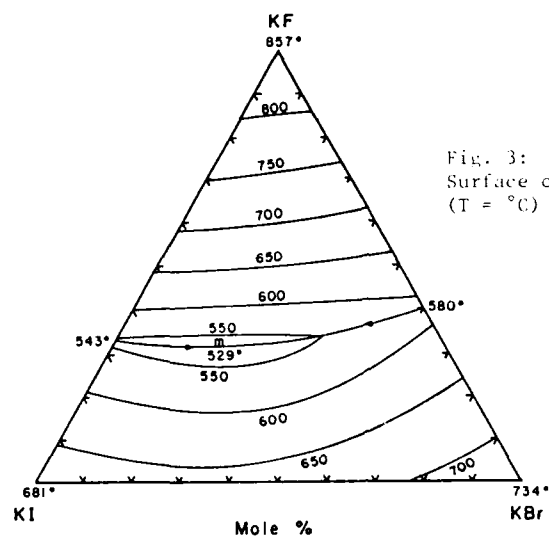


Fig. 3: Calculated (15) Liquidus Surface of the K/F,Br,I System
(T = °C)

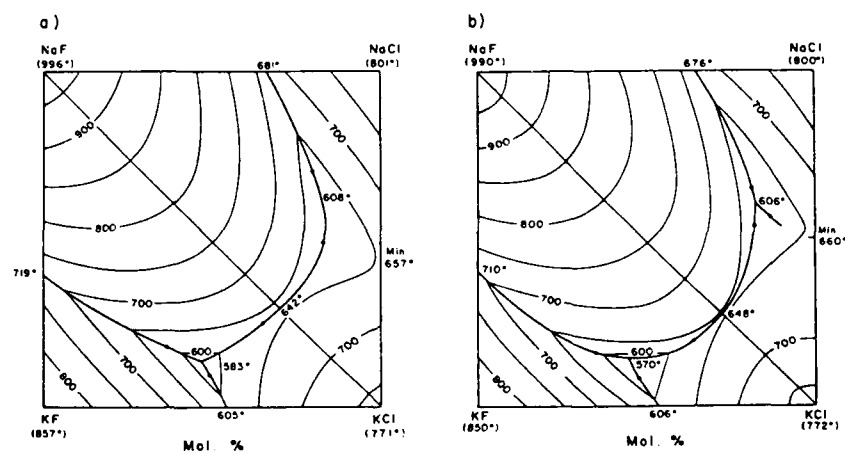


Fig. 4: Liquidus of the Na,K/F,Cl System (T = °C).
(a) Calculated via Eqs [17, 18]
(b) As Reported by (19)

TABLE 1

Input to the F*A*C*T Program EQUILIB for an Equilibrium Gas-Salt
Calculation Involving a Multicomponent Molten Salt Solution.

```

***** ENTER REACTANTS *****OR PRESS 'RETURN' FOR LAST ENTRY (DIFFERENT)
?
9.6 C#O + 7.5 C#O2 + 5.4 H#H + 12.0 H#O + 0.3 H#S + 0.1 Li#O#O3 + 0.1 Na#O#O3 + 0.1 Na#O#O4
*****
T PROD P PROD V PROD DELTA H DELTA G DELTA S DELTA U DELTA F
(K) (ATM) (L) ---- MM SPECIFY IF SUBSCRIPTS PROVIDED -----
*****
?
973 10
YOU DO(1) OR YOU DO NOT(2) WISH TO SEE THE LIST OF POSSIBLE PRODUCTS
?
1
1 LI#O#H(H#O) ---- G1 GAS 298.0 K - 5000.0 K
2 K#O#H(H#O) ---- G1 GAS 298.0 K - 5000.0 K
3 K2(O#H)2 G1 GAS 298.0 K - 8000.0 K
4 K#O#H(L) G1 GAS 298.0 K - 8000.0 K
5 K(O#H) G1 GAS 298.0 K - 8000.0 K
6 K#O(L) G1 GAS 298.0 K - 8000.0 K
7 K#O G1 GAS 298.0 K - 8000.0 K
8 K#H G1 GAS 298.0 K - 8000.0 K
9 K2 G1 GAS 298.0 K - 8000.0 K
10 K G1 GAS 298.0 K - 8000.0 K
11 (C#H3)2S#O2 G1 GAS 298.0 K - 3000.0 K
12 (C#H3)2S#O G1 GAS 298.0 K - 3000.0 K
13 C#O#S G1 GAS 298.0 K - 1800.0 K
14 H2S#O4 G1 GAS 298.0 K - 2000.0 K
15 S2O G1 GAS 298.0 K - 2000.0 K
16 S#O3 G1 GAS 298.0 K - 2000.0 K
17 S#O2 G1 GAS 298.0 K - 1800.0 K
18 S#O G1 GAS 298.0 K - 2000.0 K
:
243 K2C#O3 S1 SOLID 298.0 K - 1174.0 K
244 K(O#H) S1 SOLID-A 298.0 K - 500.0 K
245 K(O#H) S2 SOLID-B 298.0 K - 673.0 K
246 K2O2 S1 SOLID 298.0 K - 763.0 K
247 K2O S1 SOLID 298.0 K - 1154.0 K
248 K#O2 S1 SOLID 298.0 K - 675.0 K
249 K#H S1 SOLID 298.0 K - 690.0 K
250 K S1 SOLID 298.0 K - 330.0 K
251 NA2S#O4 S1 THENARDITE 298.0 K - 522.0 K
252 NA2S#O4 S2 SOLID-B 500.0 K - 980.0 K
:
MOLTEN SALT SOLUTION
290 LI#O#H
291 NA#O#H
292 K#O#H
293 LI2C#O3
294 NA2C#O3
295 K2C#O3
296 LI2S#O4
297 NA2S#O4
298 K2S#O4
ENTER CODE NUMBERS OF SPECIES TO BE CONSIDERED OR ENTER 'HELP'
?
- /1-120/290-298/243-266-251

```

TABLE 11

OUTPUT RESULTING FROM THE INPUT IN TABLE 1

$$9.8 \text{ CO} + 7.5 \text{ CO}_2 + 59.4 \text{ H}_2 + 23.3 \text{ H}_2\text{O} + 0.3 \text{ H}_2\text{S} + 0.1 \text{ Li}_2\text{CO}_3 + 0.1 \text{ K}_2\text{CO}_3 + 0.02 \text{ Na}_2\text{CO}_3 =$$

```

85.697    mol ( 0.41727      H2
+ 0.37730      H2O
+ 0.85189E-01  CH4
+ 0.67291E-01  CO2
+ 0.49418E-01  CO
+ 0.34812E-02  H2S
+ 0.19443E-04  COS
+ 0.13689E-05  KOH(H2O)
+ 0.77637E-06  LiOH(H2O)
+ 0.75659E-06  C2H6
+ 0.34233E-06  K(OH)
+ 0.29490E-06  CH2O
+ 0.27313E-06  C4H6
+ 0.13951E-06  C2H4
+ 0.49322E-07  LiOH
      .
      .
      .
+ 0.17672E-43  O3
+ 0.10943E-43  C4
+ 0.41322E-44  C5)
( 973.0, 10.0  +6)

+ 0.22373    mol ( 0.43900      Li2CO3
+ 0.43884      K2CO3
+ 0.87832E-01  Na2CO3
+ 0.15606E-01  LiOH
+ 0.15600E-01  KOH
+ 0.31224E-02  NaOH
+ 0.55912E-07  Li2SO4
+ 0.55891E-07  K2SO4
+ 0.11186E-07  Na2SO4)
( 973.0, 10.0  +SOLN 2)

+ 0.00000E+00 mol K2CO3
( 973.0, 10.0  +S1, 0.25389  )

+ 0.00000E+00 mol Li2CO3
( 973.0, 10.0  +S3, 0.98781E-01)

+ 0.00000E+00 mol Na2CO3
( 973.0, 10.0  +S2, 0.12001E-01)

```

QUASICHEMICAL MODEL FOR SILICATE MELTS

A.E. Grau* and S.N. Flengas
Department of Metallurgy and Materials Science,
University of Toronto, Toronto, Ontario, Canada

ABSTRACT

The concentration dependence of the partial molar properties of binary silicate melts is predicted by means of a thermodynamic model based on the change in short-range bonding energies which is taking place when MO reacts with SiO_2 . The model may be considered as an extension of the treatment by Toop and Samis.

The expressions derived for the activities of the MO and SiO_2 components contain an equilibrium constant K as the only adjustable parameter. The calculation of the enthalpies and entropies of mixing needs a second interaction parameter, b.

The model has been applied to available data on the systems PbO-SiO_2 , FeO-SiO_2 , CaO-SiO_2 , MnO-SiO_2 and SnO-SiO_2 , and was found to predict the activity isotherms over the available composition range, including the SiO_2 rich melts for which other theoretical models are insensitive. The derived expressions also predict the concentration dependence of the partial molar enthalpy and entropy of mixing of PbO in the PbO-SiO_2 system. The latter is the only system for which such data have been accurately obtained.

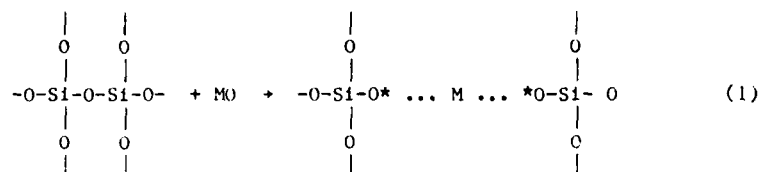
INTRODUCTION

Considering pure molten silica, it is generally accepted that each silicon is surrounded by 4 oxygen atoms, and that each oxygen is shared between 2 silicon atoms, the basic structural unit being the tetrahedrally coordinated SiO_4 . These tetrahedra share corners with each other and the structure of silica may be broadly described as a three-dimensional complex network characterized by the strongly covalent bonding between the Si and O atoms. The high viscosity and low vapour pressure of liquid silica indicates a continuity in the Si-O bonding throughout its structure, thus implying the absence of regions of lower covalency or of ionic behaviour.

When a metal oxide is added to molten silica, the resulting reaction causes drastic changes in the properties as evidenced by dramatic decreases in viscosity, the appearance of ionic conductance

* Present address: Quebec Iron and Titanium, Sorel, P.Q., Canada.

and the decrease in surface tension. This reaction is generally taken to involve a disruption in the continuity of the covalent bonds in silica due to interactions with oxygen supplied by the dissociating metal oxide, and may be written as,



Reaction (1) has been represented by Fincham and Richardson (1) as a reaction between the doubly bonded oxygen O^{**} , found within the sequence $-Si-O-Si-$, with "ionic" oxygen O^- supplied by the dissociating MO , which creates "semi-ionic" singly bonded oxygen atoms O^* found in the sequence $Si-O^* \dots M$. Reaction (1) has also been written as (1,2)



Toop and Samis (2) introduced the concept that reaction (2) represents an equilibrium between the various kinds of oxygen and calculated the relative distribution of a number of complex polysilicate anion species by assigning arbitrary values to the corresponding equilibrium constant K . According to the authors such species are created when the continuous silicate network is fragmented by the addition of a metal oxide.

In several recent publications (3-13) the thermodynamic properties of binary silicate melts have been interpreted in terms of polymer theory involving polysilicate anions.

Masson and co-workers (3-7) applied the concept of equilibrium to the calculations of the concentration of linear or branched polysilicate anions of the general formula $Si_n O_{3n+1}^{2(n+1)-}$ and calculated the "free" oxygen ion concentration which remains after the proposed poly-anions have reached equilibrium.

Activities of metal oxides in the silicate melts were obtained through the expression

$$a_{MO} = \frac{N_{O^{2-}}}{N_{O^{2-}}^0} \quad (3)$$

which was derived on the assumption that Temkin's (14) ideal solution model was applicable.

In this paper it is shown that the concentration dependence of the thermodynamic properties of binary silicate melts such as activities, enthalpies and entropies of mixing may be predicted from a simple thermodynamic model which is based on the equilibrium between the characteristic oxygen species proposed by Toop and Samis (2). The agreement between activity isotherms calculated from theory, with the experimentally obtained values, for a number of metal oxide-silica binary systems is excellent, even for silica rich compositions where other thermodynamic models are in poor agreement with the experimental data.

THERMODYNAMIC TREATMENT

According to reaction (1), the addition of a metal oxide to pure silica results in the disruption of the continuity of the Si-O-Si covalent type bonds which are responsible for the three dimensional network structure of silica. Each O^{2-} supplied by the metal oxide disrupts two Si-O bonds in SiO_2 and causes the localization of paired electrons with the result that the two Si-O* bonds produced upon reaction acquire a more "ionic" character.

One important characteristic of reaction (1) is that the SiO_4 coordination which exists in pure molten SiO_2 is also preserved in the MO- SiO_2 melts.

Considering reaction (1), because of the characteristic tetrahedral coordination of silicon and the well established strength of the covalent and semi-ionic bonds between silicon and oxygen, it will be assumed that the interactions between any oxygen species and the surrounding atoms are determined primarily by short range forces between nearest neighbours. Bonding energies representing pairs of the type Si-O**, M-O, SiO* and M-O* which are present, respectively, in the configurations Si-O-Si, M-O-M, and Si-O-M will be taken as constant and as being concentration independent. Thus the changes in bonding energy which take place during the mixing of MO with SiO_2 , are localized to the type of atomic pairs which are directly affected by the reaction, and should be independent of the detailed structure of the possible polysilicate anions created during reaction.

The silicate melt reaches a state of minimum free energy by equilibrating the characteristic oxygen species O*, O** and O^{2-} , shown in reaction (2).

For the evaluation of the activities the standard states are established at unit oxygen species fractions. Thus, for doubly bonded oxygen O**, the standard state is the state of oxygen in pure SiO_2 , for which $N_{O^{**}} = 1$. Similarly, the standard states for O* and O^{2-} are, respectively, their states in the stoichiometric ortho-silicate melt M_2SiO_4 , and in pure metal oxide MO.

Under the previously stated assumptions the species activity coefficients should be constant for all compositions, and activities could be equated to oxygen species fractions, except for compositions very near to pure metal oxide and to pure silica where deviations from the assumptions underlying the model should be expected.

The equilibrium constant for reaction (2) may be written as

$$K = \frac{N_{O^*}^2}{N_{O^{**}} \cdot N_{O_2}} \quad (4)$$

where, N_O 's are specie fractions and the equilibrium constant K should be constant and composition independent at constant temperature.

The species fractions N_{O^*} , $N_{O^{**}}$ and N_{O_2} may be calculated by following the mass balance introduced by Toop and Samis (2) and the results are shown in Table 1.

The quantity α found in Table 1 is the "degree of reaction" representing the fraction of MO reacted per mole of MO added to the melt.

By substitution in equation (4) of the corresponding species fractions N_i , the expression for the equilibrium constant is obtained as

$$K = 4 \frac{X_{MO}^2}{(1 - \alpha) \cdot (2X_{SiO_2} - \alpha X_{MO})} \quad (5)$$

This equilibrium constant is the reciprocal of that used by Toop and Samis (2) and characterizes a $MO-SiO_2$ binary system at a given temperature.

From equation (5)

$$\alpha = \frac{K \cdot (1 + X_{SiO_2})}{2X_{MO} (K - 4)} \left[1 - \left(1 - \frac{8X_{MO} X_{SiO_2} (Y - 4)}{K (1 + X_{SiO_2})^2} \right)^{1/2} \right] \quad (6)$$

where $0 \leq \alpha \leq 1$.

Plots of α versus composition generated for selected values of K are shown in Fig. 1. It may be seen that very large K values correspond to totally reacted silicate systems in which the maximum amount of the orthosilicate species SiO_4^* is present. K values between 100 and 1 represent various equilibrium conditions, while smaller values of K indicate a tendency towards immiscibility.

TABLE 1
Number of Various Oxygen Species Present
in 1 g mole of Melt at Equilibrium

	Before mixing	After mixing
O**	$2 X_{\text{SiO}_2} \cdot N$	$(2 X_{\text{SiO}_2} - \alpha X_{\text{MO}})N$
O*	-	$2 \alpha X_{\text{MO}} \cdot N$
O ²⁻	$X_{\text{MO}} \cdot N$	$(1 - \alpha) X_{\text{MO}} \cdot N$

(N is the Avogadro number)

Number of characteristic bonds at equilibrium

Bond Type	Before mixing	After Mixing	Bond Energy
Si-O	$4 X_{\text{SiO}_2} N$	$(4 X_{\text{SiO}_2} - 2 \alpha X_{\text{MO}}) N$	$\epsilon_{\text{Si-O}}$
M-O	$z X_{\text{MO}} N$	$z(1 - \alpha) X_{\text{MO}} N$	$\epsilon_{\text{M-O}}$
Si-O*	-	$2 \alpha X_{\text{MO}} N$	$\epsilon_{\text{SiO-O*}}$
M-O*	-	$2 \alpha X_{\text{MO}} N$	$\epsilon_{\text{M-O*}}$

(N is the Avogadro number)

* X_{SiO_2} and X_{MO} are initial moles of SiO₂ and MO per mole of solution

The degree of reaction α may also be used to determine the number of the different kinds of bonds present in a system at equilibrium. Thus, each doubly bonded oxygen O** corresponds to two Si-O type bonds, and each "free" oxygen ion O²⁻ determines the existence of z M-O type bonds. The coordination number z for oxygen in the metal oxide is taken to remain unchanged in the molten solution. Finally, each singly bonded oxygen O* creates one M-O* and one SiO* type bonds.

The numbers of the different kinds of bonds at equilibrium per mole of silicate containing X_{MO} moles of MO and X_{SiO_2} moles of SiO₂ are also shown in Table 1.

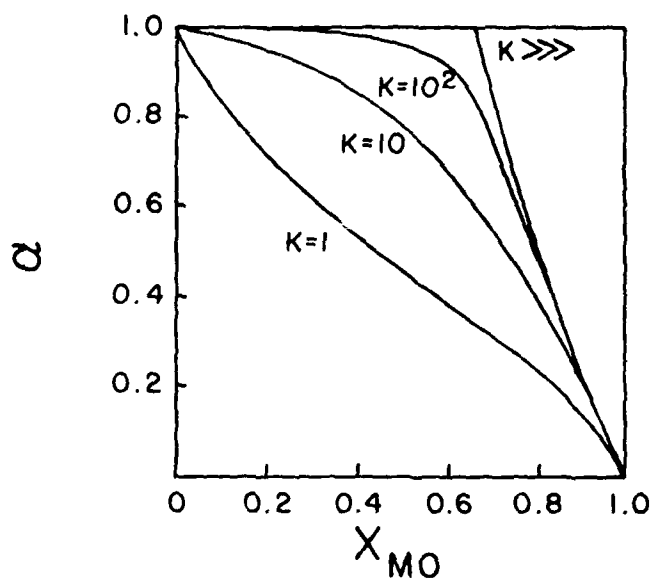
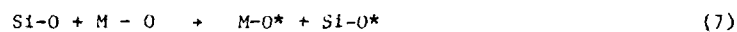


Fig. 1. Plots of the degree of reaction α versus composition X_{MO} for selected values of K .

CONCENTRATION DEPENDENCE OF THE SOLUTION PROPERTIES

For the calculation of the enthalpy change during mixing, reaction (1) can be taken as the exchange reaction



(as in pure SiO_2 and MO) (as in the reacted system)

The internal energy change during mixing ΔE_{mix} , per gram-mole of solution may be written as

$$\Delta E_{\text{mix}} = E_{\text{solution}} - X_{\text{MO}} E_{\text{MO}}^0 - X_{\text{SiO}_2} E_{\text{SiO}_2}^0 \quad (8)$$

where E_{solution} , E_{MO}^0 , and $E_{\text{SiO}_2}^0$ are respectively, the internal energy contents per mole, and X 's are mole fractions.

If it is considered that the mixing process affects only the energy of the bonds shown in Table 1, then equation (8) may be written as

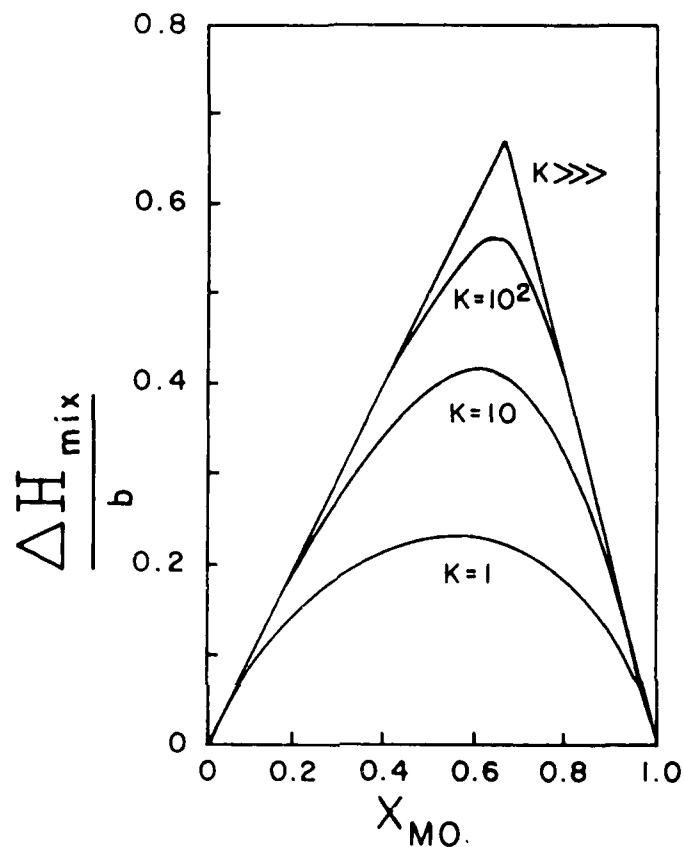


Fig. 2. Plots of $\Delta H_{\text{mix}}/b$ versus composition (X_{MO}) at selected values of K .

$$\begin{aligned}
 \Delta E_{\text{mix}} = & N[(4X_{\text{SiO}_2} - 2\alpha X_{\text{MO}})\epsilon_{\text{Si-O}} + z(1 - \alpha)X_{\text{MO}}\epsilon_{\text{M-O}} \\
 & + 2\alpha X_{\text{MO}}\epsilon_{\text{M-O}^*} + 2\alpha X_{\text{MO}}\epsilon_{\text{Si-O}^*}] \\
 & - N[4X_{\text{SiO}_2}\epsilon_{\text{Si-O}} + zX_{\text{MO}}\epsilon_{\text{M-O}}]
 \end{aligned} \quad (9)$$

which is readily reduced to

$$\Delta E_{\text{mix}} = \alpha X_{\text{MO}} [N(2\epsilon_{\text{M-O}^*} + 2\epsilon_{\text{Si-O}^*} - 2\epsilon_{\text{Si-O}} - z\epsilon_{\text{M-O}})] \quad (10)$$

Under the postulates of this model the term in parentheses is constant for a given temperature and independent of concentration, and may be replaced by an interaction parameter b which is characteristic of the metal oxide added. b can also be interpreted as the heat of reaction when 1 g mole of MO reacts totally with SiO_2 according to reaction (1).

As pressure-volume effects on the energy of mixing of liquid silicates are negligibly small, equation (9) becomes,

$$\Delta H_{\text{mix}} = bX_{\text{MO}} \quad (11)$$

where ΔH_{mix} is the enthalpy change for the mixing process. Combination of equations (6) and (11) yields,

$$\Delta H_{\text{mix}} = b \frac{K(1 + X_{\text{SiO}_2})}{2(K - 4)} (1 - B) \quad (12)$$

where

$$B = \left[1 - \frac{8X_{\text{MO}}X_{\text{SiO}_2}}{(1 + X_{\text{SiO}_2})^2} \cdot \frac{K - 4}{K} \right]^{1/2} \quad (13)$$

Plots of $\Delta H_{\text{mix}}/b$ versus composition generated for a number of selected K values are shown in Figure 2. It is seen that the totally reacted systems are represented by very large values of K and show a characteristic orthosilicate peak at $X_{\text{MO}} = 0.667$.

To calculate the partial molar heat of mixing for MO, the right hand side of equation (11) is multiplied by $n_{\text{MO}} + n_{\text{SiO}_2}$, and then partially differentiated. The resulting expression is,

$$\bar{\Delta H}_{\text{MO}} = \frac{\partial}{\partial n_{\text{MO}}} [(n_{\text{MO}} + n_{\text{SiO}_2}) \Delta H_{\text{mix}}] n_{\text{SiO}_2} \quad (14)$$

Introducing equation (6), it is readily shown that:

$$\bar{\Delta H}_{\text{MO}} = b \frac{K}{2(K - 4)} \left[1 - B + \frac{4(K - 4)}{KB} \cdot \frac{X_{\text{SiO}_2} (2 - 3X_{\text{MO}})}{(2 - X_{\text{MO}})^2} \right] \quad (15)$$

Plots of $\bar{\Delta H}_{\text{MO}}/b$ for various selected values of K are included in Fig. 3. It is seen that for a totally reacted system, $\bar{\Delta H}_{\text{MO}}$ becomes zero at $X_{\text{MO}} = 0.667$, and for all concentrations where $X_{\text{MO}} < 0.667$, $\bar{\Delta H}_{\text{MO}}$ is equal to b .

For a reacting system, the total entropy of mixing is also due to reaction (1) and may be calculated following the same treatment as

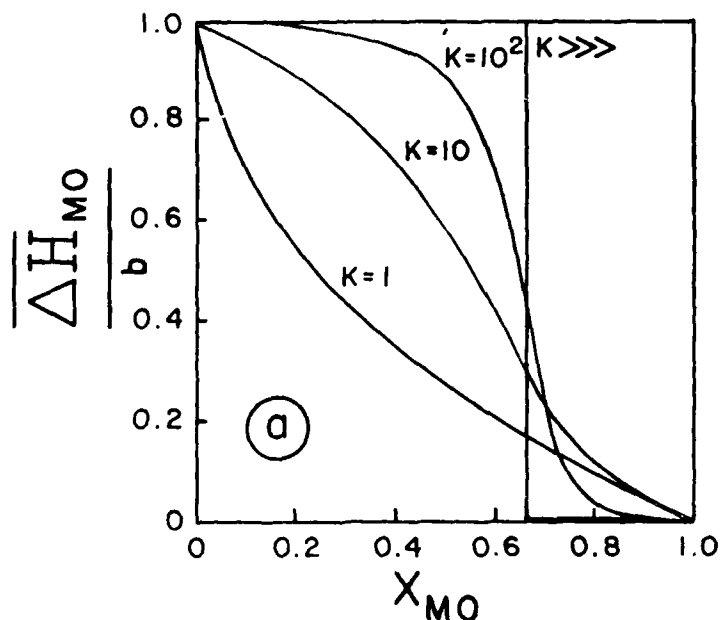


Fig. 3. Plots of $\Delta \bar{H}_{MO}/b$ versus composition (X_{MO}) at selected K-values.

for the enthalpy of mixing, with the main difference that the interaction parameter b should now be replaced by an entropy parameter. If δ is taken to represent the entropy change when one mole of MO reacts totally with SiO_2 following reaction (1), then

$$\Delta S_{mix} = \alpha X_{MO} \delta \quad (16)$$

The partial molar entropy of mixing for MO can be obtained by partial differentiation as

$$\Delta \bar{S}_{MO} = \delta \frac{K}{2(K-4)} \left[1 - B + \frac{4(K-4)}{KB} \cdot \frac{X_{SiO_2}(2 - 3X_{MO})}{(2 - X_{MO})^2} \right] \quad (17)$$

The values calculated from equation (17) which is similar in form to expression (15), represent the change of entropy due to reaction (1) when the number of reaction units is proportional to the

degree of reaction α . The latter is defined by the value of the equilibrium constant K for a given system at a given temperature.

The molar and partial molar entropies of mixing calculated by this model account for the randomness in the system.

For example, the partial molar free energy of mixing for any of the oxygen specie present is given as

$$\Delta G_i = RT \ln N_i \quad (18)$$

and the corresponding partial molar entropies of mixing are given by expressions of the type,

$$\overline{\Delta S}_i = -R \ln N_i - RT \frac{d \ln N_i}{dT} \quad (19)$$

The latter expression contains the configurational term for entropy, in which N_i is a temperature and composition dependent quantity.

It should be emphasized that the term ΔS_i for an oxygen species does not represent the partial molar entropy of MO as this is obtained by partial differentiation of the total entropy change of the system.

The partial molar free energy of mixing ΔG_{mix} for MO can be obtained by combining the partial molar enthalpies and entropies of mixing according to the Gibbs-Helmholtz relationship,

$$\overline{\Delta G}_{MO} = \overline{\Delta H}_{MO} - T \overline{\Delta S}_{MO} \quad (20)$$

From equations (15) and (17) the following expression is obtained.

$$\overline{\Delta G}_{MO} = (b - \delta T) \left[1 - B + \frac{4(K - 4)}{KB} \cdot \frac{X_{SiO_2} (2 - 3X_{MO})}{(2 - X_{MO})^2} \right] \cdot \frac{K}{2(K - 4)} \quad (21)$$

The term $b - \delta T$ represents the "standard" free energy change for reactions (2) and therefore it can be equated to $-RT \ln K$.

The expression for the activity of the metal oxide in the solution, a_{MO} , referred to the pure liquid MO as the standard state, is readily derived from equation (21) as,

$$\ln a_{MO} = \frac{K}{2(K - 4)} \left[1 - B + \frac{4(K - 4)}{KB} \cdot \frac{X_{SiO_2} (2 - 3X_{MO})}{(2 - X_{MO})^2} \right] \ln \frac{1}{K} \quad (22)$$

where the value of the term B is given in equation (13).

From equation (22) it is readily seen that the concentration dependence of activities is predicted using K as the only adjustable parameter. For large K values the a_{MO} term becomes zero for the composition range defined by $0 < X_{MO} < 0.67$. For compositions more basic than the ortho-silicate $X_{MO} > 0.667$, a_{MO} becomes unity. For low values of K near unity the activities for dilute solutions of MO show pronounced positive deviations from ideality.

In general, high K -values indicate a highly reacted system, while low K -values indicate a tendency towards immiscibility.

With regard to the activities of MO , it is evident that, as the temperature is increased, both the oxygen pressure in equilibrium with the molten silicate and the "oxygen anion activities" in the melts should increase. Such an increase should be accompanied by a decrease in the K values and should describe the weakening of the bonds which are binding the oxygen species in the melts. This decrease in the K -values with increasing temperature is consistent with the observed exothermic enthalpies of mixing and the negative b values which are calculated for binary silicate systems.

Limiting values for the activities of MO should not be calculated from equation (22) because for very dilute solutions the assumption that the equilibrium constant K is truly independent of concentration should no longer be valid.

Thus, at compositions representing very dilute solutions of MO in SiO_2 , all the oxygen anions supplied by MO should be trapped within the $Si-O^*-M$ type configurations and the "free" oxygen anion population should be approaching zero.

COMPARISON WITH EXPERIMENTAL RESULTS

Figure 4c shows a comparison between experimental (15) activity data for PbO at $1000^\circ C$ and the calculated values as predicted from equation (22) with a value of $K = 20$. It may be seen that the agreement is excellent within the entire concentration range for which the system was investigated. The b value which is calculated from equation (15) from a single experimentally measured value of the partial molar heat of mixing and the previously obtained value $K = 20$, is $b = -3,600 \text{ cal.mole}^{-1}$.

These two values for K and b may be used in equation 15 to predict the partial mole heats of mixing over the entire concentration range. In Fig. 4a the points are experimental and the solid line represents the calculated partial molar heats of mixing.

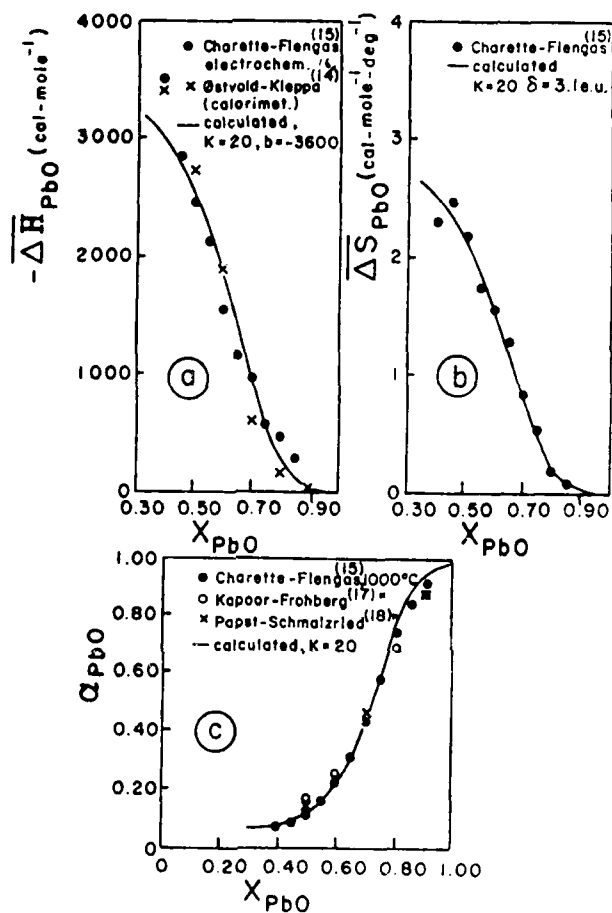


Fig. 4. (a) Plot of ΔH_{PbO} versus X_{PbO} for the PbO-SiO₂ system. Solid line is calculated from theory (Eqn. (15)). Points are taken from experimental data.

(b) Plot of ΔS_{PbO} versus X_{PbO} for the PbO-SiO₂ system. Solid line is calculated from theory (Eqn. (17)). Points represent experimental data.

(c) Plot of Q_{PbO} versus X_{PbO} for the PbO-SiO₂ system. Solid line is calculated from theory (Eqn. (22)). Points represent experimental data.

It should be emphasized that the PbO-SiO₂ binary system is the only system for which complete thermodynamic data are available in the literature. Partial molar enthalpies of mixing measured both calorimetrically (16) and electrochemically (15) are in good agreement. Also recent activity data for PbO reported by various authors (15,17,18) are in good agreement.

Comparison between data from various sources is shown in Figs. 4a, 4b, and 4c.

Accordingly, the partial molar entropies of mixing for PbO have been calculated with confidence and the results are included in Fig. 4b. In Fig. 4b the points represent the experimentally obtained entropy values while the line is calculated from the thermodynamic model.

Values of the parameter δ are obtained by combining the K and b values, according to

$$-RT \ln K = b - T\delta \quad (22)$$

For $T = 1273^\circ\text{K}$, $K = 20$ and $b = 3,600$ cal/mole, δ is found to be equal to 3.1 e.u. The good agreement between the experimental data for the partial molar entropies of mixing of PbO and the curve predicted by equation (22) is shown in Fig. 4b.

Activities of FeO referred to the pure liquid FeO as the standard state have been determined in the temperature range 1250-1400°C by equilibrating CO-CO₂ (19) and H₂-H₂O (20) gas mixtures with melts contained in iron crucibles. More recently, activities of FeO have been measured in the range 1785-1960°C (21) by equilibrating molten levitated beads of iron with liquid FeO-SiO₂ slags and by analyzing for the oxygen content in the iron.

Because of the non-stoichiometry of FeO, the system is not a true binary and may be considered as a ternary containing FeO, SiO₂ and small amounts of Fe₂O₃. Several attempts (3,22) have been made to correct the published data for the effect of the non-stoichiometry of FeO but it is felt that such corrections could introduce deviations larger than the inherent uncertainty in the experimental data.

The activity plot of Fig. 5 indicates the good agreement between the experimental activities at 1300°C and at 1785°C with those predicted from equation (22) with K values of 8 and 5, respectively.

From the expression

$$\frac{d \ln K}{dT} = \frac{b}{RT^2} \quad (23)$$

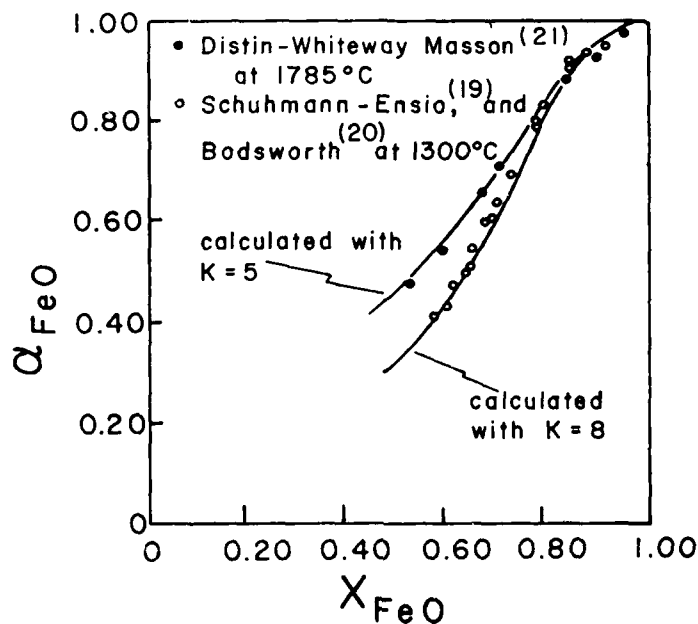


Fig. 5. Plots of a_{FeO} versus X_{FeO} for the FeO-SiO₂ system at 1785°C and 1300°C, respectively. Points are experimental, solid lines are calculated from equation (22).

and the available K values at two different temperatures, an approximate value of the parameter b for this system is given as -6,270 cal/mole. The corresponding approximate value of δ is 0.2 e.u.

The activities of CoO in CoO-SiO₂ melts have been measured at 1500°C by equilibrating melts held in Pt-Rh containers with known oxygen potentials (23). The original data are given with respect to the solid CoO as the standard state and have been recalculated with reference to pure supercooled liquid CoO (23). For this conversion the entropy of fusion of CoO has been taken (4) to be the same as for FeO, as 4.25 e.u. The experiments could only cover the concentration range between 55 and 70 mole % CoO.

Figure 6 shows a comparison between the experimental activities at 1500°C (referred to liquid CoO) and those predicted by equation (22) with K = 7. In view of the apparent uncertainty of these data, the agreement is acceptable.

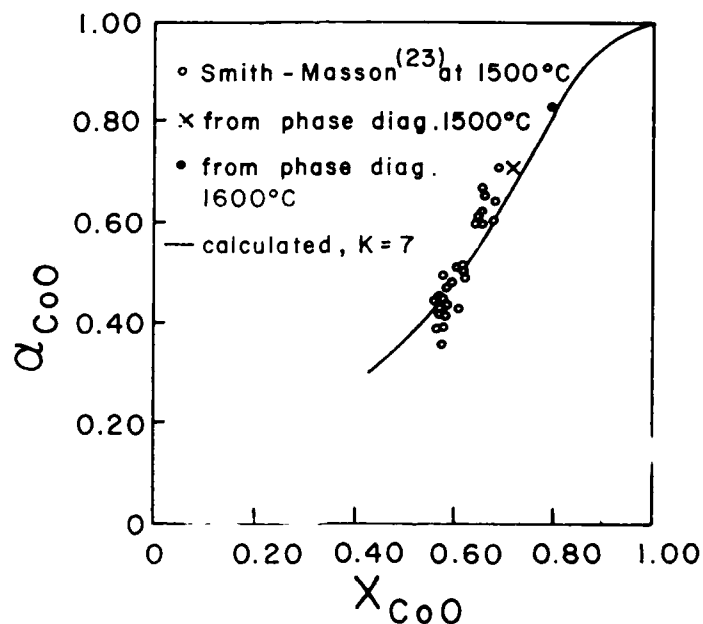


Fig. 6. Plot of a_{CoO} versus X_{CoO} for the CoO-SiO_2 system at 1500°C . Points are experimental. Solid line is calculated from equation (22) with $K = 7$.

Activities of the MnO at 1600°C referred to pure solid MnO as the standard state, have been determined by equilibrating various gas mixtures of $\text{H}_2\text{-CO}_2\text{-N}_2$ with solid Mn and liquid slags containing MnO and SiO_2 (24). The accurate conversion of these data to activities referring to pure supercooled MnO at 1600°C is difficult because of the lack of knowledge on the heat of fusion of MnO and the uncertainty regarding the melting point of the oxide. However, it has been assumed (4), that the entropy of fusion of MnO is the same as for FeO , e.g. 4.5 e.u., and that the melting point is 1875°C (25). The activities with regard to molten MnO as the reference state have been calculated from the well-known expression.

$$\ln \frac{(a_{\text{MnO}})_{\text{liq.}}}{(a_{\text{MnO}})_{\text{sol.}}} = - \frac{\Delta f_{\text{fusion}}}{RT} \quad (24)$$

Figure 7 shows a comparison between the converted experimental activities and the values predicted by equation (22) with $K = 19$. It may be seen that the agreement is satisfactory in the concentration range for which the experimental data are available.

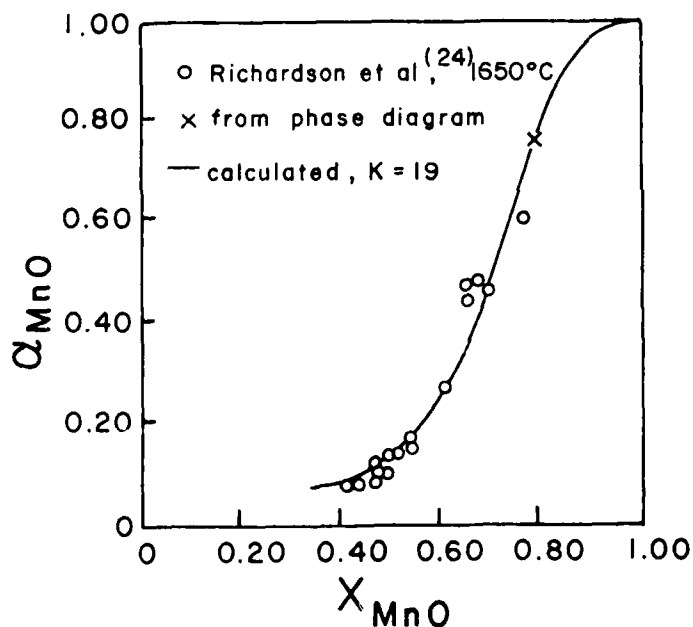


Fig. 7. Plot of a_{MnO} versus X_{MnO} for the MnO-SiO_2 system at 1650°C . Points are experimental. Solid line is calculated from equation (22) with $K = 19$.

Activities of CaO have not been experimentally determined with respect to the pure liquid oxide as the reference state. The only data available representing the mixing of supercooled CaO are the free energies of mixing at 1600°C estimated by Darken and Gurry (26) from which activities for both components may be obtained (21,23). A comparison between these approximate activities of CaO and those obtained from equation (22) with $K = 200$ is shown in Fig. 8.

The CaO-SiO_2 binary is a highly reacted system in which the almost complete formation of the orthosilicate configuration is observed at 67 mole % CaO .

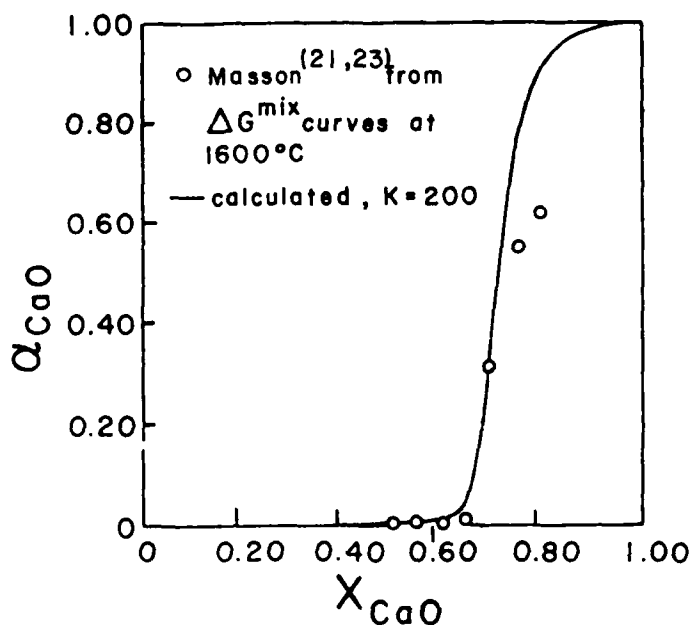


Fig. 8. Plot of a_{CaO} versus X_{CaO} for the CaO-SiO_2 system at 1600°C. Points are experimental. Solid line is calculated from equation (22) with $K = 22$.

The activities of SnO in the binary SnO-SiO_2 system have been obtained (27) in this laboratory from emf measurements.

Figure 9 shows a comparison between the experimental activities of SnO at 1000°C, with respect to molten SnO as the state of reference, and those calculated from equation (22) using a K -value equal to 2.7.

Such a low K -value suggests that SnO is one of the most acidic oxides with respect to silica.

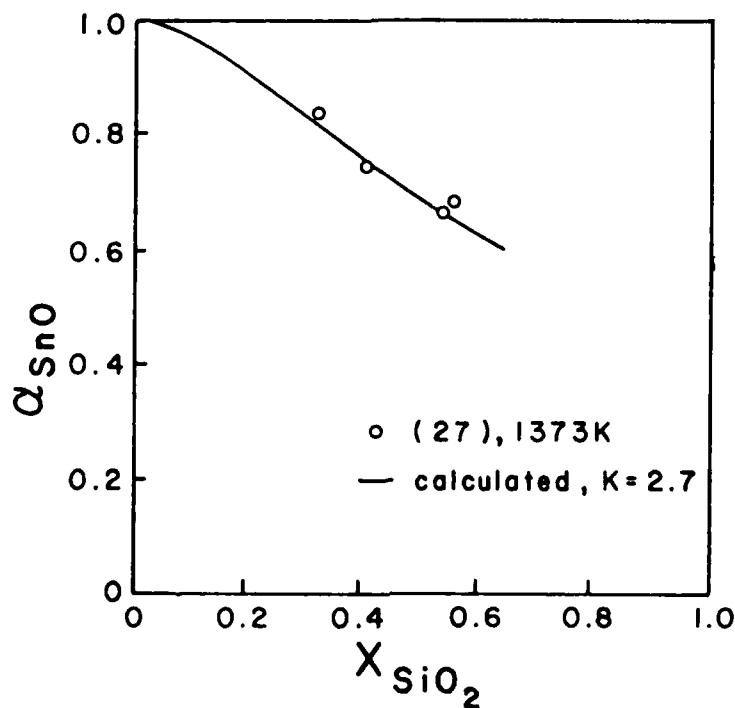


Fig. 9. Plot of a_{SnO} versus X_{SiO_2} for the system SnO-SiO₂. Points are experimental. Solid line is calculated from theory with $K = 27$.

REACTIVITY SCALE IN BINARY SILICATE MELTS

The energy released during the mixing of a metal oxide with silica according to reaction (1) is represented by the interaction parameter \underline{b} . The magnitude of \underline{b} depends upon the ability of the metal oxide to release its oxygen, which reacts with silica in order to form the SiO-O*-M type configurations. The overall energy for a configuration of the type Si-O*-M depends upon the competing interactions of the oxygen with the surrounding Si and M atoms and is expected to decrease proportionally with the formation potential of the metal-oxygen atom pair.

Metal oxides having strong metal to oxygen interactions are less effective as oxygen donors than those in which the interactions are weak. Since the strength of the metal to oxygen bond is expected to be inversely proportional to the interatomic distance \underline{d} , the interaction parameter \underline{b} should change in proportion to $1/\underline{d}$.

If the entropy change associated with reaction (1) is taken to be small, the "standard" free energy change, which is equal to $-RT \ln K$, could be approximated by b . Then, the value of the quantity $-RT \ln K$ should also be proportional to the reciprocal of the metal-oxygen distance d in the pure solid metal oxide. This assumption appears to be valid in the case of the FeO-SiO₂ system for which the available data indicate an entropy parameter of only 0.2 e.u. Low values of δ can also be expected for the remaining metal oxides having the same NaCl cubic structure.

The plot of $-RT \ln K$ versus $1/d$ shown in Fig. 10 includes only cubic metal oxides like CaO, FeO, MnO and CoO, and the relationship appears to be linear.

A cubic oxide like PbO, which has a layer structure, does not behave in this manner and is expected to indicate different trends.

Approximate K values for the binary silicates containing other cubic oxides like NiO, MgO, SrO and BaO, for which experimental activities are not available, may be obtained by extrapolation in Fig. 10. Such K -values may be used in equation (22) to predict the activities of the metal oxides with respect to pure liquid oxides as the reference states.

Thus, estimated activity isotherms for the systems BaO-SiO₂ and SrO-SiO₂ at 1900°C, are shown in Fig. 11.

A summary of the experimentally available, as well as extrapolated K -values for the various cubic systems, are given in Table 2.

TABLE 2
Scale of Basicity of Cubic Metal Oxides Towards Silica

Metal oxides	Equil. constant K	Inter-atomic distance $d(\text{\AA})$	Metal-oxygen attraction z^2/d	$-RT \ln K$, or b , cal/mole
BaO	11,000 (1873K)	2.771	1.44	-34,500
SrO	1,300 (1873K)	2.560	1.54	-26,600
CaO	200 (1873K)	2.406	1.66	-19,700
MnO	19 (1923K)	2.218	1.80	-11,300
FeO	6.5 (1873K)	2.148	1.84	-6,700
CoO	7 (1773K)	2.127	1.87	-6,800
NiO	2 (2000K)	2.071	1.93	-2,600

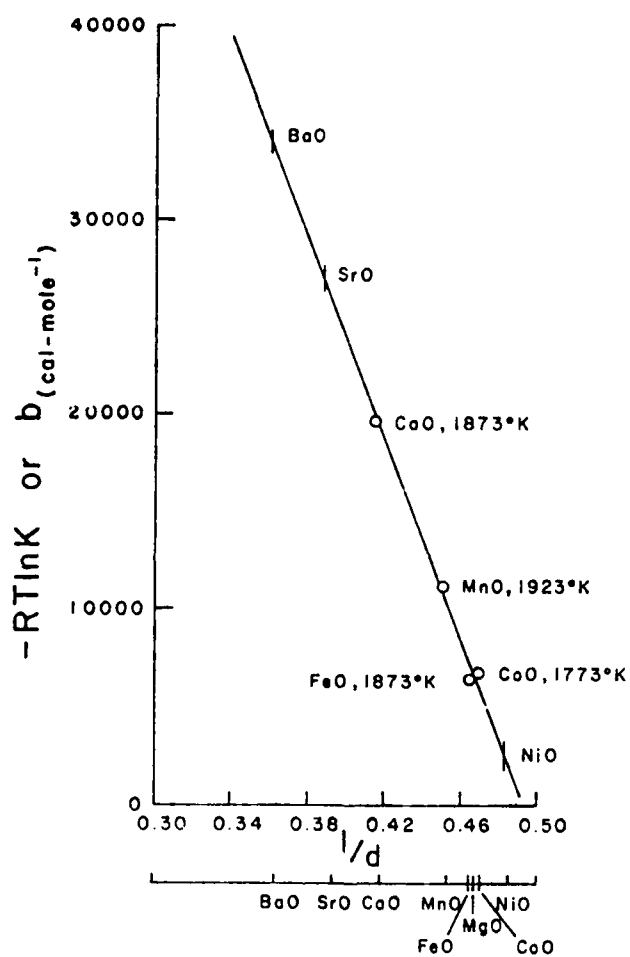


Fig. 10. Plot of $-RT \ln K$ or " b " versus $1/d$.

Table 2 also includes a list of interatomic distances and of atom-pair potentials, expressed as z^2/d , where z is the valence of a metal cation. The last column, which represents either b or $-R \ln K$, may be taken to represent a "basicity" or "reactivity" scale for the various metal oxides listed. This scale is a measure of the ability of a given metal oxide to disrupt the silicate network.

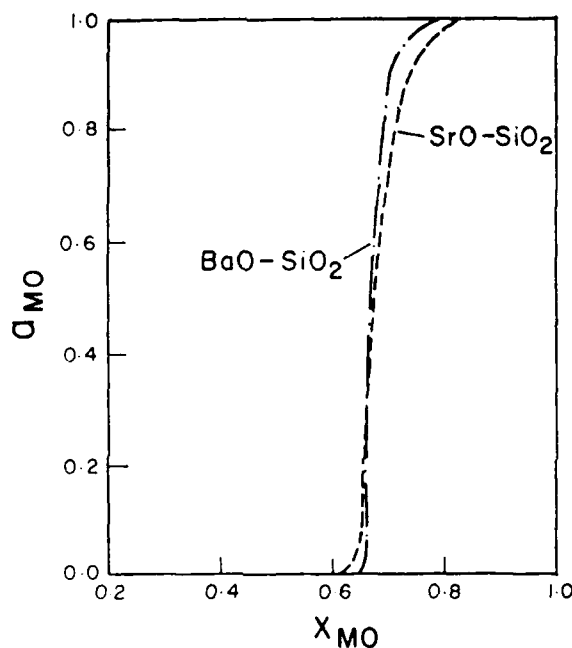


Fig. 11. Activity isotherms for the molten systems BaO-SiO₂ and SrO-SiO₂ at 1900°C estimated from the K-values shown in Fig. 10.

CONCLUSIONS

The equilibrium constant concept for binary silicate melts introduced by Toop and Samis (12) has been employed for the derivation of analytical expressions which describe the concentration dependence of partial molar properties, such as, activities, the partial molar enthalpies and entropies of mixing. The thermodynamic model is capable of describing within the limits of experimental uncertainty the concentration dependence of these properties.

For the calculation of the activities it is only necessary to use the equilibrium constant K as an adjustable parameter. However, once K for a given binary system has been calculated from activity data, the heats of mixing for the system may be calculated over its entire concentration range using one additional adjustable parameter, b , which has a unique value for each binary silicate system.

The partial molar entropies of mixing are then readily calculated.

In comparison with available experimental data the present thermodynamic model has been found capable of expressing, within the limits of experimental error the concentration dependence of the molar and partial molar properties in binary silicate melts over a wide composition range, including the SiO_2 rich regions for which most polymeric type thermodynamic models are non-applicable. The present model should be unrealistic for dilute solutions particularly in systems which are characterized by low K -values. In composition ranges near pure MO and near pure SiO_2 the assumption that K is a concentration independent quantity should not be expected to be valid.

In recent papers by Dron (28-30), the concept of an equilibrium between the various oxygen species proposed by Fincham and Richardson (1) and by Toop and Samis (2), has been expanded to account for possible differences in the thermodynamic states of doubly bonded oxygen, in accordance with the number of the reacted oxygen atoms carried by the adjacent silicon atoms. However, the treatment of such multiple equilibria requires the use of several equilibrium constants and general applicability becomes questionable.

In their modified quasichemical approach, pair-bonding enthalpy and non-configurational entropy contributions associated with reaction (1) have also been considered by Pelton and Blander (3-32). It is shown that the thermodynamic properties of binary (31) and higher order systems (32) may be expressed by semi-empirical equations which are suitable for data treatment and computer optimization.

The simple thermodynamic model developed in this paper shows that the properties of silicate melts are determined primarily by the interaction of oxygen ions with silica. These interactions involve only nearest neighbours and the magnitude of the partial molar properties appear to depend on the degree of completion of reaction (2) which represents the equilibrium between the various oxygen species. Because of the predominance of such short range interactions, the thermodynamic treatment does not require the exact knowledge of the detailed structure of the poly-silicate complex configurations that may form during reaction.

REFERENCES

1. C.J. Fincham and F.D. Richardson, Proc. Roy. Soc., A223, 40, 1954.
2. G.W. Toop and C.S. Samis, Trans. Metall. Soc. AIME, 224, 878-887, 1962.
3. C.R. Masson, Proc. Roy. Society, A, 287, 201-221, 1965.
4. C.R. Masson, J. Am. Cer. Soc., 51, 134-143, 1968.
5. S.G. Whiteway, I.B. Smith and C.R. Masson, Can. J. Chem., 48, 33-45, 1969.
6. C.R. Masson, I.B. Smith and S.G. Whiteway, Can. J. Chem., 48, 1456-1464, 1970.
7. C.R. Masson, I.B. Smith and S.G. Whiteway, Can. J. Chem., 48, 201-202, 1970.
8. M.L. Kapoor and M.G. Froberg, Chemical Metallurgy of Iron and Steel - Iron and Steel Institute, London, England, p.17-23, 1973.
9. M.L. Kapoor, G.M. Mehrotra and M.G. Froberg, Arch. Eisenh., 45, 663-669, 1974.
10. M.L. Kapoor, G.M. Mehrotra and M.G. Froberg, Proc. Australas. Inst. Min. Metall., 254, 11-17, 1975.
11. D.R. Gaskell, Metall. Trans., 4, 185-192, 1973.
12. D.R. Gaskell, "Activities and Free Energies of Mixing in Binary Silicate Melts", Metall. Trans. B, 8, 131-145, 1977.
13. P.L. Lin and A.D. Pelton, Met. Trans. B., 0 B, 667-675, 1979.
14. M. Temkin, Acta Physicochim. U.S.S.R., 20, 41, 1945.
15. G.G. Charette and S.N. Flengas, Can. Met. Quarterly, 7, 191, 1968.
16. T. Ostwald and J. Kleppa, J. Inorganic Chem., 8, 78, 1969.
17. M.L. Kapoor and M.G. Froberg, Arch. Eisenh., 42, 5, 1971.
18. G. Papst and H. Schmalzried, Z. Phys. Chem. N.P., 82, 206, 1972.
19. R. Schuhmann and P.J. Ensio, Trans. AIME, 191, 401, 1951.
20. C. Bodsworth, J. Iron and Steel Inst., London, 193, 13, 1959.
21. P.A. Distin, S.G. Whiteway, C.R. Masson, Can. Met. Quarterly, 10, 73, 1972.
22. C. Bodsworth and I.M. Davidson, Phys. Chem. of Process Metallurgy, Part 1, Interscience Publishers, 1959, p.233.
23. I.B. Smith and C.R. Masson, Can. J. Chem., 49, 683, 1971.
24. K.P. Abraham, M.W. Davies and F.D. Richardson, J. Iron Steel Inst., 196, 82, 1960.
25. F.P. Glasser, Am. J. Sci., 256, 398, 1958.
26. L.S. Darken and R.W. Gurry, Phys. Chem. of Metals. McGraw Hill, 1953, p.340.
27. A.E. Grau and S.N. Flengas, J. Electrochemical Soc., 123, 852, 1976.
28. R. Dron, Compt. Rend. Ser. C, 289, 397-400, 1979.

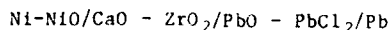
29. R. Dron, Compt. Rend. Ser. C, 289, 4370440, 1979.
30. R. Dron, J. Non-Cryst. Solids, 53, 267-278, 1982.
31. A.D. Pelton and M. Blander, "Second International Symposium on Metallurgical Slags and Fluxes". The Metallurgical Society of AIME. Ed. H.A. Fine and D.R. Gaskell, 1984, pp.281-294.
32. M. Blander and A.D. Pelton, Ibid, pp.295-304.

THERMODYNAMIC PROPERTIES OF THE MOLTEN PbO-PbCl₂ SOLUTIONS

A. Hacetoğlu* and S.N. Flengas
Department of Metallurgy and Materials Science,
University of Toronto,
Toronto, Ontario, Canada M5S 1A4

ABSTRACT

Partial molar and integral molar properties of mixing for the PbO-PbCl₂ melts have been investigated by using solid electrolyte galvanic cells of the type:



The thermodynamic properties, such as activities and the partial molar enthalpies of mixing, calculated from the measured cell potentials show pronounced negative deviations from ideality.

To explain this behaviour and to predict the concentration dependence of the thermodynamic properties of these solutions, a theoretical model based on a number of possible reaction mechanisms has been developed.

It is shown that in a non-ideal solution, the activity of any component A_B is given as:

$$a_{A_B} = (N_A^{x+} \cdot N_B^{y-})_{\text{equilibrium}}$$

where N_A^{x+} and N_B^{y-} are respectively the cation and anion fractions in a solution which has reached the ionic composition representing a specific reaction mechanism at equilibrium.

From the activity data, the limiting experimental conditions for removing the oxygen impurity from PbCl₂ melts, and for recovery of Pb and O₂ by fused salt electrolysis have been established.

INTRODUCTION

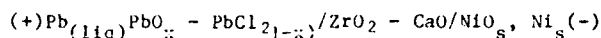
The PbO-PbCl₂ molten solutions represent the only metal oxide-metal chloride system in which oxide solubility occurs over a wide concentration and temperature range at relatively low temperatures.

* Cyanamide of Canada, Niagara Falls, Ontario, Canada.

Recently the phase diagram of the system has been revised by Renauld et al. (1) and significant differences from the earlier work by Ruer (2) and Varoni (3) have been found. At a temperature of 700°C, the range of liquid solutions extends from pure PbCl_2 to about 80 mole % PbO .

Activities of PbO in this system have been measured electrochemically by Sugawara et al. (4) at temperatures between 506 and 1063°C.

In the present investigation the reversible emf of the cell,



was measured for PbO compositions varying between pure PbO to 1 mole % PbO , and in the temperature range 450 to 950°C.

From the results the thermodynamic properties of PbO and of PbCl_2 in the PbO-PbCl_2 melts have been calculated. In addition to its theoretical significance, the thermodynamic information may be used to predict the limiting equilibrium conditions for the chlorination of PbO at high temperatures, for the preparation of pure PbCl_2 through the electrochemical removal of an oxygen impurity and for the recovery of metallic lead by fused salt electrolysis of the PbO-PbCl_2 solutions in the temperature range 500 to 600°C.

EXPERIMENTAL

The design of the cell for the emf measurements is given in Fig. 1. The reference electrode consisted of a CaO stabilized zirconia tube containing 13 mole % CaO , closed at one end, having a total length of about 30 cm. To make this electrode, nickel wire 1 mm in diameter having a spiral end was inserted into the zirconia tube and was covered with 2 to 3 cm of a compacted mixture of Ni and NiO powders. The open end of this tube was closed with a glass bell cemented into place and the entire system could be evacuated and sealed under vacuum. During its operation the thermal decomposition of NiO at the temperature of the experiment established the oxygen gas pressure and the emf measurements did not contain errors due to mixed potentials which are created by non-equilibrium oxygen pressure conditions (5).

The indicator electrode was molten lead in contact with the PbO-PbCl_2 melt contained in a zirconia crucible. Electrical contact to the lead was through iridium wire, about 1 mm in diameter and 10 cm long, connected to a platinum wire lead.

The entire electrode assembly, including the crucible with the salt mixture, was placed in a silica tube closed at one end. The top of this tube was covered with a nickel plate machined to contain

entry ports for the various cell components, as shown in Fig. 1. Vacuum tight seal was provided by De Khotinsky cement covering the entire surface of the top plate and all openings. To prevent the escape of the volatile PbCl_2 from the zirconia crucible containing the PbO-PbCl_2 melt, the top of the crucible was also closed with a boron nitride lid machined to fit tightly. This lid had openings for the insertion of the reference electrode and the other cell components shown in Fig. 1. A further precaution against possible volatilization of PbCl_2 was provided by operating the indicator electrode compartment under a static blanket of purified argon. A gas valve, connected in parallel with the argon supply to the cell, maintained a slightly positive gas pressure while it prevented the flow of gas and created semi-static conditions.

Materials losses due to possible volatilization were determined by weighing the contents of the crucible before and after a run, during dummy runs that duplicated the experimental conditions in terms of melt composition, temperature and duration. No significant loss of materials was observed. For example, for a total melt weight of 50 grams containing 70 mole % PbCl_2 , at a temperature of 750°C , over a period of 10 hours the weight loss was only 0.2 gram. Accordingly, melt compositions did not have to be corrected for losses due to volatilization.

The PbO and PbCl_2 used for these experiments were anhydrous high purity reagents and argon was dehydrated and oxygen purified by using the appropriate getters (Ti pellets at 1000°C).

Potential measurements taken during a heating and cooling cycle at each composition, were in agreement to within ± 2 millivolts. Maximum duration of a run was about 10 hours.

RESULTS AND DATA TREATMENT

Reversible potentials were measured as a function of temperature and composition and the results are shown in Figs. 2 and 3. The data have been calculated by least squares to correspond to linear equations of the form:

$$E \text{ (in mV)} = A - BT \quad (1)$$

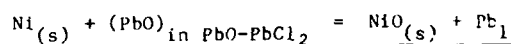
where A and B are constants for a given composition and T is given in degrees Kelvin. The constants, and the calculated standard and maximum deviations, are given in Table 1.

The activities of PbO were calculated from the Nernst equation given as:

$$E = (E_{\text{NiO}}^\circ - E_{\text{PbO}}^\circ) - RT/2F \ln a_{\text{PbO}} \quad (2)$$

TABLE 1

emf Measurements Representing the Overall Cell Reaction



Note: Negative emf values imply a reversal in the electrode reaction.

X_{PbO}	T Temp. Range (°K)	E = A - BT		Standard deviation (mV)	Maximum deviation (mV)
		A (mV)	B		
0.01	778-914	-15.933	0.15322	± 0.90	± 1.5
0.05	778-873	-39.228	0.05184	± 1.16	± 2.5
0.1	762-874	-32.380	0.02944	± 1.34	± 2.9
0.2	775-874	-14.103	0.00106	± 0.92	± 1.6
0.3	474-926	19.579	0.01716	± 2.08	± 3.6
0.4	781-935	29.452	0.000066	± 0.30	± 0.5
0.5	921-1010	78.821	0.01374	± 0.88	± 1.6
0.6	956-1062	117.207	0.02322	± 0.51	± 1.3
0.7	967-1064	158.435	0.03938	± 0.34	± 1.2
0.8	1016-1094	204.462	0.06705	± 1.03	± 1.7
1.0	160-1371	222.98	0.05052	± 0.57	± 1.0

TABLE 2

Standard Electrode Potentials

Electrode	Temp. Range (°K)	Cell Potential $E^\circ = A^\circ - B^\circ T$		Standard Deviation (mV)	Maximum Deviation (mV)
		A° (mV)	B°		
$\text{Ni}_{(s)} + 1/2 \text{O}_{2(g, \text{lat})} = \text{NiO}_{(s)}$ (5)	911- 1376	1,210.83	0.43993	± 0.57	± 1.0
$\text{Pb}_{(l)} + 1/2 \text{O}_{2(g, \text{lat})} = \text{PbO}_{(l)}$ (5)	1160-	987.5	0.38941	± 0.51	± 0.8
$\text{Pb}_{(l)} + \text{Cl}_{2(g, \text{lat})} = \text{PbCl}_{2(l)}$ (19)	773-	1,742.5	0.602	-	-

where a_{PbO} is the activity of PbO calculated with respect to pure molten PbO as the standard state. R and F have the values of 1.987 cal.mole⁻¹ and 23,066 cal.volt⁻¹, respectively. E is given in volts and E_{NiO}° and E_{PbO}° are respectively the formation potentials of pure solid NiO and pure molten PbO at the same temperature as T. T is given in degrees Kelvin.

The formation potentials for pure solid NiO at various temperatures have been established in previous investigations (5-11). With regard to pure molten PbO the standard Gibbs free energies reported by several investigators (12-14) and by Charette and Flengas (5) are in substantial agreement to within 2 to 4 mV. Accordingly, the standard formation potentials for NiO and for PbO used for the calculation of the activities from equation (2) are those reported in our previous work (5). The latter were obtained by emf measurements in closed cells similar to those used in the present investigation. The data for the standard potentials of NiO and PbO are given in Table 2.

The activities of PbO at the selected temperatures of 750°C and 850°C are given in Table 3. The activities of PbCl₂ which are also included in Table 3, have been calculated using the well known Gibbs-Duhem relationship (15).

TABLE 3

x_{PbO}	750°C		850°C		$\Delta H_{\text{PbO}}^{**}$ Kcal/mol
	a_{PbO}	a_{PbCl_2}	a_{PbO}	a_{PbCl_2}	
0.1	0.005	0.890	0.008	0.899	-11.80
0.2	0.010	0.765	0.020	0.796	-10.90
0.3	0.022	0.620	0.035	0.660	-9.40
0.4	0.045	0.440	0.065	0.475	-8.90
0.50	0.085	0.240	0.115	0.300	-6.60
0.60	0.160	0.110	0.200	0.150	-4.80
0.7	0.280	0.035	0.325	0.060	-2.90
0.8	0.450	0.010	0.480	0.018	-0.80
0.9	-	-	(0.760)*	(0.001)*	

* Extrapolated

** The uncertainty in the values of the partial molar heats of mixing is about ± 1.0 Kcal/mole.

The partial molar enthalpies of mixing for PbO, given in Table 3, have been calculated from the A-constants which are presented in Table 1, using the readily derived expression:

$$\Delta H_{\text{PbO}} = 46,132 (A - 0.2233) \quad (3)$$

These values are given in cal.mole⁻¹ and may be converted to S.I. units by multiplication with 4.184 Joules.

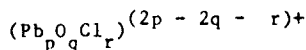
Activities of PbO in this system reported by Sugawara et al. (4) are in disagreement with the present results, particularly at high PbO contents. For solutions containing more than 80 mole % of PbO, the reported activities are greater than unity, which is thermodynamically impossible for the chosen reference states which were the same as in the present calculations. For compositions lower than 30 mole % PbO, there is better agreement with the present results, although the temperature dependences of the emf's differ.

Activity isotherms for the PbO and the PbCl₂ components are shown in Fig. 4. Activities calculated by Sugawara et al. (4) are also included for comparison.

DISCUSSION

The pronounced negative deviations from ideality shown by the activity data in Table 3 and by the strongly exothermic partial molar heats of mixing for PbO, are indicative of strong interactions between the solute ions in the PbO-PbCl₂ melts.

The result of such interactions could be the formation of complex oxychloride configurations of the general type,



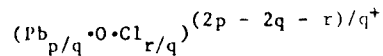
similar to the incongruently melting compounds 3PbCl₂·2PbO, PbCl₂·PbO, PbCl₂·2PbO and PbCl₂·4PbO, which have been identified as existing in a solid state within the phase diagram of the system (1-3).

Considering a solution which initially contains n₁ and n₂ moles of PbO and PbCl₂, respectively, it will be assumed that a complex forming reaction is taking place until equilibrium is reached.

If *a* is the fraction of the initial oxygen which has reacted and has been incorporated in the complex oxychloride, then the enthalpy change for the formation of the solution is given as:

$$\Delta H_m = n_1 a \Delta H_r^\circ \quad (4)$$

where ΔH° is the enthalpy change for the formation of one mole of oxychloride species containing one gram-atom of oxygen, such as in



The "reaction" part of the enthalpy of mixing is considered to be a major contribution to the total energy released during mixing, and any other secondary interactions between the solute atoms in the reacted system will not be taken into account.

The total entropy of mixing is considered to consist of two major contributions; the entropy for the formation of the amount of oxychloride complex present at equilibrium and the configurational contribution for the random mixing of the various species i present at equilibrium.

The total entropy of mixing may be written as:

$$\Delta S_m = n_1 \Delta S_r^\circ - R \sum_i n_i \ln N_i \quad (5)$$

where n_i and N_i are, respectively, the number of moles and the ionic fractions of species i present in the mixture at equilibrium.

Combination of equations (4) and (5) into the Gibbs-Helmholtz relationship yields the the Gibbs free energy of mixing as:

$$\Delta G_m = n_1 \Delta (\Delta H_r^\circ - T \Delta S_r^\circ) + RT \sum_i n_i \ln N_i \quad (6)$$

where

$$\Delta H_r^\circ - T \Delta S_r^\circ = -RT \ln K \quad (7)$$

K is the equilibrium constant for a given oxychloride formation reaction, which is specific to each system.

The expression for the activities of PbO is obtained by partial differentiation of equation (7) with respect to n_1 at constant n_2 and under the restriction that:

$$\sum N_i = 1, \text{ at equilibrium} \quad (8)$$

The final equation takes the form:

$$\ln a_{\text{PbO}} = \sum_i \left[\ln N_i \left(\frac{dn_i}{dn_1} \right)_{n_2} \right] - \left[n_i \left(\frac{da}{dn_1} \right)_{n_2} + a \right] \ln K \quad (9)$$

It is readily seen that the expression for the activity of PbO contains the equilibrium constant K as the only adjustable parameter

The solution of equation (9) is readily found by considering the mass balances representing various reaction mechanisms. Irrespective of the scheme chosen, the expression for the activity is found to have the following form:

$$a_{\text{PbO}} = (N_{\text{Pb}^{2+}} \cdot N_{\text{O}^{2-}})_{\text{at equil.}} \quad (10)$$

In equation (10), $N_{\text{Pb}^{2+}}$ and $N_{\text{O}^{2-}}$ are respectively the ionic fractions for Pb^{2+} and O^{2-} in a molten mixture of PbO and PbCl_2 which has reacted internally in accordance with a specific reaction mechanism and has reached a state of equilibrium.

From similar considerations it may be shown that the activity of PbCl_2 is given by the expression:

$$a_{\text{PbCl}_2} = (N_{\text{Pb}^{2+}} \cdot N_{\text{Cl}^-}^2)_{\text{at equil.}} \quad (11)$$

For the PbO- PbCl_2 solutions several reaction mechanisms have been considered, such as the formation of the complex oxychlorides, Pb_2OCl^+ , Pb_2O_2^+ , $\text{PbCl}_2\text{O}_2^-$, as well as the compositions representing the various incongruently melting compounds mentioned earlier.

From all these possible schemes the experimental data appear to be best represented by the reaction:



The mass balance representing equation (12) is given in Table 4. The equilibrium constant is written as:

$$K = \frac{N_{\text{Pb}_2\text{OCl}^+}}{N_{\text{Pb}^{2+}}^2 \cdot N_{\text{O}^{2-}} \cdot N_{\text{Cl}^-}} \quad (13)$$

for which the expressions for the ionic fractions are given in Table 4.

Degrees of reaction α have been estimated for various selected K values from equation (13), and are given in Table 5.

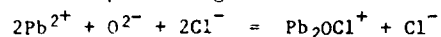
From the equilibrium ion-fractions given in Table 4, the activities for PbO and PbCl_2 are readily calculated as:

$$a_{\text{PbO}} = \frac{1 - 2\alpha X_1}{1 - \alpha X_1} \cdot \frac{X_1(1 - \alpha)}{1 + X_2 - 2\alpha X_1} \quad (14)$$

and

TABLE 4

Ionic Composition of the PbO-PbCl₂ Molten Solutions
Representing the Reaction



UNREACTED MELT			Melt composition when reaction has reached equilibrium	
Compo- sition	No of moles	Mole fractions	Mole numbers at equilibrium	Ion fractions
PbO	n_1	X_1	$n_{\text{Pb}^{2+}} = n_1 + n_2 - 2an_1$	$N_{\text{Pb}^{2+}} = \frac{1 - 2aX_1}{1 - aX_1}$
PbCl ₂	n_2	X_2	$n_{\text{Pb}_2\text{OCl}^{+}} = an_1$	$N_{\text{Pb}_2\text{OCl}^{+}} = \frac{aX_1}{1 - aX_1}$
			$n_{\text{O}^{2-}} = n_1(1 - a)$	$N_{\text{O}^{2-}} = \frac{X_1(1 - a)}{1 + X_2 - 2aX_1}$
			$n_{\text{Cl}^{-}} = 2n_2 - an_1$	$N_{\text{Cl}^{-}} = \frac{2X_2 - aX_1}{1 + X_2 - 2aX_1}$

$$a_{\text{PbCl}_2} = \frac{1 - 2aX_1}{1 - aX_1} \cdot \left| \frac{2X_2 - aX_1}{1 + X_2 - 2aX_1} \right|^2 \quad (15)$$

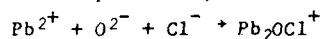
where X_1 and X_2 in these expressions are respectively the primary mole fractions of PbO and PbCl₂ in the "unreacted" mixture.

The activity isotherms shown in Fig. 4 were calculated from equations (14) and (15) (solid lines), while the points are experimental. The 1023 isotherm was calculated from the a -values corresponding to $K = 15$. The isotherm at 1123K was calculated from the a -values based on $K = 10$.

It should be noticed that at constant composition the activity of a_{PbO} increases as K decreases.

TABLE 5

Dependence of Degree of Reaction α on the Equilibrium Constant, K ,
at Various Compositions, for the Reaction



K	1	10	15	100	1,000	10,000	∞
x_{PbO}	α	α	α	α	α	α	α
0.0	1	1	1	1	1	1	1
0.1	0.32183	0.81296	0.86579	0.97676	0.99762	0.99976	1
0.2	0.30941	0.78486	0.84143	0.97038	0.99691	0.99969	1
0.3	0.29576	0.74659	0.80520	0.95713	0.99525	0.99952	1
0.4	0.28035	0.69702	0.75367	0.92370	0.98886	0.99881	1
0.5	0.26216	0.63809	0.68849	0.84653	0.93307	0.96991	1
0.6	0.23926	0.57257	0.61545	0.74321	0.80369	0.82380	0.83333
0.7	0.20976	0.49620	0.53292	0.64094	0.69062	0.70674	0.7142857
0.8	0.16765	0.37906	0.40544	0.47618	0.49709	0.49970	0.50000
0.9	0.09229	0.19302	0.20171	0.21883	0.22188	0.22219	0.22222
1.0	0	0	0	0	0	0	0

The integral enthalpy of mixing for the system were calculated from the expression:

$$\Delta H_m = X_1 \bar{\Delta H}_{\text{PbO}} + X_2 \bar{\Delta H}_{\text{PbCl}_2} \quad (16)$$

For the calculation the partial molar enthalpies of mixing for PbCl_2 were obtained from the partial molar enthalpies of mixing of PbO using the Gibbs-Dubem relationship.

The results of these calculations are given in Fig. 5. On this graph points are experimental, while the dotted line has been derived from equation (4) written in the form:

$$\Delta H_m = aX_1 \Delta H_r^\circ \quad (17)$$

which represents the enthalpy of mixing per mole of solution.

For the calculation the degrees of reaction, based on reaction (12) for $K = 10$, have been used. The value for the ΔH_r° term which must be common for all compositions is $-13,500 \text{ cal. mole}^{-1}$.

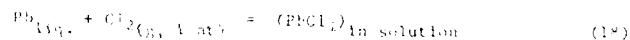
Entropies of mixing, calculated from the enthalpies of mixing and the corresponding Gibbs free energies, are plotted in Fig. 6 as a function of composition. Here the solid line 1 represents the experimental values for the total integral entropy of mixing, while the points are calculated from equation (5), as applied to reaction (12), for $K = 10$. For this calculation the a -values that correspond to $K = 10$ and a common value of $\Delta S_r = -7.3$ e.u. were found to satisfy the entire composition range. Curve 2 in Fig. 6 represents only the configurational component of the total integral entropy of mixing.

Considering the uncertainty which is always present when calculating entropies, the agreement between the experimental and the theoretical entropies of mixing and, particularly, the correct prediction of their concentration dependence, indicates the validity of the present thermodynamic model.

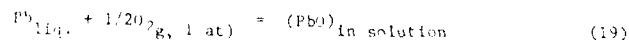
ELECTROLYTIC BEHAVIOUR OF THE PbO-PbCl₂ MELTS

From equation (2) and its equivalent for PbCl₂, it is possible to calculate the reversible potentials for the electrochemical separation of Pb and O₂, or of Pb and Cl₂, from a molten solution of PbO and PbCl₂.

For the reactions:



and



the reversible electrode potentials at 850°K and at 1023°K, respectively, were calculated using the previously derived activity values, and the standard potentials given in Table 2.

The results of these calculations are plotted in Fig. 7. Because of the wide potential separation, the electrolysis of PbO-PbCl₂ are almost independent of melt composition and consequently, lead chloride melts may be de-oxygenated by pre-electrolysis.

Fused salt electrolysis of PbO dissolved in a PbCl₂ solvent is expected to produce as cathodic and anodic products lead and oxygen, respectively.

CONCLUSIONS

The thermodynamic properties of the PbO-PbCl₂ molten solutions show pronounced negative deviations from ideality which indicate strong interactions between the ionic species in solution. To

explain this behaviour and to predict the concentration dependence of the activities of PbO and of PbCl_2 of the enthalpies and of the entropies of mixing, a thermodynamic model based on the presence of strong complex oxychloride species has been developed. In this model the concentration dependence of the activities at each temperature requires the equilibrium constant K as the only adjustable parameter. The concentration dependence of the enthalpy of mixing is predicted from equation (17) in which the only other adjustable parameter is the term ΔH_F° , which, however, is constant over the entire composition range. The calculation of the entropies of mixing does not require any other adjustable parameters. K and ΔS_F° are related by equation (7) and ΔS_F° cannot be adjusted independently.

It is shown that in non-ideal solutions the activity of any component $A_x B_y$ is expressed by the simple relationship:

$$a_{A_x B_y} = (N_A^{x+} \cdot N_B^{y-})_{\text{equilibrium}}$$

In this expression N_A^{x+} and N_B^{y-} are the respective cation and anion fractions in a solution which has the ionic composition corresponding to a specific reaction mechanism at equilibrium.

Thus Temkin's rule (16) is of general validity to ideal and non-ideal solutions, providing that the correct reaction mechanism and dissociation schemes are formulated.

In this treatment non-ideality is attributed to changes in the composition of a solution as the result of complex forming reactions. The theory does not account for secondary interactions between the reaction products. Equilibrium ion fractions of the assumed ionic forms are used throughout, the basic assumption being that the reactivity of the simple ionic species like Pb^{2+} , O^{2-} or Cl^- has been satisfied through the formation of the complex and that all other interactions are not too significant.

Under such circumstances, the equilibrium constant K is expected to be composition independent and to depend only on temperature over the composition range within which the above assumptions are valid.

REFERENCES

1. M. Renauld, E. Poidatz, F.E. Choix, Can. J. Chem., 2016-2020, 1970.
2. R. Ruer, Z. Anorg. Chem., 29, 372, 1906.
3. A. Varoni, Atti. Accad. Naz. Lincei, Rend. Classe Sci. Fis. Nat., 20, 384, 1934.

4. H. Sugawara, K. Nagata, K.S. Goto, *Met. Trans.* 8B, 511-514, 1977.
5. G.G. Charette, S.N. Flengas, *J. Electrochem. Soc.*, 115, 796-804, 1968.
6. K. Kiukkola, C. Wagner, *J. Electrochem. Soc.*, 104, 308-316, and 379-387, 1957.
7. C.B. Alcock, T.N. Belford, *Trans. Faraday Soc.*, 60, 822, 1964.
8. J.F. Elliott, M. Gleiser, *Thermochemistry for Steel Making*, vol. 1, 1960, Addison-Wesley.
9. R.A. Rapp, *Trans. Am. Inst. Min. Engrs.*, 227, 371-374, 1965.
10. B.C.H. Steele, C.B. Alcock, *Trans. Am. Inst. Min. Engrs.*, 233, 1359-1367, 1965.
11. B.C.H. Steele, "Electromotive Force Measurements in High Temperature Systems", Ed., C.B. Alcock, pp.3-27, 1968, Elsevier, New York.
12. A. Leung, W.T. Thompson, *Can. Met. Quart.*, 15, 227-233, 1976.
13. M. Iwase, K. Fujimura, T. Mori, *Trans. JIM*, 19, 377-384, 1964.
14. Y. Matsushita, K. Goto, *J. Fac. Eng. Tokyo Univ.*, Ser. B, 27, 217-280, 1964.
15. D.R. Gaskell, *Intro. Metall. Therm.*, 2nd Ed., 1981, McGraw Hill, New York, p.327.
16. M. Temkin, *J. Phys. Chem. USSR*, 20, 105-110, 1946.

ACKNOWLEDGEMENTS

The authors acknowledge the valuable contribution by Peter King to the initial part of this work. The financial assistance by the Natural Sciences and Engineering Research Council of Canada is also gratefully acknowledged.

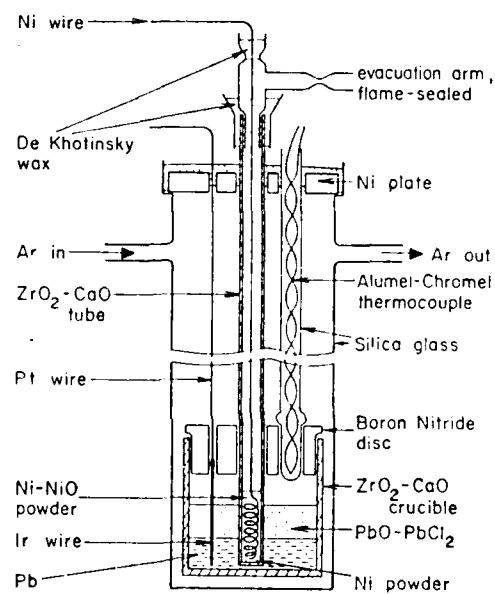


Fig. 1. Schematic drawing of the experimental emf cell.

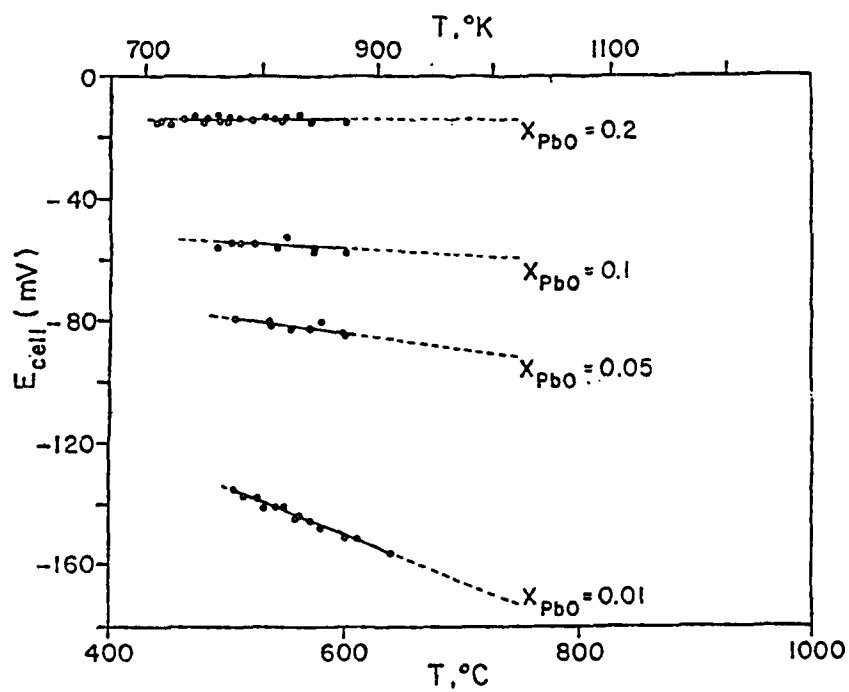


Fig. 2. Temperature dependence of the cell emf for various PbO mole fractions.

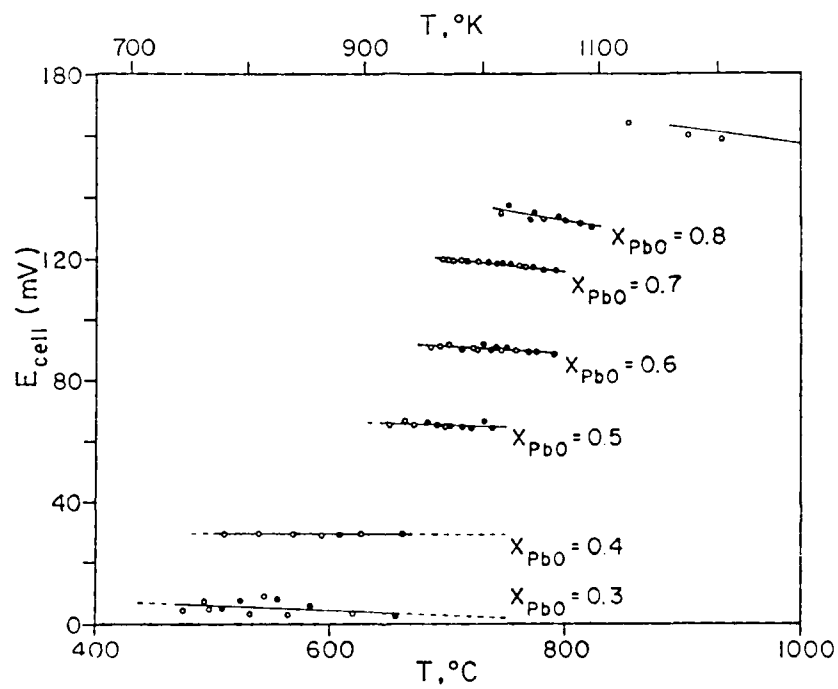


Fig. 3. Temperature dependence of the cell emf for various PbO mole fractions.

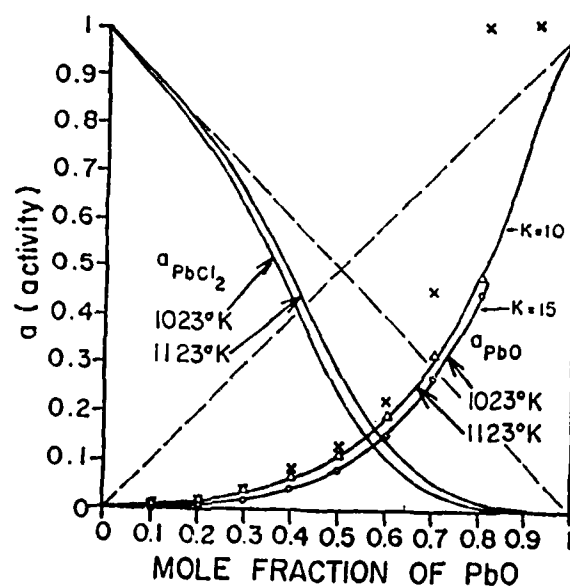


Fig. 4. Activity isotherms for PbO and PbCl_2 at 1023°K and 1123°K , respectively. Points (circles and triangles) are from experimental work. Solid lines are calculated from equations (10) and (11). x's are experimental activity data for PbO reported by Sugawara et al. (4).

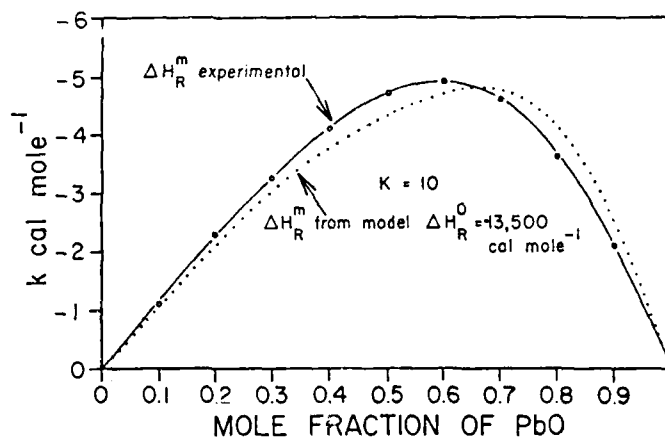


Fig. 5. Plot of the integral heat of mixing as a function of the PbO mole fraction in the PbO-PbCl₂ melts. Dotted line has been calculated from equation (17) for $K = 10$.

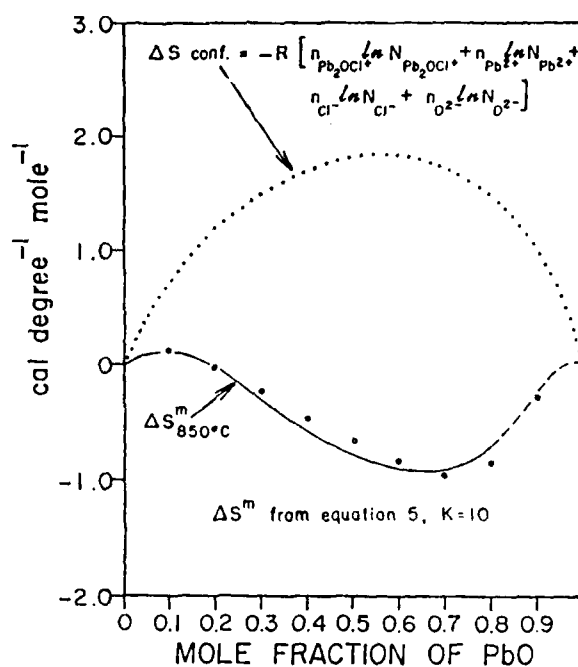


Fig. 6. Integral molar entropies of mixing plotted as a function of the PbO content in the PbO-PbCl₂ melts. Solid line represents the total entropy calculated from equation (5) for K = 10. Points are from the experimental results. Dotted line represents the configurational component of the total entropy.

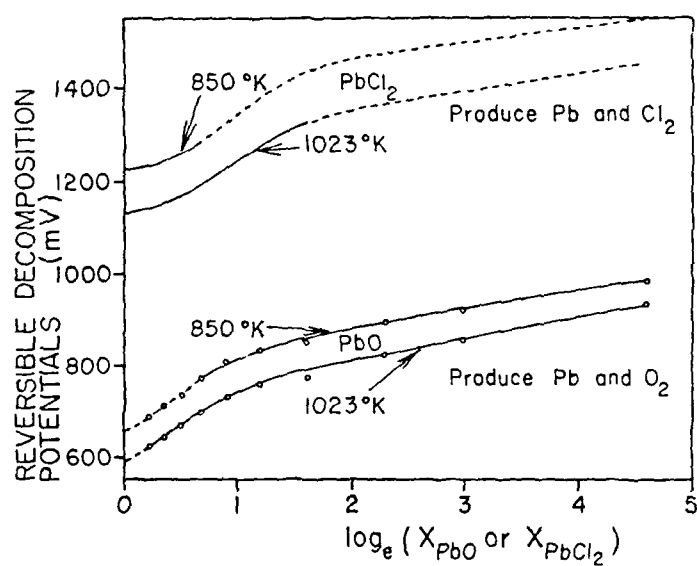


Fig. 7. Reversible decomposition potentials for PbO and PbCl₂ in the PbO-PbCl₂ melts at 850°K and 1023°K, respectively.

CONDENSED AND GASEOUS PRODUCTS CHEMISTRY IN THE COMBUSTION AND GASIFICATION OF HIGH-SULFUR COAL

S. Sinha, K. Natesan, and M. Blander

Argonne National Laboratory
9700 South Cass Avenue
Argonne, IL 60439

ABSTRACT

A recently developed computer program, based on geometric programming, is used to calculate condensed and gaseous products chemistry in the combustion or conversion of high-sulfur Illinois #6 coal. Under 30% air-excess and 30% air-deficient conditions, product chemistries were calculated as a function of temperature. For the temperature ranges of 1800-1100 K, condensed phases are saturated with solid silica, and the major "Na" and "Cl" bearing gaseous species are NaCl and HCl. The concentration of sulfates (under oxidizing conditions) or sulfides (under reducing conditions) in the silica-saturated molten silicate solutions increases progressively with a decrease in temperature. The liquid condensates appear to be more complex than believed, and "hot corrosion" by silicates could be important.

INTRODUCTION

Combustion and gasification of coal is of considerable importance in industrial power generation. The presence of elements, such as, for example, S, Na, and Cl, in relatively small amounts in coal, often leads to the formation of thin layers of molten condensates, and results in accelerated deterioration of downstream components in these industrial processes.

Some experimental studies of the chemistry of these industrial processes are available. Unfortunately, the global chemistry of all the gaseous and condensed products are not available because of the difficulties inherent in performing calculations in very complex systems. Comprehensive understanding of all the chemistry is essential in order to explain and predict the corrosive behavior of the combustion and gasification products. The present work describes the methods we are developing to calculate the total chemistry of coal combustion and gasification systems.

Typically, in such systems, one must consider a large number of elements, 13-15, which form as many as 300-500 species distributed between several condensed phases and a gaseous phase. Furthermore, nonequilibrium conditions are possible due to kinetic factors. Treatment of such a complex system poses many difficulties for researchers of this area.

In the present work, we shall discuss the use of a recently developed computer program, based on geometric programming, to calculate the chemistry of this system. This program is capable of handling up to 300 species, including 150 condensed phases and several solution phases. As a first approximation in this initial paper, the solution phase will be assumed to be ideal and, fortuitously, the condensed phase constituents can be chosen in a manner which makes this a reasonable approximation. We shall calculate the composition of all the equilibrium products as a function of temperature for the temperature range of 1800-1100 K (1527-827°C). In addition, we shall incorporate an expected nonequilibrium condition to illustrate the feasibility of using such options in our methods. Results are presented as a function of decreasing temperature to simulate the condition in which the hot combustion or gasification products are cooling as they pass through downstream components away from the hot zone.

CALCULATIONAL PLAN

The computer program is based on an unique algorithm which utilizes geometric programming (1). The program is linked to a critically analyzed data base consisting of the thermodynamic properties of about 1800 species (2). We shall not describe the details here because of space limitations, but the program is capable of handling large chemical systems.

To illustrate our method, high-sulfur Illinois #6 coal was chosen for the present work. Table 1 gives the composition of this coal which has 3.41 wt% S. The theoretical oxygen requirement for combustion is the amount of oxygen required to convert the carbon, sulfur, and hydrogen to carbon-dioxide, sulfur-dioxide, and water, respectively, minus the free oxygen present in coal. In our calculations, 30% excess and 30% deficient O₂ as dry air is supplied to deduce the chemistries for oxidizing and reducing conditions, respectively. Table 2 shows the selected species in the solution phases under oxidizing and reducing conditions. These solution phases are chosen by performing several trial calculations, with several possible combinations of components of solution phases, based on a knowledge of solution chemistry and the tendency of components to form. Ideal solutions are assumed for the present illustrative calculations. Solution components were chosen in a manner which best illustrates the chemical properties and simultaneously formed solutions that do not deviate greatly from ideality. This procedure was a reasonably good approximation for most of the temperatures for which we

performed calculations. Nonideality of the solutions will be considered in future work.

RESULTS AND DISCUSSIONS

Oxidizing Conditions: Figures 1 and 2 and Table 3 show the results for oxidizing conditions. Of the 120 gaseous species in the results of these calculations, only the most important species are shown in Figure 1. Under equilibrium conditions, very sharp changes in the partial pressures of several species occur around 1390 K in Figure 1 (continuous lines). This is the temperature where the glassy $\text{Al}_2\text{O}_3\cdot\text{Na}_2\text{O}\cdot 6\text{SiO}_2(\text{s})$ forms by reaction of solids with the solution phase. Figure 2 shows that the solution phase disappears at this temperature (at about 1390 K) and $\text{Na}_2\text{SO}_4(\text{s})$ or an Na_2SO_4 rich liquid solution does not form under equilibrium conditions to temperatures as low as 1100 K (Table 3). However, in real systems the formation of glassy $\text{Al}_2\text{O}_3\cdot\text{Na}_2\text{O}\cdot 6\text{SiO}_2(\text{s})$ from two or more condensed phases is probably very slow because the two phases have to be in contact to react. Hence calculations were repeated for the non-equilibrium case where the glassy $\text{Al}_2\text{O}_3\cdot\text{Na}_2\text{O}\cdot 6\text{SiO}_2(\text{s})$ does not form. Such a case simulates one kinetic constraint in a realistic practical environment. Figure 2 shows that, under this constraint, the corrosive solution phase extends to temperatures as low as 1160 K.

The major gaseous carriers of sodium and chlorine are NaCl and HCl under all conditions (Figure 1). Under nonequilibrium conditions, the concentration of NaCl(g) below 1390 K is higher than those under equilibrium conditions. The relative concentrations of $\text{Na}_2\text{O}\cdot 2\text{SiO}_2(\text{l})$ and $\text{Na}_2\text{SO}_4(\text{l})$ in the solution phase (Figure 2) vary drastically as the temperature of the solution phase changes from 1800 K to 1100 K. The solution is high in $\text{Na}_2\text{O}\cdot 2\text{SiO}_2(\text{l})$ and $\text{FeO}\cdot\text{SiO}_2(\text{l})$ above 1600 K; at 1250 K the solution phase is largely $\text{Na}_2\text{SO}_4(\text{l})$. Within the temperature range of 1600 K to 1160 K (under nonequilibrium conditions), the concentration of $\text{Na}_2\text{SO}_4(\text{l})$ increases from a mole fraction of less than 0.01 to almost 1, with a corresponding decrease of $\text{Na}_2\text{O}\cdot 2\text{SiO}_2(\text{l})$ to less than 0.01. The concentration of NaCl(l) stays around 0.001 below 1350 K. It may be noted that the condensed phases are saturated with $\text{SiO}_2(\text{s})$ at all temperatures. Because of the assumption of ideal solution of species in the solution phase, the exact values of concentrations in the real nonideal solution phase is likely to be somewhat different. The concentrations are least accurate from about 1350-1500 K because of the deviations from ideality expected. However, the general nature of results at the temperatures where $\text{Na}_2\text{O}\cdot 2\text{SiO}_2(\text{l})$ or $\text{Na}_2\text{SO}_4(\text{l})$ is in dilute solution will be very similar in both ideal and nonideal solution phases. Consequently, the general pattern of variations in the concentrations of silicates and sulfates as a function of temperature will be similar to Figure 2 in practical cases.

These results present an approximate, but general, behavior of solution phases under oxidizing conditions; the solution phase becomes progressively more concentrated in $\text{Na}_2\text{SO}_4(\text{l})$ as the temperature of the gaseous and condensed phase decreases from 1800 K (1323°C) to around 1200 K (923°C). The compositional changes reflect differences in the corrosive behavior. The silicate liquid may be even more corrosive than sulfates because of the high temperatures and because the solubility of protective oxide coatings of metals of construction in combustion systems is likely to be higher in silicates than in sulfates. Our results make it clear that for coal combustion, the corrosive liquids are not just simple sulfates, but are much more complex liquids than have been considered heretofore.

Reducing Conditions: Results of calculations under reducing conditions are presented in Figure 3 and Table 4. Again, only the most important gaseous species are shown in Figure 3. Calculations are repeated for nonequilibrium conditions where the glassy $\text{Al}_2\text{O}_3\cdot\text{Na}_2\text{O}\cdot 6\text{SiO}_2(\text{s})$ is not allowed to form below 1390 K.

The condensed phases are saturated with $\text{SiO}_2(\text{s})$ at all temperatures (Table 4). The partial pressure of $\text{NaCl}(\text{g})$ in the gaseous phases at 1100 K (923°C) is almost one order of magnitude higher under reducing conditions (Figure 3) than for oxidizing conditions (Figure 1). At high temperatures the solution phase is largely $\text{FeO}\cdot\text{SiO}_2(\text{l})$ and $\text{Na}_2\text{O}\cdot 2\text{SiO}_2(\text{l})$ and is largely $\text{FeS}(\text{l})$ at low temperatures. Considerable amounts of S as $\text{FeS}(\text{l})$ or $\text{Na}_2\text{S}(\text{l})$ are present in the liquid phase at all temperatures. The concentration of S bearing species under reducing conditions in the solution phase is much higher (0.1 at 1800 K) than the S bearing species $\text{Na}_2\text{SO}_4(\text{l})$ (less than 0.001 at 1800 K) under oxidizing conditions. At 1300 K, the concentration of S as $\text{FeS}(\text{l})$ in the solution phase is 0.33 under nonequilibrium conditions. For 1800-1400 K, the concentration of "Fe" in the solution phase increases with a decrease in temperatures. The solution phase is present below 1100 K (923°C) under nonequilibrium conditions, and even under equilibrium conditions, the solution phase exists down to temperatures as low as 1260 K (987°C).

SUMMARY AND CONCLUSIONS

Corrosive molten condensates from the combustion of coal under oxidizing conditions are much more complex than has been considered previously. Mixtures of silicates and sulfates are probable; these could be more corrosive than sulfates. Under reducing conditions, molten sulfides appear to be present down to very low temperatures. Such chemistries would have to be dealt with in coal conversion processes. Thus, our preliminary calculations provide us with the ability to calculate the global chemistry in the oxidation of coal. Further work, which accurately represents the complex nonideal solutions, which includes silicates, and

which incorporates kinetic effects on the chemistry will greatly enhance our ability to analyze the global chemistry in coal combustion and conversion and aid in developing methods for minimizing corrosion.

ACKNOWLEDGMENTS

This work is supported by the U.S. Department of Energy, Division of Materials Science, Office of Energy Sciences, under Contract W-31-109-ENG-38.

REFERENCES

1. M. Minkoff, R. Land, and M. Blander, "Computation of Chemical Equilibria Via Primal Geometric Programming," CALPHAD XI Conf., Argonne National Laboratory, May 16-20, 1982.
2. R. Kumar, M.-L. Saboungi, and M. Blander, unpublished information.

Table 1. The Composition of High Sulfur Illinois #6 Coal
Used For the Present Work

	<u>Wt %</u>		<u>Ash</u>
C	60.15	SiO ₂	45.57
H	4.25	Fe ₂ O ₃	15.80
N	0.97	Al ₂ O ₃	17.99
S	3.41	CaO	6.88
Cl	0.05	MgO	1.09
H ₂ O	10.54	SO ₃	4.22
O	7.33	Na ₂ O	4.84
Ash	13.30		

Table 2. The Solution Phases for the Oxidizing and Reducing Conditions

<u>Solution Phase for Oxidizing Conditions</u>	<u>Solution Phase for Reducing Conditions</u>
1. Na ₂ O·2SiO ₂ (l)	1. Na ₂ O·2SiO ₂ (l)
2. Na ₂ SO ₄ (l)	2. Ni ₂ O·SiO ₂ (l)
3. NaCl(l)	2. 'FeO·SiO ₂ '(l)
4. Na ₂ S(l)	4. Na ₂ S(l) or FeS(l)
5. 'FeO·SiO ₂ '(l)	

Table 3. Approximate Amounts and Temperature Ranges of Stability of Solid Condensed Phases Under Oxidizing Conditions*

	<u>1800 K</u>	<u>1400 K</u>	<u>1100 K</u>
SiO ₂ (s)	75.0	68.5	<u>52.7</u> 52.2
Al ₂ O ₃ ·Na ₂ O·6SiO ₂ (s)			<u>1.7</u> 0
Na ₂ SO ₄ (s)			<u>0</u> 7.4
Al ₂ O ₃ ·2CaO·SiO ₂ (s)	8.1	8.3	
CaSO ₄ (s)			<u>13.3</u> 11.4
Al ₂ O ₃ ·SiO ₂ (s)			<u>17.9</u> 16.7
3Al ₂ O ₃ ·2SiO ₂ (s)	3.9	5.4	
Al ₂ O ₃ ·MgO(s)	4.2		
MgO·SiO ₂ (s)		4.2	<u>3.4</u> 2.9
Fe ₃ O ₄ (s)	8.8		
Fe ₂ O ₃ (s)		13.6	<u>11.0</u> 9.4

*The numerical values are % moles of the corresponding species in the mixture of all the condensed phases excluding the solution phase. Equilibrium and nonequilibrium (see text) values at 1100 K are above and below the lines, respectively.

Table 4. Approximate Amounts and Temperature Ranges of Stability of Solid Condensed Phases Under Reducing Conditions*

	<u>1800 K</u>	<u>1400 K</u>	<u>1100 K</u>
$\text{SiO}_2(\text{s})$	77.0	79.2	<u>28.5</u> 56.2
$\text{Al}_2\text{O}_3 \cdot \text{Na}_2\text{O} \cdot 6\text{SiO}_2(\text{s})$			<u>13.7</u> 0
$\text{FeS}(\text{s})$			<u>35.0</u> 15.2
$\text{Al}_2\text{O}_3 \cdot \text{SiO}_2(\text{s})$			<u>6.8</u> 17.0
$3\text{Al}_2\text{O}_3 \cdot 2\text{SiO}_2(\text{s})$	9.0	8.2	
$\text{Al}_2\text{O}_3 \cdot 2\text{CaO} \cdot \text{SiO}_2(\text{s})$	14.0	12.6	<u>10.6</u> 8.8
$\text{MgO} \cdot \text{SiO}_2(\text{s})$			<u>5.5</u> 2.8
$\text{Al}_2\text{O}_3 \cdot \text{FeO}(\text{s})$			

*The numerical values are % moles of the corresponding species in the mixture of all the condensed phases excluding the solution phase. Equilibrium and nonequilibrium (see text) values at 1100 K are above and below the lines, respectively.

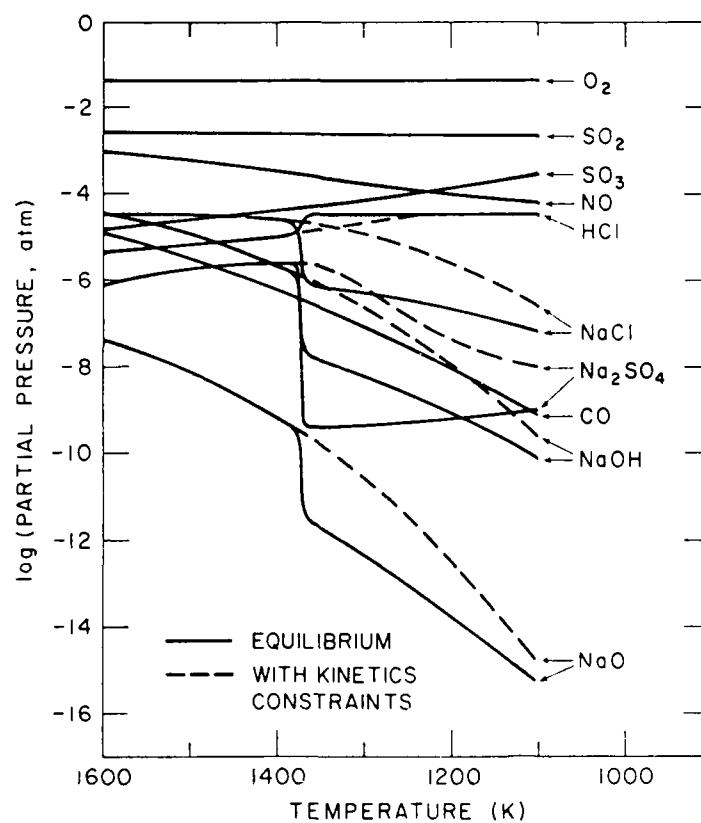


Figure 1. Partial Pressures of Important Gaseous Species During the Combustion of Illinois #6 Coal. 30% Excess Oxygen is Used for the Combustion.

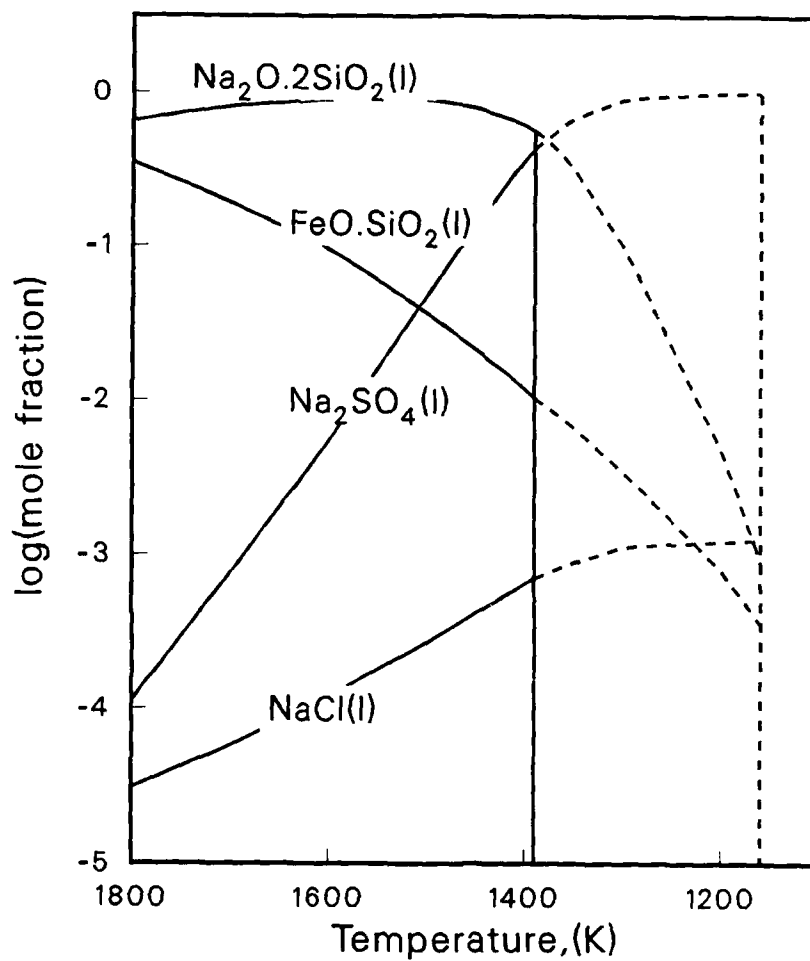


Figure 2. Composition of the Solution Phase Under Oxidizing Conditions. Continuous Line (—) and the Dotted Lines (- - -) Represent the Compositions Corresponding to Equilibrium and Nonequilibrium Conditions, Respectively. The Concentration of $\text{Na}_2\text{S}(\text{l})$ is Less Than 10^{-8} at All Temperatures.

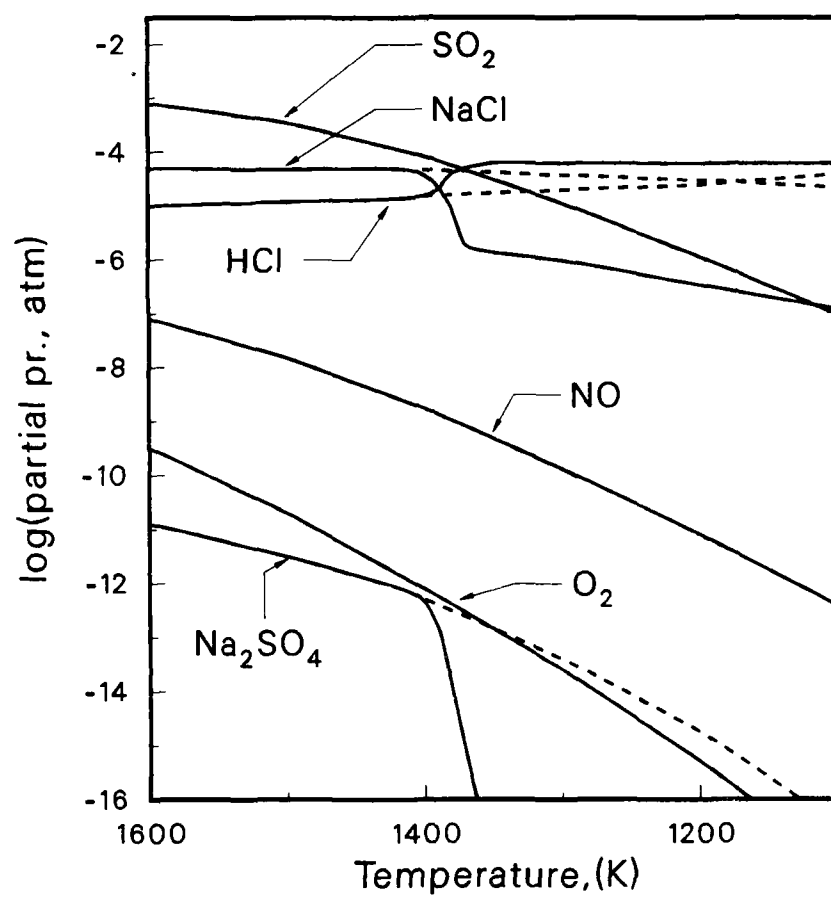


Figure 3. Partial Pressures of Important Gaseous Species During the Gasification of Illinois #6 Coal. 30% Deficient Oxygen is Used in This Case.

A MODEL AND DATA FOR -
FREEZING TEMPERATURE LOWERING OF 4 TO 7
COMPONENT MOLTEN SALT MIXTURES

H. William Prengle, Jr. and Sandeep P. Shah
Chemical Engineering Department
Wayne E. Wentworth
Chemistry Department

University of Houston, Houston, Texas 77004 USA

ABSTRACT

Research was conducted to find molten salt mixtures, compatible with alkali metal sulfates, as media for ammonium hydrogen sulfate reactions. Mixtures of mono- and divalent metal sulfates having freezing temperatures of ~ 550 K were sought, pure sulfates melt at 1000 to 1300 K. Nine divalent metal sulfates with three alkali metal sulfates were used.

For interpretation of experimental data a thermodynamic model was developed, the key parameter being the "excess entropy-enthalpy function", positive values of the excess function produce greatest effect. Results gave for 4-components 640 K; for 5-components 631 K; for 6-components 596 K; and 7-components 593 K.

INTRODUCTION

The Ammonium-Hydrogen-Sulfate (AHS) energy storage cycle was proposed 11 years ago by Wentworth and Chen (1), followed by process configurations proposed by Prengle and coworkers (2,3). The duplex modification of the cycle proposed by Prengle in 1984 is based on conducting the two endothermic chemical reactions (4) in a compatible molten salt (CMS) mixture. The first reaction (450-600 K) produces NH_3 , H_2O , and $\text{S}_2\text{O}_7^{2-}$ by reaction of ammonium hydrogen sulfate with an alkali metal sulfate, and the second (650-950 K) produces SO_3 by decomposition of the pyrosulfate. The duplex version of the cycle contemplates using the sensible energy in the excess CMS immediately; whereas the exothermic recombination of the three product molecules would be accomplished for later use of the stored energy.

The research described in this paper concerns the search for CMS mixtures of alkali metal, alkaline earth, and transition metal sulfates which could be used as reaction media for the two reaction steps mentioned above. Specifically, the objective of the work was to discover mixtures of mono- and divalent metal sulfates with freezing temperatures of ~ 550 K, a significant lowering as the pure components melt

in the range of 1000-1300 K.

LITERATURE SEARCH

Data on thirty-two sulfate eutectic mixtures were obtained from the literature (5,6,7), including the alkali metal components Li, Na, K, the alkaline earths Mg, Ca, Ba, and the transition metals Zn, Cu, Cd, Pb, Co and Mn. It was hoped that some preliminary answers would be revealed to the three questions: -the possible amount of freezing temperature lowering, -the effect of specific metal ions, and -the number required to get 500-600 degree lowering.

By analogy with the thermodynamic mixing property, a preliminary lowering criterion can be defined. For example, for a local minimum enthalpy, the mixing property, ΔH^M , will be,

$$\Delta H^M = \sum X_i (\bar{H}_i - H_i) \quad (1)$$

where X_i , \bar{H}_i , H_i , are the mole fraction, partial mole enthalpy, and pure component enthalpy respectively. Similarly, for a molten salt eutectic mixture freezing temperature will be,

$$\Delta T_f = \sum X_i (T_f - T_{fi}) \quad (2)$$

$$\text{and,} \quad \sum X_i (T_f - T_{fi}) / \Delta T_f = \sum X_i \xi_i = 1 \quad (3)$$

each term in the series representing the fraction lowering, ξ_i , of the freezing temperature for a given component. Using this method of analysis, Table 1 presents the results for mixtures of alkali metal and alkaline earth sulfates, indicating that in a preliminary way Li^+ had the greatest effect, K^+ was next highest, and Na^+ and Ba^{+2} were lowest.

The remaining eighteen mixtures of alkali metal sulfates with Group IB, IIB and VIB, VIIB and VIII were analyzed similarly. As a preliminary guide to further experimental work, the final ranking of the components, based on all thirty-two mixtures, in descending order with some overlap was,

$$\xi(\text{Li}) > \xi(\text{K}) > \xi(\text{Zn}) > \xi(\text{Mg})$$

$$\xi(\text{Pb}) > \xi(\text{Cd}) > \xi(\text{Ca}) > \xi(\text{Na}) > \xi(\text{Ba})$$

$$\xi(\text{Cu}) > \xi(\text{Co}) > \xi(\text{Mn})$$

Table 1 - ξ_i Contributions of Alkali Metal and Alkaline Earths

Mixture	$\xi_a(\text{Li})$	$\xi_b(\text{Na})$	$\xi_c(\text{K})$	$\xi_d(\text{Mg})$	$\xi_e(\text{Ca})$	$\xi_f(\text{Ba})$
L1	0.636	0.364	-	-	-	-
L2	0.748	-	0.2523	-	-	-
L3	-	0.345	0.655	-	-	-
L4	0.744	0.084	0.172	-	-	-
Conclusion: $\xi_a > \xi_c > \xi_b$						
L12	-	-	0.623	0.377	-	-
L8	-	-	0.482	-	0.518	-
L7	-	-	0.520	-	-	0.480
L20	0.657	-	-	0.343	-	-
L17	0.687	-	-	-	0.313	-
L16	0.502	-	-	-	-	0.498
L28	-	-	0.483	-	0.392	0.125
L30	-	-	0.186	0.748	0.066	-
L29	-	0.255	-	-	0.585	0.160
L32	-	0.320	0.334	0.342	-	-
Conclusion: $\xi_a > \xi_c > \xi_d > \xi_e > \xi_b > \xi_f$						

EXPERIMENTAL

The search to find the desired 550 K freezing temperature mixture(s) resulted in measurements on 45 four-seven component mixtures of Li^+ , Na^+ , K^+ sulfates with Mg^{+2} , Ca^{+2} , Ba^{+2} alkaline earth sulfates, and seven transition metal sulfates, Cd^{+2} , Co^{+2} , Cr^{+2} , Cu^{+2} , Mn^{+2} , Pb^{+2} , and Zn^{+2} . The sulfates used were reagent grade of 99% purity. Mixtures of known composition were made up, melted, and held in liquid phases for ~ 12 hours to insure ionic equilibrium, prior to determination of the cooling curve by electrical conductivity.

Figure 1 displays a typical conductivity-temperature plot, as $\ln \lambda$ vs. $1/T$, indicating an observed hysteresis cooling-heating curve. Since primary interest is in the occurrence of solidification from the liquid phase, the values of T_o and T_c were taken as more meaningful to the objectives of the project. Simultaneously the cooling curve derivative was determined and recorded electronically, displayed in Figure 2, permitting a more precise determination of the difference $\Delta T = T_o - T_c$. This difference was used as a guide for successive estimation of new compositions closer to the eutectic point. Details of the equipment

used are presented by Shah (8).

T_f - LOWERING MODEL

As the experimental work progressed it was apparent that a model for calculation of the excess entropy and enthalpy was needed to guide the composition choices, a criterion more precise than the ξ_i ordering. Consider the T-S loop cycle shown in Figure 3, starting with the pure components in the solid phase of a eutectic mixture. As the solid phase is heterogeneous a generalized composition dependent structure is not possible; instead the pure components were chosen arbitrarily as the starting point. Progressing around the cycle, points 1 to 4, the sum of the entropy terms and the corresponding enthalpy terms, are given by,

$$\sum_i X_i \bar{C}_{pci} \ln \frac{T^*}{T_f} + \Delta S_m^* + \Delta S_L^M + \sum_i X_i \bar{C}_{pli} \ln \frac{T_f}{T^*} - \Delta S_m = 0 \quad (4a)$$

$$\sum_i X_i \bar{C}_{pci} (T^* - T_f) + \Delta H_m^* + H_L^E + \sum_i X_i \bar{C}_{pli} (T_f - T^*) - \Delta H_m = 0 \quad (4b)$$

where $\Delta S_m^* = \sum X_i \Delta S_{mi}^*$, $\Delta H_m^* = \sum X_i \Delta H_{mi}^*$, and $T^* = \Delta H_m^* / \Delta S_m^*$. Solving for ΔS_m and ΔH_m gives,

$$\Delta S_m(\text{at } T_f) = \Delta S_m^* + \Delta S_L^M + \langle \Delta C_p \rangle \ln \frac{T^*}{T_f} \quad (4c)$$

$$\Delta H_m(\text{at } T_f) = \Delta H_m^* + H_L^E + \langle \Delta C_p \rangle (T^* - T_f) \quad (4d)$$

where, $\langle \Delta C_p \rangle \equiv \sum X_i \bar{C}_{pci} - \sum X_i \bar{C}_{pli}$, the difference between the crystal and liquid heat capacities. Combining by $T_f \Delta S_m = \Delta H_m$ gives,

$$T_f \Delta S_m^* + T_f \Delta S_L^M + T_f \langle \Delta C_p \rangle \ln \frac{T^*}{T_f} = \Delta H_m^* + H_L^E + \langle \Delta C_p \rangle (T^* - T_f) \quad (5a)$$

The two heat capacity terms can be combined, letting

$$\begin{aligned} g &= T_f \langle \Delta C_p \rangle \ln \frac{T^*}{T_f} - \langle \Delta C_p \rangle \frac{(T^* - T_f)}{T_f} T_f \\ &= T_f \langle \Delta C_p \rangle \left[\ln \left(\frac{T_f + \Delta T}{T_f} \right) - \left(\frac{T_f + \Delta T - T_f}{T_f} \right) \right] \\ &= T_f \langle \Delta C_p \rangle \left[\ln \left(1 + \frac{\Delta T}{T_f} \right) - \frac{\Delta T}{T_f} \right] \end{aligned} \quad (5b)$$

also letting, $y \equiv \frac{\Delta T}{T_f}$; $g = T_f \langle \Delta C_p \rangle [\ln(1 + y) - y]$; $y = 0.10$ to 0.50 ,

$$\ln(1 + y) - y \approx y - ay^2 - y = -ay^2 = -a \left(\frac{\Delta T}{T_f} \right)^2 \quad (5c)$$

where $a = 0.422 \pm 0.037$, and $g = -ay^2 \langle \Delta C_p \rangle T_f$. (5d)

Substituting into 5a and solving for T_f gives,

$$T_f = \frac{\Delta H_m^* (1 + H_L^E / \Delta H_m^*)}{\Delta S_m^* \left[1 + \frac{1}{\Delta S_m^*} (\Delta S_L^M - ay^2 \langle \Delta C_p \rangle) \right]} \quad (5e)$$

Letting $u_1 \equiv H_L^E / \Delta H_m^*$; $u_2 \equiv [\Delta S_L^M - a(\frac{\Delta T}{T_f})^2 \langle \Delta C_p \rangle] / \Delta S_m^*$

then, $T_f = \Delta H_m^* (1 + u_1) / \Delta S_m^* (1 + u_2) = T^* (1 + u_1) / (1 + u_2) = T^* \theta$

or, $\theta = \frac{T_f}{T^*} = (1+u_1)/(1+u_2) = 1 + u_1 - u_2 + [\text{higher order terms}]$

The quantity of interest is the fraction depression of T^* , called $\alpha = (1-\theta)$. Neglecting the higher order terms gives,

$$\alpha \approx u_2 - u_1 = \frac{1}{\Delta S_m^*} (\Delta S_L^M - ay^2 \langle \Delta C_p \rangle) - H_L^E / \Delta H_m^* \quad (6a)$$

Inserting the ideal entropy of mixing and the excess entropy, y^2 in terms of α , and defining $\phi^E \equiv (S_L^E - H_L^E/T^*)$ gives the model equation,

$$\alpha = \frac{R}{\Delta S_m^*} (-\sum X_i \ln X_i) + \phi^E / \Delta S_m^* - a \left(\frac{\alpha}{1-\alpha} \right)^2 \langle \Delta C_p \rangle / \Delta S_m^* \quad (6b)$$

The magnitude of the excess property function, ϕ^E , being determined primarily by the liquid phase excess entropy, which can be positive or negative depending on the liquid phase molecular configuration. For a given experimental mixture, knowing α , $\langle \Delta C_p \rangle$, and ΔS_m^* , the value of the excess function can be obtained,

$$\phi^E = \alpha \Delta S_m^* + R \sum X_i \ln X_i + a \left(\frac{\alpha}{1-\alpha} \right)^2 \langle \Delta C_p \rangle \quad (6c)$$

It is obvious that a positive excess function is desirable to obtain larger α -values.

THE CORRELATION PAIR

As a consequence of the model, combined with a Scatchard function, a correlation pair results for the freezing temperature lowering as a function of the thermodynamic variables. Examination of the α -function (Eqn. 6b) indicates that it is a cubic-in- α for which the real root $0 < \alpha < 1$ is desired, and in this region can be represented by a quadratic rather than a cubic. Defining,

$$w \equiv \Delta S_m^* / \langle \Delta C_p \rangle, \text{ and } z \equiv (\phi^E - R \sum X_i \ln X_i) / \Delta S_m^* \quad (7a)$$

followed by mathematical simplification of 6b leads to the dimensionless form,

$$\alpha = 7(zw)^{1/2}/9 - w/6 \quad (7b)$$

or the linearized form,

$$\alpha/w = 7(z/w)^{1/2}/9 - 1/6 \quad (7c)$$

Neither equations 6c or 7a,b are predictive of ϕ^E , both requiring experimental data; however, once a few values of the excess function are known as a function of composition for a particular group of mixtures, a pseudo-binary Scatchard (9) function can be used to correlate the values,

$$\phi^E = X_1 X_2 A_0 [1 + a_1(X_1 - X_2) + a_2(X_1 - X_2)^2 + \dots] \quad (7d)$$

Equations 7a or b and 7d constitute the correlation pair of equations. For the case of sulfate mixtures, X_1 and X_2 were taken as X_m and X_d , the mole fractions of the mono- and divalent metal sulfates respectively.

RESULTS

Using model equation 6c, values of the excess function were calculated for the thirty-two literature and the forty-five experimental mixtures. For the divalent metals with alkali metal sulfates, some gave positive values others negative values as indicated,

positive ϕ^E values		negative ϕ^E values	
barium	75%	cadmium	78%
calcium	of all	cobalt	of all
lead	positive	copper	negative
zinc	values	magnesium	values
		manganese	

A test of the α -correlation is presented as Figure 4 for the literature plus experimental mixtures with positive excess function values. The computer generated curve as $f(2w)$ gives a very good fit, $r=0.985$.

The positive ϕ^E -values were correlated as suggested by a Scatchard function giving,

$$\begin{aligned} \phi^E (\text{J/gmol K}) &= A_0 X_m X_d [1 + a_1(X_m - X_d) + a_2(X_m - X_d)^2] \\ &= 3.064 X_m X_d [1 + 1.559(X_m - X_d) + 16.99(X_m - X_d)^2] \quad (8a) \\ (r &= 0.990) \end{aligned}$$

Plots of $\phi^E/X_m X_d$ vs. $(X_m - X_d)$ and ϕ^E vs. X_m are shown as Figures 5a,b, the latter plot indicating that greatest temperature lowering should occur in the vicinity of $X = 0.20$ and 0.80 .

As regards our experimentally measured freezing temperatures, two

ternary mixtures reported in the literature (4,6) served as the lowest temperature starting point: 1) -an alkali metal sulfate mixture, $X(\text{Li})$ 0.780, $X(\text{Na})$ 0.085, $X(\text{K})$ 0.135, $T_f = 785$ K; and 2) -a mixture with zinc sulfate, $X(\text{Na})$ 0.190, $X(\text{K})$ 0.258, $X(\text{Zn})$ 0.552, $T_f = 661$ K, the effect of zinc being rather striking. Table 2 summarizes the 'best' 4, 5 and 7 component mixtures, and Figure 6 is a plot showing the convergence of 6-component mixtures to eutectic compositions.

Table 2. Lowest T_f for 4, 5, and 7 Component Mixtures

N	Composition X_i	X_m	α	T^*, K	T_f
4	(Li) 0.3247 (Na) 0.1579 (K) 0.0741 (Zn) 0.4433	0.5567	0.4123	1103	649
5	(Li) 0.3268 (Na) 0.1586 (K) 0.0746 (Zn) 0.3556 (Ca) 0.0842	0.5602	0.4550	1158	631
7	(Li) 0.1600 (Na) 0.2600 (K) 0.2600 (Ca) 0.0150 (Ba) 0.0100 (Mg) 0.0885 (Zn) 0.2065	0.6800	0.5220	1221	593

The research to date has achieved T_f values in the vicinity of 590 K, lower values should follow with additional work.

DISCUSSION

Three items are believed to be significant from the work, the fact that: 1) -the mixture freezing point can be reduced more than 50% of the linear combination freezing point, 2) -the proposed model can be used to guide the search to the composition regions where greatest lowering can be expected, and 3) -statistically the mono- and divalent sulfate mixtures involved showed significant excess entropy and enthalpy. Concerning the latter matter, Lumsden (11) and Bloom (12), following Hildebrand (10) have viewed molten salt mixtures as 'regular' solutions; however, it was expected that the mixtures investigated in this work would show excess entropy. The choice of the definition of the excess function, $\phi^E = S^E - H^E/T^*$, was a matter of mathematical convenience, as individually S^E and H^E can not be separated. Those mixtures with positive excess function showed values of $0 < \phi^E < 4$, J/gmol K, which is considered to be primarily entropy, as enthalpy is small when divided by T^* .

ACKNOWLEDGEMENT

The authors thank the U.S. Department of Energy and the University of Houston Energy Laboratory for financial support of the project. Also the assistance of David Jones in executing certain laboratory work and literature search, and the calculational assistance of Karen Polonczyk is acknowledged.

REFERENCES

1. W.E. Wentworth and E. Chen, Solar Energy, 18, 205 (1976).
2. H.W. Prengle, Jr., and E. C-H Sun, Solar Energy, 18, 561 (1976).
3. H.W. Prengle, Jr., J.C. Hunt, C.E. Mauk and E. C-H Sun, Solar Energy, 24, 373 (1980).
4. H.W. Prengle, Jr., and M-C. Lee, Solar Energy, 37, 293 (1987).
5. G.J. Janz, Molten Salts Handbook, Academic Press, New York (1967).
6. G.J. Janz, C.B. Allen, J.R. Downey and R.P.T. Tompkins, Eutectic Data, U.S. ERDA publication TID-27163-V1, V2 (1976).
7. E.M. Levin, H.F. McMurdie, and E.P. Hall, Phase Diagrams for Ceramists, The American Ceramic Society, Inc., (1965); ibid (supplement) (1975).
8. S.P. Shah, M.S. Thesis: Chemical Storage of Solar Energy - Compatible Multicomponent Molten Salt Mixtures for the Duplex AHS Cycle, University of Houston, Chemical Engineering Department, Aug. 1985.
9. G. Scatchard, Chem.Revs., 8, 321 (1931); ibid, Trans. Faraday Soc., 33, 160 (1937).
10. J.H. Hildebrand and E.J. Salstrom, J. Am. Chem. Soc., 52, 4641 (1930); ibid, 54, 4257 (1932).
11. J. Lumsden, Thermodynamics of Molten Salt Mixtures, Academic Press, New York (1966).
12. H. Bloom, The Chemistry of Molten Salts, W.A. Benjamin, Inc., New York (1967).

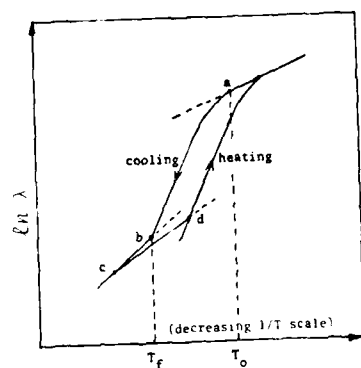


Fig.1. Dynamic Hysteresis

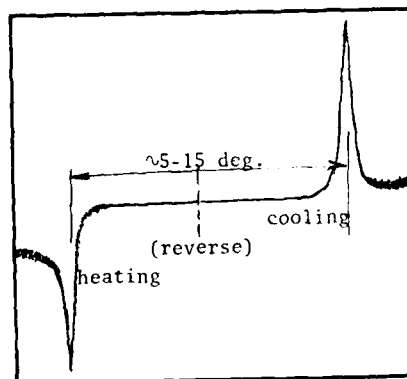


Fig.2. Typical Derivative

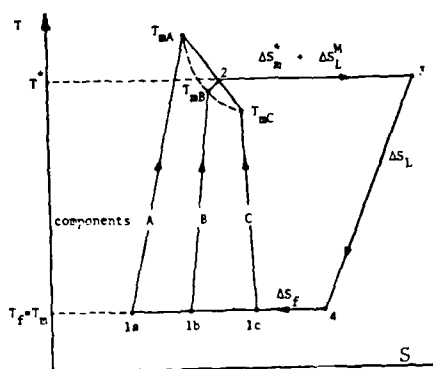


Fig.3. T-S Cycle

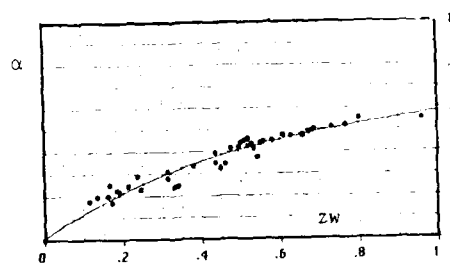


Fig.4. Temperature Lowering Correlation

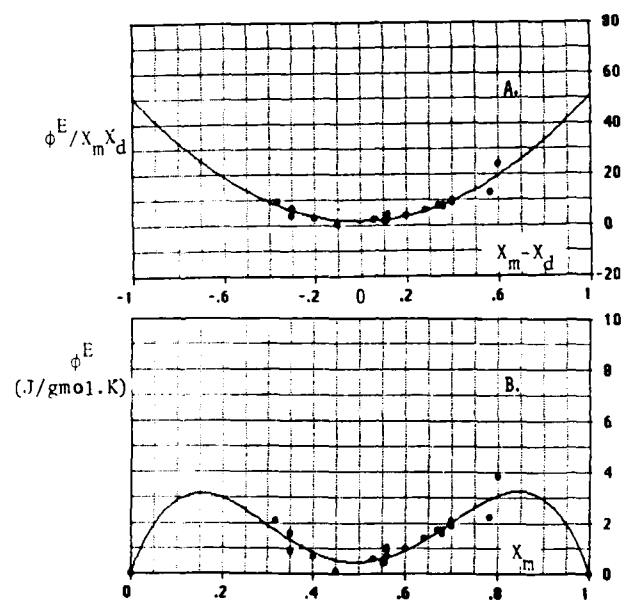


Fig.5A,B. Excess Function Correlation

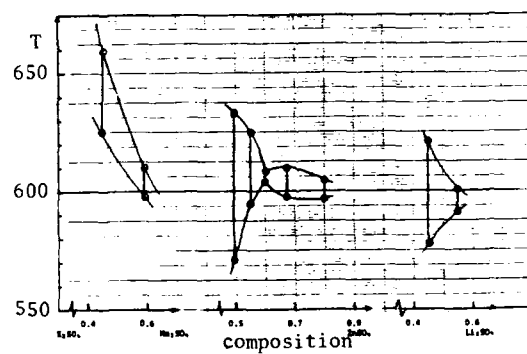


Fig.6. Freezing Temperature Convergence

THERMODYNAMICS OF 1-METHYL-3-ETHYLIMIDAZOLIUM
CHLORIDE -- ALUMINUM CHLORIDE MIXTURES

C. J. Dymek, Jr., C. L. Hussey, J. S. Wilkes and H. A. Øye*

The Frank J. Seiler Research Laboratory
United States Air Force Academy
Colorado Springs CO 80840-6528

ABSTRACT

A thermodynamic model for liquid mixtures of 1-methyl-3-ethylimidazolium chloride - aluminum chloride is presented. The model is based on EMF and vapor pressure measurements. It assumes the presence of the anions, Cl^- , AlCl_4^- , Al_2Cl_7^- , $\text{Al}_3\text{Cl}_{10}^-$, as well as Al_2Cl_6 and equilibria between them. The most remarkable feature of this system is the strong dependence of AlCl_3 activity on composition in the acidic region and the presence of $\text{Al}_3\text{Cl}_{10}^-$ as a dominant species around 75 mol % AlCl_3 .

INTRODUCTION

Melt mixtures of 1-methyl-3-ethylimidazolium chloride (MEICl) -- aluminum chloride are molten at room temperature for aluminum chloride concentrations between 30 and 67 mole % (1). Its Lewis acidity varies within a wide range from the very basic melt with excess MEICl to the acidic melts with excess aluminum chloride. The melt mixtures are of interest as a battery electrolyte, a solvent for unusual oxidation states, and as a homogeneous catalyst for organic reactions.

Recently the melts have been characterized thermodynamically between 46 and 68 mole % AlCl_3 by EMF measurements using aluminum electrodes (2). A study extended further into the acidic range is of importance to obtain a complete thermodynamic description of the melts and to clarify which species are present throughout the composition range. Using a vapor pressure method, activities with respect to liquid aluminum chloride can be calculated and a thermodynamic model can be constructed which predicts vapor pressure, activities, and the EMF's of galvanic cells.

*Permanent Address: The Technical University of Norway, N-7034
Trondheim-NTH, NORWAY

EXPERIMENTAL

The vapor pressure was obtained by a boiling point method. The principle and theory of this method have been given by Motzfeldt, Kyande, and Wahlbeck (3) and only a short outline is presented here. The sample is contained in a cell with a capillary opening, in the present case made from pyrex glass (cf. Fig. 1). The cell is placed in a recording thermobalance and brought to temperature under N_2 pressure. Theoretical treatment of the transport processes (3) gave the following expression for the rate of weight change \dot{w} :

$$-\dot{w} = C \left[\left(\frac{P \exp(\dot{w}/B)}{1 - \exp(\dot{w}/A)} \right)^2 - P_F^2 \right] \quad (1)$$

In this equation, P_F is the external pressure, and P is the equilibrium vapor pressure of the melt. The parameters A , B , and C are related to gas diffusivity, heat transfer and gas viscosity, respectively, but for the present purpose may be considered empirical constants for a given experiment at constant temperature. What is important here is that Eqn. 1 allows calculation of P from the experimental quantities, P_F and \dot{w} .

A commercial thermogravimetric analyzer was used for our studies (Perkin-Elmer TGA7 Thermogravimetric analyzer). It was connected to a MENSOR Quartz manometer/controller with a nitrogen reservoir and a vacuum pump. The TGA7 was fully computerized but could only take total weight of 5 grams including the crucible. To accommodate the crucible and achieve a larger zone of constant temperature, the low-temperature furnace of the TGA7 was replaced with a larger furnace made of a quartz tube with externally wound 0.2 mm Pt wire having the same resistance as the original furnace, 8.5Ω.

In earlier work on chloroaluminates (4,5,6), the initial outer pressure was larger than the vapor pressure and the outer pressure was then stepwise lowered, the weight loss increasing markedly when the outer pressure becomes lower than the equilibrium vapor pressure. The vapor pressure was obtained by a fitting of the mass loss data to Eqn. 1. As the evaporating gas had a composition different from that of the melt, a continuous change in melt composition resulted. This was accounted for by correction procedures (5,6).

The problem with a changing composition of the melt during the present experiment is much more serious due to the smaller sample size (2 g versus 40 g) and a very strong dependence of vapor pressure on composition. Using the procedure mentioned above led to having to "chase" a rapidly diminishing pressure. The resulting break in the weight loss curve was not sufficiently pronounced and the correction procedure was difficult to employ. It was then decided to change the

procedure and turn this apparent weakness of the present set-up into an advantage.

The first modification was to lower the initial external pressure below the equilibrium pressure, and then let the sample boil itself toward the composition which corresponds to the external pressure. The equilibrium pressure was determined from the weight loss as follows:

In the chosen pressure range where $P_f < P$, Eqn. 1 is simplified to

$$-\dot{w} = C[(P_{\text{exp}} (w/B))^2 - P_f^2] \quad (2)$$

neglecting diffusive gas flow.

As the weight change Δw for one experiment with constant P_f is small relative to the total weight and the gas consists only of aluminum chloride

$$\Delta X_A \approx k' \Delta w \quad (3)$$

$$\text{where } k' = \frac{X_A(1-X_A) + (1-X_A)^2 (M_{\text{MEICl}}/M_{\text{AlCl}_3})}{w}$$

where M is the molecular weight of the subscripted species, X_A denotes the stoichiometric mole fraction of $\text{AlCl}_3 = n_{\text{AlCl}_3}/(n_{\text{AlCl}_3} + n_{\text{MEICl}})$, and w is the sample weight.

For a limited range, the vapor pressure of Al_2Cl_6 is assumed to follow the relation

$$d \ln P = k'' d X_A \quad (4)$$

Eqns. 2-4 gives the following differential equation for the weight change rate

$$-\dot{w} = C[P_0^2 e^{a\Delta w} e^{\alpha w} - P_f^2] \quad (5)$$

where P_0 is the pressure at the start of the experiment at time $t=0$ and $\Delta w=0$, $a=2k'k''$ and $\alpha=2/B$. This equation can only be solved for $|\alpha w| < 1$, so that

$$e^{\alpha w} \approx 1 + \alpha w$$

This gives

$$-\dot{w} = \frac{CP_0^2 e^{a\Delta w} - CP_f^2}{1 + \alpha CP_0^2 e^{a\Delta w}} \quad (6)$$

and integration of Eqn. 6 gives:

$$\frac{\Delta w}{CP_f^2} - \frac{1}{a} \left[\frac{1}{CP_f^2} + \alpha \right] \ln \left[\frac{p_0^2 e^{a\Delta w} - p_f^2}{p_0^2 - p_f^2} \right] = t \quad (7)$$

The quantities P_0 and a can be obtained in an iterative fashion and the constants C and α by fitting of Eqn. 5, 6 or 7. A two point fitting is most easily done by the use of Eqn. 5 as the experiments give both \dot{w} and Δw and no approximation is involved. The fitting is done for $t=0$ where $\Delta w=0$ and for the end time, t .

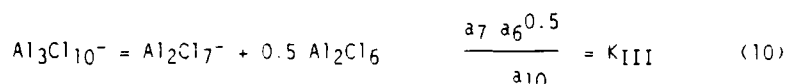
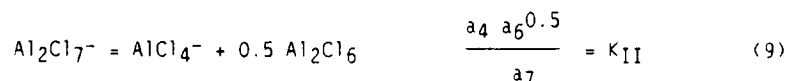
After determination of α and C , Δw for $\dot{w} = -0.1$ mg/min is calculated. The composition of the melt which has this weight change Δw is now taken to be the melt which has a vapor pressure P_f . The rationale for setting $\dot{w} = -0.1$ mg/min instead of 0 was justified from calibration experiments with ethyleneglycol combined with the fact that Eqn. 5 will extrapolate the data too far due to neglect of diffusive gas flow. Examples of experimental data are shown in Fig. 2. This procedure worked well for external gas pressures in the range 0.4 - 0.7 atm., but at lower external pressures, the time t for $\dot{w} = -0.1$ mg/min becomes exceedingly long making the extrapolation procedure uncertain.

In the second modification, the initial external pressure was again lowered below the equilibrium vapor pressure resulting in boil-off of $AlCl_3$. But the external pressure was increased in steps until boiling stopped as indicated by the levelling off of the rate of weight loss. The composition at that point corresponded to a melt which had the vapor pressure P_f . For both methods, melt mixtures from 80 to 66 mol % could be studied with a single experimental sample. It was however necessary to raise the temperature when the vapor pressure became too low for easy measurements (< 0.05 atm).

III. THERMODYNAMIC MODEL AND CALCULATIONAL PROCEDURES

The model assumed the following melt species to be present in the melt: 1-methyl-3-ethylimidazolium (MEI^+), Cl^- , $AlCl_4^-$, $Al_2Cl_7^-$, $Al_3Cl_{10}^-$, and Al_2Cl_6 .

Three independent equilibria are formulated between the species:



where

$$a_i = Y_i X_i \quad (11)$$

the subscript referring to the number of Cl's present in each species, and

$$K_i = \exp \left\{ -\frac{\Delta H_i^0(T_0)}{RT} + \frac{\Delta S_i^0(T_0)}{R} + \frac{\Delta C_p^0}{R} \left[\ln \frac{T}{T_0} + \frac{T_0 - T}{T} \right] \right\} \quad (12)$$

where T is the temperature of the experiment and T_0 is the standard temperature.

X_i is defined as a modified Temkin ion fraction (7), i.e. as an anion fraction where the neutral Al_2Cl_6 is counted among the anions. From this definition the following mass balance equilibria are obtained:

$$X_4 + 2X_7 + 3X_{10} + X_6(2 - X_A)/(1 - X_A) = X_A/(1 - X_A) \quad (13)$$

$$\text{and} \quad X_1 + X_4 + X_7 + X_{10} + X_6 = 1 \quad (14)$$

where X_A is defined as at Eqn. 3.

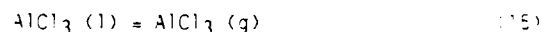
Presently the activity coefficients Y_i in Eqn. 5 are set equal to unity. This is equivalent to setting them to be constant and incorporating them into the equilibrium constants. The ΔC_p^0 in Eqn. 12 is set equal to zero. Knowing K_I , K_{II} , and K_{III} , as functions of temperature, Eqns. 8-14 can then be used to calculate the five ion fractions as well as the activity a_6 .

The program MODFIT (8) programmed for a personal computer was used to determine the equilibrium constants K_I , K_{II} , and K_{III} , by minimizing

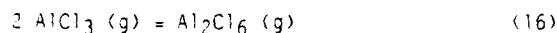
$$F = \sum (\log a_g [\text{exp}] - \log a_g [\text{calc}])^2$$

This criteria is equivalent to a relative least square fit of the values proper, but avoids the very small numbers for basic melts.

The experimental total vapor pressures were converted to activities utilizing data from the JANAF tables (9) as well as considering the small amount of AlCl_3 in the vapor phase:



$$K_{15} = \exp \{76.65 - 13159.6 T^{-1} - 9.474 \ln T + 7.93 \cdot 10^{-3} T - 3.903 \cdot 10^{-6} T^2 + 1.3 \cdot 10^{-9} T^3 - 0.1929 \cdot 10^{-12} T^4\}$$



$$K_{16} = \exp \{-23.6162 + 15588.4 T^{-1} + 0.5482 \ln T + 3.32 \cdot 10^{-3} T - 1.96 \cdot 10^{-6} T^2 + 0.774 \cdot 10^{-9} T^3 - 0.137 \cdot 10^{-12} T^4\}$$

The activity a_g is then given as:

$$a_g = \frac{P_{\text{Al}_2\text{Cl}_6}}{P_{\text{Al}_2\text{Cl}_6}^0} = \frac{B - \sqrt{B^2 - 4P_{\text{tot}}^2}}{2K_{16} \cdot K_{15}^2} \quad (17)$$

where $B = 2P_{\text{tot}} + 1/K_{16}$. As the internal transport number of MEI^+ is unity (10,11), the EMF data can be transferred to activity by the relationship (12):

$$d \ln a_g = - \frac{6F}{RT} \left[\frac{1 - X_A}{1 + 2X_A} \right] dE \quad (18)$$

The integration constant was chosen so that this EMF data overlaps with the vapor pressure data.

Although Eqns. 8-14 are a straightforward set of equations to solve for the anion fractions and the a_g activity in an iterative fashion, the solution may easily diverge if proper starting values and restrictive conditions are not introduced, especially near the equivalence points, $X_{A(\text{eq})} = 0.50, 0.667$ and 0.75 . The following procedure was successful. Close to the equivalence points, $X_A =$

$X_A(\text{eq}) \pm 0.02$, the majority species was first calculated for the equivalence composition assuming only the three most prominent species present. Then the second most prominent species was calculated for the same composition. The three remaining species were calculated from Eqns. 8-10. A better value for the second species was then calculated from Eqn. 13 by requiring the ratio between the two most prominent species to be unchanged, and an improved value was then obtained for the first species from Eqn. 14. The process was repeated until all mole fractions changed with less than ± 0.00001 . Further apart from the equivalence point, the iteration procedure was less critical and the starting values were calculated considering only the two major species. Using this procedure the final result for each composition was usually obtained with less than 10 iterations. To find the best set of K_I , K_{II} , and K_{III} , the constants were first varied one at a time and afterwards all constants were varied simultaneously.

IV. RESULTS

The original EMF data were averaged from two or three independent experiments and integrated to obtain activities using Eqn. 18 and are given below. For the three different temperatures, the activities of Al_2Cl_6 for $X_A = 0.60$ have been arbitrarily set equal to unity.

40°C

X_A	0.4745	0.4798	0.4853	0.4903	0.4952	
$\log a_6$	-29.983	-29.755	-29.446	-29.085	-28.533	
	0.5204	0.5310	0.5415	0.5504	0.5595	0.5691
	-1.869	-1.465	-1.168	0.902	-0.636	-0.506
	0.5798	0.5904	0.6003	0.6102	0.6205	0.6308
	-0.324	-0.141	0.041	0.209	0.430	0.689
	0.6411	0.6511	0.6612	0.6714		
	1.039	1.435	2.036	2.873		

50°C

X_A	0.4850	0.4906	0.4948	0.5211	0.5288	0.5387
$\log a_6$	-29.222	-27.567	-28.048	-1.806	-1.541	-1.283
	0.5509	0.5598	0.5698	0.5791	0.5897	0.5999
	-0.972	-0.767	-0.562	-0.372	-0.175	0.002

60°C

X_A	0.4648	0.4691	0.4751	0.4800	0.4852	0.4902
$\log a_g$	-29.205	-29.082	-28.854	-28.597	-28.279	-27.890
	0.4952	0.5198	0.5312	0.5410	0.5512	0.5597
	-27.263	-1.852	-1.442	-1.176	-0.926	-0.736
	0.5711	0.5784	0.5867	0.6001	0.6103	0.6212
	-0.4858	-0.3416	-0.1898	0.0046	0.2353	0.4782
	0.6296	0.6410	0.6503	0.6605	0.6713	0.6804
	0.683	1.009	1.397	1.898	2.505	3.120
	0.6909					
	3.871					

The vapor pressure data were transformed into a_g by Eqn. 17 ignoring the presence of $AlCl_3$ i.e. $a_g = P_{tot}/K_gK_8^2$:

$t^\circ C$	206	236	267	191	191	191
X_A	0.7572	0.7281	0.7114	0.7788	0.7665	0.7383
$\log a_g$	-0.611	-0.961	-1.360	-0.427	-0.552	-1.030
	219	219	265			
	0.7233	0.7118	0.7049			
	-1.278	-1.676	-1.701			

In order to get a smooth overlap between the EMF and the vapor pressure data, the value 6.5 was subtracted from all $\log a_g$ data obtained by EMF measurement. The fit gave the following parameters:

	I	II	III
ΔH (kJ)	55.40	2.81	6.21
ΔS (J/K)	-191	-53	0.9
$\log K$ (40°C)	-19.2	-3.2	-1.0

with a standard deviation in the fit equal to 0.107. Figure 3 shows the activity a_g for $t=40^\circ C$ and $t=250^\circ C$ and the calculated concentration of the different species for $t=250^\circ C$. It must, however, be stressed that the data are preliminary and more accurate data are expected to be obtained after performing further experiments. It should also be remembered that the mole fraction is calculated assuming the activity coefficients to be constants. Higher polymeric anions with four or more Al atoms may also be present.

Nevertheless three features stand out:

1. Acidic melts are stable versus gaseous decomposition up to at least 300°C even if they attain a dark color.

2. Not only is the activity change tremendous around 50 mol % AlCl_3 , but the AlCl_3 activity changes much more strongly with composition in the acidic region than for alkali chloraluminate melts.

3. Substantial amounts of higher polymers like $\text{Al}_3\text{Cl}_{10}^-$ must be present to explain the strong change in AlCl_3 activity around $x_A = 0.75$.

Raman spectroscopic studies are under way to clarify the presence of higher polymers.

ACKNOWLEDGEMENT

The expert glassblowing and other help from Mr. Fred C. Kibler is greatly appreciated as well as the sample preparation by Mr. Steve Keeley. We also thank Missy Landess for expert word processing and assisting in editing this manuscript.

REFERENCES

1. A. A. Fannin, Jr., D. A. Floreani, L. A. King, J. S. Landers, B. J. Piersma, D. J. Stech, R. L. Vaughn, J. S. Wilkes, and J. L. Williams, *J. Phys. Chem.*, **88**, 2614 (1984).
2. C. L. Hussey, T. B. Scheffler, J. S. Wilkes, and A. A. Fannin, Jr., *J. Electrochem. Soc.*, **133**, 1389 (1986).
3. K. Motzfeldt, H. Kvide, and P. G. Wahlbeck, *Acta Chem. Scand.*, **A31**, 444 (1977).
4. H. Linga, K. Motzfeldt, and H. A. Øye, *Ber. Bunsenges. Phys. Chem.*, **82**, 568 (1978).
5. B. Knudstad, H. Linga, and H. A. Øye, *Ber. Bunsenges. Phys. Chem.*, **85**, 1132 (1981).
6. K. Nakamura, T. Østvold, and H. A. Øye, *Ber. Bunsenges. Phys. Chem.*, **90**, 141 (1986).
7. H. A. Øye, E. Rytten, P. Kjaebye, and S. J. Cyvin, *Acta Chem. Scand.*, **25**, 559 (1971).
8. T. Hertzberg, "MODFIT," Inst. of Chem. Eng., Norwegian Inst. of Technol., Trondheim, Norway (1970).
9. "JANAF Thermochemical Tables," Nat'l. Stand. Ref. Data Serv., National Bureau of Standards, No. 37 (1971).
10. C. L. Hussey and H. A. Øye, *J. Electrochem. Soc.*, **131**, 1621 (1984).
11. C. L. Hussey, J. R. Sanders, and H. A. Øye, *J. Electrochem. Soc.*, **132**, 2156 (1985).
12. H. A. Øye and L. A. King, *Inorg. Nucl. Chem. Lett.*, **16**, 547 (1980).

To Thermal Balance

Figure 1. Capillary cell used for vapor pressure measurements.



0 5 10 15 20 25

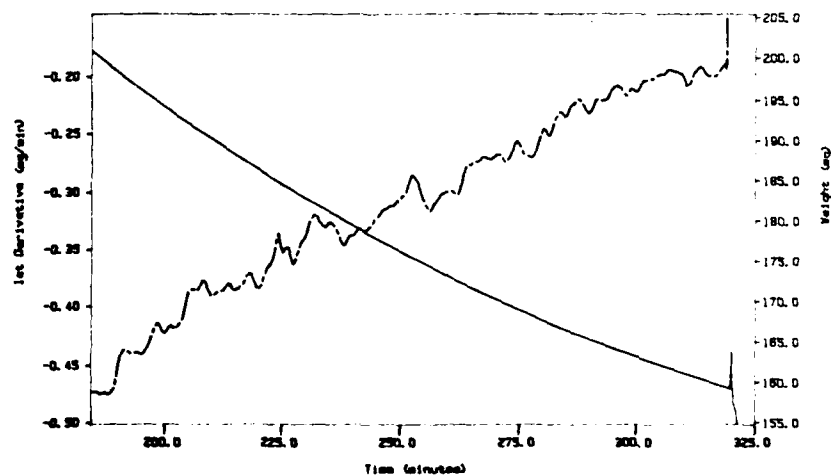
MILLIMETERS

Figure 2. Experimental weight loss data. $T = 191^{\circ}\text{C}$, outer pressure of 0.5613 atm, and composition at equilibria of $X_A = 0.7675$.

TGA 1st Derivative 1e10
Sample Weight: 0.000 mg
Fri Apr 17 22:50:24 1987

PERKIN-ELMER
7 Series Thermal Analysis System

TGA File Name: 1e10
Sample Weight: 0.000 mg
Fri Apr 17 22:50:24 1987



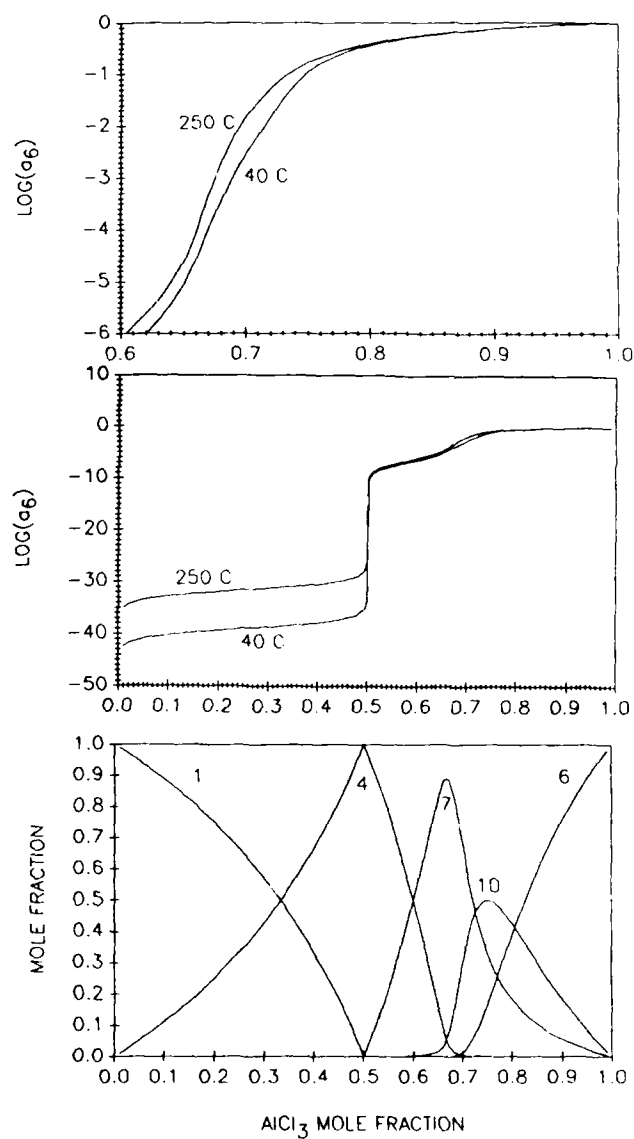


Figure 3. Activity of Al_2Cl_6 at 40 and 250°C and species concentration at 250°C from model calculations.

VAPORIZATION OF WATER FROM HYDROUS MELTS
AND CONCENTRATED ELECTROLYTE AQUEOUS SOLUTIONS

Shigehito Deki, Masaharu Fukui,
Akihiko Kajinami, and Yukio Kanaji

Department of Industrial Chemistry,
Faculty of Engineering, Kobe University
Rokkodai, Nada, Kobe, 657 Japan

ABSTRACT

Vapor pressure of hydrous melts and very concentrated electrolyte aqueous solution were measured with the systems $\text{ZnCl}_2\text{-H}_2\text{O}$ and $\text{CaCl}_2\text{-H}_2\text{O}$. The measurements were made at various temperatures in the composition range of $r(\text{water/electrolyte})=1.27\text{-}20.0$ for $\text{ZnCl}_2\text{-H}_2\text{O}$, or $r=4.23\text{-}30.0$ for $\text{CaCl}_2\text{-H}_2\text{O}$ by the transpiration method. From the temperature dependence of the vapor pressure, the enthalpy and entropy of vaporization were determined. The correlation between them showed two different types of linearity indicating Barclay-Butler rule for each system. To explain these results, the existence of different kinds of ion-water interactions were proposed.

INTRODUCTION

Hydrous melts and very concentrated electrolyte aqueous solution, containing hydrate melts, are situated near the end of the concentration scale of the electrolyte in molten salts-water systems, if it could be allowed not to take account of the difference in temperature (1). Therefore, they have two kinds of aspects, as a molten salt and an electrolyte aqueous solution. The studies on these regions are expected to do much for both of molten salt chemistry and aqueous solution chemistry. Especially, the investigations on the chemical or physical behavior of water in these systems are very interesting and important in order to understand the properties of water in molten salts at high temperature or in the hydration sheath around ions of dilute aqueous solutions. In them, most of water molecules are under restriction of ions and the water-ion interactions are highly associated with ion-ion interactions.

For the purpose of studying the physico-chemical properties of water in hydrous melts and very concentrated aqueous solutions, the vapor pressures of water for the systems $\text{ZnCl}_2\text{-H}_2\text{O}$ and $\text{CaCl}_2\text{-H}_2\text{O}$ were measured over a complete concentration range, as far as they were stable liquids at various temperatures of 30-145 °C, by

using the transpiration method.

EXPERIMENTAL

The preparation of hydrous melts and the concentrated solutions was reported earlier(2).

The vapor pressure of water over the electrolyte-water systems were determined by the transpiration method using a Karl-Fischer automatic titrator. The apparatus for the measurement is shown in Fig.1. N_2 gas was used as a carrier gas. The dried and preheated carrier gas was first equilibrated with the electrolyte-water systems at a known temperature in the sample chamber, and finally passed through anhydrous methanol in the cell of Karl-Fischer automatic titrator for the measurements at low temperatures, or through a cold trap, cooled with liquid nitrogen, for those at high temperature. On the latter case, after flowing carrier gas for the given period of time, the cold-trapped water was heated and evaporated to put into the cell of titrator with carrier gas flow. Samples were maintained at the known temperatures with a water bath or an electric furnace thermo-controlled. To prevent the vapor from condensation, the paths were kept at 5 °C higher than measuring temperature. The equilibrated vapor pressure was determined as the value at the plateau on the plot of vapor pressure v.s. flow-rate of carrier gas (3). Testing the accuracy of this method, measurements were made with pure water at different temperatures.

RESULTS AND DISCUSSION

Transpiration measurements were made mainly on the systems of $ZnCl_2-H_2O$ and $CaCl_2-H_2O$ in the temperature ranges of 30-145 °C for the former systems and 30-120 °C for the latter. Their composition ranges were 1.27-20.0 for $ZnCl_2-H_2O$ and 4.23-30.0 for $CaCl_2-H_2O$ of water/electrolyte ratio (r). On being measured under these conditions, all the samples were stable as liquids. However, not all compositions could be investigated at all temperatures because of the limitations of their melting point or solubility. Before and after the measurement, the change of the composition was negligible.

The variations of vapor pressure with the composition are shown Fig.2. For $CaCl_2-H_2O$ system, the linearity of vapor pressure in the mole ratio of water were kept up to $r=5$. For $ZnCl_2-H_2O$ system, the linearity could not be recognized, as had been reported with nitrate-water systems by Tripp (4). The relationship between activity coefficient of water and composition for the hydrous melts was shown in Fig.3. The activity coefficient was so small that it indicated water molecules intensively restricted with ions, and that of $CaCl_2-H_2O$ was smaller than that of $ZnCl_2-H_2O$ by a factor of

about two at corresponding mole ratio in the composition range up to ca. $r=6$.

From the data on the temperature dependence of vapor pressure, average enthalpy and entropy of vaporization were determined by the ordinary method. The plots of the enthalpy of vaporization v.s. composition are given in Fig.4 and 5. In spite of being determined in different temperature ranges, the plots for each system are correlated by a single line. However, the correlation for $\text{CaCl}_2\text{-H}_2\text{O}$ remarkably differs from that for $\text{ZnCl}_2\text{-H}_2\text{O}$. It has a maximum at ca. $r=6$ in the plots. For $\text{ZnCl}_2\text{-H}_2\text{O}$, the enthalpy increases with the decrease of water content and the correlation shows a discernible shoulder at $r=3-4$.

The entropy of vaporization for these systems showed similar correlation with their composition to that of the enthalpy. The plots of entropy v.s. enthalpy of vaporization, Barclay-Butler plots, are shown in Fig.6. With both systems, they give two different straight lines distinguished by the composition ranges. In the range of those composition, each correlation shows the Barclay-Butler rule which expresses the similar process of vaporization, and it is suggested that water molecules in those composition ranges are under similar restriction (5). In other words, it seems that water-ion interaction changes at $r=2.8$ for $\text{ZnCl}_2\text{-H}_2\text{O}$ and $r=5$ for $\text{CaCl}_2\text{-H}_2\text{O}$.

From these results, it is concluded that the ion-water interactions in the $\text{CaCl}_2\text{-H}_2\text{O}$ system are weakened by increasing cation-anion interaction at a water content region less than $r=5-6$ and the water molecules in the $\text{ZnCl}_2\text{-H}_2\text{O}$ system are trapped among increased aggregated species of ZnCl_2 at a water content region less than $r=3-4$.

ACKNOWLEDGEMENT

The authors make their acknowledgement for partial financial support of the Ministry of Education, Japan, a Grant-in-Aid Fundamental Scientific Research (Grant No.61530593).

REFERENCES

1. J. Braunstein, *Inorg. Chim. Acta Rev.*, **2**, 19 (1968).
2. S. Deki and Y. Kanaji, *Rep. Asahi Glass Found. Ind. Technol.*, **15**, 97, (1984).
3. H. T. Gerry and L. J. Gillespie, *Phys. Rev.*, **40**, 269 (1932).
4. T. B. Tripp and J. Braunstein, *J. Phys. Chem.*, **73**, 1987 (1969).
5. R. L. Friedman and C. V. Krishnan, in "Water" vol.3 (E. Franks, ed.) Plenum, N.Y. (1973).

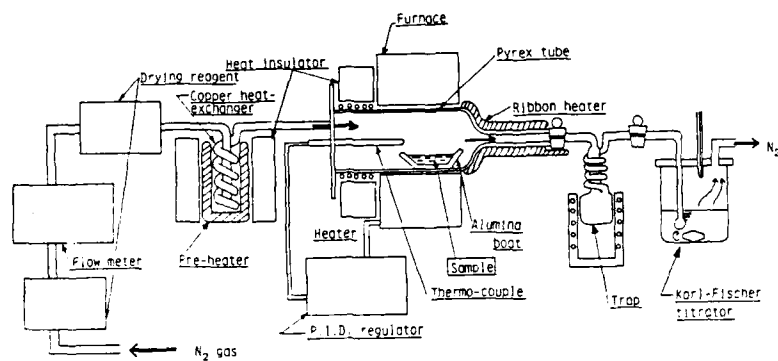


Fig.1 Schematic of Apparatus Used in the Transpiration Method for Measuring Vapor Pressures.

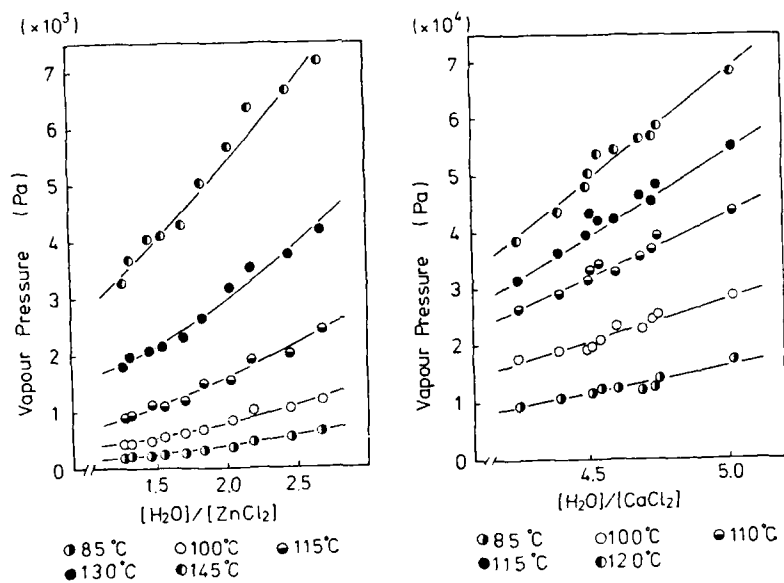


Fig.2 Vapor Pressure of Hydrated Melts at Various Temperatures.

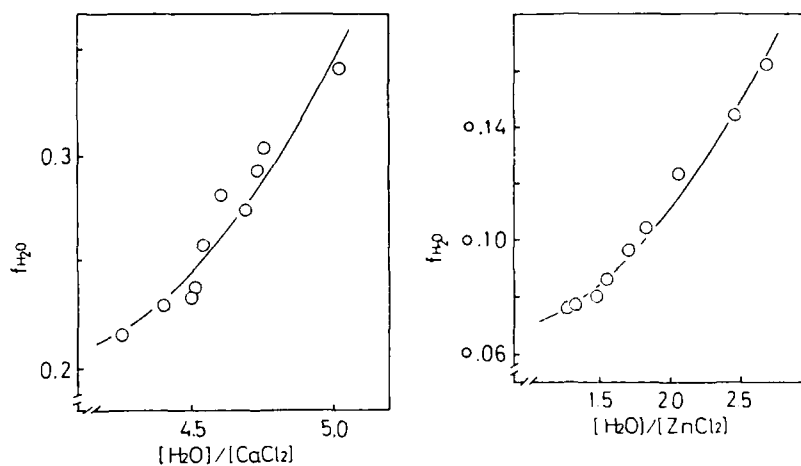


Fig.3 Activity Coefficient of Water in Hydrous Melts at 100 °C.

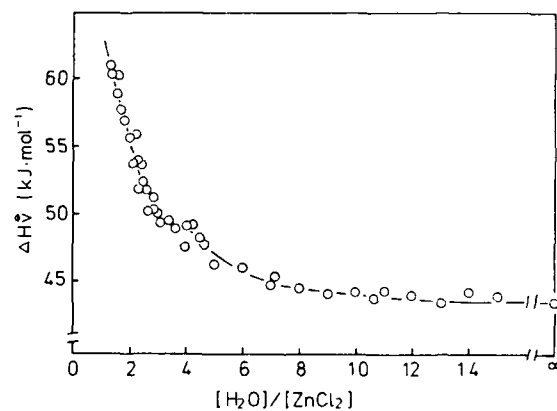


Fig. 4 Enthalpy of Vaporization from $ZnCl_2 - H_2O$ Systems.

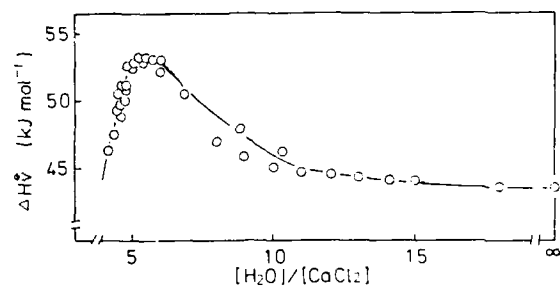


Fig.5 Enthalpy of Vaporization from $\text{CaCl}_2 - \text{H}_2\text{O}$ Systems.

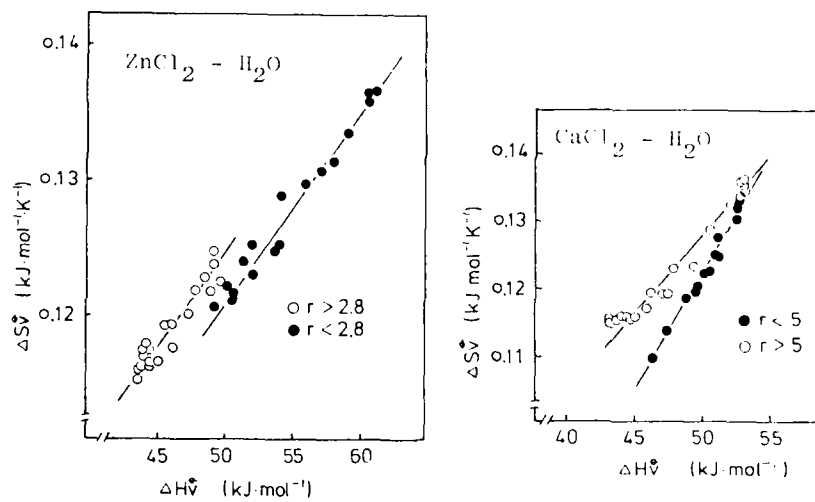


Fig.6 Plots of Enthalpy v.s. Entropy of Vaporization.

THERMODYNAMIC PROPERTIES OF MOLTEN MAGNESIUM CHLORIDE
HYDRATES IN PRESENCE OF POTASSIUM CHLORIDE

H.-H. Emons, A. Dittrich, and W. Voigt
Bergakademie Freiberg, Sektion Chemie
Leipziger Str., Freiberg 9200, Germany

ABSTRACT

Vapour pressure measurements had been performed in the ternary system $x\text{KCl} + (1-x)(\text{MgCl}_2 + R \text{H}_2\text{O})$ up to a maximum temperature of 523 K. The investigated compositions varied between $0 \leq x \leq 0.3$ and $4.6 \leq R \leq 6.0$. From the experimental vapour pressures water activities, enthalpies of evaporation, and partial molar excess entropies of water were calculated. The present results confirm the appearance of direct cation-anion contacts within the concentration range of molten hydrates due to $\text{H}_2\text{O} \rightleftharpoons \text{Cl}^-$ exchange reactions in the first coordination sphere of Mg^{2+} .

1. Introduction

Molten salt hydrates represent a class of liquids interconnecting features of aqueous solutions and molten salts. Recently, we proposed to define the concentration range of molten hydrates more generally as a range, which is characterized by a quantitative predominance of ion-water contact interactions [1,2]. A peculiar transition behaviour in the concentration dependence of thermodynamic properties is observed within this range. The sharpness of this transition is related to the strength of ion-water and cation-anion interactions. Its position on the concentration scale corresponds to the average hydration number of the strongest hydrating ion.

In this respect, MgCl_2 can be considered as a model substance, consisting of a strongly hydrating cation with almost no tendency to associate with the anion in aqueous solutions [3,4]. In agreement with the primary hydration number of Mg^{2+} , at a molar $\text{H}_2\text{O}:\text{MgCl}_2$ ratio $R \approx 6$, distinct changes in the partial molar quantities of water were revealed from vapour pressure measurements in the binary system $\text{MgCl}_2\text{-H}_2\text{O}$ [2,5,6].

On the other hand, the properties of the anhydrous molten mixtures $\text{MgCl}_2\text{-ACl}$ ($A=\text{K}, \text{Rb}, \text{Cs}$) are governed by the formation of tetrahedrally coordinated chlorocomplexes of magnesium [7,8].

There arises the question, whether chlorocomplex formation becomes important in the range of molten hydrates of MgCl_2 . A ligand exchange $\text{H}_2\text{O} \rightleftharpoons \text{Cl}^-$ at the Mg^{2+} ions should be reflected in a relative increase of the water activity. Thus, in this work the influence of KCl on the vapour pressure of molten

magnesium chloride hydrates has been investigated for molar $\text{H}_2\text{O}:\text{MgCl}_2$ ratios between six and four. Tab. 1 gives a summary of the compositions, which are covered by our measurements.

2. Experimental

The preparation and analysis of magnesium chloride hydrates have been described previously (9). Reagent grade KCl (VEB Jenapharm Laborchemie Apolda) was recrystallized and dried to constant weight at 473 K. Aliquots of magnesium chloride, potassium chloride and water were weighed directly into the teflon vessel of the autoclave to give a sample of the desired bulk composition.

A detailed description of the apparatus for vapour pressure measurements and the procedure used is given in (9).

In this study some improvements were introduced increasing the accuracy of the experiments. Two wire circuits of the Pt-100 resistance thermometers were replaced by four-wire arrangements and all measurements of voltage were performed in both current directions to compensate thermoelectric effects. The samples were homogeneously melted before evacuating the apparatus. Likewise, for the correction of slight shifts in bulk composition (± 0.5 per cent) the quantity of water vapour, exhausted during the evacuation, was weighed after freezing-out at liquid nitrogen temperature.

For all compositions given in Tab. 1 a vapour pressure polytherm was determined with temperature steps of about 12 K until a maximum temperature of 523 K. The experiments were started at a temperature about 10 K above the crystallization temperature according to the phase diagram of D'ANS and SYPIENA (10).

In order to ensure a temperature interval of at least 50 K the maximum concentration of KCl was limited to 30 mol-% related to the anhydrous salt mixture.

3. Calculation of the water activity from vapour pressure

For the calculation of the water activities from the measured vapour pressures p_w Eq. (1) was applied.

$$\ln a_w(p^*) = \ln(p_w/p_w^*) + \frac{1}{RT} \int_{p_w^*}^{p_w} (V_w'' - V_w^{0''}) dp + \frac{1}{RT} \int_{p_w}^{p_w^*} V_w' dp \quad (1)$$

Eq.(1) yields the water activity a_w at the vapour pressure of pure water p_w^* at the given temperature, where V_w is the partial molar volume of water, T the absolute temperature and R the general gas constant ($8.3144 \text{ J mol}^{-1} \text{ K}^{-1}$). The subscripts have the following meaning: 0 standard state; $*$ pure water; $''$ liquid phase and; $'''$ gas phase.

For a satisfactory accuracy in the analytical solution of the first integral of Eq.(1) up to 523 K - our upper limit in the experiments - it was necessary to take into account the third virial coefficient of water steam (Eq.(2)).

$$V_w''' = RT \cdot p_w + B + C p_w \quad (2)$$

where B and C is the second and third virial coefficient, respectively. The numerical values of B and C as a function of temperature were determined by means of multilinear regression of the PVT-data of water steam [11] from 373 to 573 K. The obtained power series are given by Eq.(3) and (4).

$$B [\text{m}^3 \text{ kg}] = a_0 + a_1 T + a_2 T^2 + a_3 T^3 + a_4 T^4 + a_5 T^5 \quad (3)$$

$$\begin{aligned} a_0 &= -3.14697 \text{ E-1} & a_3 &= 3.37919 \text{ E-8} \\ a_1 &= 7.63194 \text{ E-2} & a_4 &= -7.71229 \text{ E-10} \\ a_2 &= -7.26904 \text{ E-5} & a_5 &= 6.78403 \text{ E-12} \end{aligned}$$

$$C [\text{m}^3 (\text{kg bar})] = a'_0 + a'_1 T + a'_2 T^2 \quad (4)$$

$$a'_0 = -1.03334 \text{ E-3} \quad a'_1 = 1.26910 \quad a'_2 = -3.97580 \text{ E-2}$$

At temperatures $\leq 523 \text{ K}$ Eq.(2) to (4) represent the original data [11] within error limits of 0.15%.

From Eq.(1) it follows that the partial molar volume of water in the liquid phase has to be included into the calculation. Different approximations were used for this quantity in the literature. The reason has to be seen in a lack of precise and extensive volumetric data of water-salt systems at temperatures above 373 K and high concentrations. At lower concentrations the most reliable approach consists of the use of the molar volume of pure water V_w^* (e.g. [12, 13, 14]).

The relative contribution of the second integral in Eq.(1) increases with rising vapour pressure difference between salt solution and pure water. In the case of a magnesium chloride hexahydrate melt, with its low water activity, it amounts

to only 0.3 per cent at 423 K, but 1.5 per cent at 523 K already. Accordingly, at higher temperatures the necessary attention has to be directed to the partial molar volume of water to allow an exact calculation of the water activity from vapour pressure data. For molten hydrates, containing strongly hydrated cations as Mg^{2+} , a vigorous decrease of the partial molar volume of water should be expected. AKSMANOVIC and KREY [15] reported an equation for the density of $\text{MgCl}_2 \cdot \text{H}_2\text{O}$, which we used to calculate the partial molar volume of water. A general plot is given in Fig.1. With rising temperature the influence of the salt concentration on V_w' increases, but its maximum variation remains smaller than 10%. At the end of the compiled concentration range (45 wt% = 8.6 mol MgCl_2 kg H_2O) the uncertainty in the density derivative with respect to composition is small. Consequently, the crossing-point at about 9 mol MgCl_2 kg H_2O is not significant. In the ternary system $\text{KCl-MgCl}_2\text{-H}_2\text{O}$ the partial molar volume of water was considered as to be not influenced by the added KCl.

4. Results and discussion

The experimental results are summarized in Tab.2. The molalities in column 1 and 2 are corrected for the amount of water in the vapour phase. The temperature dependence of the vapour pressure can be described by means of relation (5),

$$\ln p_w = A_0 + A_1/T \quad (5)$$

where p_w is the vapour pressure in kPa. The numerical values of A_0 and A_1 together with the standard deviation obtained from a linear regression are listed in Tab.3.

Column 6 of Tab.2 contains the water activities a_w^{corr} , recalculated to constant compositions of the sample and rounded molar ratios $\text{H}_2\text{O/MgCl}_2$. For the temperature dependence of the water activity at constant composition, relation (6) was applied

$$\ln a_w^{\text{corr}} = A'_0 + A'_1/T \quad (6)$$

The coefficients A'_0 and A'_1 are reported in Tab.4.

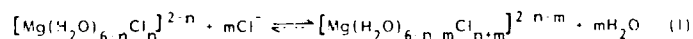
Fig.2 exhibits a graphical representation of the results at a molar $\text{H}_2\text{O/MgCl}_2$ ratio $R=6.0$. The logarithm of the water activity $\ln a_w^{\text{corr}}$ was plotted against the reciprocal absolute temperature $1/T$. The four polythermal data sets given in Fig.2a scatter within ± 1.1 per cent around the regression line. This value

can be considered as the reproducibility of our vapour pressure measurements. In Fig.2b the regression function from the present work (Fig.2a) is plotted together with previous data [9,16]. The comparison between the two figures points out the higher accuracy of the recent data. Fig.2 reveals also an unexpected result. Within the experimental uncertainty the water activity of a magnesium chloride hexahydrate melt is not changed after addition of anhydrous potassium chloride. The experimental results at lower water contents are shown in Fig.3. Filled circles and their regression lines (drawn as continuous lines) refer to a KCl content of $x = 0.3$, whereas the dashed lines represent the water activities in the binary system $\text{MgCl}_2\text{-H}_2\text{O}$ at the same molar ($\text{H}_2\text{O-MgCl}_2$) ratio R . At $R = 6$ an increase of the water activity becomes evident after addition of KCl. In Fig.4 the effect of composition variation is presented in form of isothermal plots. At a temperature of 473 K the relative increase of the water activity referred to the corresponding pure magnesium chloride hydrate melt is plotted. Fig.4a demonstrates the effect of the addition of 30 mol-% KCl in regard to the molar $\text{H}_2\text{O-MgCl}_2$ ratio, whereas in Fig.4b the variation of the water activity in regard to the KCl content is given for constant $R = 4.6$.

The most distinct effect was found at the lowest water content (Fig.4a) and after addition of the largest amount of KCl (Fig.4b). In spite of the higher total salt content the water activity is increased by 14.5 per cent. This result is in contrast to the common behaviour of aqueous solutions, where the vapour pressure decreases with growing total salt concentration.

Returning to the question formulated in the introduction, from our results it can be stated that in molten magnesium chloride hydrates ligand exchange processes $\text{H}_2\text{O} \leftrightarrow \text{Cl}^-$ become important. At $R = 6$ the release of water from the coordination sphere of Mg^{2+} ions reaches such an extent that the water activity is not only relatively increased, but absolutely.

Reactions of type (1) can be formulated to describe the coordination competition between H_2O and Cl^-



This agrees with a recent raman spectroscopic investigation [17], which proves the existence of direct cation-anion contacts in melts of magnesium chloride hydrates.

A displacement of equilibrium (1) to the right-hand side enhances the water activity and should become large as the total ratio of $\text{Cl}^-:\text{H}_2\text{O}$ in the melt is changed. Tab.5 gives the variation of this ratio in comparison to pure magnesium chloride hydrate melt Δ . With decreasing R we find increasing values of Δ , which explains the enlargement of the effect observed in this direction. At the instance of molten magnesium chloride hexahydrate, the water activity increasing effect by reaction (1) is just compensated by the simultaneous increase in total salt content. At still lower molar ratios $\text{H}_2\text{O}:\text{MgCl}_2$ reaction (1) produces an absolute enhancement of vapour pressure.

The liberation of coordinated water according to (1) is also clearly reflected in the molar enthalpy of evaporation $\Delta_v H_w$ as well as in the partial molar excess entropy of water $\Delta_m S_w^{\text{ex}}$. For the calculation of these quantities Eq. (7) and (8) were used, respectively.

$$\Delta_v H_w = T(V_w'' - V_w') dp_w dT \quad (7)$$

$$\Delta_m S_w^{\text{ex}} = -R(\ln a_w^{\text{corr}} - \ln x_w) - RT d \ln a_w^{\text{corr}} dT \quad (8)$$

where x_w is the mole fraction of water on an ionized basis. The needed vapour pressures and water activities as well as their temperature dependencies were derived from Eq. (5) and (6), respectively.

In Fig.5 both $\Delta_v H_w$ and $\Delta_m S_w^{\text{ex}}$ are plotted against the KCl content at a $\text{H}_2\text{O}:\text{MgCl}_2$ ratio, $R = 4.6$ and 473 K .

The deviation of the points at $x = 0.15$ (run 8) from the general tendency exposes the sensitivity of these quantities to relative small errors in the activity data. In preparation of run 8 obviously rest gas was not removed completely from the reference system resulting in a slightly larger slope in the temperature dependence of the water activity.

With increasing KCl concentration the absolute values of $\Delta_v H_w$ as well as of $\Delta_m S_w^{\text{ex}}$ decreases, which is adequate to a decrease of the ion-water interactions.

The present results confirm our general view of the concentration range of molten hydrates as to be characterized by dominant ion-water contacts and the appearance of direct cation-anion contacts due to coordination competition.

REFERENCES

- 11 H.-H. Emons, Th. Fanghanel, and W. Voigt, Sitzungsber. Akad. Wiss. DDR,
- 12 H.-H. Emons, Österr. Chemiker-Ztg.,
- 13 C. A. Angell and D. M. Gruen, J. Am. Chem. Soc., 88(1966),5192.
- 14 D. G. Miller, J. A. Rard, L. B. Eppstein, and J. G. Albright, J. Phys. Chem., 88(1984),5739.
- 15 W. Voigt, "Struktur und Eigenschaften von Salz-Wasser-Systemen im Übergangsbereich Lösung-Schmelze", Dissertation B, Bergakademie Freiberg, 1986.
- 16 V. Valyashko, M. Urusova, W. Voigt, and H.-H. Emons, Zh. Neorg. Khim., in Press.
- 17 M. H. Brooker and C.-H. Huang, Can. J. Chem., 58(1980),168.
- 18 H.-H. Emons and W. Voigt, Sitzungsber. Akad. Wiss. DDR, 15N (1981).
- 19 H.-H. Emons, W. Voigt, and F.-W. Wollny, Z. Phys. Chem. (Leipzig), 267(1986),1.
- 20 J. D'Ans and G. Sypiana, Kali verwandte Salze und Erdöl, 6(1942),89.
- 21 Landoldt Bornstein, Bd. IXa Technik, Teil 4 Wärmetechnik, Springer Verlag, Berlin-Heidelberg, New York, 1967.
- 22 C. T. Liu and W. T. Lindsay, J. Phys. Chem., 74(1970),341. J. Solution Chem., 1(1972),45.
- 23 W. T. Lindsay, C.-T. Liu, J. A. Hunter, et. al., U.S. Office Saline Water, Res. Dev. Progr. Rep. 1968, No 347.
- 24 E. R. Gardner, P. J. Jones, and H. J. de Nordwall, J. Chem. Soc., Trans. Faraday, 59(1963),1994.
- 25 M. Aksmanovic and J. Krey, Chem. Eng. Tech., 42(1970),1568.
- 26 F.-W. Wollny, Dissertation A, Bergakademie Freiberg, 1984.
- 27 W. Voigt and P. Klæboe, Acta Chem. Scand., 40A (1986),354.

Tab. 1 Bulk compositions of the investigated samples in the system
 $\{x\text{KCl} + (1-x)(\text{MgCl}_2 + R \text{H}_2\text{O})\}$

R	x =					
	0.05	0.10	0.15	0.20	0.25	0.30
6.0			*			*
5.5						*
5.0						*
4.6	*	*	*	*	*	*

Tab.2: Experimental vapour pressures p_w and water activities a_w

$m(\text{MgCl}_2)$ [mol/kgH ₂ O]	$m(\text{KCl})$ [mol/kgH ₂ O]	T [K]	p_w [kPa]	a_w	a_w^{corr}
1	2	3	4	5	6
MgCl₂ + 6H₂O (run 1)					
9.253		433.60	103.6	0.1731	0.1732
9.286		502.95	686.2	0.2738	0.2756
9.308		524.02	1104.7	0.3119	0.3148
MgCl₂ + 6H₂O (run 2)					
9.248		402.42	33.9	0.1315	0.1313
9.250		422.83	70.9	0.1560	0.1560
9.256		448.04	159.9	0.1896	0.1899
9.266		473.74	333.2	0.2283	0.2291
9.283		500.04	639.7	0.2685	0.2701
0.85(MgCl₂ + 6H₂O) + 0.15KCl (run 3)					
9.267	1.635	434.09	103.8	0.1714	0.1722
9.270	1.636	446.65	153.9	0.1884	0.1894
9.274	1.637	459.09	222.3	0.2064	0.2076
9.280	1.638	472.04	317.8	0.2254	0.2264
9.287	1.639	484.75	441.8	0.2446	0.2466
9.297	1.641	497.44	602.0	0.2644	0.2668
9.309	1.643	510.51	816.2	0.2865	0.2895
9.324	1.646	523.51	1089.6	0.3102	0.3138
0.70(MgCl₂ + 6H₂O) + 0.30KCl (run 4)					
9.281	3.977	469.23	294.1	0.2208	0.2224
9.287	3.980	481.68	407.2	0.2391	0.2410
9.294	3.983	494.26	553.3	0.2573	0.2596
9.305	3.988	507.41	751.1	0.2778	0.2806
9.318	3.993	520.67	1035.3	0.2995	0.3028
0.90(MgCl₂ + 4.6H₂O) + 0.10KCl (run 5)					
12.099	1.345	462.35	127.6	0.1113	0.1121
12.105	1.346	475.08	188.8	0.1271	0.1281
12.113	1.347	487.85	272.9	0.1441	0.1454
12.138	1.349	513.76	538.6	0.1819	0.1840
12.155	1.351	526.51	730.9	0.2021	0.2046
12.124	1.348	500.55	387.2	0.1630	0.1647
0.70(MgCl₂ + 4.6H₂O) + 0.30KCl (run 6)					
12.100	5.177	458.67	123.9	0.1167	0.1176
12.105	5.179	471.72	183.9	0.1323	0.1333
12.112	5.182	485.08	269.4	0.1496	0.1509
12.122	5.186	497.94	379.8	0.1672	0.1688
12.133	5.191	510.80	524.7	0.1857	0.1878
12.147	5.197	522.25	688.2	0.2030	0.2055

Tab.2: continued

1	2	3	4	5	6
0.95(MgCl ₂ + 4.6H ₂ O) + 0.05KCl (run 7)					
12.126	0.637	459.28	113.1	0.1053	0.1067
12.131	0.637	471.61	166.2	0.1199	0.1216
12.139	0.638	484.13	240.2	0.1360	0.1379
12.151	0.638	497.44	347.2	0.1544	0.1567
12.165	0.639	510.37	484.2	0.1729	0.1757
12.183	0.640	523.03	655.7	0.1914	0.1948
0.85(MgCl ₂ + 4.6H ₂ O) + 0.15KCl (run 8)					
12.081	2.130	459.53	117.5	0.1088	0.1092
12.086	2.131	472.67	178.2	0.1258	0.1263
12.094	2.132	485.41	257.9	0.1425	0.1432
12.104	2.134	498.77	371.6	0.1613	0.1624
12.116	2.136	511.24	512.4	0.1802	0.1817
12.134	2.139	523.85	706.3	0.2033	0.2053
0.80(MgCl ₂ + 4.6H ₂ O) + 0.20KCl (run 9)					
12.084	3.022	459.26	122.6	0.1142	0.1146
12.090	3.023	473.33	188.1	0.1311	0.1317
12.097	3.025	486.57	273.8	0.1479	0.1488
12.107	3.027	498.95	383.4	0.1659	0.1671
12.120	3.031	512.38	538.1	0.1857	0.1873
12.135	3.034	523.94	708.3	0.2035	0.2056
0.75(MgCl ₂ + 4.6H ₂ O) + 0.25KCl (run 10)					
12.086	4.031	458.33	121.1	0.1150	0.1155
12.091	4.033	471.83	182.9	0.1312	0.1319
12.099	4.035	485.36	268.9	0.1486	0.1495
12.108	4.038	498.58	383.2	0.1668	0.1681
12.120	4.042	511.12	524.4	0.1847	0.1863
12.134	4.047	522.86	695.0	0.2030	0.2051
0.70(MgCl ₂ + 5.0H ₂ O) + 0.30KCl (run 11)					
11.141	4.783	460.78	152.5	0.1372	0.1385
11.146	4.785	473.06	218.3	0.1526	0.1540
11.152	4.788	485.38	306.6	0.1690	0.1708
11.161	4.792	497.83	423.3	0.1863	0.1883
11.172	4.797	511.67	594.4	0.2069	0.2094
11.184	4.802	522.82	770.5	0.2245	0.2275
0.70(MgCl ₂ + 5.5H ₂ O) + 0.30KCl (run 12)					
10.074	4.325	458.54	179.1	0.1687	0.1679
10.078	4.327	470.21	249.7	0.1843	0.1837
10.083	4.329	482.94	350.1	0.2014	0.2010
10.092	4.333	497.55	505.9	0.2228	0.2228
10.101	4.337	510.90	692.8	0.2430	0.2434
10.112	4.341	522.71	902.3	0.2619	0.2626

Tab.3: Regression coefficients of Eq.(5)

run	A_0	A_1 [K]	σ ¹⁾
1 and 2	18.518	-6026.5	0.014
3	18.395	-5966.7	0.005
4	18.117	-5833.0	0.002
5	19.183	-6624.3	0.007
6	18.918	-6464.3	0.005
7	19.172	-6630.5	0.007
8	19.322	-6686.0	0.005
9	19.027	-6528.0	0.004
10	18.952	-6485.3	0.005
11	18.676	-6287.4	0.003
12	18.357	-6036.7	0.003

1) $\sigma = [\sum (\ln p_w(\text{exp}) - \ln p_w(\text{cal}))^2 / (n-2)]^{1/2}$
 with n = number of experimental points

Tab.4. Regression coefficients of Eq.(6)

run	A'_0	A'_1 [K]	$\sigma^{1)}$
1 and 2	1.7050	-1504.4	0.008
3	1.7346	-1518.0	0.004
4	1.6109	-1461.7	0.002
5	2.7616	-2287.9	0.003
6	2.4465	-2104.1	0.001
7	2.7174	-2275.1	0.002
8	2.8751	-2338.8	0.005
9	2.5789	-2180.1	0.002
10	2.4895	-2130.5	0.001
11	2.1993	-1925.0	0.002
12	1.8503	-1667.1	0.002

1) $\sigma = [\sum (\ln a_w^{\text{corr}}(\text{exp}) - \ln a_w^{\text{corr}}(\text{cal}))^2 / (n-2)]^{1/2}$
 with n : number of experimental points

Tab.5: The change of the $\text{Cl}^-/\text{H}_2\text{O}$ ratio in the system
 $\{x\text{KCl} + (1-x)(\text{MgCl}_2 + R \text{H}_2\text{O})\}$ in comparison to the pure
magnesium chloride hydrate melt

R	x =	
	0.15	0.30
6.0	0.030	0.072
5.5	0.032	0.078
5.0	0.035	0.086
4.6	0.038	0.093

Fig.1: Concentration dependence of the partial molar volume of water V'_w at several temperatures [K] in the system $\text{MgCl}_2\text{-H}_2\text{O}$ (473 K = max. compiled temperature; dashed straight line = limit of the compiled concentration range [15])

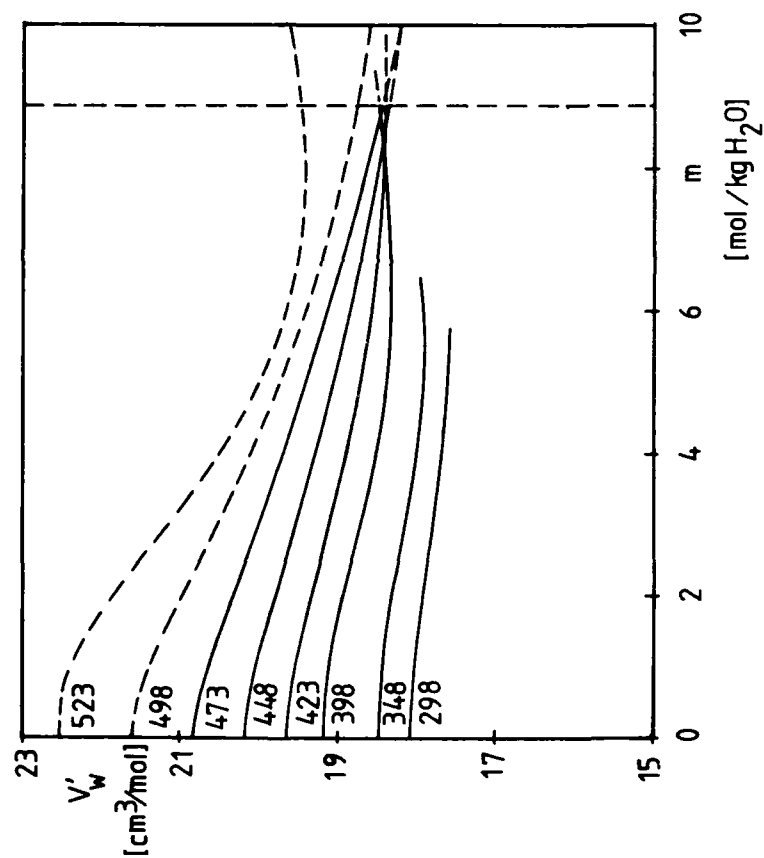


Fig. 2a: Experimental results for $\frac{1}{2}x\text{KCl} + (1-x)(\text{MgCl}_2 + 6.0 \text{H}_2\text{O})$
 (continuous line refers to the regression line of runs 1 and 2)
 Present work: + $x=0$ (run 1 and 2)
 • $x=0.15$ (run 3)
 o $x=0.30$ (run 4)

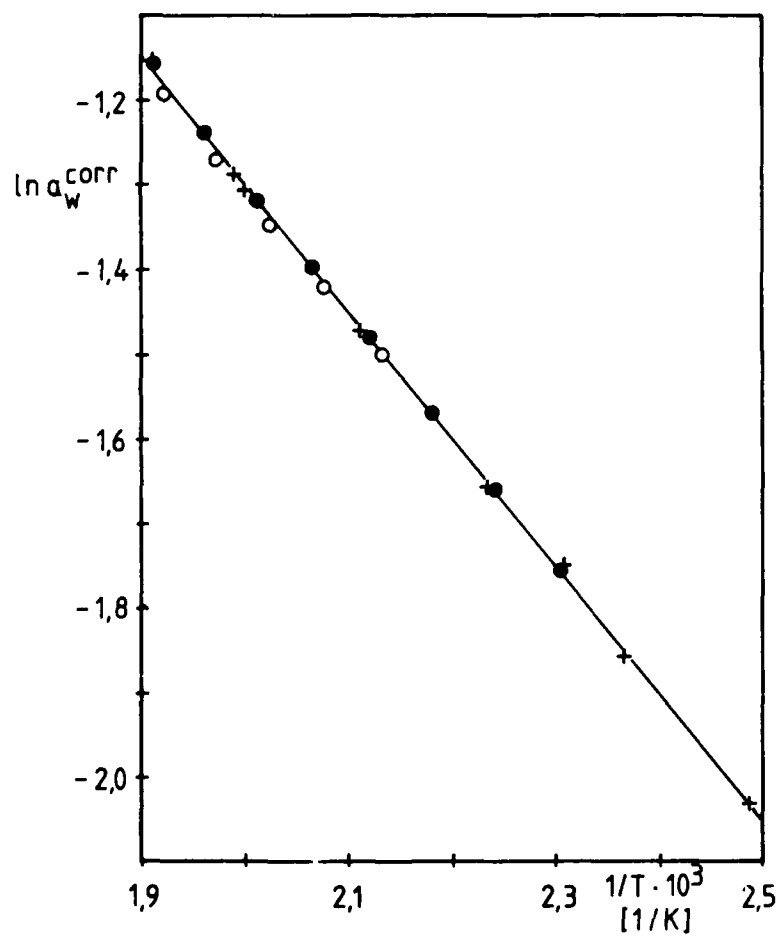


Fig. 2b: Experimental results for $[x\text{KCl} + (1-x)\text{MgCl}_2 + 6,0\text{H}_2\text{O}]$
 (continuous line refers to the regression line of runs 1 and 2)
 Previous data: + $x=0$ (from [9])
 • $x=0,10$ (from [16])
 o $x=0,20$ (from [16])

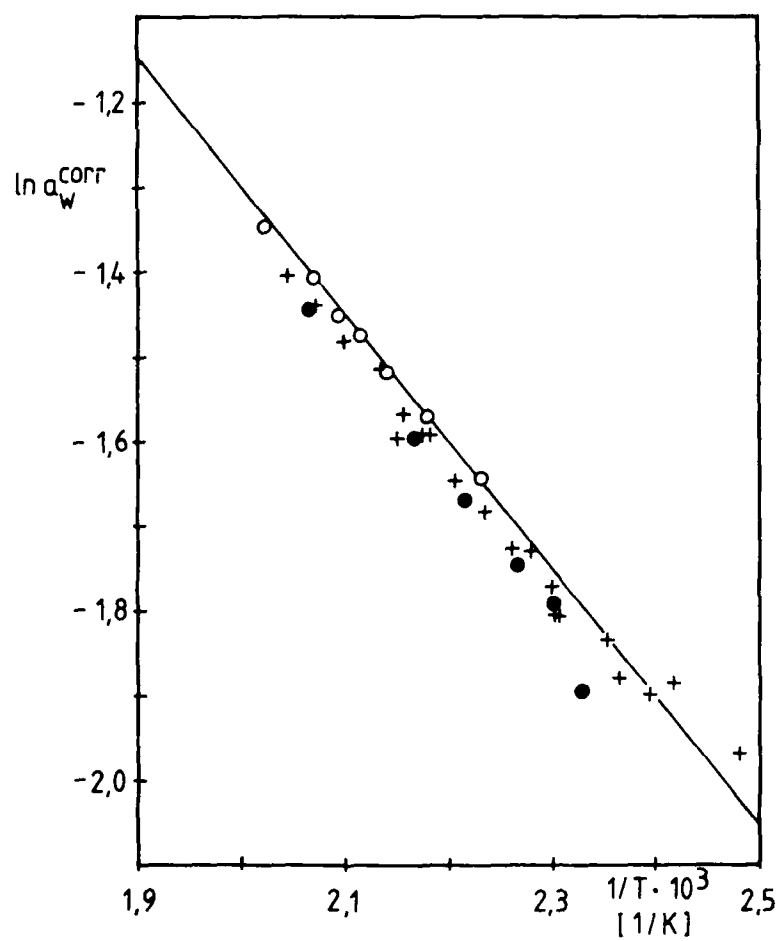


Fig.3 Experimental results for $\{x\text{KCl} + (1-x)(\text{MgCl}_2 + R \text{H}_2\text{O})\}$
 (filled circles and continuous lines refer to $x = 0.3$, whereas
 dashed lines represent the binary system $\{\text{MgCl}_2 + R \text{H}_2\text{O}\}$
 taken from [9])

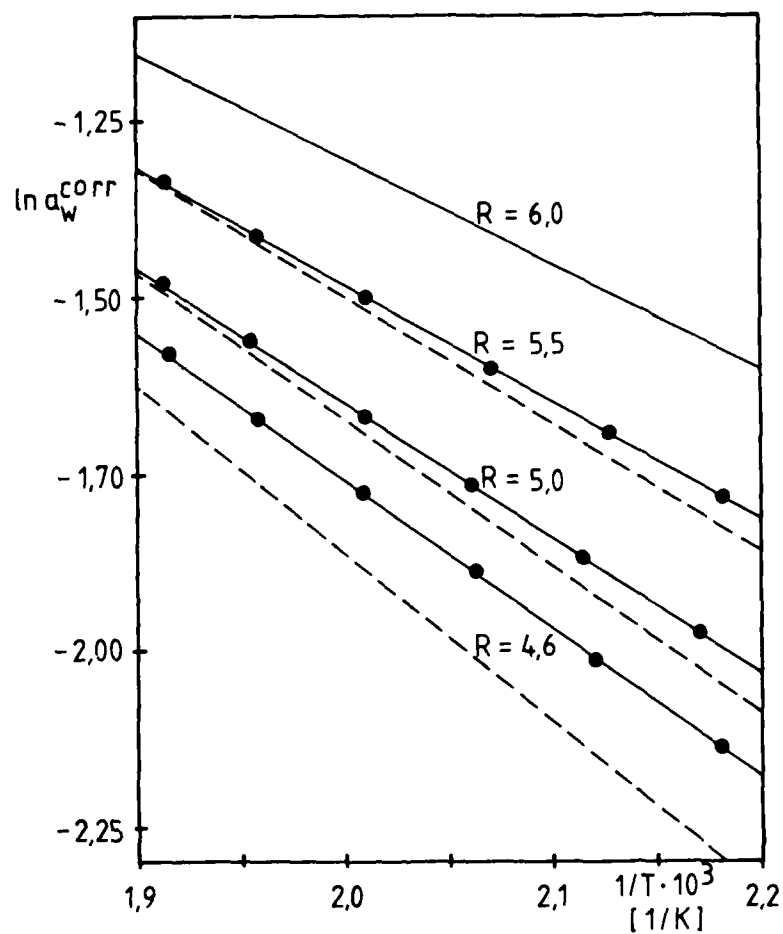


Fig. 4. Isothermal representation of the variation of water activity in the system $\{x\text{KCl} + (1-x)(\text{MgCl}_2 + R \text{H}_2\text{O})\}$ at $T = 473 \text{ K}$

a) Dependence on the molar ratio $\text{H}_2\text{O} / \text{MgCl}_2$ at $x = 0.3$

b) Dependence on the KCl content at $R = 4.6$

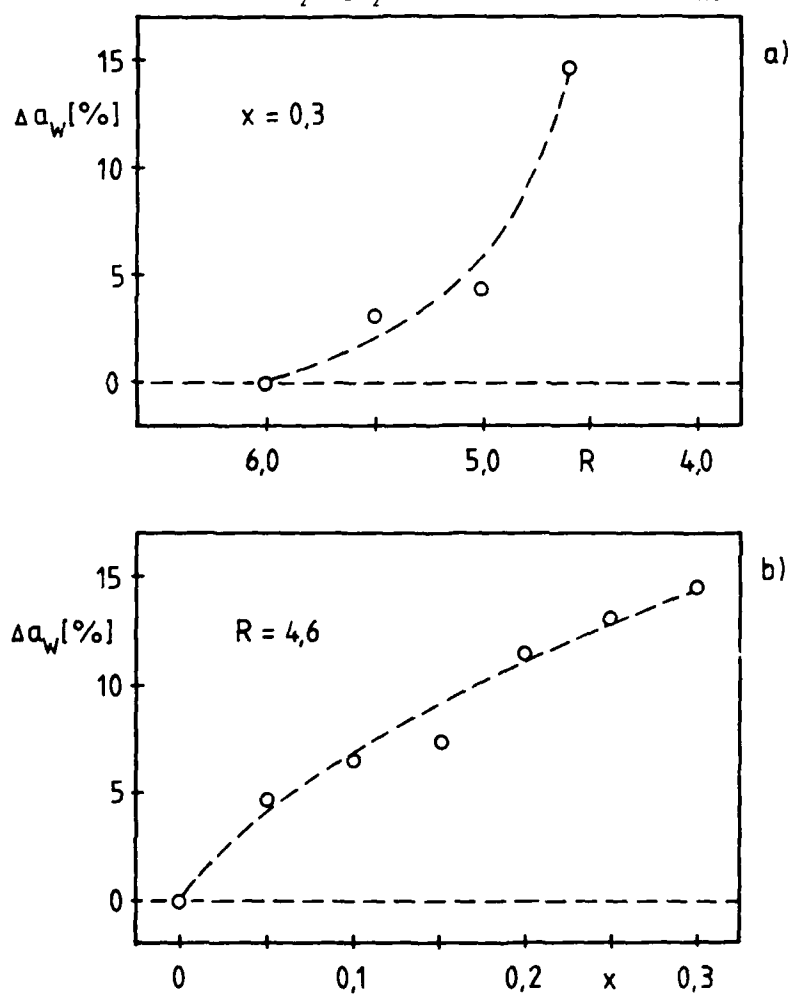
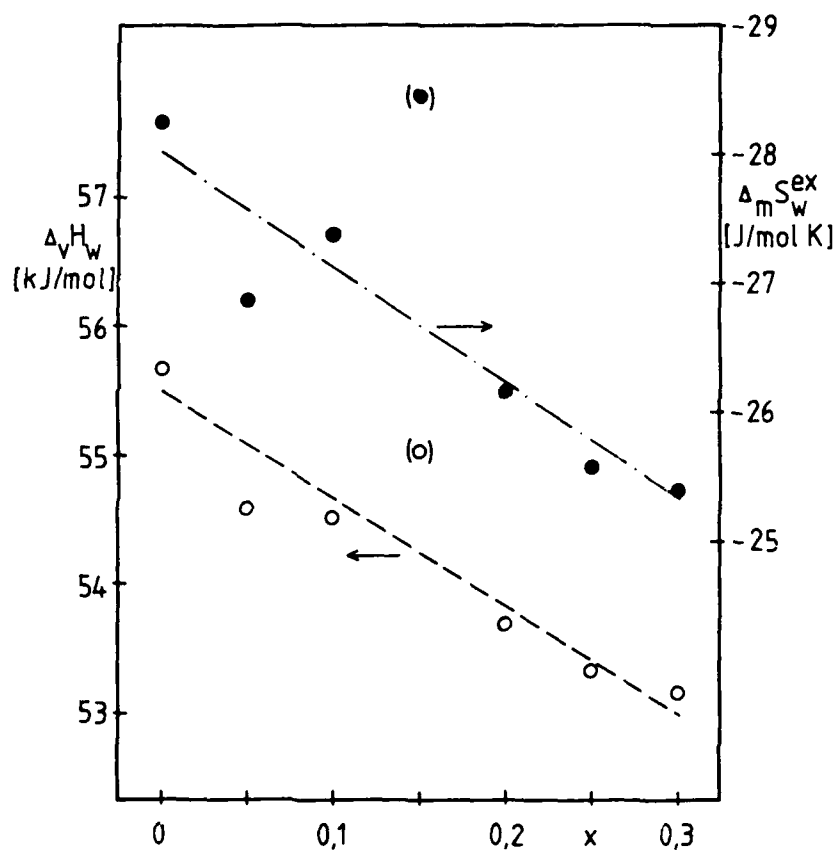


Fig. 5 Dependence of the molar enthalpy of evaporation $\Delta_v H_w$ and the partial molar excess entropy of water $\Delta_m S_w^{ex}$ on the KCl content in the system $\{x\text{KCl} + (1-x)(\text{MgCl}_2 + R \text{H}_2\text{O})\}$ at $R = 4.6$ and $T = 473 \text{ K}$



STORING ENERGY AT AMBIENT TEMPERATURES: A STUDY OF THE MELTING-FREEZING EQUILIBRIA OF $(\text{CaCl}_2, 6\text{H}_2\text{O}) - (\text{K}^+, \text{NH}_4^+)(\text{Cl}^-, \text{NO}_3^-)$ MIXTURES

J. Guion, A. Jaffrin, M. Laügt, and M. Teisseire

Laboratoire d'Ecothermique C.N.R.S.
B.P. 21, 06561 Valbonne, Cedex, France

ABSTRACT

This paper reports on research into storing energy at ambient temperatures by use of phase change materials mainly based upon $\text{CaCl}_2, 6\text{H}_2\text{O}$. This process has a highly reversible solid-liquid equilibria that will not degrade for thousands of cycles. Different compositions, from pure stabilized calcium chloride hexahydrate (phase transition $\Theta \approx 28.2^\circ\text{C}$, $\Delta H \approx 190-200 \text{ J/g}$) to multicomponent solutions with KCl and NH_4Cl (existence of two eutectic valleys, $22.5-25^\circ\text{C}$ temperature range, and $\Delta H \approx 190-200 \text{ J/g}$), have been studied and characterized by differential scanning calorimetry. Solutions containing nitrate ion and showing the existence of an anion exchange reaction lead to the formation of an eutectic compound (phase transition $\Theta \approx 1^\circ\text{C}$ and $\Delta H \approx 170-180 \text{ J/g}$). From a rough analysis of the C_p signals, which are very sensitive to slight composition changes, the influence of several parameters on the behavior of these solutions was studied.

INTRODUCTION

Various attempts have been made at storing energy from the sun as a free primary energy source and storing it for low temperature applications such as heating or cooling of buildings and growing of plants in well-controlled greenhouses. We have oriented our research toward efficient and low-cost devices using phase change materials (PCM) as storing materials. For the applications mentioned above, the main objective is temperature regulation near ambient temperature, using the latent heat involved in the phase transitions: solid-liquid in the storing part and liquid-solid in the restituting part. Many studies have been completed using salt hydrates: such PCM present a much higher thermal capacity (sensible and latent heat) than raw materials such as rocks, pebbles or concrete, and even water. This reduces by a factor of 5 to 20 the weights and volumes of thermal storage required for equal performance. The choice of PCM depends upon many parameters: transition temperature domain, transition enthalpy, thermal stability, and cost. This paper deals with calcium chloride hexahydrate solutions for use in the $20-30^\circ\text{C}$ temperature applications.

CALCIUM CHLORIDE HEXAHYDRATE

Figure 1 represents part of the phase diagram of $\text{CaCl}_2\text{-H}_2\text{O}$, showing the existence of two compounds: hexahydrate A ($\text{CaCl}_2 \cdot 6\text{H}_2\text{O}$) and tetrahydrate B ($\text{CaCl}_2 \cdot 4\text{H}_2\text{O}$). The tetrahydrate exists under three allotropic forms, the stable one being the α variety.

The liquidus branches of A and B (α -tetrahydrate) join at a peritectic point, P, which means that, starting with a solid of composition A, if melted and then cooled, one will observe formation of tetrahydrate B. This salt has a higher density than that of the liquid in equilibrium, and settles down, giving rise to a segregation phenomenon. Unfortunately, the enthalpy transition of the tetrahydrate is much lower than that of the hexahydrate. Moreover, the tetrahydrate will melt again, only at a higher temperature than the melting temperature (29.2°C) of A.

Another common feature observed for salt hydrates is the subcooling phenomenon. For chemically pure calcium chloride hexahydrate, it is very easy to get a temperature of 10 to 15°C below the melting temperature without freezing. Many studies concerning nucleation and suppression of segregation effects have been attempted. A variety of nucleating agents have been tested and may play a role in preventing subcooling (1-5). One of them, strontium chloride hexahydrate, is an epitaxial agent of calcium chloride hexahydrate with very similar crystal parameters, which may explain its possible nucleation effect. However, it is generally used in proportions less than saturation, which means that it might also slightly modify the phase diagram (6). Controversies still exist on the exact mechanism responsible for the suppression of subcooling (5-7).

Since the peritectic composition P is very near the composition of hexahydrate, this compound is often referred to as "quasi-congruent melting" compound. This may only be approached with additives which modify the phase diagram, resulting in a decrease in the melting temperature moving the relative position of P compared to pure A. Among the most effective additives are strontium chloride hexahydrate and potassium chloride; however, it is not certain whether, after many cycles, gradually increasing amounts of tetrahydrate B are formed.

Another method, referred to as the "extra water principle," simply consists of adding some water in order to operate with the P composition. This addition lowers the melting temperature by $1\text{-}2^\circ\text{C}$ and reduces the latent heat by 20-30%, but does not give complete freedom from the segregation phenomenon. Many thickening agents have been claimed as effective for preventing this phenomenon. A critical examination shows very little to moderate success of the solutions

proposed for another attractive salt hydrate, the Glauber's salt (sodium sulfate dodecahydrate) (9). We have been lucky enough to find a successful agent for calcium chloride hexahydrate, consisting of a special variety of diatomaceous earth, containing mainly acicular "synedra," with a needle form of 5000 Å length with arrays of regularly matched holes of 50 Å diameter. The effectiveness of such stabilizing agent - 10% by weight of calcium chloride - has been clearly demonstrated over thousands of cycles, and solar houses equipped with this storing material - patented under the trade name of chliarolithe (from Greek: warm stone) - in different configurations have been operating without any alteration of the PCM for nine years. How the stabilizing agent works is not yet completely understood, but the role of diatomites is generally thought of as being twofold:

1. The mechanical dispersion in mass, their distribution preventing any settling down of tetrahydrate, and then allowing its eventual redissolution upon heating, if ever formed. However, it is difficult to understand why other diatomaceous varieties (cylindrical or spiral shapes) with comparable macrophysical properties (density) do not exhibit the same behavior.
2. The microporous properties, favoring preferential nucleation of hexahydrate and orienting crystalline growth of this compound. This is quite difficult to prove. We tried some experiments with crystallization of calcium chloride hexahydrate solutions, in x-ray Guinier-Simon cells, equipped for work in controlled atmospheres and varying temperatures with time. While the thermal properties evaluated from slow heating rates with DSC calorimetry - 3°C per hour - showed a reversible melting-freezing transition process according to the typical curve of Figure 2, for the same sample of chliarolithe the x-ray diagrams did not show any lines before we reached a temperature of -11°C. The only compound identified is $\text{CaCl}_2 \cdot 6\text{H}_2\text{O}$, but these observations occurred far below the interesting melting zone.

SOLUTIONS RICH IN CALCIUM CHLORIDE WITH AMMONIUM AND POTASSIUM CHLORIDE ADDITIVES

For some building applications and greenhouse regulations, there is need for PCM melting in the 18-25°C range. The strategy followed was to take calcium chloride hexahydrate as the basic component and to try several additives in order to get lower melting temperatures and a "fair" latent transition heat.

After several experiments involving the "extra water principle" (8) and following one observation about two not well-defined compositions of $\text{CaCl}_2 \cdot 6\text{H}_2\text{O}$, KCl, and NH_4Cl mixtures (10), we pursued the exploration of this pseudo-ternary system. Working in the corner

of a rich $\text{CaCl}_2 \cdot 6\text{H}_2\text{O}$ component, within the estimated maximum solubilities area of both NH_4Cl and KCl , either along constant CaCl_2 compositions or constant $\text{KCl}/\text{NH}_4\text{Cl}$ molar ratio lines, we were able to correlate the variations of C_p curves that were very sensitive to even slight composition changes, to the possible existence of a smooth eutectic valley. On Figure 2, we represented two C_p signals and their relative contents, which may be compared to the values observed for pure $\text{CaCl}_2 \cdot 6\text{H}_2\text{O}$ and the technical chliarolithe. The curves are highly reproducible, and the melting temperatures obtained from intersection of the basis line with the extrapolated tangent at the first inflection point - onset temperature - gives 22.5°C for the eutectic "temperature." Figure 3 shows the C_p signal corresponding to the eutectic composition (MU 124, $n_{\text{CaCl}_2 \cdot 6\text{H}_2\text{O}} = 1$, $n_{\text{NH}_4\text{Cl}} = 0.242$, $n_{\text{KCl}} = 0.096$), for which the total ΔH transition value is 190-200 J/g.

It is worthwhile emphasizing how difficult it is to clearly identify what the solid phases in equilibrium in the transition zone are, while experimental x-ray work is still progressing. When cycled, the composition corresponding to MU 124 gives the extended horizontal melting level temperature versus time, at least for the first cycles. As before, segregation and subcooling might easily be observed and this makes it compulsory, for long term industrial applications, to introduce diatomites as a stabilizer.

Observations, related to the experiments where the exact ratio of water to calcium chloride was not correctly adjusted to get the hexahydrate compound, led us to explore a small part of the quaternary system CaCl_2 , H_2O , KCl and NH_4Cl . Surprisingly, within a narrow composition domain, we observed again the probable formation of an eutectic compound, with a melting temperature of 23.9°C and a heat content of 190-200 J/g (see C_p curve for the compound MU 106 on Figure 3, $n_{\text{CaCl}_2} = 0.430$, $n_{\text{H}_2\text{O}} = 2.44$, $n_{\text{KCl}} = 0.040$, and $n_{\text{NH}_4\text{Cl}} = 0.101$). This composition has been tested for stability towards segregation; with a water deficit of 5.3% compared to hexahydrate composition, we could not trigger any undesirable tetrahydrate, even by introducing external germs of this last compound. It is to be noted that the total ΔH content of 190-200 J/g is quite similar to that of chliarolithe, and this fact may be related to the high endothermic effect observed on solubilization of NH_4Cl and KCl .

RECIPROCAL SOLUTIONS RICH IN CALCIUM CHLORIDE WITH AMMONIUM, POTASSIUM CHLORIDES, AND NITRATES

Starting from the eutectic composition related to $\text{CaCl}_2 \cdot 6\text{H}_2\text{O}$, NH_4Cl , KCl , we added various quantities of either ammonium or potassium nitrate. The corresponding C_p versus temperature curves generally showed two peaks, sometimes three, more or less separated. The onset temperatures were difficult to determine, for the shape of

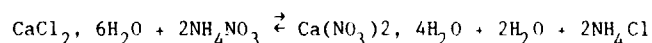
the C_p signals was similar to that in solutions where an excess of water as compared to hexahydrate was introduced (8); this resulted in observation of a pronounced drag effect before the first melting peak, reducing the latent heat content of these solutions.

We systematically analyzed the influence of the different parameters governing the behavior of these reciprocal solutions where the water content is critical. All these solutions were prepared with diatomites as a stabilizer and with pure $\text{CaCl}_2 \cdot 2\text{H}_2\text{O}$.

Figure 4 shows the variation of the importance of the ΔH content corresponding to the "drag zone," of the eutectic peak (ΔH_{m1}), and of the second peak (ΔH_{m2}) with the deficit in moles % relative to calcium chloride hexahydrate composition. The drag effect decreases linearly with increasing lack of water, while the relative importance of ΔH_{m1} and ΔH_{m2} changes from almost pure eutectic (S 29) to a signal where the second peak becomes predominant, all the other parameters being fixed.

Figure 5 shows the influence of the number of moles of NO_3^- for a given initial deficit of water of 3%, n_{CaCl_2} , $n_{\text{NH}_4\text{Cl}}$, n_{KCl} being fixed. This influence is also illustrated in Figure 6, corresponding to solutions with an initial water deficit of 8%, for the evolution of the C_p signals. S 59 with no nitrate is very near the eutectic ($\Theta_m = 23.9^\circ\text{C}$) already mentioned; increasing the nitrate content results in the decrease of this peak and the progressive formation of an intermediate peak (S 57, $n_{\text{NO}_3^-} = 0.02$). Both peaks decrease gradually from S 56 ($n_{\text{NO}_3^-} = 0.06$) to S 58 ($n_{\text{NO}_3^-} = 0.12$), while the eutectic compound ($\Theta_m = 19.7^\circ\text{C}$, $\Delta H = 170 \text{ J/g}$) growth becomes more pronounced. Variations of ammonium chloride initial content, or potassium chloride/ammonium chloride ratio, other parameters being held constant, show that the drag effect is constant, and that the relative importance of the two peaks may vary.

These experimental observations can be partly accounted for by the the exchange reaction:



The formation of the calcium nitrate tetrahydrate is accompanied by the formation of two water molecules. This may explain the drag effect observed and its correlative reduction when the initial water content of the solutions is decreased. This evidently holds if KNO_3 is used instead of NH_4NO_3 . The above reaction leads also to the formation of NH_4Cl (or KCl), thus modifying the $\text{KCl}/\text{NH}_4\text{Cl}$ ratio, which is critical for reaching the exact eutectic composition (11,12). Such solutions have been actually tested in full-scale greenhouses and have worked well for two years, thus, allowing 40% energy savings.

BIBLIOGRAPHY

- (1) TELKES M., Phase change thermal storage/a comprehensive look at developments and prospects. Monegon L+J report M 105, September 1950.
- (2) ABHAT A., Rev. Phys. Appl. 15, p. 477 (1980).
- (3) SCHNEIDER M., SYLVAIN J-D., BERGER X., JAFFRIN A., BOURDEAU L., A.N.V.A.R.-C.N.R.S. French Patent n° 79 13296 (1977)
European Patent n° 0, 019, 573 (1979).
- (4) LANE G.A. and ROSSOW H.E., U.S. patent 4, 272, 396 (1981).
- (5) CARLSSON B., STYMNE H. and WETTERMARK G., Solar Energy 23, p. 343, (1979).
- (6) LANE G.A., Solar Energy, Vol. 27, p. 73, (1981).
- (7) FEIL CHENFELD H., FUCHS J. and SARIG S., Solar Energy, Vol. 32, N° 6, p. 779 (1984).
- (8) LAUGT M., SAUZADE J-D., MAKHLOUF S., WETTERWALD M-J. and GUION J., A.F.G.A.T., Calorimetry and thermal analysis proceedings, La Gaillarde, Vol. XV, p. 22 (1983).
- (9) MARKS S.B., Solar Energy, Vol. 25, p. 255 (1980).
- (10) MEISINGSET K.K. and GRONVOLD F., Solar benefits evaluated, Birmingham Conference (September 1982).
- (11) JAFFRIN A., LAUGT M., GUION J., PELOUS E., Belgian patents 900 2448, Solvay and 900 2449 (17/5/85).
- (12) GUION J., LAUGT M. and TEISSEIRE M., Brevet C.N.R.S. 86 12346, (27 Août 1986).

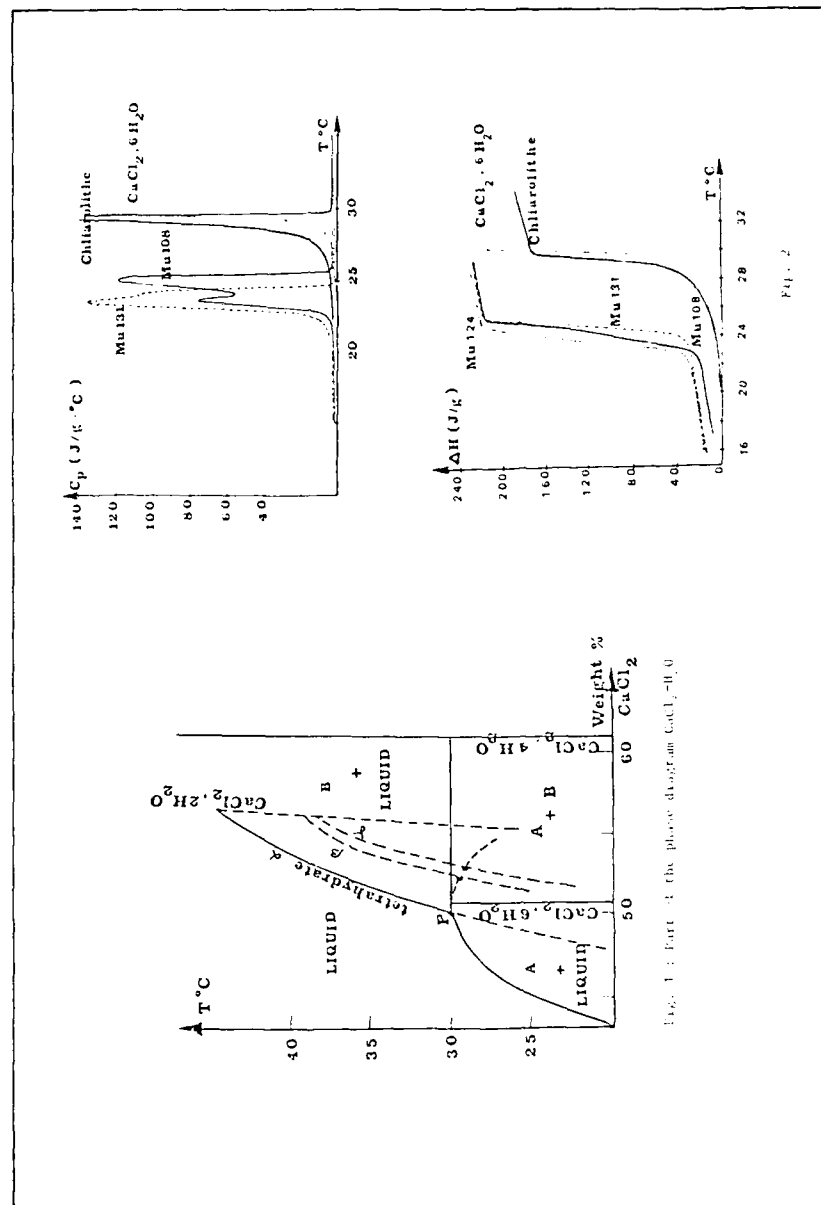


Fig. 1 : Part 1 of the phase diagram $\text{CaCl}_2\text{-H}_2\text{O}$.

Fig. 3. C_p signals for the two eutectic compositions Mu 124 and Mu 106.

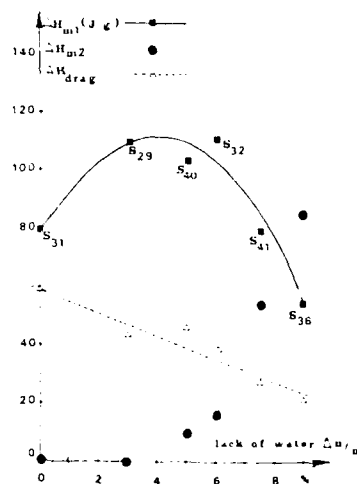
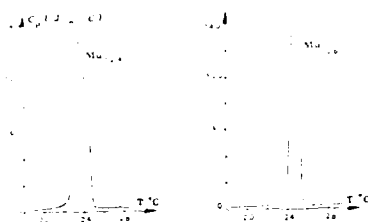


Fig. 4. Influence of lack of water on the different parts of ΔH content ($n \text{ CaCl}_2 = .75$; $n \text{ NH}_4\text{Cl} = .20$; $n \text{ KCl} = .0925$; $n \text{ NO}_3^- = .08$)

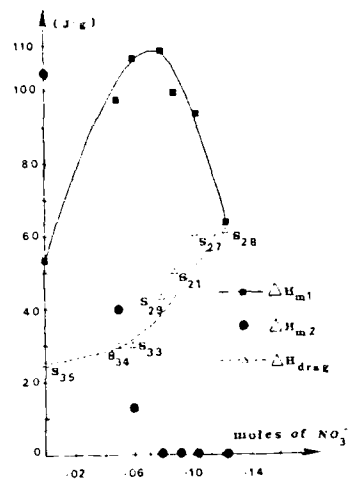
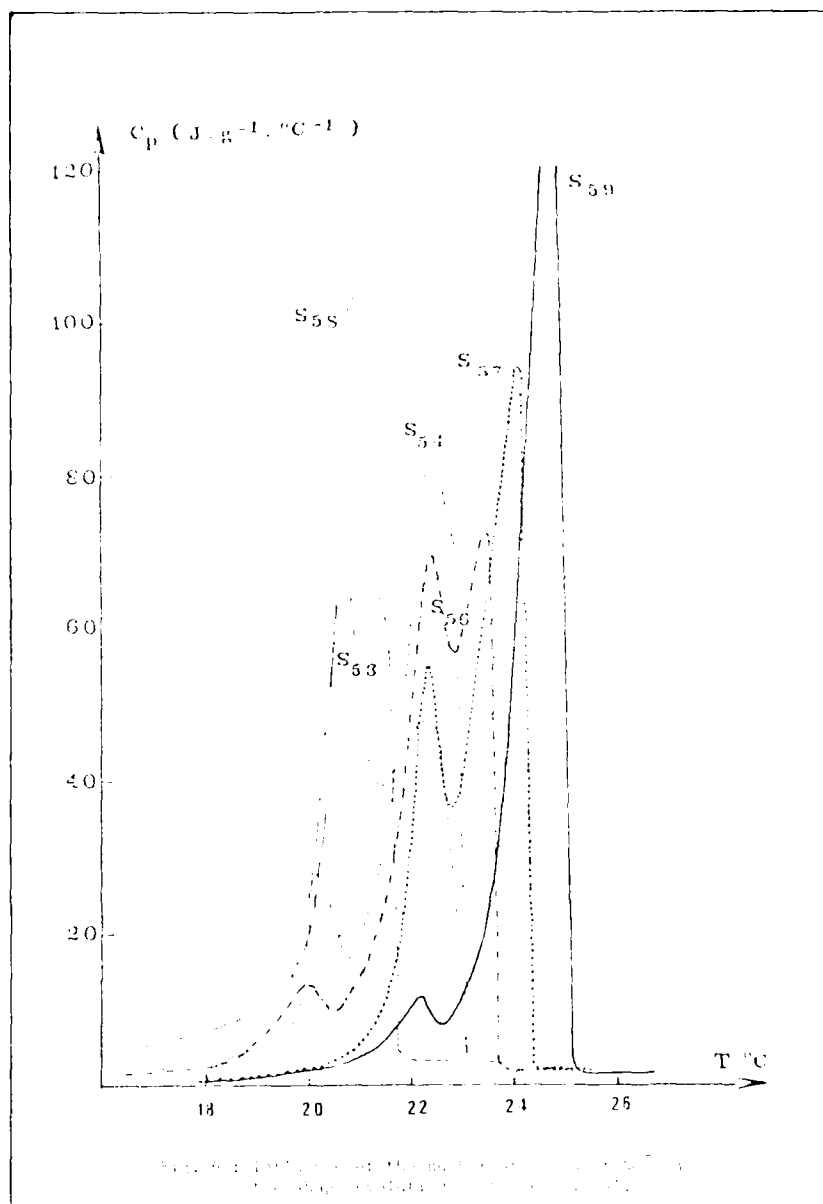


Fig. 5. Influence of the number of moles of NO_3^- ($n \text{ CaCl}_2 = .75$; $n \text{ H}_2\text{O} = 4.365$; $n \text{ KCl} = .0925$; $n \text{ NH}_4\text{Cl} = 0.20$)



THEORETICAL DETERMINATION OF EXCHANGE INTEGRALS IN SALTS

H. Sevkî Darendelioglu

Selçuk University, Department of Physics, Zindankale, Konya, Turkey

ABSTRACT

The exchange integrals of the crystal salts were investigated making use of Fourier Method. The mathematical relations between the exchange integrals were found out by determining the stability conditions for the magnetic modes, following the requirement for which the quadratic form must be definite positive. The magnetic modes and the exchange integrals which are the solutions of an eigen value problem, were studied theoretically in case of magnetite crystal.

INTRODUCTION

The signs and magnitudes of the exchange integrals are extremely important in determining the transition temperature, the magnetic structures and indeed practically all of the fundamental properties of the substances. In principle, the exchange integrals are of course calculable but in practice most calculations can claim only qualitative accuracy, although the methods and approaches are steadily improving. In this paper, we discuss the problem of determining the relations between exchange integrals of $(4e)Fe^{2+}$ ions of magnetite crystal by what might be called Fourier Method(1). The values are established by combining theoretical relations between the exchange integrals and various physical properties such as the Néel Point, with experimental data on these properties.

The exchange integrals of substances may be obtained by diverse methods. Many substances are studied by theoretical methods such as Fourier method(2), spin-dispersion method(3) or by experimental methods like neutron diffraction, heat capacity measurement(4) etc. In Fourier method one writes just the second order terms in the hamiltonian expression. In other words, one considers an hamiltonian expression as follows:

$$H = -J \sum_{i,j} \sum_{\alpha,\beta} A_{ij} \vec{S}_i^{\alpha} \cdot \vec{S}_j^{\beta}$$

In this study, we have used this form of Hamiltonian in which all invariants of the second order are just the scalar product of the two base vectors having the same representation. The spins being considered as axial vectors, one writes down the Hamiltonian expression invariant under spin reversal and symmetry operations of the crystal group.

ANALYSIS OF FOURIER METHOD

The most general expression of the second order of the interaction energy between spins \vec{S} and \vec{S}' located at the positions \vec{r} and \vec{r}' is given in dyadic notation(5) by

$$W_{P,R} = -2S(R)\vec{A}(R,R')\vec{S}'(R') \quad (1)$$

Here the dyadic $\vec{A}(R,R')$ is defined as

$$\vec{A}(R,R') = \sum_{i,j} W_{ij} \vec{a}_i \vec{b}_j \quad (i,j = 1,2,3) \quad (2)$$

where W_{ij} are scalar coefficients, \vec{a}_i and \vec{b}_j are vectors having the following property:

$$\vec{a}_i \cdot \vec{b}_j = \delta_{ij} \quad (3)$$

The nine-component dyadic $\vec{A}(R,R')$ may be decomposed into a symmetrical part and an antisymmetrical part, and then may be expressed in the following form:

$$W_{P,R} = -2J_{R,R'} \vec{S}(R) \cdot \vec{S}'(R') + J_{D-M} \vec{A}(R,R') \cdot (\vec{S}(R) \wedge \vec{S}'(R')) + \vec{S}(R) \vec{D}(R,R') \vec{S}'(R') \quad (4)$$

The interaction symbolised by J is called "isotropic or scalar interaction". Since J is a scalar and the scalar product $\vec{S}(R) \cdot \vec{S}'(R')$ is invariant under the action of rotation operations, the energy $-2J$ is just the difference between the singlet state energy and triplet state energy. The second term results from spin-spin orbit interaction, denotes antisymmetric coupling. It is also called "antisymmetric exchange" because of the fact when the spins $\vec{S}(R)$ and $\vec{S}'(R')$ are exchanged, this term changes the sign. It is introduced by Dzialoshinski and Moriya (b). The third term denotes the anisotropy. Here $\vec{D}(R,R')$ is a second order dyadic.

$$\vec{D}(R,R') = \frac{1}{2} \sum_{i,j} W_{ij} \vec{a}_i \vec{b}_j - \vec{b}_j \vec{a}_i = \frac{1}{2} \sum_{i,j} K_{ij} \quad (5)$$

When $\vec{a}_i = \vec{b}_i$ (if we neglect the constant terms) we obtain for W_R :

$$W_R = -2S(R)\vec{D}(R,R')\vec{S}'(R') \quad (6)$$

W_R is crystalline field energy of the spin at the position R . This energy is proportional to crystalline field tensor and has the symmetry elements of point R . So we can write the Hamiltonian for the system:

$$H = \sum_{R,R'} W_{R,R'} \quad (7)$$

We now consider isotropic exchange energy which is also known as Heisenberg-Néel energy H_N .

$$H_N = -2 \sum_{R,R'} g_{R,R'} \vec{S}(R) \cdot \vec{S}'(R') \quad (8)$$

Let us write again the above expression in terms of unitary spins:

$$H_N = -2 \sum_{R,R'} g_{R,R'} \hat{O}(R) \cdot \hat{O}'(R') \quad (9)$$

where $\hat{O}(R) = \vec{S}(R)/S(R)$ and $g_{R,R'} = \vec{S}(R)g_{R,R'}\vec{S}'(R')$

On the other hand, the equation of the spin motion:

$$\hbar \frac{d\vec{S}(R)}{dt} = 2 \sum_{R'} g_{R,R'} \vec{S}'(R') \wedge \vec{S}(R) \quad (10)$$

In static equilibrium the first term of the Eq. (10) must be zero. This

indicates that $\vec{S}(\vec{R})$ must be parallel to $\sum_{R'} g_{R,R'} \vec{S}'(\vec{R}')$. So using the unitary spins we may write:

$$\lambda_R \hat{S}(\vec{R}) = \sum_{R'} g_{RR'} \hat{S}'(\vec{R}') \quad (11)$$

Where λ_R is a constant of proportionality. By using Eq.(11), the Eq.(9) becomes

$$H_H = -2 \sum_R \lambda_R \hat{S}^2_R = -2 \sum_R \lambda_R \quad (12)$$

It follows from Eq.(12) that λ_R may be thought of as the contribution to the exchange energy arising from the interaction of \vec{S}_R with all neighbouring spins. On the other hand, because of λ_R is the same for every crystallographically equivalent atoms.

Let us number i (or j) = 1, 2, 3, ... in the different Bravais lattices of magnetic atoms. Here n is the number of independent sub-lattices. Multiplying the term $\lambda_i \hat{S}_i$ by the term $\exp 2\pi i \vec{k} \cdot \vec{R}_i$ and summing over all R_i , we get:

$$\lambda_i \vec{T}_i(\vec{k}) = \sum_j e_{ij}(\vec{k}) \vec{T}_j(\vec{k}) \quad (13)$$

Where

$$\vec{T}_i(\vec{k}) = \sum_j \hat{S}_j(\vec{R}_j) \exp 2\pi i \vec{k} \cdot \vec{R}_i \quad (14)$$

Since $\vec{T}_i(\vec{k})$ is the Fourier transformation of the unit spin $\hat{S}_i(\vec{R}_i)$ and g depends only on the distance $|\vec{R} - \vec{R}'|$, one has:

$$e_{ij}(\vec{k}) = \sum_{R_j} g_{R_i, R_j} \exp 2\pi i \vec{k} \cdot (\vec{R}_i - \vec{R}_j) \quad (15)$$

This sum is evaluated by fixing the atom at the position \vec{R}_i and by summing on all atoms \vec{R}_j of lattice j . The equation system (13) may be rewritten as matrix equation as follows:

$$(E(\vec{k}) - \lambda) \vec{T}(\vec{k}) = 0 \quad (16)$$

where $E(\vec{k})$ is a hermitian matrix of which elements are defined by the Eq.(15). (λ) is a diagonal matrix with elements of $\lambda_i \delta_{ij}$. $\vec{T}(\vec{k})$ defined by the Eq.(14) is a column vector of n component. $\vec{C}_j(\vec{k})$ is given by the Fourier inverse transformation of $\vec{T}_j(\vec{k})$:

$$\vec{C}_j(\vec{R}_j) = \sum_{\vec{k}} \vec{T}_j(\vec{k}) \exp(-2\pi i \vec{k} \cdot \vec{R}_j) \quad (17)$$

In resolving the equation(16), we obtain the information about spins orientation from the eigen vectors. By means of the eigen values, we obtain the propagation vectors which corresponds to every magnetic mode. Finally, using the stability conditions, we obtain the relations in the form of inequalities between the exchange integrals. The spins having the same phase are located on the same crystallographic planes. The phase expression of the spins located on such planes is given by the term $\exp 2\pi i \vec{k} \cdot \vec{R}$. Vector $\vec{k}(h, k, l)$ which defines the direction of propagation of the spins waves is a solutions of the equation:

$$\frac{d\lambda}{dn} = \frac{d\lambda}{dk} = \frac{d\lambda}{dl} = 0 \quad (18)$$

In order to study the stability conditions of the system, the quadratic form the coefficient of which are the second derivatives of λ , must be

positive. This requirement yields the relations between the exchange integrals.

APPLICATION TO $(4e)Fe^{2+}$ IONS OF MAGNETITE CRYSTAL

Firstly, we shall discuss the solid phase i.e. crystal phase rather than molten phase. Our test material is fagus magnetite crystal. Magnetite crystal belongs to the space group $I_{hmm} - (O_2H)$, and the $(4e)Fe^{2+}$ ions are (7) spread out in the following manner:

$$9(0, 1/4, 1/4) \quad 10(1/2, 3/4, 3/4) \quad 11(0, 3/4, 3/4) \quad 12(1/2, 1/4, 1/4) \quad (19)$$

The matrix elements for these ions defined by the Eq. (15) are:

$$e_{g,g} = e_{g,ga} + e_{g,gb} + e_{g,gc} \quad (21)$$

$$\text{where } e_{g,ga} = 2e_{g,ga} \cos 2x$$

$$e_{g,gb} = -2e_{g,gb} \cos 2y$$

$$e_{g,gc} = 2e_{g,gc} \cos 2z$$

and the other matrix elements are:

$$e_{g,1} = -2e_{g,1} \cos x \cos y \cos z$$

$$e_{g,11} = -2e_{g,11} \cos y \cos z \quad (22)$$

The interaction matrix defined by the Eq. (16), takes on the form:

$$E_{111} = \begin{pmatrix} e_{g,g} & e_{g,10} & e_{g,11} & e_{g,12} \\ e_{g,10} & e_{g,g} & e_{g,12} & e_{g,11} \\ e_{g,11} & e_{g,12} & e_{g,g} & e_{g,10} \\ e_{g,12} & e_{g,11} & e_{g,10} & e_{g,g} \end{pmatrix} \quad (23)$$

The reader may check that the matrix:

$$\Psi^r = \begin{pmatrix} 1 & 1 & 1 & 1 \\ 1 & 1 & 1 & 1 \\ 1 & 1 & 1 & 1 \\ 1 & 1 & 1 & 1 \end{pmatrix} \quad (24)$$

completely diagonalizes E

$$\Psi^\dagger E \Psi = n(\lambda)$$

where $n = 4$ and (λ) is the diagonal matrix formed by the following values:

$$\begin{aligned}\lambda_F &= e_{y,9} + e_{y,10} + e_{y,11} + e_{y,12} \\ \lambda_G &= e_{y,9} - e_{y,10} + e_{y,11} - e_{y,12} \\ \lambda_C &= e_{y,9} + e_{y,10} - e_{y,11} - e_{y,12} \\ \lambda_A &= e_{y,9} - e_{y,10} - e_{y,11} + e_{y,12}\end{aligned}\quad (24)$$

The corresponding eigen vectors which are the columns of the matrix are $T_1(1,1,1,1)$, $T_2(1,-1,1,-1)$, $T_3(1,1,-1,-1)$, $T_4(1,-1,-1,1)$ respectively. It should be considered the ground-state eigen value λ_F of the system.

$$\lambda_F = e_{y,9} + e_{y,10} + e_{y,11} + e_{y,12}$$

and equating its differentials with respect to x, y, z to zero, one obtains the respective solutions for the various modes which are summarized in Table I. As seen in the table, in the G-mode, spins of the same phases parallel to (110) planes, the phase of each spin being given by $\cos 2\pi x/y$.

The quadratic form, the coefficients of which are the second derivatives of λ_F with respect to x, y, z , must be positive or zero. Another method states the matrix $\frac{\partial^2 \lambda_F}{\partial x_i \partial x_j}$ must have positive roots for small but arbitrary variations of x_i . Here x_i and k_i are the equilibrium values of x and k respectively. To that end one writes the second order differentials $\delta^2 \lambda_F$. We finally find following inequalities for A-mode and G-mode respectively.

$$\begin{aligned}\delta^2 g_{y,9} + \delta^2 g_{y,10} + \delta^2 g_{y,11} + \delta^2 g_{y,12} + \delta^2 g_{y,9} + \delta^2 g_{y,10} + \delta^2 g_{y,11} + \delta^2 g_{y,12} &> 0 \\ \delta^2 g_{y,9} + \delta^2 g_{y,10} + \delta^2 g_{y,11} + \delta^2 g_{y,12} + \delta^2 g_{y,9} + \delta^2 g_{y,10} + \delta^2 g_{y,11} + \delta^2 g_{y,12} &> 0\end{aligned}$$

CONCLUDING REMARKS

It is not possible to obtain exact solution of Eq.16 for three-dimensional crystal, even if we restrict ourselves to the simplest case of nearest-neighbour-interactions only. Some form of approximation must be used and it is difficult to estimate the approximation, as there is no exact solution as a standard of comparison.

In general, we may say that the molecular field is used when there is more than one set of interactions though considerably more sophisticated and accurate methods are available for only the case of nearest-neighbour-interactions only. There are a number of examples in the literature where nearest-neighbour approximation are applied to systems which have two or more sets of interactions.

REFERENCES

1. F. Bertaut, Ann. Phys., **7**, 220 (1972)
2. F. Bertaut, Com. Rend. Acad. Sci., **26**, 252 (1961)
3. B. H. Torrie, Solid State Com., **5**, 715 (1964)
4. S. H. Charap, J. Appl. Phys., **35**, 938 (1961)
5. F. Bertaut, Compt. Rend. Acad. Sci., **252**, 2078 (1961)
6. T. Moriya, Phys. Rev., **120**, 91 (1961)
7. S. L. Abrahams and B. A. Calhoun, Acta Cryst., **8**, 257 (1955)

Propagation Vector	Modes	Phases
0 0 0	F	1
1 0 0	A	$\cos 2x$
0 1 0	C	$\cos 2y$
1 1 0	G	$\cos 2(x+y)$

Table 1 Propagation Vectors and Corresponding Modes with Phases

APPLICATION OF A MODIFIED LINDEMANN'S MELTING FORMULA
TO ISENTROPIC AND ISOTHERMAL COMPRESSIBILITIES OF
MOLTEN SALTS AT THEIR MELTING POINTS

T. Iida, T. Mizobuchi, and Z. Morita

Department of Metallurgical Engineering
Faculty of Engineering, Osaka University
2-1, Yamada-oka, Suita, Osaka 565, Japan

ABSTRACT

Simple equations for the isentropic and isothermal compressibilities of molten salts at their melting points have been derived by combining Einstein's formula for the compressibility of a solid with a modified version of Lindemann's melting formula by the authors. These equations are similar to both expressions derived on the basis of a statistical fluctuation theory, i.e. Cahn-Hilliard theory, and a hard-sphere model.

INTRODUCTION

The motions of molecules in liquids are very complicated, since they are time dependent. It would appear, however, that some properties of liquids are mainly dominated by the simple oscillatory motion of molecules. For example, the viscosity of simple liquids (1), the compressibility and thermal conductivity of non-metals (2,3) are, respectively, expressed in terms of the fundamental frequency of intermolecular vibration. In calculating the above properties of liquids, Lindemann's melting formula (4) has frequently been used for the frequency of vibration (1-3). Unfortunately, Lindemann's formula provides only rough values for the average frequency of vibration of solids at their melting points (4-7). Therefore, to evaluate the intermolecular frequencies of liquids at their melting points, we have modified Lindemann's formula using the surface tension of a liquid (8-10).

In this paper, simple equations for the isentropic and isothermal compressibilities of molten salts at their melting points have been derived by combining Einstein's compressibility formula and a modified Lindemann's formula of the authors. In addition, the equation for isothermal compressibility is compared with both expressions derived on the basis of a statistical fluctuation theory, i.e. Cahn-Hilliard theory (10-13), and a hard-sphere model (10,11,12).

DERIVATION OF LIQUID COMPRESSIBILITY EQUATIONS AT THE MELTING POINT

Einstein proposed a simple relation between the compressibility of a solid and the characteristic frequencies of molecules (14,15). The relation may be written as

$$\nu = \frac{C_i}{M^{1/3} \rho^{1/6} \kappa_S^{1/2}} \quad (1)$$

where ν is the mean frequency of intermolecular vibration, M the molecular weight (formula weight), ρ the density, κ_S the isentropic compressibility, and C_i ($i=1, \dots, 5$) a constant which is roughly the same for all materials.

According to Lindemann, the intermolecular frequency of solids at their melting points is given by

$$\nu = C_2 \left(\frac{T_m}{M V_m^{2/3}} \right)^{1/2} \quad (2)$$

where T_m is the absolute melting temperature, and V_m the molar volume at temperature T_m .

Combining eqns. (1) and (2), we have an expression for isentropic compressibility.

$$\kappa_S = \frac{C_3 V_m}{T_m} \quad (3)$$

This simple relationship has long been known (7). Figure 1 indicates this relationship for various molten salts. As can be seen from Figure 1, this relationship is not satisfactory at all, though it is said that the relationship holds approximately for liquids at or near their melting points (7). Incidentally, on the basis of the relationship in Figure 1, molten salts can be divided into some groups. For example, alkali halides lie on their own straight line. The need for this classification can be attributed to the types of intermolecular forces present within these molten salts.

Since Lindemann's melting formula is inadequate, eqn.(1) would, as a result, also seem to be inadequate. The average frequency of intermolecular vibration of liquids at their melting points is reasonably given by Lindemann's formula as modified by the authors (8-10). The modified Lindemann's formula is

$$\nu = C_4 \left(\frac{\gamma}{M} \right)^{1/2} \quad (4)$$

where γ is the surface tension of a liquid at its melting point. (The value of C_4 is approximately 6.8×10^{11} for pure liquid metals (16)).

Combining eqns. (1) and (4), we have a simple expression for the isentropic compressibility of a liquid at its melting point.

$$\kappa_S = \frac{C_5 V_m^{1/3}}{\gamma} \quad (5)$$

Figure 2 shows this relationship. As is clear from Figure 2, eqn. (5) provides good results for various molten salts with a slope of 6.0×10^{-10} ($\text{mol}^{1/3}$) as the constant of proportionality between isentropic compressibility and the grouping ($V_m^{1/3}/\gamma$).

It may be expected that the compressibility of molten salts is roughly given as a function of the reciprocal of surface tension, since molten salts have similar values of $V_m^{1/3}$. Figure 3 indicates a correlation between the isentropic compressibility and the reciprocal of surface tension of molten salts at their melting points. As can be seen, the expected correlation is roughly true for molten salts.

The isothermal compressibility κ_T can easily be calculated using the well-known thermodynamic relationship (17)

$$\kappa_T = \left(\frac{C_p}{C_v} \right) \kappa_S \quad (6)$$

where C_p and C_v are heat capacities at constant pressure and constant volume, respectively. As exhibited in Figures 4 and 5, the values of C_p/C_v are approximately equal to 1.45 for all molten salts at or near their melting points. (The values of C_p/C_v are about equal to 1.15 for all liquid metals (17,18).)

Substituting eqn. (5) into eqn. (6), we have an expression for the isothermal compressibility of molten salts at their melting points.

$$\kappa_T = \frac{C_5 C_p V_m^{1/3}}{C_v \gamma} \approx \frac{8.7 \times 10^{-10} V_m^{1/3}}{\gamma}, \text{ (in SI units)} \quad (7)$$

or

$$\kappa_T \gamma \approx 8.7 \times 10^{-10} V_m^{1/3} \quad (8)$$

According to Cahn-Hilliard theory based on a statistical fluctuation in number density, the product of the isothermal compressibility and surface tension of a liquid near its triple point is expressed as (10-13)

$$\kappa_T \gamma \approx 7 \times 10^{-2} L \quad (9)$$

where L is the surface (interface) thickness.

An analogous expression to eqn. (9) has been proposed on the basis of a hard-sphere model, and is given by (10-12)

$$\kappa_T \gamma \approx \frac{a(2 - 3\eta + \eta^3)}{4(1 + 2\eta)^2} \quad (10)$$

where a is an effective molecular diameter, and η the packing fraction. Near the triple point, with η taken as 0.45 (it would appear that the value of η for liquids is roughly equal to 0.45 over a wide range of temperature (19-21), eqn. (10) yields approximately

$$\kappa_T \gamma \approx 5 \times 10^{-2} a \quad (11)$$

Eqn. (8) by the authors is similar to independently derived relations, eqns. (9) and (11).

From eqns. (8), (9), and (11), we have simple expressions for L and a , respectively.

$$L \approx 1.2 \times 10^{-8} v_m^{1/3} \quad (12)$$

$$a \approx 1.7 \times 10^{-8} v_m^{1/3} \quad (13)$$

Using these equations, the surface thickness and the effective molecular diameter can be evaluated from the molar volume, which can be measured experimentally.

CONCLUSIONS

(1) Simple equations for the isentropic and isothermal compressibilities of molten salts at their melting points have been derived by combining Einstein's formula and a modified Lindemann's melting formula by the authors. These equations are similar to the relations derived from dissimilar routes.

(2) The surface thickness and the effective molecular diameter of molten salts can be evaluated from the molar volume obtained experimentally.

REFERENCES

1. E. N. da C. Andrade, Phil. Mag., **17**, 497 (1934).
2. I. Osida, Proc. Phys.-Math. Soc. Japan, **21**, 353 (1939).
3. A. G. Turnbull, Aust. J. Appl. Sci., **12**, 324 (1961).
4. F. A. Lindemann, Phys. Z., **11**, 609 (1910).
5. A. K. Singh and P. K. Sharma, Can. J. Phys., **46**, 1677 (1968).
6. J. N. Shapiro, Phys. Rev., **1**, 3982 (1970).
7. M. Toda, H. Matsuda, Y. Hiwatari and M. Wadati, The structure and properties of liquids. (1976). Iwanami Shoten Publishers, Tokyo (in Japanese).
8. T. Iida, A. Kasama, M. Misawa and Z. Morita, J. Japan Inst. Metals, **38**, 177 (1974).
9. A. Kasama, T. Iida and Z. Morita, J. Japan Inst. Metals, **40**, 1030 (1976).
10. T. Iida and R. I. L. Guthrie, The physical properties of liquid metals--for metallurgists and materials engineers--, Oxford University Press, (in press).
11. P. A. Egelstaff and B. Widom, J. Chem. Phys., **53**, 2667 (1970); S. W. Mayer, J. Phys. Chem., **67**, 2160 (1963).
12. N. H. March and M. P. Tosi, Atomic dynamics in liquids. (1976), MacMillan, London.
13. A. B. Bhatia and N. H. March, J. Chem. Phys., **68**, 1999 (1978).
14. A. Einstein, Ann. d. Physik, **34**, 170 (1911).
15. N. F. Mott and H. Jones, The theory of the properties of metals and alloys, **12** (1936), Clarendon Press, Oxford.
16. T. Iida, R. I. L. Guthrie and Z. Morita, The 140th Committee, JSPS, Rep. No. 132 (Dec., 1982).
17. O. J. Kleppa, J. Chem. Phys., **18**, 1331 (1950).
18. P. Ascarelli, Phys. Rev., **173**, 271 (1968).
19. N. W. Ashcroft and J. Lekner, Phys. Rev., **145**, 83 (1966).
20. N. W. Ashcroft, Physica, **35**, 148 (1967).
21. Y. Waseda, The structure of non-crystalline materials, liquids and amorphous solids, **54** (1980), McGraw-Hill, New York.

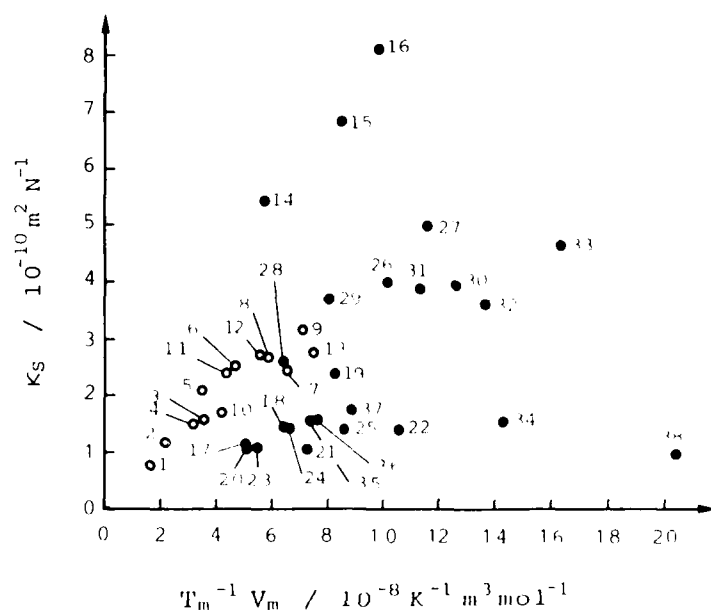


Figure 1. The isentropic compressibilities of molten salts at their melting points as a function of (V_m/T_m) .

Identification numbers are:

1. LiF 2. NaF 3. KF 4. LiCl 5. NaCl 6. KCl 7. CsCl
8. NaI 9. KI 10. LiBr 11. NaBr 12. KBr 13. CsBr
14. $MgCl_2$ 15. $MgBr_2$ 16. MgI_2 17. $CaCl_2$ 18. $CaBr_2$
19. CaI_2 20. $SrCl_2$ 21. $SrBr_2$ 22. SrI_2 23. $BaCl_2$
24. $BaBr_2$ 25. BaI_2 26. $ZnCl_2$ 27. ZnI_2 28. $CdCl_2$
29. $CdBr_2$ 30. CdI_2 31. $HgCl_2$ 32. $HgBr_2$ 33. HgI_2
34. $PbCl_2$ 35. $LiNO_3$ 36. $NaNO_3$ 37. KNO_3 38. $AgNO_3$

Open circles represent alkali halides in Figures 1 to 5. Data, except for those for $MgCl_2$, are taken from Janz (G. J. Janz, *Molten salts handbook*, 252 (1967), Academic Press, New York). Data for $MgCl_2$ from Ejima and Ogasawara (T. Ejima and M. Ogasawara, *J. Japan Inst. Metals*, 41, 778 (1977)).

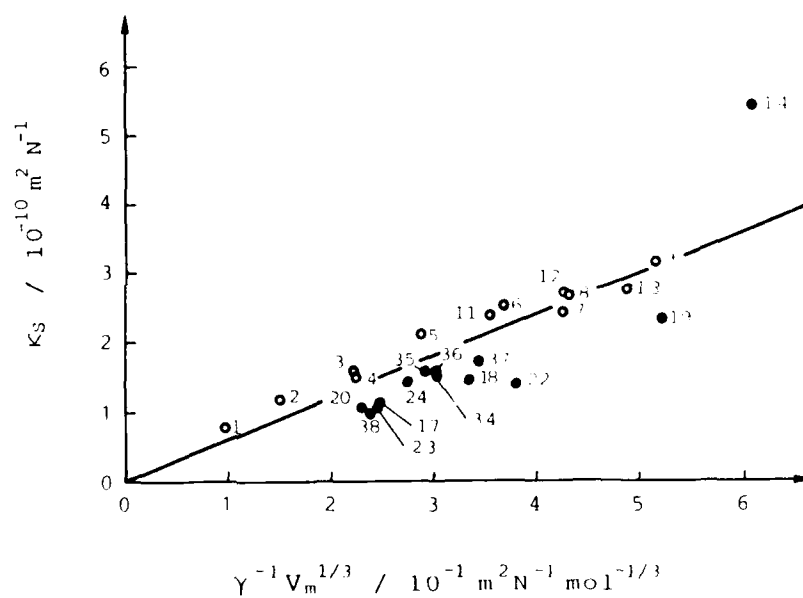


Figure 2. The isentropic compressibilities of molten salts at their melting points as a function of $(V_m^{1/3}/\gamma)$. Identification numbers in Figures 2 to 5 are the same as those in Figure 1.

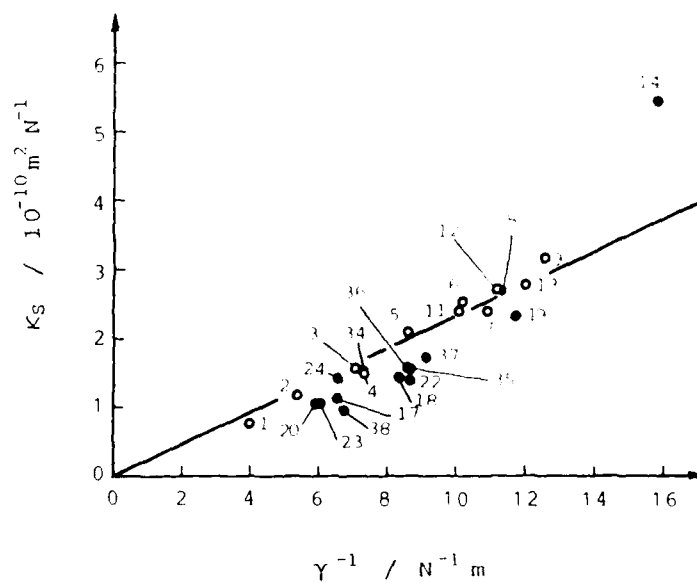


Figure 3. The isentropic compressibilities of molten salts at their melting points as a function of $(1/\gamma)$.

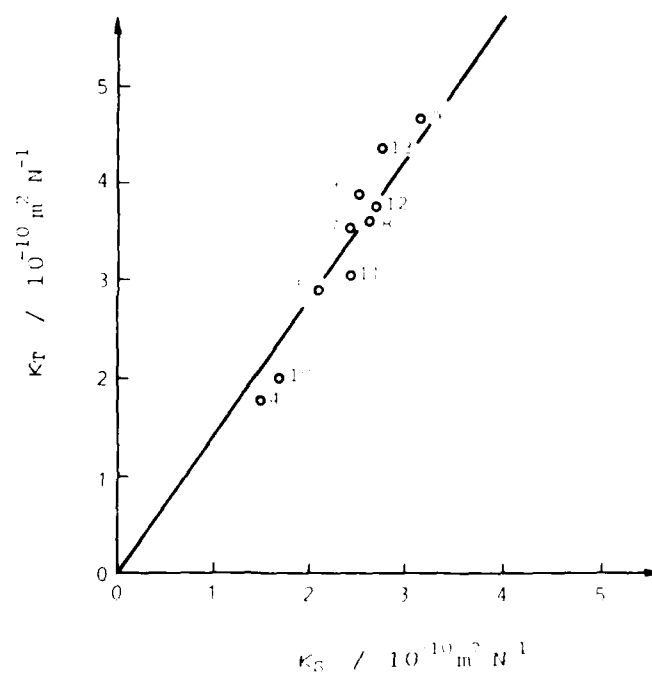


Figure 4. Isothermal compressibilities vs. isentropic compressibilities for molten alkali halides at their melting points. The constant of proportionality between κ_T and κ_S , i.e. C_P/C_V , is equal to 1.42.

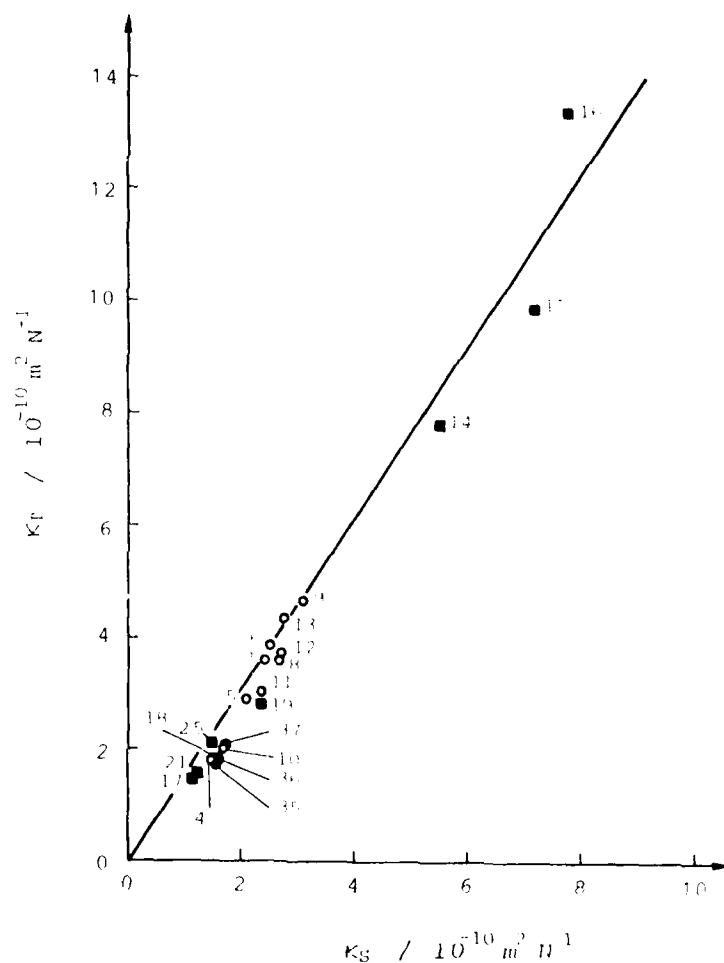


Figure 5. Isothermal compressibilities vs. isentropic compressibilities for various molten salts at or near their melting points. The constant of proportionality between κ_T and κ_S , i.e. C_p/C_v , is equal to 1.46. Open and closed circles denote alkali halides and nitrates at their melting points, respectively. Squares denote other salts at 1073K (the ratios of 1073K to their melting temperatures, i.e. $1073/T_m$, are between 1.0 and 1.2).

THERMODYNAMIC PREDICTION OF SULFIDE CAPACITIES IN $\text{Na}_2\text{O-SiO}_2$ MELTS

R. G. Reddy, M. Blander,* and B. Chen

Department of Chemical and Metallurgical Engineering
University of Nevada, Reno
Reno, Nevada 89557-0047

*Argonne National Laboratory
Chemical Technology Division/
Materials Science and Technology Program
Argonne, Illinois 60439-4837

ABSTRACT

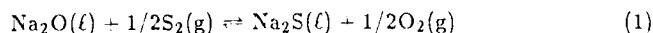
Sulfide capacities of $\text{Na}_2\text{O-SiO}_2$ melts at 1473 and 1623 K were calculated *a priori* from a model using free energies of formation of Na_2S and Na_2O and the activities of Na_2O in the binary $\text{Na}_2\text{O-SiO}_2$ melts. Our calculations are in excellent agreement with available experimental data and appear to be more more accurate than currently used empirical predictions of sulfide capacities, based on correlations with optical basicities using Pauling electronegativities.

INTRODUCTION

Recently, in industrial steelmaking, there has been increasing interest in treating hot metal with soda ash because it provides the possibility of removing sulfur and phosphorus from hot metal simultaneously. More attention has been paid to desulfurization than to dephosphorization. Sulfide capacities (which are a measure of the ability of a slag to remove sulfur from metal) of $\text{Na}_2\text{O-SiO}_2$ melts were experimentally determined by several investigators.(1-10) Comparison of the experimental data showed poor agreement among the various investigators, and also data are available only in a limited range of slag composition and temperature. A number of empirical correlations have been proposed between sulfide capacity and the basicity of slags. Very recently, we showed that sulfide capacities can be calculated *a priori*, based on a simple solution model and on a knowledge of the chemical and solution properties of sulfides and oxides. (11,12) Predictions of sulfide capacities, based on empirical correlations with basicity or optical basicity are far less accurate than those deduced from our method. In this paper, we present calculations of sulfide capacities of $\text{Na}_2\text{O-SiO}_2$ melts at the temperatures 1473 and 1623 K.

THEORETICAL CONSIDERATIONS

The sulfide equilibrium reaction can be written as



The equilibrium constant for reaction (1) is given by

$$K_{\text{Na}} = \left(\frac{P_{\text{O}_2}}{P_{\text{S}_2}} \right)^{1/2} \cdot \frac{a_{\text{Na}_2\text{S}}}{a_{\text{Na}_2\text{O}}} \quad (2)$$

Fincham and Richardson (13) defined the sulfide capacity, C_S , in terms of measurable quantities

$$C_S = (\text{wt}\% \text{S}) \left(\frac{P_{\text{O}_2}}{P_{\text{S}_2}} \right)^{1/2} \quad (3)$$

Combining equations (2) and (3), the following relation can be obtained

$$C_S = K_{\text{Na}} \cdot a_{\text{Na}_2\text{O}} \cdot \frac{(\text{wt}\% \text{S})}{a_{\text{Na}_2\text{S}}} \quad (4)$$

Equation (4) can be used to calculate C_S with the knowledge of K_{Na} , $a_{\text{Na}_2\text{O}}$, and a method of obtaining the relation between $a_{\text{Na}_2\text{S}}$ and $(\text{wt}\% \text{S})$. The method of obtaining this relationship and calculating C_S has been fully discussed. (11, 12)

For basic melts in the composition range $0 \leq X_{\text{SiO}_2} \leq 0.33$ in the Na_2O - SiO_2 binary system, the solution is considered to be a ternary mixture of Na_2O , Na_4SiO_4 , and Na_2S . The equation for C_S can then be written as

$$C_S = 100 \cdot W_S \cdot K_{\text{Na}} \cdot a_{\text{Na}_2\text{O}} \left(\frac{1 - 2X_{\text{SiO}_2}}{\bar{W}} \right) \quad (5)$$

where \bar{W} is the average molecular weight of the solution and where W_i is the molecular weight of the compound i .

For the composition range $0.33 \leq X_{\text{SiO}_2} \leq 0.5$ in the Na_2O - SiO_2 system, the solution is a mixture of sulfide anions with silicate polymer anions. Using polymer solution theory, we obtain an equation for C_S written as

$$C_S = 100 \cdot W_S \cdot K_{\text{Na}} \cdot a_{\text{Na}_2\text{O}} \cdot \frac{X_{\text{SiO}_2}}{\bar{W}} \left(\frac{\Phi_S}{a_{\text{Na}_2\text{S}}} \right) \quad (6)$$

where Φ_S is the volume fraction of S^{2-} sites defined here as $\Phi_S \approx n_S/n_{\text{Si}}$, n_S is the number of monomer sulfide sites and n_{Si} is the number of polymer sites. The relationship between Φ_S and $a_{\text{Na}_2\text{S}}$ was obtained from the adaptation of Flory's approximation for polymer-monomer mixtures to silicate melts. (14) One

parameter in the Flory theory is m , the average polymer chain length. For finite values of m , we obtain the expression

$$\ln a_{\text{Na}_2\text{O}} \approx \ln \Phi_s + \left(1 - \frac{1}{m}\right) \Phi_p \quad (7)$$

where Φ_p is $(1 - \Phi_s)$ and is generally close to unity.

Two conditions were considered, $m = 1$ at the central composition $2\text{Na}_2\text{O} \cdot \text{SiO}_2$ and a large value approaching $m = \infty$ (or $m = 1$) near the $\text{Na}_2\text{O} \cdot \text{SiO}_2$ composition.

Case I. When melts contain only monomers, i.e., $m = 1$, equation (7) reduces to

$$\frac{a_{\text{Na}_2\text{O}}}{\Phi_s} = 1 \quad (8)$$

Case II. For melts containing mostly polymers, $m = 1$ and $\Phi_p \approx 1$. Under these conditions, equation (7) reduced to

$$\frac{a_{\text{Na}_2\text{O}}}{\Phi_s} = 2.7183 \quad (9)$$

The sulfide capacities of binary $\text{Na}_2\text{O} \cdot \text{SiO}_2$ melts were calculated by substituting equation (8) and (9) into equation (6).

CALCULATION OF C_S FOR $\text{Na}_2\text{O} \cdot \text{SiO}_2$ MELTS

The calculated sulfide capacities in the binary $\text{Na}_2\text{O} \cdot \text{SiO}_2$ system at 1473 and 1623 K are presented in Figure 1. The activity of Na_2O was deduced from the experimentally measured data of Ohtani et al.¹⁵ The free energy of formation of $\text{Na}_2\text{S}(s)$ and $\text{Na}_2\text{O}(s)$ were taken from standard tables of data,¹⁶ and are presented in Table I at 1473 and 1623 K.

From the calculated values of the equilibrium constant $K_{\text{Na}_2\text{O}}$ for reaction (1) and $a_{\text{Na}_2\text{O}}$, C_S was calculated using equations (7) and (9) for the range of slag composition from $X_{\text{Na}_2\text{O}} = 1$ to 0.5 and for the two temperatures 1473 and 1623 K. The calculated values of C_S and experimental data of Nagashima and Katsura¹⁶ as compiled by Turkdogan¹⁷ at 1623 K are shown in Figure 1b; the calculated values of C_S and the experimental data of Ohtani and Terada¹⁵ at 1473 K are shown in Figure 1c. As can be seen, the agreement between the theoretically calculated and experimentally determined sulfide capacities is very good. For a given temperature, the sulfide capacity increases with an increase in the concentration of Na_2O in the $\text{Na}_2\text{O} \cdot \text{SiO}_2$ melt. It is also interesting to note that, for the composition $X_{\text{Na}_2\text{O}} = 0.5$, the sulfide capacity increases with a decrease in

temperature and for $X_{\text{Na}_2\text{O}} < 0.9$, the sulfide capacity increases with an increase in temperature. However, the effect of temperature on sulfide capacity is not very large. This observation can be explained by considering two independent factors, K_{Na} and $a_{\text{Na}_2\text{O}}$. At higher concentrations (i.e., $a_{\text{Na}_2\text{O}} \approx 1$), the equilibrium constant, K_{Na} , governs the temperature dependence of the sulfide capacity; whereas, at low concentrations of Na_2O in $\text{Na}_2\text{O-SiO}_2$ melts, the differences of the activity of Na_2O predominately control the temperature dependence of sulfide capacities (i.e., the activity of Na_2O increases with an increase in temperature).

A comparison of these sulfide capacities with the sulfide capacities of other binary systems, which were calculated in our previous publications, (11,12) is presented in Table II. Although these cannot be compared directly because of temperature differences, it is clear that the sulfide capacities of hypothetical pure molten Na_2O is higher than all the other oxides. However, for a composition of $X_{\text{SiO}_2} > 0.33$, the sulfide capacities are higher than those in the CaO-SiO_2 and MgO-SiO_2 systems and lower than those in the MnO-SiO_2 and FeO-SiO_2 systems. With an increase in the SiO_2 concentration, the sulfide capacities of $\text{Na}_2\text{O-SiO}_2$ solutions decrease very significantly because of the very large decrease in the activities of Na_2O .

From our results, it is clear that sulfide capacities of slags are directly related to two independent quantities, (1) the equilibrium constant, K_{Na} , and (2) the activity of Na_2O . This leads to the conclusion that sulfide capacities cannot be empirically correlated using a single parameter, such as basicity, but needs to be predicted in a more fundamental manner, using known thermodynamic data and data on solutions. This point can be illustrated by a comparison of the available data and our predicted sulfide capacities of $\text{Na}_2\text{O-SiO}_2$, with those based on empirical concepts of optical basicity proposed by Sosinsky and Sommerville. (22) These are given at 1623 and 1473 K in Figures 1a and 1b. As can be seen from the figures, empirical optical basicity values differ significantly from the experimental data and from our results at the compositions and temperatures considered.

CONCLUSIONS

The method we propose for calculating C_s in slags *a priori* is shown to be in very good agreement with available experimental data. The sulfide capacities of $\text{Na}_2\text{O-SiO}_2$ melts are directly proportional to two independent factors (a) the equilibrium constant K_{Na} and (b) the activity of Na_2O , and cannot be empirically correlated with any single parameter, such as basicity.

ACKNOWLEDGMENTS

This work was supported by the U.S. Department of Energy, Division of Materials Science, Office of Basic Energy Sciences under Contract W-31-109-ENG-38 with the Argonne National Laboratory. One of the authors (B.C.) expresses his appreciation to the Department of Chemical and Metallurgical Engineering and miscellaneous Program Development Funds, University of Nevada-Reno for financial support.

REFERENCES

1. F. Korber and W. Oelsen, *Stahl u. Eisen*, Vol. 58, pp. 905-14, 943-49 (1938).
2. W. Oelsen, *Stahl u. Eisen*, Vol. 58, pp. 1212 (1938).
3. W. Domalski, K. Fabian, and D. Nolle, *Stahl u. Eisen*, Vol. 88, pp. 906 (1968).
4. B. Bahout, Y. Bienvenu, and G. Denier, *Ironmaking Steelmaking*, Vol. 5, pp. 162-167 (1978).
5. R. Derici and H. B. Bell, unpublished work. H. B. Bell, *International Symposium on Metallurgical Slags*, CIM, Halifax (1980).
6. S. Nagashima and T. Katsura, *Bull. Chem. Soc. Jpn.*, Vol. 46, pp. 3099-3103 (1973).
7. R. Inoue and H. Suito, *Trans. Iron Steel Inst. Jpn.*, Vol. 22, pp. 514-23 (1982).
8. D. H. DeYoung, *Am. Chem. Soc., Div. Fuel Chem.*, Vol. 27, pp. 117-28 (1984).
9. A. H. Chan and R. J. Fruehan, *Met. Trans.*, Vol. 17B, pp. 491-496 (1986).
10. W. R. Maddocks and E. T. Turkdogan, *J. Iron Steel Inst.*, Vol. 162, pp. 249-64 (1949).
11. R. G. Reddy and M. Blander, submitted to *Met. Trans.*
12. R. G. Reddy and M. Blander, submitted to *Met. Trans.*
13. C. J. B. Fincham and F. D. Richardson, *Proc. Royal Soc., London*, Vol. 223A, pp. 40-62 (1954).
14. J. H. Hildebrand and R. L. Scott, *The Solubility of Non-Electrolytes*, 3rd Edition, Reinhold Publishing Corporation, New York, NY, pp. 347-351 (1950).
15. K. S. Goto, S. Yamaguchi, and K. Nagata, *Second International Symposium on Metallurgical Slags and Fluxes*, edited by H. A. Fine and D. R. Gaskell, TMS-AIME, Warrendale, PA, pp. 467-481 (1986).

16. D. R. Stull and H. Prophet, JANAF Thermochemical Tables, 2nd edition, NSRDS-NBS 37, Supt. of Documents, Washington, D.C. (1971).
17. E. T. Turkdogan, Physicochemical Properties of Molten Slags and Glasses, TMS, London, pp. 230-231 (1983).
18. K. P. Abraham, M. W. Davies, and F. D. Richardson, JISI, Vol. 196, pp. 309-312 (1960).
19. R. A. Sharma and F. D. Richardson, JISI, Vol. 200, pp. 372-379 (1962).
20. P. T. Carter and T. G. MacFarlane, JISI, Vol. 185, pp. 54-66 (1957).
21. R. A. Sharma and F. D. Richardson, Trans. AIME, Vol. 233, pp. 1586-1592 (1965).
22. D. J. Sosinsky and I. D. Sommerville, Metall. Trans., Vol. 17B, pp. 331-337 (1986).

Table I. Free Energy of Formation of Na_2S and Na_2O
 (ΔG_f°) cal/mole

	1473 K	1623 K
Na_2S	-49,195	-31,137
Na_2O	-41,913	-33,257
ΔG° (reaction (1))	-7,282	-6,609
K_{Na}	12.03	7.76

Table II. Sulfide Capacities of Binary Silicate Slags

System	Mole Percent Basic Oxide		
	100	50	50 (expt)
1923 K			
CaO-SiO ₂	0.476	1.45×10^{-4}	2.01×10^{-4} (19,20)
MnO-SiO ₂	0.146	4.21×10^{-3}	3.35×10^{-3} (18)
FeO-SiO ₂	8.63×10^{-2}	7.52×10^{-3}	—
MgO-SiO ₂	1.41×10^{-2}	6.09×10^{-5}	8.65×10^{-5} (21)
MgS(solid)			
1773 K			
CaO-SiO ₂	0.290	4.18×10^{-5}	7.80×10^{-5} (17,19,20)
MnO-SiO ₂	7.91×10^{-2}	2.35×10^{-3}	2.11×10^{-3} (18)
FeO-SiO ₂	4.56×10^{-2}	3.73×10^{-3}	3.89×10^{-3} (18)
			(51.67 mole %)
MgO-SiO ₂	7.76×10^{-3}	4.02×10^{-5}	
MgS (solid)			
1623 K			
Na ₂ O-SiO ₂	401	9.52×10^{-4}	3.98×10^{-3} (16)
1473 K			
Na ₂ O-SiO ₂	622	3.81×10^{-4}	3.75×10^{-4} (9)

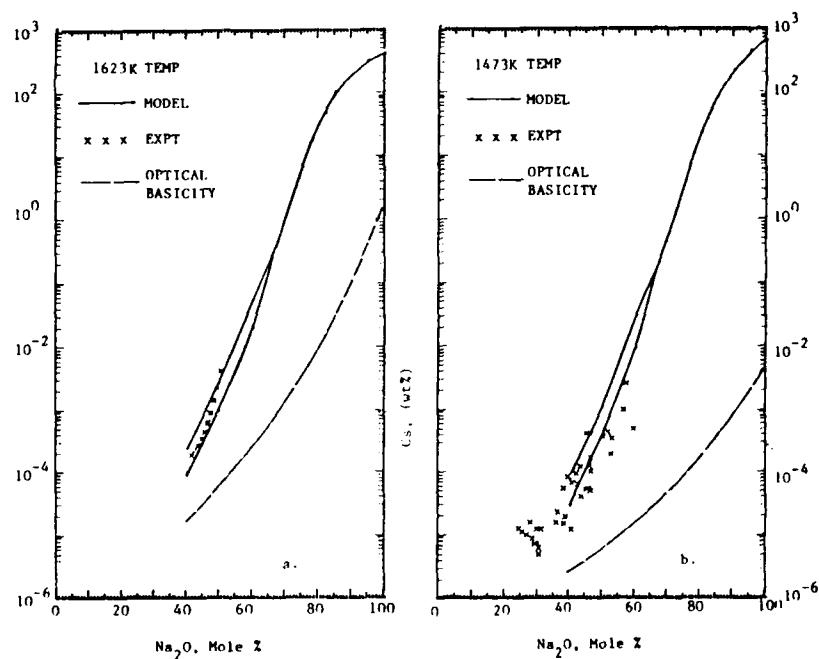


Figure 1. Plot of Sulfide Capacities Calculated Based on the Model Presented in This Paper, and on the Optical Basicity Concept (22), and Measured Sulfide Capacities (6,9,17) at (a) 1623 K and (b) 1473 K for Na_2O - SiO_2 Melts. The Upper Lines Calculated From the model Are For $m \leq 1$ and the Lower Lines are for $m > 1$.

X-RAY STRUCTURAL ANALYSIS OF
MOLTEN KF-KX(X=Cl, Br, AND I) SYSTEMS

Yoshihiro OKAMOTO, Kazuo IGARASHI, and Junichi MOCHINAGA

Department of Synthetic Chemistry, Faculty of Engineering
Chiba University, Chiba-shi 260, Japan

ABSTRACT

The structures of molten KF-KX(X=Cl, Br, and I) systems with the common cation were investigated by an X-ray diffraction method and the short range structures obtained were compared with those found in the pure melts and the molten alkali halide mixtures with the common anion. The nearest neighbor configurations of the unlike ion pairs were similar to those in the pure melts. On the other hand, the nearest distances between like ions changed by mixing, as well as the systems with the common anion.

1. INTRODUCTION

In recent years, molten alkali halide mixtures have been proposed for use as heat transfer medium and as electrolyte in molten salt batteries. The structure of the melt is important information. However, although there have been many studies on the structures of the pure melts, only a few studies on the structures of the mixture melts have been carried out. Therefore, there are few data to discuss the properties of the melts based on microscopic observation.

Okada et al.(1) investigated the structure of molten LiCl-KCl(eutectic composition) system by the X-ray diffraction analysis with the aid of molecular dynamics simulation. According to the report, the nearest neighbor distances of the unlike ion pairs such as $\text{Li}^+\text{-Cl}^-$ and $\text{K}^+\text{-Cl}^-$ were almost the same as those in the pure melts. On the other hand, the nearest distances of the like ion pairs such as $\text{K}^+\text{-K}^+$ and $\text{Cl}^-\text{-Cl}^-$ etc. changed by mixing. Recently, Igarashi et al.(2)(3) investigated the structures of molten LiF-NaF(3:2), LiF-KF(1:1), and LiF-KF-NaF(eutectic composition), called FLINAK, systems by the X-ray diffraction analysis and obtained a similar conclusion. They were all the mixtures with the common anion. The similar

results can also be expected in the mixtures with the common cation.

In this work, we chose molten KF-KX (X=Cl, Br, and I) systems, which contain K^+ ion as the common cation. The mole ratios were 1:1 for KF-KCl and KF-KBr systems, and 1:2 for KF-KI system, which were close to each eutectic composition.

2. EXPERIMENTAL

Chemicals KF, KCl, KBr, and KI were of analytical reagent grade and were dried at 400 °C under reduced pressure for 10 hours. They were weighed to the prescribed composition in an atmosphere of dried N_2 gas, and fused in a platinum crucible. Experimental temperatures were 660 °C for KF-KCl system, 700 °C for KF-KBr system, and 600 °C for KF-KI system.

Prior to the measurement, the moisture was removed thoroughly from the air-tight sample chamber. The measurement was carried out in an atmosphere of dry He gas. The temperature was controlled to maximum error of 10 °C. X-ray scattering intensity was measured on a diffractometer having θ - θ type parafocusing reflection geometry using MoK α beam. Scattering beam was monochromatized with a curved graphite crystal. Intensity data were collected over the range of scattering angle 3° to 54° for KF-KCl and KF-KBr systems, and 4° to 45° for KF-KI system, respectively. These values correspond to 14.3 and 12.5 as the maximum S value defined by the following equation.

$$S = 4\pi \sin \theta / \lambda,$$

where 2θ is the scattering angle, and λ is the wavelength.

The corrections for background, polarization, absorption, and Compton radiation were applied to the observed data by usual methods(5). Corrected data were scaled to the independent scattering factor for stoichiometric unit by the combined use of the high angle region method and Krogh-Moe-Norman method. The reduced intensity function $S_i(S)$ and the correlation function $G(r)$ were calculated by the following equations.

$$G(r) = 1 + \frac{\sum (K_m)^2}{2\pi^2 g_0 r} \int_0^{S_{max}} S \cdot i(S) \sin(rS) dS,$$

$$S \cdot i(S) = S [I_{tot}^{coh}(S) / \sum_m f_m^2(S) - 1],$$

and

$$g_0 = (\sum_m K_m)^2 \rho_0,$$

where ρ_0 is the number of stoichiometric unit per \AA^{-3} , K_m the effective electron number in the atom m , f_m the independent scattering intensity, $I_{\text{coh}}^{\text{ex}}(S)$ the total coherent intensity, and S_{max} the maximum value of S reached in the experiment.

Parameters used in the calculations are listed in Table 1.

3. RESULTS

(1) KF-KCl(1:1) system

$\text{Si}(S)$ and $G(r)$ curves for molten KF-KCl(1:1) system at 660 °C are shown in Figs. 1(a) and 2(a), respectively. $G(r)$ has the peaks at $r=3.10$, 3.70, and 4.05 Å, and the shoulder at near 2.60 Å.

Zarzycki(6) investigated the structure of the pure KF melt and reported that the nearest neighbor distance of K^+-F^- interaction was 2.65 Å. Takagi et al.(7) reported that the nearest neighbor distance of K^+-Cl^- interaction was 3.05 Å in the pure KCl melt. From those results, the shoulder at near 2.60 Å and the peak at 3.10 Å seem to correspond to the nearest K^+-F^- and K^+-Cl^- interactions, respectively. The peaks at 3.70 and 4.05 Å seem to due to the interactions of the like ion pairs such as K^+-K^+ and Cl^--Cl^- . In order to separate and determine those contributions, the following equation proposed by Narten et al.(8) was applied to the observed $\text{Si}(S)$ curve beyond $S=2.0 \text{ \AA}^{-1}$.

$$\text{Si}(S) \left[\sum_{i=1}^m f_i^2(S) \right] = \sum_{i=1}^m \sum_k f_i(S) f_k(S) \exp(-b_{ik} S^2) \sin(Sr_{ik}) / r_{ik} N_{ik}$$

where N_{ik} represents the number of interaction between ions i and k , b_{ik} the temperature factor, and r_{ik} the average distance between ions i and k .

Structural parameters were obtained by the least squares method. Those are listed in Table 2. The nearest distances of K^+-F^- and K^+-Cl^- interactions were 2.62 and 3.13 Å, and these values were almost the same as those in the pure melts. On the other hand, the nearest distances of K^+-K^+ and Cl^--Cl^- interactions were 4.02 and 3.69 Å, and these values were shorter than those in the pure melts.

The calculated $\text{Si}(S)$ curve is shown in Fig. 1(a).

(2) KF-KBr(1:1) system

Si(S) and G(r) curves for molten KF-KBr(1:1) system at 700 °C are shown in Figs. 1(b) and 2(b), respectively. G(r) has the peak at 3.25 Å, and the shoulders at near 2.70 and 4.15 Å.

The shoulder at 2.70 Å seems to correspond to the nearest K^+-F^- interaction. According to the study on the structure of the pure KBr melt by Ohno et al.(9), the nearest distance of K^+-Br^- interaction was 3.18 Å in the G(r). The peak at 3.25 Å seems to correspond to that interaction. The shoulder at near 4.15 Å seems to due to the interactions of the like ion pairs.

As well as the foregoing system, the least squares fitting was applied to the observed Si(S) curve beyond $S=2.0\text{ Å}^{-1}$, and the structural parameters were obtained. Those are listed in Table 3. The nearest distances of K^+-F^- and K^+-Br^- interactions were in good agreement with those in the pure melts, while those of K^+-K^+ and Br^--Br^- interactions were 4.12 and 4.23 Å, and these values were shorter than those in the pure melts.

The calculated Si(S) curve is shown in Fig. 1(b).

(3) KF-KI(1:2) system

Si(S) and G(r) curves for molten KF-KI(1:2) system at 600 °C are shown in Figs. 1(c) and 2(c), respectively. G(r) has the peak at 3.55 Å, and the shoulders at 2.65 Å and near 4.70 Å.

The shoulder at 2.65 Å seems to correspond to the nearest K^+-F^- interaction. The peak at 3.55 Å seems to correspond to K^+-I^- interaction. The distance of this interaction reported by Antonov(10) was 3.52 Å. The shoulder at near 4.70 Å seems to due to the interactions of the like ion pairs.

The curve fitting for the observed Si(S) as well as the foregoing two systems was carried out. In the calculation, the contribution of K^+-K^+ interaction to the total intensity was so small that it was neglected and only I^--I^- interaction was considered as the interaction of the like ion pair. The structural parameters obtained are listed in Table 4. The nearest distances of the unlike ion pairs were almost the same as those in the pure melts, while that of I^--I^- interaction was 4.64 Å. This value was slightly shorter than that in the pure melt.

The calculated Si(S) curve is shown in Fig. 1(c).

4. DISCUSSION

Some experimental studies on the structures have been performed for alkali halide pure and mixture melts, and are

listed in Table 5. The nearest neighbor distances of K^+-X^- ($X=F, Cl, Br, \text{ and } I$) interactions obtained were found to be almost the same as those in the pure melts and the mixture melts with the common anion such as $LiCl-KCl$ and $LiF-KF$ systems. The distances of the like ion pairs were found to be slightly shorter than those in the pure melts. These results show that the conclusion reported for the mixture melt of alkali chlorides by Okada et al. and for the mixture melts of alkali fluorides by Igarashi et al. applied well to the present systems. The nearest neighbor structure of the unlike ion pair unchanged by mixing, while the nearest distance of the like ion pair changed.

Moreover influence of temperature should be considered in connection with the results in this work, because the experimental temperature in each system is considerably lower than the melting point of the constituent salt. As shown in Table 5, it seems that the nearest neighbor structures between unlike ions were not appreciably influenced by the temperature, while the nearest distances between like ions obviously became shortened with a decrease of temperature. Molar volume of the melt is relatively sensitive to the structure, and generally decreases as temperature drops. The decrease of the second interionic distance seems to be occurred with the decrease of the molar volume.

5. CONCLUSION

- (1) In the mixture melts with the common cation, as well as the melts with the common anion the nearest neighbor structures between unlike ions were similar to those in the pure melts.
- (2) The nearest distances between like ions were slightly shorter than those in the pure melts. This fact is associated closely with the temperature, and parallels the decrease of the molar volume.

6. REFERENCES

- (1) I. Okada, H. Okano, H. Ohtaki, and R. Takagi, Chem. Phys. Lett., **100**, 436 (1983).
- (2) K. Igarashi, M. Murofushi, Y. Iwadate, J. Mochinaga, and H. Ohno, Chem. Lett., **1985**, 817.
- (3) K. Igarashi, M. Murofushi, Y. Iwadate, J. Mochinaga, and H. Ohno, Nippon Kagaku Kaishi, **1985**, 1821.

- (4) G.J. Janz, R.P.T. Tomkins, and C.B. Allen, J. Phys. Chem. Ref. Data, **8**, 138 (1979).
- (5) K. Furukawa, Rep. Prog. Phys., **25**, 395 (1962).
- (6) J. Zarzycki, J. Phys. Rad., Suppl. Phys. Appl., **18**, 65A (1957).
- (7) R. Takagi, H. Ohno, and K. Furukawa, J. Chem. Soc., Faraday Trans. 1, **75**, 1477 (1979).
- (8) A.H. Narten and H.A. Levy, Science, **165**, 447 (1969).
- (9) H. Ohno, K. Furukawa, R. Takagi, K. Igarashi, and J. Mochinaga, J. Chem. Soc., Faraday Trans. 2, **79**, 463 (1983).
- (10) B.D. Antonov, Zh. Strukt. Khim., **16**, 501 (1975).
- (11) H.A. Levy, P.A. Agron, M.A. Bredig, and M.D. Danford, Ann. N.Y. Acad. Sci., **79**, 762 (1960).

Table 1. Parameters used in the calculations of r.d.f.

	KF KCl 1:1	KF KBr 1:1	KF KI 1:2
Temperature °C	660	700	600
Density g/cm ³	1.7531	2.0883	2.4094
ρ A ⁻³	0.00796	0.00710	0.00620
Effective electron number			
K _L	19.7889	18.6415	17.6950
K _M	7.1719	6.7714	6.6380
K _V	17.2454	17.9440	16.1370
S_{eff} A ⁻¹	14.3	14.3	12.5

X: Cl, Br, and I

The densities used were given by Smirnov et al. (4)

Table 2. Structural parameters of KF-KCl system

	n	r	Δr
K ⁺ -F	4.0	2.62	0.289
K ⁺ -Cl	3.4	3.13	0.326
Cl ⁻ -Cl	6.1	3.69	0.494
K ⁺ -K ⁺	9.4	1.02	0.640

Table 3. Structural parameters of KF-KBr system

	n	r	Δr
K ⁺ -F	3.9	2.54	0.322
K ⁺ -Br	4.0	3.23	0.381
Br ⁻ -Br	5.7	4.23	0.623
K ⁺ -K ⁺	7.9	1.12	0.643

Table 4. Structural parameters of KF-KI system

	n	r	Δr
K ⁺ -F	4.0	2.60	0.324
K ⁺ -I	4.8	3.48	0.480
I ⁻ -I	4.6	4.64	0.674

Table 5 The interionic distances of the correlation function and radial distribution function

Mixture (Author)	K ⁺ -F ⁻	K ⁺ -Cl ⁻	K ⁺ -Br ⁻	K ⁺ -I ⁻	K ⁺ -K ⁺ & X ⁻ -X ⁻ (X)	Temp.	Ref.
KF-KCl (this work)	2.624	3.13			4.02 3.69(Cl ⁻)	660°C	
KF-KBr (this work)	2.59		3.23		4.12 4.23(Br ⁻)	700	
KF-KI (this work)	2.60			3.48	4.64(I ⁻)	600	
LiF-KF (Igarashi et al.)	2.70				3.57	545	(2) (3)
FLiNAK (Igarashi et al.)	2.59				3.43	520	
LiCl-KCl (Okada et al.)		3.08			4.41 3.85(Cl ⁻)	395	(1)
KF (Zarzycki)	2.65*				~ 4.20*	870	(6)
KCl (Takagi et al.)		3.05				900	(7)
KCl (Levy et al.)		3.10*			~ 4.70 (Cl ⁻)	—	(11)
KBr (Ohno et al.)			3.18		4.65 (Br ⁻)	750	(9)
KBr (Antonov)			3.35*			—	(10)
KI (Antonov)				3.52*	4.95* (I ⁻)	—	(10)

* the data based on r.d.f.

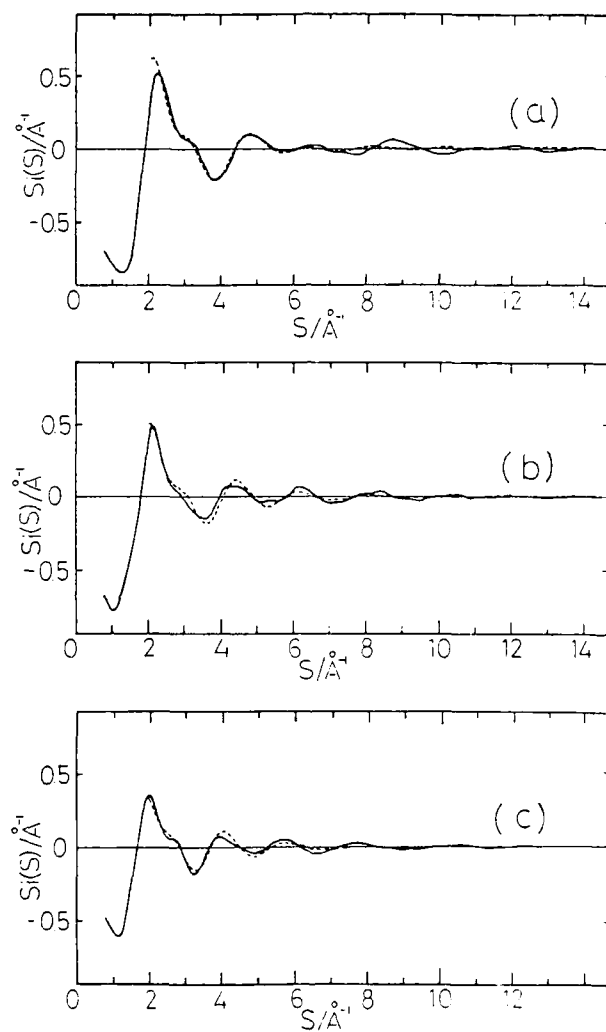


Fig.1 Observed(solid line) and calculated(dotted line)
 reduced intensity functions $S_i(S)$
 (a) KF-KCl(1:1) system at 660°C
 (b) KF-KBr(1:1) system at 700°C
 (c) KF-KI (1:2) system at 600°C

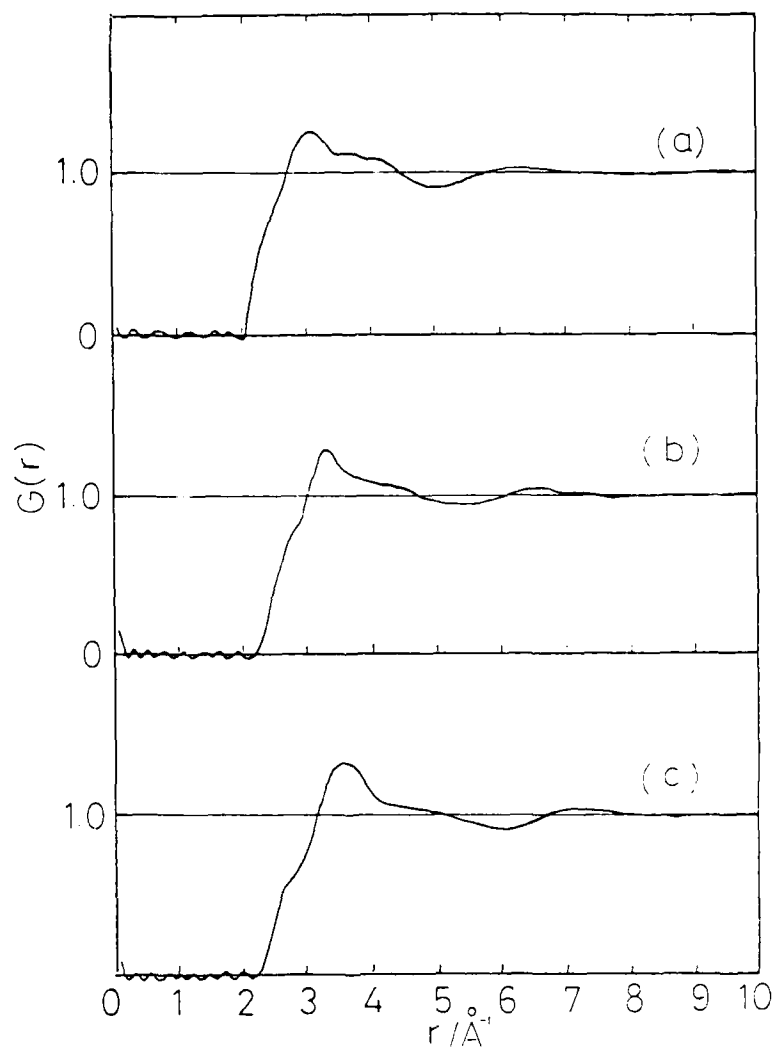


Fig. 2 Correlation functions $G(r)$
 (a) KF-KCl (1:1) system at 660°C
 (b) KF-KBr (1:1) system at 700°C
 (c) KF-KI (1:2) system at 600°C

X-RAY DIFFRACTION STUDY OF MOLTEN CaCl_2 -KCl SYSTEM

Kazuo IGARASHI, Yoshihiro OKAMOTO, and
Junichi MOCHINAGA

Department of Synthetic Chemistry, Faculty of Engineering,
Chiba University, Chiba-shi, Chiba 260, Japan

ABSTRACT

Structure of molten CaCl_2 -KCl mixtures with the compositions of 1:1, 1:2, and 1:3 as mole ratio of CaCl_2 to KCl was investigated by the radial distribution function based on X-ray diffraction intensities and was analyzed by the correlation method. The nearest neighbor distances of Ca^{2+} - Cl^- and K^+ - Cl^- pairs in the three melts were 2.76-2.78 and 3.08 Å, respectively. The first coordination number of the K^+ - Cl^- pair was ca. 4 in the three mixtures. On the other hand, the coordination number of the nearest Ca^{2+} - Cl^- pair increased from 5.5 for the 1:1 melt to 5.8 for the 1:3 melt. Similarly, a slight increase of the nearest Cl^- - Cl^- distance was observed. These results suggest that the Ca^{2+} ions surrounded octahedrally by the Cl^- ions increase with increasing KCl concentration.

INTRODUCTION

A number of physicochemical properties on molten CaCl_2 -KCl system have been investigated[1-13], but a concordant conclusion on the structure of the melt has not yet obtained from their studies. Emons et al.[1-4] have suggested the existence of the complex species such as CaCl_3^- and CaCl_4^{2-} ions in the melt. On the other hand, Grjotheim et al.[5-8] have considered that the molten CaCl_2 -KCl system does not deviate significantly from random cation mixture. A similar conclusion has also been reported by Ejima et al.[9,10].

Brooker[14] has studied the structure of molten CaCl_2 -CsCl(1:2) system by Raman spectroscopy and reported the existence of tetrahedrally shaped species.

Raman spectrum for molten CaCl_2 -KCl(1:2) mixture at 600 °C has been measured by Umesaki[15], in which the Raman bands have been observed at 110-300 cm^{-1} . He has suggested that these bands observed are attributable to an octahedral

complex species formed in the melt.

In the previous study[16], we analyzed by an X-ray diffraction method the structure of the $(\text{CaCl}_2)_x-(\text{NaCl})_{1-x}$ melts with the compositions of $x=2/3$, $1/2$, and $1/3$. In these molten mixtures, the coordination number of Cl^- ions around a Ca^{2+} ion was found to be about six.

In the present paper, the structures of molten CaCl_2 - KCl (mole ratios 1:1, 1:2, and 1:3) mixtures were investigated by the X-ray diffraction analysis.

EXPERIMENTAL

CaCl_2 and KCl of analytical reagent grade were used and dried by heating under reduced pressure for 7-8 hours. Prescribed amounts of CaCl_2 and KCl were weighed in a dry box and melted in a fused silica crucible under argon atmosphere at temperature above melting point according to the phase diagram[17]. After mixing for 10 min., the melts were quenched to prevent the segregation.

X-ray scattering intensities were measured by an X-ray diffractometer having a parafocusing reflection geometry, with a curved graphite monochromator. The observable ranges of the scattering angle were $3^\circ \leq \theta \leq 50^\circ$ for the 1:1 mixture and $3^\circ \leq \theta \leq 48^\circ$ for the others, corresponding to the ranges from 0.93 to $13.5(13.0)\text{\AA}^{-1}$ in $S(S=4\pi\sin\theta/\lambda)$ for $\text{MoK}\alpha$ radiation ($\lambda=0.7107\text{\AA}$). The measurements were made by using a step-scanning technique with fixed count. The experimental temperatures were 785°C for the 1:1 melt, 750°C for the 1:2 melt, and 650°C for the 1:3 melt and were maintained within maximum error 8°C by a temperature controlled device.

The experimental intensity data were corrected for background, polarization, absorption, and Compton radiation by the usual methods[18] and were normalized to the independent scattering factor for the stoichiometric unit using both the Krogh-Moe-Norman[19,20] and high angle region methods. The radial distribution function $D(r)$, average correlation function $G(r)$, and intensity function $i(S)$ are given by the following expressions,

$$D(r) = 4\pi r^2 \rho_0 \left(\sum_m \bar{K}_m \right) + \sum_m (\bar{K}_m)^2 2r/\pi \int_0^{S_{\max}} S \cdot i(S) \sin(rS) dS,$$

$$G(r) = 1 + \sum_m (\bar{K}_m)^2 \left(\left(2\pi^2 r \rho_0 \sum_m \bar{K}_m \right) \int_0^{S_{\max}} S \cdot i(S) \sin(rS) dS \right),$$

$$i(S) = I_{\text{expt}}(S) / \sum_m f_m^2(S) - 1,$$

where ρ_0 is the average electron density, \bar{K}_m the effective electron number in the atom m , $f_m(S)$ the independent atomic

scattering intensity, and $I_{\text{coh}}(S)$ the total coherent intensity. The densities of these melts were taken from Lillebuen's density data[21]; 1.793 g cm⁻³ (785 °C) for the 1:1 melt, 1.725(750) for the 1:2 melt, and 1.726(650) for the 1:3 melt.

RESULTS AND DISCUSSION

Reduced intensity curves $S.i(S)$ are shown in Fig. 1 together with those of molten KCl[22] and CaCl₂[16]. A slight shift to the lower angle side and a faster decay of amplitude of the $S.i(S)$ curves occurred with increasing KCl concentration. The small peak at about 3 Å⁻¹ found in the KCl melt have appeared as the shoulder at almost the same position in the $S.i(S)$ curves of the mixtures.

Figure 2 shows $D(r)$ curves and functions $D(r)/r$ obtained by Fourier transformation of the reduced intensities $S.i(S)$. The $G(r)$ curves are shown in Fig. 3 together with those of molten KCl and CaCl₂ as well as $S.i(S)$ curves. The first peaks in $G(r)$ for the mixtures changed to a slightly longer position with increase of KCl concentration. And their peak heights became progressively lower.

(1) 1:1 system

The first and second peaks in $G(r)$ as shown in Fig. 3(b) were observed at $r=2.85$ and 3.55 Å, respectively. It seems that the first peak at 2.85 Å contains contributions from both Ca²⁺-Cl⁻ and K⁺-Cl⁻ pairs. Analysis of the first peak of $D(r)$ for pure melt gives the nearest neighbor distance and coordination number of unlike ion pair. However, in a multi-component system with the similar nearest neighbor distances of unlike ion pairs it is difficult to separate these correlations from the analysis of $D(r)$. In order to determine these correlations quantitatively the correlation method based on Debye equation was applied to the observed $S.i(S)$ curve. It has been known[23,24] that in molten binary systems, the nearest neighbor distances and coordination numbers of unlike ion pairs are little affected by mixing. We, thus, set initial values in this calculation on the basis of the short range structure of molten CaCl₂[16,25,26] and KCl[22,27-29]. The calculation was performed for the correlations of Ca²⁺-Cl⁻, K⁺-Cl⁻, and Cl⁻-Cl⁻ pairs using the range of the observed $S.i(S)$ beyond $S=3.5$ Å⁻¹ because other correlations have little contributions in this region of S . The structural parameters were determined by the least squares fit and were shown in Table 1. The fit between the calculated values and observed ones was evaluated by R factor, which was 0.33 in this calculation. Comparison of the calculated $S.i(S)$ with the observed one is shown in Fig. 4(a).

The nearest neighbor distance and coordination number of K^+-Cl^- pair and the nearest $Ca^{2+}-Cl^-$ distance in the 1:1 melt were found to be almost equal to those in pure KCl and $CaCl_2$ melts. But the first coordination number of $Ca^{2+}-Cl^-$ pair seems to be slightly larger than that of the pure melt. The second peak position in $G(r)$ is considerably shorter than the analyzed distance of the Cl^-Cl^- pair. This is so because the second peak has contributions from the unlike ion pairs. A small fall between the first and second peaks suggests this.

(2) 1:2 system

The first and second peaks in $G(r)$ as seen in Fig. 3(c) are observed at 2.90 and 3.60 Å, respectively. These are slightly longer than those in the 1:1 system.

The three correlations as well as the 1:1 mixture were analyzed by the same method. The structural parameters obtained were listed in Table 2. The R value in this calculation was 0.28. The comparison of the observed $S_i(S)$ with calculated one is shown in Fig. 4(b).

Surroundings of K^+ ions in the 1:2 melt were the same as those in the 1:1 melt. But the first coordination number of $Ca^{2+}-Cl^-$ pair tends to increase with increasing KCl concentration.

Emons et al.[1-4] have suggested from studies of the physical properties that species such as $CaCl_4^{2-}$ anion exists predominantly in the melt of this composition. Brooker[14] has studied the structure of molten $CaCl_2-CsCl(1:2)$ system by Raman spectroscopy and reported the existence of tetrahedrally shaped species. The result was expected the formation of similar species in the molten $CaCl_2-KCl(1:2)$ mixture. If the complex anion as was expected exists in the melt, the number of Cl^- ions around a Ca^{2+} ion is four and the second peak corresponding to the contribution of the nearest Cl^-Cl^- pair is predicted to appear to the position at $r=4.5$ Å from the distance ratio of the tetrahedral arrangement. However, the assumed result differs from the measured one. This means that very few of tetrahedral complex species are formed in this melt. Our result suggests the existence of octahedrally shaped species rather than tetrahedral species as reported by Umesaki[15].

(3) 1:3 system

As seen in Fig. 3(d), $G(r)$ has the first peaks at 2.95 Å and broad second peak at about 3.95 Å. The short range structure of this melt was analyzed the same way. The structural parameters determined are shown in Table 3. The R value was 0.28 in this calculation. The comparison of the observed $S_i(S)$ with calculated one is shown in Fig. 4(c). The result has revealed that the surroundings of the

K^+ ions did not change with the increase of KCl concentration, but the surroundings of Ca^{2+} ions became more octahedral.

REFERENCES

- [1] G. Roewer and H.-H. Emons, Z. Anorg. Allg. Chem., **370**, 128 (1969).
- [2] H.-H. Emons, G. Bräutigam, and H. Vogt, Z. Anorg. Allg. Chem., **394**, 265 (1972).
- [3] G. Bräutigam and H.-H. Emons, Z. Anorg. Allg. Chem., **394**, 271 (1972).
- [4] H.-H. Emons, G. Bräutigam, and H. Vogt, Z. Anorg. Allg. Chem., **394**, 279 (1972).
- [5] K. Grjotheim, R. Nikolic, and H. A. Øye, Acta Chem. Scand., **24**, 489 (1970).
- [6] K. Grjotheim, J. L. Holm, B. Lillebuen, and H. A. Øye, Trans. Faraday Soc., **67**, 640 (1971).
- [7] K. Grjotheim, J. L. Holm, B. Lillebuen, and H. A. Øye, Acta Chem. Scand., **26**, 2050 (1972).
- [8] D. Dumas, B. Fjeld, K. Grjotheim, and H. A. Øye, Acta Chem. Scand., **27**, 319 (1973).
- [9] T. Ejima and T. Mitsuhashi, J. Japan Inst. Metals, **39**, 687 (1975).
- [10] T. Ejima, K. Iwasaki, and S. Genji, J. Japan Inst. Metals, **41**, 784 (1977).
- [11] T. Østvold, J. Phys. Chem., **76**, 1616 (1972).
- [12] J. J. Egan and J. Bracker, J. Chem. Thermodynamics, **1974**, 9.
- [13] P. Sem, G. Hatem, J. P. Bros, and M. Gaune-Escard, J. Chem. Soc., Faraday Trans. 1, **80**, 297 (1984).
- [14] M. H. Brooker and G. N. Papatheodorou, "Advances in Molten Salt Chemistry", Ed. G. Mamantov, Elsevir, Amsterdam-Oxford-New York-Tokyo, Vol. 5, p.51 (1983).
- [15] N. Umesaki, Doctoral Thesis, Osaka University, Osaka Japan (1981).
- [16] K. Igarashi, T. Nijima, and J. Mochinaga, Proc. First International Symposium on Molten Salt Chem. and Technol., Kyoto Japan, p.469 (1983).
- [17] T. Sato and T. Amano, Metal Research, **11**, 549 (1934).
- [18] H. Ohno, K. Furukawa, K. Igarashi, and J. Mochinaga, J. Chem. Soc., Faraday Trans. 1, **78**, 1555 (1982).
- [19] J. Krogh-Moe, Acta Cryst., **9**, 951 (1956).
- [20] N. Norman, Acta Cryst., **10**, 370 (1957).
- [21] G. J. Janz, R. P. T. Tomkins, C. B. Allen, J. R. Downey, Jr., G. L. Gradner, U. Krebs, and S. K. Singer, J. Phys. and Chem. Ref. Data, **4**, 958 (1975).
- [22] R. Takagi, H. Ohno, and K. Furukawa, J. Chem. Soc., Faraday Trans. 1, **75**, 1477 (1979).
- [23] I. Okada, H. Okano, H. Ohtaki, and R. Takagi, Chem.

- Phys. Lett., **100**, 436 (1983).
- [24] K. Igarashi, M. Murofushi, Y. Iwadate, J. Mochinaga, and H. Ohno, Nippon Kagaku Kaishi, 1985, 817.
- [25] S. Biggin and J. E. Enderby, J. Phys. C: Solid State Phys., **14**, 3577 (1977).
- [26] N. Iwamoto, N. Umesaki, T. Asahina, and M. Kosaka, Nippon Kagaku Kaishi, 1982, 920.
- [27] J. Zarzycki, J. Phys. Rad., Suppl. Phys Appl., **59**, 13A (1958).
- [28] H. A. Levy, P. A. Agron, M. A. Bredig, and M. D. Danford, Ann. N. Y. Acad. Sci., **79**, 762 (1960).
- [29] J. Y. Derrien and J. Duppy, J. Phys., **36**, 191 (1975).

Table 1 Structural parameters of molten $\text{CaCl}_2\text{-KCl}$
(1:1) system at 785°C

i - j	n_{ij}	r_{ij}	$\Delta r_{ij}^{2,3,4}$
$\text{Ca}^{2+} - \text{Cl}^-$	5.5	2.77	0.24
$\text{K}^+ - \text{Cl}^-$	3.9	3.08	0.35
$\text{Cl}^- - \text{Cl}^-$	6.8	3.80	0.45

Table 2 Structural parameters of molten $\text{CaCl}_2\text{-KCl}$
(1:2) system at 750°C

i - j	n_{ij}	r_{ij}	$\Delta r_{ij}^{2,3,4}$
$\text{Ca}^{2+} - \text{Cl}^-$	5.6	2.76	0.23
$\text{K}^+ - \text{Cl}^-$	3.9	3.08	0.33
$\text{Cl}^- - \text{Cl}^-$	7.4	3.79	0.48

Table 3 Structural parameters of molten $\text{CaCl}_2\text{-KCl}$
(1:3) system at 650°C

$i - j$	n_{ij}	r_{ij}	$(\Delta r_{ij})^{1/2}$
$\text{Ca}^{2+} - \text{Cl}^-$	5.8	2.78	0.24
$\text{K}^+ - \text{Cl}^-$	4.0	3.08	0.33
$\text{Cl}^- - \text{Cl}^-$	8.1	3.85	0.50

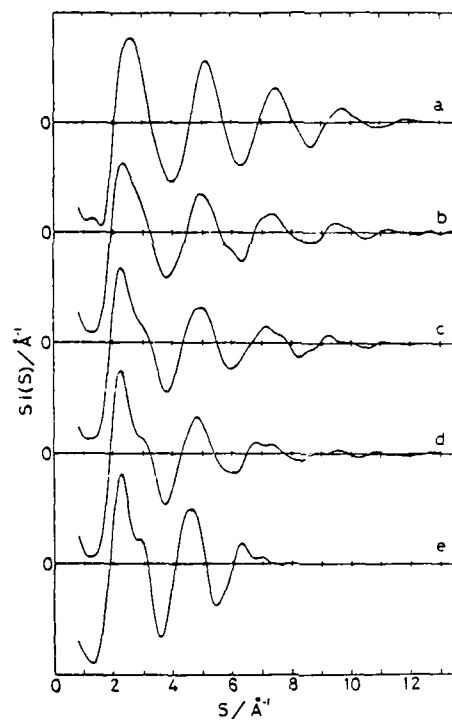


Fig. 1 Reduced intensity curves $S_i(S)$ of molten CaCl_2 (16), $\text{CaCl}_2\text{-KCl}$ mixtures, and KCl (22).
a; CaCl_2 , b; 1:1, c; 1:2, d; 1:3, e; KCl .

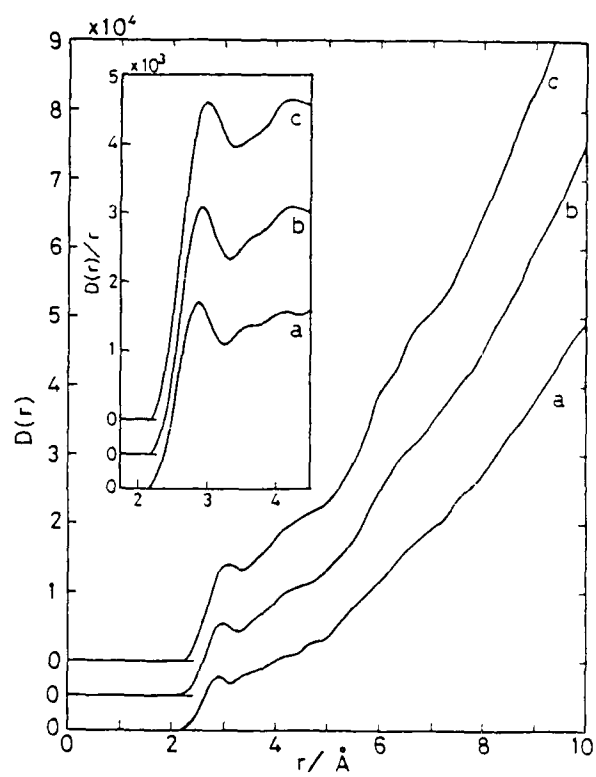


Fig. 2 Radial distribution functions $D(r)$ and functions $D(r)/r$.

a; 1:1, b; 1:2, c; 1:3.

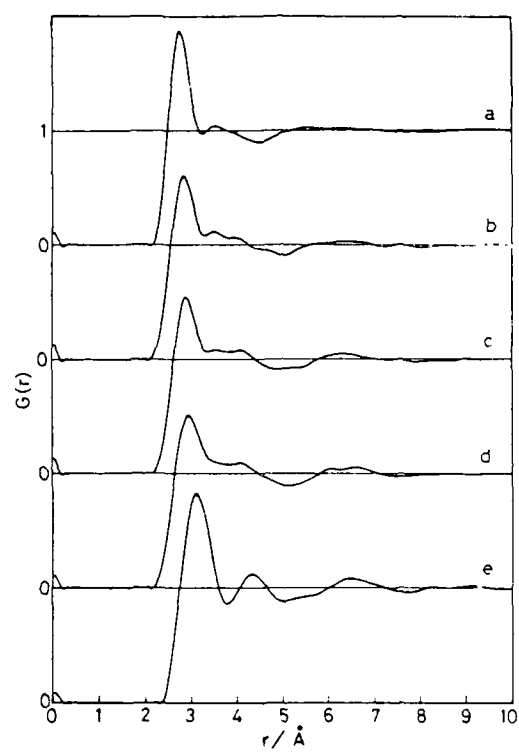


Fig. 3 Correlation functions $G(r)$.

a; CaCl_2 , b; 1:1, c; 1:2, d; 1:3, e; KCl.

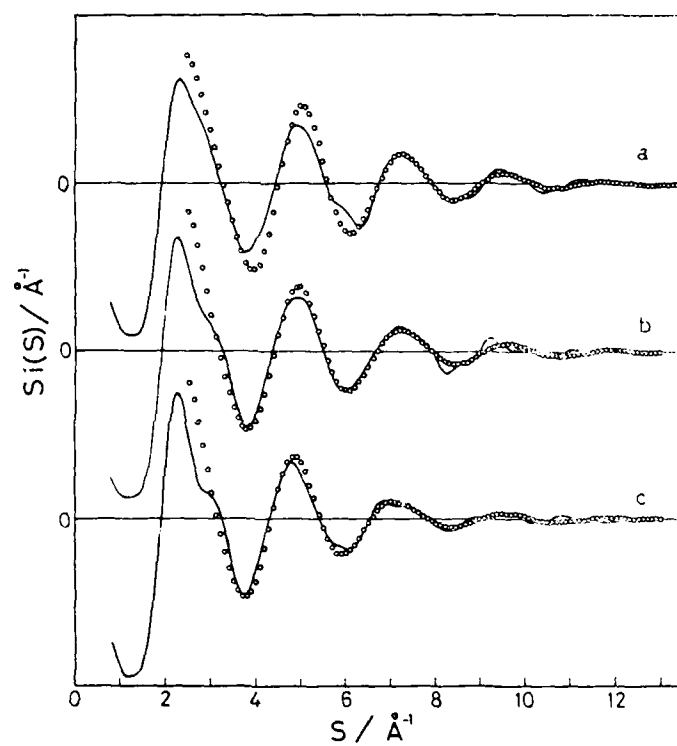


Fig. 4 Observed(—) and calculated(•••) intensity curves $S_i(S)$.

a; 1:1, b; 1:2, c; 1:3.

AB INITIO MOLECULAR ORBITAL INVESTIGATION OF THE
STRUCTURE OF Al_2F_7^- and Al_2Cl_7^-

Larry A. Curtiss
Chemical Technology Division/
Materials Science and Technology Program
Argonne National Laboratory
Argonne, Illinois 60439

ABSTRACT

The structures of Al_2F_7^- and Al_2Cl_7^- have been investigated using *ab initio* molecular orbital theory including the effects of polarization functions in the basis sets. The Al_2F_7^- ion is found to have a linear or nearly linear Al-F-Al bridge while Al_2Cl_7^- is found to have a bent Al-Cl-Al bridge with a significant barrier to inversion (4 kcal/mol). Structures with two and three halogen atoms in the bridge were also investigated and found to be less stable than the structures with one halogen atom in the bridge.

INTRODUCTION

The existence of the Al_2Cl_7^- ion in chloroaluminate melts has been investigated both experimentally (1-5) and theoretically (6). From Raman spectroscopic studies (1-3) it has been concluded that Al_2Cl_7^- consists of two AlCl_4^- tetrahedra sharing one corner. Infrared studies (4) have indicated that Li^+ stabilizes a bent Al-Cl-Al bridge while a linear (or slightly bent bridge) is preferred with the larger alkali cations. In solids containing Al_2Cl_7^- , the bent bridge is preferred (7). A theoretical study (6) using the semiempirical MNDO method has found the isolated Al_2Cl_7^- ion to have an Al-Cl-Al bridging angle of 125° . Introduction of counterions about the anion in the calculations led to little change in the bridging angle. No spectroscopic evidence has been reported for the existence of Al_2F_7^- in fluoride melts as AlF_4^- has been found to be in equilibrium with octahedrally coordinated AlF_6^{3-} .

In the work reported in this paper we have used *ab initio* molecular orbital theory to investigate the structure of the Al_2F_7^- and Al_2Cl_7^- ions. A previous *ab initio* study (8) on a series of AX_n^{m-} anions ($\text{A} = \text{Be}, \text{B}, \text{Mg}, \text{Al}$; $\text{X} = \text{F}, \text{Cl}$) has given a good account of the structural and vibrational properties of these ionic species. We have considered configurations with the AX_4^- tetrahedra having

corner, edge, and face bridging, i.e., of the type Al-X-Al, Al-X₂-Al, and Al-X₃-Al, respectively. The purpose of this work was to determine at a first principles level whether the Al-Cl-Al bridge in Al₂Cl₇⁻ is linear or bent in the absence of any counterions and the relative energies of the different bridging configurations. The Al₂F₇⁻ anion was included in this study to determine the effects of the smaller anion size on the bridge structure. Comparison is made with the results of the MNDO calculations and the spectroscopic studies on the structure of the bridge in Al₂Cl₇⁻.

THEORETICAL METHODS

All of the calculations were done at the Hartree-Fock (HF) level of calculation (9). Three basis sets were used. They are the minimal STO-3G basis set (10), the split-valence 3-21G basis (11), and the polarized split-valence 6-31G* basis set (12). The geometries of the Al₂F₇⁻ and Al₂Cl₇⁻ anions were optimized at the STO-3G and 3-21G basis set levels. The more accurate 6-31G* basis set was used to calculate the energies of the 3-21G equilibrium structures (referred to as HF/6-31G*//HF/3-21G). The STO-3G and 3-21G basis sets have previously given reasonable structures for other aluminum halide anions and neutral metal halide complexes (8,13).

The structures for Al₂F₇⁻ and Al₂Cl₇⁻ are illustrated in Fig. 1. Five corner bridged Al₂X₇⁻ structures, 1, were optimized: (a) a D_{3d} structure with a linear Al-X-Al bridge and a staggered arrangement of the terminal -AlX₃ groups, (b) a D_{3h} structure with a linear Al-X-Al bridge and an eclipsed arrangement of the terminal -AlX₃ groups, (c) a C_s structure with a bent Al-X-Al bridge and a "staggered" arrangement of -AlX₃ groups, (d) a C_{2v} structure with a bent Al-X-Al bridge and an "eclipsed" arrangement of the -AlX₃ group, and (e) a C₂ structure obtained from the C_{2v} structure by rotation of the -AlX₃ groups about the Al-X_{br} axes (X_{br} = bridging X atom) in opposite directions. An edge-bridged structure having a C_s configuration [Fig. 1, 2(C_s)] and a face-bridged structure having a C_{2v} configuration [Fig. 1, 3(C_{2v})] were also geometry optimized to assess the energies of these other bridging possibilities relative to that in the structures of type 1. All of the Al₂X₇⁻ structures were fully optimized within the given symmetry constraints with the exception that the angles between the X-Al-X_{br} planes were held fixed at 120° for each of the terminal X₃Al- groups in the C_s, C₂, and C_{2v} structures. Relaxation of this constraint led to little change in the energy when tested.

RESULTS AND DISCUSSION

The total energies of the STO-3G and 3-21G optimized structures of Al₂F₇⁻ and Al₂Cl₇⁻ are given in Table I. This table also contains 6-31G* energies at the

3-21G geometries (HF/6-31G*//HF/3-21G). The relative energies of the different structures are tabulated in Table II. Optimized geometries for the $\underline{1}(D_{3d})$ and $\underline{1}(C_s)$ structures of $Al_2Cl_7^-$ and the $\underline{1}(D_{3d})$ structure of $Al_2F_7^-$ are given in Fig. 2. We now discuss the results for the two anions.

$Al_2F_7^-$. The calculations indicate that a linear or nearly linear Al-F-Al bridge is favored for $Al_2F_7^-$. At the 3-21G level no minimum in the potential energy surface was found for the nonlinear bridge structure $\underline{1}(C_s)$. The geometrical parameters of the equilibrium $\underline{1}(D_{3d})$ structure are given in Fig. 1. The eclipsed form $\underline{1}(D_{3h})$ is 0.4 kcal/mol less stable (see Table II, 6-31G*) indicating a small barrier to rotation. The smaller basis set, STO-3G, gives a minimum for the nonlinear Al-F-Al structure (Al-F-Al angle of 158°), but it is only 0.1 kcal/mol more stable than the linear D_{3d} structure. We also carried out 6-31G* calculations at the STO-3G geometries (HF/6-31G*//HF/STO-3G). The results of these calculations (not included in Table I) indicated that the nonlinear structure is favored by 0.2 kcal/mol when polarization functions are included in the calculation. Hence, the 6-31G* results, which are expected to be the most reliable, suggest that corner-bridged $Al_2F_7^-$ has a nearly linear Al-F-Al bridge in the absence of any counterions.

The results in Table II also indicate that at the HF/6-31G*//HF/3-21G level the $Al_2F_7^-$ structures with two and three fluorines in the bridge are 12.7 and 29.1 kcal/mol less stable, respectively, than the configuration with a single fluorine in the bridge. The energy differences are much less at the STO-3G and 3-21G levels indicating that polarization functions are important in obtaining an accurate description of the bridges.

$Al_2Cl_7^-$. In contrast to $Al_2F_7^-$, a nonlinear Al-Cl-Al bridge is favored for $Al_2Cl_7^-$ with a significant barrier to inversion. The STO-3G and 3-21G geometries of the $\underline{1}(D_{3d})$ and $\underline{1}(C_s)$ structures for $Al_2Cl_7^-$ are given in Fig. 2. The Al-Cl-Al angle is 131.6° (3-21G) in the C_s structure. The C_{2v} structure illustrated in Fig. 1 has a Al-Cl-Al bond angle of 137.8° and is 0.4 kcal/mol less stable (3-21G) than the C_s structure. We also considered an alternative C_{2v} structure which has both $-AlCl_3$ groups rotated by 180° from what is shown in Fig. 1. This configuration is 0.7 kcal/mol less stable (3-21G) than the C_s structure. There is, in addition, the possibility that $Al_2Cl_7^-$ may have a C_2 structure derived from the $\underline{1}(C_{2v})$ structure by rotation of the $-AlCl_3$ groups in opposite directions. Geometry optimization of the C_2 structure for $Al_2Cl_7^-$ indicated that it was nearly equivalent in energy to the C_s structure (see Tables I and II). The Al-Cl-Al bond angle in the C_2 structure is 132.4° (3-21G). The closeness in energy (0.4 kcal/mol at the 3-21G level) of the C_{2v} , C_2 , and C_s structures reflects the small barrier to internal rotation in the $Al_2Cl_7^-$ anion.

The HF/6-31G*//HF/3-21G barrier to inversion from the nonlinear to linear bridged structure is about 4 kcal/mol if it is taken to be the difference between the $\underline{1}(C_s)$ and $\underline{1}(D_{3d})$ structures. This is an estimated number as it was not possible to

do the 6-31G* calculation on the C_s structure of $Al_2Cl_7^-$. The 4 kcal/mol value for the inversion barrier is estimated from the 6-31G* energy of the $1(D_{3d})$ structure relative to the $1(C_{2v})$ structure (3.6 kcal/mol) (14) and the HF/3-21G//HF/3-21G energy for the difference between the C_s and C_{2v} forms (0.4 kcal/mol). The barrier to inversion is much smaller at the 3-21G level (1 kcal/mol). This indicates the importance of the polarization functions, which are present in the 6-31G* basis, to the description of the bridge.

The edge- and face-bridged structures of $Al_2Cl_7^-$ are 40.2 and 47.1 kcal/mol less stable than the corner-bridged structure at the 3-21G level. No further calculations were done at the 6-31G* level because these structures were clearly less stable than the corner-bridged structure.

The inversion barrier for structure 1 of 4 kcal/mol is close to the value of 5.2 kcal/mol found by Davis et al. (6) using the MNDO semiempirical method. The two theoretical methods also find approximately the same Al-Cl-Al bond angle for the free ion (131° from the *ab initio* calculations and 124° from the MNDO method). However, preliminary results (15) at the *ab initio* level indicate that introduction of an alkali cation, which bridges the two $-AlCl_3$ groups, significantly reduces the Al-Cl-Al angle (30° - 40°), whereas the MNDO calculations indicate the presence of such a cation has little effect on the angle (1° - 2°). The results of both sets of theoretical calculations disagree with the infrared study of Hvistendahl et al. (5) who find a linear or nearly linear structure for $Al_2Cl_7^-$ in chloroaluminate melts containing cations larger Li^+ . If the predicted barrier is correct it is unlikely that a linear-averaged structure would be observed.

Finally, we explore the reason for the different $Al_2F_7^-$ and $Al_2Cl_7^-$ structures. In a classical picture, two of the factors determining whether the Al-X-Al bridge is bent or linear are the Al-Al repulsion and the polarizability of the halide anion. The longer Al-Al distance and larger anion polarizability in $Al_2Cl_7^-$ than in $Al_2F_7^-$ are consistent with the predictions here of a bent bridge in $Al_2Cl_7^-$ and a linear bridge in $Al_2F_7^-$. This picture is also consistent with the linear bridge found in $Al_2H_7^-$ (16-17) and the bent bridge found in $Al_2Br_7^-$ (18).

CONCLUSIONS

The following conclusions can be drawn from this *ab initio* molecular orbital study of the structure of the $Al_2F_7^-$ and $Al_2Cl_7^-$ anions.

- 1) The $Al_2Cl_7^-$ anion is predicted in the absence of any cations to have a bent bridge with an Al-Cl-Al angle of about 131° and a barrier to inversion of 4 kcal/mol. The Al-Cl distance in the bridge is about 0.15 Å longer than in the terminal $-AlCl_3$ groups. Three different bent bridge structures (C_s , C_2 , and C_{2v}), all related by internal rotation, differ by less than 0.4 kcal/mol in energy.
- 2) The $Al_2F_7^-$ anion is found to have a linear or nearly linear Al-F-Al bridge with

at most a very small barrier to inversion (less than 0.2 kcal/mol). The preference for a linear bridge in Al_2F_7^- is attributed to increased Al-Al repulsion and smaller anion polarizability compared to that in Al_2Cl_7^- .

3) The edge- and face-bridged structures (2 and 3) are predicted to be less stable than the corner-bridged structures for both Al_2F_7^- and Al_2Cl_7^- . For Al_2Cl_7^- they are less stable by more than 40 kcal/mol. For Al_2F_7^- the edge-bridged structure is predicted to be about 13 kcal/mol less stable and the face-bridged structure 29 kcal/mol less stable.

ACKNOWLEDGMENTS

We thank M. Blander for helpful discussions. The assistance of R. Misak, an undergraduate research participant, is also gratefully acknowledged. This work was performed under the auspices of the Division of Materials Science, Office of Basic Energy Sciences of the United States Department of Energy.

REFERENCES

1. E. Rytter, H. A. Øye, S. J. Cyvin, B. N. Cyvin, and P. Klæboe, *Inorg. Nucl. Chem.* **35**, 1185 (1973).
2. G. Torsi, G. Mamantov, and G. M. Begun, *Inorg. Nucl. Chem. Lett.* **6**, 553 (1970).
3. S. J. Cyvin, P. Klæboe, E. Rytter, and H. A. Øye, *J. Chem. Phys.* **52**, 2776 (1970).
4. J. Hvistendahl, P. Klæboe, E. Rytter, and H. Øye, *Inorg. Chem.*, **23**, 706(1984).
5. M. H. Brooker and G. N. Papatheodorou, in "Advances in Molten Salt in Chemistry," edited by G. Mamantov, (Elsevier, Amsterdam, 1983), Vol. 5 pp. 27-165.
6. L. P. Davis, C. J. Dymek, J. J. P. Stewart, H. P. Clark, and W. J. Lauderdale, *J. Am. Chem. Soc.*, **107**, 5041 (1985).
7. T. W. Couch, D. A. Lokken, and J. D. Corbett, *Inorg. Chem.* **11**, 357 (1972).
8. L. A. Curtiss and R. Nichols, Proceedings of the Fifth International Symposium on Molten Salts, The Electrochemical Society, Pennington, New Jersey, 1986.
9. J. S. Binkley, M. J. Frisch, D. J. DeFrees, K. Ragavachari, R. A. Whitesides, H. B. Schlegel, E. M. Fluder, and J. A. Pople, GAUSSIAN 82 (release A version), Carnegie-Mellon University, 1983.

10. W. J. Hehre, R. F. Stewart, and J. A. Pople, *J. Chem. Phys.* 51, 2657 (1969); W. J. Hehre, R. Ditchfield, R. F. Stewart, and J. A. Pople, *J. Chem. Phys.* 52, 2769 (1970);
11. J. S. Binkley, J. A. Pople, and W. J. Hehre, *J. Am. Chem. Soc.* 102, 939(1980); M. S. Gordon, J. S. Binkley, J. A. Pople, W. J. Pietro, and W. J. Hehre, *J. Am. Chem. Soc.* 104, 2797(1982).
12. P. C. Hariharan and J. A. Pople, *Theoret. Chim. Acta.* 28, 213(1973). M. M. Francl, W. J. Pietro, W. J. Hehre, J. S. Binkley, M. S. Gordon, D. J. Defrees, J. A. Pople, *J. Chem. Phys.* 77, 3654 (1982).
13. L. A. Curtiss, *Int. J. Quant. Chem.* 14, 709 (1978); G. N. Papatheodorou, L. A. Curtiss, and V. A. Maroni, *J. Chem. Phys.* 78, 3303 (1983).
14. This energy difference is 4.0 kcal/mol at the HF/6-31G*//HF/STO-3G level, indicating that the results are not very sensitive to the level of geometry optimization.
15. L. A. Curtiss, unpublished results.
16. J. L. Atwood, D. C. Hrncir, R. D. Rogers, and J. A. K. Howard, *J. Am. Chem. Soc.* 103, 6787 (1981).
17. J. M. Howell, A. M. Sapse, E. Singman, and G. Snyder, *J. Am. Chem. Soc.* 104, 4758 (1982).
18. E. Rytter, B. E. D. Rytter, H. A. Øye, J. Krogh-Moe, *Acta Crystallogr.* B31, 2177 (1975).

Table 1. Total Energies^a of Al₂F₇⁻ and Al₂Cl₇⁻ Anions

Anion	Structure	HF/STO-3G// HF/STO-3G	HF/3-21G// HF/3-21G	HF/6-31G*// HF/3-21G
Al ₂ F ₇ ⁻	<u>1</u> (D _{3d})	-1164.62264	-1174.25585	-1180.58495
	<u>1</u> (D _{3h})	-1164.62212	-1174.25510	-1180.58439
	<u>1</u> (C _s)	-1164.62275	--- ^b	---
	<u>1</u> (C _{2v})	-1164.62213	--- ^c	---
	<u>2</u> (C _s)	-1164.62512	-1174.24802	-1180.56466
	<u>3</u> (C _{2v})	-1164.63464	-1174.24758	-1180.53851
Al ₂ Cl ₇ ⁻	<u>1</u> (D _{3d})	-3660.81451	-3682.95323	-3700.82967
	<u>1</u> (D _{3h})	-3660.81415	-3682.95293	---
	<u>1</u> (C _s)	-3660.81820	-3682.95481	---
	<u>1</u> (C _{2v})	-3660.81716	-3682.95410	-3700.83545
	<u>1</u> (C ₂)	-3660.81824	-3682.95486	---
	<u>2</u> (C _s)	-3660.78540	-3682.89066 ^d	---
	<u>3</u> (C _{2v})	-3660.73074	-3682.87907	---

^aIn atomic units (1 a.u. = 627.5 kcal/mol). Structures illustrated in Figs. 1 and 2.

^bC_s → D_{3d}.

^cC_{2v} → D_{3h}.

^d3-21G energy at the STO-3G geometry (HF/3-21G//HF/STO-3G).

Table II. Relative Energies^a of Al₂F₇⁻ and Al₂Cl₇⁻ Anions

Anion	Structure	HF/STO-3G// HF/STO-3G	HF/3-21G// HF/3-21G	HF/6-31G*// HF/3-21G
Al ₂ F ₇ ⁻	<u>1</u> (D _{3d})	0.1	0.0	0.0
	<u>1</u> (D _{3h})	0.4	0.5	0.4
	<u>1</u> (C _s)	0.0	— ^b	—
	<u>1</u> (C _{2v})	0.4	— ^c	—
	<u>2</u> (C _s)	-1.5	4.9	12.7
	<u>3</u> (C _{2v})	-7.5	5.2	29.1
Al ₂ Cl ₇ ⁻	<u>1</u> (D _{3d})	2.3	1.0	3.6
	<u>1</u> (D _{3h})	2.5	1.2	—
	<u>1</u> (C _s)	0.0	0.0	(-0.4) ^d
	<u>1</u> (C _{2v})	0.7	0.4	0.0
	<u>1</u> (C ₂)	0.0	0.0	—
	<u>2</u> (C _s)	20.6	40.2 ^e	—
	<u>3</u> (C _{2v})	54.9	47.5	—

^aIn kcal/mol. Calculated from total energies in Table I.^bC_s → D_{3d}.^cC_{2v} → D_{3h}.^dEstimated relative energy from 3-21G results for 1 (C_s) and 1 (C_{2v}) structures.^e3-21G energy at the STO-3G geometry.

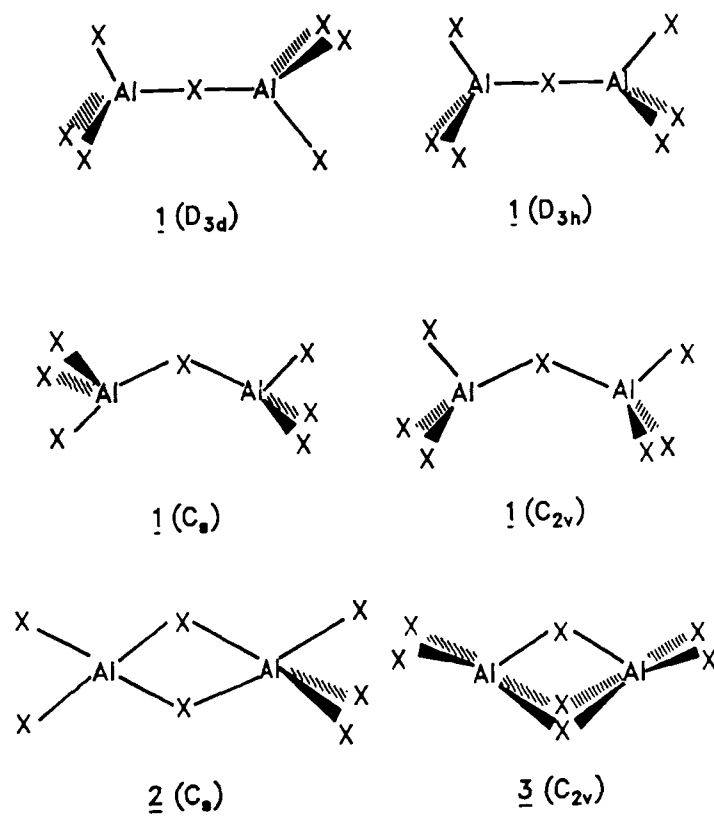
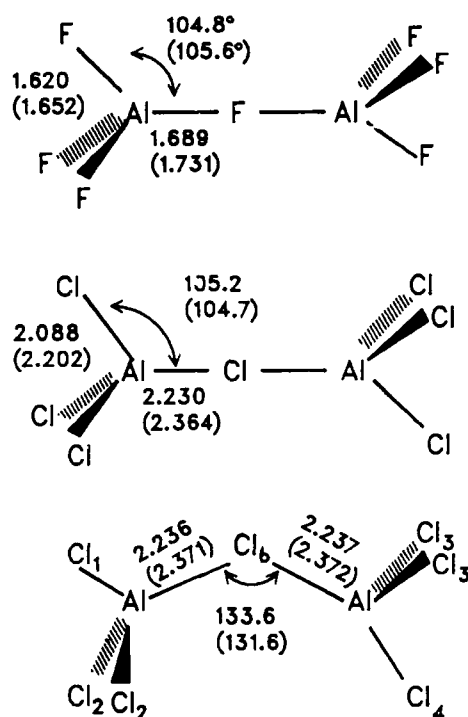


Fig. 1 Structures of Al_2X_7^- having corner (1), edge (2), and face (3) bridging.



	$r(\text{AlCl}_1)$	$r(\text{AlCl}_2)$	$r(\text{AlCl}_3)$	$r(\text{AlCl}_4)$
STO-3G	2.086	2.089	2.087	2.089
3-21G	2.199	2.203	2.200	2.203
	$< \text{Cl}_1\text{AlCl}_6$	$< \text{Cl}_2\text{AlCl}_b$	$< \text{Cl}_3\text{AlCl}_b$	$< \text{Cl}_4\text{AlCl}_b$
STO-3G	105.6°	104.8°	105.6°	103.9°
3-21G	105.1°	104.3°	105.2°	103.3°

Fig. 2 STO-3G and 3-21G optimized geometries for Al_2F_7^- [$\bar{1}$ (D_{3d}) structure] and Al_2Cl_7^- [$\bar{1}$ (D_{3d}) and $\bar{1}$ (C_s) structures]. Bondlengths in angstroms and bondangles in degrees (3-21G values in parentheses; values in the table are for the C_s structure).

LIQUID DICHLORIDES AND DICHLORIDE-MONOCHLORIDE MIXTURES

M. Rovere^{*,†} and M. P. Tosi[†]

^{*}Institut für Physik, Universität Mainz, Germany

[†]Dipartimento di Fisica and ICTP, Trieste, Italy

ABSTRACT

We give a short review of the progress done recently in the interpretation of the structure of molten divalent cation chlorides and of the stability of chloro complexes in molten salt mixtures.

INTRODUCTION

In recent years neutron scattering experiments from isotropically enriched samples have yielded a large amount of structural information on molten divalent cation chlorides, namely BaCl_2 (1), SrCl_2 (2), ZnCl_2 (3), CaCl_2 (4), MgCl_2 , and MnCl_2 (5).

The experimental results show a close connection between the structural properties in the melt and the behavior of these systems in the hot solid phase, where a variety of interesting phenomena, like fast ionic conduction or glass transition are observed. Similar liquid structures are found for BaCl_2 and SrCl_2 , both crystallizing in a fluorite type structure at high temperature. Like other fluorite type materials, they undergo a transition to a high conductivity phase (superionic) before melting. The increase of conductivity is related to the high concentration of anionic defects (6). The disorder of the anionic component and the crystalline order of the cations are reflected in the liquid in the high degree of short range order for the metal ions in comparison with the chlorine ions.

A very different structure is observed in liquid ZnCl_2 , whose glass forming tendencies are well-known (7,8). MgCl_2 and MnCl_2 have some similarities with the ZnCl_2 structure. In the liquid phase one observes a very well defined local structure of chlorines arranged in a tetrahedral coordination around the zinc ion with a close similarity to the local structure of the glass. The existence of these tetrahedral units is confirmed by spectroscopic data (9). Moreover, the addition of excess chlorine breaks the bridging of the tetrahedral units and modes are observed related to the $[\text{ZnCl}_4]^{2-}$ complexes (10).

Complexes are also found in some of the molten mixtures of polyvalent cation halides and alkali halides upon addition of alkali

halide. The experiments (11) and computer simulation (12) show for instance for mixtures of AlCl_3 and alkali halides the existence of complexes in which halogen ions are coordinated in a tetrahedral configuration around the polyvalent cation. There are, however, a number of systems like $\text{CaCl}_2\text{-2LiCl}$, where complexes are not revealed at all. In $\text{CaCl}_2\text{-2KCl}$ coexistence of sixfold and fourfold coordinated configurations around the calcium ions is observed (13).

For a liquid dichloride a first interpretation of the difference of the structural properties can be obtained just looking at the classification scheme of crystalline structures and molecular shapes for sp bonded AB_2 compounds (14-16). The increasing ionicity corresponds in the crystal to an increase in the coordination number and in the molecules to a transition from a linear to a bent molecule.

In this scheme SrCl_2 and BaCl_2 lie in the high ionicity limit, and ZnCl_2 , MgCl_2 and MnCl_2 in the low ionicity limit. It is interesting to note that the low ionicity limit seems to favor the formation of complexes.

A more accurate analysis of the liquid structure could be attempted of course by using the statistical mechanical theories and computer simulation. We give now a short review of the progress done for some of the compounds and mixtures just mentioned.

STRUCTURAL PROPERTIES OF MOLTEN SrCl_2

Detailed simulation work on molten SrCl_2 has been done by de Leeuw (17) assuming a rigid ion potential. McGreevy and Mitchell (2) found a significant disagreement with their neutron scattering data. A refined liquid theory has been applied by Pastore et al. (18), and a careful analysis has been performed.

The indications, which come out, are that the rigid ionic model gives reasonable agreement with the thermodynamics of the liquid, but large discrepancies are found in the Sr-Sr pair distribution function. The main conclusions of the work of Pastore et al. can be summarized as follows:

1. The Sr-Sr correlations, which are most sensitive to the model of interionic forces, are dominant. They determine the main features of the liquid structure. Moreover, the cation short range order drives the transition to the crystal in the superionic phase (19).
2. A simple classical jellium model works in reproducing the Sr-Sr structure when the cation-cation Coulomb repulsion is screened by the electronic dielectric constant of the material. This suggests an important role of the distortions of the electronic shells in determining the correlations.

STRUCTURE AND INTERIONIC FORCES IN MOLTEN ZnCl_2

Simulation of liquid ZnCl_2 with a rigid ionic model has been done by Woodcock et al. (20) and most recently by Gardner and Heyes (21). This model gives a reasonable agreement with the gross features of the Zn-Cl and Cl-Cl pair correlations, but it fails completely in the prediction of the Zn-Zn structure. This means that the model is not able to reproduce one of the most important conclusions of the experimental work; the close similarity between the local structure of the liquid and the glass (3,7,8). As proposed by Desa et al. (8), this structure can be seen as a distorted random close packing of chlorine ions with a Cl-Cl coordination number of the order of 8-10. The Zn ions are occupying the tetrahedral holes in such way as to maximize corner sharing of the resulting ZnCl_4 tetrahedra at the expense of edge or face sharing.

Theoretical work has been done by Ballone et al. (22). They examined a number of different models, starting from the simple charged hard sphere model, and then introducing non-additive excluded volume effects and an effective screening. Now the anion-anion correlations are the dominant ones, and by choosing suitable values of the non-additive ionic radii the authors are able to reproduce the local tetrahedral coordination. Finally, with the introduction of a distance dependent dielectric screening they get very reasonable results. They conclude that the Zn-Zn correlations reflect mostly the real binding forces, even if a combination of non-additivity of ionic radii and an effective r-dependent dielectric screening can give a reasonable account of the correlations.

STABILITY OF CHLORO COMPLEXES IN MOLTEN SALT MIXTURES

A number of experiments on molten mixtures of polyvalent cation halides and alkali halides, as said in the introduction, indicate the existence of units of halogen ions coordinated in a fourfold configuration around the polyvalent cation. For instance the existence of $[\text{AlCl}_4]^-$ units in molten LiCl-AlCl_3 has been directly established by Biggin et al. (11) by neutron scattering experiments. On the other hand in recent work with Raman spectroscopy, Sakai et al. (13) did not reveal complexes in systems like $\text{CaCl}_2\text{-2LiCl}$, $\text{CaCl}_2\text{-2NaCl}$, $\text{SrCl}_2\text{-2KCl}$ and $\text{SrCl}_2\text{-2RbCl}$. As mentioned above, in $\text{CaCl}_2\text{-2KCl}$ there is a coexistence of sixfold and fourfold coordination for the calcium ions.

Sabounji et al. (12) showed by computer simulation on an $\text{AlCl}_3\text{-NaCl}$ mixture that an ionic model can reproduce structural features of a complexing liquid. A similar kind of approach has been developed by Akdeniz et al. (23). They applied a simple ionic model to the solutions of divalent cation chlorides (MCl_2) in molten alkali chlorides. They evaluated the complex stability as a function of

the alkali chloride solvent and of the solute concentration. The complexes are dissociated when the solute concentration exceeds the "stoichiometric" composition 1/3, but it is also found that the stability is determined by the ionic screening length of the solution. A stability criterion is established in terms of a "critical" ratio between the screening length and the M-Cl distance. The dissociation of the complexes takes place when this ratio is less than 1.60. In the table below the values of the ratio for different MCl-alkali chloride mixtures are given. The prediction of complex forming (above the line) and non forming (below the line) are in agreement with the experiments.

TABLE I

	Li	Na	K	Rb	Cs
Be	1.93	1.96	1.99	2.01	2.03
Mg	1.69	1.71	1.74	1.75	1.77
Ca	1.58	1.60	1.62	1.63	1.64
Sr	1.53	1.55	1.57	1.58	1.60
Ba	1.49	1.51	1.53	1.54	1.55

REFERENCES

1. F. G. Edwards, J. E. Enderby, R. A. Howe and D. I. Page, J. Phys. C: Solid State Phys., **8**, 3483 (1978).
2. R. L. McGreevy and E. W. J. Mitchell, J. Phys. C: Solid State Phys., **15**, 5537 (1982).
3. S. Biggin and J. E. Enderby, J. Phys. C: Solid State Phys., **14**, 3129 (1981).
4. S. Biggin and J. E. Enderby, J. Phys. C: Solid State Phys., **14**, 3577 (1981).
5. S. Biggin, M. Gay and J. E. Enderby, J. Phys. C: Solid State Phys., **17**, 977 (1984).
6. M. T. Hutchings, K. Clausen, M. H. Dickens, W. Hayes, J. K. Kjems, P. G. Schnabel, and C. Smith, J. Phys. C: Solid State Phys., **17**, 3903 (1984).
7. J. Wong and F. W. Lytle, J. Non-Cryst. Solids, **37**, 273 (1980); R. Triolo and A. H. Narten, J. Chem. Phys., **74**, 703 (1981).
8. J. A. Desa, A. C. Wright, J. Wong, and R. N. Sinclair, J. Non-Cryst. Solids, **51**, 57 (1982).

9. C. A. Angell, G. H. Wegdam and J. van der Elsker, Spectrochim. Acta, **30A**, 665 (1974); F. L. Galeener, J. C. Mikkelsen, A. C. Wright, R. N. Sinclair, J. A. Desa, and J. Wong, J. Non-Cryst. Solids, **42**, 23 (1980); F. Aliotta, G. Maisano, P. Migliardo, C. Vasi, F. Wanderlingh, G. P. Schmith, and R. Triolo, J. Chem. Phys., **75**, 613 (1981).
10. J. R. Mayer, J. C. Evans, and G. Y. S. Lo, J. Electrochem. Soc., **113**, 485 (1966).
11. S. Biggin, S. Cummings, J. E. Enderby and M. Blander, Proc. Molten Salt Symposium (Las Vegas 1985).
12. M. L. Saboungi, A. Rahman, and M. Blander, J. Chem. Phys., **80**, 2141 (1984); M. Blander, M. L. Saboungi, and A. Rahman, J. Chem. Phys., **85**, 3995 (1986).
13. S. Sakai, T. Nakamura, N. Umesaki, and N. Iwamoto, Phys. Chem. Liquids, **14**, 67 (1984).
14. W. Andreoni, Helv. Phys. Acta, **58**, 226 (1985).
15. W. Andreoni, G. Galli, and M. P. Tosi, Phys. Rev. Letters, **55**, 1734 (1985).
16. M. Rovere and M. P. Tosi, Rep. Prog. Phys., **49**, 1001 (1986).
17. S. W. de Leeuw, Molec. Phys., **36**, 103 (1978); S. W. de Leeuw, Molec. Phys., **36**, 765 (1978).
18. G. Pastore, P. Ballone, and M. P. Tosi, J. Phys. C: Solid State Phys., **19**, 487 (1986).
19. B. D'Anguanno, M. Rovere, M. P. Tosi, and N. H. March, Phys. Chem. Liquids, **13**, 113 (1983); M. Rovere and M. P. Tosi, Solid State Commun., **55**, 1109 (1985).
20. L. V. Woodcock, C. A. Angell, and P. Cheeseman, J. Chem. Phys., **65**, 1565 (1976).
21. P. J. Gardner and D. M. Heyes, Physica, **131B**, 227 (1985).
22. P. Ballone, G. Pastore, J. S. Thakur, and M. P. Tosi, Physica, **142B**, 294 (1986).
23. Z. Akdeniz and M. P. Tosi, Phys. Chem. Liquids, in press.

SMALL ANGLE X-RAY SCATTERING (SAXS) AND PVTX-BEHAVIOUR
OF FLUID K_xKCl_{1-x} SOLUTIONS

E. Pfeiffer, K. Garbade and W. Freyland
FB 14 Physikalische Chemie, Universität Marburg,
D-3550 Marburg, FRG

ABSTRACT

In this paper we present first results of the small angle X-ray scattering and the pVTx behaviour of fluid K_xKCl_{1-x} solutions. In the salt rich solutions Guinier type scattering is observed. From this an electronic radius of gyration $R_g \sim 10 \text{ \AA}$ is determined which gives a first approximate measure of the extent of local density inhomogeneities around localized electronic states. Approaching the metal-nonmetal transition region the scattering law changes. Based on the pVTx results the thermodynamic equation of state has been determined the first time for a metal-molten salt solution. It is compared with a simple model calculation which is found to be in good agreement with the experimental values over the whole composition range.

INTRODUCTION

Most alkali metal (M) - alkali halide (MX) solutions exhibit spinodal decomposition into separate liquid phases below a critical temperature T_c (1). Above this critical point a continuous transformation from metallic (M) to nonmetallic (NM) states occurs with varying composition. This change in the electron-ion coupling strongly influences the microscopic structure (2) and offers a continuous challenge for the theoretical modelling of the thermodynamics of these systems (3).

Recent spectroscopic experiments (4) and theoretical studies (5,6) demonstrate that at very high metal dilution predominantly F-center like localized states form. With increasing metal concentration interaction between F-centers may lead to spin-paired (7) associated F-center dimers or dielectrons, i.e. two electrons localized in the same anion vacancy. This defect model was successfully applied to salt rich solutions to explain the thermodynamic, optical, and electronic transport properties (8). Recent quantum molecular dynamics calculations by Selloni et al. (6) also predict the occurrence of dielectron complexes in a singlet ground state. At higher metal concentrations approaching the NM-M transition it was first suggested from ESR measurements that higher associated localized states with an electron distribution comparable to metal cluster states might occur (7).

In relation with these problems the present study is concerned with the following main objectives. We have been interested in a direct information, as much as possible, on the local microscopic structure of aggregated localized states and their structural changes approaching the NM-M transition region. For this aim we have started small angle X-ray scattering (SAXS) experiments on K_xKCl_{1-x} solutions. First preliminary results have been obtained in the salt rich solutions up to the critical point ($x_c = .39$, $T_c = 788^\circ\text{C}$). In a second experiment we have studied the pVTx-behaviour of K_xKCl_{1-x} over the whole composition range from pure salt to pure metal. From this we have determined the thermodynamic equation of state which is presented for the first time for a M-MX solution. For a quantitative theoretical description of the electronic and thermodynamic characteristics of these solutions the equation of state offers a crucial test. In both experiments we have selected the K-KCl system as this is a favourite model fluid in the current theoretical investigations of M-MX solutions.

EXPERIMENTAL

The limited page number does not allow a detailed description of the experimental techniques and of the data and error analysis. So we sketch here only the principles of the applied methods and concentrate on some important points of the sample cell constructions dictated by the high temperature conditions.

A. SAXS-EXPERIMENT

Due to the high temperature requirements of the sample we had to apply a transmission method. For intensity reasons we have chosen slit-collimation and constructed a high temperature Kratky camera (9) with the following diffraction geometry: Cu- K_α X-ray source, graphite monochromator, slit-collimation system, high temperature-high vacuum furnace with sample cell and beam stop, position sensitive detector. The sample in the shape of a thin slab is fixed and perpendicular to the incoming beam with an asymmetric scattering geometry. The principle of construction of the sample cell is shown in Fig.1. The liquid film is confined between two circular windows 1.4 from sapphire or B₄C, which have a thickness of 60 μm or 400 μm , respectively, in the range of the X-ray beam. The windows are pressed against a Ta-ring 3 to achieve a vacuum tight sealing of the sample. The optimum scattering thickness of the film of μ^{-1} (μ = linear absorption coefficient) is defined by a Mo-ring spacer 2.

In order to determine the coherent scattering intensity the data have been corrected for absorption (empty container and container plus sample absorption), polarization, inelastic and multiple scattering - for details see e.g. (10) -. The background scattering of the solvent which is mainly determined by the number-number fluctuations $S_{NN}(Q)$ and is proportional to the isothermal compressibility χ_T in the long wave-

length limit has been calculated from the corresponding analytical expression (11) and the χ_T -data determined from the pVTx-measurements below. This contribution has been subtracted from the total coherent intensities. With the slit-collimation used here the deconvolution of the measured intensities is a major correction. For this aim the weight function $W(y)$ (9) which contains the smearing of the intensities due to the finite slit length and the detector entrance slit has been determined experimentally. It is well approximated by a Gaussian. The overall uncertainty of the finally corrected intensities is estimated to be below 5% as long as the counting statistics is better than 2%. For further details of this experiment, results, and data evaluation see (12).

B. pVTx-EXPERIMENT

The pVT-data at different metal mole fractions x ($0 \leq x \leq 1$) have been measured in an internally heated high pressure vessel, compressed argon gas being the pressurizing medium. At constant x the pressure and temperature dependence of the molar volume of mixing, $V_m(p, T, x)$, has been determined by a dilatometric technique as sketched in Fig. 2. The fluid sample is contained in a stainless steel bellows 1 closed at the top end by a cone fitting 2. The volume change $V_m(p, T, x)$ of the liquid mixture is monitored by a thermostated inductive device 3 inside a high pressure capillary at the cold end of the high pressure vessel. The resolution and reproducibility of this dilatation measurement is found to be $\pm 10 \mu\text{m}$ and the whole setup has been calibrated up to high temperatures and pressures with a dummy steel cell. With a filling volume of $\sim 2.5 \text{ cm}^3$ the maximum absolute error of the $V_m(p, T, x)$ results is estimated to be $\pm 1.1\%$. For pure K and KCl the results reported here agree with the corresponding literature data, (13) and (14) respectively, to better than $\pm 0.6\%$. In addition we have measured the pressure dependence of the phase diagram which is obtained from clear kinks observed in the $V_m(p, T, x)$ curves when crossing the phase boundaries. This independent information gives a valuable insight into the thermodynamic consistency of the pressure dependence of the phase boundary and the value of the molar excess volume near the critical point (15). Details of the results and the experimental techniques are described in a separate paper (16).

RESULTS AND DISCUSSION

A. SAXS-RESULTS

As discussed in the introduction, in the salt rich solutions electron localization in the form of different defect states leads to inhomogeneities in the local electron distribution $\rho_e(R)$. This is probed by the X-rays. For the interpretation of the small angle X-ray scattering due to these inhomogeneities we start from the following basic relation

for the elastic scattering intensity $I(\bar{Q})$ (9):

$$I(\bar{Q}) \propto N |F(\bar{Q})|^2 (1 + \int g(\bar{R}) \exp(-i\bar{Q}\bar{R}) d^3\bar{R}). \quad [1]$$

Here \bar{Q} is the scattering vector and N is the number of defects (particles). The structure factor $|F(\bar{Q})|$, which is the Fourier transform of $\rho_e(\bar{R})$, describes the intraparticle scattering. The integral in Eq. [1] gives the interparticle scattering determined by the Fourier transform of the pair distribution function $g(\bar{R})$. As a first approximation for salt rich solutions we may consider a two phase model: we assume that we have N identical spherical particles which are not strongly correlated and which have a homogeneous scattering length density ρ_{ep} embedded in a solution (matrix) of homogeneous scattering length density ρ_{es} . Then $|F(\bar{Q})|$ may be written as:

$$|F(\bar{Q})|^2 \propto (\rho_{ep} - \rho_{es})^2 S(\bar{Q}) \propto (\Delta\rho_e)^2 \exp(-\frac{Q^2 R_e^2}{3}). \quad [2]$$

Here the scattering function $S(\bar{Q})$ has been approximated by the Guinier scattering law (17), where the electron radius of gyration, R_e , for a spherical symmetric charge distribution around a defect is given by:

$$\langle R_e^2 \rangle = \frac{\int_0^\infty R^4 \rho_e(R) dR}{\int_0^\infty R^2 \rho_e(R) dR}. \quad [3]$$

The following discussion is based on these relations. Fig.3 shows a Guinier plot, $\ln I(Q)$ vs. Q^2 , of the SAXS-results of K_xKCl_{1-x} at a constant temperature of $\sim 775^\circ\text{C}$ for three selected compositions $x = .07$, $.10$, and $.17$. The intensities are in relative units. Below $x = .10$ a Guinier type behaviour is observed over the whole Q -range. From a best linear fit of the data (full curve) a radius of gyration of $R_g \sim 10 \text{ \AA}$ is found. This gives a first rough estimate of the extent of the inhomogeneity of the charge distribution around defect states like F-centers or dimers. Localized electrons in F-center or dimer states are stabilized by interaction with ions in first and second neighbor cation and anion shells, respectively, and thus may influence the local density over this distance range. Taking this into account the magnitude of R_e is not unreasonable.

In order to get a more quantitative insight into $\rho_e(\bar{R})$ improvements of the present results are necessary. First the scattering range has to be extended to lower Q -values which is possible with the B_4C -cells and is currently undertaken. In a further step, variation of the scattering contrast $\Delta\rho_e$ is considered. This is possible by isomorphous substitution - exchanging the cation while keeping the anion the same, e.g. comparison of NaX with KX systems - or by varying the scattering length itself - anomalous scattering - at different energies using a synchrotron light source. In particular this last technique offers

completely new possibilities. Improvements in these directions are in preparation.

With further increase of the metal concentration above $x = 0.10$ clear deviations from Guinier behaviour are observed. This is demonstrated by the upper curve in Fig.3 for $x = .17$. Concerning this concentration range the following considerations are of interest. In the more concentrated solutions the average separation between localized states is reduced and so interparticle scattering may come into play. Another interesting possibility is that the scattering law changes approaching the NM-M transition region. From the electronic properties we expect this to occur around $x_{NM-M} \approx 0.5x_c$ (18). If cluster aggregation or diffusion limited aggregation are the dominant changes in the local structure during the NM-M transition the small angle scattering should follow a characteristic power law, $S(Q) \propto Q^{-d}$ (see, e.g., (19)). For the understanding of the M-NM transition mechanism in fluid systems this problem may be of particular interest. Discussing the small angle scattering in the intermediate concentration region of the NM-M transition, a further complication arises from the nearby critical point ($x_c = .39$) and the extension of the critical scattering below x_c . Going from salt rich solutions towards the consolute composition x_c the scattering law changes and shows the characteristic Ornstein-Zernike behaviour, i.e.

$$S(Q) \propto (1 + \xi^2 Q^2)^{-1} \quad [4]$$

with the critical correlation length ξ . This is demonstrated in Fig.4 for three temperatures above T_c and $x = x_c$. Here the corrected experimental intensities (points) are compared with the calculated intensities according to [4], where the latter have been smeared with the experimentally determined weight function $W(y)$ (full curves). These curves have been normalized at $Q \approx 0.35 \text{ \AA}^{-1}$ and thus ξ is the only fitting parameter. The ξ -values determined in this way range from 25 \AA ($T \approx T_c$) to 13 \AA ($T - T_c + 50 \text{ K}$). A more detailed study of the SAXS of K_xKCl_{1-x} in comparison with the corresponding neutron results of Chieux et al. (20) for K-KBr is in progress.

B. pVTx-RESULTS

The molar volume of K_xKCl_{1-x} ($0 \leq x \leq 1$) has been measured as a function of temperature up to 920°C and at 8 different pressures up to 1600 bar (16). A selection of these results at 850°C and three different pressures is presented in Fig.5 as a function of the mole fraction x . In the salt and metal rich end V_m shows ideal mixing behaviour within the experimental error of 1.1%, whereas a slight but positive excess volume is observed in the composition range of the miscibility gap. In a first short publication (15) we presented a small negative excess volume in the salt rich end. In further measurements we could not reproduce this part which explains the changed data around $x \approx 0.1$ as presented in Fig.5. In the previous paper (15) we have discussed the thermodynamic

consistency of the measured pressure dependence of the miscibility gap, e.g. $\partial T_C/\partial p > 0$, with the observed positive excess volume near the critical point. We have also given the partial molar volumes V_K and V_{KCl} derived from $V_m(p, T, x)$. In the following we focus on the thermodynamic equation of state for K_xKCl_{1-x} .

The thermodynamic equation of state,

$$(\partial U/\partial V)_T = T(\partial S/\partial V)_T - p = T(\partial p/\partial T)_V - p, \quad [5]$$

relates the internal pressure, $P_i = (\partial U/\partial V)_T$, with the isochoric thermal pressure coefficient, $(\partial p/\partial T)_V$, and the total pressure p . The thermal pressure coefficient is given by the isobaric expansivity, α_p , and the isothermal compressibility, χ_T :

$$(\partial p/\partial T)_V = -(\partial V/\partial T)_p / (\partial V/\partial p)_T = \alpha_p / \chi_T. \quad [6]$$

With the high density of data points for $V_m(p, T, x)$ recorded at different T and p it is possible to determine α_p and χ_T from these measurements with sufficient accuracy and to calculate $(\partial U/\partial V)_T$ according to eq. [5] with an uncertainty of $\pm 1\%$. This is presented in Fig. 6 where the internal pressure of K_xKCl_{1-x} at 800 bar and 850°C is plotted versus x (open circles). Over the whole composition range a negative excess internal pressure - difference between experimental result and dashed line - is found with a minimum value of about -1.5 kbar.

Holzhey and Schirmacher recently published a simple model for the calculation of the thermodynamic properties of liquid M-MX solutions which qualitatively describes the phase separation in these systems (21). The main ingredients of this model are the following. The interaction between the metal cation and the halogen anion is treated via an electronically screened Coulomb potential and a hard core repulsion. The screening length $\lambda(x)$ is assumed to vary linearly with composition between the limits of the salt, λ_{MX} , and the metal, λ_M , i.e.:

$$\lambda(x) = \lambda_{MX} + (\lambda_M - \lambda_{MX}) \cdot x \quad [7]$$

Using a parameterization for the correlation function of concentration fluctuations they find the following analytical expression for the excess internal energy U_m^{ex} ,

$$U_m^{ex} = (-Ae^2/\sigma)(1-x)(\exp(-\lambda(x)\sigma) - \exp(-\lambda_{MX}\sigma)), \quad [8]$$

which is a mean field type approximation. In eq. [8] A is a short range order parameter of the order of 1, σ is a common hard sphere diameter of the ions, and e is the electron charge.

In order to test this model on the measured $pVTx$ -data, we have

calculated the excess internal pressure, p_i^{ex} , from eq. 8 according to

$$p_i^{ex} = (\partial U_m^{ex} / \partial V)_T = A e^2 (1-x) \left(\frac{\partial \psi(x)}{\partial V} \right)_T e^{-\psi(x)} - \left(\frac{\partial M_X}{\partial V} \right)_T e^{-\psi M_X} \quad (9)$$

For $M_X(T, V_m)$ and $M(T, V_m)$ we have taken the analytical expressions of the Debye-Hückel and Thomas-Fermi model, respectively (see, e.g. (22)). In a first rough approximation we set $A=1$ and estimated $\approx 3 \text{ \AA}$ from the ionic radii of K^+ and Cl^- . These calculated values of p_i^{ex} are included in Fig. 6 (full line). The agreement between this simple model calculation and the experimental results is surprisingly good.

ACKNOWLEDGEMENT

We are pleased to acknowledge valuable discussions with W. Ruiland on the deconvolution problem of the SAXS-data and with W. Schirmacher on the thermodynamic model. Financial support of this work by the Deutsche Forschungsgemeinschaft and, in part, the Fonds der Chemischen Industrie is gratefully acknowledged.

REFERENCES

1. M.A. Bredig in Molten Salt Chemistry, ed. M. Blander (Interscience, New York) 1964
2. J.F. Jai, J. Dupuy and P. Chieux, J. Physique Coll., C8 41, 257 (1980).
3. G. Chabrier and J.P. Hansen, J. Phys. C: Solid State Phys., 18, 4757 (1985).
4. For recent reviews, see: W.W. Warren, Jr. in The Metallic and Non-metallic States of Matter, eds. P.P. Edwards and C.N.R. Rao (Taylor and Francis, London) 1985; W. Freyland in Proc. 5th Int. Symp. Molten Salts, eds. M.L. Saboungi, K. Johnson, D.S. Newman and D. Inman, (The Electrochemical Society, Pennington, NJ) 1986.
5. M. Parrinello and A. Rahman, J. Chem. Phys., 80, 860 (1984).
6. A. Selloni, R. Car, M. Parrinello and P. Carnevali, J. Phys. Chem., 1987, (in press).
7. N. Nicoloso and W. Freyland, J. Phys. Chem., 87, 1997 (1983).
8. J.J. Egan and W. Freyland, Ber. Bunsenges. Phys. Chem., 89, 381 (1985); H. Heyer, J.J. Egan and W. Freyland, Ber. Bunsenges. Phys. Chem., 1987 (to be published).
9. O. Glatter and O. Kratky, Small Angle X-Ray Scattering (Academic Press, New York) 1982.
10. C.W.J. Wagner in Liquid Metals, Chemistry and Physics ed. S.Z. Beer (Marcel Dekker Inc., New York) 1972.
11. M. Rovere, M. Parrinello and M.P. Tosi, Phil. Mag., B 39, 167 (1979).
12. E. Pfeiffer and W. Freyland, 1987 (to be published).
13. E.E. Shpil'man, K.A. Yakimovich and A.G. Mozgovoi, Fiz. Tverd. Temp., 14, 511 (1976).
14. G. Goldmann and K. Todheide, Z. Naturforsch., 31a, 656 (1976).
15. K. Garbade and W. Freyland, LAM6 Proceedings, Z. Phys. Chem., 1987

- (in press).
16. K.Garbade, PHD Thesis, University Marburg, 1987 and K.Garbade and W.Freyland, 1987 (to be published).
 17. A.Guinier and G.Fournet, Small Angle Scattering of X-Rays (Wiley and Sons, New York) 1955.
 18. D.Nattland, H.Heyer and W.Freyland, Z.Phys.Chem.N.F. 149, 1 (1986).
 19. P.W.Schaefer, J.E.Martin, P.Wiltzius and D.S.Cannell, Phys.Rev. Lett. 52, 2371 (1984).
 20. P.Chieux, P.Damay, J.Dubuy and J.F.Jai, J.Phys.Chem. 84, 1211 (1980).
 21. Ch.Hoizney and W.Schirmacher, J.Physique Coll. C8, 373 (1985) and Proc.LAM6 Conference, Z.Phys.Chem.N.F. (in press).
 22. N.W.Ashcroft and N.D.Mermin, Solid State Physics (Holt-Saunders College, Philadelphia) 1376.

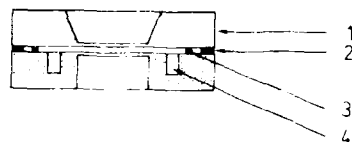


Figure 1. Cross section of the liquid sample cell for SAXS

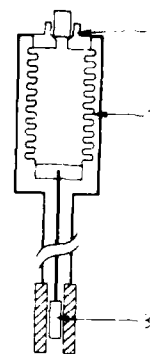


Figure 2. Sketch of the sample cell and dilatation technique used in the pVTx-measurements.

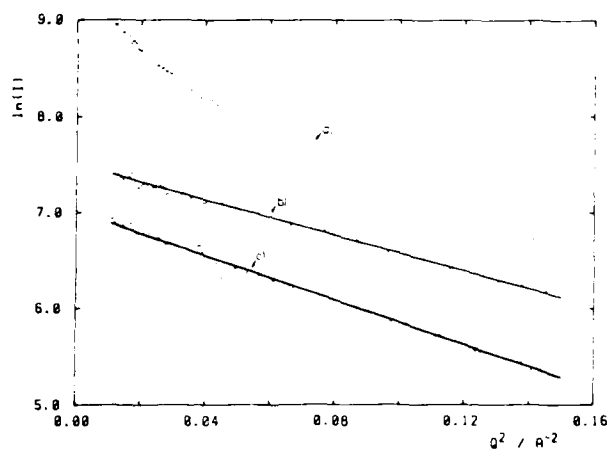


Figure 3. Guinier plots of the SAXS-results of K_xKCl_{1-x} at 775°C (c. $x = .07$; b. $x = .10$; a. $x = .17$).

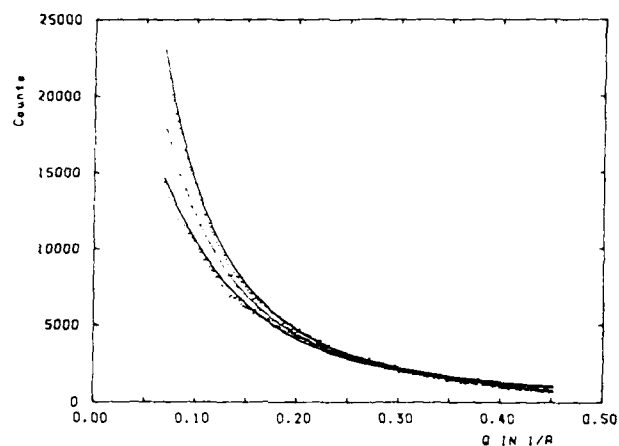


Figure 4. Critical SAXS of K_xKCl_{1-x} (Ornstein-Zernike behaviour) at $x=x_c = .39$ and three temperatures of $T \geq T_c = 788^\circ\text{C}$, $T = 813^\circ\text{C}$ and $T = 842^\circ\text{C}$ (temperature increasing from the top to the bottom curve).

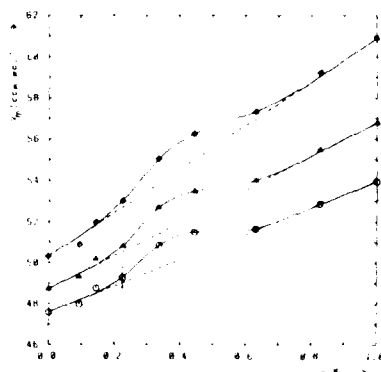


Figure 5. Molar volume of K_xKCl_{1-x} at 850°C and three different pressures of 1 bar (\diamond), 800 bar (Δ), and 1600 bar (\circ).

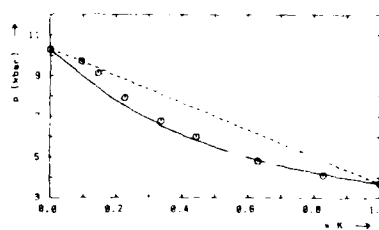


Figure 6. Internal pressure $p_i = (30U/V)_T$ of K_xKCl_{1-x} at 850°C and 800 bar; symbols give the experimental results, the full curve has been obtained from a model calculation.

STRUCTURE AND THERMODYNAMICS OF METAL-SALT SOLUTIONS:
THE THEORETICAL VIEWPOINT

Gilles Chabrier^{*}
D. P. M. Université Claude Bernard-Lyon I
69622, Villeurbanne Cedex, France

ABSTRACT

The structure and thermodynamics of solutions of alkali metals and their halides are calculated on the basis of a simple two-fluid (ion-electron) reference system and a second order perturbation expansion in the ion-electron coupling. The miscibility gap observed in these solutions is reproduced theoretically and explained in terms of screening lengths and correlation lengths, for which we obtain explicit expressions.

I. THE MODEL

The metal-salt solutions are regarded as being composed of N_1 positive ions of charge Z_1e and N_2 negative ions of charge Z_2e in a volume Ω ; the corresponding number densities and concentrations are defined as $\rho_\alpha = N_\alpha/\Omega$ and $x_\alpha = N_\alpha/N$ ($\alpha=1,2$), with $N=N_1+N_2$. The excess of positive charge⁺ is compensated by the conduction electrons which are assumed to provide a rigid, uniform background of charge e_0 , ensuring overall charge neutrality:

$$\rho_1 Z_1 + \rho_2 Z_2 + \rho_0 = \rho_{\bar{e}} + \rho_0 = 0 \quad (1)$$

The total hamiltonian of the system is written as the sum of three terms (1):

$$H = H_{ii} + H_{ee} + V_{ie} \quad (2)$$

where H_{ii} is the hamiltonian for the ions in a neutralizing uniform background, H_{ee} is the familiar helium hamiltonian for the electrons in a uniform background which exactly cancels the previous one, while V_{ie} describes the ion-electron interaction minus the interaction energy of the ions with their associated background.

1.1 THE IONIC HAMILTONIAN

The ions are assumed to interact pairwise via the simple model potential(2):

^{*}present address: Department of Physics and Astronomy,
University of Rochester, Rochester, New York 14627-0011

$$U_{\alpha\beta}(r) = Z_{\alpha}Z_{\beta}e^2/r + V_0(r) \quad (3)$$

where the short range repulsion $V_0(r)$ acts only between oppositely charged ions, and is taken to be of exponential form:

$$V_0(r) = (1 - \delta_{\alpha\beta}) A \exp\{-r/r_0\} \quad (4)$$

The potential (3) is a simplified version of the usual Born-Huggins-Mayer potential. For the parameters A and r_0 , we have chosen the values of the complete Tosl Fumi potential corresponding to the pure molten salt (3).

The ion-ion hamiltonian hence finally reads:

$$H_{ii} = K_i + \frac{1}{2\Omega} \sum_{\vec{k} \neq 0} \frac{4\pi e^2}{k^2} [\rho_{\vec{k}}^* \rho_{-\vec{k}} - N] + \sum_{i=1}^{N_1} \sum_{j=1}^{N_2} V_0(|\vec{r}_i - \vec{r}_j|) \quad (5)$$

where K_i represents the kinetic energy of the ions and $\rho_{\vec{k}}^*$ denotes the Fourier component of the ionic charge density. The corresponding ionic pair correlation functions $g_{\alpha\beta}(r)$ and their Fourier transforms the ionic structure factors $S_{\alpha\beta}(K)$ have been calculated in the framework of the hypernetted chain equations (HNC), supplemented by the Ornstein-Zernicke relations between the direct correlation functions $C_{\alpha\beta}(r)$ and the total correlation functions $h_{\alpha\beta}(r) = g_{\alpha\beta}(r) - 1$:

$$\begin{cases} g_{\alpha\beta}(r) = \exp\{-\beta U_{\alpha\beta}(r) + h_{\alpha\beta}(r) - c_{\alpha\beta}(r)\} & \text{HNC} \\ h_{\alpha\beta}(r) = c_{\alpha\beta}(r) + \sum_{\gamma=1}^2 \rho_{\gamma} \int h_{\alpha\gamma}(r') c_{\gamma\beta}(|\vec{r} - \vec{r}'|) d\vec{r}' & \text{OZ} \end{cases} \quad (6a) \quad (6b)$$

($\beta = 1/k_B T$)

Figure 1 compares the structure factors issued from the model hamiltonian (5) with the experimental results obtained by neutron diffraction for K-KCl and Rb-RbBr(8). The poorer agreement for Rb-RbBr is the consequence of the higher polarisability of this system, not included in our model.

I.2. THE ION-ELECTRON INTERACTION

The term V_{ie} of eqn. [2] can be split in two terms:

$$V_{ie} = \frac{1}{\Omega} \sum_{\alpha=1}^2 \sum_{\vec{k} \neq 0} \hat{v}_{0\alpha}(\vec{k}) \rho_{\vec{k}\alpha}^* \rho_{\vec{k}0}^* + U_0 \quad [7]$$

where $v_{0\alpha}(\vec{k})$ is the dimensionless Fourier transform of the ion-electron pseudopotential $v_{0\alpha}(\vec{r})$, and U_0 is the structure independent contribution (1.4):

$$U_0 = \frac{1}{\Omega} \sum_{\alpha=1}^2 \lim_{\vec{k} \rightarrow 0} \left[\hat{v}_{0\alpha}(\vec{k}) + \frac{4\pi Z_{\alpha} e^2}{k_B T} \right] \rho_{\vec{k}\alpha}^* \rho_{\vec{k}0}^* = \rho_0 \sum_{\alpha=1}^2 N_{\alpha} \int_{\Omega} \left[v_{0\alpha}(\vec{r}) + \frac{Z_{\alpha} e^2}{r} \right] d\vec{r} \quad [8]$$

The hamiltonian specified by eqns. [2], [5], [7] is in fact quite general and describes a number of coulombic systems besides metal-salt solutions M, MX_x : liquid metals (limit $x=1$), molten salts (limit $x=0$), binary alloys (for which $Z_1 Z_2 > 0$), and binary ionic mixtures, in which the short range repulsive term may be omitted, the electron-ion interaction being purely coulombic.

For the ion-electron pseudo-potentials occurring in eqns. [7], [8], we have chosen the Ashcroft empty core form [7] for the cation, with a core diameter determined at the melting point of the pure metal, using the sum rule for the compressibility (5). The anion-electron pseudo-potential has been chosen to be an interpolation between the Ashcroft and Shaw (6) forms (7):

$$\begin{aligned} V_{02}(\vec{r}) &= -\xi Z_2 e^2 / r_{c2} & ; r < r_{c2} \\ &= -Z_2 e^2 / r & ; r > r_{c2} \end{aligned} \quad [9]$$

For r_{c2} we have chosen, somewhat arbitrarily, the ionic Pauling radius. ξ will be the only adjustable parameter in our perturbation theory. The coordinates of the critical point which terminates the miscibility gap will depend sensitively on ξ , as we will see later. Let us note that the special case $\xi=0$ corresponds to the empty core.

I.3 THE ELECTRON GAS

The thermodynamic properties of the uniform electron gas depend on the usual density parameter r_s and the degeneracy parameter τ defined by:

$$r_s = \frac{(3/4\pi\rho_0)^{1/3}}{a_B} \quad ; \quad \tau = \frac{kT}{kT_F} \quad [10]$$

where a_B is the Bohr radius and $kT_F = \frac{1}{2} \hbar^2 k_F^2 / m_e$ is the Fermi temperature. In the Metal-salt solutions, as the metallic mole fraction decreases, the density parameter r_s increases ($r_s = \infty$ in the pure salt!) while the Fermi temperature decreases. As a consequence, the electron gas becomes more and more correlated while finite temperature corrections become non-negligible. To describe this weakly degenerate electron gas, we have used the most accurate equation of state presently available, calculated in a wide range of densities [10].

II. THERMODYNAMICS

The thermodynamic properties of the metal-salt solutions described by the hamiltonian [2] are calculated by a perturbation expansion in the ion-electron coupling V_{ie} . In the zeroth order the electronic and ionic components, neutralized by their respective uniform backgrounds, are assumed to be completely decoupled so that the Helmholtz free energy of this reference system is given by:

$$F^{(0)} = F_i + F_e \quad [11]$$

The ionic contribution is calculated from classical statistical mechanics, using the pair distribution functions obtained in §I(4). An interesting property of the HNC closure, beside the fact that it is especially adapted to coulombic systems, is that it allows a direct calculation of the excess chemical potentials μ_α , from the partial pair correlation functions [9]. Hence the excess (i.e. non ideal) free enthalpy per ion follows directly from:

$$\frac{G_i^{EX}}{NkT} = \sum_{\alpha=1}^2 x_\alpha \mu_\alpha^{EX} \quad [12]$$

The further contributions to the free energy are calculated using the standard coupling constant integration:

$$F = F(\lambda = 1) = F(\lambda = 0) + \int_0^1 \langle V_{ie} \rangle_\lambda d\lambda \quad (13)$$

where $F(\lambda=0) = F_i + F_e$ is the free energy of the reference system, whereas $\langle \rangle_\lambda$ denotes the canonical average taken over the perturbed hamiltonian. To first order in the coupling, the free energy is:

$$F^{(1)} = F_i + F_e + \langle V_{ie} \rangle_0 \quad (14)$$

with

$$\langle V_{ie} \rangle_0 = \frac{3e^2}{2a^3} \bar{Z} [N_1 Z_1 c_{e1}^2 + N_2 Z_2 c_{e2}^2 (1 - \frac{2}{3} \xi)] \quad (15)$$

The second order ion-electron contribution is calculated in the linear response approximation for the induced electron density $\langle \rho_{k0} \rangle$, which yields:

$$F_2 = \frac{1}{2} \sum_{\alpha} \sum_{\beta} (N_{\alpha} N_{\beta})^{1/2} \frac{1}{(2\pi)^3} \int \left[\frac{1}{\epsilon_e(k)} - 1 \right] \frac{k^2}{4\pi e^2} \hat{v}_{\alpha}(k) \hat{v}_{\beta}(k) S_{\alpha\beta}^{(0)}(k) d\vec{k} \quad (16)$$

the $S_{\alpha\beta}^{(0)}(k)$ denote the partial structure factors of the unperturbed ionic fluid calculated in §I. For the dielectric function $\epsilon_e(k)$ we have chosen the zero-temperature form proposed by Ichimaru and Utsumi (11), which is well adapted to the highly correlated regime ($r_s \gg 1$).

By truncating the perturbation expansion of the free energy after the second order, we restrict ourselves to linear screening in the description of the ion-electron coupling. This is a priori inapplicable in the regime of low metallic concentrations. However, since the weight of the electronic contribution to the thermodynamics of a metal-salt solution decreases with decreasing metal concentration x , we have used the results of second order perturbation theory throughout the entire range of concentration.

In that case the total free energy finally reads:

$$F^{(2)} = F_i + F_e + U_0 + F_2 \quad (17)$$

All other thermodynamic properties of the system can be derived from the free energy expression [17], by taking the appropriate derivatives with respect to the thermodynamic variables Ω , T and x . The excess Gibbs free energy of mixing is defined in the usual way as

$$\Delta G_m(P, T, x) = G_m(P, T, x) - x G_m(P, T, x=1) - (1-x) G_m(P, T, x=0) \quad [18]$$

where $G_m(T, P, x) = F_m - (P F_m / \partial \Omega_m)$, Ω_m is the molar free energy of the mixture^m at the concentration x . In practice, for fixed values of T and x , the molar volume Ω_m is varied to yield a prescribed value of the total pressure P . All the results presented here are for $P=0$. The molar volumes at zero pressure calculated from the second order perturbation theory are listed in tables for several values of the concentration, together with the various contributions to the equation of state, for the system K_xKCl_{1-x} , with $\xi=0$.

x	$\Omega / \text{cm}^3 \text{mole}^{-1}$	r_s	$\beta P_i / e$	$\beta P_e / e$	$\beta P_{ie}^{(1)} / e$	$\beta P_{ie}^{(2)} / e$
1	37.045	4.627	-14.608	-0.920	19.665	-4.135
0.8	32.868	4.790	-5.385	-0.796	10.734	-4.550
0.6	32.072	5.229	-0.869	-0.756	4.437	-3.807
0.4	39.275	6.404	0.437	-0.633	0.850	-1.786
0.2	53.203	8.928	0.895	-0.304	-0.135	-0.445
0.1	62.767	12.028	0.361	-0.122	-0.133	-0.107
0	78.901	"	0	0	0	0

TABLE 1

Molar Volumes and Various Contributions to the EOS at Zero Pressure for K_xKCl_{1-x} with $\xi=0$, at $T=1250K$. r_s is Defined by Eqn. [10]. The Subscripts^x and Superscripts i.e. (1), (2) Denote Respectively Ions, Electrons, First and Second Order.

For the pure metal, the calculated molar volume is very sensitive to the second order term in pressure, due to the fact that the zeroth and first order contributions are of opposite signs. The calculated molar volume (which is independent of ξ at $x=1$) is considerably smaller than the experimental value (68 cm³/mole at $T=1250K$). This defect may be attributed to a poor convergence of the perturbation series for the pressure in the high temperature range of expanded liquid metals (11).

For the pure salt, the calculated molar volume is larger than its experimental value for KCl (51.20 cm³/mole at $T=1250K$). But we have checked that this discrepancy is essentially due to our neglect of Van der Waals interactions in the ionic potential model of eqns. [3]-[4].

The excess molar volume of mixing $\Delta \Omega_m$ is defined as:

$$\Delta\Omega_m = \Omega_m(P=0, T, x) - x\Omega_m(P=0, T, x=1) - (1-x)\Omega_m(P=0, T, x=0) \quad [19]$$

The most striking result of our calculation is its prediction of a large negative excess volume at intermediate concentrations, as shown on figure 2. Although the large absolute values of these excess volumes may be attributed to the crudeness of our model (especially the density independence of the pseudopotentials), we believe the sign of the excess volume is real. This is to be checked by experiments. Let us note too that the results are sensitive to the value assumed for ξ .

III. MISCIBILITY GAP - CRITICAL BEHAVIOR

The various contributions to ΔG are plotted in figure 3 as a function of the molar fraction x for a typical state of K_2KCl_{1-x} . To zeroth order, when ΔG is just the sum of independent ionic and electronic contributions, ΔG is a convex function of x so that the solution would be thermodynamically unstable at all concentrations. But when the first and second order corrections due to the electron-ion coupling are added, ΔG becomes concave, signaling that the solution is going to stabilize. This behaviour contrasts with the case of binary ionic mixtures (BIM) or metallic alloys where the ionic contribution always tends to stabilize the mixture (12,13).

As figure 4 shows for one value of ξ , as ξ takes nonzero values, ΔG builds up a convex portion on the salt-rich side, signaling phase separation. The concentrations of the coexisting liquid phases are determined by the usual double tangent construction. The critical coordinates, T_c and x_c , are sensitive to ξ and are compared to the experimental values in the case of K_2KCl_{1-x} in table 2. While the calculated critical temperature can be brought into agreement by an adequate choice of ξ , the corresponding critical concentration x_c is too small. This is probably a consequence of the inadequacy of linear screening theory (and hence pseudo-potential approach) on the salt rich side of the phase diagram.

Figure 5 shows the results we get for K-KCl and Rb-RbBr for different values of ξ .

ξ	0.01	0.05	0.2	0.333	Experiment (15)
T_c / K	1250	1650	2300	2500	1073
x_c	0.25	0.25	0.35	0.40	0.35

Table 2

Critical Coordinates for K_2KCl_{1-x} Calculated for Several Values of ξ .

The demixing phenomena can be explained in terms of screening lengths. The metal-salt solutions are characterized by a competition between a Debye-Huckel type screening between the ions and a Thomas-Fermi type screening due to the rearrangement of the electronic background around each charge. These two different kinds of screening are characterized by two screening lengths or, equivalently, two dielectric functions. The electronic screening length is:

$$\lambda_e^2 = \frac{1}{4\pi e^2} \left(\frac{\partial \mu_0}{\partial \rho_0} + \frac{\partial \mu_z^{ie}}{\partial \rho_z} \right) = \frac{1}{K^2} \lim_{K \rightarrow 0} \epsilon_e(K)^{-1} \quad [20]$$

where μ_0 is the chemical potential of the continuous electron gas, whereas $\mu_z = \partial(G^{ie}/n)/\partial \rho_0$ denotes the bound electrons contribution to the total electrochemical potential. Using the Nozières-Pines (14) approximation for the correlation energy of an electron fluid at zero temperature, we obtain the following analytical expression for λ_e :

$$\lambda_e^2 = \frac{Z_2 M_1 r_2'^2 - Z_1 M_2 r_1'^2}{M_1 Z_2 - M_2 Z_1} + (0.409 r_s - 0.068 r_s^2 - 0.0017 r_s^3) a_B^2 \quad [21]$$

where $r_i' = r_i (1 - \frac{2}{3} \xi_i)^{1/2}$ is the modified radius of the pseudopotential [8]. The term $0.409 r_s a_B$ is the Thomas-Fermi screening length squared, which becomes exact in the limit of weak coupling for the electron gas ($r_s \rightarrow 0$). The first term of eqn [21] exposes the electrostrictive behavior in the response of the system, because of the finite size of the ions in the ion-electron interaction. Let us note that in the metal-salt solutions, because of the strong variation of r_s along the phase diagram, λ_e decreases quickly from metallic values to zero. This phenomenon is usually associated with the appearance of a local order (15). The screening length loses its significance in such situations. This is really different for BIM or binary alloys where the electronic screening length is always larger than the ionic one so that the screening effect is dominated by the ions.

For the ions the ionic screening length λ_i can be related to the ionic correlation length, λ_c through the equation:

$$\lambda_i^2 = \frac{\chi_0}{\chi_i} \beta \left. \frac{\partial^2 g_i}{\partial x_i^2} \right|_{T,P} \lambda_c^2 = \frac{1}{K^2} \lim_{K \rightarrow 0} \epsilon_i(K)^{-1} \quad [22]$$

Here χ_i and q_i denote respectively, the compressibility and the free enthalpy density for the ions whereas $\chi_0 = B/p$ designs the compressibility of the perfect gas. λ_c can be shown to be equal to:

$$\lambda_c^2 = \frac{S_{cc}(0)}{4\pi e \beta e^2 \bar{z}^2} = \left\{ 4\pi e \beta e^2 \bar{z}^2 \left[\beta \frac{\partial q_i}{\partial \chi_i} \right]_{T,P} + \frac{\chi_0}{\chi_i} \delta'^2 \right\} \quad (23)$$

where $S_{cc}(0)$ is the concentration-concentration structure factor at zero wave-vector which diverges at the critical point and δ' is the expansion coefficient ($\delta' = 1/p(\partial p_0/\partial \chi_1)_{P,T}$).

VI. CONCLUSION

We have shown that our really simple model reproduces qualitatively and at least semiquantitatively the structure and the miscibility gap observed in metal-salt solutions. Moreover, we have characterized this phenomenon through two screening lengths, typical of two different screening phenomena, and a correlation length, of which the scalar value let us expect that the demixing critical behaviour of metal-salt solutions is probably Ising like.

REFERENCES

1. Ashcroft, N. W., and Stroud, D., *Solid State Physics*, Vol. 33, edited by J. T. Devreese and D. Turnbull (Academic Press), (1978).
2. Chabrier, G., and Hansen, J. P. *Mol. Phys.* 50, 901, (1983).
3. Tosi, M. P., and Fumi, F. G. *J. Phys. Chem. Solid.* 25, 31, (1964).
4. Chabrier, G., and Hansen, J. P. *Mol. Phys.* 59, 1345 (1986).
5. Evans, R., and Slukin, T. J. *J. Phys. C.* 14, 3137, (1981).
6. Shaw, R. W. *Phys. Rev.* 174, 769, (1968).
7. Chabrier, G., Senatore, G., and Tosi, M. P. *Nuovo Cim. D3*, 4, (1984).
8. Chabrier, G., Jal, J. F., Chieux, P., and Dupuy J., *Physics Lett.* 93A, 1, 47, (1982). Jal J. F., These d'Etat, Universite Lyon I, (1981).
9. Baus M., and Hansen, J. P. *Phys. Rep.* 59, 1, (1980).
10. Richert W., and Ebeling W. *Phys. Stat. Sol. B*, 121, 633, (1984).
11. Kahl, G., and Hafner, J. *Phys. Rev. A.*, 29, 3310, (1984).
12. Hansen, J. P., Torrie, G. M., Vieillefosse, P. *Phys. Rev. A*, 16, 2153, (1977).
13. Henderson, R. L., and Ashcroft, N. W. *Phys. Rev. A* 13, 859, (1976).
14. Nozières P., and Pines, D. *Phys-Rev.* 111, 442, (1958).
15. Bredig, M. A., *Molten Salt Chemistry*, edited by M. Blander (Wiley Interscience), (1964).
16. Vieillefosse, P., and Hansen, J. P. *Phys. Rev. A* 12, 1106, 1975.

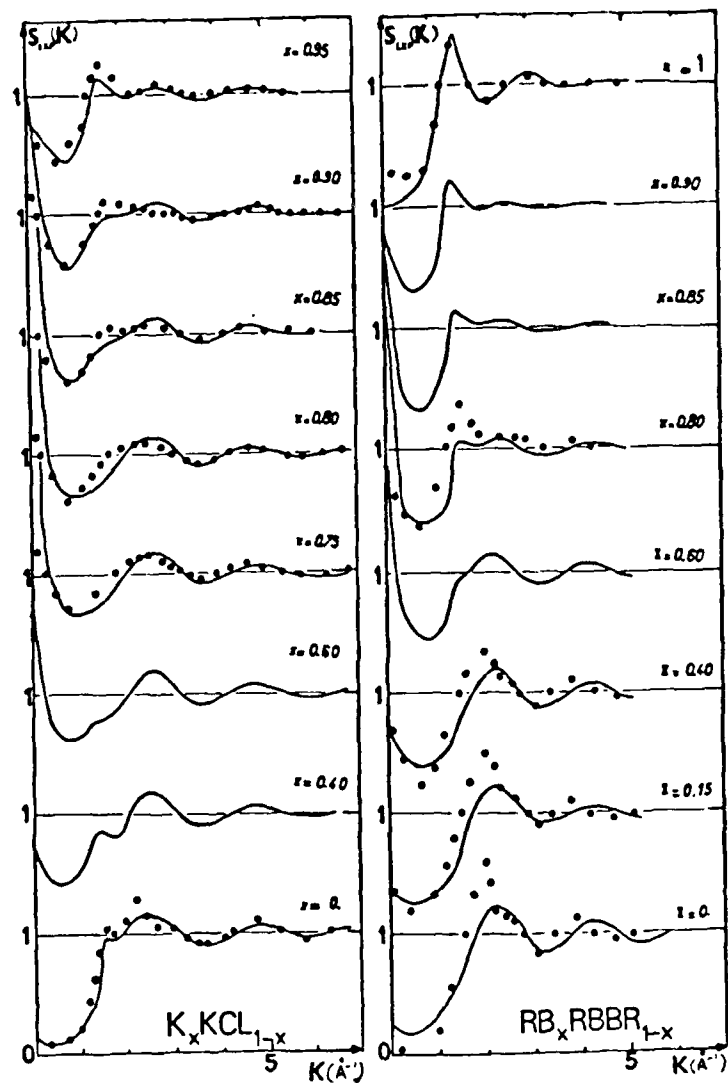


FIGURE 1

Comparison Between the Structure Factors Obtained from Neutron Diffraction (•) (dots) and from the Model Hamiltonian (—) (line).

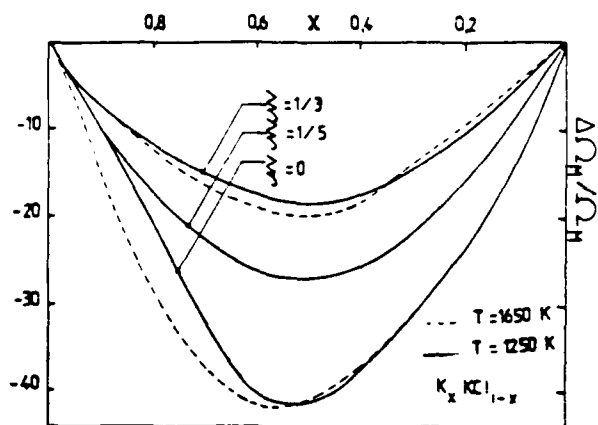


Figure 2 - Relative Excess Molar Volume versus x for K_xKCl_{1-x} Mixture at Zero Pressure.

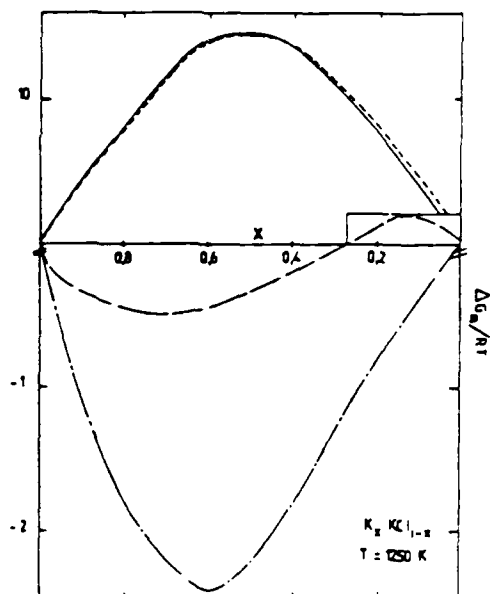


Figure 3 - Various Contributions to the Molar Gibbs Versus Molar Fraction x . Full Curve: Ionic Contribution; Dashes: Ionic and Electronic Contributions; Long Dashes: First Order Perturbation Theory; Dash-dotted Curve: Second Order Perturbation Theory.

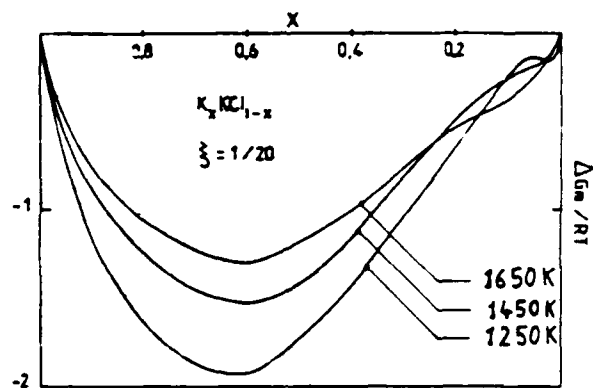


Figure 4 - Molar Gibbs Excess Free Energy Versus Molar Fraction X for a K_xKCl_{1-x} Mixture, for a Non-Zero Value of ξ .

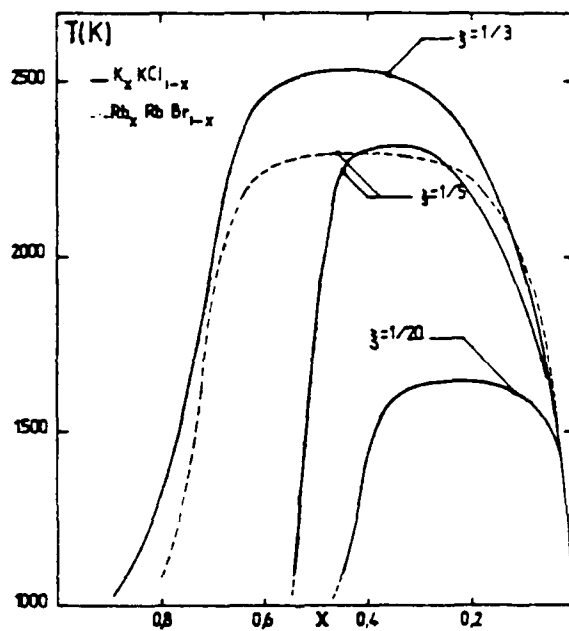


Figure 5 - Phase Diagrams of K_xKCl_{1-x} and Rb_xRbBr_{1-x} for three different values of ξ .

THEORETICAL ANALYSIS OF COLLECTIVE MODES IN
METAL-MOLTEN-SALT MIXTURES AND MOLTEN-SALT MIXTURES

Gilles Chabrier*

D. P. M. Université Claude Bernard-Lyon I
69622, Villeurbanne Cedex, France

ABSTRACT

We present the results of a theoretical analysis of long wavelength collective modes in mixtures of metal-molten salts and mixtures of salts. In the former case the calculations are made based on the assumption of a rigid background for the conduction electrons, and extended to the metal-rich concentration range by taking into account the polarisability of the electron gas. The most interesting prediction of our analysis is that sound waves should be overdamped below a critical wavenumber for a certain range of concentrations in the salt rich region of metal-salt solutions.

I. INTRODUCTION

In the following sections we give an analysis of collective modes both in metal-salt mixtures and molten-salt mixtures. We use linearized hydrodynamics, i.e. we focus on the long-wavelength, low-frequency limit, and extend our analysis for higher frequencies, using the generalized hydrodynamics, in the $K \rightarrow 0$ limit. The long wavelength domain is the region where collective modes occur. Moreover, in a strongly coupled ionic fluid, the collision frequency is large compared to all other characteristic frequencies and maintains the system locally in thermodynamic equilibrium, so that the hydrodynamic description of this high frequency mode is, at least qualitatively, correct. For the sake of simplicity, temperature fluctuations will be neglected throughout, so that the heat diffusion mode will never appear in our analysis. This is also a reasonable approximation in strongly coupled ionic systems where the potential energy dominates the kinetic energy. In other words, we assume the specific heat ratio $\gamma = c_p/c_v$ to be of order 1 (which is well verified for pure liquid metals).

For the metal-salt mixtures, the analysis is first carried out for the case of a rigid background, which applies in the salt-rich phase, and then extended to the situation where the polarisability of the gas of conduction electrons can no longer be neglected (metal-rich phase).

*present address: Department of Physics and Astronomy,
University of Rochester, Rochester, New York 14627-0011

For all these cases we have solved the equations of hydrodynamics for a charged fluid (1, 2), which express the conservation of mass density, charge density, momentum and energy density. This latter has been ignored, the coupling between temperature fluctuations and fluctuations of the other variables being neglected, as already mentioned. The resolution of these equations yields the hydrodynamic matrix of which the zeros of the determinant determine the dispersion relation of the different collective modes. Our purpose here is not to reproduce these calculations but just to summarize our results.

II. METAL-SALT SOLUTIONS - RIGID BACKGROUND MODEL

We consider mixtures of the type $M_x(MX)_{1-x}$, where x is the mole fraction of the alkali metal. The metallic ions have a mass M_1 and carry a positive charge $Z_1 e$, while the halogen have a mass m_2 and carry a negative charge $Z_2 e$. The number densities of both species are respectively ρ_1 and ρ_2 . It is convenient to choose as independent variables the temperature T and the mass and charge densities:

$$\rho_m = \sum_{i=1}^2 \rho_i m_i; \quad \rho_z = \sum_{i=1}^2 \rho_i Z_i e \quad (1)$$

The thermodynamic potential associated with these variables is the Helmholtz free energy density f , from which all thermodynamic quantities are derived. The two characteristic frequencies of our two-component system are the hydrodynamic plasma frequency

$$\omega_p = (4\pi \rho_z^2 / \rho_m)^{1/2} \quad (2)$$

which occurs naturally in the long-time, collision-dominated regime, and a frequency ω_0 , associated to the mutual diffusion between the two species or, equivalently, the ionic conductivity σ :

$$\omega_0 = 4\pi\sigma \quad (3)$$

The determinant of the hydrodynamics matrix results, in that case, in a cubic equation (3):

$$Z^3 + Z^2(\omega_k + b k^2) + Z(b k^2 \omega_k + \omega_p^2 + c^2 k^2) + k^2 c^2 \omega_0 \left[1 + \frac{k^2}{k_i^2}\right] = 0 \quad (4)$$

with

$$\omega_k = \omega_0 + k^2 \sigma \left(\frac{\partial \mu_z}{\partial \rho_z} \right)_{T, \rho_m} = \sigma \left[4\pi + k^2 \left(\frac{\partial \mu_z}{\partial \rho_z} \right)_{T, \rho_m} \right] \quad (5)$$

μ is the electrochemical potential conjugate to the charge density, b is the longitudinal kinematic viscosity, k_D^{-1} is the ionic screening length, $C = 1/\rho_m$ is the actual velocity of the mixture (in the assumption $\gamma = 1$), and $C' = \rho_m (\partial \rho_m / \partial \rho_m)_{T, \mu}$ reduces to the sound velocity c in the pure salt.

In the long-wavelength ($k \rightarrow 0$) limit, the three roots of (4) are:

$$Z_1 = 0 \quad ; \quad Z_{2,3} = -\frac{1}{2} [\omega_0 \pm (\omega_0^2 - 4\omega_p^2)^{1/2}] \quad (6)$$

Near the pure metal ($\omega_0 \rightarrow 2\omega_p$), the roots Z_2 and Z_3 are complex conjugate and correspond to two plasmon modes of frequency $\pm \omega_p$, while the root Z_1 corresponds to the $k \rightarrow 0$ limit of collective diffusion mode. In the opposite limit of the pure molten salt ($\omega_0 \rightarrow 2\omega_p = 0$), the doubly degenerate root $Z_1 = Z_3 = 0$ is the zero wavenumber remnant of propagating sound modes, while $Z_2 = -\omega_0$ corresponds to a fully damped, non-hydrodynamic, charge relaxation mode, with a relaxation time $\tau = 1/\omega_0$.

11.1. METAL RICH MIXTURES ($\omega_p \gg \omega_0$)

Perturbing around the non zero-root, we solve equation (4), and find a purely diffusive mode (Z_1 in (6)) $Z = -D_M k^2$, with a collective diffusion constant given by:

$$D_M = c'^2 (\omega_0 / \omega_p^2) \quad (7)$$

and two plasmon modes with the dispersion

$$\omega = \pm \omega_p \left[\left(1 - \frac{\omega_k^2}{8\omega_p^2} \right) + k^2 \left(\frac{c^2}{2\omega_p^2} + \frac{(b - D_M)\omega_0}{4\omega_p^2} \right) \right] \quad (8a)$$

and the damping

$$\Gamma = \tau^{-1} = \frac{1}{2} [\omega_k + \left(\frac{1}{2} b - D_M \right) k^2] \quad (8b)$$

In the limit of the pure metal ($\omega_0 = 0$), we recover the result for the OCP (9). The two main effects of the inclusion of salt ($\omega_0 > 0$) is to lower the plasma frequency ω_p and to make the damping of the plasmons finite even at zero wave number, due to inter-diffusion of the two ionic species which dominates the purely viscous damping in the pure metal. Moreover, as ω_0 decreases due to the addition of salt, the k -dependent term in [8a] becomes more and more important, and the

plasmon-like dispersion will eventually turn into an acoustic one.

II.2 SALT RICH MIXTURES ($\omega_0 \gg \omega_p$)

In this case, we solve the eqn. (4) by looking for small perturbations around the non-hydrodynamic fully damped charge relaxation mode $z \approx -\omega_0$. Following the analysis of Giaquinta et al. (4), we distinguish two wavenumber regimes according to the relative values of the two characteristic frequencies ω_0 and ck associated with charge relaxation and sound propagation respectively.

(i) At sufficiently long wavelengths, such that $k < k_0 = \omega_0/c$, the frequency ω_0 associated with charge relaxation dominates all other characteristic frequencies of the mixture. The fully damped mode has a relaxation time

$$\tau_s^{-1} = \left(\omega_k - \frac{\omega_p^2}{\omega_k} \right) - k^2 \frac{(c^2 - c'^2)}{\omega_0} \quad [9]$$

where the two last terms represent corrections relative to the pure molten salt, due to the presence of a finite concentration of metal. The two remaining roots correspond to acoustic modes $z = \pm ic_s k - \Gamma/2$ with a sound velocity

$$c_s^2 = \frac{c'^2 - b(\omega_p^2/2\omega_0^2)}{1 - (\omega_p^2/\omega_0^2)} \quad [10]$$

and an attenuation

$$\Gamma = \frac{\omega_p^2}{\omega_k} + k^2 \left(\frac{c^2 - c'^2}{\omega_0} \right) + k^2 b \quad [11]$$

Only the third term on the RHS of [11] contributes in the pure molten salt, where charge and density fluctuations are decoupled. The addition of some metal introduces a small coupling between these fluctuations, and the attenuation remains finite as $k \rightarrow 0$. The coupling between charge and mass fluctuations is also responsible for the deviation of the sound velocity [10] from its value c' in the pure salt. The most important result in this long wavelength regime is that sound propagation is not possible at all concentrations. It is possible only if the general dispersion relation (4) has two complex

conjugate roots. The condition for sound propagation is hence:

$$\Gamma^2 - 4c'^2\omega_0\tau_s k^2 < 0 \quad (12)$$

Retaining only terms up to order k^2 , we obtain the following condition, from (9), (11), (12):

$$(\omega_p/\omega_0)^4 < 4k^2 \frac{c'^2}{\omega_0^2} \approx k^2/k_0^2 \quad (13)$$

This means that for a given wavenumber k (smaller than k_0), there exists a range of concentrations, delimited by the inequalities:

$$(k/k_0)^{1/2} < \omega_p/\omega_0 < 1/2 \quad (14)$$

where all collective modes are overdamped or equivalently, for a given metallic concentration, sound propagation is possible only if the wavenumber k is larger than a critical value $k_c = k_0(\omega_p/\omega_0)^2$. At higher metal concentrations, plasmon like modes predominate (see (6)), while at lower metal concentrations the mixture sustains sound waves, but due to concentration gap [14], there is no crossover between the two types of propagating modes.

(ii) : wavelengths sufficiently short so that kk_0 , the sound wave frequency ω_k dominates the charge relaxation frequency ω_0 . In that case the relaxation time of the fully damped charge mode is:

$$\tau_s^{-1} = \omega_0 \frac{c'^2}{c^2} \left(1 + \frac{k^2}{k_i^2}\right) \quad (15)$$

The two remaining modes are sound waves of velocity

$$c_s = c \quad (16)$$

and attenuation

$$\Gamma = b k^2 + \omega_k - \omega_0 \frac{c'^2}{c^2} \left(1 + \frac{k^2}{k_i^2}\right) \quad (17)$$

The main difference between the two regimes i) and ii) lies in the sound attenuation Γ which is dominated by mutual diffusion for kk_0 .

and by viscous forces for $k \ll k_0$. Moreover sound waves propagate at any metal concentration as soon as $k \gg k_0$ and crossover directly into plasmon modes in the metal-rich phase. The difference between the two regimes is shown in figure 1.

III. METAL-SALT SOLUTIONS, EFFECT OF ELECTRON SCREENING

In the metal rich phase the electron density is high and the associated screening length λ_e is of the order of the inter-ionic spacing. Hence, whenever the wavenumber k is smaller than this electronic screening wavenumber $k_e \sim 1/\lambda_e$, the coupling of the conduction electrons to the collective modes of the solution cannot be ignored. But, because of the large ion to electron mass ratio, the adiabatic approximation for the electron gas is justified, so that frequencies characteristic of the fast electronic motions will never appear in the equations. Moreover, in the metal rich phase, we expect the ion-electron interaction to be weak so that we consider the response of the electron gas in the linear screening approximation.

The electronic contributions to the total free energy density f must be taken into account; this leads to a renormalization of the chemical potentials μ_m and μ_z . The characteristic frequency [4] is changed to:

$$\omega_k = \sigma \left[\frac{4\pi}{\epsilon_e(k)} + k^2 \left(\frac{\partial \mu_z}{\partial \rho_z} \right)_{T, \rho_m} \right] \quad [18]$$

where μ_z is now the renormalized electrochemical potential conjugate to the charge density and $\epsilon_e(k)$ is an effective electronic dielectric function which accounts for the short-range non coulombic part of the ion-electron coupling (5). Its long wavelength form determines the electron screening wavenumber by the relation $\epsilon_e(k) \sim 1 + k_e^2/k^2$. For $k \gg k_e$ we recover the case of a rigid background described previously. In the polarisable background ($k \ll k_e$), the fundamental difference arises from the fact that ω_k now vanishes with k , as:

$$\omega_k = \sigma \left[\frac{4\pi}{k_e^2} + \left(\frac{\partial \mu_z}{\partial \rho_z} \right)_{T, \rho_m} \right] k^2 = d k^2 \quad [19]$$

so that the dispersion relation [4] takes the form:

$$z^3 + z^2 [(d+b)k^2] + z \left[\left(c^2 + \frac{\omega_p^2}{k_e^2} \right) k^2 + b d k^4 \right] + \omega_0 c'^2 (k_i^{-2} + k_e^{-2}) k^4 = 0 \quad [20]$$

which is reminiscent of that for a neutral one component fluid, the thermal diffusivity in the latter being replaced by the ionic conductivity in the present case. Over the whole range of concentrations, eqn [20] has two complex conjugate roots of the form [10], corresponding to propagating sound waves, and a purely diffusive, real root, $z = -Dk^2$. The sound velocity is given by:

$$c_s^2 = c^2 + \frac{\omega_p^2}{k_e^2} = 1 / \rho_m \chi_T \quad [21]$$

where χ_m is the total (i.e. ionic plus electronic contributions) compressibility of the mixture. The sound attenuation is:

$$\Gamma = (b + d - D) k^2 \quad [22]$$

where the collective diffusion constant is given by:

$$D = 4\pi\sigma\left(\frac{c'}{c_s}\right)^2 (k_i^{-2} + k_e^{-2}) \quad [23]$$

As expected, the main effect of electronic polarisability, which occurs in the metal-rich side of the diagram is to transform the plasmon-like modes of the rigid background into acoustic modes, as in the pure metal (4).

IV. METAL-SALT SOLUTIONS. HIGH FREQUENCY BEHAVIOUR

In order to extend our analysis at higher frequencies, we outline a generalized hydrodynamics description of longitudinal collective modes in metal-salt solutions in the $k \rightarrow 0$ limit. In this limit, the frequency ω must be replaced by its frequency-dependent generalization, i.e. after Laplace transform:

$$\omega_o(z) = 4\pi\sigma(z) = \delta^2 / [z + M(z)] \quad [24]$$

where $M(z)$ is the memory function associated with the frequency dependent ionic-conductivity $\sigma(z)$, and $\delta^2 = \Omega_p^2 - \omega_p^2$ is the difference between the kinetic plasma frequency which occurs in the short-time, Vlasov type, description of ionic dynamics ($\Omega_p^2 = 4\pi\rho_a(z_a e^2)/m_a$), and the hydrodynamic plasma frequency.

Single relaxation time approximation for $M(t)$ yields:

$$M(t) = M(0) e^{-t/\tau} = \Omega_J^2 e^{-t/\tau} ; M(z) = \Omega_J^2 / (z + \tau^{-1}) \quad [25]$$

where $\Omega_J^2(k)$ is easily calculated, using standard procedures (6.3), and the relaxation time τ can be determined from the static conductivity via:

$$\sigma = \sigma(z=0) = \frac{\delta^2}{4\pi M(0)} = \frac{\delta^2}{4\pi \Omega_J^2 \tau} \quad [26]$$

The dispersion relation [4] becomes:

$$z^3 [z + M(z)] + \delta^2 z^2 + \omega_p^2 z [z + M(z)] = 0 \quad [27]$$

hence

$$z^3 + \frac{\delta^2 z^2}{z + \Omega_J^2 / (z + \tau^{-1})} + \omega_p^2 z = 0 \quad [28]$$

In the pure metal we recover the undamped plasmon modes $z = \pm i\omega$. A perturbation calculation based on [28] shows that if some salt is added, the plasmon frequency is slightly shifted to:

$$\omega = \Omega_p + \frac{1}{2} \frac{\delta^2 \Omega_J^2}{\Omega_p^3} \quad [29]$$

while the damping is given by

$$\tau_M^{-1} = \frac{\delta^2 \Omega_J^2}{2 \tau \Omega_p^4} = \frac{\omega_0}{2} \left(\frac{\Omega_J}{\Omega_p} \right)^4 \quad [30]$$

We see from [29] and [30] that the generalised hydrodynamics calculation leads to a shift above the kinetic plasma frequency Ω_p , whereas the linearized hydrodynamics predicts a frequency below the hydrodynamic plasma frequency. This is a wellknown failure of the linearized hydrodynamics (7).

On the salt-rich side, the main consequence of introducing a frequency-dependent conductivity is to predict the existence of plasmon modes, reminiscence of the 'optic' modes of the crystal. The frequency of these modes is given by:

$$\omega = \pm \Omega_P \left[1 + \frac{\Omega_P^2 \delta^2}{2 \Omega_P^4} \right] \quad [31]$$

Comparing with eq. [29], [30], we conclude that the plasmon modes of the metal-rich region do not vanish at a salt concentration, such as $\omega_0 = 2\omega_P$, as predicted by linearized hydrodynamics, but survive all the way into the salt-rich phase where they coincide with the familiar 'optic' modes of ionic systems.

V. MIXTURE OF MOLTEN-SALTS, MX_2-MX_3

We concentrate on mixtures of molten salts with the same cation M. The independent thermodynamic variables are chosen to be the temperature T, the mass density ρ_m , the charge density ρ_z and the concentration x of particles X_3 , defined respectively as:

$$\rho_z = \sum_i \rho_i Z_i e ; \rho_m = \sum_i \rho_i m_i ; x = \rho_3 Z_3 / \rho_- \quad [32]$$

where $\rho_- = \rho_2 Z_2 e + \rho_3 Z_3 e$ is the density of negative ions. The global electroneutrality condition yields $\rho_z = 0$.

We solve the equations of linearized hydrodynamics in a similar way to that in previous sections. We only have to add a current $\vec{j}_c(\vec{r}, t) = x \vec{j}_3(\vec{r}, t)$. The convective part \vec{j}_c is due to the total current of negative charges, \vec{j}_- being the mutual diffusion current between species 2 and 3. Ignoring again the energy conservation law, the determinant of the hydrodynamic matrix, is given now by a quartic equation: (10)

$$\begin{aligned} z^4 + z^3 [\omega_0 + k^2 (b + v_{zz} + v_{xx})] \\ + z^2 [k^2 (c^2 + b \omega_0 + \omega_0 v_{xx} - \omega_1 v_{zx}) + o(k^4)] \\ + z [k^2 \omega_0 c^2 + o(k^4)] + o(k^4) = 0 \end{aligned} \quad [33]$$

The v_{ij} are the elements of the generalized diffusion matrix $v_{\alpha\beta}$ ($\alpha = z, x; \beta = z, x, m$). This latter is the product of the mobility

matrix $\Lambda_{\alpha\beta}$, of which elements are expressed in the Kubo linear response theory as a correlation of the currents:

$$\Lambda_{\alpha\beta} = \frac{1}{3\Omega T} \int_0^\infty \langle \vec{j}_\alpha(0) \vec{j}_\beta(t) \rangle dt \quad \alpha, \beta = (z, x) \quad [34]$$

and the inverse susceptibility matrix, related to the chemical potentials via:

$$\chi_{\gamma\delta}^{-1} = \frac{\partial \mu_\gamma}{\partial \rho_\delta} \quad (\gamma = z, x; \delta = z, x, m; d\rho_x = \rho - d_x) \quad [35]$$

Then

$$\nu_{\alpha\beta} = \Lambda_{\alpha\gamma} \chi_{\gamma\beta}^{-1} \quad [36]$$

ω_0 and ω_1 are the two characteristic relaxation frequencies given by:

$$\omega_0 = 4\pi\sigma \quad [37a]$$

$$\omega_1 = 4\pi\Lambda_{zx} \quad [37b]$$

In the infinite wavelength limit, the four roots are easily determined:

$$z_1 = z_3 = z_4 = 0 \quad ; \quad z_2 = -\omega_0 \quad [38]$$

The dispersion and damping of these modes are determined like previously by standard perturbation up to order k^2 , starting from these zero wavenumber solutions. The fully damped mode ($z_2 = -\omega_0$) has a relaxation time τ such that:

$$\tau^{-1} = \omega_0 + k^2 \left(\nu_{zz} + \nu_{zx} \frac{\omega_1}{\omega_0} \right) + o(k^4) \quad [39]$$

Factoring out this mode yields a cubic equation which gives the three other modes dispersion relation. The discriminant of this equation, $\Delta = 4k^2 c + o(k^4)$, is always positive, indicating the existence of two complex conjugate roots corresponding to two propagating sound waves $z_{2,3} = \pm ic_k k - \Gamma/2$ and to a real root corresponding to a fully damped diffusive mode $z_1 = -DK^2$. The velocity of the sound waves at zero wavenumber is

$$C_s = C = 1 / (\rho_m \chi_r)^{1/2} \quad [40]$$

and the sound attenuation is given by:

$$\Gamma = k^2 \left[b + \frac{1}{\rho_m c^2} \frac{\partial P}{\partial x} \frac{\partial \mu_x}{\partial \rho_m} \left(\Lambda - \frac{\Lambda_{zz}^2}{\sigma} \right) \right] + o(k^4) \quad [41]$$

where $\Lambda = \Lambda_{xx}$ is the mutual mobility of the two salts, dominated by viscosity, charge diffusion and interspecies diffusion.

The most interesting result is that this sound attenuation is of the order k^2 and does not include a constant (k independent term), contrary to the case of molten-salt embedded in a rigid background, described in section I. Actually this constant term, proportional to the free electrons density ρ_e , was responsible for the overdamping of sound propagation [see eqn. 11]. In this case, although the overall electroneutrality is insured, the local electroneutrality condition is violated by any low frequency motion of the ions. The rigid background then overdamps the oscillation in order to prevent this local electroneutrality. Obviously, this phenomenon disappears in the case of a polarizable background because of the spontaneous rearrangement of the electrons, and in a mixture of molten salts because of the absence of free electrons.

The other typical result in our mixture of molten-salts is the appearance of a new diffusive mode $z_1 = -DK$, a consequence of the extra degree of freedom introduced by allowing mutual diffusion between the species MX_2 and MX_3 .

A very crude analysis within the framework of generalized hydrodynamics in the limit of zero wavenumber, like in III, confirms the existence of plasmon modes, remnant of the crystal optical modes. Let us note as an interesting result that, if the ions X_3 are replaced by "massive" electrons, this model can be viewed as a special case of metal-molten salts on the very salt-rich side of the phase diagram where the electrons are known to be trapped in localized defects as F centers (8).

VI. CONCLUSION

The main predictions of our different analysis are the following ones. For metal-salt solutions, in the rigid background model (valid in the salt rich side), linearized hydrodynamics predict propagating plasmon modes in the metal-rich region, up to a concentration such that $\omega \approx 2\omega_p$, while the generalized hydrodynamics show that these 'optic' modes persist up to the pure salt. Their frequency lies above

the kinetic plasma frequency Ω , and their damping is dominated by ionic conductivity (interdiffusion) and vanishes in the $k \rightarrow 0$ limit only for the pure metal. Interdiffusion of the two species leads to a fully damped charge relaxation mode which has a finite lifetime at zero wavenumber for any non-vanishing salt concentration. Sound waves propagate in the pure molten salt at long wavelengths but, as metal is added, the acoustic modes cease to propagate below a critical wavenumber k_c because of the coupling between charge and mass density. This overdamping of propagating waves is the consequence of the presence of a rigid electronic background of finite density. As soon as either the electron gas is more dense, i.e. in the region of higher metallic concentrations, or the electrons are trapped in "F-centers" defects and can be considered as massive negative particles, the sound waves keep propagating. However there could be a small region in the phase diagram (for metallic concentrations between 5 and 20%) where the rigid electron background might be valid and where an overdamping of the sound waves might be observed.

Screening by conduction electrons modifies the predictions of the rigid background model in the metal-rich region, where the plasmon modes are changed into hydrodynamic sound waves.

For a mixture of molten salts, most of the results of the rigid background are recovered, i.e. the charge relaxation mode and the two plasmon modes remnant of the crystal optic modes. The two main differences lie in the persistence of sound wave propagation at long wavelength and in the apparition of a central ($\omega=0$) non-thermal diffusive mode, due to the mutual diffusion of the two species.

REFERENCES

1. Kadanoff, L. P., and Martin, P. C., *Ann. Phys.* 24, 419, (1963).
2. De Groot, S. R., and Mazur P., *Non-equilibrium Thermodynamics*, North Holland (Amsterdam 1969).
3. Chabrier, G., Hansen, J. P., and Joanny, J. F., *J. Phys. C* 19, 4443, (1986).
4. Postogna, F., and Tosi, M. P., *Nuovo Cim.* 55, 399, (1980).
5. Chabrier, G., *J. Phys. C*, 20, 357, 1987.
6. De Gennes, P. G., *Physica* 25, 825, (1958).
7. Hansen, J. P., Joly F., and McDonald, I. R., *Physica* 132A, 472, (1985).
8. Senatore, G., Parinello, M., and Tosi, M. P., *Phil. Mag.* 41, 595, (1980).
9. Baus, M., *Physica* 79A, 377, (1975); Vieillefosse P., and Hansen, J. P., *Phys. Rev. A* 12, 110 (1975).
10. Chabrier, G., and Joanny, J. F., to be published (1987).

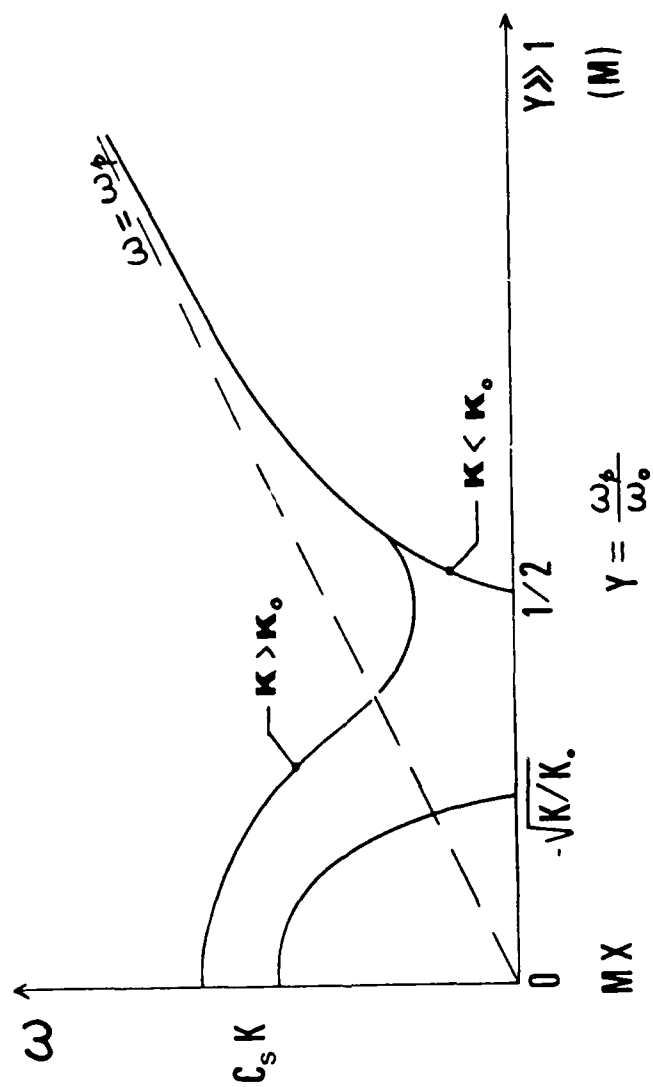


Fig. 1. Dependence of the frequency ω on the parameter X for the case of a plasma with a magnetic field.

ELECTRONIC CONDUCTION IN MOLTEN SODIUM CHLORIDE

G. M. Haarberg, K. S. Osen, and J. J. Egan

Brookhaven National Laboratory
Department of Applied Science
Upton, L.I., NY 11973

ABSTRACT

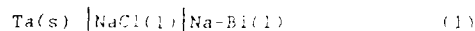
The electronic conductivity of molten NaCl was determined as a function of the activity of Na at 850 and 900°C by using the Wagner polarization technique. A new cell design, which prevented evaporation of Na, was essential for obtaining good results.

INTRODUCTION AND THEORY

Dissolution of Na in molten NaCl gives rise to an increase in the total electrical conductivity, which increases as the activity of Na increases. The same behavior has been found for other alkali metals dissolved in alkali halides as well as for mixtures of alkaline earth metals and alkaline earth halides. The increase in conductivity is believed to be electronic and may exceed the ionic conductivity. Experimental results have been reviewed by Bredig (1) and Warren (2,3).

In cases where the electronic part of the conductivity is small, i.e., when the activity of the metal is low, direct conductivity measurements must be replaced by more sensitive methods. Wagner (4,5) developed theories for treatment of galvanic cells with solid electrolytes which exhibit both ionic and electronic conduction, and the so-called polarization technique has been used for detecting small electronic contribution to the total conductivity. Egan and coworkers (6,7,8,9) and Huggins et al. (10) have applied Wagner's theories to molten salts equilibrated with metal.

The experimental relationship between steady state current and potential can be determined for a cell such as



The tantalum electrode is made negative with respect to the Na-Bi alloy which also determines the activity of Na in NaCl. The potential across the cell is always lower than the decomposition voltage of the salt. The concentration of electrons will build up at the negative electrode (Ta), and the current through the cell is caused by the concentration gradient of electrons. Ionic migration is suppressed and

electronic conduction dominates. The activity of Na at the negative electrode can be calculated from the measured potential. The activity of Na in the alloy must then be known. The electronic conductivity (κ_e) can be calculated from the experimental current versus potential curve from the following equation

$$\kappa_e = G \frac{\partial I}{\partial E} \quad (2)$$

where G is the cell constant. Since the measured potential corresponds to a certain activity of Na at the negative electrode, the electronic conductivity can be determined as a function of the activity of Na in NaCl. The theory for the polarization technique is valid provided that the mobility of electrons is constant and independent of the activity of Na.

Egan and Freyland (11) have developed a defect model for molten NaBr-Na mixtures based on studies of solid alkali halides with excess metal by Kröger (12) and Wagner (13). Upon dissolution of metal the following is a qualitative description of what takes place. In the pure stoichiometric salt the concentration of electrons and electron holes is equal. When Na is added the concentration of electrons increases. Upon further addition of Na the concentration of electrons increases in proportion to the concentration of anion vacancies. Formation of F-centers by association of electrons and anion vacancies occurs upon even further addition of Na. At high activity of Na F-center dimers are the predominant defects. The concentration of defects as a function of the activity of Na is schematically presented in Figure 1. Quantitative relationships are obtained by applying the law of mass action. In particular, the concentration of electrons is obtained as a function of Na activity. This model may also be applied to similar systems such as NaCl-Na. The model provides a quantitative correlation between the thermodynamic and optical, magnetic or electrical properties of the systems.

EXPERIMENTAL

The experimental cell, which is shown in Figure 2, consists of a tantalum crucible (6) containing NaCl (4) in contact with a Na-Bi alloy (15 mol % Na) (5), a reference electrode with a Na-Bi alloy of known composition (3) and an inert Ta electrode in a sapphire tube (8) of known geometry. The sapphire tube is filled with electrolyte, and the Ta electrode and the sapphire tube form a vacuum tight seal preventing the evaporation of Na. The activity of Na in the bulk NaCl (4) is controlled by equilibration with the Na-Bi alloy (5) of known activity. A constant current is applied through the cell making the Ta cup positive and the Ta electrode inside the sapphire tube negative. The potential between the electrodes is measured as a function of time, and the stationary value obtained after a long time (40 min) is recorded. A series of such corresponding potential versus current data is measured so that the electronic conductivity can be calculated as a function of potential according to equation 2. The cell constant

is determined by the geometry of the sapphire capillary. AC resistance measurements are also made periodically between the Ta electrode and the large Ta cup as a control. The composition of the Na-Bi alloy in the large Ta cup is also checked after each run by a titration method involving the reference electrode. All Na is coulometrically removed from the reference electrode and then added again until the potential between the reference alloy and the larger Na-Bi alloy is zero. The composition of the Na-Bi alloy is then known, and the activity of Na is calculated from thermodynamic data for Na-Bi alloys (14-17).

RESULTS AND DISCUSSION

The current versus potential data obtained for the NaCl-Na system at 900°C are shown in Figure 3. Similar results were obtained at 850°C. The experimental data were fitted to an arbitrary exponential equation, and the solid line in Figure 3 was calculated. The derivative of the current with respect to the potential was calculated for the I versus E curves for the potential region under study by using a computer program. The electronic conductivity was calculated according to equation (2), and the activity of Na was calculated as a function of potential from the measured emf. The results are presented in Figures 4 and 5 showing the relation between the electronic conductivity and activity of Na in NaCl at 850 and 900°C. Conductivity data at high activities from Bronstein and Bredig (18) are given as a comparison, and by extending the present results to high activities the agreement with literature data is reasonably good. This agreement confirms the validity of the polarization technique, and also implies that the electron mobility does not vary much with Na activity.

The present results supersede those reported by Davis et al. (8) because Na did not evaporate from the sapphire capillary. However, evaporation of Na from the crucible occurred during the experiment at 900°C. This caused a change in the composition of the Na-Bi alloy, corresponding to a drop in Na activity from $7.0 \cdot 10^{-4}$ to $6.5 \cdot 10^{-4}$. At 850°C, the alloy composition appeared to remain constant during the experiment.

Values for the transport number of electrons can be calculated from the following equation

$$t_e = \kappa_e / (\kappa_e + \kappa_{ion}) \quad (3)$$

where κ_{ion} is the specific conductivity of pure NaCl, which has been determined by Van Artsdalen and Yaffe (19). The calculated transport number of electrons and the electronic conductivity are given as a function of concentration and activity of Na in NaCl at 850 and 900°C in Tables 1 and 2. The concentration of excess Na is listed as δ , which is used as a parameter in the defect model, defined as

$$\delta = x_{\text{Na}}/(1-x_{\text{Na}}) \quad (4)$$

where x_{Na} is the mole fraction of Na in NaCl. Data for the activity of Na in NaCl have been published by Smirnov et al. (20) and shown in Figure 6 as Na activity versus δ at 900°C. These results were used for calculating δ as a function of Na activity in Tables 1 and 2.

Recent experiments in other alkali halides suggest that iron is more suitable than tantalum as the inert electrode. Transient techniques may also be applied to the same cell, and such experiments can hopefully make it possible to determine the electron diffusion coefficient and mobility.

ACKNOWLEDGMENTS

This work was supported by the Division of Chemical Sciences, U.S. Department of Energy, Washington, D.C., under contract No. DE-AC02-76CH00016. The authors would like to thank Dr. W. Freyland for supplying the sapphire capillary used in this work. This was considered an essential contribution. They are also indebted to Mr. R. J. Heus who helped in all phases of the experiments. Prof. J. Thonstad is also thanked for his continuing support.

REFERENCES

1. M. A. Bredig, "Mixtures of Metals with Molten Salts" in Molten Salt Chemistry ed. by M. Blander, p. 365, Interscience, New York, 1964.
2. W. W. Warren, Jr., "Electronic Properties of Solutions of Liquid Metals and Ionic Melts" in Advances in Molten Salt Chemistry ed. by G. Mamantov, J. Braunstein, Vol. 4, p. 1, Plenum Press, New York, 1981.
3. W. W. Warren, Jr., "Metal-Metal Halide Melts" in The Metallic and Nonmetallic States of Matter ed. by P. P. Edwards, C.N.R. Rao., p. 139, Taylor and Francis, London, 1985.
4. C. Wagner, Proc. CITCE, 7, 361 (1957).
5. J. B. Wagner, C. Wagner, J. Chem. Phys., 26, (6) 1597 (1957).
6. R. J. Heus, J. J. Egan, J. Phys. Chem., 77, (16) 1989 (1973).
7. R. J. Heus, J. J. Egan, Proc. Int. Symp Molten Salts, p. 523 (1976).
8. R. E. Davis, R. J. Heus, J. J. Egan, Ext. Abstracts ISE, 30th Meeting, p. 272 (1979).

9. R. E. Davis, R. J. Heus, J. J. Egan, Proc. Second Int. Symp. Molten Salts, p. 73 (1981).
10. G. J. Reynolds, M. C. Y. Lee, R. A. Huggins, Proc. Fourth Int. Symp. Molten Salts, p. 519 (1983).
11. J. J. Egan, W. Freyland, Ber. Bunsenges. Phys. Chem., 89, 381 (1985).
12. F. A. Kröger, "The Chemistry of Imperfect Crystals", Vol. 2, 2nd Edition, North Holland, American Elsevier, 1974.
13. C. Wagner, Ber. Bunsenges. Phys. Chem., 77, 518 (1973).
14. E. A. Miorova, A. G. Morachevskii, J. Appl. Chem. USSR, 48, (6) 1303 (1975).
15. T-S. Yih, J. C. Thompson, J. Phys. F: Met. Phys., 12, 1625 (1982).
16. M-L. Saboungi, T. P. Corbin, J. Phys. F: Met. Phys., 14, 13 (1984).
17. J. J. Egan, High Temp. Science, 19, 111 (1985).
18. M. V. Smirnov, V. V. Chebykin, L. A. Tsiovkina, Electrochim. Acta, 26, 1275 (1981).
19. H. R. Bronstein, M. A. Bredig, J. Am. Chem. Soc., 80, 2077 (1958).
20. E. R. VanArtsdalen, I. S. Yaffe, J. Am. Chem. Soc., 59, 118 (1955).

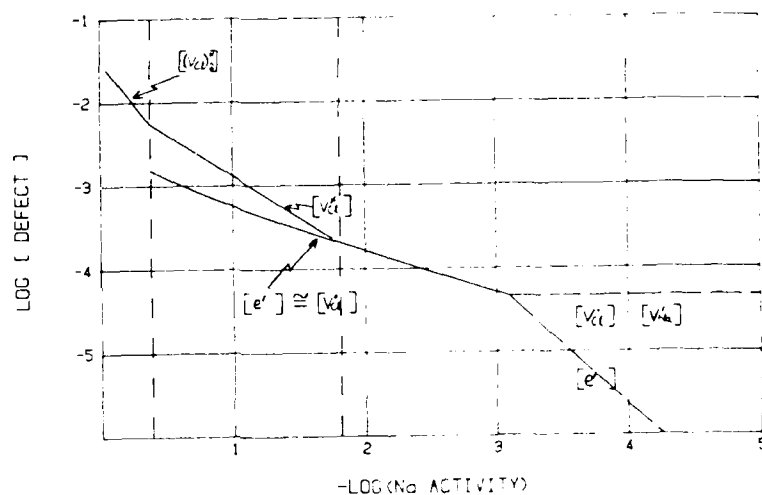


Figure 1. Schematic Representation of the Defect Concentration as a Function of Na Activity in Molten NaCl.
 e' - electron, V_{Na} - cation vacancy, V_{Cl}^* - anion vacancy,
 V_{Cl}^x - F-center, $(V_{Cl}^x)_2$ - F-center dimer

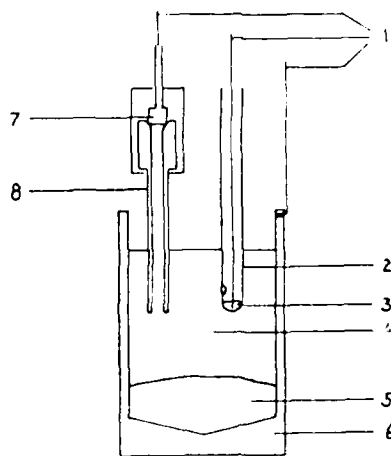


Figure 2. The Experimental Cell

- 1 - Ta leads
- 2 - alumina tube
- 3 - Na-Bi alloy, reference electrode
- 4 - NaCl (liq)
- 5 - Na-Bi alloy
- 6 - Ta crucible
- 7 - Ta electrode
- 8 - sapphire tube

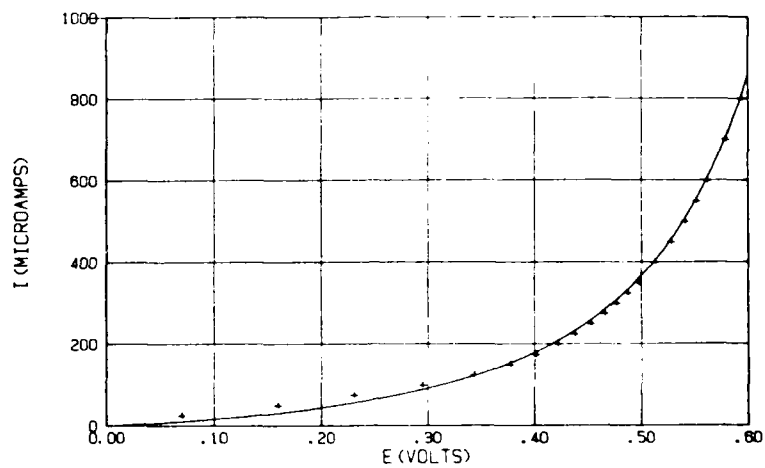


Figure 3. Current Versus Potential from Polarization Experiment in NaCl-Na at 900°C. Experimental Data and Calculated

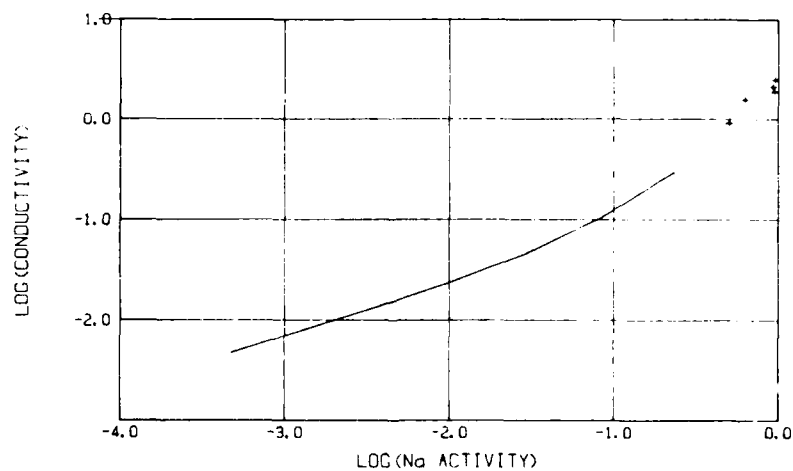


Figure 4. Electronic Conductivity as a Function of Na Activity in NaCl at 850°C.
Solid line - Calculated from polarization experiment.
Points - Data from Bronstein and Bredig (19).

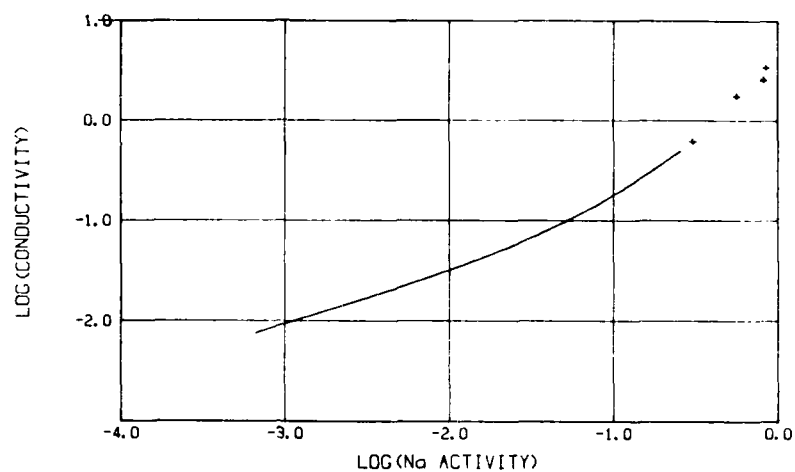


Figure 5. Electronic Conductivity as a Function of Na Activity in NaCl at 900°C.
Solid line - Calculated from polarization experiment
Points - Data from Bronstein and Bredig (19).

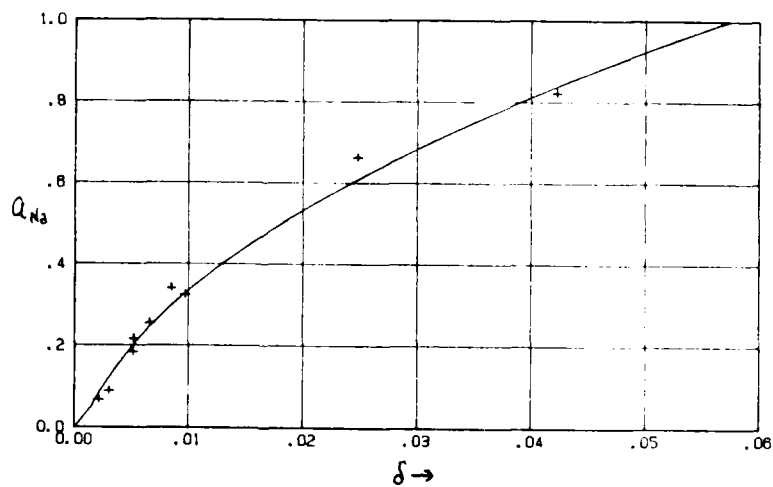


Figure 6 Activity of Na as a Function of Excess Na (δ) in NaCl at 900°C.
Activity data from Smirnov et al. (18).

Table 1. Values for the Transport Number of Electrons and the Electronic Conductivity as a Function of Excess Na (δ) and Na activity in NaCl at 850°C.

δ	a_{Na}	t_e	κ_e ohm ⁻¹ cm ⁻¹
.00016	.0005	.0013	.005
.00017	.0011	.0019	.007
.00019	.0025	.0029	.011
.00023	.0056	.0045	.017
.00032	.0129	.0072	.027
.00053	.0294	.0121	.046
.00103	.0673	.0225	.086
.00154	.1018	.0322	.125
.00191	.1251	.0391	.152
.00240	.1539	.0478	.188
.00305	.1893	.0589	.235
.00393	.2327	.0731	.296
.00513	.2862	.0913	.377
.00678	.3519	.1143	.484
.00907	.4328	.1432	.627
.01230	.5322	.1791	.818
.01688	.6545	.2228	1.075

Table 2. Values for the Transport Number of Electrons and the Electronic Conductivity as a Function of Excess Na (δ) and Na activity in NaCl at 900°C.

δ	a_{Na}	t_e	κ_e ohm ⁻¹ cm ⁻¹
.00014	.0007	.0020	.008
.00016	.0015	.0029	.011
.00019	.0032	.0044	.017
.00025	.0072	.0068	.026
.00039	.0158	.0108	.042
.00070	.0349	.0184	.072
.00149	.0770	.0348	.139
.00229	.1144	.0502	.204
.00289	.1395	.0609	.251
.00371	.1700	.0745	.311
.00480	.2072	.0915	.389
.00630	.2526	.1129	.492
.00836	.3079	.1394	.626
.01122	.3753	.1720	.803
.01523	.4575	.2116	1.047
.02090	.5576	.2586	1.348
.02897	.6797	.3130	1.761

ADDITION OF MOLTEN SALT IN MOLTEN METAL. STRUCTURE AND DYNAMICS

J.F. Jal, C. Matthieu, J. Dupuy
Département de Physique des Matériaux
Université Claude Bernard, Lyon, Villeurbanne 69622

P. Chieux
Institut Laue-Langevin, 156X Avenue des Martyrs, 38042 Grenoble

J.-B. Suck
Institut für Nukleare Festkörperphysik, D75000 Karlsruhe
Postfach 3640

Abstract

A partial structure factor analysis (based on the chlorine) isotopic substitution method in neutron scattering experiments) of the solutions $K_x(KCl)_{1-x}$ with $x = 0.8$ and 0.6 shows how strongly the hot liquid metal can be structured by the introduction of salt. The measurement of the structure factor of pure liquid potassium up to 700°C is used in the discussion. Extended sound modes measured in the metallic regime were similar to the ones observed in pure metal. With the addition of salt, strong damping effects are observed and related to the structuring effect created by the salt.

The addition of salt in a liquid alkali metal generates, over a concentration range which depends on the metal, a non-stability domain (miscibility gap) together with a strong scattering regime for conduction. Near the pure salt limit of the phase diagram, the short range order is related to full ionic bonding, the excess electron becoming localized or solvated because of fluctuations of the Coulombic potential assisted by local structure rearrangements (1) (2). On the metal rich side, although thermodynamics (3) predict a significant restructuring of the hot liquid metal by the halogen ions, analysis of conductivity or excess magnetic susceptibility data (4) indicated nearly free electron behaviour down to a very large fraction of salt ($x \approx 0.5$).

Theoretical models based on a single electron screening theory (5) can reproduce the stability conditions and take into account the screening length with a continuous fluid of electrons interacting with finite sized ions. They do not consider the restructuring of the metal atoms by the halogen ions, so that the dielectric behaviour cannot be well represented.

In this paper we want to demonstrate how the restructuring of the metal atoms by negative ions can be described as a local structure with short range order and additional strong interactions leading to medium range order. If these structural effects exist in the system, then the dynamics should be strongly affected. The existence of collective excitations in liquids, as a result of the solid state collective modes, is now well established (6) (7). In charged liquids, the appropriate dynamical variables (linked to mass and charge fluctuations) must vary in some wavenumber ranges related to the interactions existing in the system. It is therefore interesting to measure the collective modes because they point to wavenumber and energy domains where collisional processes can be involved and influence the transport properties. This could, in our case, help indirectly to specify the behaviour of the electron.

After a detailed description of the microscopic structure of the metal-molten salt solutions in the metal rich and strong scattering regime, we shall present below an analysis of the effect of salt addition on the low energy excitations connected to the density response function of liquid alkali metals.

I. Structural modifications induced in hot alkali metal by addition of salt

The structural information were obtained from neutron scattering measurements. We shall not describe here the analysis of the data, which will be presented in a specialized paper (8). We only point out the extreme difficulty in measuring low scatterers like potassium. Moreover, at high temperature, the weakness of the interference signal makes it even more difficult to separate it from the diffusion of the sample environment (furnace, container) or from contributions due to small amounts of impurities such as hydrogen. The measurement of the temperature dependence of the structure factor of liquid potassium allowed us, owing to the relative simplicity of its analysis, to crosscheck the validity of our data treatment. It also provides useful information for the discussion of the metal partial structure factor in the metal-molten salt mixture.

a) The pure metal structure

The structure factor of liquid K is known, not too far from the melting point (9). We have measured its temperature dependence, which is related to the density variation and to the number fluctuations at the $Q = 0$ limit ($Q = (4\pi/\lambda) \sin \theta$, where λ is the neutron wavelength and 2θ is the scattering angle). Comparison between experimental data and recent theoretical calculation is excellent (10). The calculation of the structure factor $S(Q)$ at a given density is made with an effective potential and a self-consistent integral equation (HMSA). This gives better results than the OCP model. The data are presented in figure 1.

b) Structure of the solutions in the metallic conduction regime

$$(12) (\sigma > 5.10^{-3} \Omega^{-1} \text{ cm}^{-1})$$

The determination of the microscopic structure allows us to obtain the local and the medium range order. Neutron scattering, using isotopic substitution, is the only technique able to give this type of information on a large momentum transfer range with possible extrapolation to the thermodynamic limit ($Q=0$). Recent improvements of the high flux reactor instruments (ILL Grenoble) have been described (11). They permit us to analyse the $K_x(KCl)_{1-x}$ structure, i.e. one of the most difficult binary mixtures studied up to now. Figures 2a and 2b give the three total structure factors obtained by varying the chlorine isotopic composition at a fixed salt concentration. The low statistical accuracy obtained with the ^{37}Cl sample comes from a corresponding relatively low counting time. These structure factors are typical of $M_x(MX)_{1-x}$ mixtures. The curves are more or less structured according to the scattering length of the chlorine isotope as compared to that of the alkali metal. The large diffusion at low momentum transfer is due to fluctuations existing in the vicinity of the phase separation region.

In figures 3a and 3b, we give the partial structure factors extracted from the resolution of the linear system of equations formed by the above total structure factors. These partial structure factors are worth a few comments.

For the composition $K_{0.8}(KCl)_{0.2}$, the potassium partial structure factor is not very different from that of the pure metal given for comparison, except at low momentum transfer. There is a correlation between the potassium and the chlorine partials, which have similar peak positions but different peak intensities. The ClK partial exhibits the enhanced stability of the unlike atom interaction at a momentum transfer value slightly smaller than in the case of pure molten salt (k_N). Medium range order effects are apparent in all partials at low momentum transfer. This produces a hump at about 1 \AA^{-1} in the ClK partial.

The partial structure factors were also obtained for a higher addition of salt into the metal, $K_{0.6}(KCl)_{0.4}$. The temperature was kept equivalent for the two concentrations ($(T_{\text{exp}} - T_{\text{m.p.}})/T_{\text{m.p.}} \approx 1.1$). We see very significant differences between the partials at 80% and 60% metal concentration: enhancement of structure of the partials at large Q values, symmetric pattern for the like-ion partials, strong structuring of the KK partial at large Q , accompanied by a significant decrease of the first peak intensity. At Q values around 1 \AA^{-1} a strong hump is now obtained in the ClK partial but we shall not comment on it. The low Q part of this diagram is still investigated for possible systematic errors. At large Q values, we have not yet quantified with accuracy the nearest neighbour coordination number between unlike ions,

corresponding to the characteristic wavenumber k_M ; nevertheless a rough analysis gives a value of 4. This fourfold coordination seems favourable in monovalent ionic systems in which Coulombic forces are involved (2). A model for electron localization with the assistance of neighbouring K^+ ion relaxation gives a coordination of four (1). In compounds where a partial covalent contribution to the binding exists, a low coordination is favoured (2), which could in turn favour a high cationic mobility. Further work is being done in order to prove if small additions (< 10%) of molten salt into a hot alkali metal could stabilize the fourfold coordination at the same time as the metallic interaction between K atoms decreases. Of course, such a structural effect in a metallic liquid must influence its dynamics, in particular, the collective particle motions.

II. Preliminaries on the dynamics of a hot alkali liquid perturbed by dissolution of salt

Neutron scattering experiments allow us to measure the coherent dynamic structure factor $S_{coh}(Q, \omega)$ related to collective particle motions in the system. The description of collective fluctuations in a liquid is well analysed by the linearized hydrodynamics as long as the wavelength of the fluctuation is much greater than the atomic size. This is the case for light scattering experiments where we can investigate heat and sound modes. For neutron scattering the wavelength of the radiation becomes of the order of the interatomic distances and the concept of extended modes is introduced (15). Neutron scattering experiments on molten Rb at temperatures slightly above the melting point, show the existence of such extended sound modes for Q values up to $Qa \approx 1$ (a , being the mean free path between collisions). The data are well represented by three Lorentzian lines corresponding to Rayleigh and Brillouin scattering or heat and sound modes, respectively. In figure 4, the sound mode of liquid rubidium shows a maximum at a Q value corresponding to half of that of the maximum in the structure factor (16). In ionic liquids, it has been proven useful to introduce the mass density and charge density fluctuation variables (2). $S_{MM}(Q, \omega)$ is, at low Q and ω , isomorphous to the hydrodynamic structure factor of a monatomic liquid.

We also present in figure 4 some experimental results on a solution of $Rb_{0.9}(RbCl)_{0.1}$, which is, in first approximation, of purely metallic character, and on $Rb_{0.8}(RbBr)_{0.2}$ sample, which should have the same structural properties as $K_{0.8}(KCl)_{0.2}$. Details on the experiment and its analysis are published separately (17).

The dispersion of the mass density as a function of momentum transfer given in figure 4 for the M-MX solutions is obtained from the side peak positions in the inelastic scattering spectra measured on a triple axis spectrometer. The positions obtained on the energy loss and on the energy gain side are represented

separately. In the hydrodynamics regime, these positions at $\pm \omega_0$ are related to the adiabatic sound velocity. Therefore the knowledge of the pure metal sound velocity allows us to draw the hydrodynamic regime limit in the case of the strongly metallic concentration.

No significant difference is detected in the dispersion law of $\text{Rb}_{0.9}(\text{RbCl})_{0.1}$ as compared to pure Rb. This confirms the assumption that at this concentration, we remain in the metallic regime. And the sound velocity should not vary much from the pure metal one. At higher dilution of the metal, the results are not equivalent. Although the weakening of the signal renders the data analysis extremely difficult, some trends seem to be observed. A gap seems to occur at 1 \AA^{-1} . A similar one is observed in argon (7). This might come from the coupling between collective acoustic motion and the structure of the liquid shown in the partial structure factors. Also interesting is the extrapolation to the hydrodynamic regime. From the shape of the dispersion law, one wonders if the isothermal sound velocity of this mixture does not become anomalous.

Further studies should be made on the damping of the collective modes, which might turn out to be of general importance for the ionic and electrolytic liquids. Indeed, in a study of collective excitations in electrolytic glasses at very low water content, we detected (18) low frequency harmonic modes (up to 4 meV), in addition to the sound modes, and a damping of these modes occurs at the glass transition. The structured picture of the M-MX solutions in the strong scattering regime and its effect on collective motions are beginning to be deciphered.

REFERENCES

- (1) G. Senatore, M. Parinello, M.P. Tosi, *Phil. Mag.* (1980) B41, 595
- (2) M. Rovere, M.P. Tosi, *Rep. Progr. Phys.* (1986) 49, 1001
- (3) H. Yokohama, O.J. Kleppa, *J. Chem. Phys.* (1982) 76, 5574
- (4) N. Nicoloso, W. Freyland, *Z. Phys. Chem.* (1983) 135, 39
- (5) G. Chabrier, *J. Phys. C* (1987) 20, 357
- (6) J.R.D. Copley, J.M. Rowe, *Phys. Rev. Lett.* (1973) 32, 49
- (7) I.M. de Schepper, P. Verkerk, A.A. van Well, L.A. de Graaf, *Phys. Rev. Lett.* (1983) 50, 974
- (8) J.F. Jal, P. Chieux, J. Dupuy, to be published
- (9) M.B. Huijben, W. van der Lugt, *Act. Cryst.* (1975) A35, 431
- (10) J.F. Jal, G. Kahl, P. Chieux, J. Dupuy, J.P. Hansen, to be published
- (11) J. Dupuy, J.F. Jal, A. Aouizerat-Elarby, P. Chieux *Trends in Physics* (Ed. Javta, J. Pantoflietch) (Prague Europ. Phys. Soc., p. 394)
- (12) M.A. Bredig (1964) in *Molten Salt Chemistry*, Ed. M. Blander, N.Y., Interscience, p. 367
- (13) J.F. Jal, P. Chieux, J. Dupuy, *J. de Physique* (1980) 41, 657
- (14) J.P. Boon, S. Yip, *Molecular Hydrodynamics*, Mc Graw-Hill, N.Y., (1980)
- (15) L.M. de Schepper, E.C.D. Cohen, *J. of Stat. Phys.* (1982) 27, 223
- (16) J.R.D. Copley, J.M. Rowe, *Phys. Rev. Lett.* (1974) 32, 49
- (17) C. Matthieu, J.F. Jal, J. Dupuy, J. Suck, P. Chieux, *Liquid and Amorphous Metals (LAM6)*, Garmisch (1986) to appear in *Z. Phys. Chem.*
- (18) J.F. Jal, A. Aouizerat-Elarby, J. Dupuy, J. Dianoux, to be published.

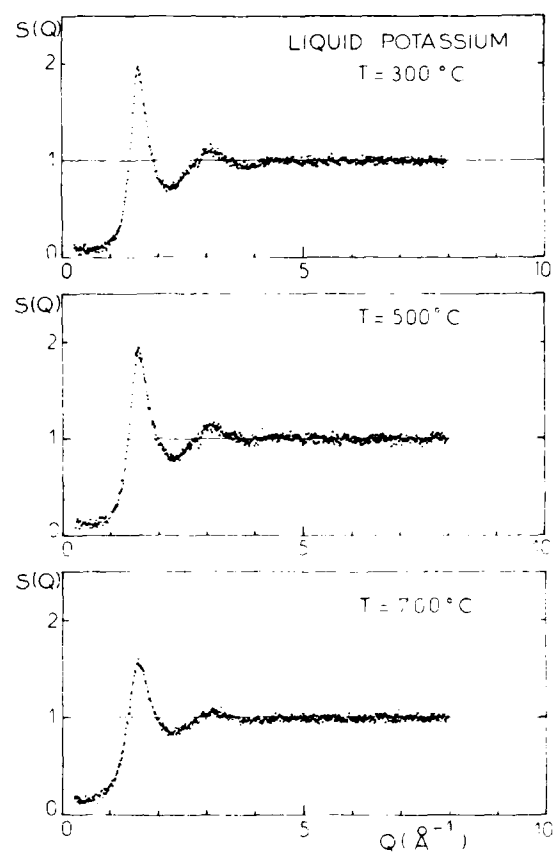


Figure 1 : Structure factor of liquid potassium at several temperatures

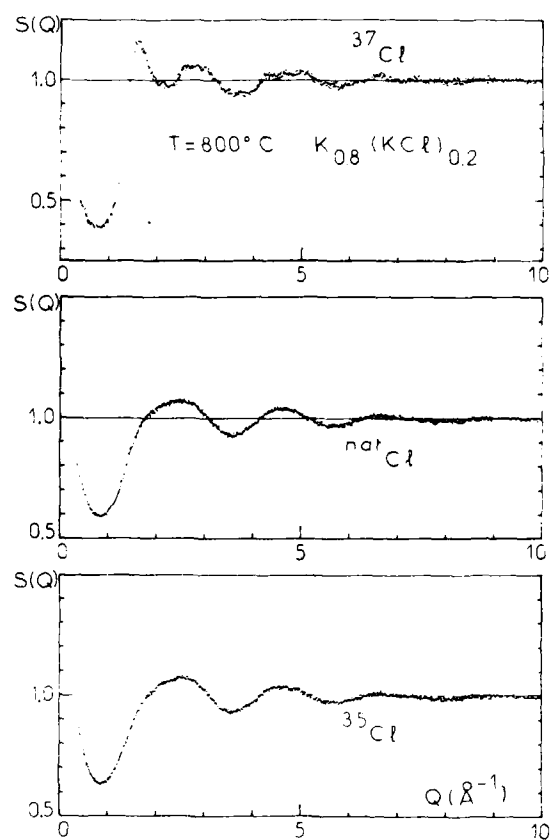


Figure 2a : Total structure factor of the $K_{0.8}(KCl)_{0.2}$ solution for three chlorine isotopic compositions

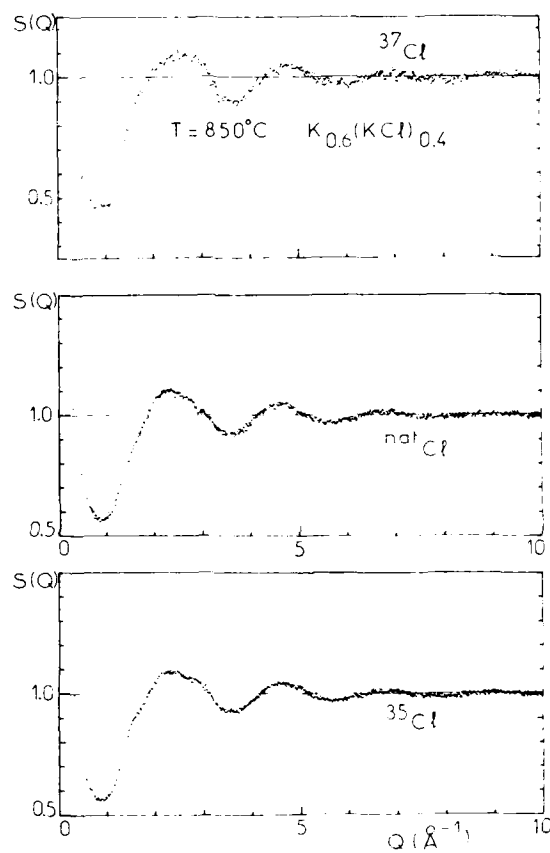


Figure 2b : Total structure factor of the $\text{K}_{0.6}(\text{KCl})_{0.4}$ solution for three chlorine isotopic compositions

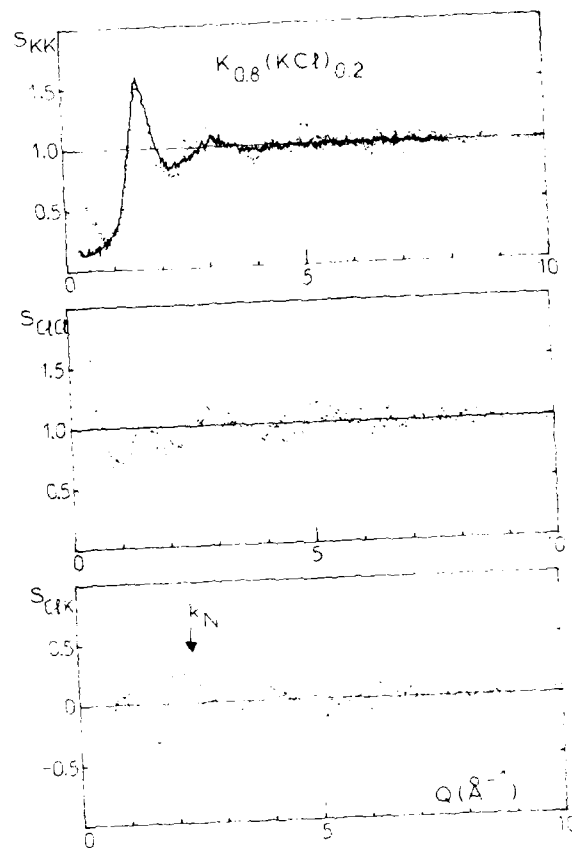


Figure 3a : Partial structure factor for the $K_{0.8}(KCl)_{0.2}$ solution. The structure factor of pure potassium at 700°C (---) is drawn for comparison on the S_{KK} partial. The central line (k_N) of the triple hump characteristic of the pure CLK pattern is marked.

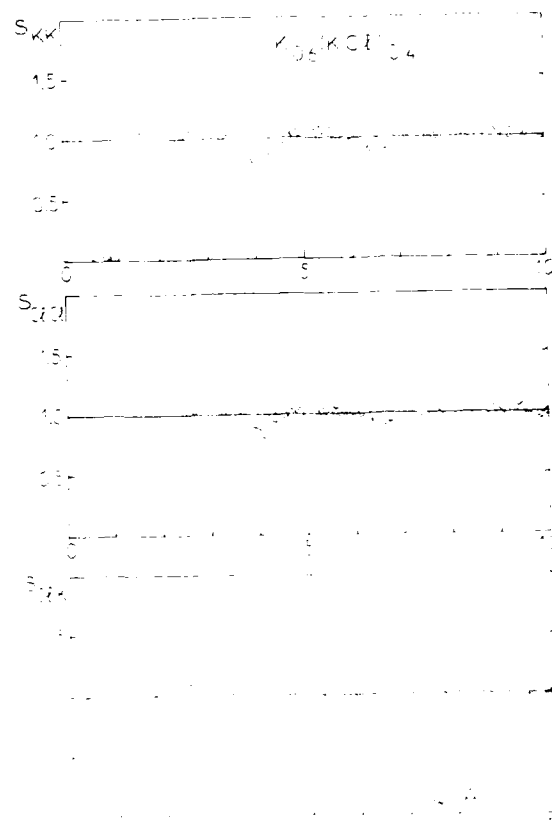


Figure 3b : Partial structure factors for the $K_{0.6}(KCl)_{0.4}$ solution.

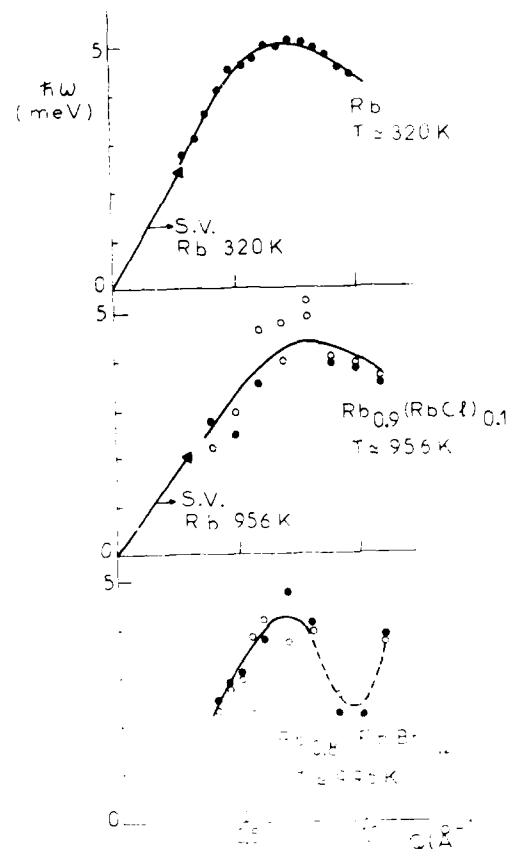


Figure 4 : Upper curve - The dispersion of the collective density fluctuations in pure liquid rubidium (ref. (16)). The arrow at low Q values is obtained from the sound velocity of the pure metal (hydrodynamic regime). Central curve - The dispersion of the collective density fluctuations in $\text{Rb}_{0.9}(\text{RbCl})_{0.1}$. Energy gain and energy loss are quoted separately. The arrow at low Q values is obtained from the sound velocity of the pure metal. Lower curve - The dispersion of the collective density fluctuations in $\text{Rb}_{0.8}(\text{RbBr})_{0.2}$.

DYNAMIC CONDUCTIVITY OF MOLTEN
3 KNO₃ · 2 Ca(NO₃)₂ AT FREQUENCIES
ABOVE 100 MHz

Klaus Funke and Jörg Hermeling*

Institut für Physikalische Chemie der
Westfälischen Wilhelms-Universität Münster,
4400 Münster, and Sonderforschungsbereich 173,
Germany

ABSTRACT

The dynamic ionic conductivity of the molten salt 3 KNO₃ · 2 Ca(NO₃)₂ has been measured in the coaxial-waveguide frequency range from 100 MHz to 18 GHz, at temperatures between 422 K and 478 K. The conductivity is found to display the dispersion that is characteristic of the so-called "universal dielectric response". A similar dispersion was observed earlier within the glass-transformation temperature range around 345 K, at frequencies below 1 MHz. The present results are interpreted in terms of a simple jump-relaxation model. The model involves only one reorientational relaxation time. This time and its temperature dependence turn out to be close to those derived with the help of other techniques.

INTRODUCTION

The glass forming molten salt 3 KNO₃ · 2 Ca(NO₃)₂ is a simple ionic system with interesting dynamic properties. Relaxation-type processes have been observed by different techniques in this system (1-6), and the (average) relaxation time has been found to vary by more than ten orders of magnitude, if the temperature is changed from 330 K to 650 K (7).

In 3 KNO₃ · 2 Ca(NO₃)₂, the glass transformation range extends roughly from 330 K to 360 K (7). Within this range, the system is known to show the characteristic features of the so-called "universal dielectric response" (8), comprising in particular the power-law behavior of the frequency dependent electrical conductivity, $\sigma'(\nu)$. The existing data are limited to frequencies below 1 MHz (4). The shape

* Present address: Institut für Physikalische Chemie der Gesamthochschule Siegen, 5900 Siegen, Germany

of $\sigma'(\nu)$ has been described by a distribution of relaxation times (7) and by a "fractional exponential" relaxation function (9,7). These are however merely formal representations which do not a priori convey any microscopic insight into the actual relaxation process.

The technique of Brillouin scattering has been applied to analyze the structural relaxation in molten $3 \text{ KNO}_3 \cdot 2 \text{ Ca(NO}_3)_2$ in the high-temperature, high-frequency regime (5,6). The spectra yield the temperature dependence of the velocity and attenuation of sound waves at frequencies of about 10 GHz. The modulus representation has been used to discuss the data, see (7), and it has been argued that a single relaxation time should suffice to describe the relaxation in the melt (5), at least if the temperature is sufficiently high, i.e., at $T > 473 \text{ K}$ (7). This assumption implies that the dynamic conductivity should be constant, showing no dispersion at frequencies close to the inverse of 2π times the relaxation time (10).

In our present study we have measured the dynamic conductivity of molten $3 \text{ KNO}_3 \cdot 2 \text{ Ca(NO}_3)_2$ at radio and microwave frequencies in order to test the validity of the above assumption and, more generally, to learn more about the short-time relaxation processes in this material. In the following we will show that even at 478 K the conductivity is found to display the typical dispersion already known from the low-temperature, low-frequency conductivity spectra mentioned above (4). Our present results will be interpreted in terms of a simple jump-relaxation model. The model involves only one relaxation time. This time and its temperature dependence turn out to be close to those derived from the Brillouin scattering data (6,7) and from the shear viscosity (7).

EXPERIMENTAL

The sample was prepared from reagent grade chemicals. $\text{Ca(NO}_3)_2 \cdot 4 \text{ H}_2\text{O}$ was dehydrated in a vacuum chamber for four days, at temperatures increasing up to 220°C . During the dehydration process, it was intermittently ground and analyzed gravimetrically. The KNO_3 was dried at 180°C for two days. The necessary amount of $\text{Ca(NO}_3)_2$ was then dissolved in the KNO_3 melt.

Fig. 1 is a block diagram of the experimental set-up used for the high-frequency measurements. An hp 8350 B sweep oscillator and an hp 8757 A scalar network analyzer

are both controlled by an hp 9000 (series 300) desktop computer. The arrangement of Fig. 1 permits fully automated swept measurements. The quantities measured are the absolute values of the complex transmission and reflection factors, $|\hat{t}|$ and $|\hat{r}|$, of the sample part of the coaxial waveguide system. An exploded view of the sample assembly is shown in Fig. 2, along with a schematic representation of the nine individual traveling waves in the various media, i.e., in air, in the window material (teflon), and in the molten salt itself. Let us denote the nine complex amplitudes of the respective radial electric fields by \hat{E}_{01} to \hat{E}_{09} . The measured scalar quantities may now be written

$$|\hat{t}| = |\hat{E}_{09}/\hat{E}_{01}| \quad (1)$$

and

$$|\hat{r}| = |\hat{E}_{02}/\hat{E}_{01}| \quad (2)$$

The eight ratios, $\hat{E}_{02}/\hat{E}_{01}$ to $\hat{E}_{09}/\hat{E}_{01}$, are uniquely determined by the dielectric and electric properties of the materials involved and by the requirement that the (transverse) electric and magnetic field components be continuous at the interfaces. The continuity conditions give us a set of eight simultaneous complex equations, which are linear in the eight ratios, $\hat{E}_{02}/\hat{E}_{01}$ to $\hat{E}_{09}/\hat{E}_{01}$, but transcendental in the dielectric and electric properties of the sample. It is therefore not easily possible to compute the complex permittivity, $\hat{\epsilon}(\nu)$, or the complex conductivity, $\hat{\sigma}(\nu) \approx i2\pi\nu\epsilon_0\hat{\epsilon}(\nu)$, directly from $|\hat{t}|$ and $|\hat{r}|$. The set of equations is however easily solved for the ratios, $\hat{E}_{02}/\hat{E}_{01}$ to $\hat{E}_{09}/\hat{E}_{01}$, if one assumes certain values of the real parts of $\hat{\epsilon}(\nu)$ and $\hat{\sigma}(\nu)$, which are called $\epsilon'(\nu)$ and $\sigma'(\nu)$. Transformation networks (σ', ϵ') \leftrightarrow ($|\hat{t}|, |\hat{r}|$) may thus be prepared, and this has been done for each frequency and each sample length. An example is shown in Fig. 3. In the experiment both permittivity and conductivity of the sample are automatically read from the relevant network and immediately plotted as functions of frequency.

RESULTS

Fig. 4 is a log-log plot of the conductivity, σ' , versus frequency at 453 K. The figure shows that different sample lengths yield consistent results. It also gives an impression of the scatter of the experimental data. The

mean values of the different 453 K runs are replotted in Fig. 5, together with data obtained at 422 K and at 478 K. It is evident that the spectra of Fig. 5 are very similar to those of Ref. (4). It is also noticeable that a trend already visible in the low-temperature results (4) is now continued: with increasing temperature the increase of $\sigma'(\nu)$ is found to begin at higher and higher frequency.

The relative permittivity, $\epsilon'(\nu)$, is found to decrease continuously within the experimental frequency range. At 453 K, for instance, it is 47 ± 5 at 100 MHz and 10 ± 4 at 18 GHz. The mutual consistency of the conductivity and permittivity spectra has been checked with the help of the Kramers-Kronig relations.

At sufficiently high frequency, when the relaxation cannot follow the changing electric field any more, $\epsilon'(\nu)$ tends to a limiting value, $\epsilon'(\infty)$. That value is not causally related to the relaxation, but independent of it. It is therefore sensible not to include $\epsilon'(\infty)$ when plotting functions that characterize the relaxation. This holds in particular true, if the relaxation is represented in the complex conductivity plane. In Fig. 6 we have thus plotted $\sigma''(\nu) - \omega\epsilon_0\epsilon'(\infty)$ against $\sigma'(\nu)$, at 453 K, assuming $\epsilon'(\infty)$ to be 7, 8, or 9. In each of these cases we observe the formation of an almost circular arc in the complex plane. The centers of the arcs are displaced below the real axis.

The measurements are being continued in the rectangular-waveguide frequency range above 18.5 GHz in order to determine $\epsilon'(\infty)$ as accurately as possible and to search for a limiting high-frequency value of the conductivity, $\sigma'(\infty)$. It will then be possible to choose the proper arc of Fig. 6 and to complete it on its high-frequency, high-conductivity side, until it meets the real axis again at $\sigma' = \sigma'(\infty)$.

DISCUSSION

The dispersion observed in the molten salt $3 \text{ KNO}_3 \cdot 2 \text{ Ca(NO}_3)_2$, see Figs. 4 to 6, is of the general type found also in many other ionic and polaronic conductors including glassy and crystalline solid electrolytes. The characteristics of the dispersion include the power-law behavior of $\sigma'(\nu)$ at sufficiently low temperature and the formation of almost circular arcs with depressed centers in the complex planes of conductivity, impedance, and permittivity. The generality of

the phenomenon was first noticed by Jonscher (8) who termed it "the universal dielectric response".

Microscopically, an understanding of the "universal dielectric response" requires the solution of a complicated many-particle problem. A very general model was put forward by Ngai (11). However, the model does not give a kinematic description of the microscopic dynamics. The same is true of other models that have been proposed (12).

More recently, a rather simple kinematic jump-relaxation model has been suggested by one of us (K.F.), see (13,14). It applies to any structurally disordered system of mobile charge carriers and is able to predict the main features of the "universal dielectric response". In particular, the solid lines of Figs. 5 and 6 have been calculated from this model. In addition to the lines, which fit the data very well, Fig. 5 also contains arrows marking particular frequencies. These are defined by $\nu = 1/(2\pi\tau)$, where τ is a reorientational relaxation time, see below. Compared with the relaxation times obtained from the shear viscosity and from Brillouin scattering (7), the present values are shorter roughly by a factor of four, but they have the same temperature dependence, see Fig. 7.

The basic idea of the jump-relaxation model is sketched in Fig. 8. In the figure, the momentary position of a mobile charge carrier (an ion) is denoted by A. The ion may hop to a neighboring position B, which requires some activation energy Δ . Now the model assumes that, if the ion resides at A, the neighborhood is structurally relaxed with respect to A. The ion therefore experiences a "conditional effective" single-particle potential which is normally higher at B than at A, see Fig. 8 a. As a consequence, the barrier height for a backward hop, δ , is smaller than Δ , at least immediately after the hop from A to B.

Suppose the ion hops from A to B at time $t = 0$. We then have to consider two competing relaxation processes at times $t > 0$:

- (i) The ion hops back to A. The correlated forward-backward hopping sequence thus performed contributes to the dynamic conductivity only at sufficiently high frequencies, but not at low frequencies.
- (ii) The neighborhood relaxes with respect to B. The reorientation of the neighborhood is characterized by some reorientational relaxation time, τ , and results in the formation of a new absolute minimum of the conditional effective potential at B. In this case

the initial hop has eventually proved successful and thus contributes to the dc conductivity.

It is important to note that the backward barrier height, $\delta_{B \rightarrow A}(t)$, see Fig. 8 b, increases as the ion stays at B. Therefore, the relaxation time of the back-hop process increases. The relaxation is thus slowed down as time goes by. The resulting spectra hence look as if there were a "distribution of relaxation times".

The model considers the probability, $W(t)$, that the correlated backward hop has not yet been performed at time t . A rate equation and simple geometrical arguments lead to a closed algebraic expression for $W(t)$, which makes use of the exponential-integral function (14). A useful approximation is

$$W(t) \approx \exp\{-2A(1-\exp(-t/\tau)) \cdot (\Delta-\delta)/kT\} , \quad (3)$$

where A is some constant of the order of one and τ is again the reorientational relaxation time of the neighborhood. The approximation of Eq. (3) is valid, if $(\Delta-\delta)/kT \leq 1$. Neglecting the finite duration of hops, the velocity autocorrelation function of the hopping motion may now be written

$$\langle \underline{v}(0) \cdot \underline{v}(t) \rangle_{\text{hops}} = \text{const.} \cdot \{\delta(t) + \dot{W}(t)\} , \quad (4)$$

where $\delta(t)$ is the delta function. The (frequency dependent) coefficient of self-diffusion is obtained from Eq. (4) by Fourier transformation, and the conductivity is formed with the help of the Nernst-Einstein equation. Cross terms are neglected. The procedure yields the expression

$$\hat{\sigma}(\omega) = (1 + \int_0^{\infty} \dot{W}(t) \exp(-i\omega t) dt) \cdot C / (r \cdot T) . \quad (5)$$

The solid lines of Figs. 5 and 6 have been obtained with the particular parameter values $A \approx 1$, $(\Delta-\delta)/k=600$ K, and $C = 8 \cdot 10^{-10} (\text{Ks})/(\Omega\text{cm})$. Instead of Eq.(3) we have however used the respective expression given in Ref. (14). The optimum values of the relaxation time τ are those plotted in Fig. 7. Note the changing slope of $\log \tau$ versus $1/T$. From our present data, this variation is found to be quite similar as in Ref.(7), see Fig. 7. The temperature dependence of the relaxation time shows that Δ is much larger than kT ($\Delta = 9.5$ kT at 493 K, see (7)). The difference, $(\Delta-\delta) \approx k \cdot 600$ K, is thus found to be considerably smaller than the barrier heights, Δ and δ , themselves. Nevertheless it is this difference that causes the entire

dispersion observed in the present study.

CONCLUSION

The dynamic conductivity of the simple molten salt $3 \text{ KNO}_3 \cdot 2 \text{ Ca}(\text{NO}_3)_2$ has been determined in the radio and microwave frequency range up to 18 GHz. A pronounced dispersion has been detected. The shape of the frequency dependent conductivity is similar to that of the low-temperature, low-frequency spectra (4). The present data have been shown to be consistent with a simple jump-relaxation model (13,14). Application of the model yields a reorientational relaxation time whose temperature dependence is in agreement with results obtained earlier from other techniques (7).

REFERENCES

1. R. Weiler, R. Bose, and P.B. Macedo, J. Chem. Phys., **53**, 1258 (1970).
2. P.B. Macedo, C.T. Moynihan, and R. Bose, Phys. Chem. Glasses, **13**, 171 (1972).
3. C.T. Moynihan, L.P. Boesch, and N.L. Laberge, Phys. Chem. Glasses, **14**, 122 (1973).
4. F.S. Howell, R.A. Bose, P.B. Macedo, and C.T. Moynihan, J. Phys. Chem., **78**, 639 (1974).
5. L.M. Torell, J. Chem. Phys., **76**, 3467 (1982).
6. L.M. Torell and R. Aronsson, J. Chem. Phys., **78**, 943 (1983).
7. C.A. Angell and L.M. Torell, J. Chem. Phys., **78**, 937 (1983).
8. A.K. Jonscher, Nature, **267**, 673 (1977).
9. G. Williams and D.C. Watts, Trans. Far. Soc., **67**, 1323 (1971).
10. See, e.g., J. Wong and C.A. Angell, Glass: Structure by Spectroscopy (Dekker, New York, 1976), Chap. 11.
11. K.L. Ngai, Solid State Ionics, **5**, 27 (1981).
12. L.A. Dissado and R.M. Hill, Solid State Ionics, **22**, 331 (1987) and references cited therein.
13. K. Funke, Solid State Ionics, **18/19**, 183 (1986).
14. K. Funke, in: Superionic Solids and Solid Electrolytes: Recent Trends, eds. A.L. Laskar and S. Chandra (Academic Press, New York, 1987); and K. Funke, Z. Phys. Chem. Neue Folge, **154**, in press (1987).
15. J.H.R. Clarke and S. Miller, Chem. Phys. Lett., **13**, 97 (1972).

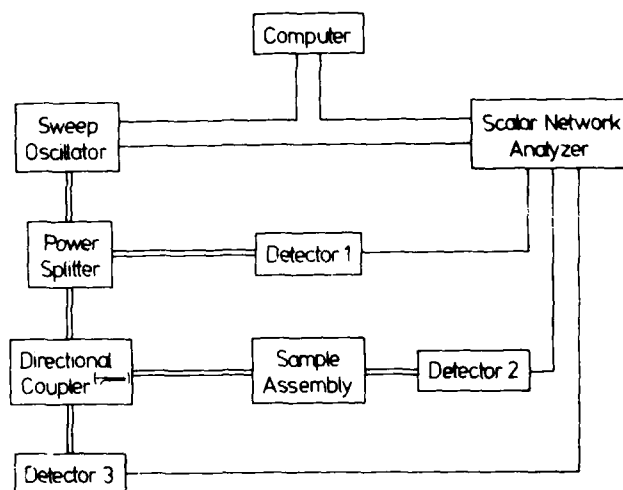


Fig. 1. Block diagram of experimental set-up.

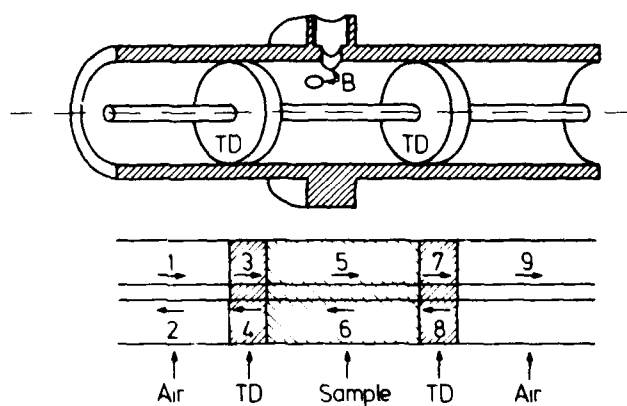


Fig. 2. Exploded view of sample assembly and travelling waves in different media. TD: teflon disks; B: inlet borings for melt.

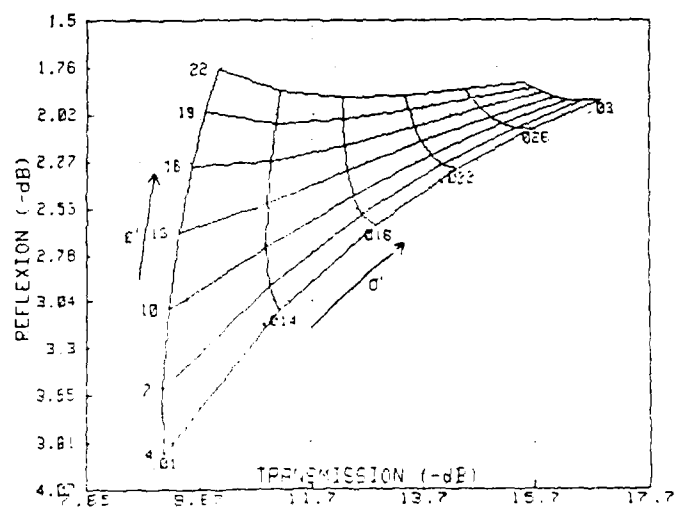


Fig. 3. A transformation network at 1.5 GHz (2 mm teflon disks, 10 mm sample); σ' is in $1/(\Omega\text{cm})$.

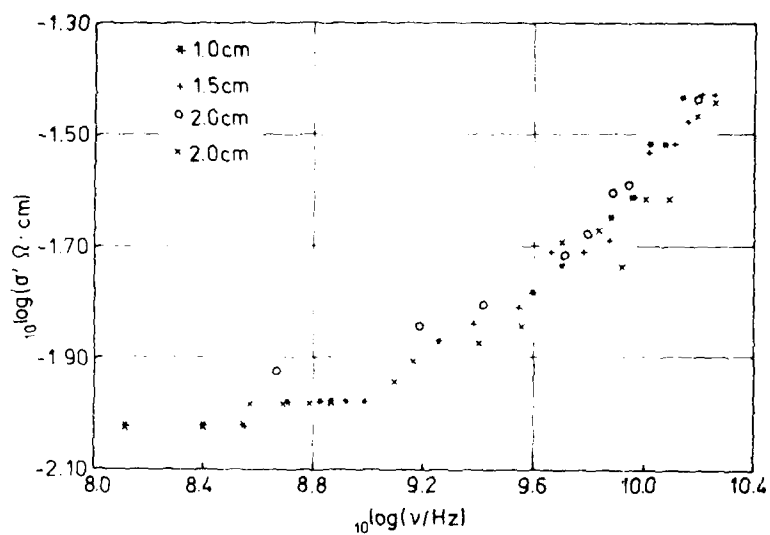


Fig. 4. Dispersion of σ' at 453 K as obtained from samples of different lengths.

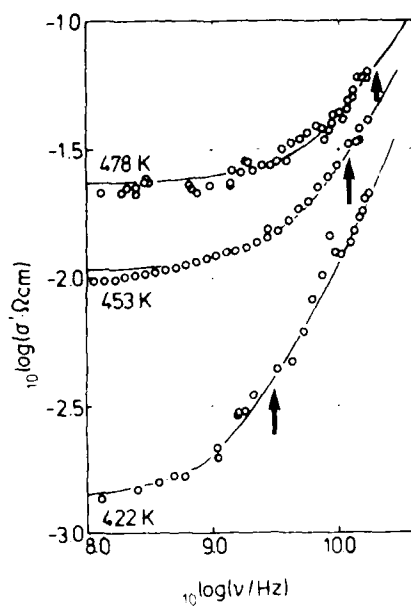


Fig. 5. Experimental and model spectra; frequencies $(2\pi\nu)^{-1}$.

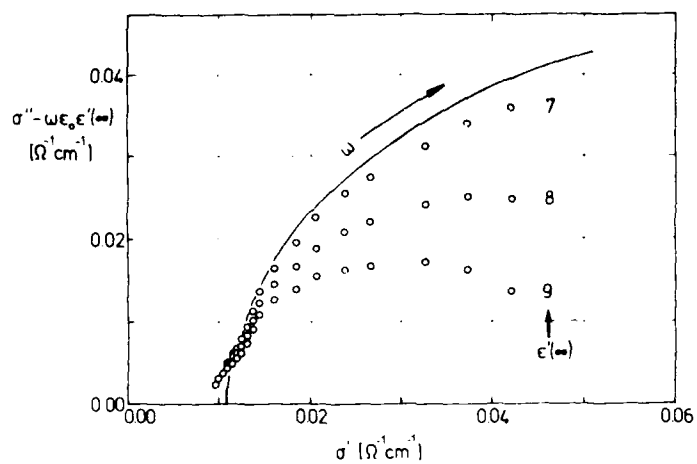


Fig. 6. Conductivity arcs, by experiment and model.

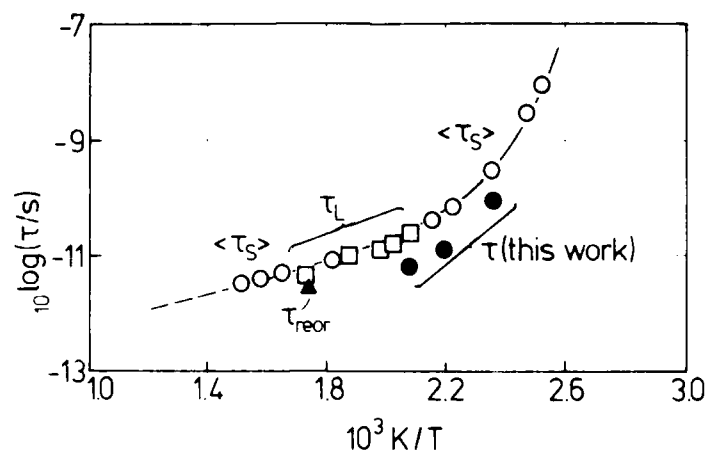


Fig. 7. Arrhenius plot of the reorientational relaxation time obtained from the present study, τ , the longitudinal relaxation time from Brillouin scattering (7,9), τ_L , and the average shear relaxation time (7), $\langle\tau_S\rangle$. The nitrate ion reorientation time, τ_{reor} , is from Raman data (15).

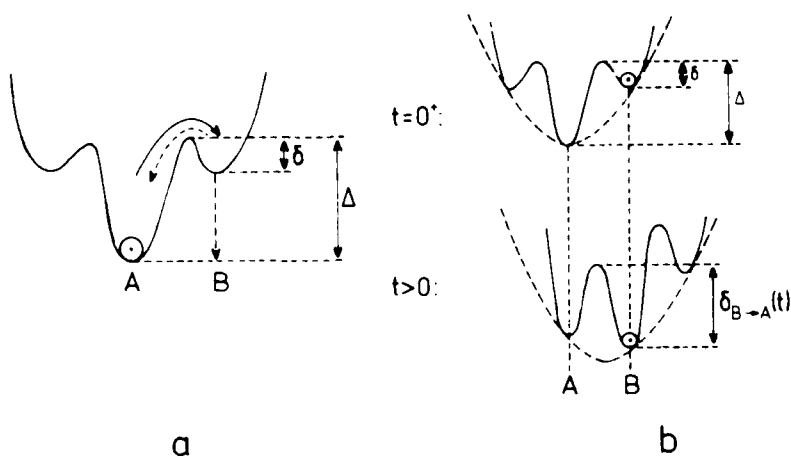


Fig. 8. Conditional effective potential and its development with time, see text.

ELECTRICAL CONDUCTIVITY OF BINARY MELTS CONTAINING
 NbCl_5 , TaCl_5 and $\text{NaCl-KCl}(1:1)$

Nobuaki Sato and Michio Nanjo
Research Institute of Mineral Dressing
and Metallurgy
Tohoku University,
Sendai 980, JAPAN

ABSTRACT

The specific electrical conductivity of the NbCl_5 - NaCl-KCl ($\text{NaCl}:\text{KCl}=1:1$) pseudo binary system was measured because of interest in the molten salt electrolysis of niobium from its chloride melts.

The phase diagrams of these systems have been determined by differential thermal analysis. The results show a trend similar to that of the NbCl_5 - NaCl and NbCl_5 - KCl systems.

The electrical conductivity of melts increases with the increase in temperature. Two liquid phases were observed in the region rich in NbCl_5 . Conductivities of pure NaCl_5 and TaCl_5 were determined between the melting point and the boiling point using a pyrex glass cell with a small cell constant.

In the same manner, the conductivity of the TaCl_5 - NaCl-KCl pseudo binary system was also considered with the goal of obtaining high purity tantalum by molten salt electrolysis.

INTRODUCTION

Niobium has recently become of major interest in high technology applications such as nuclear reactors and as a superconductor catalyst. Pure tantalum metal is also important as a capacitor.

Pyrochlore is the most important source of niobium because of its great abundance and low tantalum content (1-4). A recent trend of ore producing countries such as Brazil is that of exporting ferroniobium instead of the ore. Imported ferroniobium accounts for more than 60% of all niobium supplied to Japan.

As ferroniobium becomes a main source of the world's niobium supply, investigation of niobium production directly from ferroniobium is needed urgently. We have studied the chloride process and molten salt technology which are the most applicable to purification and synthesis of new materials (5,6). These studies present possible separation processes of niobium from ferroniobium which yield pure niobium chloride. It is feasible to consider producing niobium metal from niobium chloride by electrolysis in molten chloride salts.

In this paper, the specific electrical conductivity and the phase diagram of the NbCl_5 - NaCl-KCl pseudo binary system were investigated. Another pseudo binary system of TaCl_5 - NaCl-KCl was also considered for the production of high purity tantalum metal using chloride electrolysis.

EXPERIMENTAL

Chloride preparation

Anhydrous NbCl_5 was prepared by reacting 99.7% niobium metal powder with a small amount of carbon and dry Cl_2 gas in a chlorination apparatus at 300°C . Anhydrous TaCl_5 was prepared in the same manner using 99.5% tantalum metal. The mixture of NaCl and KCl was dehydrated by passing dry HCl gas into the $\text{NaCl-KCl}(1:1)$ melt at 750°C . These dehydrated chlorides were transferred to conductivity cells or DTA cells in an argon filled dry box.

Conductivity Measurement

The conductivity cells (a) were made of pyrex glass or quartz with a 1 mm diameter tungsten rod welded to tungsten foil as shown in Fig. 1. The cell resistance ($0.2\text{--}0.3\text{S}^{-1}$) is negligible compared to the salt bath resistance of $100\text{--}200\text{S}^{-1}$ (cell constant= $100\text{--}200\text{cm}^{-1}$). Another type of pyrex glass cell (b) with a small cell constant ($\sim 2.0\text{cm}^{-1}$) was used for pure NbCl_5 and TaCl_5 because of their small specific electrical conductivities (10^{-6} S/cm). Electrical conductivity was measured by the AC bridge method at 1-10 kHz as shown in Fig. 2.

Differential Thermal Analysis (DTA)

DTA was used to determine the phase diagrams. The cells were made of pyrex glass or quartz with a thermocouple well at the bottom (Fig.3). The cell was sealed under vacuum. The heating rate was 10°C/min .

$\text{NbCl}_5\text{-NaCl-KCl}(1:1)$ Pseudo Binary Phase Diagram

The phase diagram of this pseudo binary system is presented in Fig.4. The melting points of each component (204°C for NbCl_5 , 647°C for $\text{NaCl-KCl}(1:1)$) agree with previously reported values (204 and 645°C) (7,8). Other studies report 1:1 compounds such as NaNbCl_6 (tetragonal) and KNbCl_6 (cubic) in the $\text{NbCl}_5\text{-NaCl}$ and $\text{NbCl}_5\text{-KCl}$ binary systems (9-11). In the NbCl_5 rich region α , β , γ , and $\alpha\gamma$ interphases were observed as in the $\text{NbCl}_5\text{-KCl}$ system. In the NaCl-KCl rich region three transformations were observed as in the $\text{NbCl}_5\text{-KCl}$ system. Unfortunately there is no structural reference to the above transformations. Two liquid phases are also observed in the NbCl_5 rich region.

Specific Electrical Conductivity of NbCl_5 and TaCl_5

The specific electrical conductivities of NbCl_5 at elevated temperatures are shown in Fig. 5. The specific electrical conductivity of pure NbCl_5 from 204°C (m.p.) to 253°C (b.p.) is $1.0 \times 10^{-6}\text{ S/cm}$, a very low value, which is characteristic of molecular melts. The conductivity of NbCl_5 increases slightly with increasing temperature. The value of $9.4 \times 10^{-7}\text{ S/cm}$ (218°C) shows good agreement with that of Blitz ($2.2 \times 10^{-7}\text{ S/cm}$ at 220°C) (11). Often the very small conductivity of NbCl_5 melt is augmented by the presence of highly

conductive impurities such as HCl. However, since the measured specific conductivities are in agreement, and the NbCl_5 was prepared in different ways, it is likely that the measured conductivity arises only from the dissociation of NbCl_5 itself.

Specific Electrical Conductivity of NbCl_5 -NaCl-KCl Pseudo Binary System

Fig.6 shows the temperature dependence of the conductivity for the NbCl_5 -NaCl-KCl system. When a small amount (10mol%) of NaCl-KCl is added to pure NbCl_5 , the conductivity rises to a very large value. It also increases rapidly with increasing temperature. This suggests that the conductivity mechanism changes from molecular NbCl_5 to an ionic species. From 80 to 60 mole% composition of NbCl_5 , conductivity changes only slightly. In this composition range there are two liquid phases (Fig.4). The upper layer is pale brown, the lower is black. The conductivity of the latter liquid was measured because the electrode made contact only with the heavier black liquid. This phase corresponds to the $(\text{Na,K})\text{NbCl}_6$ eutectic melt. In the NaCl-KCl rich region, conductivity increases with the increasing concentration of ionic species.

The specific electrical conductivity isotherms for this system are shown in Fig. 7. There are three regions to the composition dependence of conductivity: I, a rapid increase region with low conductivity; II, a flat region; III, a gradually increasing region with high conductivity. Region I represents the transition from molecular to ionic conductivity. Region II corresponds to the two liquid phase of this system. Region III is influenced primarily by the contribution of the increasing concentration of the NaCl-KCl electrolyte.

The relation between $\log K$ and $1/T$ for NbCl_5 -NaCl-KCl pseudo binary system is linear for almost all compositions (Fig.8). However, in the area of 90 mol% NbCl_5 two slopes appear which correspond to the changes of the melt structure. The activation energy of 3 kcal/mol is close to that of alkali halide melts.

The phase diagram and conductivity for the TaCl_5 -NaCl-KCl pseudo binary system will be presented in detail. Viscosities and densities of the above systems will be also reported.

REFERENCES

1. H. R. Stockford, CIM Bulletin, **65**, 61(1972).
2. D. P. Gold, M. Vallee, and J. P. Charette, CIM Bulletin, **60**, 245(1967).
3. G. Perrault, Can., Mineralogist, **9**, 383(1968).
4. E. H. Nickel and R. G. Pinard, Mines Branch Invest. Rept., Dept. Energy, Mines and Resources, Canada, 70(1970).

5. A. B. McIntosh and J. S. Broadley, IMM Symposium on Extraction Metallurgy of Some of the Less-Common Metals, London, 272(1956).
6. A. Moriuchi, S. Hichimura, J. Moriyama, and I. Kushima, J. Mining Met. Inst. Japan, 76, 319(1960).
7. I. S. Morozov, Zh. Prikl. Khim., 33, 1685(1960).
8. D. S. Coleman and P. D. A. Lacy, Mater. Res. Bull., 2, 936(1967).
9. A. P. Palkin and N. D. Chikanov, Zh. Neorgan. Khim., 7, 706 (1962).
10. K. Huber, E. Jost, E. Newenschwander, M. Studer, and B. Roth, Helv. Chim. Acta, 41, 2419(1958).
11. D. R. Sadoway, A Thesis for The Doctor's Degree, University of Tront, 18(1977).
12. W. W. Elts, and A. Voigt, Z. anorg. allg. Chem., 120, 71 (1922).

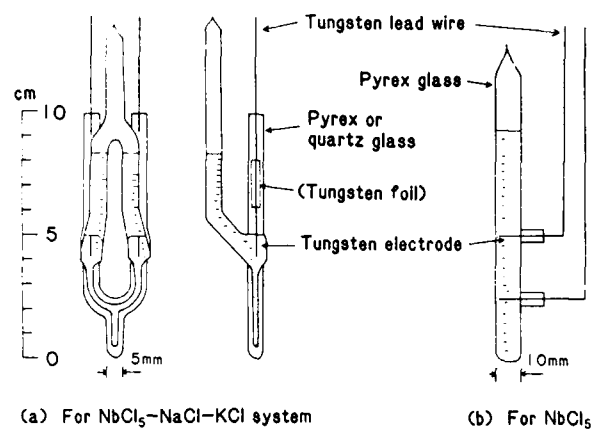


Fig. 1 Conductance cell.

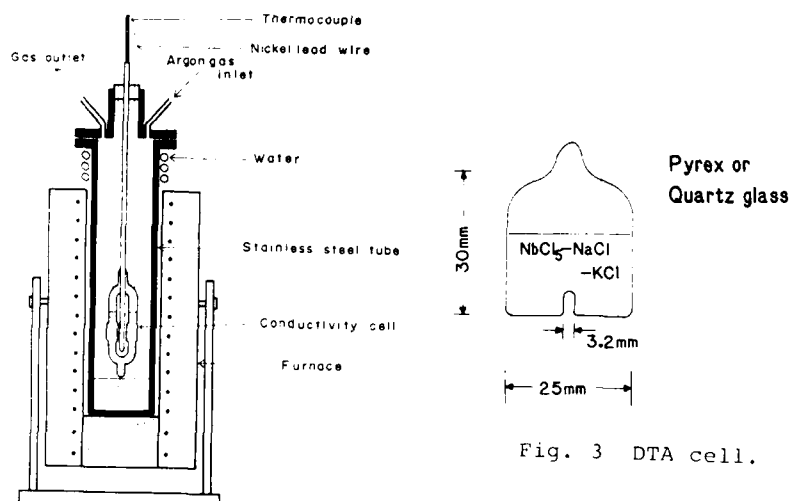


Fig. 2 Assembly for the measurement of electrical conductivity.

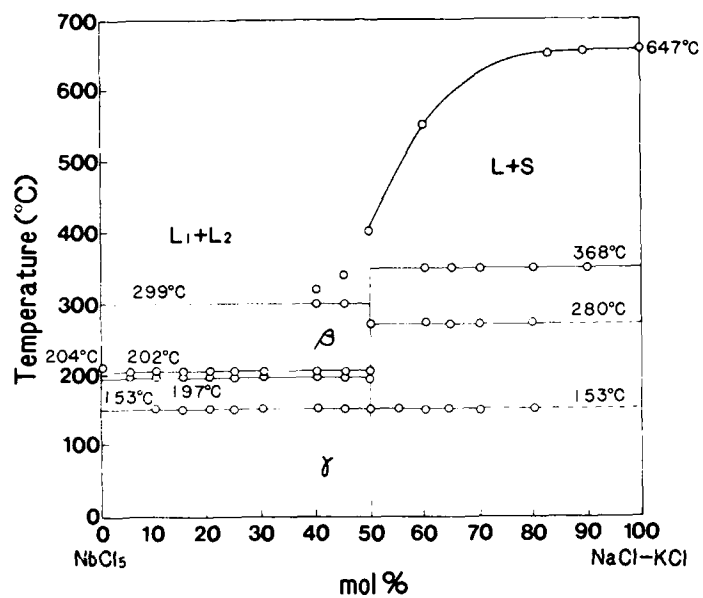


Fig. 4 Phase diagram for the NbCl_5 - $\text{NaCl-KCl}(1:1)$ pseudo binary system.

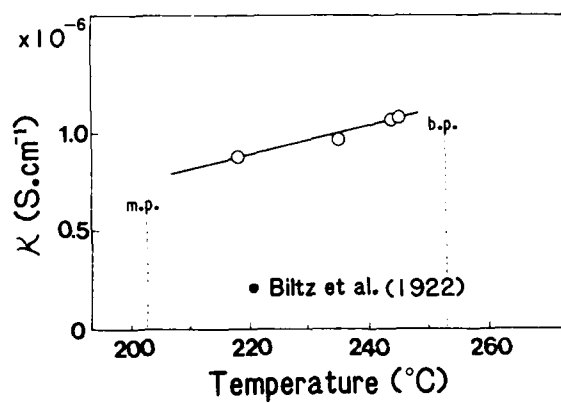


Fig. 5 Specific electrical conductivity of NbCl_5 .

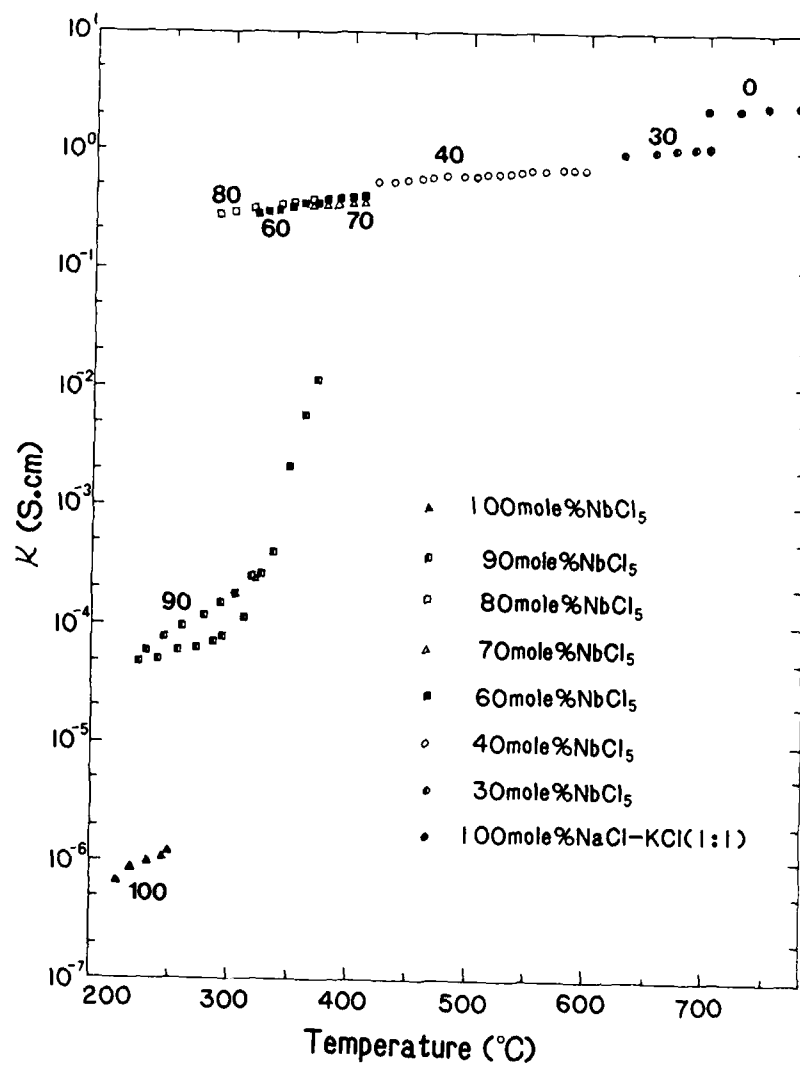


Fig. 6 Temperature dependence of conductivity for NbCl₅-NaCl-KCl(1:1) systems.

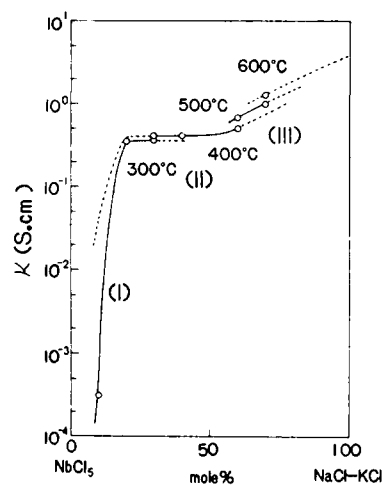
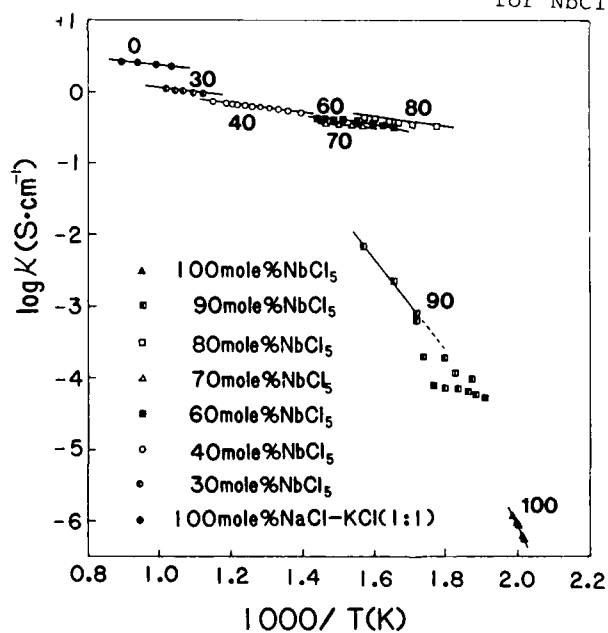


Fig. 7 Specific electrical conductivity isotherms for $\text{NbCl}_5\text{-NaCl-KCl}(1:1)$ systems.

Fig. 8 Log K vs. $1/T$ plot for $\text{NbCl}_5\text{-NaCl-KCl}(1:1)$ system.



**ENRICHMENT OF Li-6
BY COUNTERCURRENT ELECTROMIGRATION OF MOLTEN LiNO_3**

Teruo Haibara, Osamu Odawara, Isao Okada
Department of Electronic Chemistry
Tokyo Institute of Technology
Nagatsuta, Midori-ku, Yokohama 227, Japan

Masao Nomura, and Makoto Okamoto
Research Laboratory for Nuclear Reactors
Tokyo Institute of Technology
O-okayama, Meguro-ku, Tokyo 152, Japan

ABSTRACT

The internal cation mobilities of the molten binary system $(\text{Na}, \text{NH}_4)\text{NO}_3$ have been determined from the data on mobility ratios and electric conductivities; the former and the latter have been measured with the Klemm method and the direct current method, respectively. In all accessible conditions, the mobility of NH_4^+ ions is greater than that of Na^+ ions, that is, the Chemla effect occurs. Based on this information, the countercurrent electromigration method previously presented for enriching ^6Li has been improved; in the previous study ^6Li was enriched in the region of molten LiNO_3 adjoining molten NH_4NO_3 placed toward the cathode. In the present study a small zone of NaNO_3 attempted to form between these two melts in a separation tube. By this method, the outflow of Li^+ ions into the cathode compartment by electromigration, which is seriously unfavorable to enrichment of ^6Li , can be prevented. ^6Li has been enriched from 7.4% to 73.0% in 25 days without any trouble from material corrosion.

INTRODUCTION

In a previous study (1), we succeeded in enriching ^6Li by countercurrent electromigration; molten LiNO_3 and NH_4NO_3 were arranged in a separation tube and a cathode compartment, and heated at about 300°C and 180°C , respectively. A part of the separation tube was packed with alumina powder, and the boundary region between the two salts, where ^6Li was to be enriched, was formed near the end part of the separation tube adjoining the cathode

compartment.

The position of the boundary is settled by the balance of electromigration flow and countercurrent flow. When the electromigration flow overcomes the countercurrent flow, Li^+ ions flow into the cathode compartment and enrichment of ^6Li will not take place. However, maximum electromigration flow is desirable for higher enrichment of ^6Li within the limit that this flow is balanced with the counter flow.

In order to avoid an immediate outflow of Li^+ ions into the cathode compartment by an uncontrollable overcurrent flow, in the present study we have devised a way of forming a small zone of another salt between the two salts. The cation mobility of this third salt should be intermediate between those of Li^+ and NH_4^+ ions. One of the potential salts as the third salt is molten NaNO_3 . It had been known that $b_{\text{Li}} < b_{\text{Na}}$ at the whole concentration region in the system $(\text{Li}, \text{Na})\text{NO}_3$ (2) and that $b_{\text{Li}} < b_{\text{NH}_4}$ at all accessible conditions of concentration and temperature in the system $(\text{Li}, \text{NH}_4)\text{NO}_3$ (3), where b_x is the internal mobility of cation x . Thus, we have measured the internal cation mobilities in the molten binary system $(\text{Na}, \text{NH}_4)\text{NO}_3$. After confirming that $b_{\text{Na}} < b_{\text{NH}_4}$ in this mixture, we have tried to enrich ^6Li by using NaNO_3 as the third salt.

EXPERIMENTAL

Internal mobility in $(\text{Na}, \text{NH}_4)\text{NO}_3$ melt

The relative difference in the internal cation mobilities in the molten binary system $(\text{Na}, \text{NH}_4)\text{NO}_3$ was measured with the Klemm method. The electromigration cell and the procedure were similar to those previously used for the study of $(\text{Li}, \text{NH}_4)\text{NO}_3$ melts (3). The chemicals of reagent grade were used. As the salt in the large cathode compartment, a mixture of $(\text{Na}, \text{NH}_4)\text{NO}_3$ of the eutectic composition ($x_{\text{Na}}=0.20$) was employed. In the present study, an ion chromatographic analyzer (IC500S) made by Yokogawa Electric Corporation was used for quantitative analysis of Na^+ and NH_4^+ ions whereas in the previous study (3) the flame spectrophotometry and the Kjeldahl method were employed for the determination of Li^+ and NH_4^+ ions, respectively.

The electric conductivity was measured with a direct current method by use of a cell of the type proposed by Duke and Bissell (4). The cell was made of transparent silica. The cell constant was measured to be 14.40cm^{-1} with a standard KCl aqueous solution. The NaNO_3 and NH_4NO_3 were vacuum-dried at 120°C and 60°C , respectively, overnight before use. These measurements were performed in the temperature range of 160 to 180°C at $x_{\text{Na}} < 0.3$ in

the light of the phase diagram of this system (5) and the thermal decomposition of NH_4NO_3 (6).

Enrichment of ^6Li

An electromigration cell of a horizontal type was used (Fig. 1). This was similar to those used in the previous study (1). The part containing the anode compartment and the separation tube was somewhat different from the previous one; the separation tube was inserted and connected to the anode compartment tightly from the side wall and the end of the tube was turned upward as shown in Fig. 1, so that the cementation of the quartz wool by setting it from the outside became much easier than in the previous experiments. This quartz wool played a role in keeping powder dense during electromigration, which is essentially important for stable electromigration for a long period. The separation tube was packed as densely as possible with alumina powder of ca. 50 μm . The cell was wound with the nichrome tape.

Lithium nitrate of reagent grade was vacuum-dried overnight at 120°C before use. It was put into the heated separation tube through the large anode compartment. After it melted and spread over the diaphragm, a small amount of molten NH_4NO_3 and ca. 0.4 g of NaNO_3 were poured into the cathode compartment. Then the electromigration was started with increasing electric current gradually to ca. 350 mA. During the initial period of electromigration for ca. 8 hrs., more NH_4NO_3 melt was added to the planned level.

About 30 g of NH_4NO_3 melt was supplied per day to compensate the expended NH_4NO_3 due to the thermal- and electro-decomposition. A small portion of NH_4NO_3 melt in the cathode compartment was sampled for chemical analysis of Li^+ and Na^+ ions with flame spectrophotometry at intervals of a few days. For the initial few days 350 mA was supplied and the Li^+ and Na^+ contents in the cathode compartment increased considerably. Thus, it was lowered to 300 mA after 5 days from the beginning, and after that it was not necessary to adjust the current. Main experimental conditions are given in Table 1.

After 25 days, the electromigration was terminated, all the NH_4NO_3 melt in the cathode compartment and the LiNO_3 melt in the anode compartment were taken out by tilting the cell, and then the cell was allowed to cool. After rewinding the nichrome tape, the separation tube was cut into pieces for chemical analysis and the isotope ratio measurement. The isotope ratio was measured with a Varian MAT CH5 mass spectrometer.

RESULTS AND DISCUSSION

Internal mobility in $(\text{Na}, \text{NH}_4)\text{NO}_3$ melt

The relative difference, ϵ , in the internal mobilities of the two cations is defined as

$$\epsilon = (b_{\text{Na}} - b_{\text{NH}_4}) / b, \quad (1)$$

where $b = x_{\text{Na}}b_{\text{Na}} + x_{\text{NH}_4}b_{\text{NH}_4}$. The ϵ values are calculated from the amount of the cations in the separation tube and the transported charge by use of an equation presented in Ref. 7. The internal mobilities of these ions are calculated from

$$b_{\text{Na}} = (\kappa / F)(1 + x_{\text{NH}_4}\epsilon) \quad (2a)$$

$$\text{and } b_{\text{NH}_4} = (\kappa V / F)(1 - x_{\text{Na}}\epsilon), \quad (2b)$$

where κ and V are the conductivity and the molar volume of the mixture, respectively, and F the Faraday constant. The values of V for the mixture are evaluated from the two neat salts on the assumption of the additivity of the molar volume, which holds well for many mixture melts. For this evaluation the data on the molar volume of neat NH_4NO_3 melt are taken from Ref. 8 and those of neat NaNO_3 melt are extrapolated with respect to temperature from those of the melt (9). The electric conductivities measured for mixtures of some concentrations are given in Table 2. Since NH_4NO_3 is slightly decomposable even at the melting point and one of the decomposition products is water (10), the bubble and the water are supposed to have affected the conductivity measurement to some extent. Therefore, the obtained data would not be so accurate as those so far presented for such salts as alkali nitrate melts.

The isotherms of b_{Na} and b_{NH_4} are shown in Fig. 2. As seen from Fig. 2, the mobility of the larger cation, NH_4^+ , is greater than that of the smaller one, Na^+ , under all the accessible conditions; the Chemla effect occurs. Thus, as far as the mobilities are concerned, molten NaNO_3 can be used as the salt located between LiNO_3 and NH_4NO_3 in the separation tube. The reason why the Chemla effect occurs in this system is quite similar to that in the $(\text{Li}, \text{NH}_4)\text{NO}_3$ system which was previously discussed (3).

Enrichment of ^6Li

The distribution of the Li isotopes and the quantity of Li^+ , Na^+ and NH_4^+ ions in the separation tube after electromigration are shown in Fig. 3. Although NH_4NO_3 penetrated rather deeply into the separation tube, Na^+ ions were located around the boundary region between Li^+

and NH_4^+ ions. This shows that also in the ternary mixture

$$b_{\text{Li}} < b_{\text{Na}} < b_{\text{NH}_4}.$$

Since the electric current was quite high at the early period of electromigration, Na^+ ions once entering the separation tube would flow out of the tube. And the amount of Na^+ ions in the catholyte would increase. Thus, at this stage the Na^+ ions are supposed to have played a role in preventing Li^+ ions from flowing out in large quantities into the cathode compartment. Another possible merit of using NaNO_3 is that the frontal part of LiNO_3 , where enrichment of ^6Li is to be taken place, can be kept at higher temperature. The isotope effect of Li^+ ions is greater as temperature increases (11). When LiNO_3 is contiguous to NH_4NO_3 , the temperature of the adjoining part cannot be raised so high as, e.g., 300°C , because of the vigorous thermal decomposition of NH_4NO_3 (6). This merit will be quantitatively evaluated by numerical simulation of the distribution of the chemical species and the Li isotopes in the separation tube.

In the present run, ^6Li has been most enriched in fraction No.5, where the ratio $^7\text{Li}/^6\text{Li}$ is 0.3701 (73.0 ^6Li).

A distinct enrichment of ^7Li is observed in fraction No.17, where the cross sectional area changes drastically. This kind of anomalous distribution of the isotopes was observed also in the previous study (1). Klemm and Lundén have argued that this kind of anomaly is caused by the temperature gradient and the higher isotope effect of Li^+ ions at higher temperature (11). As two tubes with considerably different cross sections were connected, the temperature at the part of a smaller cross section should have been higher than that at the part of a larger one. The anomaly is not favorable to enrichment of ^6Li ; however, this is not a serious problem. In the present run, ^6Li can be enriched without any trouble on material corrosion.

The temperature of the catholyte was kept at 170°C which was about 10°C lower than in the previous run (1). This could decrease the amount of the decomposition of NH_4NO_3 ; in the present run about 30g of NH_4NO_3 was consumed per day whereas in a similar previous run (1) about 40g was. Although the melting point of neat NH_4NO_3 is 169.6°C (5), it could be kept in a molten state at 170°C probably because of the presence of water as its decomposition product.

Addition of $(\text{NH}_4)_2\text{SO}_4$ into NH_4NO_3 in the cathode compartment is now planned since it depress the decomposition of NH_4NO_3 to some extent (12).

As the separation tube was directly heated with the nichrome tape in the present run, it was difficult to keep the temperature constant and to measure it accurately. This disadvantage may be solved by using a double-walled separation tube where also in the outer part LiNO_3 melt is added to keep the temperature in the inside part constant.

A convenient means for detecting the boundary is now sought; if this is found, it will become easier to manually set the electric current to its highest possible level, which is essentially favorable for high enrichment of ^6Li .

REFERENCES

1. I. Okada, K. Gundo, M. Nomura, Y. Fujii, and M. Okamoto, Z. Naturforsch., **41a**, 1045 (1986)
2. C. Yang, R. Takaqi, and I. Okada, Z. Naturforsch., **35a**, 1186 (1980)
3. I. Okada, T. Ayano, and K. Kawamura, Z. Naturforsch., **37a**, 158 (1982)
4. F. R. Duke and L. Bissell, J. Electrochem. Soc., **111**, 717 (1964)
5. R. G. Early and T. M. Lowry, J. Chem. Soc., **121**, 965 (1922)
6. J. D. Brandner, N. M. Junk, J. W. Lawrence, and J. Robins, J. Chem. Eng. Data, **7**, 227 (1962)
7. V. Ljubimov and A. Lundén, Z. Naturforsch., **21a**, 1952 (1966)
8. F. M. A. Hoeg, Z. Anal. Chem., **81**, 115 (1930)
9. G. J. Janz, U. Krevs, H. F. Siegenthaler, and R. P. T. T. Tomskins, J. Phys. Chem. Reference Data, **1**, No. 3, 594 (1972)
10. Gmelin Handbuch der anorganischen Chemie, 8. Auflage, System-Number 23 Ammonium, Verlag Chemie, Berlin 1936, p.108
11. A. Lundén and A. Ekhed, Z. Naturforsch., **24a**, 892 (1969)
12. R. C. Saxena and S. Varma, Technology, **8**, 277 (1971)

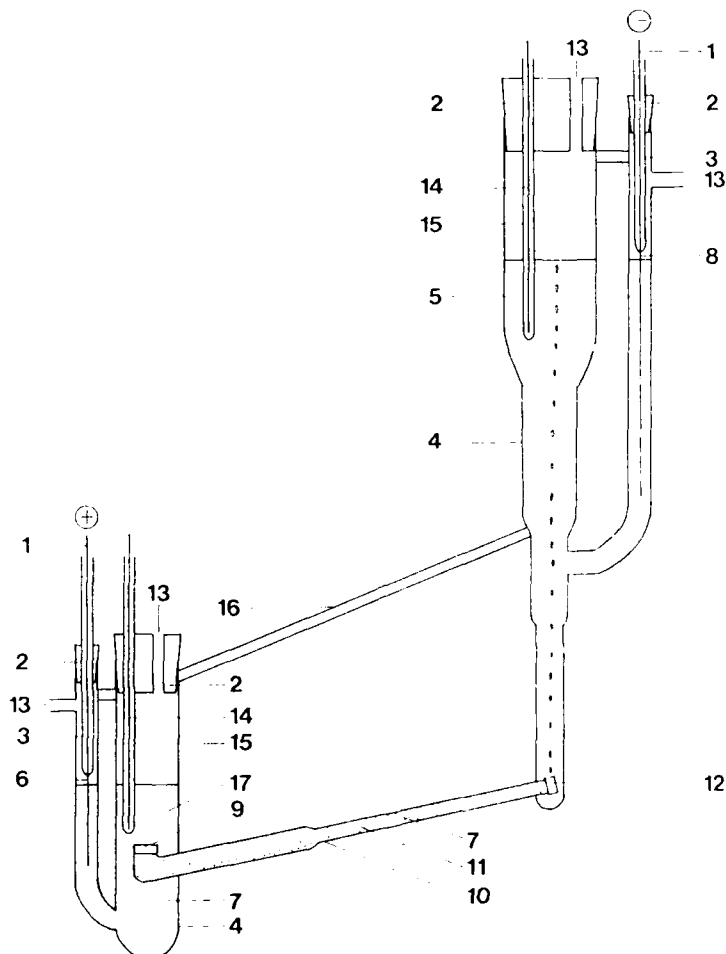


Fig. 1. Electromigration cell.

1: Mo lead wire, 2: Silicone stopper, 3: Vycor sheath for the lead wire, 4: transparent silica vessel, 5: molten NH_4NO_3 (cathode compartment), 6: Pt anode, 7: molten LiNO_3 , 8: Pt cathode, 9: quartz wool cemented to the wall, 10: transparent silica tube, 11: alumina powder, 12: quartz filter, 13: gas outlet, 14: chromel-alumel thermocouple, 15: sheath for the thermocouple, 16: support bar, 17: anode compartment.

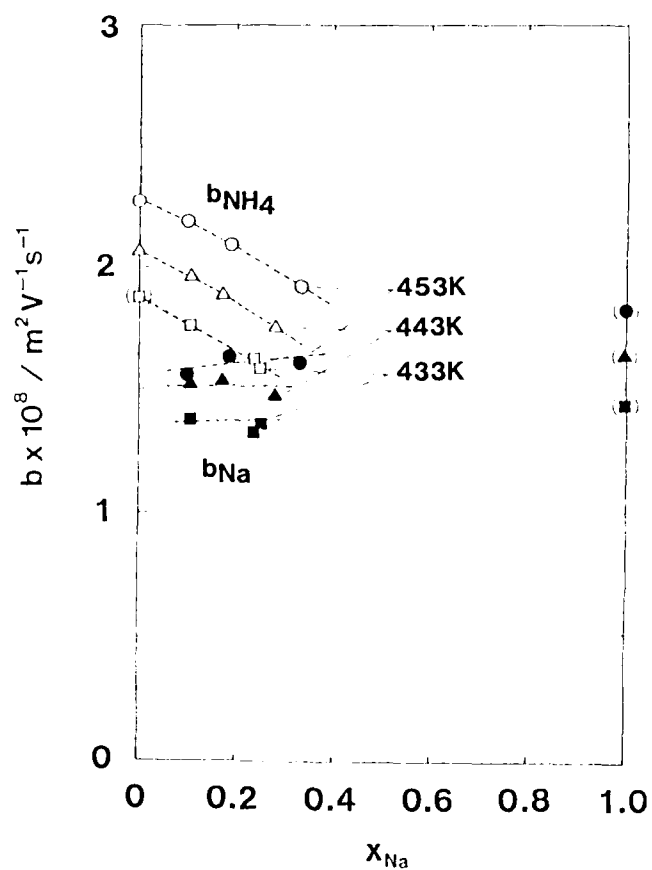


Fig. 2. Isotherms of internal cation mobility in the system $(\text{Na}, \text{NH}_4)\text{NO}_3$.

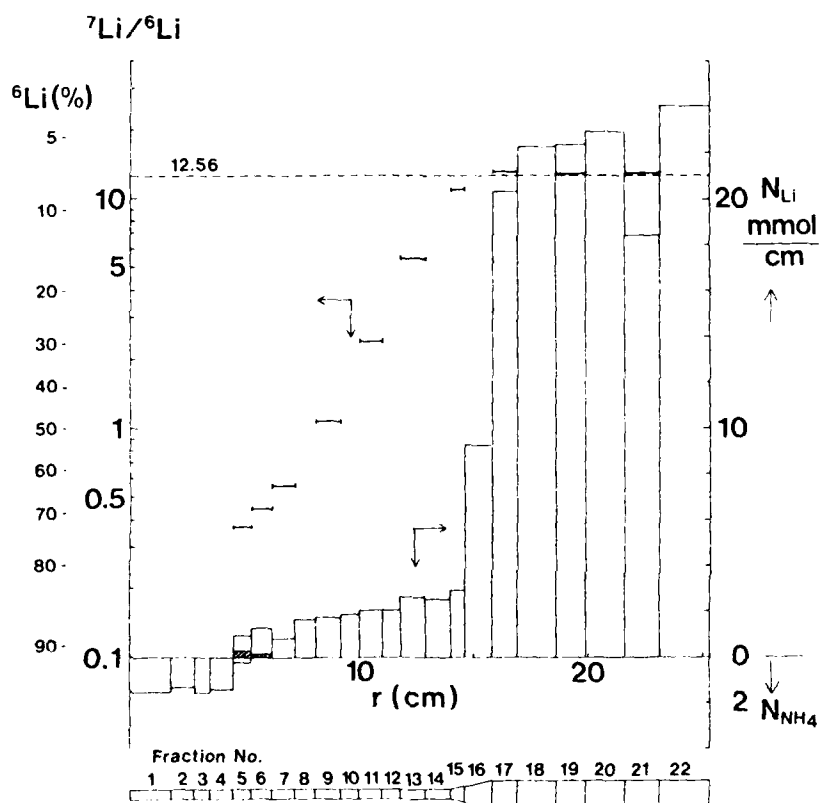


Fig. 3. Distribution of the Li isotopes and the ions Li^+ , Na^+ and NH_4^+ after the electrolysis.

The amount of Li^+ and NH_4^+ per cm of tube length are drawn upward and downward, respectively. The shadowed part shows the amount of Na^+ . The abscissa is the distance from the cathode end of the separation tube.

Table 1. Electromigration conditions.

Electric current	(mA)	320
Current density	(A/cm ²)	
4.3 mm int. diam.		3.7
12.0 mm int. diam.		0.37
Voltage	(V)	90-95
Duration	(d)	25
Transported charge	(C)	676x10 ³
Hydraulic head	(cm)	28-33
Cell material		Quartz
Packing material		Alumina
Grain size	(μm)	ca. 50
Temperature	(°C)	
LiNO ₃		ca. 300
NH ₄ NO ₃		ca. 170
Amount of salt	(g)	
LiNO ₃		ca. 160
NH ₄ NO ₃		ca. 190
Separation column		
Length	(mm)	135+113
Int. diam.	(mm)	(4.3)(12)
Isotope ratio, ⁷ Li/ ⁶ Li		
Original		12.56
In most enriched fraction		0.3701
(% ⁶ Li)		(73.0)
Overall separation factor between the most enriched fraction and the feed		33.9

Table 2. Experimental data on specific conductivities
in the system (Na,NH₄)NO₃.
 $\kappa = aT + b$ (κ in S cm⁻¹; T in K)

x _{Na}	a	b	temp. range (K)
0.000	3.70x10 ⁻³	-1.28	443 - 453
0.103	3.44x10 ⁻³	-1.18	433 - 453
0.217	3.53x10 ⁻³	-1.24	433 - 453
0.303	3.45x10 ⁻³	-1.22	433 - 453

THE CHEMLA EFFECT IN THE MOBILITIES
IN THE MOLTEN BINARY SYSTEM NaOH-KOH

Chao-Chen Yang, Osamu Odawara,
and Isao Okada

Department of Electronic Chemistry
Tokyo Institute of Technology
Nagatsuta, Midori-ku
Yokohama 227, Japan

ABSTRACT

Internal mobility ratios of two cations in the molten binary system (Na, K)OH have been measured with the Klemm method. From these and available data on the densities and conductivities, the internal mobilities of Na^+ and K^+ ions (b_{Na} and b_{K} , respectively) have been calculated. The Chemla effect occurs except at high concentration of Na^+ ions. b_{Na} and b_{K} decrease with decreasing concentrations of NaOH and KOH, respectively; b_{Na} is well expressed, except at a region of small molar volume, by

$$b_{\text{Na}} = \{A/(V-V_0)\}\exp(-E/RT),$$

where A , V_0 and E are constant independent of temperature T and molar volume of the mixture V . Negative deviation of b_{Na} from this equation at low x_{Na} region is attributed to the free space effect traceable to the small free space. The decrease of b_{K} with an increase of NaOH concentration may be interpreted qualitatively by assuming that the OH^- ions become less mobile owing to the strong interaction with the Na^+ ions.

INTRODUCTION

Molten alkali hydroxides are ionic liquids and therefore good ionic conductors. However, fundamental properties of the melts such as the structure and the mechanism of the ionic conduction have not been much as investigated as other typical ionic melts probably because of the technical difficulties due to the high chemical aggressiveness of these melts.

The order of the molar conductivities, and therefore of the internal cation mobilities b , of the following alkali hydroxides is opposed to that of other usual melts:

$$b(\text{LiOH}) < b(\text{NaOH}) < b(\text{KOH}).$$

Thus, it is interesting to elucidate the mechanism of the ionic conduction of the molten alkali hydroxides. For this purpose, it is more informative to measure mobilities in binary mixtures than in neat melts. The binary system (Na,K)OH has been chosen for the present study, since data on the densities and the conductivities (1)(2) are available. For the measurement of ratios of the internal mobilities of the two cations, the Klemm method, i.e., a countercurrent electromigration method was employed. This method is one of the most reliable and is insensitive to a small amount of impurities such as water and carbonate ions. This advantage is particularly important for the present case.

EXPERIMENTAL

The electromigration cell shown in Fig. 1 was similar to the one used for molten carbonates (3). The furnace was a transparent one made by Trans. Temp. Co., U. S. A.

A mixture LiOH-NaOH-KOH of the eutectic composition (9.5-49-41.5 mol %) (4) was used as the catholyte in the large vessel, which also played the role of a heat bath for the separation tube. These chemicals were made by Kanto Chemical Co. Japan (LiOH H_2O : min. 95 % containing max. 0.5 % Li_2CO_3 , NaOH: min. 97 % containing max. 0.8 % Na_2CO_3 and KOH: min. 86 % containing max. 0.8 % K_2CO_3). Water contained in these chemicals was mostly evaporated when they were heated.

A mixture melt (NaOH-KOH) of a chosen concentration was stored in another small vessel of alumina, and bubbled at 723 K with dry N_2 gas, which had passed through conc. sulfuric acid and molecular sieve 4A, at least for 12 hr for dehydration (5). The chemicals NaOH and KOH used in this vessel were the ones made by Merck Co. Ltd. (NaOH: min. 99 % containing max. 1 % Na_2CO_3 and KOH: min. 85 % containing max. 1 % K_2CO_3). Water content of the melt was measured with Karl Fischer's method (e.g., for a 50-50 mol % mixture less than 1.7%).

Two alumina tubes with different diameters (outer dia.: 6 mm and 16 mm ; inner dia.: 4 mm and 10 mm, respectively, α -alumina SSA-S made by Nihon Kagaku Togyo Co. Ltd.) were connected with alumina cement (Aron Ceramic D made by Toagosei Chemical, Japan) and employed as a

separation tube. The separation tube was packed over 150 mm long with alumina powder of 150-180 μm . Both the top and the bottom of the diaphragm part of the powder were installed with alumina wool for settling the powder.

The separation tube was put into the small vessel, and after the diaphragm part was filled with the melt, the tube was transferred into the electromigration cell containing the catholyte of the ternary mixture. The separation tube was set so that the connected part of the two tubes was 2-3 cm above the level of the catholyte; by this a possible short circuit between inside and outside was avoided. Then, electromigration was started with constant electric current of about 150 mA. Platinum wires of 1 mm ϕ were used as electrodes. A mixed gas of O_2 and hot water vapor was bubbled around the cathode. Conversion of the electrodeposited metal into the original hydroxide was expected to occur.

During electromigration, dry N_2 gas was passed also through the catholyte melt to remove the excess water.

After electromigration, of 2.5-3.0 hr, the separation tube was taken out, cleaned on the outside wall and cut into pieces of ca. 10 mm long. The salt in each fraction was dissolved into distilled water, and the content of the cations was determined by flame spectrophotometry.

RESULTS

The relative difference in the internal mobilities of the two cations is defined as

$$\epsilon = (b_{\text{Na}} - b_{\text{K}}) / \bar{b} \quad (1)$$

where $\bar{b} = x_{\text{Na}} b_{\text{Na}} + x_{\text{K}} b_{\text{K}}$ (x_{Na} and x_{K} are mole fractions of NaOH and KOH, respectively). The ϵ value can be calculated from the distribution of the cationic species in the separation tube and the transported charge according to a formula given in Ref. (6).

Main experimental conditions and the results are given in Table 1. As the absolute values of ϵ are large at most concentrations, relatively small transported charges in these experiments compared with those for alkali nitrates may have been enough.

Internal mobilities of the two cations are calculated from ϵ and available data on the density and conductivity (1)(2) by using

$$b_{Na} = (x V/F)(1 + x_K \epsilon) \quad , \quad (2a)$$

$$b_K = (x V/F)(1 - x_{Na} \epsilon) \quad , \quad (2b)$$

where V is the molar volume of the mixture and F the Faraday constant.

DISCUSSION

The isotherms of b_{Na} and b_K are shown in Fig. 2. The b_{Na} and b_K decrease with decreasing x_{Na} and x_K , respectively. In a certain range of concentration the Chemla effect (7,8) occurs, that is, the internal mobility of the smaller cation Na^+ is smaller than that of the larger one K^+ . The Chemla crossing point shifts toward higher concentration of the smaller cation, as temperature increases; this is observed also in other binary systems.

We have found that, in other mixture melts with a common anion such as alkali nitrates where Coulombic interaction between cations and anions is the predominant factor influencing the mobilities, the cation internal mobilities are well expressed by

$$b = [A/(V-V_0)] \exp(-E/RT) \quad , \quad (3)$$

where A , E , V_0 are the parameters characteristic of the cation of interest and almost independent of the concentrations and temperature (9).

In order to see explicitly whether such an equation holds, we have plotted the reciprocal values of b_{Na} and b_K against V and found that b_{Na} is well expressed with such an equation except at low molar volume (as for b_{Na}^{-1} , see Fig. 3). The solid lines are drawn with the parameters $A = 0.494 \times 10^{-11} m^5 V^{-1} s^{-1}$, $E = 11.34 kJ mol^{-1}$ and $V_0 = 11.51 \times 10^{-6} m^3 mol^{-1}$. The negative deviation of b_{Na} from Eq. (3) with the parameters given above is attributable to the small effective free space. (In Fig.3 the negative deviation appears as a positive one since the reciprocal of b_{Na} is taken.)

Our interpretation why b_{Na} decreases with decreasing x_{Na} is quite similar to that often stated for other systems such as binary alkali nitrates (10).

It is rather surprising that the profile of the isotherms of b_K is quite different from that of b_{Na} , whereas the ionic sizes of these cations are not so different. The profile for K^+ ions in the present system

is quite different from that in the binary system (Na, K)NO₃, and rather similar to that of self-diffusion coefficients in glasses exhibiting the "mixed alkali effect" (11).

It is also surprising that the molar conductivity of neat KOH is greater than that of neat NaOH. The external cation transport numbers in NaOH and KOH have been reported by Shvedov and Ivanov (10) to be 0.10 ± 0.03 and 0.03 ± 0.03 , respectively. These suggest that the mechanisms of ionic conduction may be considerably different in these melts.

It is known that in alkali chloride melts internal mobilities are strongly related with a separating motion of neighboring cations defined as the self-exchange velocity (SEV) (11). Thus, the internal mobilities also in the present system may be explained in terms of the SEV. At high x_K region, the motion of OH⁻ ions may be great and the contribution of this motion to the SEV in K⁺-OH⁻ pairs is much greater than that of the K⁺ ions. As x_K decreases, that is, x_{Na} increases, separating motion of OH⁻ ions from K⁺ ions will become less vigorous owing to the stronger interaction between Na⁺ and OH⁻ ions. Therefore, with decreasing x_K , b_K considerably decreases. This decrease of b_K could not be attributed to the smaller free space in the present case. If this were due to the free space effect, the rate of decrease of b_K would become more sharp with decreasing x_K . If it is assumed that, in mixture melts, Na⁺, K⁺ and OH⁻ ions move mainly in the Na⁺-OH⁻ and K⁺-OH⁻ pairs, respectively, the rather strange isotherm of b_K can qualitatively be interpreted.

According to a study of infrared spectrometry on molten NaOH, the spectral data are interpreted in terms of hydrogen bonding or polymer formation (12). This is not inconsistent with the data on b_{Na} in the present mixture. It needs to be studied further in connection with the ionic mobilities and the difference in the structure between NaOH and KOH melts.

In conclusion, the profile of the isotherms of b_{Na} and b_K is quite different, and the Chemla effect clearly occurs except at high concentration of NaOH. The profile of b_{Na} is similar to that found in other ionic melts such as alkali nitrates, but that of b_K is rather different from those so far found. This is interpreted by assuming that the external transport number of OH⁻ ions in the neat KOH is considerably great and decreases with increasing concentration of NaOH.

The expenses of this study were financially supported by the Grant-in-Aid for Special Project Research No. 61134043 from the Ministry of Education, Japan.

REFERENCES

- (1) C. Dauby, J. Glibert, and P. Claes, Electrochimica Acta, **24**, 35 (1979).
- (2) P. Claes and J. Glibert, J. Electrochem. Soc. **132**, No.4 (1985).
- (3) C. Yang, R. Takagi, K. Kawamura, and I. Okada, to be published.
- (4) N. A. Reshetnikov and N. I. Vilutis, Zhur. Neorg. Khim. **4**, 123 (1959).
- (5) P. Claes and J. Glibert, p.83, Vol.1, Molten salt techniques.
- (6) V. Ljubimov and A. Lunden, Z. Naturforsch. **21a**, 1592 (1962).
- (7) J. Perie and M. Chemla, C. R. Acad. Sci. **250**, 3986 (1960).
- (8) I. Okada, R. Takagi, and K. Kawamura, Z. Naturforsch. **34a**, 498 (1979).
- (9) C. Yang, R. Takagi, and I. Odada, Z. Naturforsch. **35a**, 1186 (1980).
- (10) C. Yang, R. Takagi, and I. Okada, Z. Naturforsch. **38a**, 135 (1983).
- (11) Delbert E. Day, J. Non-Crystalline Solids **21**, 343 (1976).
- (12) V. P. Shvedov and I. A. Iranov, Russ. J. Phys. Chem. **39**, 396 (1965).
- (13) I. Okada, R. Takagi, and K. Kawamura, Z. Natruforsch. **35a**, 493 (1980).
- (14) J. Greenberg, and L. J. Hallgreen, J. Chem. Phys. **35**, 180 (1961).

Table 1. Experimental conditions and relative difference in internal cation mobility.

x_{Na}	T/F	Q/C	t/hr	ϵ
0.249 \pm 0.001	620	1370	2.7	0.1169 \pm 0.0081
0.249 \pm 0.001	640	1191	2.6	0.1225 \pm 0.0123
0.249 \pm 0.001	673	1532	2.7	0.0620 \pm 0.0038
0.249 \pm 0.001	699	1442	2.3	0.0076 \pm 0.0018
0.249 \pm 0.001	745	1430	2.3	0.0265 \pm 0.0153
0.487 \pm 0.003	470	1448	2.7	0.0454 \pm 0.0063
0.487 \pm 0.003	480	1423	2.8	-0.0481 \pm 0.0066
0.487 \pm 0.003	500	1462	2.7	-0.0918 \pm 0.0120
0.487 \pm 0.003	518	1478	3.0	-0.1102 \pm 0.0071
0.487 \pm 0.003	593	1436	4.0	-0.1124 \pm 0.0179
0.487 \pm 0.003	645	1034	2.7	-0.1343 \pm 0.0180
0.487 \pm 0.003	699	1465	2.7	-0.1208 \pm 0.0120
0.487 \pm 0.003	723	1320	2.7	-0.1607 \pm 0.0096
0.698 \pm 0.001	697	1276	2.4	-0.3781 \pm 0.0084
0.698 \pm 0.001	735	1168	2.3	-0.3880 \pm 0.0088
0.698 \pm 0.001	783	1651	2.4	-0.4160 \pm 0.0043
0.807 \pm 0.003	723	1297	2.3	-0.4612 \pm 0.0310
0.807 \pm 0.003	753	1513	3.0	-0.4802 \pm 0.0180
0.807 \pm 0.003	790	1326	2.3	-0.5463 \pm 0.0220

Q is the transported charge and t the duration.

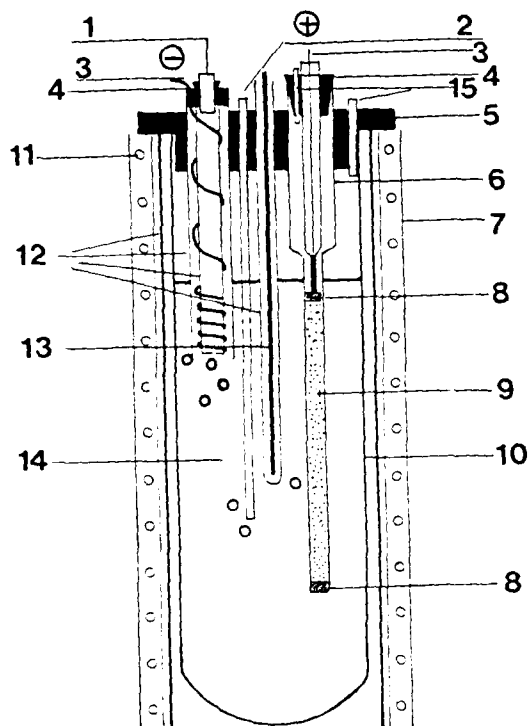


Fig. 1. Electromigration cell

1: gas inlet ($O_2 + H_2O$), 2: gas inlet (N_2), 3: Pt electrode, 4: Silicone stopper, 5: graphite cover, 6: separation tube made of alumina, 7: electric furnace, 8: alumina wool, 9: alumina powder, 10: alumina vessel, 11: nichrome heater, 12: alumina tube, 13: alumel-chromel thermocouple, 14: catholyte melt of the eutectic composition of (Li, Na, K)OH, 15: gas outlet (N_2 or H_2O).

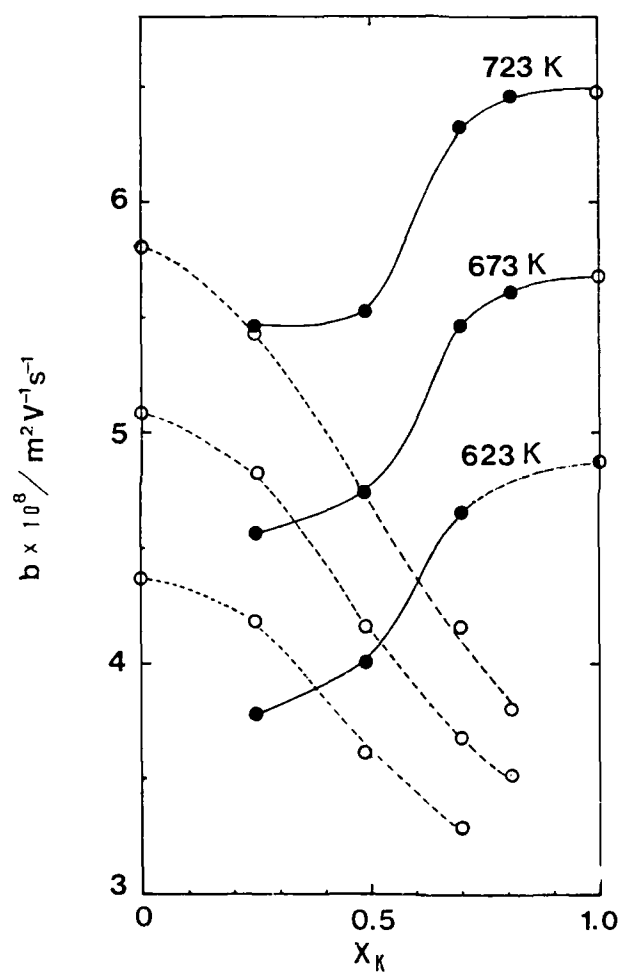


Fig. 2. Isotherms of internal mobilities of Na^+ and K^+ ions.

b_K for neat KOH at 623 K, which is estimated from the extrapolated conductivity data.

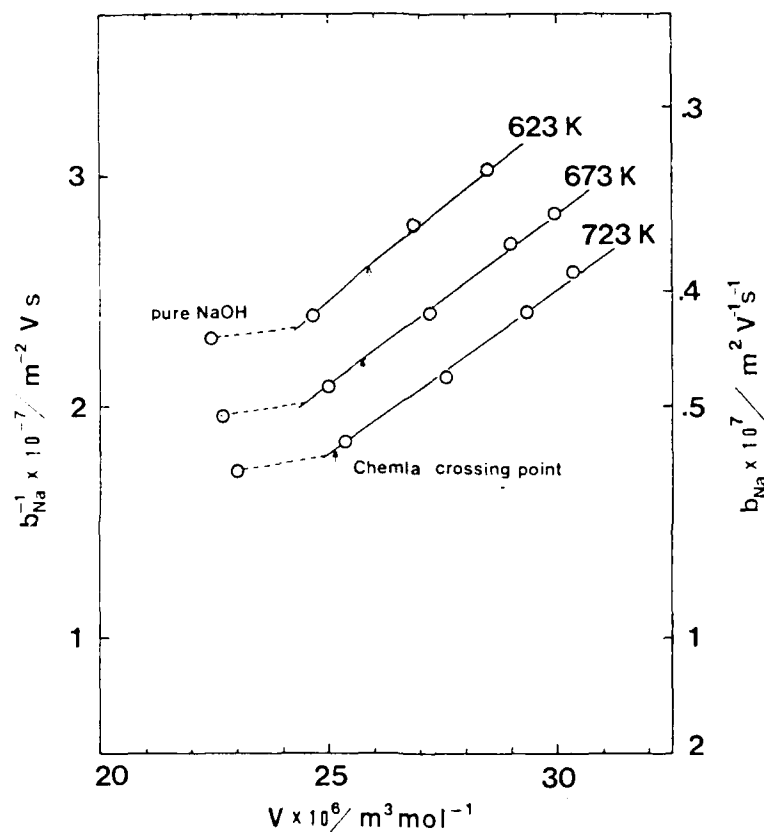


Fig. 3. The reciprocal of b_{Na} plotted vs. molar volume.

The lines are drawn according to Eq.(3) with the given parameters. The values corresponding to the Chemla crossing point are marked.

**PREDICTION OF THE OCCURRENCE OF THE ANION CHEMLA EFFECT
--- SELF-EXCHANGE VELOCITY IN THE MOLTEN BINARY SYSTEM
Li(Cl, Br) STUDIED BY MD SIMULATION**

Shipra Baluja, Akira Endoh, and Isao Okada

Department of Electronic Chemistry
Tokyo Institute of Technology
Nagatsuta, Midori-ku
Yokohama 227, Japan

ABSTRACT

Molecular dynamics (MD) simulation of the equimolar mixture of LiCl and LiBr melts has been performed at about 1000 K to evaluate the velocity of separating motion of adjacent unlike ion pairs defined as the self-exchange velocity (SEV). The SEV of Li-Br pairs is greater than that of Li-Cl pairs. This predicts that in this mixture the internal mobility of Br⁻ ions would be greater than that of Cl⁻ ions, that is, the "anion Chemla effect" will occur. For comparison, MD simulation of pure LiCl and LiBr melts has also been done.

INTRODUCTION

In previous studies, we have measured internal mobilities of cations in various molten binary mixtures with a common anion. In most of the systems the Chemla effect (1, 2) occurs in some concentration range, that is, the mobility of the larger cation is greater than that of the smaller one. This has been interpreted in terms of the difference in the Coulombic forces exerted on large and small cations by the anions.

We have found that in molten alkali chlorides internal mobilities are strongly related with the velocity of the separating motion of neighboring cation and anion defined as the self-exchange velocity (SEV) (3), which can be evaluated by molecular dynamics (MD) simulation. For example, in the molten mixture of (Li, K)Cl the Chemla effect for the internal mobilities (4) has been reproduced by the corresponding SEV's (5).

If the Chemla effect is caused by the difference in the Coulombic forces between two kinds of unlike ion pairs, it is expected that also in a binary mixture with a common cation the anion Chemla effect will occur. Thus,

in the present study the SEV's in the equimolar mixture of LiCl and LiBr melts have been calculated to learn whether the anion Chemla effect in the SEV's occurs. For comparison, the SEV's of neat LiCl and LiBr melts have been calculated. MD simulation of LiBr melt (6) as well as LiCl melt had been performed; however, the SEV of alkali bromide melts had not been studied.

MOLECULAR DYNAMICS SIMULATION

For all the systems, 432 ions were taken in the cubic cell. In the case of the equimolar mixture, 216 Li^+ , 108 Cl^- and 108 Br^- ions were disposed in the cell. The edge length L of the cubes was calculated from the data on the densities (7, 8). The pair potentials of the Born-Mayer-Huggins type were adopted:

$$u_{ij}(r) = z_i z_j e^2 / 4\pi \epsilon_0 r - A_{ij} b \exp[(z_i + \sigma_j - r)/c] - c_{ij}/r^6 - d_{ij}/r^8, \quad (1)$$

where z is the charge number, e the elementary charge, ϵ_0 the permittivity of vacuum, and A the Pauling factor. Parameters b , σ , a , c and d were taken from those presented for the crystals by Tosi and Fumi (9); for the mixture the combination rule presented by Larsen et al. (10) was employed. The parameters used are given in Table 1. The Ewald method (11) was employed for the calculation of the Coulombic force. The MD-simulations were performed with a constant energy procedure. The step time was 4 fs. The average pressure was 0.24 GPa for LiCl, 0.21 GPa for LiBr and 0.18 GPa for Li(Cl, Br), and the temperatures were 1004 K, 1002 K and 991 K, respectively. After about 3000 time steps for equilibration, the configurations for the following 3000 time steps were employed for various calculations of the properties for each system.

RESULTS AND DISCUSSION

Pair correlation function

The characteristic values of the pair correlation functions $g(r)$ are given in Table 2. In Fig. 1, $g(r)$ and the running coordination number $n(r)$ are shown for the unlike ion pairs. The positions of the first maximum R_{M1} for g_{LiCl} and g_{LiBr} are almost the same in the pure salts and the mixture, while the peak heights decrease with increasing concentration of LiBr. Similar behavior has been observed in such systems as (Li, Rb)Cl (3). This can be explained as follows: with increasing concentration of LiBr, the average distance between neighboring Li^+ ions increases, as is seen also from the positions of the first maximum of $g_{\text{LiLi}}(r)$ in Table 2, and the halide ions are

more structured with the nearest neighboring Li^+ ions by experiencing less interference from other surrounding Li^+ ions. This feature distinctively appears also in the self-exchange velocity which will be stated later.

Angular correlation function

For further insight into the short range structure, the angular correlation function defined by Eq. (2) was calculated:

$$P_{+-}(\theta) = C \, d n(\theta) / [\sin \theta \, d\theta] \quad (2)$$

where C is the normalization constant taken so that $\int_0^{\pi} P_{+-}(\theta) \, d\theta = 1$ and $d n(\theta)$ is the number of the anions around an Li^+ ion within distance R_2 between $\theta - \Delta\theta/2$ and $\theta + \Delta\theta/2$ ($\Delta\theta = 1^\circ$); R_2 is the position where $g(r)$ crosses unity for the second time and may be regarded as the end of the nearest neighbor interaction (12). The $P_{+-}(\theta)$ in the neat salts and in the mixture are shown in Fig. 2. The first peak position is located around 102° for P_{+-} and P_{++} in all the cases. This indicates that with high probability each ion is coordinated by the counter-ions nearly regular-tetrahedrally in these melts.

Self-exchange velocity (SEV)

The average velocity of separating motion of unlike ion pairs can be expressed in terms of the self-exchange velocity (SEV), v , defined by

$$v = (R_2 - \bar{R}_2) / \tau \quad (3)$$

where \bar{R}_2 is the average distance between unlike ions located within distance R_2 . The anions within distance R_2 from each Li^+ ion are marked. With the lapse of time, the marked anions will move from \bar{R}_2 to R_2 . The time needed for this movement is τ . During the same time the loss of the coordinating anions around the cation is compensated by the anions entering this region from the outside.

The SEV's for Cl^- - Li^+ and Br^- - Li^+ pairs are given in Table 3. The SEV was calculated for the anions coordinating to totally 43200 Li^+ ions for each system. In the mixture the SEV of Cl^- - Li^+ pairs is greater than that of Br^- - Li^+ pairs. Thus, the Chemla effect for the SEV occurs.

The SEV's so far calculated by MD simulations with the Tosi-Fumi potentials (9) are plotted against the experimentally obtained internal mobilities in Fig. 3. In these MD simulations the obtained pressures are usually in the order of 0.1 GPa, whereas the internal mobilities taken in Fig. 2 are those at ambient pressure. However, there seems to be strong correlation between v and b . The b in pure LiCl is minimally greater than that in pure LiBr at 1000 K, if the data on the conductivities and the den-

sities in Ref. (8) are taken. If the data are taken from another reference (7), this order is reversed. As for the SEV, it is slightly greater in LiCl than in LiBr, as shown in Table 3.

For further insight, the motion of distinct ion pairs is examined. Time evolution of the distances of distinct Cl^- and Br^- ions within the respective R_2 's at $t=0$ from a distinct Li^+ ion in the mixture is shown in Fig. 4. This motion can be classified into four processes (4, 13).

(i) The anion which starts within R_2 at $t=0$ passes R_{m1} for the first time after passing R_2 for the last time at the time t (oscillating motion = O-process); R_{m1} is the position of the first minimum of $g(r)$.

(ii) The anion passes R_2 for the last time at the time $t=0$ and passes R_{m1} for the first time at time t (leaving motion = L-process).

(iii) The cation passes R_{m1} at the time $t=0$ in the outward direction at the time $t=0$ and does not pass R_2 (wandering motion = W-process).

(iv) The cation passes R_{m1} in the inward direction at the time $t=0$ and passes R_2 for the first time at the time t (coming-back motion = C-process).

The C-process and L-process of Cl^- and Br^- ions are compared in the mixture. In Fig. 5 percentage of the anions terminating the O-process for the first time are plotted against time. This figure shows that the O-process of Cl^- ions is longer than that of Br^- ions. This is because, at the same number density of Li^+ ions, Cl^- ions are more associated with the nearest neighboring Li^+ ions than Br^- ions are, owing to the stronger Coulombic interaction. In other words, Cl^- ions are more associated with Li^+ ions than Br^- ions are.

On the other hand, the average velocity of Cl^- ions in the L-process v_L is greater than that of Br^- ions; they are $(1399 \pm 33) \text{ m s}^{-1}$ and $(1326 \pm 30) \text{ m s}^{-1}$, respectively, and lie on an empirical equation $v_L = (0.577 \pm 0.005) \times (v_c + v_a)$, where $v_c = \sqrt{8 R T / \pi M_c}$ and $v_a = \sqrt{8 R T / \pi M_a}$ (M_c and M_a : masses of the cation and anion, respectively) (5). In the L-process the velocity is mainly dependent on the masses of cation and anion of interest and temperature (5). Since a Cl^- ion is lighter than a Br^- ion, it is reasonable that in the L-process Cl^- ions are faster than Br^- ions are.

As the contribution of the O-process is greater than that of the L-process in the present mixture, the SEV of Br^- ions is greater than that of Cl^- ions, although in the

L-process the velocity of the former is smaller than that of the latter.

Self-diffusion coefficient

The self-diffusion coefficients of the ions, D , have been evaluated from the mean square displacements, which have been taken over 8 ps from different 40 time origins. The evaluated values are given in Table 5 along with the experimental values for LiCl (14). This table shows that D of Cl^- ions is greater than that of Br^- ions in the mixture as well as in the pure melts. That is, the Chemla effect does not occur for the self-diffusion coefficients. The self-diffusion coefficient refers to the motion of the ions with reference to their original position, whereas the internal mobility of the anions is related to the motion with reference to their counter-ions. Therefore, the self-diffusion coefficient of the smaller and lighter ions should be generally greater than that of the larger and heavier ones.

Table 5 indicates also that D for Cl^- and Br^- ions are greater in the pure melts than in the mixture. This may be explained as follows. The Cl^- ions are more associated in the mixture than in the pure salt, and therefore D is smaller in the former than in the latter. As for Br^- ions, these may be more associated in the pure melt than in the pure salt, but the free space is smaller in the former than in the latter. Thus, the effect of free space must be greater than the effect of association for such large ions as Br^- ions, as far as the motion with reference to their original position is concerned.

In conclusion, the Chemla effect occurs for the SIV in the equimolar mixture of LiCl and LiBr melts. This predicts that the Chemla effect would occur for the mobilities of the two anions. This is to be ascertained experimentally.

The expenses of this study were defrayed by the Grant-in-Aid for Special Research No. 61134043 from the Ministry of Education, Japan. The calculation was performed with HITAC M-680 H and M-280 H at the Institute for Molecular Science at Okazaki and the High Energy Physics Institute at Tsukuba, respectively. The Computer time made available for this study is gratefully acknowledged.

REFERENCES

1. J. Périć and M. Chemla, C. R. Acad. Sci. Paris, **260**, 3986 (1960).

2. I. Okada, R. Takagi, and K. Kawamura, Z. Naturforsch., **34a**, 498 (1979).
3. I. Okada, R. Takagi, and K. Kawamura, Z. Naturforsch., **35a**, 493 (1980).
4. A. Lundén and I. Okada, Z. Naturforsch., **41a**, 1034 (1986).
5. I. Okada, Z. Naturforsch., **42a**, 21 (1987).
6. F. Lantelme and P. Turq, Mol. Phys., **38**, 1003 (1979).
7. G. J. Janz, F. W. Dampier, G. R. Lakshminarayanan, P. K. Lorenz, and R. P. T. Tomkins, Molten Salts: Vol. 1, Electrical Conductance, Density, and Viscosity Data, NSRDS-NBS **15**, Nat. Bur. Stand., Washington 1968.
8. G. J. Janz, R. P. T. Tomkins, and C. B. Allen, Phys. Chem. Ref. Data, **8**, 125 (1979).
9. M. P. Tosi and F. G. Fumi, J. Phys. Chem. Solids, **25**, 45 (1964).
10. B. Larsen, T. Fjørland, and K. Singer, Mol. Phys., **26**, 1521 (1973).
11. P. P. Ewald, Ann. Phys., **64**, 253 (1921).
12. G. Pálinkás, W. O. Riede, and K. Heinzinger, Z. Naturforsch., **32a**, 1137 (1977).
13. I. Okada, Z. Naturforsch., **39a**, 880 (1984).
14. R. Lenke, W. Uebelhack, and A. Klemm, Z. Naturforsch., **28a**, 881 (1973).

Table 1. The parameters used for the MD simulation.

Table 1a

	Li-Li	Cl-Cl	Br-Br	Li-Cl	Li-Br	Cl-Br
A	2.00	0.75	0.75	1.375	1.375	0.75
σ /pm	163.2	317.0	343.2	240.1	253.2	330.1
$\frac{c}{10^{-79} \text{J m}^6}$	0.073	111.0	185.0	2.00	2.50	143.0
$\frac{d}{10^{-99} \text{J m}^6}$	0.030	223.0	423.0	2.40	3.30	307.1

$$b = 0.338 \times 10^{-19} \text{ J}$$

Table 1b

System	/pm	L/pm	Ref.
LiCl	34.2	2187.9	(7)
LiBr	35.3	2345.3	(7)
Li(Cl, Br)	34.8	2274.8	(8)

Table 2. Characteristic values of the pair correlation functions $g_{ij}(r)$.

System	i	j	R_1 (pm)	R_{M1} (pm)	$g(r_{M1})$	R_2 (pm)	R_{m1} (pm)	$g(r_{m1})$
Li(Cl, Br)	Li	Cl	188	219	4.29	279	353	0.42
	Li	Br	211	241	3.40	304	367	0.50
	Li	Li	327	385	1.80	477	553	0.72
	Cl	Cl	323	369	2.19	455	527	0.62
	Br	Br	350	397	2.13	491	577	0.65
	Cl	Br	335	381	2.14	469	551	0.63
LiCl	Li	Cl	192	223	3.72	281	353	0.46
	Li	Li	318	371	1.82	459	535	0.69
	Cl	Cl	324	373	2.13	455	537	0.65
LiBr	Li	Br	207	239	3.78	302	369	0.47
	Li	Li	341	397	1.79	494	573	0.70
	Br	Br	349	401	2.14	487	573	0.63

R_1 is the position where $g(r)$ crosses unity for the first time.

Table 3. Self-exchange velocity of neighboring unlike ions at about 1000 K.

System	Cl^-Li^+ (m s ⁻¹)	Br^-Li^+
Li(Cl, Br)	119	134
LiCl	145	---
LiBr	---	120

Table 4. Self-diffusion coefficients at about 1000 K.

System	Li^+ (10^{-9} m ² s ⁻¹)	Cl^- (10^{-9} m ² s ⁻¹)	Br^-
Li(Cl, Br)	10.5	7.0	4.7
LiCl	9.2 [14.2]	8.2 [7.2]	---
LiBr	10.0	---	6.2

The values in brackets are the experimentally obtained ones at 1000 K at ambient pressure (14).

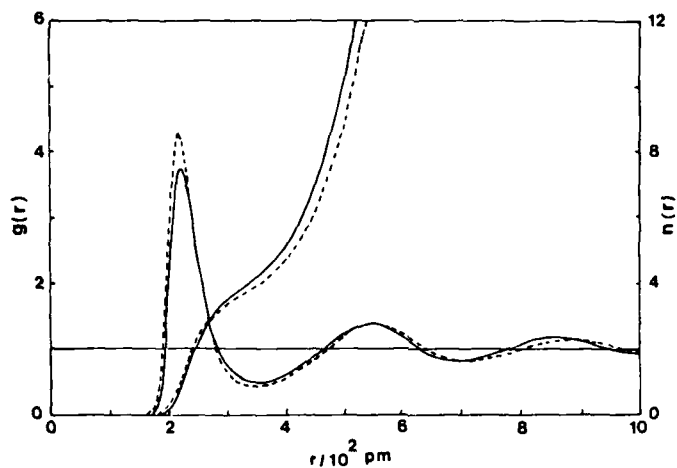


Fig. 1a. Pair correlation function $g_{\text{LiCl}}(r)$ and running coordination number $n(r)$ of Li^+ ions around a Cl^- ion.
 — : LiCl ; ---- : $\text{Li}(\text{Cl}, \text{Br})$.

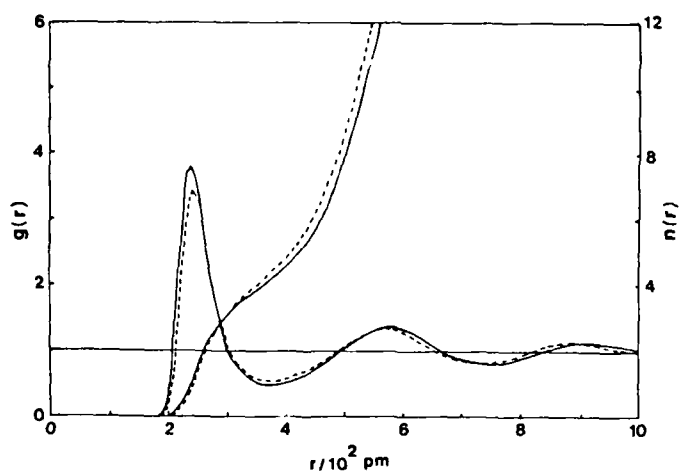


Fig. 1b. Pair correlation function $g_{\text{LiBr}}(r)$ and running coordination number $n(r)$ of Li^+ ions around a Br^- ion.
 — : LiBr ; ---- : $\text{Li}(\text{Cl}, \text{Br})$.

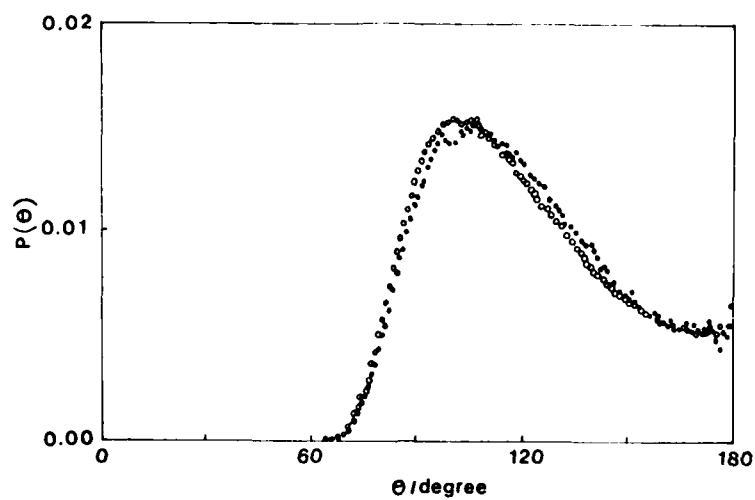


Fig. 2a. Angular correlation function $P(\theta)$ for $\angle \text{Cl-Li-Cl}$. \circ : LiCl; \bullet : Li(Cl, Br).

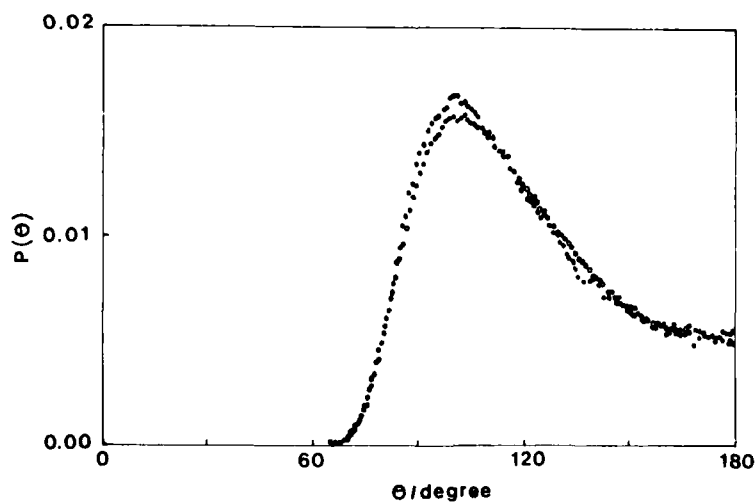


Fig. 2b. Angular correlation function $P(\theta)$ for $\angle \text{Br-Li-Br}$. \circ : LiBr; \bullet : Li(Cl, Br).

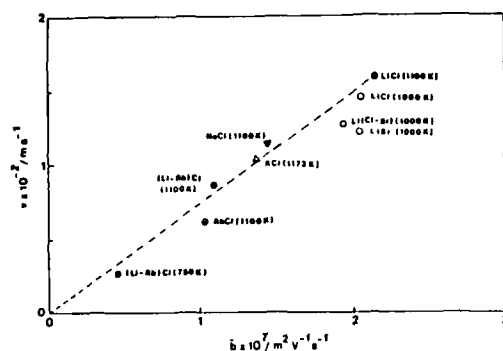


Fig. 3. Relationship between v and b in some alkali halides.

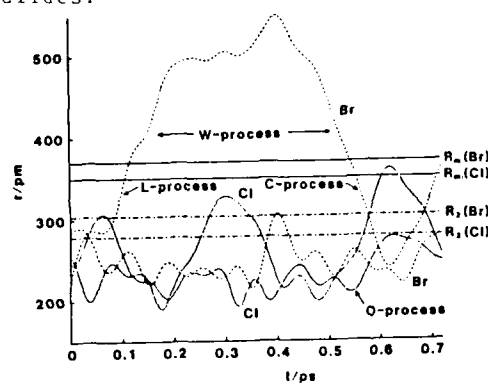


Fig. 4. Time evolution of the distances of the anions (located within R_2 at $t=0$) from an arbitrary Li^+ ion.

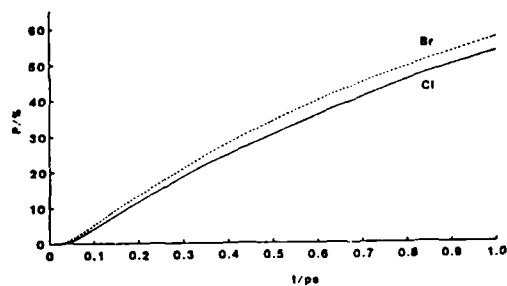


Fig. 5. Percentage of the halide ions terminating the Q-process for the first time.

STRUCTURE EFFECTS ON BINARY ORGANIC
CLASS FORMING MOLTEN SALT SOLUTION
TRANSPORT PROPERTIES

A.M.Elias and M.E.Elias

Department of Chemistry, Lisbon University, FCL,
1294 Lisbon Codex, Portugal.

ABSTRACT

The viscosities and electrical conductances of molten salts solutions in two superficially similar organic systems, γ -piccolinium chloride+ α -piccolinium chloride and quinolinium chloride+ α -piccolinium chloride have been measured and shown to have a characteristic behavior. In the first case the conductivity and fluidity increase as 4-methyl-pyridinium chloride is added to the 2-pyridinium-chloride while with quinolinium chloride addition for a small concentration, 5.3% a maximum occurs followed by a decrease. The differences are attributed to organic complex formation and different geometric configuration of solute which can be seen to act as Lewis acids. Both fragile molten salt systems exhibit considerable regions of glass formation, and correlations of the transport behavior with glass transition temperatures can be made.

INTRODUCTION

In the literature on molten salts much attention has been given to the problem of the structure of organic systems (1-6) little attention, however, has been given to the relation among glass-formation, cohesive parameters, the structure of the melt involving ionic configuration and transport properties of the solution mixtures.

In a previous study 2-methyl-pyridinium chloride functions as strong Lewis base solvent with inorganic salts (7,8); In addition, it has a good glass formation capability.

The present work analyses the consequences of replacing the inorganic salts by two other organic compounds, 4-methyl-pyridinium chloride and quinolinium chloride and shows the extent of structural and energetic aspects of the basic mass transfer process and its relation to glass formation.

EXPERIMENTAL SECTION

2-methyl-pyridinium chloride, designated hereafter α -picHCl was prepared by combination of α -picoline (Fluka) with hydrochloric acid. The product was purified by distillation as described elsewhere (7). This was followed by a vacuum sublimation which yielded a white solid with melting point 91-91.5°C.. Both 4-methyl-pyridinium (γ -picHCl) and quinolinium (QHCl) chlorides were prepared in similar procedures. The melting points of the final anhydrous products were 165.2°C. and 135°C., respectively. The sublimed materials were then melted dropwise into liquid nitrogen and stored as dry beads for convenient manipulation.

Binary melts were prepared by fusing the preweighed components under dry nitrogen and checking for weight loss, all operations being carried out under nitrogen in a dry box atmosphere. The transport properties were measured immediately after the melt preparation.

Differential scanning calorimetry (DSC) and differential thermal analysis (DTA) were performed, respectively, to determine (a) the phase diagram in the case of the quinolinium and γ -piclinium chlorides (b) the glass transition temperatures of both systems. For DSC studies, samples were hermetically sealed into aluminium pans in a dry box and scanned at 10°C., using the Perkin-Elmer DSC-1 instrument. Only one scan was performed on each sample to avoid the danger of contamination by the aluminium sample pan once melting had occurred. The T_g values were determined by DTA of small samples contained in 4mm pyrex tubes scanning at 8°C. min⁻¹. EMF were recorded using a Houston instrument X-V 3000 recorder.

Kinematic viscosities of both organic binary systems were determined using a Ubbelohde capillary viscometer with $C=4.998 \times 10^{-2}$ cSt s⁻¹. Electrical conductivities were determined on the samples using the hybrid Ubbelohde capillary viscocell with cell constant $a=26.82$ cm⁻¹ (8).

All melts were hot-filtered before admission to the measuring cell, both filtration and cell-filling operations being conducted in the dry box. Flow times were measured by a TC-13 Advanced Electronics LTD and conductivities were

determined using a Wayne-Kerr B641 autobalance universal bridge at 1592 Hz. The temperature control ($\pm 0.1^\circ\text{C}$) was performed by a photodiode system described elsewhere (9).

RESULTS AND DISCUSSION

The temperature-kinematic viscosity data for the system α -picHCl+QHCl are plotted in figure 1. Results show a dependence which is typical for this sort of systems. Figure 2 and figure 3 present electrical conductivity and kinematic viscosity for α -picHCl+ γ -picHCl system whose behavior also appears as expected. Isotherms of conductivity and viscosity are represented in figures 4 and 5 for the last system. Conductivities shows a steadily increase, as γ -picHCl content increases and this is more pronounced for higher temperatures. On the other hand, viscosity shows a minimum around 20% in γ -picHCl. Data for this system only covers the range 0-35 % in γ -picHCl due to the lack of homogeneity found beyond that composition. The α -picHCl+QHCl system presents solubility for all ranges of compositions. Viscosity isotherms for α -picHCl+QHCl (Fig.6.) show an almost steadily decrease between 0-60% in α -picHCl, the same applies in the range 0-5,3% in QHCl, however the decrease is sharp coming to a minimum around that composition. A range of constant viscosity is found between 60 and 90% in α -picHCl.

A partial phase diagram for α -picHCl- γ -picHCl is represented in figure 7 and the phase diagram for α -picHCl-QHCl is represented in figure 8. Both diagrams present a simple eutectic. In first case that point occurs for the composition $X=26\%$ γ -picHCl and in the second system for 38% in QHCl. In figure 7 is also shown glass transition temperature, T_g ; the values of the ideal temperatures are plotted in figure 9, for α -picHCl+ γ -picHCl. The values of T_g and T_0 for α -picHCl+QHCl are shown in figure 8. For both cases the values of T_0 were computed at constant values of B parameter making use of VTF equation

$$\ln W = A - (B/(T-T_0))$$

where W is a transport property and A is a constant.

Figure 10 and figure 11 present activation energy as a function of $(T/(T-T_0))^2$ for both systems. Also, T_g -reduced Arrhenius plots are presented in figures 12 and 13.

The minimum in viscosity which occurs in α -picHCl+QHCl for 5.3% QHCl is due to the break of the complex (7,10) $[\alpha\text{-picH}\dots\text{Cl}\dots\text{H}\alpha\text{-pic}]^+$, which forms in molten α -picHCl. This situation is not found in the systems containing γ -picHCl. A minimum is found only at 20% of 4-methyl-pyridinium chloride with a corresponding maximum in electrical conductivity for the same composition. These features are well correlated with glass transition parameters. In fact, T_g and T_o for QHCl system present a minimum, for concentration 5.3% and then a systematic increase up to the value in pure QHCl. In the case of γ -picHCl system, for glass transition temperatures a minimum occurs in the region 20-30% γ -picHCl. The glass forming range in α -picHCl- γ -picHCl collapses for compositions higher than 35.5% in γ -picHCl, and γ -picHCl itself is nonglass forming (11). The domain of glass forming in α -picHCl-QHCl system is from 40 to 100% in α -picHCl and also QHCl is nonglass forming (12).

Considering the activation energy E_a in the case of α -picHCl+ γ -picHCl (figure 10) and E_a in the case of α -picHCl+QHCl (figure 11) as function of $(1-(T_o/T))^{-1}$, two sets of straight lines are found and in both cases they converge to the origin. The energetic parameter for conductivity shows a systematic increase from 0 to 35.5% in γ -picHCl, on the other hand for the system containing QHCl again a minimum in the energetic parameter for viscosity, occurs for 5.3% in QHCl (figure 11). This is due because the values of configurational entropy are higher in QHCl system than the values for γ -picHCl containing system. In fact, for this sort of liquid it is reasonable to assume that C_p is approximately the same, so that relative changes in T_g and T_o may indeed be qualitatively estimated from relative changes in configurational entropy, S_c . So, the collapse of the organic complex present in molten α -picHCl gives an increase in S_c . This is consistent with Moynihan and Angell's (13) thesis that configurational energy, E_c , determines T_g .

The range of constant kinematic viscosity shown by the isotherms in the domain of composition $X=0.0-60.0\%$ in 2-methyl-pyridinium chloride is probably due to the occurrence of complex ionic species which lead to the removal of Cl^- and increase in T_o and T_g . The increase of viscosity above $x=40\%$ in QHCl is mainly due to the molecular volume of QHCl in addition to the effect of Cl^- ion transfer; as the composition approaches the pure component, fluidity decreases. In the first case configurational, translational, and rotational energies are expected to have lower values than those for compositions $X>40\%$ in α -picHCl. Here, unstable ion complexes, like $(\text{QH})_2\text{Cl}^+$ and $\text{Cl}\alpha\text{-picHCl}^+$ may be present, lowering the value of S_c and increasing T_o .

If we consider the values of viscosity and the additivity deviation for α -picHCl+QHCl, it is found that the deviation is negative and this fact is in agreement with the theory which relates organic cation dimensions with the values of those differences. These negative differences (2) are higher or lower when the organic cations are more or less distinct. In the present study the dimension (V_M) of 2-methyl-pyridinium chloride is approximately half of V_M^{QHCl} .

The fragility of the two systems (8,14) is apparent from figures 12 and 13, T_g-reduced Arrhenius plots, in spite of the results reported in kinematic viscosity. This fragility is related to the facility with which the molecular order can reorganize particularly in the intermediate distance. In α -picHCl+ γ -picHCl the fragility in the glass forming range is remarkably the same for the different compositions we have studied (figure 13). In the case of QHCl system, fragility increases with QHCl content due to the shift (in the reduced Arrhenius plot for viscosities) toward the center of general pattern (figure 13). In accordance with the complex formation decrease for $X < 94.7\%$ α -picHCl in the glass forming range.

CONCLUSIONS

This study has shown that the consequences of the γ -picHCl and QHCl addition to α -picHCl depend on the relative compositions of the binary mixtures, and on the concentration of organic complex species present in the molten systems.

The increase in the QHCl content gives a rise of fragility in the liquid structure of the systems, but in the other hand the increase in γ -picHCl content does not significantly change the intermediate range order of the systems. For this case the rate of temperature structural degradation remains the same.

REFERENCES

1. A.R.Ubbelohde, "The Molten State of Matter", John Wiley and Sons, Chichester (1978).
2. "Thermodynamic and Transport Properties of Organic Salts" IUPAC Chemical Data n°28, Pergamon Press (1980).
3. H.Bloom and V.C.Reinsborough, Aust. J. Chem., 21, 1525

- (1968)
4. J.Vedel and B.Trémillon, Bull.Soc.Chim.France, 220 (1966).
 5. D.S.Newman, W.Rohr and D.Kirklin, J.Electrochem.Soc., 119,797 (1972).
 6. D.S.Newman, R.T.Tillack, D.P.Morgan and W.C.Wan, J. Electrochem.Soc., 124,856 (1977).
 7. A.M.Elias and C.A.Angell, J.Phys.Chem., 87,4704 (1983).
 8. A.M.Elias and C.A.Angell, in press.
 9. A.M.Elias and M.H.Pereira, Rev.Port.Quim., 15,6 (1973).
 10. J.W.Shuppert and C.A.Angell, J.Chem.Phys., 67,3050 (1977).
 11. A.M.Elias and M.E.Elias, Proc. 2nd Mat.Port.Soc. Meeting tema III, Oporto (1985).
 12. F.F.Peres, M.E.Elias and A.M.Elias, Proc.3rd Mat.Port. Soc. Meeting, tema I, Braga (1987).
 13. C.A.Angell and C.T.Moynihan, in "Molten Salts: Characterization and Analysis", ed, G.Mamantov, M.Dekker, New York (1969).
 14. C.A.Angell, J.Non-Cryst.Solids, 73,1 (1985).

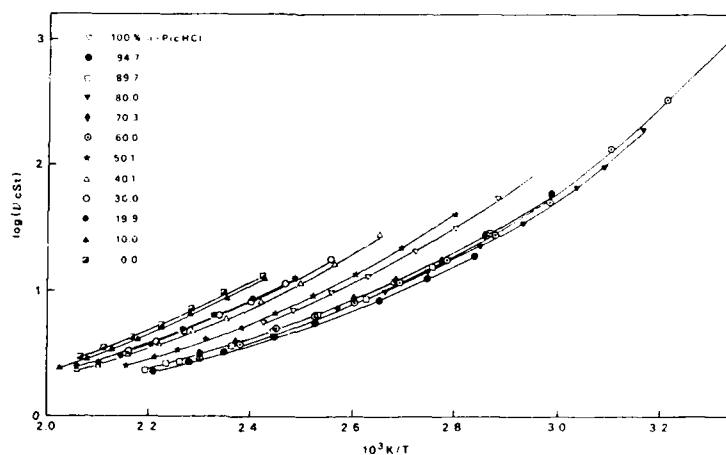


Fig. 1. Arrhenius plot of kinematic viscosity for solutions in the system α -pichCl+QHCl.

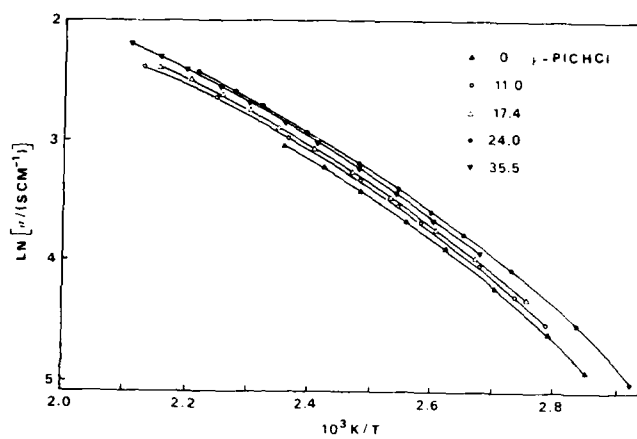


Fig. 2. Arrhenius plot of electrical conductivity for solutions in the system α -picHCl + γ -picHCl.

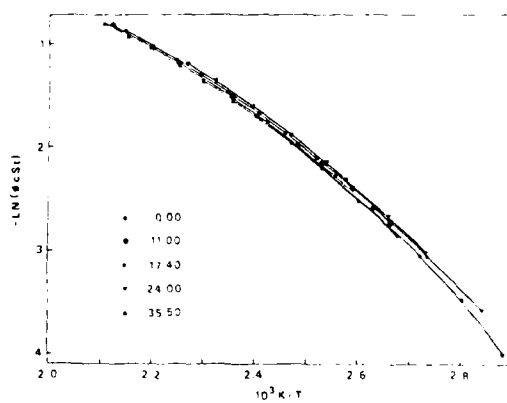


Fig. 3. Arrhenius plot of kinematic fluidity for solutions in the system α -picHCl + γ -picHCl.

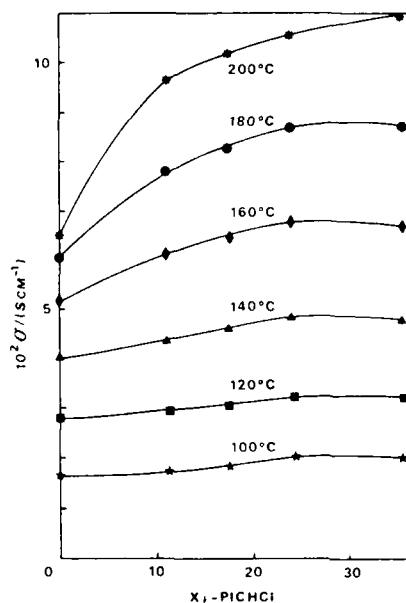
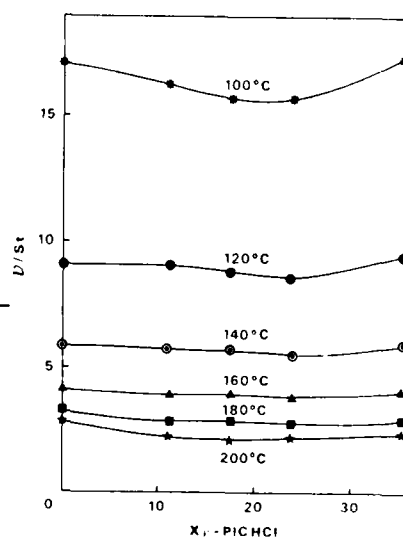


Fig. 4. Isothermal plots of electrical conductivity as a function of γ -picHCl content in the system α -picHCl + γ -picHCl.

Fig. 5. Isothermal plots of kinematic viscosity as a function of γ -picHCl content in the system α -picHCl + γ -picHCl.



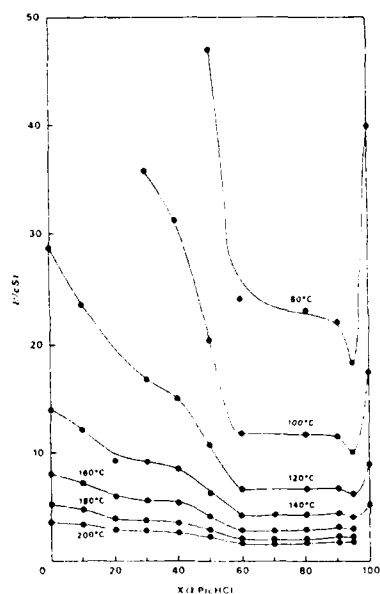


Fig. 6. Isothermal plots of kinematic viscosity as a function of α -picHCl content in the system α -picHCl+QHCl.

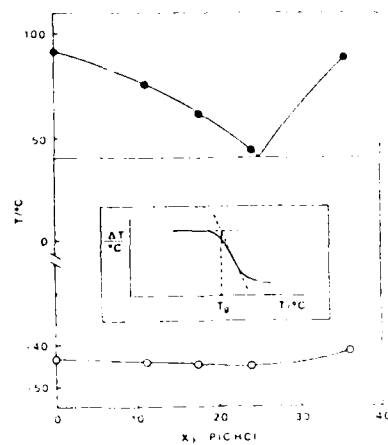
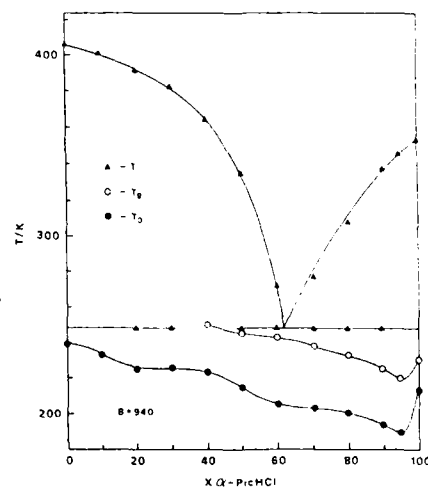


Fig. 7. Partial phase diagram for the system α -picHCl+ γ -picHCl and glass transition temperatures.

Fig. 8. Phase diagram for the system α -picHCl+QHCl and glass transition temperatures.



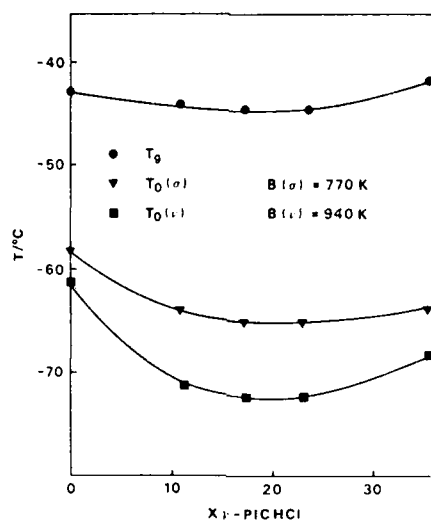


Fig. 9. Glass transition temperatures $T_0(\sigma)$, $T_0(\nu)$ and T_g for the system α -picHCl + γ -picHCl.

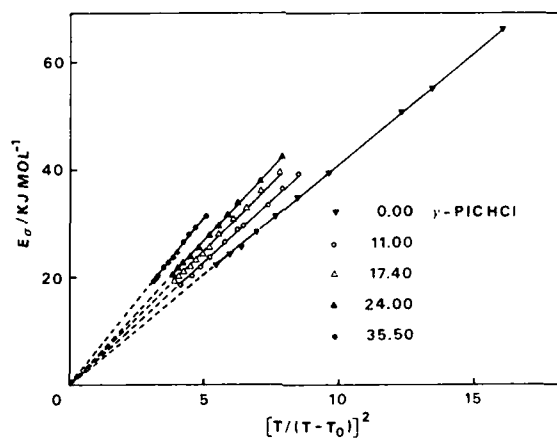


Fig. 10. Activation energy as a function of $(T/(T-T_0))^2$ for the system α -picHCl + γ -picHCl.

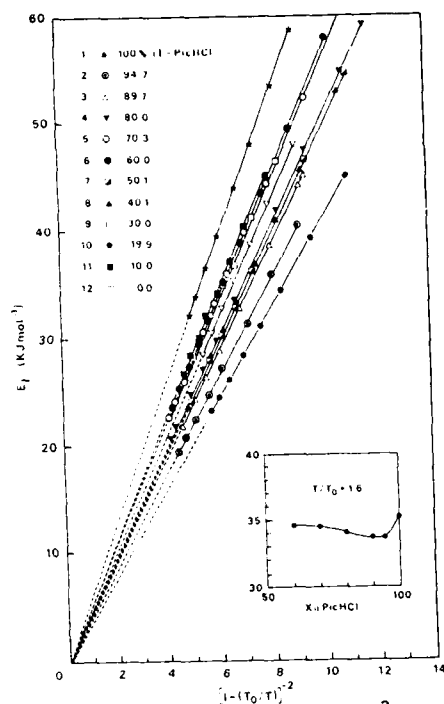
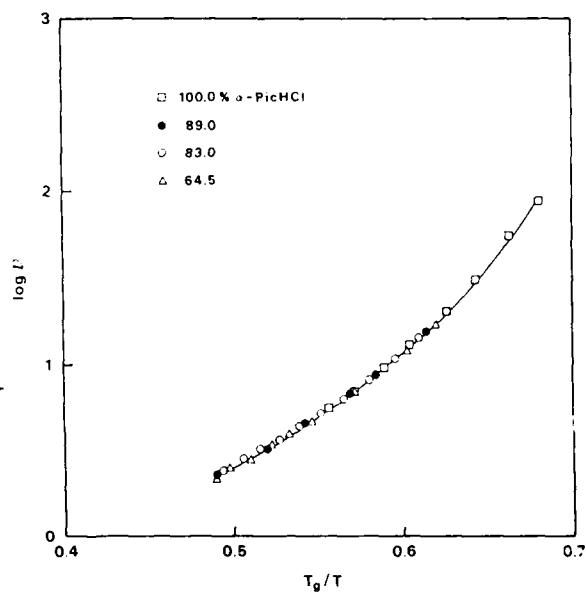


Fig. 11. Activation energy as a function of $(1 - (T_0/T))^{-2}$ for the system α -picHCl + γ -picHCl.

Fig. 12. T_g -reduced Arrhenius plot of viscosity for the system α -picHCl + γ -picHCl



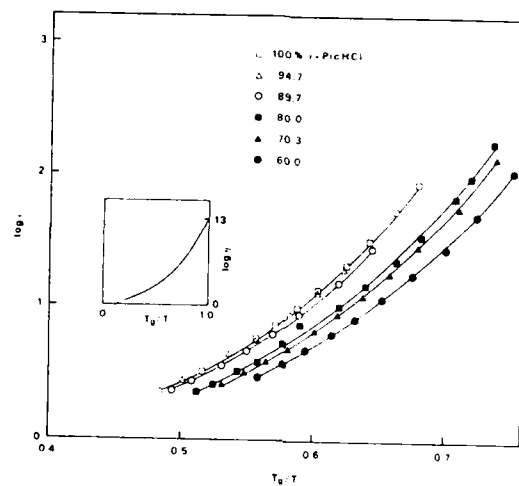


Fig. 13. T_g -reduced Arrhenius plot of viscosity for the system α -picHCl+QHCl.

Viscosity Measurements: Molten Ternary Carbonate Eutectic.

Tatsuhiko Ejima, Yuzuru Sato, Tsutomu Yamamura, Kyoko Tamai, and Masayuki Hasebe
Department Of Metallurgy, Faculty Of Engineering, Tohoku University
Sendai 980, Japan

Mark S. Bohn
Solar Energy Research Institute, Thermal Research Branch, Golden,
Colorado 80401, USA

George J. Janz
Rensselaer Polytechnic Institute, Molten Salts Data Center, Department Of Chemistry, Troy, New York 12181, USA.

ABSTRACT

Modelling calculations of falling molten salt films in direct absorption solar energy receivers led directly to questions concerning the reliability of the viscosity data for the ternary carbonate eutectic. The present work was undertaken to resolve this dilemma. A number of performance problems were encountered. The resolution of these and the results for viscosity measurements to 900°C for this molten carbonate system are reported. The results differ markedly from the earlier work, and possible reasons for this are examined.

INTRODUCTION

The molten ternary carbonate eutectic is of interest as a candidate heat transfer medium in solar energy storage applications(1-3). Doubts on the reliability of the previously measured values have emerged in recent heat transfer calculations by Bohn, and quite independently and almost concurrently, from viscosity data by Ejima and Sato for molten Na_2CO_3 . In the former it was found necessary to assume viscosities approx. 3.5 times larger in order to bring the modelling calculations into agreement with the observed thicknesses of the flowing salt films. The present work was undertaken to try to resolve this dilemma. The investigation was extended to include some work with eutectics from commercial grade quality carbonates, and these results are also reported.

EXPERIMENTAL

All measurements were made with the high temperature facility at Tohoku University in which the damped oscillational technique and working equations for calculating the viscosities on an absolute basis are used. The viscometer, as seen from Figs. 1 and 2, is computer-coupled for data acquisition and data reduction to final values. For the torsion wire, the Kestin alloy (8% W - 92% Pt) was used. This alloy has a stable constant of elasticity, a low internal friction, and is easily annealed stress free(4,5).

Samples of the eutectic (mol %: Li_2CO_3 , 43.5; Na_2CO_3 , 31.5; K_2CO_3 , 25.0; m.pt. 397°C) were prepared in kg. amounts from Reagent Grade salts, and melted to gain sample homogeneity. To repress decomposition, all transfers were under CO_2 atmospheres. For further pretreatment of samples in the viscometer, see later.

In Fig.3 measurements for molten NaCl are shown. The performance of the viscometer is thus confirmed to be within 2.5% of the recommended values from the Molten Salts Standard Program (6,8). However when measurements were started with the eutectic, a series of performance problems were encountered. As these appeared unique to work with molten carbonates, the resolution of these were important steps to meaningful results.

Log(visc) vs. T^{-1} Correlation: The temperature - viscosity data for "well behaved" ionic salt systems generally may be expressed by an exponential function of the form:

$$\text{viscosity} = A \exp (E/RT)$$

and from this, the correlation:

$$\log(\text{visc}) = \text{constant} + (E/R)\{T^{-1}\}$$

provides a ready graphical check on the progress of the measurements, i.e., a straight line having a slope of (E/R) . In the early stages of the present measurements with the molten eutectic, an apparent failure of this criterion was observed. As seen in Fig.4, the correlation held well for measurements above 700°C , but failed quite abruptly and dramatically at approx. 700°C . When measurements were extended to lower temperatures, the slope changed as shown from positive to negative values. When the cause for this "failure" was resolved, it was found to be due not to anomalous melt properties, but rather to the limitations of the viscometer. The dimensions of the crucible in this series of measurements were [20mm i.d. x 88mm], and this size is suitable for fluids with viscosities up to $\approx 10 \text{ mPa}\cdot\text{s}$. Apparently in the work with the molten eutectic, this limit was being reached at 700°C , and being exceeded below this temperature. With larger cru-

cibles meaningful measurements could be extended down to 600°C as the lower limit. The physical limitations imposed by the hot zone dimensions precluded further increases in crucible size; the temperature range for the measurements in the present study was limited accordingly.

Melt Creep: In the damped oscillational technique, as in this work, the molten salt is virtually hermetically sealed in the (cylindrical) crucible via a tightly fitting cap. The viscosities are derived from measurements of the damping effects of the fluid thus confined on the oscillations of the crucible. With the molten carbonate, it was found that the measured viscosity at each temperature did not remain constant, but continued to vary. Inspection of the crucible "post measurements" showed that the outer surfaces had been wetted by the melt, and, indeed, a small pendant drop of the carbonate was hanging externally on the crucible bottom. This melt creep complication was resolved through a series of steps as follows. Melt treatment: The eutectics were rigorously pretreated, as already noted, by heating under vacuum up to the melting point (397°C), and then CO₂ equilibrated by bubbling the gas through the melt for ≈ 12 hr at 700°. An atmosphere of [helium with 50 Torr CO₂] was used in the viscometer during the measurements. This CO₂ partial pressure is larger than the equilibrium dissociation pressures of molten carbonates at these temperatures and yet less than the pressures that introduce instability to the oscillations of the crucible. In this way the melt compositions were effectively held invariant. Gold plating: To minimize wetting by the molten carbonate, the nickel crucible surfaces were gold plated. Venting: Through a series of test measurements, it was observed that the melt creep occurred principally in the initial stages of a measurement series, i.e., as if melt degassing was occurring, and this apparently led to a forced "gushing" of the melt through the (machine threaded) seal. Accordingly, two small holes as vents were drilled in the crucible cap. The "vented cap" modification proved very effective in minimizing this "gushing" and was used throughout the measurements reported herewith.

The overall weight loss from the crucible was thus minimized to 0.3% or less. Corrections for this were made in the iterative calculations of viscosities.

A further correction, namely the "meniscus effect correction", has been quantitatively examined by Brockner, Tørklep, and Øye (10). Under the conditions used in the present study (refer: above), the uncertainties due to this possible error source appear to be less than 2%, i.e., well within the overall accuracy limits of $\pm 3\%$ for the present measurements.

RESULTS AND DISCUSSION

Table 1 lists the measured viscosities for Reagent Grade ter-

nary carbonate eutectic. Each value is the average of 4 - 6 determinations. Measurements were limited to $\approx 650^{\circ}\text{C}$ as the lower limit so as to stay well above the cut-off of 600°C (see, earlier). The correlation from this data set, is:

$$\text{visc}(\text{mPa}\cdot\text{s}) = 0.10120 \exp(33400/RT)$$

where $R = 8.3143 \text{ J K}^{-1}\text{mol}^{-1}$. Use of this for extrapolations down to 500°C , and lower receives firm support from the linearity of the $\{\log(\text{visc}) - T^{-1}\}$ criterion.

In Fig.5, these results are compared with the measurements reported earlier by Janz and Saegusa(11). The confidence level in the present work is high. The problem, thus, is to understand the factors in the earlier work that led to such markedly lower values.

In the earlier work, melt densities (in the calculations) were estimated from single salts data and theoretical principles. In the present work, measured values(12) were used. The estimated densities would lead to viscosities $\approx 10\%$ lower than the correct values.

A "voids effect" as a possible error source suggests itself directly from a result found in the present study, namely the need for the "vented cap" for measurements with the carbonate eutectic. The adherence of the gases on the interior crucible walls (as a firmly adsorbed gaseous film) would lead to a "voids effect". Since a radius larger than the actual radius of the melt is now being "input" into the working equations, the calculated viscosities would be smaller than the true viscosities. Modelling calculations (based on the parameters of the viscometer in the present work) show that for voids equivalent melt radius decrease of $\approx 20\%$, the calculated viscosities would be $\approx 65\%$ lower than the true (correct) values.

Additional factors as possible error sources could be listed, but the magnitudes cannot be estimated quantitatively and further discussion is deferred accordingly. From the preceding considerations, it appears that the disagreement can be resolved in large part through the possible presence of a firmly adsorbed gaseous film on the inner crucible surface, and that this "voids effect" undoubtedly escaped detection in the earlier study.

As stated earlier in the communication, measurements were extended to eutectics from commercial grade quality carbonate salts (overall purity: 98.4%, based on carbonate content). Without the CO_2 equilibration of these (see: melt treatment), meaningful measurements were not possible. After these were CO_2 equilibrated, the viscosities were virtually the same as the values found for the Reagent Grade ternary carbonate eutectic herewith (Table 1).

ACKNOWLEDGMENTS

This work was made possible, in large part, by financial support at RPI and at Tohoku University from the Solar Energy Research Institute under Contract DE-AC02-83CH110093 at that site.

REFERENCES

1. R.T.Coyle, R.J.Copeland, R.W.Burrows, and R.M.Gaggin, "High Temperature Molten Salts For Use In Solar Thermal Energy Systems". SERI/TR-255-2001 (1983); Solar Energy Research Institute, Golden, CO 80401.
2. M.S.Bohn, H.J.Green, G. Yeagle, J.Siebarth, O.D.Asbell, and C.T. Brown, "Direct Absorption Receiver Experiments And Concept Feasibility". SERI/TR-252-2884 (Oct.1986); Solar Energy Research Institute, Golden, CO. 80401.
3. M.S.Bohn, J.Solar Energy Eng.(ASME), 107, 208 (1985).
4. J.R.Kestin and J.M.Mosynski, Brown University Report AF891/11 (July, 1958); AFOSR-7N-752, ASTIA Doc. # 201,576.
5. R.S.Marvin, J.Research Nat.Bur.Stds., 75A, 535 (1971).
6. K.Tørklep and H.A.Øye, J.Phys.E.Sci.Inst., 12, 875 (1979).
7. T.Ejima, K.Shimakage, Y.Sato, H.Okuda, N.Kamada, and A.Ishigaki, Nippon Kagaku Kaishi, 6, 961 (1982).
8. G.J.Janz, J.Phys.Chem.Ref.Data, 9(4), 791 (1980).
9. G.J.Janz, T.Yamamura, and M.Hansen, MSDC-RPI, pre-publication results (1986).
10. W.Brockner, K.Tørklep, and H.A.Øye, Ber.Bunsenges.Phys.Chem., 83, 1 (1979).
11. G.J.Janz and F.Saegusa, J.Electrochem.Soc., 110, 452 (1963).
12. A.T.Ward and G.J.Janz. Electrochimica Acta, 10, 849 (1965).

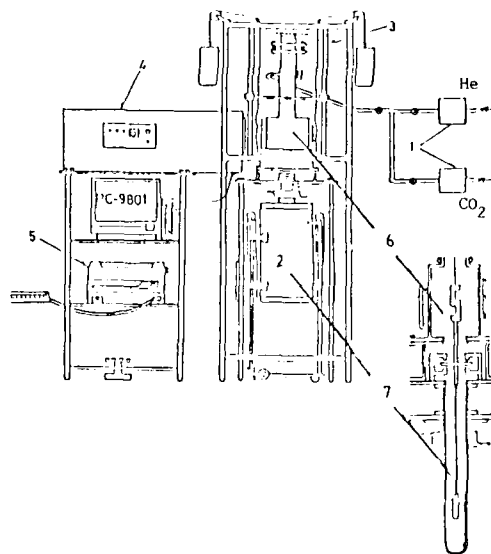


Fig.1. High Temperature Viscometer Facility

- 1: gas purifier
- 2: resistance furnace
- 3: guides
- 4: recording device
- 5: data processing computer
- 6: Mirror
- 7: Crucible

Fig.2. Iterative Calculation Of Viscosity

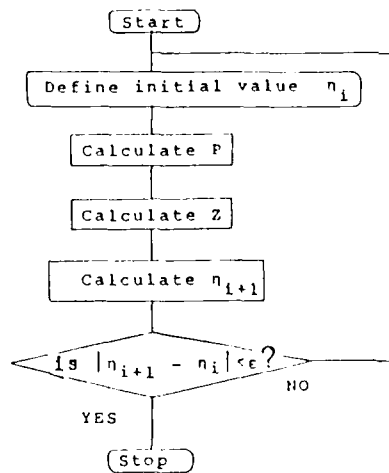


Table 1. Eutectic Viscosity: Measured Values.

T (K)	Viscosity (mPa·s)
922.6	8.058
972.2	6.326
1021.9	5.090
1071.5	4.290
1122.1	3.635
1172.1	3.148
970.9	6.184

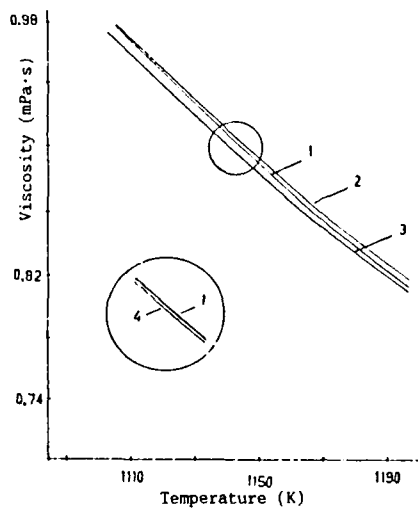


Fig.3. Comparisons Of NaCl Measurements

Shown: curve 1,(6,8); curve 2,(7); curve 3, this work; curve 4 [inset], predicted (9).

Fig.4. Eutectic Viscosity.

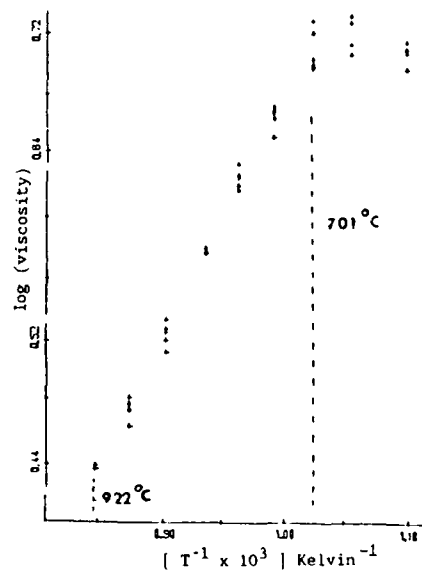
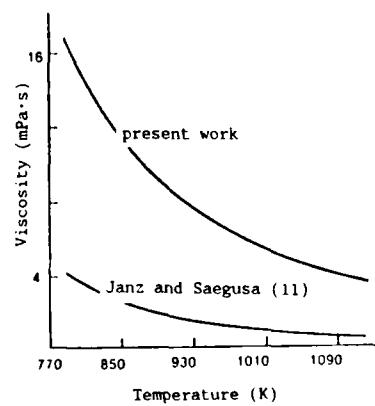


Fig.5. Comparisons with Previous Work.



ULTRASONIC AND HYPERSONIC SPECTROSCOPY OF ALKALI
NITRATE SINGLE AND BINARY MELTS

T. Ejima, T. Yamamura and K. Zhu

Department of Metallurgy, Tohoku University
Sendai 980, Japan

ABSTRACT

Sound propagation in the molten alkali nitrate single salts, LiNO_3 , NaNO_3 , RbNO_3 and CsNO_3 and the binary melts, $\text{NaNO}_3\text{-LiNO}_3$, -RbNO_3 and -CsNO_3 , have been studied over the frequency range of 5-25 MHz and 3-8 GHz by means of pulse and Brillouin scattering methods, respectively. A dispersion of sound propagation is observed at the frequency between ultra- and hyper-sound region for KNO_3 , RbNO_3 and CsNO_3 . The thermodynamic properties derived from the sound velocity are approximately additive for the binary melts investigated. The bulk viscosity, η_b , was derived from the absorption coefficient determined. The value of $d\eta_b/dT$ is negative and temperature dependence of η_b/η_s is insignificant for the molten alkali nitrate single salts. The bulk viscosity of the binary melt decreases rapidly with the addition of the component having smaller bulk viscosity in pure salt.

INTRODUCTION

Molten alkali nitrate mixtures have been considered as one of the most promising candidates for a heat storage medium at high temperatures because of its wide temperature range of chemical stability. However, the structure of molten alkali nitrate is not as simple as a typical ionic melt such as an alkali halide because of the existence of associated species. Sonic spectroscopy is one of the most effective methods of detecting the existence of associated species which cause the structural relaxation in sound propagation. In the present study, sound velocities in the molten alkali nitrate single salts, LiNO_3 , NaNO_3 , KNO_3 , RbNO_3 and CsNO_3 and binary salts, $\text{NaNO}_3\text{-LiNO}_3$, $\text{NaNO}_3\text{-RbNO}_3$, $\text{NaNO}_3\text{-CsNO}_3$ have been measured over the frequency ranges of 5-25MHz and 3-8GHz by means of pulse and Brillouin scattering methods, respectively. Ultrasonic and hypersonic velocities measured are compared with each other to elucidate the relaxation process of sound propagation in the melts. Ultrasonic absorption coefficients have been measured to determine the bulk viscosities for the binary melts. Relaxation times have been derived from the hypersonic and ultrasonic velocities and bulk viscosity on the basis of a relaxation theory with a single relaxation time. Thermodynamic properties such as adiabatic compressibility, constant pressure heat capacity, isothermal compressibility and internal pressure were obtained.

EXPERIMENTAL

ULTRASONIC SPECTROSCOPY

The propagation velocity of ultrasound in molten alkali nitrate has been measured by the use of a pulse method. Details of the pulse method was described elsewhere¹¹. The sound pulses piezoelectrically generated by a X-cut quartz crystal are introduced into the melts through a lower conduction rod made of fused quartz. The sound pulses propagated through the melt are received by an upper conduction rod made of fused quartz and is transduced into electrical signals by a quartz crystal attached to the end of the upper conduction rod. The sound velocity and absorption coefficient are determined from the measured delay time and the amplitude change accompanying the displacement of the spacing between the upper and lower conduction rods. The measurement was carried out over the temperatures ranging from the melting point of the salt to about 150K above it. The maximum of the error is estimated to be less than 0.2% for the sound velocity and 3% for the absorption coefficient determination.

BRILLOUIN SCATTERING METHOD

As predicted by Brillouin, the light scattered by a homogeneous liquid consists of a central Rayleigh line with the same frequency as that of a exciting light, and a doublet of which the components are shifted in frequency symmetrically from the frequency of the exciting light. The latter is induced by the collision of a photon and a phonon in the liquid under thermal equilibrium. The frequency shift $\Delta \nu$ between the Brillouin peak is expressed as follows:

$$\Delta \nu = \pm 2 \nu_l n (V_s / c) \sin \theta \quad (1)$$

where ν_l is the frequency of the exciting light, n is the refractive index of the liquid, V_s and c are the velocities of sound wave and light respectively, and θ is the scattering angle. The frequency shift is also equal to the frequency of sound wave which induces the light scattering. The sound velocity can be obtained from the frequency shift and the scattering angle.

A schematic diagram of the experimental apparatus used for the measurement of Brillouin scattering is shown in Fig.1. The system is composed of a light source, a high temperature cell, and a Fabry-Perot interferometer. The light from the He-Ne gas laser is modulated to 225Hz by the use of an optical chopper. The modulated light is then focused upon the cell placed in an electric furnace. The light scattered at an angle of θ is focused on a pin hole with a collecting lens and is collimated with a lens. The light passed through the interferometer is focussed and is changed into electrical signals with a photomultiplier. Reagent grade alkali nitrate is dried at 393K for 24 h in vacuo, melted in argon atmosphere and filtered through a sintered Pyrex glass disk to remove small suspended inclusions. The filtrate is poured into a cylindrical cell made of Pyrex glass and the cell is sealed under vacuo.

RESULTS AND DISCUSSION

SOUND VELOCITY AND ABSORPTION OF ALKALI NITRATE SINGLE SALTS

Frequency shifts of Brillouin peaks for molten alkali nitrates were measured over the temperature range of their melting points to 820K at scattering angles of 45, 90 and 135 deg. The velocity of hypersound was determined from the observed frequency shifts in the sound frequency ranges of 7-8 GHz for LiNO_3 , 2-7 GHz for NaNO_3 , and 3-8 GHz for CsNO_3 . In these frequency ranges sound velocity appears to be independent of frequency.

Ultrasonic velocity were measured in the frequency range of 5-25 MHz for LiNO_3 , NaNO_3 and KNO_3 , and 5-15 MHz for RbNO_3 and CsNO_3 . The ultrasonic velocity does not exhibit frequency dependence for these salts.

The ultrasonic and hypersonic velocities obtained were plotted against temperature and are shown in Fig.2. It can be seen from Fig.2 that both ultrasonic and hypersonic velocities monotonously decrease with increasing temperature. However, in case of ultrasonic velocity a curve linear relation is found for all the single salts investigated. As shown in Fig.2 both ultrasonic and hypersonic velocities decrease with increasing cation-size except for LiNO_3 . When the hypersonic and ultrasonic velocities are compared with each other for each alkali nitrate, both velocities agree well within the limit of the experimental error for molten LiNO_3 and NaNO_3 . On the contrary, the difference between hypersonic and ultrasonic velocities clearly exceeds the limit of the experimental error for KNO_3 , RbNO_3 and CsNO_3 . The observed dispersion of the sound propagation indicates that the relaxation frequency of KNO_3 , RbNO_3 and CsNO_3 are more than the highest of the ultrasonic measurement and less than the lowest frequency of the Brillouin scattering measurement. The relaxation frequencies of LiNO_3 and NaNO_3 are more than the highest frequency of the Brillouin scattering measurement. Relaxation behavior of the single salt will be examined in detail later in this section.

The absorption coefficient, α of the ultrasound was determined over the frequency range of 5-25 MHz for molten alkali nitrate single salts. The ratio of the absorption coefficient to the square of the frequency, α/f^2 are plotted against temperature and shown in Fig.3. The value of α/f^2 decreases monotonously with increasing temperature. The bulk viscosity was determined from the absorption coefficient measured by the use of the following equation,

$$\eta_s = 4\eta_s ((\alpha_{obs} / \alpha_s) - 1)/3 \quad (2)$$

where η_s is the shear viscosity, α_{obs} is the observed absorption coefficient and α_s is the absorption coefficient due to shear viscosity expressed by Eq. (3).

$$\alpha_s = 8 \pi^2 f^2 \eta_s / 3 \rho v^3 \quad (3)$$

where f is the frequency, ρ , the density, v , the velocity of ultrasound. As shown in Fig. 4 showing the temperature dependence of the bulk viscosity, the bulk viscosity decreases with increasing temperature and cation-size for alkali nitrates. Figure 5 shows the temperature dependence of the ratio of η_B / η_s . The values of η_B / η_s are approximately constant with temperature change for LiNO_3 and NaNO_3 . Even in maximum case of KNO_3 , the change of the value is less than 15 % with the temperature change of 150 K. As the origin of the bulk viscosity in the molten alkali nitrates thermal relaxation and structural relaxation are possible. The former arises from the slow interchange of energy between the external and internal degrees of freedom and is typical for nonassociated liquids. On the other hand, the latter is the case for the associated liquids which has structural order due to strong intermolecular bonding. According to the classification of Higgs and Litovitz¹² in the associated liquid $d\eta_B/dT$ is negative, and η_B / η_s is approximately constant with temperature and rarely has a value above 5. As described above, negative $d\eta_B/dT$ and constancy of η_B / η_s with temperature observed in this study suggest that the bulk viscosity of the alkali nitrate originates in the structural relaxation and the molten alkali nitrate appears to be an associated liquid. However, it should be noted that the values of η_B / η_s of KNO_3 , RbNO_3 and CsNO_3 exceed by far 3.5 which is the maximum for the hydrogen bonded associated liquids. This fact suggests that the long range coulombic interaction among the constituent ions in the molten alkali nitrates causes the structural relaxation more than the hydrogen bond does.

Since the dispersion of sound propagation was observed in the alkali nitrates, detailed consideration has been given to the relaxation behavior under the assumption that relaxation with a single relaxation time, which has been successfully applied to some molten salts by Knappe and Torelli¹³ can also be applied to the present results. On the assumption that relaxation has a single relaxation time τ , an equation for a static bulk viscosity η_B has been derived by Montrose et al.¹⁴

$$\eta_B = \rho (V_\infty^2 - V_0^2) \tau \quad (4)$$

where ρ is the density of the medium, V_∞ and V_0 are sound velocities at the limiting high and low frequencies respectively. The relaxation time was calculated from the ultrasonic velocity for V_0 , the ultrasonic bulk viscosity for η_B and hypersonic velocity for V_∞ . The relaxation times determined at 700 K are listed in Table I. The relaxation time increases with increasing cation-size in accord with the behavior of bulk viscosity with cation-size.

SOUND VELOCITY AND ABSORPTION IN ALKALI NITRATE BINARY MELTS

Sound velocity of NaNO_3 , LiNO_3 , RbNO_3 and CsNO_3 binary melts have been measured over the frequency range of 5-25 MHz by means of the pulse method. Figure 6 shows the composition dependence of the adiabatic compressibility at 650 K and 600 K for NaNO_3 - RbNO_3 binary melts. In Fig. 6, thin solid line represents the adiabatic compressibility calculated on the

basis of the volume additivity. The observed compressibility deviates positively from the additive line. But the extent of the deviation is as small as 2 % even at the maximum. The composition dependence of such thermodynamic properties as isothermal compressibility, constant pressure heat capacity and internal pressure have been examined, and it has been found that these thermodynamic properties of the alkali nitrate mixtures do not deviate much from the values calculated on the basis of the additive rule.

On the contrary to the thermodynamic properties, the bulk viscosities of NaNO_3 - LiNO_3 , NaNO_3 - RbNO_3 , and NaNO_3 - CsNO_3 binary melts deviate from the linear additivity as clearly shown in Fig.7 showing the relation between the bulk viscosity and composition. As shown in Fig.7, the bulk viscosities of NaNO_3 - CsNO_3 and NaNO_3 - RbNO_3 binary melts decrease rapidly with increasing NaNO_3 content upto 20 mol% NaNO_3 . Further addition of NaNO_3 decreases the bulk viscosity slightly. As for NaNO_3 - LiNO_3 binary melts, bulk viscosity decreases monotonously with increasing LiNO_3 content. Since the difference between the bulk viscosities of NaNO_3 and LiNO_3 is small, a change in the bulk viscosity with composition is slight. However, the same composition dependence of the bulk viscosity as that of NaNO_3 - RbNO_3 and NaNO_3 - CsNO_3 can be seen, i.e., the bulk viscosity of the binary melt decreases rapidly to approach that of the pure additive on addition of a component which has smaller bulk viscosity in pure melt. The observed behavior of the composition dependence of the bulk viscosity may be explained in terms of relaxation time in the following manner. The relaxation of the sound propagation in the binary melts seems to be structural one in analogy with the relaxation process of the pure component melts. The relaxation time of the binary melts may be controlled by the motion of the constituent having shorter relaxation time in pure component melt because the relaxation time is related to the time in which rearrangement of the constituent particles occur upon the passage of sound wave. Therefore, the viscosity of the binary melts decreases rapidly with the addition of the component having smaller bulk viscosity in the pure melt and approach the value of the pure melt of the additive.

REFERENCES

- (1) T. Ejima and T. Mitsuhashi, *J. Japan Inst. Metals*, **39**, 687(1975).
- (2) R. W. Higgs and T. A. Litovitz, *J. Acoust. Soc. Am.*, **32**, 1108(1960).
- (3) L. M. Torell and H. E.C. Knape, *Z. Naturforsch.*, **34a**, 899(1979).
- (4) C. J. Montrose, V. A. Solov'yev and J. A. Litovitz, *J. Acoust. Soc. Am.*, **43**, 117(1968).

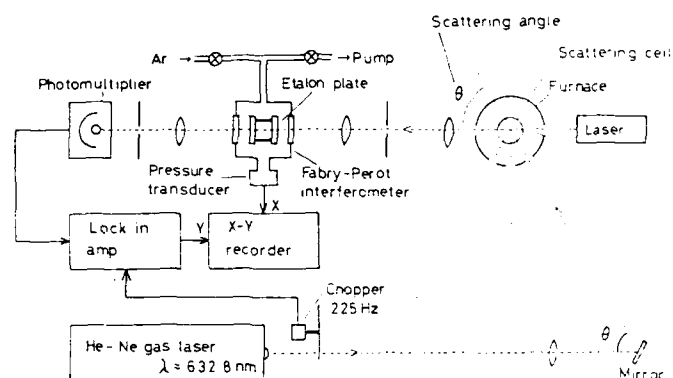


Fig. 1 Experimental arrangement for Brillouin scattering measurement.

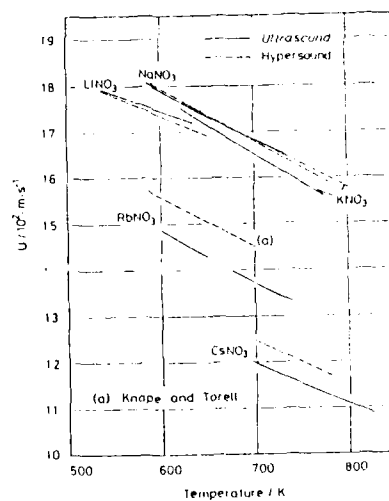


Figure 2 Temperature Dependence of Ultrasonic and Hypersonic Velocities for Molten Alkali Nitrate Single Salts.

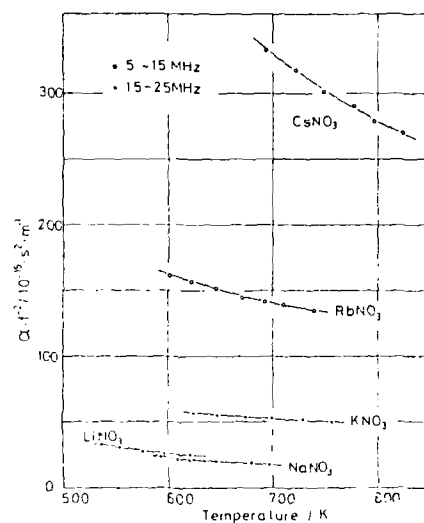


Figure 3 Temperature Dependence of Absorption in Molten Alkali Nitrate Single Salts.

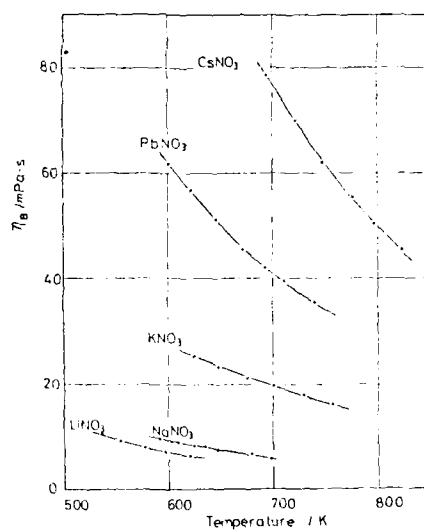


Figure 4 Temperature Dependence of Bulk Viscosity for Molten Alkali Nitrate Single Salts

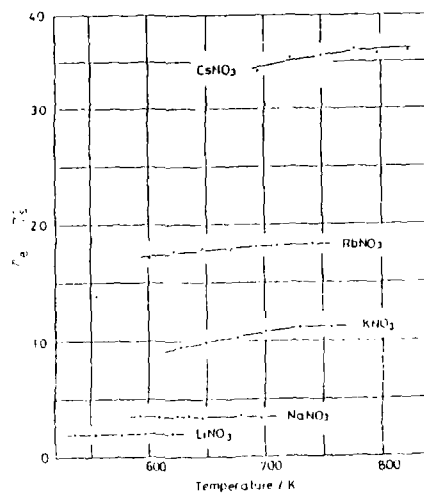


Figure 5 Temperature Dependence of η_s / η_L for Molten Alkali Nitrate Single Salts.

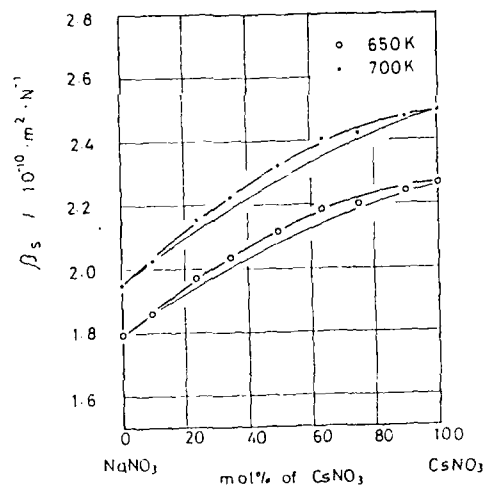


Figure 6 Composition Dependence of Adiabatic Compressibility for NaNO₃ - RbNO₃ binary melts.

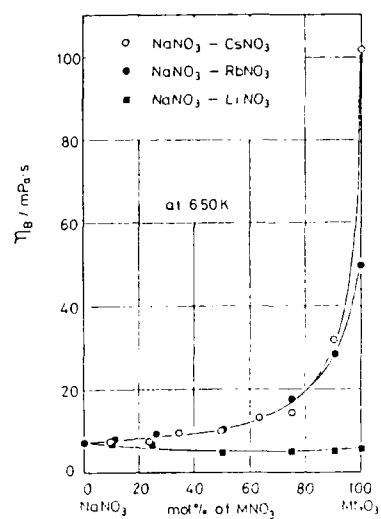


Figure 7 Composition Dependence of Bulk Viscosity for NaNO₃ - MNO₃ (M:Li,Rb,Cs) Binary Melts.

Table 1 Relaxation Time of Alkali Nitrate at 700 K

Salt	Relaxation Time/10 ⁻⁹ s
KNO ₃	0.045
RbNO ₃	0.085
CsNO ₃	0.23

SUPERCOOLING PHENOMENA IN ELECTROLYTE-AMIDE BINARY MIXTURES. ULTRASONIC AND DIELECTRIC STUDY SHOWING THE PRESENCE OF POLYMERIC STRUCTURES IN SUPERCOOLED MIXTURES : NaCNS , LiNO_3 , $\text{KCNS}/\text{CH}_3\text{CONH}_2$.

Gianfrancesco Berchiesi , Giovanni Vitali,
Giancarlo Gioia Lobbia and Ryszard Plowiec

Dipartimento di Scienze Chimiche dell'Università
Via S. Agostino 1, 62032 Camerino ; Italy

ABSTRACT

Cryoscopy, ultrasonic and dielectric measurements on Electrolyte-Amide binary systems show that at an amide mole fraction of about 0.5 complex structures are built. These structures are responsible for high values of dielectric constant.

INTRODUCTION

Binary mixtures of salts and organic compounds represent an intermediate situation between a typical ionic melt, where the interaction is prevalently electrostatic and a molecular melt, where the interaction is Van der Waals, hydrogen bond or dipole-dipole. The systems we are studying (amides+salt) are related to these problems and are of great interest because the interactions yield remarkably complex structures in a concentration and temperature range around the eutectic point, figure 1.

RESULTS AND DISCUSSION

Cryoscopy (1-9) : salts derived from strong acids mixed with amides give highly viscous liquids that supercool easily in the eutectic zone.

In some cases (principally with Na^+ ion) the liquid supercools spontaneously and reaches the glass transition temperature ; in other cases (with other ions) the liquid supercools but can also crystallize; and sometimes the crystallization temperature depends on the cooling rate as well as

on the thermal history of the liquid (3).

Viscoelasticity (10-12) : Some of these mixtures have been studied with ultrasonic techniques. Using shear waves and the method of reduced variables, the viscoelastic relaxation spectrum has been determined for the mixtures NaCNS-Acetamide ($X_{\text{NaCNS}}=0.225$) and LiNO_3 -Acetamide ($X_{\text{LiNO}_3}=0.204$). In both the spectra a shift towards high frequencies in comparison with the Maxwell model has been observed; the shift is more accentuated in the system with NaCNS. The shift indicates the presence of retardation phenomena, whose nature is probably related to the formation of polymeric structures in these liquids, as the high values of viscosity (10) also allow us to hypothesize. Mathematical analysis of the results indicates that the polymeric structures are larger in the NaCNS mixture (12); figure 2 shows that in the NaCNS mixture the shift is half a decade, in the LiNO_3 mixture the shift is 1/5 of a decade. That is, in the NaCNS mixture 20-40% of the viscosity, and in the LiNO_3 system 62% of the viscosity is involved in the viscoelastic process; the remaining part is involved in retardation phenomena.

Ultrasonic spectrum (11-13) : Analysis of the ultrasonic relaxation spectra shows that:

- 1) in the system with Na^+ structural as well as chemical equilibria are present.
- 2) in the systems with Li^+ and K^+ only chemical equilibria are evident.

It is significant that the structural process in the NaCNS system is present in the ultrasonic range while in many liquids it occurs in a higher frequency range; this fact may be related to the presence of polymeric structures which are larger in comparison to other mixtures.

The chemical process disturbs both structural and viscoelastic processes and may be ascribed to the rotation of polar groups (CONH_2) as also observed with dielectric methods.

Figure 3 shows the trend of the reduced imaginary part of the complex longitudinal modulus for the NaCNS mixture. In the other mixtures a reduced plot was not obtained. (n_v/n_s)=2/3 for the NaCNS mixture in all temperature ranges investigated (structural process); (n_v/n_s) depends on temperature, for the other mixtures (chemical process), table 1.

Dielectric relaxation (14) : The mixture NaCNS-Acetamide ($X_{\text{NaCNS}} = 0.225$) has also been investigated using the dielectric relaxation technique. Two relaxation phenomena have been found.

The radiofrequency phenomenon may be ascribed to the rotation of polar groups, the low frequency phenomenon (whose relaxation time is of the order of a second) is probably due to ionic migration, cooperative in nature, that is justified by the polymeric nature of this mixture. The cooperative motion of ions may explain the high value of the dielectric constant ($\sim 10^6$).

CONCLUSIONS

As a result of this research, we believe that three important points can be made:

- 1) Experimental evidence indicates that the salt-amide mixture may build polymeric structures in the eutectic zone.
- 2) The stability of these structures and their size do not only depend on the polarizing power of the ions. The alkali salts studied with ultrasonic technique exhibit the following order: $\text{NaCNS} > \text{LiNO}_3 > \text{KCNS}$.
- 3) These structures promote cooperative motion of the ions that is the cause of the megavalue of the dielectric constant.

Table 1. Ratio n_v/n_s at different temperatures

Salt	T, K	(n_v/n_s)
KCNS	300.2	0.16
	304.1	0.60
	308.3	0.90
LiNO_3	283.2	15.40
	298.2	1.73
	308.3	1.27

REFERENCES

- 1) F. Castellani, G. Berchiesi, F. Pucciarelli, V. Bartocci, J. Chem. Eng. Data, **26**, 150 (1981)
- 2) F. Castellani, G. Berchiesi, F. Pucciarelli, V. Bartocci, J. Chem. Eng. Data, **27**, 45 (1982)
- 3) G. Berchiesi, G. Gioia Lobbia, V. Bartocci, G. Vitali, Thermochim. Acta, **70**, 317 (1983)
- 4) G. Gioia Lobbia, G. Berchiesi, Thermochim. Acta, **72**, 301 (1984)
- 5) G. Gioia Lobbia, G. Poeti, Thermochim. Acta, **74**, 247 (1984)
- 6) G. Gioia Lobbia, G. Berchiesi, Thermochim. Acta, **74**, 251 (1984)
- 7) G. Gioia Lobbia, G. Berchiesi, G. Poeti, Thermochim. Acta, **75**, 297 (1984)
- 8) G. Berchiesi, G. Gioia Lobbia, M. A. Berchiesi, G. Vitali, J. Thermal Anal., **29**, 729 (1984)
- 9) G. Gioia Lobbia, A. Amico, Thermochim. Acta, **87**, 257 (1985)
- 10) G. Berchiesi, G. Vitali, P. Passamonti, R. Pkowiec, J. Chem. Soc., Faraday Trans. 2, **79**, 1257 (1983)
- 11) R. Pkowiec, A. Amico, G. Berchiesi, J. Chem. Soc., Faraday Trans. 2, **81**, 217 (1985)
- 12) G. Berchiesi, G. Vitali, A. Amico, J. Mol. Liquids, **32**, 99 (1986)
- 13) G. Berchiesi, F. Castellani, F. Pucciarelli, J. Pure Appl. Ultrason., **5**, 66 (1983)
- 14) A. Amico, G. Berchiesi, C. Cametti, A. Di Blasio, J. Chem. Soc., Faraday Trans. 2, in press (1987)

GLOSSARY

- n_v volume viscosity
 n_s shear viscosity

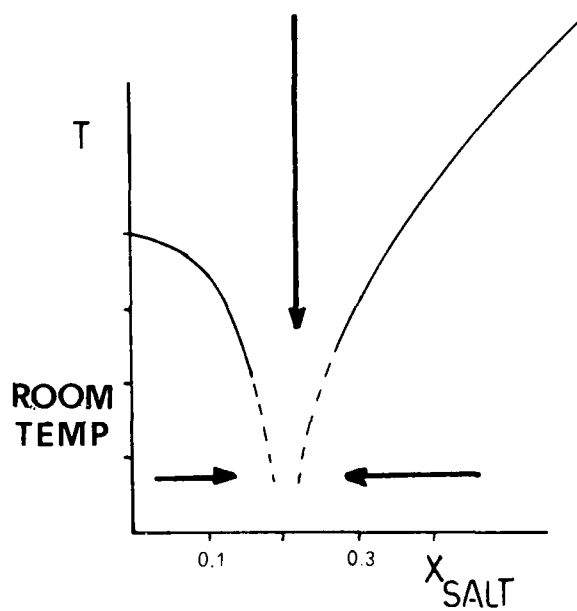


Figure 1. Schematic trend of Liquid-Solid equilibrium curve in binary systems Electrolyte-Amide. Supercooling phenomena occur in the dashed lines. The arrows indicate the increasing structural complexity of the mixture.

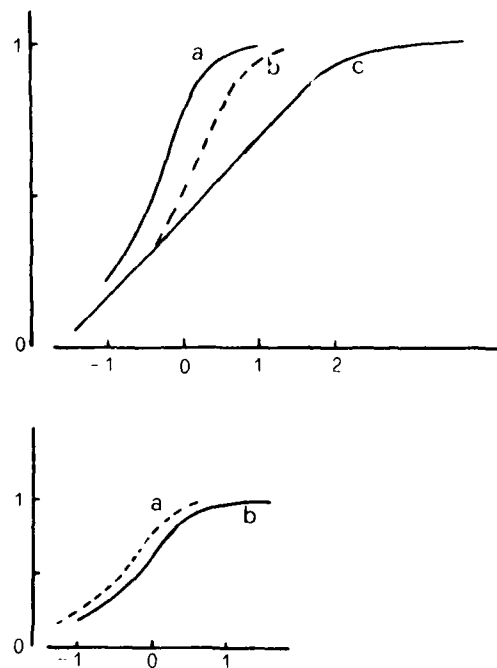


Figure 2. Vertical axis: reduced real part of the mechanical impedance. Horizontal axis: logarithm of the reduced angular frequency. Upper part: NaCNS-Acetamide mixture; a, Maxwell model; b, curve obtained at 31 and 87 MHz; c, curve obtained at 10 MHz. Lower part: LiNO₃-Acetamide mixture; a, Maxwell model; b, experimental curve.

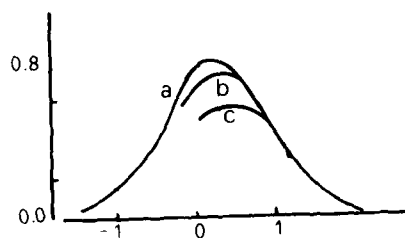


Figure 3. Vertical axis: reduced imaginary part of the longitudinal modulus. Horizontal axis: logarithm of the reduced angular frequency. Curve a, structural process; Curves b,c chemical processes concerning the mixture NaCNS-Acetamide.

SPACE THERMAL DIFFUSION EXPERIMENT IN A MOLTEN AgI-KI MIXTURE
"Theoretical Convection Approach
and Relation with in situ Measurement Results"

J. Bert, D. Henry,* H. Mellon, J. Dupuy

Universite Claude Bernard, Departement de Physique des Materiaux
69622 Villeurbanne Cedex

*Ecole Centrale de Lyon, Laboratoire de Mecanique des Fluides
B.P. 163, 69631 Ecully Cedex

ABSTRACT

The first measurement in Space of a Soret effect with an AgI/KI molten mixture is discussed as a new method of evaluating transport properties of molten salts without the perturbations of convection. The possibilities and requirements for this Space experiment are analyzed theoretically and experimentally, and new results are given dealing with wetting, interfacial properties of molten salts, and variations of the thermoelectric power with time. In each case, the comparison is made between the behavior of the molten salt on Earth and in Space, and the conditions for the theoretical convective stability are given. As a conclusion, the authors show that the interdiffusion coefficient in Space is significantly smaller than measured on Earth. This confirms some recent other Space diffusion experiments on liquid metals. It also confirms that the Soret coefficient corresponds to AgI migrating towards the cold end of the cell.

I. INTRODUCTION

The study of the liquid transport properties--electrical conductivity, diffusion, viscosity and thermal diffusion--should improve our understanding of the physical and chemical phenomena from a thermodynamic and dynamic point of view. In the case of ionic molten salts, the problem is simplified because of the absence of the usual dipolar solvent and because of the relative simplicity of these compounds. When a temperature gradient is applied throughout a binary mixture, a diffusion phenomenon appears, which leads to the partial separation of the constituents; this effect is called thermal diffusion or Soret effect. The separation created by the thermal diffusion expressed with a coefficient D' is limited by a back-diffusion with a coefficient D . An equilibrium state is reached in the system and is characterized by the Soret coefficient $S_T = D'/D$, which will be considered positive when the "heaviest" component migrates towards the cold side.

The Soret effect was intensely studied for molten salts in the sixties, either by direct analysis or by thermoelectric power measurements, see, for example, references (1) to (8). After 1970, most of these investigators left these studies for two reasons: first, they encountered theoretical difficulties interpreting their results; the problem was complex compared to the theoretical knowledge of the processes involved. Second, a great dispersion in the experimental results was generally obtained and attributed to convective disturbances (3), which could not be controlled and impeded further experimentation. Since this time, numerous computations, for instance molecular dynamics simulations, have been performed, thus offering a renewal of the interpretation possibilities. An important improvement for performing scientific experiments in new conditions has been offered by the multiplication of Space flights. This led to a new development of the transport properties studies in the liquids because the microgravity conditions allow one to assume complete disappearance of convection. However, the flight conditions only diminished quite notably the gravity levels, but did not annul them. It was then necessary to develop new kinds of calculations in order to know the influence of such reduced gravity levels.

In the case of molten salts, it is impossible to measure a Soret effect in normal gravity conditions (9). In a perfectly vertical situation, which should be the best situation, an equilibrium state is reached, which could be destabilized if the parameters of the system exceed the critical values corresponding to the onset of the instabilities. During an Earth experiment, the parameters correspond to the unstable domain where a convective motion is generated, except in the case of top heating with a positive Soret coefficient, which is an unconditionally stable situation. In fact, the perfectly vertical situation is impossible to obtain and small experimental imperfections cannot be avoided. In the case of top heating and a positive S_T , small departures from verticality will generate convective motions strongly perturbative if S_T is small. In addition, the thermal boundary conditions can create radial thermal gradients that will also generate convective perturbations. The complete numerical study (9) that we performed has permitted us to explain those problems encountered by experimenters, as mentioned above. Whatever the situation on Earth, the separation created by the thermal diffusion is always reduced, compared to the perfect one mentioned above, which only takes in account diffusive phenomena. This led us to perform our experiment on a molten AgI/KI mixture during the S1-Spacelab flight of October 1985 and also to control the convection effects in such a microgravity environment by simultaneous numerical simulations.

2. DEFINITION OF THE SPATIAL EXPERIMENT

2.1 Important Experimental Parameters

As has been seen above, the main problems encountered when measuring processes related to the diffusion in liquids are those coming from usual convection. However, this is not the only cause, and perturbations can be generated for at least two more reasons:

1. The surfaces, which are necessary because the experimental cell cannot have infinite dimensions, thus, in addition to the volume convection, a surface convection must be considered.
2. The free volumes existing inside the cell create bubbles, which will involve a continuous remixing of the molten mixture since their mobility could be much larger than that of the diffusion species. A supplementary surface effect can be added to the bubbles if they exist (Marangoni effect). The eviction of the free volumes is one of the most difficult problems that we had to solve, but we were helped by the salt expansion upon melting; all the excess volume could be absorbed by a porous material during the melting operation, if the material wetting and interfacial properties are known.

These first studies were performed during 1976-78 by Mellon (10), who defined the best conditions necessary for a successful Space experiment. He then calculated theoretically the isotherm surface tension for several molten mixtures with a model which had been successfully applied to binary and ternary metallic systems. In this model, the surface parameters are analogous to those of regular solutions proposed by Guggenheim (11) and by Defay and Prigogine (12) (quasi-structure of the liquid phase with no long distance interaction and separation of the degrees of freedom). Then the volumetric phase is related to the thermodynamic properties and the surface tensions when the physicochemical equilibrium is reached. It is concluded that, in contrast to liquid metals, the simple statistical model is not sufficient to explain the deviation from ideality observed for the surface tension measurements in molten salt mixtures. This study was then followed by calculations of the contact angles and shapes of the equilibrium meniscus as a function of the gravity values. Experimental $1-g$ determinations of the wetting properties (contact angles and surface tensions) of a molten AgI/KI mixture were also made by Mellon; he concluded that such an equimolar mixture wets imperfectly all materials with various contact angles ($40^\circ < \theta < 90^\circ$). The evolution with temperature is slight, but usual. We are now able to state that no fundamental change of these values appears under microgravity conditions.

2.2 Choice of the Experiment

The Space experiment consists of the measurement of the separation coefficient in a molten $\text{AgI}_{0.75}\text{KI}_{0.25}$ submitted to a strong temperature gradient. The choice of the type of molten salt has been discussed earlier (13, 14). Let us only mention that this salt has valuable characteristics from the thermal point of view (small thermal diffusivity compared to that of a liquid metal), as well as from the electrical point of view (very good ionic conductor). This led to a theoretical study for which we obtained a decoupling between the mass flux and the heat flux (9), and for which the microgravity will be of great interest, thus permitting the mass transfer created by the temperature gradient. Another reason for using this salt involves the method which can be used for the detection of the diffusion phenomenon in real time: the measurement of thermoelectric power. This type of measurement is greatly facilitated by using a silver salt, which allows the use of silver electrodes without being impeded by Space charge capacitance effects induced by blocking electrodes. The mixture composition (eutectic) has been determined while taking into account the minimum electrical power requirements (melting point 260°) as well as the probable maximum separation effect (related to the interdiffusion coefficient). In Figure 1, we give the most recent AgI/KI phase diagram obtained by Claudy and Letoffe (15), which is slightly different from others given in the literature, especially around the eutectic area.

The choice of the experimental cell takes into account the various problems, which are:

- no free volume (100% cell filling)
- electrically insulated cell with the possibility of measuring the thermopotential with silver electrodes
- chemical inertia and tightness at all temperatures
- maximum temperature gradient obtained by the heat flux inside the furnace
- flight security.

We chose to absorb the salt volume increase when melting occurs (10%) by use of a porous material cylinder (special variety of alumina) surrounding the salt. The choice of porous material was guided by its thermal characteristics, its wetting by the liquid, and its chemical reactivity. Some preliminary experiments helped us in the choice of the porosity (18% volume and $30\text{ }\mu\text{m}$ pore diameter) (16). The cell was made of an impervious alumina tube, this material having the best qualities for solving the problems mentioned above. For flight security, we were obliged to enclose the total cell inside a stainless steel tube. The experimental cell design inside the Space cartridge is given in Figure 2.

2.3 Determination of the Experiment Duration

The furnace used was the Gradient Heating Facility designed by the C.N.E.S. for a great number of users and mounted inside the Spacelab Material Science Double Rack. It is composed of three identical 22 mm diameter cartridges. The heating program has been carefully calculated as well as the thermal and geometric characteristics of the cartridges in order to obtain, in the shortest time, a stable temperature gradient (about 70°C/cm) combined with a minimum electric consumption (Space requirements). Successive trials on Earth combined with calculations gave a good value for the thermal coupling between the cell and diffusers. The thermal kinetics curve is given in Figure 3, which shows that the stable gradient is obtained within less than one hour. It can be maintained with a precision better than two degrees during several hours of experiments. The experiment duration was determined based on a preliminary result of Mellon (10), who measured the self-diffusion coefficients of the silver and potassium ions on Earth. He then calculated the interdiffusion coefficient of AgI/KI as a function of the mole fraction of KI and different temperatures. The curves given by Mellon clearly show that the interdiffusion coefficient is maximum for the eutectic composition (22% KI, according to Claudy and Letoffe). The maximum obtained D value is about $27 \cdot 10^{-5} \text{ cm}^2/\text{s}$. The evolution of the Soret effect separation with time can be approximated to the first order, by an exponential form. The time constant τ of this evolution is bound to L, length of the experimental cell, and to D, interdiffusion coefficient:

$$\tau = \frac{L^2}{\pi^2 D}$$

A quick calculation indicates that τ approaches one hour when $L = 3 \text{ cm}$.

One of the important problems of Space experiments is the experiment duration, for two reasons. The first comes from the economics of a Space flight, which encourages completing the maximum number of experiments. The second comes from the energy, which is necessary for an experiment to be undertaken. Both the flight organizers, as well as the experimenters, have to take into account these problems. According to these requirements, it has not been possible for us to maintain isothermal conditions during a sufficient time for equilibrium or to use the total cartridge volume in order to complete two different experiments in each of the three cartridges. Other problems come from the fact that, because the maximum number of experiments must be performed in a minimum volume, some perturbations can be induced by other experiments working at the same time. These perturbations can come from the vacuum system, which is common to several racks, as well as from movements (astronauts or experiments) inducing residual accelerations, as well as from astronauts

themselves who have to undertake considerable work, sometimes when being space-sick, or more simply missing some experiments despite their long training on Earth before the flight.

We thus fixed our experiment duration to five hours, with stable gradient, assuming that the stationary state is obtained. This adds up to about six hours with the furnace working, and seven hours when taking into account the checking of the cartridges and the heating program, plus the time necessary to obtain a sufficient vacuum. We must add that the total experiment was automatic after the astronauts had closed the furnace door (the heating program had been prepared on memories, which could not be modified when running, except for the total break off of the experiments).

3. RESULTS

3.1 Thermoelectric Potential Evolution

This first Soret-effect Space experiment on a molten salt was fully successful. We were able to measure a thermoelectric emf in the three closed impervious cells containing the molten salt. In addition, it was decided during the flight itself that another run with three cartridges could be performed at the end of the mission, when all other experiments had been made. This supplementary experiment was made with the Space cartridges, which had been loaded on board the Spacelab. This second run further confirmed, with three new cartridges, the possibility of measuring thermoelectric power under good conditions in Space. In fact, these two runs were performed under quite different conditions: during the first run, there were continuous activations-deactivations coming from other experiments, thus creating vacuum problems involving temperature variations. On the other hand, the second run was made during very quiet conditions, with no resulting temperature problems. In each experiment, we used two sizes of porous tubes:

- small salt diameter; inside 3 mm, outside 7 mm
(2 mm thickness)
- large salt diameter; inside 5 mm, outside 7 mm
(1 mm thickness)

These two different geometries should permit us to vary the convective stability conditions.

Figure 4-a gives the thermoelectric signal obtained on Earth (vertical cell), and Figure 4-b the signal obtained in Space with large diameter cells, together with the chromel-alumel thermocouple indication of the temperature difference. We see that the Earth signal, which started quite smoothly, shows perturbations after three hours of experiments. These perturbations are probably due to contact problems or oxidation on the top electrode.

Figure 10 gives the x-ray photographs of these last cells: (a) before salt melting, (b) after melting on Earth, (c) after melting in Space. It should be noted that all the x-ray photographs given in this paper have been made after complete cooling down to ambient temperature. In these three photographs, the porous tube is almost invisible, which tends to prove that the salt did not penetrate inside the porous material. The remainder of the cell-free volume before melting was sufficient for the expansion. The problems appearing during the Earth experiment are not visible on the 10-b photograph.

Figure 5 gives the thermoelectric signal and temperature difference signal obtained on Earth, with two other cells maintained vertical (small diameter cells). Note that the thermoelectric signal 5-a is perturbed, with no contact at the beginning of the experiment. This signal then starts with a lower value and maintains a low value all during the experiment. Oppositely, curve 5-b looks quite normal. Figure 11 shows the corresponding x-ray photograph. One can see the great differences between these three photographs. The second photograph shows the liquid level after a shrinkage, which is due to a large liquid absorption by the porous alumina tube, clearly visible here. On the third photograph, no problem occurred, the liquid absorption being very slight. This shows that the contact concerning Figure 5-a appeared after the salt had been absorbed by the porous material toward the top electrode. The small potential value can be explained by the temperature difference, which is smaller than expected in the diffusion zone of the molten salt.

As a conclusion for these thermoelectric measurements, one can say that measurement is possible in Space with a completely filled cell and with a reproducibility of 100% over six cells. Second, the porosity combined with the interfacial salt properties never resulted in the salt absorption being under the sole influence of capillarity. However, some supplementary absorption is obtained on Earth under the influence of the salt weight. In space, one always obtains a thermoelectric potential, which corresponds to complete cell filling.

3.2 Theoretical Stability Conditions

We undertook numerical simulation of the convection for long, differentially heated cylinders corresponding to our experimental cells. We were mainly concerned with microgravity situations characterized by a gravity (g), which is reduced by a factor 10^3 to 10^4 with regard to the Earth gravity (g_0), but with an unknown orientation. The equations, the dimensionless parameters, and the numerical method are given in previous papers (9, 17). This study has been performed for various values of the parameters. Various temperature differences and gravity levels were taken into account with the use of the Grashof number Gr_H ($0.01 < Gr_H < 10$). We

consider all the possible cell orientations with regard to gravity (γ , angle between the gravity and the cell axis, $0^\circ < \gamma < 180^\circ$). The Soret coefficient appears in the separation parameter S ($-0.75 < S < 1$). Finally, the physical properties of the molten salts are used to determine the Prandtl and Schmidt numbers ($Pr = 0.6$, $Sc = 60$). For such a system, the convective motion corresponds to a single regular roll, which has no influence on the isotherm contours (small Pr value). On the contrary, the deformation of the isomass fraction contours can be important, particularly when Gr_H increases (Figure 6). The influence of the motion on the separation, an important result for the experimenters, is given by the variable X_{bot} , mean mass fraction at the end of the cylinder, normalized to one for the perfect Soret separation (purely diffusive without convective motion). For different S values, we present the variation of X_{bot} as a function of Gr_H (for $\gamma = 90^\circ$, Figure 7) and as a function of γ (Figure 8): the separation is almost perfect for small Gr_H values or for certain vertical situations, but decreases quite strongly outside this domain. These curves will allow the experimenters to estimate the degree of perturbation of their experiment. Another interesting result is that the diminution of cell radius, which decreases the perturbations induced by convection, can be used to improve the experimental conditions. These theoretical results applied to the acceleration values measured during the flight have permitted us to ensure that our experiment was not perturbed by convection.

4. CONCLUSION

In conclusion, our first Soret-effect experiment in Space has shown the possibility of measuring thermoelectric power under low convective conditions. The evolution with time of this thermoelectric power measured in Space is given in Figure 9 and compared with the corresponding Earth variation.

The observed variation seems characteristic of a diffusion process, but the phenomenon is much slower than expected; after five hours, the stationary state had not been reached. This corresponds to a smaller diffusion coefficient in Space than measured on Earth. This fact has also been noticed by other authors using liquid metals (18), with a factor of four between Earth and Space coefficients. The Soret coefficient cannot be calculated because the stationary state is too far from being obtained, but the variation indicates that the Soret coefficient is positive, corresponding to the migration of AgI towards the cold side of the cell. The Earth variation given in Figure 9 is at least two times smaller than the Space variation; it then confirms the impossibility of a correct measurement on Earth, although the system is theoretically stable, the hot side of the vertical cell being up.

5. REFERENCES

- 1) S. Gustafsson, A. Lunden, Z Naturforsch., 17a, 550 (1962)
- 2) S. Gustafsson, J. Chem. Phys., 183 (1963)
- 3) V. Backlund, J. Dupuy, S. Gustafsson, A. Lunden, Z. Naturforsch., 22a, 471 (1967)
- 4) B.R. Sundheim, Fused Salts, Mac Graw-Hill, New-York, 1964
- 5) R. Connan, J. Dupuy, J. Leonardi, G. Poillierat, J. Chimie Physique, octobre, 64 (1969)
- 6) R. Connan, J. Dupuy, Electrochim. Acta, 15, 977 (1970)
- 7) J. Richter, Angew. Chem. Internat. Edit. 13, 7 (1974)
- 8) E. Pezzati, A. Shiraldi, A. Magistris, Z. Naturforsch., 28a, 1334, (1973)
- 9) D. Henry, Thesis, Lyon (1986)
- 10) H. Mellon, Thesis, Lyon (1978)
- 11) E.A. Guggenheim, Mixtures, Oxford University Press (1952)
- 12) R. Defay and I. Prigogine, Tension superficielle et adsorption, Editions Desoer, Liège (1951)
- 13) J. Bert et al, Space experiment on thermal diffusion - Preparation and theoretical analysis, Proc. 5th European Symposium on Material Sciences under Microgravity, Schloss Elmau (F.R.G.), 5-7 november 1984, ESA SP-222, 347-352
- 14) J. Bert et al, Space thermal diffusion experiment in a molten AgI-KI mixture, D1 Symposium - Scientific results of the German Spacelab D1 mission, Nordeney (F.R.G.), 27-29 august 1986
- 15) P. Claudy and J.M. Letoffe, private communication
- 16) B. Gourland, Thesis, Lyon (1983)
- 17) D. Henry, B. Roux, Phys. Fluids, 29, 3562 (1986)
- 18) G. Froberg, K.H. Kraatz, H. Wever, Scientific results of the German Spacelab D1 mission, Nordeney (F.R.G.), 27-29 august 1986

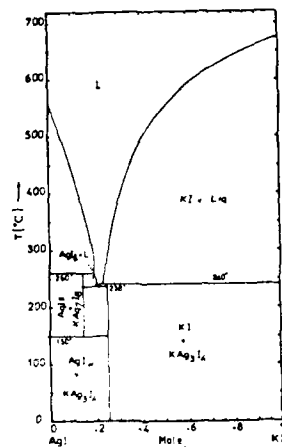


Figure 1 :
AgI/KI phase-diagram
from Claudy and Letoffe
(Ref. 15)

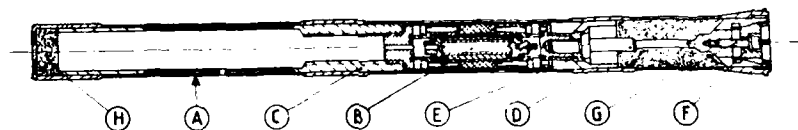


Figure 2 : Experiment cell inside the Space cartridge
A-Pyrad 490 cartridge, B-Thermodiffusion cell, C and
D-Piece of copper to hold the cell, E-Thermal coupling
copper piece, F-Expansile copper cone, G-Stainless steel
screw for expansion, H-Carbon fiber for compensation
of thermal expansion.

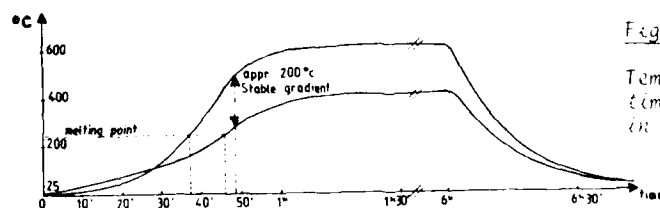


Figure 3 :
Temperature-
time curve obtained
in the cell

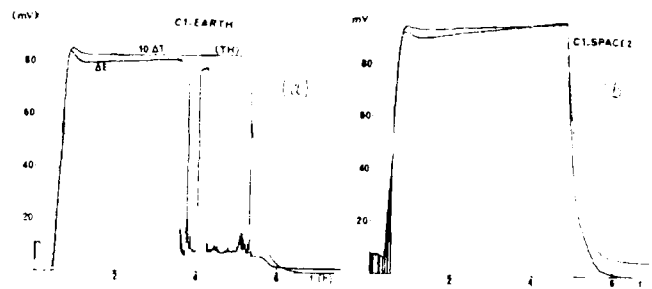


Figure 4:
Intermittent
Discharge Limit
of Space 1
Space 2
Cable 1000

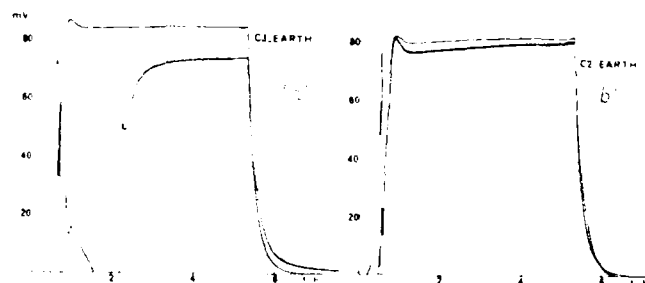


Figure 5:
Intermittent
Space 1
Space 2
Cable 1000

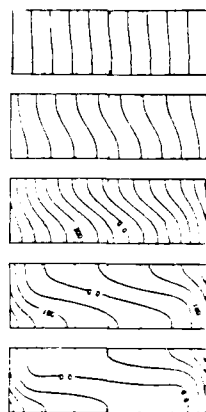


Figure 6 :
Iso-mass fraction contours
a) $G_{*H} = 0.1$, $x_{bet} = 0.999$
b) $G_{*H} = 0.5$, $x_{bet} = 0.915$
c) $G_{*H} = 1$, $x_{bet} = 0.733$
d) $G_{*H} = 3$, $x_{bet} = 0.308$
e) $G_{*H} = 5$, $x_{bet} = 0.196$

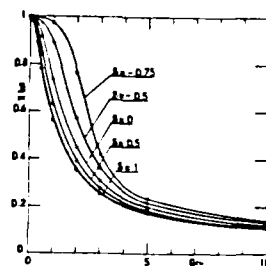


Figure 7 :
 x_{bet} versus G_{*H}
for different S
 $AZ = 6$

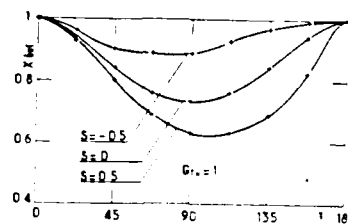


Figure 8 : x_{bet} Versus θ for different
 S at $AZ = 6$, $Pr = 0.5$, $Sc = 60$,
 $G_{*H} = 1$

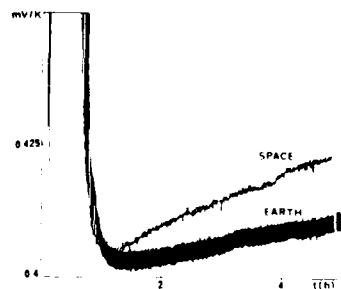


Figure 9 : Comparison of the
thermoelectric power in Space
and on Earth as function of
time

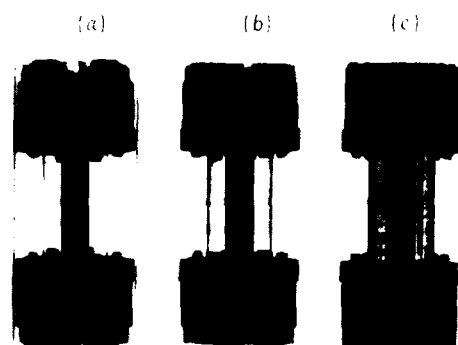


Figure 10:

X-ray photographs of large
diameter cells :
a) Before melting
b) after melting on Earth
(Cell C1-Earth)
c) After melting in Space
(Cell C2-2)

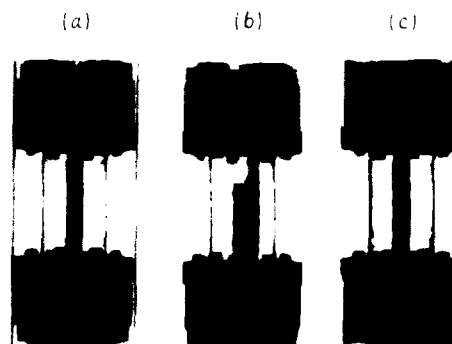


Figure 11 :

X-ray photographs of small
diameter cells :
a) Before melting
b) After melting on Earth
(Cell C3)
c) After melting on Earth
(Cell C2)

**A NEW INFRARED DETECTION SYSTEM AND ITS DATA PROCESSING FOR
THE THERMAL CONDUCTIVITY MEASUREMENTS OF MOLTEN SALTS**

Hiromichi Ohta* and Yoshio Waseda

Research Institute of Mineral Dressing and Metallurgy
(SENKEN), Tohoku University, Sendai 980, Japan.

* Department of Metallurgy, Faculty of Engineering,
Ibaraki University, Hitachi 316, Japan.

ABSTRACT

A new infrared measuring system for extended application of the laser flash method to the determination of the thermal conductivity of molten salts at high temperature with a remote sensing germanium detector has been developed. This system detects the temperature response curve of a thin platinum disk in contact with a semi-infinite column of molten salt sample. Its data processing is presented with measurements for molten sodium carbonate at 1132K. This modification minimizes the effects of electrical noise frequently observed in the previous experiments that were conducted with thermocouples.

INTRODUCTION

The importance of thermal properties such as thermal conductivity or diffusivity of molten carbonates at high temperature has been well recognized in parallel with recent progress in fuel battery technology at high temperature and solar energy storage systems. There have been various attempts at thermal conductivity measurements for relatively low conductivity melts such as oxides and nitrides. However, at sample temperatures above 1000K, these measurements were not successful, mainly due to experimental difficulties and did not permit quantitative discussions for several reasons. For example, the radiative heat flow is known to play a significant role at higher temperatures, but the effect of radiation is difficult to evaluate. The volatilized species from the sample liquid sometimes are known to cause electrical or electrochemical problems such as induced noise or short-circuit of the temperature measuring system in the high temperature region.

The use of a two-layered laser flash method first developed by Tada et al. (6) appears to reduce these difficulties. However, the full potential of this relatively

new technique has been assessed only recently, due to the coexistence of the radiative and conductive components in the measured temperature response curve. Ohta et al. (7,8) proposed the method for the separation of radiative component that is significant at high temperatures above 1000 K from the measured temperature response curve which involves both radiative and conductive heat flows. The basic idea of their data processing is to evaluate thermal conductivity (κ) of a sample liquid as well as the radiative component parameter, denoted by R_p in this paper, and the initial temperature rise of the plate (T_0) by comparing the measured temperature response curves with theoretical values using the least-square curve fitting technique. The usefulness of their method has been well-recognized but the data process for deriving thermal conductivity of liquid sample is rather complicated and requires long calculation time by the high speed large computer.

In the previous experimental assembly (7,8) to obtain the temperature response curve a thermocouple has been successfully used at relative low temperature or in high vacuum (less than 10^{-4} Pa) at high temperature. However, when the certain volatilized or gaseous species increase at high temperature, most likely in the measurements for molten salts, the significant noise prevents us from accurate measurement due to the ionization of the volatilized species by flashed laser beam, and such effect appears to be accelerated by the oscillatory electric field induced in the heating element. In such case, the noise frequently overcomes the temperature response signal even when the rectified alternating current was supplied to the heater because of the small residual ripple current. Since the vapor pressure of most molten salts is relatively high, the inert gas to prevent from volatilization is frequently required for the thermal conductivity measurements. Thus, the experimental assembly with a thermocouple is known to be strictly limited, particularly for the measurements at high temperature. The main purpose of this work is to present the improved temperature response acquisition system with a infrared ray detector of germanium. The new data processing not required the high speed large computer has also been developed for separating the radiative component from the measured temperature response curve.

The usefulness of the present improved system and data processing is demonstrated by measuring thermal conductivity of molten sodium carbonate at 1132K.

EXPERIMENTAL

The schematic diagram of the laser-pulse apparatus for measuring thermal conductivity of liquid and its cell-assembly are given in figures 1 and 2, respectively. The entire cell-assembly is enclosed by a bell jar under vacuum of the order of 10^{-4} Pa (10^{-6} Torr).

The two-layered cell system consists of two parts: a detector metal plate for measuring the temperature response curve and a column of sample liquid adhered to the metal plate. A platinum plate (0.2 mm in thickness and 6 mm in diameter) is employed as a detector plate, which is suspended by three fine platinum wires attached to the surface of the sample melt. A platinum sample vessel is placed on the tantalum pedestal, which has an elevator mechanism to precisely adjust its position. The cell system is placed in a tungsten mesh heating element.

In this work, a 45° half mirror was inserted in the laser beam path, for accurate monitoring the incident beam intensity by a silicon photo detector. To evaluate the initial temperature rise of the platinum disk and the thermal radiation heat loss from its disk, the temperature response curve without touching sample liquid were measured at various temperatures.

The germanium infrared detector was employed in this work to measure the temperature response curve excluded from external noises in the reasonable level. The schematic diagram for this modification is shown in figure 3. The infrared ray emitted from platinum plate passed through the upper quartz window and was reflected by a 45° gold mirror with a hole in its center, where the hole is used for the laser beam path. The infrared ray focused on the screen by quartz lens and the image of platinum plate by transmitting through quartz fiber-optic guides to a germanium infrared detector. To prevent multiple reflection of the focusing equipment, its inner surface was covered with black felt.

At the desired temperature, a pulsed laser beam is flashed on the top surface of a detector plate and its temperature response curve is stored in a digital transient memory from which the data is read by a micro computer system for evaluating thermal conductivity.

Samples were prepared from powder of high grade sodium carbonates. They are premelted in platinum crucible in air at 1200K. About one gram of premelted sample is put into the sample vessel and melted and held for about two hours under vacuum to remove bubbles.

After removal of bubbles, the sample vessel is elevated

to touch the sample surface to the plate and a liquid column of sample is made by lowering of the holder by 0.65 mm.

RESULT AND DISCUSSION

A system composed of thin metal plate and transparent liquid as shown in figure 2 is considered to the theoretical heat transport equations. Before heating by a laser beam, the temperature, T_0 , of a detector plate is in thermal equilibrium with the liquid layer. At $t=0$, a pulse of laser beam is flashed on the plate and the absorbed heat of the plate discharges into both sample liquid and surroundings by conduction and radiation as schematically illustrated by figure 2. As is given by Ohta et al. (8,9), the theoretical temperature decay of the platinum plate in this system is shown as figure 4. This figure also show the calculated theoretical value of Tada et al. (6) for the case where the effect of radiative heat transfer is negligible ($R_n=0$). The platinum plate is thin and has large thermal diffusivity as compared with sample liquid layer. Thus, in deriving these temperature response curves of platinum disk, we can consider liquid layer is semi-infinite and the temperature in the metal plate is uniform at any moment.

The initial temperature rise of the platinum plate, T_0 , and the ratio in the non dimensional form of radiative and conductive heat transfers, R_n , are expressed as follows.

$$T_0 = Q/(\rho_d C_{Pd} l_d) \quad (1)$$

$$R_n = 4(1+n^2)\epsilon\sigma\theta_0^3(\rho_d C_{Pd} l_d / \lambda_s \rho_s C_{Ps}) \quad (2)$$

$$h = [\lambda_s C_{Ps} \rho_s / \rho_d^2 C_{Pd}^2 l_d^2]^{1/2} \quad (3)$$

$$t = h^2 t \quad (4)$$

where the suffixes s and d indicate the sample and the detector plate, t is time, l_d is the thickness of the detector plate, T_0 is a temperature rise of the plate at time t from the equilibrium temperature, and C_p , ρ and λ denote specific heat capacity, density, thermal conductivity, respectively. σ is the Stefan-Boltzmann constant, ϵ is the total hemispherical emittance and n is the refractive index of the sample liquid. Q is the

absorbed heat of detector plate from a laser beam.

Based on these fundamental equations, the following useful relation for the quantity of h corresponding to the thermal conductivity may be readily obtained.

$$h = \sqrt{t_{1/2}/K_{Rn}} \quad (5)$$

where $t_{1/2}$ is the time from the initiation of the pulse until the detector plate temperature decrease reaches one half of its initial value, T_0 , and K_{Rn} is a constant value relevant to the radiative component of R_n . Figure 5 provides the numerical examples for K_{Rn} as a function of R_n . The values of h can be evaluated from the measured $t_{1/2}$ value coupled with the results of figure 5.

The initial temperature rise, T_0 , can not be directly measured because of the noise at $t=0$ caused by electricity supplied to laser. However, the initial temperature rise and the radiation heat transfer component concerning detector plate can be determined by measuring the temperature response without liquid sample. The essential point of this process is as follows(9).

The temperature response of thin plate heated by a laser pulse is expressed by eq.(6).

$$-\frac{d \ln(T - T_0)}{dt} = H \quad (6)$$

where

$$H = \frac{8\sigma\epsilon_0^3}{d^2 C_P d} \quad (7)$$

Figure 6 shows the observed logarithmic temperature response with time. The slope corresponds to the value of H and the T_0 value can be obtained by the extrapolation to $t=0$ since the laser energy of each shot appears frequently to show the slight fluctuation. Thus, such effect was corrected in this work by the following procedure. The initial temperature rise, T_0 , is directly proportional to the laser beam intensity as expressed in eq.(1). Therefore, the initial temperature rise for each thermal conductivity measurement of sample liquid may be determined by the following equation.

$$T_0 = (I/I')T_0' \quad (8)$$

where I is the intensity of laser beam measured by the laser intensity monitor. I' is the value derived from the run without touching sample liquid. T_0' is the value evaluated by the extrapolation for each run. The following relation may also be noteworthy in practice.

$$R_n = \left(\frac{1+n^2}{2}\right)H/h^2 \quad (9)$$

The value of h is derived as follows. At first, the preliminary h value is evaluated from the measured $t_{1/2}$ value and result of figure 5 with the assumption of $R_n = 0$. Next, the value of R_n is calculated by eq.(9) coupled with the refractive index n and H . The evaluation of h from the results of figure 5 is repeated so as to get the reasonable convergence by iteration. Then the thermal conductivity of sample liquid can be evaluated using the relation of eq.(3).

By applying the new infrared detection system and its data processing, the thermal conductivities of molten sodium silicate and carbonate have been determined. The values are $0.428 \text{ W m}^{-1} \text{ K}^{-1}$ for sodium silicates at 1133K and $0.478 \text{ W m}^{-1} \text{ K}^{-1}$ at 1273K for sodium carbonate at 1132 K, respectively. The former is found to agree well with the literature value(8). It would be interesting to extend the present method to determine the thermal conductivity of various molten salts at high temperature.

The authors are grateful for the support and encouragement by Professors A.Yazawa, Y. Shiraishi (SENKEN, Tohoku University), R.Suzuki and Y.Tomoda (Department of Metallurgical Engineering, Ibaraki University). The financial support from the Kawasaki Steel Corporation, Technical Research Division in 1986/1987 should also be greatly appreciated.

REFERENCES

1. J.T.Schriempf, Rev. Sci. Instrum., **43** 1781 (1972); High Temp. High Press., **4** 411 (1972).
2. J.L.Bates "Thermal Diffusion and Electrical Conductivity of Molten and Solid Slags" Battelle Pacific Northwest Lab. Rep.(1976).
3. R.E.Taylor and H.J.Lee Rep. 14th thermal Conductivity Conf., 135 (1974).

4. C.S.Ang H.S.Tan and S.L.Chen J.Appl.Phys., 44 687 (1973).
5. C.S.Ang S.L.Chen and H.S.Tan J.Appl.Phys., 45 179 (1974).
6. Y.Tada, M.Harada, M.Tanigaki and W.Eguchi, Indust. Eng. Chem. Fundam., 20 333 (1981).
7. T.Sakuraya, T.Emi, Y.Waseda and H.Ohta, Japan Inst. Metals, 46 1131 (1982).
8. H.Ohta, Y.Waseda, and Y.Shiraishi, Proc. 2nd Inter. Conf. on Metallurgical Slags and Fluxes. Lake Tahoe, Nevada, (1984), The Met. Soc. AIME, p.863 (1984).
9. H.Ohta, HighTemp. Mater. Processes, 7 185 (1986).
10. H.Ohta, Y.Waseda and Y.Shiraishi, J. High Temp. Soc. Japan, 11 81 (1985).

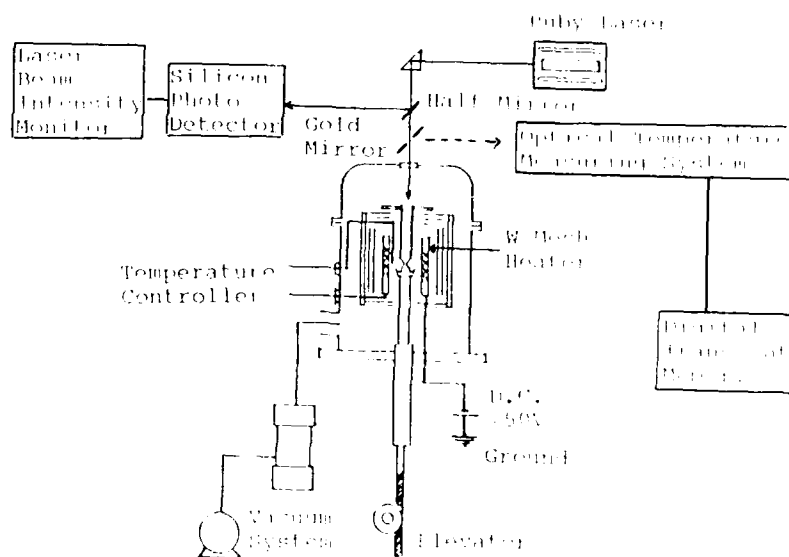


Figure 1. Block Diagram of Experimental Apparatus for The Thermal Conductivity Measurement by The Laser-Flash Method.

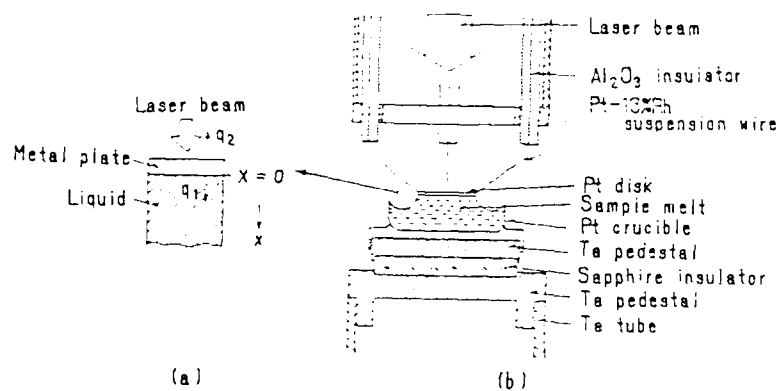


Figure 2. (a) Schematic Diagram of a Cell in The Two-Layered Laser-Flash Method; (b) Schematic Diagram of the Sample-Cell Assembly.

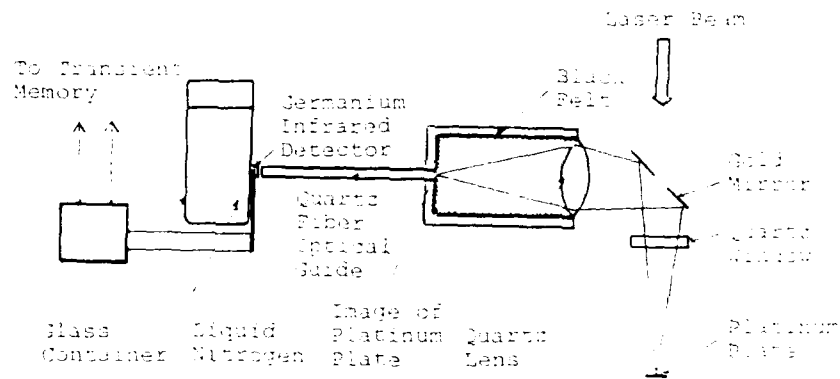


Figure 3. Optical Temperature Response Acquisition System employed in this work.

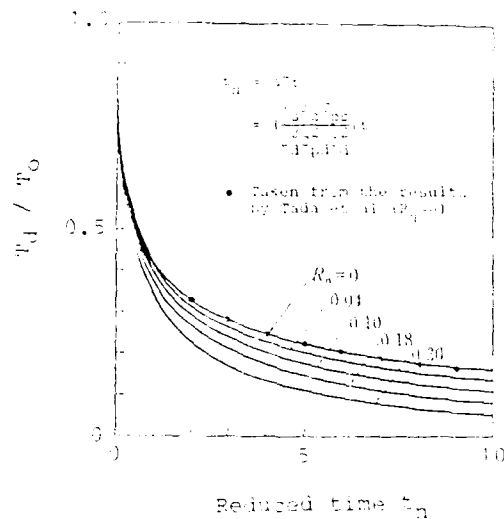


Figure 4. Calculated Temperature Response Curves with Various Radiative Effect of R_n (7).

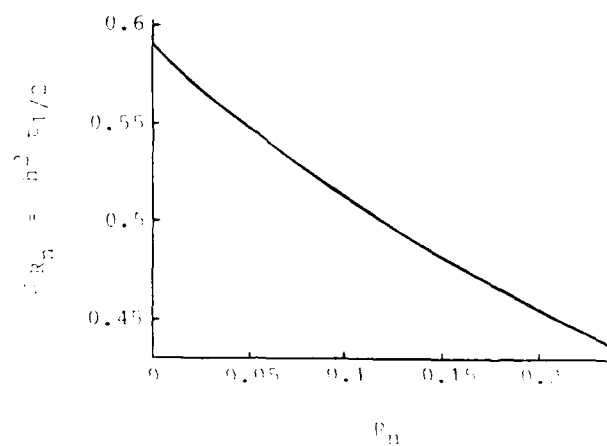


Figure 5. Half Decay Time of The Temperature Response as a Function of R_n .

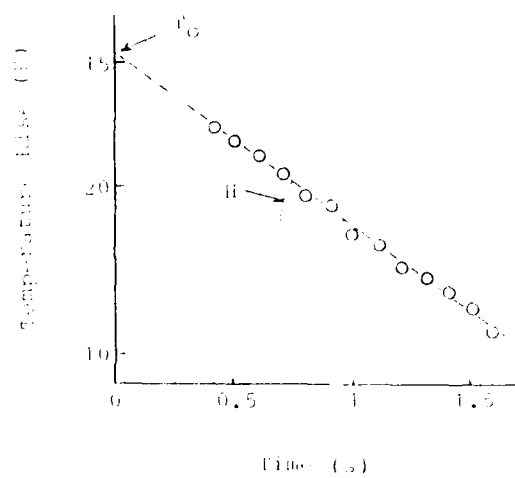


Figure 6. Observed Logarithmic Temperature Response Without Liquid Sample.

GENERATION OF CATIONIC SPECIES IN CHLOROALUMINATE MELTS : STRATEGIES BASED ON PROTONIC SUPERACID CHEMISTRY

T.A. O'Donnell

Department of Inorganic Chemistry, University of Melbourne,
Parkville, Victoria, 3052, Australia.

ABSTRACT

Initially this paper provides a quantitative basis for the levels of acidity in protonic superacids above which individual homopolyatomic cations of non-metals and metals are capable of stable existence and below which they are unstable through disproportionation. It relates these reactions in superacids to similar behaviour of these cations in chloroaluminate melts of varying acidity or basicity. Monatomic cations of *d*- and *f*-transition metals in unusually low oxidation states, e.g. U^{3+} , Ti^{2+} , Sm^{2+} etc., are shown to be stabilized in superacids, the acidity of which has been enhanced by Lewis acids. Again, the parallel with chloroaluminate melt chemistry is demonstrated. The novel feature of this presentation is the postulate that, in acidic media, whether superacids or melts, cations are the normally expected species and that they disproportionate with increase in basicity. Finally, strategies are outlined for generation of cationic species in melts. These strategies give a more specific synthetic approach than that adopted in much past work.

HOMOPOLYATOMIC CATIONS OF HALOGENS AND CHALCOGENS IN HYDROGEN FLUORIDE, FLUOROSULFURIC ACID AND ACIDIC CHLOROALUMINATES

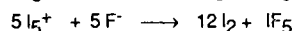
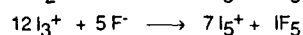
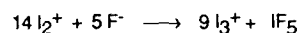
In recent work at Melbourne (1) we have established the thresholds of acidity in the solvent anhydrous hydrogen fluoride (AHF), as defined by values of the Hammett Acidity Function H_0 , above which the homopolyatomic cations I_5^+ , I_3^+ and I_2^+ are stable in solution. Some I_5^+ , together with I_3^+ , is observed by UV-visible spectroscopy in "natural" HF, i.e. triply-distilled HF which has been stored in KeilF containers.

Gillespie and Liang (2) have determined a value of -15.1 for H_0 for pure anhydrous HF. This value was not determined directly for the "pure" liquid itself. SnF_5^- (the Lewis acid of the solvent system) and F^- (the base) were added in concentrations that "swamped" any impurity effects. H_0 values were obtained for a range of acid concentrations and for a range of base concentrations and H_0 for pure HF was determined by interpolation. "Natural" distilled HF will contain minute concentrations of impurities which will be protonated. The concentration of F^- will then be slightly enhanced and H_0 may be about -11.

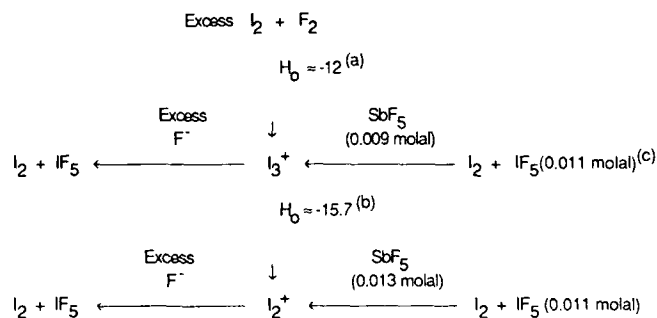
When H_0 is about -12 (saturated PF_5 in HF), I_3^+ is the only cationic species observed spectroscopically. At $H_0 = -15.17$ (0.25 NbF_5 in HF), some I_5^+ is observed and

I_2^+ is the only species detected for HF solutions more acidic than $H_0 \approx -15.7$ (0.11 M NbF_5). The most acidic solution investigated in this part of the work was 0.2 M SbF_5 in HF, for which $H_0 = -20.2$, I_2^+ being the only cationic species present.

When excess F^- — the base of the HF solvent system — is added to a solution containing any of the polyatomic cations of I_2 , the cations disproportionate to elemental I_2 (as indicated by UV-visible spectroscopy) and IF_5 (shown by Raman spectroscopy). Gradual additions of F^- to solutions containing I_2^+ would yield I_3^+ , I_5^+ and I_2 in turn in accordance with the equations :



Acidity was shown to be the major, if not the sole determinant of the nature of the cations formed in some experiments in which I_2 and IF_5 were allowed to mutually reduce and oxidize in HF of fixed acidity. It did not matter whether oxidant or reductant was in excess. The flow-sheet below summarizes the dependence of cation formation on the basicity or acidity of the medium. IF_5 is a good fluoride donor. When it is slightly in excess of SbF_5 , the strong Lewis acid of the system, $IF_4^+SbF_6^-$ is formed and the residual IF_5 gives a slightly basic solution. When SbF_5 is slightly in excess the solution is weakly acidic.



(a,b) H_0 values for (a) PF_5/HF , (b) NbF_5/HF : Reference 2.

(c) The amount of solid elemental I_2 was such that IF_5 was in a ten-fold excess relative to I_2 in the experimental volume of HF solution which was 0.011 molal in IF_5 .

In other Melbourne work, we have investigated the levels of acidity in HF above which the cations S_{19}^{2+} , S_8^{2+} and S_4^{2+} become stabilized. The absolute acidities at

which these cations are formed are "compressed" into a much higher range than for the cations of I_2 and so acid-base dependent discrimination is much less. Consequently we have put the I_2 -HF system forward as the best "indicator" system yet reported.

There are no reports to suggest that the ability to discriminate within protonic solvents other than HF or in melts is as great as in the HF solvent system. This is not surprising when it is recognized that, for each protonic solvent, the approximate range of H_0 values in going from 0.1 mole % base to 0.1 % mole acid is $\ll 0.5$ for H_2SO_4 (3), 3 for HSO_3F (4) and 9.5 for HF (2). Unfortunately there is no relatively simple acidity scale, comparable with the Hammett scale, to define acidity-basicity conditions in melts.

Despite these difficulties, a very recent review (5) correlates initially the conditions of acidity under which polyatomic cations of the halogens and of the chalcogens are stabilized in the protonic solvents, HF, HSO_3F and oleums, and in chloroaluminate melts. It is reported there that Gillespie generated I_5^+ , I_3^+ and I_2^+ in HSO_3F by oxidizing I_2 with the strong oxidant $S_2O_6F_2$. By controlling the ratio $S_2O_6F_2 : I_2$ he found that I_5^+ and I_3^+ were stable in HSO_3F ($H_0 \approx -14$) but that I_2^+ slowly decomposed in that medium, but was stable in HSO_3F-SbF_5 ($H_0 \approx -18$). Bromine cations are less stable. Whereas I_3^+ is stable in HSO_3F at $H_0 \approx -14$, Br_3^+ decomposes slowly and needs a more acidic medium $SbF_5 \cdot 3SO_3-HSO_3F$ ($H_0 \approx -19$). Cl_3^+ cannot be generated in protonic solvents.

For molten salt chemists, it is highly significant that I_5^+ and I_3^+ (as chloroaluminates) are stable in neutral melts (6) i.e. when $Cl^- : AlCl_3$, 1:1. I_2^+ was generated in acidic $AlCl_3$ and disproportionated as the medium was made more basic (7). This system will be discussed later.

For polyatomic cations of the chalcogens, the same trends apply. For example S_4^{2+} , S_8^{2+} and S_{10}^{2+} can be stabilized in oleums with H_0 values of -14.1, -13.2 and -12.7 respectively. That is, stabilization of sulfur cations with higher charge-to-element ratios require progressively higher acidities. An alternative statement is that as the acidity of the medium is increased the complexity of the cation decreases. On the other hand, the cations S_4^{2+} , Se_4^{2+} and Te_4^{2+} can be stabilized in H_2SO_4 -based media of decreasing acidity, the respective H_0 values being -14.1, -11.9 and -11. Ease of stabilization of "high-charge" cations increases with increasing atomic number of the chalcogen, as was the case with the halogens.

HOMOPOLYATOMIC CATIONS OF METALLIC ELEMENTS IN CHLOROALUMINATE MELTS AND ACIDIC FLUORIDE MEDIA

The experimental evidence for homopolyatomic cations of metals is much less comprehensive than for non-metals and, in the main, is drawn from molten salt chemistry. An important difference from the polyatomic cations of non-metals is that the charge-to-element ratio decreases, i.e. the complexity of the cation increases, as the

acidity of the medium increases, whether that medium be a molten salt or a protonic superacid.

The only diatomic cation of a metal to exist in water is Hg_2^{2+} and that disproportionates as base is added to an aqueous solution. Mamantov and coworkers obtained spectroscopic and polarographic evidence for Hg_3^{2+} in AlCl_3 and determined the structure of Hg_3^{2+} in $\text{Hg}_3(\text{AlCl}_4)_2$ isolated from the melt (8). Gillespie's group (9) generated $\text{Hg}_3(\text{AsF}_6)_2$ and $\text{Hg}_3(\text{Sb}_2\text{F}_{11})_2$ in the weakly basic solvent SO_2 and these compounds disproportionated slowly even in HSO_3F . $\text{Hg}_4(\text{AsF}_6)_2$ was generated in the weakly basic solvent AsF_3 in equilibrium with $\text{Hg}_3(\text{AsF}_6)_2$, but Hg_4^{2+} disproportionated in SO_2 .

Although there are several sketchy reports of generation of cations such as M_2^{2+} by reduction of metal dichlorides by the metal in melts — often the molten dichlorides themselves — the polyatomic cations other than those of Hg which have been well characterized are those of Cd and Bi. Corbett reported that reduction of CdCl_2 by Cd was at a maximum in *acidic* melts, when the $\text{AlCl}_3:\text{CdCl}_2$ ratio was beyond about 3:1 i.e. when there was at least one mole of AlCl_3 in excess of the amount required to form AlCl_4^- with the chlorides released from CdCl_2 . He isolated $\text{Cd}_2(\text{AlCl}_4)_2$ from these melts (10). He observed a Raman band at 183 cm^{-1} ascribed to Cd_2^{2+} in the melt which can be related to a band at 175 cm^{-1} in the isolated solid. Cutforth, Gillespie and Ummat synthesized more complex cations of Cd by oxidizing excess Cd with AsF_5 in liquid AsF_3 and isolating the solids $\text{Cd}_3(\text{AsF}_6)_2$ and $\text{Cd}_4(\text{AsF}_6)_2$ (11).

Corbett (12) isolated compounds containing polyatomic cations of Bi by adding metallic Bi to stoichiometric, i.e. *neutral*, melts where the $\text{BiCl}_3:\text{AlCl}_3$ ratio was 1:3. These compounds had formulae Bi_4AlCl_4 , which presumably contains the cation Bi_4^{2+} , and $\text{Bi}_5(\text{AlCl}_4)_3$. The latter compound appears to be related to his compound $\text{Bi}^+\text{Bi}_4^{5+}(\text{HfCl}_6)_3$ which he characterized crystallographically by reducing the *neutral* 3:2 mixture of HfCl_4 and BiCl_3 with Bi (13). The Bi cation system would appear to warrant further investigation in acidic melts in which, to use the fundamental concept of this paper, polyatomic cations would be stabilized more easily.

MONATOMIC CATIONS OF d- AND f-TRANSITION METALS IN VERY LOW OXIDATION STATES IN HF AND IN MELTS.

Treatment of metallic uranium, previously chemically cleaned of all surface oxide, with a solution of BF_3 in HF yielded a stable lilac-colored solution of HF-solvated U^{3+} , with H_2 being evolved through reduction of HF (14). This contrasts with attempts to prepare U^{3+} in aqueous solution. U^{3+} reduces water to H_2 and is itself oxidized to U(IV) . However, continuous electrolytic reduction during recording of the spectrum, gives a

spectrum for aquo- U^{3+} which is very similar to that for U^{3+} , solvated by HF, in HF solution. When excess F^- as a solution of NaF in HF, was added to U^{3+} in BF_3 -HF, the solution became colourless and the insoluble solids were U and UF_4 (15). Disproportionation had occurred :



In molten salt work in 1963 (16), it was reported that UCl_3 was produced *in situ* in fused salts in sealed tubes and reduced by metallic Al, the volume of Al being comparable with that of the melt phase in each case. After quenching, the immiscible melt and metallic phases were analyzed for U and the ratio of U in each phase interpreted in terms of reduction of U(III) by Al. The $AlCl_3/KCl$ ration in the melt was varied from 0.39 (basic) to 2.0 (acidic) in different experiments. It was observed that the ratio of U in the metallic phase to that in the melt was very small in acidic and in basic melts but had a value of 10 or greater in near-neutral melts. In a second paper (17) the experimental results were reported as showing that the extent of reduction depended on whether the predominant anionic species in the systems investigated were $Al_2Cl_7^-$, $AlCl_4^-$ or Cl^- . It will be shown latter in this paper that it is more reasonable to interpret the results in terms of the stable cation U^{3+} in acidic media, stable chloro-uranate (III) anions in basic systems and disproportionation of U^{3+} near neutrality.

Following the generation of U^{3+} in HF, metallic Cr and V reacting with HF acidified with the weak Lewis acid BF_3 were shown to yield, not surprisingly, solvated Cr^{2+} and V^{2+} . Whereas Ti was expected to give Ti^{3+} , comparison of HF spectra with those in molten $AlCl_3$ and in crystalline NaCl (with Ti^{2+} doped at 1% level) showed that solvated cations Ti^{2+} were stable in solution when cleaned Ti was reacted with 2-3M SbF_5 in HF (18). SbF_5 is a very strong Lewis acid of the HF solvent system. Increasing the basicity of this solution by adding the base F^- as NaF in HF caused disproportionation of Ti^{2+} to Ti and TiF_4 .

This work on Ti^{2+} in HF has direct relevance to spectroscopic studies of $Ti(II)$ in molten chloroaluminates. Øye and Gruen (19) interpreted their spectrum for $Ti(II)$ in pure $AlCl_3$ as indicating an octahedral chloride environment for $Ti(II)$. Lever (20) states that this spectrum is "presumably derived from the $[TiCl_6]^{4-}$ ion". In passing, it can be noted that Lever states explicitly that the spectrum recorded by Øye and Gruen (19) for $V(II)$ in $AlCl_3$ is that of octahedral $[VCl_6]^{4-}$. Based on discussion later in this paper it seems that it is much more reasonable to postulate that the absorbing species in that case is $AlCl_3$ -solvated V^{2+} . Sørlie and Øye (21) recorded spectra for $Ti(II)$ and $Ti(III)$ in melts ranging from 100% $AlCl_3$ through melts with $AlCl_3:KCl$ ratios of 51:49 to those of 49:51, i.e. from strongly acidic to weakly basic. The $Ti(III)$ spectrum shows little change to $AlCl_3:KCl$, 67 : 33, but appears to change to an anionic species, namely tetrahedral $TiCl_4^-$, at the ratio 51:49 and is mainly octahedral $TiCl_6^{3-}$ at 49:51. A new peak grows into the $Ti(II)$ spectrum as Cl^- is introduced into the melt and continues to grow in intensity with increasing Cl^- fraction, but then remains essentially unchanged until neutrality. At $AlCl_3:KCl$, 49:51, i.e. in a slightly basic melt, the spectrum appears to be that of $Ti(III)$ as $TiCl_6^{3-}$ and it is reported that metallic

Ti is deposited from the melt. This system will be discussed below in terms of Ti^{3+} and Ti^{2+} as the species present in acidic melts.

In the Melbourne program, cations of other metals in unusually low oxidation states stabilized in HF include Zr^{3+} , Eu^{2+} , Yb^{2+} and Sm^{2+} (22). The Zr^{3+} spectrum in HF correlates nicely with spectra for $Zr(III)$ in $AlCl_3$, $AlBr_3$ and AlI_3 (23).

POSTULATION OF CATIONIC SPECIES IN INTERPRETATION OF SOME ACID/BASE DEPENDENT REACTIONS IN MELTS

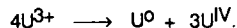
The Melbourne work on stabilization of the HF-solvated cations U^{3+} and Ti^{2+} can be used directly to re-interpret or to simplify earlier interpretations of some reported reactions in molten salts, using as a basis for the new interpretation the postulation of the existence in acidic melts of *cationic species* which disproportionate with increase in basicity of the melts. Comparison of the $U(III)$ systems in both media provides an excellent example of this approach.

Spectroscopic and direct chemical evidence supports the proposition that $U(III)$ is present in HF made slightly acidic with BF_3 as HF-solvated U^{3+} and that, as the base of the solvent system F^- is added, U^{3+} disproportionates as indicated above.

Morrey and co-workers (16, 17) observed an apparent direct reduction of $U(III)$ by Al in nearly-neutral chloroaluminate and stated that such reduction was slight in both the acidic and the basic melts. They appear to have rationalized these observations by analysis of their results, using the changing concentrations of UCl_6^{3-} , $Al_2Cl_7^-$, $AlCl_4^-$ and Cl^- as the basis for their analyses. They do not appear to offer chemical explanations for the acid/base dependence of "reduction" of $U(III)$ on the nature of the different anions.

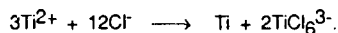
It appears much more satisfying to postulate, as they have done, that $U(III)$ is present in the basic melt as an anion $[UCl_{3+n}]^{n-}$, where n may or may not be 3, but that it is present in the $AlCl_3$ -rich melt as U^{3+} solvated by $AlCl_3$, or better, by the bidentate Al_2Cl_6 . This need not be a shocking postulate. Morrey himself published spectra for $U(IV)$ in various chloride melts (24). He recorded spectra of UCl_4 in the acidic melts $AlCl_3$ and $ZnCl_2$, of pure UCl_6^{2-} and of UCl_6^{2-} and UCl_4 in basic (chloride-rich) melts. His spectra in basic media all resembled that of UCl_6^{2-} . So $U(IV)$ must be expected to be anionic in basic melts. His acidic spectra are very similar to that of aquo- U^{4+} in acidified H_2O and so it can be postulated that $U(IV)$ is present in acidic melts as solvated U^{4+} . It is then even more reasonable to postulate that the cation of lower positive charge U^{3+} would be in solution as solvated U^{3+} . Unfortunately, no spectra for $U(III)$ in acidic melts appear to be available. It is highly significant that Morrey and co-workers reported that "on moving to the $AlCl_3$ -rich region the absorption spectrum, typical of UCl_6^{3-} is no longer observed" (16).

Once it is postulated that the U^{3+} cation exists in acidic melts it is easy to see that as the melt system approaches neutrality, U^{3+} will disproportionate :

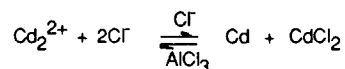


$U(IV)$, probably present as UCl_6^{2-} , would then be reduced by Al to U^{3+} which would disproportionate giving a cyclic process for production of metallic uranium, in which it is not necessary to propose that $U(III)$ is reduced by Al at all.

The $Ti(III)$ and $Ti(II)$ system in chloroaluminate melts (21) requires much less drastic reinterpretation than the $U(III)$ system. $Ti(III)$ is probably present as solvated or partly-complexed Ti^{3+} in acidic melts. The spectra suggest that, slightly on the acidic side of neutrality, the dominant species is the tetrahedral anion $TiCl_4^-$ and that this is largely replaced by octahedral $TiCl_6^{3-}$ on the basic side. The spectrum for $Ti(II)$ in pure $AlCl_3$ is best interpreted, on the basis of the spectra in HF and in doped NaCl, as indicating solvated Ti^{2+} . With increase in basicity of the melt (67% $AlCl_3$ — 33% KCl) a new peak starts to grow in at about $22,000\text{ cm}^{-1}$. This could be due to a lowering of symmetry because of replacement of Al_2Cl_6 ligands by $Al_2Cl_7^-$ or, more likely, due to some chlorocomplexation yielding solvated $TiCl^+$, with the high-energy band resulting from a charge-transfer process. The important observation is that, with slight modification, these spectral features are retained until the melt contains 51% $AlCl_3$ and 49% KCl. At 51% KCl, the spectrum is that of $Ti(III)$ in $TiCl_6^{3-}$ and Sørli and Øye reported metal deposition on the cell windows. This is consistent with disproportionation of the *cationic* species, whether partly complexed or not :

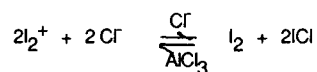


Corbett's observation that Cd_2^{2+} is stable in acidic chloroaluminates is consistent with the general proposition put forward in this paper. If the acidity were to be reduced, Cd_2^{2+} would disproportionate in accordance with the equilibrium :



It is this writer's opinion that Corbett complicates the interpretation of his observations unnecessarily by discussing preferential isolation of $Cd_2(AlCl_4)_2$ or $Cd(AlCl_4)_2$ in terms of the lattice energies of the compounds isolated (25). It is sufficient to postulate that Cd_2^{2+} is formed by reduction of Cd^{2+} by Cd if the melt is sufficiently acidic and that this reaction is reversible on increase of the basicity of the melt. The isolation of the product is an unrelated matter. Corbett would probably be better to have used the anion $HfCl_6^{2-}$, that he used so profitably in the isolation of Bi cations, for the reasons given below.

It is significant within the framework of this paper that the two iodine cations I_5^+ and I_3^+ were generated in neutral melts, i.e. when stoichiometric amounts of I_2 , ICl and $AlCl_3$ were melted together to give $Cl^- : AlCl_3$, 1:1 (6). Using anodic oxidation or chemical oxidation by Cl_2 , Mamantov (7) generated I_2^+ in acidic melts ($AlCl_3 : NaCl$, 63:37) but not in neutral melts. This indicates that I_2^+ , stable in acidic $AlCl_3$ -rich melts, disproportionates as the base Cl^- is added :



Mamantov couched the explanation of his observed reactions in terms of disproportionation of ICl . This is unlikely since there is nothing to suggest that I^{III} is forming by the disproportionation of I^I in ICl .

Mamantov's work with iodine cations suggests that if acidic rather than neutral melts had been used in the work with Cd and Bi , cations species such as Cd_n^{2+} (with $n > 2$) and Bi cations with lower charge-to-metal ratios than those isolated, may have been generated.

STRATEGIES FOR GENERATION AND ISOLATION OF COMPOUNDS CONTAINING UNUSUAL CATIONS FROM MOLTEN SALTS.

All-too-often in the synthesis of cationic compounds in melts and in other media, the roles of acids or bases, oxidants or reductants and counter-ions for isolation of the required cations have been confused or "telescoped" inefficiently.

An example drawn from fluoride chemistry has been that in the generation of cations, SbF_5 has been used to fix the acidity of the system, as an oxidant (thereby producing SbF_3) and as the source of anions such as SbF_6^- or $Sb_2F_{11}^-$. Not only has this multiple use of a single reagent limited synthetic control, but the solid products have often been impossible to characterize properly because they contain involatile SbF_3 . Similarly in work with oleums and fluorosulfuric acid, SO_3 and HSO_3F have been used as oxidants and to increase the acidity.

In work in chloroaluminates, $AlCl_3$ has been used to control the acidity and to be the source of the $AlCl_4^-$ counter-anion to the cation sought. One particular implication, deliberate or otherwise, is that "neat" or stoichiometric reacting proportions of oxidant, reductant and acid have been used, e.g. I_2 , ICl and $AlCl_3$ to give $I_5^+ AlCl_4^-$ and $I_3^+ AlCl_4^-$. Under these conditions the reacting system is always neutral, precluding the possibility of obtaining cations of higher charge for polyatomic non-metals or of lower charge for metallic ions. Mamantov obtained I_2^+ in **acidic** chloroaluminate. Bi cations were generated in neutral melts. New Bi cations might be possible in acidic melts.

To overcome these problems synthetic strategies based on at least three steps seem to be necessary :

- (a) *Adjust the acidity* — It may be necessary to work in AlCl_3 (or some other acidic melt) which, at the completion of the reaction, will contain only that amount of chloride ion which is unavoidable from the reaction conditions.
- (b) *Use a simple, specific oxidant or reductant* — In the case of polyatomic metal cation generation, use of the metal itself is usually acceptable as a reductant for a cation of that metal in a higher ("normal") oxidation state. However cathodic reduction and anodic oxidation are employed all-too-infrequently. In general, electrons are the cleanest and best oxidants or reductants. Voltammetric oxidation and reduction are often used to characterize species in the melt — or, at least, near the electrode. This has dangers in that species generated in the electrode diffusion zone may not be capable of existence in the bulk of the melt because of the level of its acidity or basicity. In chloroaluminates, elemental chlorine is a simple oxidant, easy to control quantitatively.
- (c) *Provision of a neutral counter-ion* — As experience builds up, selective precipitants can be identified e.g. we have established in HF chemistry that SiF_6^{2-} and GeF_6^{2-} and, to a less extent $\text{Ta}_2\text{F}_{11}^-$, are excellent precipitants for cations, particularly dispositive ones. Thus we isolated SmGeF_6 as a solid so insoluble that it did not react with atmospheric moisture over a period of several hours. Not surprisingly, from a lattice-energy point of view, it seems that di-negative anions and di-positive cations yield very insoluble compounds.

If Cd_3^{2+} or Cd_4^{2+} or polyatomic cations of Bi or other metals were to be sought, it would appear to be profitable to reduce the "normal" chlorides with the metal in almost pure AlCl_3 and then to add an anion such as HfCl_6^{2-} , SnCl_6^{2-} or TiCl_6^{2-} to isolate the solid containing the new cation.

CONCLUSION

The primary aim of this paper has been to establish that **solvated cations are the normal species in protonic superacids and in acidic chloroaluminates** and that, as the media are made progressively more basic, the cations undergo disproportionation. Discussion of the acid-base dependence of the stability of cations has been restricted deliberately to protonic superacids and to chloroaluminate melts. It seems highly probable that the same general principles apply to other melts, e.g. fluorides, nitrates, sulfates, silicates, etc.

One final point that is vitally important is the recognition that the corollary of what has been written here is that, just as the generation of unusual cationic species is favoured by increasing the acidity of the medium, formation of unusual stable anions occurs in basic media.

The best-known homopolyatomic anions are the so-called Zintl ions, e.g. Sn_9^{4-} , Pb_7^{4-} , Pb_9^{4-} , Sb_7^{3-} , Bi_3^{3-} , Bi_5^{3-} and Bi_7^{3-} . Many of these were postulated from analysis of the solids obtained when alloys of Na and the appropriate metal were dissolved

in liquid NH_3 . Subsequently many of them were recovered more efficiently from the basic medium ethylenediamine using cryptated Na^+ or K^+ as the counter-ion, to sequester the cation and prevent electron-transfer from the anion to the cation (27). Polychalconide chain anions have been isolated from extremely basic aqueous solution with $(\text{CH}_3)_4\text{N}^+$ as the counter-cation. The extreme case is Na^- , identified in NH_3 and ethylenediamine, and crystallized from ethylamine with cryptated Na^+ as the counter-cation (28).

The known existence of S_x^{2-} and S^{3-} in amides is consistent with reports that stable sulfur-containing species in basic melts are anionic. Future investigation of anionic species in melts would appear to call for strongly basic media.

REFERENCES

1. J. Besida and T.A. O'Donnell, unpublished observations.
2. R.J. Gillespie and J. J.-N. Liang, Ph.D. Thesis, McMaster University (1976).
3. R.J. Gillespie, T.E. Peel and E.A. Robinson, *J. Amer. Chem. Soc.* **93**, 5083 (1971).
4. R.J. Gillespie and T.E. Peel, *J. Amer. Chem. Soc.* **95**, 5773 (1973).
5. T.A. O'Donnell, *Chem. Soc. Rev.* **16**, 1 (1987).
6. D.J. Merryman, J.D. Corbett and P.A. Edwards, *Inorg. Chem.* **14**, 428 (1975).
7. K. Tanemoto, G. Mamantov and R. Marassi, *J. Inorg. Nucl. Chem.* **43**, 1779 (1981).
8. G. Torsi, K.W. Fung, G.M. Begun and G. Mamantov, *Inorg. Chem.* **10**, 2285 (1971).
9. B.D. Cutforth, C.G. Davies, P.A.W. Dean, R.J. Gillespie, P.R. Ireland and P.K. Ummat, *Inorg. Chem.* **12**, 1343 (1973).
10. J.D. Corbett, W.J. Burkland and L.F. Druding, *J. Amer. Chem. Soc.* **83**, 76 (1961).
11. B.D. Cutforth, R.J. Gillespie and P.K. Ummat, *Revue de Chim. Minerale* **13**, 119 (1976).
12. J.D. Corbett, *Inorg. Chem.* **7**, 198 (1968).
13. R.M. Friedman and J.D. Corbett, *Inorg. Chem.* **12**, 1134 (1973).
14. M. Baluka, N. Edelstein and T.A. O'Donnell, *Inorg. Chem.* **20**, 3279 (1981).
15. L. Dawkins and T.A. O'Donnell, unpublished observations.
16. R.H. Moore, J.R. Morrey and E.E. Voiland, *J. Phys. Chem.* **67**, 744 (1963).
17. J.R. Morrey and R.H. Moore, *J. Phys. Chem.* **67**, 748 (1963).
18. C.G. Barraclough, R.W. Cockman, T.A. O'Donnell and W.S.J. Schofield, *Inorg. Chem.* **21**, 2519 (1982).
19. H.A. Øye and D.M. Gruen, *Inorg. Chem.* **3**, 836 (1964).
20. A.B.P. Lever, "Inorganic Electronic Spectroscopy" 2nd Ed. pp. 399-417 Elsevier (1984).
21. M. Sørlie and H.A. Øye, *Inorg. Chem.* **20**, 1384 (1981).
22. R.W. Cockman, Ph.D. Thesis, University of Melbourne (1983).
23. E.M. Larsen, J.W. Moyer, F. Gil-Arno and M.J. Camp, *Inorg. Chem.* **13**, 574 (1974).
24. J.R. Morrey, *Inorg. Chem.* **2**, 163 (1963).
25. J.D. Corbett, "Progress in Inorganic Chemistry", Vol. 21 pp. 129-158. John Wiley (1976).
26. R.G. Teller, L.J. Krause and R.C. Haushalter, *Inorg. Chem.* **22**, 1809 (1983).
27. J.D. Corbett, *Chem. Rev.* **85**, 383 (1985).
28. J.L. Dye, *Angew. Chem. Int. Ed. Engl.* **18**, 587 (1979).

INFLUENCE OF THE ACIDO-BASICITY AND OF THE CATIONIC
COMPOSITION ON THE CHEMICAL PROPERTIES IN MOLTEN HYDROXIDES
P. Claes, G. Peeters and J. Glibert
Catholic University of Louvain, Department of Chemistry
Place L. Pasteur, 1 - B1348 Louvain-la-Neuve, Belgium

ABSTRACT

The chemical behaviour of Sn(IV) in the molten NaOH-KOH eutectic mixture at 483 K and in pure molten sodium hydroxide at 623 K has been investigated. In the molten eutectic mixture, Sn(IV) is soluble ($s < 10^{-1} \text{ M}$) as SnO_3^{2-} in basic medium; in acidic solution, SnO_3^{2-} is in equilibrium with solid Na_2SnO_3 ($s = 6.8 \pm 0.6 \cdot 10^{-4} \text{ M}$) or with SnO_2 ($[\text{SnO}_3^{2-}][\text{H}_2\text{O}] = 2.9 \cdot 10^{-5} \text{ mol}^2/\text{L}^2$) depending on the water concentration. In pure sodium hydroxide Sn(IV) is only scarcely soluble as SnO_4^{4-} in basic solutions, the solid phase being Na_4SnO_4 ($s < 10^{-3} \text{ M}$); in acidic melts the solid phase is Na_2SnO_3 probably in equilibrium with very low concentrations of SnO_3^{2-} and SnO_4^{4-} . A particular solubility effect has been observed in the molten eutectic mixture, Na_2SnO_3 is significantly more soluble in basic than in acidic melts.

1. INTRODUCTION

Recently, the chemical and electrochemical properties of various solutes in molten hydroxides have been extensively studied in our laboratory. Particularly, we succeeded in carefully analysing the properties of various solutes containing zinc or carbonide elements in two solvents: NaOH-KOH (49 M%) eutectic mixture at 483 K and sodium hydroxide at 623 K.

The investigated chemical properties are the stoichiometry and the solubility of the dissolved species, as well as their dependence on the acido-basicity of the melts. The data described and discussed in this paper are part of the results reported in a very recent Ph.D. thesis (1) which will be published in the near future. In this contribution, we would like to present the chemistry of Sn(IV) containing species which gives a good illustration of the dependence of chemical properties on the acido-basicity of the melts and on their cationic composition.

2. EXPERIMENTAL

2.1. Reagents

Sodium hydroxide and potassium hydroxide used as solvents were Merck analytical grade reagents. Potassium hydroxide contains 15.2 weight% water with a remarkable con-

stancy.

Sn(IV) was introduced into the melt as SnO_2 (A.G. Merck reagent) or as $\text{CaSnO}_3 \cdot 3\text{H}_2\text{O}$ synthesized in our laboratory.

2.2. Acido-basic properties of the melts

The acido-basicity of the molten eutectic mixture was measured by determining the concentration of oxide or water by linear sweep voltammetry. At 483 K and under a light stream of dry nitrogen, the water concentration remained constant during the experiments.

In the case of molten sodium hydroxide, sodium oxide may still be used in order to get basic media but the acidity of the melt must be controlled by equilibrating the liquid with a gaseous atmosphere with a known partial pressure of water (2). Equation [1] relates the concentration of water to its partial pressure in the gas phase.

$$P_{\text{H}_2\text{O}} = k_{\text{H}_2\text{O}} C_{\text{H}_2\text{O}} \quad [1]$$

The Henry's coefficient $k_{\text{H}_2\text{O}}$ used in this work was determined by Hoyt (3) and yielded $2.195 \text{ mm.Hg.M}^{-1}$ at 623 K. Experiments confirm this value.

2.3. Experimental device

The melts were contained in glassy carbon crucibles (Carbone Lorraine VN25). The electrochemical determinations were carried out with a PRG5 Tacussel polarograph coupled with a X1733 Goerz recorder.

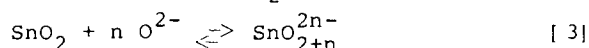
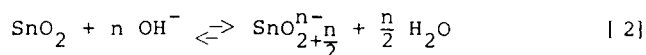
The counter electrode and the reference electrode were coiled platinum wires. The working electrode was either a plane bright platinum electrode welded to a low diameter conductor or a cylindrical electrode (0.5 mm and 1 mm diameter platinum wire respectively in NaOH and in NaOH-KOH) with a variable immersion depth (4).

2.4. Measurement of the solubilities

The solubilities were either measured in situ by means of electrochemical techniques or determined by analyzing aqueous solutions of samples taken from the melt.

2.5. Determination of the stoichiometries

The stoichiometries were characterized by accurately measuring the amounts of water produced in acidic media or the amounts of oxide ions consumed in basic media during the dissolution of given quantities of SnO_2 according to equations [2] and [3] (5).

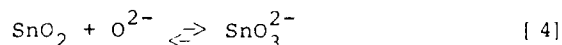


The determination of water and oxide ions have been carried out by linear sweep voltammetry (6).

3. COMPARISON OF THE STOICHIOMETRIES IN THE MOLTEN EUTECTIC MIXTURE AND IN MOLTEN SODIUM HYDROXIDE

3.1. Eutectic mixture

The dissolution of tin dioxide in the basic eutectic mixture is a slow process; it takes about 30 hours to dissolve a quantity of 100 mg SnO_2 in 100 ml of the molten eutectic mixture. Figure 1 shows the dependence of the concentration of oxide ions on the number of moles of tin dioxide added for 1 liter of melt. A consumption of 1.04 mole of oxide ions for 1 mole of SnO_2 is calculated from the slope of the experimental straight line. According to equation [4], the dissolved species is found to be trioxostannate (IV) :



The solubility of tin dioxide in acidic eutectic mixture is too slow in order to yield reliable quantitative results: the electrochemical detection of Sn(IV) is impossible even twenty days after the addition of SnO_2 . Therefore, two different experiments have been carried out :

1. Acidification up to a concentration of water of 10^{-2} M of a solution of stannate (IV) in a basic eutectic mixture. The results are shown in figure 2.

2. Dissolution of $\text{CaSnO}_3 \cdot 3\text{H}_2\text{O}$ in an acidic eutectic mixture. The time dependence of the concentration of water is shown in figure 3.

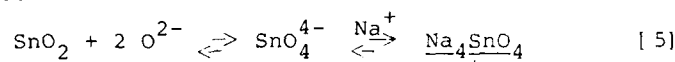
The rapid diminution of the water concentration in figure 2 is due to the neutralization of oxide ions; the slow disappearance of Sn(IV) from the solution is explained by the formation of a clearly observable insoluble phase. As shown in figure 2, the precipitation does not consume or produce any water; it must be concluded that the insoluble product is sodium or potassium stannate (IV). In fact, anhydrous sodium stannate (IV) was unambiguously identified by X ray diffraction.

The increase of the water concentration in figure 3 exactly corresponds to the amount of water contained in the quantity of $\text{CaSnO}_3 \cdot 3\text{H}_2\text{O}$ introduced into the melt. As shown by x-ray diffraction, the solid deposit was again Na_2SnO_3 , indicating an

exchange reaction of sodium ions for calcium ions.

3.2. Sodium hydroxide

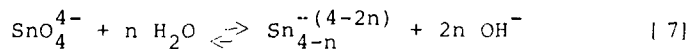
Tin oxide is only scarcely soluble in basic sodium hydroxide. Even when SnO_2 is added to a previously saturated solution, it reacts with the solvent as shown by the ion oxide consumption. The molar concentration of oxide ions is plotted as a function of the added amount of tin dioxide per liter in figure 4. The number of moles of oxide ions consumed per mole of tin dioxide introduced into the melt is 1.95 clearly indicating the formation of tetraoxostannate (IV) in the liquid phase ($s(\text{Sn(IV)}) < 10^{-3}\text{M}$) and in the precipitate.



The formula of the tin (IV) species in acidic sodium hydroxide was determined from a water balance calculation applied to the acidification of a basic solution of Sn(IV) . If the stoichiometry of this species is the same in acidic and basic solutions, then the excess concentration of water may be directly calculated from the number of moles of water added to 1 liter of melt ($C_{\text{H}_2\text{O}}^{\text{Add}}$) and from the initial concentration of oxide ions $C_{\text{O}^{2-}}$:

$$C_{\text{H}_2\text{O}}^{\text{Add}} - C_{\text{O}^{2-}} = C_{\text{H}_2\text{O}}^{\text{Exc}} \quad [6]$$

If the number of oxygen atoms bound to the Sn atom is reduced during the shift from the basic solution to the acidic melt, a complementary number of water molecules will be consumed and the excess concentration of water will be reduced to an extent related to the change of coordination:



n may be calculated from equation [8].

$$n = \frac{C_{\text{H}_2\text{O}}^{\text{Add}} - C_{\text{O}^{2-}} - C_{\text{H}_2\text{O}}^{\text{Exc}}}{C_{\text{SnO}_4^{4-}}} \quad [8]$$

where $C_{\text{SnO}_4^{4-}}$ is the initial concentration of tetraoxostannate (IV) ions in the basic melt.

The experimental result for n is 0.82 suggesting that SnO_4^{4-} is transformed to SnO_3^{2-} when the melt is acidified. Trioxostannate (IV) is only very scarcely soluble in the acidic melt and a solid phase identified as Na_2SnO_3 precipitates.

pitates. However, owing to the weak solubility of Sn(IV) in acidic solution, it is impossible to state whether the dissolved species is SnO_3^{2-} or SnO_4^{4-} or a mixture of these ions.

3.3. Discussion

With regard to a comparison of the investigated solvents, the results described in this section point out that oxo-anions with a higher coordination number are generated in sodium hydroxide. This is summarized in figure 5.

As far as an isolated complex or molecular species is concerned, a temperature increase is favourable to a reduction of the coordination number. Thus, a larger coordination number at a higher temperature implies that the absolute basicity is stronger in sodium hydroxide than in the molten eutectic mixture.

The difference of absolute basicity between both solvents is due either to the temperature difference or to the cationic composition of the melts. It is worthy of note that if the cationic composition of the liquid is the reason for the coordination change, then the acido-basic properties of molten hydroxides would exhibit a mixed alkali effect. Indeed, although the acidity of molten alkali hydroxides increases from cesium to lithium, the molten eutectic mixture, instead of having an intermediate acidity, would be more acidic than its two pure molten components.

Chemical properties in the molten eutectic mixture at 623 K are now being investigated in our laboratory, and we hope that a definite answer to this question might very soon be available.

4. SOLUBILITY OF SN(IV)

4.1. Eutectic mixture

Sn(IV) is soluble as SnO_3^{2-} in the basic eutectic mixture ($s > 10^{-1}\text{M}$); when the solution is acidified, precipitation occurs. The peak intensity of the linear sweep voltammogram for the reduction of Sn(IV) was measured as a function of the water concentration of the melt. The results are shown in figure 6; the concentration of Sn(IV) remains constant up to a concentration of water $C_{\text{H}_2\text{O}} = 4 \cdot 10^{-2}\text{M}$, afterwards the peak intensity decreases with the water concentration. The solubility of SnO_3^{2-} was measured by analysing samples taken from the solution. A value of $(6.8 \pm 0.6) 10^{-4}\text{M}$ was found for the low water concentration region.

4.2. Molten sodium hydroxide

Sn(IV) is only slightly soluble as SnO_4^{4-} in basic molten sodium hydroxide ($s < 10^{-3}\text{M}$). When the melt was acidified,

SnO_4^{4-} and solid Na_4SnO_4 were changed into insoluble Na_2SnO_3 . The concentration of Sn(IV) in acidic solution was lower than the limit of detection of the analytical technique ($s < 10^{-6}\text{M}$); it was impossible to state whether Sn(IV) was dissolved as SnO_3^{2-} or as SnO_4^{4-} .

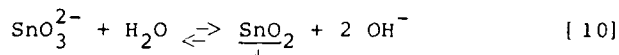
4.3. Discussion

The pH_2O independence of the solubility of Sn(IV) in the slightly acidic region (fig. 6) indicates that SnO_3^{2-} is in equilibrium with solid Na_2SnO_3 in the molten eutectic mixture.

The equilibrium concentrations of SnO_3^{2-} and H_2O in the non-constant solubility region are in good agreement with a solubility constant defined by:

$$K_S = [\text{SnO}_3^{2-}][\text{H}_2\text{O}] \quad [9]$$

Consequently, the following precipitation equilibrium occurs:



The mean value of the K_S calculated for the experimental points is $(2.9)10^{-5} \text{ mol}^2/\text{L}^2$. Depending on the pH_2O of the liquid, the dissolved SnO_3^{2-} ion is thus in equilibrium with two different solid phases: SnO_2 at $C_{\text{H}_2\text{O}} > 4.10^{-2}\text{M}$ and Na_2SnO_3 at $C_{\text{H}_2\text{O}} < 4.10^{-2}\text{M}$.

In the case of sodium hydroxide, the shift from the Na_2SnO_3 solid phase in acidic melts to the Na_4SnO_4 precipitate in basic melts implies an equilibrium between SnO_3^{2-} and SnO_4^{4-} species in the liquid phase with limiting concentrations prescribed respectively by the solubilities of Na_2SnO_3 and Na_4SnO_4 . The low solubilities of these compounds preclude an accurate determination of the limiting concentration and hence a more quantitative description of these phenomena.

Another point of interest is the much higher solubility of sodium trioxostannate in the basic eutectic mixture than in the acidic melt. Similar trends in solubility involving the same dissolved and precipitated species have been observed in both solvents for various solutes (1). Such changes which, at our knowledge, have never been described in the literature might of course not be explained by classical equilibrium laws. A tentative explanation might eventually be found in a destabilization of the liquid quasi-lattice by water molecules leading to the precipitation of the most labilized species. Such a mechanism is to be compared with

the "salt effect" which occurs in molecular solvents and might be called a "reverse salt effect".

REFERENCES

- (1) G. Peeters, thèse de doctorat, Louvain-la-Neuve, April 1987.
- (2) P. Claes and J. Glibert, Molten Salt Techniques, Vol.1, p.89, Ed. D.G. Lovering and R.J. Gale, Plenum, New York and London (1983).
- (3) E.B. Hoyt, J. Chem. Eng. Data, 12, 461 (1967).
- (4) C. Canoo and P. Claes, Electrochim. Acta, 19, 37 (1974).
- (5) P. Claes, G. Peeters and J. Glibert, Bull. Soc. Chim. Belg., 94, 809 (1985).
- (6) P. Tilman, J.P. Wiaux, C. Dauby, J. Glibert and P. Claes, J. Electroanal. Chem., 167, 117 (1984).

ACKNOWLEDGEMENTS

The authors are much indebted to the FRFC (Fonds de la Recherche Fondamentale Collective) for financial assistance in this research.

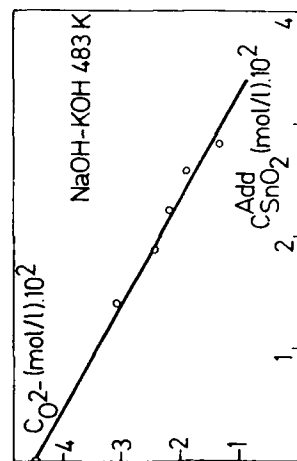


Figure 1 : Basic eutectic mixture at 483 K : oxide ion concentration dependence of the tin (IV) concentration.

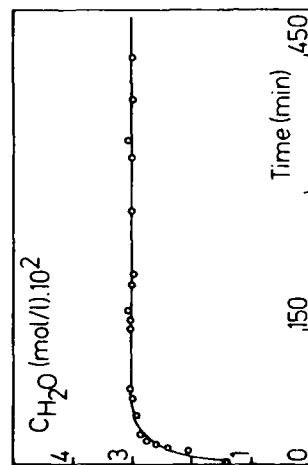


Figure 3 : Time dependence of the concentration of water after introduction of $\text{CaSnO}_3 \cdot 3\text{H}_2\text{O}$ in the acidic eutectic mixture.

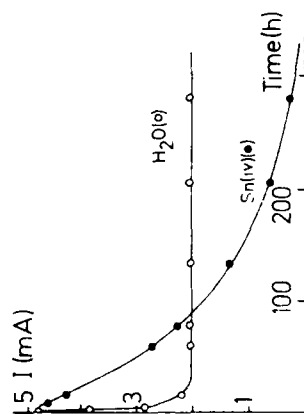


Figure 2 : Time dependence of the peak intensities of lithium sweep voltammograms for the reduction of water and of Sn(IV) .

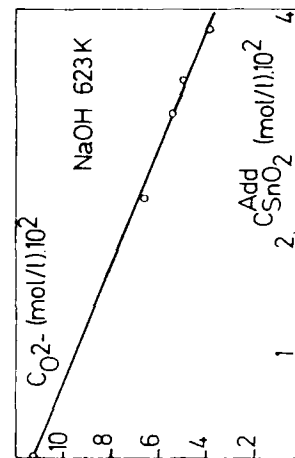


Figure 4 : Basic sodium hydroxide at 623 K : oxide ion concentration as a function of the added amount of SnO_2 .

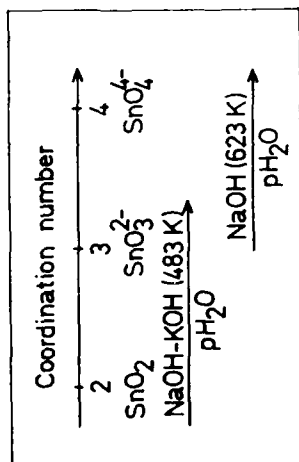


Figure 5 : Comparison of the solvents with regard to the coordination number of Sn(IV) .

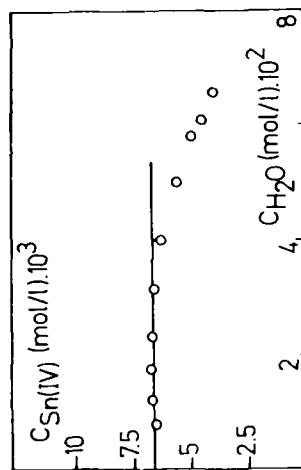


Figure 6 : Water concentration dependence of the solubility of SnO_3^{2-} .

OPTICAL BASICITIES IN SOME OXIDE - HALIDE SYSTEMS

T.Nakamura and Y.Ueda

Department of Metallurgical Engineering, Faculty of Engineering,
Kyushu Institute of Technology,
Kitakyushu, JAPAN. 804

T.Yanagase

Department of Chemical Engineering, Faculty of Engineering,
Kyushu Sangyo University,
Fukuoka, JAPAN. 814

ABSTRACT

The optical basicities in some halide compounds and in oxide - halide systems such as $\text{CaO} - \text{CaF}_2$, $\text{CaO} - \text{CaCl}_2$ systems have been measured using photoacoustic spectroscopy in order to examine an application of the optical basicity concept for oxide - halide systems. The optical basicities measured in this study were compared with the values of the theoretical optical basicity based on the concept of the average electron density (D). The optical basicities measured were in agreement with the theoretical optical basicities in $\text{CaO} - \text{CaF}_2$ and $\text{CaO} - \text{CaCl}_2$ systems. On the other hand, two values of the optical basicity were obtained from the sample in $\text{CaO} - \text{NaCl}$ system. One of them was considered to correspond to the optical basicity of CaO .

INTRODUCTION

The basicity in slags, salts and glasses is an important concept when considering the reactivity of those melts from a point of view acid - base behaviour. A number of expressions and models for basicity have been proposed over the years(1)-(3). The concept of capacity summarized by Wagner played a distinct role in understanding the basicity of metallurgical slags(4). Duffy and Ingram tried to define the basicity of oxyacids and salts from the concept of Lewis basicity and proposed the optical basicity(5)-(8).

The scale of the optical basicity was set up by the nephelauxetic effect in the outer s and p orbitals of probe ions such as Tl^+ , Pb^{2+} and Bi^{3+} and was normalized with the optical basicity of CaO which is unity. The theoretical optical basicity based on the Pauling type electronegativity and a calculation method of it in the multi-components were also proposed by Duffy and Ingram(6). Since the values of the theoretical optical basicity showed a good agreement

with the values of the optical basicity measured in oxyacids, the theoretical optical basicity has been applied to the metallurgical slags(9)-(11). However, the values of the theoretical optical basicity of transition metal oxides could not be calculated. A new scale of the theoretical optical basicity was defined by two of the authors using the concept of the average electron density(12) to overcome this difficulty (13). It is also possible to calculate the theoretical optical basicities of the multi-component systems containing even halides using a new scale. Therefore, the optical basicities of alkali halides and alkaline earth oxide - halide systems were measured to determine whether the new theoretical optical basicity can be used as a scale.

EXPERIMENTAL

Sample Preparation

All samples were made from extra high purity grade alkali or alkaline carbonates and halides which were anhydrous. The preparations such as mixing the samples were carried out in the dry box.

The glassy samples doped with 1.0×10^{-4} - 1.0×10^{-3} mass% PbO were prepared for measuring the optical basicity. These glasses were melted in Pt or alumina crucible at 1273 - 1873K, depending on the melting point. After melting, the melts were quenched by double-roll technique.

Photoacoustic Spectroscopy

UV spectra of samples due to $Pbs-p$ transition were measured on an edt-OAS 400 photoacoustic spectrometer. The wavelength of this spectrometer ranges from the ultraviolet to far infrared region. A schematic diagram is shown in Fig.1. It has two locked-in amplifiers and a mechanical chopper which covers the modulation frequency from 20 Hz to 240 Hz. The cell is constructed from aluminum, with a fused silica window. The photoacoustic signal is detected with a high sensitive microphone which is located at the back of the cell. The photoacoustic signals are recorded with a micro computer and displayed on a X-Y recorder.

RESULTS AND DISCUSSION

Theoretical Optical Basicity Based on The Average Electron Density

A new scale of the theoretical optical basicity was established by means of the concept of the average electron density instead of the Pauling type electronegativity. The basicity moderating parameters of the new theoretical optical basicity have a linear relationship with the average electron density values, as shown in

equation (1)(13).

$$\gamma = 1.34 \cdot (D + 0.6) \quad (1)$$

The average electron density was defined as equation (2).(13)

$$D = \alpha \frac{Z}{r^3} \quad (2)$$

where α : a parameter due to anion
 Z : valence of cation
 r : interionic distance between anion and cation

The selected values of the theoretical optical basicity are shown in Table 1. The optical basicity values of transition metal oxides could be found in Table 1, which were not able to be calculated from the Pauling type electronegativity. The values of acidic oxides such as SiO_2 and P_2O_5 in Table 1 are very close to the values of the theoretical optical basicity by Duffy and Ingram. On the other hand, the values of K_2O , Na_2O and BaO in Table 1 are lower than those by Duffy and Ingram. Although the optical basicity of GeO_2 is higher than that of SiO_2 in the theoretical optical basicity scale by Duffy and Ingram, the contrary order is obtained in the new scale. The optical basicity values in germanate systems measured by Sumita et al(14) were smaller than those in silicate systems. Therefore, it is considered that the theoretical optical basicity based on the average electron density is better than that based on the Pauling type electronegativity.

Optical Basicity in Oxide - Halide Systems

The concept of the optical basicity could apply to not only oxiacid systems but also halide systems(5). Angell and Benett measured the optical basicity of chloride melts and reported that the change of optical basicity values corresponded to that of activity(15). Bruce and Duffy also measured the optical basicity in fluoride systems and demonstrated a possibility to use the optical basicity for a basicity scale in fluoride - oxide systems. However, they have not presented the theoretical optical basicity values of halide compounds which are able to use even in the oxide - halide systems(16)(17).

The theoretical optical basicity values of alkaline earth fluoride and chloride compounds were obtained using equations (1) and (2). Since the values of α were necessary to calculate the optical basicity values in the systems, those values were decided by the optical basicity values of CaF_2 and CaCl_2 respectively which were calculated from the Pbs-p spectra peaks measured by photoacoustic spectroscopy.(13) The results are shown in table 2. Generally speaking, the optical basicity values of chloride systems are larger than those of fluoride systems. The optical basicity in oxide - halide systems were calculated using the same technique in the multi-

components oxide systems, by means of equation (3) and (4).

$$\Lambda = \sum_i (\Lambda_i \cdot X_i) \quad (3)$$

$$X_i = \frac{(V_i/2) \cdot n_i \cdot N_i}{\sum_i (V_i/2) \cdot n_i \cdot N_i} \quad (4)$$

X_i : theoretical optical basicity of i component
 V_i : valence of anion in i component
 n_i : number of anion in i component
 N_i : mole fraction of i component

The values of the optical basicity in $\text{CaO} - \text{CaF}_2$ system were measured in order to compare with the theoretical optical basicity. Pbs-p spectra of glassy samples in $\text{CaO} - \text{CaF}_2$ systems are shown in Fig.2. X-ray diffraction technique was used for a confirmation of glassy state of the samples. 250 nm was obtained as a peak wave length of pure CaF_2 . Although the Pbs-p spectra were not sharp, the peak shift was clearly observed. The wave length of peak shifted to long-wave length side when increasing the CaO content in the $\text{CaO} - \text{CaF}_2$ system. The change of the measured optical basicity values with CaO content is shown in Fig.3 with that of the theoretical optical basicity. Both of them increase with an increase of CaO content. The measured values show a good agreement with the theoretical values. The same plots in $\text{CaO} - \text{CaCl}_2$ system are shown in Fig.4. Although the differences between both measured and theoretical values increase with increasing CaO content, both values increase also with increasing CaO content as in Fig.3. It is understood from the results of Fig.3 and 4 that the theoretical optical basicity calculated from the average electron density can work as a basicity scale in $\text{CaO} - \text{CaF}_2$ and $\text{CaO} - \text{CaCl}_2$ systems.

The optical basicity values of alkali chloride compounds were measured by the same method. The results are shown in Table 3 with the theoretical values calculated by equations (1) and (2) using $\lambda = 4.9$. Although a difference of absolute value between the measured and theoretical values exists, the theoretical values qualitatively correspond to the measured values as the basicity increases in order of $\text{LiCl} < \text{NaCl} < \text{KCl}$. It also indicates a possibility of the application of the theoretical optical basicity in alkali chloride system. Furthermore, the optical basicity in $\text{CaO} - \text{NaCl}$ system as measured. Samples were melted at 1673 K and quenched by double-roll technique since no phase diagram is available for this system. After checking the samples by X-ray diffraction method, a broad diffraction pattern of CaO was obtained even in $\text{NaCl} + 5 \text{ mol\% CaO}$ sample. It is suggested that a solubility of CaO in NaCl melt is very small at 1673 K. A typical Pbs-p spectrum is shown in Fig.5 with Pbs-p spectrum of pure NaCl . Two peaks were observed in the range of 200 - 400 nm, a lower peak at 266 nm and a higher one at 343 nm. The lower peak is considered to correspond to the basicity of NaCl rich melt, while

the higher peak to the basicity of CaO which is about unity. It is estimated that the probe ions, Pb^{2+} , occupy two sites, one is the position which expresses the basicity of NaCl rich melt and the other is the basicity of CaO.

CONCLUSION

The optical basicity in CaO - CaF_2 , CaO - $CaCl_2$, alkali chloride and CaO - NaCl systems was measured using photoacoustic spectroscopy. The measured values of the optical basicity showed a qualitative agreement with the calculated values from the average electron density. Therefore, the theoretical optical basicity based on the average electron density could work as a wide range basicity scale in some oxide - halide systems.

REFERENCES

- (1) C.J.B. Fincham and F.D. Richardson, *Proc. Roy. Soc.*, **223**, 40 (1954)
- (2) M.R. Kalyanram, T.G. Macfarlane and H.B. Bell, *JISI*, **195**, 58 (1960)
- (3) K. Niwa and T. Yokokawa, *Trans JIM*, **10**, 3 (1969)
- (4) C. Wagner, *Met. Trans B*, **6B**, 405 (1975)
- (5) J.A. Duffy and M.D. Ingram, *J. Amer. Chem. Soc.*, **93**, 6448 (1971)
- (6) J.A. Duffy and M.D. Ingram, *J. Inorg. Nucl. Chem.*, **36**, 43 (1974)
- (7) J.A. Duffy and M.D. Ingram, *J. Inorg. Nucl. Chem.*, **37**, 1203 (1975)
- (8) J.A. Duffy and M.D. Ingram, *J. Non-Crystal. Solids*, **21**, 373 (1976)
- (9) J.A. Duffy, M.D. Ingram and I.D. Sommerville, *J. Chem. Soc. Farad. Trans.*, **74**, 1410 (1978)
- (10) D.R. Gaskell, *TISI Japan*, **22**, 997 (1982)
- (11) H. Suito and R. Inoue, *TISI Japan*, **24**, 47 (1984)
- (12) R.T. Sanderson, *Chemical Bonds and Bond Energy*, 2nd Ed., Academic Press, New York (1971)
- (13) T. Nakamura, Y. Ueda and J.M. Toguri, *J. Jap. Inst. Met.*, **50**, 456 (1986)
- (14) S. Sumita, Y. Mastumoto, K. Morinaga and T. Yanagase, *Trans JIM*, **27**, 360 (1982)
- (15) C.A. Angell and P.D. Bennett, *J. Amer. Chem. Soc.*, **93**, 6304 (1982)
- (16) A.J. Bruce and J.A. Duffy, *Phys. Chem. Glasses*, **23**, 53 (1982)
- (17) A.J. Bruce and J.A. Duffy, *J. Chem. Soc. Farad. Trans.*, **78**, 907 (1982)

Table 1. The selected values of the basicity moderating parameter and the theoretical optical basicity in oxide compounds.

Compound	γ	Λ	Compound	γ	Λ
Li ₂ O	0.95	1.05	CuO	1.12	0.89
Na ₂ O	0.91	1.10	B ₂ O ₃	2.40	0.42
K ₂ O	0.87	1.15	Al ₂ O ₃	1.47	0.68
Rb ₂ O	0.86	1.16	Fe ₂ O ₃	1.44	0.69
Cs ₂ O	0.85	1.18	Cr ₂ O ₃	1.44	0.69
MgO	1.09	0.92	As ₂ O ₃	1.39	0.72
CaO	1.00	1.00	Sb ₂ O ₃	1.25	0.80
SrO	0.96	1.04	Bi ₂ O ₃	1.14	0.87
BaO	0.93	1.08	CO ₂	2.49	0.40
MnO	1.05	0.95	SiO ₂	2.11	0.47
FeO	1.07	0.93	GeO ₂	1.64	0.61
CoO	1.07	0.93	TiO ₂	1.56	0.64
NiO	1.14	0.87	P ₂ O ₅	2.60	0.38
ZnO	1.13	0.89	SO ₃	3.48	0.29

Table 2. The values of the theoretical optical basicity in alkaline earth fluoride and chloride compounds.

Compound	γ	Λ
MgF ₂	1.82	0.55
CaF ₂	1.49	0.67*
SrF ₂	1.33	0.75
BaF ₂	1.25	0.80
MgCl ₂	1.59	0.63
CaCl ₂	1.39	0.72*
SrCl ₂	1.28	0.79
BaCl ₂	1.20	0.83

*measured

Table 3. The values of the theoretical optical basicity in alkali chloride compounds.

Compound	measured Λ	calculated Λ
LiCl	0.67	0.83
NaCl	0.72	0.91
KCl	0.79	1.02

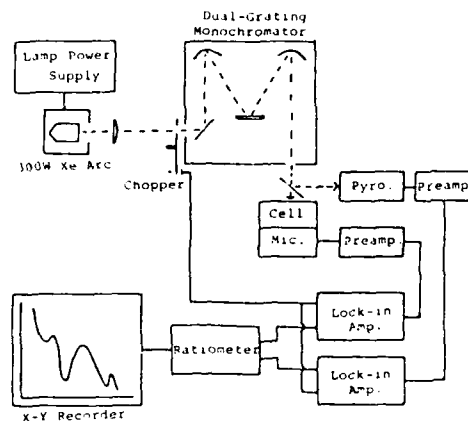


Figure 1. Schematic diagram of the double beam photoacoustic spectrometer.

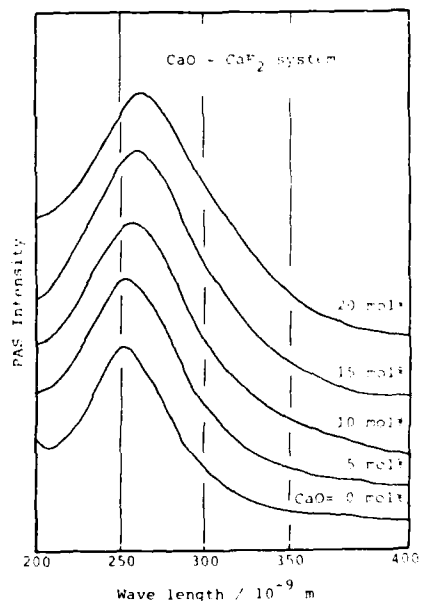


Figure 2. Pbs-p spectra in CaO - CaF₂ system.

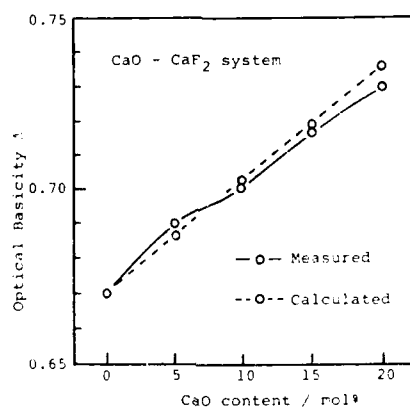


Figure 3. Change of the optical basicity with CaO mol% in CaO - CaF₂ system

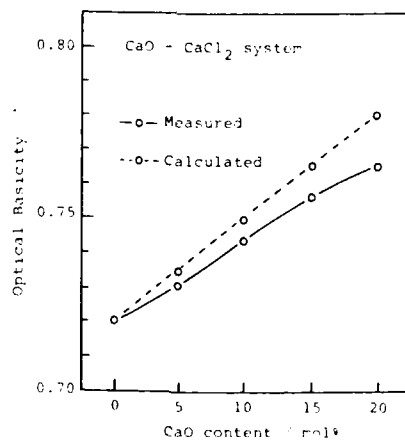


Figure 4. Change of the optical basicity with CaO mol% in CaO - CaCl₂ system.

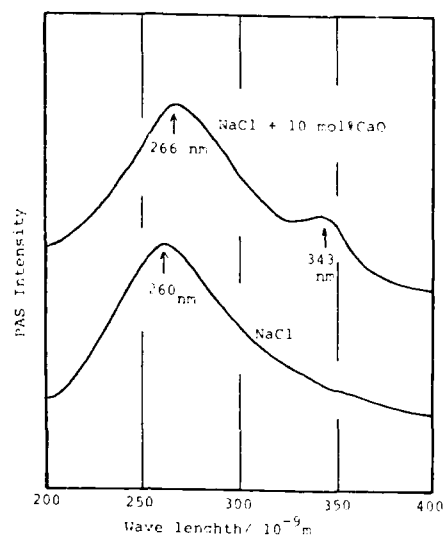


Figure 5. Pbs-p spectra in CaO - NaCl system.

INFRARED REFLECTION SPECTRA OF AlCl_3 - MCl_2
($\text{M} = \text{Mg}, \text{Ca}, \text{Sr}, \text{Ba}, \text{Mn}$ and Zn) AND OXOCHLOROALUMINATE MELTS

Mari-Ann Einarsrud and Erling Rytter

Institute of Inorganic Chemistry, The Norwegian Institute of Technology,

University of Trondheim, N-7034 Trondheim-NTH, Norway.

ABSTRACT

Infrared (IR) reflection spectra have been recorded of melts in the systems MgCl_2 - AlCl_3 , CaCl_2 - AlCl_3 , SrCl_2 - AlCl_3 , BaCl_2 - AlCl_3 , MnCl_2 - AlCl_3 , ZnCl_2 - AlCl_3 as well as of molten oxochloroaluminates. In mixtures of AlCl_3 with MgCl_2 or MnCl_2 , AlCl_4^- acts as both a tri- and bidentate ligand towards M^{2+} , whereas in the ZnCl_2 - AlCl_3 system only C_{2v} perturbation of AlCl_4^- has been found. These melts are considered to contain essentially neutral species. In the more ionic CaCl_2 , SrCl_2 and BaCl_2 systems, both perturbed and unperturbed AlCl_4^- are present. The magnitude of the observed splitting of the antisymmetric stretching vibration, $\nu_3(\text{F}_2)$, for both C_{2v} and C_{3v} perturbation of AlCl_4^- show an approximately linear dependence on the ionic potential of the cation, z/r_c . Splitting of the antisymmetric stretching vibration of the symmetric AlCl_3 top for Al_2Cl_7^- indicates a bent Cl-Al-Cl bridge, probably stabilized by interactions with the divalent cations. The oxochloroaluminate compound $\text{NaAl}_2\text{OCl}_5$ has been synthesized. Infrared spectra have been recorded of molten $\text{NaAl}_2\text{OCl}_5$ and mixtures with AlCl_3 . The complex ion $\text{Al}_4\text{O}_2\text{Cl}_{10}^-$ is proposed to be present in molten $\text{NaAl}_2\text{OCl}_5$.

INTRODUCTION

From previous spectroscopic and electrochemical measurements chloroaluminate melts are considered to contain the species: AlCl_4^- , Al_2Cl_7^- , higher polymers as for instance $\text{Al}_3\text{Cl}_{10}^-$ and Al_2Cl_6 as the concentration of AlCl_3 increases (1-4). Due to experimental difficulties only a few infrared measurements of high temperature molten salts are reported in the literature (1,5). A number of Raman measurements, however, have been carried out (6).

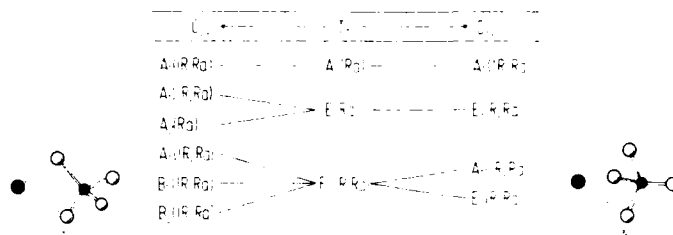
The four fundamental frequencies observed for tetrahedral AlCl_4^- in CsAlCl_4 by Raman spectroscopy are (2):

- $\nu_1(\text{A}_1) = 344 \text{ cm}^{-1}$ (symmetric stretch)
- $\nu_2(\text{E}) = 120 \text{ cm}^{-1}$ (bend)
- $\nu_3(\text{F}_2) = 483 \text{ cm}^{-1}$ (antisymmetric stretch)
- $\nu_4(\text{F}_2) = 178 \text{ cm}^{-1}$ (bend).

From infrared measurements the following frequencies are observed by Hvistendahl *et al.* (1,7) 182, 346 and 474 cm^{-1} . The $\nu_1(\text{A}_1)$ mode is observed even though it should be inactive in the infrared for a regular tetrahedron.

A correlation diagram for the activation and splitting of the fundamental frequencies from AlCl_4^- (T_d) to C_{2v} and C_{3v} symmetry is given in Table 1. Only one of the two F_2 fundamentals for the regular tetrahedron is included in the table.

Table 1. Correlation diagram applicable to the vibrational modes of AlCl_4^- with T_d , C_{2v} and C_{3v} symmetry.



If two of the chlorines in AlCl_4^- are different from the other two the ion will have C_{2v} symmetry. From the table it is seen that the $\nu_3(\text{F}_2)$ frequency will split into three frequencies (A_1 , B_1 and B_2) and the $\nu_1(\text{A}_1)$ frequency will be activated in the infrared. On the other hand, if only one of the chlorines in AlCl_4^- is different from the others, the symmetry of the anion is C_{3v} , and the $\nu_3(\text{F}_2)$ mode will split into two species (A_1 and E) and the totally symmetric $\nu_1(\text{A}_1)$ frequency will be activated. From Raman (6) and infrared (1,5) measurements on AlkCl-AlCl_3 (Alk = alkali) melts only small perturbation from the ideal tetrahedral structure of AlCl_4^- is found. Rytter *et al.* (2) have proposed a D_{3d} symmetry for Al_2Cl_7^- in these systems. However, Hvistendahl *et al.* (1) observed a splitting of the $\nu_{11}(\text{E}_g)$ band for Al_2Cl_7^- (D_{3d}) in molten LiAl_2Cl_7 . The splitting was interpreted as a stabilization of a bent bridge for $\text{Li}^+\text{Al}_2\text{Cl}_7^-$.

For the melts studied in this work large perturbations of the AlCl_4^- and Al_2Cl_7^- anions are expected due to interactions with the divalent cations present. Higher polymers as $\text{Al}_3\text{Cl}_{10}^-$ are not likely to be present in these melts as cations with a large ionic potential probably are able to distort any polymers.

This assumption is verified by the Raman spectra of $\text{ZnCl}_2\text{-AlCl}_3$ melts where mainly ZnCl_2 and Al_2Cl_6 were considered to be present (8). In $\text{SnCl}_2\text{-AlCl}_3$ melts a Raman splitting of $\nu_3(\text{F}_2)$ has been reported (9,10).

The spectra were recorded on a Bruker 113v FTIR Interferometer employing a closed diamond windowed cell as described previously (11). The nominal resolution of the spectra is 8 cm^{-1} .

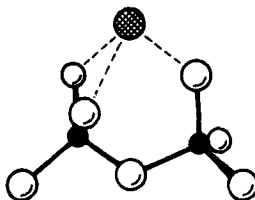
ALKALINE EARTH CHLORIDE OR TRANSITION METAL CHLORIDE - ALUMINIUM CHLORIDE SYSTEMS

MnCl₂-AlCl₃

In analogy with the Mg system (12) Fig. 1 indicates that both the C_{2v} and C_{3v} configurations of AlCl_4^- are present in the Mn system. The frequencies 400 , 488 and 574 cm^{-1} are supposed to reflect the splitting of the antisymmetric stretch, $\nu_3(\text{F}_2)$ of the tetrahedral AlCl_4^- , upon perturbation from T_d to C_{2v} symmetry, and the strong bands at 574 and 450 cm^{-1} have their origin in descent in symmetry from T_d to C_{3v} symmetry. The appearance of the totally symmetric stretch, $\nu_1(\text{A}_1)$, at 339 cm^{-1} verifies that distortions do take place.

The degeneracy at 574 cm^{-1} deserves a comment. A parallel situation was found for molten $\text{MgCl}_2\text{-AlCl}_3$ mixtures (C_{2v} : 573 , 498 and 404 cm^{-1} and C_{3v} : 573 and 452 cm^{-1}) (12) and for solid TiAl_2Cl_8 and $\text{TiAl}_2\text{Cl}_8 \cdot 6\text{C}_6\text{H}_6$ with known structures (C_{2v} : 554 , 504 and 442 cm^{-1}) and (C_{3v} : 552 and 446 cm^{-1}) (13). It is intriguing, however, that the degeneracy is found for all $\text{MCl}_2\text{-AlCl}_3$ mixtures and that the resulting band is fairly sharp.

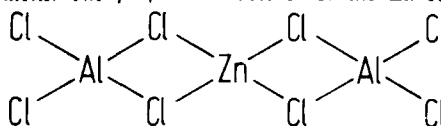
For the Mn system, it is proposed that the strong polarizing power of the manganese cation stabilizes a bent (C_s) structure rather than a linear (D_{3d}) structure of Al_2Cl_7^- .



This interaction is manifested by the observed splitting of $\nu_{11}(\text{E}_g)$ from 530 cm^{-1} for molten KAl_2Cl_7 (Fig. 4) to 589 and 493 cm^{-1} upon perturbation from D_{3d} to C_s symmetry. The observed splitting for $\text{Mg}^{2+}\text{-Al}_2\text{Cl}_7^-$ is 596 and 500 cm^{-1} and for $\text{Li}^+\text{-Al}_2\text{Cl}_7^-$ 570 and 506 cm^{-1} (Fig. 4). Thus, the counterions with high charge/radius ratio strongly perturb both the symmetric Cl-AlCl_3 tops of Al_2Cl_7^- . An alternative structure to the figure above is that two cations perturb each Al_2Cl_3 -entity of Al_2Cl_7^- . At higher aluminium chloride concentrations, strong bands of Al_2Cl_6 at 617 , 475 , 412 and 318 cm^{-1} appear.

$ZnCl_2-AlCl_3$

The $ZnCl_2$ system (Fig. 2) is distinctly different from other chloroaluminates investigated in our laboratory. The spectra are interpreted in terms of superpositions of the spectra of perturbed $AlCl_4^-$ and Al_2Cl_6 . For $AlCl_4^-$ the $\nu_3(F_2)$ is split into three dominant bands (389, 483 and 589 cm^{-1}), indicating only a C_{2v} perturbation from the tetrahedral model. Due to the almost equal Lewis acidity of $AlCl_3$ and $ZnCl_2$, the molecular species $Zn(AlCl_4)_2$ and Al_2Cl_6 probably are present in the melts. The proposed structure for the Zn-complex is:



Begun *et al.* (8) have recorded Raman spectra of the same mixtures. They interpreted the spectra as $ZnCl_2$ aggregates and Al_2Cl_6 , and they concluded that no appreciable amounts of the anions $AlCl_4^-$, $Al_2Cl_7^-$ or $ZnCl_4^{2-}$ were formed in any of the samples. The authors found two bands in the Al-Cl stretching region at 592 and 490 cm^{-1} (608 and 512 cm^{-1} in pure $AlCl_3$) and assigned them to Al_2Cl_6 . These frequencies correspond to the bands at 589 and 483 cm^{-1} observed in this work.

The authors also observed the following trends which they could not explain: (1) The intensity of the band at 119 cm^{-1} attributed to Al_2Cl_6 decreased with the concentration of $AlCl_3$ in the melts (2). The disproportionate decrease in the intensity of the 341 cm^{-1} band relative to the 512 cm^{-1} peak. These two observations are expected when the melts are considered to contain $Zn(AlCl_4)_2$ (with local symmetry C_{2v} for $AlCl_4^-$) and Al_2Cl_6 . A reassignment of the Raman data is included in Table 2.

Only two of the three antisymmetric stretching bands originating from C_{2v} perturbed $AlCl_4^-$ are observed in the Raman spectra. The band at 490 cm^{-1} has a higher intensity in the Raman spectra than the band at 592 cm^{-1} and probably is the symmetric mode A_1 . This interpretation has been verified by normal coordinate calculations (15). The band should be polarized in Raman as observed by Begun *et al.* (8). As further verification of the new melt model for the Zn system a band at *ca.* 310 cm^{-1} has been reported, even in a basic melt. This band is in agreement with the dominant $\nu_2(A_g)$ band for $Al_2Cl_7^-$ (2). The presence of $Al_2Cl_7^-$ in a formally basic melt indicates almost equal Lewis acidity of $ZnCl_2$ and $AlCl_3$.

$SnCl_2-AlCl_3$

Taulelle and Gilbert *et al.* (9,10) have measured Raman spectra of $SnCl_2-AlCl_3$ -mixtures. From a spectrum of an acidic melt (71 mol%) they concluded that the $\nu_3(F_2)$ of $AlCl_4^-$ was split into three frequencies at 425, 480 and 575 cm^{-1} . Only the band at 425 cm^{-1} was shown to be polarized.

An alternative interpretation (see Table 2) is supported by the polarized band at

ca. 310 cm^{-1} present in the reported spectrum. In previous Raman investigations (2) of chloroaluminate melts polarized bands at ca. 310 and 430 cm^{-1} were assigned to Al_2Cl_7^- . Thus an alternative interpretation of the band observed at 425 cm^{-1} is $\nu_1(\text{A}_{1g})$ of Al_2Cl_7^- . This conclusion is confirmed by the fact that the B_2 antisymmetric stretching component of C_{2v} perturbed AlCl_4^- was not observed by Begun *et al.* (8) for the ZnCl_2 -system, but was found in the corresponding IR spectrum. The polarized band of the three ν_3 components in C_{2v} symmetry (B_1 , A_1 and B_2) is predicted from theoretical calculations (15) to be the one in the middle. The polarization observed by Taulelle and Gilbert *et al.* (9,10) appears not to be in agreement with this prediction. However, as the origin in the unperturbed AlCl_4^- is a depolarized band, the A_1 component is expected only to be slightly polarized.

Table 2. Assignment of IR and Raman frequencies observed in the ZnCl_2 - AlCl_3 and SnCl_2 - AlCl_3 systems.

Al_2Cl_6	IR Zn		Raman ^a Zn		Raman ^b Sn	IR Al_2Cl_6	Raman ^c Al_2Cl_6
	67 % AlCl_3	80 % AlCl_3	70 % AlCl_3	90 % AlCl_3	71 % AlCl_3		
$\nu_{18}(\text{B}_{2u})$		144				145	
$\nu_7(\text{B}_{1g})$			165	165			166
$\nu_9(\text{B}_{1u})$		173				178	
$\nu_3(\text{A}_g)$			218	218			218
$\nu_{17}(\text{B}_{3u})$	312	316				316	
$\nu_2(\text{A}_g)$			340	339			341
$\nu_{13}(\text{B}_{2u})$	409	408				410	
$\nu_1(\text{A}_g)$				500			512
$\nu_{16}(\text{B}_{3u})$		474				473	
$\nu_{11}(\text{B}_{2g})$				605			610
$\nu_1(\text{A}_g)$							
$\nu_8(\text{B}_{1u})$		612				614	
$\text{M}(\text{AlCl}_4)_2$							
$\nu_4(\text{E})$	170	170	165				
$\nu_1(\text{A}_1)$	335	334	340	340	341		
$\nu_3(\text{B}_2, \text{C}_{2v})$	389	385					
$\nu_3(\text{A}_1, \text{C}_{2v})$	483	492	490		480		
$\nu_3(\text{B}_1, \text{C}_{2v})$	589	590	592		575		

^aBegun *et al.* (8), ^bTaulelle and Gilbert *et al.* (9,10), ^cTomita *et al.* (14).

Perturbations of AlCl_4^-

Perturbations of AlCl_4^- and Al_2Cl_7^- by interactions with the cations K^+ , Li^+ , Ba^{2+} , Sr^{2+} , Ca^{2+} , Mg^{2+} , Mn^{2+} and Zn^{2+} are studied as the ionic potential of the cations changes. Introduction of polarizability gave poorer correlations.

whereas shielding only has been considered qualitatively.

Spectra of AlkAlCl_4 ($\text{Alk} = \text{Li, K}$), $\text{M}(\text{AlCl}_4)_2$ ($\text{M} = \text{Ba, Ca, Mn and Zn}$) and 30 mol% MgCl_2 :70 mol% AlCl_3 are compared in Fig. 3. For the Ca, Sr and Ba mixtures the spectra are interpreted in terms of unperturbed AlCl_4^- observed as the intense bands at 459, 470 and 471 cm^{-1} , respectively, in addition to AlCl_4^- perturbed by the cation. In analogy with the Mg and Mn systems a C_{3v} type of perturbation dominates, cf. Table 3.

Table 3. Observed frequencies for C_{2v} and C_{3v} perturbed AlCl_4^- in MCl_2 - AlCl_3 melts.

	Ba	Sr	Ca	Mg ^b	Mn	Zn
C_{2v} $\begin{cases} \text{B}_2 \\ \text{A}_1 \\ \text{B}_1 \end{cases}$		470 vs ^a	459 vs ^a	404 sh	400 sh	389 m
		508 sh	514 sh	498 sh	488 sh	483 vs
		559 m	558 s	573 vs	574 vs	589 vs
C_{3v} $\begin{cases} \text{E} \\ \text{A}_1 \end{cases}$	471 vs	470 vs ^a	459 vs ^a	452 s	450 vs	
	556 sh	559 m	558 s	573 vs	574 vs	

^aThese bands are also interpreted as due to $\text{AlCl}_4^-(\text{T}_d)$.

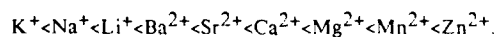
^bFrom Einarsrud *et al.* (12).

Observed splitting of $\nu_3(\text{F}_2)$ for C_{2v} (B_1 and B_2 species) and C_{3v} (A_1 and E species) perturbed AlCl_4^- given as a function of the ionic potential of the cation, gives essentially straight lines in Figs. 5 and 6. The cation radii used are the crystal radii from Shannon (16) with coordination number of six for Li^+ and the alkaline earth metal cations, both six and four for Mn^{2+} and four for Zn^{2+} .

A better fit to the line was obtained using the radius for coordination number four for Mn^{2+} . This observation may be an artifact due to a larger effective ionic potential for a transition metal.

The B_1 antisymmetric stretching component of $\nu_3(\text{F}_2)$ for C_{2v} perturbed AlCl_4^- in SnCl_2 - AlCl_3 is observed at 575 cm^{-1} (9,10). If $\text{Sn}(\text{AlCl}_4)_2$, with four coordination for Sn^{2+} , is present in the melts, the B_2 component of the antisymmetric stretching vibration is estimated to be at ca. 390 cm^{-1} . Indeed, a shoulder appears to be present at ca. 390 cm^{-1} .

To summarize, increased interactions between M^{n+} and AlCl_4^- , i.e. increased splitting of $\nu_3(\text{F}_2)$, are observed in the series



Perturbations of Al_2Cl_7^-

Spectra of $\text{AlkAl}_2\text{Cl}_7$ ($\text{Alk} = \text{K and Li}$) and $\text{M}(\text{Al}_2\text{Cl}_7)_2$ ($\text{M} = \text{Ba, Ca, Mg, Mn and Zn}$) are compared in Fig. 4.

For all the cations in the systems investigated, except K^+ , the $\nu_{11}(E_u)$ band is split into two frequencies, indicating a perturbation of $Al_2Cl_7^-$ from D_{3d} to C_s (bent structure) symmetry.

Increased interactions, *i.e.* splitting of $\nu_{11}(E_u)$, are observed when going from K^+ to Ca^{2+} . For $Mg(Al_2Cl_7)_2$ and $Mn(Al_2Cl_7)_2$ the picture is more complicated because the spectra are superpositions of $M(AlCl_4)_2$, $M(Al_2Cl_7)_2$ and Al_2Cl_6 . For $Zn(Al_2Cl_7)_2$ no bands attributable to $Al_2Cl_7^-$ were detected.

Coordination of M^{2+} in MCl_2-AlCl_3 melts

Bands which cannot be attributed to $AlCl_4^-$, $Al_2Cl_7^-$, ... or Al_2Cl_6 are interpreted as a direct observation of interactions between the divalent cation and the chloroaluminate complexes, *i.e.*, $M^{2+}Cl$ vibrations (Table 4).

Table 4. Observed $M^{2+}Cl$ frequencies, $M = Mg$ (12), Ca , Sr , Ba , Mn and Zn , relative half-widths of the strongest bands and $M-Cl$ stretching force constants.

M	Frequencies (cm^{-1})	Half-width (cm^{-1})	f_{M-Cl} ($10^{-2} N \cdot m^{-1}$)
Mg	288	120	0.66
Ca	223	60	0.55
Sr	209	35	0.61
Ba	203	20	0.63
Mn	232, 250 sh	70	0.64
Zn	288	80	1.10

For the alkaline earth systems a broad band for the $M^{2+}Cl$ stretchings is observed which shifts to higher frequencies and larger band-widths when the polarizing power of the cation increases. The force constants show that the shift is not only a mass effect, but reflects the strength of the interaction.

The IR spectra of $MnCl_2-AlCl_3$ mixtures (Fig. 1) contain two peaks assigned to $M^{2+}Cl$ stretching vibrations of four and six coordinated manganese. The spectra show a decrease in the intensity of the band at 250 cm^{-1} , whereas the band at 232 cm^{-1} seems to become more intense with increasing $MnCl_2$ content. The presence of coordination number four, contrary to only six coordination reported earlier (17) is supported by the following arguments:

- The observed splitting of $\nu_3(F_2)$ for $AlCl_4^-$ is larger than can be predicted from the ionic potential for Mn^{2+} in octahedral coordination (see Fig. 3 and 4).
- The pale yellow colour of the melts indicates that some Mn^{2+} is four coordinated, because the characteristic colour of MnX_4^{2-} is yellow-green while six coordinated manganese usually is pink (18).
- Structural changes do occur for compositions above 30 mol% $MnCl_2$, manifested by a steep rise of the melting point (19).

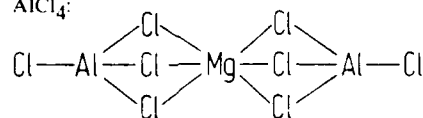
- (d) The presence of some AlCl_4^- which is perturbed to C_{2v} symmetry.

The spectra of the $\text{ZnCl}_2\text{-AlCl}_3$ (Fig. 2) system show a broad band at about 288 cm^{-1} which is attributed to $\text{Zn}\cdots\text{Cl}$ stretching for Zn^{2+} in tetrahedral coordination. A tetrahedral coordination for Zn^{2+} in these melts is expected for the following reasons:

- A C_{2v} perturbation of AlCl_4^- .
- Raman bands at 288 and 298 cm^{-1} observed for $\text{Cs}_2\text{ZnCl}_4(\text{s})$ (with tetrahedral configuration) and 277 cm^{-1} for Cs_2ZnCl_4 correspond to the $\text{Zn}\cdots\text{Cl}$ stretching frequency observed in this work (8).
- $\text{Zn}^{2+}(\text{d}^{10})$ has no octahedral site stabilization energy (OSSE) (20).
- The observed splitting of $\nu_3(\text{F}_2)$ for AlCl_4^- is in agreement with a four coordination for Zn (see Fig. 5).

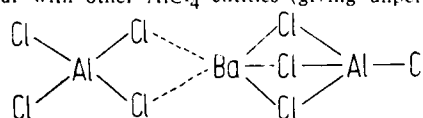
The following structural models for the alkaline earth melts are proposed:

- For the Mg-system the chloroaluminate species are bonded to the cation with almost equal M-Cl bond strengths as demonstrated for C_{3v} perturbation of AlCl_4^- :



Mobility of the chloroaluminate anions is possible. The presence of C_{2v} distorted AlCl_4^- in these melts indicates an intermediate structure for the exchange of AlCl_4^- where one of the Mg-Cl bonds above is broken.

- For the Ba-system one AlCl_4^- is attached tightly to Ba^{2+} , whereas only weak interactions occur with other AlCl_4^- -entities (giving unperturbed AlCl_4^-):



Dynamics in the melt is possible by migration of Ba^{2+} from one AlCl_4^- to another.

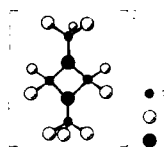
Apart from the found distortion of the anion, these models are supported by the following observations:

- Both perturbed and unperturbed AlCl_4^- are supposed to be present in the Ca, Sr and Ba systems, while only perturbed AlCl_4^- is found in the Mg system.
- The relative band-widths for the observed M-Cl stretching vibrations decrease in the series Mg, Ca, Sr and Ba, indicating a more well-coordinated complexation around Ba^{2+} than Mg^{2+} . Although this observation does not contain information on the proposed structures, *per se*, it at least is compatible with a gradual shift in the structure of the melts.
- There is only a slight decrease in the observed M-Cl stretching frequency when going from Ca to Sr and Ba. A larger decrease is expected when only the mass effect is considered.
- Mainly molecular species are expected to be present in the Mg-system, particularly as no immiscibility gap is present (12), whereas the Ca, Sr and

Ba systems are more ionic.

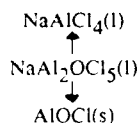
OXIDES IN CHLOROALUMINATE MELTS

The compound $\text{NaAl}_2\text{OCl}_5$ has been prepared by reacting AlCl_3 , NaCl and $\text{AlCl}_3 \cdot 6\text{H}_2\text{O}$ in a quartz ampoule at 120°C . A metastable melt phase is formed. Jentsch et al. (21) have prepared the disilver decachlorodioxotetraaluminate salt ($\text{Ag}_2[\text{Al}_4\text{O}_2\text{Cl}_{10}]$) by a similar procedure. This salt is built up by Ag^+ and $\text{Al}_4\text{O}_2\text{Cl}_{10}^{2-}$ ions. The anion also was found in the complex $[(\text{C}_6(\text{CH}_3)_6)_2\text{Nb}_2\text{Cl}_4]^{2+}[\text{Al}_4\text{O}_2\text{Cl}_{10}]^{2-} \cdot 2\text{CH}_2\text{Cl}_2$ by Thewalt and Stollmaier (22). The structure of the $\text{Al}_4\text{O}_2\text{Cl}_{10}^{2-}$ ion as determined by single crystal X-ray crystallography (21,22), is



and shows a four coordination for aluminium, oxygen in a three coordinated position and only terminal chlorines. This structure is likely to be present in solid $\text{NaAl}_2\text{OCl}_5$ as well.

When the compound $\text{NaAl}_2\text{OCl}_5$ is heated to 200°C for several hours a white solid starts to precipitate, confirming the metastability of the melt. This solid was separated from the rest of the liquid. IR transmission spectra of the solid and the remaining liquid are compared with spectra of $\text{NaAl}_2\text{OCl}_5(\text{s})$ and $\text{AlOCl}(\text{s})$ in Fig. 7. The precipitated solid is determined to be AlOCl (with impurities of NaAlCl_4) and the remaining liquid is NaAlCl_4 . Thus, it is verified that $\text{NaAl}_2\text{OCl}_5$ is a stoichiometric complex, which decomposes at 200°C , following the scheme:



The spectra of $\text{NaAl}_2\text{OCl}_5$ in the molten and solid state are very similar (Figs. 7 and 8) and the same complex probably is present in both phases. The bands are of course sharper for the solid and two of the most prominent bands are split into two, and therefore may belong to a degenerate species.

In infrared spectra of molten alkali chloroaluminates (1,5,7) two weak bands at ca. 680 and 790 cm^{-1} are assigned to combination bands. But from the present spectra it is apparent that these two bands are due to oxide species in the melt.

The intensity and position of the two bands are very stable for all the melt compositions studied (Fig. 8), and therefore probably are due to the same structural entity. In solid $\text{NaAl}_2\text{OCl}_5$ the band with the highest frequency is split into 787 and 809 cm^{-1} and the lowest oxide band is observed at 676 cm^{-1} . Because of the degeneracy, the highest frequency is assigned as an antisymmetric stretching of Al-O and the lowest to a symmetric stretch of the parent Al_3O entities.

These assignments can be justified as follows:

In an analysis of the Al-O vibrations, the Al_4O_2 entity may as a first approximation be considered as composed of two regular triangles of D_{3h} symmetry. As they combine to a D_{2h} skeleton, the stretching modes can be classified as

	Local Symmetry	Site symmetry	Skeletal symmetry	
	D_{3h}	C_{2v}	D_{2h}	
$2 \nu_{\text{Al-O}}$	A'_1	A_1	A_g	$2 \nu_{\text{Al-O}}$ sym. stretch
$2 \nu_{\text{Al-O}}$	E		B_{1g}	$\nu_{\text{Al-O}}$ ring stretch
		B_2	B_{2u}	$2 \nu_{\text{Al-O}}$ a.sym. stretch
			B_{3u}	$\nu_{\text{Al-O}}$ ring stretch

The more detailed nature of the fundamental vibrational modes in this fairly complex skeletal structure will be disclosed through a normal coordinate analysis.

In AlOCl the oxygen also is in a three coordinated position, and Al-O stretching frequencies are observed at 680, 713 and 826 cm^{-1} (Fig. 7). Apparently, the semi-degeneracy seems to be in the lowest frequencies in this case. A pyramidal compared to a planar entity may explain the difference.

In the Al-Cl stretching region two intense bands are observed for $\text{NaAl}_2\text{OCl}_5(l)$ (493 and 558 cm^{-1}) and in the solid state the lowest one of them is split into 495 and 512 cm^{-1} . The band at 493 cm^{-1} is assigned as the antisymmetric degenerate Al-Cl stretching of the axial AlCl_3 -groups, whereas the band at 558 cm^{-1} consequently is the antisymmetric Al-Cl-stretching in the equatorial AlCl_2 -groups. The equatorial frequency is higher than the axial because of one compared to two bridging ligands on aluminium, cf. the corresponding 614 cm^{-1} band of Al_2Cl_6 and 520 cm^{-1} of molten NaAl_2Cl_7 .

The frequency reduction from the chlorine to the oxygen bridged entities (614 \rightarrow 558 cm^{-1} and 520 \rightarrow 493 cm^{-1}) may be due to the larger electron affinity of oxygen. Indeed, the Al-Cl_{terminal} frequency reduction is twice as large for the entities with two adjacent Al-O_{bridge} bonds.

REFERENCES

1. Hvistendahl, J., Klæboe, P., Rytter, E. and Øye, H.A., *Inorg. Chem.* **23** (1984) 706.
2. Rytter, E., Øye, H.A., Cyvin, S.J., Cyvin, B.N. and Klæboe, P., *J. Inorg. Nucl. Chem.* **35** (1973) 1185.
3. Fung, K.W. and Mamantov, G. in *Advances in Molten Salt Chemistry*. Vol. 2, Braunstein, J., Mamantov, G. and Smith, G.P., Eds., Plenum Press, New York, 1973, p. 218.
4. Poulsen, F.W., *J. Raman Spectrosc.* **11** (1981) 302.
5. Smyrl, N.R., Mamantov, G. and McCurry, L.E., *J. Inorg. Nucl. Chem.* **40** (1978) 1489.
6. Brooker, H.M. and Papatheodorou, G.N. in *Advances in Molten Salt Chemistry*. Vol. 5, Mamantov, G. and Mamantov, C.B., Eds., Elsevier, New York 1983, p. 26.
7. Hvistendahl, J., *Thesis*, Institutt for uorganisk kjemi, NTH, Norway, 1982.
8. Begun, G.M., Brynestad, J., Fung, K.W. and Mamantov, G., *Inorg. Nucl. Chem. Letters* **8** (1972) 79.
9. Gilbert, B., Chimie Analytique, Université de Liege, Belgium, private communication.
10. Taulelle, F., *Thesis*, Université Pierre et Marie Curie, France, 1983.
11. Rytter, E., Hvistendahl, J. and Tomita, T., *Mol. Struct.* **79** (1982) 323.
12. Einarsrud, M.-A., Justnes, H., Rytter, E. and Øye, H.A., *Polyhedron*, in print.
13. Justnes, H., Rytter, E. and Andresen, A.F., *Polyhedron* **1** (1982) 393.
14. Tomita, T., Sjogren, C.E., Klæboe, P., Papatheodorou, G.N. and Rytter, E., *J. Raman Spec.* **14** (1983) 415.
15. Einarsrud, M.-A., *Thesis*, Institutt for uorganisk kjemi, NTH, Norway, 1987.
16. Shannon, R.D., *Acta Cryst.* **A32** (1976) 751.
17. Bues, W., El-Sayed, L. and Øye, H.A., *Acta Chem. Scand.* **31A** (1977) 461.
18. Cotton, A. and Wilkinson, G., *Advanced Inorganic Chemistry*. 4rd. ed., Wiley-Interscience, New York, 1980.
19. Levin, E.M., Robbins, C.R. and McMurdie, H.F., *Phase Diagrams for Ceramists*. Supplement, The American Ceramic Soc., Columbus, 1969.
20. Purcell, K.F. and Kotz, J.C., *Inorganic Chemistry*. W.B. Saunders Company, Philadelphia, 1977.
21. Jentsch, D., Jones, P.G., Schwarzmam, E. and Sheldrick, G.M., *Acta Cryst.* **C39** (1983) 1173.
22. Thewalt, U. and Stollmaier, F., *Angew. Chem. Int. Ed. Engl.* **21** (1982) 133.

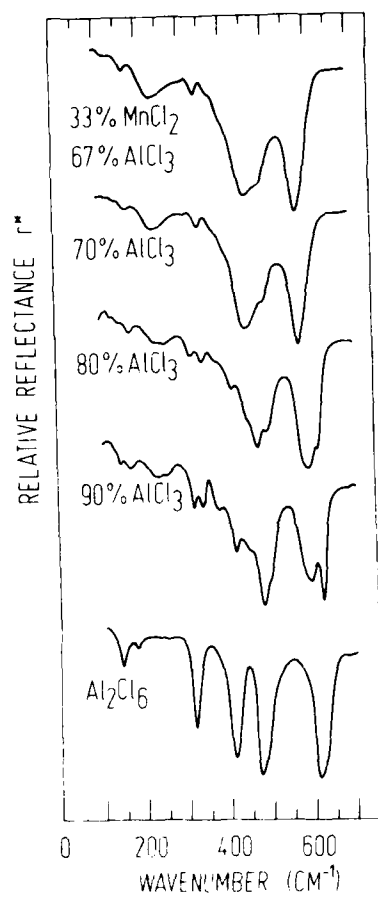


Figure 1. Infrared reflectance spectra of molten mixtures in the MnCl_2 - AlCl_3 system at 200 to 300 $^{\circ}\text{C}$.

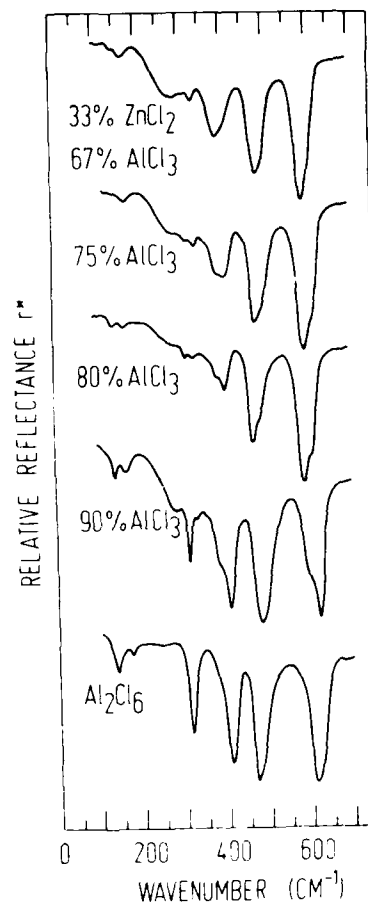


Figure 2. Infrared reflectance spectra of molten mixtures in the ZnCl_2 - AlCl_3 system at 200 to 250 $^{\circ}\text{C}$.

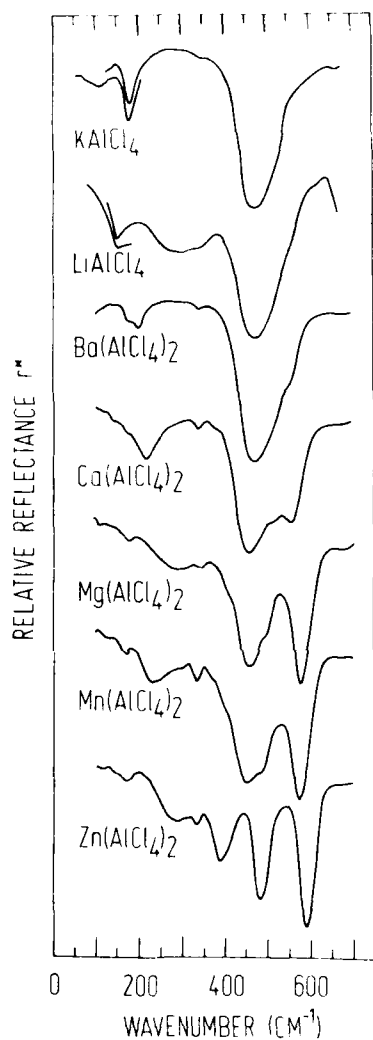


Figure 3. Infrared spectra of molten AlkAlCl_4 , $\text{Alk} = \text{K}, \text{Li}$, $\text{M}(\text{AlCl}_4)_2$, $\text{M} = \text{Ba}, \text{Ca}, \text{Mn}$ and Zn , and 30 mol% MgCl_2 :70 mol% AlCl_3 . The emission spectra are reproduced from Hvistendahl (7).

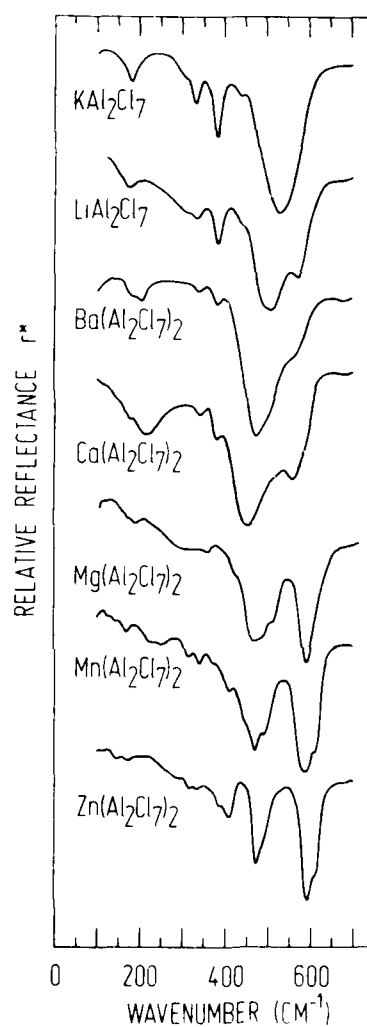


Figure 4. Infrared reflectance spectra of $\text{AlkAl}_2\text{Cl}_7$, $\text{Alk} = \text{K}$ and Li , and $\text{M}(\text{Al}_2\text{Cl}_7)_2$, $\text{M} = \text{Ba}, \text{Ca}, \text{Mg}, \text{Mn}$ and Zn .

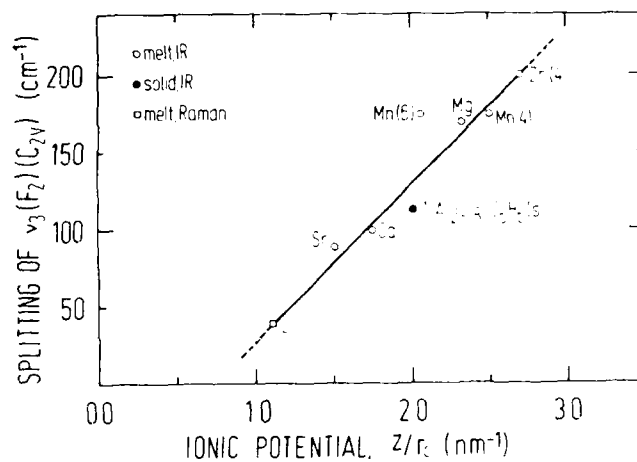


Figure 5. Observed splitting of $\nu_3(F_2)$ for $AlCl_4^-$ (C_{2v}) into B_1 and B_2 species by interactions of the cations: $Li^+(2)$, Sr^{2+} , Ca^{2+} , Mg^{2+} , $Ti^{2+}(13)$, Mn^{2+} and Zn^{2+} .

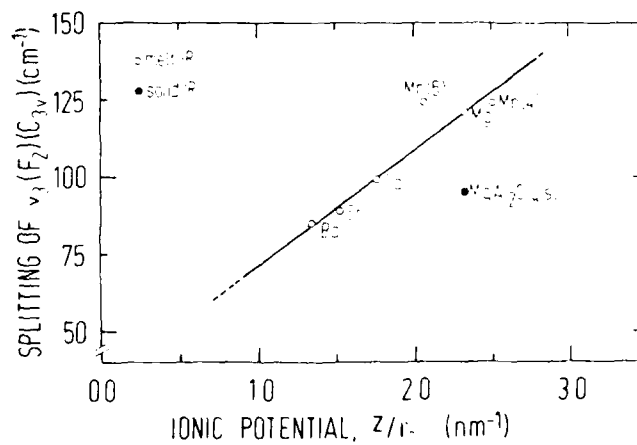


Figure 6. Observed splitting of $\nu_3(F_2)$ for $AlCl_4^-$ into A_1 and E species by interaction of the cations: Ba^{2+} , Sr^{2+} , Ca^{2+} , $Mg^{2+}(12)$ and Mn^{2+} .

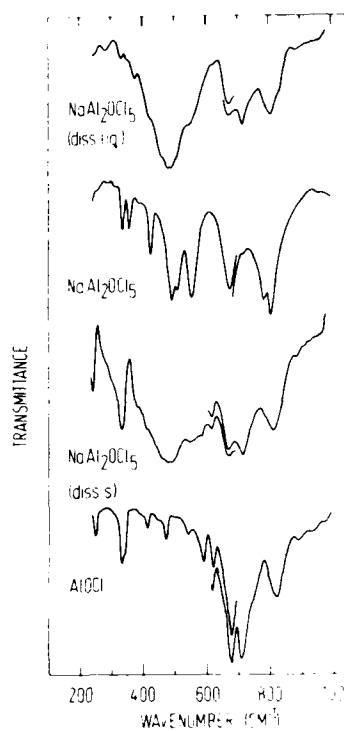


Figure 7. Infrared transmission spectra of
 (a) the remaining liquid after dissociation of $\text{NaAl}_2\text{OCl}_5$ (diss. liq.)
 (b) $\text{NaAl}_2\text{OCl}_5$
 (c) the precipitate from dissociation of $\text{NaAl}_2\text{OCl}_5$ (diss. s.)
 (d) AlOCl

All the samples were in the solid state.

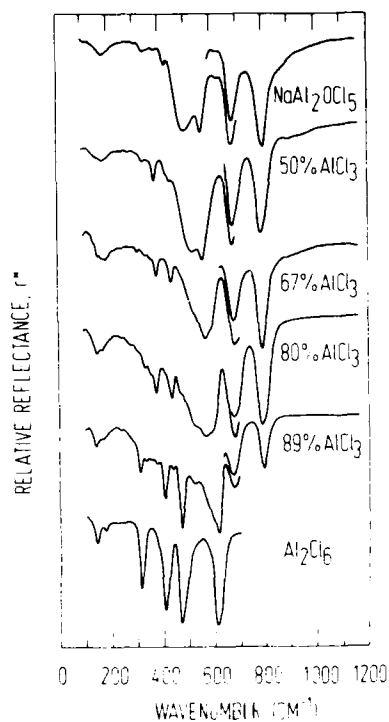


Figure 8. Infrared reflectance spectra of molten $\text{NaAl}_2\text{OCl}_5$ and mixtures with AlCl_3 at 200°C .

THE CHEMISTRY OF WATER IN AMBIENT-TEMPERATURE CHLOROALUMINATE
IONIC LIQUIDS: NMR STUDIES

by Thomas A. Zawodzinski Jr. and R. A. Osteryoung
Department of Chemistry
State University of New York at Buffalo
Buffalo, NY 14214

ABSTRACT

^{17}O NMR spectroscopy has been used to study the species formed upon addition of water to room-temperature molten salts composed of mixtures of AlCl_3 with 1-methyl, 3-ethyl imidazolium chloride (ImCl) at various mole ratios.

In basic melts, a single resonance peak is observed; in acidic melts, 3 separate peaks are observed and the nature of the various ^{17}O sites can be deduced.

^2H NMR has been employed to study the chemistry of protons in these melts. DCI interacts with a second chloride ion in basic melts whereas it interacts only weakly in acidic melts.

INTRODUCTION

Room-temperature ionic liquids composed of mixtures of AlCl_3 and organic chloride salts, RCI ($\text{R} = \text{N}-(1\text{-butyl})\text{-pyridinium cation}$ (BuPy $^+$) or 1-methyl, 3-ethyl imidazolium cation (Im $^+$)), have been used as solvents for a wide variety of chemical studies (1). These molten salts have several desirable properties including a high chloride ion activity for basic (molar excess RCI) melt compositions, high Lewis acidity, and nearly aprotic conditions. However, residual protons and oxide present in the melt have been found to have significant effects on the chemistry of certain solutes (2,3,4,5,6). Since these impurities are nearly always present, it is important to understand their chemistry.

A titration procedure for the determination of oxide impurities in melts (1,6) has been developed using Ti(IV) , which shows two voltammetric reduction waves, the first due to the reduction of the hexachlorotitanate anion and the second to the reduction of the titanium oxytetrachloride anion. Surprisingly, the addition of water to a solution of Ti(IV) with a known oxide content shifted the equilibrium between TiCl_6^{2-} and TiOCl_4^- away from the oxychloro-complex (5). This was believed to be due to the formation of an Al-OH containing species. Subsequent infrared work (7) indicated that an $-\text{OH}$ moiety is indeed formed upon addition of water to both basic and acidic melts.

The reduction on a Pt electrode of protons from water added to melts was studied (8) and it was shown that limiting currents increased linearly with increasing water concentration in basic melts. Less current was observed for an equivalent amount of water added to an acidic melt. Finally, the addition of water to nearly neutral melts apparently results in a release of 2 protons per water molecule (9).

As part of an ongoing effort to study the chemistry of water in the room-temperature chloroaluminate melts, we have used ^{17}O and ^2H NMR of water added to the melt to obtain information on the speciation of oxide and protons. We find that these techniques allow a qualitative description of water chemistry in chloroaluminate melts.

EXPERIMENTAL

The preparation, purification, and handling of melt components and solutions are fully described elsewhere (10). Water enriched to 20 or 30% ^{17}O was obtained from Cambridge Isotope Labs and was used as received. The synthesis of ImOCl_2 was similar to that of the H analog, (11).

^{17}O and ^2H NMR spectra were measured using a JEOLCO FX-270 NMR spectrometer operating at 36.54 or 41.7 MHz. Proton decoupling was carried out using broad-band, pseudo-random noise decoupling. All ^{17}O spectra were obtained at 90°C since baseline resolution of all spectral lines could be obtained at this temperature.

RESULTS AND DISCUSSION

^{17}O NMR spectra of solutions of water in acidic melts consist (generally) of three peaks as shown in Figure 1. The relative intensities of these peaks vary with composition (Figure 1) and concentration (Figure 2). As the mole ratio of AlCl_3 to ImCl is increased, the peak furthest downfield (Peak C) increases in relative intensity. The peak at 49.7 ppm (Peak A) is the most intense peak in the spectrum in melts less acidic than approximately 1.5:1.0. The intensity of the peak at 73 ppm (Peak B) decreases as the melt composition is made more acidic and is nearly negligible in very acidic melts.

Figure 3 is a plot of the total integrated intensity of the three lines observed in a 1.2:1.0 melt with various concentrations of added H_2O . The linearity of the plot implies that peaks A, B, and C account for all of the water added. The relative intensity of Peak A increases sharply with increasing concentration while that of Peak B

increases gradually with concentration. The relative intensity of Peak C decreases as the concentration of water is increased.

The spectrum shown in Figure 4 is that which results when HCl gas is bubbled through the solution whose spectrum is shown in Figure 1a. Addition of this proton donor results in the disappearance of peaks B and C, implying that peak A corresponds to oxygen present in a hydroxy-chloroaluminate species. The highly acidic nature of the medium leads us to infer that protons and AlCl_3 units (from Al_2Cl_7^-) compete for oxide sites and that peaks B and C are for oxygen atoms in bridging environments between aluminum atoms. This is further supported by the downfield chemical shift of these two lines relative to peak A, due to additional " AlCl_n " moieties surrounding the ^{17}O nucleus, and by the observed composition dependence of their intensities. By the same token, Peak C must correspond to a more highly substituted environment than Peak B.

O-bridging oxychloroaluminate species have been proposed for high temperature chloroaluminate melts (12) and have been shown to exist by crystallographic investigations of inorganic salts formed with the oxychloroaluminate as a counterion (13). Preliminary attempts at fitting the ^{17}O data discussed above to models which take into account the stoichiometry of all species formed suggest that species similar to those in references 12 and 13 are formed and concur with the qualitative conclusions reached above.

Spectra of dissolved water at several concentrations in a basic melt are shown in Figure 5. In all cases, a single line is observed. However, the position of the peak shifts with increasing water concentration. The effect of bubbling HCl through a solution of water in a basic melt is to shift the peak upfield. As in the acidic melts, the peak which results is inferred to be due to an " Al-OH " moiety. Fast chemical exchange between two or more oxygen environments, probably " Al-O " and " Al-OH " moieties, is indicated by the presence of a single peak with a variable chemical shift. The observed concentration dependence then indicates that the " Al-O " moiety is the predominant oxide environment at low concentrations while " Al-OH "-containing species are more important at higher concentrations. This suggests that the discrepancy between the infrared (7) and electrochemical (9) results is due to the higher water concentrations used in the former case relative to those typically employed in the neutral melt amperometric titration technique utilized in the latter case. These results also provide direct evidence for the type of equilibrium used to explain the behavior of the Ti(IV) system upon addition of H_2O . In the latter experiment, relatively large H_2O concentrations were added to the titanium solutions.

Further information on water chemistry in the chloroaluminate melts can be obtained from ^1H NMR studies of D_2O added to the melt.

We have also synthesized the DCl salt of ImCl , (11), hereafter referred to as ImDCl_2 , for use as a proton donor. ^1H spectra of ImDCl_2 solutions in basic and acidic melts are shown in Figure 6. The "DCl" resonance peak, the major peak in the spectrum, shifts downfield as the melt is made more basic. This is due to the interaction of DCl with a second chloride ion in basic melts, probably in an H-bonding interaction, effectively forming DCl_2 ions. The proton chemical shift of the corresponding HCl_2 ion in the ImHCl_2 liquid is 13 ppm relative to TMS. In acidic melts, protons are present as free or weakly complexed HCl.

The ^2H spectrum of a 50 mM solution of D_2O in an acidic melt is shown in Figure 7. In addition to the DCl peak, there is a second D-containing species present. This is the "Al-OH" species discussed above. Spectra of D_2O in basic melts have but a single peak. This is probably due to fast chemical exchange, as discussed above.

In conclusion, ^{17}O and ^2H NMR studies have enabled us to deduce the nature of the speciation in H_2O solutions in melts. In acidic melts, three oxygen containing species are formed; one hydroxychloroaluminate and two O-bridged oxychloroaluminate species. In basic melts, rapid exchange precludes determination of the exact number of species formed, but we can qualitatively conclude that an oxychloroaluminate, probably in a terminal environment, and a hydroxychloroaluminate are present, with the latter species being the predominant form at high water concentrations. ^1H NMR studies of protonic environments suggest that protons are present as DCl in acidic melts, but are strongly associated with a second chloride in basic melts.

ACKNOWLEDGEMENT

This work was supported in part by the Air Force Office of Scientific Research.

REFERENCES

1. C. L. Hussey in "Advances in Molten Salt Chemistry", G. Mamantov, Ed., Ch. 5, Elsevier, NY (1983).
2. Z. Karpinski, C. Nanjundiah and R. A. Osteryoung, *Inorg. Chem.*, 23, 3358 (1984).
3. S. P. Zingg, A. S. Dworkin, M. Sorlie, D. M. Chapman and G. P. Smith, *J. Electrochem. Soc.*, 131, 1603 (1984).
4. R. T. Carlin and R. A. Osteryoung, manuscript in preparation.
5. H. Linge, Z. Stojek and R. A. Osteryoung, *J. Am. Chem. Soc.*, 103, 3754 (1981).
6. Z. Stojek, H. Linge and R. A. Osteryoung, *J. Electroanal. Chem.*, 119, 365 (1981).
7. S. Tait and R. A. Osteryoung, *Inorg. Chem.*, 23, 4352 (1984).
8. S. Sahami and R. A. Osteryoung, *Anal. Chem.*, 55, 1970 (1983).
9. M. Lipsztajn, S. Sahami and R. A. Osteryoung, *Inorg. Chem.*, 25, 549 (1986).
10. T. A. Zawodzinski, R. J. Kurland and R. A. Osteryoung, *J. Phys. Chem.*, 91, 962 (1987).
11. T. A. Zawodzinski and R. A. Osteryoung, manuscript in preparation.
12. R. W. Berg, H. A. Hjuler and N. J. Bjerrum, *Inorg. Chem.*, 23, 557 (1984).
13. V. Thewalt and F. Stollmaier, *Angew. Chem. Int. Ed. Eng.*, 21, 133 (1982).

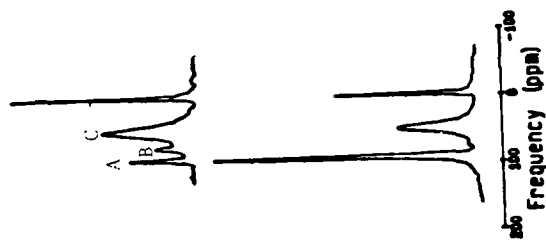


Fig. 1. ^{17}O NMR spectra of 50 mM solutions of H_2O in (a) 1.2:1 melt and (b) 1.73:1.0 melt.

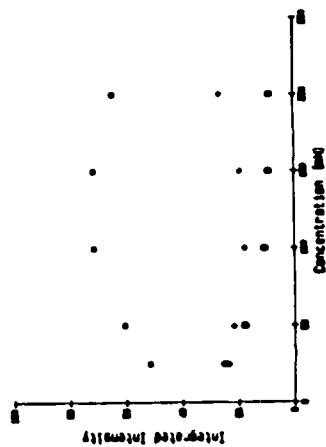


Fig. 2. Plot of relative intensities (integrated intensity for peak divided by total integrated intensity) for the three peaks as a function of water concentration in a 1.2:1.0 $\text{AlCl}_3\text{:ImCl}$ melt.

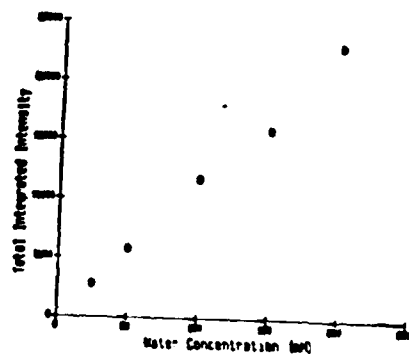


Fig. 3. Plot of total integrated intensity (sum of integrated intensities for individual peaks in spectrum) as a function of concentration of water added to a 1.2:1.0 AlCl_3 :ImCl melt.



Fig. 4. Spectrum of solution from Figure 1(a) after bubbling HCl through it.

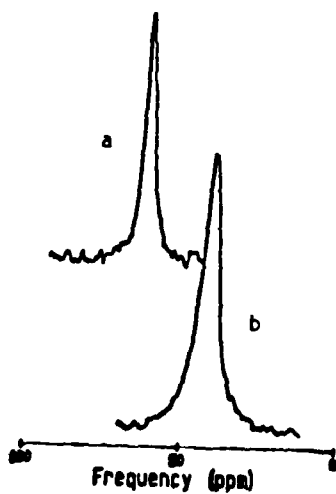


Fig. 5. Spectra of water at various concentrations in a 0.8:1.0 melt (a) 50 mM; (b) 200 mM.

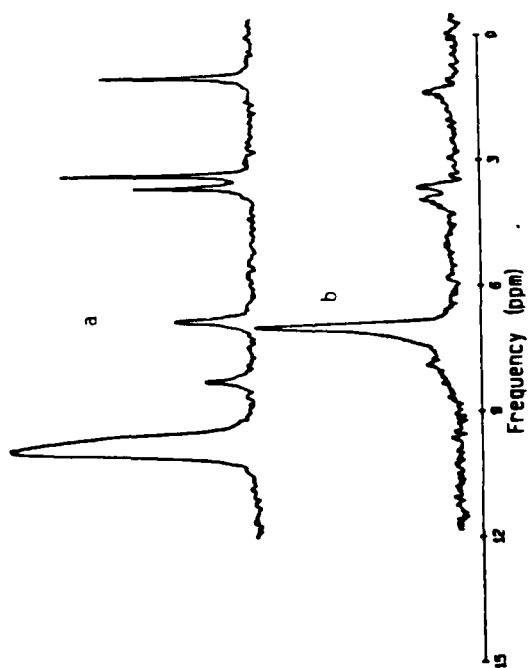


Fig. 6. Spectra of 50 mM solutions of ImDCl₂ in (a) 0.88 and (b) 1.32:1.0 melts.

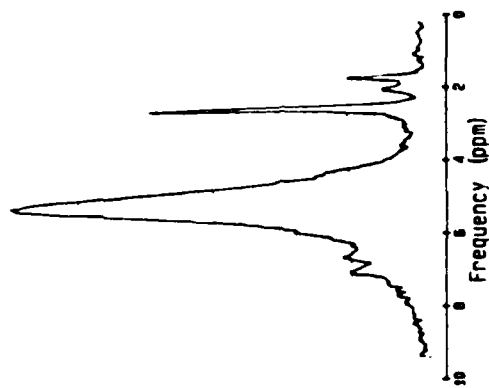


Fig. 7. Spectrum of a 50 mM solution of D₂O in a 1.32:1.0 melt.

Ionic Structure and Interactions in 1-Methyl-3-Ethylimidazolium
Chloride/ AlCl_3 Molten Salts

Kenneth M. Dieter, Chester J. Dymek, Jr., Norman E. Heimer,
John W. Rovang, and John S. Wilkes

Frank J. Seiler Research Laboratory
United States Air Force Academy
Colorado Springs, CO 80840-6528

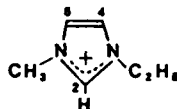
ABSTRACT

Room temperature chloroaluminate molten salts formed by mixing 1-methyl-3-ethylimidazolium chloride (MEICl) with AlCl_3 are of interest as electrolytes and non-aqueous reaction media. We have done NMR, IR, and theoretical studies on this system to elucidate the still unresolved picture of ionic structure and interactions in these melts. NMR studies of MEI^+ in melts of various composition (determined by the mole fraction, N , of AlCl_3 used in forming a melt) were originally explained by a stack model. In this model, the anions (Cl^- and AlCl_4^- in basic melts and AlCl_4^- and Al_2Cl_7^- in acidic melts) are located between stacked "parallel" MEI^+ ring planes. However, IR and Raman spectra were interpreted as evidence that Cl^- formed ion pairs with MEI^+ by a H-bonding interaction through the H on the C-2 in the ring, disputing the stack model. Our IR studies now indicate that while the hydrogen on the C-2 does interact with the Cl^- , it is clearly not the only point of interaction. It appears that the Cl^- affects the hydrogens at C-4 and C-5 members of the ring as well. Semi-empirical molecular orbital calculations support a model in which Cl^- interacts with two MEI^+ 's while occupying an equilibrium position approximately equidistant between the C-2's of adjacent near parallel MEI^+ 's.

INTRODUCTION

One of the most widely studied room temperature melt systems is the 1-methyl-3-ethylimidazolium chloride- AlCl_3 (MEICl-AlCl_3) melt which is liquid at room temperature for compositions between 33-67 mole% AlCl_3 (1,2). This melt exhibits acid-base chemistry which can be controlled by varying the composition. When the mole fraction of AlCl_3 (N) used in preparing the melt is less than 0.5, it contains an excess of Cl^- and is basic. For compositions $N > 0.50$, the melt is considered acidic because it contains an excess of Al_2Cl_7^- . In $N = 0.50$ melt the melt is neutral, containing only AlCl_4^- anions.

This melt exhibits several attractive features such as a large electrochemical window and high conductivities. The structure of MEI^+ is shown below:



A better understanding of the physical and chemical properties of these melts has been sought through investigation of the ion-ion interactions in these melts. The crystal structure of the iodide analog, MEII , has been reported, and based upon the C-2 hydrogen-iodide distance, an interaction involving hydrogen bonding through the C-2 hydrogen has been suggested (3). Previous investigations have used this model to explain variations in the IR spectra of basic MEICl-AlCl_3 melts (4). In this work we studied both normal and deuterated MEI^+ in melts of various composition. We studied the effects of solvent addition and replacement of the C-2 hydrogen with methyl. Our studies indicate that the changes in the IR spectra may not be attributed entirely to hydrogen bonding interactions between the MEI^+ and Cl^- anion. Semiempirical molecular orbital calculations have been used to support our experimental evidence for this conclusion. Other possible structures in which the interaction is not a hydrogen bond have been considered.

EXPERIMENTAL

General Procedures: The preparation of the melts has been presented earlier(1). Benzene- d_6 (Aldrich) and dichloromethane- d_2 (Aldrich) were used as received. Benzene (Aldrich, HPLC grade) and dichloromethane (Baker, HPLC grade) were purified by refluxing over P_2O_5 for several days followed by fractional distillation.

The IR spectra were recorded on an IBM model 32 FTIR spectrometer. The solutions were run between two NaCl plates (Wilmad, 41 x 32 x 6 mm) as thin films or with lead spacers of appropriate size. All loading of IR cells was done in a He-filled dry box with less than 10 ppm $\text{H}_2\text{O}/\text{air}$.

Preparation of 2- d_1 - MEICl : A solution of 4 g of MEICl was allowed to stand in 10 mL of $\text{d}_2\text{-H}_2\text{O}$ for 3 days. The water was evaporated under reduced pressure and then, to remove the remaining water, the resulting material was suspended in benzene and distilled until the distillate was clear. Analysis (IR) of the material dried by this procedure showed that there was still a small amount of water present so the material was suspended in about 30 mL benzene and treated with about 0.5 mL of thionyl chloride. After standing for 0.5 h, the benzene and thionyl chloride were removed under reduced pressure and the resulting semi-solid was stored under vacuum overnight. The material prepared in this manner showed no

water when analyzed by IR, and its ^1H -NMR spectrum showed only a small peak, c.a. 0.04 proton for the hydrogen at C-2.

Theoretical Considerations: Theoretical calculations were carried out using the standard AM1 (5) and MNDO (6) models as incorporated in the MOPAC program (7). Geometries were fully optimized using the DFP method (8) and refined by minimizing the scalar gradient of the energy (9). True minima were characterized by the absence of negative force constants (9), and vibrational frequencies were calculated for the normal modes (10).

AM1 was preferred over MNDO due to the problem of excessive long range repulsions associated with MNDO and the capability of AM1 to reproduce hydrogen bonding (5,11). Unfortunately, there are, as of yet, no AM1 parameters for aluminum. Consequently, the MNDO parameters for aluminum were used in AM1 calculations involving the interaction of AlCl_4^- ions with MEI^+ . This less than ideal procedure is justified in this study since the AM1 results for AlCl_4^- are similar to MNDO results (12) and the interaction between AlCl_4^- and MEI^+ is primarily electrostatic in nature or involves only the chlorine atoms. There is no direct interaction of aluminum with the MEI^+ and essentially no change in bonding to aluminum is involved.

RESULTS AND DISCUSSION

I. Experimental

The vibrational spectra of the MEICl-AlCl_3 ambient temperature melts carried out by Tait and Osteryoung (4) were re-examined. They found that the IR spectra of MEI^+ in acidic and neutral melts were the same, but that in basic melts some bands were apparently shifted. They proposed that Cl^- forms a hydrogen bond with the C-2 hydrogen of the MEI^+ cation to explain this shift. In other work (3) the crystal structure of MEII suggested that an interaction occurs between the I^- and the C-2 hydrogen.

In ^1H NMR studies the proton chemical shifts of the C-2 hydrogen show the largest changes as the composition of the melt is changed. This provides supportive evidence for the hydrogen bonded complex, but it was noted that the chemical shifts of the hydrogen at 4 and 5 ring positions are also affected by melt acidity (Fig. 1). Our results suggest that Cl^- is interacting with the π orbitals of the imidazolium ring instead of hydrogen bonding at the C-2 hydrogen.

Our conclusions are based on an analysis of the CH and CD stretching bands in the IR spectrum, in particular the behavior of the rather broad band at 3049cm^{-1} . The intensity of this band decreases as the mole fraction of AlCl_3 in the melt is increased (Fig. 2). It also decreases with the addition of benzene- d_6 and dichloromethane- d_2 (Fig. 3). In neutral melt, this band does not appear (Fig. 2). Its frequency appears at higher wavelengths in the

MEIBr-AlBr₃ basic melt (Fig. 4). The IR spectrum of N=0.50 MEICl-AlCl₃ melt is unaffected by the addition of benzene-d₆ or dichloromethane-d₂ and is identical to the neutral MEIBr-AlBr₃ melt. Thus, we conclude that the 3049cm⁻¹ band is due to MEI⁺ which is interacting with Cl⁻. Since the tetrahalocaluminate ion is the predominant ion in neutral melt, the IR spectra give no information on the interaction between the ions at this melt composition.

To determine whether the band previously assigned to the C-2 hydrogen stretch perturbed by a bonding interaction is a correct assignment, melts were prepared using the 1,2-dimethyl-3-ethyl imidazolium chloride salt (MMEICl). This salt is similar to MEICl except the C-2 proton has been replaced with a CH₃ group -- a group with which no hydrogen-bonding interaction is expected. The IR spectrum of an N = 0.33 melt prepared from MMEICl shows the 3049cm⁻¹ band (Fig. 5). The intensity of this band decreases as the melt is titrated to neutrality (Fig. 5). This is the same behavior as was found for the 3049cm⁻¹ band observed in the IR of MEICl-AlCl₃ basic melts. These results indicate that the 3049cm⁻¹ band cannot be due solely to the C-2 proton stretch perturbed by hydrogen bonding but must involve other vibrations. The spectrum of the N=0.50 MMEICl-AlCl₃ melt differs from the MEICl-AlCl₃ melt. In the IR spectrum of MMEICl-AlCl₃ neutral melt, the band centered around 3119cm⁻¹ seen in the MEICl-AlCl₃ melts is not observed. We thus conclude that this band in MEI⁺ results from the C-2 proton stretch (Fig. 5).

Another band appears at 1595cm⁻¹ whose intensity increases as the melt is titrated from basic toward neutral (Fig. 7). The change in intensity of this band is opposite to what is observed for the 3049cm⁻¹ band. This band has been assigned to an imidazolium ring stretch vibrational mode. The changes in the band intensity indicates that the interaction of MEI⁺ with Cl⁻ inhibits this vibrational mode. The intensity of this band increases as the melt is neutralized because of the conversion of Cl⁻ to AlCl₄⁻ which appears to interact weakly with the MEI⁺ cation (1).

If the interaction between Cl⁻ and the hydrogen at C-2 hydrogen were due to hydrogen bonding, this should be readily observable by examination of the IR spectrum of material with a deuterium at C-2. The C-2 deuterium vibration will shift away from the vibrations of the other C-H bonds in the molecule so that changes in its vibrational frequencies would be easy to see. The IR spectrum of pure 2-d₁-MEICl, N=0.0, in which hydrogen bonding might be important, showed an IR peak at 2267cm⁻¹ for the C-2 deuterium bond and C-H vibrations as a broad band in the region from 2990 to about 3200cm⁻¹ with a maximum at 3058cm⁻¹. The IR spectra of N=0.33 and N=0.50 melts of 2-d₁-MEICl/AlCl₃ are shown in Fig. 8. The IR spectrum of the N=0.50 melt shows the C-2 deuterium stretch at 2350 cm⁻¹. In the spectrum of the N=0.33 melt, this band is reduced in intensity and a new band at 2283cm⁻¹ has appeared, presumably due to an interaction of the C-2 deuterium with Cl⁻. However, this shift

in frequency due to Cl^- interaction also appears for the vinylic C-H stretching frequencies. If the interaction were due to only hydrogen-bonding, no significant shifts would be expected in the C-4 and C-5 hydrogen stretching frequencies. In the spectrum of the $N=0.50$ melt, the C-4 and C-5 hydrogen stretching bands appear at 3170 and 3149 cm^{-1} . In the spectrum of the $N=0.33$ melt, these bands are reduced in intensity and the broad Cl^- -interaction band at 3079 cm^{-1} appears. Thus the C-H stretches on C-2, C-4, and C-5 are all being affected by Cl^- in essentially the same way. We conclude that this non-specific interaction cannot be characterized as hydrogen bonding.

II. Theoretical

While AM1 and MNDO are parameterized using gas phase data, MNDO results were previously shown to be consistent with the experimental IR spectra of the Al_2Cl_7^- in molten KAl_2Cl_7 (14). For the isolated MEI^+ ion, AM1 results (Fig. 9) again provide a reasonable model of the 2900-3300 cm^{-1} region of the experimental IR spectrum results for the $N=0.50$ AlCl_3 melt, in which there is no Cl^- to interact with the MEI^+ . While the intensity of the C-2 hydrogen stretch is overestimated, its position, as well as the positions and relative sizes of alkenyl and alkyl C-H stretches, are well represented.

When a Cl^- was positioned to hydrogen bond to the C-2-hydrogen and the geometry optimized, the C-2-hydrogen bond was almost totally broken, the C-2-hydrogen and H-Cl distances optimizing at 1.56 and 1.40 Å, respectively. Consequently, the C-2-hydrogen stretch was strongly coupled with the H-Cl stretch; two vibrations appearing at 1565 and 711 cm^{-1} . These results are no doubt exaggerated due to AM1 underestimating the stability of the chloride anion (ΔH_f -37.7 kcal/mol calcd, -55.9 kcal/mol exptl [15]). Interestingly, however, when an AlCl_4^- was substituted for the Cl^- , the interaction between one chlorine atom and the C-2 hydrogen was strong enough to shift the C-2-hydrogen stretch from 3118 cm^{-1} in the isolated MEI^+ to 2492 cm^{-1} in the complex. This shift is too large to be explained fully by the change in reduced mass. While this result is again exaggerated due to the treatment of the complex as a totally isolated ion pair, it is reasonable to expect that a hydrogen bond between a Cl^- and the C-2 hydrogen would cause a larger red shift in the C-2-hydrogen stretch than to 3049 cm^{-1} .

According to AM1 calculations, the $p\pi$ orbital of the C-2 contributes 50% of the lowest unoccupied molecular orbital (LUMO) of the isolated MEI^+ . When a Cl^- was centered above the ring and the geometry optimized, the Cl^- shifted to form a covalent bond with the C-2. The heat of formation for this covalent species was 4.6 kcal/mol less than that for the "hydrogen bonded" complex, and the frequency of the C-2 hydrogen stretch was predicted to be 2951 cm^{-1} . When a second MEI^+ was positioned parallel to the first MEI^+ , with the Cl^- centered between the two rings, and the geometry fully optimized, a minimum was located with the Cl^- located slightly in

front of the two C-2's and nearly equidistant from both (C-2-H 2.48Å, C-2'-H 2.42Å). This complex was predicted to be 8.4 kcal/mol more stable than the covalent $C_6H_{11}N_2Cl$ species plus an isolated MEI^+ . The C-2-hydrogen stretch for the complex was red shifted relative to that of the isolated MEI^+ , its frequency being $3107cm^{-1}$. It is not unexpected that this is higher than the $3049cm^{-1}$ observed experimentally, since calculated vibrational frequencies are typically too high (10).

CONCLUSION

In basic melts of $MEICl$ and $AlCl_3$, Cl^- interacts with MEI^+ to cause similar shifts in the frequencies of the C-2, C-4, and C-5 hydrogen stretches. This nonspecific interaction cannot be characterized as hydrogen bonding. In fact, it is consistent with a stack model for the interaction of MEI^+ with the anions in the melt.

REFERENCES

1. J. S. Wilkes, J. A. Levisky, R. A. Wilson, and C. L. Hussey, Inorg. Chem., **21**, 1263 (1982).
2. J. S. Wilkes, J. A. Levisky, J. L. Pflug, C. L. Hussey, and T. B. Scheffler, Anal. Chem., **54**, 2378 (1982).
3. A. K. Abdul-Sada, A. M. Greenway, P. B. Hitchcock, T. J. Mohammed, K. R. Seddon, and J. A. Zora, J. Chem. Soc., Chem. Commun., 1753 (1986).
4. S. Tait and R. A. Osteryoung, Inorg. Chem., **23**, 4352 (1984).
5. M. J. S. Dewar, E. G. Zoebisch, E. F. Healy, and J. J. P. Stewart, J. Am. Chem. Soc., **107**, 3902 (1985).
6. M. J. S. Dewar and W. Thiel, J. Am. Chem. Soc., **99**, 4899 (1977).
7. J. J. P. Stewart, Quantum Chem. Prog. Exchange Bull., **6**, 91 (1986); QCPE Program 455, Version 3.1.
8. (a) R. Fletcher and M. J. D. Powell, Comput. J., **6**, 163 (1963). (b) W. C. Davidon, Ibid., **10**, 406 (1968).
9. (a) A. Komornicki and J. W. McIver, Chem. Phys. Lett., **10**, 303 (1971). (b) A. Komornicki and J. W. McIver, J. Am. Chem. Soc., **94**, 2625 (1971).
10. M. J. S. Dewar, G. P. Ford, M. L. McKee, H. S. Rzepa, W. Thiel, and Y. Yamaguchi, J. Mol. Struct., **43**, 135 (1978).
11. M. J. S. Dewar and K. M. Dieter, J. Am. Chem. Soc., **108**, 8075 (1986).
12. The MNDO heat of formation for AlCl_4^- is -273.4 kcal/mol, the Al-Cl bond length is 2.15 Å, and the atomic charges on Al and Cl are 0.90 and -0.47, respectively. The corresponding AM1 results are -263.2 kcal/mol, 2.07 Å, 0.64 and -0.41.
13. A. A. Fannin, Jr., L. A. King, J. A. Levisky, and J. S. Wilkes, J. Phys. Chem., **88**, 2609 (1984).
14. L. P. Davis, C. J. Dymek, Jr., J. J. P. Stewart, H. P. Clark, and W. J. Lauderdale, J. Am. Chem. Soc., **107**, 5041 (1985).
15. M. W. Chase, Jr., C. A. Davis, J. R. Downey, Jr., D. J. Frurip, R. A. McDonald, and A. N. Syverud, JANAF Thermochemical Tables, 3rd Ed., National Bureau of Standards: Gaithersburg, MD, 1986.

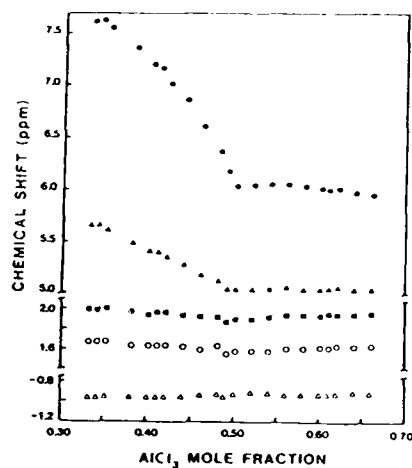


Fig. 1: Proton chemical shifts in $\text{MEI}^+\text{-AlCl}_3$ melt vs N at 30°C (\bullet) H-2, (Δ) H-4 and H-5 (average of unresolved doublet), (\blacksquare) N- CH_2 protons, (\circ) N- CH_3 protons, (\triangle) CH_3 protons. The chemical shifts were referenced to Me_2SO external reference (13).

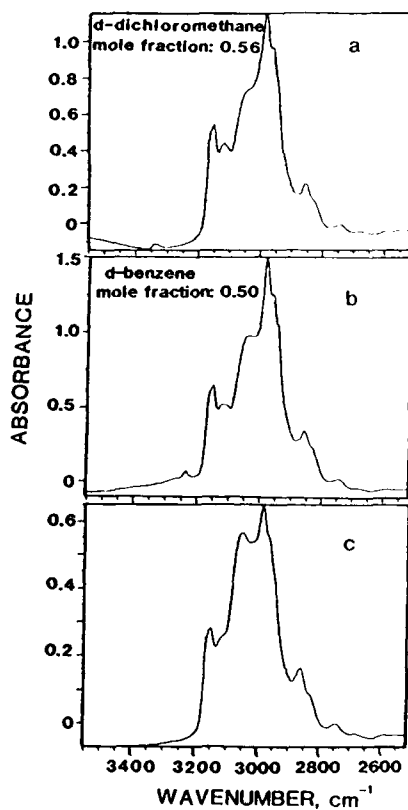


Figure 3: IR spectra of CH bands of MEI^+ in $N=0.33$ melt and nonaqueous solutions of this melt. (a) dichloromethane- d_2 , (b) benzene- d_6 , (c) neat melt.

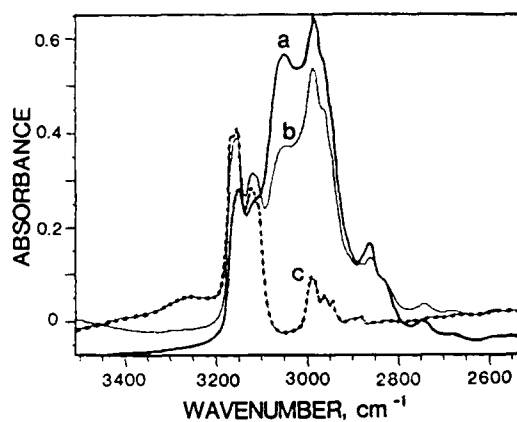


Figure 2: IR spectra of CH bands of MEI^+ in $\text{MEI}^+\text{-AlCl}_3$ melt at: (a) $N=0.50$, (b) $N=0.40$, (c) $N=0.33$.

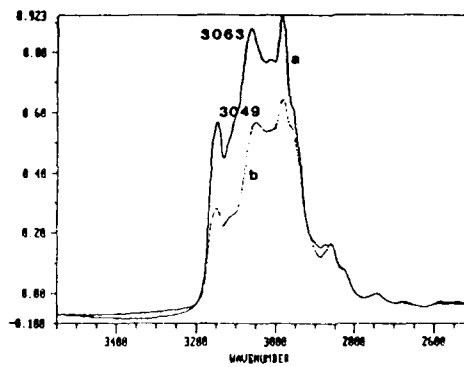


Figure 4: IR spectra of CH bands of MEI^+ in two different $N=0.33$ room temperature melts. (a) MEIBr-AlBr_3 , (b) MEICl-AlCl_3 .

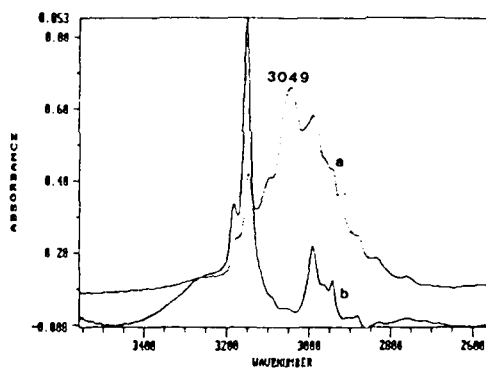


Figure 5: IR spectra of CH bands of MMEI^+ in MMEICl-AlCl_3 melt at: (a) $N=0.33$, $T=140^\circ\text{C}$, (b) $N=0.50$, $T=100^\circ\text{C}$.

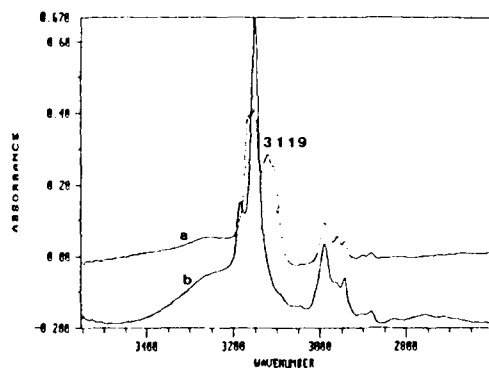


Figure 6: IR spectra of CH bands of (a) MEI^+ and (b) MMEI^+ both in $N=0.50$ melt.

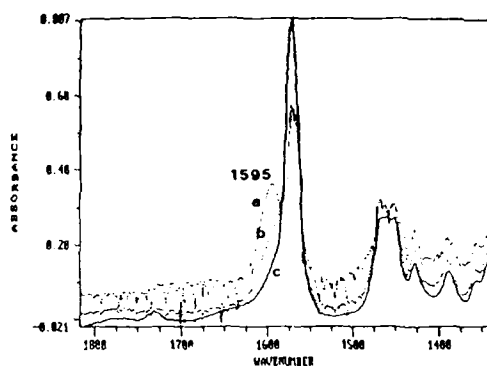


Figure 7: IR spectra showing the 1595cm^{-1} band as function of N for a MEICl-AlCl_3 melt: (a) $N=0.50$, (b) $N=0.40$, (c) $N=0.33$.

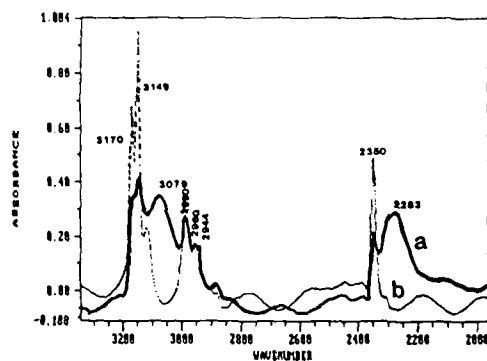


Figure 8: IR spectra of $2\text{-d}_1\text{-MEICl-AlCl}_3$ melt at: (a) $N=0.33$, (b) $N=0.50$.

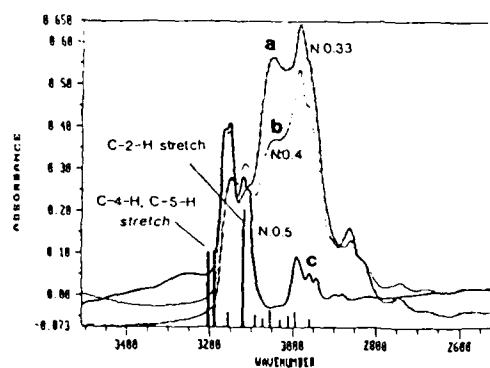


Figure 9: IR spectra of MEICl-AlCl_3 of different compositions. The bands obtained using AM1 calculations for the gas phase MEI^+ are shown as straight lines.

NUCLEAR SPIN RELAXATION OF CESIUM-133 IN THE MOLTEN
LITHIUM NITRATE - CESIUM NITRATE SYSTEM

Yoshio Nakamura, Jun Funaki, and Shigezo Shimokawa*

Department of Chemistry, Faculty of Science, and
*NMR Laboratory, Faculty of Engineering,
Hokkaido University, 060 Sapporo, Japan.

ABSTRACT

The spin-lattice relaxation times of cesium-133 nuclei in the molten (Li-Cs)NO₃ system have been measured as a function of composition and temperature. The relaxation rates, $1/T_1$, decrease with increasing LiNO₃ concentration. The rates decrease also with increasing temperature. These results are interpreted by the quadrupolar interaction of the nuclei with the surrounding nitrate ions, which changes with composition and temperature.

INTRODUCTION

In previous papers (1,2) we have reported that the chemical shifts of thallium-205 in some binary molten salt mixtures with common anions can be interpreted in terms of the anion polarization due to the difference in ionic radii of the constituent cations. This anion polarization effect has further been examined in a study of the quadrupolar relaxation of lithium-7 in the molten binary system, (Li-Cs)NO₃(3). In binary molten salt mixtures with common anions, the anions are polarized toward the smaller cation, which causes an increase of the electric field gradient at the smaller cation. Thus, the quadrupolar relaxation rates are expected to increase for the smaller cation and to decrease for the larger cation by mixing. The relaxation rates of lithium ions in the (Li-Cs)NO₃ system have been found to increase with increasing CsNO₃ concentration in accordance with this expectation (3). The purpose of the present study is to confirm this anion polarization model by measuring the relaxation rates of cesium-133 ($I=7/2$) in the same system, in which the quadrupolar interaction is predominant.

EXPERIMENTAL

The salts used were obtained from Wako Pure Chem. Co.

Ltd. and their stated purity was 99.9% for LiNO_3 and 99% for CsNO_3 . Sample mixtures were prepared by mixing precisely weighed amounts of the respective components in an NMR cell of 6 mm i.d., drying under vacuum at 110°C , and then melting thoroughly. Prior to sealing the cell, the samples were degassed by freeze-pump-thaw cycles just above the melting temperature of each sample.

NMR measurements were made with a Bruker CXP pulse FT spectrometer, operating at 5.107 MHz for Cs-133. The spin-lattice relaxation times, T_1 , were determined by the usual 180° - τ - 90° pulse sequence method. The temperature range of measurements was from the melting point of the samples to 425°C . Temperatures were controlled within $\pm 1^\circ\text{C}$. The details of the high-temperature NMR probe have been described elsewhere (2).

RESULTS AND DISCUSSION

Figure 1 shows the temperature dependence of the relaxation time of Cs-133 for the mixture with 30 mol% LiNO_3 , or $X_{\text{LiNO}_3}=0.3$. The relaxation time increases with increasing temperature. Circles and triangles in the figure denote different runs with different samples. It is noted that the slight decomposition of nitrate ions at high temperatures yields paramagnetic impurities such as NO or O_2 , which reduces the relaxation time with the additional mechanism due to the paramagnetic interaction (3,4). Therefore, the measurements were limited to the temperature range where the observed relaxation time was reproducible during heating and cooling cycles. The decomposition effect was found above 400°C for the sample with $X_{\text{LiNO}_3}=0.3$.

Figure 2 shows the composition dependence of the relaxation rates, $1/T_1$, of Cs-133 at 325°C . The relaxation rates decrease with increasing the content of LiNO_3 , in contrast to those of lithium-7, which increase with increasing the content of CsNO_3 (3). At 325°C , CsNO_3 -rich samples were solidified and measurements were limited to the samples with $X_{\text{LiNO}_3} \geq 0.3$.

The spin-lattice relaxation rate due to the electric quadrupolar interaction, $(1/T_1)_Q$, in a molten salt may be written as (4)

$$\left(\frac{1}{T_1}\right)_Q = \frac{3}{40} \frac{2I+3}{I^2(2I-1)} \left[\frac{(1-\eta)e^2qQ}{\pi} \right]^2 \tau_c \quad (1)$$

I is the nuclear spin number, Q is the electric quadrupole moment, and q is the electric field gradient at a nucleus by the surrounding ions. $(1-T_1)_X$ denotes the additional contribution arising from the polarization of the electron shells of the ions under study. τ_c is the correlation time of the field gradient fluctuation. It is estimated that the fluctuations of the field gradient occurs in much shorter time scale as rattling motion of the first shell composed of nitrate ions than the diffusion time of the ions over an average interionic distance (3,5). We suppose, therefore, that the values of τ_c are not very dependent on composition, and that the change in the field gradient, q, mainly contributes to the composition dependence of the relaxation rates.

In the polarization model, the ratio of the relaxation rate at the composition $X\text{LiNO}_3$, to that of the pure CsNO_3 is given by (3)

$$(1/T_1)_X / (1/T_1)_0 = 1 - 12 \epsilon R X \text{LiNO}_3 / R_0^3 d_0^3, \quad (2)$$

where ϵ is the polarizability of NO_3^- , R_0 and d_0 are distances Cs-N and Cs-O, respectively. R is the difference in the ionic radii of the cations, $R = R(\text{Cs}^+) - R(\text{Li}^+)$. The calculated results from eqn (2) are given in Figure 2 by a dotted line, which is in reasonable agreement with the observed results.

REFERENCES

1. Y. Nakamura, S. Shimokawa, Y. Kitazawa and M. Shimoji, Proc. First Intl. Symp. Molten Salt Chem. Tech. 1983, Kyoto, p.378.
2. Y. Nakamura, Y. Kitazawa, M. Shimoji and S. Shimokawa, J. Phys. Chem., **87**, 5117 (1983).
3. Y. Nakamura and S. Shimokawa, Ber. Bunsenges. Phys. Chem., **89**, 371 (1985).
4. D. Harold-Smith, J. Chem. Phys., **60**, 1405 (1974).
5. W. Wolney Filho, R. L. Havill, and J. M. Titman, J. Mag. Res., **49**, 296 (1982).

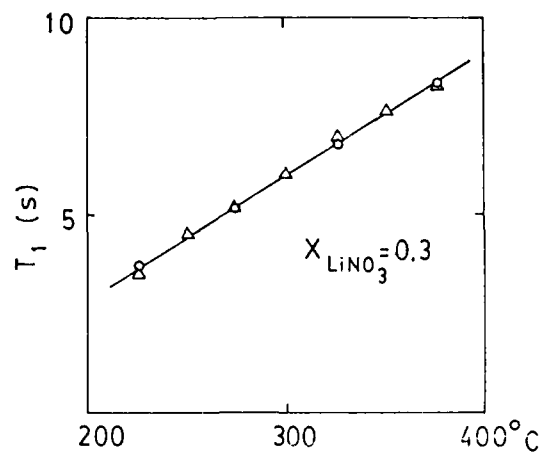


Figure 1. Temperature dependence of the spin-lattice relaxation time of Cs-133 in the molten (Li-Cs)NO₃ mixture with $X_{\text{LiNO}_3}=0.3$.

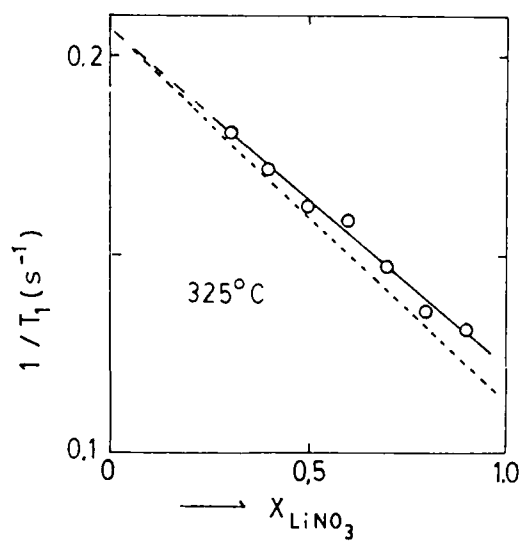


Figure 2. Composition dependence of the relaxation rate of Cs-133 in the molten (Li-Cs)NO₃ system at 325°C. -----:calculated from eqn.(2).

SPECTROSCOPICAL STUDY OF ANODIC
MICRO-PLASMAS OBSERVED DURING
ANODE EFFECT IN MOLTEN LiCl-KCl
MIXTURES.

Jean-Paul Bardet, Jean-Claude
Valognes, Pierre Mergault

Laboratoire de Physique des
Liquides Ioniques,
Université Pierre et Marie Curie
Tour 15 - 4 Place Jussieu,
75252 Paris Cedex 05, France

ABSTRACT

The values of the main parameters of an anodic plasma obtained by electrolysis of a molten LiCl-KCl equimolecular mixture are stated, under a theoretical computation of the $1f(dip-2p)$ $1s(1)$ lineshape, using Magnus frame for electronic perturbation and taking into account the effect of dynamic ion broadening: electric radial field intensity $|\vec{E}| = 160 \text{ kV cm}^{-1}$, electronic density $N_e = 1.2 \times 10^{17} \text{ cm}^{-3}$, temperature between 5000 and 5300 K. For the chosen composition of the electrolytic bath, the runaway of electrons is inhibited by the fact that the micro-plasmas are both very thin (50 μm) and partially ionised, but for a pure LiCl electrolytic bath, there is runaway.

INTRODUCTION

In 1963, our laboratory began the spectroscopical study of the light emitted at the anode during anode effect (A.E.), in the purpose of obtaining data about the gaseous "plasma" surrounding the anode (1,2,3). As a matter of fact, in well-chosen electrolytic bathes, electrodes, electrolytic cell feed voltages, the light emission is intense enough during a time long enough to permit a spectroscopic study. As is shown by using a high-speed cine-camera, there are only one or two electrical discharges on the anode surface at the same time (4), but they follow one another at random in

such a way that the whole surface seems to emit light with the same average brightness, provided the electrolytic voltage is great enough and has been applied between the electrodes after a lapse of an adequate period of time (a few seconds). Moreover, the short life created micro-plasmas locally vaporize the electrolytic bath and the heat they radiate is sufficient to maintain the gaseous sheath existence.

The life of the emission is only limited by the anode erosion, which depends on the electrolytic bath composition. Diagnostic methods of plasma spectroscopy are well suited to study the anodic plasma, because they do not modify the state of the sheath, neither in space, nor in time. Thus, theoretical spectroscopic line profiles are computed and compared with experimental data until they agree reasonably well.

EXPERIMENTAL RESULTS AND MAIN COMPUTATION HYPOTHESIS

The chosen method is better for very broad lines and, after several experiments (1,3,5,6), we have chosen to study the semi-degenerate $4f4d4p-2p$ Li(I) lines, using a molten equimolecular LiCl-KCl mixture as an electrolytic bath. A first computation of theoretical profiles in the frame of the impact approximation of the relaxation theory (7,8), considering an important self-absorption led (9) to a result close to experimental profiles (fig. 1). However, there were differences between experimental and theoretical profiles and we thought that a uniform electric field could be one reason for these differences; it was then necessary to modify the computation in order to account for this field (9,10).

The uniform electric field \vec{E} is polarized along the direction of observation (perpendicular to the anode axis); so, one observes only the σ components of the lines. Furthermore, it is necessary to take the splitting of atomic energy levels into account in the theoretical computation, before the electronic and ionic microfields perturbations. At last, the electric field \vec{E} can produce an inhomogeneity of the micro-plasmas.

was carried out under the following assumptions:

- the micro-plasma is cold
- the micro-plasma is subjected to the action of an electric field
- the validity of the Debye law
- a concentration of each element of the micro-plasma equal to the ionic concentration in the electrolytic bath.

A computation of temperature distributions was made by solving, for various values of \vec{E} , the energy balancing equation. The anodic micro-plasmas were shown to be cold (electronic temperature $T \approx 7000$ K) and, from this value obtained for the correlation factor:

$$r = \frac{1}{2} \left(1 + \frac{1}{\sqrt{1 + \frac{N_e^2}{2 \epsilon_0 k T}}} \right)$$

(N_e : electronic density, k : electronic charge)
 indicates however that the hypothesis of a quasi-static ionic microfield was not suitable (12), whatever the value of \vec{E} may be.

The computation of theoretical electronic profiles based on the Griem-Baranger theory (7,8) and taking \vec{E} into account permitted us to evaluate $|\vec{E}|$ to be of the order of 10^6 kV cm⁻¹. For this value, the optical depth of the micro-plasma is very weak and thus, self-absorption is negligible.

THEORETICAL PROFILE'S COMPUTATION

We computed again the theoretical profile of the H₁ line (H₁(I) line) by taking into account the effect of dynamic line broadening. Then, the total profile is a convolution product:

$$I(\omega) = \sum_{a,a'} \int_{-\infty}^{+\infty} \bar{I}(\omega', a, a') \bar{I}(\omega - \omega'; a', a) d\omega' \quad [1]$$

$$\bar{I}_i(\omega; a, a') = \frac{1}{\pi} \operatorname{Re} \left[\sum_{b,c} \int_{-\infty}^{+\infty} e^{i\omega t} \exp\left(i \frac{E_L t}{\hbar}\right) \rho_{ba}(t) \times \right. \\ \left. \times \langle a | \vec{D} | b \rangle \langle b | \vec{D} | c \rangle \langle c | \left\{ \bar{I}_i(t) \right\}_{a'} \right] dt \quad [2]$$

$$I_e(\omega, a', a) = \frac{1}{\eta} \operatorname{Re} \left[\int_0^{\infty} e^{-i\omega t} \langle a' | \{ U_e(t) \}_{Ae} | a \rangle dt \right] \quad [3]$$

(where $\{ U_e(t) \}_{Ae}$ is the thermal average of the evolution operators, the dipolar moment operator, $|a\rangle$, $|a'\rangle$, $|a''\rangle > U(1)$ energy levels of main quantum number $n=1$, perturbed by the field \vec{E} . At last:

$\rho(t) = \langle a | \rho(t) | a \rangle$, where $\rho(t)$ is the density matrix operator).

The partial ionic profiles $I_j(\omega; a, a')$ are obtained by using the adiabatic solutions (13) of the equation:

$$i\hbar \frac{\partial \psi(t)}{\partial t} = [H_0 + V(t)] \psi(t)$$

In a first study, we computed the partial electronic profiles $I_j(\omega; a', a)$ in the frame of the instant approximation of the relaxation theory (7.8), (see also our former studies (9,10,12)). So, we did the computation of $I_j(\omega; a, a')$, $I_j(\omega; a', a)$ and of $I(\omega)$ for several values of \vec{E} , N_e and the corresponding values of α coming from the thermodynamic study.

The theoretical profile showing the best agreement with the experimental one was obtained for:

$$N_e = 1,2 \times 10^{17} \text{ cm}^{-3} \quad (T_e = 6200 \text{ K}) \quad \text{and} \quad \|\vec{E}\| = 1,5 \times 10^5 \text{ V cm}^{-1}$$

A posteriori, the obtained value of $\|\vec{E}\|$ justifies the use of the adiabatic solutions in the computation of the partial ionic profiles $I_j(\omega; a, a')$, since it satisfactorily separates the forbidden line from the permitted one, even for the relatively great value of N_e .

One can also notice that $\|\vec{E}\|$ is two or greater than the critical electric field E_c :

$$E_c = \frac{e \hbar \omega}{8 \eta \epsilon_0 \rho_0^2} \quad \text{where} \quad \Lambda = \frac{1,5 e^3 (4 \eta \epsilon_0 \hbar \omega)^{3/2}}{(\eta N_e)^{1/2}}$$

(ρ_0 : Bohm's radius).

but one can reasonably suppose that the ion-sound phenomenon (11) is probably inhibited by the fact that the plasma is both very thin (5 μ m) and partially ionized (neutral atoms are ten times as numerous as the electrons) (15).

However, the great value of \bar{E} sets the problem of the nature of the electron-atom collisions, justifying again the computation of the partial electronic problem.

It was then necessary to go through the study by using a better representation of the electronic perturbation, which permits:

- to introduce chronologic effect
- to take into account the strong electron collisions, in another way than using a correcting term as in the previous models (9,10,12,15).

To this effect, we chose to evaluate the electronic perturbation in the Magnus frame, which has the property to take for every term of the development a linear operator. As a matter of fact, written the evolution operator $T(t)$ under the form:

$$T(t) = \exp\left(-i \frac{H_0 t}{\hbar}\right) U(t)$$

where: $U(t) = \exp[\Omega(t)]$,

Magnus chooses (16) that the equation:

$$i \hbar \frac{\partial U(t)}{\partial t} = \tilde{V}(t) U(t)$$

where:

$$\tilde{V}(t) = \exp\left(-i \frac{H_0 t}{\hbar}\right) V(t) \exp\left(-i \frac{H_0 t}{\hbar}\right)$$

(with, as $V(t)$, the electronic perturbation potential), is equivalent to the equation:

$$\frac{d\Omega(t)}{dt} = A(t) + \frac{1}{2} [A(t), \Omega(t)] + \sum_{n=2}^{\infty} \frac{(-1)^n}{2n!} B_n \left[\dots [A(t), \Omega(t)], \Omega(t) \dots \right]$$

$2n \text{ times}$

where $A(t) = \frac{\tilde{V}(t)}{i \hbar}$

(B_n : Bernoulli number.).

One has, for $\Omega(t)$, $\Omega(t) = \sum_{k=1}^{\infty} \Omega_k(t)$,
 with, for the two first terms of the development :

$$\Omega_1(t) = \int_0^t A(t_1) dt_1 \quad (\text{strong or weak collisions})$$

$$\Omega_2(t) = \frac{1}{2} \int_0^t \int_0^{t_2} [A(t_2), A(t_1)] dt_1 dt_2 \quad (\text{chronologic effect})$$

We did a systematic computation of the matrix elements of the operator $\Omega(t)$, for every alkaline, for strong or weak electronic collisions.

Then, the impact approximation leads to the thermic average :

$$\gamma_e(t) = \left\langle e^{-\frac{\Omega(t)}{A_v}} \right\rangle = 2\pi N_e \int_{v_{min}}^{+\infty} v f(v) dv \int_{p_{min}}^{p_{max}} dp \int_0^{+\infty} \left[e^{-\frac{\Omega(\sigma, t, t)}{A_v}} - 1 \right] dt$$

(where we take for $f(v)$ a maxwellian velocities distribution).

The width and the distance between peaks of the experimental profile lead, for the N_e values which are to be considered, to the impact limit :

At last, the total theoretical profile (computed by using the formula [1], [2], [3]) giving the best agreement with the experimental profile is obtained for (17) :

$\|\vec{E}\| = 150 \text{ kV cm}^{-1}$ and $N_e = 10^{17} \text{ cm}^{-3}$, values which are very near to those obtained by the latter study (15).

CONCLUSIONS

The Magnus profiles corrected with dynamic ion broadening have a greater width than the corrected Griem profiles (from 50 to 80%), but the widths of all the computed profiles are less important than the experimental widths. According to us, the main cause of this difference is the rapid evolution in time of the sheath geometry, which cor-

tainty profiles. During the life of each micro-plasma, a rapid evolution of \bar{n} . Experimental profiles are the result of an integration, in space and time, of profiles which correspond to several numerical values of the parameter in A.E., when the computed profiles correspond to the average value of these parameters.

However, one can accept that the "micro-plasma" is cold ($T_e \approx 5200^\circ K$), with a strong electronic density ($n_e \approx 10^{17} \text{ cm}^{-3}$), highly correlated, and perturbed by a polarized electric field of the order of 100 kV/cm.

Furthermore, one can state that the local thermodynamic equilibrium (L.T.E.) is bounded to the electrostatic path perpendicular. As a matter of fact, the an equilibrium mixture of H^+ and H^- ions, or more, since K is very close to infinity as 11, the electronic density is great enough to prevent the runaway of electrons (since the critical field is proportional to n_e , $\|\vec{E}\|$ is only to be greater than E_c); but, it is sure, as we saw, both the mean voltage \bar{V} and the distance between the electrodes, $\|\vec{r}\|$ will be fairly close to great as E_c , and the number of neutral atoms (proportionally the same as in the previous case) will be too small to prevent the electron runaway; then, there will not be L.T.E. This is experimentally observed, since the spectra are clearly visible over A.E. as detailed in an elementary form of our paper [5] (13).

REFERENCES

1. P.Mergault and J.C.Valogne, Communication at the 14th meeting of the C.I.T.U.I., Budapest (1963).
2. B.Letzeltrier, J.C.Valogne and P.Mergault, *Spektrochim.Acta* 18, 955 (1971).
3. J.C.Valogne and P.Mergault, *J. Phys. Chem.* 74, 24 (1970).
4. C.Guilpin and J.Garbarz-Cilleles, *J. Chim. Phys.* 75, 723 (1978).
5. P.Mergault, J.C.Valogne and C.Guilpin, *Ann. Phys. Chem. Acad. Sci. Paris* 273F, 25 (1971).
6. P.Mergault, J.C.Valogne, J.Garbarz-Cilleles and C.Guilpin, *C.R. Hebd. Seances Acad. Sci. Paris* 272, 211 (1972).
7. H.R.Grien, *Fluorescence Spectroscopy*, G. Greinert, New York (1964).
8. H.R.Grien, *Spectral Line Broadening by Fluorescence*, Academic Press, New York (1961).
9. T.Bier, J.C.Valogne and P.Mergault, *J. Chem. Phys. Radiat. Transf.* 10, 21 (1971).
10. J.C.Valogne and P.Mergault, *J. Phys. Chem.* 74, 24 (1970).
11. J.C.Valogne, J.Boekelja, T.Bier and P.Mergault, *Rev. Int. Ha. Temp. Phys.* 11, 78 (1971).
12. J.C.Valogne and P.Mergault, *J. Chem. Phys. Radiat. Transf.* 25, 11 (1971).
13. A.J.Barker, J.Boekelja and J.A. Jones, *J. Chem. Phys. Radiat. Transf.* 10, 1033 (1971).
14. J.Boekelja, J.A. Jones, N.A. Buchyn, Jr., *The Particle Kinetics of Fluorescence*, Academic Press, New York (1969).
15. J.F.Bardet and J.C.Valogne, *J. Phys. Chem.* 74, 24 (1970).
16. W. Parnis, *Ann. Phys. Chem.* 7, 11 (1951).
17. J.F.Bardet and J.C.Valogne, *J. Phys. Chem.* 74, 24 (1970).
18. J.C.Valogne, J.F.Bardet and P.Mergault, *Spektrochim.Acta* 17B, 315 (1967).

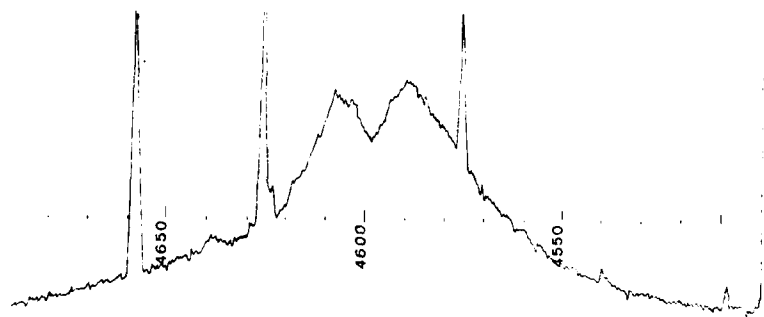


Fig.1-Experimental profile of the semi-degenerate $4f4d4p \rightarrow 2p$ Li(I) line (no perturbed frequency: 4602.9 Å).

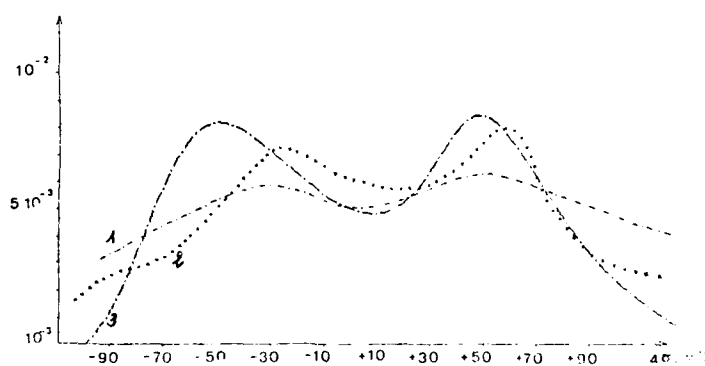


Fig.2-Comparison between the typical experimental profile and the best theoretical profiles-1:Experimental profile; 2:Corrected-Griem theoretical profile ($\|E\|=150$ kV/cm, $N_e=1.2 \times 10^{17}$ cm $^{-3}$); 3:Corrected-Magnus theoretical profile ($\|E\|=150$ kV/cm, $N_e=10^{17}$ cm $^{-3}$).

AN ELECTROCHEMICAL APPROACH FOR THE DETERMINATION OF OXIDE
IMPURITIES IN ACIDIC ALKALI CHLOROALUMINATES

Jean-Paul Schoebrechts, Paul A. Flowers and Gleb Mamantov

Department of Chemistry
The University of Tennessee
Knoxville, TN 37996 - 1600

ABSTRACT

The chemistry of tungsten hexachloride in an acidic sodium chloroaluminate (63 mole % AlCl_3) has been investigated by electrochemical and spectroscopic techniques at temperatures of 150 and 175°C. Tungsten hexachloride undergoes several reduction steps in the melt, the first of which is sensitive to the presence of oxide containing impurities. UV-visible absorption measurements indicate that tungsten hexachloride reacts with oxides in the melt to form the oxide tetrachloride WOCl_4 . Comparison between spectroscopic results and electrochemical data indicates that the first voltammetric wave is due to the reduction of WCl_6 . The initial amount of oxide in the melt as well as the equilibrium constant for formation of WOCl_4 can be obtained from a plot of reduction current of WCl_6 vs. the formal concentration of W(VI) .

INTRODUCTION

The determination of oxide impurities in molten chloroaluminates has been the subject of several studies during the last ten years (1-5). These impurities are very difficult to avoid in such melts (6) and may have pronounced effects on the behavior of other solute species of interest (7-9). Moreover, understanding the oxide chemistry in halide melts is of considerable importance to industrial electrolytic processes for the production of aluminum. Most of the methods reported for quantifying oxide levels in chloroaluminate melts are based on electroanalytical techniques and use a transition metal ion as a probe solute (such as Ti(IV) (3) and Ta(V) (4)). They are limited to basic melts only (3,4). On the contrary, the most recent method developed in our laboratory employs infrared measurements and is useful for acidic as well as basic melts (5).

The chemistry of tungsten in an acidic molten sodium chloroaluminate (63 mole % AlCl_3) is currently being reinvestigated in our laboratory. Results obtained several years ago (10) indicated that this element exhibits a wide variety of stable oxidation states in the acidic melt (+6, +3, +2, +11/6 and 0) some of which involve cluster species such as $\text{W}_6\text{Cl}_8^{4+}$. Recent results have shown that in the presence of oxide impurities, hexavalent tungsten is involved in an equilibrium between two electroactive species, the hexachloride WCl_6 and the oxide tetrachloride WOCl_4 . In this paper, an electroanalytical method for determining oxide levels based on the previous equilibrium is proposed.

EXPERIMENTAL

The preparation of the melts has been reported previously (11). However, no aluminum metal was added to the melts and no electrolysis between aluminum electrodes was performed in order to purify the melts.

The purification of commercially available tungsten hexachloride (Alfa Products) has been described earlier (10). Tungsten oxide tetrachloride (from Alfa Products) was sublimed once at 110°C prior to use.

Anhydrous sodium carbonate (Fisher Scientific) was dried under a CO_2 stream at 300°C for one day prior to use.

Aluminum oxide chloride was synthesized following the method described by Hagenmuller, *et al.* (12)

The electrochemical experiments were conducted using a PAR 174 polarographic analyzer, a PAR 175 Universal Programmer and a Houston 2000 X-Y recorder.

Molecular absorption spectra in the visible and ultraviolet regions were obtained using sealed cells and a Cary 14 spectrometer. Spacers were used to reduce the absorbance of the solutions when necessary. Neutral density filters were used in the reference compartment to record spectra with absorbances higher than 2.

X-ray powder patterns were obtained using sealed capillaries and a Phillips Unit, Model XR9-2600.

RESULTS AND DISCUSSION

Figure 1 shows a typical cyclic voltammogram for a solution of WCl_6 in a 63/37 $AlCl_3$ - $NaCl$ melt. Several reduction steps were observed before the cathodic limit of the melt, the first of which is under investigation in this study.

Analysis of cyclic voltammograms recorded at different scan rates (0.01 to 0.5 V/s) and for different concentrations (up to 20 mM WCl_6) indicates that the reduction is a reversible one-electron diffusion-controlled step. A plot of the function $\log(i_d - i/i)$ vs. E , where i_d is the limiting reduction current of the normal pulse voltammogram and E is the potential, is linear with a slope in agreement with the previous conclusion. The half-wave potential was found to be +1.650 V vs the potential of aluminum in the same melt.

The limiting current of the wave increases with the formal concentration of WCl_6 as shown in Figure 2. At low WCl_6 levels (below 3.5×10^{-3} mole- L^{-1}), the current is unexpectedly low but it then increases linearly with the concentration as the latter becomes higher than 5.5×10^{-3} mole- L^{-1} . The intercept of this straight line with the concentration axis has a positive value, indicating that something has to be neutralized before appearance of the voltammetric wave.

Figure 3 shows the change of the UV-visible absorption spectrum of a WCl_6 solution as the tungsten concentration is varied. For the most concentrated solutions, the spectra exhibit one intense absorption band at 333 nm. When the solution is diluted, that band disappears, and two new ones are observed at 355 and 230 nm, suggesting that hexavalent tungsten is involved in an equilibrium between different species. It is worthwhile pointing out that these changes occur in the same concentration range as for the voltammetric current-concentration plot.

It is known that WCl_6 easily reacts with oxide-containing species (13) to produce tungsten oxide tetrachloride, $WOCl_4$. Since the melt was probably contaminated with oxide (2,6), it was assumed that $W(VI)$ was involved in an equilibrium between an oxychloro- and a chloro- species.

The UV-visible absorption spectra of WCl_6 and $WOCl_4$ in the vapor phase (where both compounds are known to be monomeric (13)) are represented in Figures 4 and 5. $WOCl_4$ has absorption bands at 460, 355, 270 (shoulder = sh), 250 (sh), and 220 nm, while WCl_6 exhibits bands at 430 (sh), 375 (sh), 328, 275 (sh) and 255 nm. Comparison with the spectra of WCl_6 solutions indicates clearly that at low formal tungsten concentrations, the oxide tetrachloride is the only tungsten entity present in the melt, while at higher concentrations, WCl_6 also exists. This suggests that dissolved WCl_6 reacts with oxide-containing impurities initially present in the melt. The intercept of the linear part of the current-

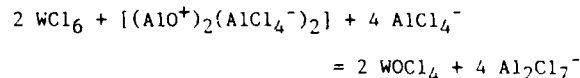
concentration curve with the concentration axis should give directly the initial concentration of oxide in the melt (expressed as "O²⁻"). Values obtained from three different experiments were in the range 2.6 to 3.3×10^{-3} mole/l of "O²⁻".

In order to confirm the previous deductions, oxide was deliberately added to a concentrated WCl₆ solution (Figure 6) by successive additions of Na₂CO₃. The voltammetric wave decreased in intensity after the first addition of oxide (Figure 6b) and then vanished when the amount of oxide exceeded that of WCl₆ (Figure 6c). Calculations based on the decrease of the voltammetric current and on an initial amount of oxide obtained from the extrapolated calibration curve (Figure 2, curve obtained at 175°C) are in agreement with a one to one reaction between WCl₆ and O²⁻.

Figure 6d shows that WOCl₄ is also electroactive in the melt but at more cathodic potentials than WCl₆, as the wave below +1.6 V increases upon addition of WOCl₄.

The fact that WCl₆ appears to be a stronger oxoacid than AlCl₃ was confirmed by reacting WCl₆ with AlOCl at 180°C. The reaction produced quantitatively WOCl₄ and AlCl₃ as shown by X-ray diffraction analysis of the products.

From the linear and non-linear parts of the calibration curve at 150°C (Figure 2), we have estimated the value of the apparent equilibrium constant for the following reaction (the concentrations of AlCl₄⁻ and Al₂Cl₇⁻ have been assumed constant)



A value of 7.3×10^4 l/mol was found.

ACKNOWLEDGEMENTS

We gratefully acknowledge the support of this research by grants from the Air Force Office of Scientific Research and Martin Marietta Laboratories.

REFERENCES

1. B. Tremillon, A. Bermond and R. Molina, J. Electroanal. Chem. Interfacial Electrochem., 74, 53 (1976).
2. R. W. Berg, H. A. Hjuler and N. J. Bjerrum, Inorg. Chem., 23, 557 (1984).
3. Z. Stojek, H. Linga and R. A. Osteryoung, J. Electroanal. Chem. Interfacial Electrochem., 119, 365 (1984).
4. T. M. Laher, L. E. Mc Curry and G. Mamantov, Anal. Chem., 57, 500 (1985).
5. P. A. Flowers and G. Mamantov, Anal. Chem., 59, 1062 (1987).
6. G. Mamantov and R. A. Osteryoung, in "Characterization of Solutes in Non-Aqueous Solvents"; G. Mamantov, Ed., Plenum Press, New York, 1978; pp. 223-249.
7. G. Ting, Ph. D. Dissertation, University of Tennessee, 1973.
8. H. Linga, Z. Stojek and R. A. Osteryoung, J. Am. Chem. Soc., 103, 3754 (1981).
9. J. B. Scheffler, C. L. Hussey, K. R. Seddon, C. M. Kear and P. D. Armitage, Inorg. Chem., 22, 2089 (1983).
10. D. L. Brotherton, Ph. D. Dissertation, University of Tennessee, 1974.
11. R. Marassi, J. Q. Chambers and G. Mamantov, J. Electroanal. Chem., 69, 345 (1976).
12. P. Hagenmuller, J. Rouxel, J. David, A. Colin and B. Le Neindre, Z. Anorg. Allg. Chemie, 323, 1 (1963).
13. J. R. Canterford and R. Colton, "Halides of the Second and Third Row Transition Metals", John Wiley and Sons Ltd, New York, 1968; pp. 220-221.

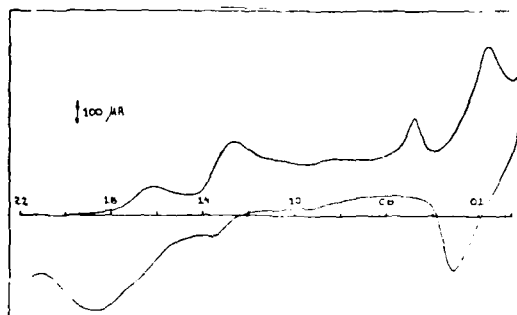


Fig. 1. Cyclic voltammogram for W(VI) at a glassy carbon electrode at 175 °C in $\text{AlCl}_3\text{-NaCl}$ (63-37 mol%). Electrode area, 0.07 cm^2 ; concentration, $1.38 \times 10^{-2} \text{ F}$; reference electrode, Al(III)/Al in the same melt; scan rate, 0.1 V/s .

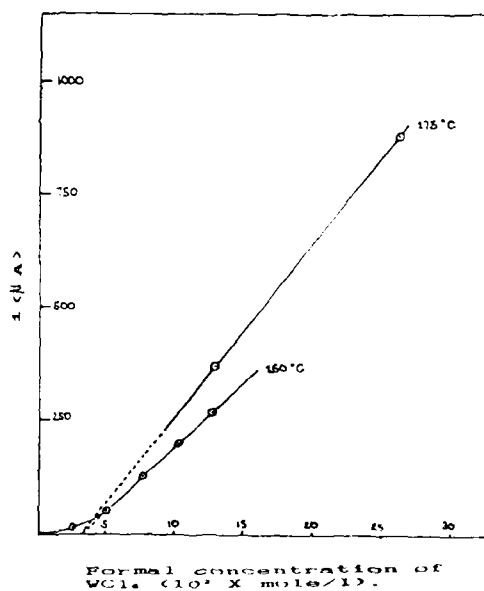


Fig. 2. Normal pulse voltammetric limiting current vs. formal concentration of WCl_6 in $\text{AlCl}_3\text{-NaCl}$ (63-37 mol%).

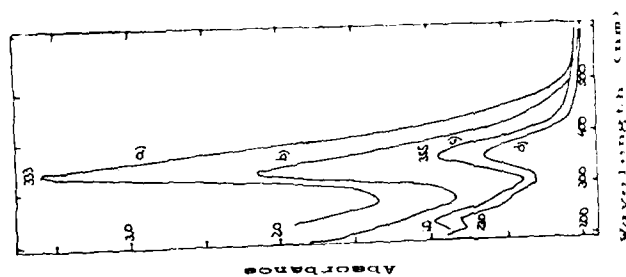


Fig. 3. UV-visible absorption spectra of $W(VI)$ in $AlCl_3-NaCl$ (63-37 mol%) at 150°C. $W(VI)$ concentration (mol/l): a) 0.011, b) 0.0071, c) 0.0035, d) 0.0018; path length, 0.025 cm.

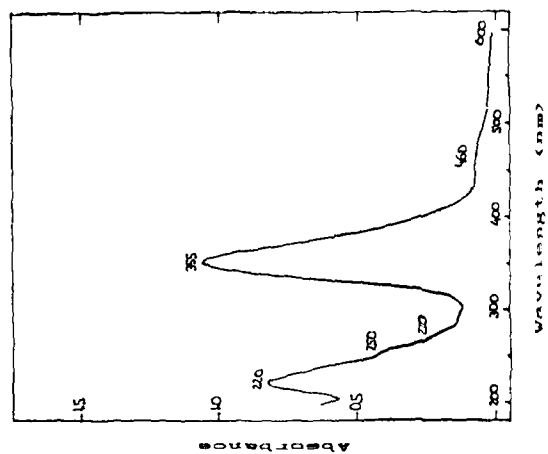


Fig. 4. UV-visible absorption spectrum of $WOCl_4(g)$ at 121°C. Path length, 1.0 cm.

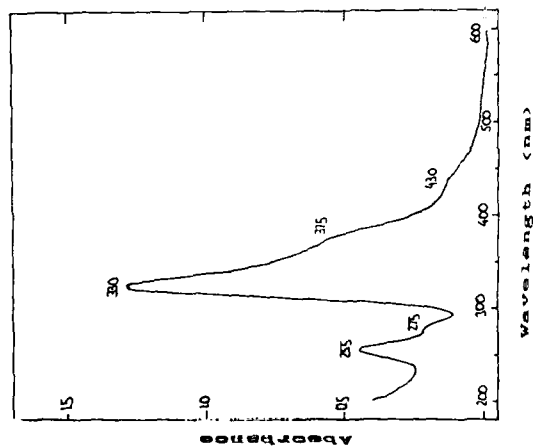


Fig. 5. UV-visible absorption spectrum of $WCl_6(g)$ at $183^\circ C$. Path length, 0.3 cm.

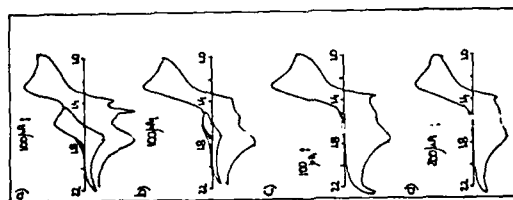


Fig. 6. Cyclic voltammograms of $W(VI)$ solutions at a glassy carbon electrode at $175^\circ C$ in $AlCl_3-NaCl$ (63-37 mole %). Electrode area, 0.07 cm^2 ; scan rate, 0.1 V/s ; reference electrode, $Al(III)/Al$ in the same melt; quantities added ($10^4 \times$ mole): a) WCl_6 , 7.41; b) Na_2CO_3 , 4.47; c) Na_2CO_3 , 7.93; d) WCl_6 , 4.61.

SPECTROELECTROCHEMISTRY IN ROOM TEMPERATURE HALOALUMINATE IONIC LIQUIDS

E. Haynes Ward, Paul A. Barnard, I-Wen Sun
and Charles L. Hussey*

Department of Chemistry
The University of Mississippi
University, MS 38677

ABSTRACT

A fiber optic based, microprocessor controlled spectroelectrochemistry system suitable for the remote acquisition of transmission spectroelectrochemical data is described. This system utilizes a commercial fiber optic spectrophotometer and employs a reticulated vitreous carbon optically transparent electrode. It can be used to collect data in reactive liquids that are isolated in a glove box or other controlled atmosphere environment. The system is completely controlled by two linked microprocessors that collect both electrochemical and spectral data simultaneously. The application of this system is demonstrated through experiments with the tris(2,2'-bipyridine)ruthenium(II)/(III) and hexachloroiridate(III)/(IV) redox systems in the aluminum chloride-1-methyl-3-ethylimidazolium chloride room temperature ionic liquid.

INTRODUCTION

The application of spectroelectrochemical techniques to investigations in molten salts has been reviewed (1). Research in this area has been conducted in both high temperature melts (2-5) and in ionic liquids that are molten at or near room temperature (6,7). Research in our laboratory is concerned with transition metal halide and oxide halide complex chemistry in room temperature

haloaluminate ionic liquids (8) like aluminum chloride-1-methyl-3-ethylimidazolium chloride ($\text{AlCl}_3\text{-MeEtimCl}$) (9). In order to fully explore this chemistry, we have constructed a microprocessor controlled fiber optic based spectroelectrochemistry system and a cell with a reticulated vitreous carbon optically transparent electrode (RVC-OTE) (10). The latter was constructed from Teflon and fused silica. This cell is designed specifically for use with these reactive solvents. The properties of reticulated vitreous carbon or glassy carbon foam electrodes have been discussed (11).

The main advantage of the spectroelectrochemistry system described herein is that it can be used to acquire data directly inside a controlled atmosphere glove box while the spectrophotometer and electrochemical instrumentation remain outside and accessible. Some of the techniques that can be carried out with this system are chronoamperometry, chronocoulometry, chronoabsorptometry, voltammetry, voltabsorptometry, and spectropotentiostatic experiments. In this article we describe this spectroelectrochemical system and illustrate the implementation of these techniques in room temperature haloaluminate melts.

SPECTROELECTROCHEMISTRY SYSTEM

The construction of the RVC-OTE cell and cell holder have been described (10). The major instruments that comprise the spectroelectrochemistry system are a Guided Wave Model 100-2 optical waveguide spectrum analyzer, a Tandy Model 1000 microcomputer, a 16 bit microcomputer (IBM PC AT equivalent), an AMEL Model 552 potentiostat, an AMEL Model 506 function generator, and a PARC Model 379 digital coulometer with a BCD output.

The Guided Wave spectrophotometer was equipped with both tungsten and deuterium light sources, a silicon diode detector, and a 1200 lines mm^{-1} concave holographic grating. The Tandy computer was equipped with 128 Kb RAM on the mother board, an RS-232 serial communications board, and a TanPak 512 Kb RAM expansion card (Hard Drive Specialist) with an additional serial port and quartz clock. The 16 bit microcomputer was equipped with 1 Mb RAM, a 20 Mb hard disk, a serial interface card, a parallel I/O BCD card (Meta-Byte), and an ADALAB PC (Interactive Microwave) interface card. This card was furnished with both differential integrating and

successive approximation 12-bit analog/digital converters, two 12-bit digital analog converters, and a four channel multiplexer. A schematic diagram of the system is shown in Figure 1.

The Tandy computer was used to control the Guided Wave spectrophotometer and acquire spectral data through a proprietary interface card and software supplied by the instrument manufacturer. The 16-bit computer, which served as the master unit, was used to control the start of an experiment by simultaneously triggering the AMEL function generator through a digital trigger and initiating spectral acquisition by the Tandy 1000 Guided Wave spectrophotometer through a serial communications link. The sweep voltage from the function generator was monitored with one channel of the four channel multiplexer by using the integrating A/D converter. The second channel was used to sample the current at the coulometer during an experiment. The BCD link was used to monitor the charge. Alternately, one of the digital/analog converters was sometimes used in place of the analog function generator to generate waveforms. Processing of both spectral and electrochemical data was carried out with LOTUS 123 software.

A unique aspect of the RVC-OTE cell is the positioning of a porous barrier between the OTE cavity and the reference and counter electrode compartments (10). This barrier virtually eliminates the edge currents common to many OTE cells, especially those constructed from minigrids, where one or more edges of the OTE electrode are exposed to the bulk solution containing the electroactive solute. No bulk solution containing electroactive solute need be present in this cell. In addition, the solution for analysis can be weighed directly into the OTE compartment; no prior calibration of the volume of this compartment is necessary.

SPECTROELECTROCHEMISTRY EXPERIMENTS

Room temperature haloaluminate melts are relatively viscous compared to conventional solvents. As a consequence, the diffusion coefficient for a given electroactive species in these melts is usually one or more orders of magnitude smaller than in conventional solvents like water or acetonitrile. Hence, the current observed during an electrochemical experiment

with the melt is much less than that observed with most conventional solvents, and longer times are required to accumulate the charge corresponding to complete electrolysis of a given number of moles of solute. Consequently, sweep experiments like cyclic voltammetry must be undertaken at very slow voltage scan rates.

Chronocoulometry and Chronoabsorptometry. Chronoabsorptometric techniques involve selective monitoring of the absorbance arising from one or more of the species consumed or produced during an electrode reaction initiated with a potential step. Chronocoulometric charge-time and chronoabsorptometric absorbance-time plots for the oxidation of tris(2,2'-bipyridine)ruthenium(II) cation ($[\text{Ru}(\text{bipy})_3]^{2+}$) in the 60 mole % AlCl_3 -MeEtimCl melt, which resulted from stepping the potential of the RVC-OTE from 0.70 to 1.50 V versus Al in the 66.7 mole % AlCl_3 -MeEtimCl melt, are shown in Fig. 2. The $[\text{Ru}(\text{bipy})_3]^{2+}/3^+$ electrode reaction has been found to be reversible and uncomplicated by coupled homogeneous chemical steps in a similar molten salt system, aluminum chloride-1-butylpyridinium chloride (12). The chronoabsorptometric plot was obtained by monitoring the $[\text{Ru}(\text{bipy})_3]^{2+}$ absorbance maximum located at 454 nm. The theoretical charge expected based on the exhaustive one-electron oxidation of the $[\text{Ru}(\text{bipy})_3]^{2+}$ cation in the solution that was weighed into the RVC-OTE was 0.01221 coulombs. An uncorrected experimental value of 0.01224 coulombs was recorded during this experiment, and this value suggests that $n \approx 1.00$. These results illustrate the complete retention of the electroactive solute in the RVC-OTE, and they suggest that $[\text{Ru}(\text{bipy})_3]^{2+}$ undergoes the expected one-electron oxidation to $[\text{Ru}(\text{bipy})_3]^{3+}$. The chronoabsorptometric plot is essentially a mirror image of the chronocoulometric plot. The flat response of the latter plot (Fig. 2), which is observed after approximately 2800 s have elapsed, illustrates the absence of edge effects associated with this cell.

Voltammetry and Voltabsorptometry. Voltabsorptometric techniques involve the simultaneous acquisition of both potential and absorbance data during a potential sweep experiment (13). These techniques are especially useful for selective monitoring of an electrode reaction in the presence of large background currents or currents arising from other electroactive solutes that are oxidized or reduced in the same potential region as the

species of interest. In order to apply these techniques, an accessible spectral region must be available in which either the oxidized or reduced form of the redox couple of interest exhibits absorption and in which there is no absorption by any species that may be participating in parallel redox reactions.

The cyclic voltammetric and voltabsorptometric responses that were obtained from the application of a 0.2 mV s^{-1} potential sweep program to the RVC-OTE, which contained the same $[\text{Ru}(\text{bipy})_3]^{2+}$ solution used in Fig. 2, are shown in Figs. 3 and 4, respectively. The triangular potential sweep program that was used for these experiments extended from 0.90 to 1.50 and back to 0.90 V. The wavelength was monitored at 454 nm in order to record the voltabsorptometric response.

The differential voltabsorptometric wave (Fig. 4b) was obtained by differentiation of the data in Fig. 4a, and it matches Fig. 3 closely for this reversible, uncomplicated electron transfer reaction. Half-wave potentials of 1.24 V were calculated from both Figs. 3 and 4b. These values are in good agreement with the estimate of $E_{1/2} = 1.22 \text{ V}$ that was determined with cyclic voltammetry at a glassy carbon disk electrode in a separate experiment.

Spectropotentiostatic Experiments. The spectropotentiostatic technique involves the measurement of absorption spectra after Nernstian equilibrium has been attained at the OTE following steady-state potential steps (14). This technique is useful for obtaining estimates of iR free formal cell potentials, E^0 (14). Significant potential errors due to uncompensated cell resistance are sometimes present in formal potentials originating from voltammetric measurements. The spectropotentiostatic technique provides a viable non-potentiometric method for estimating E^0 . In these experiments the applied potential, E_a , is used to control the ratio $[\text{Red}]/[\text{Ox}]$; when equilibrium has been achieved in the solution entrained in the OTE, the absorption spectrum is recorded. Both E^0 and n for a redox reaction can be calculated from a series of absorption spectra recorded at different E_a by monitoring the absorbance of the electroactive species in the OTE at a selected wavelength and then plotting the data according to the following equation (14):

$$E_a = E^{0'} - 2.3RT/nF \log([A_{\text{Red}} + A]/[A + A_{\text{Ox}}])$$

A_{Red} , A_{Ox} , and A correspond to the absorbance of the completely reduced solution, the absorbance of the completely oxidized solution, and the absorbance of the solution at some E_a value intermediate between those used to establish A_{Red} and A_{Ox} , respectively.

A series of spectropotentiostatic experiments for the $[\text{IrCl}_6]^{2-/3-}$ redox system in the 49.0 mole % AlCl_3 -MeEtImCl room temperature ionic liquid are shown in Fig. 5. In each experiment, the RVC-OTE was held at E_a until current ceased to flow and the optical response at 494 nm became constant. A plot of E_a versus $\log([A_{\text{Red}} + A]/[A + A_{\text{Ox}}])$, which was derived from the series of spectropotentiostatic experiments shown in Fig. 5, is shown in Fig. 6. The slope of this plot is 0.062 V at 40.0 °C (0.062 V is expected for $n = 1$), and the intercept is $E^{0'} = 0.37$ V. The latter compares favorably with a value of $E^{0'} = 0.37$ V that was calculated from voltammetric data obtained with a glassy carbon rotating disk electrode.

REFERENCES

1. V. E. Norvell and G. Mamantov in "Molten Salt Techniques", D. G. Lovering and R. J. Gale, Eds., Chap. 7, Plenum Press, N. Y. (1983).
2. G. Mamantov, V. E. Norvell, and L. N. Klatt, *J. Electrochem. Soc.*, **127**, 1768 (1980).
3. M. Sorlie, G. P. Smith, V. E. Norvell, G. Mamantov, and L. N. Klatt, *ibid.*, **128**, 333 (1981).
4. V. E. Norvell, K. Tanemoto, G. Mamantov, and L. N. Klatt, *ibid.*, **128**, 1254 (1981).
5. B. L. Harward, L. N. Klatt, and G. Mamantov, *Anal. Chem.*, **57**, 1773 (1985).
6. D. M. Chapman, G. P. Smith, M. Sorlie, C. Petrovic, and G. Mamantov, *J. Electrochem. Soc.*, **131**, 1609 (1984).
7. D. M. Chapman, A. C. Buchanan, III, G. P. Smith, and G. Mamantov, *J. Am. Chem. Soc.*, **108**, 654 (1986).
8. C. L. Hussey in "Advances in Molten Salt Chemistry", Vol. 5, G. Mamantov, Ed., pp. 185-230, Elsevier, Amsterdam (1983).

9. J. S. Wilkes, J. A. Levisky, R. A. Wilson, and C. L. Hussey, *Inorg. Chem.*, **21**, 1263 (1982).
10. E. H. Ward and C. L. Hussey, *Anal. Chem.*, **59**, 213 (1987).
11. V. E. Norrell and G. Mamantov, *ibid.*, **49**, 1470 (1977).
12. S. Sahami and R. A. Osteryoung, *Inorg. Chem.*, **23**, 2511 (1984).
13. W. R. Heineman, F. M. Hawkridge, and H. N. Blount in "Electroanalytical Chemistry", Vol. 13, A. J. Bard, Ed., pp. 72-74, Marcel Dekker, New York (1984).
14. W. R. Heineman, F. M. Hawkridge, and H. N. Blount, *ibid.*, pp. 17-30.

ACKNOWLEDGEMENT

This work was supported by National Science Foundation through Grant CHE-8412730

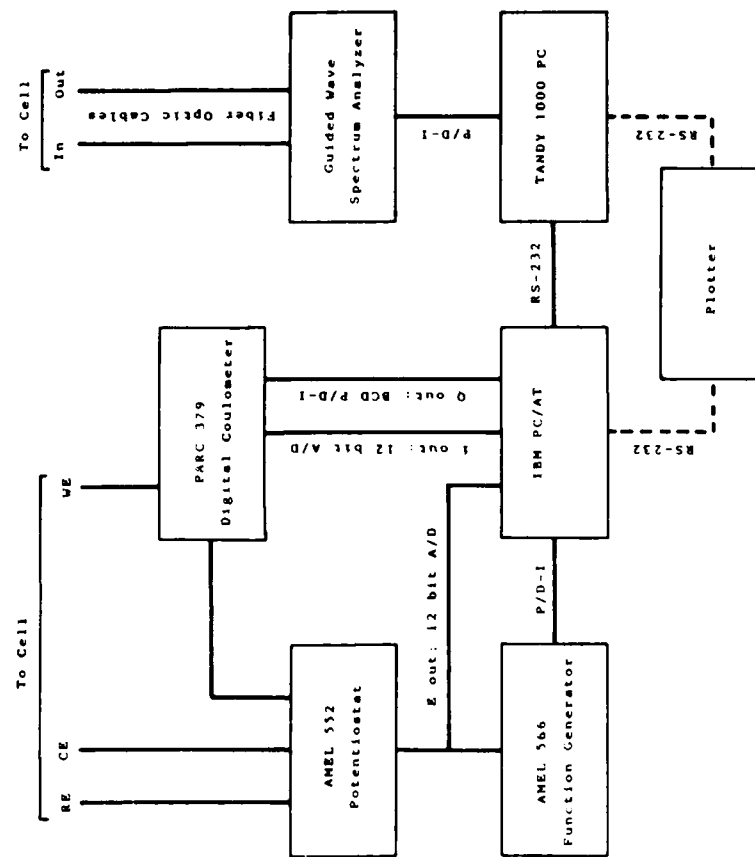


Figure 1. Schematic diagram of the spectroelectrochemistry system.

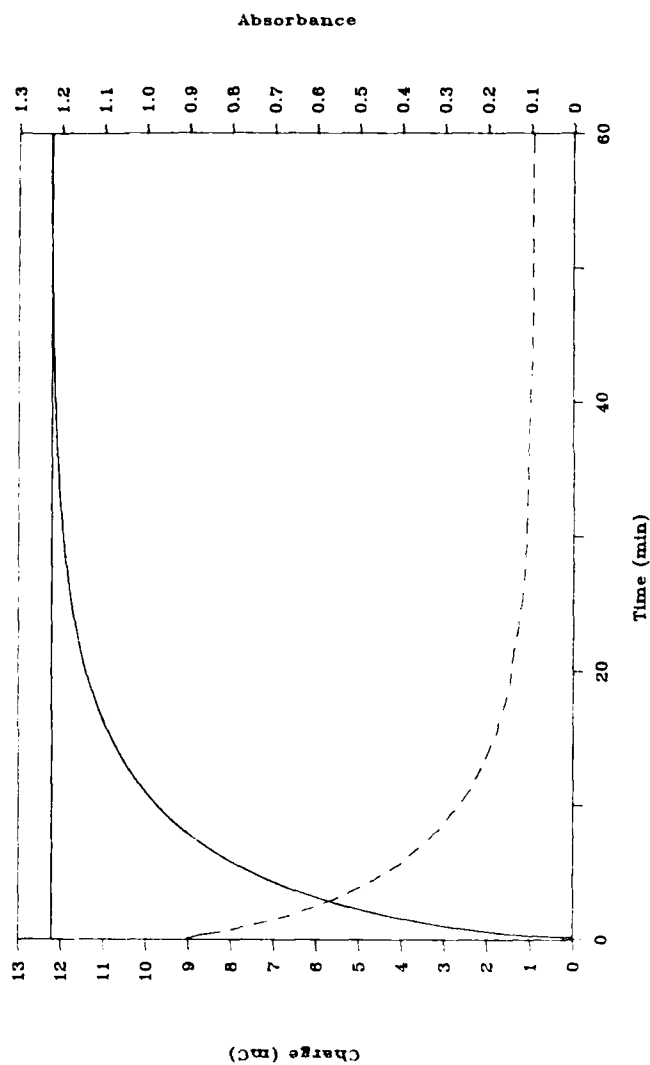


Figure 2. Chronocoulometric (—) and chronoabsorptometric (---) responses for the oxidation of a 0.60 mM solution of $[\text{Ru}(\text{bipy})_3]^{2+}$ in 60.0 mole % $\text{AlCl}_3\text{-MeEtimCl}$ at 40.0 °C at the RVC-OTE. The potential was stepped from an initial value of 0.70 to 1.50 V, and the wavelength was monitored at 454 nm.

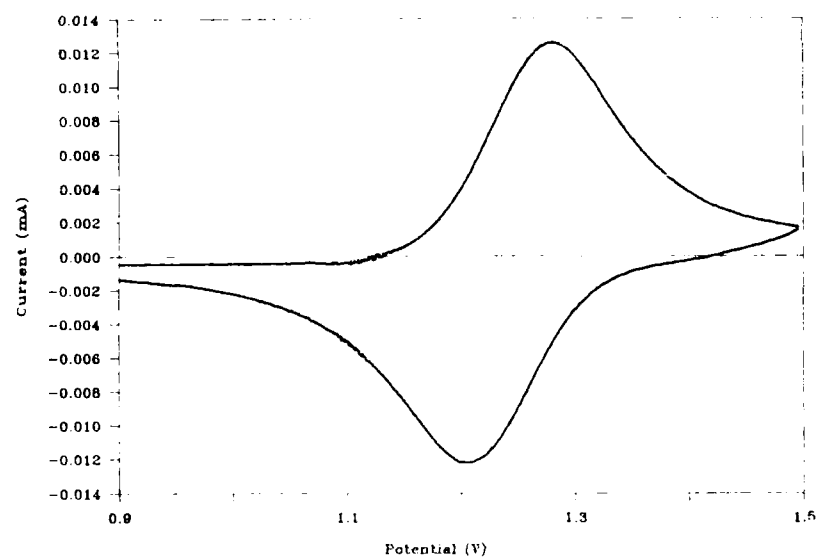


Figure 3. Cyclic voltammogram wave for the solution described in Fig. 2 at the RVC-OTE. The scan rate was 0.20 mV s^{-1} .

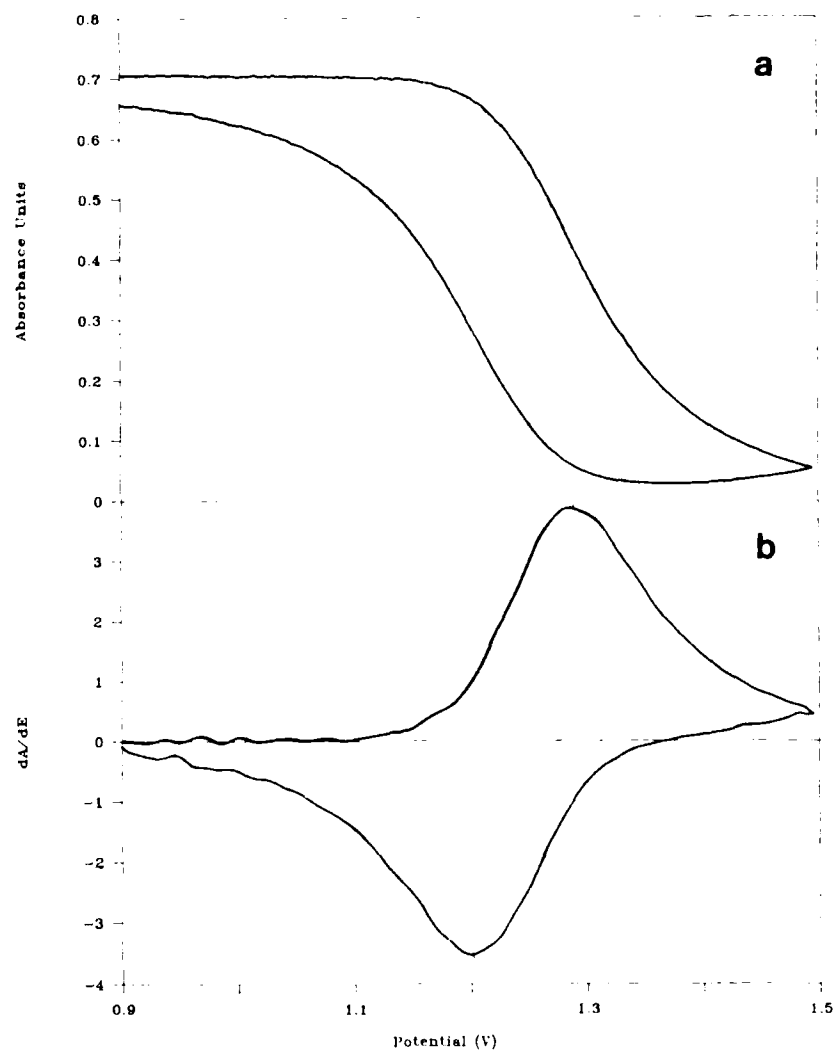


Figure 4. (a) Cyclic voltabsorptometric and (b) differential cyclic voltabsorptometric waves for the solution described in Fig. 2 at the RVC OTE. The scan rate was 0.20 mV s^{-1} , and the absorbance was monitored at 454 nm.

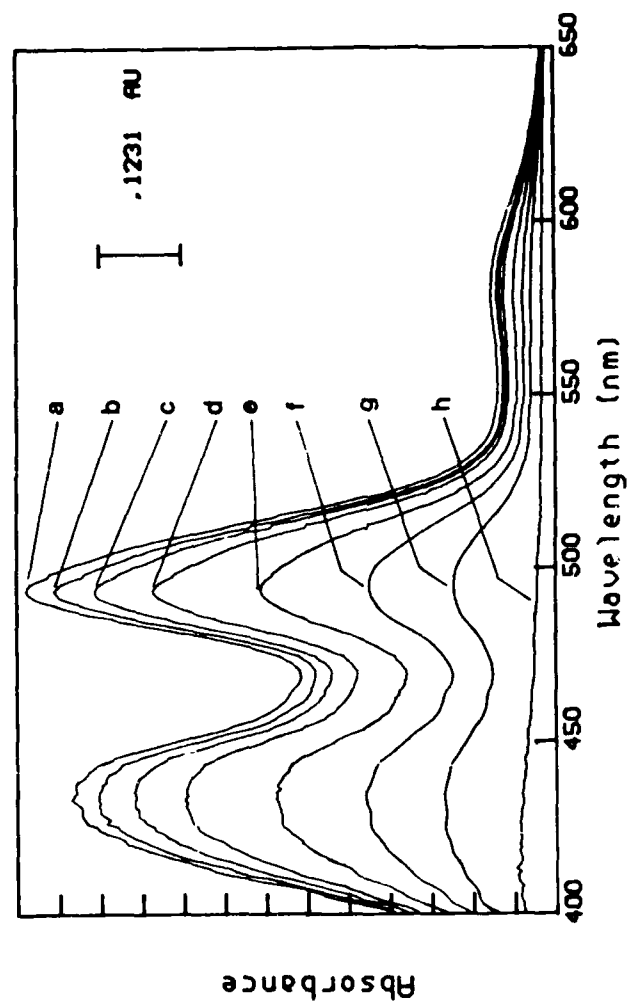


Figure 5. Absorption spectra that were recorded at various applied potentials during a spectro-potentiostatic experiment with 2.09 mM $[\text{IrCl}_6]^{2-}$ in 49.0 mole % $\text{AlCl}_3\text{-MeEtImCl}$ at 40.0 $^\circ\text{C}$. at the RVC-OTE: (a) 0.600, (b) 0.450, (c) 0.425, (d) 0.400, (e) 0.375, (f) 0.350, (g) 0.325, and (h) 0 V.

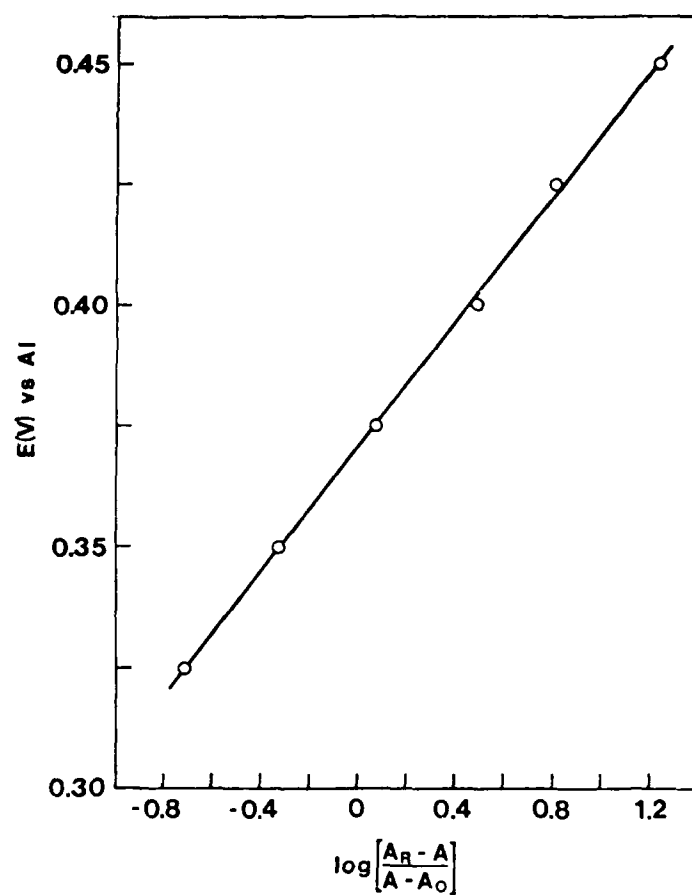


Figure 6. Plot of E_a versus $\log[(A_{Red} - A)/(A - A_{Ox})]$.

SPECTROCHEMICAL AND ELECTROCHEMICAL PROPERTIES OF SOME LANTHANIDES AND ACTINIDES IN ROOM TEMPERATURE MELT

Shyama P. Sinha
Department of Chemistry, University of Dayton
Dayton, Ohio 45469, U.S.A.

Spectroscopic and electrochemical behavior of melts consisting of 1-methyl-3-ethylimidazolium chloride and AlCl_3 and solutions of Ce(III), Tb(III) and U(V) in 0.4 (basic) melt have been investigated. The predominant species in solution was found to be $[\text{MCl}_6]^{3-}$. The melt has been modified by treating it with gaseous HCl to increase the conductivity. NMR data shows the presence of a highly acidic proton, and a melt:HCl ratio of 1:1.

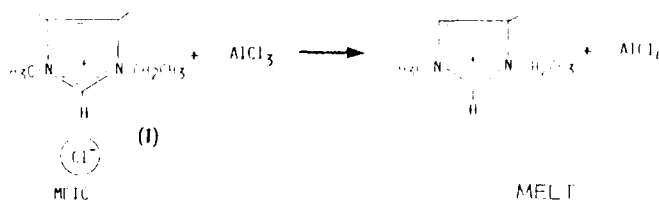
The family of ambient temperature melts resulting from 1,3-dialkylimidazolium chloride and AlCl_3 was discovered at the Frank J. Seiler Laboratories of the U.S. Air force Academy in Colorado Springs [1]. The most extensively investigated room temperature melts consist of a mixture of 1-methyl-3-ethylimidazolium chloride (MEIC) (I) and AlCl_3 in various mole ratios. These melts possess very interesting solvent properties. Some of the typical advantages and disadvantages are:

Typical Advantages

- *Stable and relatively easy to prepare
- *Low liquidus temperature
- *Liquid over a wide temperature range (-80 to -70°C)
- *Large variability of Lewis acid/base properties
- *Anhydrous aprotic solvent
- *Large electrochemical window (2.6 V)
- *Good UV/VIS spectral transparency (down to 250 nm)
- *Conductivities of the ambient temperature melts are comparable to that of the molten salts and aqueous electrolytes
- *Miscibility with organic solvents

Disadvantages

- High sensitivity to air and moisture
- Corrosive
- High viscosity



1.1 Spectroscopic Properties of the Chloroaluminate Melt

The hydrated chloride ion $[(Cl^-)(H_2O)_x]$ absorbs in the far UV region. In aqueous solution the first band appears around 194 nm possibly due to the charge transfer transition. The alkali metal ions that do not absorb in this range has virtually no effect on the position of this band. Aqueous solution of 1-methyl-3-ethylimidazolium chloride (MEIC) (I) showed a broad band at 208 nm (Fig. 1) with molar absorptivity of $4.33 \times 10^3 \text{ M}^{-1} \text{ cm}^{-1}$ agreeing with previous measurements [2]. The high absorbance peak is due to the organic chromophore of the MEIC cation (I).

The melts containing less than 0.5 mole fraction of $AlCl_3$ (i.e. basic melts) exhibit an absorption edge cut off at 250 nm. The $AlCl_4^-$ species present in these melts probably absorbs strongly around 246 nm and excludes the possibility of observing the peak due to MEIC cation moiety. However, as the mole fraction of $Al_2Cl_7^-$ is increased, the acidic melts are found to absorb strongly around 280 nm (Fig. 2). The sample containing virtually 100% $Al_2Cl_7^-$ ($N = 0.6665$) also showed a broad band at 335 nm beside the peak at 280 nm. The high wavenumber shoulder is probably due to other oligomeric forms of chloroaluminate, $[(AlCl_3)_x]$.

We have examined a solution of $LiAlCl_4$ in acetonitrile. The spectrum is shown in Fig. 3. The band at 240 nm in this spectrum is due to $[AlCl_4]^-$ anion agreeing with the strong absorption edge observed for the basic melts containing the same species. On hydrolysis, the peak at 240 nm is displaced by a peak at 260 nm (Fig. 3) possibly due to the hydrolysis of the chloroaluminate anion to produce $Al(III)$ aquo ion, $[Al(OH_2)_6]^{3+}$. It is found that $Al(III)$ aquo ion at a pH 0.9 exhibits the same spectrum profile with a peak at 258 nm. Recent spectroscopic investigation of McIntyre et al. [3] on the hexaquo- $Al(III)$ ion confirmed the presence of other equilibria involving the aquo ion, hydroxide ion and the counter anions.

The excitation and emission spectra of 1-methylimidazole (MIM), MEIC and 0.4 melt were investigated. Both MIM and MEIC show a strong and sharp excitation peak at 245 nm and a broad photoluminescence peak at 445 nm. This luminescence is due to $\pi^* \rightarrow \pi$ transition of the imidazolium moiety. The excitation spectrum of the melt (0.4) consisted of three peaks at 270, 355 and 395 nm. On excitation with 270 and 355 nm radiation, we were able to observe a strong emission band at 445 nm similar to that observed for MIM and MEIC solutions (Fig. 4). However, excitation of the melt (0.4) with 395 nm radiation produced a new luminescence peak at 470 nm, which is tentatively assigned to the coexcited chloroaluminate species. Fluorescence studies on other melt compositions are in progress and will be reported elsewhere.

Further characterization of the melts may be carried out from the observed difference in the far IR spectra due to the presence of different chloroaluminate species ($AlCl_4^-$, $Al_2Cl_7^-$) (Fig. 5). The spectral difference in the 600-200 cm^{-1} region is due to the difference in symmetry of the two prominent chloroaluminate species described earlier. We were also able to observe characteristic difference in the hydrogen bonding region (3300-2900 cm^{-1}) between a 0.4 and a 0.6 melt. This region is complicated by the presence of CH vibrations from the methyl and ethyl groups and definite conclusion have to wait further analysis. The present author, however, strongly

believes that a considerable amount of hydrogen bonding exists between the 2H of MEIC moiety and the chloride ion or the AlCl_4^- anion in the basic melts.

1.2 Electrochemical Properties

The electrochemical window of the chloroaluminate melt is limited by the reduction of imidazolium cation and the oxidation of Cl^- , AlCl_4^- , and Al_2Cl_7^- anions. Below 0.5 mole fraction the anodic potential is governed by the oxidation of Cl^- and is limited to about 1.0V. Our basic melt (0.4) exhibited an electrochemical window 1.4V with respect to a Al in 0.6 melt, at a scan rate of 50 mV/s agreeing well with that determined by Wilkes et al. [1]. The electrochemical windows are:

0.4 melt: 0.97 to -1.6 V
0.6 melt: 2.35 to -0.05 V

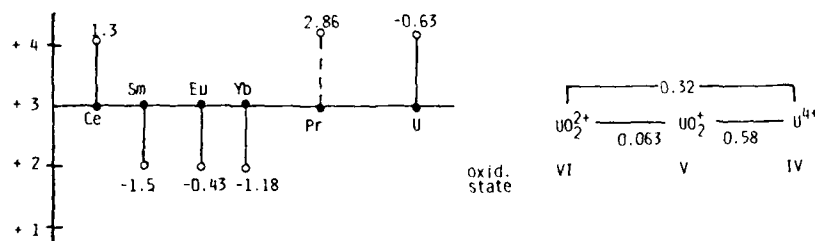
Other physical properties like the transport numbers [2], densities, phase transitions, conductivities, viscosities [4] have been measured. Comprehensive NMR studies [5] and theoretical molecular orbital calculations [6] have also been carried out.

2 Properties of Some Lanthanides and Actinides in Chloroaluminate Melt

Lanthanides and actinides are groups of very similar elements which exhibit a wide variation of oxidation states. The aqueous redox potentials of several of these ions are summarized below. In certain lanthanides these redox potentials show drastic change due to complexation and/or change in solvent polarity (cf. Ce(III)). Added advantages in working with the lanthanides and actinides are that UV/VIS and/or fluorescence spectra may be used for identification of the species present in melt solution.

2.1 Ce(III) Ion ($4f^1$):

The redox behavior of Ce(III)/Ce(IV) couple is strongly dependent on the nature of the counter ion present in aqueous solution. While the non-coordinating anion like perchlorate results in a E° value of 1.70V, the strongly coordinating carbonate anion is found to produce a drastic change in the redox potential value (0.05V) [7]. The following anion dependence E° values are observed: 1.70V (1M HClO_4), 1.61V (1M HNO_3), 1.44V (1M H_2SO_4), 1.28V (2M HCl) and 0.05V (5.5M K_2CO_3).



The redox behavior of Ce(III)/Ce(IV) couple in MEIC-AlCl₃ melt (0.4) has been extensively studied by us [8] using a glassy carbon electrode. The redox process is found to be quasi-reversible with a $E_{1/2}$ value of 0.79V against a reference electrode consisting of Al in 0.6 MEIC-AlCl₃ melt. Fig. 6 shows the variation of the cyclic voltammetric profile for Ce(III) in 0.4 melt with scan rate. The calculated rate constant (k^0) for this one electron transfer redox process is 1.20×10^{-3} cm/sec.

The species present in the melt was found to be the hexachloro complex of cerium from its charge transfer spectrum between 310 and 350 nm and the Ce-Cl stretching frequency at 280 cm^{-1} in the infrared region (Fig. 5) [9]. The final confirmation of the tervalency of cerium in 0.4 melt, before the electrochemical oxidation, came from the observation of ionic fluorescence at 370 nm for the cerium containing melt (Fig. 7). The Ce(IV) solutions do not exhibit this type of ionic fluorescence. Combining the electrochemical and spectroscopic data we find the electroactive species to be hexachloro-cerium(III) ion, $[\text{CeCl}_6]^{3-}$.

2.2 Tb(III) ($4f^8$) Ion:

It is tempting to assume that Tb(III) ion with one more electron than the half-filled configuration, $4f^7$, will easily lose an electron. Unfortunately, it has not been possible to oxidize Tb(III) to Tb(IV) in aqueous solution. The estimated E^0 value for Tb(III)/(IV) couple is above 2.8V, and Tb(IV), if present, in aqueous solution will tend to oxidize water.

Attempts to measure the Tb(III)/(IV) couple in 0.4 melt (MEIC-AlCl₃) has also been unsuccessful. However, we were able to observe the characteristic green ionic fluorescence from Tb(III) in 0.4 melt. Excitation of the Tb(III) solution at the ligand (MEIC) absorption band (348 nm) resulted in a very broad fluorescence band of the organic moiety with a maxima at 450 nm. No sharp fluorescence due to Tb was noticeable. A time-resolved fluorescence study (Fig. 8) revealed a rise time of $\sim 50 \mu\text{s}$ for the ionic fluorescence. The sharp fluorescence from 5D_4 level of Tb(III) to the ground 7F_J multiplets became evident.

We were interested in measuring the lifetime (τ) of the excited 5D_4 level by monitoring the time dependent decay of the green fluorescence at 450 nm due to the $^5D_4 \rightarrow ^7F_5$ transition of Tb(III). An average value of $\tau = 2.34 \text{ ms}$ was observed. A comparison of this data with that of the aquo ion and Tb(III) in other anhydrous solvents is presented below. The lifetime of the 5D_4 level in 0.4 melt is about five times that of the aquo ion and it is higher than that of TbCl₃ in AlCl₃ vapor phase complex. The τ -value is very close to that of the anhydrous laser liquid, POCl₃:SnCl₄. It is conceivable that 0.4 MEIC-AlCl₃ melt may compete favorably with anhydrous POCl₃:SnCl₄ solvent as a laser liquid. From a series of spectroscopic measurements and a charge transfer band of Tb(III) in 0.4 melt, it is concluded that the active species present in solution is probably $[\text{TbCl}_6]^{3-}$ ion.

Comparison of the Lifetime (msec) Data:

Levels	Aquo ion	TbCl ₃ -(AlCl ₃) _x	Tb:POCl ₃ :SnCl ₄	Tb-MEIC-AlCl ₃
5D_3	-	0.29(250°C)	0.29(25°C)	0.40(25°C)
5D_4	0.43(25°C)	1.52(250°C)	2.75(25°C)	2.34(25°C)

2.3 Sm(III) 4f⁵, Eu(III) 4f⁶, Yb(III) 4f¹³ Ions:

Trivalent Sm, Eu and Yb could be easily reduced in aqueous solution. We have recently measured the M(III)/(II) redox couple in aqueous solution (1M KCl). The $E_{p/2}$ values(V) obtained from the cyclic voltammograms are -0.5 (Eu), -1.6 (Sm) and -1.2 (Yb). These values are in agreement with those predicted by Nugent et al. [10]. Recently, Schoebrechts et al. [11] have conducted cyclic voltammetric studies on these ions, but using 1-butylpyridinium chloride (BPC) and $AlCl_3$ melt. Electrochemical and spectroscopic studies were carried out in acidic BPC- $AlCl_3$ melt (0.6). These authors reported the following $E_{p/2}$ values(V): +1.86 (Eu), +0.66 (Sm) and +1.23 (Yb). They proposed the presence of species like MCl_2^+ (Sm, Yb), $YbCl_2^+$, $YbCl^+$ beside the free M^{3+} and M^{2+} ions. It is, however, difficult to see how the acidic melts have contributed to the formation of the lower chloro-species, unless these species have resulted from the dissociation of the lanthanide trichlorides used in these studies. We are at present systematically studying these systems in MEIC- $AlCl_3$ melts and the results will be reported in the near future.

2.4 U(V) 5f¹ Ion:

Uranium present an interesting challenge to the electrochemists. The oxidation state may vary between 3 and 6. In aqueous solution "naked" U(V) and U(VI) are rare. We were interested in preparing a solution of U(IV) by dissolving UCl_4 in 0.4 MEIC- $AlCl_3$ melt. The resulting solution was green in color, showing the presence of U(IV) ion in solution. However, within a few hours the green solution bleached to a clear yellow color. Spectroscopic examination of this yellow liquid showed no absorption bands due to U(IV) nor did it exhibit the characteristic peaks of the UO_2^{2+} ion in the visible region. The spectrum profile (Fig. 9) [11], however, corresponded closely to the reported [12] U(V)-chloro complex, UCl_5^- , in nitromethane solution. The species responsible for causing oxidation of U(IV) to U(V) is believed to be the proton (H^+) generated from the minute amount of water present as water of crystallization in MEIC and acting as a strong oxidizing agent in almost-anhydrous chloroaluminate melt.

Cyclic voltammetric studies were performed on this unusual solution of UCl_5^- by scanning the glassy carbon electrode between 0.6 and -1.2V. In dilute solution a cathodic peak (U(V) \rightarrow (IV)) was observed around -0.7V but no anodic peak was found. It was apparent that reoxidation of the reduced U(IV) species is taking place before the anodic potential is reached. In a more concentrated solution (0.04 M) strong hysteresis (Fig. 10) was observed and the cathodic peak occurred at -0.55V. This system is being further investigated.

3 Modification of Chloroaluminate Melts:

Arising from the previous work that a proton (H^+) may coexist in chloroaluminate melts, the author has conducted preliminary experiments to increase the conductivity of these melts by treating the melts with dry HCl gas. Fig. 11 shows the measured specific conductivities of a 0.36 melt at 27°, -23° and -64° C. Treatment of this melt with dry HCl gas noticeably increased

(3-fold) the conductivity of the melt both at 27° and -23° C. The conductivity of the HCl-treated melt at -23° (melt remains fluid, although slightly more viscous) is comparable to that of the untreated melt at 27° C. The very low conductivity of the melt and the HCl-treated melt at -64° is due to the glassy transition of the melt at this temperature with significant increase in internal resistivity.

To gain further insight and have some idea of the nature of the species present in the HCl-treated melt, we have examined the HCl-treated melt by H-nuclear magnetic resonance (NMR) spectroscopy. The presence of a highly acidic proton at 0.6 ppm downfield from 2H of the imidazolium ring (2H is the most acidic proton in MEIC) is detected (Fig. 12). A semi-quantitative analysis of the intensities revealed the composition to be 1:1 MEIC:HCl. This composition did not seem to alter over a period of at least two weeks at room temperature. Further investigation on the composition, conductivities and electrochemical properties of the HCl-treated melt is under progress.

Acknowledgments

The work described here was performed under an Air Force Wright Aeronautics/Aeropropulsion Laboratory, Wright-Patterson Air Force Base, contract. The author wish to thank Dr. Fritts, Dr. Keil, Dr. Wilkes, Dr. Dymek and Dr. Knachel for stimulating discussions during the tenure of this work.

REFERENCES

1. (a) B. J. Piersma and J. S. Wilkes, Frank J. Seiler Res. Lab. Report, FJSRL-TR-82-0004, Sept. 1982. (b). J. S. Wilkes, J. A. Levisky, R. A. Wilson, and C. J. Hussey, *Inorg. Chem.*, **21**, 1263 (1982).
2. C. L. Hussey and H. A. Oye, *J. Electrochem. Soc.*, **131**, 1621 (1984).
3. D. F. McIntyre, R. T. Foley, and B. F. Brown, *Inorg. Chem.*, **21**, 1167 (1982).
4. A. A. Fannin, D. A. Floreani, L. A. King, J. S. Landers, B. J. Piersma, D. J. Stech, R. L. Vaughn, J. S. Wilkes, and J. L. Williams, *J. Phys. Chem.*, **88**, 2614 (1984).
5. A. A. Fannin, L. A. King, J. A. Levisky, and J. S. Wilkes, *J. Phys. Chem.*, **88**, 2609 (1984).
6. L. P. Davis, C. J. Dymek, J. J. P. Stewart, H. P. Clark, and W. J. Lauderdale, *J. Amer. Chem. Soc.*, **107**, 5041 (1985).
7. D. E. Hobart, K. Samhoun, J. P. Young, V. E. Norvell, G. Mamantov, and J. R. Paterson, *Inorg. Nucl. Chem. Letters*, **16**, 321 (1980).
8. S. P. Sinha and R. G. Keil, *Proc. Electrochem. Soc. (Extended Abstract No. 542)*, 769 (1985), Spring Meeting, Toronto, Canada, May 1985.
9. D. M. Adams and D. M. Morris, *J. Chem. Soc.(A)*, 694 (1968).
10. L. J. Nugent, R. D. Baybarz, J. L. Burnett, and J. L. Ryan, *J. Phys. Chem.*, **77**, 1528 (1973).
11. S. P. Sinha, *Lanthanide Actinide Res.*, **1**, 195 (1986).
12. J. L. Ryan, *J. Inorg. Nucl. Chem.*, **33**, 153 (1971).

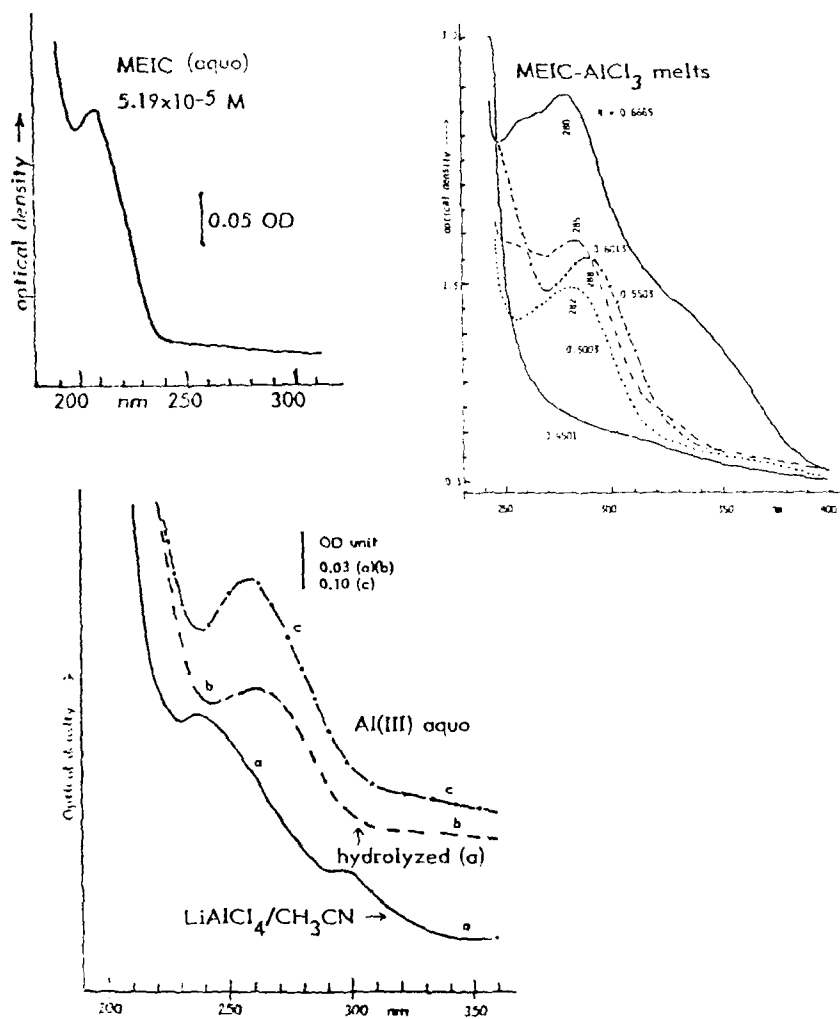


Fig. 1. Ultraviolet absorption spectrum of aqueous 1-methyl-3-ethylimidazolium chloride (1 cm pathlength).
 Fig. 2. Ultraviolet absorption profile of MEIC- AlCl_3 melts containing varied amount of AlCl_3 mole fractions(N) (3mm pathlength).
 Fig. 3. Ultraviolet absorption spectra of (a) satd. LiAlCl_4 in acetonitrile, (b) hydrolyzed solution of (a), and (c) Al(III) aquo ion of pH 0.9.

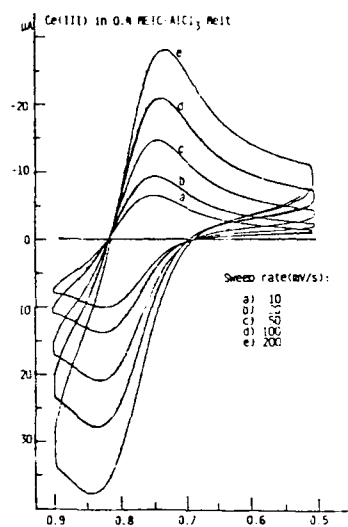
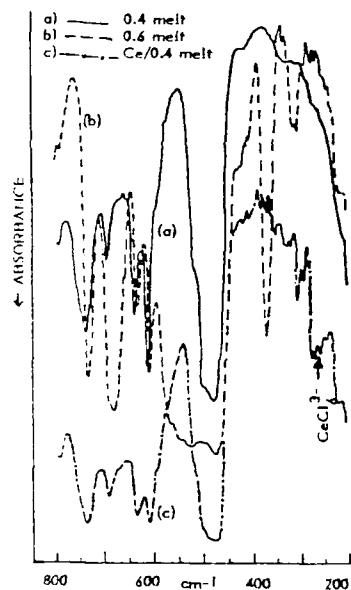
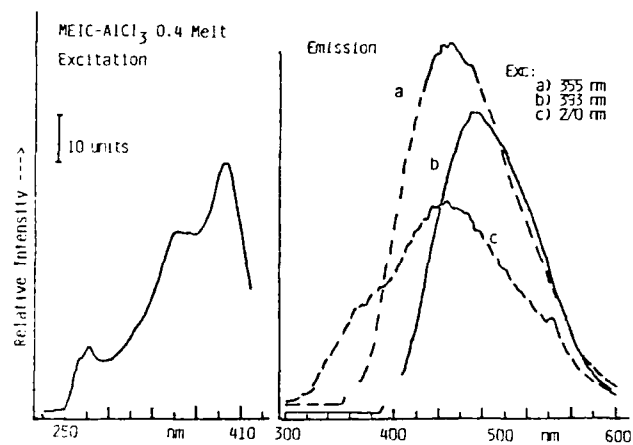


Fig. 4. Fluorescence/excitation spectrum of 0.4 (basic) MEIC-AlCl₃ melt.
Fig. 5. Far IR spectra of (a) 0.4, (b) 0.6 melts and (c) Ce(III) in 0.4 melt.
Fig. 6. Variation of cyclic voltammograms of Ce(III) solution (0.08 M) in 0.4 (basic) melt at a glassy carbon electrode at 25°.

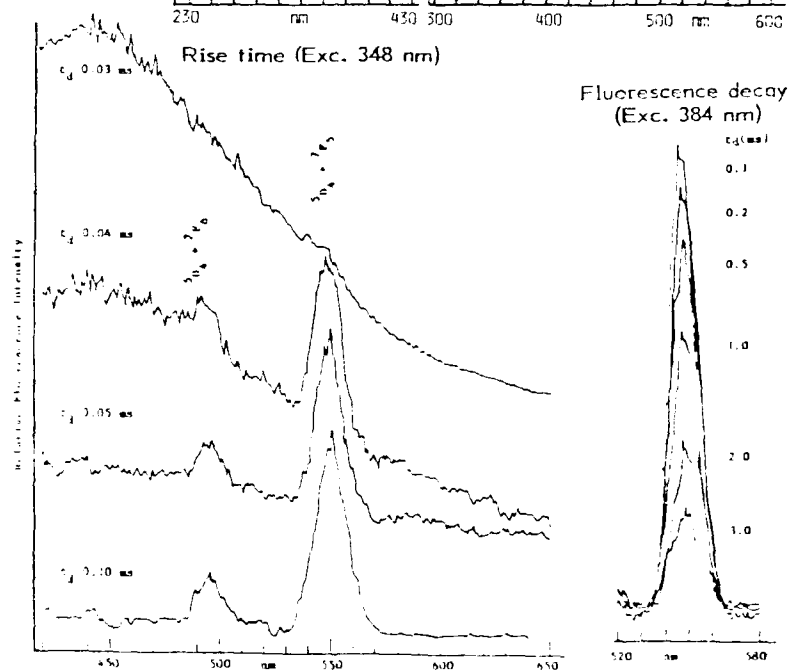
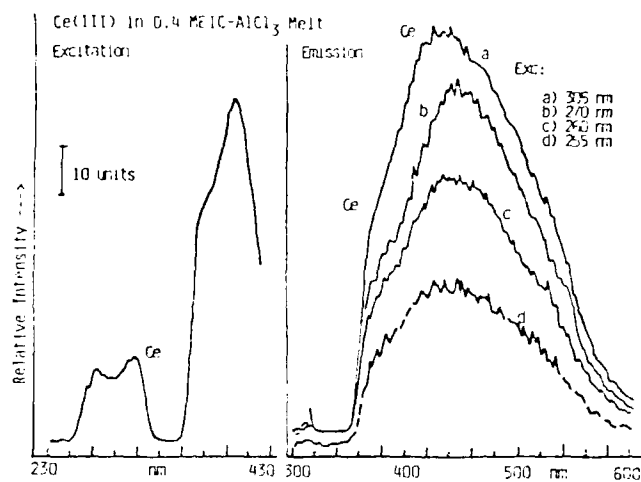


Fig. 7. Excitation and emission spectra of Ce(III) in 0.4 (basic) melt.
Fig. 8. Time resolved fluorescence spectra showing (a) rise time (exc. 348) and (b) fluorescence decay (exc. 384) of $^5D_4 \rightarrow ^7F_5$ band of Tb(III).

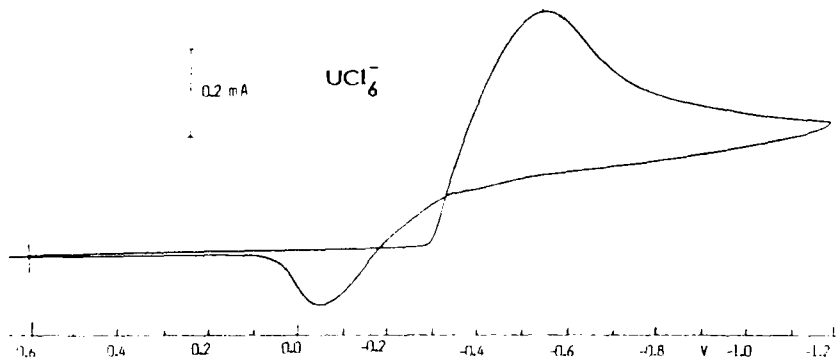
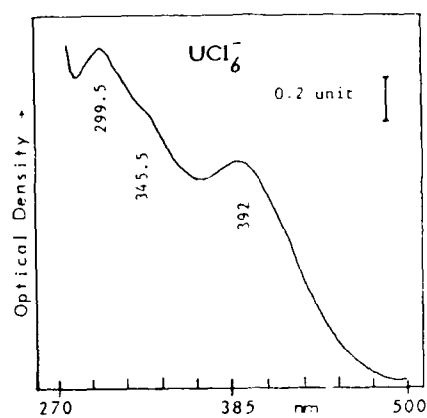


Fig. 9. Ultraviolet absorption spectrum of the yellow solution resulted after oxidation of a UCl_4 solution in 0.4 melt and exhibiting charge transfer bands of UCl_6^- species.

Fig. 10. Cyclic voltammogram of the yellow UCl_6^- solution in 0.4 MEIC- AlCl_3 melt (0.04 M) at glassy carbon electrode and showing strong hysteresis.

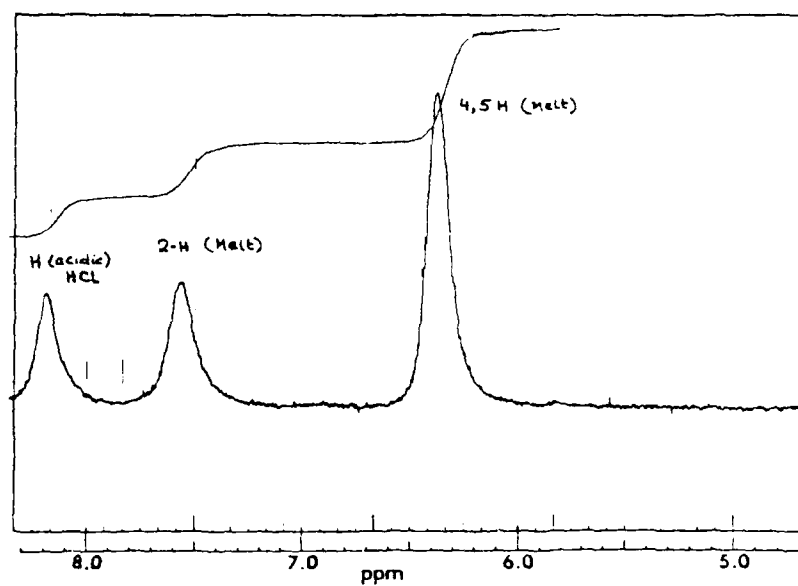
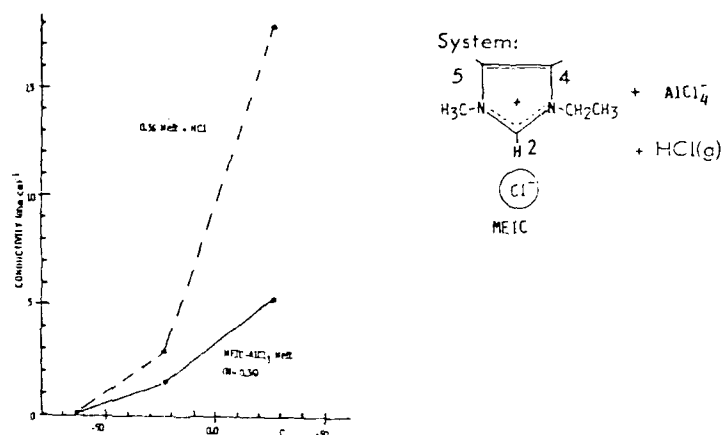


Fig. 11. Variation of electrical conductivity of a 0.36 MEIC-AlCl₃ melt and the same melt after treatment with HCl(g) as a function of temperature.

Fig. 12. H-NMR spectrum of the HCl-treated melt showing the presence of an acidic proton at ~0.6 ppm upfield of 2-proton in MEIC (melt).

POTENTIOMETRIC STUDIES OF SOME OXYANIONS
IN MOLTEN FLUORIDES

Kurt H. Stern
Chemistry Division
Naval Research Laboratory
Washington, D.C. 20375

ABSTRACT

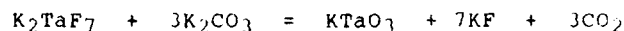
The dissociation of several oxyanions: WO_4^{2-} , SiO_3^{2-} , TaO_3^- , and TiO_3^- in molten FLINAK has been studied potentiometrically with a stabilized zirconia electrode. The interaction of these melts with O^{2-} has similarly been studied. All of these ions appear to be stable in FLINAK, but SiO_3^{2-} and TaO_3^- take up O^{2-} to form higher oxides, probably SiO_4^{4-} and TaO_4^{3-} , respectively. A method for determining the equilibrium constant of these reactions is presented.

The behavior of the Pt electrode in these melts is quite complex. Its potential varies with $\ln[\text{O}^{2-}]$, the slope being RT/F or larger.

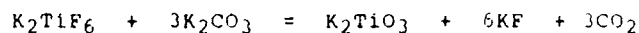
INTRODUCTION

The process whereby refractory metals can be electroplated from molten fluorides, invented by Senderoff and Mellors (1) in the 1960's, is well known. More recently we have tried to combine this process with carbonate reduction to electroplate refractory carbides. Tantalum carbide was electroplated by this procedure (2) from molten FLINAK at 750°C but the coatings tended to consist of mixtures of TaC , Ta_2C , and Ta . On the other hand, excellent adherent coatings of W_2C were obtained by the simultaneous reduction of WO_4^{2-} and CO_3^{2-} (3).

In the course of reinvestigating the tantalum carbide problem and attempting to extend the general procedure to the plating of other carbides, we noticed gas evolution from FLINAK melts containing either K_2TaF_7 or K_2CO_3 to which the other reagent had been added (4). Mass-spectrometric identification of the gas as CO_2 showed that the reaction was of the acid-base type:



The carbide can then be plated only if this reaction does not go to completion, or if TaO_3^- can be reduced. Since similar results were obtained with K_2SiF_6 and K_2TiF_6 , viz:



we have begun an electrochemical study of oxyanion reduction in molten FLINAK to see if TaO_3^- , SiO_3^{2-} can be reduced as WO_4^{2-} can be.

As a preliminary step we have investigated possible oxide equilibria involving these ions, using a stabilized zirconia (SZ) electrode as a specific O^{2-} electrode. In addition, we have studied the behavior of the platinum electrode in these melts, since it would be useful as a quasi-reference electrode if its potential were independent of melt composition.

EXPERIMENTAL PART

All experiments were carried out in a glovebox with recirculating helium atmosphere in which O_2 and H_2O were generally below 1 ppm. A Teledyne (Model 311) trace

oxygen analyzer was used to measure the oxygen pressure in the glove box. All melts were contained in nickel 200 crucibles, a 99% nickel alloy.

Reagents. The alkali metal fluorides were vacuum-dried individually at 500°. The FLINAK mixture was then melted under vacuum before use. Reagent grade Na₂O (Alfa), K₂SiO₃ (Atomergic), K₂SiO₃ (Puratronic), and KTaO₃ (Puratronic), were used without purification. Na₂WO₄ was prepared by dehydration of the dihydrate (Fisher Scientific).

Electrodes. A Ni₁Ni(II) reference electrode consisting of NiF₂(sat) in FLINAK, contained in a boron nitride envelope, as described by Jenkins, Mamantov, and Manning (5) was used. By increasing the BN wall thickness slightly over that used by these authors, the electrodes could be used for several runs, and they were easily replaced. An intercomparison of several showed that they differed by < 10mV from each other and from a more elaborate reference electrode which utilizes a LaF₃ crystal to make contact with the melt (6).

A Corning 1372 8% yttria-stabilized zirconia tube was loaded with a Ni-NiO mixture. A nickel wire was pushed into this mixture which was covered with powdered soft glass which, on softening, covered the Ni-NiO mixture to exclude air.

A coiled platinum wire served as secondary indicator.

All electrodes were suspended in the melt through holes in a lava block over the top of the crucible.

RESULTS

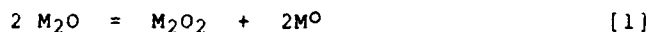
Oxide Melts

Before proceeding with the various oxyanion studies, the behavior of SZ and Pt electrodes in FLINAK melts, to which Na_2O had been added, was studied. The SZ electrode is now well established as an O^{2-} ion specific electrode in various molten salts (7). In molten FLINAK, as in the other salts, the potential-determining electrode reaction is $1/2\text{O}_2 + 2e = \text{O}^{2-}$ (8). Thus, at constant p_{O_2} , the slope of an E vs $\ln a_{\text{O}^{2-}}$ -plot has a slope of $RT/2F$. In the present study p_{O_2} is fixed by the equilibrium $\text{Ni} + 1/2 \text{O}_2 = \text{NiO}$. In dilute solutions activity coefficients are constant and the dependence of E on concentration (mole fraction in this paper) should be $RT/2F$ also.

A complicating factor is the possible transformation of the added oxide (O^{2-}) to other oxide species such as O_2^{2-} (peroxide) and O_2^- (superoxide). In NaCl (9) and Na_2SO_4 (10) reactions such as $\text{O}^{2-} + 1/2 \text{O}_2 = \text{O}_2^{2-}$ are known to occur at temperatures used in this study, although O_2^- is almost certainly negligible. At the extremely low O_2 pressures in this work, the equilibrium constants are such that very little ($< 1\%$ O^{2-}) is transformed to O_2^{2-} .

Pt is "inert" in molten fluorides and therefore constitutes an attractive and easy-to-use quasi-reference electrode. However, the potential-determining reaction(s) on the Pt surface are not known. In a previous study (8) of CO_3^{2-} in FLINAK using a Pt reference, we noticed that the cathodic limit of the melt became less negative with added K_2CO_3 concentration (at 500°C) and surmised that

this was due to increased O^{2-} resulting from the thermal dissociation of CO_3^{2-} . A plot of the cathodic limit vs $\ln [CO_3^{2-}]$ is linear with a slope of RT/F . A plot of E vs $\log X_{O^{2-}}$ at 500° is also linear with a slope of $2.3RT/F$ at lower concentrations ($< 10^{-3}$) but with a tendency toward increasing slope at higher concentrations (Fig. 1). A repetition of this experiment at 750° using both SZ (Fig. 2) and Pt indicator (Fig. 3) electrodes vs. a Ni/NiF₂ reference, showed an $RT/2F$ dependence for the former and $\sim RT/F$ dependence for the latter at lower concentrations, and larger slopes at higher concentrations. At the conclusion of this experiment it was noted that bright orange vapor emanated from all the electrodes when they were lifted out of the melt and that all relatively cool surfaces, e.g. the lava block, reacted with water to produce copious amounts of gas, and the resulting solution was highly alkaline. All of these observations are consistent with the formation of alkali metal. In this experiment O_2 was virtually absent ($p_{O_2} < 1$ ppm) and therefore it is likely that added oxide undergoes an auto-oxidation-reduction:

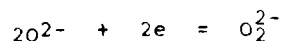


When $M = Na$ the equilibrium constant of this reaction (11) is:

$$K = 1.34 = \frac{a_{Na_2O_2}}{a_{Na_2O}^2} P_{Na}^2 \quad [2]$$

Results are similar for Li and K. Unfortunately we do not have an independent measurement of O_2^{2-} and so P_{M^0} cannot be calculated, but the rather large value of K suggests that reaction [1] is not insignificant. We conclude that

at 750° the SZ electrode is reversible to O^{2-} at least at lower concentrations. However, the behavior of the Pt electrode is more complex. The RT/F slope at lower concentration requires a one-electrode process. In terms of reaction [1] the equilibrium



requires two electrons unless the peroxide ion functions as O^- . Whatever the potential-determining equilibrium on Pt is, the shape of the E vs $\ln X_{O^{2-}}$ plot clearly increases with concentration above 0.1 mol% at very low oxygen pressures to values which have no clear meaning in terms of simple reversible oxidation-reduction reactions. This behavior also occurs when Na_2O is added to a FLINAK melt already containing various oxyanion species (see below). Similar conclusions about the complexity of the Pt electrode behavior were also expressed by Brookes and Inman (7c). It is thus clear that Pt can not be used as a reference in molten salts unless it can be shown that it remains constant with respect to a thermodynamically reversible reference in a particular system.

Oxyanion Melts

Before discussing the individual oxyanion systems, the rationale underlying this study is outlined. From the preceding section it is clear the emf of the cell



becomes more negative (i.e. the SZ indicator electrode becomes more negative) with increasing O^{2-} . This is also true if Pt is used as indicator, although the functional dependence of E on $\log X_{O^{2-}}$ then becomes more complex.

We can then distinguish the following possibilities, keeping in mind that the O^{2-} concentration in a "clean" melt is $\sim 10^{-2}$ mol%.

A. Addition of oxyanion to "clean" melt

$$\Delta E = 0$$

Implies

a. material is insoluble

or

b. material does not react with O^{2-} .

$$\Delta E < 0$$

anion dissociates to yield O^{2-}

$$\Delta E > 0$$

anion reacts with impurity O^{2-}

B. Addition of O^{2-} to melt containing oxyanion - SZ electrode

$$\Delta E < 0, \text{ slope} = RT/2F$$

no reaction of O^{2-} with oxyanion

$$\Delta E < 0, \text{ slope} < RT/2F$$

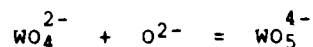
O^{2-} reacts with oxyanion

Results with the individual systems are now described.

(1) Na_2WO_4

This compound is known to be quite soluble in FLINAK (3). Higher tungstates, such as Na_4WO_5 ($\text{Na}_2\text{WO}_4/\text{Na}_2\text{O} = 1$), are also well known in the solid state, but have not been studied in molten salts.

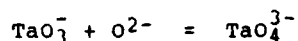
Figure 4 shows the effect of adding Na_2WO_4 and Na_2O on the emf of cell A. The emf becomes only slightly less negative on adding Na_2WO_4 , while the subsequent addition of Na_2O yields a slope of $RT/2F$. Both of these results indicate that the equilibrium



lies far to the left, i.e. WO_4^{2-} is quite stable in FLINAK. When a Pt electrode is substituted for the SZ indicator electrode, the results on addition of Na_2O results in a slope several times RT/F .

(2) KTaO_3

The addition of KTaO_3 to FLINAK changes the emf of cell A in the direction indicating lower oxide, with a slope $< RT/2F$ (Fig. 5). This is consistent with the formation of TaO_4^{3-} :

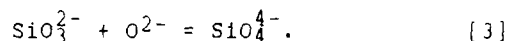


but at a rate indicating only partial conversion. Above 0.075 mol% TaO_3 the emf becomes independent of added tantalate. The most likely explanation is that this represents the solubility. When oxide is added to the

melt containing both dissolved and undissolved tantalate, the slope is less than $RT/2F$, indicating some uptake of O^{2-} by the tantalate in suspension and/or solution.

(3) K_2SiO_3

Visual observation showed that K_2SiO_3 is quite soluble in FLINAK. Figure 6 shows that the emf of cell A becomes more positive with the addition of this compound, with both SZ and Pt indicator electrodes, consistent with a decrease of O^{2-} with addition of SiO_3^{2-} . Below 0.1 mol% this decrease occurs with a slope of $< RT/2F$, indicating a partial conversion of SiO_3^{2-} to SiO_4^{4-} , but above 0.1 mol% the slope is $1.8 RT/F$ which indicates that more than one mole O^{2-} is removed for every mole SiO_3^{2-} . However, no silicate fitting such a requirement is known, at least in the solid state. Thus the most likely reaction is:



Interestingly, both SZ and Pt electrodes show similar dependence in this part of the experiment. When Na_2O is added to the silicate-containing melt, however, the slopes are quite different: $RT/2F$ for the SZ electrode, $1.77RT/F$ for Pt. Even the first result is unexpected, unless whatever silicate is in the melt prior to oxide addition is the highest oxide-containing silicate.

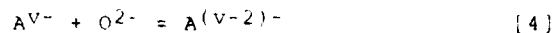
(4) KTiO_3

The results for this compound resemble those for Na_2WO_4 , i.e. addition of KTiO_3 produces no change in emf. However, whereas Na_2WO_4 is so soluble that it can easily be observed to dissolve, KTiO_3 seems, by visual examination, to be insoluble. The subsequent addition of oxide produces a slope somewhat larger than $RT/2F$.

DISCUSSION

The results presented in this paper constitute an exploration of how potentiometric measurements might be used to determine oxide equilibria involving various oxyanions in molten salts. Oxide-ion-specific stabilized zirconia electrodes have been used to solve a wide variety of problems of which those described in references 7-9 constitute only a portion.

For example, the equilibrium constant for a reaction of the type



where AV^- represents an oxyanion and $\text{A}^{(\text{V}-2)-}$ represents an oxyanion with one more O^{2-} , can be determined by the titration of AV^- in the melt with O^{2-} . If O^{2-} does not react with AV^- then

$$E_{\text{th}} = E^0 - RT/2F \ln [\text{O}^{2-}]_{\text{a}} \quad [5]$$

where $[\text{O}^{2-}]_{\text{a}}$ represents added O^{2-} .

In general

$$E = E^0 - n \frac{RT}{2F} \ln [O^{2-}] \quad [6]$$

where n measures the fraction of the expected $RT/2F$ slope.

Subtracting [5] from [6] yields

$$\exp \frac{E - E_{th}}{(RT/2F)} = \frac{[O^{2-}]_a}{[O^{2-}]^n} \quad [7]$$

Since all quantities except $[O^{2-}]$ are known, the latter can be calculated. The equilibrium constant for reaction [3] can be written as:

$$K = \frac{[A^{V-}] [O^{2-}]}{[A^{(V-2)-}]} \quad [8]$$

$$\text{Also } [A^{V-2-}] + [A^{V-}] = [A^{V-}]_a$$

where $[A^{V-}]_a$ represents the originally added concentration.

Also

$$[A^{(V-2)-}] = [O^{2-}]_a - [O^{2-}] \quad [9]$$

$$[A^{V-}] = [A^{V-}]_a - ([O^{2-}]_a - [O^{2-}]) \quad [10]$$

Substituting [9] and [10] into [8] yields

$$K = \frac{[A^{V-}]_a - ([O^{2-}]_a - [O^{2-}])}{[O^{2-}]_a - [O^{2-}]} [O^{2-}]$$

From each emf a value of K can be determined, and therefore the method lends itself to a statistical treatment.

The data obtained in this work are only semi-quantitative and therefore do not justify such elaborate treatment.

SUMMARY

1. The measurement of oxide activity on successive addition of oxyanions and oxide can be used to gain information on the dissociation of the oxyanion and/or its reaction with oxide.
2. WO_4^{2-} is a stable ion in FLINAK. It does not dissociate nor does it take up O^{2-} to form tungstates such as WO_5^{4-} .
3. K_2SiO_3 is quite soluble in FLINAK. SiO_3^{2-} appears to react with O^{2-} to form SiO_4^{4-} .
4. The solubility of KTaO_3 in FLINAK is ~ 0.075 mol%. TaO_3^- appears to react with O^{2-} to form TaO_4^{3-} .
5. The solubility of KTiO_3 is too low to measure.
6. The potential of the Pt electrode in FLINAK varies as RT/F with $\ln[\text{O}^2]$ up to 0.1 mol% and 2-3 times RT/F above that concentration.

REFERENCES

1. S. Senderoff and G.W. Mellors, *Science* 153, 1475 (1966), *J. Electrochem. Soc.*, 112, 266, 841 (1965); 113, 60, 66 (1966).
2. K.H. Stern and S.T. Gadomski, *J. Electrochem. Soc.*, 130, 301 (1983).
3. K.H. Stern and M.L. Deanhardt, *J. Electrochem. Soc.*, 132, 1892 (1985).
4. K.H. Stern, unpublished results.
5. H.W. Jenkins, G. Mamantov, and D.L. Manning, *J. Electroanal. Chem.*, 19, 385 (1968).
6. H.R. Bronstein and D.L. Manning, *J. Electrochem. Soc.*, 119, 125 (1972).
7. (a) R. Combes, J. Vedel, and B. Tremillon, *Electrochim. Acta* 20, 191 (1975); (b) K.H. Stern, *Electrochim. Acta*, 127, 2375 (1975); (c) H.C. Brookes and D. Inman, *Proc. Fifth International Symp. on Molten Salts*, The Electrochemical Society, Vol. 86-1, 128 (1986).
8. M.L. Deanhardt, K. H. Stern, and A. Kende, *J. Electrochem. Soc.*, 133, 1149 (1986).
9. K.H. Stern, Rm. Panayappan, and D.R. Flinn, *J. Electrochem. Soc.*, 124, 642 (1977).
10. K.H. Stern, M.L. Deanhardt, and R. Panayappan, *J. Phys. Chem.*, 83, 2848 (1979).
11. JANAF Thermochemical Tables, D.R. Stull and H. Prophet, 2nd Ed. NSRDS-NBS 37, (1971).

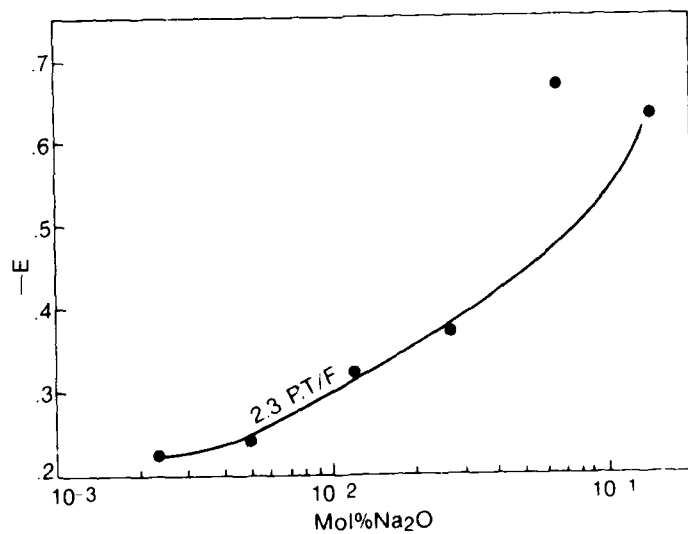


Figure 1 Emf of cell A with Pt indicator electrode
500°C. Na₂O solute

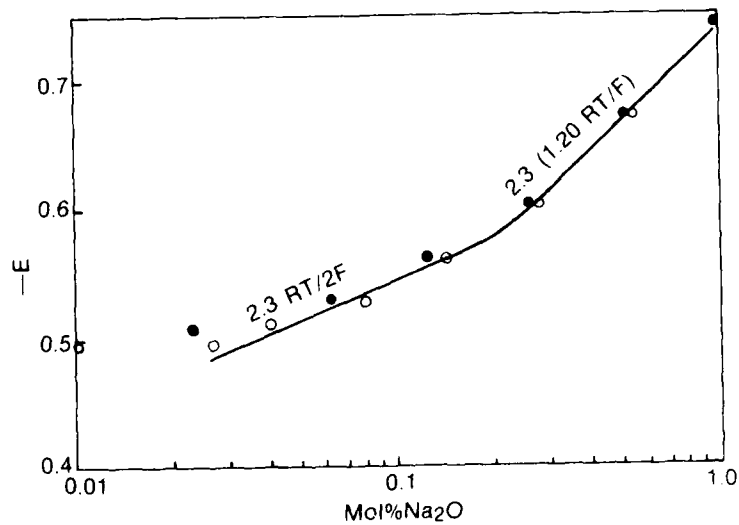


Figure 2 Emf of cell A with SZ indicator electrode 750°C ● Based
on weighed Na₂O ○ Corrected for Na₂O impurity

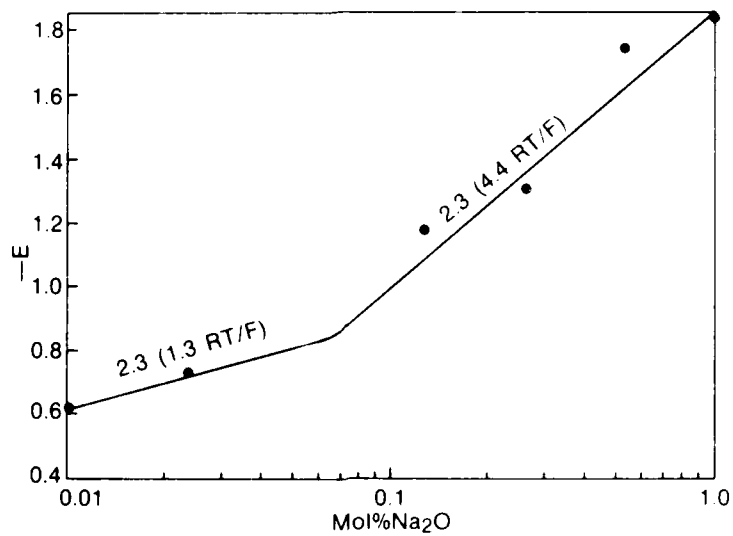


Figure 3 Emf of cell A with Pt indicator electrode
750°C. Na_2O solute

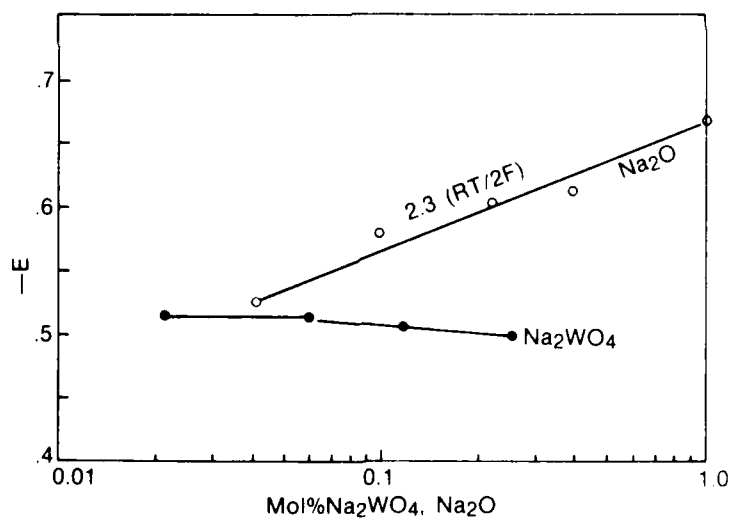


Figure 4 Emf of cell A with SZ indicator electrode
750°C. • Na_2WO_4 , o Na_2O

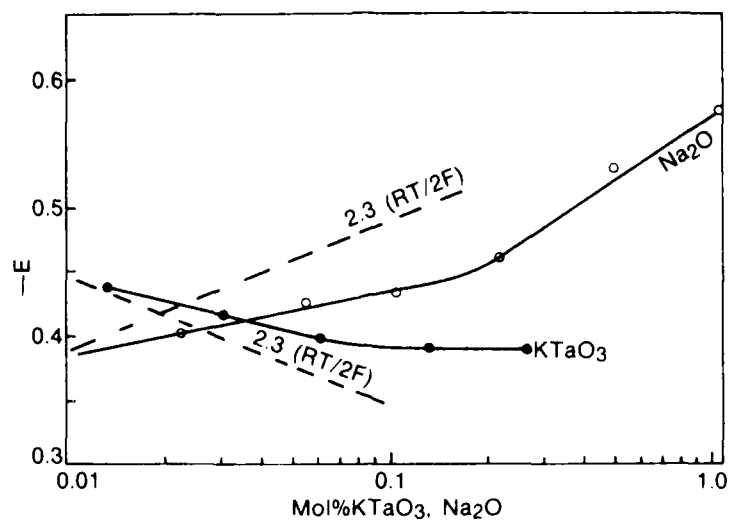


Figure 5 Emf of cell A 750°C. SZ indicator electrode.
 • KTaO₃. o Na₂O

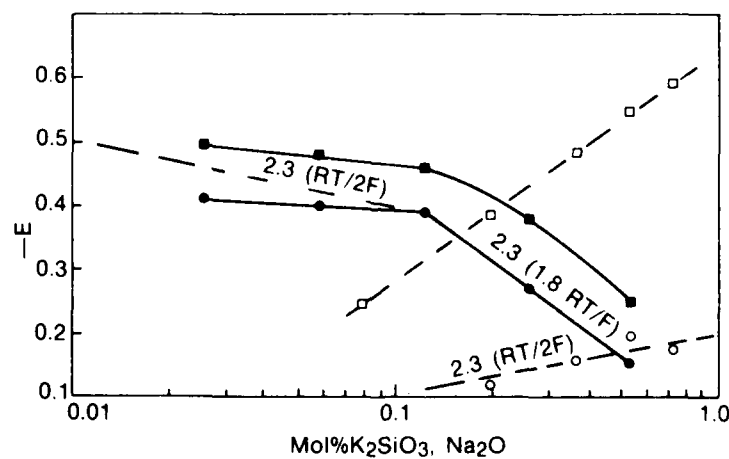


Figure 6 Emf of cell A 750°C. SZ indicator electrode • K₂SiO₃. o Na₂O.
 Pt indicator electrode. ■ K₂SiO₃. □ Na₂O

REDOX POTENTIAL OF Pb^{2+}/Pb^0 IN BORATE AND SILICATE MELTS

Miyuki Shimizu, Katsuyuki Kawamura, and Toshio Yokokawa

Department of Chemistry, Faculty of Science
Hokkaido University, Sapporo 060, Japan

ABSTRACT

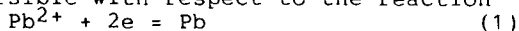
Among redox pairs in borate and silicate melts, Pb^{2+}/Pb^0 is important; the reduced species are metallic and reactive with the Pt in the solid in linear sweep voltammetry. Since Pb metal is soluble in solid Pt, and any excess deposit of Pb over the solid solubility limit yields a liquid alloy on the electrode, the current-potential curve bends at that point. A computer simulation of the process confirmed this interpretation. The application of this technique seems quite valuable to compare the basicity of various melts. The effect of alumina on the basicity of sodium silicate melts is discussed.

INTRODUCTION

Linear sweep voltammetry has been applied to oxide melts for redox equilibrium measurements (1-4). The usefulness of this technique in spite of difficulties due to high operating temperature lies evidently in this direct measurement compared with chemical analyses of reduced and oxidized species in quenched melts. Thus, Ce^{4+}/Ce^{3+} and Fe^{3+}/Fe^{2+} equilibria in sodium borate melts were measured as functions of solvent basicity and temperature (3,4). In the course we met with the problem when the couple Pb^{2+}/Pb^0 was to be measured. The current-potential curve showed an abrupt bending and a large anodic peak which was characteristic of a system of the reduced species adsorbing on the electrode. In this report, the electrode process is discussed and the application to sodium aluminosilicate melts is described.

EXPERIMENTAL

Linear sweep voltammetry. The working electrode is a platinum wire of 0.4 mm diameter whose end has been coiled in order to provide a large surface area. This electrode is assumed to be reversible with respect to the reaction



The current due to the unavoidable reaction



in the anis-electrode-oxide melt coexisting phases was calculated and described. The reference electrode is a sealed platinum wire of 0.4 mm diameter and was positioned to just contact the melt surface. It is reversible with respect to the reaction (2). The platinum crucible functions as the counter electrode. The measurement was carried out in pure oxygen.

Sample melts. The sample melts were prepared in the following procedure. Sodium, lead and aluminum nitrates of needed compositions were dissolved in nitric acid, and ethyl silicate with ethanol is added. The latter was hydrolyzed by adding ammonium hydroxide solution. The resultant gel mixture was dried and heated to powder anhydrous. It was finally melted in a platinum crucible, then the cell assembly was immersed. The content of lead oxide was fixed to one mole % in finally established runs.

Experimental results. Examples of the current-potential curves are shown in Fig. 1. It is noted that the curves are quite different from those in ordinary redox couples. Thus, the cathodic current rises abruptly after being low in the anodic curve shows a large peak characteristic of desorption of reduced species on the electrode.

Computer simulation of i.e.v. process. The mode of the calculation will be described as follows.

(1) Before the bending point is reached, Pt-Pb solid solution is formed on the electrode. The current is very low because of the low diffusivity and the low concentration of Pb in the solid solution.

(2) When the concentration of Pb reaches the solubility limit, a liquid metal phase starts to appear. The current increases because the diffusivity of Pb is quite high and Pb dissolves in the liquid keeping the activity of Pb constant at the solid-liquid boundary, and the current is determined by the diffusivity of Pb^{2+} in the oxide melt.

(3) In the reverse sweep, a large cathodic peak appears because the reduced species is concentrated near the electrode surface and because of the large diffusivity of Pb in the liquid alloy.

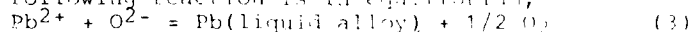
(4) The current suddenly approaches zero when the liquid metal disappears.

(5) The electrode reaction is reversible and Nernst equation gives the activity ratio at the electrode surface.

The computer simulation was carried out to solve the difference equation in place of the differential equation of Fick's 2nd law. The system is divided into sufficiently small parts ($1 \cdot 10^{-5}$ cm in the melt and $2 \cdot 10^{-7}$ cm in the electrode) in the direction perpendicular to the electrode

surface. The concentration of each part is calculated at each time increment of 1×10^{-5} sec. An example of the simulated current-potential curve is shown in the left part of Fig. 2. The agreement is satisfactory. Instead of the simplified Laplace transform method, where the concentration at the electrode surface is given, the concentration profile near the surface is visualized. The right side of Fig. 2 shows the concentration profiles at the times denoted on the voltammogram. Here the vertical axis is the concentration of Pb^{2+} or of Pb in a conventional scale. The far right side of the figure shows those of the liquid alloy phase, whose height is much lowered for drawing convenience.

Fig. 2 shows that at the bending point the Pb^{2+} concentration is not much lower than the original level (the straight line) and the Pb content in the liquid alloy is approximated by that in solid-liquid equilibrium of Pt-Pb system at the experimental temperature. The activity of lead in this system has been measured by Schwerdtfeger (5). Therefore, at the potential of the bending point, E_{dep} , the following reaction is in equilibrium,



$-2E_{dep}F = \Delta G^0(3) + RT \ln(a_{Pb}PO_2^{1/2}/a_{Pb^{2+}}a_{O^{2-}})$ (4)
where $\Delta G^0(3)$ is the standard free energy change of reaction (3). One must note that the standard state of the left hand side is not pure PbO , since O^{2-} here is the component of the solvent.

If the activity of Pb^{2+} is a function of only the basicity of the solvent irrespective of the solvent component and if the basicity is properly expressed by the activity of Na_2O , E_{dep} will be a function of the latter. Fig. 3 shows an example of the potential in silicate and aluminosilicate melts, where alumina content ranged 5 to 15 mole %. The activity of Na_2O in these melts has been measured previously (6,7). Fig. 3 shows the above prediction is fulfilled. The experimental results including those of other redox pairs will be discussed in more detail.

REFERENCE

1. K. Takahashi & Y. Miura, J. Non-Cryst. Solid **38&39** 527 (1980)
2. K. W. Semkow, R. A. Rizzo, L. A. Haskin & D. J. Lindstrom, Geochim. Cosmochim. Acta **46** 1879 (1982)
3. A. Sasahira and T. Yokokawa, Electrochim. Acta **29** 533 (1984)
4. A. Sasahira and T. Yokokawa, Electrochim. Acta **30** 441 (1985)
5. Schwerdtfeger, Trans. AIME **236** 23 (1966)
6. T. Yokokawa and S. Kosaka, J. Chem. Eng. Data, **24** 167 (1979)
7. H. Itoh and T. Yokokawa, Trans. JIM **25** 879 (1984)

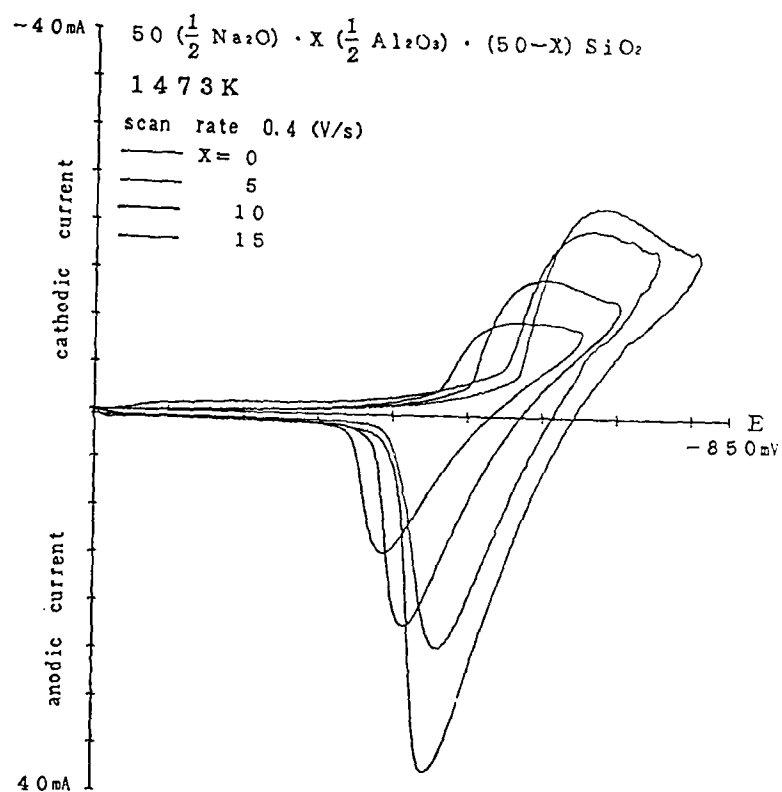


Figure 1. Linear sweep voltammogram in sodium aluminosilicate melts.

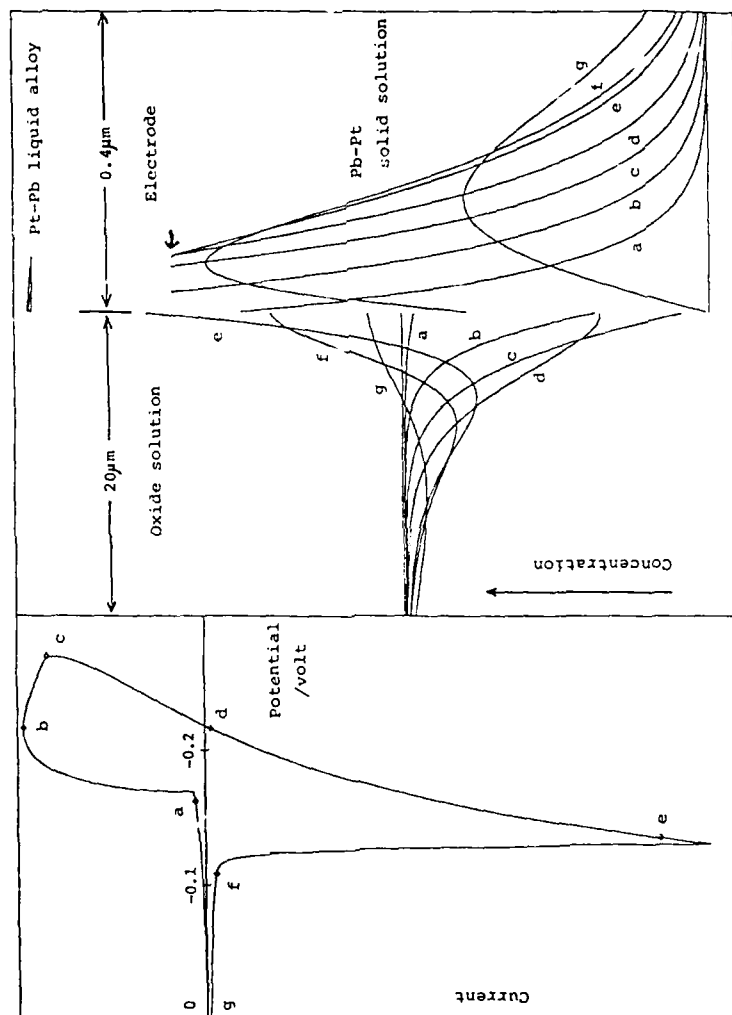


Figure 2. Computer simulation of voltammogram and concentration profile

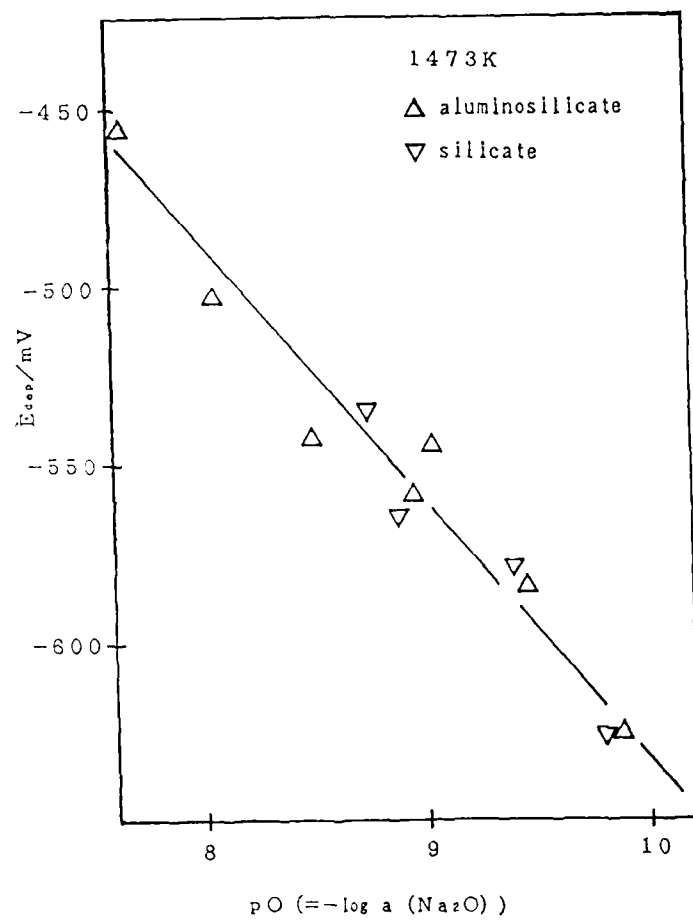


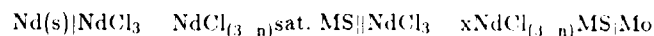
Figure 3. Potential at the bending point in sodium silicate and aluminosilicate melts as function of their basicity.

AN INVESTIGATION OF THE DISSOLUTION OF NEODYMIUM IN MOLTEN NEODYMIUM TRICHLORIDE

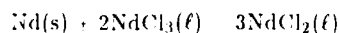
Q. T. Lu, S. X. Li, R. L. Yu, S. G. Chen
Department of Metallurgical Engineering
Shanghai University of Technology, Shanghai, China

ABSTRACT

In the temperature range 780-950° C, the relationship between temperature and EMF is reported for the concentration cell:



where MS refers to a molten salt. Also given are (1) the solubility of Nd in molten NdCl_3 , (2) the temperature dependence of the solubility of Nd, and (3) the equilibrium constant K , as well as ΔG° of the reaction:

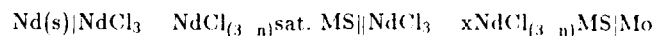


INTRODUCTION

In recent years, the methods for producing Nd and its alloys have received special attention because neodymium is the material for making a new permanent magnet Nd-Fe-B (1). The molten salt electrolysis of chloride, or oxide, is one of the main methods for producing rare earth (RE) metals. However, the current efficiency of electrolysis is usually as low as 20-50% due to the high solubilities of RE metals in their own halides. The interaction between La or Ce, with its own chloride, has been studied (2-4); however, the dissolution of Nd in its molten chloride has seldom been investigated. The aim of the present paper is to investigate the reaction of Nd with NdCl_3 by an electrochemical method.

EXPERIMENTAL

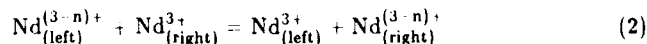
In order to investigate the mechanism of the dissolution of metals, the following cell has been designed



where a molybdenum rod is used as conductor and stirrer for the molten salt (MS). A schematic of the cell is given in Fig. 1. The half-cell consists of a Nd electrode and neodymium trichloride molten salt saturated with Nd; it is an equilibrium system of Nd metal with NdCl_3 - NdCl_2 melt. The right half-cell is composed of a Mo electrode and NdCl_3 molten salt in which the dissolved amount of Nd changes from zero to saturation and the Mo rod is used as the indicating electrode for measuring the redox potential $\Phi_{\text{Nd}^{3+}/\text{Nd}^{2+}}$, where

$$\Phi_{\text{Nd}^{3+}/\text{Nd}^{2+}} = \Phi_{\text{Nd}^{3+}/\text{Nd}^{2+}}^0 + \frac{RT}{nF} \ln \frac{[\text{Nd}^{3+}]}{[\text{Nd}^{2+}]} \quad (1)$$

From the value of n , the dissolution mechanism of Nd (2-3) may be determined. In agreement with the reaction of the concentration cell:



and equation (1), the EMF equation of the concentration cell can be expressed as:

$$E = \frac{RT}{nF} \ln \frac{a_{\text{Nd}^{3+}}}{a_{\text{Nd}^{2+}}} + \frac{RT}{nF} \ln \frac{a_{\text{Nd}^{3+}}}{a_{\text{Nd}^{2+}}}$$

By knowing the values of R , F , n and substituting the concentration of Nd for activity, we obtain:

$$E = 1.984 \times 10^{-4} T \log \frac{[\text{Nd}^{3+}]_{\text{eq}}}{[\text{Nd}^{2+}]_{\text{eq}}} + 1.984 \times 10^{-4} T \log \frac{[\text{Nd}^{3+}]_{\text{right}}}{[\text{Nd}^{2+}]_{\text{right}}} \quad (3)$$

When the dissolved amount of Nd in the right half-cell increases from zero to saturation, measuring $E = f(T)$ will yield by regression analysis a series of equations:

$$E = a + bT \quad (4)$$

for various amounts of dissolved Nd. From equations (3) and (4), the following equation:

$$\log \frac{[\text{Nd}^{3+}]_{\text{eq}}}{[\text{Nd}^{2+}]_{\text{eq}}} = \log \frac{[\text{Nd}^{3+}]_{\text{right}}}{[\text{Nd}^{2+}]_{\text{right}}} + \frac{10^4 b}{1.984} - \frac{10^4 a}{1.984 T} \quad (5)$$

can be obtained. The value for $f(T) \sim \log \frac{[\text{Nd}^{3+}]_{\text{eq}}}{[\text{Nd}^{2+}]_{\text{eq}}}$ was determined using the coefficients a and b defined in equation (4). From equation (5), the solubility of Nd in NdCl_3 can be calculated using various temperatures.

RESULTS AND DISCUSSION

In the temperature range 780-950°C, the temperature dependence of the EMF's was determined for different neodymium compositions, i.e., with neodymium additions, by mole percent (m%) of Nd, of 2.98, 7.13, 12.4, 16.7, 21.3, 28.4, 31.2, and 33 m%. The $E = f(T)$ relationships are shown in Fig. 2. It is obvious that the experimental points of the same Nd addition all fall on a straight line. By mathematical treatment, we have derived the following relations:

1. $\text{NdCl}_{2.91}(2.98 \text{ m\% Nd}) \quad E_1 = -0.123 + 9.03 \times 10^{-4}T$
2. $\text{NdCl}_{2.79}(7.13 \text{ m\% Nd}) \quad E_2 = -0.119 + 8.02 \times 10^{-4}T$
3. $\text{NdCl}_{2.63}(12.4 \text{ m\% Nd}) \quad E_3 = -0.116 + 7.03 \times 10^{-4}T$
4. $\text{NdCl}_{2.50}(16.7 \text{ m\% Nd}) \quad E_4 = -0.627 + 9.60 \times 10^{-4}T$
5. $\text{NdCl}_{2.36}(21.3 \text{ m\% Nd}) \quad E_5 = -0.123 + 3.32 \times 10^{-4}T$
6. $\text{NdCl}_{2.15}(28.4 \text{ m\% Nd}) \quad E_6 = -0.149 + 3.50 \times 10^{-4}T$
7. $\text{NdCl}_{2.06}(31.2 \text{ m\% Nd}) \quad E_7 = -0.123 + 3.13 \times 10^{-4}T$
8. $\text{NdCl}_{2.03}(33 \text{ m\% Nd}) \quad E_8 = -0.211 + 3.00 \times 10^{-4}T$

The isotherms at temperatures of 800, 850, and 900°C were consequently calculated and are shown in Fig. 3. From Fig. 3, it can be seen that, except for the compositions ranging from $\text{NdCl}_{2.50}$ to $\text{NdCl}_{2.15}$, in which the electronic conductivity increases (2-3), the remaining experimental points for various concentrations lie on the relevant isotherms.

By mathematical treatment of the relative data of $E = f\left(\log \frac{[\text{Nd}^{3+}]}{[\text{Nd}^{2+}]}\right)$, the following equations of the EMF isotherms were obtained:

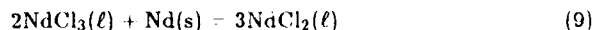
$$E_{800^\circ\text{C}} = 0.563 + 0.29 \log \frac{[\text{Nd}^{3+}]}{[\text{Nd}^{2+}]} \quad (6)$$

$$E_{850^\circ\text{C}} = 0.595 + 0.309 \log \frac{[\text{Nd}^{3+}]}{[\text{Nd}^{2+}]} \quad (7)$$

$$E_{900^\circ\text{C}} = 0.627 + 0.322 \log \frac{[\text{Nd}^{3+}]}{[\text{Nd}^{2+}]} \quad (8)$$

The coefficients in front of the logarithmic term of the above equations indicate that $n \approx 1$. It is obvious that the dissolution mechanism for Nd in NdCl_3 molten

salt is in agreement with the following reaction:



and that $\text{NdCl}_3\text{-NdCl}_2$ is a normal solution, i.e., $r_{\text{Nd}3+}/r_{\text{Nd}2+} = \text{const}$. Therefore, we can substitute concentration for activity, putting the coefficients (a and b) of equation $E = f(T)$, as well as the corresponding composition of molten salt, in equation (5); the following equation was thus derived:

$$\log \frac{[\text{Nd}^{3+}]_{\text{eq}}}{[\text{Nd}^{2+}]_{\text{eq}}} = -2.75 + \frac{620}{T} \quad (10)$$

In the temperature interval, 780-950°C, the solubility of Nd in NdCl_3 molten salt is roughly 32.9 m% Nd, in agreement with chemical analysis results of 31.7 m% Nd. This value also agrees with the 31-33 m% Nd based on the phase diagram of Nd-NdCl₃ (5).

Using equation (10), the temperature dependence of the equilibrium constant and of the Gibbs energy of the dissolution reaction was derived:

$$\log K = 5.52 - \frac{1264.1}{T} \quad (11)$$

$$\Delta G_T^\circ = 24172.4 - 105.6T \text{ J/mol} \quad (12)$$

According to these results, it is obvious that:

- (1) In the temperature range, 850-900°C, the equilibrium constant of the interaction between Nd and NdCl_3 varies from $2.2 \cdot 10^4$ to $2.44 \cdot 10^4$; the enthalpy and entropy of reaction have positive values, which indicate that the reaction is endothermic. Therefore, high temperature would further promote the interaction between Nd and NdCl_3 , and low temperature would decrease the solubility of Nd in NdCl_3 .
- (2) According to references (4,6), in the temperature range, 805-1000°C, the solubility of the other rare earth metals is in m% units:
La, 12-17; Ce, 9; Pr, 22-26; Sm, 33.3.

It is clear that the solubility of Nd is close to that of Sm. Thus, in the molten salt electrolysis of Nd, the dissolution loss of Nd is inevitable.

CONCLUSION

1. In the temperature range, 780-950°C, the thermodynamics of Nd in solution in NdCl_3 were derived and can be summarized by

$$\log \frac{[\text{Nd}^{3+}]}{[\text{Nd}^{2+}]} = -2.75 + \frac{620}{T}$$

$$\log K = 2.52 - \frac{1264.1}{T}$$

and

$$\Delta G_T^\circ = 24172.4 - 105.6T \text{ J/mol}$$

2. The dissolution mechanism of Nd in NdCl_3 consists of chemical interaction of Nd with NdCl_3 . The solubility of Nd in NdCl_3 is roughly 32.9 m% Nd in the temperature interval, 780-950°C.

REFERENCES

1. M. Sagawa *et al.*, J. Appl. Phys. **55**, 2083 (1984).
2. M. V. Smirnov, Doklad Akad. Nauk USSR **151**, No. 3, 591-594 (in Russian) (1963).
3. M. V. Smirnov, Elektrokhiymya **1**, No. 7, 833-383 (in Russian) (1965).
4. F. J. Keneshea, J. Chem. Eng. Data **6**, 507 (1961).
5. F. Druding Leonard, J. Amer. Chem. Soc. **83**, 2462-2467 (1961).
6. G. W. Mellors and S. Senderoff, J. Phys. Chem. **63**, 1110 (1959).

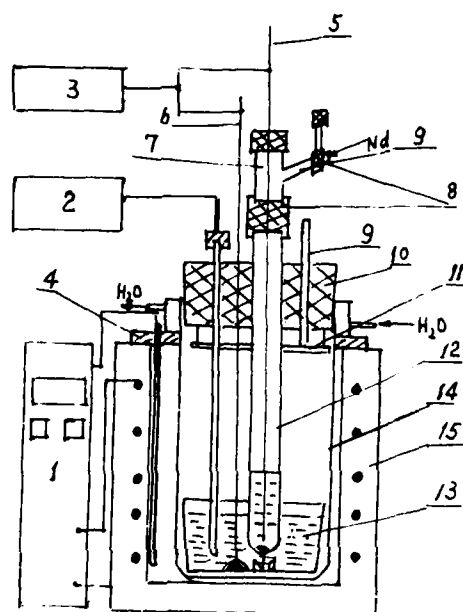


Fig. 1 Schematic Drawing of the Concentration Cell for Measuring EMF.

1. DWK-702 temperature controller.
- 2.,3. PZ-8 direct current digital voltmeter for measuring temperature and EMF of the cell.
4. Pt-Pt.Rh thermocouple.
5. Molybdenum electrode and stirrer.
6. Mo conductor for connecting Nd metal melt.
- 7.,12. Porcelain test tubes, the latter contains NdCl_3 .
8. Joint bast.
9. Inlet for argon and vacuum.
10. Rubber cover.
11. Carbon screen.
13. Porcelain crucible (left half-cell).
14. Stainless steel crucible.
15. Resistance-type furnace.

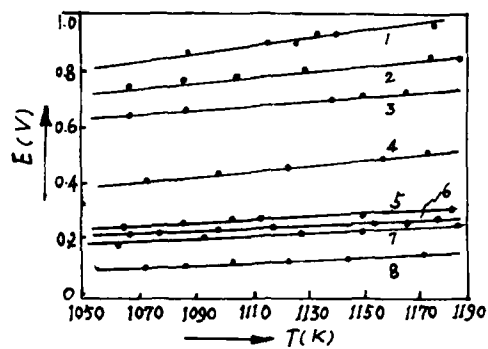


Fig. 2 Temperature Dependence of the EMF's.

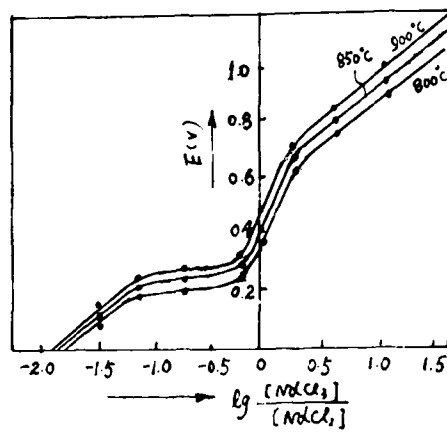


Fig. 3 The EMF Isotherms.

THE ACTIVITY OF LANTHANA IN
NaF-AlF₃-Al₂O₃-La₂O₃ MELTS

Liu Xuliang; Shen Shiyang

Northeast University of Technology,
Shenyang, Liaoning, P.R. of China

ABSTRACT

The concentration cell was assembled by using MgO-stabilized ZrO₂ solid electrolyte. The high precise regression equation of lanthana activity (a) was obtained according to results of the electromotive force of cell.

The paper also discussed the influence of several factors on the activity of lanthana.

I. INTRODUCTION

Al-RE alloys are widely used in several areas because of their high strength and good properties. It is remarkable that the Al-RE alloys of lower and higher contents and the Al-Mg-Si-RE alloy of the high strength were produced in aluminum cells by rare earth oxide addition jointly by Northeast University of Technology and several aluminum reduction plants. The Al-RE alloy was also produced by rare earth carbonate addition to aluminum cells.

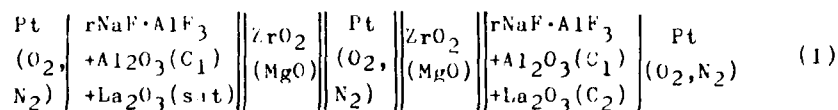
Recently, the research work on physical properties of cryolite-aluminum fluoride-alumina-rare earth oxide melts has been done^[1,2,3]. But activity measurements of rare earth oxide in these melts has not been published.

Lanthana activity in the melts was obtained in the present work by using the concentration cell assembled with MgO-stabilized ZrO₂ solid electrolyte.

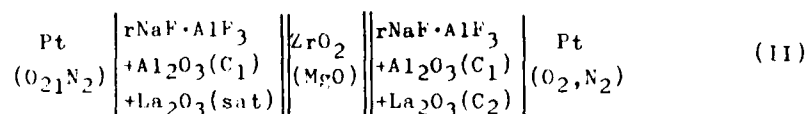
II. EXPERIMENTAL

1. Consideration of cell design

The following concentration cell was designed for use with MgO-stabilized ZrO₂ solid electrolyte.



Theoretically the cell (I) is equivalent to the cell:



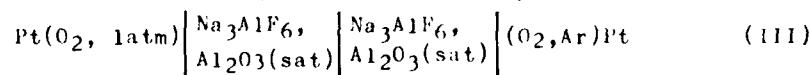
However, the structure of the cell (I) is simpler than that of the cell (II), and the cell (I) is also assembled easily.

In order to prove that the EMF of two cells are equal, we did seven contrast experiments (with different melts at different temperatures). The results for the same conditions show that the differences of the EMF of two cells (ΔE) are smaller than ± 2 mv. This result proves that the cell (I) is the same as the cell (II) electrochemically.

Besides, the adopted oxygen electrode has many advantages. For example, it is easily assembled and there is no interaction between molten salts and container.

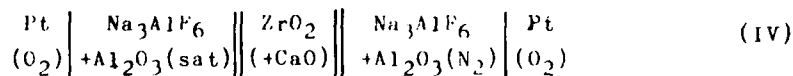
In the past several decades, oxygen electrode has widely been applied in measuring physical chemistry and electrochemistry properties of melts.

Sterten [4] et al. used the cell (III) in order to study the behavior of oxygen electrode in cryolite-alumina melts.



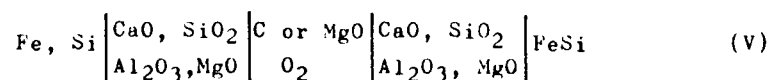
The results showed that $\text{Pt}(\text{O}_2)$ in the melts is a reliable and reversible oxygen electrode.

Shen Shiyong [5] obtained alumina activity in cryolite-alumina melts (with different content of alumina) by measuring EMF of the cell (IV)



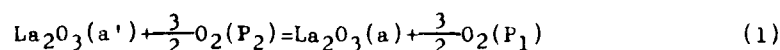
Esin [6] used oxygen bridge connecting two chemical cells

in order to form a concentration cell when researching the state of the silica in liquid slags.



The research results showed that C (or MgO) contacting air and molten slags is an oxygen electrode. Esin also pointed out that the electric potential of oxygen electrode depends on the activity ratio oxygen on electrode to oxygen ions in melts. This is the reason that oxygen electrode was adopted in the present work.

The electrochemical reaction of the cell (II) is:



According to Nernst Equation, the EMF of the cell is

$$E = - \frac{RT}{6F} \ln \frac{a P_1^{3/2}}{a' P_2^{3/2}} \quad (2)$$

Where P_1 and P_2 are oxygen pressures on the surfaces of two electrodes, a is the activity of lanthana in the melts which is not saturated, and a' is the activity of lanthana in the melts saturated with lanthana. Setting the activity of the melts saturated with lanthana equals to unity ($a'=1$), and considering that the two electrodes of the cell (II) are in air, so P_1 equals to P_2 . We obtain the equation:

$$\ln a_{\text{La}_2\text{O}_3} = -69628 E/T \quad (3)$$

If EMF of the cell is determined at a temperature, T , equation (3) can be used to calculate the activity of lanthana in the melts.

2. Experimental Method

MgO-stabilized ZrO_2 solid electrolyte tubes used in present work were produced by Shenyang Ceramic Plant.

The experimental apparatus consists of an electric resistance furnace controlled by DWK-702, a P48 digital voltmeter and a LY4 digital printer (See Fig. 1). Before experiment, it was proved that the temperature field is uniform about 60 mm above the furnace bottom when the temperature is between 1200K and 1300K. In order to prove that MgO-stabilized ZrO_2 solid electrolyte tubes can resist the corrosion of cryolite-alumina melts, two tubes were

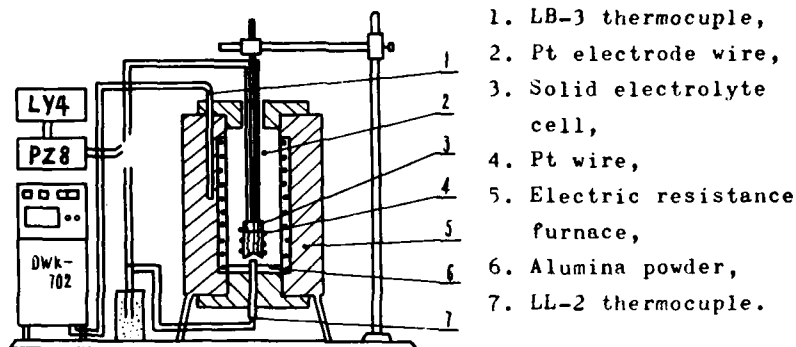


Fig.1 Experiment apparatus

soaked in the melts for eight hours at 1273K. The experimental results showed that the tubes do not show visible corrosion.

The EMF of the cell (II) was recorded by PZ8 digital voltmeter with LY4 digital printer, six times a minute. The average of the EMFs for 3 minutes was considered as an experimental datum. The experimental reagents are as follows: Lanthana, La_2O_3 is more than 99.99% (wt), Yuelong Chemical Plant, Shanghai; Alumina, analytically pure, Shenyang the Third Reagent Plant; NaF, analytically pure, Dandong the Fourth Chemical Plant; Cryolite, $r=3.0$, Shanghai the Third Reagent Plant and $r=2.05$, Fushun Aluminum Reduction Plant.

III. RESULTS AND DISCUSSION

1. Regression Equation and its Precision

The combinatorial design with orthogonal regression was adopted and experimental plan and results are given in table 1. The regression equation (4) was obtained on the basis of the experimental data.

$$\begin{aligned}
 a = & -80.1885 + 0.5274C_1 + 0.2574C_2 - 2.8452r + 0.13192T \\
 & - 0.005298C_1C_2 - 0.0002937C_1T - 0.0001862C_2T - 0.01904C_1^2 \\
 & - 0.001436C_2^2 + 0.5141r^2 - 5.1889 \times 10^{-5}T^2
 \end{aligned} \quad (4)$$

Where a is the activity of lanthana, C_1 and C_2 are concentrations (%wt) of alumina and Lanthana respectively, r is cryolite ratio, and T is temperature (K).

Table 1. Experimental plan and results

No.	Al ₂ O ₃ %(wt)	La ₂ O ₃ %(wt)	T	T	La ₂ O ₃ activity
1	2	2	2.4	1233	0.00976
2	2	2	2.4	1293	0.02708
3	2	2	3.0	1233	0.01193
4	2	2	3.0	1293	0.01419
5	2	10	2.4	1233	0.1649
6	2	10	2.4	1293	0.09629
7	2	10	3.0	1233	0.1393
8	2	10	3.0	1293	0.07703
9	6	2	2.4	1233	0.1197
10	6	2	2.4	1293	0.09552
11	6	2	3.0	1233	0.1041
12	6	2	3.0	1293	0.03512
13	6	10	2.4	1233	0.4762
14	6	10	2.4	1293	0.3214
15	6	10	3.0	1233	0.3974
16	6	10	3.0	1293	0.2521
17	1.172	6	2.7	1263	0.04674
18	6.828	6	2.7	1263	0.1741
19	4	0.344	2.7	1263	0.00679
20	4	11.656	2.7	1263	0.4267
21	4	6	2.276	1263	0.4027
22	4	6	3.124	1263	0.3078
23	4	6	2.7	1220.6	0.2975
24	4	6	2.7	1305.4	0.04113
25	4	6	2.7	1263	0.1954

The analysis of variance ($F=17.87 > F_{0.01}(11, 13)=4.03$) showed that the regression equation is very precise. In order to examine the reliability of the equation again, we did eight contrast experiments at random. The deviations of lanthana activity calculated and measured is smaller than ± 0.02 in the same condition. The result proves that

the equation is very precise and reliable.

2. Influence of Several Factors on Activity of Lanthana

According to the equation (4), the influence of several factors on lanthana activity was given in Fig. 2-Fig. 5.

Fig. 2. Shows clearly that the activity of lanthana increases with increasing concentration when other factors do not change. The gradient of increase relates to the concentration of alumina. The reason is that AlOF_2 ions increase with increasing the concentration of alumina.

When cryolite ratio is equal to 2.7, the influence of the concentration of alumina on the activity of lanthana is plotted in Fig. 3. As can be seen from this figure, when

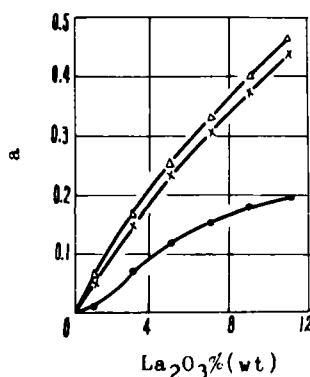


Fig. 2 Variation of activity of lanthana (a) with its concentration ($\text{La}_2\text{O}_3\%$ (wt)) at 1248K

▲- $r=2.5$, $\text{Al}_2\text{O}_3=6\%$;
 x- $r=2.9$, $\text{Al}_2\text{O}_3=6\%$;
 •- $r=2.5$, $\text{Al}_2\text{O}_3=2\%$.

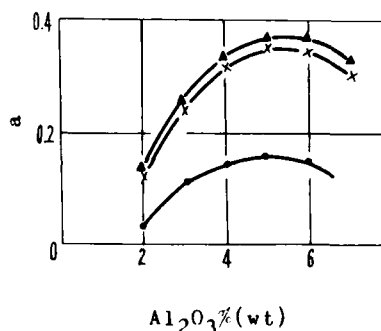


Fig. 3 Variation of activity of lanthana (a) with concentration of alumina ($\text{Al}_2\text{O}_3\%$ (wt)) ($r=2.7$)

▲- $T=1248\text{K}$, $\text{La}_2\text{O}_3=9\%$;
 x- $T=1263\text{K}$, $\text{La}_2\text{O}_3=9\%$;
 •- $T=1248\text{K}$, $\text{La}_2\text{O}_3=3\%$.

the concentration of alumina is smaller than 5% (wt), the activity of lanthana increases with increasing the concentration of alumina, and when the concentration of alumina is higher than 6% (wt), the slope reverses. The results may be that complicated complex ions is formed by combination of Al-O-F ions^[7], so the concentration of AlOF_2 ions decreases.

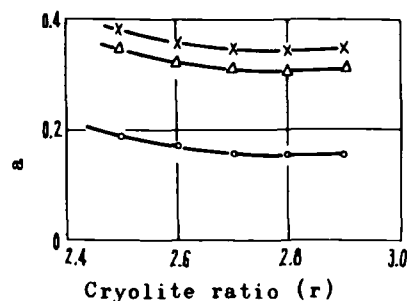


Fig. 4 The influence of cryolite ratio on the activity of lanthana (a) at 1263K

x-Al₂O₃=6%, La₂O₃=9%;
 Δ-Al₂O₃=4%, La₂O₃=9%;
 •-Al₂O₃=4%, La₂O₃=3%.

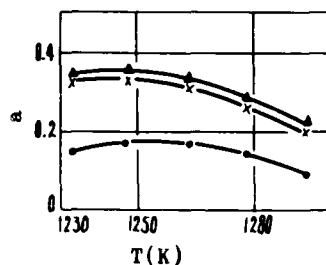


Fig. 5 The influence of temperature on the activity of lanthana (a) (Al₂O₃=4% (wt))

Δ-r=2.6, La₂O₃=9%;
 x-r=2.8, La₂O₃=9%;
 •-r=2.6, La₂O₃=3%.

The influence of cryolite ratio on the activity of lanthana is illustrated in Fig. 4. It is shown that the activity of lanthana decreases slightly with increasing cryolite ratio.

Fig. 5 shows the influence of temperature on the activity of lanthana. The curves in the figure show that the activity of lanthana first increases and then decreases slightly with increasing the temperature. This is the results of two reasons. First, increasing temperature causes complex ions to decompose, and this increases the activity of lanthana. Second, the solubility of lanthana in melts increases with increasing temperature, so its activity decreases.

3. The Isogram of Lanthana Activity

In order to examine the influence of several factors on the activity, the isogram of lanthana activity is illustrated in Fig. 6. The figure shows that when the concentration ratio lanthana to alurina is equal to some datum, the activity of lanthana is the highest. Cryolite ratio has little influence on this result.

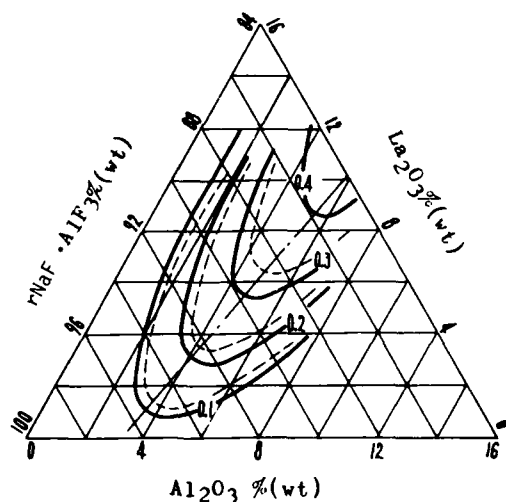


Fig. 6 Iso-activity lines of lanthana in
 $r\text{NaF} \cdot \text{AlF}_3\text{-Al}_2\text{O}_3\text{-La}_2\text{O}_3$ melts at 1253K
 — $r=2.5$; - - $r=2.7$

IV. CONCLUSION

1. A highly precise regression equation of lanthana activity was obtained.
2. The experimental results show that the activity of lanthana in melts increases with increasing its concentration, and the concentration of alumina has a large influence on the activity of lanthana. When the concentration of alumina is about 5%, the activity of lanthana reaches a maximum.
3. The Isogram shows that the activity of lanthana reaches a maximum as a function of the lanthana/alumina ratio.

REFERENCE

1. Wei Xujun; Xu Xiuzhi; Liu Xuliang; Zhao Yifa, Journal of The Chinese Rare Earth Society, 1985, 3(3), 44-47.
2. Shen Shiyang; Zhao Keqi; Zhang Yijing, Xi Tu, 1983,

No.3, 1.

3. Shen Shiyong; Zhao Keqi; Zhang Yijing, Xi You Jin Shu, 1984, No. 2, 23.

4. Sterten, A.; Haugen, S.; Hamberg, K., Electrochim Acta, 1976, 21, 589-592.

5. Shen Shiyong, Journal of Northeast University of Technology, 1983, No.4, 34.

6. Esin, O. A. Dokl, Acad. USSR. 1953, 88, 713.

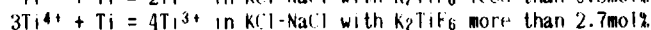
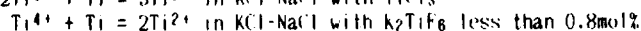
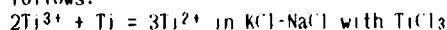
7. Grjothim, K. et al., Aluminium Electrolysis, Aluminium-verlag Gmb H, 1977.

ELECTROCHEMICAL STUDIES ON DISPROPORTIONATION REACTION OF TITANIUM AND TITANIUM IONS IN KCl-NaCl MOLTEN SALTS

Takeo Oki, Masazumi Okido and Chen Guang-sen
Faculty of Eng., Nagoya University, Furo-cho, Chikusa-ku, Nagoya, 164, Japan

ABSTRACT

The reaction between titanium and titanium ions was investigated by means of electrochemical and physical methods in KCl-NaCl molten salts with K_2TiF_6 or $TiCl_3$ at 973K. The reactions were considered as follows.



And also, it was clarified that the fluoride ions affected on the reduction reaction of titanium ions (Ti^{4+}) by the electrochemical and physical measurements in the molten salts with KF.

INTRODUCTION

The electrodeposition of titanium from molten salt systems has been investigated by many researchers(1-6). However, the process is very complicated due to lower valent compounds of titanium(Ti^{2+} , Ti^{3+}) which exist in the electrolytic bath and the reactions between metallic titanium and tetra- or trivalent titanium ions(7-10). There are currently a number of papers concerning the equilibrium between titanium metal and chloride molten salts containing $TiCl_4$ or $TiCl_3$ (10-13) but few reports concerning the mechanism and kinetic behavior of the interaction between titanium metal and titanium ions in various compositions of molten salts. This is of importance, not only for the electrodeposition of titanium from molten salt systems, but also for the applications of the disproportionation reaction to the formation of thin films(14). In this paper, the interaction reaction of titanium and titanium ions was investigated and discussed by the use of the immersion test and the electroreduction of Ti ions(K_2TiF_6) by linear sweep voltammetry, chronoamperometry and Faradaic impedance measurements in NaCl-KCl molten salts. Also, the effects of F^- ions on the reaction and behaviour of electroreduction of Ti^{4+} ions were investigated.

EXPERIMENTAL

The experimental cell for electrochemical measurements is shown in Fig.1. All experiments were carried out in a protective purified argon atmosphere at a temperature of 973 ± 2 K. The reference electrode consisted of Ag-0.1N AgCl in equimolar KCl-NaCl molten salts and a very thin mullite tube as diaphragm. A Ti wire

(1.6mm ϕ) or a Pt wire(0.5mm ϕ) was used as a working electrode. The counter electrode was Pt wire with a large surface area.

As a supporting electrolyte, an equimolar KCl-NaCl mixture was used after holding at their melting point in a vacuum enough to dehydrate. K_2TiF_6 and $TiCl_3$ were both used as a source of titanium ions. Also, KF was added into the molten salts to examine the effects of fluorine ions on the reaction behaviour of titanium ions. Linear sweep voltammetry and chronoamperometry were achieved by means of a conventional potentiostat. The impedance measurements were performed using a digital frequency response analyzer(15). Alternating voltage with an alternate ΔE_p of about 10 mV was superimposed.

Also, the weight changes of Ti plates with 10×10×2mm were measured after being immersed in the molten salts with various compositions of K_2TiF_6 , $TiCl_3$, KF and so on. The molten salts after experiment were cooled in the inert atmosphere and solidified salts were leached with boiled distilled water to dissolve the alkali chlorides and to separate the insoluble products formed by the reaction between titanium and Ti^{4+} ions (K_2TiF_6). The separated products were analyzed by X-ray diffraction to obtain the information about the valency state of Ti.

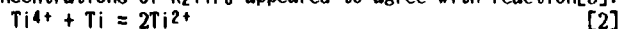
RESULTS AND DISCUSSION

1. Reaction between Ti metal and Ti ions

Typical potential changes of titanium plates of 10×10×2(mm) in KCl-NaCl with $TiCl_3$ or K_2TiF_6 are shown in Fig.2. It was found that the mixed potential E increased with the increase of $TiCl_3$ or K_2TiF_6 concentration in the molten salts and a steady state was obtained in about 30-60 minutes. Then, the immersion time was taken as 70 minutes to determine the weight change of Ti plates in the molten salts. The Ti weight changes associated with the reaction between Ti metal and Ti ions in KCl-NaCl molten salts with $TiCl_3$ or K_2TiF_6 are demonstrated in Fig.3. The lines represent the theoretical weight change in accordance with various possible interaction mechanisms. The experimental results in the bath with $TiCl_3$ was in good agreement with the theoretical line, which follows this reaction.



But the interaction between titanium metal and the molten salts with K_2TiF_6 was not simple. The experimental values in the bath with lower concentrations of K_2TiF_6 agreed with the theoretical line of reaction[2] and those in the bath with higher concentrations of K_2TiF_6 appeared to agree with reaction[3].



From the results shown in Fig.3, the mechanism of the interaction between titanium metal and the molten salts containing K_2TiF_6 appears complex, so it was necessary to determine the products of the interaction in order to clarify the reaction mechanism.

2. X-ray analysis

Typical results of the X-ray diffraction of insoluble materials through water leaching of the solidified salts are given in Fig.4. Besides the fluorides of trivalent titanium (K_2NaTiF_6 , $KTiF_4$, $NaTiF_4$, K_3TiF_6 , Na_3TiF_6), the lines for titanium metal were very strong in Fig.4(a), less stronger in Fig.4(b) and very weak in Fig.4(c).

3. Impedance characteristics

Fig.5 shows typical complex impedance diagrams ($Z=R+jX$, $j=\sqrt{-1}$) for the interaction reactions between titanium metal and the KCl-NaCl molten salts containing $TiCl_3$ or K_2TiF_6 at mixed potentials. And it is the result of Ti electrode in the molten salts with 1.37mol% K_2TiF_6 or 0.276mol% $TiCl_3$. It is evident that the complex impedance diagrams consist of two parts for both $TiCl_3$ and K_2TiF_6 , the loop on the higher frequency side is due to a charge transfer reaction, and the straight line with a slope of about 45° on the lower frequency side is attributed to diffusion of reactants or reaction products.

Fig.6 shows a relation between the reaction resistance ($1/R_i^*$) obtained from the impedance data and the average weight change rate (ΔW mg/hr.cm²) of titanium immersed in KCl-NaCl molten salts with $TiCl_3$ or K_2TiF_6 . There was a straight line relation for titanium metal in the molten salts with $TiCl_3$, but in the case of K_2TiF_6 a straight line relation was not observed. The implication is that the mechanism of the reaction between titanium metal and the molten salts containing K_2TiF_6 changed with the K_2TiF_6 content.

4. Reaction between Ti and K_2TiF_6

From the results in Fig.3,4 and 6, the interaction between titanium metal and the molten KCl-NaCl- K_2TiF_6 was different from the reaction between titanium metal and the molten KCl-NaCl- $TiCl_3$. When the content of K_2TiF_6 was higher than 2.76mol% (about 9.1wt.%), the weight change of the titanium specimen agreed well with the theoretical values calculated as the reaction of eq.[3], where the products were determined as titanium trifluoride group in Fig.4(c). These results were consistent with those obtained by many researchers(15-18). Therefore, the interaction between titanium metal and the molten salts with higher than about 9wt.% K_2TiF_6 content can be indicated as the eq.[3].

When the concentration of K_2TiF_6 was less than approximately 0.8mol%, the experimental results were in close agreement with the theoretical values calculated by the reaction of eq.[2]. However, only titanium trifluoride compounds and titanium metal in the products were detected according to X-ray diffraction analysis results. This may be because of the decomposition of Ti^{2+} (fluoride) during cooling(19-20). The reaction of titanium metal in the molten salts with less than about 0.8mol% K_2TiF_6 content proceeded according to reaction[2]. And from the results in Fig.3 and 4(b), the interaction reaction between titanium metal and the molten salts containing K_2TiF_6 of 0.8~2.7mol.% was represented by

reactions [2],[3].

5. Effects of F⁻ ions on the reaction between Ti and Ti⁴⁺ ions

The behaviour of the reaction between Ti metal and Ti⁴⁺ ions in equimolar KCl-NaCl molten salts with K₂TiF₆ was more complex in comparison with the case of TiCl₃. Therefore, the experiment was made to clarify the effects of F⁻ ions on the reaction. Fig.7 shows Ti weight changes with the concentration of KF in KCl-NaCl-KF-3wt%(or 10wt%)K₂TiF₆. The dashed lines present the theoretical weight changes in accordance with various possible mechanisms provided that these reactions proceed completely. In KCl-NaCl-3wt%K₂TiF₆, the Ti weight changes in the bath with below 3wt% KF were in close agreement with the reaction of eq.[2]. However, the weight changes decreased with the increase of KF concentration. It was caused that the reaction changed from eq.[2] to eq.[3]. In KCl-NaCl-10wt.% K₂TiF₆ molten salts with various composition of KF, the Ti weight changes were independent of the KF concentration. These values agreed well with the theoretical those calculated from the reaction of eq.[3].

As discussed above, it can be concluded that the reaction of Ti and Ti⁴⁺ ions with less fluorine ions occurred to act like that in alkali chloride melts. Also, there existed an intermediate fluorine ion range in which reactions of eq. [2] and eq.[3] occurred simultaneously and were in equilibrium.

6. Polarization behavior of Ti and Ti⁴⁺

It was observed that fluorine ions played a important role in the reaction as shown above. The cathodic reactions of Ti⁴⁺ ions and anodic reactions of Ti will be presented in this section. Typical linear voltammograms for electroreduction of Ti⁴⁺ ions in KCl-NaCl-3wt%K₂TiF₆ and anodic reaction of Ti metal in KCl-NaCl molten salts are given in Fig.8. Curve(1) in this figure is the cathodic current density-potential curve for the reduction of Ti⁴⁺. According to this result and the result obtained at the same Pt electrode in pure KCl-NaCl molten salts, it was found that the current increased from less potential than -2.0V corresponded to the reduction of alkali cation ions. Then, the reduction of Ti⁴⁺ ions consisted of four steps(discussed later in this paper). This differed from the results published in the literature[15-18] in which it was pointed that the reduction of Ti⁴⁺ ions in fluoride or chloride-fluoride mixed melts (K₂TiF₆ > 10 wt.%) had following steps: $Ti^{4+} + e = Ti^{3+}$, $Ti^{3+} + 3e = Ti(Pt \text{ alloy})$.

Curve(2) in Fig.8 presents the anodic behavior of Ti metal in pure KCl-NaCl molten salts. It was composed of three different straight relations between log(i) and potential(V). According to standard potential of Ti/Ti⁴⁺(or Ti³⁺ or Ti²⁺) system, it was reasonably considered that they corresponded to the following three different anodic reactions.



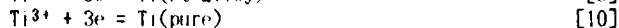
Also it was noted that part (A) of the anodic curve, which corresponds to eq.(4), intersected with part(b) of the cathodic one.

A typical linear voltammogram for the reduction of Ti^{4+} in KCl-NaCl molten salts with 10wt.% K_2TiF_6 is shown in Fig.9. It differed from the electroreduction of Ti^{4+} ions in the molten salts with 3wt.% K_2TiF_6 . In this case, three steps were observed. Fig.10 showed typical linear voltammograms for electroreduction of Ti^{4+} ions in KCl-NaCl-3wt.% K_2TiF_6 molten salts with 10wt.%KF and anodic reaction of Ti metal in KCl-NaCl melts containing 10wt.%KF. In comparison with the results in Fig.8 and 9, the cathodic behaviour of Ti^{4+} ions were close to that in KCl-NaCl molten salts with 10 wt.% K_2TiF_6 and the anodic characteristics were similar to that in pure KCl-NaCl melts. However, part (B) of the anodic curve intersected with part (c) of the cathodic one. This point was different from that shown in Fig.8.

It was shown that the reduction of Ti^{4+} ions at a Pt electrode was (quasi) reversible process and mainly diffusion controlled. Therefore, the following equation can be used for estimation of the electron number involved in the electrochemical reduction steps, if both the reactants and products are soluble.

$$E_p - E_{1/2p} = E_{pc} - E_{pa} = -2.20RT/(nF) \quad [7]$$

The electron numbers were also obtained from the slope $[RT/(nF)]$ of the proportional relations between $\log[(i_d - i)/i]$ for a steady voltammogram. Table 1 and 2 showed the mean values calculated by these two methods. X-ray diffraction analysis was used to determine the products obtained on a Pt electrode after electrolysis at various potentials. The electrochemical reduction of Ti^{4+} ions on a Pt electrode in fluoride-chloride mixed melts with higher fluorine ions was suggested as follows.



When the concentration of F⁻ ions in the molten melts was less, the reduction reaction was proposed as the following four sequential steps.



The reaction between Ti metal and the molten salts containing Ti ions can be deduced from the cathodic reaction and anodic reaction at the intersection point of these(cathodic or anodic) voltammograms. According to the results shown in Fig.8, the cathodic reactions was eq.[11] and eq.[12] and the anodic one was eq. [4] at the mixed potential which was approximately equal to that at the intersection point. Then, the reaction between Ti metal and KCl-NaCl-3wt.% K_2TiF_6 were the same with reaction of eq.[2].

CONCLUSION

The reaction between titanium and titanium ions was considered to proceed at 973K as follows.

$2\text{Ti}^{3+} + \text{Ti} = 3\text{Ti}^{2+}$ in KCl-NaCl with TiCl_3

$\text{Ti}^{4+} + \text{Ti} = 2\text{Ti}^{2+}$ in KCl-NaCl with K_2TiF_6 less than 0.8mol%

$3\text{Ti}^{4+} + \text{Ti} = 4\text{Ti}^{3+}$ in KCl-NaCl with K_2TiF_6 more than 2.7mol%

The effects of the fluorine ions on the reduction reaction of titanium ions (Ti^{4+}) have been clarified. The reduction of Ti^{4+} ions changed from $\text{Ti}^{4+} + e = \text{Ti}^{3+}$, $\text{Ti}^{3+} + e = \text{Ti}^{2+}$ and $\text{Ti}^{2+} + 2e = \text{Ti}$ three step process to $\text{Ti}^{4+} + e = \text{Ti}^{3+}$, $\text{Ti}^{3+} + 3e = \text{Ti}$ two step process with the increase of F^- concentration.

REFERENCES

- 1) I.A.Menzies, D.L.Hill, G.J.Hill, Young and Jom Bockris, J.Electroanal. Chem., vol1 (1959/60)161
- 2) W.E.Reid, J.Electrochem.Soc., 108 (1957)393
- 3) F.Ouemper, D.Deroo, N.Rigard, ibid. 119 (1972)1353
- 4) E.CHASSAING, F.Basile and G.Lorthioir, J.less-com. metals 68 (1979)153-158
- 5) S.Tokumoto, E.Tanaka, and Ogisu, J.of Metal 27(Nov)(1975)18
- 6) S.Mori, T.Kuroda and K.Kawamura, Denki Kagaku, 42 (No.4) (1974)175
- 7) M.B.Aipert, F.J.Shultz, W.F.Sullivan, J.Electrochem.Soc. 104 (1957)555
- 8) M.B.Aipert, J.A.Hamilton, F.J.Shultz, W.F.Sullivan, ibid. 106 (2)(1959)142
- 9) K.Komarek, P.Herasynenko, ibid 105 (4) (1958)210
- 10) M.V.Smirnov and O.V.Skiba, Electrochemistry of molten and solid electrolytes, vol.2, Consultants Bureau, New York (1964)21
- 11) P.M.Vsov and M.V.Smirnov, Electrochemistry of molten and solid Electrolytes vol.3, Consultants Bureau, New York (1966)1
- 12) M.E.Sibert, O.H.Kenna, J. Electrochem. Soc. 102 (1955)252
- 13) G.Ervin, H.F.G.Geltz, M.E. ibid 106, (1959)144
- 14) T.Oki and J.Tanigawa, Molten Salts 25 (1982)115
- 15) J.G.Wurm et al, J.Electrochem. Soc. 104 (1957)301
- 16) N.F.H.Bright and J.G.Wurm, Can.J.Chem. 36 (1958)615
- 17) R.VYTLacil and A.NEKEL, Wien Metall, 34 (1980)538
- 18) F.R.Claytau and G.Mamantov, J. Electrochem. Soc., 120 (1973)1193
- 19) L.Thakur and B.B.Sandwar, J.Indian Chem. Soc., 56(7) (1979)663-665
- 20) V.K.BRODEREN and W.Ruporff Z.Anorg Allgem Chem. 131 (1954) 121

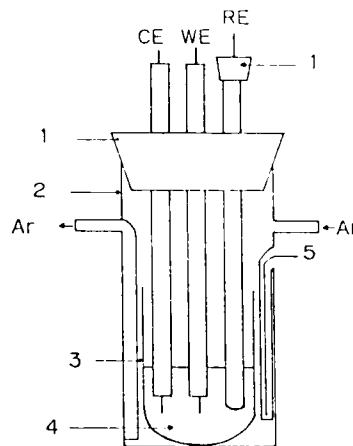


Fig.1 Electrolysis cell. (1) silicon rubber; (2) quartz tube; (3) crucible; (4) CA thermocouple.

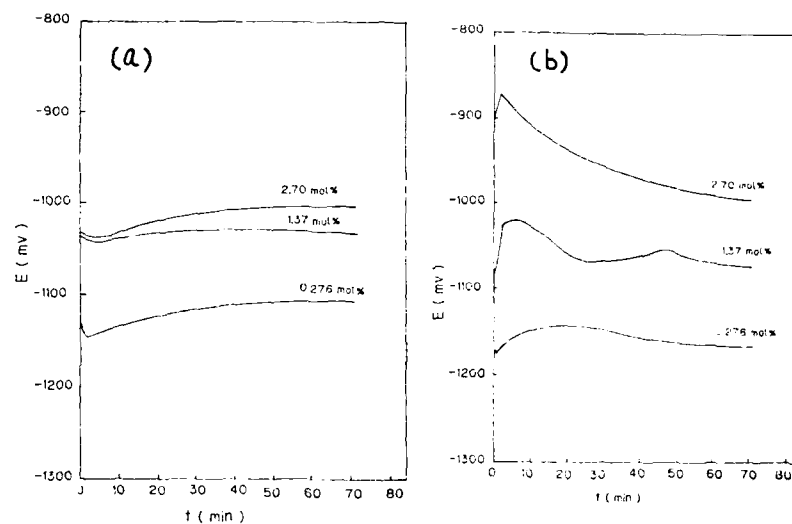


Fig.2 Time dependence of mixed potential of Ti plates in KCl-NaCl melts with various compositions of (a) TiCl_3 ; (b) K_2TiF_6 at 973K

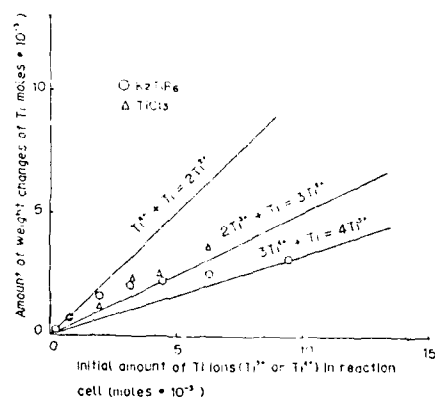


Fig.3 Weight changes of the Ti specimens in KCl-NaCl(15g) with TiCl_3 or K_2TiF_6 for 70 minutes at 973K. The lines represent theoretical weight changes with various possible reactions.

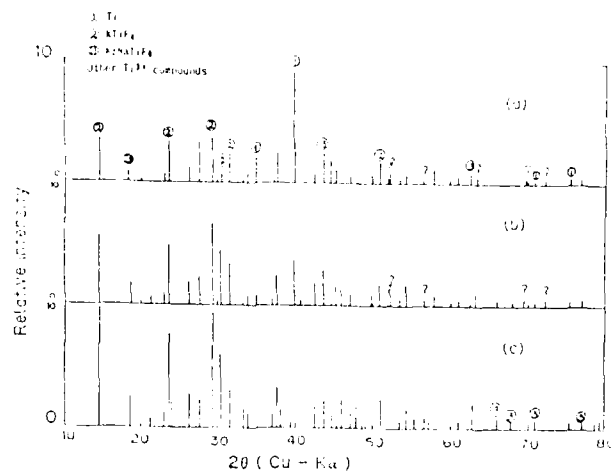


Fig.4 X-ray diffraction of the products of the reaction between Ti metal and Ti ions in KCl-NaCl melts with k_2TiF_6 : (a) 0.276mol%; (b) 1.37mol%; (c) 3.99mol%.

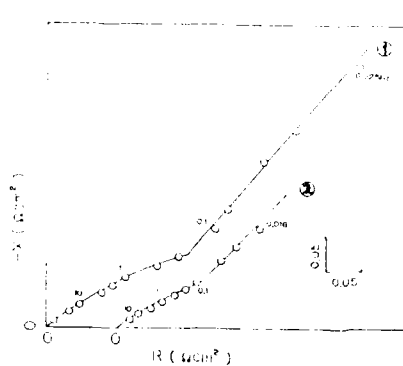


Fig.5 Complex impedance diagrams of a Ti electrode in KCl-NaCl melts at mixed potential at 973K: (1) 0.276mol% $TiCl_3$; (2) 1.37mol% k_2TiF_6 .

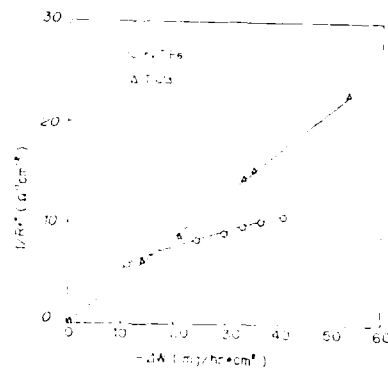


Fig.6 Relation between Ti weight change rate and the charge transfer resistance of Ti electrode at mixed potential in KCl-NaCl melts with $TiCl_3$ or k_2TiF_6 .

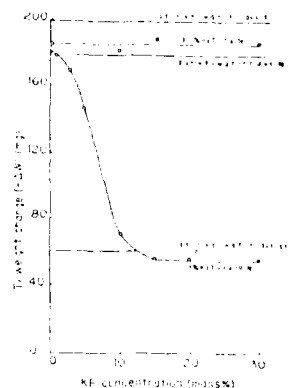


Fig. 7 Effects of KF concentration on the Ti weight changes in KCl-NaCl-KF(30g) melts with K_2TiF_6 for 3hrs.

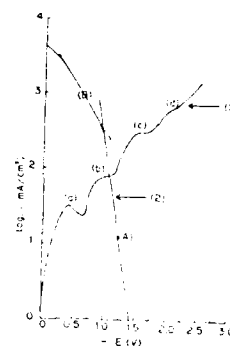


Fig. 8 (1) Cathodic polarization curve for Ti^{4+} ions in KCl-NaCl melts with 3wt.% K_2TiF_6 ; (2) Anodic one for a Ti electrode in KCl-NaCl at 973K. Scan rate: 50mv/s.

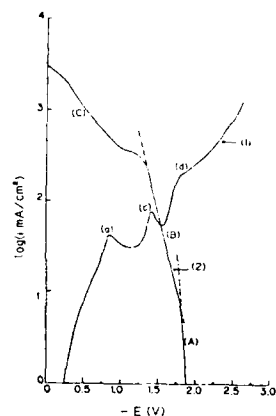


Fig. 9 (1) Cathodic polarization curve for Ti^{4+} ions in KCl-NaCl melts with 3wt.% K_2TiF_6 and 10wt.% KF; (2) Anodic one for a Ti electrode in KCl-NaCl-10wt.% KF at 973K. Scan rate: 50mv/s

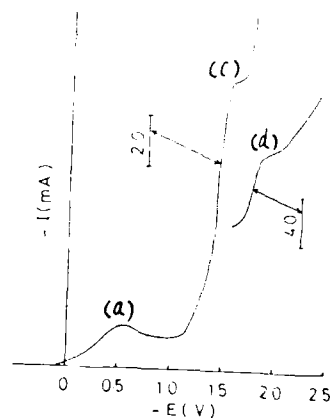


Fig. 10 Linear sweep voltammogram for reduction of Ti^{4+} ions in KCl-NaCl-10wt.% K_2TiF_6 at 973K. Pt: 0.159cm²; scan rate: 50mV/s.

Table 1 Mean values of electron number for reduction of Ti^{4+} in KCl-NaCl with K_2TiF_6 on a Pt electrode at 973K

Reduction step	(a)	(b)	(c)	(d)
1wt.% K_2TiF_6	0.99	1.10	1.89	1.91
10wt.% K_2TiF_6	1.01		2.82	3.02

Table 2 Mean values of electron number for reduction of Ti^{4+} in KCl-NaCl-3wt.% K_2TiF_6 melts with KF on a Pt electrode at 973K

Reduction step	(a)	(b)	(c)	(d)
0wt.%KF	0.92	0.95	2.01	1.94
3wt.%KF	1.02	0.90	1.86	
10wt.%KF	1.01		2.99	
20wt.%	0.92		2.96	

**PULSE AND A.C. IMPEDANCE STUDIES OF THE ELECTROCHEMICAL
SYSTEMS OF TITANIUM
IN LiCl-KCl EUTECTIC MELT AT 743 K.**

D.M. Ferry, G.S. Picard and B.L. Trémillon
Laboratoire d'Electrochimie Analytique et Appliquée
associé au C.N.R.S. (U.A. 216)
E.N.S.C.P., 11 rue P. et M. Curie
75231 Paris Cedex 05 - France

ABSTRACT

The electrochemical systems of titanium in LiCl-KCl eutectic melt have been investigated by means of pulse techniques and A.C. impedance measurements. $Ti^{3+}/Ti(IV)$ electrochemical system appears reversible while Ti^{3+}/Ti^{2+} is quasi-reversible and metallic titanium deposition from Ti^{2+} is irreversible. Kinetic constants related to these redox systems have been determined as also the thickness of the diffusion layer, the double layer capacitance and the electrolyte resistance.

1. INTRODUCTION

The electrodeposition of metallic titanium from titanium (IV) chloride in molten chlorides melt aroused a lot of investigations since the early fifties. Nevertheless the important discrepancies between the various results available in literature led us to perform a systematic study of the thermodynamic stability of titanium chlorides and oxides in a particular bath, the molten eutectic LiCl-KCl at 743 K.

First we determined the standard potentials of the three different redox systems of titanium [$Ti(0)/Ti(II)$, $Ti(II)/Ti(III)$ and $Ti(III)/Ti(IV)$] and the solubility products of all the titanium oxides (1). Secondly, because of the lack of information on the kinetic parameters of the electrochemical systems of titanium, we have undertaken their determination by using pulse and A.C. impedance techniques. This is the subject of this paper.

2. TECHNICAL

2.1. Preparation of melt and apparatus.

The eutectic melt (45 wt % LiCl - 55 wt % KCl) was contained in a pyrex crucible placed inside a pyrex reactor. This mixture was fused under vacuum as was described earlier (2), and then maintained at the working temperature (743 K) under an inert atmosphere of dry argon. Heating was achieved by means of a Renat furnace connected to a temperature-controlled device Microcor Chauvin-Arnoux.

2.2. Products and electrodes.

Lithium and potassium chlorides (minimum purity 99%) were supplied by Merck. Solid titanium(III) chloride (purity $\geq 98\%$), from Alpha Ventron, was kept in a dry glove-box until its use. $TiCl_3$ was added into the melt by means of a "powder burette" (3).

The working and counter electrodes were tungsten wires (surface area $S = 0.24 \text{ cm}^2$) and the reference electrode was the silver-silver chloride (0.75 mol.kg^{-1}) reference previously described (3). Metallic wires were supplied by Johnson Matthey (W purity : 99.98 % ; Ag : 15 ppm of impurities). Silver chloride was a Merck product (99 %). Potentials are referred in this paper to the chlorine (1 atm)-chloride electrode whose potential is + 1.023 V versus our reference electrode.

2.3. Pulse techniques.

Chronoamperograms and chronopotentiograms have been recorded by using a PAR Model 176 potentiostat-galvanostat connected, via an interface Model 273, to an Apple IIe microcomputer. Experimental data have been stored onto 5¹/₄ flexible disks and then plotted with a 7470 A Hewlett-Packard plotter.

2.4. A.C. Impedance measurements.

Experiments were performed with a Z Computer system Tacussel coupled to a Hewlett-Packard 9826 microcomputer. Measurements have been carried out using a 15 mV amplitude sine wave signal and a frequency range from 100 kHz to 50 mHz. The usual operating precautions (Faraday cage surrounding the electrochemical cell, connecting screened wires,...) were taken. Interpretation of experimental data was realized by comparing them with computerized curves according to a mechanism model. An HP 9000 "Series 300" microcomputer and a 7470 A HP plotter was used for that purpose.

3. RESULTS AND DISCUSSION

3.1. Chronoamperometric studies of the oxidation and reduction of titanium(III) solutions.

From $E = -2.5 \text{ V}$ to $E = 0 \text{ V}$, it was experimentally observed that chronoamperograms exhibit a current constant value, due to thermal convection, for each potential when times are greater than 10 s. These steady state potential-dependent current values were used for obtaining the i - E curves represented in figure 1a.

We can notice on figure 2a that the diffusion limiting current of the oxidation wave is practically equal to the one of the first reduction wave and to the half of the second reduction wave. Besides, a logarithmic analysis of the i - E oxidation curve (figure 1b) indicates a bilogarithmic behavior when potential is lower than the half-wave potential (current densities less than 13 mA.cm^{-2}) corresponding to a reversible charge transfer involving one electron suggesting the formation of soluble Ti^{4+} ions. For potentials greater than the half-wave potential, we observe a deviation from the bilogarithmic behavior which can be explained by considering the solubility of gaseous TiCl_4 . By such an analysis, we can verify that the number n of exchanged electrons is close to the unity ($n = 1.2 \pm 0.1$). From these results, we can deduce that the first step of the Ti^{3+} ion reduction leads to titanium(II), followed by the reduction of Ti(II) into metallic titanium.

By plotting the variation of the current versus the reciprocal value of the square root of time at a potential corresponding to the diffusion limiting current of the i - E oxidation curve (point P on figure 1a), we demonstrate that experimental data obey

Cottrell's law (figure 1c). The straight line obtained has a slope of $45 \pm 6 \text{ mA.cm}^{-2}.\text{s}^{-1/2}$ from which the diffusion coefficient D of Ti^{3+} ion has been calculated by using for the number of exchanged electrons the value $n = 1$ determined above. We found $D = (1.9 \pm 0.5) \cdot 10^{-5} \text{ cm}^2 \text{ s}^{-1}$. By using (i) this value of D , (ii) the one of the thickness δ of the diffusion layer deduced from the limiting current density, and (iii) those of the standard potentials of the electrochemical systems $\text{Ti}^{3+}/\text{Ti}^{2+}$ and $\text{Ti}^{2+}/\text{Ti}(0)$ [previously determined potentiometrically (1,5,6)], it was possible to obtain a simulated curve (solid line on figure 1a) which fits well the experimental points, thus verifying the consistency of the proposed electrochemical reactions. From this analysis, we have obtained the values of the intrinsic rate constants k_0 and of the transfer coefficients α of these two redox systems (Table 1). $\text{Ti}^{3+}/\text{Ti}^{2+}$ can be considered as quasi-reversible whereas titanium deposition appears irreversible.

3.2. Chronopotentiometric analysis of the titanium electrochemical systems.

$\text{Ti}^{3+}/\text{Ti(IV)}$ electrochemical system.

Figure 2a gives typical chronopotentiograms obtained at a tungsten electrode for imposed anodic current density values ranging from 29 to 42 mA.cm^{-2} . We observe waves whose quarter wave potentials $E_{t/4}$ are very close to the value of the $\text{Ti}^{3+}/\text{Ti(IV)}$ standard potential (itself equal to the half wave potential $E_{1/2}$ of the oxidation curve of figure 1a). For times higher than the transition times τ , potentials reach values relative to the oxidation of chloride ions into chlorine. Analysis of the variation of the transition time as a function of imposed current density values j_0 (figure 2b) confirms that the electrochemical reaction is diffusion-controlled (Sand's law). From the slope of the straight line obtained by plotting j_0 versus $\tau^{-1/2}$, we obtained for the diffusion coefficient D of Ti^{3+} the value $D = (1.0 \pm 0.1) \cdot 10^{-5} \text{ cm}^2.\text{s}^{-1}$ which is slightly lower than the value determined by chronoamperometry.

Current reversal chronopotentiometry has given the following additional information. By reversing the current at various times of electrolysis (and for several current values) as shown in figure 2c, we have been able to demonstrate that titanium(IV) is produced as a soluble species. In fact, the ratio of τ_{red} (transition time corresponding to the reduction of part of the species formed during electrolysis of duration t_{ox}) to t_{ox} is close to 1/3 whatever the imposed current values (figure 2d).

Ti^{3+} reduction.

Concerning the reduction of Ti^{3+} , chronopotentiometric transients show that this reduction effectively occurs in two successive steps (figure 3a). By measuring the corresponding transition times τ_1 and τ_2 , we observe that τ_2 is about eight times higher than τ_1 . This result is in good agreement with an exchange of one electron for the first reduction step, and of two electrons for the second one (7a).

By using current reversal techniques (figure 3b), we can prove the formation of

soluble titanium(II) species during the first electrochemical reaction followed by the electrodeposition of metallic titanium. In fact, the ratio of the reoxidation transition time τ_{ox} to the global reduction electrolysis time t_{red} takes the value of 1/3 for potentials ranging from -1.95 to -2.15 V, and takes the value 0.6 for potentials lower than -2.3 V. A value close to 0.6, and not unity which is generally observed for a one step electrochemical deposition, is obtained because of the intermediate step leading to Ti^{2+} ions.

3.3. A.C. Impedance measurements.

The analysis of the i-E reduction curves performed above allowed us to determine the kinetic characteristics of the electrochemical reactions of the Ti^{3+} reduction. Concerning the $Ti^{3+}/Ti(IV)$ redox system, which appears reversible from i-E oxidation curve, we had to use another technique for obtaining the corresponding value of the intrinsic rate constant and that of the transfer coefficient. Because of the large frequency range which can be explored, A.C. impedance measurements had proved to be the best method for that study.

Experimental data resulting from measurements performed at a potential equal to -0.50 V are reported in the complex plane (Nyquist plot) in figure 4a and as a function of frequency (Bode plots) in figures 4b and 4c. These spectra clearly show one capacitive loop at high frequencies (from 100 to 5 kHz) and a Warburg behavior for frequencies ranging from 5 kHz to about 0.1 Hz (the phase angle tends towards -45°). Below this last frequency value, as indicated by the Bode phase plot (figure 4c), we can observe a decrease in the phase angle due to the thermal convection leading to a finite thickness diffusion layer δ (already determined).

Relying on the results obtained by pulse techniques, impedance spectra have been computerized by using a simple model involving two mass transfer steps (Ti^{3+} and produced $Ti(IV)$ diffusions) and one electron charge transfer step. Simulated curves are represented as solid lines in figures 4. The good fit obtained corresponds to the kinetic parameter values given in Table 1, to a double layer capacitance C_d of $(125 \pm 40) \cdot 10^{-6} \text{ F.cm}^{-2}$ and to an electrolyte resistance R_e of $(0.08 \pm 0.01) \Omega$ (for a working electrode surface area equal to 1 cm^2).

4. CONCLUSION.

By using both pulse and A.C. impedance techniques, it was possible to accurately determine the kinetic parameters characterizing the mass and the charge transfers occurring, in the electrochemical oxidation and reduction reactions of Ti^{3+} ions.

Dahl *et al.* had estimated the diffusion coefficient of Ti^{2+} ion at 723 K from their study on electrodeposition of titanium from $TiCl_2$ solutions (8). They considered that this diffusion coefficient is in the range of $(1-3) \cdot 10^{-5} \text{ cm}^2 \cdot \text{s}^{-1}$. By comparing with our work we can assert that the diffusion coefficients of Ti^{3+} and Ti^{2+} are close to each other. Moreover, we have been able to put a figure to the effect of thermal convection by determining the resulting thickness δ of the diffusion layer. The value obtained is in good agreement with that which can be estimated by using the relation $\delta = \sqrt{2Dt}$ (7b) knowing

the value of the diffusion coefficient of Ti^{3+} and that of the duration t for which steady-state diffusion conditions due to thermal convection are reached. In fact from the corresponding value of t ($\sim 10s$) deduced from the chronoamperometric measurements, we find $\delta = 0.017 \pm 0.005$ cm.

Concerning the intrinsic rate constants k_0 of the electrochemical systems of titanium, only the one related to the $Ti^{2+}/Ti(0)$ redox system is available in the literature. Haarberg *et al.* (9) considered that the electrodeposition of titanium from Ti^{2+} is irreversible, as we have demonstrated in this work. The value of k_0 which can be calculated from their work ($1.5 \cdot 10^{-6} cm^{-1}$) is very close to ours.

The results described in this paper complete those of our previous work concerning the thermodynamic properties of titanium and its compounds with iron and oxygen (1,4).

ACKNOWLEDGEMENTS.

We wish to thank the C.N.R.S. for its financial support (A.T.P. N° 70.0002).

REFERENCES.

- (1) D.M. Ferry, G.S. Picard and B.L. Trémillon, Trans. Inst. Min. Met., Sect. C, (1987), in press.
- (2) G. Picard, F. Séon and B. Trémillon, J. Electrochem. Soc., **129** (1982) 1450.
- (3) F. Séon, G. Picard and B. Trémillon, Electrochim. Acta, **28** (1983) 209.
- (4) D. Ferry, E. Noyon and G. Picard, J. Less Common Metals, **97** (1984) 331.
- (5) D.M. Ferry, G.S. Picard and B.L. Trémillon, Communication presented at the EUCHEM Conference on Molten Salts (1986) Geiranger, Norway.
- (6) D.M. Ferry, G.S. Picard and B.L. Trémillon, 170th Meeting of the Electrochemical Society, Extended Abstracts. Vol 86-2, p 988, San Diego, California, USA (1986).
- (7) A.J. Bard and L.R. Faulkner in "Electrochemical Methods. Fundamentals and Applications". John Wiley and Sons Editors, New-York, 1980.
a) p 268, b) p129.
- (8) G. Dahl, A. Hjelset, W.R. Rolland, Å. Sterten, J. Thonstad and R. Tunold, 34th meeting of the International Society of Electrochemistry; Extended Abstracts; (1983) p. 1131; held in Erlangen (Germany), Sept. 18-23, 1983.
- (9) G.M. Haarberg, W.K. Rolland, Å. Sterten, J. Thonstad and S. Øye, Communication presented at the EUCHEM Conference on Molten Salts (1986) Geiranger, Norway.

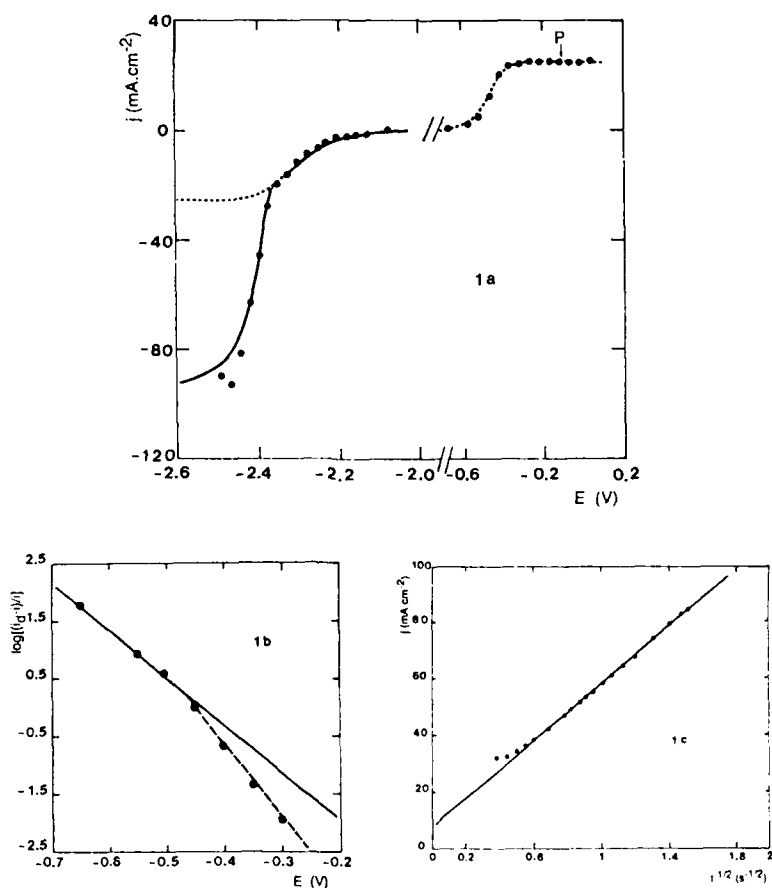


Figure 1 : a) i - E curves in the steady-state conditions due to thermal convection (concentration of $\text{Ti}^{3+} = 0.11 \text{ mol.kg}^{-1}$).
 b) Bilogarithmic analysis of the oxidation wave.
 c) Verification of Cottrell's law at a potential corresponding to the diffusion limiting current (point P in figure 1a).

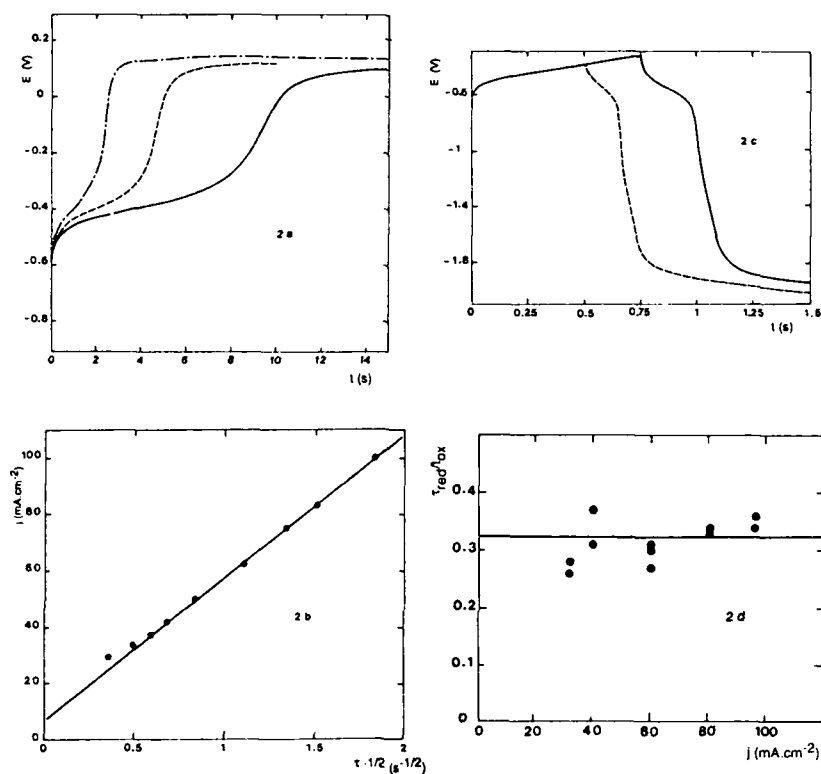


Figure 2 : a) Typical chronopotentiograms for the oxidation of Ti^{3+} ions (concentration of these ions : $8 \cdot 10^{-2} \text{ mol.kg}^{-1}$). Current densities : $j = 29, 33$ and 42 mA.cm^{-2} .
 b) Verification of Sand's law.
 c) Chronopotentiograms with current reversal. $j = 62 \text{ mA.cm}^{-2}$.
 d) Ratio of τ_{red} (transition time corresponding to the reduction of the species formed during electrolysis of duration t_{ox}) to t_{ox} for various current densities.

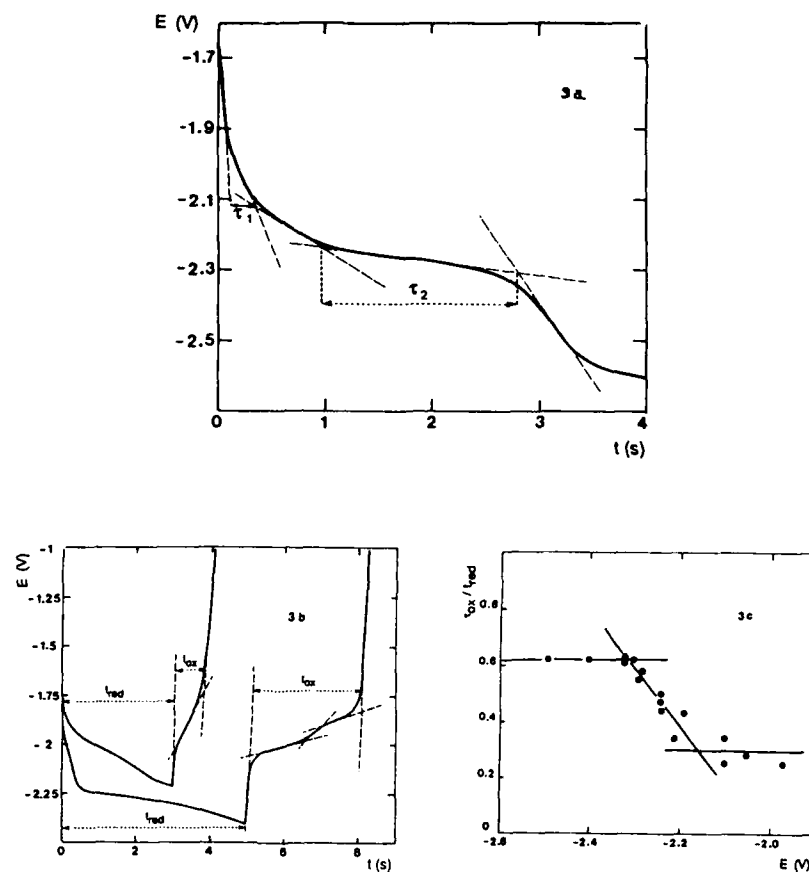


Figure 3 : a) Typical chronopotentiogram for the reduction of Ti^{3+} into Ti^{2+} and metallic titanium (concentration of Ti^{3+} : $7.5 \cdot 10^{-2} \text{ mol.kg}^{-1}$).
 b) Chronopotentiograms with current reversal at potentials corresponding to the first reduction step (formation of Ti^{2+} ions) and to the second reduction step (leading to the electrodeposition of metallic titanium).
 c) Variation of the ratio τ_{ox}/τ_{red} versus reversal potential.

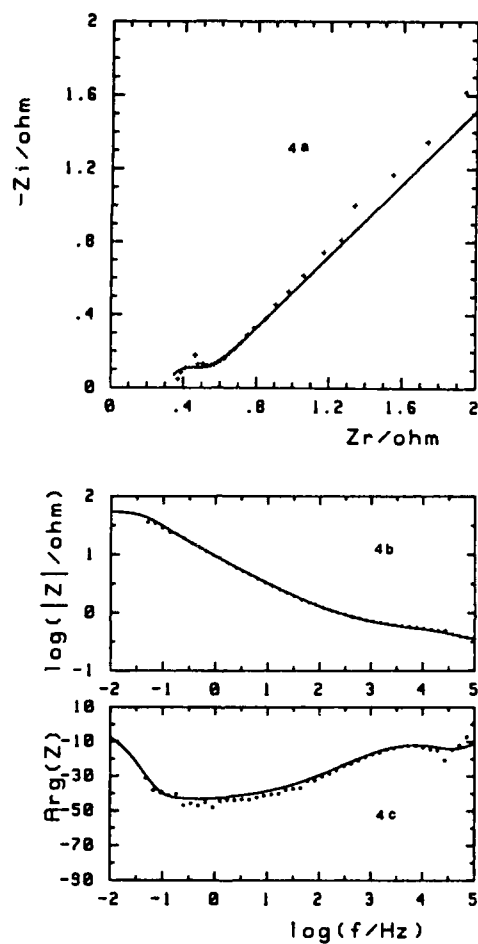


Figure 4 : Nyquist (a) and Bode (b-c) diagrams of the oxidation of Ti^{3+} (imposed potential : -0.5 V) and corresponding simulated curves.

Electrochemical system	E° (V) ref: $\text{Cl}^-/\text{Cl}_2(1 \text{ atm})$	k_0 (cm.s^{-1})	α
$\text{Ti}^{3+}/\text{Ti(IV)}$	-0.44 ± 0.02	0.2 ± 0.1	0.70 ± 0.05 (ox)
$\text{Ti}^{2+}/\text{Ti}^{3+}$	-1.94 ± 0.01	$(2 \pm 1)10^{-3}$	0.50 ± 0.05
$\text{Ti(0)}/\text{Ti}^{2+}$	-2.05 ± 0.01	$(3 \pm 1)10^{-6}$	0.60 ± 0.05 (red)

Table 1 : Kinetic characteristics of the different redox systems of titanium in LiCl-KCl eutectic melt at 743 K.

CARBON ANODE REACTION AND INTERCALATION
COMPOUNDS IN FLUORIDE MELT

Nobuatsu WATANABE

Applied Science Research Institute, 49
Ooi-cho, Tanaka, Sakyo-ku, Kyoto, 606,
Japan

and

Tsuyoshi NAKAJIMA

Department of Industrial Chemistry, Faculty
of Engineering, Kyoto University, Sakyo-ku,
Kyoto, 606, Japan

ABSTRACT

The large overpotential on carbon anode in fluoride melt is due to a strong chemical interaction of discharged fluorine with carbon, which provides graphite fluoride film having an extremely low surface energy. When carbon anode is somewhat covered by thin graphite fluoride film, the wettability of anode by electrolyte decreases and anode effect occurs. Graphite fluoride film is directly detected by ESCA. Graphitization of carbon anode significantly affects the critical current density for anode effect. Namely amorphous carbon gives a higher critical current density than high quality graphite because graphite fluoride film easily decomposes to fluorocarbon gases. Recent investigation has revealed that a small amount of water contained in KF_2HF melt gives serious effect to the formation of graphite fluoride film on carbon anode. The effect of LiF addition to the melt first appears when water content is less than 0.02%. The role of LiF is the catalytic action for fluorine intercalation in graphite to give a highly conductive intercalation compound.

INTRODUCTION

The study on the mechanism of anode effect in fluoride melts had already started at the end of 19th century, being concerned with the electrolytic production of aluminum metal in cryolite melt. The first theory was that a high resistivity film was formed on the carbon anode by discharge of fluoride ion(1). This is similar to the passivating state of metal, which was supported for 20 years. However, it was found in 1916 that voltage increase is not so high as that experimentally observed when calculated from the resistivity of the film. Second theory was that gas film was formed between electrode and electrolyte by vaporization of molten salt due to abnormal generation of Joule heat(2). This

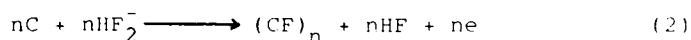
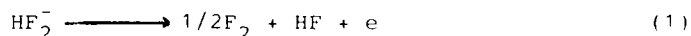
view had an advantage that anode effect was understandable from charged gas bubbles, surface tension of molten salt, viscosity, density and so on.

The authors proposed a new interpretation on the basis of the studies on wettability of carbon electrode by electrolyte (3) and overpotential in fluorine evolution reaction (4). Carbon anode reactions including anode effect are understood by the formation and properties of graphite intercalation compound on the anode surface. This paper summarizes carbon anode reactions in KF2HF melt.

RESULTS AND DISCUSSION

1. Overpotential for the discharge reaction of fluoride ion on carbon electrode

Two kinds of overpotentials are always observed on carbon anode reaction in KF2HF melt (Fig.1). One increases rapidly as soon as the circuit is closed (π_p), but another increases slowly with time (π_s). Tafel equation is applicable at a current density less than 2 Adm^{-2} where π_p is under 1 V (Fig.2). However, π_s varies with time and reaches such a high potential at which anode effect occurs as the current density increases. Fig.2 shows that π_p obeys the Tafel relation, however, π_s is strongly dependent on the crystallinity of carbon electrode, i.e. being different between carbon and graphite electrodes. Fig.3 is the variation of cell voltage and a contact angle of electrolyte on anode as a function of time. Variation of the contact angle is very large compared with that of cell voltage. This phenomenon is interpreted as follows. Discharge of fluoride ion on carbon electrode is given by equation (1).



However, $(\text{CF})_n$ film formation proceeds at the same time by the reaction of discharged fluorine with carbon. If this film has a low surface energy, it becomes gradually difficult that carbon electrode is wetted by electrolyte. With increasing contact angle, a real current density also significantly increases, which would facilitate the reaction of discharged fluorine with carbon. The low surface energy of $(\text{CF})_n$ is demonstrated by contact angle measurement of $(\text{CF})_n$ prepared by direct fluorination of graphite at a high temperature (Table 1). Fig.4 is a cyclic voltammogram of carbon electrode in KF2HF melt containing a small amount of water. The solid line indicates the first scan, in which peak B shows the discharge of OH^- ion (oxygen evolution) and peak F is the discharge of F^- ion (fluorine evolution). The

dashed line is the second scan, in which the peak corresponding to oxygen evolution disappears and only fluorine evolution is observed. A shoulder D is observed only in the first scan. This has not been clarified for a long time. However, a recent study suggests that peak D corresponds to the formation of graphite oxide film, which is decomposed by the attack of fluorine. If a low surface energy film is partly formed on the anode after first scan, the surface energy of anode might be decreased. This would result in the difficulty in water adsorption on anode surface. However, the adsorption of fluoride ion is possible because of the lower surface tension of HF than water. A large overpotential observed on carbonaceous anode is thus understood by postulating a low surface energy film on anode. Anode effect is considered to be such a state that anode potential extremely increases with decrease in the wettability of anode by electrolyte. The film on carbon anode cannot be detected by X-ray diffraction probably because it is too thin to be detected. $(CF)_n$ film is confirmed by ESCA measurement. Fig. 5 shows ESCA spectra of pyrolytic graphite anode which is obtained immediately after anode effect. C_{1s} peak around 288-289 eV indicates C-F covalent bond and another peak at 284.3 eV corresponds to C-C bond of graphite.

2. Several factors influencing anode effect

Occurrence of anode effect is strongly affected by crystallinity of carbon anode and fluoride additives. Fig. 6 is the critical current density (the highest current density just before anode effect happens) as a function of graphitization degree of carbon anode. Critical current density remarkably decreases when graphitization degree exceeds 50%. This is more clearly observed in the melt containing NiF_2 . Amorphous carbon reacts more easily with fluorine than high quality graphite. However, since the reaction of amorphous carbon with discharged fluorine proceeds more faster than graphite, it produces fluorocarbons such as CF_4 and C_2F_6 , giving new carbon surface with high roughness. On the other hand, the reaction of graphite with fluorine gives a more stable $(CF)_n$ film. This is similar to the behavior of layer plane and edge plane of pyrolytic graphite as shown in Fig. 5.

3. Effect of a trace of water and solid LiF on anode effect

LiF is often added to the electrolyte so that fluorine evolution may be continued at a high current density. The solubility of LiF in KF_2HF melt is 0.6-0.8 wt% at 100 °C. The addition of LiF over the solubility gives a colloidal solution of KF_2HF melt, in which the increase in the electrolytic current is first observed. The impregnation of LiF in carbon electrode is more effective than the addition of LiF to the melt for preventing the anode effect. This is

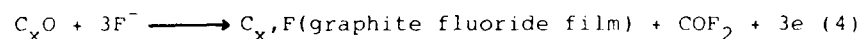
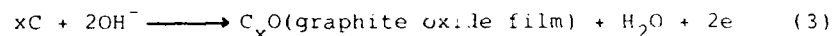
shown in Fig.7, which suggests that solid LiF acts at anode/electrolyte interface.

The following explanation was proposed concerning the role of LiF suspended in KF₂HF melt. Fluorine gas bubbles having a negative charge are strongly attracted to anode surface by anodic polarization. LiF particles having a positive charge are adsorbed onto the surface of fluorine gas bubbles at anode/electrolyte interface. Neutralization of the charges facilitates the separation of gas bubbles from anode surface(5). Based on this interpretation, it was attempted to measure the potential of LiF particles in liquid hydrogen fluoride. However, no potential was detected by such an experiment(6).

Recently, a new fluorine-graphite intercalation compound was successfully synthesized in the presence of metal fluoride such as LiF, CuF₂, or AgF(7-9). It shows high electrical conductivity and stability. The intercalated fluorine has a nearly ionic bond with graphite, and the carbon layer is still plane after intercalation of fluorine. Based on the formation of fluorine-graphite intercalation compound in the presence of LiF, a new proposal was given on the role of solid LiF suspended in KF₂HF melt or impregnated in carbon electrode(10). It is that the occurrence of anode effect may be suppressed by the formation of graphite intercalation compound(GIC) which gives a high electrical conductivity to carbon anode and ensures the wettability of anode surface by electrolyte.

Fig.8 is the variation of anode potential under various conditions as a function of quantity of electricity. When water content in KF₂HF melt is relatively large, that is, ca. 0.05%, anode effect occurs in a short time compared with the case that water content is less than 0.02%, almost independently of whether LiF is added to the melt or not. Anode effect occurs only slightly later in the melt containing 3 wt% LiF. However, when water content is less than 0.02%, the effect of LiF added to the melt distinctly appears as shown in Fig.8. In this case, it is required that addition of LiF is made after water content is decreased to less than 0.02% by preelectrolysis. When preelectrolysis is done after addition of LiF to the melt, LiF give no effect on the suppression of anode effect probably because water in the melt is adsorbed by LiF particles. This is supported from the fact that water content decreases from 0.05% to 0.03% by addition of 3 wt% LiF.

Fig.9 shows the GIC and graphite fluoride film formed during electrolysis under various conditions. In the melt containing ca. 0.05% H₂O, GIC is not formed but graphite fluoride film is easily prepared and anode effect occurs by a small quantity of electricity.



However, when water content is less than 0.02%, stage 6 and 4 GIC's are formed even in the melt without LiF, giving 23.7 Å and 16.2 Å as the repeat distance. Since no LiF is contained in the melt, this would be due to the electrochemical intercalation of HF_2^- into graphite.



The repeat distance(d_c) of this GIC is expressed as follows as a function of stage number, n.

$$d_c(\text{Å}) = 6.05 + 3.35(n - 1) \quad (6)$$

When LiF is added to the melt containing a trace of water less than 0.02%, the lower stage GIC(stage 3) is formed without occurrence of anode effect. This would be due to the intercalation of fluorine in graphite by the catalytic action of solid LiF in addition to the electrochemical intercalation of HF_2^- .



As the product is a mixture of $C_n^+HF_2^-$ and $C_n^+F_m^-$, it is described as $C_xF(HF)_y$.

There are two roles of solid LiF in KF2HF melt. One is the adsorption of water in the melt which contains a relatively large amount of water. Water-adsorbed LiF particles have no function to suppress the occurrence of anode effect. The film of adsorbed water on LiF particles would prevent the interaction of fluorine with LiF. LiF should be added to the melt after water content is decreased by preelectrolysis. When water content in KF2HF melt is less than 0.02%, water adsorption by suspended LiF can be neglected because the peak ratios for oxygen and fluorine evolution in cyclic voltammograms are the same before and after addition of LiF to the melt.

Another effect is the intercalation of fluorine in graphite as indicated in equation (7). This appears when water content is small, less than 0.02%. The reaction (7) occurs together with the electrochemical intercalation of HF_2^- in graphite, giving a lower stage GIC than that formed in the melt without LiF. The formation of GIC having a high electrical conductivity would ensure the sufficient wettability of anode by KF2HF melt.

REFERENCES

1. M. Guntz, *Compt. Rend.*, **117**, 732 (1883)
2. V. Czepinski, *Z. anorg. Chem.*, **19**, 245 (1899)
3. G. Oesterheld and E. Brunner, *Z. Electrochem.*, **22**, 38 (1916)
4. N. Watanabe, M. Ishii and S. Yoshizawa, *Denki Kagaku*, **29**, 492 (1961)
5. N. Watanabe, M. Ishii and S. Yoshizawa, *ibid.*, **30**, 171 (1962)
6. N. Watanabe, M. Inoue and S. Yoshizawa, *J. Electrochem. Soc. Jpn.*, **31**, 113 (1963)
7. H. Imoto, *Thesis of Kyoto University* (1977) p.93
8. T. Nakajima, M. Kawaguchi and N. Watanabe, *Synthetic Metals*, **7**, 117 (1983)
9. T. Nakajima, I. Kameda, M. Endo and N. Watanabe, *Carbon*, **24**, 343 (1986)
10. T. Nakajima, T. Ino, N. Watanabe and H. Takenaka, submitted to *Carbon*
11. N. Watanabe, *Proceedings of the first International Symposium on Molten Salt Chemistry and Technology*, Kyoto, Japan (1983) p.21

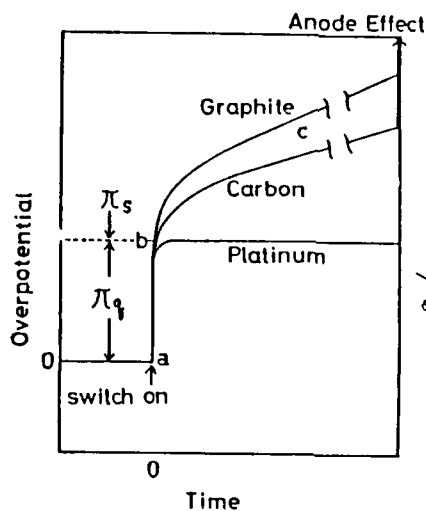


Fig.1 Overpotentials of carbon anode

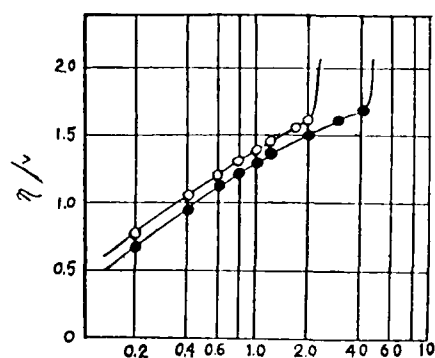


Fig.2 Relation between overpotential and current density

O:graphite, ●:carbon

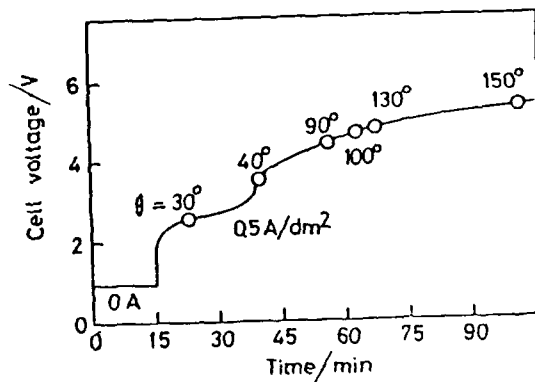


Fig.3 Change in cell voltage and contact angle as a function of time

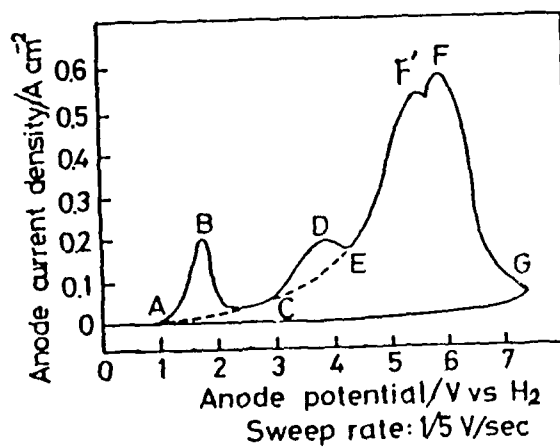


Fig.4 Polarization curves of carbon anode in KP₂HF melt at 100°C

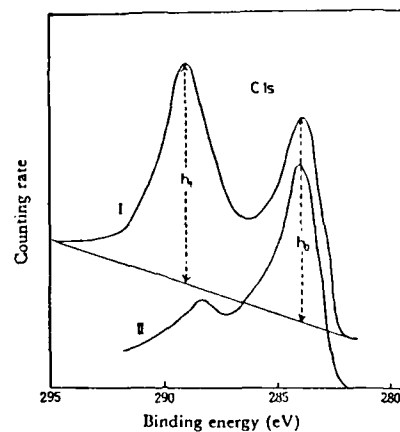


Fig. 5 ESCA spectra of pyrolytic graphite anodes immediately after the anode effect.
I: Layer-plane,
II: edge plane.

Table 1 Surface Free Energies Obtained from Contact Angles

Solid	γ_s^d / erg cm ⁻² ^a	Surface Composition
Graphite fluoride, [CF] _n	6±3	≥CF for basal plane. >CF ₂ , -CF ₃ for edge plane
Perfluorododecanoic acid (on Pt)	10.4	-CF ₃
Poly(hexafluoropropylene)	18.0	-CF ₃ , >CF ₂ , ≥CF
Poly(tetrafluoroethylene)	19.5	>CF ₂

^a erg = 10⁻⁷ J.

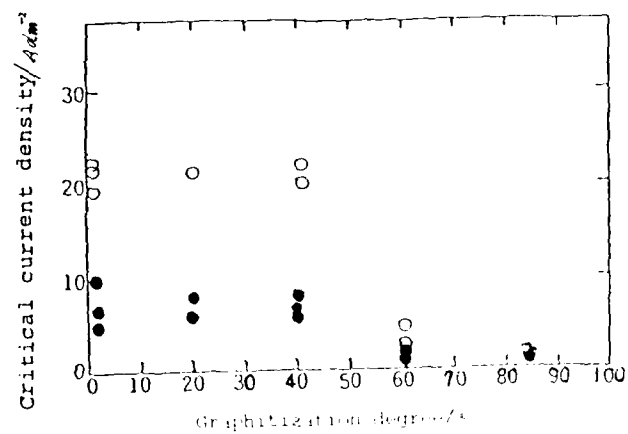


Fig.6 Effect of graphitization degree on critical current density

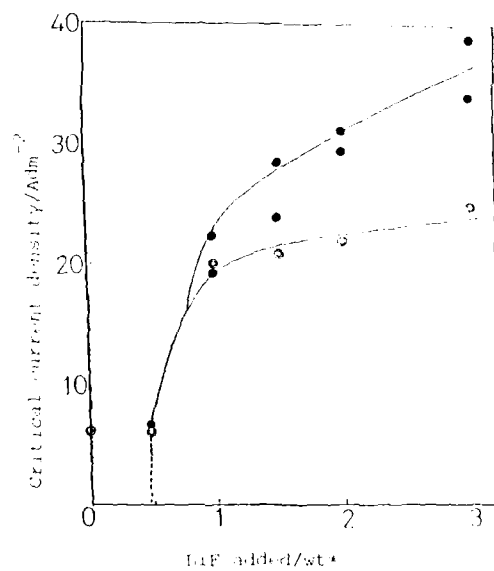


Fig.7 Effect of LiF added to KF₂HF melt and impregnated in carbon electrode

○: added to KF₂HF, ●: impregnated in electrode

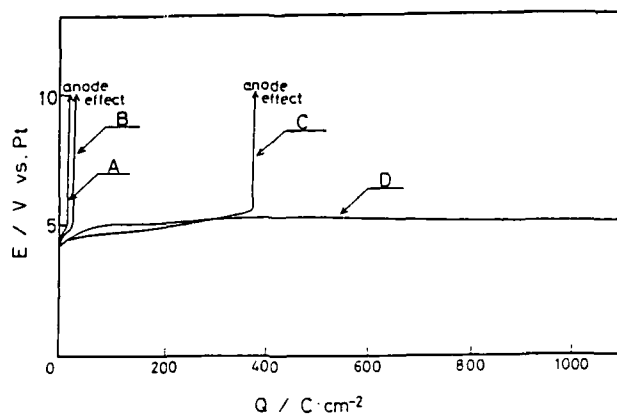


Fig.8 Variation of anode potential with electrolysis

A, $H_2O \approx 0.05\%$, LiF:0 wt%, B, $H_2O \approx 0.05\%$, LiF:3 wt%,
C, $H_2O < 0.02\%$, LiF:0 wt%, D, $H_2O < 0.02\%$, LiF:3-6 wt%

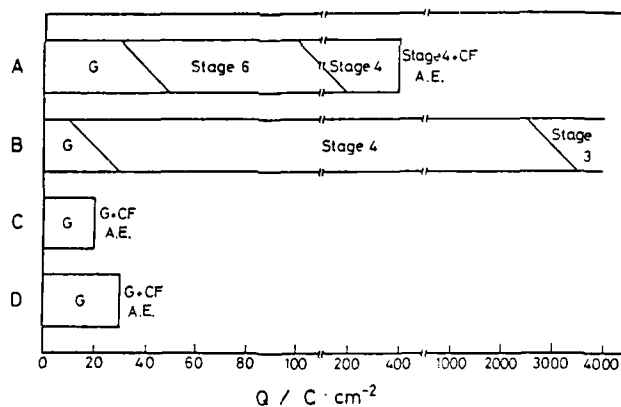


Fig.9 Stage number of GIC formed in grafoil anode

A, $H_2O < 0.02\%$, LiF:0 wt%, B, $H_2O < 0.02\%$, LiF:3-6 wt%,
C, $H_2O \approx 0.05\%$, LiF:0 wt%, D, $H_2O \approx 0.05\%$, LiF:3 wt%

G:graphite, CF:graphite fluoride film,

A.E.:anode effect

ELECTROCHEMICAL AND CHEMICAL INTERCALATION
OF FLUORINE IN GRAPHITE IN THE KF₂HF MELT

Tsuyoshi NAKAJIMA and Toru OGAWA
Department of Industrial Chemistry, Faculty
of Engineering, Kyoto University,
Sakyo-ku, Kyoto, 606, Japan

Nobuatsu WATANABE
Applied Science Research Institute,
49 Ooi-cho, Tanaka, Sakyo-ku, Kyoto, 606, Japan

ABSTRACT

Effect of a trace of water on graphite anode reaction has been investigated in the KF₂HF melt at 100°C. Cyclic voltammetry shows that with increasing water content from 0.01% to 0.05%, anode potential for the formation of graphite oxide and graphite fluoride film on graphite electrode is shifted to a lower potential. This would be due to the increase in anode surface area by the decomposition of graphite oxide film, which is caused by the reaction with discharged fluorine.

When water content is ca. 0.05%, anode effect occurs in a short time, namely graphite fluoride having a low surface energy is easily formed on graphite. However, when it is 0.01%-0.02%, stage 4 intercalation compound of graphite, C⁺HF₂⁻ is prepared. Addition of 3-6 wt% LiF to the KF₂HF melt gives stage 3 C_xF(HF)_y without occurrence of anode effect.

INTRODUCTION

Fluorine gas is generally produced by electrolysis of KF₂HF melt at 100°C. It is difficult due to anode effect to electrolyze KF₂HF melt at a high current density. Anode effect is caused by a low surface energy of graphite fluoride film formed on carbon anode, i.e. the wettability of anode surface by electrolyte extremely decreases owing to the low surface energy of graphite fluoride film. Addition of a metal fluoride such as LiF having a low solubility to KF₂HF melt is effective for preventing anode effect. However, the role of LiF suspended in the melt or impregnated in anode has not been clarified for a long time.

Recently we synthesized a new fluorine-graphite intercalation compound in the presence of a metal fluoride such as LiF, CuF₂ or AgF(1-3). The metal fluoride is considered to act as a catalyst for fluorine intercalation in graphite. Among metal fluorides examined, AgF shows the highest

catalytic ability because of the strong chemical interaction with fluorine and the low melting point. Based on the formation of fluorine-graphite intercalation compound, a new interpretation was proposed on the role of solid LiF(4). It is that the occurrence of anode effect may be suppressed by the formation of graphite intercalation compound(GIC) which gives a high electrical conductivity to carbon anode and ensures the wettability of anode surface by electrolyte. Recent investigation on this problem has revealed that not only LiF but also a trace of water contained in the melt give serious effects to graphite anode reaction(5). In this paper, we report the effect of a trace of water on graphite anode reaction and intercalation of fluorine in graphite in the KF2HF melt.

EXPERIMENTAL

The electrolytic cell is made of polytetrafluoroethylene and polytrifluorochloroethylene. Working electrode and counter electrode are grafoil(graphite sheet, 35X6 mm) and nickel plate with a large surface area, respectively. Reference electrode is Pt wire. Fluorine evolution is made by cyclic voltammetry and galvanostatic electrolysis at 33 mAcm⁻². The water content in the melt was estimated by the same method reported previously(5). After electrolysis, graphite anode was analyzed by X-ray diffractometry.

RESULTS AND DISCUSSION

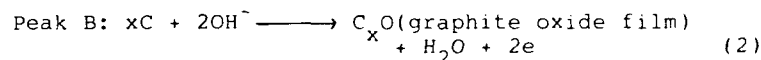
1. Effect of a trace of water on the anode reaction

Fig.1 shows the cyclic voltammograms for graphite anode in the KF2HF melts containing different amounts of water. All the voltammograms were obtained at first scan. It has been pointed out in a previous paper(5) that a small amount of water (less than 0.1%) significantly influences the fluorine evolution reaction on graphite anode. It is known that peak A corresponds to oxygen evolution reaction by electrolysis of water contained in the melt.

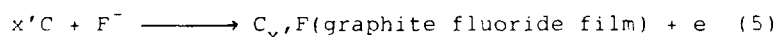
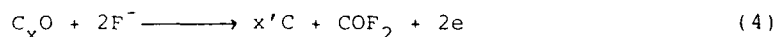


With decreasing water content from 0.05% to 0.01%, the intensity of peak A decreases. Peak A disappears after 2nd scan because the wettability of anode by electrolyte decreases due to graphite fluoride prepared at 1st scan. Peaks B and C, however, move to higher potentials with decreasing water content. Peak B, observed as a shoulder in most cases, also disappears after 2nd scan. This has not been identified for a long time. When the water content is relatively large, anode effect immediately occurs, i.e. graphite fluoride is easily prepared on graphite anode(5).

It has been also found that graphite oxide is easily fluorinated to be graphite fluoride at 100-200°C because graphite oxide is more unstable than fluoride. From these facts, peak B would be the formation of graphite oxide on the anode surface.



Graphite oxide has a covalent bond as well as graphite fluoride, therefore it is an electric insulator. After peak B, since fluorine evolution occurs vigorously, graphite oxide is attacked by discharged fluorine, which would give the anode more active and larger surface than that of pristine graphite. This facilitates the reaction of graphite anode with discharged fluorine, i.e. the formation of graphite fluoride film. Thus the following reactions would occur between peak B and peak C.



Therefore with increasing water content, the formation of graphite oxide and graphite fluoride are both accelerated. This would be the reason why the peaks B and C are shifted to higher potentials with decreasing water content.

2. Intercalation of fluorine in graphite

When water content in the melt is ca. 0.05%, anode effect occurs in a short time, i.e. anode surface is covered with graphite fluoride at least to some extent without formation of ionic intercalation compound of graphite. This is almost the same even when LiF is added to the melt(4). However, with decreasing water content, GIC having an ionic bond is prepared electrochemically while the formation of graphite fluoride becomes difficult.

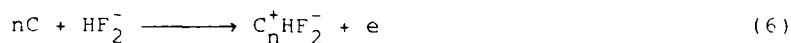


Fig.2 is the X-ray diffraction patterns of pristine grafoil and GIC's prepared in KF2HF melt containing 0.01-0.02% water. GIC formed was a mixture of stage 4-6 till 100 C.cm⁻² (Fig.2 (C) (D)), after which stage 4 GIC was observed until anode effect occurred (Fig.2 (E) (F)), though the crystallinity of GIC increased as shown in the figure. On the other hand, when LiF was added to the melt by 3-6 wt%, intercalation of fluorine was considerably accelerated without occurrence of anode effect. This is due to the

catalytic intercalation of fluorine in graphite by solid LiF suspended in the melt as reported previously(5).



GIC of stage 4+5 was first formed and stage number remained 4 till 1000 C·cm⁻². When quantity of electricity reached 3000 C·cm⁻², stage 3 GIC became a main component. Fig.3 (G) shows the typical stage 3 GIC obtained at 4000 C cm⁻².

REFERENCES

1. T. Nakajima, M. Kawaguchi and N. Watanabe, Synthetic Metals, **7**, 117 (1983)
2. T. Nakajima, I. Kameda, M. Endo and N. Watanabe, Carbon, **24**, 343 (1986)
3. T. Nakajima, T. Ino, N. Watanabe and H. Takenaka, submitted to Carbon
4. N. Watanabe, Proceedings of First International Symposium on Molten Salt Chemistry and Technology, p.21, Kyoto, Japan (1983)
5. T. Nakajima, T. Ogawa and N. Watanabe, J. Electrochem. Soc., **134**, 8 (1987)

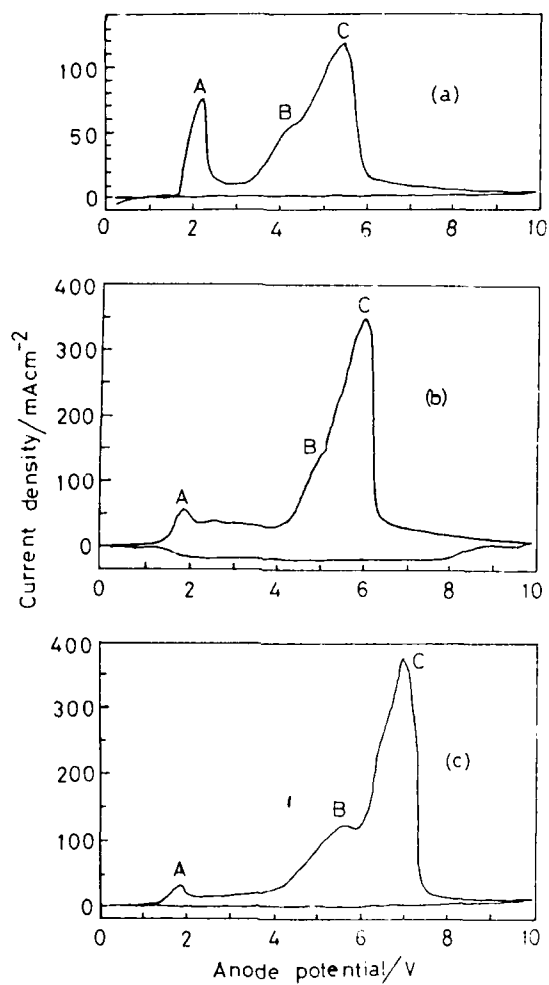
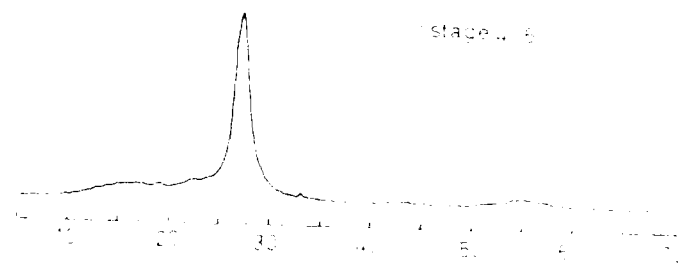
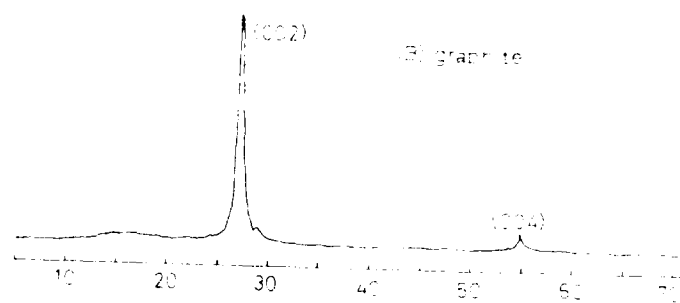
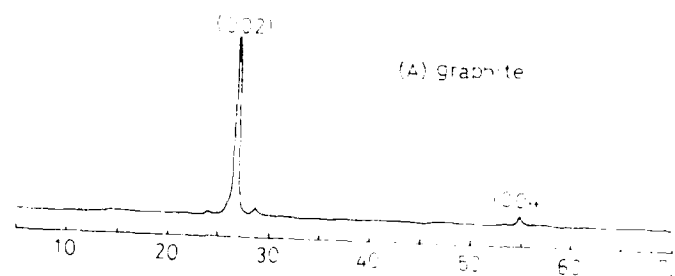


Fig.1 Cyclic voltammograms for graphite anode in KF₂HF melt
 Water content: (a) 0.05%, (b) 0.03%, (c) 0.01%
 Scan rate: 10 mV/sec



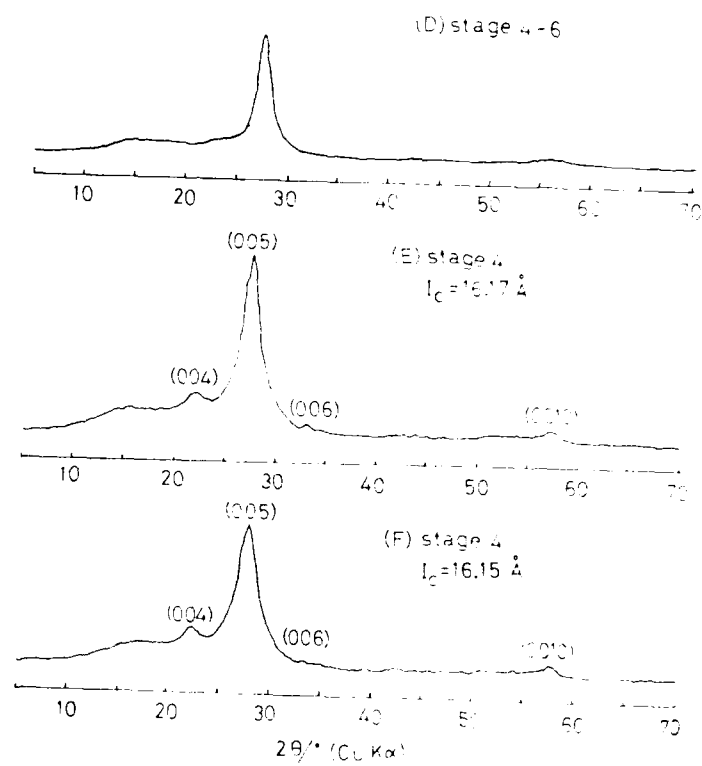
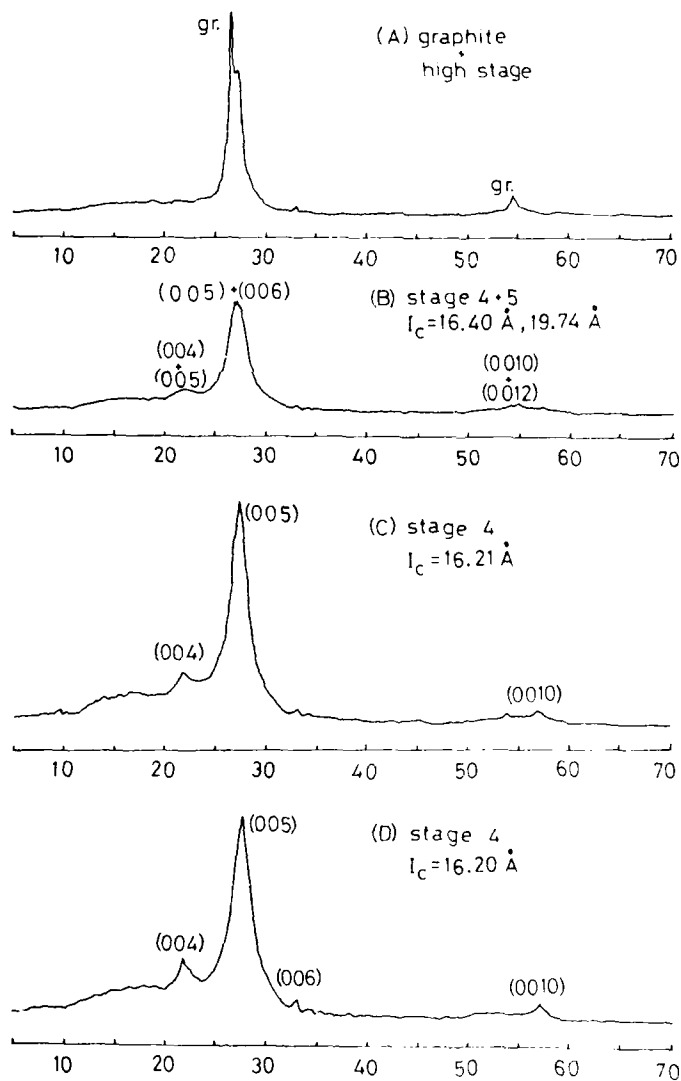


Fig.2 Change in X-ray diffraction patterns obtained in the salt containing 0.2% - 0.02% water as a function of quantity of electricity

Quantity of electricity (C·cm²): (A)0, (B)20, (C)60, (D)100, (E)150, (F)300



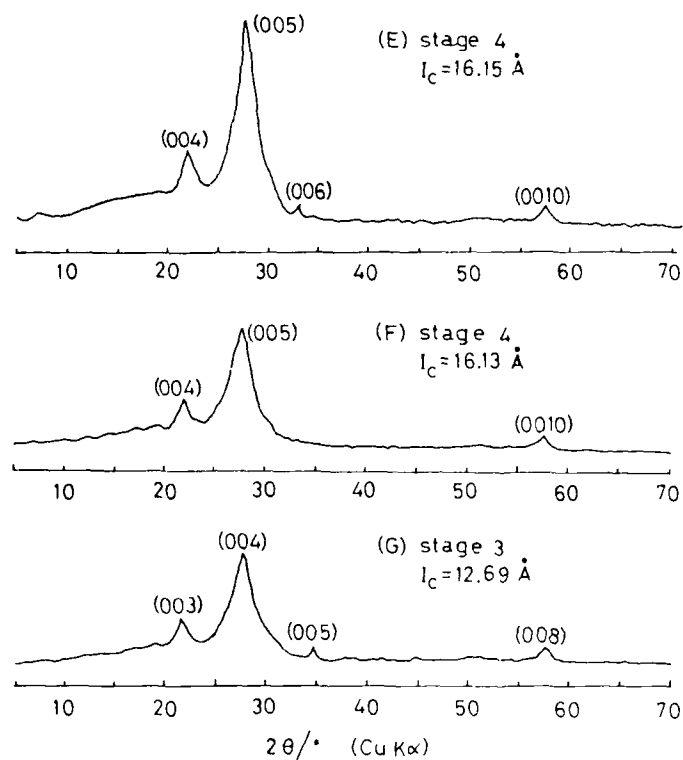


Fig.3 Change in X-ray diffraction patterns obtained in the melt containing 0.01 -0.02% water and 3-6 wt% LiF as a function of quantity of electricity

Quantity of electricity($C \cdot cm^{-2}$): (A)20, (B)60, (C)100, (D)200, (E)400, (F)1000, (G)4000

STUDY OF CF_x PASSIVATING LAYERS ON CARBON ELECTRODES IN RELATION TO FLUORINE PRODUCTION

M. CHEMLA and D. DEVILLIERS

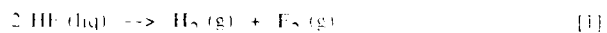
Universite P. & M. Curie : Laboratoire d'Electrochimie
4, Place Jussieu : 75252 PARIS Cedex 05

ABSTRACT

The electron transfer for fluorine evolution reaction on carbon anodes takes place through a non-homogeneous film of solid graphite fluoride. The deep layers are characterized by a good electrical conductivity whereas the external layers constitute a thin insulating film which acts as an energy barrier through which the current flows by tunnel effect. The consequence is that very low values are found for the β transfer coefficient. Chronopotentiometry experiments confirm the existence of two kinds of CF_x , depending on the potential of the working electrode. The reversibility of the redox system is discussed; then, the behavior of the CF_x formed on graphite and carbon anodes in the $2HF-KF$ melt is interpreted by an electrochemical formation reaction coupled with both diffusion and thermal decomposition processes.

INTRODUCTION

Fluorine is produced by the electrolytic decomposition of molten anhydrous $2HF-KF$, according to the equation:



Although it does not appear in this equation, the nature of the anodic material has a great influence on the overall mechanism. In all industrial cells, the evolution of fluorine takes place on graphite-free carbon anodes at about 100°C. The thermodynamic potential of decomposition of HF was demonstrated to be equal to 2.90 V, taking into account the activity of HF in the melt (1). However, a voltage of 8 to 12 volts is necessary in order to obtain the working current density $i = 10$ to $15 A dm^{-2}$. About 3 volts are required to overcome bath resistivity and more than 3 volts correspond to the electrode overvoltage. It results a poor energy efficiency and a considerable quantity of heat needing to be eliminated: nearly 150,000 joules per hour for an output of 4 kg of fluorine (2).

Since other electrolytes which have higher conductivity (such as $\text{NH}_4\text{F-nHF}$ melts) generate more corrosion, it seems that progress can be obtained in lowering the anodic overvoltage by a better understanding of the overall electrochemical mechanism.

It has been shown (1) that the thermodynamic potential of decomposition of HF leading to the formation of a layer of solid graphite fluoride CF_x on the anode surface is equal to 1.45 V whereas the fluorine evolution reaction only occurs at 2.90 V. Experimental evidence of the formation of graphite fluoride, starting at 2 V versus a platinum reference electrode, was given by ESCA measurements performed by Professor N. Watanabe and co-workers (3), and by mass-spectrometry experiments performed in our laboratory (4).

Among the properties of graphite fluoride, we must first consider the surface properties: graphite fluoride has a very low surface energy, so, the carbon anode covered with CF_x are not "wetted" by the melt: it means that the contact angle at the electrode-electrolyte interface is high, and thus the fluorine bubbles are lenticular and adherent to the electrode. In consequence, the electroactive surface of the anode is small since the gaseous layer acts as a very insulating barrier. One may partially solve this problem by using porous carbons for which the evolution of the gas takes place through the matrix of the electrode: the fragility may be avoided by using composite anodes which comprise a cylinder of dense carbon covered with a layer of porous carbon (5).

Now, let us consider the electrical properties of graphite fluoride: the electrical conductivity strongly depends on the stoichiometry of the compound. For example, Bartlett and co-workers (6) have shown that the conductivity is divided by 10^7 when x increases from 0.3 to 0.5. When x is greater than 0.5, the compound may be considered as an insulator. Due to its insulating properties, the CF_x film acts as a high potential barrier, which is responsible for the large energy loss in the electron transfer reaction at the interface. It has been suggested that the discharge of fluoride ions, leading to fluorine evolution, involves electron tunneling across the passivating film (7,8). The main characteristics of such a process are recalled in the next paragraph, as well as experimental results which support this hypothesis.

MECHANISM OF ELECTRON TRANSFER BY TUNNEL EFFECT

The general aspects of the Gurney-Gerischer theory have been reviewed in reference (9). In this theory, an electrochemical oxidation reaction is treated as an

elastic tunnel transition of the electron from an occupied level in the electrolyte to an unoccupied term in the other phase, i.e., the conduction band of the metallic anode for example. It is important to bear in mind that the intensity of the current strongly depends on the thickness d of the insulating layer since the probability W of the quantum-mechanical tunnel transition is expressed as follows :

$$W(d,E) \sim \exp [-4\pi d (2mE)^{1/2} / \hbar] \quad [2]$$

where E is the mean height of the potential barrier and m the electron mass.

Gerisher (10) has shown that the expression of the current may be simplified as follows :

$$I = I_0 [\exp \beta \eta F/RT - \exp -(1-\beta) \eta F/RT] \quad [3]$$

where η is the overpotential.

A simple law identical to Tafel's law is obtained, but its meaning is quite different ; the β coefficient may be much lower than 0.5.

In Table 1, we have reported experimental values of the transfer coefficient β , calculated from classical steady-state current-potential curves (13,14) or from potential decay curves (7,11,12), following the method developed by Busing et al.(15). We have determined β from this last method for graphite-free carbon C205 electrodes produced by *Le Carbone Lorraine*. It consists in applying a long galvanostatic pulse to the electrode ; the decreasing potential immediately following an interruption in the circuit is recorded ; β is extracted from the slopes $b = -2.3RT/\beta F$ of the linear diagrams $E = f(\log t)$. It depends on the anodic material and on the final value of the potential E_f , obtained at the end of the galvanostatic oxidation step. We think that only the electrochemical CF_x formation reaction occurs, but not the evolution of fluorine when $E < 4V$. This explains the differences between the results obtained for the same electrodes by ourself and (13) on one hand ($\beta < 0.14$ if $E > 4V$) and by (12) and (14) on the other hand ($\beta > 0.21$ if $E < 4V$). It may be noticed that all the values obtained for the fluorine evolution reaction are consistent with the electron tunneling mechanism since they are generally much lower than 0.5.

We have mentioned that, for a tunnel effect process, the probability of electron transfer depends on the thickness and the height of the potential barrier. Therefore, it is important to study the characteristics of the CF_x layers, in relation to the electrode material, the operating voltage, the electrolyte composition, and so on.

ELECTRICAL PROPERTIES OF CF_x LAYERS ON CARBON ANODES

In a previous paper, we showed that the capacitance of the interface anode/electrolyte decreases very sharply in the 2HF-KF melt, in consequence of the increase of the thickness of insulating CF_x layers (16). Cyclic voltammetry is also a convenient technique for investigating the electrochemical behavior of different kinds of carbonaceous anodes (1). Further quantitative investigations have led to the conclusion that the passivation of carbon or graphite in the fluoride melt obeys the law of formation of a low-conducting film under ohmic-resistance control (17).

The shape of the voltammograms obtained with graphite is very typical : for small values of E , $I = f(E)$ is a straight line ; for increasing values of E , the curve deviates from the linear behavior ; after the current peak, I decreases sharply as the degree of coverage tends to 1. As expected, the magnitude of the current peak and the corresponding potential increase linearly with the square root of the potential sweep rate (v). The charge Q_a required to cover the whole surface area may be calculated by integrating the I vs E curves. It depends on v : larger values of Q_a are obtained for slow sweep rates. Values as large as 0.3 coulomb may be found for scans performed at $v = 0.4 \text{ V s}^{-1}$ with G208 graphite produced by Le Carbone Lorraine, corresponding to thicknesses about one micrometer, on the assumption that a homogeneous film of carbon-monofluoride $(CF)_n$ is formed. These too large values are not compatible with the classical theory of the tunnel effect since the overpotential derived from Eq. [2] would be extremely high. However, our results may be interpreted if we consider that the electrodes are covered with a non-homogeneous film (18) in which the deep layers should be characterized by a good electrical conductivity, i.e., a stoichiometric coefficient x lower than 0.4, and a thickness being about one micrometer. Then, the external layers should constitute the thin dielectric film, a few angströms thick, through which the current flows by tunneling effect. This hypothesis of a non-homogeneous film of CF_x has been proposed by other authors studying the anode overvoltage in fluorine cells (19).

For graphite-free carbon electrodes, the quantity of passivating compounds is at least divided by ten ; thus, quantitative investigations are more difficult to perform and experiments must be carried out in a pure electrolyte free of oxidable impurities such as water which give residual currents needing to be taken into account.

Chronopotentiometric behavior of graphite and carbon anodes

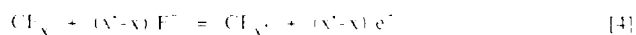
Chronopotentiometry experiments confirm that it is necessary to distinguish the formation of several kinds of CF_x compounds, depending on the final potential E_f reached by the working electrode at the end of the oxidation pulse.

We present hereafter the results obtained with G208 graphite :

1) if E_f remains lower than 2.2 volts during the oxidation step, the compound may be easily reduced by means of a reverse electrochemical pulse (figure 1). The uncompensated resistance R_u between the working electrode and the reference electrode includes the resistance of the electrolyte, negligible in our case, and the resistance of the passivating layer. When the current is reversed, one can notice a negligible ohmic drop IR_u , proving that the CF_x previously formed has a high electrical conductivity. A cathodic transition time τ_c is observed on the chronopotentiogram when the reduction of the compound is achieved. After this process, hydrogen evolution occurs.

The reversibility of the redox system leads us to assume that the conducting fluorinated compound may correspond to the graphite intercalation compound $C_x^{+}HF_2^{-}$ chemically prepared by other authors (6,20). However, as shown in the first part of Table 2, the charge Q_c used during the reduction step ($Q_c = \tau_c I_c$) is always smaller than the charge Q_a consumed during the oxidation step ($Q_a = t_a I_a$). In addition, the ratio Q_c/Q_a increases for consecutive identical experiments with the same electrode (sample 1).

2) when very long oxidation steps at low current or larger intensity pulses are imposed to the electrode (figure 2), a sudden increase of the potential is observed after a transition time τ_a . We assume that this phenomenon corresponds to the irreversible formation of a second kind of graphite fluoride, according to Equation [4] :



After the transition time, the evolution of fluorine may also begin to occur, since E_f reaches values greater than 4 volts. The very large value of the ohmic drop observed when the current is reversed proves that the new compound acts as an insulator; it cannot be reduced easily and the evolution of hydrogen immediately takes place during the cathodic pulse.

The charge Q_a needed to "saturate" the whole electrode with the first kind of CF_x ($Q_a = \tau_a I_a$) decreases when I_a increases, as shown in the second part of Table 2.

(samples 2-5). These values are in good agreement with those obtained from cyclic voltammetry experiments.

For graphite-free carbon electrodes, a quantitative interpretation of the experiments is more difficult. Instead of a reversible redox behavior, a more rapid increase of the potential, attributed to a continuous variation of the stoichiometric coefficient x , is observed. After the ohmic drop, it is scarcely possible to reduce the CF_x compounds even when they are formed at about 4 volts. See figure 3 (C205 carbon - Le Carbone Lorraine) and figure 4 (vitreous carbon V25 - Le Carbone Lorraine).

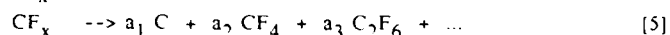
Discussion

It is obvious that the hexagonal structure of graphite allows the formation of large quantities of intercalation compounds. When the potential is made more anodic, they are partially transformed into insulating perfluorinated CF_x ; the consequence is that graphite is not a suitable material for fluorine-cell anodes. On the other hand, graphite-free carbons have an amorphous structure, which does not allow the formation of thick layers of insulating compounds; as a matter of fact, the electron transfer in the fluorine evolution reaction by tunneling process is easier. With vitreous carbon, Q_d values are very small and partial reduction of the CF_x is observed. However, the material completely lacks porosity and passivation by fluorine bubbles makes it unsuitable for further studies (see Introduction).

Several hypothesis may be proposed to explain the oxido-reduction behavior of the CF_x compounds of the first kind especially the value of the ratio Q_c/Q_d for the experiments reported in Table 2 :

- (i) a fraction of the oxidation current is used by side reactions : evolution of fluorine, evolution of oxygen or oxygen fluoride due to the oxidation of traces of moisture in the melt. However, in highly purified electrolytes the concentration of water is too low to support this idea, and for the investigated potentials lower than 4 volts the evolution of fluorine does not take place.
- (ii) the reduction of CF_x is an incomplete process and all the carbon active sites cannot be restored especially those which have been perfluorinated (4). It is often observed that the reversibility is obeyed for active materials used in electrochemical generators if the compounds are non-stoichiometric ; if the stoichiometry is reached, irreversible oxidation transformations occur.

(iii) a consumption reaction of the passivating compound is coupled with the electrochemical process ; in a previous paper (16), devoted to the interpretation of cyclic voltammetry experiments with graphite electrodes, we concluded that thermal decomposition of CF_x according to Equation [5] must be taken into account :



This hypothesis is supported by the results of the analysis of the anodic gases evolved from laboratory or industrial cells : trace amounts of gaseous fluorocarbons are always present even at low potentials for which the evolution of fluorine does not occur, showing that these gases do not result from the combustion of the carbon electrode with elemental fluorine (4). We have developed a theoretical model including the electrochemical growth of an insulating layer under ohmic resistance control coupled with a first order decomposition of the passivating compound ; it gives a quantitative interpretation of voltammograms and chronopotentiograms but leads to too large values of the first order rate constant when it is applied to graphite electrodes : for example, $k = 0.05 \text{ s}^{-1}$ for the experiment presented in figure 1. This means that thermal decomposition must be taken into account, but it is not the major phenomenon.

(iv) if, during the anodic pulse at low potentials, slow diffusion of the fluorinated intercalation compound occurs in the matrix of the graphite electrode, one may understand that Q_c/Q_a is always lower than 1 since the electroactive species have diffused too far in the matrix of the electrode to be reduced entirely. In the scope of this hypothesis, increasing values of Q_c/Q_a are obtained for consecutive oxidation-reduction cycles as well as smaller values of Q_a for increasing values of I_a (or high sweep rates in cyclic voltammetry) : for slow experiments, Q_a is more important because the compound may diffuse deeper in the matrix of the electrode. On the other hand when I_a increases, the final value of the potential E_f increases, leading to the formation of perfluorinated compounds more and more difficult to reduce ; this means that Q_c/Q_a decreases for the experiments reported in Table 2 (samples 2-5).

CONCLUSION

Previous results lead to the conclusion that, during the fluorine evolution, the carbon electrodes are covered with a non-homogeneous film of graphite fluoride. The deep layers (thickness greater than one hundred angströms), which are directly in contact with the carbon matrix, are characterized by a high electrical conductivity. The external layers form a thin dielectric film, a few angströms thick, through which the

current flows by tunnel effect. This solid compound acts as a high potential barrier and is responsible for the large energy loss in the electrochemical process, but its presence is effective to prevent the combustion of the carbon electrode in contact with elemental fluorine.

We think that the oxido-reduction behavior of the CF_x formed on graphite anodes in the 2HF-KF melt may be interpreted by an electrochemical formation reaction coupled with both diffusion and thermal decomposition processes.

A better comprehension of the fundamental phenomenon of electron transfer by tunnel effect is necessary in order to find the most suitable anodic material which will make this transfer easier and thus contribute to lower the energy consumption during the fluorine production process.

REFERENCES

1. D. Devilliers, F. Lantelme and M. Chemla, *J. Chim. Phys.*, **80**, 267 (1983).
2. R. Papp and R.J. Romano, Centenary of the discovery of Fluorine, International Symposium p. 193, Paris (1986).
3. H. Imoto and N. Watanabe, *Bull. Chem. Soc. Jpn.*, **49**, 1736 (1976).
4. D. Devilliers, M. Vogler, F. Lantelme and M. Chemla, *Analytica Chim. Acta*, **153**, 69 (1983).
5. A. Marshall (B.N.F. plc.), UK Patent GB 2 135 334 (1983).
6. T. Mallouk and N. Bartlett, *J. Chem. Soc., Chem. Commun.*, 103 (1983).
7. N. Watanabe, *J. Fluorine Chem.*, **22**, 205 (1983).
8. D. Devilliers, Thesis, P. and M. Curie University, Paris, France (1984).
9. J.W. Schultze and K.J. Vetter, *Electrochimica Acta*, **18**, 889 (1973).
10. H. Gerischer, *Z. physik. Chem. N.F.*, **26**, 223 (1960).
11. A.J. Arvia and J. Bebezzuck de Cusminsky, *Trans. Faraday Soc.*, **58**, 1019 (1962).
12. N. Watanabe, M. Inoue and S. Yoshizawa, *J. Electrochem. Soc. Jpn.*, **31**, 168 (1963).
13. D.M. Novak and P.T. Hough, *J. Electroanal. Chem.*, **144**, 121 (1983).
14. D. Devilliers, F. Lantelme and M. Chemla, *J. Chim. Phys.*, **76**, 428 (1979).
15. W.R. Busing and W. Kauzmann, *J. Chem. Phys.*, **20**, 1129 (1952).
16. M. Chemla, D. Devilliers and F. Lantelme, in "Proceedings of the first International Symposium on Molten Salt Chemistry and Technology", p. 301, Kyoto, Japan (1983).
17. D. Devilliers, F. Lantelme and M. Chemla, *Electrochimica Acta*, **31**, 1235 (1986).

18. D. Devilliers, F. Lantelme and M. Chemla, Centenary of the discovery of Fluorine, International Symposium, p. 216, Paris (1986).
19. O.R. Brown and M.J. Wilmott, Centenary of the discovery of Fluorine, International Symposium, p. 218, Paris (1986).
20. H. Touhara, K. Kadono, H. Imoto and N. Watanabe, Centenary of the discovery of Fluorine, International Symposium, p. 152, Paris (1986).

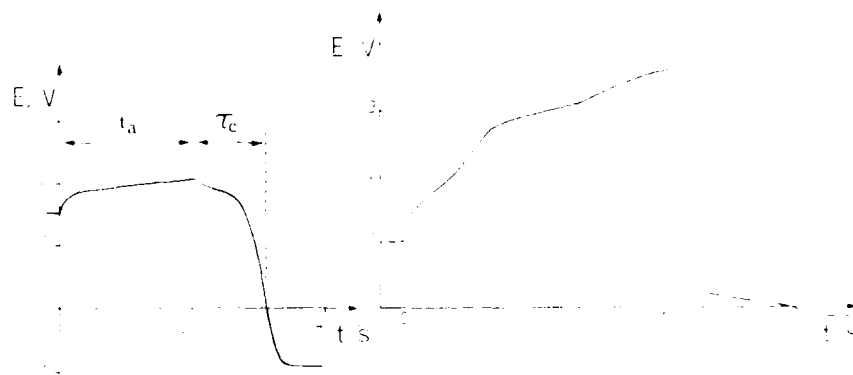


Figure 1. Chronopotentiogram on G2oS Graphite:
 $S = 0.06 \text{ cm}^2$
 anodic pulse: $I_a = 2 \text{ mA}$
 cathodic pulse: $I_c = 1 \text{ mA}$

Figure 2. Chronopotentiogram on G2oS Graphite:
 $S = 0.06 \text{ cm}^2$
 anodic pulse: $I_a = 2 \text{ mA}$
 cathodic pulse: $I_c = 0.5 \text{ mA}$

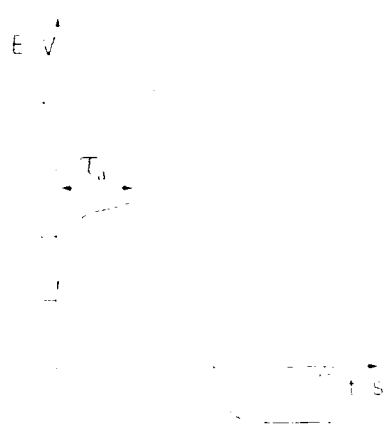


Figure 2. Chronopotentiogram on G2oS Graphite:
 $S = 0.06 \text{ cm}^2$
 anodic pulse: $I_a = 2 \text{ mA}$
 cathodic pulse: $I_c = 0.5 \text{ mA}$

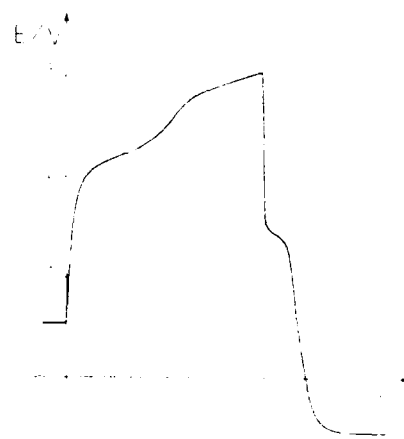


Figure 3. Chronopotentiogram on G2oS Graphite:
 $S = 0.06 \text{ cm}^2$
 anodic pulse: $I_a = 2 \text{ mA}$
 cathodic pulse: $I_c = 0.5 \text{ mA}$

Electrolyte	Temperature (K)	anodic material	β	Ref.
KF 0.7 M in anhydrous HF	273	nickel, $E < 4V$	0.068	(7)
		nickel, $E > 4V$	0.043	
HF-KF	525	carbon, graphite	0.18	(11)
2HF-KF	373	carbon, $I < 1A/dm^2$	0.225	(12)
		graphite	0.21	
		platinum, $I < 2A/dm^2$	0.23	
2HF-KF	354	carbon, $E < 4.5V$	0.10	(13)
		carbon, $E > 4.5V$	0.14	
		carbon with a shielded top	0.14	
2HF-KF	357	carbon C205 LCL, $E < 4V$, $I < 1A/dm^2$	0.27	(14)
2HF-KF	357	carbon C205 LCL		this work
		$E_f = 4.2V$	0.080	
		$E_f = 4.4V$	0.060	
		$E_f = 5.9V$	0.077	

Table 1 : Transfer Coefficient β for the F^-/F_2 System

(i) For ref.(11), average value of β for carbon and graphite electrodes
(ii) reference electrodes : graphite (11), Cu/CuF₂ (7), C-H₂ (12), Pd-H₂ (13), Pt-H₂ for (14) and for this work.
(iii) E_f is the potential reached by the electrode at the end of the galvanostatic pulse, prior to the interruption in the circuit.

Electrode sample	E_f (V)	I_a (mA)	t_a (s)	τ_a (s)	Q_a (mC)	I_c (mA)	τ_c (s)	Q_c/Q_a
1	2.00	2	20	-	40	1	10	0.25
1	2.02	2	20	-	40	1	14	0.35
1	2.06	2	20	-	40	2	11	0.55
2	3.9	2	-	2100	4200	2	231	0.110
3	4.3	6	-	570	3420	6	48	0.084
4	4.48	8	-	360	2880	8	21	0.058
5	4.5	10	-	245	2450	10	12	0.049

Table 2 : Galvanostatic Experiments on G208 LCL Graphite Electrodes ($S = 1 \text{ cm}^2$)

$Q_a = I_a t_a$ for the three consecutive experiments with sample 1
 $Q_a = I_a \tau_a$ for the experiments with samples 2-5
 $Q_c = I_c \tau_c$

Copy available only if IC does not
permit fully legible reproduction

KINETIC STUDY OF $O^{2-}/1/2O_2$ ELECTRODES IN MOLTEN SALTS

Hiroyo Numata, Ki-ichiro Asako, Tetsuo Kakosaki,
Akiko Momma and Shiro Hatayama

Department of Metallurgical Engineering
Tokyo Institute of Technology, 2-12-1 O-okayama, Meguro-ku,
Tokyo 152, Japan

ABSTRACT

The kinetics of the $O^{2-}/1/2O_2$ reaction on fully and partially immersed Au electrodes in molten chloride and carbonate have been studied with the galvanostatic double-pulse and a.c. impedance methods. The cathodic reduction of oxygen in both the melts proceeds via a two-step mechanism and the rate of the rapid charge-transfer step was found to be of the order of $10^{-4} A \cdot cm^{-2}$ from the galvanostatic double-pulse measurement. The Cole-Cole plot of the impedance of the oxygen electrodes exhibited a semicircle at high frequencies and a Warburg behavior at low frequencies. The exchange current obtained from the diameter of the semicircle was one order magnitude less than that obtained from galvanostatic double-pulse method, and probably corresponds to that of the slow reaction step. The Cole-Cole plot of the impedance on a partially immersed electrode exhibited a slightly deformed semicircle, which corresponds to the slower reaction step, without exhibiting Warburg impedance.

INTRODUCTION

Molten salts have much interest as media for fuel cells, heat storage systems and molten salt nuclear and chemical reactors. Studies of the kinetics of oxygen electrodes in molten salts are of great importance for understanding electrochemical processes in these devices. Although the reversibility and the standard electrode potential of oxygen in LiCl-KCl and NaCl-KCl melts have been extensively studied with potentiometric and current-potential measurements, much remains uncertain regarding the kinetics (1).

In this paper, the kinetics of $O^{2-}/1/2O_2$ electrode

reaction on fully and partially immersed electrodes in molten chloride and carbonate have been studied with galvanostatic double pulse and a.c. impedance methods. Emphasis was placed on the kinetics at the three phase boundary.

EXPERIMENTAL

Electrode Working electrodes (Pt, Au and Pd) for NaCl-KCl melt were prepared by sealing platinum, gold and palladium wires 5×10^{-4} m in diameter into a pyrex tube, which were inserted into an alumina tube. The gap between glass and alumina tubes was clogged with alumina or zirconia cements in order to minimize the contact of pyrex glass with the melts. The electrode was polished with emery paper #1500 and washed with methanol. A Au electrode prepared by casting Au wire into an alumina tube (1.0×10^{-3} m in inner diameter) was also used in Na_2CO_3 - K_2CO_3 melt. All the electrodes were fixed into an alumina stem which was fixed to a silicon rubber stopper. The reference electrode was Ag/Ag⁺ (0.05 m.f.) electrode (NaCl-KCl melt) and Ag/Ag⁺ (0.1 m.f.) electrode (Na_2CO_3 - K_2CO_3 melt) with a mullite membrane. Electrode potentials are referred to the Ag/Ag⁺ (0.05) and Ag/Ag⁺ (0.1) electrodes.

Apparatus Experimental cell was an alumina cylinder which was placed at the center of the furnace. Temperature was kept at $1023 \pm 3\text{K}$ except as otherwise noted. The partial pressure of O_2 , CO_2 and Ar was controlled by the ratio of the flow rates of these gases. The mixture of Ar- O_2 gas was dried through silica gel, CaCl_2 and P_2O_5 , and CO_2 gas through P_2O_5 .

Polarization curves Measurement of current-potential curves was made with an electronic potentiostat using a potential sweep of $1 \times 10^{-5} \text{ V}\cdot\text{s}^{-1}$.

Galvanostatic double pulse method The double pulse method consists of polarizing the electrode by two consecutive rectangular pulses. The first pulse current, i_1 , is chosen so that the derivative of the potential is zero at its end and η_0 is the overpotential for charge transfer corresponding to the second pulse current, i_2 . In order to separate a residual contribution of diffusion from the overpotential, the data were treated by the following equation proposed by Matsuda, Oka and Delahay (2).

$$\eta_0 = (RTi_2/zF) [1/i_0 + (4N/3\sqrt{\pi}) \sqrt{t_1}] \quad [1]$$

$$N = (1/zF) (1/C_0\sqrt{D_0} + 1/C_R\sqrt{D_R}) \quad [2]$$

where C represents bulk concentration, D the diffusion coefficient, and suffixes O and R denote oxidant and reductant, respectively.

The exchange current density increases with increasing the concentration of either oxide ion or the partial pressure of oxygen. Thus

$$i_0 = zFk_s pO_2^{\frac{(1-\alpha)}{2}} [O^{2-}]^\alpha \quad [3]$$

where k_s indicates the standard rate constant and α the transfer coefficient. Therefore, $\log i_0 - \log pO_2$ and $\log i_0 - \log [O^{2-}]$ plots yield straight lines, the slope of which gives the transfer coefficient.

A.C. impedance method Impedance measurements were made with the Frequency Response Analyser (NF Circuit Co.Ltd.) over the frequency range between 100 K and 0.01 Hz. The impedance data were plotted on a complex plane (Cole-Cole plot). When the electrode process consists of charge transfer and diffusion, the complex plane plot of the interfacial impedance exhibits a semicircle at high frequencies and a straight line with the slope of 45 degree at low frequencies. The exchange current density i_0 and double layer capacitance C_{dl} are obtained from the diameter r_t and the frequency ω_m at the top of the semicircle, respectively. Thus

$$r_t = RT/zFi_0, \quad \omega_m = 1/r_t C_{dl} \quad [4]$$

RESULTS and DISCUSSIONS

1. Reversibility of $O^{2-}/1/2O_2$ (Pt, Au and Pd) electrode

The reversible potential of oxygen electrode in molten salts is written as



$$E = E^\circ + (RT/2F) \ln \left\{ (pO_2)^{1/2} / [O^{2-}] \right\} \quad [6]$$

where E° represents the standard potential and $[O^{2-}]$ is molar concentration ($\text{mol} \cdot \text{m}^{-3}$). The activity of oxide ion in $\text{Na}_2\text{CO}_3\text{-K}_2\text{CO}_3$ melt is known to respond to the partial pressure of CO_2 according to the following reaction (3):



In order to confirm the establishment of the reversible

oxygen potential, the electrode potentials in NaCl-KCl melt were measured while varying the partial pressures of O_2 and the concentrations of O^{2-} . The stationary potentials were obtained within several minutes after changing the partial pressures of O_2 and some ten minutes after the addition of Na_2CO_3 . Figure 1 shows the change in the electrode potential of Pt with time after changing the partial pressures of O_2 . Similar behavior was observed on Au and Pd electrodes (4).

Figure 2 (a) and (b) shows the Nernstian plots of the stationary potential of Au and Pd electrodes, where the slopes of the graphs are 0.19, 0.09 for Au and 0.085, 0.075 for Pd, respectively. The slope for Au is consistent with the theoretical value, while that of Pd exhibits a slightly lower value. Nernstian plots of $O^{2-}/1/2O_2$ (Au) electrode in Na_2CO_3 - K_2CO_3 were remarkably similar to those observed in molten chloride.

2. Cathodic reduction of oxygen in molten salts

The cathodic reduction of oxygen in molten salts was studied at first by sweep voltammetry. Figure 3 shows the current-potential curves for the reduction of oxygen at the Pt electrode in the molten chloride containing O^{2-} ($2.5 \text{ mol} \cdot \text{m}^{-3}$) under different partial pressures of O_2 . The cathodic currents increase steeply with the start of the cathodic scanning, showing the polarographic waves. This behavior is characteristic of a reversible electrode, i.e. a MZ^{n+} electrode in molten salts. The cathodic polarization curve up to $-0.4V$ exhibits a limiting current. Figure 4 shows that the cathodic currents at $-1.0V$ are approximately proportional to the partial pressures of O_2 . Similar proportionality was observed on Au and Pd. Occurrence of the diffusion limiting current indicates that the charge transfer step of the $O^{2-}/1/2O_2$ electrode is very rapid and the current is controlled by diffusion, only poor information regarding the mechanism of cathodic reduction of oxygen can be obtained from the stationary polarization experiment.

On the basis of the results of the non-stationary experiments, however, it is widely believed that, in molten chloride, molecular oxygen is quite stable and the cathodic reduction of oxygen proceeds via a two-step mechanism, thus

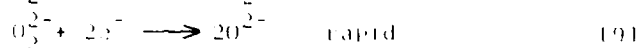
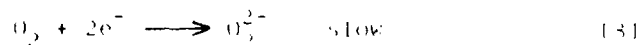
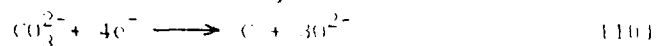
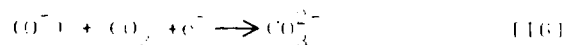
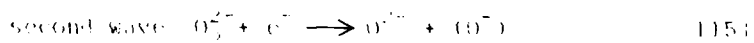
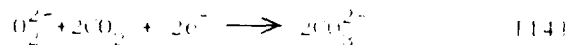
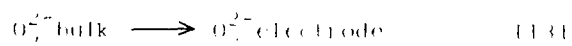
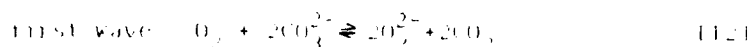
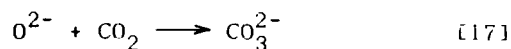


Figure 5 shows cathodic polarization curves of a $0.7/1/20_3(\text{Au})$ electrode in the molten carbonate under different partial pressures of O_2 . The cathodic currents in molten carbonate are much lower than those in chloride melts, exhibiting neither a Tafel region nor a limiting current. It has been well established that the increase in current at the potentials below -1.5 V is attributable to the cathodic reduction of CO_3^{2-} (5), thus

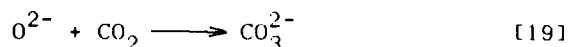
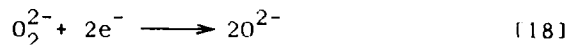


The cathodic current at the potentials noble to -1.5 V is weakly dependent on the partial pressures of either O_2 or CO_2 . With increased potential sweep rates, however, the voltammograms exhibit two current waves around -0.9 and -1.4 V , respectively. The potentials at the wave maxima shift in the less noble direction with increasing sweep rates (Fig. 6). The square root of the shift of the maximum potentials was proportional to the logarithm of the sweep rate and the slopes of the graphs are close to $RT/4$ (0.200 V/decade). The maximum currents of both waves were proportional to the square root of the sweep rate. These observations indicate that the two current waves correspond to different reaction processes, both of which are controlled by diffusion as was suggested by Appleby et al. (7). It is widely accepted from thermodynamic considerations (6) that the oxygen molecule is transformed to O_2 and O_2^{2-} in $\text{Na}_2\text{CO}_3\text{-K}_2\text{CO}_3$ melts. Therefore, the cathodic reduction of oxygen takes place via the peroxide or superoxide ions. Appleby et al. (7) reported that the reaction orders for O_2 and CO_2 are 0.30 and 0.33 , respectively for the first wave and 0.75 and 0.50 , respectively for the second wave. They proposed the reaction mechanism for each wave as





The reaction step [14] can be split into charge transfer and chemical reaction steps, as



3. Impedance and double pulse studies of $O^{2-}/1/2O_2$ electrode in molten salts

The measurements of the charge transfer rate of the $O^{2-}/1/2O_2$ reaction on Pt were made in NaCl-KCl melt under different partial pressures of oxygen by the galvanostatic double pulse method. The η_0 values measured are plotted against the square root of the pulse width t_1 in Fig.7. As was expected from Eq.[1], η_0 is proportional to the square root of t_1 . Similar graphs were obtained by the for different concentrations of O^{2-} . Extrapolation of the graphs to the intercept of the vertical axis yields the exchange current density of the charge transfer step shown as Eq. [9]. The exchange current densities thus obtained are plotted against the partial pressures of O_2 and the concentrations of O^{2-} in Fig.8. The graphs exhibit straight lines as was expected from Eq.[3], and the transfer coefficients for Pt, Au and Pd electrodes were 0.25, 0.20 and 0.14 ± 0.04 , respectively. The exchange current densities of the $O^{2-}/1/2O_2$ electrode in the chloride melts are of the same order of magnitude as those of the reversible metal electrode in chloride melts hitherto reported (8).

Complex plane plots of the impedance on the Pd electrode in NaCl-KCl melt are shown in Fig.9. The diagram consists of a semicircle at high frequencies and a much depressed semicircle at low frequencies. The depressed semicircle is attributable to the Warburg impedance under Nernst diffusion layer limitation. The transfer resistance that corresponds to the diameter of the semicircle at high frequencies decreases with increasing partial pressures of O_2 (Fig.9 (b)). The exchange current densities obtained from the diameter of the semicircle and galvanostatic double pulse method in NaCl-KCl melt are summarized in Table I.

As was mentioned above (Eq.[8] and Eq.[9]), the cathodic reduction of oxygen in molten chloride proceeds via a two-step mechanism strongly inhibited by diffusion.

The exchange current densities obtained from the transfer resistance are an order of magnitude less than those obtained by the double pulse method and probably correspond to the slower transfer step shown as Eq.[8].

Thus, the equivalent circuit for the impedance of the oxygen electrode in molten chloride can be written as Fig.10 where C_{dl} represents the double layer capacitance, R_t the transfer resistance corresponding to Eq.[9], C_p the pseudo capacitance, R_t' the transfer resistance corresponding to Eq.[8], and W the Warburg impedance. Since the R_t value is very small, the semicircle corresponding to R_t is barely discernable on the graph. The R_t value is obtained only by the galvanostatic double pulse method. Similar results were obtained on Au and Pd electrodes in NaCl-KCl melt.

Figure 11 shows the complex plane plots of the impedance on Au electrode in the molten carbonate under different partial pressures of oxygen. The graphs consist of a depressed semicircle at high frequencies and a somewhat deformed Warburg impedance at low frequencies. The diameter of the semicircle decreases with increasing partial pressures of oxygen and probably corresponds to the chemical reaction resistance shown as Eq.[19]. The equivalent circuit in this case is similar to that of Fig.10, where R_t' indicates the chemical reaction resistance.

4. Cathodic reduction of oxygen on partially immersed Au electrode

Cathodic polarization experiments were made on a partially immersed Au electrode in the molten carbonate under different partial pressures of O_2 and CO_2 . The partially immersed electrode has a very thin liquid layer at the meniscus and simulates an electrode which has a three phase boundary, as reported for an aqueous fuel cell (9).

Figure 12 shows the polarization curves of the cathodic reduction of O_2 on the partially immersed Au electrode under different partial pressures of O_2 . The current on the partially immersed electrode is much greater than that on the fully immersed electrode, exhibiting a Tafel region and a limiting current. Therefore, it is likely that most of the current flows in the vicinity of the three phase boundary, where the inhibition by diffusion is greatly eliminated. The cathodic currents on the partially immersed electrode increase with increasing the partial pressures of either O_2 or CO_2 .

Copy available. This does not
permit fully legible reproduction

Simultaneous results were also obtained. At $(P_{O_2}, P_{CO_2}) = (0.10, 0.10)$ and $(0.10, 0.10)$ respectively, again at $100^\circ C$. The slopes of the 15-min. linear plots of the current against the partial pressures of O_2 and CO_2 are found to be 0.403 and -0.131 respectively. The impedance of the oxygen reaction on the partially immersed electrode under different partial pressures of O_2 and CO_2 is plotted on a complex plane (Cole-Cole plot) in Fig. 1(a) and (b). The diagrams exhibit a deformed semicircle and the Warburg impedance is not observed. The deformed portion of the semicircle indicates the existence of another semicircle at high frequencies, although it is barely discerned. The diameter of the semicircle, which probably corresponds to the chemical reaction step shown in Eq. (19), decreases with either increasing the partial pressure of O_2 or decreasing the partial pressure of CO_2 . The reaction orders regarding the partial pressures of O_2 and CO_2 are 0.413 and -0.159, respectively. These values are consistent with the reaction orders obtained from the current-potential measurements, although the value of the exchange current density is several times larger than the latter. Further studies are needed on the oxygen electrode reaction at the three phase boundary.

CONCLUSION

Cathodic reduction of oxygen on Au, Pd and Pt electrodes in molten salts proceeds via a two-step mechanism. The rate of the rapid charge transfer step measured with the galvanostatic double pulse method was of the order of $10^{-4} A/cm^2$. The Cole-Cole plot of the impedance of the oxygen electrode exhibited a semicircle at high frequencies and a Warburg behavior at low frequencies. The exchange current obtained from the diameter of the semicircle was one order of magnitude less than that obtained from galvanostatic double pulse method, and probably corresponds to that of the slower reaction step.

The rate of cathodic reduction of oxygen increased greatly on a partially immersed Au electrode. The Cole-Cole plot of the impedance on the partially immersed electrode exhibited a slightly deformed semicircle. The diameter of which corresponds to the rate of the slower reaction step, without exhibiting Warburg impedance.

ACKNOWLEDGMENT

The authors would like to acknowledge Dr. J. L. R. Scharif, Illinois Institute of Technology, for helpful discussions.

REFERENCES

1. D. Lamm and H. J. Achever, *J. Electroanal. Chem.*, **51**, 45 (1974).
2. Y. Katozaki and H. Fukunishi, *J. Electroanal. Chem.*, **52**, 339 (1975).
3. D. L. Lamm and G. Lammox, *J. Electrochem. Soc.*, **124**, 480 (1977).
4. J. L. Debarbied and K. H. Stern, *J. Electrochem. Soc.*, **127**, 2600 (1980).
5. H. J. Achever, S. Oka, and P. Delahay, *J. Am. Chem. Soc.*, **81**, 5077 (1959).
6. Y. Horiuchi et al., *J. Power Sources*, **16**, 75 (1985).
7. K. Asako, H. Nomura, and S. Haruyama, *Proc. of 18th Symp. Polym. Solid Chem.*, in Japan, p. 5, (1985).
8. J. L. Debarbied, P. Baro, and G. J. Janz, *Electrochim. Acta*, **11**, 1629 (1966).
9. B. K. Andersen, *Polym. Electrolyte Flow*, Tech. Univ. of Denmark, Lyngby, Denmark (1975).
10. A. J. Appleby and S. E. Nicholson, *J. Electroanal. Chem.*, **5**, 105 (1974).
11. H. A. Laitinen, R. P. Fricker, and D. L. Rice, *J. Electrochem. Soc.*, **117**, 546 (1970).
12. S. Haruyama, H. Nomura, and A. Nishikawa, *Proc. 10th Int. Symp. on Polym. Solid Chem. and Tech.*, Polym. Solid Chem. Soc. Japan, **1**, p. 173 (1983).
13. J. L. Debarbied, *J. Electrochem. Soc.*, **119**, 145 (1972).
14. H. Omiya, Y. Horiuchi, K. Imata, and T. Shirogami, *Denki Kagaku*, **54**, 430 (1996).

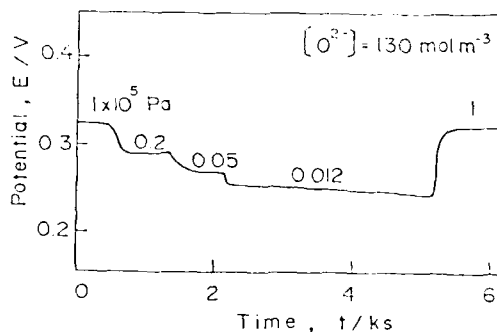


Figure 1. Change in Potential (vs. Ag/Ag⁺ (0.1)) with Time after Changing the Partial Pressure of O₂, [O²⁻]=130 mol·m⁻³. Numbers in the Figure: Partial Pressure of O₂ (Pa).

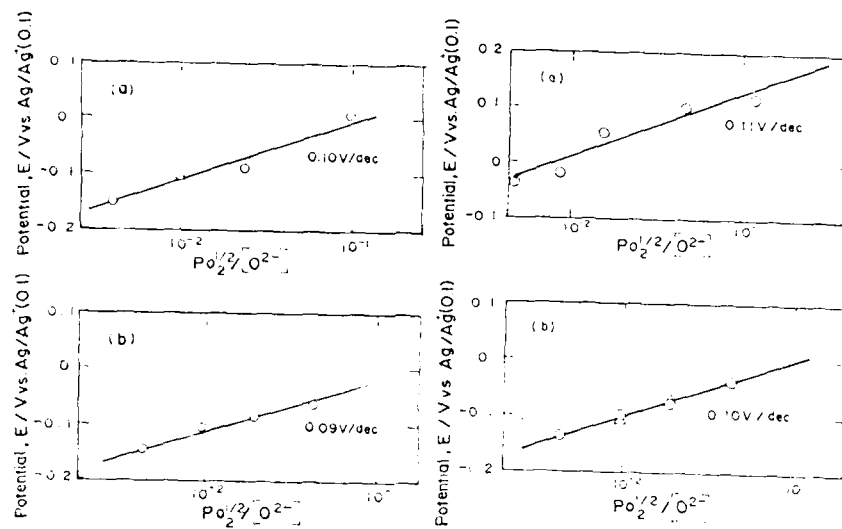


Figure 2. Nernst Plots of Potential, E/V vs. $Ag/Ag^+(O.I)$ for $O_2^{1/2}/1/2O_2(Pt)$ Electrode in NaCl-KCl Melt at 1023K. (a) $Po_2 = 0.001$, (b) $Po_2 = 0.001$, (c) $Po_2 = 0.01$, (d) $Po_2 = 0.01$.

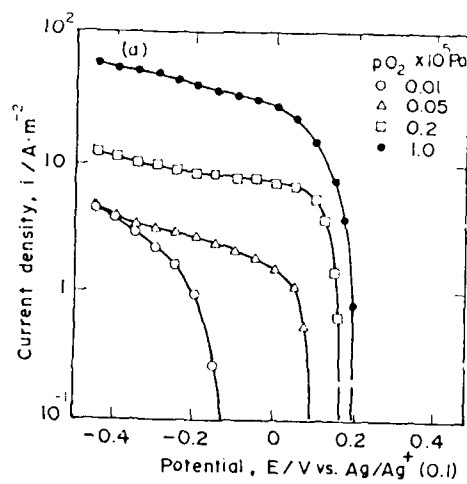


Figure 3. Polarization Curves for $O_2^{1/2}/1/2O_2(Pt)$ Electrode in NaCl-KCl Melt Having Different Partial Pressures of O_2 at 1023K, $[O_2^{1/2}] = 1.30 \text{ mol} \cdot m^{-3}$.

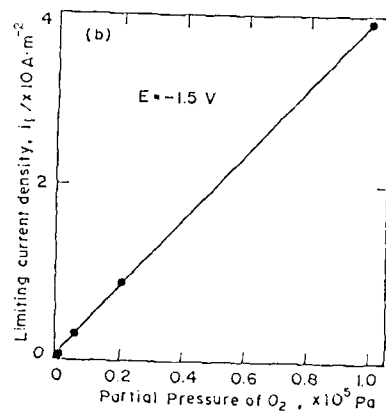


Figure 4. Dependence of Limiting Current Density at -0.15 V on Partial Pressure of O_2 , $[\text{O}^{2-}] = 136 \text{ mol} \cdot \text{m}^{-3}$.

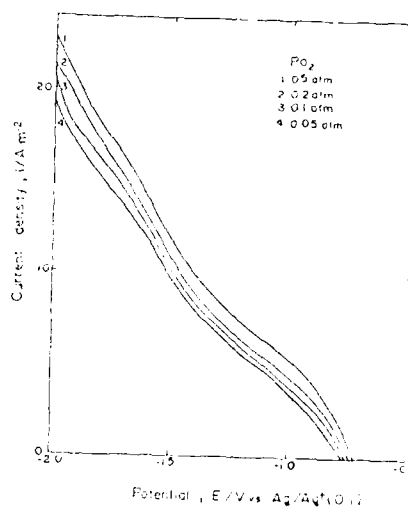


Figure 5. Cathodic Polarization Curves of $\text{Pt}/120_2$ (Au) Electrode in $\text{Na}_2\text{CO}_3\text{-K}_2\text{CO}_3$ Melt at 1023 K , $\text{PO}_2 = 0.1 \times 10^5$.

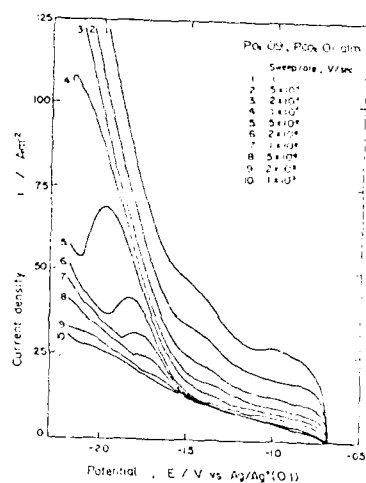


Figure 6. Sweep Voltammogram of $\text{Pt}/120_2$ (Au) Electrode in $\text{Na}_2\text{CO}_3\text{-K}_2\text{CO}_3$ Melt at 1023 K , $\text{PO}_2 = 0.1$, $\text{PO}_2 = 0.1 \times 10^5$.

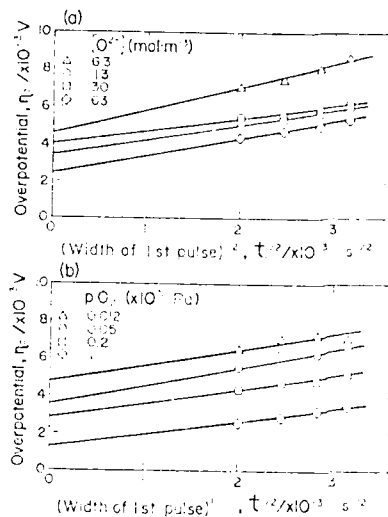


Figure 7. Plots of Overpotential, η , against Square Root of t_1 in NaCl-KCl Melt (a) $T=1023\text{K}$, $p\text{O}_2=0.2 \times 10^{-3}$, $[\text{O}^{2-}]=6.3, 13.3, 31, 130 \text{ mol}\cdot\text{m}^{-3}$ (b) $T=1023\text{K}$, $[\text{O}^{2-}]=13 \text{ mol}\cdot\text{m}^{-3}$, $p\text{O}_2=0.012, 0.05, 0.2, 1.0 \times 10^{-3}$

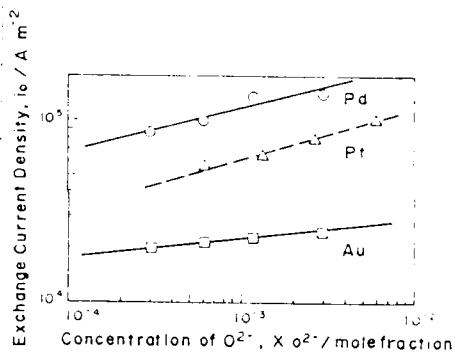


Figure 8. Exchange Current Density of O^{2-} in Pt, Au, Pd Electrodes Having Different Concentration of $[\text{O}^{2-}]$ in NaCl-KCl Melt at 1023K . Galvanostatic Double Pulse Method

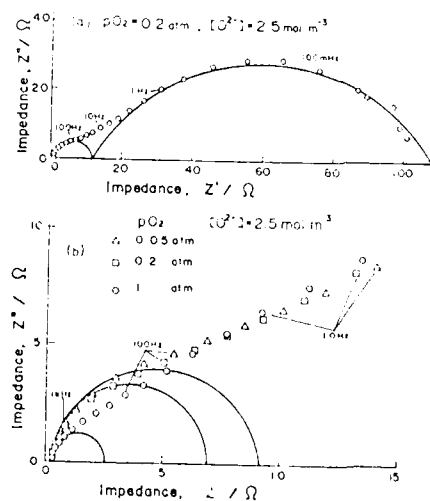


Figure 9. Cole-Cole Plots of Z'' vs Z' for Pt Electrode in NaCl-KCl Melt at 1023K , $p\text{O}_2=0.05, 0.2, 1 \text{ atm}$, (a) Low Frequency Region (b) High Frequency Region

Table 1 Exchange current density measured by the galvanostatic double pulse and a.c. impedance methods

	$[O^{2-}]$ mol·m ⁻³	Double pulse x10 ⁴ A·m ⁻²	pO_2 x10 ⁵ Pa	A.C. impedance x10 ³ A·m ⁻²
Pt	6.2	5.6		
$pO_2 =$	13.3	6.3		
0.2×10^5	30	7.8		
	62	9.9		
Au	6.9	2.0	Au ₂ ⁻	0.01
$pO_2 =$	13.8	2.2	$[O^{2-}] =$	0.11
0.2×10^5	23.0	2.3	25 mol·m ⁻³	1.0
	69.2	2.5		0.59
Pd	6.9	6.9	Pd ₂ ⁻	0.05
$pO_2 =$	13.8	9.0	$[O^{2-}] =$	0.064
0.2×10^5	23.0	15.0	2.5 mol·m ⁻³	0.2
				0.088
				0.26

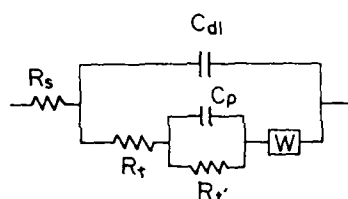


Figure 10. Equivalent Circuit of the Oxygen Electrode in Molten Chloride.

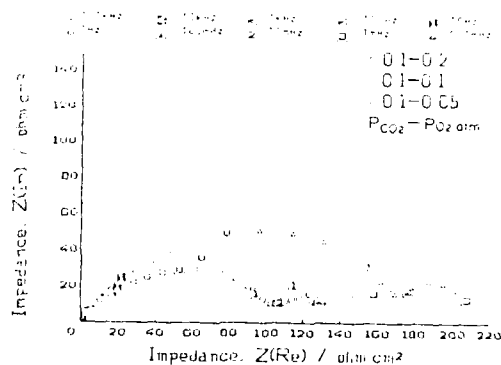


Figure 11. Cole-Cole Plots of $O^{2-}/1/2O_2(Au)$ Meniscus Electrode in $Na_2CO_3-K_2CO_3$ Melt at 1023K Having Different Partial Pressure of O_2 . $pCO_2=0.1 \times 10^5$.

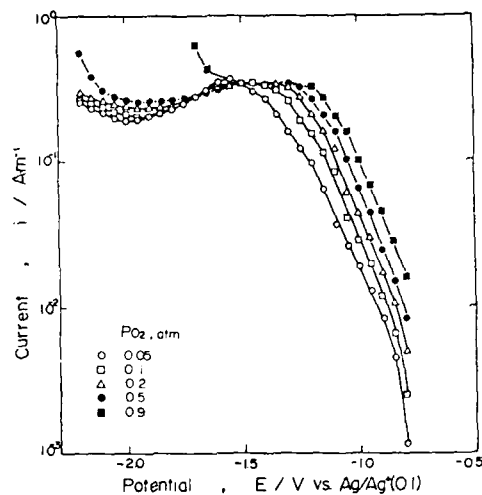


Figure 12 Cathodic Polarization Curves of $O_2^-/1/2O_2(Au)$ Meniscus Electrode in $Na_2CO_3-K_2CO_3$ Melt at 1023K, $pCO_2=0.1 \times 10^{-5}$.

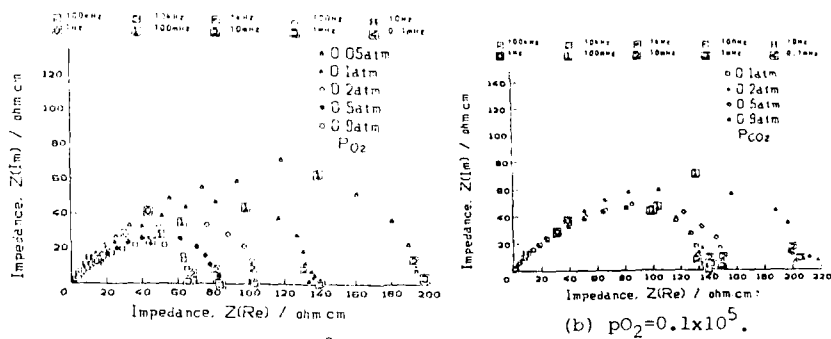


Figure 13. Cole-Cole Plots of $O_2^-/1/2O_2(Au)$ Meniscus Electrode in $Na_2CO_3-K_2CO_3$ Melt at 1023K Having Different Partial Pressure of O_2 and CO_2 . (a) $pCO_2=0.1 \times 10^{-5}$,

(b) $pO_2=0.1 \times 10^{-5}$.

KINETIC STUDY OF HYDROGEN OXIDATION
IN MOLTEN ALKALI CARBONATE

Isamu Uchida, Tatsuo Nishina, and Masaya Takahashi

Department of Applied Chemistry, Faculty of Engineering,
Tohoku University
Aramaki-Aoba, Sendai 980, Japan

ABSTRACT

The hydrogen oxidation reaction in (62+38)mol% (Li+K)CO₃ at 650°C has been studied at Au, Ag, Cu, Pt, Ir, Pd, Ni, Co, and Fe electrodes by using cyclic voltammetry, ac impedance and potential-step methods. Impedance data were analyzed by computer fitting with an equivalent circuit taking into account the hydrogen adsorption. The exchange current density increased with the following series under the gas composition of P(H₂)/P(CO₂)/P(H₂O)=0.691/0.236/0.013; Pd(118.9 mA/cm²)>Ni>Pt>Ir>Au>Ag (16.1 mA/cm²). The effect of the nature of metals on the electrode kinetics is discussed.

INTRODUCTION

The hydrogen oxidation in molten carbonates is an important process in the development of molten carbonate fuel cells. It has received renewed attention recently from the electrode kinetics[1-4] because extensive work is needed to improve the anode efficiency and the performance degradation. Ang and Sammells obtained kinetic parameters, including the exchange current density, on nickel and cobalt electrodes in Li/K, Li/Na and Li/Na/K carbonates by using a potential step method[1]. The potential step has been used for other systems such as conducting ceramic electrodes [2] and copper electrodes[3] in the Li/K carbonate. Throughout the previous studies[1-4], including early work on polarization data for various metals[5], the kinetic features, especially for i_0 values, are little dependent on the nature of the electrode materials. Apparently, there is not drastic variation in i_0 values with the metal as is observed in the aqueous system. The present work was undertaken to examine extensively the influence of metals on hydrogen oxidation by using an ac impedance method and potential step techniques, including chronocoulometry.

EXPERIMENTAL

The eutectic mixture of alkali carbonate, (62+38)mol% (Li+K)CO₃, was used as a solvent at 650°C. Experimental techniques, melt purification, apparatus, and the cell assembly were described elsewhere[6-8]. Electrode potentials were given with respect to the oxygen gas reference electrode of $P(O_2)/P(CO_2)=0.33/0.67$, i.e., (1:2)O₂/CO₂. Inlet fuel gases were initially (7:3)H₂/CO₂ and (3:7)H₂/CO₂. They were fed into the cell after moistening with water vapor.

The working electrodes were fully immersed flag type electrodes with a geometrical area of 0.4 cm². They were commercially available, smooth and thin foils (3N-up purity, 0.05 mm thickness) cut out with a paper punch (0.5 cm in diam.). Fine gold wire was welded to the punched foils as electrical leads in order to minimize the meniscus effect bringing about a high local current at the metal/gas boundary. Selected metals were Au, Ag, Cu, Pt, Ir, Co, Ni, Fe and Pd.

Cyclic voltammetry and potential step experiments were carried out by using a PAR model 273 potentiostat coupled with a Nicolet 4094 digital oscilloscope. Solartron 1186 and 1286 potentiostats were also used for this purpose. For pulse experiments the resultant transients were recorded with the microprocessor-controlled oscilloscope and were stored on floppy disks for subsequent signal conditioning and analyses. Impedance measurements were carried out using a Solartron 1250 frequency response analyzer coupled with the 1186 (or 1286) electrochemical interface. Frequencies were changed from 1 Hz to 60 kHz and the signal amplitude was 5 mV rms. Data were transferred to microcomputers (HP 85 and NEC PC-9800) and subjected to the faradaic impedance analysis.

RESULTS AND DISCUSSION

Voltammetric behavior

Cyclic voltammograms (CV) for hydrogen oxidation yield characteristic waves for anode metals as shown in Fig. 1. Hydrogen oxidation takes place at the rising portion of CV. However, metal dissolution follows the hydrogen oxidation for the Ni, Co, and Cu cases. At Co and Fe electrodes, the onset potentials of metal dissolution are very close to the hydrogen oxidation, and the current peak can not be distinguished as observed in the Ni and Cu cases. The single peaked wave observed at Ni, Cu, Au, Ag, Pt, and Ir electrodes are ascribed to the hydrogen oxidation process. It is noted here that the peak height depends on the nature

of the metal. Whereas the peak potential seems almost independent of scan rates up to 0.5 v/s as reported for Cu electrodes[3].

Pd electrodes showed extraordinarily large peaks as shown in Fig. 2. The peak shape indicates an adsorption-like behavior. Considering a quite large amount of charge passing during the scan, this behavior can not be ascribed to a surface redox process of monolayer adsorption, suggesting that a hydride-like compound formed inside the electrode surface participates in the anodic process.

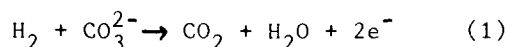
AC impedance behavior

Figures 3 to 5 show impedance plane plots for different metals measured at the rest potential. Inlet gas composition was $\text{PH}_2:\text{PCO}_2:\text{PH}_2\text{O}=0.691:0.296:0.013$ atm and the frequency range selected here was 1 Hz to 6 kHz.

As shown in Fig. 3, the Cole-Cole plots for Au and Ag electrodes were very similar, indicating circular arcs at high frequencies. Copper showed a somewhat different locus and the diffusion impedance observed usually at low frequencies was not well defined. Ni and Co electrodes gave very linear plots as shown in Fig.4. The diffusion impedance was predominant throughout the measured frequencies. Comparing the two, the latter was more resistive in the diffusion impedance. Fig.5 shows the comparison between three metals of the Pt family. The behavior of Pd was almost identical with that of Ni. Pt showed a small circular arc at high frequencies while Ir had a large arc comparable to that of Au.

Faradaic impedance analysis

The overall hydrogen oxidation reaction is



The process involves adsorption intermediates



The reaction mechanism following Eq.(2) has been discussed recently[1,3,9]. Taking into account the adsorption step, we searched several equivalent circuits capable of well interpreting the impedance data. Using a curve fitting program[6,7] with postulated circuits, we found that the circuit shown in Fig.6 gave good results. Examples of the computational results are shown in Fig.7 in comparison with the experimental results, and parameters thus determined

are summarized in Table 1 together with i_0 values calculated from the activation resistance ($\theta = RT/nFi_0$). Parameters for Cu and Co electrodes are omitted in the table because fitting accuracy was poor for the circuit of Fig.6. We simply note the i_0 values; 43.8 mA/cm² for Cu and 32.9 mA/cm² for Co.

The double layer capacity shows little dependency on the nature of metal (60 to 80 $\mu\text{F}/\text{cm}^2$) except for Ni and Pd. Although there are no data about the true C_d values at various metals under a hydrogen atmosphere, the above values seem to be reasonable. Smirnov et al. reported the double layer capacity on Pt electrodes at 650°C under a CO₂ atmosphere [10]. Although their results showed a large scatter of absolute values depending on the prepolarization, the C_d values were about 10 to 60 $\mu\text{F}/\text{cm}^2$ at the corresponding potential region.

The Warburg coefficient, σ , changed with the nature of metals. The σ value represents the magnitude of diffusion impedance, being related to the reciprocal of $C\sqrt{D}$ [11]. Therefore, the observed dependency is curious because the hydrogen partial pressure and the melt composition were identical through the experiments. This unexpected behavior, which was also noted in the peak height of voltammograms, can be attributed to the hydrogen incorporation into metals or hydride formation on electrode surfaces. The small σ values and the large C_d and C_{ad} values noticed at Ni and Pd electrodes suggest complicated kinetics caused by a transport process taking place inside the electrode. Vogel et al. described the effect of hydrogen diffusion through Ni and Pd metals on hydrogen oxidation kinetics at meniscus electrodes [4].

Potential step experiments

Potential step measurements were carried out to determine i_0 values with Allen-Hickling plots. Results are shown in mA/cm² as follows; Pd(75.7) > Ni(61.0) > Pt(43.9) > Cu(37.3) > Au(20.5).

In order to get further insight to the mixed transport process of metal side and melt side, chronocoulometry was employed. Potential was stepped from the rest potential to a potential positive by 0.2 V. Typical chronocoulometric responses for different metals are shown in Fig.8. When the potential step is sufficiently large to attain the diffusion-limited condition, the transient is given by the integral of the Cottrell equation, showing a linear plot with a slope providing the $C\sqrt{D}$ [11]. As shown in Fig.8, the variation of slopes with the kind of metal confirms the difference in transport process between the metals. The

trend of kinetic behavior is in agreement with that of values mentioned in Table 1. Qualitative analysis of chronocoulometric data is in progress.

ACKNOWLEDGMENT

This work was supported by Grant-in-Aid for Scientific Research of The Ministry of Education, Science and Culture.

REFERENCES

1. P.G.P.Ang and A.F.Sammells, J. Electrochem. Soc., **127**, 1287(1980).
2. A.F.Sammells, S.B.Nicholson, and P.G.P.Ang, J. Electrochem. Soc., **127**, 350(1980).
3. S.H.Lu and J.R.Selman, J. Electrochem. Soc., **131**, 2827 (1984).
4. W.M.Vogel, L.J.Bregoli, and S.W.Smith, J. Electrochem. Soc., **127**, 833(1980).
5. L.P.Kletsov, G.G.Arhipov, and G.K.Stepanov, Sov. Electrochem., **3**, 785(1967).
6. I.Uchida, T.Nishina, Y.Mugikura, and K.Itaya, J. Electroanal. Chem., **206**, 229(1986).
7. I.Uchida, Y.Mugikura, T.Nishina, and K.Itaya, J. Electroanal. Chem., **206**, 241(1986).
8. I.Uchida, T.Nishina, Y.Mugikura, and K.Itaya, J. Electroanal. Chem., **209**, 125(1986).
9. L.K.Bieniasz, J. Electroanal. Chem., **197**, 387(1986).
10. M.V.Smirnov, L.A.Tsiiovkina, and V.A.Oeinikova, Electrochemistry of Molten and Solid Electrolytes, **8**, 61(1968).
11. A.J.Bard and L.R.Faulkner, "Electrochemical Methods" p.200, John Wiley & Sons, New York (1980).

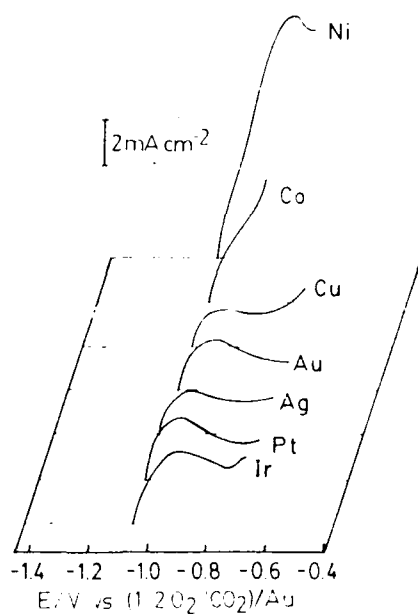


Fig. 1. Cyclic voltammograms for hydrogen oxidation at various metal electrodes. $P(H_2)/P(CO_2)/P(H_2O) = 0.691/0.296/0.013$, $v = 0.2$ V/s.

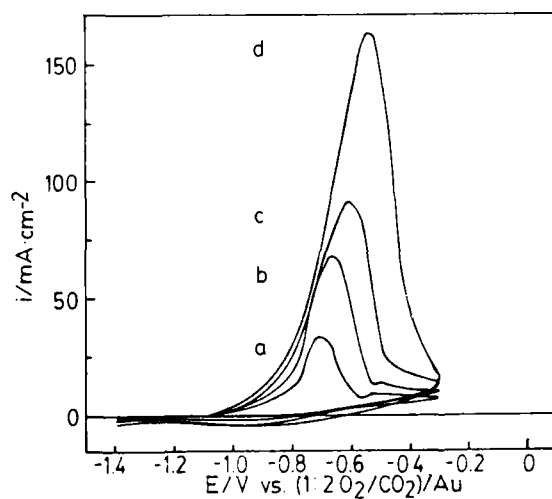


Fig. 2. Cyclic voltammograms for hydrogen oxidation at Pd electrodes. Scan rate, a: 0.02, b: 0.05, c: 0.10, d: 0.20 V/s, respectively.

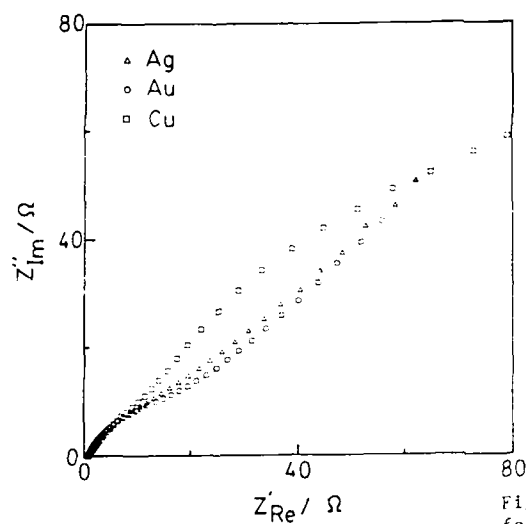


Fig. 3. Impedance plane plots for Ag, Au, and Cu electrodes at the rest potential. $f=1$ Hz to 6 kHz, Gas composition as in Fig. 1.

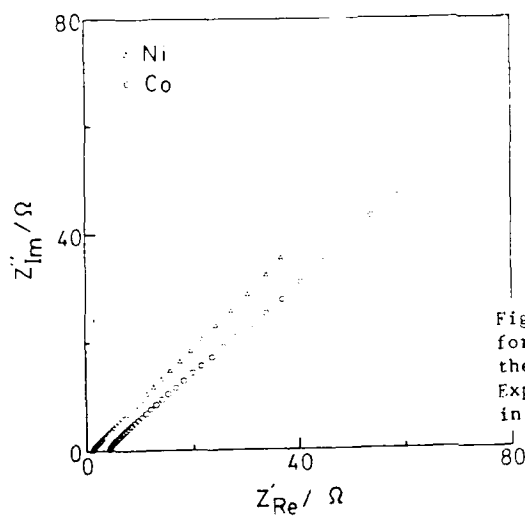


Fig. 4. Impedance plane plots for Ni and Co electrodes at the rest potential. Experimental conditions as in Fig. 3.

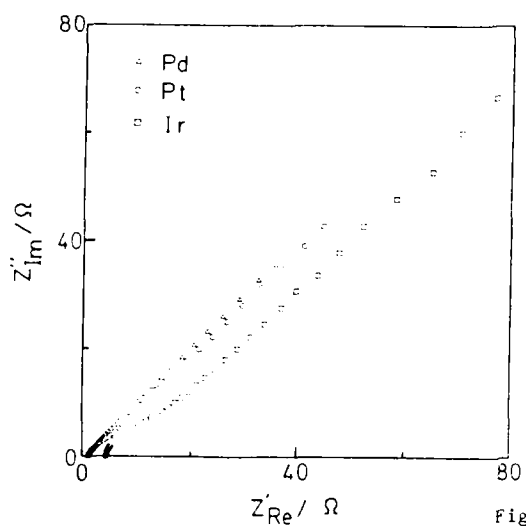


Fig. 5. Impedance plane plots for Pt, Ir, and Pd electrodes at the rest potential. Experimental conditions as in Fig. 3.

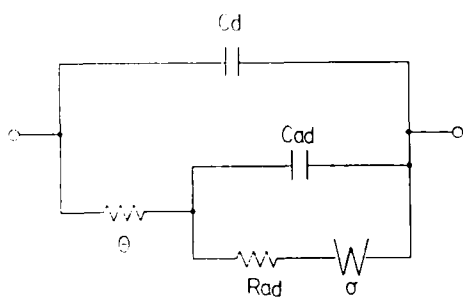


Fig. 6. Equivalent circuit for hydrogen electrode. Cd: double layer capacity, R : charge transfer resistance, Cad: adsorption pseudo-capacity, Rad: adsorption resistance, σ : Warburg coefficient.

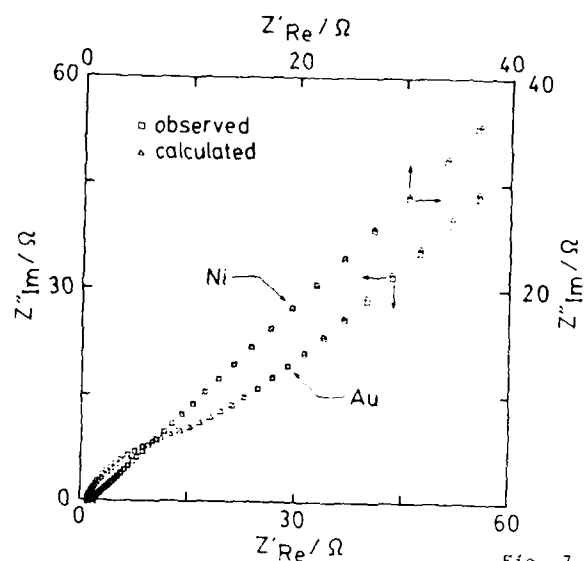


Fig. 7. Fitting of impedance data.

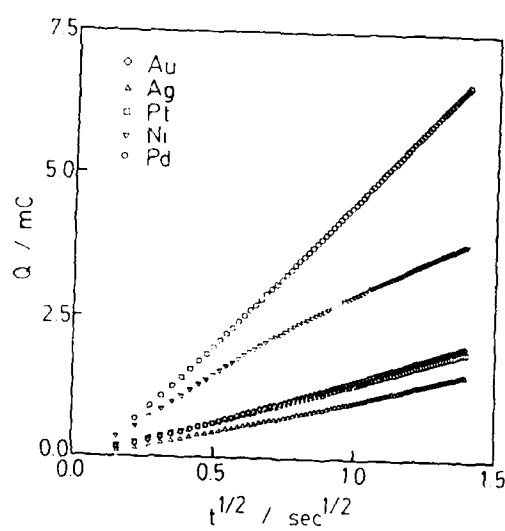


Fig. 8. linear plots of chronocoulometric response at various metals. Step potential: +200 mV from the rest potential. Experimental conditions as in Fig. 3.

Table 1. Parameters obtained by faradaic impedance analysis based on the equivalent circuit of Fig. 6.

Material	τ [cm ² sec ^{1/2}]	ω [cm ²]	Cd [μ Fcm ⁻²]	Cad [μ Fcm ⁻²]	Rad [cm ²]	i_0 [mAcm ⁻²]
Ag	63.2	2.48	64	98	3.53	16.1
Au	57.1	1.98	66	98	1.57	20.0
Ir	53.2	1.59	73	93	1.13	25.0
Pt	42.9	0.76	80	128	0.49	56.5
Ni	33.5	0.38	104	173	0.21	105.2
Pd	36.0	0.33	198	181	0.25	118.9

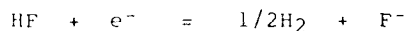
BEHAVIOUR OF HF/H₂ ELECTRODE IN A MOLTEN LiF-KF SYSTEM

Keiko Ema, Yasuhiko Ito, Toshihide Takenaka
and Jun Oishi

Department of Nuclear Engineering
Faculty of Engineering
Kyoto University
Sakyo-ku, Kyoto 606, Japan

ABSTRACT

Cathodic behaviour of HF in a molten LiF-KF system has been investigated in detail by using both immersion type and semi-immersion type platinum electrodes. In the case of immersion type electrode, clear current peak due to the reduction of HF dissolved in the melt:



was observed on a potential sweep voltammogram, at the potential of 1.5-1.6 V (vs. Li,K / Li⁺, K⁺ electrode). The dependence of peak current on the square root of scan rate as well as on the partial pressure of HF in the atmosphere suggests a diffusion controlled reaction. In the case of semi-immersion type gas electrode, equilibrium potential of the above reaction has been determined to be:

$$E = (2.019 \pm 0.024) + 2.303(RT/F) \log P_{\text{HF}}/(P_{\text{H}_2})^{1/2}$$

(V. vs. Li,K/Li⁺,K⁺ electrode) on the platinum gauze as an electrode at 570°C. And at this electrode, cathodic polarization was very small even at the apparent current density of 0.15 A/cm², which is interesting from the technological viewpoint.

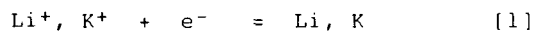
INTRODUCTION

Molten fluoride is a useful material for use in many future engineering applications. Thus, systematic studies of molten fluoride systems are to be conducted extensively. From this viewpoint, in the authors' laboratory, LiF-KF eutectic melt has been selected as an

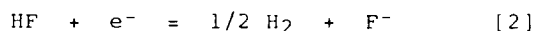
example of fluoride melt, and a series of electrochemical studies has been conducted. However, in these studies, it is very difficult to find stable and reliable reference electrode with thermodynamic significance, so that thermodynamic considerations of experimental results are very difficult to achieve. Then the authors conventionally have been using $\text{Li,K/Li}^+, \text{K}^+$ electrode as a reference electrode. This electrode is reproducible when it is used as a dynamic reference electrode. As mentioned later, this electrode can be easily obtained by a constant current electrolysis immediately before the potential measurement. But thermodynamic significance of its potential is not so clear yet. So, in this paper, relation between potential of this dynamic reference electrode and HF/H_2 gas electrode has been measured to make certain of the potential value of this dynamic reference electrode. Since the thermodynamic significance of the potential of HF/H_2 electrode is clear, the potential measured against the $\text{Li,K/Li}^+, \text{K}^+$ electrode can be easily converted to the potential value with thermodynamic significance.

EXPERIMENTAL METHOD AND APPARATUS

The experimental cell is shown in Fig.1, and the whole experimental system is shown in Fig.2. Commercial LiF and KF (Reagent Grade, Wako Chemicals Co., Ltd) were mixed, and the eutectic mixture was vacuum dried for over two nights at 200°C , after which it was placed in a carbon crucible (Ibigawa Denko Co., Ltd., T-5) and kept further for 20 hours at 350°C under vacuum condition in the cell assembly, and then it was melted and kept at a finite experimental temperature such as 570°C under vacuum. As counter and quasi-reference electrode, glassy carbon rods (Tokai Carbon Co., Ltd., GC30-S) were used. The potential of the quasi-reference electrode was calibrated versus the $\text{Li-K/Li}^+, \text{K}^+$ dynamic reference electrode before use. By means of a constant current electrolysis between the glassy carbon anode and the nickel rod cathode, Li-K alloy of a finite composition ($\text{Li} : \text{K} = 2 : 1$) was deposited on the cathode. By each measurement, this alloy deposition has been newly conducted and very stable and reproducible value (equilibrium potential of this alloy electrode) could be obtained. Fig.3 schematically shows an example of potential build-up and decay of this electrode during constant current electrolysis. The problem of this alloy electrode is that the thermodynamic significance of the equilibrium potential of the reaction:



is not so clear. In order to clarify this, the potential of this alloy electrode should be calibrated versus the potential of the electrode which has very clear thermodynamic significance. For this purpose, HF/H₂ gas electrode has been constructed by using platinum gauze or perforated platinum cylinder as electrode material. These electrodes are expected to show equilibrium potential of the reaction :



Total experimental system is composed of three main parts, ie., electrolytic cell, HF gas supplying part and HF gas recovering part. Pipes and valves in the system are made of nickel or stainless steel, and the system was kept gastight.

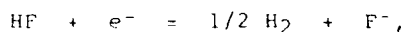
After melting the salt, pure hydrogen gas (purity 99.9999%) was introduced into the cell at first, then mixture of H₂ and HF of a finite composition was introduced into the cell. Partial pressure of the mixture was controlled by passing H₂ gas over NaF-HF pellet (Morita Kagaku Kogyo Co., Ltd.) which was kept at a finite temperature. After the equilibrium has been reached, rest potential of this electrode was measured.

The rest potential was obtained by extrapolating both cathodic and anodic polarization curves to the point of zero current. And in order to clarify the influence of contaminants and the existence of the side reaction, as well as to clarify the cathodic reduction behaviour itself, potential sweep method was also applied.

RESULTS AND DISCUSSION

1. Cathodic Behaviour of HF by Voltammetry

Before measuring the equilibrium potential, in order to get the whole understanding of the cathodic reduction of HF as well as to investigate the influence of the contaminants and the existence of the side reaction, voltammogram of the dissolved HF was investigated in a wide potential range, by the use of immersion type electrode. Gold wire was used as a working electrode. Fig.4 shows a sample voltammogram. In the figure, three peaks are observed: at 1.5-1.6 V (Peak 1), around 1 V (Peak 2), and around 0.7 V (Peak 3), respectively. And at about 0.5 V, sharp current increase can be observed. These are the peaks due to the reaction:



the peak due to the reduction of H_2O , and the peak due to the reduction of OH^- ion or the formation of the alkali metal-gold alloy. Sharp current increase at about 0.5V is due to the deposition of alkali metal alloy.

Fig.5 shows dependence of the peak current of Peak 1 on the potential scanning rate, and Fig.6 shows relation between this peak current and the square root of scanning rate. From the linear relation on the figure, this reaction is suggested to be diffusion controlled.

Though there can be seen a linear relation between peak current and partial pressure of HF in the atmosphere at very low partial pressure range, as it increases, the peak current tends to deviate from linearity and to become saturated. This suggests the very low solubility of HF in the melt. Thus it is clear that by the measurement of the equilibrium potential, gas diffusion type electrode is absolutely necessary to assure three phase zone among gas, molten fluoride, and electrode material.

2. Measurement of Polarization Curve and Equilibrium Potential by the Use of Semi-Immersion Type Gas Electrode

Two kinds of semi-immersion type electrode have been used to measure polarization characteristics and equilibrium potential, i.e., perforated cylinder electrode and platinum gauze electrode.

2-1. Perforated Cylinder Electrode

Fig.7 shows cathodic and anodic polarization characteristics obtained at several partial pressures of HF, by the use of perforated platinum cylinder electrode. Both polarization curves coincide at the current of 0 mA. And the polarization characteristics depend on the partial pressure of HF. Fig.8 shows cathodic polarization curves obtained in a wide potential range. Three plateaus are observed in the figure. Taking into consideration three peaks observed in the voltammogram of the dissolved HF described above, these three correspond to the reduction of HF, the reduction of H_2O and the alkali metal deposition, respectively, in the order from noble to base potential. If we change the current from high to low value, here we observed four plateaus, as seen in the same figure, the reason of which is not clear yet. From the plateau due to the reduction of HF, limiting current i_l of the cathodic reduction of HF is rather high, which is interesting from the technological viewpoint. That is, there is some possibility to use this cathodic reaction

for an electrolytic reaction of producing some useful material at an anode.

Rest potentials measured at several HF partial pressures are plotted against $\log P_{\text{HF}}/(P_{\text{H}_2})^{1/2}$ with open circles in Fig.9. From this figure, relation between rest potential and the partial pressure of gases is given by the following equation :

$$E = (2.015 \pm 0.078) + 2.303(RT/F)\log P_{\text{HF}}/(P_{\text{H}_2})^{1/2} \quad [3]$$

In the root mean square calculation, the slope of the line is fixed at the value of Nernst relation. This equation [3] gives the equilibrium potential of reaction [2].

2-2. Platinum Gauze Electrode

Fig.10 shows examples of cathodic and anodic polarization curves obtained by the use of platinum gauze electrode. For this electrode, platinum gauze was rolled to form gauze cylinder and the bottom of the cylinder was closed by flattening and spot welding. When ohmic loss is corrected, both cathodic and anodic polarizations are almost zero. Rest potentials at several HF partial pressures are plotted with closed circles in Fig.10. From this figure, relation between rest potential and partial pressures of gases is given by the following equation :

$$E = (2.019 \pm 0.024) + 2.303(RT/F)\log P_{\text{HF}}/(P_{\text{H}_2})^{1/2} \quad [4]$$

In the calculation, the slope of the line is fixed at the Nernst relation. This equation [4] gives the equilibrium potential of reaction [2]. Equation [3] and equation [4] are almost coincident and the results of both experiments described above are considered to be reasonable. However, taking into consideration that the platinum gauze electrode is more suitable for the direct gas reaction and in fact the precision is higher in equation [4] than in equation [3], the equilibrium potential of HF/H₂ electrode expressed versus alkali metal electrode is concluded to be given as in equation [4].

ACKNOWLEDGEMENT

This work was supported by a Grant-in-Aid from the Ministry of Education, Science and Culture. The authors thank Morita Kagaku Kogyo Co., Ltd., for supplying NaF·HF pellet for controlling the partial pressure of HF gas.

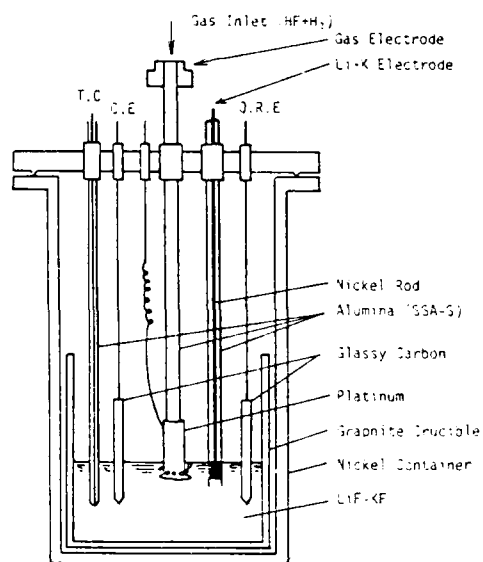


Fig.1 Experimental Cell

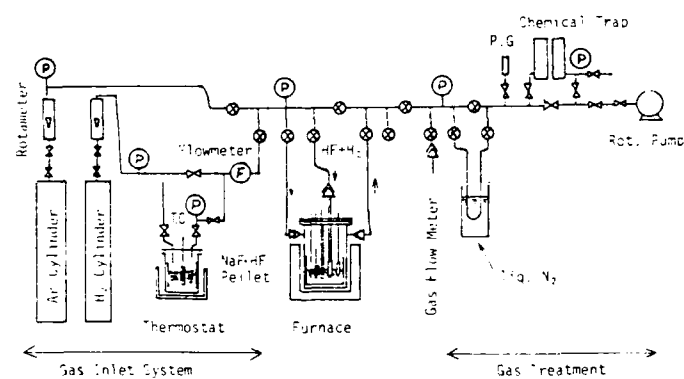


Fig.2 Experimental System

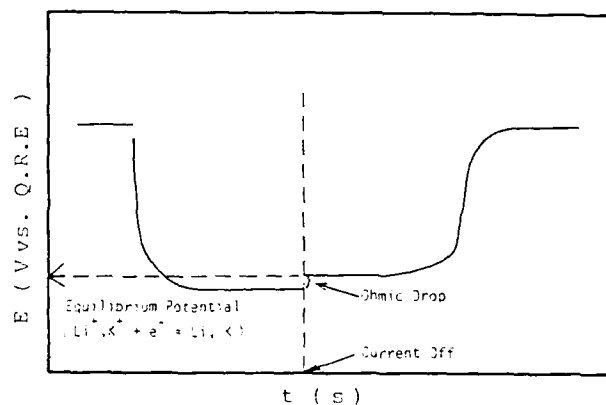


Fig.3 Schematic Representation of the Potential Response of Alkali-Metal Electrode (Potential Decay after the Constant Current Electrolysis; Potential is referred to the Glassy Carbon Quasi-Reference-Electrode)

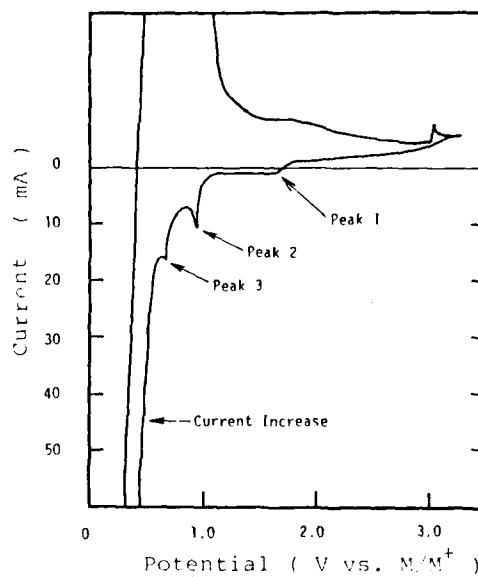


Fig.4 Voltammogram ($P_{HF} = 2.56 \times 10^{-1}$ ata, Sweep Rate 100 mV/s, Au Electrode)

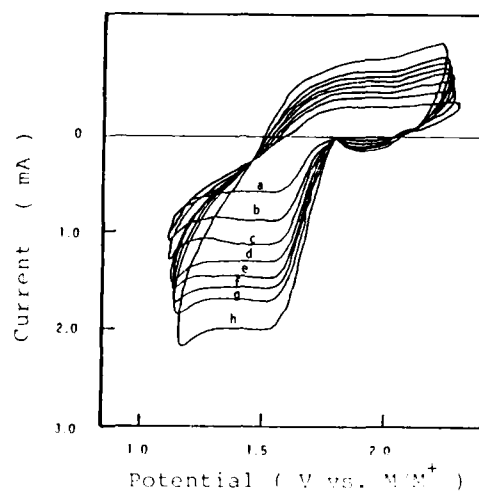


Fig.5 Voltammogram ($P_{HF} = 9.39 \times 10^{-2}$ ata, Sweep Rate; a = 100 mV/s, b = 200, c = 300, d = 400, e = 500, f = 600, g = 700, h = 1000)

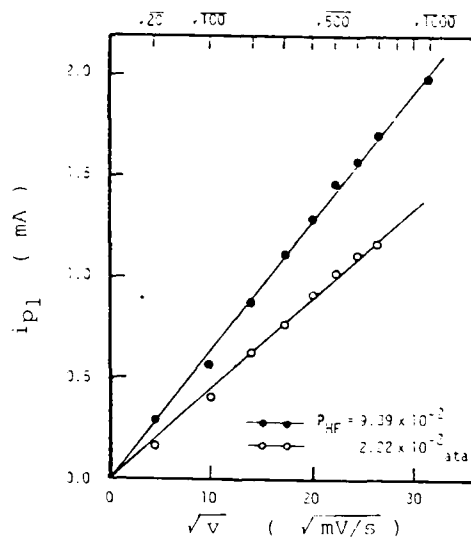


Fig.6 Relation between Peak Current i_{p1} and Square Root of Sweep Rate \sqrt{v}

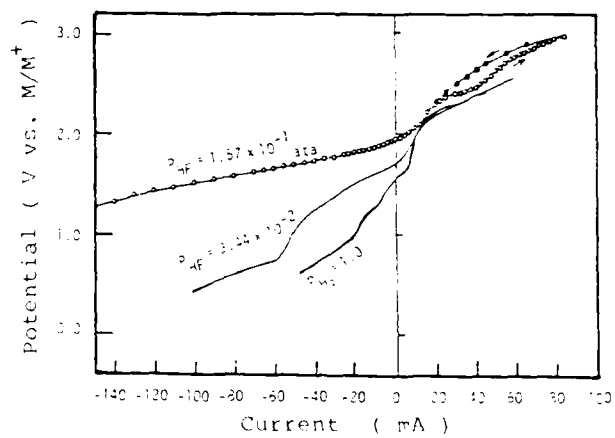


Fig. 7 Polarization Curve

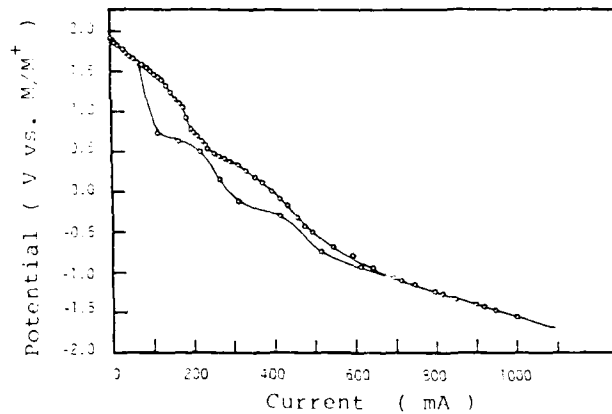


Fig. 8 Polarization Curve ($P_{HF} = 1.57 \times 10^{-1}$ ata)

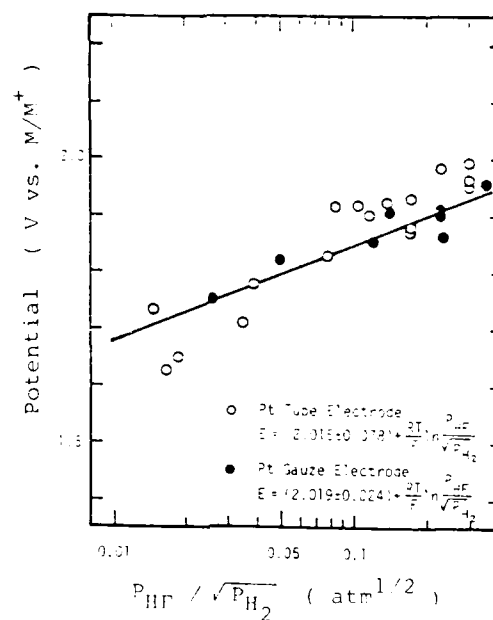


Fig.9 Relation between Potential and $P_{HF} / \sqrt{P_{H_2}}$

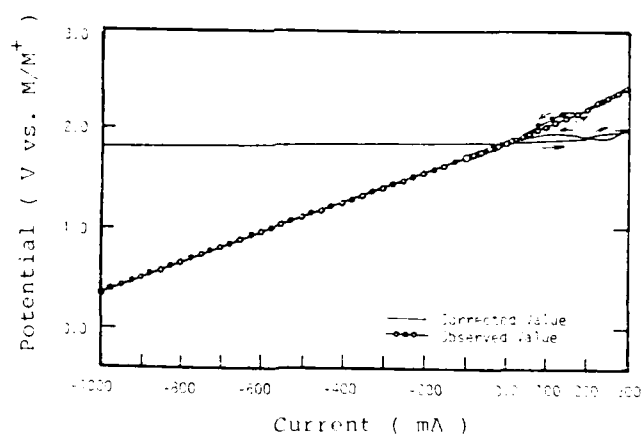


Fig.10 Polarization Curve
 ($P_{HF} = 2.25 \times 10^{-1}$ ata, Pt Tube Electrode)

GALLIUM SPECIES ELECTROCHEMISTRY IN ROOM TEMPERATURE
CHLOROALUMINATE MELTS

S.P. Wicelinski and R.J. Gale
Department of Chemistry
Louisiana State University
Baton Rouge, LA 70803

ABSTRACT

Constant potential and current electrolyses have been used to study Ga(I) ions in room temperature chloroaluminate melts. A potentiometric analysis of Ga(I) ion, produced by anodization in 1.5:1 mole fraction AlCl_3 :1-butylpyridinium chloride (BPC) system, 35°C, gave $E^\circ \text{Ga(I)}/\text{Ga(0)} = +0.339 \text{ V}$ vs. Al(2:1) reference and one-electron Nernst slope. Potentiometry of Ga(I) species, produced by anodization and by reduction of added GaCl_3 , as a function of melt acidity, indicates that GaCl_2^- ion may be the predominant lower valence gallium species in the basic regime. Little, if any, dependence of Ga(I) was found on melt acidity at acidic melt compositions. Deposition of Ga(0) was possible from acidic but not basic melts. A small voltammetric wave, assigned to Al underpotential deposition on Ga, is reported for slow scans in acidic melts. Prospects for depositing pure films of the compound semiconductor GaAs are discussed briefly.

INTRODUCTION

Though the electrochemistry of Ga has received much attention in aqueous media, relatively little is known concerning the electrochemical kinetics of Ga species reduction in nonaqueous media (1). Verdieck and Yntema reported that solutions of Ga(III) in an AlCl_3 -NaCl-KCl molten eutectic at 156°C showed a reduction process at +0.83 V and deposition at about +0.2 V vs. Al reference electrode (2). Anders and Plambeck have investigated the electrochemistry of Ga in an AlCl_3 -NaCl-KCl melt at 135°C (3). Using potentiometric and voltammetric techniques, they demonstrated that chloroaluminate melts favored the existence of the lower valence Ga(I) ionic species more than aqueous media or chloride melts. Shafir and Plambeck reported that the stable oxidation states of gallium in a LiCl-KCl eutectic at 450°C are the metal and the trivalent ion (4). Tremillon and coworkers have investigated the acidobasic properties of molten potassium tetrahalogenogallates (5). They reported that molten tetrahalogenogallates were chemically similar to tetrahalogenoaluminates, however, the existence of the Ga(I) lower oxidation state complicated the determination of melt acidity. More recently, von

Barner has reported the results of potentiometric investigations of the complex formation of Ga(III) in KCl-AlCl₃ melts at 300°C (6).

As part of an investigation of the prospects of electrodepositing films of the commercially important III-V semiconductor gallium arsenide, of useful quality, we have attempted to better understand the electrochemistry of gallium species in room temperature chloroaluminate melt systems (7). GaAs films have potential applications for high efficiency solar cells cf. (8,9) or other semiconductor devices.

EXPERIMENTAL

Preparation of melts and equipment for cyclic voltammetry have been reported elsewhere (7). Constant potential and current electrolyses were made with cells in a dry box under a purified argon atmosphere. Controlled potential coulometric investigations were performed with a PAR 173 Potentiostat/Galvanostat equipped with a PAR 179 Digital Coulometer or an EG&G 273 Potentiostat/Galvanostat. Working electrode cells consisted of a Pt crucible with a maximum melt capacity of about 15 ml and a C crucible which could accommodate about 50 ml of melt. Electrolyses were usually with stirred melts containing less than 75 mg of electroactive species. Crystalline, anhydrous GaCl₃ of 99.999% purity (Aesar) was obtained in sealed ampoules and used as received. Constant current coulometry was performed with a Brinkman (E524) coulostat. Gallium working electrodes were prepared from ingots of Ga metal of 99.99% purity (Alfa). A Keithley 179 TRMS digital voltmeter was used for potentiometric measurements.

RESULTS AND DISCUSSION

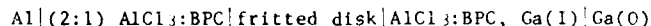
Potentiometric Investigations

In order to understand better the formation and stability of Ga(I) ion species in low temperature melts, constant potential and current electrolyses were performed on acidic melts. Earlier cyclic voltammetric measurements had shown that an exhaustive (theoretical) two-electron reduction depleted the melt entirely of Ga(III) species, added as GaCl₃, thereby allowing electrochemical or spectroscopic examinations of the Ga(I) ion species (7). It has been reported previously that Ga(III) species in a KCl melt at 300°C could not be reduced directly to Ga(0) (5). Although gallium chlorocomplexes behave in many respects similar to aluminum chlorocomplexes, unlike the Ga(I) ion, the Al(I) species has not been shown to be prevalent in either acidic or basic chloroaluminate melt media at 175°C (10). In low temperature basic chloroaluminate melts, it was not possible to reduce the Ga(I) species prior to reduction of the butylpyridinium cation, e.g., cyclic voltammetric studies did not produce current

responses for Ga(I) species (produced by constant potential electrolysis and added to a basic melt). Thus, attempts to electrodeposit gallium in basic melts, similar to the chloride system, were unproductive. In our voltammetric studies of Ga(III) species in low temperature chloroaluminate melts, glassy carbon, tungsten and platinum working electrodes were employed. However, the best electrochemical responses were achieved at platinum. Thus, similar to the case for Al in acidic and basic chloroaluminates, it appears that Ga may be deposited from acidic gallium species but not from the basic complexes which form in the presence of an excess of Cl^- ion in these systems.

Anodization of a pure gallium electrode can be used to determine the standard reduction potential, E_0 , of the Ga(I)/Ga(0) couple. The Nernst plot, shown in Figure 1, was obtained by varying the Ga(I) activity, produced by anodization of Ga at low current densities in a 1.5:1 AlCl_3 :BPC melt, and measuring the emf of the Ga(I)/Ga(0) half-cell vs. Al(2:1) reference electrode. The least squares slope was calculated to be 59 ± 2 mV (theory value for $n = 1$ at 35°C is 61 mV) and the intercept value for the standard electrode potential on the mole fraction scale is $E_0 = 0.339 \pm 0.005$ V vs. Al (2:1) reference. This value may be compared to the E_0 value of 0.199 V obtained at 135°C for Ga(I)/Ga(0) in a ternary AlCl_3 -NaCl-KCl melt (3). No corrections for liquid junction potentials (likely insignificant), nor reference electrode temperature differences are available.

The form of the Ga(I) ion species also may be studied with potentiometry by varying the Lewis acidity (Cl^- ion activity) of the melt. Note that the above Nernst plot of Ga(I)/Ga(0) was uncorrected for any melt acidity change for the Ga(I) ion mole fraction range 3.27×10^{-4} to 2.04×10^{-2} . Such a correction requires a knowledge of the competitive equilibria with free melt Cl^- ion in the acidic regime and the implicit assumption is that the Ga(I) is essentially noncomplexed. Potentiometric titrations of AlCl_3 :BPC melts containing a fixed Ga(I) mole fraction were performed by addition of BPC. The potentiometric measurements involving the Ga(I)/Ga(0) couple were carried out using the cell formally depicted by



Emf measurements were made versus an Al (2:1) reference as a function of melt composition with a high impedance voltmeter. Typical data are illustrated in Figure 2. It may be noted that in the acidic composition range the Ga(I) ion potential is practically unaffected by the melt acidity which may mean that Ga(I) is noncomplexed or in a complex form which does not vary with the melt acidity.

The formation of various types of mononuclear chloro complex ions of the type GaCl_m^{1-m} was considered in the basic composition regime. Information concerning the identity and stability of these complex ions can be obtained by curve fitting basic melt titration data to the

expression

$$E = E_o + (RT/F) \ln X_{GaCl_m}^{1-m} + (RT/F) \ln K - (mRT/F) \ln X_{Cl^-} + E_j$$

where the equilibrium constant, K, is defined by

$$K = X_{Ga(I)} (X_{Cl^-})^m / X_{GaCl_m}^{1-m}$$

E_j , the cell liquid junction potential, can be assumed small and neglected. The Ga(I) ion mole fraction in the basic composition range can be calculated at each of the measured emf values from the Nernst equation,

$$E = E_o + (RT/F) \ln a_{Ga(I)}$$

using the standard electrode potential and assuming that the activity of Ga(I) approximates the mole fraction of Ga(I). Representative data associated with the ion mole fractions for the potentiometric titration of Ga(I) are contained in Tables I and II. Analysis of the potentiometric titration data indicated that Ga(I) is complexed mainly as $GaCl_2^-$ ion in the basic melt.

Table I contains data obtained after the reduction of Ga(III) to Ga(I) in an initial 1.5:1 AlCl₃:BPC melt. The data contained in Table II was obtained after the anodization of a gallium electrode in a 1.25:1 AlCl₃:BPC melt, to produce Ga(I). Figure 3 contains a plot of E vs. $\log X_{Cl^-}$ constructed from the data shown in Tables I and II (indicating a second-power dependence on chloride ion). For the basic emf values obtained from Table I, a graph of emf vs. $\log X_{Cl^-}$ gave a line of slope 0.110 ± 0.01 V (theory value at 35°C is 0.122 V) with a correlation coefficient of 0.95. The least squares slope of the data from Table II, plotted in Figure 3, is 0.106 ± 0.008 V (theory value at 40°C is 0.124 V) with a correlation coefficient of 0.99. Deviation from ideality with respect to the second-power dependence on Cl⁻ ion mole fraction might arise from an inadequate model or the presence of adventitious oxidants. The presence of these oxidants caused difficulties in obtaining accurate emf values, however, it is reasonable to infer from these results that $GaCl_2^-$ ion is the predominant species in the basic regime.

Voltammetric Investigations

As mentioned above, platinum proved to be the best substrate electrode material for resolving voltammetric waves. Unfortunately, as reported earlier (7), even with platinum, the reduction waves Ga(III)/Ga(I) and Ga(I)/Ga(0) had quasi-reversible characteristics and showed evidence of complications as a function of acidity in the 1:1 to 2:1 melt composition range.

Cyclic voltammetric studies also have been performed using AlCl₃:1-methyl-3-ethylimidazolium chloride (MEIC) melts at various melt

compositions. The Ga(III), added as GaCl₃ to the AlCl₃:MEIC melts, exhibited behavior similar to that obtained when added to AlCl₃:BPC melts. Two poorly defined reduction waves, Ga(III)/Ga(I) (or Ga(0)) reduction followed by Ga(I)/Ga(0) reduction, occur in the acidic regime. However, an oxidation peak in the acidic AlCl₃:MEIC melts, at approximately +1.3 V vs. Al (1.5:1) reference (Figure 4) is sharper than the oxidation peak in the corresponding AlCl₃:BPC melts. The sharp anodic peak at circa +1.3 V presumably is the Ga(0) stripping peak and the shoulder at positive potentials may be due to Ga(I)/Ga(III) oxidation. Especially at scan rates below 100 mV/s, stripping peaks were obtained which possessed shoulders. Broad stripping peaks or stripping peaks with shoulders are likely to be indicative of composite behavior of two or more species being oxidized. The consequence of slow electron transfer kinetics has meant that a large excess of gallium species over arsenic species is required to obtain codeposited films of GaAs. For this reason, we have recently commenced a study of chlorogallate melts from which, it is hoped, more favorable electron transfer kinetics can be achieved (11).

Aluminum Underpotential Deposition

A second reason to use chlorogallate media would be to reduce the possibility of unwanted Al codeposition, possibly as AlAs, in GaAs films. Deposition of metals at potentials more positive than their thermodynamic reversible potentials is a phenomenon termed underpotential deposition (UPD). This phenomenon precedes the bulk deposition of the metal, which occurs negative to the reversible potential. Metal ion adsorption occurs in an area described as the underpotential range, which may extend over a potential of a few hundred millivolts positive of the equilibrium potential. The underpotential, E_u , may be expressed by

$$E_u > E_o + (RT/zF) \ln a_M z^+ / a_M$$

In this expression, E_o is the equilibrium potential of the deposited metal-metal ion electrode.

The deposition of a metal at potentials significantly positive to that of bulk deposition has been observed in aqueous systems for Ag(I), Tl(I) and Cu(II), e.g. (12), on Au. In addition, this same phenomenon is well known with regards to the formation of monolayers of atomic hydrogen on Ir, Pt and Rh electrodes (13). Similar behavior occurs in molten salt systems. For example, using a LiCl-KCl molten salt systems, Schmidt investigated the deposition of Ag(I), Cd(II), Ni(II) and Pb(II) ions and briefly addressed monolayer formation processes (14). Hills et al. have studied the deposition of Ag and Ni on Pt from the LiCl-KCl eutectic at 400°C (15) and they observed predeposition of Ni at 0.5 V positive to the equilibrium potential, and predeposition of Ag at 0.1 V positive to the reversible potential.

During investigations of the electrochemistry of gallium in the room temperature chloroaluminate melts, cyclic voltammograms were obtained that perhaps indicate the presence of the UPD phenomenon. Figure 5 contains a voltammogram of Ga(III) at a slow scan rate (5 mV/s) in a very acidic, $\text{AlCl}_3\text{:BPC}$ melt. After the second reduction wave, $\text{Ga(I)} \rightarrow \text{Ga(0)}$, a third, sharp reduction wave was obtained. This reduction peak at circa +0.16 V vs. Al (2:1) reference is presumably the underpotential deposition of Al onto Ga. After reversing the direction of the voltammetric sweep, an anodic peak (Al stripping) was obtained at approximately +0.24 V. Successive scans past 0.0 V showed that bulk deposition of Al occurred at potentials near -0.1 V vs. Al (2:1) reference. Thus, the underpotential deposition occurs at a potential about 150 mV positive of the equilibrium potential. Integration of the currents, for the UPD of Al and the subsequent stripping, showed that the charge for Al predeposition on the cathodic sweep is nearly equal to the charge on the anodic sweep. The UPD phenomenon has been explained in terms of the existence of stronger attractive forces between atoms of the depositing metal and foreign atoms of a substrate than between similar atoms of the bulk metal (16). It is difficult to state if a GaAl intermetallic compound is responsible for this effect. This appears to be the first reported case for aluminum underpotential deposition.

REFERENCES

1. T. I. Popova, I. A. Bagotskaya and E. D. Moorhead, "Encyclopedia of Electrochemistry of the Elements", A. J. Bard (Ed.), Vol. VIII, Marcel Dekker, Inc. (1978), p. 207.
2. R. G. Verdieck and L. F. Yntema, *J. Phys. Chem.*, **48**, 268 (1944).
3. U. Anders and J. A. Plambeck, *Can. J. Chem.*, **47**, 3055 (1969).
4. J. M. Shafir and J. A. Plambeck, *Can. J. Chem.*, **48**, 2131 (1970).
5. I. G. Dioum, J. Vedel and B. Tremillon, *J. Electroanal. Chem.*, **137**, 219 (1982).
6. J. H. von Barner, *Inorg. Chem.*, **24**, 1686 (1985).
7. S. P. Wicelinski and R. J. Gale, "GaAs Film Formation from Low Temperature Chloroaluminate Melts", Proc. 5th Int. Symp. on Molten Salts, Vol. 86-1, The Electrochemical Society (1986), p. 144.
8. F. A. Shirland and P. Rai-Choudhury, *Rep. Prog. Phys.*, **41**, 1839 (1978).
9. H. J. Hovel, "Semiconductors and Semimetals", Vol. 11, Academic Press (1975), p. 217.
10. R. J. Gale and R. A. Osteryoung, *J. Electrochem. Soc.*, **121**, 984 (1974).
11. S. P. Wicelinski, R. J. Gale and J. S. Wilkes, *J. Electrochem. Soc.*, **134**, 262 (1987).
12. W. J. Lorenz, H. D. Hermann, N. Wuthrich and F. Hilbert, *J. Electrochem. Soc.*, **121**, 1167 (1974).
13. S. Hadzi-Jordanov, H. Angerstein-Kozłowska, M. Vukovic and B. E. Conway, *J. Phys. Chem.*, **81**, 2271 (1977).
14. E. Schmidt, *Electrochim. Acta*, **8**, 23 (1963).

15. G. J. Hills, D. J. Schiffrin and J. Thompson, J. Electrochem. Soc., 120, 157 (1974).
16. A. R. Despic, "Comprehensive Treatise of Electrochemistry", Vol. 7, B. E. Conway, J.O'M. Bockris, E. Yeager, S. U. Khan and R. E. White (Eds.), Plenum Press (1983), p. 451.

Table I. Ion Mole Fractions and Potentials for Titration of 4.64×10^{-3} M Ga(I) in a 1.5:1 AlCl₃:BPC Melt at 35°C.

E, V	Ga(I)	Cl ⁻ in excess to 1:1	GaCl ₂ ⁻	Cl ⁻ ^a
-0.963	5.21×10^{-22}	1.63×10^{-2}	4.39×10^{-4}	1.55×10^{-2}
-0.968	4.28×10^{-22}	3.99×10^{-2}	4.28×10^{-4}	3.90×10^{-2}
-1.026	4.76×10^{-23}	7.23×10^{-2}	4.14×10^{-4}	7.15×10^{-2}
-1.049	2.02×10^{-23}	1.11×10^{-1}	3.97×10^{-4}	1.11×10^{-1}
-1.065	1.12×10^{-23}	1.64×10^{-1}	3.73×10^{-4}	1.63×10^{-1}

^a) Excess chloride ion fraction less the amount complexed with Ga(I).

Table II. Potentials and Ion Mole Fractions for Titration of 5.93×10^{-2} M Ga(I) in a 1.25:1 AlCl₃:BPC Melt at 40°C.

E, V	Ga(I)	Cl ⁻ in excess to 1:1	GaCl ₂ ⁻	Cl ⁻ ^a
-0.920	2.57×10^{-21}	1.02×10^{-2}	6.01×10^{-3}	6.16×10^{-3}
-0.983	2.32×10^{-22}	2.94×10^{-2}	5.94×10^{-3}	1.75×10^{-2}
-1.002	1.15×10^{-22}	4.53×10^{-2}	5.88×10^{-3}	3.33×10^{-2}
-1.021	5.69×10^{-23}	6.54×10^{-2}	5.72×10^{-3}	5.39×10^{-2}
-1.037	3.069×10^{-23}	8.90×10^{-2}	5.58×10^{-3}	7.78×10^{-2}
-1.054	1.65×10^{-23}	1.06×10^{-1}	5.47×10^{-3}	9.52×10^{-2}

^a) Excess chloride ion fraction less the amount complexed with Ga(I)

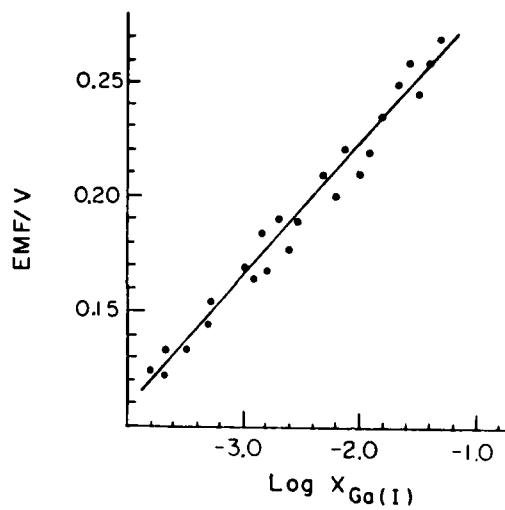


Figure 1. Nernst plot of $Ga(I)/Ga(0)$ vs. $Al(2:1)$ ref. for a 1.5:1 $AlCl_3:BPC$ melt, $35^\circ C$.

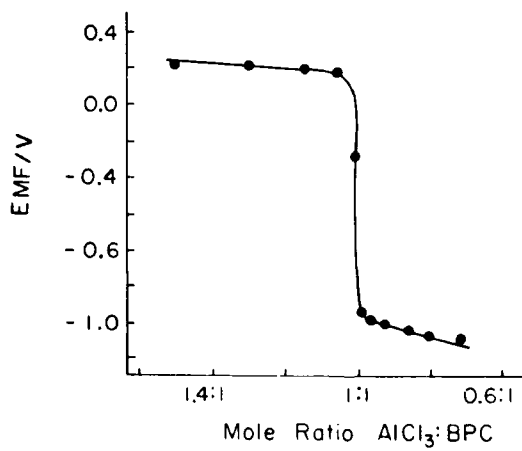


Figure 2. Potentiometric titration of $Ga(I)$ as a function of $AlCl_3:BPC$ melt acidity, $35^\circ C$.

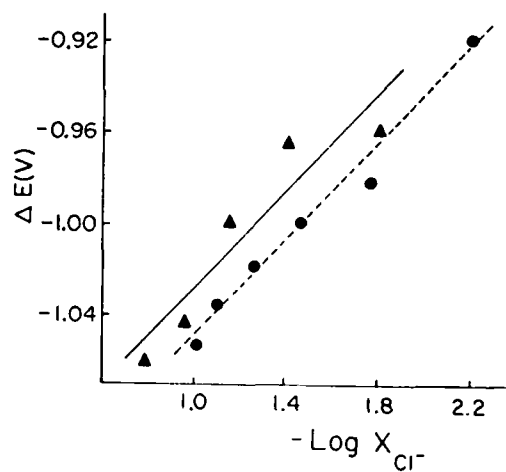


Figure 3. Variation of the cell potential with the calculated chloride ion mole fraction in basic $\text{AlCl}_3\text{:BPC}$.
 (▲) Basic emf values at 35°C, Ga(I) produced by reduction of Ga(III).
 (●) Basic emf values at 40°C, Ga(I) produced by anodization of Ga(0) working electrode.

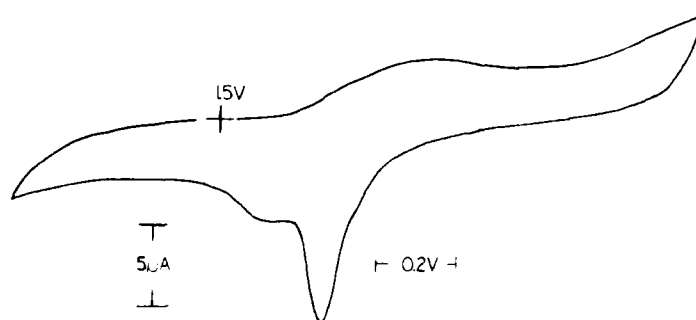


Figure 4. CV of ~30 mM Ga(III) at 50 mV/s, W electrode area 7.06 mm², in (1.1:1) $\text{AlCl}_3\text{:MEIC}$, 25°C.

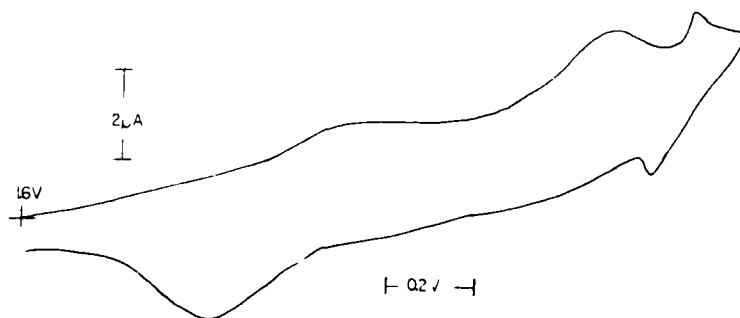


Figure 5. CV of ~ 15 mM Ga(III) at 5 mV/s, Pt button area 0.810 mm^2 , in (1.87:1) AlCl_3 :BPC, 40°C .

ON THE INITIATION OF ANODE EFFECT IN CHLORIDE MELTS

Ulf Erikson and Reidar Tunold

Institutt for Teknisk Elektrokjemi
Norges Tekniske Høgskole (NTH)
Universitetet i Trondheim
7034 NTH, NORWAY

ABSTRACT

The gas evolution process and the initiation of anode effect (AE) have been studied in chloride melts on different shapes of electrodes made of various materials. The critical cd (ccd) has been determined as a function of composition. The value of ccd varied from about 1 A cm^{-2} in pure NaCl melts to $20\text{--}35 \text{ A cm}^{-2}$ in melts containing 20-30wt% MgCl_2 .

The formation and detachment of bubbles have been studied by visual inspection and by short film sequences.

A mechanism for the initiation of anode effect is proposed.

INTRODUCTION

The anode effect (AE) which manifests itself as a blocking of the anode surface inhibiting current transfer, is a well-known phenomenon especially occurring in molten salt systems such as in cryolite/alumina and other halide based melts. It is even found in aqueous solutions where it also occurs in connection with the cathodic hydrogen evolution, making this phenomenon a general electrode effect. The mechanism for initiation of AE may however be different in different systems. Several possible causes for AE have been proposed, which can be summarized briefly as follows:

- i) Formation of an insulating solid compound on the anode surface (1-4)
- ii) Deteriorating wettability between the anode and the melt due to:

- a) changes in surface tension (5,6)
- b) formation of surface-compounds (7-12) or gaseous anode products (13,14)

iii) Mass transfer problems due to

- a) transport of gas bubbles away from the anode surface becoming rate controlling, resulting in gas blanketing of the surface (15,16)
- b) spontaneous formation of a gas film from a supersaturated melt in the vicinity of the anode surface (17,18)

iv) Electrostatic attraction of negatively charged gas bubbles to the anode (19,20)

v) Thermal effects, IR-heating of the anode/electrolyte interface resulting in vapourization of the electrolyte close to the anode (21).

A main problem in proposing a comprehensive theory is the rather large differences in critical cds observed in different melts, from about 0.1 A cm^{-2} in some fluoride melts (22) to $20\text{-}35 \text{ A cm}^{-2}$ in some chloride melts and in aqueous solutions, as found in the present investigation.

In the present work we have studied AE in chloride melts. The critical cd for the onset of AE has been studied as a function of the MgCl_2 -content in the binary mixture with NaCl and in quaternary mixtures with NaCl, KCl and CaCl_2 in the temperature range of $750\text{-}830^\circ\text{C}$. The gas evolution process including bubble formation and detachment, and the formation of a gas film, was studied visually and by making film sequences. A mechanism for the initiation of AE is proposed.

EXPERIMENTAL

Cell, melts and electrodes

Most of the experiments were carried out in a transparent gold film silica furnace (Trans Temp. Inc., USA).

Alkali chlorides were purified by heating in vacuum, melting and recrystallization. Magnesium chloride and calcium chloride were heated by slowly increasing the temperature to about 400°C in HCl-atmosphere. The magnesium chloride was thereafter distilled in vacuum. Calcium chloride was finally melted under HCl atmosphere and then filtrated through a silica frit. All handling of the purified salts was performed in a dry box atmosphere. The final salt mixture was contained in a transparent silica-tube (55 mm ϕ) with bottom.

The following types of anodes were used:

- Spectrographic graphite, Grade II (4.56 mm ϕ) from Johnson, Matthey Chemical Ltd., England, encapsulated in boron nitride. These electrodes were conically shaped with the active anode area facing downwards and with a typical area of 0.5 cm²
- Glassy carbon rods, 3mm ϕ , type GC-30 from Tokai Carbon Co., Ltd., Japan
- Spectrographic graphite rods, same quality as above
- A tungsten rod, 1.8 mm ϕ (99.9% purity), from Tungsten Manufacturing Co. Ltd., England

As a counter electrode, a Mg/Ni alloy rod shielded by a quartz tube was employed.

Measuring procedures

The ccd was measured by using a voltage sweep method at two different sweep-rates, $v = 0.33 \text{ Vs}^{-1}$ and $v = 3.44 \text{ Vs}^{-1}$. Occasionally a "semi-potentiostatic" method was employed, where the cell voltage was kept constant allowing the cell current to stabilize before proceeding to a higher voltage.

The gas evolution process and the onset of AE was filmed by a 16 mm movie camera.

Melt samples were taken after each addition of MgCl_2 and analyzed by atomic absorption spectrometry.

RESULTS AND DISCUSSION

The critical cd

Values for the critical cd as a function of MgCl_2 -content are shown in Fig. 1 and 2, measured by the voltage sweep method. In Fig. 1 results from the measurements in the binary system MgCl_2 -NaCl are shown. The ccd seems to increase from values of 1-4 A cm⁻² in pure NaCl to about 30 A cm⁻² at 25 wt% MgCl_2 , with no further increase at higher content. The same general trend is found in the quaternary system as shown in Fig. 2, but with a somewhat lower ccd. The reproducibility of the current values at different electrodes was not good and was even slightly worse at lower sweep rates. At lower sweep rates the measured ccds were somewhat reduced.

The main difference between the pure alkali chloride melts (and in

mixtures with CaCl_2) and melts with MgCl_2 , is the interfacial tension which is reduced by adding MgCl_2 to the melts. Pure CaCl_2 has a surface tension of 147 dyn cm^{-1} at 800°C and pure NaCl 116 dyn cm^{-1} ($T=850^\circ\text{C}$), whereas the surface tension of MgCl_2 is 62 dyn cm^{-1} (23). The contact angle between a graphite surface and chlorine bubbles in molten chlorides have been determined to $120 - 175^\circ\text{C}$ in pure NaCl and to $36 - 40^\circ\text{C}$ in pure MgCl_2 (24). This means that the melt is wetting the surface better the more MgCl_2 is added, leading to smaller contact angles between the electrode and the gas bubbles and therefore to smaller bubbles.

Visual observations

Visual observations reveal large differences in the gas evolution process in NaCl melts and in melts with low MgCl_2 content, compared with melts with more than about 5 wt% of MgCl_2 . The difference is shown in Fig. 3 and 4. The effect of anode geometry is also pronounced.

Gas evolution and the initiation of AE on rod-shaped anodes

Visual observations show that the gas evolution process in pure NaCl and in melts with a low MgCl_2 -content ($\leq 5 \text{ wt}\%$) is distinctly different from how it appears in melts with higher MgCl_2 -content, as shown in Fig. 3 compared to Fig. 4. The arrows in the figures indicate bubble movements. The numbers (1) to (3) are showing stages in the gas evolution process during a continuously increasing cell voltage/current sweep.

Fig. 3 shows gas evolution in pure NaCl .

- (1): The gas evolution has started and a few bubbles coalesce. The bubbles, having a large contact area with the anode, are nonsymmetrical and rather flat. This means the contact angle θ is large (see Fig. 5). No bubbles leave the anode surface directly, but move upwards in a "creeping" manner still adhering to the electrode, until they meet the boundary atmosphere/melt, where they disappear into the gas phase.
- (2): The situation is similar except that the cd (and cell voltage) is higher, giving a faster growth of the bubbles. At the same time more bubbles coalesce, giving as a total effect, an increasingly larger area covered by gas bubbles.
- (3): Ultimately a few large bubbles coalesce suddenly, resulting in AE. A thin continuous gas film covering the entire anode surface appears. The current immediately drops to a very small value of about 0.01 A cm^{-2} . The ccd in such cases is $1-3 \text{ A cm}^{-2}$.

In fig. 4, 5-10 wt% MgCl_2 has been added to the melt.

- (1): The reaction has started, producing small circular bubbles having a much smaller contact area with the anode than the bubbles in fig. 3. This is probably due to the improved wetting conditions at the melt/anode-interface, resulting in a smaller contact angle θ (Fig. 5).
At this stage (i.e. at low cd) the bubbles move upwards on the surface and a few coalesce, still adhering to the electrode.
- (2): When the cd is increased, more and more bubbles start to leave the electrode surface directly to the melt.
- (3): After a while the gas evolution process becomes quite vigorous at very high cd s. Then, suddenly, the gas evolution stops and a thin gas film is observed at the anode surface, corresponding to the onset of AE. The cd in this case is very high, $\approx 10-35 \text{ A}\cdot\text{cm}^{-2}$.

The interfacial potential seems to stabilize the gas film. When the potential sweep is reversed to a value somewhat lower than the voltage at the moment of initiation, the gas film disappears and normal gas evolution starts. The film vanishes from the lower end of the electrode and upwards, during a period of one to two seconds.

Conically shaped anodes, encapsulated in boron nitride

Figure 6 shows a corresponding sequence from (1) to (3) as in Fig. 3 observed in melts with a low MgCl_2 content.

In this case, however, the interface boron nitride/graphite seems to hinder the upward motion of the bubbles. Ultimately a few large bubbles coalesce, forming one large bubble covering the entire anode surface. This bubble remains at the electrode in the same way as the gas film observed on rod shaped electrodes, until the voltage is reduced to a value below the critical cell voltage necessary for initiating AE. Then the gas evolution will start as prior to AE.

At higher MgCl_2 -content ($\geq 5 \text{ wt}\%$) gas bubbles will leave also this electrode directly to the melt. The critical cd is very high ($10-35 \text{ A}\cdot\text{cm}^{-2}$) and the gas evolution becomes vigorous. The detachment of bubbles, however, seems not to be hindered by the edge between the graphite and the encapsulation. The AE occurs in the same manner as with the rod shaped electrodes. A thin gas film is formed spontaneously with a corresponding abrupt fall in the cd .

Changes of electrode materials and electrolyte

Tungsten anode

When using a tungsten rod as an anode in the chloride melt, the same development of AE was observed as with graphite rod electrodes. Gas evolution took place at the same time as tungsten dissolved anodically. The total ccd was about 15 A cm^{-2} in a NaCl-MgCl_2 melt containing 10 wt% MgCl_2 . In this value the anodic dissolution current is also included. This means that the mechanism of the AE is probably independent of the electrode material.

Aqueous solutions

The anode (electrode) effect was also studied in an alkaline aqueous solution where oxygen was evolved on a conically shaped graphite electrode encapsulated in boron nitride and a Pt wire electrode. The critical cd was very high, 30-40 A cm^{-2} , on both types of electrodes. Very small bubbles were detached from the electrode surface in the same manner as shown in Fig. 4. The gas evolution became very vigorous with increasing cd. No large bubbles could be observed on the surface before the anode effect took place. The anode effect was initiated very suddenly also in this case. In case of the encapsulated graphite electrode one large bubble covering the whole surface was formed. On the Pt wire AE resulted in a thin gas film, as on the graphite rod electrode in the melt.

That this film really was a hydrogen film and not water vapour could be seen by the fact that the film was stable while the potential was kept constant or increased. With the reduced heating any water vapour should then condense. When reducing the potential, the film disappeared in the same way as in the molten salt systems.

GENERAL DISCUSSION

If only physical properties of the electrode/electrolyte interface are determining the initiation of AE, one should anticipate rather reproducible ccds. It seems, however, that the ccd is rather irreproducible and that geometrical factors are participating. This indicates that the gas evolution process and the detachment of bubbles are the main determining factors.

We have earlier shown that AE can occur during very high current pulses before any bubble formation (17). In that case a thin gas film is probably formed from the supersaturated melt in the vicinity of the interface. Calculations have shown that in such a transient, concentration of chlorine might become thousand to ten thousand times the equilibrium saturation value in a film of thickness 10^{-4} cm . A gas film from such a layer would have a volume that is

about ten times the corresponding melt volume (17).

In melts with good wetting properties, i.e. in melts with a high content of MgCl_2 , there seem to be no large effects of geometry. Bubbles detach readily from the surface. The active surface becomes smaller with increasing cd due to the increasing amount of bubbles on the surface. At the onset of AE a gas film is suddenly formed at the active surface area, covering the whole electrode. In this case the ccd is very high.

In melts with inferior wetting properties the bubbles stick to the electrode and coalesce to large bubbles with irregular shapes and which move along the electrode surface, adhering to it. The movements of the bubbles will depend on geometrical factors. The active area becomes very small with increasing current and AE occurs either by the coalescence of all existing bubbles or also here, by the sudden formation of a gas film from the supersaturated melt between the bubbles. This effect will bring about total coalescence of all bubbles.

If the active electrode surface continues into the atmosphere, the bubbles disappear into the gas phase and only a thin gas film is retained at the electrode. If an edge or another obstacle hinders the bubble movement, the electrode seems to be covered by a gas blanket. This probably also depends on the size of the electrode.

CONCLUSIONS

The critical cd for the initiation of anode effect depends on the wetting properties of the melt/electrode interface, being large in melts with good wetting properties and rather small in melts with high interfacial tensions.

The wetting properties as well as geometrical factors, decide the size of gas bubbles and the coalescence, detachment and transport of bubbles away from the surface. The AE is probably created by the sudden formation of a gas film from the supersaturated melt. The magnitude of the ccd then depends on the active, bubble free interface.

REFERENCES

- (1) K. Arndt and H. Probst,
Z. Electrochem. 29, 323 (1923)
- (2) L.N. Antipin and N.B. Tyurin,
Zhur. Fiz. Khim. 31, 1103 (1957)
- (3) E. Pruvot, Allumina 22, 709 (1953)
- (4) Y. Kanaya and N. Watanabe,
Denki Kagaku 40, (6) 417 (1972)
- (5) K. Grjotheim and C. Krohn,
Freiberger Forschungshefte B82, 63 (1964)
- (6) E.A. Zhemchuzhina,
Izv. Akad. Nauk. SSSR Met. (3) (1965)
- (7) W. Rüdorff, G. Rüdorff, J. Endell and G. Ruess,
Z. Anorg. Chem. 256, 126 (1948)
- (8) C. Krohn,
Lic. Thesis, Inst. Uorg. Kjemi NTH (1963)
- (9) Yu.I. Aleksandrov and V. P. Mashovets,
J. Appl. Chem. USSR 39, (11) 2346 (1966)
- (10) V.P. Mashovets and Yu.I. Aleksandrov,
J. Appl. Chem. USSR 43, (3) 814 (1970)
- (11) P. Mergault,
C.R. Acad. Sc. Paris 240, 765 (1955)
- (12) N. Watanabe and T. Asaue,
J. Electrochem. Soc. Japan 39, 107 (1971)
- (13) M. Fréjaques,
Bull. Soc. Franc. Electr. 9, 684 (1949)
- (14) A. Vajna,
Met. Ital. 44, 585 (1952)
- (15) R. Piontelli, A. Berbenni, B. Mazza and P. Pedeferrri
Electrochim. Met. 1, (3) (1966)
- (16) B. Mazza, P. Pedeferrri and G. Re,
Electrochim. Acta. 23, 87 (1978)
- (17) R. Tunold and T. Berge,
Electrochim. Acta 19, 849 (1974)
- (18) H. Vogt,
Electrochim. Acta 29, (2) 167 (1984)
- (19) H. Wartenberg,
Z. Elektrochem. Met. 32, 330 (1926)

- (20) P. Drossbach and P. Krah1,
Z. Elektrochem. 62, 178 (1958)
- (21) H.H. Kellogg
J. Electrochem. Soc. 97, (4) 133 (1950)
- (22) J. Thonstad, F. Nordmo and J.K. Rodseth,
Electrochim. Acta 19, 761 (1974)
- (23) K. Grjotheim, J.L. Holm, B. Lillebuen and H.A. Oye,
Acta Chem. Scand. 26, 2050 (1972)
- (24) K. Grjotheim, A.H. Schultz and H.A. Oye,
Met. 26, 236 (1972)

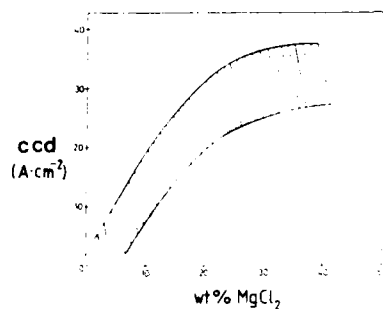


Figure 1.
Critical Current Density (CCD) vs
 MgCl_2 Content, Binary System
 NaCl-MgCl_2 , Voltage Sweep
Measurements, $v=3.44 \text{ V s}^{-1}$,
 $T = 830 \pm 5^\circ\text{C}$.

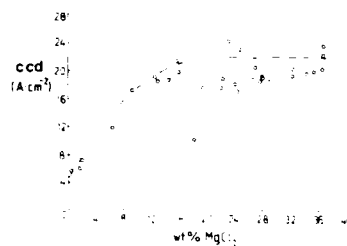


Figure 2.
CCD vs MgCl_2 Content, Quaternary
System $\text{NaCl-KCl-CaCl}_2\text{-MgCl}_2$, Voltage
Sweep Measurements, $v=3.44 \text{ V s}^{-1}$,
 $T = 750^\circ\text{C}$.

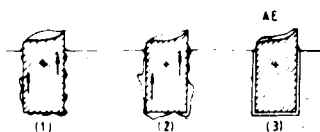


Figure 3.
Gas Evolution on a Rod Shaped
Anode in Pure NaCl , Low CCD.

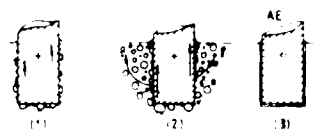


Figure 4.
Gas Evolution in $\text{MgCl}_2\text{-NaCl}$ Melt,
High CCD.

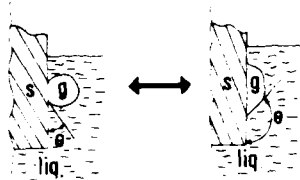


Figure 5.
Gas Bubble and Contact Angle,
Melt/Solid/Gas in Melts with
a) Good Wetting Properties,
b) Inferior Wetting Properties.

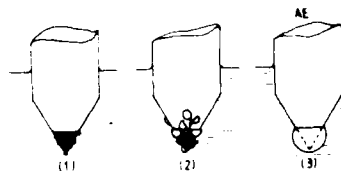


Figure 6.
Gas Evolution on Conically Shaped
Anodes Encapsulated in Boron
Nitride, in Melts without MgCl_2
or with a Low MgCl_2 -Content.

CONCEPTS AND REALITIES OF CHEMICAL AND
ELECTROCHEMICAL REACTIONS IN MOLTEN SALTS

Keith E. Johnson and E. Wayne Yerhoff

Department of Chemistry, University of Regina
Regina, Saskatchewan, Canada S4S 0A2

ABSTRACT

Our present knowledge of the electrolytic reduction of molten nitrates is reviewed. Direct and catalytic reduction may both occur and the former is particularly sensitive to the cation present. This may arise because of the different structural energetics of oxide, peroxide and superoxide coordination by cations. Such coordinations are extended to other solvents. Acid-base equilibria pertinent to nitrate, chloroaluminate and antimony chloride salts are discussed with emphasis on acidity-oxidative power relations. The usefulness of the silver(I)-silver potential and of transition metal ion coordination site detection are pointed out.

INTRODUCTION

During the last 40 years molten salt chemistry developed against a background of (a) aqueous chemistry, including acid-base equilibria and a transformation and rationalization of coordination chemistry; (b) a viewpoint of inorganic chemical facts; and (c) a developing mechanistic approach to first organic, and later inorganic reactions. It should come as no surprise to find molten salt chemistry and electrochemistry explained in a variety of ways: either along the lines that a new field allows for other chemistries to be forgotten, or in terms of fitting all the results to models derived from the extant science.

It is the purpose of this paper to discuss several molten salt chemistry results in terms of thermodynamics, complexation, acid-base equilibria, kinetics, electrochemical studies and spectroscopy. We shall attempt: (a) to distinguish between concepts, useful or otherwise, and established realities; and (b) to comment on mechanisms and postulates consistent with observation

and species identification. The systems considered include molten nitrates, oxygen anions, the stabilization of silver ions in melts and the chemistry of aluminum, zinc and antimony chloride systems.

MOLTEN NITRATES

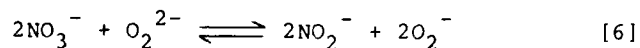
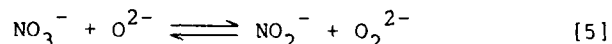
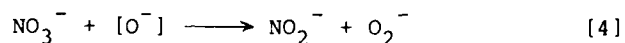
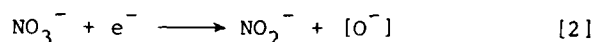
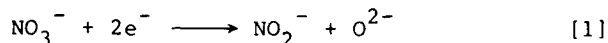
The oxidative power of molten alkali nitrates is well known; it suggests that few metals or non-metals should be stable in contact with the melts, and it is consistent with their decomposition into oxygen and nitrite at moderate temperatures with some peroxide formation at higher temperature (1). It was no surprise therefore to find nitrate as one electroreduction product of alkali nitrates (2), but what else was produced was not so obvious. Hittorf in 1847 (3) proposed that peroxide was formed at platinum electrodes in sodium and potassium nitrates. Several groups observed the inhibition of electro-reduction of nitrate in lithium- or sodium-based melts and ascribed it to alkali monoxide precipitation (2,4,5). Eventually, Zamboni and Jordan (6,7) identified peroxide and superoxide in addition to nitrite in electrolysed $\text{NaNO}_3\text{-KNO}_3$, provided the melts were dry, and suggested that water catalysed the reduction of nitrate in wet melts. NO_2 (or N_2O_4) has not been isolated in molten nitrate reductions.

The oxygen chemistry of the alkali metals features Li_2O , Na_2O_2 and KO_2 as the most stable compounds, with Li_2O_2 and Na_2O also being formed on burning the metals in air. Na_2O (and K_2O) are best obtained by the reduction with Na(K) of the peroxide, hydroxide or nitrite.

Voltammetric studies of water and several metal ions (e.g. Pb^{2+}) in solution in alkali nitrates show reduction waves prior to the solvent wave. The reduction currents are proportional to solution concentration, but the temperature dependence of these currents (8) indicates a process with activation energy comparable to that of the solvent reduction (2,4). The original assumption was that water was reduced to hydrogen, but that metal ions were reduced to metal which then reacted with the nitrate to yield metal oxide (9) and nitrite (not identified). Attempts to anodically oxidize such metals to the ions in solution failed: the metal grew an oxide coat.

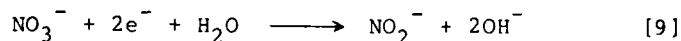
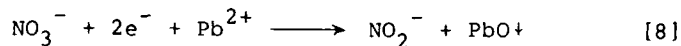
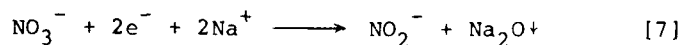
From these summarized observations we can conclude that the following processes occur when molten nitrates are electrolysed.

(a) Nitrate itself is reduced to nitrite and oxidic species by one or more of the following:



The observation that: (i) after a bulk electrolysis of $\text{NaNO}_3\text{-KNO}_3$, superoxide concentration slowly increases at the expense of peroxide (7); (ii) NaNO_3 electrolysis yields more peroxide than superoxide and KNO_3 electrolysis yields the reverse (10); and (iii) the reduction peaks occur at more negative potentials in the sequence $\text{LiNO}_3\text{-KNO}_3$, $\text{NaNO}_3\text{-KNO}_3$, NaNO_3 (20% w/w) in KNO_3 (11), make it appear that, as in the thermal combustion of the metals, O_2^- formation is favoured by Li^+ , O_2^{2-} formation by Na^+ and O_2^- formation by K^+ . This necessarily implies that the oxidic species in solution is cognizant of its alkali metal ion environment. One could then imagine reactions [1], [5] and [6] occurring in mixed melts, reaction [1] only in LiNO_3 and reactions [2], [4] and [3] in KNO_3 .

(b) The reduction of nitrate is catalysed by species which can form stable insoluble (e.g. PbO , Na_2O , Li_2O) or soluble (OH^-) oxides:

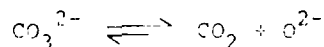


Reactions [7], [8] and [9] could be considered as a combination of reaction [1] followed by MgO , PbO and OH^- formation, but then the potentials should be identical and this is not found. The recent postulate of metal ion catalysis (12) is energetically simpler. It has yet to be determined how many reactions from schemes (a) and (b) can occur simultaneously, e.g. is the nitrate peak reaction [7] the sole electrode process in a dry melt? It is established that [7] and [9] can both occur in a wet one (2,4,11).

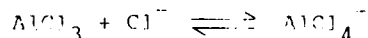
We note in passing that there have been numerous attempts to establish oxygen electrodes in molten salts including chlorides, nitrates, sulfates and carbonates. The electrodes based on solvent oxidation - Cl_2/Cl^- , $\text{NO}_2 + \text{O}_2/\text{NO}_3^-$, $\text{SO}_3 + \text{O}_2/\text{SO}_4^{2-}$ and $\text{CO}_2 + \text{O}_2/\text{CO}_3^{2-}$ have been shown to function reasonably, but O_2/O^{2-} electrodes have caused numerous problems and controversies, mainly because the cation role was not always realized. The suggestions of Appleby and Nicholson (13) should be considered for all solvents: the monoxide, peroxide or superoxide preferences of the cations likely determine either the electrode reaction or the following chemical reaction, or both.

ACID-BASE CONCEPTS

The Lux-Flood acid-base concept for molten salt equilibria is centred upon the idea of oxide ion as the reference base and species such as NO_2^+ , CO_2 and SO_3 as the corresponding acids in oxyanion melts, e.g.:



It is a particular example of the Lewis concept which again finds application in aluminum halide based systems, where AlCl_3 is the acid:

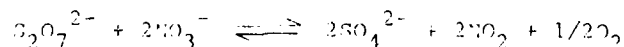


Further, oxidants are of course Lewis acids and reductants Lewis bases. The difference between an actual redox reaction and an acid-base reaction is then one of degree: in the former case electron transfer between species is complete while in the latter a mere sharing of

redistribution of electrons originating within a species takes place.

ACID-BASE REACTIONS IN NITRATES

When either pyrosulfate or lithiumate and lead ions are added to a nitrate melt, nitrogen dioxide and oxygen are liberated (14):



One can postulate, as did Duke (15), that the process involves the acid NO_2^+ , rather than NO_2O , and write an acidity sequence $\text{S}_2\text{O}_7^{2-} > \text{Cr}_2\text{O}_7^{2-} \sim \text{H}_2\text{O}_5(\text{NO}_2^+)$. However, NO_2^+ has not been observed directly in melts and there is no reason per se for NO_2O to behave in acidic nitrates the way it does in H_2O and other non-aqueous solvents (16).

Although some of the active participants in SbCl_3 -based melts require better definition, the acidity and oxidative power are purported to be related but not necessarily identical (17). SbCl_3 itself is a molecular liquid which can either donate Cl^- to acidic molecules such as AlCl_3 to form AlCl_4^- or accept Cl^- from alkyl or quaternary ammonium chlorides to form SbCl_4^- (or 5- or 6-coordinate species as found in isolated complexes). The identity of the Lewis acid formulated as SbCl_2^+ is no more certain than is the existence of NO_2^+ in nitrates. Two different modes of action (acid-base and redox) have been cited in the transalkylation and radical cation production from diphenylmethane and 11-2-anthylmethane, respectively (17).

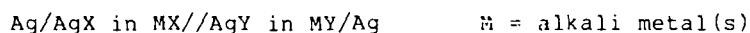
Whether the reduced form of antimony produced is the metal ($n = 3$) or some oxidation state n less than 3, the antimony redox reaction will have a potential

$$\begin{aligned} E &= E_{\text{basic}}^0 + \frac{RT}{nF} \ln \frac{[\text{SbCl}_3]}{[\text{Cl}^-]^2 [\text{SbCl}_{3-n}]} \\ &= E_{\text{acidic}}^0 + \frac{RT}{nF} \ln \frac{[\text{SbCl}_2^+]}{[\text{Cl}^-]^{n-1} [\text{SbCl}_{3-n}]} \end{aligned}$$

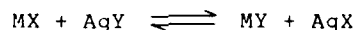
where $E_{\text{acidic}}^0 = E_{\text{basic}}^0 - \frac{RT}{nF} \ln K_d$ and K_d is the dissociation constant of SbCl_3 . It appears that radical cation production requires a lesser oxidant than does transalkylation since the latter occurs more readily in the AlCl_3 -dominated system. Hydride abstraction, if it occurs in the latter case, does not necessitate the formation of an intermediate such as HSbCl_3 containing H^- .

METAL ION STABILIZATION IN MELTS

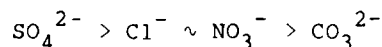
Many years ago (18) we carried out or collected together measurements of the e.m.f.'s of cells such as



and constructed an e.m.f. series of anions, X^-, Y^- . Disregarding the small uncertainties of liquid junction potentials, the e.m.f.'s may be seen to express several things: (a) the different activities of silver ions in the two media; (b) the Gibbs free energy change (or equilibrium constant) of the exchange reaction



(c) the preference of Ag^+ for X^- and Y^- ; (d) the relative "acidity" or oxidizing power of Y^- vs. X^- . The results of these measurements were a preference order for Ag^+ of $\text{Cl}^- > \text{CO}_3^{2-} \sim \text{NO}_2^- > \text{SO}_4^{2-} \sim \text{NO}_3^-$. The inclusion of cell e.m.f. data (17) involving the oxidation of common anions led to the development of a sequence of anion oxidation potentials in alkali metal salt melts



If we extend the comparison of silver potentials to the chloraluminate systems we find a 20 mv difference between $E_{\text{Ag}^+, \text{Ag}}^0$ values in AlCl_4^- and Al_2Cl_7^- melts.

However, the Al^{3+}/Al , $\text{Fe}^{3+}/\text{Fe}^{2+}$, Fe^{2+}/Fe , $\text{Cu}^{2+}/\text{Cu}^+$ and Cu^+/Cu potentials differ by 455, 450, 320, 496 and 61 mv, respectively (19), always with the electrode in the Al_2Cl_7^- system the more positive. Referring to LiCl-KCl as solvent (20) we find $E_{\text{Ag}^+, \text{Ag}}^0 - E_{\text{Al}^{3+}, \text{Al}}^0 = 1.040 \text{ V}$

compared to 1.086 V for NaAlCl_4 and $E_{\text{Cu}^+/\text{Cu}}^0 - E_{\text{Al}^{3+}/\text{Al}}^0 = 0.805$ V compared to 1.073 V for NaAlCl_4 . Thus Ag^+/Ag can be considered a good reference electrode in acid-base melts with Cu^+/Cu a fair second choice. The Ag^+/Ag potential reflects only the nearest neighbor's presence. The usual bidentate inclination of the d^{10} ions Ag^+ and Cu^+ compared to the tetrahedral and higher coordinations of the other ions is probably the primary determining factor. The transition metal ions possess their own acid-base character which confuses the picture.

Transition metal ions do offer probe characteristics because of coordination preference and thus coordination detection through spectral (color) properties. Co^{2+} ions are particularly useful since they take on tetrahedral (blue), octahedral (pink) or dodecahedral (purple) coordination in various molten salts (21) whereas Cr^{3+} ions either find octahedral sites, an unusual but possible situation in LiCl-KCl (22) or no sites as in ZnCl_2 where the tetrahedral network makes CrCl_3 virtually insoluble (23). One must be careful to distinguish between the behavior of melts such as AlCl_3 and ZnCl_2 due to their acidity and the behavior due to their structure, which two characteristics need not be totally correlated.

REFERENCES

1. B.D. Bond and P.W.M. Jacobs, J. Chem. Soc. A, 1265 (1966).
2. H.S. Swofford and H.A. Laitinen, J. Electrochem. Soc., **110**, 814 (1963).
3. W. Hittorf, Poggendorfe Ann. Phys., **72**, 481 (1847).
4. G.J. Hills and K.E. Johnson, "Advances in Polarography", p. 974, Pergamon Press, London (1961).
5. H.E. Bartlett and K.E. Johnson, J. Electrochem. Soc., **114**, 64 (1967).
6. P.G. Zambonin and J. Jordan, J. Amer. Chem. Soc., **89**, 6365 (1967); **91**, 225 (1969).
7. P.G. Zambonin, J. Electroanal. Chem., **24**, 365 (1970).
8. N. Nachtrief and M. Steinberg, J. Amer. Chem. Soc., **72**, 3558 (1950).
9. D. Inman and J. O'M. Bockris, J. Electroanal. Chem., **3**, 126 (1962).
10. K.E. Johnson and P.S. Zacharias, J. Electrochem. Soc., **124**, 448 (1977).

11. K.E. Johnson, Ph.D. Thesis, London (1959).
12. M.H. Miles, G.E. McManis and A.N. Fletcher, J. Electrochem. Soc., **134**, 614 (1937).
13. A.J. Appleby and S.B. Nicholson, J. Electroanal. Chem., **33**, App. 13 (1972); **53**, 105 (1974); **83**, 308 (1977); **112**, 71 (1980); J. Electrochem. Soc., **127**, 759 (1980).
14. F.R. Duke and M.L. Iverson, J. Amer. Chem. Soc., **80**, 5061 (1958).
15. F.R. Duke and S. Yamamoto, J. Amer. Chem. Soc., **81**, 6378 (1959).
16. N.W. Greenwood and A. Earnshaw, "Chemistry of the Elements", p. 526, Pergamon Press, Oxford (1934).
17. A.C. Buchanan, D.M. Chapman and G.P. Smith, J. Org. Chem., **50**, 1702 (1985).
18. L.G. Boxall and K.E. Johnson, J. Electroanal. Chem., **30**, 25 (1971).
19. L.G. Boxall, H.L. Jones and R.A. Osteryoung, J. Electrochem. Soc., **121**, 212 (1974).
20. H.A. Laitinen and C.H. Liu, J. Amer. Chem. Soc., **80**, 1015 (1958).
21. K.E. Johnson and J.R. Dickinson, "Advances in Molten Salt Chemistry II", p. 135 (1973).
22. G. Harrington and B.R. Sundheim, Ann. N.Y. Acad. Sci., **79**, 930 (1960).
23. D.H. Kerridge and I.A. Sturton, Inorg. Chem. Acta, **8**, 27 (1974).

EVALUATION OF LiCl-LiBr-KBr ELECTROLYTE
FOR Li-ALLOY/METAL DISULFIDE CELLS

Thomas D. Kaun
Argonne National Laboratory
Chemical Technology Division
9700 South Cass Avenue
Argonne, IL 60439-4837

ABSTRACT

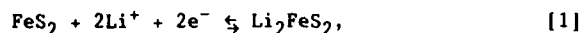
The physical properties of a new molten salt electrolyte for lithium-alloy/metal disulfide cells, 25 mol % LiCl-37 mol % LiBr-38 mol % KBr, were investigated. In earlier cells, a LiCl-KCl electrolyte was used. Cyclic voltammetry of FeS_2 in the new molten salt at 375-425°C indicated improved electrochemistry and stability of the reaction on the upper voltage plateau (1.75 V vs. LiAl). The new electrolyte provides an opportunity to operate an upper-plateau (U.P.) FeS_2 electrode at a lower temperature, 400°C, and with a higher activity of lithium ion in the electrolyte. The broad liquidus of this molten salt at 400°C also supports operation at high current density. Testing of 24- to 48-Ah cells indicated greater than 50% improved energy and power density over the conventional two-plateau FeS_2 cell with LiCl-KCl electrolyte. The conventional FeS_2 cells would lose 50% of their upper-plateau capacity within 200 cycles. The elimination of this capacity decline problem was demonstrated by 400 cycles and 5400 h of stable operation with a dense U.P. FeS_2 electrode cell, which maintained 89% utilization of theoretical capacity throughout the test.

INTRODUCTION

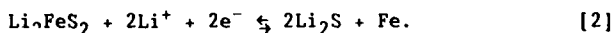
A new molten-salt electrolyte is a key component of a substantially improved LiAl/ FeS_2 cell. With this electrolyte, the cell's energy and power density were increased by at least 50% and cycle-life stability problems were alleviated (1). This electrolyte, 25 mol % LiCl-37 mol % LiBr-38 mol % KBr (m.p. 310), has many interesting properties which give it preference over the commonly used 58 mol % LiCl-42 mol % KCl (m.p. 352°C). The LiCl-LiBr-KCl-KBr system was initially examined by investigators in the U.S.S.R. (2) for crystallization of solid solutions in reciprocal ternary systems. The properties of the above LiCl-LiBr-KBr composition are currently being investigated at Argonne National Laboratory in its development of high-performance battery cells. This paper will report on the physical properties of the electrolyte, the electrochemistry of the FeS_2 electrode, and the LiAl/ FeS_2 cell performance with the LiCl-LiBr-KBr electrolyte.

A second feature of the improved LiAl/FeS₂ cell is its exclusive operation on the higher of two discharge voltage plateaus, along with an increased loading of active material in the FeS₂ electrode from 32 vol % FeS₂ (1.5 Ah/cm³) to 50 vol % FeS₂ (2.4 Ah/cm³). The energy density of this "dense U.P. FeS₂ electrode" is potentially greater than that of the two-plateau (T.P.) FeS₂ electrode--with the added advantage of a 0.3 V increase in cell voltage at 80% depth of discharge (DOD), Fig. 1.

The discharge reaction of the dense U.P. FeS₂ electrode (1.75 V vs. LiAl) can be written as:



although it is a series of three consecutive reactions (3), as will be seen later. In the conventional T.P. FeS₂ cell, the lower-voltage reaction (1.33 avg V vs. LiAl) is also used. This reaction is:



The discharge product of the U.P. FeS₂ reaction, Li₂FeS₂, has a much higher density (2.8 g/cm³) in comparison to the Li₂S (1.6 g/cm³) produced in the T.P. FeS₂ electrode operation. Consequently, a higher loading of active material for the dense U.P. FeS₂ electrode develops higher electrode energy density, Wh/cm³.

The earlier T.P. FeS₂ cells with LiCl-KCl electrolyte were operated at 425-450°C and had unacceptably high capacity decline rates of 0.10-0.25% per cycle. Approximately 50% of the upper-plateau FeS₂ capacity would be lost in the first 200 cycles of operation. This phenomenon was explained by sulfur migrating from the positive electrode into the separator region of a cell and depositing there as Li₂S (4). Therefore, a U.P. FeS₂ cell design was not a practical approach for development of a high-performance cell with the LiCl-KCl electrolyte. The LiCl-LiBr-KBr molten salt offers physical properties that allow stable operation of the dense U.P. FeS₂ electrode without degrading cell performance. Several unique characteristics of the U.P. FeS₂ cell with LiCl-LiBr-KBr electrode were identified. As related to FeS₂ cell design and fabrication, some of the physical properties of the LiCl-LiBr-KBr were determined directly and some were observed. The FeS₂ electrode electrochemistry was investigated by slow-scan cyclic voltammetry in a temperature range of 375-425°C. Compact prismatic cells were operated to demonstrate the improved performance of the LiAl/LiCl-LiBr-KBr/FeS₂ system.

EXPERIMENTAL

The electrolyte was polarographic grade LiCl-LiBr-KBr of the eutectic composition (25 mol % LiCl-37 mol % LiBr-38 mol % KBr, m.p. 310°C), which was obtained from Anderson Physics Laboratory (APL). Melting point and cooling curves were determined by APL in the course of producing this melt. The FeS₂ was purchased from the University of

Minnesota as purified mineral and was determined to be approximately 95% pure by x-ray diffraction analysis. The LiAl electrodes used 23 wt % lithium-aluminum particles from Foote Mineral Co.

The cyclic voltammetry experiments were conducted in cells consisting of FeS_2 working electrodes and Li-Al reference (about 1-Ah capacity) and counter (about 10-Ah capacity) electrodes. The FeS_2 electrode (25 mg FeS_2) was positioned in proximity to other electrodes in about 200 g of electrolyte. The LiAl electrodes employed cylindrical stainless steel housings which were covered with 325-mesh stainless steel screens. The Li-Al powder was mixed with aluminum powder to reduce the lithium concentration to about 35 at. % Li. The working electrode employed a molybdenum housing for 0.25-cm² electrode area and 0.6-mm depth and is faced by 100-mesh molybdenum screens.

The cyclic voltammograms were generated with a PAR 175 universal programmer, a PAR 173 potentiostat, a PAR 179 coulometer, and a HP 7045A X-Y recorder. Steady-state voltammograms were obtained from repeated cathodic and anodic sweeps at a sweep rate of 0.02 mV/s with a potential range of no greater than 1.1 to 2.15 V vs. Li-Al.

Cell performance characteristics were assessed in sealed prismatic bicells of 24- to 48-Ah capacity. The electrodes (8.7-cm high x 6.3-cm wide) were contained behind perforated-sheet current collectors--molybdenum for the central FeS_2 electrode and 1008 steel for the two Li-Al electrodes. The electrode area, based on the area of the BN felt separator (0.2-cm thick, 10 vol % BN, Kennecott Corp.), was 100 cm². The positive electrodes contained FeS_2 with 15 mol % CoS_2 additive for a theoretical capacity of either 24 or 48 Ah on the upper plateau. The slurry-formed negative electrodes (5) contained 53 at. % Li-Al alloy of either 35- or 70-Ah capacity with 0.9 Ah/cm³ loading density. Cells were assembled with a BN-powder feedthrough seal and were operated in an argon glovebox. Cycle-life testing at an 8-h charge rate (25 or 50 mA/cm²) and 4-h discharge rate (50 or 100 mA/cm²) was controlled between voltage cutoffs of 2.10 and 1.25 V, respectively. A $\text{Ni/Ni}_2\text{S}_3$ reference electrode indicated working-electrode potentials during the deep discharge cycling.

RESULTS AND DISCUSSIONS

The physical properties of LiCl-LiBr-KBr were investigated relative to the design, fabrication, and operation of LiAl/U.P. FeS_2 cells. As reported earlier (2), the new electrolyte has a melting point of 310°C. Also, its liquidus range of 1.25 to 2.6 Li^+/K^+ ratio at 400°C is of particular interest to the dynamic conditions of electrode operation at high current density. For LiCl-KCl, the liquidus range at 400°C is only 1.25 to 1.81 Li^+/K^+ ratio. The broader liquidus for LiCl-LiBr-KBr would tend to prevent salt crystallization from the Li^+ ion flux of current conduction. Melting point and cooling curve determinations at APL (6) indicated a melting point of 312±1°C, but once liquid, this molten salt exhibits a lower freezing point of 296±4°C. Accordingly, test cells begin to exhibit

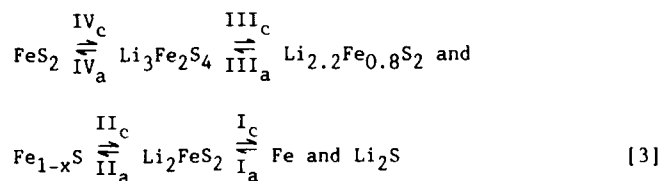
voltage at $310 \pm 10^\circ\text{C}$. With regard to the expanded liquidus range of the LiCl-LiBr-KBr, the improved performance of the Li-Al/U.P. FeS_2 cell at 400°C (reported below) is supportive of this property.

Determinations of the density of LiCl-LiBr-KBr correlated well with the calculated density based on component densities. At 400°C , the liquid density is about 2.2 g/cm^3 . (Room-temperature density is 2.7 g/cm^3 .) The liquid density was determined from the weight of an established volume of electrolyte in a graphite crucible at $400 \pm 5^\circ\text{C}$. The liquid meniscus is dealt with by placing a graphite cap having a small hole (to take up excess melt) on the top of the crucible. It was observed that the LiCl-LiBr-KBr electrolyte wets electrode materials (LiAl , FeS_2 , CoS_2) and cell components (MgO-treated BN felt, steel, and molybdenum) quite well. Generally, a vacuum was required to fully infiltrate LiCl-KCl electrolyte into the cell. The cells with LiCl-LiBr-KBr have attained full cell capacity without vacuum-assisted infiltration. This good wetting characteristic is important for the development of "electrolyte-starved" cells.

The specific resistivity of the molten salt and solubility of the metal disulfide electrode materials are linked to Li^+ ion activity and temperature. An added consideration is the thermal stability of FeS_2 . It has been determined (7) that thermal decomposition of FeS_2 at 400°C is rather slow and that thousands of hours would pass before a significant amount of decomposition would occur, whereas at 500°C decomposition would occur within a few hours. Earlier studies have documented the increased solubility of Li_2S in molten salts due to higher Li^+ ion content (8). Solubility at 450°C is 1860 ppm Li_2S for 65 mol % LiCl-35 mol % KCl and 840 ppm Li_2S for 55 mol % LiCl-45 mol % KCl. The all- Li^+ ion salt, LiCl-LiBr-LiF, at 465°C has a much higher Li_2S solubility (9), 6840 ppm. Generally, a 50°C temperature rise in the range of 400 - 500°C will approximately double Li_2S solubility for all of these molten salts. The solubility of Li_2S in LiCl-LiBr-KBr at 400°C based on a 62 mol % Li^+ content is approximated at 1100 ppm Li_2S . The specific resistivity of LiCl-KCl eutectic at 400°C , which is approximately 0.8 ohm-cm , decreases as the LiCl mole fraction is increased, but the melting point rapidly increases to 400°C for the LiCl-rich composition of 65 mol % LiCl-35 mol % KCl. It is apparent that, compared with LiCl-KCl eutectic, the LiCl-LiBr-KBr electrolyte provides lower temperature operation ($\sim 400^\circ\text{C}$), which minimizes thermal decomposition and solubility of electrode material, and higher Li^+ ion activity, which enhances FeS_2 electrode performance. •

The electrochemistry of FeS_2 in LiCl-LiBr-KBr was examined by cyclic voltammetry, as shown in Fig. 2, at three temperatures: 375°C , 400°C , and 425°C . The potential sweep rate was 0.02 mV/s , and the potential range was 1.10 to 2.10 V. These conditions generated about one cycle per day. Achieved capacity, based on summed areas of either anodic or cathodic peaks, exceeded 80% of the theoretical capacity. The dominant features of these voltammograms are consistent with those of FeS_2 in LiCl-KCl eutectic, which were reported by Preto et al. (3). Roman numerals label the peaks, with "a" for anodic and "c" for cathodic. The corresponding sequence of phases at the various states

of charge are assigned according to the work of Tomczuk et al. (10) as follows:



These are equilibrium phases and do not imply reaction mechanisms. Of particular interest for this study is the separation of the anodic and cathodic high-voltage peaks (IVa and IVc), which indicates irreversibility of this reaction. A notable difference between the cyclic voltammograms of Fig. 2 and those of FeS_2 in LiCl-KCl is that this peak separation (difference in leading edge potentials, LEP) is less--95 mV vs. 120 mV, respectively. Also, the leading edge of peak IVa does not exhibit the shoulder found for FeS_2 in LiCl-KCl (3). These differences indicate improved reversibility from a molten salt with higher Li^+ ion activity. As seen in Table 1, peak separation between IVa and IVc (LEPa-LEPc) lessens with increased operating temperature.

A unique characteristic of the high voltage reactions (FeS_2 to Li_2FeS_2) is their strong entropic cooling. The potentials of the leading edges of peak IVc at 375, 400, and 425°C (Fig. 2) exhibit a positive temperature coefficient, which correlates well with the change in the equilibrium potentials of these peaks due to temperature. The emf for the $\text{FeS}_2 \rightarrow \text{Li}_3\text{Fe}_2\text{S}_4$ phase transition has been reported by Tomczuk et al. (11) as:

$$\text{Emf} = 1.542 + 0.0005231 T(^{\circ}\text{C}) \quad [4]$$

As shown in Table 1, a 50°C change in temperature raises the potential of the leading edge of peak IVc by 20 mV. Calculating the difference between the equilibrium potentials of the reaction peaks with their leading-edge potentials, LEP, for peaks IVa and IVc (Table 1) indicates the overpotentials for these reactions. The cathodic overpotentials are quite small (4-14 mV), while the anodic overpotential of peak IVa is about 85 mV at 400°C. Most significantly, the overpotential of charging the high voltage reaction of FeS_2 (IVa) in LiCl-LiBr-KBr at 400°C is 20 mV less than it is in LiCl-KCl eutectic.

The cyclic voltammograms indicate rather good stability of FeS_2 in LiCl-LiBr-KBr. At 425°C or less, soluble polysulfides are not generated, as evidenced by the lack of activity in the voltage region 1.95 to 2.10 V vs. LiAl. Generation of soluble polysulfides would lead to electrode capacity loss. Unlike FeS_2 , CoS_2 and NiS_2 generate Li_2S in charging their high voltage reaction, which can be further oxidized to soluble Li_2S_2 (3). In Fig. 2, the diminution of peaks IVa

and IVc at 425°C may be attributed to lengthy operating times (200 h) for the 25-mg FeS₂ electrode and/or physical loss of active material.

Tests of the LiAl/LiCl-LiBr-KBr/dense U.P. FeS₂ cell at 400°C demonstrated at least a 50% improved energy density in comparison to that of the LiAl/LiCl-KCl/T.P. FeS₂ cell at 427°C (12). As seen in Fig. 1, capacity utilization is about 50% greater, along with a 10% higher average discharge voltage. Cell power density was improved by at least 100% because of two factors. First, the cell voltage at 80% DOD was about 0.3 V higher than that of a T.P. FeS₂ cell. Second, cell resistivity was lower for the dense U.P. FeS₂ cell at 400°C, ranging from 0.65 to 0.85 ohm-cm² for 5-80% DOD compared with 1.2 to 1.6 ohm-cm² for the T.P. FeS₂ cell at 427°C. The higher voltage and lower resistivity of the U.P. FeS₂ cell increased power density from 0.3 to 0.8 W/cm² of separator area at 80% DOD.

The high utilization, about 80% at the higher current densities of 100-150 mA/cm², attests to extremely good electrode kinetics for the U.P. FeS₂ electrode in the LiCl-LiBr-KBr electrolyte. As seen in Fig. 3, utilizations at these high current densities are approximately double those of the T.P. FeS₂ system. Cells have been operated at temperatures as low as 380°C, but as seen in Fig. 3, sensitivity to cell operating temperature begins to show at temperatures less than 400°C. At a 1-h discharge rate (150 mA/cm²), 78% utilization is achieved at 400°C.

Stable cycle life is a particular concern for the dense U.P. FeS₂ cell in that cell capacity loss for earlier cells was exclusively due to loss of upper-plateau (high sulfur activity) capacity. The cell capacity vs. cycle number for the U.P. FeS₂ cell is shown in Fig. 4. (Its coulombic efficiency was +99%.) At 50 mA/cm², the upper-plateau FeS₂ capacity utilization was 89%. The cell capacity remained constant through 400 cycles and 5400 hours, after which problems with the test facility terminated the test. During this test, the cell was charged at 25 mA/cm² to a charge cutoff of 2.05 V. These values are greater than those that could be used with the LiAl/LiCl-KCl/T.P. FeS₂ and still maintain stable capacity (12). This is further indication of improved FeS₂ electrode kinetics. Electrode potentials (vs. the Ni/Ni₃S₂ reference electrode) indicated that discharge cell capacity was limited by the upper-plateau FeS₂ capacity of the positive electrode. The 89% utilization of the upper-plateau FeS₂ capacity provided quite good accounting of the sulfur capacity throughout the cycle-life test. Apparently, both time- and cycle-related capacity loss mechanisms have been eliminated in this advanced cell.

CONCLUSION

The physical characteristics of the molten salt LiCl-LiBr-KBr provide a unique opportunity to operate a U.P. FeS₂ cell at a substantially lower temperature (400 vs. 450°C) along with a higher Li⁺ ion activity (62 vs. 58 mol % Li⁺ ion) than is possible with LiCl-KCl. Additionally, its broad liquidus at 400°C supports high current

density (100-150 mA/cm²) operation at high utilization (about 80% of the U.P. FeS₂ capacity). The electrochemistry of U.P. FeS₂ in LiCl-LiBr-KBr exhibits increased reversibility, as indicated by reduced peak separation of the high-voltage reaction peaks in the cyclic voltammograms. The capacity stability of the dense U.P. FeS₂ is aided by improved electrode kinetics at the lower operating temperature of 400°C. Thermal decomposition and solubility of the FeS₂ electrode are held in check at this temperature. Also, generation of soluble polysulfides at potentials of 1.95-2.1 V was not indicated in cyclic voltammograms for this electrode/electrolyte system.

Based on the improved U.P. FeS₂ electrode performance, we expect to develop sealed monopolar cells with specific energy of 150-175 Wh/kg at a 3-h rate and specific power of 200-300 W/kg at 80% DOD for the electric-vehicle application. The dense U.P. FeS₂ electrode and LiCl-LiBr-KBr electrolyte have resulted in a cell with very stable cycle life. The expected cycle life is greater than 1000 cycles. The unique feature of strong entropic cooling for the U.P. FeS₂ discharge reaction provides an additional incentive for development of this system for high-power applications. A bipolar battery design for the production of intense power could be operated adiabatically.

ACKNOWLEDGMENT

This work was supported by the U.S. Department of Energy, Office of Energy Storage, under contract W-31-109-Eng 38. The assistance of M. Pytosh, T. Hashman, and T. Holifield as student researchers was highly valued. The author is grateful to M. F. Roche and J. E. Battles for their support.

REFERENCES

1. T. D. Kaun, J. Electrochem. Soc. 132, 3063 (1985).
2. A. G. Bergman and A. S. Arabadzhan, Russ. J. Inorg. Chem. (English Trans.) 8, 369 (1963).
3. S. K. Preto, Z. Tomczuk, S. Von Winbush, and M. F. Roche, J. Electrochem. Soc. 130, 264 (1983).
4. J. E. Battles, F. C. Mrazek, and N. C. Otto, Argonne National Laboratory Report ANL-80-130 (1980).
5. T. D. Kaun, U.S. Patent No. 4,358,513 (1983) and U.S. Patent No. 4,446,212 (1984).
6. K. Johnson, private communication, Anderson Physics Lab.
7. G. Barlow, Proc. of Int'l Workshop on High-Temperature Molten Salt Batteries, ANL-86-40, p. B-130 (1986).

8. D. Warin, Z. Tomczuk, and D. R. Viszers, J. Electrochem. Soc. 130, 64 (1983).
9. Z. Tomczuk, D. R. Viszers, and M.-L. Saboungi, Proc. of 4th Int'l Symp on Molten Salts, M. Blander, Ed., J. Electrochem. Soc. Vol. 84-2, 352 (1984).
10. Z. Tomczuk, B. Tani, N. C. Otto, M. F. Roche, and D. R. Viszers, J. Electrochem. Soc. 129, 925 (1982).
11. Z. Tomczuk and D. R. Viszers, J. Electrochem. Soc. 133, 2504 (1986).
12. F. J. Martino, W. E. Moore, and E. C. Gay, Argonne National Laboratory Report ANL-83-62, pp. 29-38 (1983).

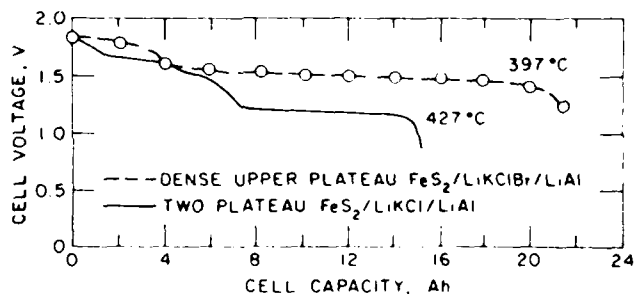


Figure 1. Voltage/Capacity Curves at a Discharge Rate of 50 mA/cm².

Table 1. Equilibrium and Lead-Edge Potentials (LEP) for FeS₂ & Li₃Fe₂S₄ in LiCl-LiBr-KBr (310° m.p.)

Electrolyte	Temp. (°C)	LEP _c (V)	Emf (V)	LEP _a (V)	LEP _a - LEP _c (V)
LiCl-LiBr-KBr	375	1.730	1.734	1.835	0.105
	400	1.740	1.751	1.835	0.095
	425	1.750	1.764	1.835	0.085
LiCl-KCl(a)	400	1.735	1.751	1.855	0.120

(a) From References 3 and 11.

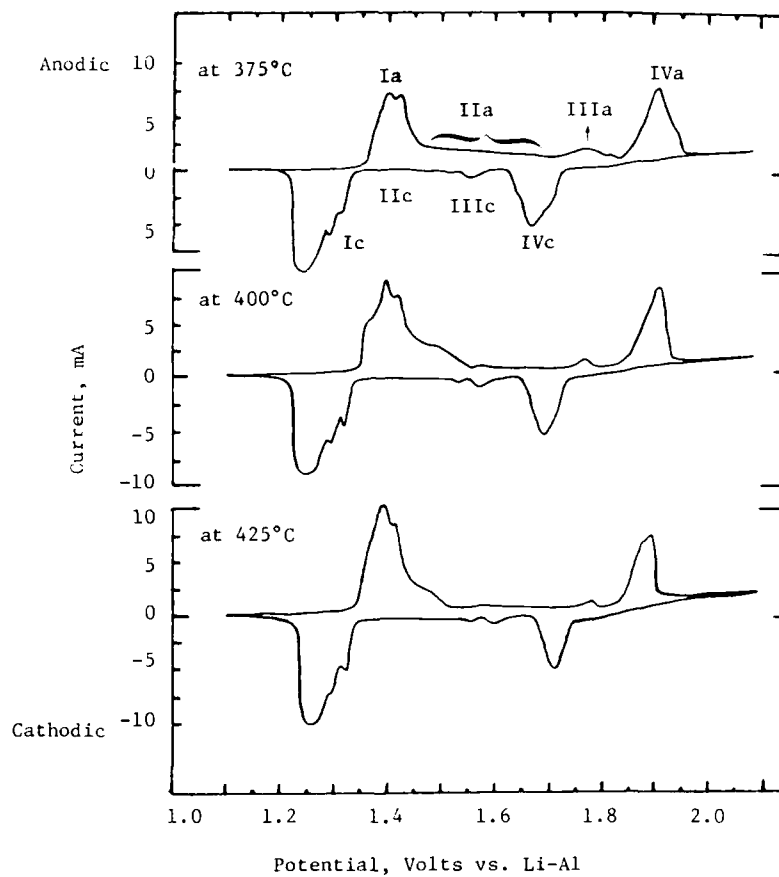


Figure 2. Cyclic Voltammograms of FeS_2 in LiCl-LiBr-KCl (310 m.p.) Electrolyte at Three Temperatures: 375, 400, and 425°C (sweep rate, 0.02 mV/s). The peaks are labeled according to the reactions of Eq. (3).

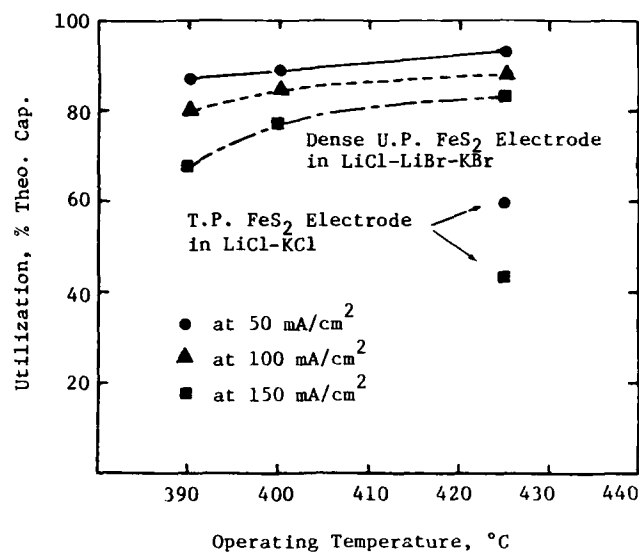


Figure 3. Utilization vs. Temperature of Operation for Li-Al/FeS₂ Cells of 100-cm² Separator Area.

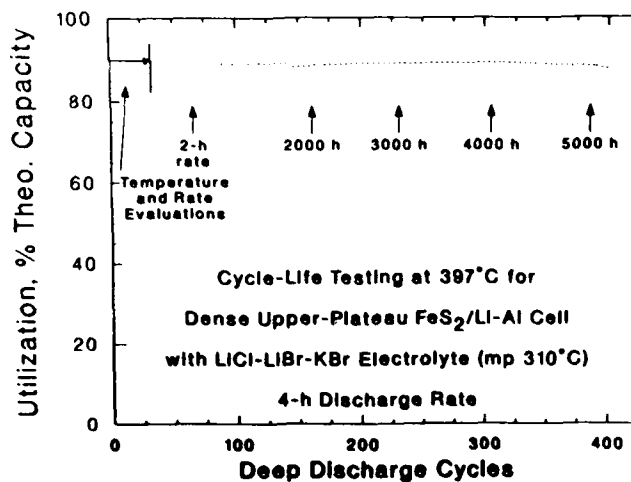


Figure 4. Cell Discharge Capacity (Utilization of the U.P.-FeS₂ Capacity) as a Function of Cycle Life.

OVERCHARGE PROTECTION IN Li-ALLOY/METAL DISULFIDE CELLS

Laszlo Redey

Argonne National Laboratory
Chemical Technology Division
9700 S. Cass Avenue, Argonne, IL 60439

ABSTRACT

Charge and overcharge reactions of FeS_2 , NiS_2 , and $(\text{Fe-Ni})\text{S}_2$ electrodes were studied in half-cell and full-cell experiments to investigate the electrochemical stability of these materials at high charge potentials. In Li_2S -saturated (LiCl-KCl , LiF-LiCl-LiBr , and LiCl-LiBr-KBr) electrolytes, a new plateau appeared at 2.05-2.1 V vs. Li-Al and was associated with polysulfide anion formation. The polysulfide seems to stabilize the transition-metal sulfides against overcharge-related dissolution, even at 2.2 V. The anodically formed polysulfide provides overcharge tolerance for Li-alloy/ MS_2 cells by an electrochemical-chemical sulfide/polysulfide cycle.

BACKGROUND

The present Li-alloy/metal sulfide cells require voltage-limited charge termination. An experimentally determined limit (about 1.9 to 2.05 V for the Li-alloy/ FeS_2 cells [1,2]) is set to prevent unwanted electrode reactions. Although both the negative and the positive electrodes are affected by this problem, only those problems that are associated with the latter are discussed in this paper. Above the voltage limit, if the charge is continued, detrimental overcharge reactions occur, such as soluble transition-metal salt formation from the active material and anodic dissolution of the current collector. Overcharge reactions of the metal sulfide electrodes have been studied extensively [3-6], and a review on this topic is available [7]. The overcharge reactions shorten cell life to a great extent by decreasing capacity and causing metal to precipitate in the separator, which then short circuits the electrodes. The deleterious effect of the overcharge reactions is proportional to the charge applied above the critical voltage limit.

Overcharge of the weak cells of a battery is a serious problem whenever the utilizable capacities of the cells become uneven. Maintaining the charge voltage at or below the voltage limit and simultaneously reaching equal capacity in each serially connected cell of a metal sulfide battery over many cycles are difficult tasks. To overcome this difficulty, a special integrated charger-battery system

has been developed [8]. This system, which has interconnections between each cell and the charger, removes any cell from charge individually that reaches the charge voltage limit.

Ideally, the battery overcharge control, however, should rely on a built-in chemical mechanism that furnishes the cells with an inherent overcharge tolerance. A similar mechanism is available in lead-acid and Ni-Cd cells.

EXPERIMENTS AND RESULTS

To explore the possibility of chemical overcharge protection, charge and overcharge reactions of FeS_2 , NiS_2 , and $(\text{Fe-Ni})\text{S}_2$ electrodes in 58% LiCl - 42% KCl eutectic, 22% LiF - 31% LiCl - 47% LiBr all- Li^+ -cation, and 25% LiCl - 37% LiBr - 38% KBr "low melting" electrolytes (composition in mol%) were studied by intermittent galvanostatic cycling. The electrolytes were Li_2S -saturated, i.e., they contained more sulfide than the stoichiometrically needed quantity to form the heavy-metal disulfides from their respective metals.

Two sets of experiments were carried out: (i) half-cell experiments to study the charge properties of the sulfides and (ii) full-cell experiments to investigate the interaction between the positive and negative electrode in an arrangement that simulates the conditions of the compact engineering cells. Details of the cell design and the method used in the half-cell study are described elsewhere [9,10]. For the full-cell study, a sulfide electrode was combined with a Li-alloy negative electrode into a cell sandwich; this cell was designed for performing experiments under a wide variety of conditions, including open and sealed operations. Both types of cells were cycled, at least, 50 to 150 times before the experiment was terminated.

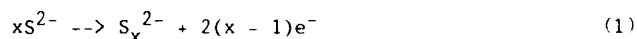
The half-cell experiments revealed a new plateau at about 2.05-2.1 V vs. Li-Al (IR-free closed-circuit value). This potential range had been considered to be beyond the safe charge voltage limit and subject to detrimental overcharge reactions. The half-cell experiments suggested an electrode reaction at 1.95-2.1 V potential that was not directly related to the transition-metal sulfide process because (i) the charge passed during this plateau was not recoverable in the subsequent discharge, (ii) the recoverable useful discharge capacity of the transition-metal sulfide was hardly affected by the length of the overcharge plateau, and (iii) the useful discharge capacity did not decline in the following cycles, even after several overcharging cycles. The results in Table 1 show the charge and discharge capacities of an FeS_2 electrode before, during, and after "overcharge" (i.e. when the electrode potential is higher than 1.9 V).

Similar results were obtained in the full-cell experiments with the three listed metal disulfides. Figure 1 shows the voltage variation of a Li-Al-Si/(Fe-Ni) S_2 sealed cell when cycled between discharge and charge voltage limits of 1.0 and 2.1 V, respectively. The voltage oscillations seen on the curve are traces of the voltage excursions during 15-s current interruptions, which were applied regularly to measure area-specific cell impedance [10]. In the 21st charge (C-21), when the voltage limiter relay was inactivated, the cell was overcharged with a current density of 50 mA/cm² to approximately 2.5 times the theoretical capacity. In spite of this unusual treatment, no damage occurred in the electrodes. This observation is substantiated by the fact that the plot recorded in the pre-overcharge cycle is unaltered from that obtained in the subsequent cycles. Furthermore, the cell showing good capacity retention performed many more cycles and several overcharges.

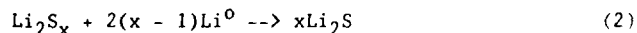
DISCUSSION

Both the half-cell and full-cell experiments suggested that transition-metal disulfide electrodes in Li₂S-saturated electrolyte will undergo beneficial overcharge reactions that provide overcharge tolerance.

The mechanism of the overcharge tolerance can be explained by the action of an electrode reaction-chemical reaction (ER-CR) cycle. At high positive potentials, the abundant S^{2-} ions of the electrolyte are oxidized to polysulfide on the sulfide electrode in the electrode reaction



where $x \leq 2$. Then, the polysulfide, after having been diffused to the negative electrode, is reduced back to sulfide on the Li alloy in the chemical reaction



The symbol Li^0 in Eq 2 represents the excess lithium content of the alloy that is produced during the overcharge. The sulfide produced in Eq. 2 diffuses and migrates back to the positive electrode and short circuits the ER-CR cycle. Although the polysulfide and the excess lithium in the alloy are produced continuously during overcharge, they do not accumulate to an unacceptably high level because the counteracting chemical reaction, when steady state is reached, consumes them at the same rate as that of their formation. The high solubility of the polysulfide assures a high diffusion rate and, therefore, fast consumption at the negative electrode. Consequently, the ER-CR cycle can maintain a self-regulated charge voltage limit, which is set by the current density and temperature.

A key element of the proposed ER-CR cycle is that the polysulfide formation takes over the charge transfer from the transition-metal sulfide electrode reactions, thus providing an electron source for the inert-metal current collector while the overcharging current is flowing.

Previous findings support the polysulfide formation under the conditions of our experiments. Cyclic-voltammetric experiments indicated that Li_2S was readily oxidized in various complicated anodic reactions on inert electrodes to various polyanions of sulfur in the potential range of 1.9 to 2.2 vs. Li-Al [11,12]. The lower end of this range coincides with the potential of the FeS_2 formation [12]. However, because the FeS_2 formation takes place at high overpotential [12], the polysulfide anion formation is energetically favored relative to the transition-metal disulfide formation. The polysulfide may eventually help the FeS_2 formation from the lower sulfur activity phases in a chemical interaction. This reaction mechanism would explain the observed [13] good charge acceptance and high utilizations of the disulfide electrodes in Li_2S -saturated electrolytes.

The term disulfide is used in this paper only in the generic sense, indicating the transition-metal sulfide phase(s) of highest sulfur activity; the actual compound present at the end of the charge is not known. The surplus of Li_2S in the described experiments may dictate a phase transformation sequence that is different from the presently known one [12] that is valid for the disulfides at $4\text{Li}:\text{Fe}:\text{S}$ atom ratio.

CONCLUSION

Identified in this work was an effective overcharge mechanism that protects the transition-metal disulfide electrodes in Li_2S -saturated electrolyte against anodic dissolution and sets a self-regulated charge voltage limit. The resulting overcharge tolerance of the cells, which is believed to be due to the ER-CR cycle, should eliminate the need of voltage-limited cell charge and allow the use of standard cyclers for charge equalization in cells of the battery. This would reduce the initial and operating cost of Li-alloy/MS_2 batteries.

ACKNOWLEDGMENT

This work was supported by the U.S. Department of Energy, Office of Energy Storage under contract No. W-31-109-Eng-38. The author is grateful to Drs. P. A. Nelson and J. E. Battles for their encouragement and support.

REFERENCES

1. F. J. Martino, W. E. Moore, and E. C. Gay, Argonne National Laboratory Report, ANL-83-62, pp. 29-38 (1983).
2. T. D. Kaun, J. Electrochem. Soc., 132, 3063 (1985).
3. M. F. Roche, Progress Report ANL-8109, Argonne National Laboratory (1975).
4. Z. Tomczuk, R. E. Hollins, and R. K. Steunenberg, Proc. Symp. Workshop Adv. Battery Res. Design, ANL-76-8, Argonne National Laboratory (1976).
5. Z. Tomczuk and A. E. Martin, Progress Report ANL-76-9, Argonne National Laboratory (1976).
6. Z. Tomczuk, A. E. Martin, and R. K. Steunenberg, Ext. Abst. 150th Electrochem. Soc. Meeting, p. 131 (1976).
7. J. R. Selman and M. L. Saboungi, Electrochemistry of Sulfur in Halide Melts, chapter in "The Sulfur Electrode" ed. R. P. Tischer, Academic Press, p. 113 (1983).
8. W. H. DeLuca, A. A. Chilenskas, and F. Hornstra, Proc. of 14th IECEC, Boston, MA, August 5-10, 1979, Vol. 1, p. 665 (1979).
9. L. Redey and D. R. Vissers, Extended Abstracts, 163rd Electrochem. Soc. Meeting, San Francisco, CA, Vol. 83-1, p. 69 (1983).
10. L. Redey, D. R. Vissers, J. Newman, and S. Higuchi, Proc. Symp. on Porous Electrodes: Theory and Practice, H. C. Maru et al., eds, The Electrochem. Soc. Inc., Pennington, NJ, Vol. 84-8, p. 322 (1984).
11. J. R. Birk and R. K. Steunenberg, Adv. Chem. Ser., No. 140, p. 186 (1975).
12. S. K. Preto, Z. Tomczuk, and M. F. Roche, J. Electrochem. Soc., 130, 264 (1983).
13. L. Redey, Proc. of the First Intl. Workshop on High-Temperature Molten Salt Batteries, Argonne, IL, April 16-18, 1986, ANL-86-40, p. B-131 (1986).

Table 1. Charge/Discharge Imbalance of FeS_2 Electrode^a

Cycle No.	Charged ^b (mAh)	Overcharged ^c (mAh)	Cut-off V vs. Li-Al	Discharged ^d (mAh)
128	325	0	1.90	320
129	322	0	1.90	321
130	320	215	2.15	327
131	315	280	2.20	325
140	323	170	2.15	317
141	325	310	2.20	330
142	321	0	1.90	317
150	325	0	1.90	315

^a All- Li^+ -cation electrolyte, 100 mA/cm^2 , 475°C

^b Charged to 1.90 V

^c Measured above 1.90 V

^d Discharged to 1.5 V

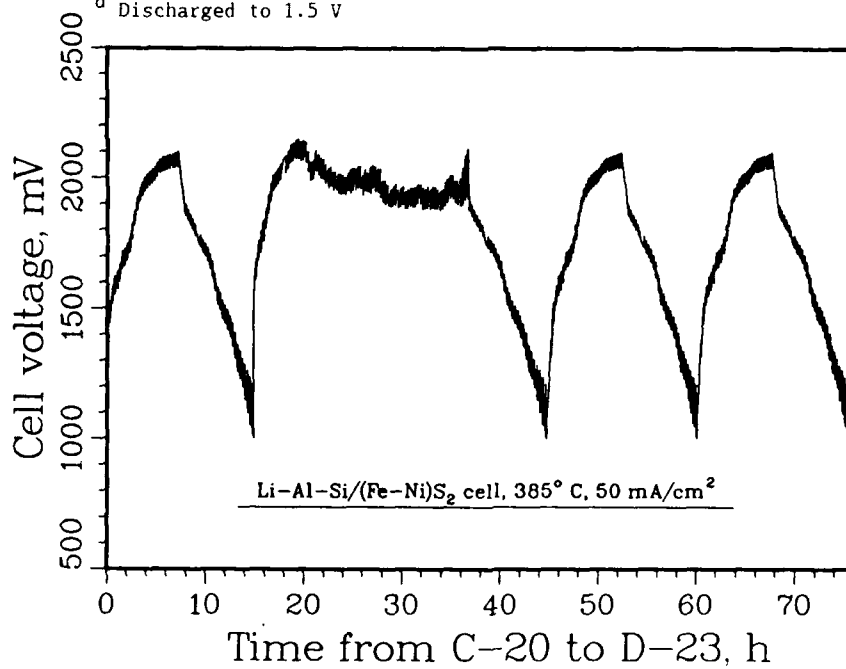


Figure 1. Evidence of Overcharge Tolerance in Cycle 21

MOLTEN SALT ELECTROCHEMISTRY FOR HIGH TEMPERATURE
THERMOCHEMISTRY AND KINETICS OF THE SYSTEM Li-Fe-S

A. Rabenau, B. Schoch, and W. Weppner

Max-Planck-Institut für Festkörperforschung
D-7000 Stuttgart 80, Germany

ABSTRACT

LiCl-KCl eutectic molten salts are employed as high temperature electrolytes for the electrochemical investigation of phase equilibria and fundamental thermodynamic and kinetic properties of the ternary system Li-Fe-S. Emf measurements in combination with electrochemical variations of the composition shows the presence of the phases $\text{Li}_3\text{Fe}_2\text{S}_4$ and Li_2FeS_2 with wide ranges of stoichiometry. The standard Gibbs energies of formation of Li_2FeS_2 and $\text{Li}_3\text{Fe}_2\text{S}_4$ are determined by integration of the cell voltage to be -543 and -894 kJ/mol at 420°C, respectively. The electrochemical reaction of lithium with Li-FeS₂ electrodes is rate determined by diffusion. The chemical diffusion coefficients are of the order of $10^{-5} \text{ cm}^2\text{sec}^{-1}$ at 420°C for both phases Li_2FeS_2 and $\text{Li}_3\text{Fe}_2\text{S}_4$. The diffusion is enhanced by internal electrical fields.

INTRODUCTION

The application of molten salt electrolytes shows many advantages for studying phase equilibria, thermodynamics and kinetics in high temperature chemistry. Electrochemical techniques (1-4) do not require quenching the samples for characterization in contrast to most other (e.g., metallographic or diffraction) methods. The equilibration process may be directly monitored by the change of the cell voltage with time. An analysis before the sample has equilibrated or after annealing for an unrequired long period of time is avoided. Thermodynamic data, phase equilibria and kinetic parameters may be obtained from the same experiment without destruction of the sample from reading conveniently measurable electrical quantities such as currents and voltages. A comparatively small number of sample preparations is required since the composition may be varied by electrochemical titration. Precision and resolution are extremely

high. Voltages may be readily measured within an error bar of 1 mV which corresponds to an uncertainty in the Gibbs energy of formation of 100 J/mol. Electrical charge transfers smaller than 1 μ Asec may be readily applied which corresponds to a mass change of about 10^{-16} g or a variation in stoichiometry of the order of 10^{-7} assuming a sample mass of 1 g. The electrochemical reactions may be also easily studied in-situ by X-ray or neutron diffraction while the sample is inserted into the molten salt which does not contribute to the diffraction pattern (5).

There are, however, several problems related to the application of molten salts. Besides high volatility, problems may be caused by the solubility of the solid electrode in the electrolyte and by chemical reactions. Stability may be generally not supported by kinetic impedances because of the high mobility of all electrolyte components. Thermodynamic stability requirements have to be taken into consideration in most cases.

The merits and problems of application of molten salt electrolytes will be illustrated by the investigation of the ternary system Li-Fe-S. This material is of special practical interest in combination with LiCl-KCl(e) molten salts because of the application in lithium-sulphur cells for high energy and power density secondary and thermally activated batteries (6-8). In spite of the large amount of work on this system, several fundamental questions on the thermodynamics, phase equilibria and kinetics are still open or debatable. Most phase diagram studies were performed by metallographic examination, X-ray and chemical analysis on samples cooled to room temperature. A variety of ternary phases is reported, e.g., LiFeS₂ (9), Li_{1.35}FeS₂ (9), Li_{1.5}FeS₂ (7), Li₁FeS₂ (7,10-12), Li_{1.5}Fe₂S₃ (7), and Li₁Fe₂S₃ (7). Emf measurements are described as a function of temperature for several plateaus in the discharge curve (13,14).

MOLTEN SALT ELECTROLYTE/ELECTRODE STABILITY

Stability of the molten salt electrolyte against reaction with the electrodes is required for any state of discharge of the galvanic cell. The salt should have a large decomposition voltage for battery type applications and should be stable at high activity of the electrochemically active component. In the case of solids it is difficult to combine these requirements with the condition of high ionic conductivity since the activation enthalpy for the motion of ions and the Gibbs energy of formation of the compound tend to

be inversely proportional. Molten salt electrolytes show advantages in this regard. The conductivity is generally very high. However, the melting point of the salt tends to increase in temperature with increasing thermodynamic stability.

Binary lithium compounds with high negative Gibbs energies of formation in the lowest oxidation state are suitable from a thermodynamic point of view. E.g., LiCl has a decomposition voltage of 3.4 V at 650°C, but the melting point is as high as 614°C. Various ternary chlorides show much lower melting temperatures, e.g., as low as 146°C in the case of LiAlCl₄. This material has a very wide stability range ($E_{\text{decomp}} = 2.38$ V at 200°C) but only at very low lithium activities (15). The much lower stability of AlCl₃ ($E_{\text{decomp}} = 2.03$ V at 200°C) as compared to LiCl (3.84 V, 200°C) leads to reaction with Li to form the more stable lithium chloride. To avoid this problem, a thermodynamically more stable chloride than LiCl needs to be added to form a ternary molten electrolyte. The choice is very limited, however. KCl is one exception and forms a eutectic melt with LiCl (molar ratio LiCl/KCl = 1.38; melting point 352°C).

ELECTROCHEMICAL TECHNIQUE

Methods that were developed for the investigation of complex systems (3) were employed to bring clarification in several details of the phase diagram of the ternary system Li-Fe-S and to obtain thermodynamic and kinetic information. The emf E is related to the chemical potential μ of the electroactive component Li and the Gibbs energy ΔG_r of the virtual cell reaction by

$$E = -\Delta G_r / \delta q \quad (1)$$

q and δ are the elementary charge and the variation of the lithium content by the considered cell reaction. Including the variation of E with temperature, comprehensive thermodynamic information may be derived.

Phase equilibria are determined from the variation of E as a function of composition (3). The cell voltage is independent of the composition as long as only the relative amounts of the existing compounds are changed by the cell reaction. This is the case when the maximum number of phases, i.e., 3 in the case of a ternary system, is present. The emf is in this case related to the standard Gibbs energies of formation ΔG_f° of all present phases according to

$$E = \frac{1}{qd} \sum_{n=1}^3 (-1)^n d_{n1} \Delta G_f^0(\text{Li}_{x_n} \text{Fe}_{y_n} \text{S}_{z_n}); \quad d = \begin{vmatrix} x_1 & y_1 & z_1 \\ x_2 & y_2 & z_2 \\ x_3 & y_3 & z_3 \end{vmatrix} \quad (2)$$

d is the determinant formed by the stoichiometric numbers of all three compounds in equilibrium; d_{n1} is the minor of d formed by eliminating the column of the stoichiometric numbers of the conducting ions (i) and the line of the running number (n). The minor d_{n1} is zero if the corresponding phase is not involved in the cell reaction. The cell voltage is then determined by 2 phases. This means, the ratio of the stoichiometries of two components remains unchanged for any phase during a reversible cell reaction.

The presence and extension of the various regions of the phase diagram are also obtained by varying continuously the composition by coulometric titration using various starting compositions along the binary Fe-S leg or within the ternary field. Single and two-phase regions are recognized by a drop in voltage. If originally a sample without any Li content is brought in contact with the electrolyte, the latter will be decomposed and the available Li will react with a sample as long as the Li activity of the sample exceeds the decomposition voltage. Vice versa, this amount of Li in the sample may not be removed electrochemically by titration, but this error may be neglected in most cases. An important check of the correctness of the phase diagram is to prove the monotonous increase of the voltage for any direction of the phase diagram with increasing Li content.

The electrical work of a reversible electrochemical reaction corresponds to the difference of the chemical energy which is the change of the Gibbs energy of formation between the starting and the final composition. The Gibbs energy for any composition of the sample is therefore obtained by integration of the emf along the path of variation of lithium content (3)

$$\Delta G_f^0(\text{Li}_\delta \text{Fe}_y \text{S}_z) = q \int_{\delta_0}^{\delta} E(x) dx + \Delta G_f^0(\text{Li}_{\delta_0} \text{Fe}_y \text{S}_z) \quad (3)$$

This allows to determine the Gibbs energy of formation for any composition and along any direction of the phase diagram, e.g., also along quasi-binary sections which are not directed toward the Li corner.

An electrochemical transfer of ions through the galvanic cell produces compositional inhomogeneities in the electrodes. The current describes the flux of ions in the electrode at the interface with the electrolyte. The cell voltage indicates the concentration of Li at the same position

but superimposed by polarizations. The time dependence of the cell voltage and current may be employed to analyse the effective chemical diffusion under the influence of electrochemical potential gradients. In principle, any initial and boundary condition may be used to solve Fick's second law. It is convenient to start with a homogeneous composition and to fix either the voltage or the current, or to provide a short current pulse (4,16). The technique of constant currents is employed in the present investigation of the Li-Fe-S system. The cell voltage changes with the square root of time in this case:

$$dE/d\sqrt{t} = \alpha i_0 dE/d\delta \bar{D}^{-1/2}; \alpha = 2V_M/q N_A \sqrt{\pi} \quad (4)$$

(i_0 : current density, \bar{D} : chemical diffusion coefficient, V_M : molar volume, N_A : Avogadro's number) The variation of E with the stoichiometry, $dE/d\delta$, is obtained from the difference of the equilibrium cell voltages before and after the current flux. This quantity is proportional to the enhancement factor

$$W = \partial \ln a / \partial \ln c = - (q\delta/kT) dE/d\delta \quad (5)$$

(a : activity, c : concentration, k : Boltzmann's constant) which relates to the diffusivity D , electrical mobility u , and tracer diffusion coefficient D_T (4). This electrochemical technique has been developed for binary systems (16) and is extended to ternary systems in the present work. Complications arise from the fact that the additional component produces an additional degree of freedom. Variation of the stoichiometry of one component results in changes of the chemical potentials of both other components. The predominantly mobile component will move and may drive the composition locally away from the path of equilibrium compositions.

EXPERIMENTAL

Molten salt electrolytes were prepared from eutectic mixtures of LiCl (purum p.a., >98%) and KCl (puriss. p.a., >99%), both from Fluka, Buchs CH. Crucibles made of alumina (Haldenwanger, Berlin, 4 cm wide and 6 cm high) and resistance furnaces were employed. All preparations and experiments were performed in an argon filled dry box. The melt was heated over night at 400°C before the electrodes were inserted. The counter and reference electrode were prepared electrochemically from aluminum wire (Ventron, Karlsruhe D, 0.1 cm in diameter) which was wound to a spiral to accommodate easily to the large expansion by the uptake of lithium without breaking apart. Molten lithium (Cerametals,

New York, 99.9 %) adherent to a molybdenum sheet was employed as anode using molten LiCl-KCl(e) electrolytes at 400°C. The electrochemical reaction proceeded under constant current until an equal molar amount of LiAl (β -phase) and Al (α -phase) was obtained. The samples were prepared from Fe (Merck, Darmstadt, > 99.5%), $\text{Fe}_{0.9}\text{S}$, FeS, and Li_2S (all from Cerac, Driebergen NL, > 99.9%). The appropriate mixtures of the powders were pressed to pellets (pressure: 30 kN) of 6 mm in diameter and 1-2 or 2-5 mm in thickness for samples employed for coulometric titration or static emf measurements, respectively. The pellets were annealed in small evacuated sealed glass ampoules at 420°C for 10 hours before they were inserted into small pockets made from molybdenum sheet (Ventron, > 99.9%; 0.1 mm in thickness). These sample holders were open to the melt from the top. If part of the sample should break off, this material is collected within the pocket and participates further in the titration process. Molybdenum wires were used as electronic leads to all electrodes.

Currents of the order of 7-15 mA/cm² electrode surface area were provided by constant current sources (Keithley, models 220/227). Emfs were measured by electrometers (Keithley, models 616/619, input impedance > $2 \times 10^{14} \Omega$). The coulometric titrations and kinetic transient measurements were computer controlled. Generally 50 steps were taken for a full forward and backward titration. The operating temperature was kept within the regime of $420 \pm 20^\circ\text{C}$ at the position of the sample.

RESULTS AND DISCUSSION

Fig. 1 shows one of the results of the coulometric titrations. FeS_2 is used as starting material in this case. Three voltage plateaus are observed indicating the presence of ternary or quasi binary equilibria. The results for forward and backward titration are in good agreement except for the intermediate small plateau which shows a value which is 20 mV higher if lithium is taken out of the sample rather than inserted. Also, the voltages are smaller close to $\delta=4$ when lithium is added rather than taken out of the sample. This may be understood by kinetic impedances due to the formation of Li_2S (besides Fe) which is an ionic conductor and equilibrates very slowly. Wide intermediate regimes of dropping voltages indicate the presence of large single- and two-phase fields.

The information obtained from the coulometric titration curves is transferred into the phase diagram as shown in Fig. 2. In addition, the results of static emf measurements

are included. Identical cell voltages are indicated by the same symbol. The other investigated compositions fall within single- and two-phase regions. The results are in agreement which shows that the exposure of the sample to the molten salt for extended periods of time does not give rise to uncontrolled variations of the composition, e.g., by the loss of sulphur or electronic conductivity of the electrolyte. Areas of identical plateau voltages and static emfs are combined in triangles of three-phase equilibria. The presence of 2 ternary phases, Li_2FeS_4 and $\text{Li}_2\text{Fe}_2\text{S}_5$, is confirmed. The ranges of non-stoichiometry are, however, much wider than assumed previously. These are indicated by the shaded areas. The static emf measurements indicate the equilibrium of $\text{Li}_2\text{Fe}_2\text{S}_5$ with Li_2S . Discrepancies with earlier work may be due to the present in-situ investigation at 420°C while other examinations were performed at room temperature.

The Gibbs energy of the reaction of lithium with FeS_2 is plotted in Fig. 3 employing equation (3) through all 1-, 2- and 3-phase regions up to the formation of $2\text{Li}_2\text{S} + \text{Fe}$ ($\delta=4$). The ternary and quasi binary regions are indicated as straight lines. Taking into account literature data (17) for the Gibbs energy of formation of FeS_2 (-138 kJ/mol), the standard Gibbs energy of formation of stoichiometric Li_2FeS_4 from the elements is found to be -543 kJ/mol. The corresponding value for the compound $\text{Li}_2\text{Fe}_2\text{S}_5$ is -894 kJ/mol. The compositional dependence of the standard Gibbs energy of formation of the compounds along the quasi binary section $\text{FeS}-\text{Li}_2\text{S}$ is obtained from integration of the emf between the Fe-S leg and the final composition. The results are shown in Fig. 4. A literature value of -419.5 kJ/mol for the formation of Li_2S at 420°C (17) is used.

The galvanostatic currents produce variations of the cell voltage with the square root of time in the initial stage as long as a semi-infinite sample may be assumed (Fig. 5). This shows that this reaction process is rate determined by diffusion in the bulk of the sample. Deviations from the linear $E - \sqrt{t}$ behaviour are also due to non-linearities of the slope $dE/d\delta$ of the coulometric titration curves which causes changes of the enhancement factor and chemical diffusion coefficient with the variation of the composition at the interface with the molten salt. Fig. 6 shows the time dependence in the reverse direction. The slope is in agreement within the limits of experimental error. Similarly, linear $E - \sqrt{t}$ relations are obtained in the case of the presence of $\text{Li}_2\text{Fe}_2\text{S}_5$ (Fig. 7). A plateau is observed after the sample has polarized at the interface with the molten salt enough so as to form the 3-phase region $\text{Li}_2\text{Fe}_2\text{S}_5 - \text{Li}_2\text{FeS}_4 - \text{Fe}_{0.9}\text{S}$. The reaction is sufficiently fast in this

case and equilibrium is maintained until only Li_2FeS_4 is present at the interface. The variation of the chemical diffusion coefficient for the various phases crossed in the course of discharge of an FeS_2 electrode is given in Fig. 8. The diffusion process is fast and shows a chemical diffusion coefficient of the order of 10^{-5} cm²/sec for solid Li_2FeS_4 and Li_2FeS_3 . The diffusion of lithium in FeS_2 is 1 - 2 orders of magnitude slower but still higher than typically in metallic systems. This enhanced diffusion is related to internal electrical fields to drive the ions in addition to the concentration gradient.

REFERENCES

1. Chen Li-chuan and W. Weppner, Naturwiss., **65**, 505 (1978).
2. W. Weppner, Chen Li-chuan and A. Rabenau, J. Solid State Chem., **31**, 257 (1980).
3. W. Weppner, Chen Li-chuan and W. Piekarczyk, Z. Naturforsch., **35a**, 381 (1980).
4. W. Weppner and R.A. Huggins, Ann. Rev. Matls. Sci., **8**, 269 (1978).
5. C. Riekel and W. Weppner, to be published.
6. D.R. Vissers, Z. Tomczuk, R.K. Steunenberg, J. Electrochem. Soc., **121**, 654 (1974).
7. D.R. Vissers, in: Materials for Advanced Batteries (D.W. Murphy, J. Broadhead and B.C.H. Steele, Eds.), Plenum Press, New York, London, 1980, p.47.
8. B.J. Burrow, K.W. Nebesny, N.R. Armstrong, R.K. Quinn and D.E. Zurawski, J. Electrochem. Soc., **128**, 1919 (1981).
9. R.A. Sharma, J. Electrochem. Soc., **123**, 448 (1976).
10. C. Melendres and B. Tani, J. Phys. Chem., **82**, 2850 (1978).
11. Z. Tomczuk, S.K. Preto and M.F. Roche, J. Electrochem. Soc., **128**, 760 (1981).
12. Z. Tomczuk, B. Tani, N.C. Otto, M.F. Roche and D.R. Vissers, J. Electrochem. Soc., **129**, 925 (1982).
13. Z. Tomczuk and D.R. Vissers, J. Electrochem. Soc., **133**, 2505 (1986).
14. D. Bernardi, Ph. D. Thesis, Univ. of California, Berkeley, 1986.
15. W. Weppner and R.A. Huggins, Solid State Ionics, **1**, 3 (1980).
16. W. Weppner and R.A. Huggins, J. Electrochem. Soc., **124**, 1569 (1977).
17. I. Barin and O. Knacke, Thermochemical properties of inorganic substances, Springer Verlag, Heidelberg, 1973, Supplement 1977.

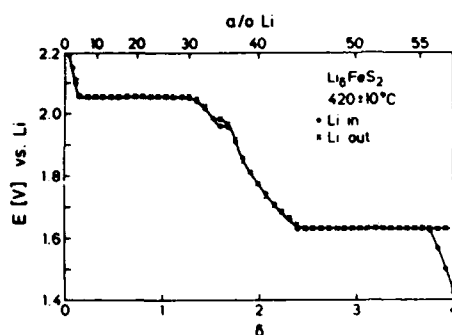


Fig. 1. Coulometric titration curve for the reaction of Li with FeS_2 in molten LiCl-KCl (e) salts at 420°C

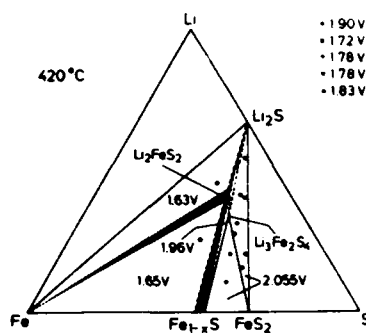


Fig. 2. Phase diagram of the ternary systems Li-Fe-S at 420°C (from coulometric titration and static emf-measurements)

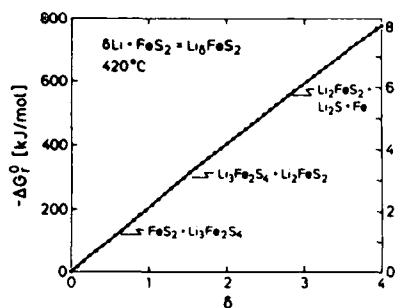


Fig. 3. Gibbs energy of reaction of Li with FeS_2 as a function of composition at 420°C

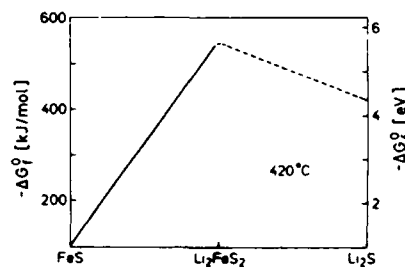


Fig. 4. Variation of the standard Gibbs energy of formation along the quasibinary section $\text{FeS-Li}_2\text{S}$

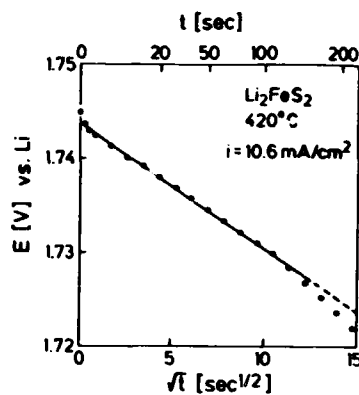


Fig. 5. Variation of the cell voltage with the square root of time for the galvanostatic insertion of Li in Li_2FeS_2 .

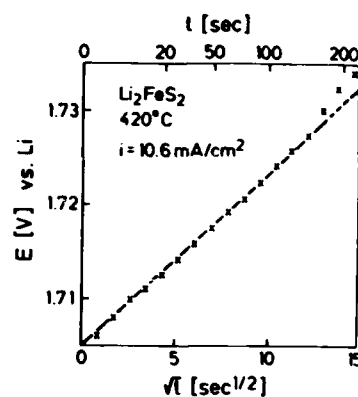


Fig. 6. Variation of the cell voltage with the square root of time for taking Li out of Li_2FeS_2 galvanostatically.

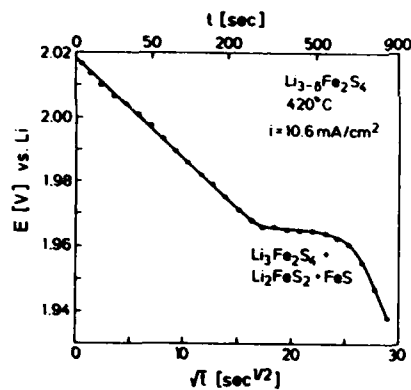


Fig. 7. Variation of the cell voltage with the square root of time for the electrochemical reaction of Li with $\text{Li}_3\text{Fe}_2\text{S}_4$. The plateau indicates the formation of a 3-phase equilibrium.

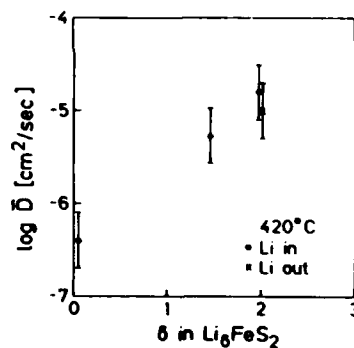


Fig. 8. Chemical diffusion coefficient of Li in Li_6FeS_2 as a function of composition at 420°C .

A COMPARATIVE STUDY OF THE ELECTROCHEMISTRY OF
THE LiAl ANODE IN MOLTEN SALT AND ORGANIC MEDIA

Y.S. Fung,
Department of Chemistry,
University of Hong Kong,
Hong Kong

ABSTRACT

The electrochemistry of the LiAl anode in molten salt and organic media was investigated using cyclic voltammetry, chronopotentiometry and chronoamperometry. Electrochemical formation of the β -LiAl phase was shown highly dependent on the nucleation polarisation in both media and the difference observed is attributed to the difference in the operation temperature. Development of the anode as indicated by lowering polarisation potential and expanding electrode structure was observed upon cycling. The impurities was shown to have a greater effect on the cycling efficiency using the organic solvent. Moreover, an unstable passive film was formed at the electrode surface as a result of the interaction with the organic solvent, which occurred continuously over a wide span of the cathodic potential. On the other hand, the anode/solvent interaction under the molten salt medium was affected by the liberation of potassium as a vapour, which only occurred at a highly cathodic potential.

INTRODUCTION

Due to the high electronegativity and low atomic weight, lithium and its alloys provide promising anode materials for various advanced battery systems (1,2). The alloying of lithium with aluminium in the form of LiAl anode is at present the most promising anode due to the good retention of the corrosive lithium metal and a moderate lowering of the voltage of the cell (3-5). The LiAl anode has thus been used in the molten salt batteries and in the organic lithium cells. The use of an organic medium has the advantage of operating the cell under ambient temperature, whereas the use of the molten salt medium provides a cell with high current drain. It could be interesting to compare the electrochemical behaviour of LiAl in these two media so as to identify the limiting areas in each system and to provide a direction for searching new media to be used in the secondary lithium battery. In the present study, LiCl.KCl eutectic system was chosen as the molten salt medium and methyl acetate as the organic medium.

Three electrochemical techniques, the cyclic voltammetry, chronopotentiometry and chronoamperometry, were employed for the investigation of the electrochemical kinetics for the formation of the LiAl anode in the two selected media.

EXPERIMENTAL

The LiCl-KCl eutectic mixture was prepared by mixing appropriate amounts of LiCl and KCl and purified by fusion under vacuum, preelectrolysis and filtration. Methyl acetate was purified by first shaking with anhydrous potassium carbonate to remove acidic impurities, then refluxed with acetic anhydride (85 mL/g) for 6 hours to remove water, then distilled to remove methanol, finally refluxed and distilled with phosphorus pentoxide under argon atmosphere to reduce the moisture content and only the middle cut was collected after distillation. The purified solvent was kept in the dry box with dehydrated molecular sieve. All the lithium salts used were finely ground and dried under vacuum at 160°C for 48 hours before use. The experiments were performed inside the dry box.

Aluminum wire or aluminum rod encased in teflon tubing was used as the working electrode for the molten salt and the organic system. The electrode was first degreased with acetone, then mechanically polished to a mirror shine surface with alumina powder, followed by cleaning in an ultrasonic bath with methyl acetate. Electrochemically formed LiAl (50 a/o) electrode was used as the reference electrode for the molten salt study, whereas 0.1 M Ag⁺/Ag electrode in acetonitrile was used as reference electrode for the organic medium. Lithium metal or thermally preformed LiAl alloy was used as the counter electrode to provide a source of lithium for the electrochemical experiment.

A Princeton Applied Research (PAR) 175 Universal Programmer, a PAR 173 Potentiostat/Galvanostat and a PAR 170 Digital Coulometer/Current-to-Voltage Converter was used for cyclic voltammetric studies and chronoamperometric studies, while a PAR 83 Potentiostat/Galvanostat was used to provide constant currents for chronopotentiometric studies. For fast transient signal, DataLab M 501 transient recorder with a Tektronix 504 oscilloscope attachment was used for recording, whereas Houston Instrument Omniscribe X-Y recorder or Esterline Angus (Model 975) X-Y recorder was used for recording slow signal. In the cyclic chronopotentiometric studies, a self-constructed electronic automatic switching unit was used to limit the coulomb of charges plated onto the electrode surface, as well as to reverse the current direction at the end of the deposition process. The adjustable timing trigger was supplied by the Chemical Electronic Model 61 Waveform Generator.

RESULTS AND DISCUSSION

Electrochemical formation of the Li/Al intermetallic phases

The appearance of a critical potential (E_c) for the electrochemical formation of the β -LiAl phase indicates the occurrence of nucleation polarisation, which is clearly shown to occur in freshly prepared aluminium electrode. The occurrence of a potential spike and large polarisation potential during charging and discharging were attributed to the nucleation polarisation, as both of them are markedly decreased in the use of nonalloying substrate such as nickel metal (7). The nucleation of the β -LiAl on aluminium substrate was studied using chronoamperometry and the results are shown in fig. 1. The normal i - t curves were obtained upon small potential step. However, a current minimum, followed by a current growth curve was found to occur after the potentials were stepped above a critical value in both the molten salt and the organic media.

The growth in the current growth region for the β -LiAl formation was shown (8) to follow a three-dimensional growth of the lithium in the direction from surface to the bulk of the aluminium. As the charge transfer rate for metal deposition is generally high, the current observed will be limited by mass diffusion. Under such conditions, the current density for a fixed number of crystallites, N_0 , growing by hemispherical diffusive flux, is given by the following equation (9):

$$I(t) = nFN_0 \left(\frac{1}{2} \sqrt{\frac{D}{\pi t}} \right) \frac{1}{M} \frac{1}{d}$$

- where $I(t)$ = current at time t in Amperes;
 n = number of electron transferred;
 F = Faraday constant in coul. equiv. $^{-1}$;
 D = the diffusion coefficient of the electroactive species in $\text{cm}^2 \text{s}^{-1}$;
 C = the concentration of the electroactive species in mol cm^{-3} ;
 M = the molecular weight of the electroactive species in gram;
 and d = the density of the deposited species in g cm^{-3} .

The $1/t^{1/2}$ as indicated to be constant by the above equation was verified (10) in the LiAl system. The constancy of $1/t^{1/2}$ was further shown to be dependent on potential and a change in the nucleation growth mechanism was shown to occur during the electrochemical deposition of lithium at aluminium at intermediate potential (11).

The difference in the nucleation behaviour under molten salt and organic media is mainly due to the difference in temperature (fig. 1).

Both systems exhibit the existence of a critical potential and the change in the nucleation growth mechanism at a given stepping potential. The chronoamperograms differ in the response time and the charge density. Under molten salt media, the nucleation rate is more affected by potential and it is in general much faster than the use of the organic solvent.

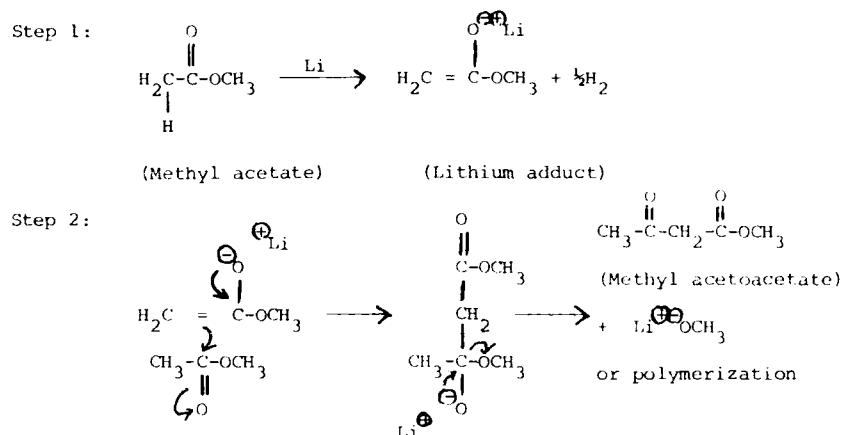
Cycling studies

The cyclability of the LiAl anode is shown in fig. 2. The polarisation potential between charging and discharging is shown to be much less in the molten salt medium. Moreover, well defined plateaus for other lithium rich intermetallic phases are clearly shown using the molten salt system and only one plateau was observed under the organic medium. This is due to the occurrence of numerous lithium rich intermetallic phases and the chemical reactivities of the anode towards the organic solvent at ambient temperature.

The LiAl anode is shown to develop upon cycling under both high and low temperature systems. The polarisation potential was shown (10,11) to decrease upon cycling and the morphology of the electrode was expanded and developed into a well characterised structure under cycling with suitable c.d. The nucleation polarisation was also decreased upon cycling. However, impurities like H_2O or oxide was shown (10) to have a more marked influence on the cycling efficiency for the organic than the molten salt system.

Anode/solvent interaction

The interaction between the anode and the solvent was studied using the cyclic voltammetric technique, as the system can be temporarily exposed to high activity lithium alloys during the cathodic scan. The results are shown in fig. 3. Cyclic voltammograms for the high lithium activity alloys are well characterised in the molten salt study and scanning into very cathodic potential leads to the appearance of oscillating current in the stripping voltammogram due to the liberation of potassium as a vapour from the LiCl.KCl eutectic. More interesting interaction was observed for the organic system. Three cross-over points are observed in the cyclic voltammogram upon successive cathodic scan. The first cross-over is due to the activation of the electrode surface by the deposition of the β -LiCl. Thus, the electrode can accept more lithium at the reverse scan. The second cross-over is due to the formation of a passive film at the electrode surface, leading to a reduction in current. Further cathodic scan leads to a breakdown of the passive film with subsequent increase in current and the appearance of a wavy voltammogram. Based on the evidence from the identification of the reaction products by the i.r. and N.M.R. techniques (10), the following reaction mechanism is proposed with a two step reaction initiated by the abstraction of an acidic α hydrogen from methyl acetate.



CONCLUSION

The formation of the β -LiAl is shown to be strongly affected by the nucleation of the β phase, which grows rapidly three-dimensionally after the potential was stepped above a critical value. The difference in the nucleation polarisation under molten salt and organic media is mainly due to the difference in temperature, which affects the nucleation rates and the current density. The LiAl anode is shown to develop upon cycling under both high and low temperature system. The polarisation potential was found to decrease while the electrode structure was developed upon cycling. However, only one plateau was observed under the organic solvent while other lithium rich alloy phases were suppressed due to their activities with the solvent. For the same reason, impurities in the solvent affect the cycling efficiency more under the organic solvent. The anode/solvent interaction as studied by cyclic voltammetry indicates a continued interaction of the solvent with the anode over a wide potential span in the organic medium, whereas the molten salt medium only deteriorates at highly cathodic potential with the liberation of potassium vapour. The formation of an unstable passivated film in the organic medium leads to further interaction of the anode and the solvent. Although a better passive film can be made by the use of LiAsF_6 (12, 13), the reactivity between the anode and the organic solvent is a major problem facing the use of the organic solvent. The recent development of the room temperature molten salt system may provide a medium with suitable conductivity and inertness towards lithium and its alloys. Initial promising results were obtained in the preliminary work (14,15) and the compatibility of various room temperature molten salt systems towards lithium and its alloys is at present investigated in our laboratory.

ACKNOWLEDGEMENT

The author would like to thank the Ministry of Defence in U.K. and the Research Grant Committee in H.K.U. for the financial support for the above work.

REFERENCES

1. H.V. Venkatesetty, "Lithium Battery Technology", Wiley-Interscience, New York, 1984, p. 61-78.
2. J.P. Gabano, "Lithium Batteries", Academic Press, London, 1983.
3. J.R. VanBeek and P.J. Rommers, Power Sources, **7**, 595 (1979).
4. J.R. Selman, D.K. DeNuccio, C.J. Sy and R.K. Steunenbergh, J. Electrochem. Soc., **124**, 1160 (1977).
5. C.J. Wen, B.A. Boukamp, R.A. Huggins and W. Weppner, J. Electrochem. Soc., **126**, 221-8 (1979).
6. Y.S. Fung, D. Inman and S.H. White, J. Appl. Electrochem., **12**, 669 (1982).
7. Y.S. Fung and D. Inman, Proc. Internat. Symp. on Recent Aspects of Electroanal. Chem. and Electrochem. Technol., Chandigarh, Dec. 28-30, 1982, 36 pp.
8. G. Staikov, P.D. Yankulov, K. Mindjov, B. Aladjov and E. Budevski, Electrochim. Acta, **29**, 661 (1984).
9. G. Gunawardena, G. Hills, I. Montenegro and B. Scharifker, J. Electroanal. Chem., **138**, 225 (1982).
10. Y.S. Fung and H.C. Lai, J. Appl. Electrochem., 1985, in preparation.
11. Y.S. Fung, D. Inman and S.H. White, Proc. Internat. Symp. on Molten Salt 1980, Florida, Electrochem. Soc., **F1**, 167 (1981).
12. V.R. Koch, J. Electrochem. Soc., **126**, 181 (1979).
13. F.W. Dampier and S.B. Brummer, Electrochim. Acta, **22**, 1339 (1977).
14. C.D. Desjardins, Report - MDP/83/27, 1984, 25 pp.
15. J.S. Wilkes, J.A. Levisky, R.A. Wilson and C.L. Hussey, Inorg. Chem., **21**, 1263 (1982).

Fig. 1. Chronoamperometric study of the nucleation of β -LiAl

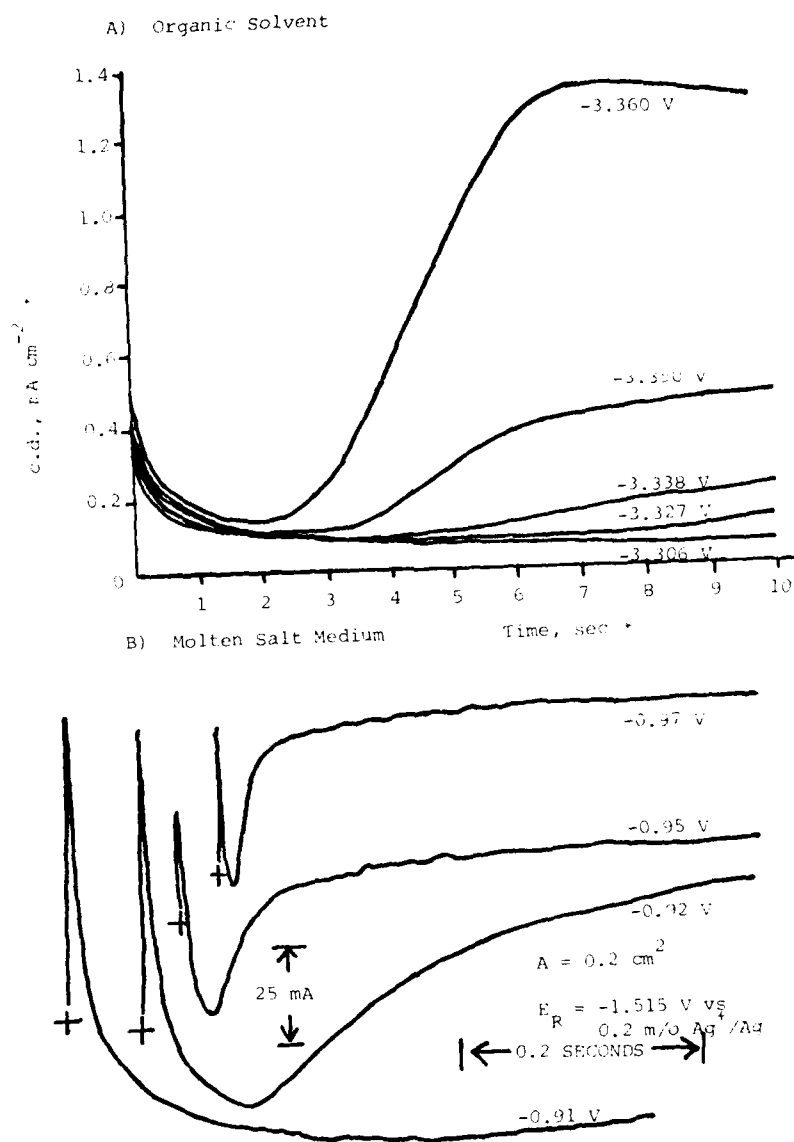
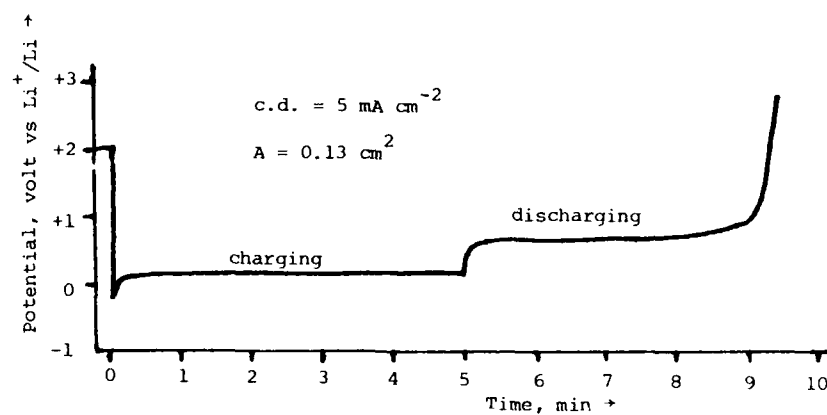


Fig. 2. Chronopotentiometric study of the LiAl anode

A) Organic Solvent



B) Molten Salt Medium

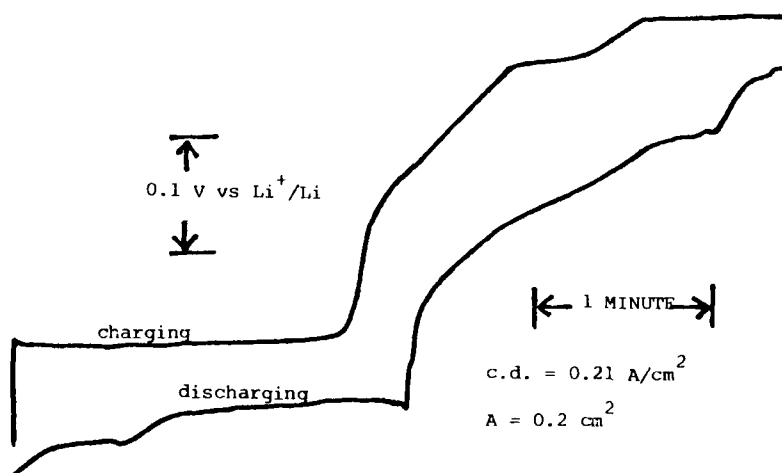


Fig. 3. Cyclic Voltammetric Study of the Li/Al anode

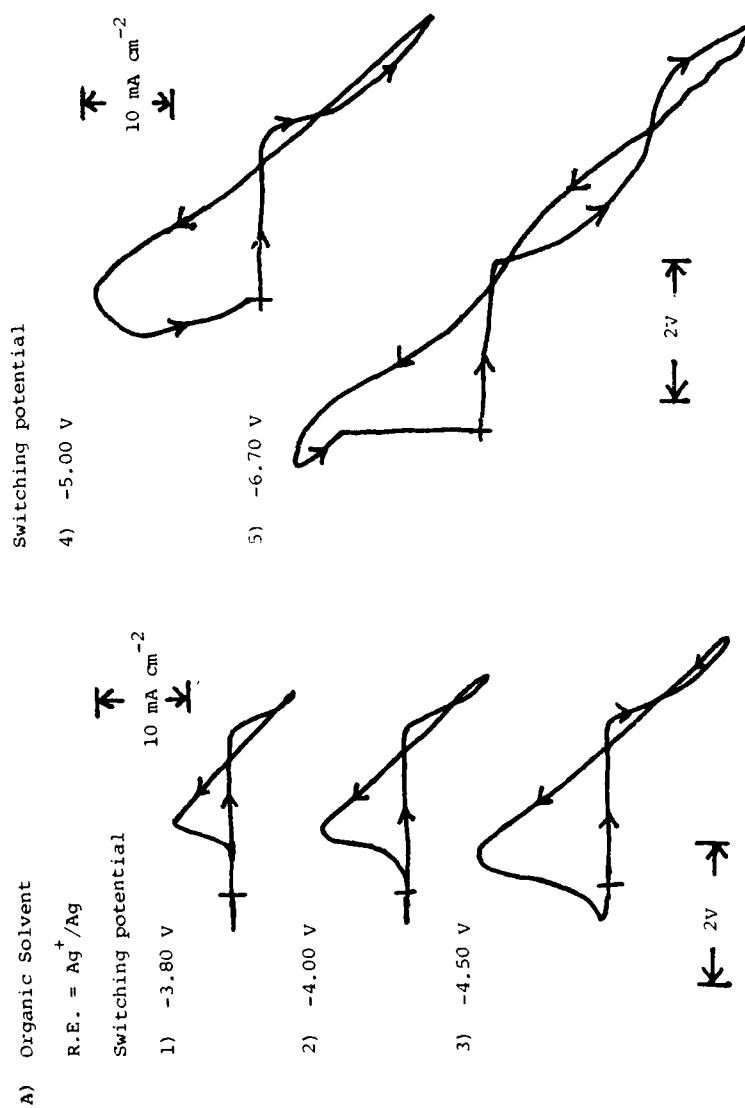
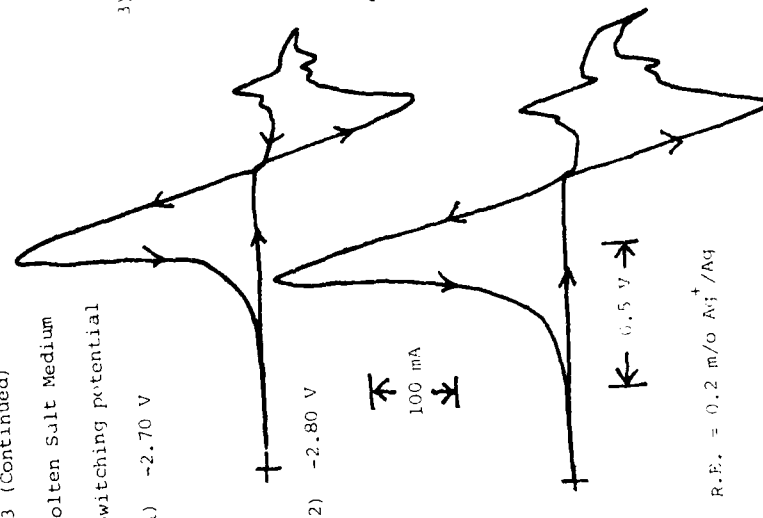


Fig. 3 (Continued)

B) Molten Salt Medium

Switching potential

1) -2.70 V



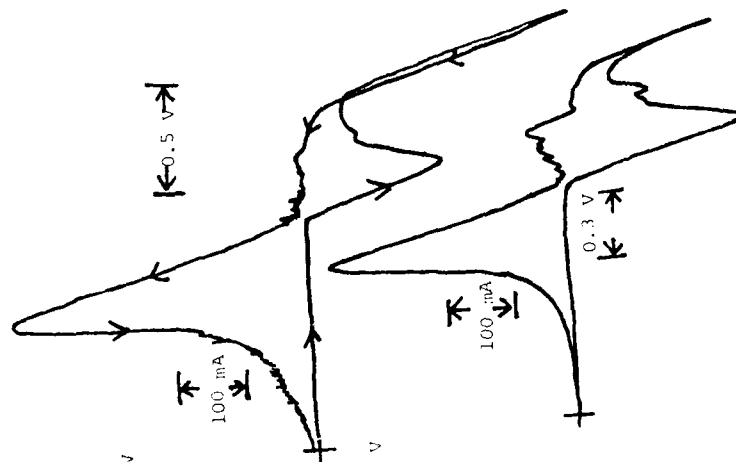
2) -2.80 V

100 mA

0.5 V

R.E. = 0.2 m/o Ag^+/Ag

3) -2.90 V



4) -3.05 V

100 mA

0.5 V

A NOVEL INORGANIC LOW MELTING ELECTROLYTE
FOR SECONDARY ALUMINUM-NICKEL SULFIDE BATTERIES.

H.A. Hjuler* , S. von Winbush[†] , R.W. Berg* and N.J. Bjerrum*.

*Molten Salts Group, Chemistry Department A, Building 207,
The Technical University of Denmark, 2800 Lyngby, Denmark.

[†]State University of New York at Old Westbury,
New York, USA.

A B S T R A C T

A new, inorganic low melting electrolyte with the composition LiAlCl_4 - NaAlCl_4 - NaAlBr_4 - KAlCl_4 (3:2:3:2) (or equivalently LiAlBr_4 - NaAlCl_4 - KAlCl_4 (3:5:2)) has been developed. The melting point for this neutral melt is 86°C; the decomposition potential is approximately 2.0 Volts; the ionic conductivity is measured in the range 97-401°C and is at 100°C 0.142 $\text{ohm}^{-1}\text{cm}^{-1}$ and the density is 2.07 g cm^{-3} . The conductivity seems to be an almost linear combination of the conductivities of the four individual halo salts which form the melt. The electrolyte is employed in the rechargeable battery system $\text{Al}/\text{electrolyte}/\text{Ni}_3\text{S}_2$ at 100°C. The open circuit voltage of this system with the low melting electrolyte is from 0.83 to 1.0 Volts. Dendrite free aluminum deposits are obtained. The cycling behaviour of the battery system is reported.

I N T R O D U C T I O N

The need for better rechargeable batteries is well-known, but most authors have been working with alkali metal anodes. In the last few years, aluminum has instead been investigated for battery suitability, especially in Denmark (1-3), Japan (4) and other countries. Melts of NaCl-AlCl_3 or KCl-NaCl-AlCl_3 have been the most popular electrolytes in the temperature range from 130 to 240°C, but room temperature molten salts, like imidazolium- or butylpyridinium-chloride aluminum chloride mixtures, have also been used in a number of cases (see ref. 5 for a recent survey).

The advantage of electrolytes that can be used at room temperature is obvious, but unfortunately the above mentioned large-cation organic melts have low ionic conductivities and high weights compared to the inorganic medium-

or high-temperature melts. Further the organic melts are less stable - depending on composition - in contact with aluminum metal.

Therefore, it is desirable to develop an inorganic electrolyte which is molten at room temperature. So far NaAlCl_4 has been used at 175°C in most of our battery work (1-3). When pure it melts at $156.7 \pm 0.1^\circ\text{C}$ (6). If NaCl is mixed with KCl and sufficient AlCl_3 is added, it is possible to reach very low melting acidic compositions; melting points down to 70°C have been reported (7). Unfortunately the ionic conductivity is low and the vapor pressure is not vanishing. This makes acidic melts (i.e. excess of AlCl_3) undesirable as battery electrolytes.

We adopted another policy in trying to find a low-temperature electrolyte, mixing alkali tetrahalo-aluminate salts which are neutral. By careful purification of the chemicals, followed by mixing various amounts, we have so far succeeded in obtaining an electrolyte with a rather low melting point, as described elsewhere (8). Here, preliminary determinations of some physicochemical properties are reported.

Finally, to examine the applicability of the melt, three test batteries have been constructed in a new cell design. The batteries were tested at 100°C and compared to earlier (1-2) measurements on a similar battery system with a NaAlCl_4 electrolyte at 175°C .

EXPERIMENTAL

All manipulations with the chemicals were performed in nitrogen-filled glove-boxes.

The alkali halides were made from analytical grade reagents purified in the molten state by flushing with dry, analytical grade hydrogen halide gas (6). The aluminum halides were purified by distillation (6).

The individual alkali aluminum halide salts were made from the above mentioned salts and purified by recrystallization or zone refining, as described recently (9). The electrolyte was finally made by weighing the three salts in the wanted ratios and sealing the ampoule. After equilibration at 125°C in a rocking furnace, the electrolyte was taken out, solidified and ground in a glove box. This material was kept in sealed ampoules until used.

The nickel sulfide electrodes were made from Ni_3S_2 (from

Cerac 99,9%), active carbon powder (Darco G60 from Fluka) and a teflon dispersion (from Dupont). As separator a boron nitride felt obtained from Argonne Natl. Lab., USA, was used.

The conductivity measurements were performed as earlier described (10).

Determination of the particular mixture having the lowest possible melting point was done as described elsewhere (8).

The density was determined visually, using an ampoule with markers immersed in a thermostated oil bath.

The quality of electrolytically deposited aluminum was examined in the cell shown in Figure 1. Of special interest is the question whether or not dendrites will be formed during charging (i.e. the plateability). For the cell in Figure 1, square pyrex tubing was used to facilitate observations of the electrodes. The cell, filled with electrolyte, was placed such that it could be observed and photographed directly while inside an oven of our own construction, heated with circulated air and controlled by a PID regulator. The electrodes of the cell were observed using a Zeiss Jena Technical 2 Stereo Microscope equipped with an Olympus OM-2 SLR-camera and a Schott KL 1500 cold light source. For cycling of the cell, a high-precision chronoamperostat, built in this laboratory (11) was used, connected to a chart recorder. The same cell and experimental set-up was used also to determine the electrochemical window of the electrolyte.

The testing of the batteries was performed using a oil bath with mechanical stirring and a PID-regulator. The battery test equipment has been described elsewhere (1). The battery test cell design is shown in Figure 2.

RESULTS AND DISCUSSION

Melting point. By observing the melting points of a large number of mixtures (8), it was found that the 3:5:2 LiAlBr_4 - NaAlCl_4 - KAlCl_4 melt was the one which remained totally liquid down to the lowest temperature: $86 \pm 1^\circ\text{C}$.

Density. The density ρ of the mixture was measured at ca. 100°C to be $2.07 \pm 0.02 \text{ g}\cdot\text{cm}^{-3}$.

Plateability. In the cell shown in Figure 1, aluminum was deposited on the carbon electrode (D) by electrolysis. Cathodic current densities from 1.4 to $706 \text{ mA}/\text{cm}^2$ was used. The time was chosen so that the passed total charge was ca. 2 C in each case, i.e. $30 \text{ C}/\text{cm}^2$. This amounts to an aluminum

layer of 0.01 mm. During electrolysis the potential was recorded.

After formation, the aluminum deposit was photographed. In all experiments with 1.4-70 mA/cm² a dense layer of aluminum was obtained. This corresponds to a high plateability, in contrast to what was found previously for NaAlCl₄ melts (12). At the highest current densities 0.14-0.7 A/cm² the deposits were, however, more porous (i.e. the layer appeared thicker and less dense) but absolutely no dendrites nor other well-defined crystals were seen, (in contrast to what was seen in NaAlCl₄ electrolytes, cf. Figure 3).

No passivation phenomenon was observed.

After each plating, the aluminum was stripped off again, by reversing the potential. The glassy carbon electrode was made perfectly smooth (mirror-like) before a new deposition electrolysis was started.

Anodic decomposition potential. Reverse electrolysis (electrode stripping) was used to determine the "electrochemical window" of the electrolyte. The anodic current was measured as a function of the applied potential. At the same time the cell was being observed for finding the potential at which evolution of a brown gas started. By plotting the current versus voltage and extrapolating towards zero current and comparing to visual observation of bromine evolution, a decomposition value of 2.0±0.1 Volts at 100°C was obtained.

This value should be compared to a value of 2.5±0.1 Volt, obtained at 175°C by extrapolation of similar measurements (13) on a near neutral NaCl-AlCl₃ molten salt in the temperature range 300-660°C. Our own determination of the decomposition potential of molten NaAlCl₄ at 175°C was 2.4±0.1 Volt (12). In this case, a yellow gas evolved (according to the reaction $4\text{AlCl}_4^- \rightarrow \text{Cl}_2 + 2\text{Al}_2\text{Cl}_7^- + 2\text{e}^-$). The lower decomposition potential of the low-temperature electrolyte is not to be ascribed to a temperature phenomenon, since decomposition potentials normally increase at lower temperatures (13). Instead, it is due to Br₂ formation.

Conductivity of the low melting electrolyte. The results of our measurements are presented in Figure 4. The known conductivity κ_i , $i = 1, 2, 3, 4$, of the four tetrahalo compounds (10, 14-16) from which the low melting system can be made (i.e. LiAlCl₄-NaAlCl₄-NaAlBr₄-KAlCl₄ (3:2:3:2)) are also included. It can immediately be seen that the conductivity of the low melting mixture cannot be far from a weighted average based on the molar fractions X_i of the

four individual salts.

A quantitative examination of this idea in the temperature range 267-349°C where comparison can be made shows that the difference between the weighted average conductivity ($\kappa_{\text{model}} = \kappa_1 X_1 + \kappa_2 X_2 + \kappa_3 X_3 + \kappa_4 X_4$) and the measured conductivity κ_{obs} varies between 0.8-3.0%. In this respect we are dealing with almost ideal liquids.

The conductivity of the low melting system naturally decreases with decreasing temperature but even at the melting point of the mixture, a fairly high conductivity is found (extrapolated value of $\kappa_{\text{obs}} = 0.117 \text{ ohm}^{-1} \text{ cm}^{-1}$ at 86°C). The measured conductivities are given in Table 1.

Test of batteries. The battery cell design is shown in Figure 2. A representative number of cycles are shown in Figure 5. Cell A, B and C differed by the shape of the cathode: a flat circular-, a cylinder wall- and a thick cylinder-wall-cathode, respectively. The open circuit voltage was - after assembly - 0.87V, 1.0V and 0.83V, respectively. The cell testing conditions were the same for cell A and B whereas for cell C, the charge/discharge currents were increased successively after cycle no. 39, as described in the caption of Figure 5.

A graphical presentation which helps evaluation of the results is shown in Figure 6. The charge efficiency is defined as (mAh, discharge)/(mAh, charge) and the energy efficiency is defined as the charge efficiency times (average discharge voltage)/(average charge voltage). The cell performance seems not good compared to the Al/NaCl-AlCl₃/Ni₂S₃ system at 175°C (1-2). The lower temperature may be causing some of the difference.

The metal housing excludes visual observation of the interior of the battery. The highly fluctuating efficiencies are probably related to shorting problems at the glass feed-through (Figure 2B), which in principle can be solved. The fact that the cells can exhibit high efficiencies can be interpreted to show that the battery system is promising. More work has to be done in this field.

A C K N O W L E D G E M E N T S

We would like to thank J.E. Battles, Argonne National Laboratory, USA for a sample of boron nitride felt, and GN Batteries A/S (former Hellesens Batteries A/S) for a sample of teflon dispersion. We would like to thank the Danish Ministry of Energy, the Danish Technical Science Research

Foundation and Director Ib Henriksens Foundation for financial support. Also, T.L. Lauridsen is thanked for measuring the conductivities.

R E F E R E N C E S

1. Hjuler, H.A.; Berg, R.W.; Bjerrum, N.J.: Power Sources 1985, 10, 1-21.
(Proceedings from the 14th International Power Sources Symposium 1984, Brighton, England).
2. Hjuler, H.A.; Berg, R.W.; Bjerrum, N.J.: 31st Power Sources Symposium (Proceedings) 1984, 60-73.
3. Hjuler, H.A.; Berg, R.W.; Bjerrum, N.J.: J. Electrochem. Soc., submitted.
4. Takami, N.; Koura, N.: *Denki Kagaku* 1986, 54, 498-503 (and references therein).
5. Wilkes, J.S.: "A Bibliography of Room Temperature Chloroaluminate Molten Salts", FJSRL-TM-84-0006, 1984 (Available from the F.J. Seiler Research Laboratory, USAFA, Colorado Springs, Colorado 80840-6528, USA).
6. Berg, R.W.; Hjuler, H.A.; Bjerrum, N.J.: *Inorg. Chem.* 1984, 23, 557-565.
7. Fischer, W.; Simon, A.L.: *Z. Anorg. Allg. Chem.* 1960, 306, 1-12.
8. Berg, R.W. et al. work in progress.
9. Berg, R.W.; Østvold, T.: *Acta Chem. Scand.* 1986, A40, 445-451.
10. Hjuler, H.A.; Berg, R.W.; Zachariassen, K.; Bjerrum, N.J.: *J. Chem. Data* 1985, 30, 203-208.
11. Fehrmann, R.; Bjerrum, N.J.; Poulsen, F.W.: *Inorg. Chem.* 1978, 17, 1195-1200.
12. Hjuler, H.A.; Berg, R.W.; Bjerrum, N.J.: Unpublished results.
13. Kher, M.G.; Mene, P.S.: *Indian J. Chem.* 1963, 1, 185-186.

14. Carpio, R.A.; King, L.A.; Kibler, F.C.; Fannin Jr., A.A: J. Electrochem. Soc. 1979, 126, 1650-1654.
15. Boston, C.R.: J. Electrochem. Soc. 1971, 118, 425-428.
16. Boston, C.R.; Grantham, L.F.; Yosim, S.J.: J. Electrochem. Soc. 1970, 117, 28-31.

Table I. Specific Conductivity of $\text{LiAlBr}_4\text{-NaAlCl}_4\text{-KAlCl}_4$ (3:5:2) as a Function of Temperature:

$t, ^\circ\text{C}$	$\kappa_{\text{obs}}, \Omega^{-1}\text{cm}^{-1}$
97.0	0.136
108.0	0.155
127.8	0.198
151.3	0.252
177.3	0.313
200.8	0.367
248.3	0.472
297.3	0.572
324.0	0.623
346.5	0.662
375.8	0.709
400.5	0.747

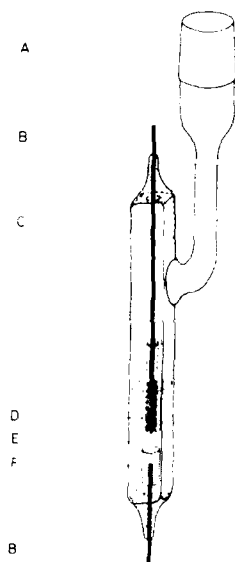


Figure 1. Electrolysis cell for plateability experiments: A, conical joint; B, tungsten wire; C, square pyrex glass tubing; D, electrode fixed into pyrex glass; E, electrolyte; and F, Al-counter-electrode.

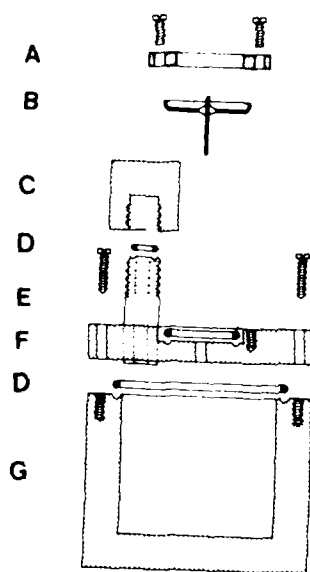


Figure 2. Vacuum-tight battery housing of test battery: A, aluminum disc to hold kovar disc (B) in its place; B, kovar disc with glass feed-through and stainless steel wire as positive terminal; C, filling tube cap; D, o-ring; E, electrolyte filling tube; F, cell lid; G, aluminum cell house (negative electrode).

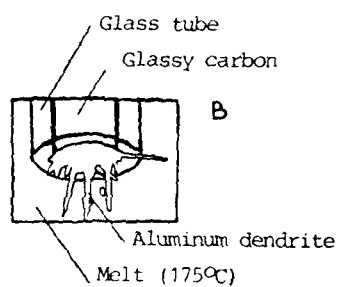
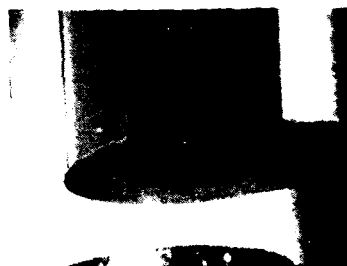
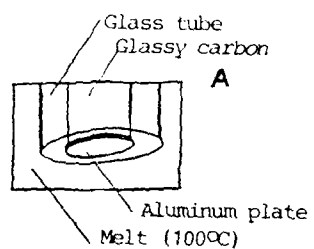


Figure 3. Photographs showing typical deposits obtained during plateability experiments, using A: The new low temperature melt at 100°C, B: The NaAlCl₄ electrolyte at 175°C, in both cases using a current density of 1.4 mA/cm². In A a dense Al plate, in B Al dendrites are formed.

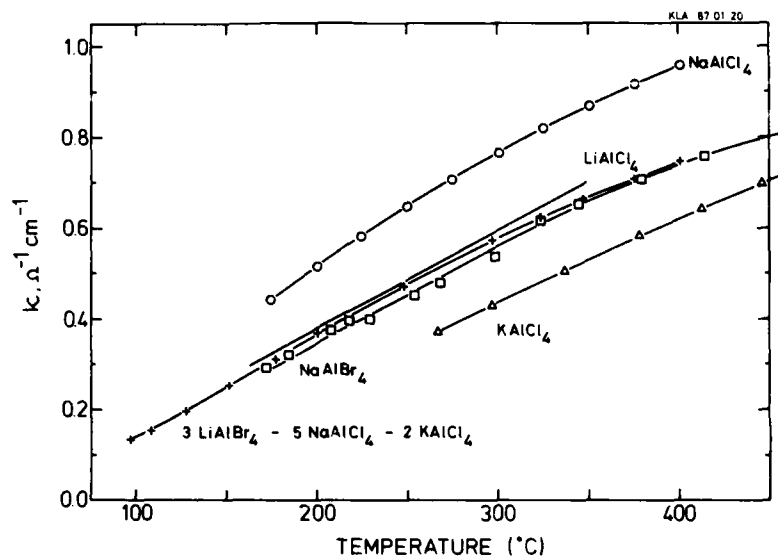


Figure 4. Conductivity of the LiAlBr_4 - NaAlCl_4 - KAlCl_4 (3:5:2) system as a function of temperature compared with the conductivity of the four tetrahalo compounds which alternatively can form this low melting neutral system: -○- LiAlCl_4 data (14), ○: NaAlCl_4 data (10), □: NaAlBr_4 data (15), △: KAlCl_4 data (16) (taken from graph), +: present measurements.

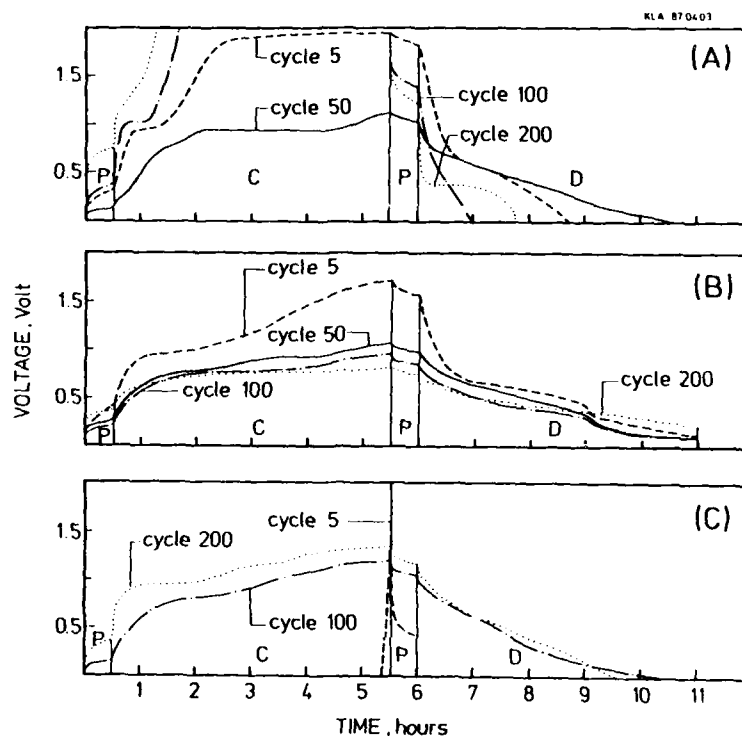


Figure 5. Charge/discharge curves for three experimental battery cells: (A) theoretical cathode capacity 204 mAh; charge/discharge conditions 5 mA and 5 h. (B) theoretical cathode capacity 1133 mAh; charge/discharge conditions 5 mA and 5 h. (C) theoretical cathode capacity 7586 mAh; charge/discharge conditions 5 mA and 5 h until cycle 39, 10 mA and 5 h until cycle 68, 15 mA and 5 h until cycle 89, 20 mA and 5 h until cycle 108, 25 mA and 5 h until cycle 128 and 50 mA and 5 h until test was terminated.

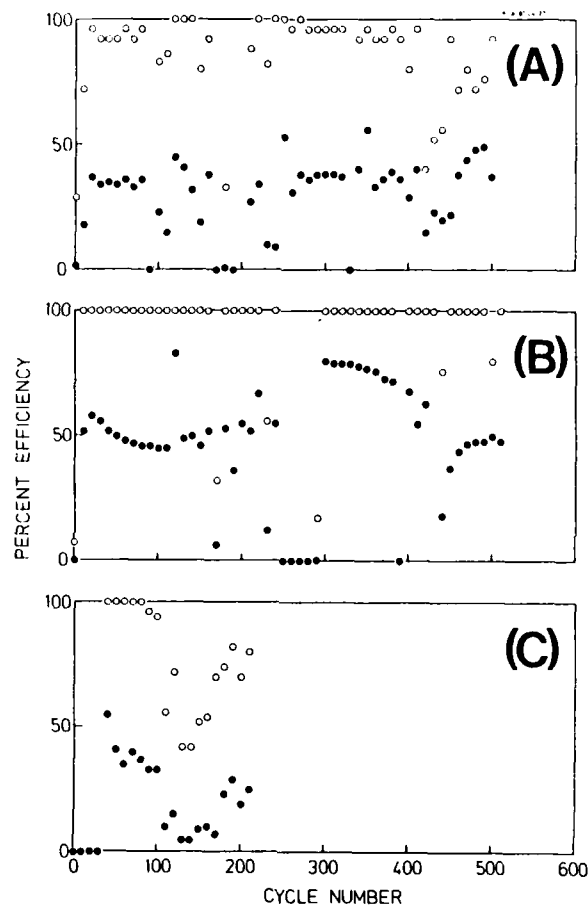


Figure 6. Experimental batteries: results calculated for every tenth cycle. Charge efficiency: O and energy efficiency: ● for cell A, B and C.

PERFORMANCE OF Na/Se(IV) MOLTEN CHLOROALUMINATE BATTERIES

Morio Matsunaga and Kunisuke Hosokawa

Department of Industrial Chemistry
Kyushu Institute of Technology
Tobata, Kitakyushu 804, JAPAN

ABSTRACT

This paper describes recent progress in the development of a new rechargeable cell, sodium/tetravalent selenium in $\text{AlCl}_3\text{-NaCl}$ melts. From the theoretical consideration of the energy density of sodium/molten chlorides battery the utilization of basic chloroaluminate melts is discussed. A cell with current collector of carbon felt shows high energy density (~ 415 Wh/kg), when it operates within both acidic and basic melts. The design of the positive compartment is also discussed.

INTRODUCTION

Several kinds of batteries, which utilize aqueous, organic, molten salt, and solid electrolytes, have been extensively studied for the load leveling and electric vehicle applications. A new rechargeable Na/X cell is one of the most attractive batteries because of high voltage, high energy density, and high energy efficiency. This type cell is composed of sodium anode, molten salt cathode, and a separator conductive to sodium ions. Several kinds of molten salts could be utilized in this type cell, in which only sodium ions could permeate the solid electrolyte. Especially, acidic melts such as haloaluminates offer many advantages for the battery applications; i.e., low liquidus temperature and high conductivity.

Several kinds of Na/X type cells with a molten chloroaluminate electrolyte have been reported; e.g., Na/ SbCl_3 (1), Na/S(IV) (2-4), Na/Se(IV) (5,6), Na/ Cl_2 (7), and Na/Fe(II) (8). Among them the cells which utilize tetravalent sulfur or selenium show quite high open circuit voltage and high energy density. This report describes the theoretical consideration on energy density of Na/X cells and the improvement of positive mix composition of a Na/Se(IV) cell as well as the material and design of positive current collector.

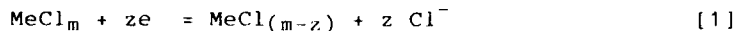
EXPERIMENTAL

Commercial reagents of AlCl_3 and NaCl were purified as follows. AlCl_3 was sublimed through a glass filter after reaction with aluminum metal(m5N) for one day. NaCl was dried under vacuum for several days at 400°C . Commercial grade of selenium(m6N) was used without pretreatment. Salt mixtures were prepared with purified chemicals in a glove box filled with high-purity nitrogen. Sodium metal was purified by double filtration.

Typical cell arrangements used in this study are shown in Fig.1. Each cell consisted of a Pyrex glass compartment filled with positive mixture, which was separated from the sodium electrode by means of a beta"-alumina tube (NGK Spark Plug Co.). Carbon felts(GF-20, Nippon Carbon Co.) and tungsten spiral were used as the cathode and anode current collectors, respectively.

RESULTS AND DISCUSSION

High energy density is one of the most important characteristics required for new batteries which will be applied for load leveling and electric vehicle. To develop high performance sodium/molten chlorides cells, the theoretical energy density is discussed in relation to the range of melt composition changed during a charge-discharge cycle. As an example we consider the following cathode reaction for a Na/X cell,



here MeCl_m and MeCl_{m-z} correspond to the positive active species at charged and discharged states, respectively. Although these species usually exist as anions in melts, we will treat all the species as neutral molecules to simplify the discussion. From Eq.[1] the total cell reaction with z electron transfer becomes as follows



Here we will consider the cells which use molten AlCl_3 - NaCl as the positive solvent. In this cell the sodium chloride content increases and the melt becomes basic with discharging. The range of melt composition changed during the cycle, therefore, relates to the energy density of a Na/X cell. When the molar ratio, $N(\text{AlCl}_3)/N(\text{NaCl})$, is $x/(1-x)$ at fully discharged and $y/(1-y)$ at fully charged state, the energy density of the cell will be

$$\text{ED/Whkg} = \frac{2.68 \times 10 (1/x - 1/y)(E_{\text{ave}}/V)}{74.90 + 58.44/x + (M/z)(1/x - 1/y)} \quad [3]$$

In this equation M is the molecular weight of discharged product $\text{MeCl}_{(m-2)}$ and E_{ave} is the average cell voltage. Fig.2 represents the relations between equivalent weight of the positive active mass and the theoretical capacity density of a cell which operates within four ranges of melt composition. In this figure the scale to estimate the theoretical energy density from the average cell voltage is also shown. These results suggest that there are two ways to improve the energy density of Na/X batteries. One is utilization of the positive material of which equivalent weight is low. The other method is to operate the cells within wider range of melt composition. Although a Na/S(IV) cell has quite high electromotive force and good charge-discharge behavior (2-4), this cell can work only in an acidic region such as between 80/20 and 50/50 of $\text{AlCl}_3/\text{NaCl}$ molar ratio. On the other hand, tetravalent selenium and tellurium are stable in both acidic and basic $\text{AlCl}_3\text{-NaCl}$ melts. In this study the performance of Na/Se(IV) cells has been investigated to demonstrate this consideration on the energy density of Na/X cells.

At first the performance of two kinds of Na/Se(IV) cells were studied, of which the positive current collectors were simple tungsten spiral. The positive melt in one cell kept basic during the operation, and the other utilized both acidic and basic melts. The Na/Se(IV) cell can discharge smoothly, when the melt composition is in an acidic region. When the melt is saturated with sodium chloride, the cell voltage at discharging abruptly changed and the tungsten electrode is covered with transparent solid which might be sodium chloride. These results suggest that the Na/Se(IV) cell operating in basic melt region requires new positive current collector of which surface area is quite large.

To find the discharging limit of melt composition in basic region, the performances of three cells, CS-52, CS-53 and CS-54, have been studied which utilize carbon felt current collector as shown in Fig.1. The melt composition and the amount of $\text{AlCl}_3\text{-NaCl}$ melt at fully charged state are almost the same in these cells as shown in Table 1. The typical charge-discharge curves observed in these cells are shown in Fig.3. Each cell shows stable discharging voltage before the $\text{AlCl}_3/\text{NaCl}$ molar ratio in melts approaches 35/65, and sodium chloride content at the discharging limit becomes richer with an increase of theoretical capacity. The dependence of energy density and

percent utilization of tetravalent selenium on discharge current density is shown in Fig.4. This figure depicts also the energy efficiency observed when the charging current is a half of discharging. Each cell shows high energy density more than 300 Wh/kg with lower discharging current density at 225°C, and the highest value was obtained for a cell CS-54. On the other hand, the percent utilization decreases with an increase of the theoretical capacity. In these cells the discharge limit relates to the coverage of the carbon felt with solid sodium chloride. The results obtained here, therefore, suggest that the $\text{AlCl}_3/\text{NaCl}$ molar ratio at full discharge should be in the range between 35/65 and 30/70. Of course this melt composition depends on the ratio of the surface area of current collector to the amount of positive mixture. The electric conductance of carbon felt and the design of the positive compartment also influence the capacity.

The cell CS-54 shows lower polarization than the other two cells as observed in Fig.3. Especially the cell voltage at charging is quite flat in this cell. The cell design of these cells was similar, since that of CS-52 and CS-53 was A-I type in Fig.1, and CS-54 was B-I. However, the carbon felt was wholly dipped in the positive melt in the cell CS-54, although only impregnated with melt in the cells CS-52 and CS-53. This difference influences the polarization especially at the charging. In cells CS-52 and CS-53 the distribution of melt composition is not uniform because of the low viscosity of the melt. At charging the melt in the upper part of carbon felt easily changes to be acidic, although that in the lower part keeps basic. As it is known that higher polarization is observed at charging in an acidic melt, the high voltage at the end of charging as shown in Fig.3 might be due to the above phenomenon. On the other hand, cell CS-54 has an uniform distribution of melt composition, and then flat voltage at charging was observed.

It has become apparent that a Na/Se(IV) cell could discharge even if the positive melt would be saturated with sodium chloride. To improve the energy density we prepared an experimental cell CS-61 which would work theoretically within the melt composition range between 65/35 and 30/70 as shown in Table 1. The structure of this cell corresponds to C-II type in Fig.1, and the positive current collector is wholly dipped in the melt similar to cell CS-54. The typical charge-discharge curves observed in this cell are shown in Fig.5. The dependence of the energy density, percent utilization, and energy efficiency on discharge current density is shown in Fig.4 together with the results in the above three cells. This cell shows

relatively low polarization at charging and discharging. Only at the end of charging the polarization had increased due to the change of melt composition to be acidic. The energy density obtained at 1.0 A discharging is quite high such as 415 Wh/kg in this cell. The percent utilization of tetravalent selenium, however, becomes low with higher current than 2.0 A. This poor performance at high current densities might relate to the design of positive current collector. Then it would be necessary to improve the design and material of the current collector in order to obtain better performance at high current density.

We have reported a Na/S(IV) cell with tungsten positive current collector had run for 17 months at nearly 100% depth of discharging with no significant rate of degradation (4). For Na/Se(IV) cells with carbon felt current collector, however, the degradation of percent utilization and energy efficiency was usually observed as shown in Fig.6. When graphite powder is suspended in chloroaluminate melts with tetravalent chalcogens, graphite intercalation compounds are formed. Then the above degradation of performance might relate to the formation of intercalation compounds. The other materials such as porous vitreous carbon should be used for this type cell.

ACKNOWLEDGEMENT

This work was partially supported by Grant-in-Aid for Scientific Research No.60040025 and No.61040019 from Ministry of Education, Science, and Culture.

REFERENCES

1. J. Werth, EPRI Report EM-230 (1975), EM-751 (1978)
2. G. Mamantov, R. Marassi, M. Matsunaga, Y. Ogata, J. P. Wiaux and E. J. Frazer, J. Electrochem. Soc., **127**, 2319 (1980)
3. G. Mamantov, K. Tanemoto, and Y. Ogata, J. Electrochem. Soc., **130**, 1528 (1983)
4. M. Matsunaga and K. Hosokawa, "Research on Energy Conversion and Storage Through Chemical Processes," SPEY vol.13, pp.217-226
5. R. Marassi, D. Calasanzio and G. Mamantov, in "Materials for Advanced Batteries," pp.223-227, Plenum Press(1981)
6. M. Matsunaga, K. Kitagawa, and K. Hosokawa, Denki Kagaku, **51**, 847 (1983)
7. J. Y. Cherng and D. N. Bennion, in extended abstracts in 170th Electrochem. Soc. Meeting, No.129, pp.187-8(1986)
8. R. J. Bones, J. Coetzer, R. C. Calloway, and D. A. Teagle, ibid, Abstract No.763, pp.1122 (1986)

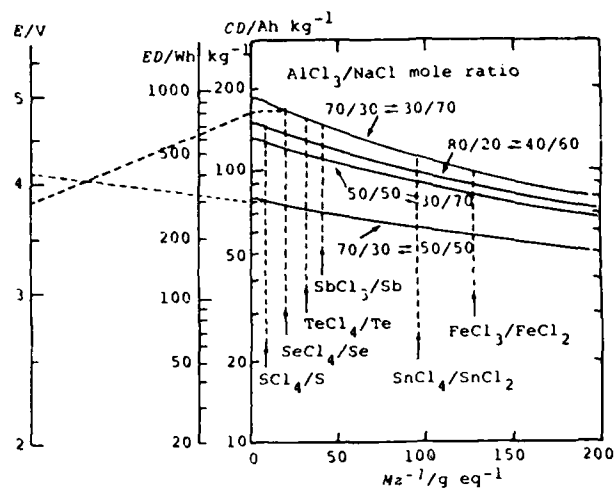


Figure 2 . Theoretical Capacity and Energy Densities of Na/X Cells Which Utilize AlCl₃- NaCl Melts

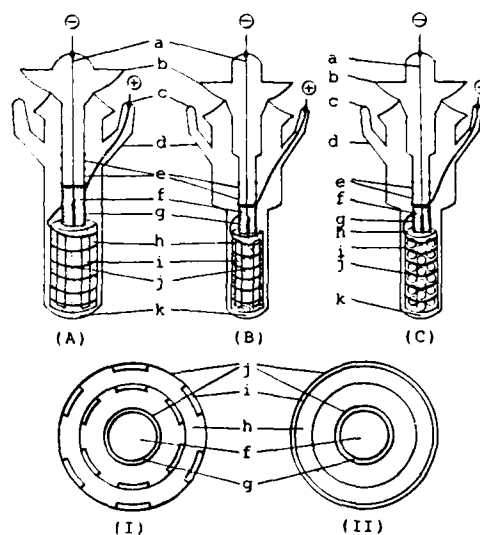


Figure 1 . Schematic Diagrams of Experimental Cells.
 (a) Tungsten Wire (b) Sodium Inlet (c) Positive Mix Inlet (d) Pyrex Glass (e) Sealing Glass (f) Sodium (g) Beta"-Alumina (h) Carbon Felt (i) Molybdenum Sheet (j) Tungsten Spiral

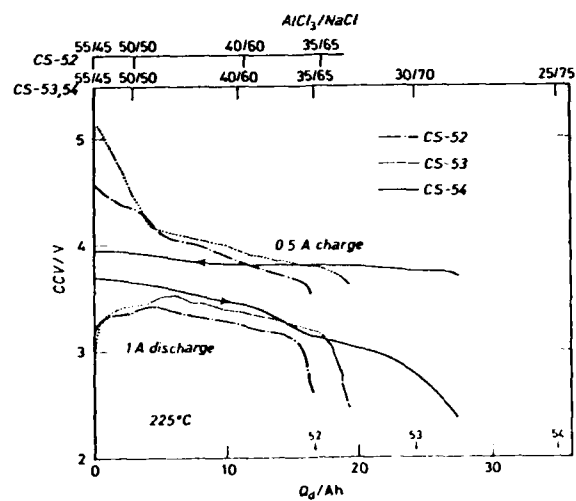


Figure 3. Charge-Discharge Curves of Three Na/Se(IV) Cells at 225°C.

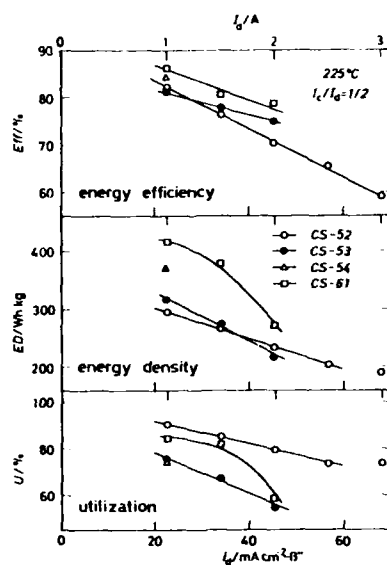


Figure 4. The Dependence of Cell Performance on Discharge Current Density for Na/Se(IV) Cells at 225°C.

Table 1. Specifications for Four Na/Se(IV) Cells

	AlCl ₃ /NaCl molar ratio		weight of active masses	theoretical capacity
	fully charged	fully discharged		
CS-52	55.30/44.70	35.04/64.96	175.0 g	17.32 Ah (98.94 Ah/kg)
CS-53	54.91/45.09	29.89/70.11	195.3 g	24.58 Ah (124.8 Ah/kg)
CS-54	54.45/45.55	24.98/75.02	224.5 g	35.04 Ah (156.1 Ah/kg)
CS-61	65.07/34.93	30.00/70.00	196.6 g	28.91 Ah (147.1 Ah/kg)

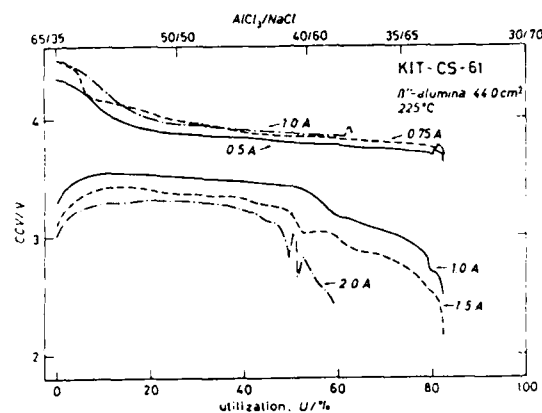


Figure 5. Charge-Discharge Curves of A High Energy Density Na/Se(IV) Cell at 225°C.

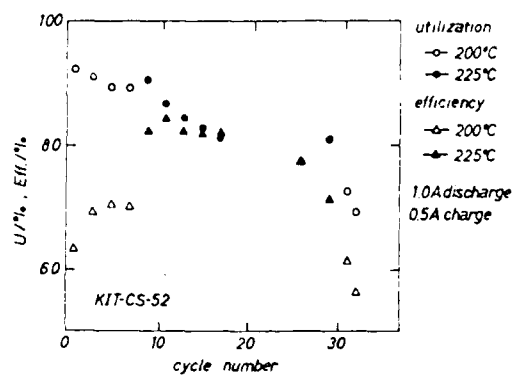


Figure 6. Change of Performance of A Na/Se(IV) Cell with Number of Cycles

ON THE TECHNOLOGICAL STATUS OF MOLTEN CARBONATE FUEL CELLS

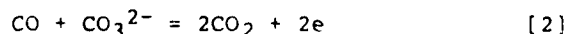
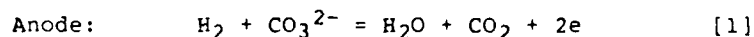
Nguyen Quang Minh
Garrett/AiResearch
2525 190th Street
Torrance, California 90509, USA

ABSTRACT

Molten carbonate fuel cells (MCFCs) are presently under development for electric utility power generation. Much progress has been made in the MCFC technology during the last ten years. This paper examines and summarizes the technological status of the MCFC. Emphasis is placed on discussion of technical issues such as cathode dissolution corrosion, electrode deformation, electrolyte loss, sulfur contamination, and internal reforming. A brief discussion of the importance of electrolyte basicity in MCFCs is also given.

INTRODUCTION

The molten carbonate fuel cell (MCFC) represents one of the most important applications of molten salts. The fuel cell employs molten carbonates as the electrolyte. Carbonate mixtures are the only electrolytes which are invariant with respect to the electrochemical combustion of hydrogen and carbon monoxide, thus providing the basis for the fuel cell. The overall reactions are as follows:



The state-of-the-art MCFC consists of a porous stabilized nickel anode (fuel electrode) and a porous lithium-doped nickel oxide cathode (oxidant electrode), separated by a lithium aluminate matrix filled with lithium and potassium carbonates (62-70 mol% Li_2CO_3) as the

electrolyte. The cell is operated at a temperature of about 925 K and at a pressure of 1 to 10 atm; the fuel gas is a humidified mixture of H_2 and CO , and the oxidant is a mixture of O_2 and CO_2 which may contain water vapor.

Present MCFC designs are based on a planar geometrical configuration. Practical electrical power generation is achieved by stacking a series of cells to build voltage. A bipolar plate carries electrons from the anode of one cell to the cathode of the next in electrical series. The essential components of a MCFC stack is shown in Fig. 1.

The MCFC operating temperature (about 925 K) is high enough to produce valuable waste heat. The waste heat can be used to supply heat for bottoming cycles and/or cogeneration purposes (process or space heat). In an MCFC power plant using natural gas fuel, the most important process heat use will be for the reforming of methane. For MCFCs, internal reforming of methane is possible (i.e., the waste heat is directly available within the fuel cell for the conversion of methane directly to hydrogen and carbon monoxide in a driven reforming reaction in the anode region of the fuel cell). The internal reforming capability of the MCFC offers higher system efficiencies.

The MCFC, following a very intensive development effort during the last ten years, may be approaching the threshold of commercialization. The MCFC market includes electric utility, cogeneration, and on-site applications. This paper examines and summarizes the technological status of the MCFC. A brief discussion of the importance of electrolyte basicity in MCFCs is also given.

TECHNOLOGICAL STATUS OF MOLTEN CARBONATE FUEL CELLS

Commercial MCFCs are expected to range in cell area from 0.37 to 1.5 m^2 (4 to 16 ft^2). The number of cells per stack is expected to range from 75 to 700, giving a total stack height range of 0.46 to 5.1 m (18 to 200 inches). An electrical generating plant will contain one or more of these stacks, each of which will have an output of 5 kW to 1 MW (1). Recent MCFC developments in the U.S. are focused on stack design and operation and development of a fundamental understanding of reactions, materials, kinetics, and processes in an operating fuel cell. Although there are as yet no stacks in operation of the size envisioned for commercialization, results on subscale stacks [20 cells with 930 cm^2 (1 ft^2)/cell] are very encouraging. A subscale stack was operated for 5000 h (1).

The average cell performance of the stack met prediction and duplicated the single cell data (Fig. 2) (2). Testing of an 0.74-m^2 (8-ft^2) short stack (20 cell) is in progress (2). Several major technical issues have been identified, and the status of each of these issues is discussed below.

* Cathode dissolution: The instability of NiO during cell operation is now considered one of the major technical difficulties facing MCFC development (3). Nickel oxide has a small degree of solubility in the carbonate electrolyte in the fuel cell cathode environment (about 10-15 ppm). However, the dissolved nickel ions diffuse, under a concentration gradient, from the cathode toward the anode. At some location between the two electrodes and under the influence of reducing conditions caused by the anode gas, the dissolved nickel precipitates as nickel metal. The precipitation of nickel creates a sink for the nickel ions, which facilitates further NiO dissolution. Thus, the dissolution of NiO can be a major life-limiting factor for the MCFC. The present industrial efforts attempt to prolong NiO life by employing low partial pressure of CO_2 and high- Li_2CO_3 electrolyte. Additives (e.g., MgO) to the carbonate electrolyte to lower NiO dissolution are also attempted. Although the lifetime of NiO can be extended under those conditions, it is not clear whether lowering the CO_2 partial pressure or changing other operating conditions will make the NiO cathode endure 40,000 operating hours required for commercial applications. Alternative cathode materials are being developed. Two materials, LiFeO_2 and Li_2MnO_3 , have been identified as potential MCFC cathode materials. These materials were extensively tested and meet the requirements of stability, low solubility, and nonmigration. Adequate conductivities under realistic cell conditions can be achieved by doping the materials (4,5). The emphasis has now shifted toward fabricating appropriate cathode microstructures with doped materials, then testing them in cells (5).

* Corrosion: Another important question being addressed in MCFC technology concerns resistance to corrosion of current collectors/bipolar plates. In MCFCs, the bipolar plates are coated with a thin film of molten carbonate electrolyte and in contact with the cathode and the oxidant gas on one side and with the anode and fuel gas on the other side. They are therefore susceptible to hot corrosion attack (6,7). Corrosion of bipolar plates causes decline in cell performance and can lead to cell failure by allowing direct reaction of oxidant and fuel. The 316 stainless steel (SS) specified in the past for bipolar plates in laboratory cells was found not to be suitable for full-scale cells which have a life goal of 40,000 h.

Severe attack of the bipolar plate made of 316 SS, especially the anode side of the plate, was frequently observed in cells operated for a few hundred to a few thousand hours (8). Nickel cladding for protecting the anode side of 316 SS was attempted (8-10). However, there was still significant amount of corrosion on the cathode side of the plate. Corrosion and cell tests with 310 SS and INCO 825 indicated that plates made of these materials had better corrosion resistance in the fuel cell environment. These materials, however, did not show sufficient corrosion resistance to meet endurance goals on the anode side. In current MCFC stack tests, plates made of 310 SS or INCO 825 are nickel-coated on the anode side for corrosion protection. At present, a satisfactory bipolar plate material has not yet been identified.

* Electrode deformation: In MCFCs, the anode and cathode structures should be dimensionally stable. Any compaction of the structures not only decreases the active surface area but also may cause loss of contact and high resistances between components. Compaction may also cause significant tolerance requirements for stack hardware design. The porous nickel anode sinters at the cell operating temperature and compresses somewhat as a result of the cell holding force. Nickel anodes have been stabilized by dispersing small amounts of certain oxides such as chromia and alumina in nickel. Stack tests verified that the anode compaction goal has been attained with this stabilization method (1). Metal-coated ceramic anodes with good compaction resistance are also being developed (1). Recently, with the advent of dimensionally stable anodes, the compaction of the NiO cathode has been observed. For example, the average compaction of NiO cathodes in one stack test was found to be approximately 0.09 mm (3.5 mils) per cell (cell thickness of about 2.54 mm or 100 mils) (11). This degree of compaction is believed to be unacceptable for stacks used in commercial applications. Recent efforts to improve cathode compaction resistance emphasize heat treating and oxidation (1).

* Electrolyte loss: Long-term stability of cell and stack performance is, to a large extent, dependent on limiting electrolyte loss by corrosion and volatilization. Corrosion loss is largely limited to the first 2,000 h of operation. Loss by volatilization is a slow but continuing process. These two losses are considered to be manageable (excess electrolyte is stored or added), at least up to 10,000 h. Another problem is electrolyte leakage through the wet seal. This leakage occurs because the ambient oxygen which surrounds the cell is reduced to form carbonate ions on the outer surface of the cell (Fig. 3)

(12). More carbonate ions are produced on the anode than on the cathode because the anode is at a lower potential. Some of the carbonate ions migrate and react at the anode. The remainder of the charge necessary for neutrality is transferred by the migration of alkali ions to the outer surface of the cell. The leaked electrolyte then migrates along the manifold gaskets to the top of the stack. Several engineering approaches to minimize electrolyte migration have been developed, and encouraging results have been obtained in subscale stack tests that operated over 5,000 h.

* Sulfur contamination: It is generally acknowledged that even ppm levels of sulfur may cause an unacceptable loss of cell voltage. Performance loss of a MCFC due to the presence of sulfur in the fuel and oxidant gases occurs primarily at the anode. The sensitivity of the nickel anode to hydrogen sulfide has been demonstrated in many studies and cell tests (13). The presence of sulfur dioxide in the oxidant (due to recycling of burned fuel to the cathode or in air) does not affect cathode polarization but affects anode performance, because sulfur dioxide in the oxidant will react to produce sulfate in the electrolyte and then be transported to the anode. In a cell, a concentration gradient of sulfate ions between cathode and anode is established, as hydrogen in the anode reduces sulfate to hydrogen sulfide. While there is a general agreement on the negative impact of hydrogen sulfide on fuel cell performance, the exact mechanism responsible for the performance loss is not clearly defined. Several possible mechanisms exist which may account for the decrease in cell performance: (a) Hydrogen sulfide can poison the hydrogen oxidation reaction by adsorbing on anode active sites and thereby blocking the desired molecules from adsorbing. (b) Adsorbed hydrogen sulfide can poison the water shift reaction, causing a hydrogen deficiency in the fuel cell, which in turn causes a drop in cell voltage (14). (c) Recently, it has been suggested that poisoning of the Ni anode is the result of electrochemical formation of a layer of nickel sulfide on the anode. The layer forms by reaction between the Ni electrode and dissolved sulfide ions in the electrolyte (15). Sulfur tolerant anode materials are being investigated.

* Internal reforming: It has been demonstrated that internal reforming in MCFCs is technically feasible (16). Internal reforming MCFCs can operate up to 5,000 h without performance decay. The performance of internal reforming cells is identical to that obtained with cells using simulated reformed fuels. However, the nickel reforming

catalyst used for internal reforming in MCFCs can be affected by one or another form of deactivation. To date, MgO-supported catalysts have demonstrated the best stability in the fuel cell (17). However, the catalyst slowly decays at longer times. The cause for the decay is physical blockage of catalyst active sites by the carbonate electrolyte. The electrolyte on the catalyst was found to be rich in potassium, indicating electrolyte transfer to the catalyst by vapor phase as well as creepage. Recent work on internal reforming emphasizes on developing a way to control electrolyte vapor transport and electrolyte creepage from the anode to the catalyst. It appears that finding a means to prevent both electrolyte vapor transport and electrolyte creepage for long periods of time is a major technical challenge.

IMPORTANCE OF ELECTROLYTE BASICITY IN MOLTEN CARBONATE FUEL CELLS

As discussed earlier, two of the critical issues in the development of MCFCs are cathode dissolution and bipolar plate corrosion. In cathode dissolution, the most important factor which determines the rate of NiO dissolution and transport (and, thus, the cathode lifetime) is the magnitude of the NiO solubility under fuel cell operating conditions. Therefore, knowledge of NiO solubility under various conditions is essential for evaluating NiO cathode endurance. In bipolar plate corrosion, accelerated corrosion of stainless steels in the anode gas atmosphere is due to oxide scale fluxing. The protective qualities of the scale is destroyed by the dissolution of the oxide in the carbonate electrolyte and precipitation of the oxide elsewhere as a non-protective porous mass. Thus, understanding the solubility of oxides in molten carbonates is important. In this respect, the electrolyte basicity plays an important role.

The solubility of an oxide depends on the basicity of the molten salt, and, in some cases, on oxygen partial pressure as well. The theory of the acid/base behavior of oxyanion salts is analogous to the Bronsted theory for aqueous solutions. In molten oxyanion salts, the oxide activity defines the basicity of the system. Thus, for a solvent such as $\text{Li}_2\text{CO}_3\text{-K}_2\text{CO}_3$ under a partial pressure of CO_2 , the basicity of the molten salt is given by the equilibrium



The basicity of the melt may be altered by varying

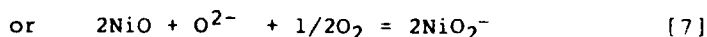
the partial pressure of CO_2 and by varying the mole fraction of the components.

The dissolution of oxides in molten carbonates can be classified as basic and acidic. In basic dissolution, the solubility increases as the basicity increases. In acidic dissolution, the solubility decreases as the basicity increases. Plotting the logarithm of the concentration of a dissolved oxide in the molten salt (assuming an ideally dilute behavior corresponding to a concentration-independent activity coefficient) versus the basicity of the melt yields two straight lines, one corresponding to the acidic dissolution and one corresponding to the basic dissolution, and a minimum solubility is observed (Fig. 4).

In the case of NiO cathodes, for example, NiO is an amphoteric oxide and can dissolve as a base or as an acid (18,19). In a relatively acidic melt, NiO dissolves by dissociation



In a basic melt, NiO reacts with oxide to produce one of two forms of nickelate ions



In the MCFC cathode environment, the melt is relatively acidic and the acidic dissolution is important.

For the acidic dissolution of NiO in molten carbonates, the solubility of the oxide decreases with increasing basicity of the melt. Therefore, making the MCFC cathode environment more basic is a means to lower the solubility of NiO and prolong the life of the NiO cathode. Basicity of the molten carbonate can be altered by (i) a change in the gas phase in equilibrium with the melt (e.g., lowering the partial pressure of CO_2 increases basicity), and (ii) a change in the carbonate melt composition (e.g., increasing the lithium content in $\text{Li}_2\text{CO}_3\text{-K}_2\text{CO}_3$ or adding basic oxides increases basicity).

The basicity of the molten carbonate can also play an important role in determining the properties of materials synthesized in the molten salt via its influence on the material stoichiometry. An example is the alternative cathode material LiFeO_2 . The electronic resistivity of LiFeO_2 synthesized in carbonates was found to be dependent on the partial pressure of CO_2 above the

carbonate melt (thus the basicity of the melt). Synthesis with partial pressure of $\text{CO}_2 < 0.005$ atm produced LiFeO_2 with lower resistivity and the resistivity decreased with decreasing CO_2 partial pressure (20). This observation can be explained as follows. The partial pressure of CO_2 will affect the basicity of the carbonate melt (the activity of lithium oxide) and, in that way, can affect the cation ratio (Li/Fe) of the lithium iron oxide synthesized in the melt. Low partial pressure of CO_2 enhances the activity of lithium oxide, which tends to result in a more lithium-rich compound, i.e., a LiFeO_2 compound with a Li/Fe ratio > 1 . Therefore, LiFeO_2 synthesized in more basic electrolyte is nonstoichiometric. As a result, a lower resistivity is observed.

REFERENCES

1. Morgantown Energy Technology Center, "Fuel Cells-Technology Status Report," DOE/METC-86/0241, 1985.
2. C. A. Reiser, C. R. Schroll, and M. J. Smith, 1986 Fuel Cell Seminar, p.140, Tucson, AZ, October 26-29, 1986.
3. N. Q. Minh, "Technological Status of Nickel Oxide Cathodes in Molten Carbonate Fuel Cells," submitted to Journal of Power Sources.
4. G. H. Kucera, N. Q. Minh, J. L. Smith, and F. C. Mrazek, 1985 Fuel Cell Seminar, p.158, Tucson, AZ, May 19-22, 1985.
5. J. L. Smith, G. H. Kucera, and N. Q. Minh, 1986 Fuel Cell seminar, p.163, Tucson, AZ, October 26-29, 1986.
6. P. Singh, in "Proceedings of the Symposia on Corrosion in Batteries and Fuel Cells and Corrosion in Solar Energy Systems," C. J. Johnson and S. L. Pohlman, eds., p.124, The Electrochemical Society, Pennington, NJ (1983).
7. D. A. Shores and P. Singh, in "Proceedings of the Symposium on Molten Carbonate Fuel Cell Technology," J. R. Selman and T. D. Claar, eds., p.271, The Electrochemical Society, Pennington, NJ (1984).
8. General Electric, "Development of Molten Carbonate Fuel Cell Power Plant," Final Report, DOE/ET/17019-20, March 1985.

9. International Fuel Cells, "Development of Molten Carbonate Fuel Cell Power Plant Technology," Quarterly Technical Progress Report No.21, October-December 1984, DOE/ET/15440-197.
10. Energy Research Corporation, "Development of Molten Carbonate Fuel Cell Technology," Technical Progress Report, October-December 1984, DOE/ET/11304-34.
11. International Fuel Cells, "Development of Molten Carbonate Fuel Cell Power Plant Technology," Quarterly Technical Progress Report No.22, January-March 1985, DOE/ET/15440-1944.
12. "Assessment of Research Needs for Advanced Fuel Cells," p.171, DOE/ER/30060-TI, November 1985.
13. S. W. Smith, H. R. Kunz, W. M. Vogel, and S. J. Szymanski, in "Proceedings of the Symposium on Molten Carbonate Fuel Cell Technology," J. R. Selman and T. D. Claar, eds., p.246, The Electrochemical Society, Pennington, NJ (1984).
14. R. J. Remick and G. L. Anderson, "Effects of H₂S on Molten Carbonate Fuel Cells. Topical Report: Literature Survey of Water-Gas Shift Reaction," DOE/MC/20212-1714, January 1985.
15. R. J. Remick, "Effects of H₂S on Molten Carbonate Fuel Cells," Progress Report for April 1-June 30, 1984, DOE/MC/20212-1739, March 1985.
16. M. Tarjany, L. Paetsch, R. Bernard, and H. Ghezeli-Ayagh, 1985 Fuel Cell Seminar, p.177, Tucson, AZ, May 19-22, 1985.
17. Energy Research Corporation, "Development of Molten Carbonate Fuel Cell Technology," Technical Progress Report, July-September 1984, DOE/ET/11304-33.
18. D. A. Shores, in "High Temperature Corrosion," p.493, National Association of Corrosion Engineers, Houston, TX (1983).
19. R. A. Rapp and K. S. Goto, in "Proceedings of the Second International Symposium on Molten Salts," p.159, The Electrochemical Society, Pennington, NJ (1981).

20. N. Q. Minh, G. H. Kucera, and J. L. Smith, in "Proceedings of the Fifth International Symposium on Molten Salts," M. L. Saboungi et al., eds., p.597, The Electrochemical Society, Pennington, NJ (1986).

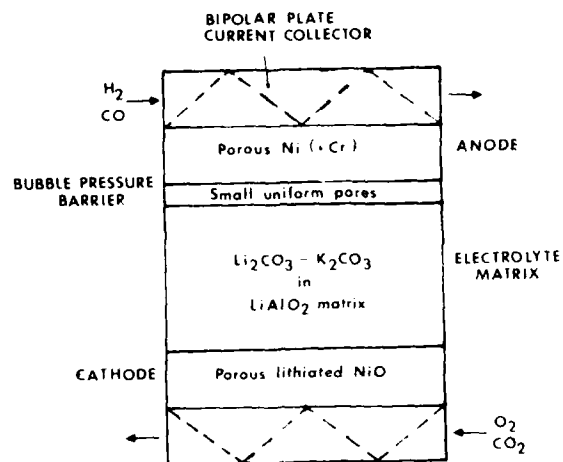


Fig. 1. Essential Components of a Molten Carbonate Fuel Cell Stack

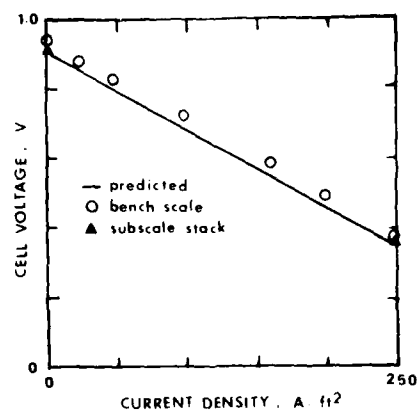


Fig. 2. Subscale Stack Performance (2)

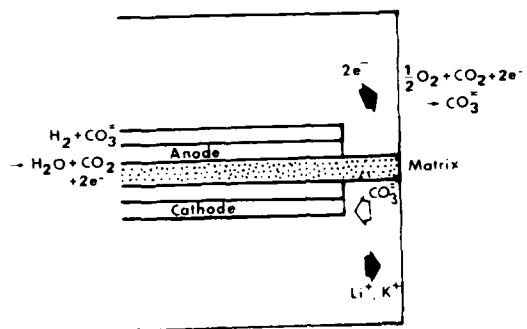


Fig. 3. Electrolyte Leakage through Wet Seal in a Bench-Scale Molten Carbonate Fuel Cell

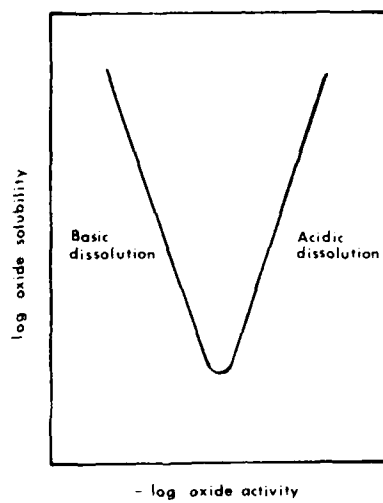


Fig. 4. Solubility vs. Oxide Activity

**INFLUENCE OF THE ACIDITY ON THE UNSTABLENESS AND
THE CORROSIVENESS AT HIGH TEMPERATURE OF MOLTEN
NITRATES AND NITRATE-NITRITE MIXTURES.
A DEMONSTRATIVE EXAMPLE SHOWING THE INTEREST OF
CONTROLLING THE ACIDITY IN MOLTEN SALTS.**

Bernard L. TREMILLON
Laboratoire d'Electrochimie Analytique et Appliquée
associé au C.N.R.S (UA 216)
Ecole Nationale Supérieure de Chimie de Paris
Université Pierre et Marie Curie
11 rue P. et M. C.Curie
75231 PARIS Cedex 05 - France

ABSTRACT

Research objectives which fit into the prospect of promoting the applications of molten nitrates are to reduce their thermic unstableness and define conditions which favor the passivation of metallic materials at their contact. Quantitative considerations about the decomposition reactions of the nitrate melts lead to establish that two essential conditions must be fulfilled in order to obtain an optimal stability allowing the utilization of these melts at temperature up to about 500-550°C : i) The addition of a certain percentage of nitrite ; ii) The control of the melt acidity (pO^{2-}) by means of a proper pO^{2-} buffer system (OH^-/H_2O). Concerning the corrosion of metallic materials, the acidity has also to be controlled, generally, in order to achieve the formation of oxidized layers (due to the strong oxidizing power of the nitrate anion) showing the best passivating properties. In the case of iron (and steel) considered in this study, the formation of ferrate $NaFeO_2$, which occurs in an intermediate pO^{2-} range corresponding again to the OH^-/H_2O buffer system, leads to a maximal passivation effect.

1. INTRODUCTION

It is likely that no other melt has been concerned by so many fundamental works as the alkaline nitrates, in spite of their small number of applications. The latter may be explained on one hand by the thermic unstableness of these melts and on the other hand by their corrosive power towards metals and alloys, related to the strong oxidizing character of the NO_3^- ion. Therefore, reducing the thermic unstableness and defining conditions which favor the passivation of metallic materials are research objectives which fit into the prospect of promoting the applications of melted nitrates.

In our laboratory, we were led to work towards these objectives some years ago, within the framework of a research to adjust the use of the so-called "HITEC" mixture (KNO_3 53%, NaNO_3 40%, NaNO_2 7% w/w) as a heat transfer liquid in the experimental solar power station "Themis" built by Electricité de France. As a matter of fact, the normal working of this power station supposed the possibility that the temperature of the melt rises to over 500°C , which required an optimisation of the stability conditions of the melted mixture. The corrosion effects on the iron alloy containers and tubing in contact with the 500 tons of molten salts at temperatures varying between about 250 and 500°C was at the same time an important matter of concern which justified a thorough study.

The work realized to reach these objectives consisted in making a serie of experimental determinations by electrochemical methods whose results, in combination with thermodynamical data, allowed to predict the reactions which may occur, using an analytical reasoning.

I shall here describe the principal results we obtained -- without insisting on technical aspects of the study which have already been described elsewhere [8,21] --, mainly with the purpose of pointing out the successive steps of the reasoning.

At this point, some general characteristics of molten nitrates must be redefined in order to make the whole description clear.

2. REACTIONS OF DECOMPOSITION

Because the anion NO_3^- can be considered theoretically as an oxobase (donor of O^{2-}), the first explanations of the behavior of the molten alkaline nitrates postulated the intervention of the following autodissociation system [1] :



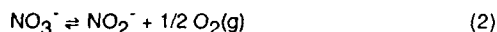
considering the nitronium cation NO_2^+ as the strongest oxoacid existing in solution in these media. But two facts came to invalide this assumption :

(i) The cation NO_2^+ (and nitrogen hemipentoxide N_2O_5 , originated by $\text{NO}_2^+ + \text{NO}_3^-$) is unstable and undergoes a decomposition if set in the conditions leading to its formation (acidificating the melt). As this decomposition produces nitrogen oxide and oxygen, it corresponds to a redox reaction which follows the dissociation of NO_3^- .

(ii) The anion O^{2-} cannot stay in a free state at an appreciable concentration (in NaNO_3 - KNO_3) because of the oxidizing power of the NO_3^- ion : peroxide ions O_2^{2-} and superoxide ions O_2^- (already observed in NaOH - KOH [2], are formed as well as nitrite ions NO_2^- (as the product of the reduction of NO_3^-) [3].

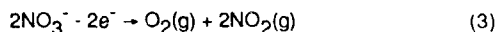
Hence, in order to specify the "oxoacidobasic" characteristics and especially the size of the acidobasicity range actually accessible in molten nitrates, it is convenient to start examining these chemical unstablenesses, related to the redox properties of the nitrate ion.

Independently of the above-mentioned decompositions, which correspond to acidity or basicity effects, the decomposition of the nitrate ion according to the following reaction (independant of the acidity) also occurs [4] :

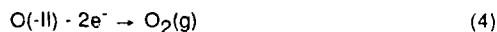


This redox reaction corresponds to both systems that fix the limits of the electrochemical stability of the solvent.

As a matter of fact the two limits are caused by oxidation and reduction of the NO_3^- ion. The reduction leads to the formation of nitrite NO_2^- , with the liberation of an oxide ion O^{2-} . The oxidation leads to the formation of oxygen (as the nitrogen of NO_3^- is already in its maximal oxidation state), the initial step being the liberation of the cation NO_2^+ that decomposes into NO_2 and oxygen. So, the whole electrochemical reaction is :



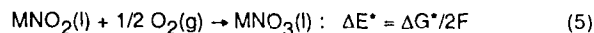
But the formation of NO_2 doesn't take place any longer if the melt is kept at a sufficient basicity level (by the presence of an oxobase) ; a simple release of oxygen is then observable, corresponding to the system :



In a strongly basic melt, the free O^{2-} ion becomes oxidizable to peroxide O_2^{2-} or superoxide O_2^- , before O_2 is formed (in NaNO_3 , KNO_3 and their mixtures).

Thermochemical calculations, completed by experimental results, allow to establish the **equilibrium potential-acidity diagram E-pO^{2-} that corresponds to the stability area** (from the thermodynamical point of view) limited by these different reactions. As an example, figure 1 presents this diagram, in the case of equimolar NaNO_3 - KNO_3 at 230°C and NaNO_3 at 470°C.

With respect to the straight line giving the variation of the equilibrium potential of the oxygen electrode (system $\text{O}(-\text{II})/\text{O}_2(\text{g})$), it is possible to place the line that represents the variation of the equilibrium potential of the system $\text{NO}_3^-/\text{NO}_2^-$, which has the same slope $2.3\text{RT}/2\text{F}$, by calculating the e.m.f. that corresponds to the reaction :



As it has been shown that the nitrate-nitrite mixtures behave ideally [5], the equilibrium potential difference between the systems $\text{O}(-\text{II})/\text{O}_2$ (1 atm) and $\text{NO}_3^-/\text{NO}_2^-$ (dissolved in NO_3^-) is then obtained from the simple relation :

$$\begin{aligned} \Delta\text{E} &= \Delta\text{E}^* + 2.3\text{RT}/2\text{F} \log \text{N}(\text{NO}_2^-) \\ &= \Delta\text{E}^* + 2.3\text{RT}/2\text{F} [\log m(\text{NO}_2^-) - 1.026] \end{aligned} \quad (6)$$

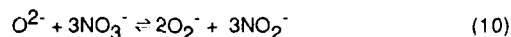
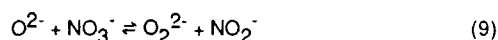
(N : molar fraction ; m : molality). Thus one predicts that the **thermodynamical stability range only corresponds to a very small potential interval** (only 120 mV at 470°C with $m(\text{NO}_2^-) = 1 \text{ mol.kg}^{-1}$) and that the molten nitrate cannot be free from nitrite : according to the calculation, the equilibrium concentration under

$P(O_2) = 0.2 \text{ atm}$ must be about $6 \cdot 10^{-2} \text{ mol.kg}^{-1}$ at 470°C (a value the experience appreciably confirms).

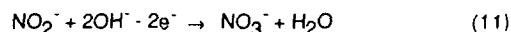
A similar calculation leads to the variation of the equilibrium potential corresponding to the system $\text{NO}_3^-/\text{NO}_2(\text{g})$ [i.e. $\text{NO}_3^- + \text{e}^- \rightleftharpoons \text{NO}_2(\text{g}) + \text{O}^{2-}$, (7)] as well as to the system $\text{NO}_3^-/\text{NO}(\text{g})$ [i.e. $\text{NO}_3^- + 3\text{e}^- \rightleftharpoons \text{NO}(\text{g}) + 2 \text{O}^{2-}$, (8)], for it is known that NO_2 is unstable (which is confirmed by the respective positions, in the E- pO^{2-} diagram, of the achieved straight lines : the reduction of NO_3^- into NO appears to be thermodynamically easier than the one into NO_2).

Then, to complete the stability diagram, it is possible to process experimental data from electrochemical studies :

(a) The unstableness of the free O^{2-} ion is demonstrated by the voltammogram (2) of figure 2 A, given by a diluted solution of Na_2O (in $\text{NaNO}_3\text{-KNO}_3$ at 230°C [3]) : in fact the solution contains a mixture of peroxide O_2^{2-} (oxidizable into O_2^- and further into O_2) and superoxide O_2^- (reducible into O_2^{2-} and oxidizable into O_2) that comes from the reactions :



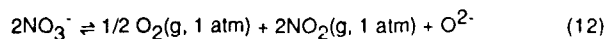
The voltammogram also shows the presence of NO_2^- through the appearance of an anodic wave that corresponds to the oxidation $\text{NO}_2^- - \text{e}^- \rightarrow \text{NO}_2$ (notice that, in the absence of a donor of O^{2-} , the oxidation of the nitrite can only occur by this reaction. But due to the presence of an oxobase this oxidation may produce again NO_3^- ions : see for example voltammogram (5) of figure 2 B, that corresponds to the oxidation reaction in presence of the oxobase OH^- :



This reaction occurs at a lower potential than the reaction $\text{NO}_2^- - \text{e}^- \rightarrow \text{NO}_2$, voltammogram (4)).

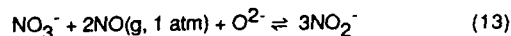
Owing to the determination (from voltammetric measurements) of values of standard potentials and equilibrium constants for the disproportionation reactions of superoxide and peroxide ions into oxide and oxygen, the E- pO^{2-} diagram can be completed for basic media as shown in figure 1.

(b) Further, to complete it on the acidic side, it is sufficient to obtain the coordinates of a point like P that corresponds to the chemical equilibrium :



Such a point is located on the straight line that gives the variation of the equilibrium potential of the system $\text{O}(-\text{II})/\text{O}_2(\text{g}, 1 \text{ atm})$ and consequently it is only necessary to measure its potential (potential of a platinum electrode in molten nitrate

under bubbling of a gaseous mixture $\text{NO}_2 + \text{O}_2$, as it has been done at about 230°C [6] (see figure 1 A). It is also possible to use the point P' (see figure 1 B) that corresponds to the chemical equilibrium :



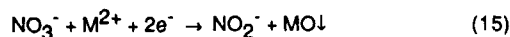
and whose pO^{2-} value has been experimentally measured with a stabilized zirconia membrane indicator electrode [8] (*).

Electrochemical decomposition

From the point of view of electrochemical decomposition, some important observations have to be made.

1) The oxidation of $\text{O}(-\text{II})$ into oxygen and that of NO_2^- into NO_3^- depend, as far as the potentials at which they occur are concerned, on the presence of an oxobase and on its strength (O^{2-} donor power). On the opposite, the reduction of NO_3^- into NO_2^- depends on the presence of an oxoacid (acceptor of O^{2-}) and on its strength. As a matter of fact, such an oxoacid as H_2O fixes the O^{2-} ion liberated by the reduction of NO_3^- and this reduction turns easier : thus on the voltammogram (curve (6), figure 2 B), a cathodic wave whose current is limited by the diffusion of H_2O (**) appears before the reduction of the pure nitrate. The same thing happens in presence of the oxoacid CO_2 , and the difference in half-wave potentials $E_{1/2}$, with respect to the diffusion wave of H_2O , corresponds to a greater oxoacidic power for CO_2 than for water (curve (7), figure 2 B).

Other oxoacids act in the same way : they are metallic cations. With the exception of Ag^+ which is cathodically reduced into metal [11], most of the metallic ions lead to a cathodic reduction wave which has been shown (for example for Ca^{2+} and Ba^{2+} [12], as well as Cd^{2+} , In^{3+} , Pb^{2+} , Tl^+ , Zn^{2+} [13]) not to correspond to the formation of a metal but to the reduction of NO_3^- into NO_2^- in the presence of the oxoacid (acceptor of O^{2-}) M^{2+} :



(*) At $230\text{--}250^\circ\text{C}$ the decomposition of NO_2 into $\text{NO} + 1/2 \text{O}_2$ is slow enough for equilibrium (12) to be realized. This no longer occurs at 470°C , in that case the possible equilibrium is : $2\text{NO}_3^- \rightleftharpoons 3/2 \text{O}_2(\text{g}) + 2\text{NO}(\text{g}) + \text{O}^{2-}$, (14).

The use of the stabilized zirconia membrane pO^{2-} -indicator electrode (ZME) in molten nitrate has been described in previous papers [9].

(**) Though the limiting current corresponds to the diffusion of water, here this one plays the role of an oxoacid and not that of a reducible substance, because no production of hydrogen is observed [10].

This interpretation is consistent in so far as only cations of high oxidizing power (Ag^+ , Hg^{2+} ...) can lead to metal formation, for the reduction of a metallic ion can only be observed if it is easier than that of the anion NO_3^- .

2) In a mixture of pure molten nitrates, the potential range between the two limits due to reduction and oxidation of NO_3^- (non-electroactivity range of the pure solvent) has an extent of over 2.5 Volts at 230°C , which the E-pO^{2-} diagram can explain. As the oxidation produces oxygen and NO_2 , it takes place in medium conditions, near the electrode, that correspond to point P. On the contrary, the reduction produces oxygen and NO_2 , it takes place in medium conditions, near the electrode, that correspond to point P. On the contrary, the reduction produces nitrite and O_2^{2-} ions (and O_2^{2-} or O_2^-) and thus occurs in the conditions of the strongest basic medium next to the cathode. According to the E-pO^{2-} diagram, this leads to a difference of over 2 V between the anodic and cathodic potentials (plus the overpotentials related to the kinetics of both electrochemical processes).

On the other hand, if in the molten nitrate there is a pO^{2-} buffer system that forces anode and cathode to work in the same medium conditions, the non-electroactivity range of the NO_3^- ions reduces to the potential difference between the two (parallel) lines limiting the stability diagram (lines which correspond to the formation of oxygen and nitrite), that is (including overpotentials) less than 1 Volt. This change appears on figure 2 C where curve (8) corresponds to the presence of the buffer system $\text{H}_2\text{O}/\text{OH}^-$ (in this case, the formation of NO_2 at the anode and that of O_2^{2-} or O_2^- at the cathode are suppressed).

3. CONDITIONS FOR OPTIMAL STABILITY

Starting from the foregoing thermodynamic considerations, it is now possible to discuss the optimal stability conditions of molten nitrates.

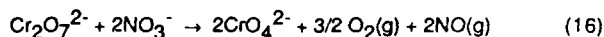
The previously established E-pO^{2-} diagrams point out that the pO^{2-} scale in molten nitrates is limited at both ends by the intervention of the described decomposition reactions. Quantitative data concerning these reactions allow to define these limits precisely. Thus, in the case of the equimolar mixture $\text{NaNO}_3\text{-KNO}_3$ at 230°C in equilibrium with air [$\text{P}(\text{O}_2) = 0.2 \text{ atm}$], if one wishes to limit the formation, on one side, of O_2^- at a maximal molality of $10^{-2} \text{ mol.kg}^{-1}$ and, on the other side, of NO_2 at a maximal pressure of 10^{-2} atm , it is foreseen that pO^{2-} must remain in the range :

$$6.6 < \text{pO}^{2-} < 34$$

(the maximal value is even lowered to 27 if the formation of NO instead of NO_2 is contemplated, with the same partial pressure limit of 10^{-2} atm). At 470°C , the data connected with the diagram in figure 2 B point out that the limits are only about 2.5 and 12.

In fact, adding a strong oxoacid which has a tendency to rise the pO^{2-} over the

maximal value defined in this way produces decomposition of the nitrate into NO_2 or NO . This happens for example with dichromate (at 470°C) [9] :

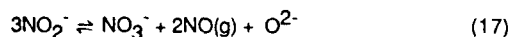


Therefore, two actions favor the stability of molten nitrate :

1') The addition of a certain proportion of nitrite, which by shift of equilibrium (2) lowers the equilibrium oxygen pressure and thus slows down the progressive thermic decomposition by oxygen release.

From the values of equilibrium constants given in ref. [14], in the case of the melt $\text{NaNO}_3 + \text{NaNO}_2$ 1 mol.kg^{-1} (nitrite proportion very close to that of the HITEC mixture) the equilibrium oxygen pressure remains under 10^{-2} atm until a temperature of about 500°C is reached (with the equimolar mixture $\text{NaNO}_3\text{-NaNO}_2$, this temperature would rise up to 630°C).

Through lowering of the redox potential of the melt, the presence of nitrite also reduces the formation of O_2^{2-} and O_2^- and permits to reach the most oxobasic media (lowest values of pO_2^-). Per contra, the upper limit of pO_2^- is lowered by the intervention, at high pO_2^- , of the disproportionation of NO_2^- according to the reaction :



In the case of the melt $\text{NaNO}_3 + \text{NaNO}_2$ 1 mol.kg^{-1} , figure 3 A (curve 1) shows how this upper limit varies with the temperature (according to ref. [14]) so that the partial pressure of NO should remain under 10^{-2} atm.

2') By means of a proper pO_2^- buffer system, pO_2^- is kept in the stability range previously defined. As it is practically very difficult to avoid the presence of moisture, the oxoacid/oxobase system which one can most naturally think about is the system $\text{H}_2\text{O}/\text{OH}^-$. The measured values [14] of the constant (K_1) of the equilibrium $2\text{OH}^- \rightleftharpoons \text{H}_2\text{O}(\text{g}) + \text{O}^{2-}$ show that this system is quite convenient for the required buffer effect : according to the values of $P(\text{H}_2\text{O})$ and $m(\text{OH}^-)$, the value of pO_2^- fixed by the buffer varies within 2 units around $\text{p}K_1$, which varies according to the temperature from 4.4 at 310°C to 2.3 at 500°C . Curves 3, 3', 3" in figure 3 A show that the addition of 1% (w/w) soda to the melt $\text{NaNO}_3 + \text{NaNO}_2$ 1 mol.kg^{-1} is convenient to avoid an appreciable decomposition of the melt up to $T = 500^\circ\text{C}$, taking in account a partial pressure of steam above 10^{-2} atm.

In the absence of OH^- , the single oxoacid H_2O imposes high pO_2^- values that produce, when temperature rises, the decomposition of NO_2^- with release of nitrogen oxide vapors, as indicated by curve 4 of figure 3 A.

Concluding, to stabilize nitrate melts in order to heat them to temperatures as high as possible (about $500\text{-}550^\circ\text{C}$), it is necessary, on

one hand to add a certain proportion of nitrite (*), and on the other hand to add a small proportion of soda (about 1% w/w) and to keep a sufficient percentage of moisture so as to realize the buffering of pO_2 at a convenient level.

4. CORROSIVE ACTION. THE CASE OF IRON

It has been shown experimentally that the strong oxidant nitrate ion attacks metals, with the exception of the noblest among them (Ag, Au, Hg, Pt). Generally, an insoluble oxide forms in the neutral melt (the end of the attack on the metal depends on the passivating power of this oxide).

It is easy to predict this property by means of the $E-pO_2$ diagrams, as on these diagrams the position of the variations of the equilibrium potentials E_{eq} of the systems $M(s)/metal\ oxide(s)$ can be established by thermochemical calculations which connect this position to that of the straight line corresponding to the system $O(-II)/O_2$. Thus, for example, at 230°C, the system $Ni(s)/NiO(s)$ gives an E_{eq} variation located 0.1 Volt under the straight line corresponding to the reduction system of NO_3^- into NO_2^- ($1\ mol.kg^{-1}$), which implicates the oxidizability of nickel by NO_3^- .

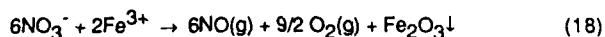
This oxidizability of metals corresponds to the previously mentioned irreducibility of metallic cations in nitrate melts.

This does happen in the case of iron which will be detailed now.

The attack of iron and its alloys by nitrate melts and nitrate + nitrite mixtures, with the formation of a superficial iron oxide layer, has already been observed and pointed out several times [15-18]. Generally the formation of Fe_2O_3 (hematite $\alpha-Fe_2O_3$) is considered; but other compounds may also play a role, according to the acidobasicity level of the melt, especially the ferrate FeO_4^{2-} whose formation has already been demonstrated for other melts (hydroxides [19], alkali chlorides [20]). Hence an experimental study proved to be necessary to clear up the nature of the (stable) oxidation products of iron in molten nitrates as a function of pO_2 . This study, quite recently published [21], led to the following main results.

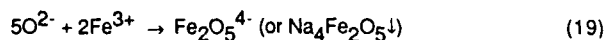
It has been observed that the addition of ferric nitrate to the neutral melt leads to the precipitation of Fe_2O_3 [22,23], which can be identified by X-ray diffraction. Besides, the simultaneous apparition of nitrogen oxide induces to assign the formation of Fe_2O_3 to the decomposition of the nitrate caused by the oxoacidic character of the Fe^{3+} ion:

(*) Diagram 3 B points out that in order to keep both partial pressures of the gaseous decomposition products O_2 and NO smaller than $10^{-2} atm$ it is necessary to choose a mixture of optimal composition close to $NaNO_3 + NaNO_2\ 2.5\ mol.\ kg^{-1}$ (about 15% w/w) to be able to reach the maximal temperature of 550°C, buffering pO_2 at a lower value than 1.5. A mixture containing more nitrite involves a decomposition of the latter at lower temperature.



On the other hand, the addition of ferric nitrate to a melt which has been made basic by a previous addition of OH^- (and dissociation $2\text{OH}^- \rightarrow \text{O}^{2-} + \text{H}_2\text{O}$ through bubbling of dry nitrogen) gives a reaction between the O^{2-} and Fe^{3+} ions without the decomposition of NO_3^- (except after the total consumption of the O^{2-} ions). This reaction has been studied quantitatively realizing the titration of O^{2-} through progressive addition of Fe^{3+} and following the variations of pO^{2-} during the titration with a ZME. Typical curves are represented in figure 4.

One can observe on these curves that a steep rise in pO^{2-} occurs, which corresponds to an end point $\alpha_1 = 0.4$. The reaction that corresponds to this value is :



This reaction occurs during the first step of the titration, between $\alpha = 0$ and $\alpha = \alpha_1$.

Notice that, if the decomposition (18) occurred before the consumption of O^{2-} ions and the latter combined further with the Fe_2O_3 formed, the end point would correspond, for the same compound $\text{Fe}_2\text{O}_5^{4-}$, to the value $\alpha = 1$, very far from the observed one.

In the second place, pO^{2-} remains invariable from $\alpha_2 = 0.5$ on. This invariance must correspond to an equilibrium between two precipitated forms of iron (III) : α - Fe_2O_3 , which appears (by decomposition of NO_3^-) at the end of the reaction due to the initial free O^{2-} , and a form of scarcely soluble ferrate obtained from the reaction of Fe^{3+} on $\text{Fe}_2\text{O}_5^{4-}$. Identified by X-ray diffraction, this ferrate is NaFeO_2 (allotropic form β , although the stable form at the temperatures of the experiments is the α one ; but it has been shown previously that at $T > 300^\circ\text{C}$ the reaction between Fe_2O_3 and NaOH gives the β form whose allotropic transformation $\beta \rightarrow \alpha$ is very slow [24]). It can be deduced that, in the range [$\alpha_1 = 0.4$; $\alpha_2 = 0.5$], the following reaction must occur :



The value $\alpha_2 = 0.5$ corresponds indeed to the end point of the global reaction :



As a matter of fact, the mathematical analysis of the variation of pO^{2-} in the interval [α_1 ; α_2] induces to admit that both the identified ferrates have non negligible solubilities whose orders of magnitude, in the range of temperature 420 - 520°C , are 0.02 mol.kg^{-1} for $\text{Na}_4\text{Fe}_2\text{O}_5$ and 0.03 mol.kg^{-1} for NaFeO_2 [21].

Thus it appears possible to form three compounds of iron (III) by a contact with

molten nitrate, each being stable in a different acidity range : Fe_2O_3 in an acidic melt, $\text{Na}_4\text{Fe}_2\text{O}_5$ in a strongly basic one, NaFeO_2 at middle basicity. The pO^{2-} values corresponding to the successive equilibria between two solid forms ($\text{Fe}_2\text{O}_3/\text{NaFeO}_2$ and $\text{NaFeO}_2/\text{Na}_4\text{Fe}_2\text{O}_5$) which have been deduced from this experimental study, in combination with the standard potential values of the redox systems formed by iron and its solid oxides, calculated with respect to the system of oxygen by means of the values of the Gibbs energies of formation given in the literature [25], allow to establish the E- pO^{2-} diagram of iron, shown on figure 5. Through the superposition of the variations of the potentials imposed by the systems of the melt ($\text{NO}_3^-/\text{NO}_2^-$ or $\text{NO}_3^-/\text{NO(g)}$), according to the pO^{2-} range), thus it is confirmed that the only stable species of iron in contact with molten nitrates can be those of iron(III).

But from the point of view of the corrosion of the metal, besides the existence of insoluble oxidation products forming a well-adhesive layer at the surface of the metal, the important point is the passivating power of this layer which fixes the velocity of corrosion. As it is possible to postulate that the part of the oxidized layer which is in contact with the melt is made out of the compound in equilibrium with the latter, whose nature depends on the acidity, and as a priori the passivating power of different insoluble compounds must be different, one can expect that the velocity of corrosion varies with the acidity of the melt. Hence, for the applications, it is convenient to fix the acidity (by means of a proper pO^{2-} buffer system, as in the case of the stabilization of the melt) at a level that corresponds to the formation of the oxidized compound which has the greatest passivating power. The results of the experimental works of EL HOSARY et al [15] and SPITERI [18] agree with this hypothesis : they show that the corrosion velocity is the lowest in a moderately basic medium and that in these conditions sodium ferrate NaFeO_2 forms as the corrosion product of iron. Our quite recent electrochemical study with impedance measurements, described by G. PICARD in another paper presented at this meeting, corroborates this conclusion precisising the attack mechanism. It appeared that the layers formed in the conditions of acidity corresponding to the stability area of NaFeO_2 (that is pO^{2-} about 4.5 to 5 at 420°C) present the greatest resistance to charge transfer, which allows to assign the lowest porosity and further the lowest corrosion velocities to this compound.

Hence, in conclusion, the best protection layer of iron (and in all probability of its alloys) is obtained fixing the pO^{2-} of the melt, for which the use of the buffer system $\text{OH}^-/\text{H}_2\text{O}$ is again the easiest way. The positionning of the stability area of $\text{NaFeO}_2(\text{s})$ on the diagram in figure 3 A shows that, in the case of the melt $\text{NaNO}_3 + \text{NaNO}_2$ 1 mol.kg $^{-1}$, the choice of the conditions $m(\text{OH}^-) = 0.06$ mol.kg $^{-1}$ (that is 0.25% of NaOH w/w) and $P(\text{H}_2\text{O}) = 0.1$ atm would be consistant with the seek for both an optimal stabilization effect of the melt and the best protection of the steel elements in contact with the melt.

Note. Experimentally, it has been possible to put in evidence a nitruration of the steels in contact with a nitrate melt. As a matter of fact the formation of compounds like Fe_4N may be originated by the presence of nitrogen oxide (NO) coming from the decomposition of NO_2^- or from the reduction of NO_3^- (in a very acidic medium), or from that of NO_2^- .

Yet a thermodynamical diagram, $\log P(\text{O}_2)/\log P(\text{NO})$, in which the stability areas of the different iron oxides and nitrides, as well as the area corresponding to the molten mixtures $\text{NaNO}_3\text{-NaNO}_2$ could be represented (figure 6), shows that no nitride may have a stable existence in contact with these mixtures. Hence it appears that the effective formation of such a compound must be interpreted putting forward the diffusion of nitrogen oxide into the lower layers of the oxidized film, next to the metal, where a tiny partial pressure of oxygen holds.

5. CONCLUSION

To conclude, at the end of this talk, I think I showed the importance of controlling the acidity (or basicity) level of a melt to achieve the optimal conditions of use of this medium (for the same reason that it is important to control the pH when working on aqueous solutions). This appears to be quite important in the case of molten nitrates at relatively high temperature because of the decomposition reactions that they undergo, whose effects nevertheless can be minimized by a sensible control of the pO_2 with the buffer system $\text{OH}^-/\text{H}_2\text{O}$.

REFERENCES

- [1] F.R. Duke et al, J. Phys. Chem., **62**, 417 (1958) ; J. Am. Chem. Soc., **80**, 5061 (1958) ; Anal. Chem., **31**, 1233 (1959) ; J. Am. Chem. Soc., **81**, 6378 (1959).
- [2] J. Goret and B. Trémillon, Bull. Soc. Chim. Fr., 67 (1966).
- [3] P.G. Zambonin and J. Jordan, J. Am. Chem. Soc., **89**, 6365 (1967) ; **91**, 2225 (1969) ; P.G. Zambonin, J. Electroanal. Chem., **24**, 28, 365 (1970) ; **33**, 248 (1971) ; **35**, 251 (1972).
- [4] R.N. Kust and J.D. Burke, Inorg. Nucl. Chem. Lett., **6**, 335 (1970).
- [5] E. Freeman, J. Phys. Chem., **60**, 1487 (1956).
- [6] L.G. Boxall and K.E. Johnson, J. Electrochem. Soc., **118**, 885 (1971).
- [7] A. De Haan and H. Van Der Porten, Bull. Soc. Chim. Fr., 2894 (1973).
- [8] G. Picard, T. Flament and B. Trémillon, J. Electrochem. Soc., **132**, 863 (1985).
- [9] B. Trémillon and G. Picard, in "Proceedings of the 1st International Symposium on Molten Salt Chemistry and Technology", Kyoto, Japan, April 1983, The Electrochemical Society of Japan, p. 93 (1983).
- [10] E. Desimoni et al, J. Electroanal. Chem., **84**, 323 (1977).
- [11] M.H. Miles et al, J. Electrochem. Soc., **131**, 2075 (1984).
- [12] S. Sternberg and T. Visan, Electrochim. Acta, **26**, 75 (1981).

- [13] M.H. Miles et al, *Electrochim. Acta*, **32**, 247 (1987) ; *J. Electrochem. Soc.*, **134**, 614 (1987).
- [14] G. Picard, T. Flament and B. Trémillon, in "Proceedings of the 1st International Symposium on Molten Salt Chemistry and Technology" , Kyoto, Japan, April 1983, The Electrochemical Society of Japan, p. 85 (1983) ; in "Molten Salts", M. Blander et al ed., The Electrochemical Society Softbound Proceedings Series, Pennington, NJ, p. 649 (1984) ; *J. Electrochem. Soc.*, **132**, 863 (1985).
- [15] A.A. El Hosary et al, *Br. Corros. J.*, **11**, 44, 163 (1976).
- [16] H.V. Venkasetty and D.J. Saathoff, in "Molten Salts", J.P. Pemsler et al ed., The Electrochemical Society Softbound Proceedings Series, Princeton, NJ, p. 329 (1976).
- [17] T. Notoya and R. Midorikawa, *Denki Kagaku*, **39**, 930 (1971).
- [18] P. Spiteri, EDF report D 554 MAT/T 40 (1984).
- [19] R.G. Doisneau and B. Trémillon, *Bull. Soc. Chim. Fr.*, 1419 (1976).
- [20] G. Picard, F. Séon and B. Trémillon, *J. Electrochem. Soc.*, **129**, 1450 (1982).
- [21] G. Picard, H. Lefèbvre and B. Trémillon, *J. Electrochem. Soc.*, **134**, 52 (1987).
- [22] D.H. Kerridge and A.Y. Khudhari, *J. Inorg. Nucl. Chem.*, **37**, 1893 (1975).
- [23] G. Tridot et al, *Compt. Rend. Acad. Sci. Paris*, **270 C**, 204 (1970).
- [24] R. Collongues and J. Théry, *Bull. Soc. Chim. Fr.*, 1141 (1959).
- [25] I. Barin, O. Knacke and O. Kubaschewski, "Thermochemical Properties of Inorganic Substances", Springer Verlag, Berlin-Heidelberg - New York (1973).

Table I. Constants K of chemical equilibria

Equilibrium	Mass action law expression	$\text{p}K = A + B/1000/T$	
		A	B
$2 \text{OH}^- = \text{H}_2\text{O(g)} + \text{O}^{2-}$	$K = \text{PH}_2\text{O(m)} \cdot \text{m(OH)}^{-1}$	-4.80	5.48
$3\text{NO}_2^- = \text{NO}_3^- + 2\text{NO(g)} + \text{O}^{2-}$	$K = \text{PNO}_3\text{(m)} \cdot \text{m(NO}_2\text{)}^{-3} \cdot \text{m(NO)}^{-2}$	-15.8	15.75
$\text{NO}_3^- = \text{NO}_2^- + \frac{1}{2} \text{O}_2\text{(g)}$	$K = \text{PO}_2 \cdot \text{NINO}_2 \cdot \text{m(NO}_2\text{)}^{-1} \cdot \text{m(NO)}^{-1/2}$	-5.47	5.88
$2\text{NO}_2^- = 2\text{NO(g)} + \frac{1}{2} \text{O}_2\text{(g)} + \text{O}^{2-}$	$K = \text{PO}_2 \cdot \text{PINO}_2 \cdot \text{m(NO}_2\text{)}^{-2} \cdot \text{m(NO)}^{-1}$	-21.4	21.6
$2\text{NO}_2^- = 2\text{NO(g)} + 3/2 \text{O}_2\text{(g)} + \text{O}^{2-}$	$K = \text{PINO}_2 \cdot \text{PINO}_2 \cdot \text{PINO}_2 \cdot \text{m(NO}_2\text{)}^{-3}$	-32.3	33.4
$\text{NO(g)} + \frac{1}{2} \text{O}_2\text{(g)} = \text{NO}_2\text{(g)}$	$K = \text{PINO}_2 \cdot \text{PINO}_2 \cdot \text{PINO}_2 \cdot \text{m(NO)}^{-1/2}$	3.99	-3.06
$2\text{NO}_2^- + \frac{1}{2} \text{O}_2\text{(g)} = \text{NO}_3\text{(g)} + \text{O}^{2-}$	$K = \text{PINO}_2 \cdot \text{m(O}^{2-}\text{)} \cdot \text{PINO}_2 \cdot \text{m(NO}_2\text{)}^{-2}$	-13.4	15.5
$2\text{NO}_2^- + \text{NO}_2\text{(g)} + \frac{1}{2} \text{O}_2\text{(g)} + \text{O}^{2-}$	$K = \text{m(O}^{2-}\text{)} \cdot \text{PINO}_2 \cdot \text{PINO}_2 \cdot \text{m(NO}_2\text{)}^{-1}$	-24.3	27.3
$3\text{NO}_2\text{(g)} + \text{O}^{2-} = 2\text{NO}_3^- + \text{NO(g)}$	$K = \text{NINO}_2 \cdot \text{PINO}_2 \cdot \text{PINO}_2 \cdot \text{m(O}^{2-}\text{)}^{-1}$	20.3	-24.2

Table II. Redox equilibria and standard potentials E° ($\lambda = 2.3RT/F$)

Electrochemical system	Equilibrium potential	$E^\circ = A + B \cdot 10^{-3}/T$	
		A	B
$\text{NO}_2^- + 2e^- = \text{NO}_2^- + \text{O}^{2-}$	$E = E^\circ + \frac{\lambda}{2} \log \frac{\text{NINO}_2^-}{\text{NINO}_2^-} + \frac{\lambda}{2} \text{pO}^{2-}$	-1.317	0.50
$\text{NO}_2^- + e^- = \text{NO(g)} + \text{O}^{2-}$	$E = E^\circ + \lambda \log \frac{\text{NINO}_2^-}{\text{PINO}_2} + \lambda \text{pO}^{2-}$	-2.887	2.08
$\text{NO}_2^- + 3e^- = \text{NO(g)} + 2 \text{O}^{2-}$	$E = E^\circ + \frac{\lambda}{3} \log \frac{\text{NINO}_2^-}{\text{PINO}_2} + \frac{2\lambda}{3} \text{pO}^{2-}$	-1.840	1.03
$\text{O}_2\text{(g)} + 4e^- = 2 \text{O}^{2-}$	$E = E^\circ + \frac{\lambda}{4} \log \text{PIO}_2 + \frac{\lambda}{2} \text{pO}^{2-}$	-0.731	-0.045
$\text{NO}_2^- + e^- = \text{NO}_2\text{(g)} + \text{O}^{2-}$	$E = E^\circ + \lambda \log \frac{\text{NINO}_2^-}{\text{PINO}_2} + \lambda \text{pO}^{2-}$	-3.453	2.38
$\text{NO}_2\text{(g)} + 2e^- = \text{NO(g)} + \text{O}^{2-}$	$E = E^\circ + \frac{\lambda}{2} \log \frac{\text{PINO}_2}{\text{NINO}_2} + \frac{\lambda}{2} \text{pO}^{2-}$	-1.036	0.353

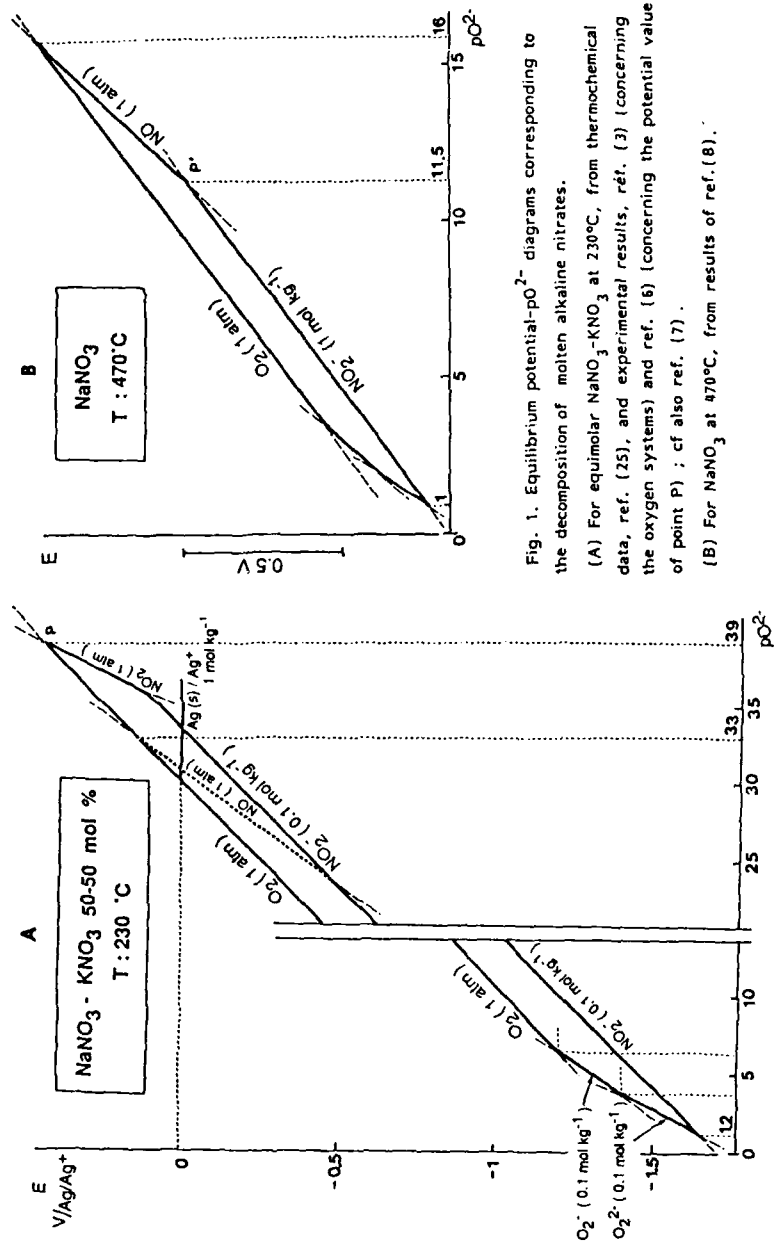


Fig. 1. Equilibrium potential- $p\text{O}_2$ diagrams corresponding to the decomposition of molten alkaline nitrates.
 (A) For equimolar NaNO_3 - KNO_3 at 230°C , from thermochemical data, ref. (25), and experimental results, ref. (3) (concerning the oxygen systems) and ref. (6) (concerning the potential value of point P); cf also ref. (7).
 (B) For NaNO_3 at 470°C , from results of ref. (8).

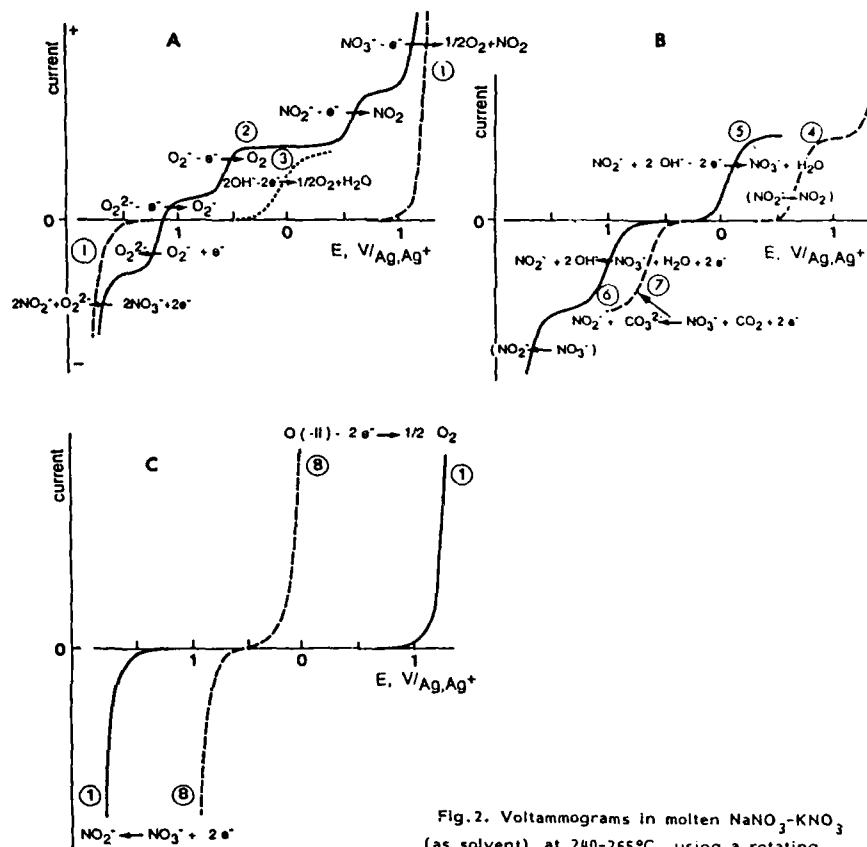


Fig.2. Voltammograms in molten NaNO₃-KNO₃ (as solvent) at 240-265°C, using a rotating platinum microelectrode.

- (1) pure solvent ;
- (2) addition of Na₂O 1 mmole/kg ;
- (3) oxidation of OH⁻ ions ;
- (4) oxidation of NO₂⁻ in the pure solvent ;
- (5) oxidation of NO₂⁻ in the presence of OH⁻ ;
- (6) reduction of NO₃⁻ in the presence of H₂O ;
- (7) reduction of NO₃⁻ in the presence of CO₂ (1 atm) ;
- (8) oxidation and reduction in the presence of H₂O/OH⁻ buffer.

[from ref.(3) and (10)]

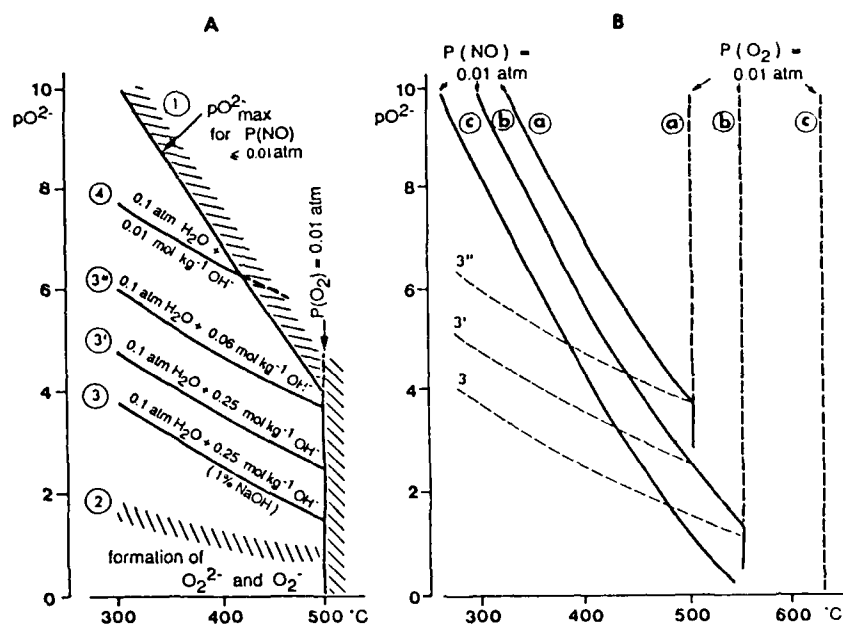


Fig. 3. Diagrams showing the variation of the values of pO_2^- which correspond to different limiting or buffering conditions, in molten $NaNO_3 + NaNO_2$ (under an inert atmosphere : $P(O_2) < 0.01$ atm), as a function of temperature.

A - $NaNO_3 + 1 \text{ mol kg}^{-1} NaNO_2$

B - a - $NaNO_3 + 1 \text{ mol kg}^{-1} NaNO_2$

b - $NaNO_3 + 2.5 \text{ mol kg}^{-1} NaNO_2$

c - $NaNO_3 - NaNO_2$ 50-50 mol %

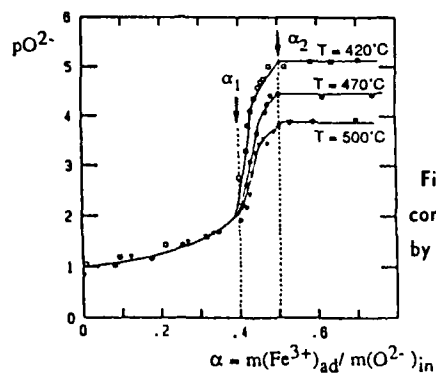


Fig. 4. Titration curves of sodium oxide (initial concentration : 0.21 mol kg^{-1} , under N_2) by iron(III) nitrate, in $NaNO_3 - NaNO_2$ (99 - 1)

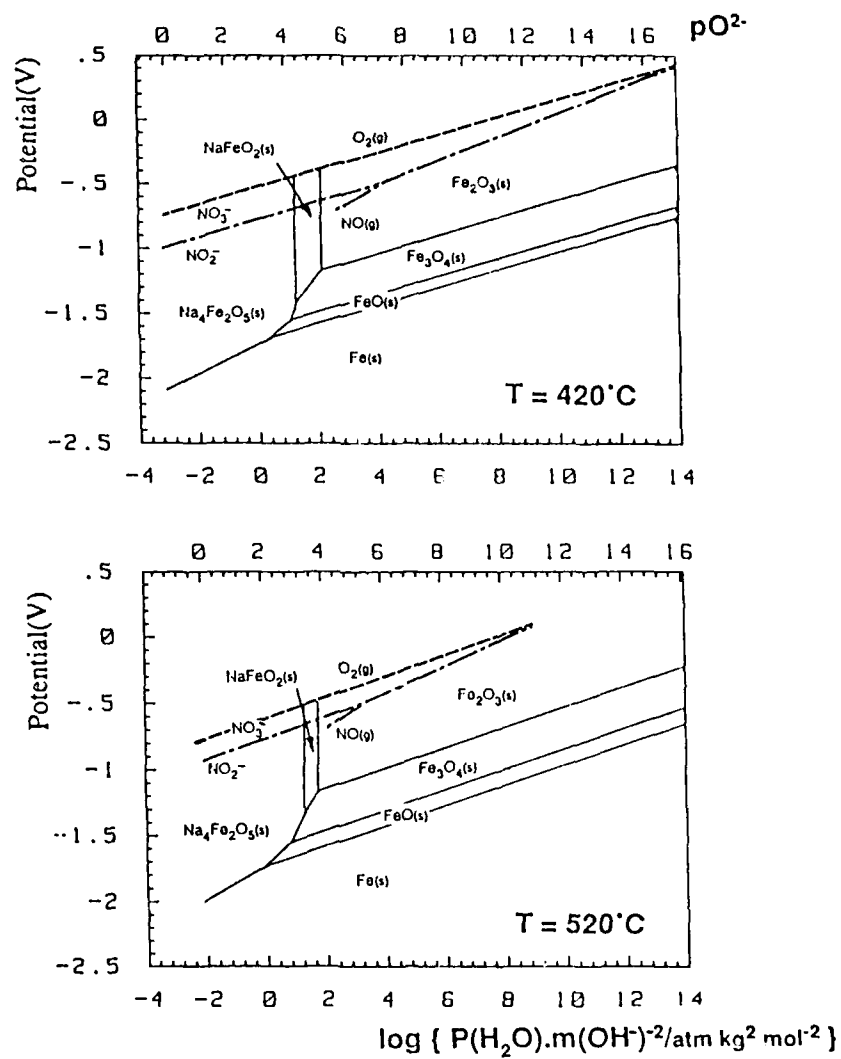


Fig. 5. Potential- $p\text{O}^{2-}$ and potential- $\log [P(\text{H}_2\text{O}) \cdot m(\text{OH}^-)^{-2}]$ diagrams:

- iron systems
- — NaNO_3 - NaNO_2 - NO system and --- O_2/O^{2-} system.

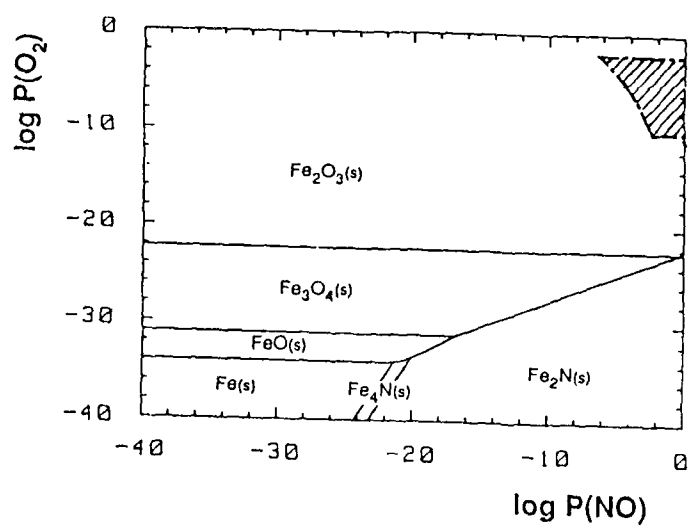


Fig. 6. $\log P(\text{O}_2)$ - $\log P(\text{NO})$ diagram for iron oxides and iron nitrides.
 $T = 693 \text{ K}$. ▨ Stability area of the sodium nitrate-nitrite mixtures.

The Solubilities of Metal Oxides in Fused Na_2SO_4 Solutions

Y.S. Zhang and Robert A. Rapp*

Shanghai Institute of Metallurgy, Shanghai PR China

*Department of Metallurgical Engineering, The Ohio State University
116 West 19th Ave., Columbus, Ohio 43210 USA

ABSTRACT

The basicity-dependent solubilities of NiO , Cr_2O_3 , iron oxides, and SiO_2 in fused Na_2SO_4 at 1200K are presented and explained in terms of high temperature Pourbaix-type diagrams. The activity coefficients of solute species in Na_2SO_4 melt are summarized. A comparison of the solubilities of CeO_2 in a pure Na_2SO_4 melt and in a $0.7 \text{ Na}_2\text{SO}_4$ - 0.3NaVO_3 solution is also reported.

INTRODUCTION

Metals and alloys may be subjected to accelerated oxidation when covered with a thin condensate or deposit of fused salt in an oxidizing gaseous environment. This type of attack is called hot corrosion. Because of its high thermodynamic stability, Na_2SO_4 is the most usual or dominant salt involved. As indicated in much work, dissolution of metal oxides comprising the protective scale is involved in hot corrosion processes. Therefore, a knowledge of the solubility behavior of metal oxides is important in understanding any fluxing mechanisms of hot corrosion. Likewise, the subject serves to characterize better our thermodynamic knowledge for these systems. In this paper, the basicity-dependent solubilities of NiO , Cr_2O_3 , iron oxides, and SiO_2 in fused Na_2SO_4 at 1200 K, as well as the solute activity coefficients are presented and interpreted in terms of high-temperature Pourbaix-type phase stability diagrams. The solubility of CeO_2 in a pure Na_2SO_4 melt is compared to that in a $0.7 \text{ Na}_2\text{SO}_4$ - 0.3NaVO_3 solution.

1. Solubilities of Metal Oxides in Pure Fused Na_2SO_4

Fused Na_2SO_4 , like any other oxyanion fused salt, exhibits an acid-base chemistry. The basicity of pure fused Na_2SO_4 can be defined as $\log a_{\text{Na}_2\text{O}}$, which can be measured by using a sodium sensor combined

with an oxygen probe (1). At 1200 K, the Na_2SO_4 melt basicity is related to the voltage between these two reference electrodes:

$$E(V) = 1.4943 + 0.119 \log a_{\text{Na}_2\text{O}} \quad (1)$$

The oxygen activity in the melt is determined from the voltage between a platinum working electrode and the oxygen probe:

$$E(V) = 0.0403 + 0.0595 \log P_{\text{O}_2} \quad (2)$$

As expected thermodynamically, the solubility of NiO in fused Na_2SO_4 at 1 atm O_2 is basicity-dependent, as shown in Figure 1 (1). The basic and acidic solutes were inferred from the experimental slopes to be NiO_2^- and Ni^{2+} , respectively.

As indicated by the phase stability diagram for the Na-Cr-S-O system in Figure 2, the measurement and explanation of the solubility of Cr_2O_3 in fused Na_2SO_4 offered a special challenge because of the possibility of forming four solute species, dissolved Na_2CrO_4 , NaCrO_2 , $\text{Cr}(\text{SO}_4)_{1.5}$ and CrS , depending upon melt basicity and P_{O_2} . The solubility of Cr_2O_3 at 1200 K was measured as a function of basicity for two different oxygen activities (1.01×10^5 and 3.19×10^{-9} Pa) the experimental results are shown as solid lines in Figure 3 (2). The experimental slopes demonstrate the existence of all four solute species in the Na_2SO_4 melt. The dashed lines in Figure 3 represent the calculated solubility for Cr_2O_3 at several other oxygen activities, assuming that the activity coefficient for each dilute solute is constant.

Figure 4 (3) shows the solubilities of the two oxides Fe_2O_3 and Fe_3O_4 in Na_2SO_4 at 1200 K as four solutes $\text{Fe}(\text{SO}_4)_{1.5}$, FeSO_4 , FeS , and NaFeO_2 for the entire range of stability for the two oxides. The measured solubilities at three different oxygen activities are shown as solid lines in Figure 4. This solubility behavior is in excellent agreement with the theoretical expectations from the Pourbaix-type diagram for the Na-Fe-S-O system in Figure 5. As is frequently done for aqueous solutions, Figure 6 divides the field of oxide stability into regimes of dominance for the several solutes of the iron oxides.

The solubility of SiO_2 in Na_2SO_4 was also measured at 900C, and it was found that the solubility is not dependent upon melt basicity

(4). A stability diagram also shows that molecular SiO_2 , and not any ionic solute, is stable. The presence of a slightly soluble SiO_2 molecular solute is consistent with the known excellent resistance of SiO_2 to acidic fluxing in hot corrosion.

A compilation of measured solubilities in fused Na_2SO_4 at 1200 K and 1 atm O_2 for the oxides of principal interest to high temperature alloys and coatings is presented in Figure 7 (5).

2. Solutes and Their Activity Coefficients

From solubility measurements, the solutes and their activity coefficients in fused Na_2SO_4 at 1200 K are derived, as summarized in Table 1 (1-3, 6). As mentioned earlier, some uncertainty in these activity coefficient values may result from the uncertainties in the thermodynamic formation energy data for compounds, and from experimental errors.

3. Solubility of CeO_2 in Fused Na_2SO_4 - NaVO_3

Recently, the solubilities of CeO_2 , HfO_2 and Y_2O_3 in fused Na_2SO_4 -30 mol.% NaVO_3 and, for comparison, of CeO_2 in pure Na_2SO_4 were measured at 900 C (7). Figure 8 is a plot comparing the solubilities of CeO_2 in pure Na_2SO_4 and in 0.7 Na_2SO_4 -0.3 NaVO_3 at 900 C and 1 atm O_2 . Although the basic solubilities do not differ importantly, the magnitude of the acidic solubility is increased greatly over a wide regime of melt basicities. At the minimum solubility for CeO_2 in pure Na_2SO_4 , the solubility is increased by three orders of magnitude in the vanadate solution. The dependence of acidic solubility upon basicity implies that the increase does not result because Ce^{4+} cations complex importantly with vanadate anions, but rather because the metavanadate anions strongly complex oxide ions to form orthovanadate anions. For this reason, the increase in acidic solubility should be observed generally for all oxides in vanadate solutions. The effect is significant in explaining the highly corrosive attack by vanadate solutions.

Acknowledgments

This research was sponsored by the National Science Foundation, Metallurgy Program of the Division of Material Research, under Grant 75-17204 and 791190.

References

1. D.K. Gupta and R.A. Rapp, J. Electrochem. Soc., **127**, 2194 and 2656 (1980).
2. Y.S. Zhang, Ibid., **133**, 655 (1986).
3. Y.S. Zhang and R.A. Rapp, Ibid., **132**, 734 and 2498 (1985).
4. D.Z. Shi and R.A. Rapp, Ibid., **133**, 849 (1986).
5. R.A. Rapp, Corrosion, **42**, 568 (1986).
6. P.D. Jose, D.K. Gupta, and R.A. Rapp, J. Electrochem. Soc., **132**, 735 (1985).
7. Y.S. Zhang and R.A. Rapp, Solubilities of CeO_2 , HfO_2 and Y_2O_3 in Fused Na_2SO_4 -30 m/o NaVO_3 and CeO_2 in Pure Na_2SO_4 at 900 °C, accepted for publication in Corrosion (1987).

Table 1: Activity coefficients of Solutes in Na_2SO_4 at 1200K

solute	NaFeO_2	NaCoO_2	NaNiO_2	NaCrO_4	NaCrO_2	$\text{Fe}(\text{SO}_4)_{1.5}$	FeSO_4	FeS	CoSO_4	NiSO_4	$\text{Cr}(\text{SO}_4)_{1.5}$	CrS
activity coefficient	430	50	50	4.6	2.3	3.6×10^{-3}	0.83	180	2.5	0.12	5.8	20

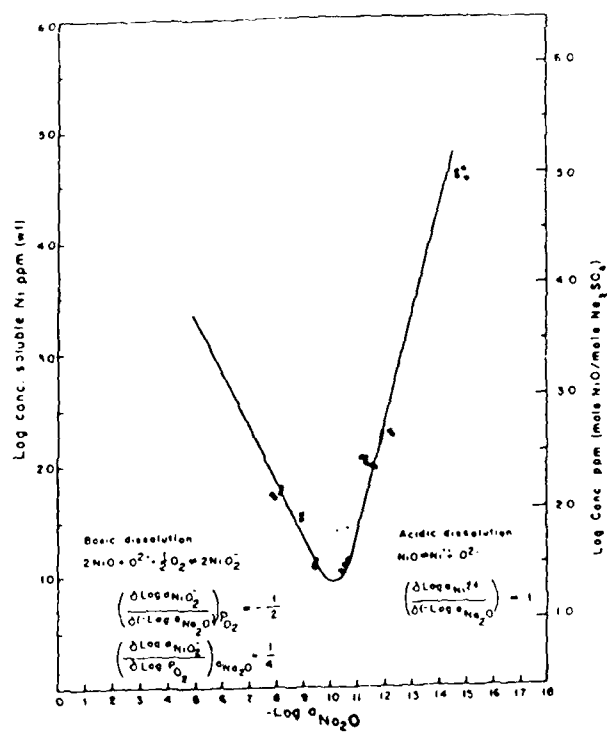


Figure 1. Solubility of NiO in fused Na₂SO₄ at 1200K

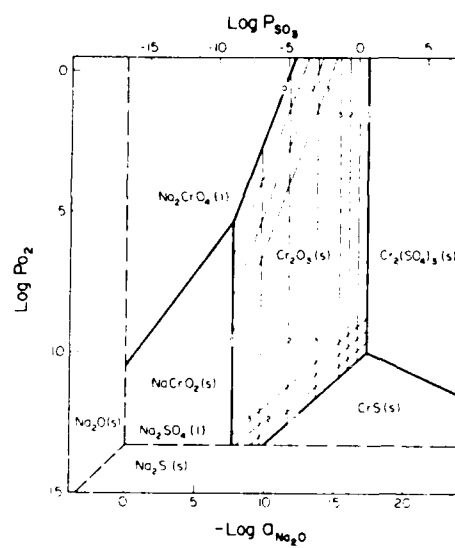


Figure 2. Na-Cr-S-O phase stability diagram for 1200K

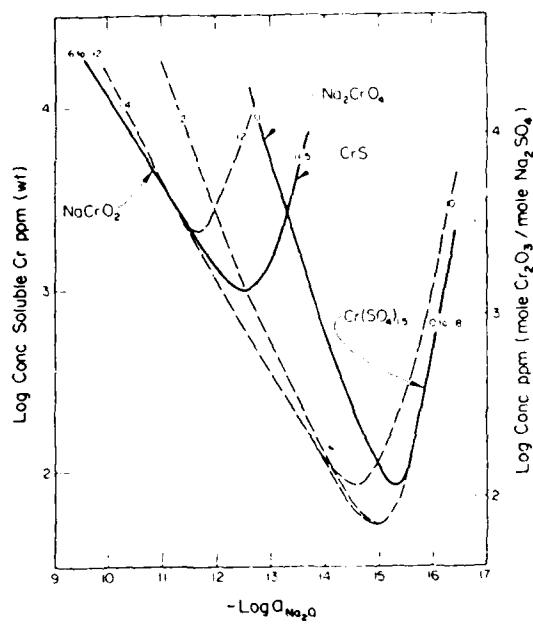


Figure 3. Measured and calculated solubilities of Cr_2O_3 in fused Na_2SO_4 at 1200K for several oxygen activities

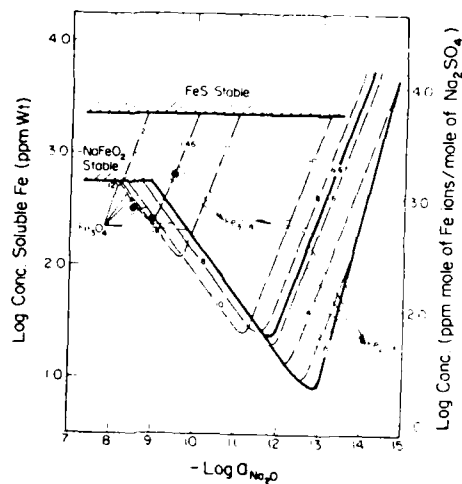


Figure 4. Measured and calculated solubilities of Fe_2O_3 and Fe_3O_4 in fused Na_2SO_4 at 1200K for several oxygen activities.

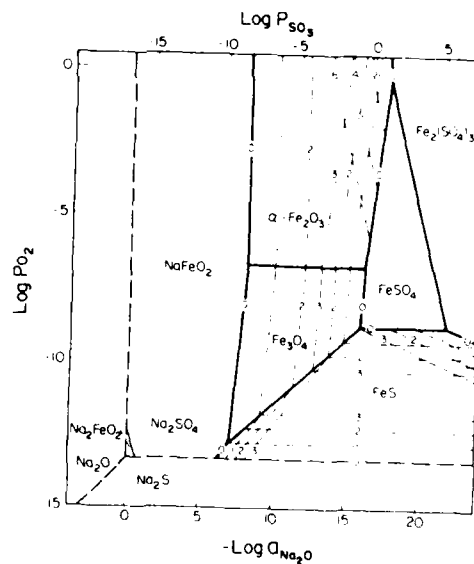


Figure 5. Na-Fe-S-O phase stability diagram for 1200K

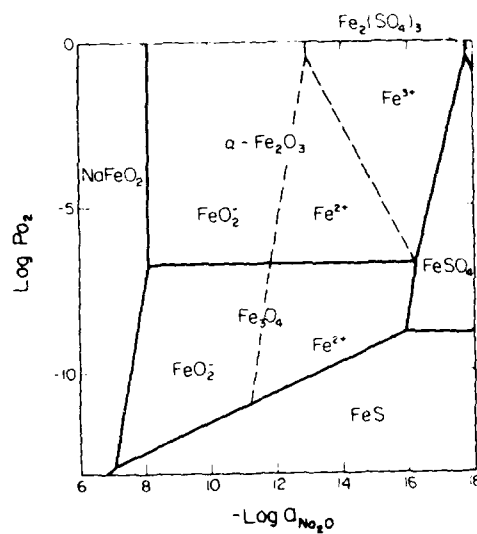


Figure 6. Dominant iron solute species in the Na-Fe-S-O system at 1200K.

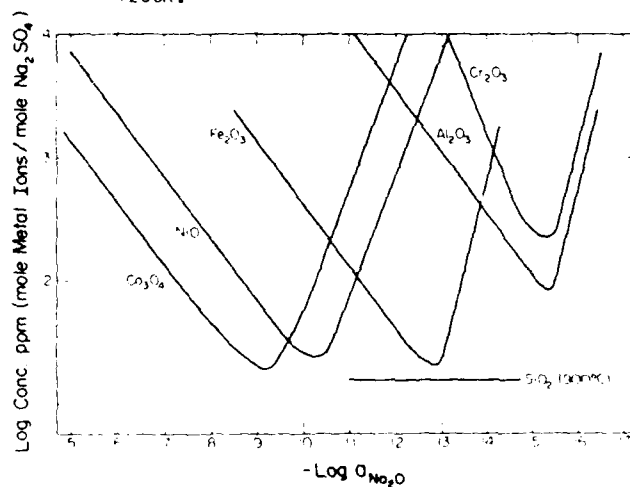


Figure 7. Measured oxide solubilities in fused Na_2SO_4 at 1200K and $P_{\text{O}_2} = 1.01 \times 10^5 \text{ Pa}$

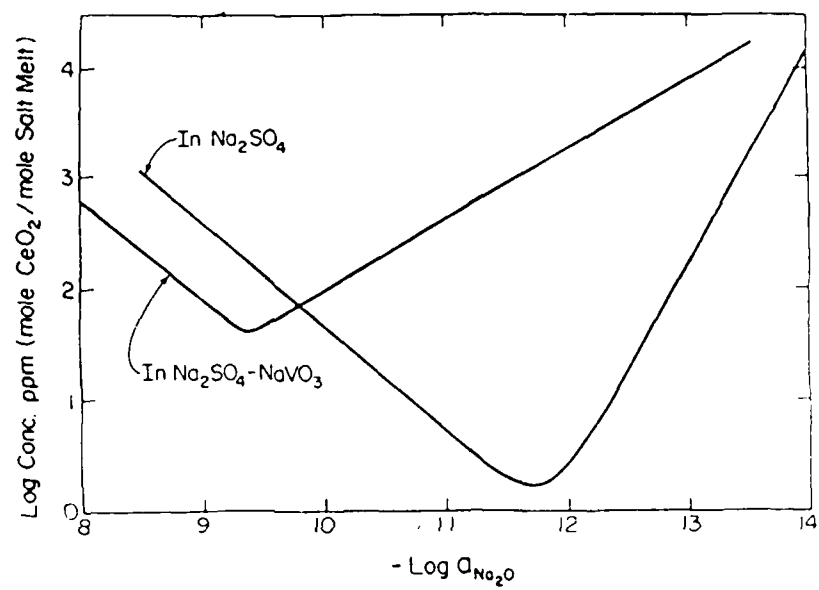


Figure 8. Comparison of CeO_2 solubility in pure Na_2SO_4 and in Na_2SO_4 -30 mol.% NaVO_3 solution at 900 C and $P_{\text{O}_2} = 1.01 \times 10^5 \text{ Pa}$

CORROSION OF HOT-PRESSED SILICON NITRIDE
IN ALKALI CARBONATE MELTS

Koji Tajiri, Toshiyuki Nishio, Tadashi Asahina,
and Mineo Kosaka

Government Industrial Research Institute, Nagoya
1-1 Hirate-cho Kita-ku Nagoya 462, Japan

ABSTRACT

The corrosion behavior of hot-pressed Si_3N_4 in alkali carbonate melts was investigated under air, N_2 , and CO_2 environments. The rate of corrosion could be shown by weight loss per unit surface area of Si_3N_4 . From the experiments at 800-1000°C, the apparent activation energies of the reactions in Li_2CO_3 , Na_2CO_3 , and K_2CO_3 were 163, 138, and 153 kJ/mol, respectively. The rate of corrosion in Li_2CO_3 was about twenty times faster than that in Na_2CO_3 and about two-hundred times faster than that in K_2CO_3 . The rates of corrosion in Li_2CO_3 - Na_2CO_3 or Li_2CO_3 - K_2CO_3 mixtures were in the middle of the rates in each pure carbonate. The rate became faster with the increase in the mole fraction of Li_2CO_3 . From the above results and SEM observations, the corrosion mechanism was discussed. Under CO_2 environment, the rate of corrosion was slower than that under atmosphere. Thus, it was suggested that the basic oxide concentration in molten carbonate had an effect on the rate of corrosion.

INTRODUCTION

Non-oxide ceramics, such as Si_3N_4 and SiC , are being considered as structural materials to be used in corrosive environments at high temperature. This consideration also includes the applicability of such ceramics to structural materials in the molten carbonate fuel cell. However, relatively little work has been done on the corrosion of such ceramics in molten salts.[1-3] Moreover, quantitative analysis of the reaction rate is very limited.[4]

Therefore, for the first step of the study on the reaction of ceramics with molten salts, we selected hot-pressed Si_3N_4 as a non-oxide ceramics and the alkali carbonates as molten salts. We investigated the effects of parameters such as temperature, kinds of alkali carbonates, and environment, on the corrosion behavior of this material in alkali carbonate melts.

EXPERIMENTAL

Ceramic samples were prepared as commercial hot-pressed Si_3N_4 (Toshiba Co. Ltd., 7% $(\text{Y}_2\text{O}_3\text{-Al}_2\text{O}_3)$, 3.25 g/cm^3) cut into $5.2 \times 4.4 \times 1.8 \text{ mm}^3$ sizes by a diamond cutter. The carbonates used were analytical grade (Wako Chemical Co.).

Figure 1 shows a schematic diagram of the reaction apparatus. About 0.1 mole of specified carbonate, pure or mixed, in a Pt crucible was heated by an electric furnace. After the temperature of the carbonate reached a fixed value, a Si_3N_4 sample, which was weighed and measured precisely, was put into the crucible. After heat treatment, the crucible was taken out and quenched in air. The sample was washed in water and HCl solution, rinsed, dried, weighed, and measured.

The corrosion experiments in N_2 or CO_2 environments were the same as that mentioned above only with 250 ml/min. of gas flow from the gas inlet.

Scanning Electron Microscopy (SEM) was carried out with an Akashi Alpha-10.

RESULTS AND DISCUSSION

(1) Reaction Kinetics

As an example, the weight loss of a Si_3N_4 specimen in Li_2CO_3 melt is shown in figure 2. By measuring of dimensional change of the specimen, this reaction was considered to proceed isotropically. Therefore, the relation between the reaction time and the weight loss of the specimen per unit surface area was plotted. The plots of the reaction in Li_2CO_3 and of that in Na_2CO_3 are shown in figures 3 and 4, respectively. The relations were approximately linear. Consequently, the reaction could be regarded as being controlled by surface reaction. Then, the factor of the rate of corrosion, k , would be defined as a unit of the speed of weight loss per unit area. The k value would be used in subsequent analyses.

(2) The Effects of Reaction Temperature

As shown in figures 2-4, the rates of corrosion varied significantly with changes in the temperature. Figure 5 shows the Arrhenius plots of these reaction rates. From these plots, apparent activation energies of the hot-pressed Si_3N_4 with molten Li_2CO_3 , Na_2CO_3 , and K_2CO_3 were obtained as 163, 138, and 153 kJ/mol, respectively. It has been reported that the value of the corrosion of Si_3N_4 in K_2SO_4 melt was 724 kJ/mol. Comparing these values, it could be postulated that the apparent activation energy was strongly effected by the kind of anion constituting each melt.

(3) The Effects of the Kinds of Carbonate

Figure 5 also shows the effects of the kind of alkali carbonate on the rate of corrosion. As shown in figure 5, at the same temper-

ature, the rate of corrosion in Li_2CO_3 was about twenty times faster than that in Na_2CO_3 , and about two-hundred times faster than that in K_2CO_3 . It seemed that the smaller the radius of the alkali ion, the faster the rate of corrosion.

When binary mixtures, $\text{Li}_2\text{CO}_3\text{-Na}_2\text{CO}_3$ or $\text{Li}_2\text{CO}_3\text{-K}_2\text{CO}_3$, were used as the melts, the relations between the composition of carbonate and the rate of the corrosion are given in figure 6. The values of the rate of corrosion in the mixture are in the middle of that in each pure carbonate. The logarithm of the value of the rate of corrosion had a linear relation with the mole fraction of Li_2CO_3 on the $\text{Li}_2\text{CO}_3\text{-Na}_2\text{CO}_3$ system.

(4) SEM Observations

The microstructures of the surface and the section of the Si_3N_4 samples, both original and corroded, are shown in figure 7. Because of corrosion, the surface of the sample became rough with the appearance of Si_3N_4 grains. This means that the grain boundary of the sample was eroded faster than the Si_3N_4 grains in the sample.

The microstructure of the section of the corroded sample indicates that the region, where structural change by the corrosion occurred, is limited only near the surface.

From these observations, it could be supposed that the reaction of the Si_3N_4 samples with carbonate melts was not completed on the surface of the samples, but proceeded by the mechanism that Si_3N_4 grains in the samples were eliminated with the erosion of the grain boundary.

If this assumption was accepted, the difference of the rate of corrosion of the Si_3N_4 sample by the kinds of carbonates could be explained partly as the difference of the diffusivities of alkali ions into the grain boundary of the Si_3N_4 sample by the difference of the ion radius. However, the determination of the reaction rate of pure Si_3N_4 with carbonate melt, the composition analysis of the carbonate in the reacting crucible, and other factors are needed in order to verify this assumption.

(5) The Effects of Environment

Some of the results of the experiments, which were carried out under N_2 or CO_2 environment, are also shown in figures 2-4. The rate of corrosion in carbonate under N_2 environment was fast, and that under CO_2 environment was slow, compared with that under air environment.

The following explanation has been reported [2,4] on the corrosion behavior in each environment. Under an air environment; SiO_2 film is formed on the surface of the Si_3N_4 , and the film suppresses the reaction. But under an N_2 environment, SiO_2 film is not formed; therefore, the reaction proceeds rapidly.

It seems that the results of the experiments under a CO_2 environment suggests that the basic oxide concentration in the carbonate melt affects the rate of corrosion of the Si_3N_4 sample. Under an air environment, some of the carbonate would decompose to

basic oxide. But under a CO_2 environment, the decomposition would be suppressed. It might be considered that the higher the basic oxide concentration in the carbonate melt, the faster the rate of corrosion. This also was suggested from the result that the corrosion of the sample occurred faster when the amount of carbonate initially in the crucible was decreased.

However, more precise experiments under a controlled environment are needed to assure the above suggestion.

SUMMARY

The corrosion behavior of hot-pressed Si_3N_4 in alkali carbonates melts was investigated, and the following results were obtained:

- a) The corrosion was apparently controlled by surface reaction.
- b) Apparent activation energies were obtained. These energies did not vary greatly for different alkali carbonates.
- c) The differences in the rates of corrosion among the alkali carbonates were large and increased in the order $\text{Li}_2\text{CO}_3 > \text{Na}_2\text{CO}_3 > \text{K}_2\text{CO}_3$.
- d) The rate of corrosion of the hot-pressed Si_3N_4 in carbonates under an N_2 environment was fast, while that under a CO_2 environment was slow, compared to the rate under an air environment.

REFERENCES

1. R. E. Tressler, M. D. Meiser and T. Yonushonis, J. Am. Ceram. Soc., **59**, 278 (1976).
2. D. W. Mackee and D. Chatterji, J. Am. Ceram. Soc., **59**, 441 (1976).
3. N. Nassif and S. B. Hanna, Thermochim. Acta, **79**, 305 (1984).
4. T. Sato, Y. Kanno, T. Endo and M. Shimada, Yogyou-Kyokai-Shi, **94**, 123 (1986). (in Japanese)

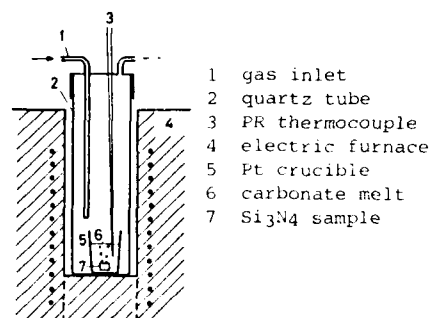


Figure 1. Schematic Diagram of the Reaction Apparatus.

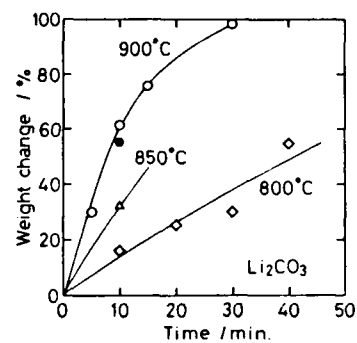


Figure 2. Weight Loss of Si_3N_4 Samples in Li_2CO_3 Melt under Air Environment. (except \bullet at 900°C , under CO_2 environment)

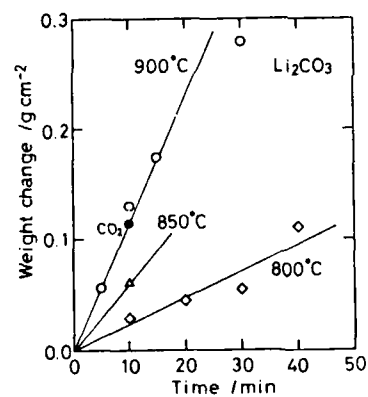


Figure 3. Plots of the Reaction time vs. Weight Loss per Unit Area for the Reaction in Li_2CO_3 under Air Environment. (except \bullet)

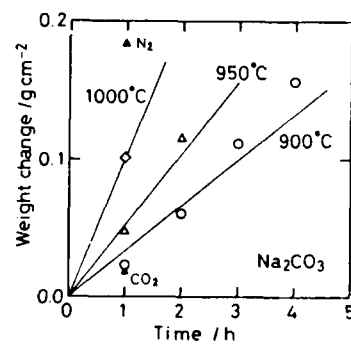


Figure 4. Plots same as Figure 3 for the reaction in Na_2CO_3 .

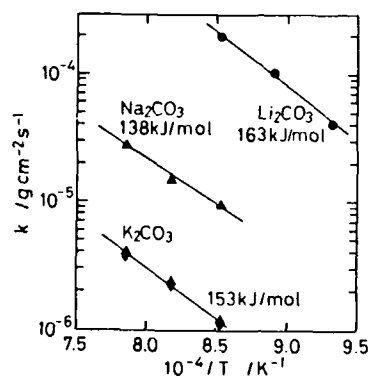


Figure 5. Arrhenius Plots for the Reaction

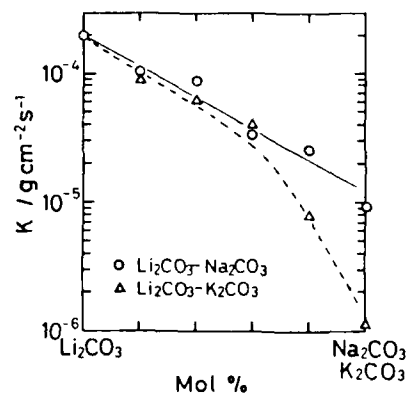


Figure 6. Effects of the Composition of Carbonate Melt to the Reaction Rate.

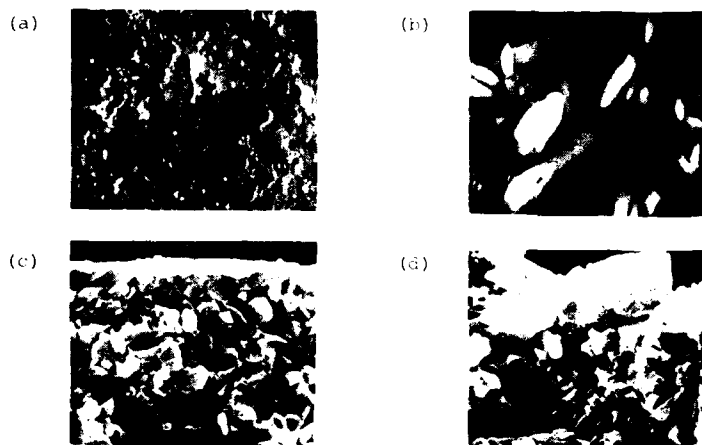


Figure 7. Microstructure of the Si_3N_4 sample. (a) the Surface of the Original Sample. (b) the Surface after Corroded. (c) the Section of Original Sample. (d) the Section after Corroded.

HOT CORROSION OF HEAT-RESISTANT ALLOYS INDUCED
BY MOLTEN FLUORIDE MIXTURES

Masahiro Kawakami, Masato Kawabe^{*1},
Masaru Okuyama^{*2} and Koin Ito

Toyohashi University of Technology
Hibariyaka, Tempaku-cho, Toyohashi 440 JAPAN

ABSTRACT

Heat resistant alloys have been heated with the coating of molten fluoride mixture at 500 - 700 °C, either in air or in Ar. The weight change was monitored with a thermogravimetric balance for 20 hrs.. The air oxidation of Hastelloy-N, Inconel 625 and N-155 was accelerated significantly with NaBF_4 -NaF coating. The electrochemical polarization revealed that the corrosion current corresponded well to the rate of accelerated oxidation. With LiF-Bef_2 coating, some volatile materials are formed, and oxidation is accelerated.

INTRODUCTION

It is well known that high temperature oxidation of heat resistant alloys are accelerated by the adhesion of molten salts(1,2). The accelerated oxidation of nickel base alloys by molten Na_2SO_4 has been investigated extensively by many researchers (3-6). Those by molten Na_2CO_3 , NaNO_3 (7-9) and NaCl-KCl (10) have also been reported. But it is not known whether molten fluorides do induce the accelerated oxidation of alloys. Molten fluoride mixtures, such as NaBF_4 -NaF and LiF-Bef_2 , are considered as candidates for heat transfer media in molten salt reactors. Therefore, it might be of some interest to examine the hot corrosion of alloys induced by such salts, although the accelerated oxidation can be avoided in the practical reactor design even if it happens.

In the present work, hot corrosion (including accelerated oxidation) of several heat resistant alloys have been investigated with coating of the above fluoride mixtures. The experimental methods are thermogravimetric measurements and electrochemical polarization measurements.

Present address; ^{*1} Suzuki Motor Co. Ltd., Sototakatsuka, Hamamatsu 432-29 JAPAN, ^{*2} Oyama National College of Technology, 771 Nakagaki, Oyama 323 JAPAN.

EXPERIMENTALS

(1) Materials

Composition of the fluoride mixtures are 92mol%NaBF₄-8mol%NaF and 66mol%LiF-34mol%BeF₂, which are considered as the heat transfer media in the secondary cooling loop of molten salt reactors.

The heat resistant alloys are commercial Hastelloy-N(M.M.), home-made Hastelloy-N(h.m.), commercial Inconel 625 and commercial N-155. Compositions of the alloys are shown in Table 1.

Table 1. Composition of the alloys.(wt%)

Alloys	Elements						
	Cr	Fe	Co	Mo	Si	Mn	Ni
Hastelloy-N (M.M.)	7.0	4.0	--	16.7	0.3	0.5	Bal.
Hastelloy-N (h.m.)	7.1	--	--	16.7	0.3	0.4	Bal.
Inconel 625	23.9	3.5	--	11.7	0.5	--	Bal.
N-155	22.0	30.5	19.3	3.7	1.9	--	19.8

(2) Thermogravimetric measurements

Test pieces of 5mmx10mmx1mm were cut out from the alloy stock and polished with dry abrasive paper of #1000. The fluoride mixtures were pre-fused in Ar. The test piece coated with the salt mixture was set in a thermogravimetric balance, and heated up to the desired temperature either in air or in Ar. The weight of the test piece was continuously measured for 20 hrs. After the measurement, the scale formed on the test piece was examined by EPMA.

(3) Electrochemical polarization measurements

Figure 1 shows the schematic diagram of experimental apparatus. The working electrode was cut out from the alloy stock and graphite rod in the form of plate or cylinder. The reference electrode was a kind of Ag-AgF electrode. The counter electrode was made of platinum net. NaBF₄ and NaF powders of reagent grade were mixed in the composition shown above and kept in a dry box for 24 hrs. before the experiment. The salt mixture was put in a high alumina crucible, fused at 400 °C and dehydrated with Ar for 10 min.; then, the salt mixture was heated up to the experimental temperature. Three electrodes were dipped into the fused salt. The rest potential of the working electrode was measured with a potentiometer. After getting a stable rest potential, the working electrode was polarized in noble direction down to -1.6 V in order to reduce oxide film on the electrode surface. Then, polarization in less-noble direction was carried out. The potential was raised 25 mV every 30 sec up to +2.0 V.

RESULTS AND DISCUSSION

(1) Thermogravimetric measurements with NaBF_4 -NaF mixture

(1)-1 Decomposition of the salt mixture

Figure 2 shows the heating pattern and the weight change with time. The test piece of Hastelloy-N(M.M.) was heated with 43.3 mg/cm^2 of the salt mixture in Ar. Temperature was raised linearly up to 700°C for 30 min., and kept constant. When the temperature reached 400°C , the weight began to decrease remarkably. The weight change per unit surface area, $\Delta W/S$, reached down to -17.1 mg/cm^2 for 40 min. and -20.2 mg/cm^2 for 1200 min.. No change was observed in the appearance of test piece. Thus, the weight loss was attributed to the decomposition of NaBF_4 to NaF and BF_3 which had very high vapor pressure. Assuming that the whole weight loss should correspond to the amount of evaporated BF_3 , the composition of salt mixture changed to $31\text{mol}\%\text{NaBF}_4$ - $69\text{mol}\%\text{NaF}$, after 1200 min. Referring to the phase diagram, this composition was in solid-liquid two phase region at 700°C . The fractions of weight loss during heating in Ar were nearly the same in all experiments. Thus, the salt mixture was considered to be in solid-liquid co-existing state in all oxidation experiments. The rate of weight loss after 40 min. was not high and could be negligible, compared with the oxidation rate as will be shown later. Thus, the air was introduced at 40 min. from the beginning of heating to start the oxidation experiment.

(1)-2 Oxidation curve of alloys

Figure 3 shows the oxidation curves of Hastelloy-N(M.M.) with and without salt coating at 700°C . The air oxidation was very much accelerated with the salt coating. The accelerated oxidation curve could be divided into three time periods, namely, an incubation period in which the oxidation was very slow, a catastrophic period and a moderate acceleration period. With larger amount of salt coating, the catastrophic oxidation started later and lasted longer. But, the rate of oxidation in the moderate acceleration period was the same, regardless of the amount of salt coating.

Figure 4 shows the oxidation curves of Hastelloy-N(h.m.) at different temperatures. The oxidation was very much accelerated by the salt coating at 700°C . The shape of oxidation curve with the salt coating was similar to that shown in Figure 3. At 600°C , the weight decreased initially due to the salt decomposition and increased after 800 min.. At 500°C , the weight decreased monotonously. From microscopic observation of the test piece heated at 500°C , no oxide film could be found on the surface. From these, it can be said that the oxidation was significantly accelerated at 700°C , but no accelerated oxidation was observed at a temperature lower than 600°C . Figure 5 shows the effect of amount of salt coating on the oxidation curve. The amount of oxidation was larger with larger amount of salt

coating, although crossover was observed with the curve of 6.8 and 4.8 mg/cm² from 500 to 800 min..

Figure 6 shows the curves of Inconel 625 with and without salt coating at different temperatures. The accelerated oxidation did occur from 600 °C. The amount of accelerated oxidation was larger at higher temperature. The shape of accelerated oxidation was different from those of Hastelloy-N. Neither incubation nor catastrophic periods were observed, although the initial oxidation rate was very fast.

Figure 7 shows the oxidation curves of N-155 at different temperatures. The accelerated oxidation was observed at every temperature. The shape of the oxidation curves are nearly the same as those of Inconel 625.

(1)-3 Comparison of the accelerated oxidation behavior among alloys

The amount of oxidation is sometimes expressed as the following function of time,

$$\Delta W/S = a t^b \quad \dots\dots\dots(i)$$

where, t is time, a and b are parameters. In figure 8, the accelerated oxidation curves of alloys at 700 °C are replotted in log-log form. From the slope of lines, the value of b was estimated. The oxidation is called "catastrophic", when b is larger than unity, and "moderate acceleration", when b is less than unity. In the cases of Hastelloy-N(M.M.) and Hastelloy-N(h.m.), b was about 2 in an early period of time and 0.36-0.4 in later period. But the absolute amount of oxidation was larger in Hastelloy-N(M.M.) than in Hastelloy-N(h.m.). In the case of Inconel 625, b was slightly less than unity initially and almost constant at 0.1 in later periods. This small value of $b=0.1$ shows very slow oxidation and is favorable from the view point of hot corrosion resistance. In the case of N-155, b changed from 0.7 in early periods to 0.4 in later periods. It can be said from the figure that Hastelloy-N(h.m.) should be the best with respect to hot corrosion resistance, among the present alloys.

The effect of chromium content on the accelerated oxidation can be seen by comparing the result of Hastelloy-N(M.M.) to that of Inconel 625, because compositions of the two alloys are similar to each other, but chromium content in Inconel 625 is more than 3 times larger than in Hastelloy-N(M.M.). Significant differences can be seen in later periods. The value of b in Inconel 625 was very small. Thus, chromium can be considered effective for hot corrosion resistance. The effect of iron content can be seen by comparing the result of Hastelloy-N(M.M.) to that of Hastelloy-N(h.m.). The amount of oxidation of Hastelloy-N(M.M.) was always larger than that of Hastelloy-N(h.m.). Since Hastelloy-N(h.m.) contains no iron, iron can be considered detrimental with respect to hot corrosion resistance. This detrimental effect can also be seen by comparing

the result of Inconel 625 to that of N-155. Protective effect of chromium seen in Inconel 625 was cancelled by the detrimental effect of iron in N-155, because the latter contained a much larger amount of iron.

(1)-4 Morphology of the scale formed by accelerated oxidation

Photo. 1 shows microscopic picture of the scale formed on Hastelloy-N(M.M.) at 700 °C and distribution map of elements. The scale was of 500 μ m thickness and had a kind of multi-lamellar structure. Map of elements shows that the scale was mainly composed of nickel oxide and contained some amounts of iron, chromium and molybdenum oxides uniformly. Sodium was concentrated in the outer layer. Thus, the outer layer might be a mixture of oxides and salt. No concentration gradient of elements was observed in the alloy phase, showing no preferential oxidation. The feature of scale formed by the accelerated oxidation with NaBF_4 -NaF mixture was similar to that shown in Photo. 1, in all alloys.

(2) Thermogravimetric measurements with LiF-BF_2 mixture

(2)-1 Vaporization of salt and hot corrosion of Hastelloy-N(h.m.)

Triangles in Figure 9 show the weight loss of salt coated on platinum net. The vaporization of the salt occurred during heating at 700 °C, but its rate was not so fast. Circles in the figure show the weight change of Hastelloy-N(h.m.) with the salt coating heated in air. The weight decreased till 1000 min. and increased later. Squares in the figure show the weight change when the alloy with the salt coating was heated in Ar. The weight decreased faster in the initial period of time than heated in air and continued to decrease throughout the heating time. Therefore, it can be said that two kinds of reaction occurred simultaneously, when the alloy was coated with LiF-BF_2 and heated in air. The one might be the formation of some volatile material, and the other is the accelerated oxidation.

(2)-2 Weight change of Inconel 625 and N-155

Figure 10 shows the weight change of Inconel 625 with the salt coating heated in air at different temperature. The weight decreased initially and increased later. The formation of some volatile material and the accelerated oxidation occurred simultaneously, also in the case of Inconel 625. The rate of both reactions were faster at higher temperature.

Figure 11 shows the weight change of N-155 with the salt coating heated in air at different temperature. No weight loss was observed, contrary to the other two alloys. The oxidation was significantly accelerated. The amount of oxidation was larger at higher temperature. The oxidation curve was not smooth but stepwise.

(2)-4 Morphology of the scale

Photo. 2 shows the microscopic picture of the scale formed on Inconel 625 with the salt coating heated in air at 700 °C. The feature of scale was globular and very different from that in the case of NaBF₄-NaF mixture. Although the weight change was negative at the end of experiment, oxide phase was found in the scale. Oxide phase was composed of chromium and iron oxides with a small amount of molybdenum oxide. Nickel oxide was scarcely found in the oxide phase. Porous layer was found in the alloy phase, just beneath the salt-alloy interface. The layer was deficient in chromium and iron contents. Outside of the layer, some precipitates were found, which might be the intermetallic compound of nickel and molybdenum. The morphology of the scale on the other alloys was nearly the same as that shown in Photo. 2.

(3) Electrochemical polarization measurement in NaBF₄-NaF

Figure 12 shows polarization curves of Inconel 625 and N-155 in Ar at 600 °C. I_a and I_c are anodic and cathodic currents, respectively. The polarization curves were similar to each other, although the anodic current of Inconel 625 was smaller in higher potential region than that of N-155. The anodic current had an active dissolution peak at -0.3V and showed the passivation around 0 V. Figure 13 shows polarization curves of a graphite electrode at 600 °C, in air and in Ar. The cathodic current in air was larger than that in Ar. Thus, the cathodic current can be attributed to the reduction of dissolved oxygen in the salt, in the potential range from -0.4 to 0.3 V.



This potential range coincided with that where active dissolution of alloy electrode occurred, as shown in Figure 12.



Thus, it can be postulated that the accelerated oxidation might occur electrochemically by the coupling of reactions (2) and (3).

Figure 14 shows polarization curves of the alloys at 700°C. The anodic current of Hastelloy-N(h.m.) was much smaller than those of others, in the above potential range. This accorded with the result of thermogravimetric measurement, where the amount of accelerated oxidation of Hastelloy-N(h.m.) was the smallest among the alloys. Figure 15 shows the polarization curve of Hastelloy-N(h.m.) in air at 700 °C. The corrosion current was estimated as 1.32 mA/cm² by extrapolating cathodic and anodic currents with the aid of the Tafel relation. The rate of accelerated oxidation of Hastelloy-N(h.m.) was estimated from the slope of the curve shown in Figure 4, between 400 and 1000 min. and converted to the current density of 1.7 mA/cm², assuming di-valent electrode reaction and the mean atomic weight of

60. These two current densities seem to be in accordance with each other.

CONCLUSION

The air oxidation of the present alloys is significantly accelerated by the adhesion of $\text{NaBF}_4\text{-NaF}$. The amount of accelerated oxidation is larger with larger amount of the salt mixture and at higher temperature. The result of electrochemical polarization measurement indicates that the electrochemical mechanism, in which the anodic dissolution of metallic element is coupled with the cathodic reduction of oxygen, plays an important role. When the nickel based alloys are heated with LiF-BF_2 coating in air, the weight decreased initially and increased later. Thus, it is seen that some kind of volatile material might be formed simultaneously with the accelerated oxidation.

ACKNOWLEDGEMENT

The present work is financially supported by Grant-in Aid for Energy Research, The Ministry of Education, Science and Culture, Japan.

REFERENCES

1. M. Kawakami, K.S. Goto and R.A. Rapp, *Trans. ISIJ*, 20, 646(1980).
2. J. Stringer, *Annual Reviews of Materials Science*, 477 (1977).
3. E.L. Simons et al., *Corrosion NACE*, 11, 505 (1955).
4. C. Tedmon and A.U. Seybolt, *Corros. Sci.*, 8, 125 (1968).
5. J.A. Goebel et al., *Met. Trans.*, 4, 261 (1973).
6. R.A. Rapp and K.S. Goto, *Proc. Symp. Fused Salt*, Oct. (1978).
7. N.S. Bornstein and M.A. DeCresente, *Trans. AIME*, 245, 1947(1969).
8. N.S. Bornstein and M.A. DeCresente, *Corrosion*, 26, 209 (1970).
9. N.S. Bornstein and M.A. DeCresente, *Met. Trans.*, 2, 2875 (1971).
10. M. Kawakami et al., *Proc. JIMIS-3; High temperature Corrosion*, 279 (1983).
11. M.W. Rosenthal et al., "The Developmental States of Molten Salt Breeder Reactors", *ORML-4812*, (1972).
12. M.W. Rosenthal et al., *JAERI-M*, 5181 (1973).

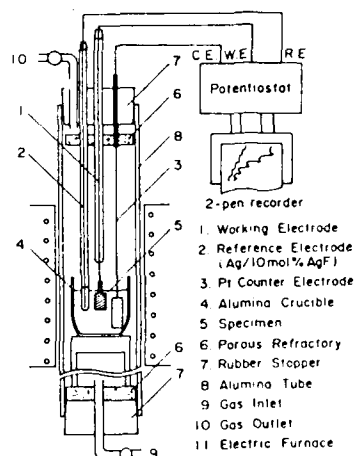


Figure 1. Schematic diagram of the apparatus in electrochemical polarization experiment.

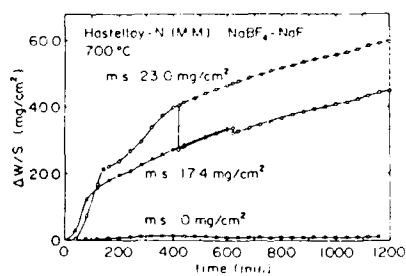


Figure 3. Oxidation curves of Hastelloy-N(M.M.) with and without $\text{NaBF}_4\text{-NaF}$ coating at 700°C .

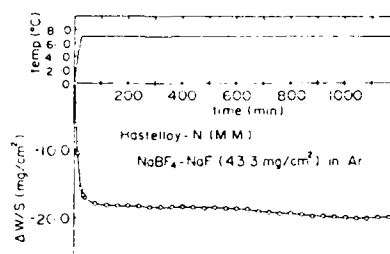


Figure 2. Weight change of Hastelloy-N(M.M.) heated in Ar.

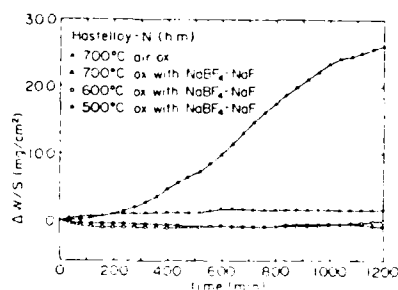


Figure 4. Oxidation curves of Hastelloy-N(h.m.) with and without $\text{NaBF}_4\text{-NaF}$ coating at different temperature.

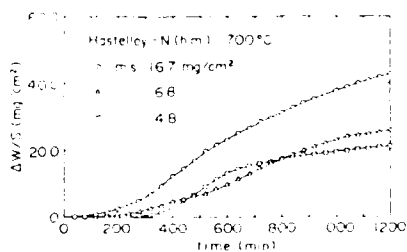


Figure 5. Effect of the amount of $\text{NaBF}_4\text{-NaF}$ on the oxidation curve of Hastelloy-N(h.m.) at 700°C .

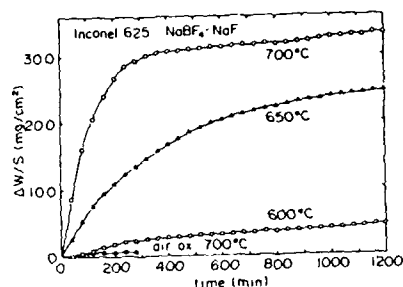


Figure 6. Oxidation curves of Inconel 625 with and without $\text{NaBF}_4\text{-NaF}$ coating at different temperature.

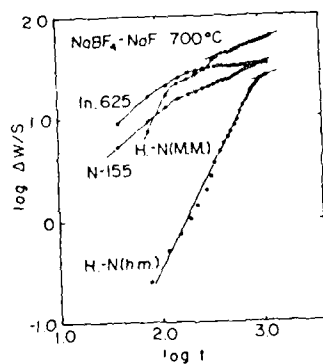


Figure 8. Comparison of accelerated oxidation among alloys.

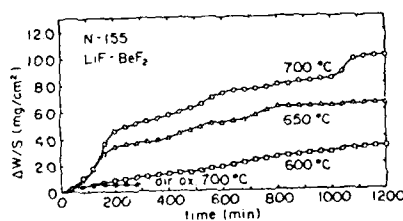


Figure 11. Weight change of N-155 heated in air with LiF-Bef_2 coating.

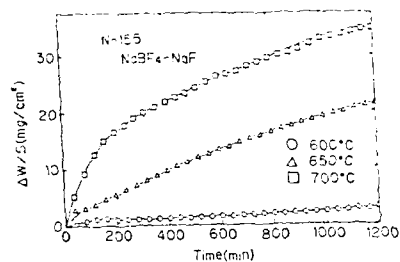


Figure 7. Oxidation curves of N-155 with $\text{NaBF}_4\text{-NaF}$ coating at different temperature.

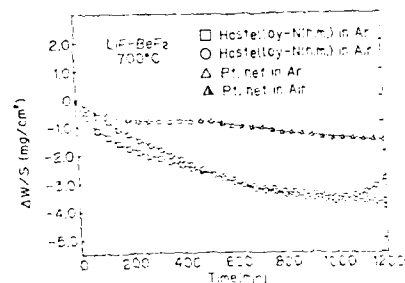


Figure 9. Weight change of Pt net and Hastelloy-N(h.m.) with LiF-Bef_2 coating in Ar and air.

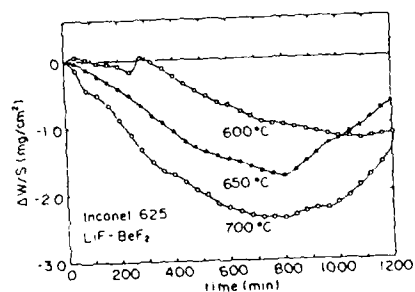


Figure 10. Weight change of Inconel 625 heated in air with LiF-Bef_2 coating.

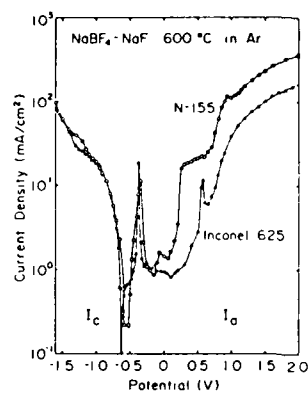


Figure 12. Polarization curve of alloys in $\text{NaBF}_4\text{-NaF}$ at 700°C .

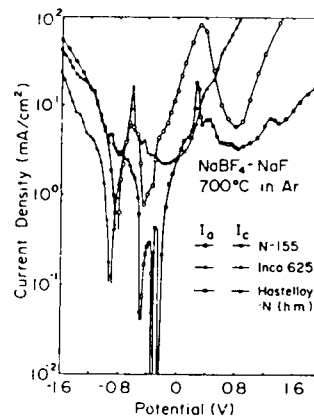


Figure 14. Polarization curve of alloys in $\text{NaBF}_4\text{-NaF}$ at 700°C .

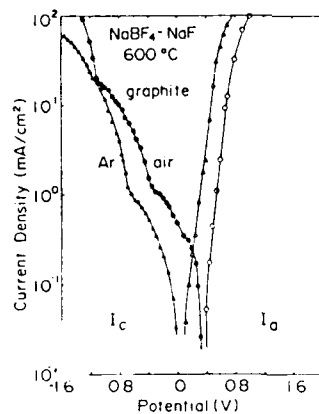


Figure 13. Polarization curve of oxygen in $\text{NaBF}_4\text{-NaF}$ at 600°C .

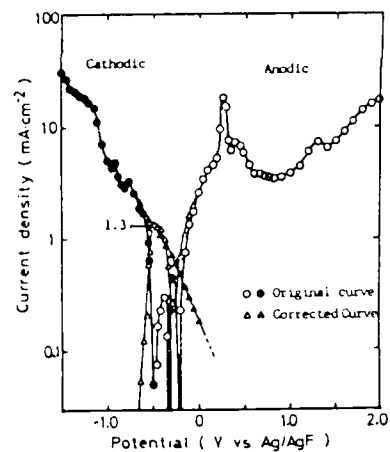
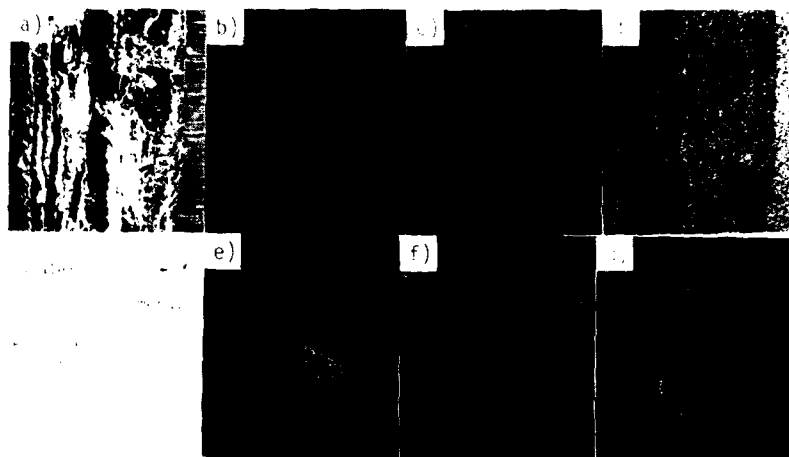
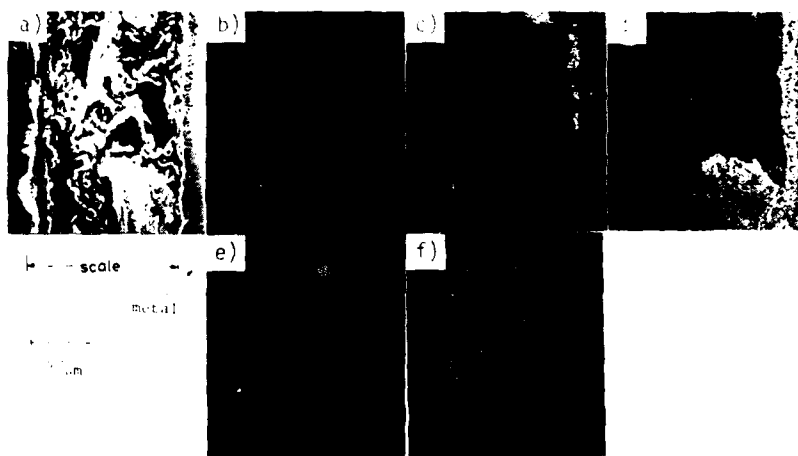


Figure 15. Polarization curve of Hastelloy-N(h.m.) in $\text{NaBF}_4\text{-NaF}$ at 700°C in air flow.



a) SEM Image b) Fe Image c) Cr Image d) Ni Image
e) Mo Image f) O Image

Photo. 1 Microscopic picture of the scale formed on Hastelloy-N(M,M) with $\text{NaBF}_4\text{-NaF}$ coating at 700°C , and map of elements.



a) SEM Image b) Fe Image c) Cr Image d) Ni Image
e) Mo Image f) O Image

Photo. 2 Microscopic picture of the scale formed on Inconel 625 with LiF-BF_2 coating at 700°C , and map of elements.

A DESIGN PRINCIPLE OF BIPOLAR ELECTRODES FOR ELECTROWINNING CELL FROM CHLORIDE MELTS

Tatsuo Ishikawa, Shoichi Konda and Toshio Narita

Department of Metallurgical Engineering,
Faculty of Engineering, Hokkaido University,
Kita-13, Nishi-8, Kita-Ku, Sapporo 060, Japan

ABSTRACT

A design principle of bipolar electrodes for liquid metal electrowinning cell was discussed theoretically. By taking into consideration of volume balance and homogeneous circulation of the chloride melt, general equations were deduced for determination of each sectional area of the bipolar electrodes. The values of design parameters were checked experimentally by operating the laboratory-scale cells constructed with the proposed design principle in which following variables were supposed to be known: the number of the inter-spacing reaction zones and a total sectional area of the cell, an average surface area and thickness of the bipolar electrodes, a distance between electrodes, specific conductivity of the chloride melts and decomposition voltage of aluminum chloride in the melt at various concentrations at operational temperatures.

INTRODUCTION

Experimental studies on the electrowinning of liquid aluminum from the chloride melts containing aluminum chloride in the bipolar electrode cells have been carried out for many years in our laboratory to develop a novel process for electric energy saving (1)-(3). This electrowinning process is the same in principle as that opened by Aluminum Company of America in 1973.

As well known, in the ALCOA bipolar electrode cell, all electrodes having a horizontal surface are stacked and also both products from the anode and the cathode move counter-currently in the cell. On the other hand, in the bipolar electrode cell developed in our laboratory the surfaces of the electrodes have a slope to the horizontal plane and so the anodic and the cathodic products can be separately moved in the cell.

In this paper, the prerequisite was firstly discussed for homogeneous circulation of the melt through the center holes, the inter-spacing reaction zones, and the periphery clearances in the bipolar electrode cell. The general equations were derived for determination of the

sectional areas of the bipolar electrodes stated above. According to these equations, nine kinds of bipolar electrode cells were constructed and the values of design parameters were checked by the laboratory-scale tests.

THEORETICAL

Prerequisites for homogeneous circulation of melts

At first, let us consider a circulating path of the chloride melt in the bipolar electrode cell under steady state conditions during electrowinning of liquid aluminum.

The chloride melt, replenished with aluminum chloride in the upper part of the cell, is flowing down through the center hole of the electrodes and enter into each of the inter-spacing reaction zones wherein aluminum chloride decomposes to liquid aluminum at the cathode and chlorine gas at the anode surface. The residual melt and the chlorine gas evolved will move toward the cell wall and then rise up as bubbles through the periphery clearance between the electrodes and the cell wall. Finally, the chlorine gas as bubbles transfer from the melt into gas phase at the upper part of the cell.

Driving force for such circulation of the melt is owing to the gas lift effect in the periphery clearance. Accordingly, in order to supply a fresh melt containing aluminum chloride into each of the inter-spacing reaction zones between the electrodes without any delay in all bipolar electrodes, it is necessary for the melt to move at a constant velocity by means of a gas bubble lift force irrespective of levels of the melt. For the prerequisite of a constant volume ratio of the melt and the gas, bubbles have to be maintained at any level of the melt within the periphery clearances. As shown in Fig.1, this condition can be satisfied by making decreases of both sectional areas of center holes and periphery clearances in integer series. However, it is not so easy to determine practically these values because each of the electrode surfaces, which gives directly the gas volume from the anode, has to be determined from difference between the sectional area of the cell and the area summation of the center hole and the periphery clearance. The latter area is also dependent upon the gas volume. Therefore, it seems that an universal design principle for construction of the bipolar electrode cell is essential and will be discussed in the next paragraph.

Design rules of bipolar electrodes

The volume of chlorine gas evolved from anode surface is proportional to the effective current I_E through the bipolar electrode. This gas volume seems to be almost independent of the bipolar electrodes because the effective current is expressed to be nearly the same as those for all of the electrodes. Since the value of I_E can not be measured directly,

the value of an applied current I_T was used tentatively instead of the I_E value.

Taking the gas volume evolved from the anode surface into consideration, the following relationship should be obtained at the lowest bipolar electrode.

$$S_g^0 \times i_g = \bar{S}_E \times i_T \quad (1)$$

In this equation S_g^0 is a sectional area occupied by the gas bubbles in the periphery clearance at the lowest bipolar electrode. i_g is a current density which is defined as the current through the bipolar electrode divided by the cross sectional area of the gas bubbles, which can move upward smoothly in the periphery clearance. \bar{S}_E is an average surface area of the electrodes, and i_T is an applied current density. The value of \bar{S}_E in equation (1), which can be finally obtained after decision of all parameters, might be assumed to equal that at the middle level of the bipolar electrodes, namely, the $n/2$ bipolar electrode, because the bipolar electrodes have a similar shape to each other and vary their sizes systematically.

At the $n/2$ bipolar electrode at the middle level, a total sectional area of the cell vessel S_T is given by the following relationship,

$$S_T = S_E^{n/2} + (n/2) \cdot (S_C^0 + S_P^0 + S_g^0) \quad (2)$$

where S_C^0 and S_P^0 are sectional areas for the center hole and for the melt in the periphery clearance, respectively, at the lowest bipolar electrode as defined for S_g^0 .

In order to represent these areas of S_C^0 and S_P^0 as a function of S_g^0 two additional parameters were newly introduced, namely,

$$V_g = S_P^0 / S_g^0 \quad (3)$$

and

$$V_m = S_C^0 / S_P^0 \quad (4)$$

In these equations V_g denotes the sectional area ratio of the melt to the gas bubbles in the periphery clearance and V_m the sectional area ratio of the melt in the center hole to that of the periphery clearance. Substitution of the equations (3) and (4) into the equation (2) yields a following relationship.

$$S_T = S_E^{n/2} + (n/2) \cdot (V_g \cdot V_m + V_g + 1) \cdot S_g^0$$

$$= S_E^{n/2} + (n/2) \cdot (V_g \cdot V_m + V_g + 1) \times S_E^{n/2} \cdot (i_T / i_g) \quad (5)$$

Providing the values of n , i_T , i_g , V_g and V_m , the values of $S_E^{n/2}$ can be determined for the cell with a total sectional area of S_T as follows:

$$S_E^{n/2} = S_T / [1 + (n/2) \cdot (V_g \cdot V_m + V_g + 1) \times (i_T / i_g)] \quad (6)$$

$$S_g^0 = S_E^{n/2} \cdot (i_T / i_g) \quad (7)$$

By using the equation (7), sectional areas for the electrode surface S_E^m , the center hole S_C^m , and the periphery clearance ($S_g^m + S_p^m$) can be determined by following equations and schematically shown in Fig.2.

$$S_E^m = S_T - m \cdot (V_g \cdot V_m + V_g + 1) \cdot S_g^0 \quad (8)$$

$$S_C^m = m \cdot V_g \cdot V_m \cdot S_g^0 \quad (9)$$

$$(S_p^m + S_g^m) = m \cdot (V_g + 1) \cdot S_g^0 \quad (10)$$

In these equations m is positive integer and denotes the number of bipolar electrodes stacked, that is, the electrode with number $m=1$ is the lowest bipolar electrode, which was opposite to an end-cathode connected with a DC supplier, whereas the electrode of number $m=n$ is an end anode. The aluminum particles are falling down through the center hole and nitrogen gas as a carrier gas is introduced along with aluminum chloride vapor. In the above consideration these effects of volume of aluminum particles and carrier gas were ignored for the volume and lifting velocity of the melt. Furthermore, it was assumed that the gas bubbles were completely separated from the melt into the gas phase at the top level of the melt.

EXPERIMENTAL

Electrode

The bipolar electrodes, both end-anode and end-cathode and terminals were cut from a graphite rod to possess fifty four kinds of the electrode shapes specified according to the design rule stated in the preceeding section. The parameters adopted for the cell design are as follows:

Total sectional area of the quartz cell vessel, S_T , is 100.3 cm^2 ; number of the inter-spacing reaction zones, n , is five. The applied current density, i_T , is 1.0 A/cm^2 and the value of i_g is supposed to be 75 A/cm^2 . Two parameters of V_g and V_m are variable, i.e., 2, 3, and 5 for V_g as well as 0.4, 0.7, and 1.0 for V_m , respectively.

As one of the examples, the horizontal sections of each electrode designed for $V_g=3$ and $V_m=0.4$ are given in Fig. 3. In the cell design, a diameter for the smallest center hole was determined to allow aluminum particles drop from the cathode surface without any interference, and also the largest bipolar electrode limited its diameter within the allowable difference between thermal expansion coefficients of the cell wall and electrode materials. The electrolytic cell consisted of a transparent quartz tube, 113 mm in diameter and 1 m in length, and is heated externally by a nichrome wire wound furnace with an electric power capacity of 4 kw. To look at the inside of the cell during electrolysis a long rectangular window was scooped through the furnace bricks. Further, this furnace is possible to be divided into four blocks and surrounded by the separable walls for heat-insulation. The structure of the cell and the furnace are represented schematically in the center region of Fig. 4.

Melt preparation and supply of aluminum chloride

The mixture of magnesium chloride and sodium chloride in the proportion of 25 and 75 mol% was used as a solvent melt with a melting point of 660°C . The solvent melt was firstly melted in additional furnace and then poured into the cell at about 700°C . The bottom of the quartz tube cell was self-sealed by freezing of the melt and sodium chloride granules at relatively low temperatures. The total amount of the solvent melt is about 4.5 Kg in each run.

From the results obtained in our previous studies, it was found that the concentration of aluminum chloride in the melt has to be kept as low as possible during electrolysis at 750°C in order to establish high current efficiency and low bath voltage. In this investigation an automatic supplier of aluminum chloride was developed after several modifications. This new equipment consisted of a large glass container for aluminum chloride and a vibrational rotary feeder. As shown in Fig. 4, solid particles of aluminum chloride first fall down through the rotary feeder into the melt composed of sodium chloride and aluminum chloride mixtures. The aluminum chloride is able to vaporize and is purified at the same time since the impurities accompanied by the aluminum chloride remain in the melt in the boiler. Aluminum chloride vapor can be transferred by nitrogen gas stream into the melt in the electrolytic cell. The amount of aluminum chloride supplied in this way can be precisely determined by monitoring the weight of whole system of aluminum chloride supplier; also the supply rates were controlled easily by using the rotary feeder with various revolution rates.

Exhaust of chlorine gas

As shown in Fig. 4, chlorine gas evolved during electrolysis will move toward the 10% sodium hydroxide solution through the exhaust systems by pumping with an aspirator under nitrogen gas stream used for supply of aluminum chloride into the cell. Aluminum chloride from the cell and other volatile matters were collected in glass condenser and plastic separator connected to the exhaust system.

Electrolytic procedures

Prior to the start of electrolytic experiment, pre-electrolysis was carried out for 30 minutes in order to remove the impurities contained in the solvent melt. Then aluminum chloride was supplied into the melt, according to the procedures described. After the concentration of aluminum chloride in the melt reached an appropriate level, aluminum electrolysis was commenced and continued for five hours.

During the electrolytic experiment, bath voltage was recorded every 3 minutes, and the relationships between applied currents and bath voltages were measured every 30 minutes. At the same time, a small amount of the chloride melt was sampled for chemical analysis of aluminum chloride, and also the sodium hydroxide solution was exchanged to determine the total amounts of chlorine gas evolved during electrolysis in the 30 minute intervals. After a run, the melt was exhausted from the bottom of the cell by melting down the self-sealed salt.

RESULTS

Several examples of the relationship between the applied current and bath voltage are given in Fig. 5 for different design parameters. From the results shown in the figures, it was clearly observed that every bipolar electrode can be operated in a so-called multi-cell when the bath voltages are larger than about 10 V.

In the intermediate range of the applied current the bath voltage is directly proportional to the applied current, whereas with increase in the applied current the deviation of the bath voltage from the linear relationships was demonstrated, shifting toward higher values. It seems that this deviation is due to the gas bubbles that can not rise smoothly through periphery clearance due to its great volume.

DISCUSSION

The linear relationship between the applied current density and the bath voltage could be determined theoretically according the calculative procedures (3,4), providing physico-chemical properties of the chloride

melt. As shown in Fig.5, the calculated bath voltages for various applied current densities obey the linear relationship between them. The linear relationships calculated for nine kinds of the bipolar electrode cells were compared with the experimental results obtained for fifty four cases. From these comparisons it was found that the calculated relationships were in fairly good agreement with the experimental ones for the cases of relatively small values of V_g and V_m .

Meanwhile, with increases in these values of V_g and V_m , the calculated results tended to deviate from the experimentally determined ones as demonstrated in Fig.5 for the case of $V_g = 5$ and $V_m = 0.4$. It can be considered to arise from the heterogeneous distribution of the by-pass current through the periphery clearance.

As shown in Fig.5, in the large values of the applied current the deviation of the bath voltage was observed from the linear relationship between them. The upper current density, at which the deviation was initially observed, was denoted as the i_T^{up} in the present investigation.

Figure 6 shows the dependencies of V_g on the upper current density obtained for various values of V_m . The effective current, I_E , which corresponds to the rate of gas evolution at the lowest bipolar electrode, was calculated with the modified equivalent circuit (3) at the upper applied current I_T^{up} . The value of I_E was firstly divided by the area of the periphery clearance at the lowest bipolar electrode and further divided by the value of i_T^{up} . In order to reexamine the value of i_g , which was 75 A/cm^2 at $i_T = 1.0 \text{ A/cm}^2$, the current densities for smooth gas lift obtained above, i_g^0 , were calculated for various values of V_m . It was found that the values of i_g^0 varied from 50 to 60 A/cm^2 with increase of V_g , irrespective of the values of V_m . Therefore, the value of 60 A/cm^2 should be used for the design of the bipolar electrode cell.

CONCLUSION

In the present study the design principle was first considered for the bipolar electrode cell. In the experimental study the bipolar electrode cells with five units were constructed with the proposed design principle and then operated for electrowinning of liquid aluminum from the chloride melts at 750°C .

It was demonstrated for the moderate values of V_g and V_m that the calculated and observed relationships between the bath voltage and the applied current density are fairly in good agreement. However, with increases in both the values of V_g and V_m , the calculated relationships tend to deviate gradually from the observed ones. This means that the by-pass resistance, R_S , in the equivalent circuit (3) might be changed because of the heterogeneous distribution of by-pass current in the periphery clearance of the bipolar electrode cell.

It is worthwhile to note from the point of view for saving energy that the applied current should exist within the linear relationships between the bath voltage and the applied current, and the cell design parameters such as V_g , V_m , i_g and i_T should be selected as low as possible to avoid decrease in the cell efficiency of the bipolar electrode cell and increase in the bath voltage.

REFERENCES

1. Ishikawa, T. and Konda, S., Bulletin of the Faculty of Engineering, Hokkaido University, No.110, 107 (1982).
2. Ishikawa, T. and Konda, S., DENKI KAGAKU, 51,199 (1983).
3. Ishikawa, T. and Konda, S., Proc. of the First International Symposium on Molten Salts Chemistry and Technology (Kyoto), p.5 (1983).
4. Ishikawa, T., YOUYUEN (Fused Salt), 28, No.3, 197 (1985).

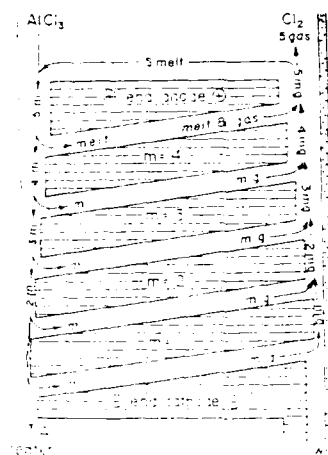


Figure 1. Circulating Path of Melt in each section of the bipolar electrolytic cell.

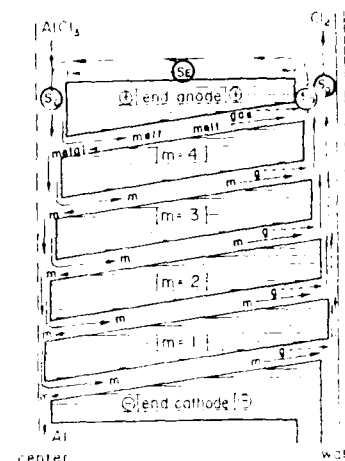


Figure 2. Constitution of total sectional areas in the bipolar electrolytic cell.

$Q = 1, V_0 = 0.4$ diameter of cell = 113 mm
 $r = 10.4 \text{ cm}, r_0 = 75.4 \text{ cm}, s_0^2 = 14 \text{ cm}^2$

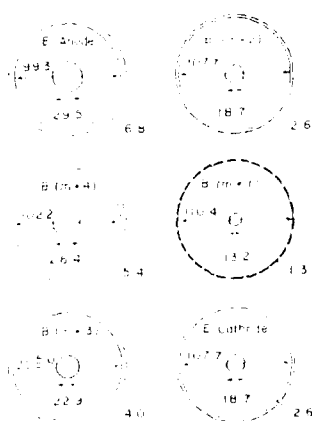


Figure 3. An example of horizontal sections in the bipolar electrolytic design.

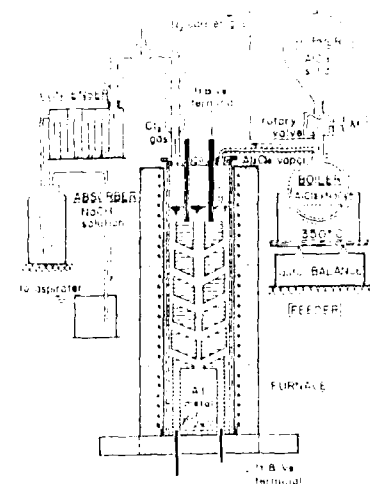


Figure 4. Schematic diagram of experimental apparatus.

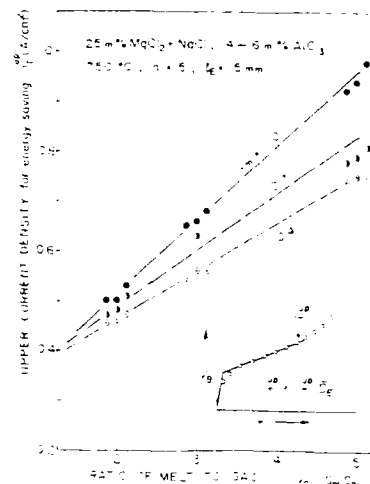
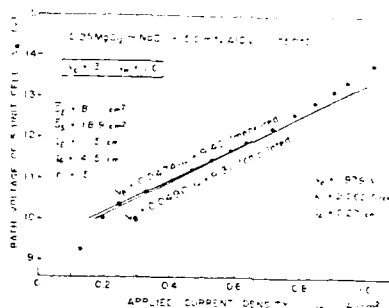
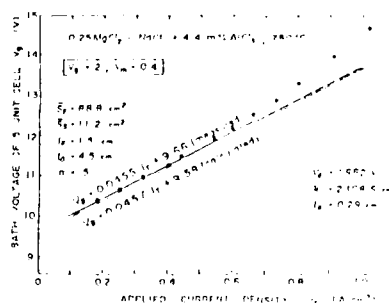
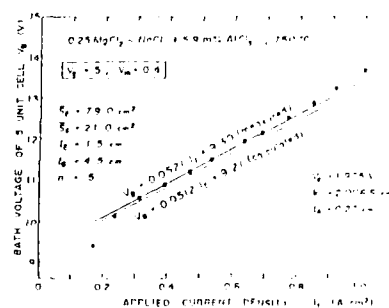


Figure 4. Relationship between Upper Current Density and ratio of melt to gas.

Figure 5. Relationship between Bath Voltage and Applied Current Density for the Design Cell.

A STUDY OF THE ELECTROCATALYTIC ACTIVITY OF DOPED
CARBON ANODES IN CRYOLITE-ALUMINA MELTS

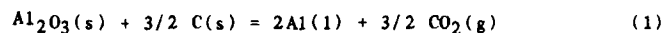
Liu Yexiang, Xiao Haiming, and Liu Longyu
Dept. of Metallurgy
The Central South Univ. of Technology
Changsha, China

ABSTRACT

The anodic overvoltage of a carbon anode in the existing aluminium electrolysis process is 0.4-0.6V. This paper aims at reducing the anodic overvoltage for saving energy by increasing the catalytic activity of the carbon anode with dopants. The anodic overvoltage of carbon anodes in $\text{Na}_3\text{AlF}_6\text{-Al}_2\text{O}_3$ (sat) melt was measured by using a steady state technique. Obvious electrocatalytic activities were observed on the carbon anodes with Ru, Cr, and Li dopants. The anodic overvoltage was reduced more than 0.2V under the industrial current densities. The estimated energy saving will be 6.0% when using this technique. A primary discussion related to the function of dopants in the carbon anode and the mechanism of the aforementioned electrochemical process is given also.

INTRODUCTION

Carbon is almost the only material employed for anodes in the production of aluminium by electrolysis in a bath of cryolite alumina melt. The major cell reaction is



with a standard reversible potential of 1.13V at 1273K. According to the results obtained from laboratory tests and industrial cells, the counter electromotive force (cemf) of the cell is 1.6-1.7V higher than the standard reversible potential. The difference between the cemf and the reversible potential, i.e., the polarization potential, equals the sum of the cathodic overvoltage and the anodic overvoltage. Many measurements have shown that the cathodic overvoltage of the existing aluminium reduction cell is very low, around 40-80 mV(4). Therefore, the polarization potential is mostly attributed to the anodic overvoltage (η_a) and is as high as 0.4-0.6V. The later results in a great deal of electrical energy loss. How to reduce the anodic overvoltage in the Hall-Heroult process is very interesting, but very few reports on investigations of this aspect have been published. According to the electrocatalytic prin-

ciple in aqueous solution, it is possible to reduce the η_a by doping the carbon anodes for aluminium electrolysis with electrocatalysts. The effects of some dopants on the electrocatalytic activity of the carbon anode in cryolite alumina melts was studied.

EXPERIMENTAL

Preparation of anodes with dopants

Pure spectrographic graphite rods ($\phi 10$ mm) were employed as anodes. Catalysts were (A.R.) CrCl_3 , MnCl_2 , CoCl_2 , NiCl_2 , RuCl_3 , Li_2CO_3 , and NaCl . After cleaning and drying, the graphite rods were treated by a special doping method so that the catalysts were dispersed not only on the surface, but in the bulk of the graphite electrode. The same kind of graphite electrodes but without dopants were also used in measurements for comparison. The effective area of the graphite anode tested was $0.78\text{--}0.79\text{ cm}^2$.

Measurement technique

Steady state polarization curves were recorded on a X-Y recorder by using a potential step generator (XFD-8) and a JH-2C potentiostat. Scan rates of $10\text{--}20\text{ mV/sec}$ were found to be suitable for increasing as well as decreasing the potential. The reference electrode was a graphite electrode, which was protected by an alumina tube. A graphite crucible containing 100 g of cryolite alumina melt was the counter electrode (3).

Reference electrode

Many workers (4-6) have reported that the graphite electrode, when equipped properly, is stable and can be used as a reference electrode. The graphite electrode, which does not require flushing with gas, is very convenient and simple. We adopted it in this work. It is necessary to evaluate the stability of the electrode. Two identical graphite electrodes were dipped into cryolite melt and the deviation of the potential difference between them versus time was measured. The results showed that the potential deviation is within 8 mV for a long time (5 hours), which proved that this kind of reference electrode was reliable.

RESULTS AND DISCUSSION

Typical steady anodic polarization curves for graphite electrodes with different dopants are presented in Fig. 1 and Fig. 2.

At the beginning of a measurement prior to electrolysis, it was found that the open circuit potential of the working electrode and counter electrode vs the reference, respectively, was very close. After polarization, the potential of the counter electrode vs the reference electrode still remained unchanged. Due to the large area

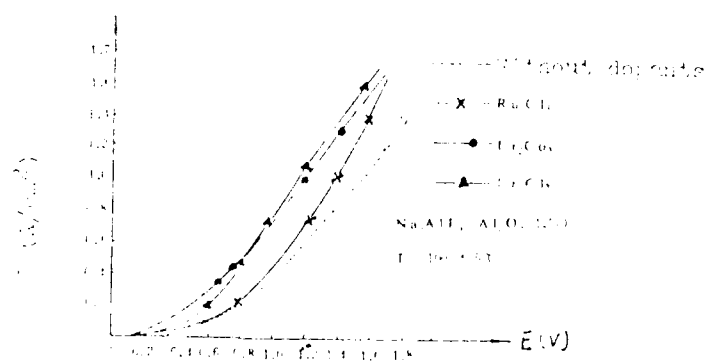


Fig. 1 Tafel polarization curves for graphite anodes with different depolarizers.

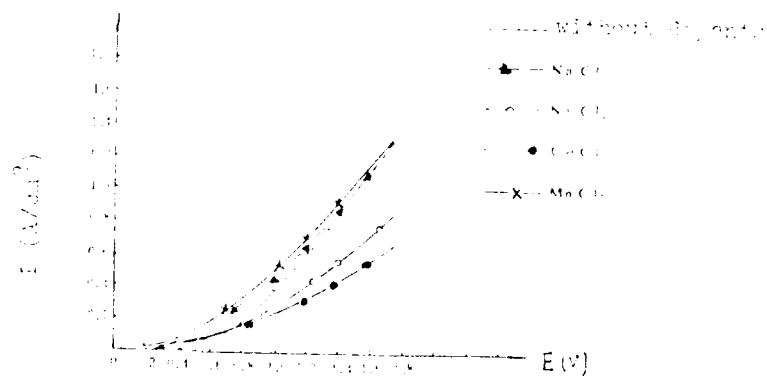


Fig. 2 Tafel polarization curves for graphite anodes with different depolarizers.

of the counter electrode (graphite crucible), much polarization occurred only on the anode during electrolysis.

To obtain the anodic overvoltage (η_a), the standard reversible potential at the temperature tested for reaction (1) (1.13V) was subtracted from the polarization data (anode-reference). The overvoltage data for graphite anodes with different dopants under industrial current density are presented in Table I.

Table I Overvoltages on graphite anodes with different dopants at industrial current densities
(Na_3AlF_6 - 12% (wt) Al_2O_3 , $1000 \pm 5^\circ\text{C}$)

I η_a doping (M)	Current Densities (A/cm^2)				
	0.70	0.85	1.00	1.15	1.30
none	0.147	0.286	0.424	0.562	0.690
RuCl_3	0.064	0.136	0.212	0.286	0.360
CrCl_3	-0.112	0.011	0.135	1.258	0.382
MnCl_2	0.099	0.229	0.357	0.486	0.615
NiCl_2	0.339	0.487	0.636	0.789	0.903
NaCl	0.176	0.283	0.390	0.497	0.604
CoCl_2	0.487	0.730	0.917	1.215	1.459
Li_2CO_3	-0.130	0.105	0.249	0.393	0.537

* Ohmic voltage drop was not eliminated.

Electrocatalytic activity of the carbon anode

Oxygen and fluorine containing ions discharged on a carbon anode in the aluminium electrolysis reaction process would produce various intermediate compounds such as CFO . Because of the mechanism of this anodic process is quite complicated, it is not suitable to identify the electrocatalytical activity of the electrodes by means of the reaction kinetic parameters obtained from the above tests. In order to evaluate the electrocatalytic activities of various anodes, a comparison of the anode overvoltage at constant current density is a better criterion. The lower the anodic overvoltage the better the electrocatalytic activity.

It is evident from the data in Table I as well as from Fig. 1 and Fig. 2 that some of the doping agents have a remarkable electrocatalytic effect on the anodic reaction. In particular, CrCl_3 , Li_2CO_3 and RuCl_3 have a strong positive effect, the anodic overvoltage at 1.0 A/cm^2 being reduced by 0.2V compared with no dopant in the electrode. MnCl_2 and NaCl are also beneficial. Doping with NiCl_2 and CoCl_2 has a negative influence. The electrocatalytic function of carbon anodes with dopants may result from changes in the stoichiometry, valence, crystal structure nature of conduction and surface states. Generation of more active sites in the bulk carbon after doping would be favorable to the adsorption and discharge of oxygen containing ions, which may result in a higher rate of anodic reaction or lower overvoltage. Following Rao's (6) studying on the burning process of carbon and the catalysis of the Boudouard reaction, Li_2CO_3 had a strong catalytic effect on the burning of carbon. This agrees with the effects of doping Li_2CO_3 into carbon anodes in present work. In fact, the anodic reaction on carbon anodes in the aluminium electrolysis process is an electro-oxidation reaction of carbon (7).

The lifetime of the electrocatalytic activity of doped carbon anodes

The lifetime of the electrocatalytic activity of a doped carbon anode is important for its application and worthy of study. The results obtained are shown in Fig. 3.

Both anodes with dopants and without dopants were polarized at

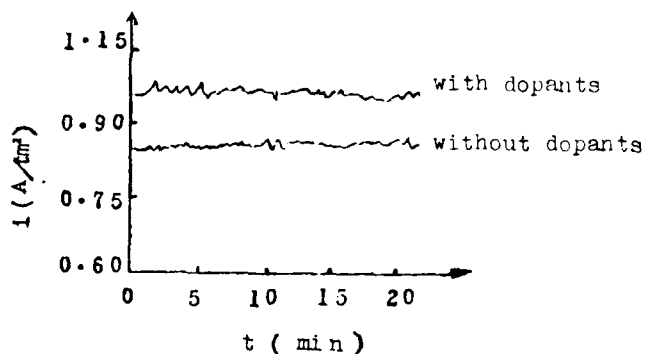


Fig.3 The lasting time of electrocatalytic activity of doped carbon anode ($E = 1.4 \text{ v}$)

the same potential ($E = 1.4\text{V}$). A higher current density was observed to pass through the doped anode. As shown in Fig. 3, no electrocatalytic activity decline was observed on the well prepared doped anodes within the test period. With a few exceptions, the

electrocatalytic activity of some doped carbon anodes began to decline after several minutes. This may be ascribed to both degeneration of the electrocatalyst and to the low probability that the catalyst could remain in the anode during the consumption of the carbon anode. Especially, when the doping agents were not distributed homogeneously inside the bulk of the electrode or distributed mainly on the surface of anode, the electrocatalytic activity of the anode obviously declines. In this case, adopting an inert anode to replace the existing carbon anodes in aluminium electrolysis will be advantageous, because the anodes will not be consumed and the catalysts will be present for a longer time. Although carbon anodes are consumable, this doping technique, which is simple and can be adapted to industrial use with ease, is available and exhibits good prospects as a technique for saving energy.

Estimation of the power saving resulting from reduction of the overvoltage on carbon anodes

In aluminium electrolysis, the power required per ton of metal produced is calculated as:

$$P = 2980 \frac{V_c}{CE} \quad (\text{KWH/T}) \quad (2)$$

where CE = current efficiency (decimal);

V_c = average pot voltages, (volts).

$$V_c = E^0 + \eta_a + \eta_c + \Sigma IR$$

where E^0 is standard reversible potential; η_a and η_c are anodic and cathodic overvoltage, respectively; I is the current; ΣR is the sum of ohmic resistances of electronic and ionic conductors in the cell. When all other condition are kept constant, energy saving can be realized by reducing the η_a . The estimation of energy saving per ton of aluminium produced at 0.85 A/cm^2 is presented in Table II. It can be seen that, as a consequence of adopting doped carbon anodes, the amount of electrical energy used can be reduced. The highest efficiency of saving energy is 6.0%.

Since the concentration of doping agents in the carbon anodes was very low, the aluminium produced would not be contaminated by them, especially in the case of doping with Li_2CO_3 . Lithium salts were always used as additives in Hall baths and there was no contamination problem.

The doping technique used in this test is very simple and can be realized in the anode workshop. Neither additional expense nor other equipment is needed. It is predicted that employing these techniques in the aluminium electrolysis industry will be beneficial.

However, the doping technique still needs study in order to select doping elements with a more extended range and to look for

Table II Estimation of energy saving by the
reducing of anodic overvoltage when
using doped carbon anode

Doping agent	anodic over- voltage at 0.85 A/cm ² _(v)	anodic over- voltage at reduced (v)	D.C. KWH/T	energy saving	
				KWH/T	%
none	0.286	0	15238	0	0
RuCl ₃	0.139	-0.147	14740	497	3.3
CrCl ₃	0.011	-0.275	14307	930	6.1
Li ₂ CO ₃	0.105	-0.181	14625	612	4.0
MnCl ₂	0.229	-0.057	15045	192	1.3
NaCl	0.283	-0.003	15228	10	0.06

* Estimated from Eq. (2) as $V_c = 4.5$ V, $CE = 0.88$

factors which prolong the lifetime of the electrocatalytic activity of the doped carbon anodes. Meanwhile, the mechanism of the electrocatalytic effect of dopants and the consumption of carbon anodes must also be considered.

REFERENCES

1. S. Trasatti and G. Lodi, in Electrodes of Conductive Metallic Oxides Part A, p. 301, Elsevier, Amsterdam, (1981).
2. Liu Yexiang, Non-Ferrous Metals (China), (quarterly), (1985), No 3, pp. 53-58.
3. Xiao Haiming, Liu Yexiang, Non-Ferrous Metals (China), (quarterly), (1986), No. 4, pp. 57-62.
4. K. Grjotheim, et al., Aluminium Electrolysis, Aluminium-verlag GmbH Dusseldorf, (1982), p. 200.
5. Zhang Mingjie, et al., Journal of Northeast Institute of Technology, (China), (1984), No. 1, pp. 46-50.
6. Y. K. Rao, Journal of Metals, (1983), No. 7, pp. 46-50.
7. W. E. Haupin and W. B. Frank, Comprehensive Treatise of Electrochemistry, Vol. II, Ed. by J. O. M. Bockris, et al., p. 309, Plenum Pub., (1979).
8. Liu Yexiang, Journal of the Central South Institute of Mining and Metallurgy, (1982), No. 3, pp. 66-73.

STUDIES OF THE ANODIC PROCESS AT SnO_2 -BASED ELECTRODES IN ALUMINIUM ELECTROLYSIS

Liu Yexiang and Xiao Haiming
Dept. of Metallurgy
The Central South Univ. of Technology
Changsha, China

ABSTRACT

The use of inert anodes and stable cathodes in the aluminium electrolysis industry is of important significance for saving energy.

The electrochemical characteristics of SnO_2 -based electrodes in aluminium electrolysis are interesting not only for understanding the mechanism of the anode process and inferring indirectly the structure of cryolite-alumina melt, but also for developing new techniques for aluminium metallurgy with inert anodes.

The anode process on SnO_2 -based electrodes in aluminium electrolysis has been studied by several electrochemical methods and some initial results have been obtained.

Prior to the above mentioned studies, a new reference electrode that is itself a SnO_2 -based electrode has been tested and inspected at the same time an aluminium reference electrode was employed. It was discovered that the potential of a SnO_2 -based electrode dipped into cryolite-alumina melt was stable for a long time and fluctuated within a few mV ($\pm 8\text{mV}$). The performance of a SnO_2 -based electrode was reproducible and reversible. As a reference electrode, its construction was simple, and it was convenient to use. The potential relationship between a SnO_2 -based electrode and an aluminium reference electrode could be expressed as follows:

$$E_{\text{SnO}_2} = 1.8062 - 0.3332 \log N_{\text{Al}_2\text{O}_3} - 5.1409 \times 10^{-4} T + E_{\text{Al}}$$

The anode overvoltage on a SnO_2 -based electrode was found to be 0.1-0.2V at industrial current densities by the steady state technique. The occurrence of two straight segments on the anodic Tafel plot implied a two-step oxygen discharge reaction.

The linear potential sweep curves obtained from a SnO_2 -based anode showed that oxygen and fluorine discharged separately. No anode effect appeared at high current densities ($i = 12 \text{ A/cm}^2$), which could be explained from the good wetting of SnO_2 materials by the molten electrolyte.

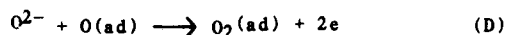
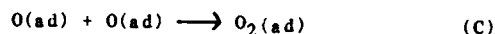
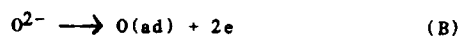
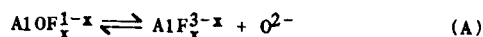
According to chronogalvanic measurements, oxygen evolution on a SnO_2 -based anode was a irreversible process. The current-time relation could be described as follows

$$I = nFAKC \exp\left(\frac{K_f^2 t}{D}\right) \left(1 - \int_0^y K_f t^{1/2} / D^{1/2} e^{-y^2} dy\right)$$

where $K_f = 0.001 \text{ cm s}^{-1}$.

It has been discovered from chronopotentiometric measurements that the oxygen evolution on a SnO_2 -based electrode was an irreversible process preceded by a chemical reaction. The values of K , K_f , and K_b involved in this chemical reaction could be calculated ($K = 0.6$, $K_f = 750.8 \text{ s}^{-1}$, $K_b = 1251.5 \text{ s}^{-1}$) where K was the equilibrium constant of the reaction, K_f was the rate constant of the forward reaction, and K_b was that of the backward reaction. Also $\beta_{n_a} = 0.85$ was obtained from the chronopotentiometric technique. In the case of $\beta_{n_a} = 0.5$, thus $n_a = 1.7 = 2$. It appeared that there were two electrons transferred in the rate-determining step.

Based on all the results obtained from different electrochemical measurements, the mechanism of oxygen evolution on the SnO_2 -based anode was thought to be



(B) was the rate-determining step.

ELECTRIC FIELD IS CALCULATED BY SOLVING LAPLACE'S EQUATION
ON A CYLINDRICAL GRAPHITE ANODE IN MOLTEN NaF AND Na₃AlF₆.

Christiane Brunet and Pierre Mergault

Laboratoire de Physique des Liquides Ioniques,
Université Pierre et Marie Curie, Tour 15,
4, Place Jussieu, 75252 PARIS CEDEX 05, FRANCE.

ABSTRACT

We have shown repeatedly in our laboratory (1.9) and it is confirmed by some recent papers (10.13) that the surface of the graphite anode available for electrolysis diminishes when time increases; this produces a growing resistance R in the cell and an increasing current density (the role of fluorine in the insulation phenomenon of the anode is of prime importance). To calculate R , Laplace's equation is numerically resolved to have a potential map of the cell, whence $\vec{E}, \vec{J} = \gamma \vec{E}, I = \int \vec{J} \cdot d\vec{S}$, $R = V/I$. In any case, the ultimate step before anode effect occurs, is the insulation of the anode by vaporization of the liquid near the surface of the not yet insulated anode.

EXPERIMENTS AND RESULTS

We showed (5,7) that the ohmic drop R_a on an anode measured at the interruption of the current, is greater after an electrolysis of molten NaF or Na₃AlF₆ between graphite electrodes (in our case, the crucible and a central electrode with a symmetry of revolution around a common vertical axis, see fig.1) and even before anode effect (AE) occurs; the anode may be one of these two electrodes. This anodic ohmic drop is not a constant and can reach very high values whereas on the cathodic side, the ohmic drop R_c is small and constant: this last result permits to assert that the bath does not significantly change.

When AE occurs, the current intensity I observed for example on a storage oscilloscope display, decreases down to zero or almost. A discussion of this experimental result shows that $I = 0$ if the anode is completely

surrounded by an insulating sheath and then, $R = R_0 + R_1$ is infinite (2). As a consequence of these experiments, we may interpret the high values of the ohmic drop on the anode side as due to a partial coverage of the anode by an insulating sheath. This first supposition is quite logical and does not imply any hypothesis concerning the nature of this sheath (adsorbed sheath, gaseous sheath, and so on...)

RESOLUTION OF THE LAPLACE'S EQUATION

Then it is necessary to have a relation between the insulating coverage of the anode, $\theta = S_1/S$ (with $S = S_1 + S_2$, where S is the whole surface of the anode, S_1 the surface of the insulated part and S_2 the "free" surface of the anode, that is to say the surface allowing the passage of the current between bath and graphite) and R . Since there is no analytical solution of Laplace's equation, $\Delta V = 0$, for the geometry we used, we calculate R for a given coverage θ by numerically solving $\Delta V = 0$ in order to obtain a potential map with the V values at every point of a regular network. Then we can deduce the electric field \vec{E} , and by assuming γ constant in the whole bath, we have \vec{J} by Ohm law, $\vec{J} = \gamma \vec{E}$, $I = \int_S \vec{J} \cdot d\vec{S}$ and $R = V/I$.

Some more assumptions are yet necessary to simplify the calculation:

1-Thermal and electrical conductivities are constant throughout the bath.

2-The electrical conductivity of the bath γ_b being very much smaller than the graphite one γ_g , $\gamma_g/\gamma_b \approx 500$, we may consider γ_b as infinite. This hypothesis permits to have \vec{E} and \vec{J} perpendicular to the "free" surface of the anode (the electric field in the bath near the insulated surface of the graphite is tangential to this surface).

3- S_1 is an increasing function of time, that is to say that we do not take account of the usual statistical aspect of the coverage phenomenon.

4-The increase dS_1 of the insulated graphite surface part S_1 at a given time occurs to the detriment of S_2 , $S_1 + S_2 = S$ leads to $dS_1 + dS_2 = 0$, on those parts of S_2 where $|\vec{J}|$ is maximal. This hypothesis permits to keep the symmetry of revolution of the problem.

5-This "mechanism" of anode coverage is quite different from that observed by T.Utgard and J.M.Toguri (1) wherein the underside of the anode is first insulated from the bath by a large gas bubble. To take account of this experimental result, we take a S value which does not comprise the anode underside surface.

Even in this framework, the solution of Laplace's equation is analytically impossible and we have resorted to numerical calculations. These calculations are carried out for different values of the coverage in a frame of cylindrical coordinates with the z axis coinciding with the symmetry axis. Then the Laplace's equation becomes:

$$\Delta V = (1/r)(dV/dr) + (d^2V/dr^2) = 0.$$

In doing so, we used the Frankel-Young method while using an optimisation factor determined by the Gauss-Seidel method (14,15) and with a network of 3744 points (the distance between two nearest points is 0.5mm in the bath): thus we obtain the curve of figure 2. In a recent paper (16), we showed that even if the surface of an electrode is progressively insulated by an electrochemical process, as is the case for a graphite anode in molten fluorides or chlorides, there is always a time after which the Joule effect gets to play a leading role in making up the layer needed for a complete insulation of the electrode (electrode effect (EE) onset). It is straightforward in the case of electrode effects (EE) without electrochemical (or chemical) insulating of the electrode and the demonstration is very easy in the case of an electrochemical insulating coverage proportional to the quantity of electricity:

$$dQ = I \cdot dt = -k \cdot dS,$$

where k and I are constant (this condition fulfills the hypothesis 3- and 4- above): this demonstration is also valid for $\alpha < 2$ when we have:

$$Q = k \cdot (S_0 - S)^{\alpha} = I \cdot (t - t_0),$$

although it is very difficult to think up an electrochemical process with $\alpha > 1$.

DISCUSSION

At first view, it seems that it is necessary to take into consideration the heat of vaporization of the bath in the calculation of the induction time of EE. But in the case wherein there is no gaseous emittance on the considered electrode, the constitution of an insulating gaseous layer around the electrode in question corresponds to the theoretical and experimental intervals of induction time of the EE. This shows that we do not have to take into account the vaporisation heat (17). This interpretation remains valid for fused salts (4) and, in particular, for fluorides baths.

REFERENCES

1. P.Mergault and C.Brunet, C.R.Acad.Sc.Paris, **269**, 1, 102, (1969).
2. P.Mergault, J.C.Valognes, D.Lefebvre, J.Garbarz-Olivier and C.Guilpin, 23rd I.S.E. Meeting, Stockholm, 1972, Abstracts, p. 345.
3. P.Mergault, C.Brunet and J.C.Valognes, C.R.Acad. Sc. Paris, **275**, C, 601 (1972).
4. C.Guilpin and J.Garbarz, Thermochim. Acta, **13**, 467 (1975).
5. C.Brunet-Lefort, These d'Etat, Université Pierre et Marie Curie, Paris (1977).
6. C.Brunet and P.Mergault, 30th I.S.E. Meeting, Trondheim (Norway) Abstracts, p.167 (1979).

7. C.Brunet and P.Mergault, Rev. Int. Hautes Temp. Refract. (France), 20, 17 (1983).
8. C.Brunet and P.Mergault, International Symposium: Centenary of the Discovery of Fluorine, Paris, Abstracts, p.211 (1986).
9. J.C.Valognes, J.P.Bardet and P.Mergault, Spectrochim. Acta, 42 B, 445 (1987).
10. T.Utigard and J.M.Toguri, Light Metals 1986, New-Orleans, Proceedings of the technical sessions (Ed. by R.E.Miller), 405 (1986)
11. P.T.Hcugh and D.M.Novak-Antoniou, International Symposium: Centenary of the Discovery of Fluorine, Paris, Abstracts, p.211 (1986).
12. D.Devilliers, F.Lantelme and M.Chemla, International Symposium: Centenary of the Discovery of Fluorine, Paris, Abstracts, p.211 (1986)
13. D.Devilliers, F.Lantelme and M.Chemla, Electrochimica Acta, 31, 1235 (1986).
14. E.Durand, Electrostatique et Magnetostatique (Paris 1953), Ed. Masson et Cie.
15. E.Durand, Electrostatique, Tome I- Les Distributions. (Paris 1964).
Tome II- Problemes Generaux. Conducteurs (Paris 1966).
Tome III- Methodes de Calcul. Dielectriques (Paris 1966).Ed. Masson et Cie.
16. P.Mergault and C.Brunet, Proceedings of the First International Symposium on Molten Salt Chemistry and Technology p.B-105, Kyoto (Japan), 1983.
17. J.Garbarz-Olivier and C.Guilpin, C.R.Acad.Sc.Paris, 275 C, 1359 (1972).

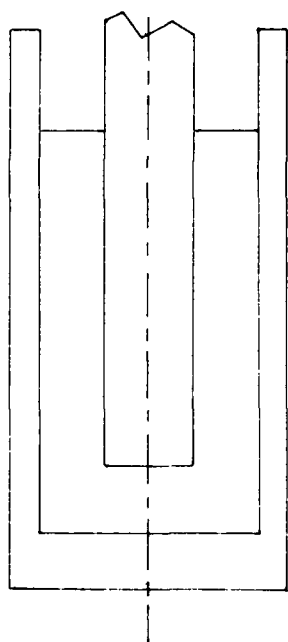
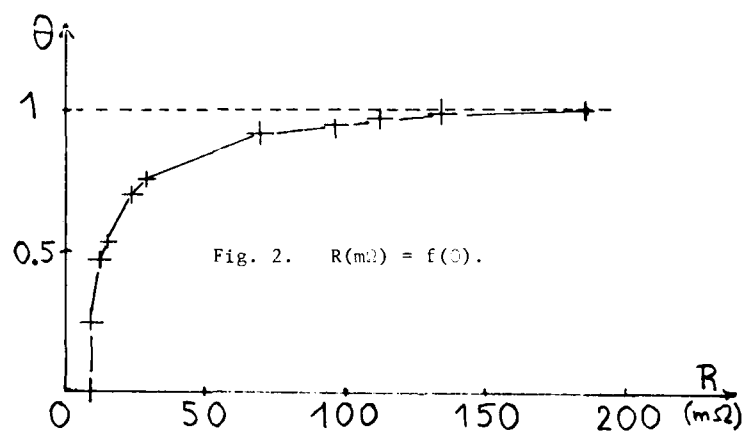


Fig. 1. Crucible:

$\varnothing = 50-40$ mm.

Central anode:

$\varnothing = 16$ mm.



THE INFLUENCES OF MgO ON THE DIFFUSION OF MAGNESIUM ION IN MAGNESIUM ELECTROLYSIS

Zhang Yueqiang, Lin Jingfu

Department of Non-ferrous Metallurgy
Northeast University of Technology,
Shenyang, Liaoning, CHINA

ABSTRACT

The influences of different sorts of magnesium oxide on the diffusion rate of magnesium deposition in the MgCl_2 - NaCl - KCl - CaCl_2 molten salt system have been investigated with a multiple electrochemical measuring system.

The variances of the limiting current density of the deposition of magnesium ion with the amount of MgO added have been measured with linear voltage scan methods. The diffusion coefficient and the diffusion reactivity energy of magnesium ion have been determined and the effects of MgO on them have also been studied.

It was shown that different sorts of MgO have different influences on the diffusion coefficient, and the MgO obtained from the hydrolysis of $\text{MgCl}_2 \cdot 6\text{H}_2\text{O}$ has the most obvious effects on it.

INTRODUCTION

Magnesium oxide has unfavourable effects on the electrolysis process of magnesium production. As a result of its tiny particles and strong reactivity, MgO, from the hydrolysis of the magnesium electrolyte in the electrolysis process, is prone to being absorbed by the cathode and causing the cathode to be polarized.

The present paper refers to the magnesium electrolyte system in industrial electrolysis and applies linear voltage scan electrochemical technique to study the influences of MgO on the diffusion coefficient and the limiting current density of the deposition of magnesium ion.

EXPERIMENTAL

Conditions

The chlorides used in the experiments were predried in oven, then in predried gaseous HCl until they were melted. The experiments were performed in atmosphere of argon at ambient pressure and at the temperature of 700°C.

Electrodes

The electrode system involved anode, working electrode and reference electrode. A stable Ag/AgCl reference electrode with ceramic diaphragm was used. The anode was made of spectral purity carbon and the working electrode of molybdenum.

The electrolyser was set in a quartz glass container.

RESULTS AND DISCUSSION

The Influences of MgO on the Diffusion Coefficient and the Limiting Current Density

Fig. 1 and Fig. 2 are respectively the linear voltage scan voltammograms at different scan rate with the electrolyte containing 0% (wt.) and 0.6% (wt.) MgO.

From the voltammograms we know that, at the same scan rate, the peak current density is obviously reduced after adding a small amount of MgO into the electrolyte, and the deposition voltage of Mg^{++} is also reduced a little vs. Ag/AgCl electrode. These all show that the MgO is absorbed by the cathode. Therefore, the diffusion of Mg^{++} to the cathode surface is impeded, the diffusion rate and the diffusion current density is lowered, and the cathodic concentration polarization is more obvious.

On the curves, it is also noticed that the peak current decreased correspondingly with the decrease of the scan rate. Based on the fundamental electrochemistry, the peak current (I_p) and the scan rate (V) satisfy the following electrochemical equation:

$$I_p = 0.661(nF)^{3/2}(D_0V/\pi T)^{1/2}AC_0 \quad (1)$$

Where A is the area of the cathode, D_0 is the diffusion coefficient (cm^2/sec) of reactant, and C_0 is the bulk

concentration (mol/cm^3) of reactant.

The plots of I_p vs. $v^{1/2}$ are shown in Fig. 3. The slope (t_{gA}) of a plot is derived from the equation (1).

$$t_{\text{gA}} = 0.661(nF)^{3/2}(D_0/RT)^{1/2}A C_0 \quad (2)$$

From the equation (2), the diffusion coefficient D_0 can be determined. The results are shown in Fig. 4.

Fig. 4 shows that the smaller the amount of MgO is, the more obvious the influences on the diffusion coefficient are. The similar effects on the limiting current density are shown in Fig. 5. With the adding amount of MgO increasing from 0% (wt.) to 0.3% (wt.), the diffusion coefficient D_0 and the limiting current density I_d decrease rapidly. Then, the amount increasing further, there is only a little decrease of D_0 and I_d . That is, the effects of MgO become weaker and weaker.

According to the analysis above, it is assume that the increase of the absorbed MgO film on the cathode ceased when the MgO increased to a certain amount. On one hand, the film obstructs the diffusion of magnesium ion to the cathodic surface. On the other hand, it also obstructs the further absorption of the cathode.

The Diffusion Activation Energy

Generally, the diffusion coefficient D_0 increases with the temperature, and they observe the following equation:

$$\ln D_0 = A - (W/nT)$$

Here A is a constant, W is the diffusion activation energy. With the electrolyte containing 0.3% (wt.) MgO , the magnesium diffusion coefficients were measured with linear voltage scan method at different temperatures. And the plot of $\ln D_0$ vs. $1/T$ is shown in Fig. 6. From the slope of this plot, the diffusion activation energy was calculated to be 3200 cal/mol.

The Influences of Different Forms of MgO

The reactivity of MgO is related to the method and process of its production. The experiments of the influences of agent MgO , hydrolysis MgO and MgOHCl on the diffusion of magnesium ion have been made. The results are shown in Fig. 7.

Like the preceding discussion, all the magnesium oxides have apparent influences on D_0 with the amount of MgO ranging from 0% to 0.3% (wt.). At the same amount, the influence of hydrolysis MgO on the D_0 is the most, the $MgOHCl$ influence is smaller, and the agent MgO one is the smallest. The differences of the influences show that there are different reactivities with different sources of MgO .

The apparent reactivity of $MgOHCl$ is smaller than the hydrolysis one. Actually, $MgOHCl$ will rapidly decompose and produce MgO at the experimental temperature when it is added into the electrolyte so that the influences really are performed by MgO . The weight ratio of MgO to HCl is about 1:1. If $MgOHCl$ is almost completely decomposed, 0.3% (wt.) $MgOHCl$ will produce 0.15% hydrolysis MgO . Based on this hypothesis, the curve of D_0 ($MgOHCl$) vs. MgO (produced from the decomposition of $MgOHCl$) have been made out. As shown in Fig. 8, it is very closed to the curve of hydrolysis MgO within 0.6% (wt.) $MgOHCl$. The similarity of the two curves shows that most of the $MgOHCl$ decomposes into MgO instead of the $MgOH^+$ ion. The fact that there is only a small current peak of $MgOH^+$ on the wide range linear voltage scan voltammogram is one of the evidences for the hypothesis, too.

CONCLUSION

MgO , the impurity in the electrolyte, is absorbed on the cathode and cause it to be polarized. Therefore, the limiting current density and the diffusion coefficient are lowered.

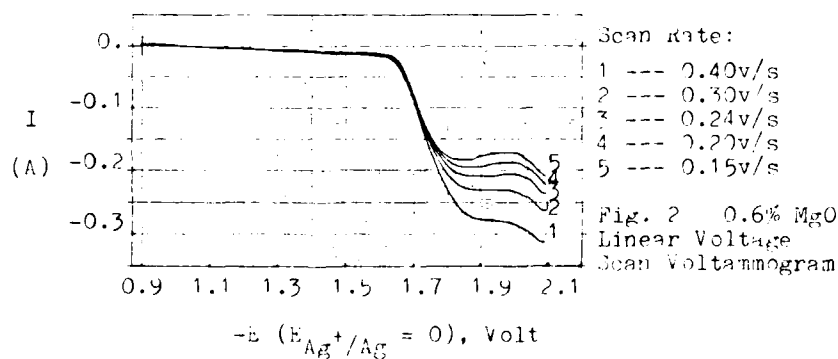
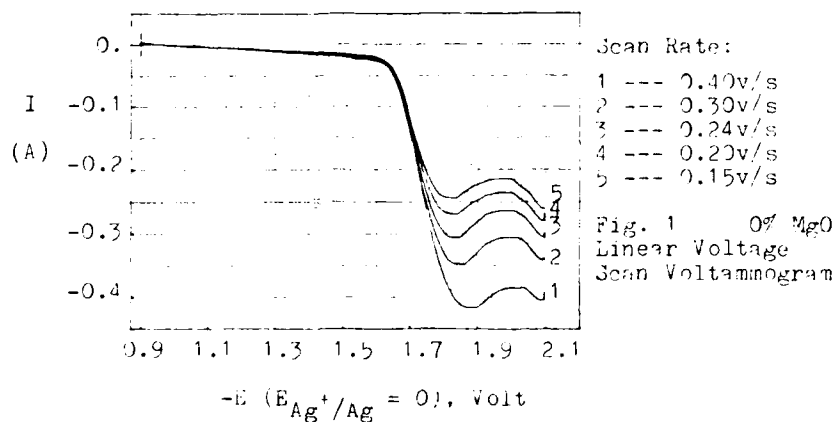
At the electrolysis temperature, with the content of MgO increasing from 0% (wt.) to 0.3% (wt.), the diffusion coefficient D_0 and the limiting current density I_d are decreased rapidly. Then, with the further increasing of the content of MgO , the decrease of D_0 and I_d disappears gradually.

MgO from different sources possesses different reactivity. The hydrolyzed electrolyte ($MgOHCl$) is probably mostly decomposed into MgO , and there is very little to be dissolved into $MgOH^+$ in the molten salts.

REFERENCES

1. Xu Riyao, Zhang Yueqiang, Magnesium Metallurgy.
2. Light Metals (China national magazine), No.3, P.38, (1981).

3. Light Metals P.949, (1980).
4. Tian Shaowu, Electrochemical Research Methods.
5. Shanghai Metallurgical Institute, Ag/AgCl Reference electrode with Ceramics Diaphragm Available to Molten Salt System, (1981).
6. Lin Qingfu, The Influences of MgO on the Cathodic Deposition Processes in magnesium electrolysis, the thesis for an MS degree, (1985).



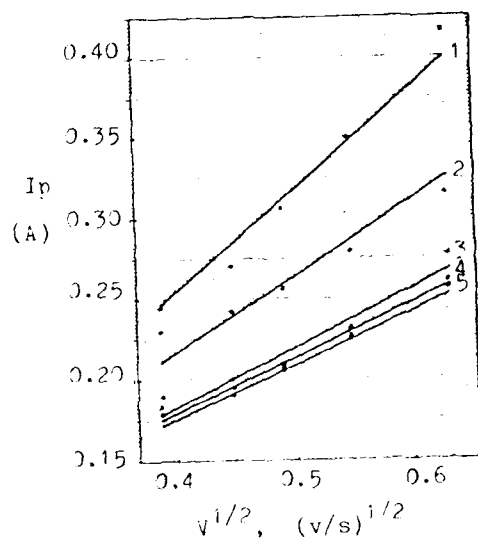


Fig. 3
Lines of I_p
vs. $v^{1/2}$

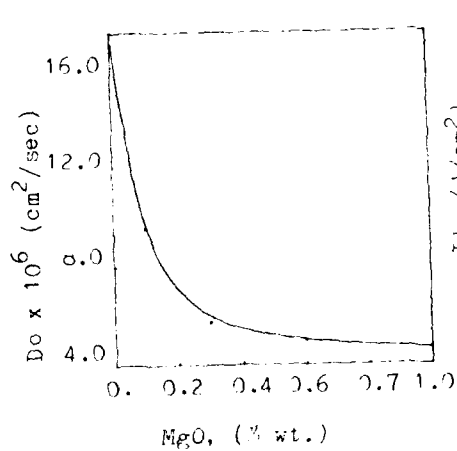


Fig. 4 Curve of
 D_o vs. $MgO \%$

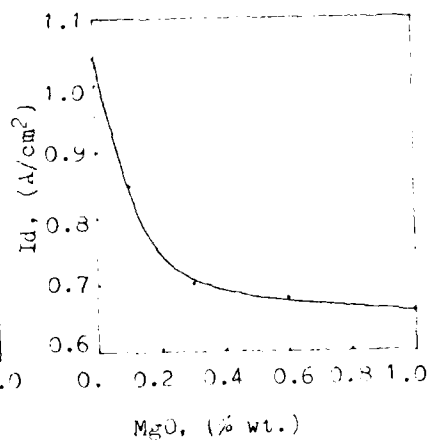


Fig. 5 Curve of
 I_d vs. $MgO \%$

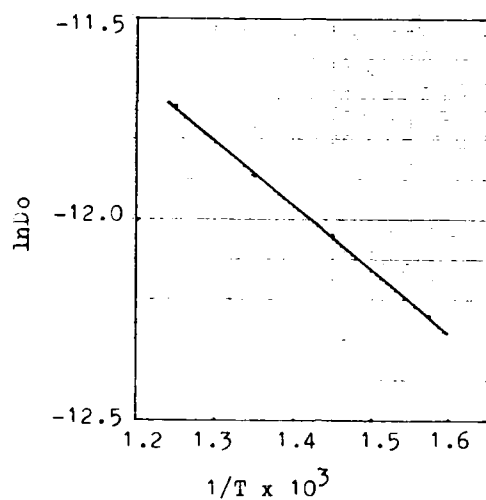
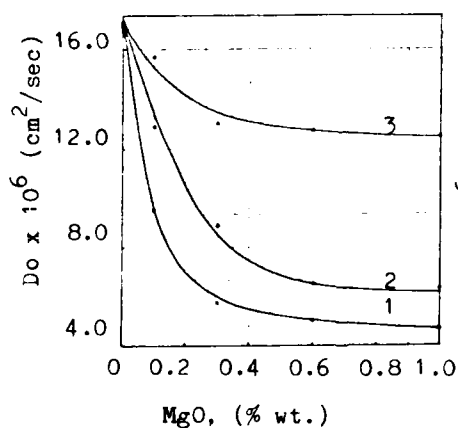
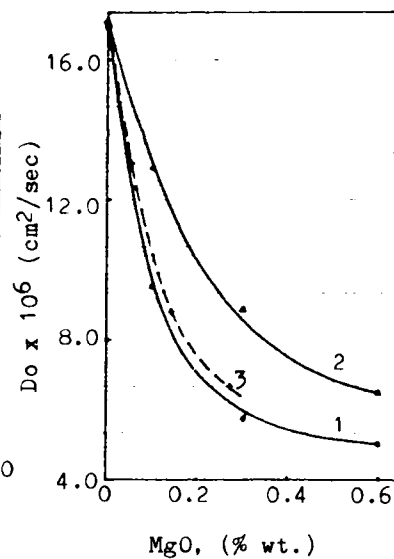


Fig. 6
Line of
 $\ln D_o$ vs. $1/T$



1--- MgO (hydro.)
2--- MgOHCl
3--- MgO (agent)

Fig. 7 Curves of
 D_o vs. MgO% from
Different Sources



1--- MgO (hydro.)
2--- MgOHCl
3--- MgO (in MgOHCl)

Fig. 8 Curve of
 $D_o(\text{MgOHCl})$ vs. MgO %

DISPROPORTIONATION REACTION IN MOLTEN SALTS AND THEIR APPLICATION TO SURFACE COATING TREATMENT

Takeo Oki

Faculty of Eng., Nagoya University, Furo-Cho, Chikusa-Ku,
Nagoya, 464, Japan

ABSTRACT

Surface coating treatment by chemical transport using disproportionation reaction in molten salts was studied comprehensively. The metal such as Si, Cr, Ti, V, Zr, Ta and etc. was deposited to form alloy and compound coating on the surface by application of the disproportionation reaction in molten halide salts KCl-BaCl₂-NaF-Me-Me salt system. The overall reaction can be represented as follows.

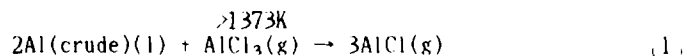


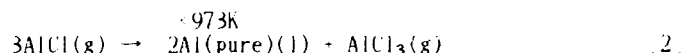
Various films were coated on steels by this method; ferro-silicon and ferrosilicon graphite composite, chromium carbide, titanium carbide, vanadium carbide, tantalum carbide and boride films of these metals. The surface hardness (Hv) of these films ranged from 1000 to 3000 and they had very high wear resistance.

INTRODUCTION

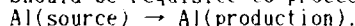
Many surface treatments have been done in an attempt to improve the performance characteristics of material surface(1). The diffusion treatment is well known as a representative one. The disproportionation in molten salts can precipitate an active metal on the surface, which is able to alloy and compound by reaction with the component of substrate. In this investigation, activity change of metal at the same temperature was used for the surface coating of alloy and compounds. This method by means of disproportionation is one of the chemical transport process in molten salts.

The disproportionation reaction is defined as the redox reaction of metal ions with the same metal, like the following disproportionation reaction of Al(2)(formula 1, and 2). Disproportionation reaction can be performed by two kinds of driving force; the one is the difference in temperature between reaction system and production system, and the other is that in activity. The former has been utilized for refining Aluminium(2). The reactions can be described as follows.

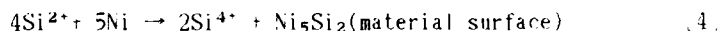
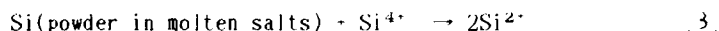




Temperature difference should be requisite to proceed this reaction.



On the other hand, the latter can be applied to coating of substrate by precipitation in molten salts. For example, Gay and his coworkers(2) found that nickel can be siliconized by dipping into molten $\text{KCl-NaCl-NaF-Na}_2\text{SiF}_6$ salts containing silicon powder. The reaction was described as follows.



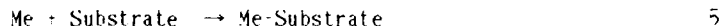
The difference in activity of silicon between powder and intermetallic compound should be requisite to perform these disproportionation reactions [3 and 4] at the same temperature. Here in this paper the latter disproportionation will be applied to produce the coated films on substrate.

RESULTS AND DISCUSSION

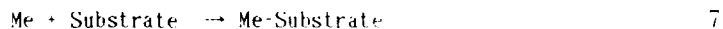
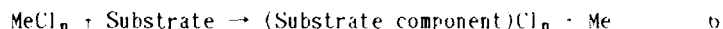
1. Pre-consideration about the mechanism of precipitation in molten salts

The mechanism of precipitation in molten salts was suggested as the following processes.

(1) Collision mechanism



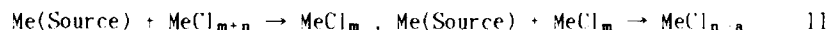
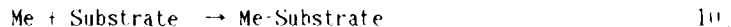
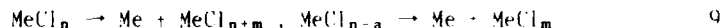
(2) Exchange mechanism



(3) Disproportionation mechanism



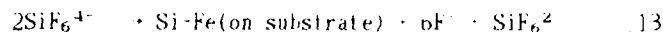
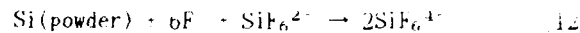
or



There were many discussions about these mechanisms(3)-(10), where there are many results for which the collision mechanism cannot give an explanation. This experiment was performed in order to evaluate the disproportionation mechanism and apply it to preparation of surface coating on substrate.

2. The formation of ferrosilicon and ferrosilicon-graphite composite film on steel as alloy film formation(11),(12)

Table 1 shows the chemical composition and the original hardness of the specimens. It was immersed into the molten salts NaCl-KCl-NaF at 973~1173K, which contained Na₂SiF₆ and silicon powder as additives. After dipping of 3.6 ~10.8ks, the specimen was taken out of the crucible, washed with water, dried and used in several tests. In this treatment, the following disproportionation was speculated.



Silicon which deposits on the material surface diffuses into the material and forms intermetallic compounds. Therefore the activity of deposited silicon is lower than that of silicon powder. Then the reactions 12, 13 occurred steadily.

Fig.1 shows the relationship between the amount of coating and the molar ratio of silicon powder to Na₂SiF₆. The amount of coating increased with added silicon powder.

Fig.2 shows the relationship between the amount of coating and NaF or Na₂SiF₆ quantity, while the amount of silicon powder was constant. The amount of coating increased with increasing these components. Also the lack of either Si or silicon salts resulted in non-coating. All these results suggest that Si precipitation occurs through the disproportionation reaction.

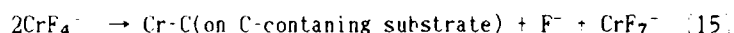
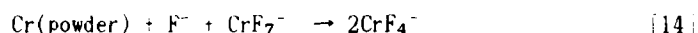
And X-ray analysis confirmed that the ferrosilicon films were formed inwardly from surface to reduce silicon ratio in this order: FeSi₂, FeSi, Fe₃Si. The hardness H_v at the vicinity of the surface was about 700.

3. Chromium carbide and other(TiC, VC, ZrC and TaC) films on steel as metal carbide film formation(12)-(14)

In this experiment, CrF₃ and chromium powder were added into fused NaCl-KCl-NaF. The specimen was dipped into the molten mixture salt at 1173K for 10.8ks.

Fig.4 shows the profile of Vickers hardness in the surface area

of the specimen. It was about 1200 ~ 2000. Cr_7C_3 and Cr_2C were confirmed in surface films by X-ray analysis. The amount of coating was influenced by the concentration of NaF , CrF_3 and chromium powder. (Fig.5) It increased with increasing concentration of each element under constant concentration of the others. These results suggest also the following disproportionation.

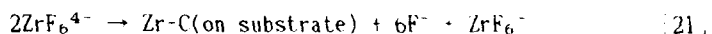
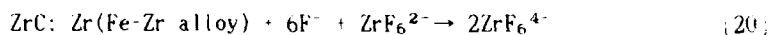
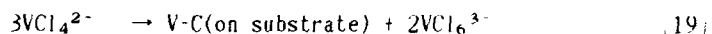
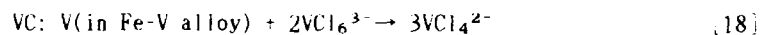
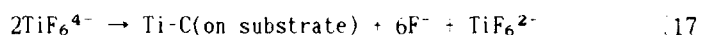
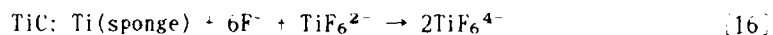


In addition, it was proved that the proportion of chromium ions before the treatment ($44\%\text{Cr}^{3+} + 56\%\text{Cr}^{6+}$) changed with reaction, and that the relative concentration of Cr^{3+} increased. (After the treatment, $96.1\%\text{Cr}^{3+}$, $3.9\%\text{Cr}^{6+}$). This change suggests that the reaction [14] proceeds faster than the reaction [15] at last stage. In other words, the formation of chromium carbide may be controlled by consumption of precipitated chromium.

The other carbide films could be formed on steel by the same method. The molten $\text{KCl-BaCl}_2\text{-NaF}$ salts were used as main supporting salts in all cases. K_2TiF_6 and sponge titanium for titanium carbide, VCl_3 and Fe-V alloy for vanadium carbide, K_2ZrF_6 and Fe-Zr alloy for zirconium carbide, K_2TaF_7 and tantalum for tantalum carbide were used as additives, respectively. SKD11(JIS) (1.5%C) was used as C-containing substrate for all cases and moreover S55C(JIS)(0.5%C) and SKD3(JIS)(1.0%C) especially for TaC film.

Fig.6 shows the effect of the treatment temperature on the amount of coating for TiC, VC and ZrC (treatment time: 3.6ks). In either case, the amount of coating increased with increasing temperature. The each film thickness at 1273K are indicated in Fig.6.

The effects of additives on the amount of coating for ZrC, TiC and VC are showed by Fig.7 and Fig.8. And the lack of either metallic salt or metal made it difficult to form carbide films. These results suggest the following disproportionation for each carbide films.



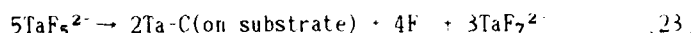
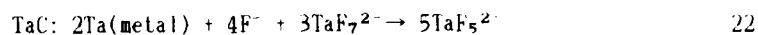


Fig.9 shows the profiles of vickers hardness in surface areas for ZrC, TiC and VC coating. The hardness at the immediate vicinity of surface for each film is 1490, 1750 and 3400, respectively. Fig.10 represents the profiles of hardness for TaC film coating. It reached about 2800~3000 (Hv) at the immediate vicinity of the surface.

4.The formation of boride film on steel(15) as boride film formation

The boriding of metal substrate in molten salts was investigated by means of disproportionation reaction, too. B_2O_3 and ferrobaboron were added as additives into the molten $\text{KCl-BaCl}_2\text{-NaF}$ salts. The reaction temperature ranged from 973 to 1173K. 10.8ks was adopted as treatment time.

The dipping of SKD11 in these molten salt resulted in the formation of Fe_2B film, which was confirmed by X-ray analysis. It is indicated in Fig.11 ~13 that the amount of coating depends on the concentration of NaF, B_2O_3 and ferrobaboron. This suggests the following disproportionation reaction for film formation.

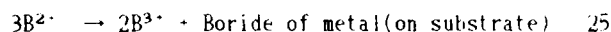
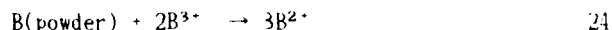


Fig.14 shows the profiles of vickers hardness in surface areas. When austenitic stainless steel(AISI304,316) were dipped, CrB film were formed on its surface.

On the other hand, dipping Cr plated steel resulted in the formation of Cr_2B film, which showed high corrosion resistance.

Besides, other various boride films on steel were formed by combination of carbide formation and boriding. The specimen with TiC, VC and ZrC film were immersed in boride forming molten salts, and TiB_2 , VB and ZrB films were made. This indicates that the affinity of metal-boron is much greater than that of metal-carbon. The Vickers hardness of all these boride films ranged from 1200 ~3000.

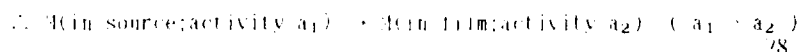
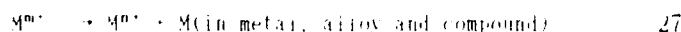
5.Crystal orientation of the produced films

The crystal orientation of various carbide films were investigated by X-ray analysis. The special orientation could not be found for TiC, WC and ZrC films. On the contrary, (002) plane was preferentially oriented for VC film and (421) plane for Cr_7C_3 film. The orientation of Cr_7C_3 film could not be found under the lack of

NaF. The orientation of film is intimately and complicatedly connected with it's formation process, and it is supposedly of great value to examine it furthermore.

7. Conclusion

It was turned out that ferrosilicon and ferrosilicon-graphite composite film, various carbide films and boride films could be formed by utilizing the useful disproportionation reaction in molten salts. The specimen was immersed into molten salts at high temperature, which contained the metal for coating (M) and its salt. In general, the following reaction occurred.



The precipitated M onto the specimen diffused immediately inward to form various type films. These forward and backward disproportionation reactions proceeded at the same temperature. This method can be called one of the chemical transportation method in molten salts.

REFERENCES

- (1) e.g. Materials Science and Technology 2(1986)201-326
- (2) S.Nishi, T.Oki: The complete works of Inorganic Chemistry, X 1-1, Aluminium, published by Maruzen, Japan (1975), 65.
- (3) A.J.Gay and J.Quakernaat: J.Less Common Metals, 40(1975), 21.
- (4) M.E.Straumanis, S.T.Shih and A.W.Schlechten: J.Electrochem.Soc., 104 (1957), 17.
- (5) K.Hosokawa, M.Ceda, T.Tamura: J.Japan Inst.Metals, 41(1977), 94.
- (6) S.T.Shih, M.E.Straumanis and A.W.Schlechten: J.Electrochem.Soc., 103 (1956), 395.
- (7) T.Arai et al.: J.Japan Inst.Metals, 39(1975), 217., 40(1976), 925., 41 (1977), 68., 41(1977), 138., 41(1977), 332
- (8) N.Uchida: J.Iron and Steel Inst., Japan, 67(1981), No12, S1041., S1045.
- (9) J.B.Steimann, R.V.Karnock, C.G.Root and A.R.Stetson: J.Electrochem. Soc., 114 (1967), 1018
- (10) N.Koura, T.Nakada: J.Metal Finishing Soc., Japan, 32(1981), 29
- (11) T.Oki, J.Ianikawa: J.Metal Finishing Soc., Japan, 31(1980), 56
- (12) T.Oki, J.Ianikawa: Molten Salt Japan, 25(1982), 115
- (13) T.Oki: The 61th Symposium of Metal Finishing Soc., Japan, (1980), C21
- (14) T.Oki and J.Ianikawa: Proceedings of the First International Symposium on Molten Salt Chemistry and Technology, Electrochemical Soc., Japan, (1983), 265
- (15) T.Oki et al.: The 19th Symposium on Molten Salt Chemistry, (1986) 99

Table 1 Chemical composition(mass%)
and hardness(Hv) of the specimens

	C	Mn	P	S	Si	Hv
A	0.1	0.22	0.013	0.019	.	149
B	0.8	0.30	0.030	0.030	0.35	210
C	3.5	0.30	0.01	0.02	0.5	162

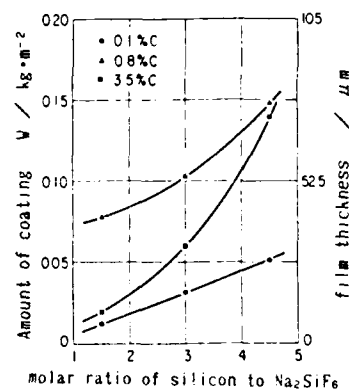


Fig.1 The relationship between the
amount of coating and molar ratio
of silicon

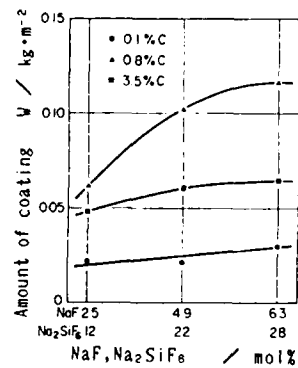


Fig.2 The relationship between the
amount of coating and NaF, Na₂SiF₆
concentration

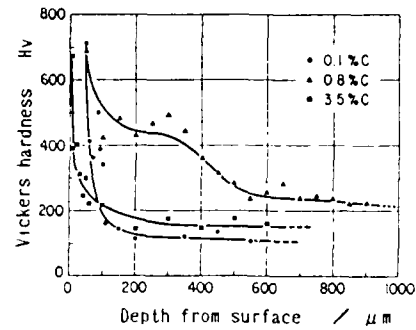


Fig.3 The profiles of Vickers
hardness(Hv) in ferrosilicon-graphite
composite film

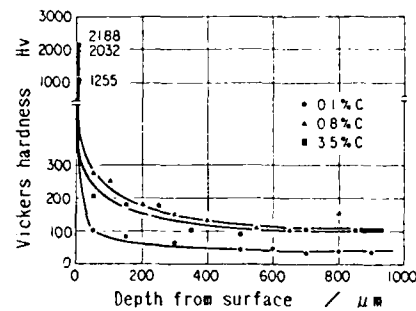


Fig.4 The profiles of Vickers
hardness(Hv) in chromium carbide film

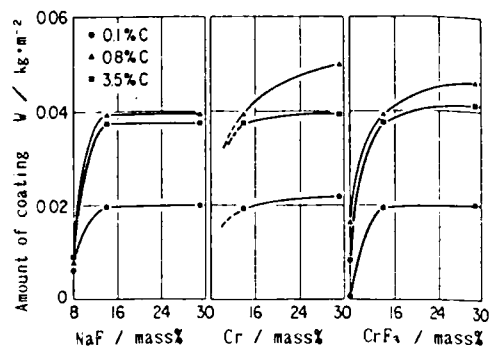


Fig.5 The effect of NaF, Cr and CrF_3 concentration on chromium carbide coating

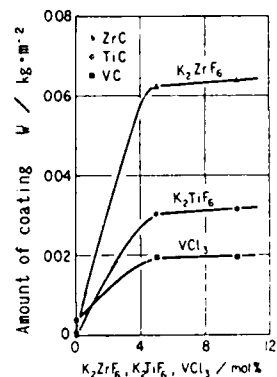


Fig.7 The effect of K_2ZrF_6 , K_2TiF_6 and VCl_3 concentration on ZrC, TiC and VC coating, respectively

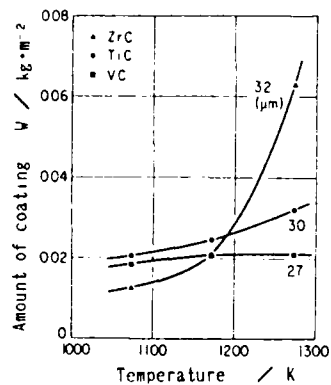


Fig.6 The effect of treatment temperature on ZrC, TiC and VC coating

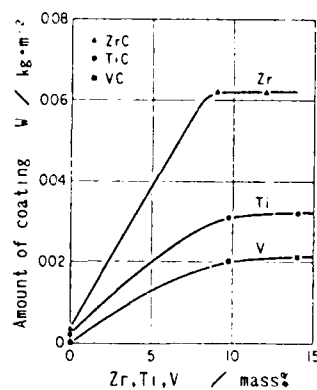


Fig.8 The effect of added Zr, Ti and V quantity on ZrC, TiC and VC coating respectively

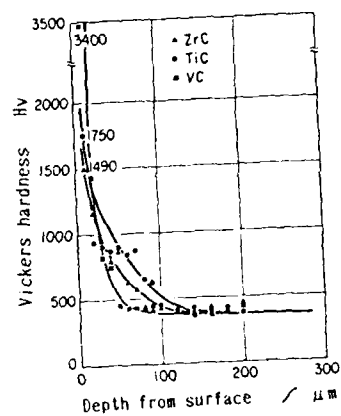


Fig.9 The profiles of Vickers hardness in ZrC, TiC and VC films

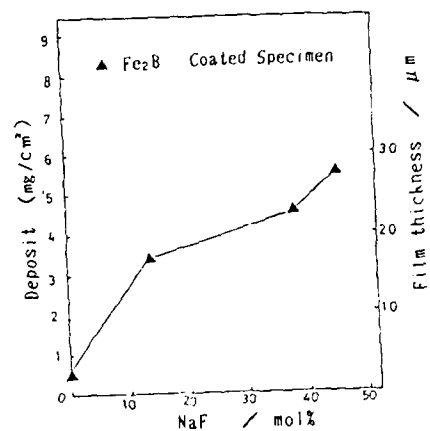


Fig.11 Relation between deposit and NaF

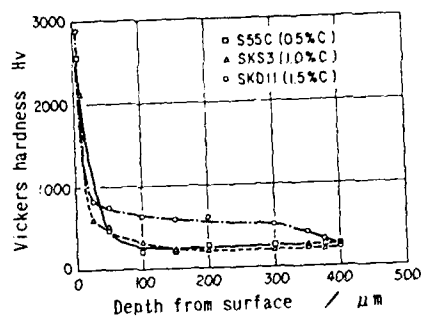


Fig.10 The profiles of Vickers hardness in TaC film

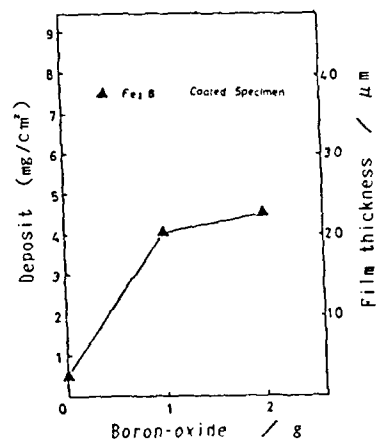


Fig.12 Relation between deposit and metal oxide

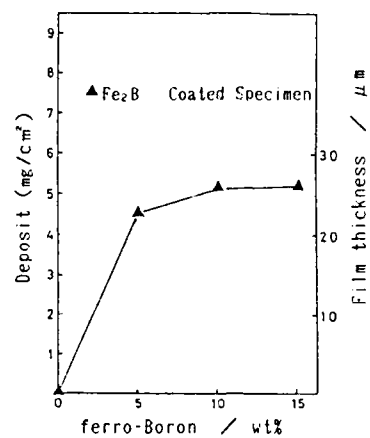


Fig.13 Relation between deposit and ferro-alloy

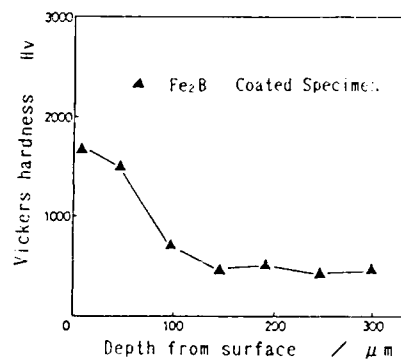


Fig.14 Vickers hardness profiles from surface

ELECTRODEPOSITION OF TITANIUM FROM CHLORIDE MELTS

Willy Rolland, Asmund Sterten and Jomar Thonstad

Laboratories of Industrial Electrochemistry,
The Norwegian Institute of Technology,
7034 Trondheim NTH, Norway

ABSTRACT

Electrodeposition of titanium from alkali chloride melts containing $\text{TiCl}_2/\text{TiCl}_3$ was studied in a small laboratory cell in the temperature range 450-850 °C. The reduction step and the subsequent anodic dissolution of the deposit gave well defined voltammetric peaks, while the red-ox reaction $\text{Ti(II)} \rightleftharpoons \text{Ti(III)} + e^-$ gave broadened, ill-defined peaks. The diffusion coefficient for the metal deposition step in KCl-LiCl eutectic at 456 °C was $1.1 \cdot 10^{-5} \text{ cm}^2/\text{s}$. Potential step measurements gave indications of instantaneous nucleation of titanium on stainless steel cathodes. The nature of the titanium deposit varied considerably with the cd, the composition of the melt and the temperature.

It is more than 80 years since preparation of titanium by fused salt electrolysis was reported for the first time by Huppertz (1). He claimed to have obtained a reasonably pure product by electrolysis of TiO_2 dissolved in CaCl_2 . At present, TiCl_4 seems to be the most suitable raw material for electrowinning of titanium. A stepwise reduction to the intermediate stages TiCl_3 and TiCl_2 is expected before Ti metal is deposited at the cathode. This process could be performed in either alkali chloride or alkali fluoride/chloride based systems at temperatures from 450 to 850 °C. In fluoride/chloride mixtures, Ti(III) is supposed to be reduced directly to the metal (2). In chloride melts the temperature can be lowered substantially (to ~120 °C) by addition of AlCl_3 (3), which allows application of low melting apparatus.

The fact that titanium is present in different valences involves the risk of red-ox, disproportionation and reoxidation reactions leading to severe losses in current efficiency. Although there are a large number of patents and papers suggesting various solutions to the

multi-valency problem, there is still no process adapted for industrial application. The use of various types of diaphragms to separate the anolyte and catholyte or circulation of the electrolyte between two separate cells have been proposed. In the latter case prereduction of Ti(IV) to Ti(II) is performed in one cell and reduction to metallic titanium in the other (4).

The melting point of titanium is very high (1670 °C), so the metal is deposited in the solid state. The cathode product can have different forms:

- powder
- dendritic crystals
- thin sheets

This necessitates periodic removal and stripping or replacement of the cathode. If it is equipped with more than one cathode, the electrolyzer can still be adapted for continuous operation. A continuous process is one reason why electrolysis looks attractive compared to today's batch processes, such as the Kroll process which is based on metallothermic reduction. However, steady improvements of the Kroll process using batches of up to 10 tons of titanium makes this process more competitive as the time passes.

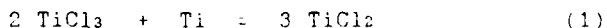
A technical break-through is not the only factor leading to success for a new process. The price and the demand for titanium products must also be considered. Earlier the main applications of titanium were found in the military, aircraft and aerospace industries and to some extent in the chemical industry. However, new applications are developing. One example is the replacement of special steel alloys by titanium in the offshore oil industry (eg. seawater piping application). The medical application of titanium as an implant material is also well known.

The purpose of the present work was to determine electrochemical properties of titanium in selected chloride melts, and to study the nature of the titanium metal deposit as a function of the operating parameters. It is believed that some of the difficulties encountered in process development can be overcome by a proper understanding of the chemistry of the process.

EXPERIMENTAL

The experiments were carried out in a transparent gold film furnace (Trans Temp Inc., USA). Two types of cell containers were used; i.e. transparent silica tubes and sintered alumina crucibles. The cell was preheated under an argon atmosphere, filled with salts inside a dry-box and then placed in the furnace without exposing the purified salts to air. Argon gas which was passed through the furnace was purified by passing through magnesium perchlorate to remove moisture and over titanium sponge at 600-700 °C to remove oxygen.

The melt consisted of mixtures of KCl, LiCl and NaCl. Titanium was introduced by adding solid TiCl_3 . It was allowed to equilibrate with titanium metal in the form of sheet which was present in the melt, according to the heterogeneous reaction:



The total titanium chloride content in the melt was determined by atomic absorption spectrophotometry of melt samples dissolved in acidic aqueous solutions. The temperature of the melt was varied in the range 450-850 °C. Three different cathode materials were tested; stainless steel, tungsten and iron. The anode materials were titanium and carbon (spec. pure) and the reference electrode was a titanium rod (or a platelet).

The electrode reactions were studied using linear sweep voltammetry, chronoamperometry and constant current electrolysis. The measurements were carried out with a PAR Model 173 potentiostat/galvanostat with an IR compensation unit and a PAR Model 175 universal programmer. Slow responses were measured by a x-y recorder whereas fast responses were recorded and stored on a Nicolet Explorer III A oscilloscope.

RESULTS AND DISCUSSION

Voltammetric Studies.

Linear sweep voltammetric curves were recorded at speeds ranging from 0.001 V/s to 1 V/s (in extreme cases up to 75 V/s). A voltammogram recorded in the lower range of sweep rates is shown in Figure 1. The deposition reaction took place at a more negative potential than expected. Although the cathode peak had a lower peak current than the anodic peak, the ratio of cathodic to

anodic charges during a full cycle is close to unity. This indicates that deposition of titanium metal (insoluble product) and stripping of the same (soluble product) was taking place. In certain cases the cathodic charge exceeded the anodic charge, probably due to the background current or nucleation or pre-peak reactions. The values of the cathodic peak potential, the cathodic half peak separation and the total peak separation were considerably higher than the theoretical values for purely diffusion controlled processes, indicating some irreversibility of the system Ti(II)/Ti .

The zero current potential with respect to the titanium reference electrode occurred in the range from +10 to +100 mV when operating between the potential limits shown in Fig.1 (-250 to +150 mV). When the potential scan was extended to more positive limits, the diagram exhibited a new and rather broad anodic peak, represented by wave (B') in Figure 2. The peak current of this wave (B') increased when the charge transferred in the wave (A') was increased by depositing more titanium metal cathodically and then reoxidizing it. An increase in the cathodic current in a broad range (B) was also observed. As shown in Fig.2, the peak potential of (A) shifted to more negative potentials in the third cycle. The process that takes place during the upper part (anodic potentials) of the diagram is probably the oxidation of Ti(II) to Ti(III) (at B'), with the corresponding reduction back to Ti(II) at (B). This process seems to be rather irreversible, as shown by the extensive broadening of the waves. A significant cathodic pre-shoulder sometimes occurred at a potential of -50 mV. Figure 3 shows more distinct waves for (B) and (B'), probably caused by a higher content of TiCl_3 in the bulk of the melt.

Plots of the cathodic peak current of peak (A) vs. the square root of the sweep rate were linear, but they exhibited positive intercepts. These plots indicated pure diffusion control and did give some indication about slow nucleation taking place prior to the deposition peak. The results of the voltammetric studies show that in the presence of Ti(III) the metal deposition reaction occurs in two steps.

Potential Step Amperometry Studies.

Figure 4 shows transients typical of a diffusion controlled process. Linear $I-t^{1/2}$ relations were obtained. As the steps were increased to an overpotential of about -300 mV, a significant change in the $I-t$ transients occurred, as shown in Figure 5. After the

initial double layer charging the current dropped to a minimum and then rose with time. At even more negative overpotentials the current still passed through a minimum, and then attained a maximum before finally decaying in the usual way with time. This behavior indicates that nucleation and growth phenomena play a part in the overall deposition process. Such behavior was difficult to detect below about 590 °C and at concentrations lower than a few weight percent TiCl_2 . After every run the deposited titanium was removed from the surface by polarizing the working electrode anodically. The rising part of the I-t transients obeyed an I vs. $t^{1/2}$ linear relationship which shows that instantaneous nucleation of titanium occurs on a stainless steel surface.

Diffusion Coefficients.

For the determination of diffusion coefficients the melt was equilibrated with a large titanium sheet to ensure that equilibrium (1) was established. In the calculation it was assumed that all TiCl_3 was converted to TiCl_2 . The diffusion coefficients were determined from voltammetric and potential step measurements at relatively low concentrations (1.0×10^{-4} mol/cm³). From linear plots of $v^{1/2}$ vs. i_p and $t^{-1/2}$ vs. i_{lim} the value of D_{TiCl_2} was calculated to be 1.1×10^{-5} cm²/s in KCl-LiCl eutectic at 456 °C for both methods. The temperature dependence of the diffusion coefficients showed a linear relationship between $\log D$ and $1/T$ for both voltammetric and potential step measurements. The diffusion coefficients determined from the voltammetric studies increased more rapidly with temperature, mainly due to a rise in the background current. This could be corrected for in the potential step measurements, and the activation energy of diffusion was calculated to be about 50 kJ/mol from Fig. 6. (Uncorrected voltammetric measurements gave about 70 kJ/mol).

Constant Current Electrolysis Using a Consumable Anode.

During "long time" electrolysis (2 - 20 hrs) titanium metal was deposited at the cathode while the titanium anode dissolved. The cathode was a stainless steel rod of 6 mm diameter and about 2.5 cm² surface area. The rods were pretreated by wet rubbing with waterproof emery paper (silicon carbide p1000B). After a run the cathode was replaced by a new rod without admitting air to the system. Most of the experiments were carried out at current densities between 20 and 400 mA/cm².

Results of visual inspection of the deposited metal are given in Table 1. These data might be summarized as

follows concerning the effect of melt composition and temperature:

KCl-LiCl eutectic, 450 °C : small crystals, low coverage.
KCl-LiCl eutectic, 830 °C : larger crystals (than above), better coverage.
KCl-NaCl eutectic, 700 °C : large crystals, good adherence and good coverage.
NaCl 850 °C : large crystals, good adherence and low drag-out ratio.
LiCl-KCl-NaCl (20:40:40 mol%), 630 °C : poorly reproducible results.

In KCl-LiCl at 450 °C it was observed that an initial current pulse of up to 400 mA/cm² for a few seconds resulted in a considerably better coverage on the cathode.

The current efficiency was usually low, i.e. no better than about 30%. At the highest current densities the current efficiency sometimes reached 90%. Experiments with KCl-NaCl at 750 °C indicated better current efficiency than at 700 °C. The reproducibility of current efficiency determinations became poor after a period of one week using the same melt. The lack of reproducibility was usually observed for the kinetic experiments as well if the measurements lasted for more than one week.

Appreciable amounts of blackish powder and flakes were formed in the melt during the experiments. It tended to settle at the bottom of the cell and to deposit on the walls. It was identified by x-ray analysis as titanium with some oxygen in the lattice. This dark product has been reported earlier by Baboian et al. (5) and by Straumanis and Chiou (6) who identified it as being TiO_x (~TiO_{0.198}) initially which later was oxidized to TiO and TiO₂ in the presence of oxygen. The oxygen might originate from the salt itself, from the walls of the cell or it could be introduced during replacement of the cathode.

In the electrowinning of titanium an inert chlorine evolving anode will be used. In experiments using a graphite anode for chlorine evolution it was observed that the anode chamber was free from black deposits. In the beginning of the experiment the anolyte acquired a bluish color which is indicative of Ti(III) and subsequently a yellow color due to chlorine. The melt in the cathode chamber was greenish, typical of Ti(II). A

cathodically polarized nickel diaphragm was used to separate the two chambers.

REFERENCES

- (1) Huppertz, W., Electrochem. Met. Ind., 3 (1905) 35
- (2) Chassing, E., Basile, F. and Lorthoir, G.,
J. Appl. Electrochem., 11 (1981) 187
- (3) Burgess, J., Brown, G.T. and Roberts C.W.,
J. Appl. Chem., 8 (1958) 6
- (4) Ginatta, M.V., "Method of Producing Metals by Cathodic Dissolution of Their Compounds,"
US. Patent 4,400,247, Aug.23,1983
- (5) Baboian, R.L., Hill, D.L. and Bailey, R.A.,
Can. J. Chem., 43 (1965) 187
- (6) Straumanis, M.E. and Chieu, Ch.,
Z. Elektrochem., 62 (1958) 201

Table 1. Nature of the Electrodeposited Metal		Base electrolyte containing about 5 wt% TiCl_2			
Cathodic current density (mA/cm ²)		(KCl-LiCl) sat	(KCl-LiCl) sat	(KCl-NaCl) sat	NaCl
		450 °C	830 °C	700 °C	850 °C
High 150 - 400	Low 20 - 50	<ul style="list-style-type: none"> - no deposit OR: - thin film - grey colour - porous - good coverage - poor adherence 	<ul style="list-style-type: none"> - no deposit 	<ul style="list-style-type: none"> - no deposit OR: - fine coherent deposit - short needle shaped dendrites - even growth of dendrites - very good coverage - good adherence 	<ul style="list-style-type: none"> - no deposit OR: - extreme types of growth at the underside of the cathode - lustrous - poor coverage - poor adherence - coarse
	Low 20 - 50	<ul style="list-style-type: none"> - even surface - short, needle shaped dendrites - some lustrous - films - porous - poor coverage - poor adherence 	<ul style="list-style-type: none"> - uneven, coarse film - lustrous - good adherence - poor coverage - growth was concentrated on the lower part of the cathodes 	<ul style="list-style-type: none"> - as above, but - larger quantity of coarse crystals - some sword-shaped dendrites 	<ul style="list-style-type: none"> - large quantity of sword shaped dendrites (up to 5 mm) - lustrous - poor coverage - poor adherence
	Medium 50 - 150	<ul style="list-style-type: none"> - as above, but - lustrous - some nodules - thinner film than above 	<ul style="list-style-type: none"> - more coarse than above - some sword shaped dendrites - large mirror like areas (up to 1x3 mm) - good adherence - good coverage 	<ul style="list-style-type: none"> - as above, but - larger quantity of sword-shaped dendrites on the lower part of the cathodes 	<ul style="list-style-type: none"> - as above, but - up to 15 mm long dendrites facing downwards - better coverage

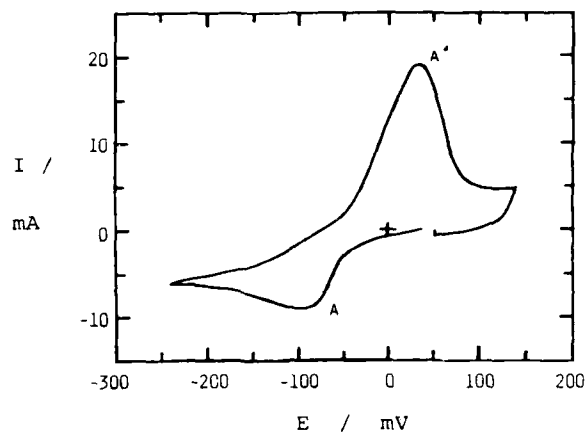


Figure 1. Cyclic Voltammogram at a Tungsten Electrode during the Reduction of Ti(II) (A) and the Oxidation of Ti (A') in KCl-LiCl Eutectic at 456°C . Sweep Rate: 5 mV/s , Electrode Area 0.4 cm^2 , Concentration of TiCl_2 : $1.0 \times 10^{-4}\text{ mol/cm}^3$.

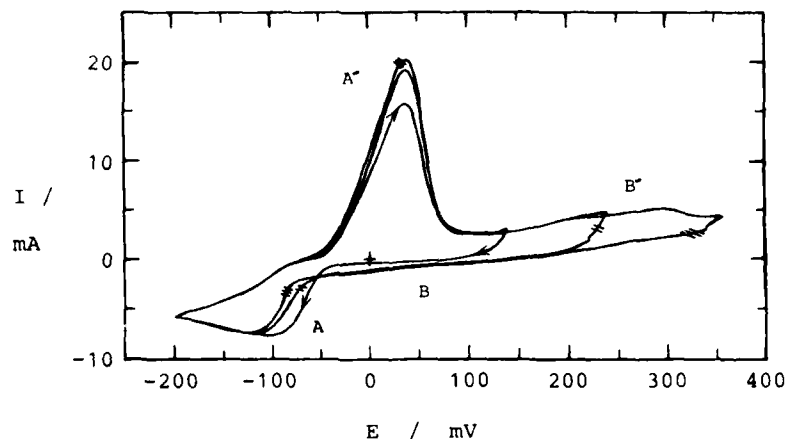


Figure 2. Repeated Voltammograms on a Tungsten Electrode with Increasing Upper Limit (more anodic) in KCl-LiCl Eutectic at 456°C . The Same Conditions as in Fig.1.

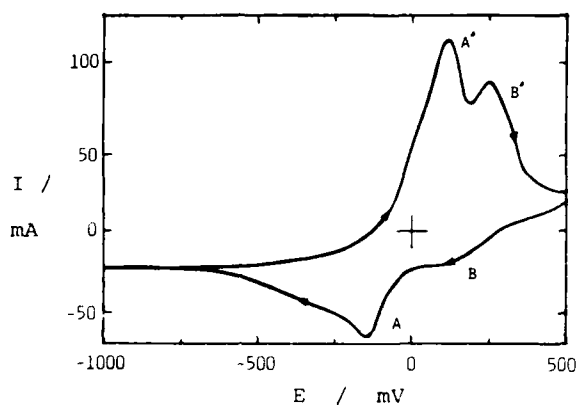


Figure 3. Voltammogram Showing the Same Waves as in Fig. 2. Tungsten Electrode With Surface Area 0.40 cm^2 at 450°C . LiCl-KCl Eutectic. Total Titanium Content Calculated as TiCl_2 ($3.2 \times 10^{-4} \text{ mol/cm}^3$). Sweep Rate 100 mV/s .

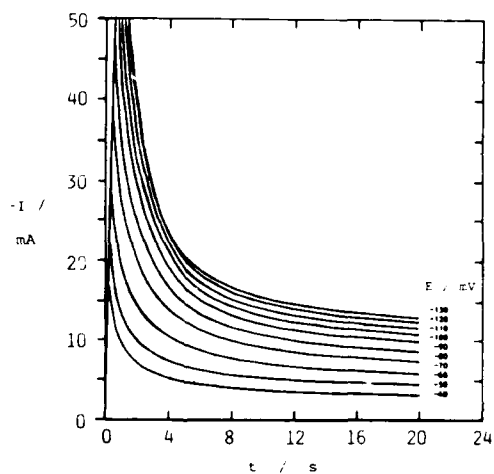


Figure 4. Cathodic Current vs. Time Obtained at Different Potential Steps (Potentials are Indicated on the Curves, for the Deposition of Ti on Tungsten (0.45 cm^2) in KCl-LiCl Eutectic with 0.7 wt\% TiCl_2 at 511°C . Initial Potential $+30 \text{ mV}$.

Figure 5. Potentiostatic Current Transients for the Electrodeposition of Titanium on Stainless Steel (0.45 cm^2) in KCl-LiCl Eutectic with 4.0 wt% TiCl_2 at 602°C . (Potentials are Indicated on the Curves). Initial Potential +10 mV.

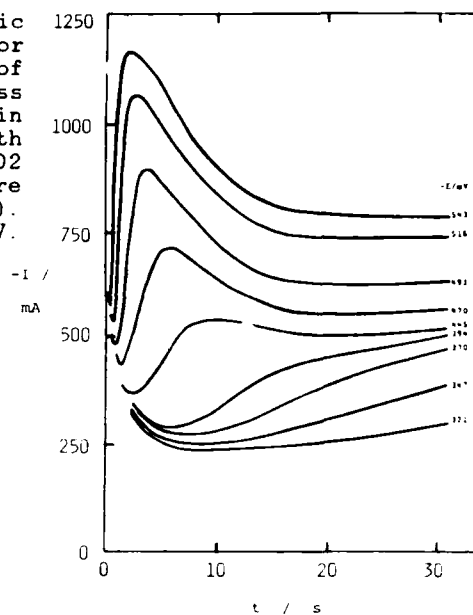
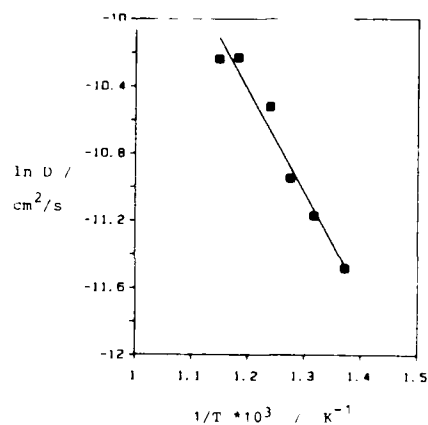


Figure 6. The Logarithm of the Diffusion Coefficient of TiCl_2 vs. the Inverse Temperature in the Range $456\text{--}598^\circ\text{C}$. Tungsten Electrode. KCl-LiCl Eutectic With $1.0 \times 10^{-4} \text{ mol/cm}^3$ TiCl_2 . Potential Step Measurements.



THE SYNTHESIS OF β -VANADIUM BRONZE AND
VANADYL PHOSPHATE BY MOLTEN SALT ELECTROLYSIS

Yoshikazu Kaneko, Hiroaki Hashida and
Hironao Kojima

Faculty of Engineering, Yamanashi University
Kofu, Yamanashi, 400, Japan

ABSTRACT

The good electrical conducting compounds of alkali vanadium bronze and the layered vanadyl phosphate were obtained from molten $\text{LiVO}_3 + \text{K}_4\text{P}_2\text{O}_7$ and $\text{V}_2\text{O}_5 + \text{Li}_3\text{PO}_4$ systems by electrolysis. The experimental conditions of electrolysis were determined from the results of cathodic polarization curves and cyclic voltammograms of melts at 700-800°C. The single crystals obtained were $\text{Li}_x\text{V}_2\text{O}_5$ and $\text{Li}_x\text{VOPPO}_4$ and showed semiconducting behavior. The activation energies were calculated from the linear dependence of electrical resistivity on the temperature.

INTRODUCTION

The lithium vanadium bronzes ($\text{Li}_x\text{V}_2\text{O}_5$) have attracted much attention because of their electrical properties. The β - $\text{Li}_x\text{V}_2\text{O}_5$ ($0.22 < x < 0.62$) shows one-dimensional ion conductivity because Li^+ ion resides in tunnels of the distorted V_2O_5 lattice. They may be of use for the cathode of a lithium cell[1]. The lithium vanadium bronzes have α , β , and γ phases depending on the amounts of Li^+ ion they contain. The vanadium bronzes have been synthesized mainly by solid state sintering of V_2O_5 , V_2O_3 and MVO_3 mixtures, but the Czochralski method has been reported for

β phase sodium vanadium bronze[2].

Electrical crystallization from molten salts is advantageous in that the compounds having unstable atomic valence state can be synthesized at elevated temperature. This is because the electrical techniques facilitate control of the atomic valence state through oxidation-reduction reactions on the electrodes. A limited number of compounds, such as sodium tungsten bronze, NaB_6 , and molybdenum bronzes have been synthesized using molten salt electrolysis[3-5]. The $\beta\text{-Li}_x\text{V}_2\text{O}_5$ crystals were synthesized from molten sulfate and carbonate melts by electrolysis[6].

In this report, attempts were made to synthesize $\beta\text{-Li}_x\text{V}_2\text{O}_5$ using molten salt electrolysis from vanadate and phosphate melts. In addition, the synthetic conditions needed and the properties of vanadyl phosphate, which was formed during the electrolysis of molten vanadate and phosphate baths, were investigated.

EXPERIMENTAL

The systems of $\text{LiVO}_3 + \text{K}_4\text{P}_2\text{O}_7$, $\text{KVO}_3 + \text{K}_4\text{P}_2\text{O}_7$, $\text{LiVO}_3 + \text{Li}_3\text{PO}_4$ and $\text{V}_2\text{O}_5 + \text{Li}_3\text{PO}_4$ were used as the electrolytic baths. The electrolytic cell was constructed with a Mullite tube with one end sealed (dia. 8 cm, depth 40 cm), and a copper flange, which was water-cooled to protect its rubber O ring seal. Approximately 200 g of molten salt was placed in the Pt crucible (dia. 5.5 cm, depth 12 cm), and a Pt wire (dia. 0.5 mm) was used as the cathode, a Pt wire (dia. 0.5 mm) or a glassy carbon rod (dia. 5 mm) was used as the anode and a Pt wire (dia. 0.5 mm) was used as the reference electrode. They were inserted into the molten electrolytic bath and held at 1 cm below the melt surface. Prior to electrolysis, the cyclic voltammograms were recorded in order to find the oxidation-reduction potential of vanadyl ion in the melt using a Hokuto Denko model HA301.

The electrolysis was carried out at 600-800 °C with constant current or constant voltage in an atmosphere of N_2 gas. At the end of the electrolysis, the cathode was raised above the melt and the crystals formed were recovered from the electrode surface. The products,

containing impurities like the solvent, were washed with acids and distilled water. In the case of the products, which were deposited not on the cathode but in the electrolyte, the melt was cooled to a solid, and then the solvent was removed by washings to obtain the crystals.

The electrical resistivity was measured in the range of room temperature to 400 °C by using a complex impedance method.

RESULTS AND DISCUSSION

Cyclic Voltammogram

The cathodic polarization curves of $\text{LiVO}_3 + \text{K}_4\text{P}_2\text{O}_7$ (33 mol%) melt at 650 °C are shown in Figure 1. The peak at -0.6V could be assigned to the reduction of V^{5+} to V^{4+} . This value corresponds to the value of -0.35 V for $\text{Li}_2\text{SO}_4 + \text{LiVO}_3$ melt and -0.4 V for $\text{M}_2\text{SO}_4 + \text{LiVO}_3$ melt already reported[6]. The reduction potential of the phosphate bath was slightly negative of the sulfate bath.

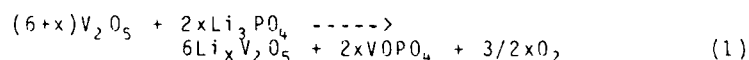
Cyclic voltammograms of the phosphate melt ($\text{LiVO}_3 + \text{K}_4\text{P}_2\text{O}_7$) are shown in Figure 2. The potential was scanned between -1.2 V and 1.2 V. The scan rates were applied both at 100 mV^{-1} (curve a) and 300 mV^{-1} (curve b). From Figure 2, it was observed that the reduction potential at the rapid scan was -0.7 V compared to -0.6 V at lower rate, and the current was increased. Similar potential changes depending on the scan rate were observed in the $\text{KVO}_3 + \text{K}_4\text{P}_2\text{O}_7$ melt at 750 °C such as -9.5 V at 100 mV/s , -10.0 V at 300 mV/s , -10.8 V at 600 mV/s and -1.5 V at 1000 mV/s . The potential changes dependence on the scan rate in this study seemed to show that chemical reactions followed the charge transfer on the cathode[7]. Also, the linear relation between the reduction peak current and the square root of the scan rate was obtained in $\text{KVO}_3 + \text{K}_4\text{P}_2\text{O}_7$ melt at 750 °C and is shown in Figure 3. From these results, the formation mechanism of vanadium bronzes was postulated to be charge transfer to produce V^{4+} followed by reaction with species containing Li^+ ion in the melt. It was confirmed that the diffusion was rate determining for the cathodic reaction.

The anodic polarization curve of $\text{LiVO}_3 + \text{K}_4\text{P}_2\text{O}_7$ melt

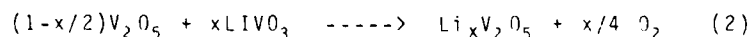
at 650 °C showed a peak at +0.2 V. This peak seemed to be the oxidation dissolution of the vanadium bronze, which was formed by the cathodic polarization and in contrast the dissolution potentials for other melts were -0.15 V for $\text{LiVO}_3 + \text{Li}_2\text{SO}_4$ melt and -0.2 V for $\text{LiVO}_3 + \text{M}_2\text{SO}_4$ melt. From these results, the vanadium bronzes formed by electrolysis seemed to be more stable in the phosphate melt than in the sulfate melt. Also, these results suggest the kinds of electrolytic baths that should be chosen to obtain δ - vanadium bronze.

Crystal Deposition

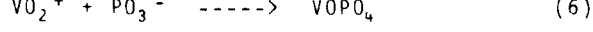
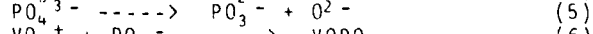
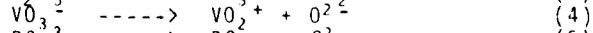
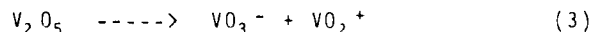
The experimental conditions and results are summarized in Table 1. It was observed that the crystals were deposited on the cathode easier in the phosphate melt than in the sulfate melt. Also, the crystals of δ -vanadium bronze were obtained easily from $\text{Li}_3\text{PO}_4 + \text{V}_2\text{O}_5$ melt compared with non-phosphate melts. The formation reaction of vanadium bronze accompanying the formation of vanadyl phosphate (VOPO_4) from the melt containing phosphate ion is believed to be as shown in the following equation:



When lithium meta-vanadate was used for the electrolytic bath, the formation reaction of vanadium bronze was estimated by the following equation[6].



When the electrolysis of phosphate melts was carried out at 800 °C for 9 hours with a constant voltage of 1.5 V, the crystals obtained were 2 cm (length) x 0.8 cm (width) x 0.2 cm (thick) and trigonal prism shaped. However, the crystals obtained from $\text{LiVO}_3 + \text{V}_2\text{O}_5$ melt were plate-like in shape and appeared as needles. The crystal habits were changed by the melt composition. When we continued to electrolyze the phosphate melt ($\text{Li}_3\text{PO}_4 + 99.1 \text{V}_2\text{O}_5$), the concentration of oxide ion in the melt was decreased through the evolution of oxygen gas at the anode, and then VO_2^+ and PO_3^- were formed these ions combined to form VOPO_4 at the anode according to the following equations:



Formation of Li_xVPO_4 with the layered VPO_4 intercalating the Li^+ ion in the melt seemed to be favored.

Electrical Resistivity

Electrical resistivities were measured in the range 12-450 °C for the β - $\text{Li}_x\text{V}_2\text{O}_5$ ($x=0.25, 0.30$) and $\text{Li}_{0.68}\text{VPO}_4$. The resistivities were of the order of $10^4 \Omega \cdot \text{cm}$ for β - $\text{Li}_{0.25}\text{V}_2\text{O}_5$, $10^2 \Omega \cdot \text{cm}$ for β - $\text{Li}_{0.3}\text{V}_2\text{O}_5$, and $30 \Omega \cdot \text{cm}$ for $\text{Li}_{0.68}\text{VPO}_4$ at room temperature. At higher temperatures, the electrical resistivities were lowered to $50 \Omega \cdot \text{cm}$, $25 \Omega \cdot \text{cm}$, $2 \Omega \cdot \text{cm}$, at 350 °C, respectively. These compounds showed typical semiconducting behavior. The resistivities were linearly temperature dependent. Their activation energies were 0.35, 0.19 and 0.12 eV, respectively. The reason why the resistivity of lithium vanadyl phosphate was lower than that of the other vanadium bronzes could be due to the difference of the lithium content because these compounds have the layered structure.

REFERENCES

1. N. Ueda, A. Yano and K. Shiratori, "Electronic Conduction in Oxides," pp. 200, Syokabo, Tokyo, (1983).
2. N. Sol and P. Merends, J. Crystal Growth, **46**, 557 (1979).
3. R. A. Fredleis and A. Damjanovic, J. Solid State Chem., **4**, 91 (1979).
4. E. Edweli, J. A. Zubeck, R. S. Geigelson and R. A. Huggins, J. Crystal Growth, **29**, 65 (1975).
5. P. Strobel and M. Greenblatt, J. Solid State Chem., **4**, 91, (1981).
6. H. Kojima, Y. Kinoko and H. Udagawa, Proc. Int. Chinese-Japanese Bilateral Symp. on Molten Salt Chem. and Techn., pp. 20 (1986).
7. R. S. Nicholson and J. Stein, Anal. Chem., **36**, 706 (1964).

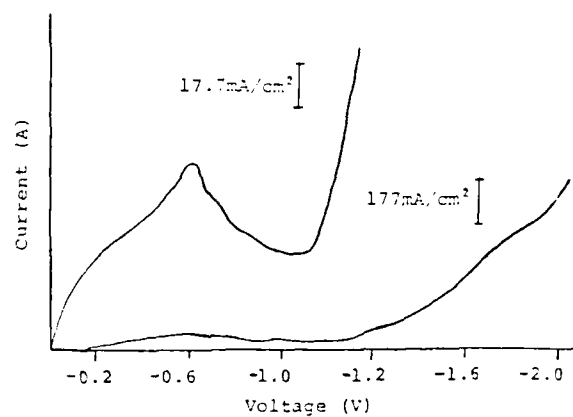


Figure 1. Cathodic Polarization Curve of $\text{LiVO}_3 + \text{K}_4\text{P}_2\text{O}_7$ melt at 650°C .

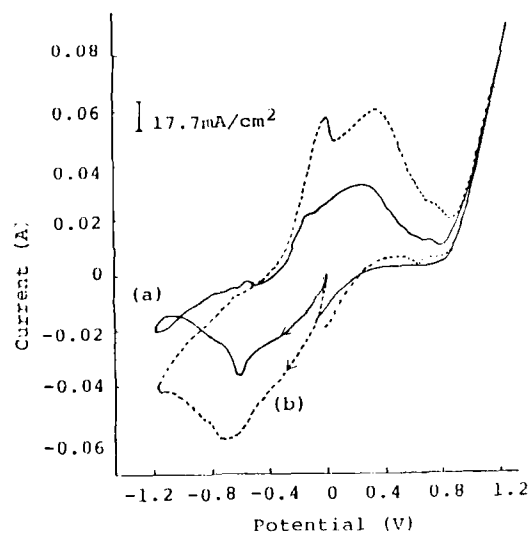


Figure 2. Cyclic Voltammograms of $\text{LiVO}_3 + \text{K}_4\text{P}_2\text{O}_7$ at 657°C . Scan Rate (a) 100mV/sec , (b) 300mV/sec

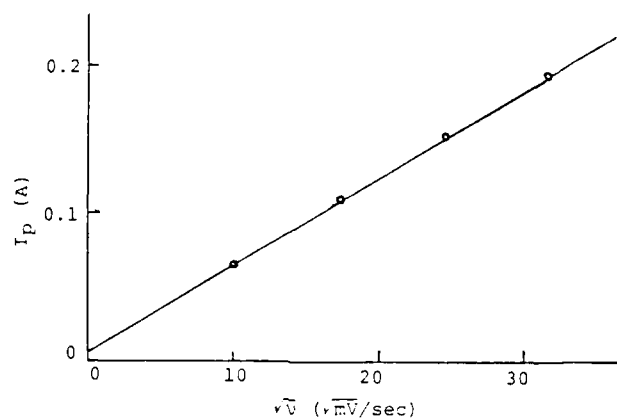


Figure 3. Relationship between Peak Current(I_p) and Square Root of Scan Rate(\sqrt{v}) in Cyclic Voltammograms of $KVO_3 + K_4P_2O_7$ at 750 C.

Table 1. Experimental Conditions and Results.

Electrolytic bath (Composition)	Conditions		Crystals obtained
	Temperature (°C)	Voltage (V)	
LiVO ₃ +K ₄ P ₂ O ₇ (33.3mol%)	700	1.2	γ -Li ₃ V ₂ O ₅
	650	1.2	"
LiVO ₃ +Na ₄ P ₂ O ₇ (25.0mol%)	650	0.7	γ -Li ₃ V ₂ O ₅
	650	1.2	"
	650	2.0	"
NaVO ₃ +Na ₄ P ₂ O ₇ (25.0mol%)	700	0.6	Na ₄ V ₂ O ₇
			Na ₃ V ₂ O ₅
	700	1.5	Na ₃ VOP ₂ O ₄
KVO ₃ +K ₄ P ₂ O ₇ (25.0mol%)	600	1.5	"
	700	1.5	K ₄ V ₂ P ₄ O ₁₇
LiVO ₃ +Li ₃ PO ₄ (16.7mol%)	700	1.5	K(VO ₂), PO ₄
	750	0.9	VOP ₂ O ₄
			"
LiVO ₃ +Li ₃ PO ₄ (16.7mol%)	700	1.5	γ -Li ₃ V ₂ O ₅
	750	2.0	"
	800	1.0	"
Li ₃ PO ₄ +V ₂ O ₅ (66.7mol%)	750	1.5	VOP ₂ O ₄
			Li ₃ VOP ₂ O ₄
			β -Li ₃ V ₂ O ₅
Li ₃ PO ₄ +V ₂ O ₅ (90.9mol%)	750	0.4	β -Li ₃ V ₂ O ₅
	750	0.6	"
	750	1.0	"

SMOOTH ELECTRODEPOSITS OF MOLYBDENUM FROM KF-B₂O₃-Li₂MoO₄ MELT

Koichiro Koyama and Yasuhiko Hashimoto

Department of Metallurgy and Materials Science, Himeji
Institute of Technology, 2167 Shosha, Himeji
671-22(Japan).

ABSTRACT

Adherent and visually smooth deposits of molybdenum have been electrolytically deposited on copper, nickel, molybdenum, and graphite substrates in a KF-B₂O₃-Li₂MoO₄ melt at temperatures in the range 1023-1173 K and current densities in the range 110-880 Am⁻². The use of a graphite anode also gave a smooth deposit of molybdenum although its hardness (Hv: 274 at 200 g load) was higher than that (Hv: 157 at 200 g load) of the deposit obtained when using a molybdenum anode.

INTRODUCTION

Molybdenum metal has good physical properties at high temperatures and excellent corrosion resistance against molten salts, especially against sulfur-containing molten salts(1). However, it is very expensive and is difficult to fabricate. Therefore, it is a good idea to coat an inexpensive metallic substrate with molybdenum metal or to obtain molybdenum metal in the form of a sheet or rod. Previous papers have revealed that visually smooth coatings of molybdenum can be obtained electrolytically on metal substrates such as copper and nickel substrates in KF-B₂O₃-MoO₃, KF-B₂O₃-Na₂MoO₄, KF-B₂O₃-K₂MoO₄, KF-Li₂-B₄O₇-Li₂MoO₄, KF-Na₂B₄O₇-Na₂MoO₄, KF-K₂B₄O₇-K₂MoO₄ and KF-Na₂B₄O₇-K₂MoO₄ salt melts(2-8). Analogous to these melts, a KF-B₂O₃-Li₂MoO₄ melt was expected to give visually smooth coatings of molybdenum. Thus, this work was undertaken to study the electrodeposition of molybdenum in a KF-B₂O₃-Li₂MoO₄ melt and, in particular, to determine the ranges of bath composition, temperature and current density that give a visually smooth and adherent deposit of molybdenum. This salt was found to give molybdenum deposits with lower hardness than that of commercially available molybdenum metal. The literature on the electrodeposition of molybdenum from fused salts has been reviewed in a previous paper(2).

EXPERIMENTAL

Figure 1 shows schematic diagrams of the electrolytic cell assemblies. The preparation of electrodes were the same as described previously(7). The fused salts were prepared from KF(guaranteed reagent grade), B_2O_3 (guaranteed reagent grade) and Li_2MoO_4 (99% purity). The method for preparation of the bath was also the same as described previously(7). The electrolysis was carried out at constant current densities(110, 220, 330, 440, 550, 660, 770, 880 and 990 Am^{-2}) and at constant temperatures(998, 1023, 1073, 1123, 1153 and 1173 K). The procedures for electrolysis and the examination of electrodeposits were also the same as described previously(7). The current efficiencies were calculated from the changes in the mass of electrodes by assuming the anodic dissolution of Mo^{6+} and the cathodic deposition of Mo from Mo^{6+} .

RESULTS AND DISCUSSION

1) Effects of bath composition on the molybdenum deposition

To determine the optimal bath composition range, which gave a visually smooth deposit of molybdenum, 15 different baths were used for the electrolysis. Figure 2 shows the results of the visual examination and X-ray diffraction analysis for the electrodeposits. The $KF-Li_2MoO_4$ binary baths of series I and II gave no cathodic deposit of molybdenum metal nor of a molybdenum-containing compound. The addition of B_2O_3 to the $KF-Li_2MoO_4$ binary baths of series I and II gave visually smooth deposits of metallic molybdenum without dendrites at the edges of the substrates. However, the addition of a large amount of B_2O_3 resulted in the deposition of powdery molybdenum or a black matter. Figure 3 shows the X-ray diffraction pattern of the black matter. This matter was composed of MoO_2 and the unknown compound A, which has been described in a previous paper(3). On the other hand in series III the addition of B_2O_3 to the $KF-Li_2MoO_4$ binary bath did not give a deposit of metallic molybdenum, but gave a codeposit of MoO_2 and the compound A.

Figure 4 shows the variation in cathode current efficiency with the concentration of B_2O_3 . The cathode current efficiencies were almost 100 % when molybdenum metal was deposited.

Figure 5 shows the variation in anode current efficiency with the concentration of B_2O_3 . The anode current efficiencies were almost 100 % except for the $KF-Li_2MoO_4$ binary melts.

Figure 6 shows the variation in cell voltage with the concentration of B_2O_3 . The cell voltage varied with the concentration of B_2O_3 in a way similar to that in the other KF-borate-molybdate systems reported previously(2-8).

2) Effects of bath temperature and current density on the molybdenum deposition

To study the effects of bath temperature and current density on the molybdenum deposition, a $KF(60)-B_2O_3-(10)-Li_2MoO_4(10 \text{ mol}\%)$ bath was selected as a representative bath because, as can be seen from Fig.7, it had the lowest melting point(926 K) among the baths that gave smooth deposits of molybdenum under the electrolytic conditions described above. Table 1 lists the electrolytic conditions used and the results obtained. The lowest temperature which gave a visually smooth deposit without dendrites at the edges of the substrate was 1023 K(750°C).

The upper limits of the cathode current density that gave visually smooth deposits without dendrites at the edges of the substrates were 330 A m^{-2} at 1023 K, 550 A m^{-2} at 1073 K, 770 A m^{-2} at 1123 and 880 A m^{-2} at 1173 K. Figure 8 shows the comparison of these values with those of the other KF-borate-molybdate systems reported previously(3-8), indicating that the present system is superior to the other KF-borate-molybdate systems with regard to the upper limit of the cathode current density at low temperatures.

3) Deposition of molybdenum on different substrates

Copper, nickel, molybdenum, stainless steel(SUS304), mild steel(S20C) and graphite were tested as substrate materials. All the deposits were visually smooth without dendritic formation at the edges of the substrates. The deposits were of columnar structure, and firmly attached to the copper, nickel, molybdenum, and graphite substrates. In the case of the stainless steel and mild steel substrates, the adherence was good in appearance, but a black matter, which looked like an oxide under an optical microscope, was present here and there at the interfaces of the substrates and the molybdenum coatings. However, when the mild steel and stainless steel substrates were immersed in the bath with an applied voltage, the adherence was greatly improved.

The use of a graphite anode also gave a smooth and adherent deposit on a nickel substrate.

4) Hardness of the deposits

Table 2 lists the values of the Vickers microhardness of the deposits on the nickel, copper, molybdenum, stainless steel and mild steel substrates(a graphite

container was used). The hardness varied with changing substrate, indicating that the substrate metals somewhat diffused into the molybdenum coatings. Figure 9 shows the variation in the Vickers microhardness of the molybdenum deposits on the molybdenum substrates with the bath container material and the electrolytic temperature. The hardness of the deposits from the graphite container was a little higher than that of the deposits from the platinum container. This fact indicates that the use of a graphite container only a little contaminates the deposits that are obtained from the present fused salt system. Furthermore, the hardness of the deposits from the graphite container as well as the platinum container at 1073 K, 1123 K, and 1153 K was much lower than the hardness (Hv:198) of a molybdenum button that was prepared by plasma arc melting the commercially available Mo sheet that was used as an anode, while the hardness of the deposit at a low temperature of 1023 K was comparable with that of the molybdenum button. Therefore, it was found that the present fused salt system gives a molybdenum deposit with higher purity than or purity comparable with that of the commercially available molybdenum metal. The hardness of the deposit decreased with an increase in electrolytic temperature; for the explanation for this fact, further investigations are necessary. Table 3 lists the values of the Vickers microhardness of the deposits obtained at different cathode current densities; the hardness did not vary with cathode current density.

The value of the Vickers microhardness of the deposit obtained at 1153 K when using a graphite anode was 274 and much higher than that (152) obtained when using a molybdenum anode under otherwise identical conditions. This is probably due to the carbon (Mo_2C) in the deposits.

CONCLUSION

To find a fused salt giving a smooth, adherent deposit of molybdenum, $\text{KF-B}_2\text{O}_3\text{-Li}_2\text{MoO}_4$ fused salt baths were subjected to electrolysis. The results are summarized as follows:

- (1) Visually smooth deposits of molybdenum were obtained from $\text{KF-B}_2\text{O}_3\text{-Li}_2\text{MoO}_4$ fused salt baths.
- (2) The upper limits of the cathode current density that gave a visually smooth deposit in the $\text{KF-B}_2\text{O}_3(10)\text{-Li}_2\text{MoO}_4(10 \text{ mol}\%)$ fused salt bath were: 330 A m^{-2} at 1023 K, 550 A m^{-2} at 1073 K, 770 A m^{-2} at 1123 K and 880 A m^{-2} at 1173 K.
- (3) The adhesion of the smooth deposits of molybdenum to copper, nickel, molybdenum and graphite substrates was

very good.

(4) The Vickers microhardness of the smooth deposits was lower than or comparable with that of commercially available molybdenum metal even when a graphite crucible was used as a container of the bath.

(5) The use of a graphite anode also gave a smooth molybdenum deposit although its hardness was higher than that of the smooth deposit obtained when using a molybdenum anode.

REFERENCES

1. J. E. Battles, in "Critical Materials Problems in Energy Production," C. Stein, Ed., Academic Press, New York, p. 801(1976).
2. K. Koyama, Y. Hashimoto, S. Omori and K. Terawaki, Trans. Jpn. Inst. Met., 25(1984), 265.
3. K. Koyama, Y. Hashimoto, S. Omori and K. Terawaki, Trans. Jpn. Inst. Met., 25(1984), 804.
4. K. Koyama, Y. Hashimoto, S. Omori and K. Terawaki, Trans. Jpn. Inst. Met., 26(1985), 198.
5. K. Terawaki, K. Koyama, Y. Hashimoto and S. Omori, Nippon Kinzoku Gakkaishi, 50(1986), 303.
6. K. Koyama, Y. Hashimoto, S. Omori and K. Terawaki, J. Less-Common Met., 123(1986), 223.
7. K. Koyama, Y. Hashimoto and K. Terawaki, J. Less-Common Met., in press.
8. K. Koyama, Y. Hashimoto and K. Terawaki, J. Less-Common Met., in press.

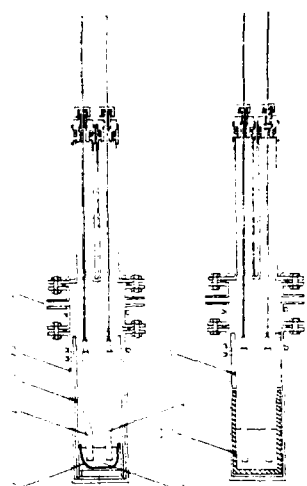


Fig.1 Schematic Diagrams of Electrolytic Cell Assemblies.

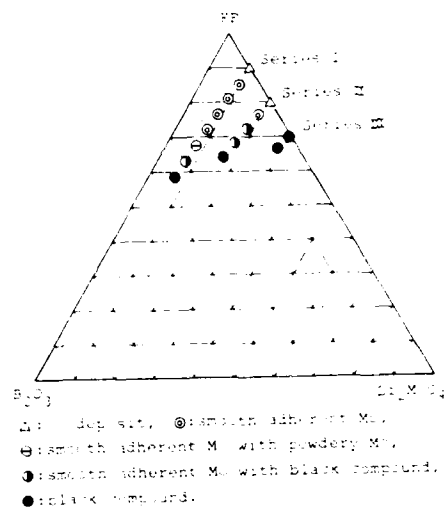


Fig.2 Results of Visual Examination and X-ray Diffraction Analysis.

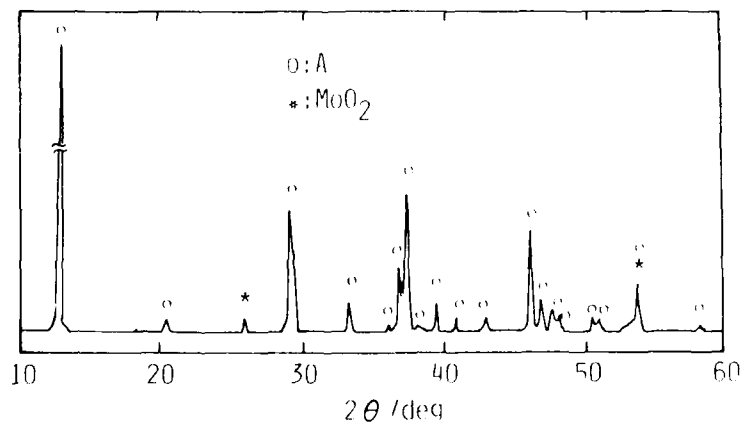


Fig.3 X-Ray Diffraction Pattern for Black Compound (CuK α).

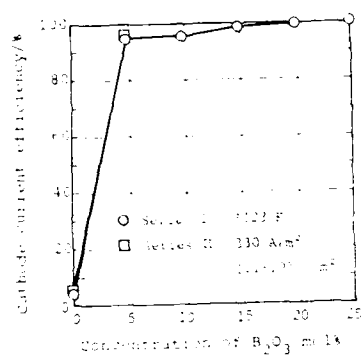


Fig. 4 Variation in Cathode Current Efficiency with B_2O_3 Concentration (Series I: $KF:Li_2MoO_4 = 9:1$; Series II: $KF:Li_2MoO_4 = 8:2$).

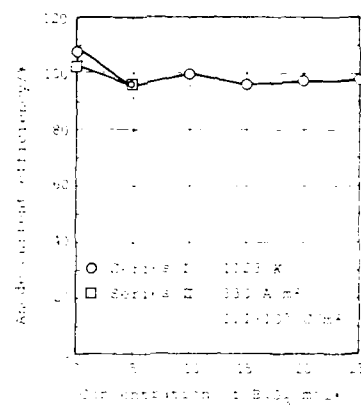


Fig. 5 Variation in Anode Current Efficiency with B_2O_3 Concentration (Series I: $KF:Li_2MoO_4 = 9:1$; Series II: $KF:Li_2MoO_4 = 8:2$).

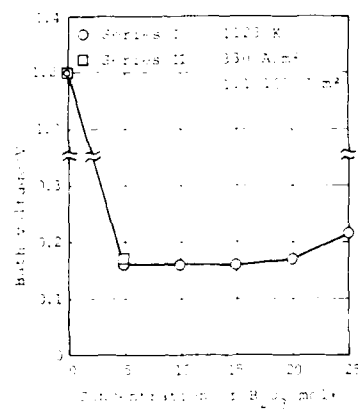


Fig. 6 Variation in Cell Voltage with B_2O_3 Concentration (Series I: $KF:Li_2MoO_4 = 9:1$; Series II: $KF:Li_2MoO_4 = 8:2$).

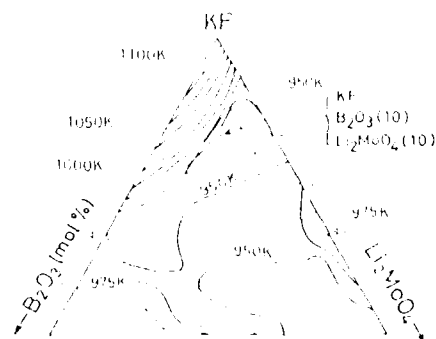


Fig. 7 Compositional Area giving Smooth Deposits and Composition of Representative Bath.

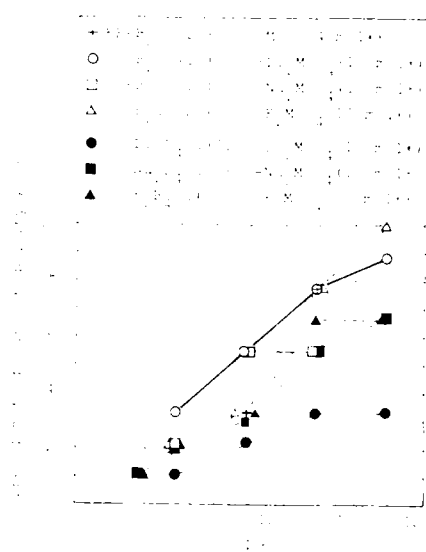


Fig. 8 Upper Limits of Cathodic Current Density giving Smooth Deposits without Dendrites at Edges of Substrate.

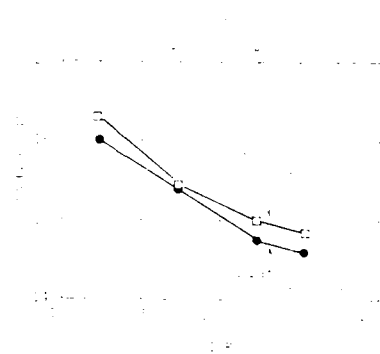


Fig. 9 Variation in Vickers Micro-hardness with Bath Container Material and Electrolyte Temperature.

Table 1 Effects of Temperature and Current Density on Deposition of Molybdenum from $\text{KF-B}_2\text{O}_3(10)\text{-Li}_2\text{MoO}_4(10 \text{ mol}\%)$ Bath.

Temp. (K)	Current density (Am^{-2})	Morphology of deposit	X-ray diffraction analysis	Cathode current eff. (%)	Cell voltage (V)
998	110	Smooth deposit, Lamellar deposit	Mo, MoO_2 , Unknown compound(B)	-	0.14
1023	110	Smooth deposit	Mo	95.3	0.11
	330	Smooth deposit	Mo	98.5	0.26
	440	Smooth deposit, Dendrite	Mo	99.6	0.31
1073	110	Smooth deposit	Mo	93.2	0.16
	550	Smooth deposit	Mo	100.7	0.30
	660	Smooth deposit, Dendrite	Mo	100.7	0.36
1123	110	Smooth deposit	Mo	98.5	0.07
	770	Smooth deposit	Mo	102.2	0.31
	880	Smooth deposit, Dendrite	Mo	101.4	0.37
1173	110	Smooth deposit	Mo	98.5	0.05
	880	Smooth deposit	Mo	102.2	0.33
	990	Smooth deposit, Dendrite	Mo	100.6	0.37

Electrolytic conditions: Molybdenum anode, Nickel cathode, Amount of electricity of $1.1 \cdot 10^6 \text{ Cm}^{-2}$, and Platinum container.

Table 2 Vickers Microhardness of Deposits on Several Substrates(200 g load)

Substrate	Mo	Ni	Cu	Stainless steel	Mild steel
Hardness	157	152	185	179	184

Electrolytic conditions: $\text{KF-B}_2\text{O}_3(10)\text{-Li}_2\text{MoO}_4(10 \text{ mol}\%)$ bath, 1123 K(850°C), 330 Am^{-2} , Amount of electricity of $5.6 \cdot 10^6 \text{ Cm}^{-2}$, Molybdenum anode, and Graphite container.

Table 3 Vickers Microhardness of Deposits Obtained at Different Cathode Current Densities(200 g load)

Current density(Am^{-2})	220	330	440
hardness	169	168	169

Electrolytic conditions: $\text{KF-B}_2\text{O}_3(10)\text{-Li}_2\text{MoO}_4(10 \text{ mol}\%)$ bath, 1073 K(800°C), Amount of electricity of $5.6 \cdot 10^6 \text{ Cm}^{-2}$, Molybdenum anode, Molybdenum substrate, and Platinum container.

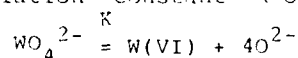
ELECTRODEPOSITION OF TUNGSTEN AND TUNGSTEN CARBIDE FROM MOLTEN HALIDE

Hideki Yabe, Yasuhiko Ito, Keiko Ema and Jun Oishi

Department of Nuclear Engineering, Faculty of Engineering,
Kyoto University, Sakyo-ku, Kyoto 606, Japan

ABSTRACT

The behavior of tungstate ion, such as its reduction potentials and dissociation equilibria in several molten halide systems, has been investigated, and using these data, electrodeposition of tungsten and tungsten carbide has been conducted. The reduction potentials of tungstate ion in a molten LiF-KF eutectic system at 973K were about 0.8V and 0.3V (vs. Li,K/Li⁺,K⁺). And dissociation constant K of the reaction;



was $K=5(+1)\times 10^{-12}$ (mole fraction unit). Taking these data into consideration, tungsten and tungsten carbide have been electrodeposited from both molten fluoride and chloride. The electrodeposit from the fluoride was dumpy or mossy.

INTRODUCTION

In this study, at first, oxyanions of tungsten, or tungsten and carbon, were dissolved in a molten LiF-KF system, and the dissociation constant and behavior of oxyanion were investigated by potential sweep method(1), chronopotentiometry(2) and zirconia sensor method(3)(4). Next, using these results, electrodeposition of tungsten metal and tungsten carbide has been conducted. Tungsten and carbon were added to the molten salt as oxyanions because of their stability and simplicity of the experimental procedure.

In this field, several experimental results have been reported, eg., electrodeposition of tungsten etc. from molten fluoride by Senderoff et al.(5)(6), electrodeposition of tungsten bronzes from molten alkali polytungstates by Meites et al.(7), electrodeposition of tungsten carbide from sodium tungstate, graphite anode serving as the source of carbon in molten sodium chlorides by Gomes et al.(8), and electrodeposition of tungsten

carbide etc. from molten fluoride by Stern et al. (9)(10)(11). But reference electrode used in these studies didn't have stability and reproducibility. So, their results can not be regarded as standard reference in considering electrolytic conditions quantitatively. For example, Ni/NiF₂ electrode, which was used by Senderoff et al., doesn't have a stability because of occurrence of Ni/NiO potential by contaminated oxide ion. While platinum electrode, which was used by Stern et al., lacks reproducibility, as well as thermodynamic significance. So, in this study, to avoid such difficulties, alkali metal electrode M/M⁺ (M:Li,K)(12) was used as a reference electrode, which had good reproducibility and has thermodynamic significance. Furthermore, in their studies, relation between ion concentrations and morphology of electrodeposit was not considered. Then, to make it clear, dissociation constant of tungstate ion in a melt was determined by using a zirconia-air oxide ion indicator. By this experiment, it has become possible to conduct electrodeposition by monitoring concentration of oxide ion and of all other ions in the melt.

EXPERIMENTAL

Experimental apparatus is shown in Fig.1. As an electrolyte, LiF-KF eutectic or LiCl-KCl eutectic was used. Then, it was contained in a high purity alumina or carbon or nickel crucible, and was dried under vacuum at just under the melting point for a few days. After that, it was melted under an argon atmosphere and kept at experimental temperature. A nickel wire was dipped into the eutectic salt saturated with nickel oxide contained in a mullite tube (Nippon Kagaku Togyo Co., Ltd.), which was used as a Ni/NiO reference electrode. As an Ag/AgCl electrode, a silver wire was dipped into the eutectic salt containing silver chloride in a pyrex glass tube whose tip was very thin. Moreover, for potential calibration, alkali metal electrode M/M⁺ (M:Li,K)(12) was used, for which alkali metal was electrodeposited on the nickel wire in molten salt. The electrode thus prepared showed good reproducibility. As an anode, glassy carbon was used, and as a cathode, a nickel plate which was placed inside the alumina tube was used. Besides, zirconia-air electrode(4) (Nippon Kagaku Togyo Co., Ltd.) was used as an oxide ion indicator or as a reference electrode.

After melting the salt, vacuum dried potassium tungstate, or potassium tungstate and potassium carbonate of about 0.02~2.0mol% were added, and the electrodeposition was conducted on the cathode at 823~973K with current density of 20~500mA/cm². The potential was kept

more negative than reduction potential of tungsten determined from voltamograms. For analyses of the samples, IR, EDXA, EDX, ESCA, RBS and X-ray diffraction were used.

RESULTS AND DISCUSSION

1. The behavior of tungstate ion

At first, the reduction potentials of tungsten were investigated both by potential sweep method and chronopotentiometry. A typical voltammogram at 973K in a LiF-KF is shown in Fig.2. This figure was obtained when 0.1mol% potassium tungstate was added, and the scan rate was 0.3V/sec. The peak indicating the reduction of tungstate ion can be seen at about 0.8V and 0.3V against the alkali metal electrode, respectively. And an example of chronopotentiogram is shown in Fig.3. In this case, also, plateau which indicates the reduction of tungstate ion is observed at about 0.8V.

Next, dissociation constant K of tungstate ion dissociation,



at 973K in a molten fluoride, can be determined as follows: Equation [1] was used as a basis of calculation, though there are some possibilities of partial dissociation. After careful estimation, it was concluded that the assumption of eq.[1] is satisfactory enough. Then, from eq.[1], the dissociation constant in mole fraction unit is written as

$$K = \frac{[\text{W(VI)}]_{\text{bulk}} [\text{O}^{2-}]_{\text{bulk}}^4}{[\text{WO}_4^{2-}]_{\text{bulk}}} \quad [2]$$

As the tungstate ion concentration ($[\text{WO}_4^{2-}]_{\text{add}}$) is increased, the oxide ion concentration and the tungsten ion concentration in bulk vary according to the following equations:

$$[\text{O}^{2-}]_{\text{bulk}} = [\text{O}^{2-}]_{\text{initial}} + 4[\text{W(VI)}]_{\text{bulk}} \quad [3]$$

$$[\text{WO}_4^{2-}]_{\text{bulk}} = [\text{WO}_4^{2-}]_{\text{add}} - [\text{W(VI)}]_{\text{bulk}} \quad [4]$$

Substituting these relations into eq.[2], and using the theoretical equation

$$E = E_0 - 2.303 \frac{RT}{2F} \log [\text{O}^{2-}]_{\text{bulk}} + 2.303 \frac{RT}{2F} \log (1 + K' [\text{O}^{2-}]_{\text{bulk}}) \quad [5]$$

of the zirconia-air electrode which we derived before(4), the relation between the potential of zirconia-air electrode and added tungstate ion can be deduced. Here, E_0 shows characteristic nature of the individual zirconia-air electrode. While K' is a constant reflecting deviation from the Nernst line at high oxide ion concentration. These constants (called zirconia constants in our previous paper(4)) depend on individual zirconia-air electrode, which can be evaluated by experiments. Then, from the curve fitting similar to that described in our previous paper(4), K can be determined. The alternate method for determining K value is to titrate definite amount of tungstate ($[WO_4^{2-}]_{add(initial)}$) with oxide ion ($[O^{2-}]_{add}$). Oxide ion, tungsten ion and tungstate ion concentration vary according to:

$$[O^{2-}]_{bulk} = [O^{2-}]_{bulk(initial)} + [O^{2-}]_{add} - 4[W(VI)]_{dec} \quad [6]$$

$$[W(VI)]_{bulk} = [W(VI)]_{bulk(initial)} - [W(VI)]_{dec} \quad [7]$$

$$[WO_4^{2-}]_{bulk} = [WO_4^{2-}]_{bulk(initial)} + [W(VI)]_{dec} \quad [8]$$

Substituting these relations into eq.[2], and using eq.[5], K can be determined by computer curve fitting.

Here, $[WO_4^{2-}]_{bulk(initial)}$, $[W(VI)]_{bulk(initial)}$ and $[O^{2-}]_{bulk(initial)}$ are deduced from eq.[2], [3] and [4]. And, $[W(VI)]_{dec}$ is a decreased concentration of $W(VI)$ by addition of oxide ion. Fig.4 shows relation between the potential of zirconia-air electrode against the alkali metal electrode, and the concentration of tungstate ion, where open circles and solid line show experimental values and calculated values, respectively. For the calculation, zirconia constants of $E_0=2.17V$ (vs. $Li, K/Li^+, K^+$) and $K'=0$, and dissociation constant of $K=5 \times 10^{-12}$, and the initial oxide ion concentration of $[O^{2-}]_{initial}=1.3 \times 10^{-4}$ mole fraction were used. The measured and calculated values are very close to each other in a wide concentration range. Fig.5 shows relation between the potential of zirconia-air electrode and concentration of oxide ion. Open circles show experimental data when the concentration of initial tungstate ion was $[WO_4^{2-}]_{add(initial)}=1.78 \times 10^{-3}$ mole fraction, and solid line shows calculated values. For the calculation, zirconia constants of $E_0=2.00V$ (vs.

Li,K/Li⁺,K⁺) and $K'=350$, and dissociation constant of $K=6 \times 10^{-12}$, and initial oxide ion concentration of $[O^{2-}]_{\text{initial}}=4.0 \times 10^{-4}$ mole fraction were adopted. The measured and calculated values almost agreed. And the equilibrium constants estimated by these two different ways were almost consistent. From the results of several experiments, the dissociation constant of the tungstate ion in LiF-KF eutectic melt has been calculated to be $5(\pm 1) \times 10^{-12}$ at 973K.

2. Electrodeposition of tungsten

Tungsten was electrodeposited under several conditions, in which concentrations of three ionic species in eq.(1) were monitored and the reduction potential was controlled. Fig.6 shows SEM of sample electrodeposited at 973K, by a current density of 50 mA/cm^2 in a LiF-KF, containing 1.0mol% of K_2WO_4 ($[WO_4^{2-}]=6.3 \times 10^{-4}$, $[W(VI)]=3.7 \times 10^{-4}$, $[O^{2-}]=1.7 \times 10^{-3}$ mole fraction). In the figure, mossy deposit can be seen. From EDX spectrum, the deposition of tungsten could be observed. X-ray diffraction was clearly recognized that tungsten metal alone was deposited. By ESCA and RBS, also, the deposition of tungsten was confirmed.

3. Electrodeposition of tungsten carbide

Fig.7 shows a SEM sample electrodeposited at 973K by a current density of 100 mA/cm^2 from LiF-KF containing 1.0mol% of K_2WO_4 and 2.0mol% of K_2CO_3 . In this figure, uniform coating is observed, which main component was concluded from EDX to be tungsten. ESCA analyses show that tungsten and carbon are contained in the sample. X-ray diffraction spectrum is shown in Fig.8. From the spectrum, it is clear that WC and W_2C were electrodeposited. Peak of nickel and lithium fluoride on the spectrum came from the cathode plate itself and salt on the surface, respectively. Fig.9 shows an influence of deposition potential on the morphology of deposits. These samples in the figure were all obtained by electrodeposition containing 1.0mol% of K_2WO_4 and 1.0mol% of K_2CO_3 at 973K from LiF-KF, and (a) is a sample electrodeposited at 0.8V against alkali metal electrode, while (b) and (c) are obtained at 0.6V and 0.4V, respectively. X-ray diffraction showed that they were all tungsten carbide. These SEM show that the more noble the potential is, the more uniform become the deposits.

4. Electrodeposition from molten chloride

Electrodeposition of tungsten and tungsten carbide from molten chloride was also conducted in order to find dependence of morphology and composition of the deposit on anion and on a small amount of additive element in a melt. These results will not be described here for want of space, and will be described in detail in our separate paper "ELECTROCHEMICAL REACTION OF WO_4^{2-} ION IN LiCl-KCl EUTECTIC MELT" appearing in this proceedings.

ACKNOWLEDGMENTS

We would like to thank Mr. Teruyoshi Umezaki of the Kyoto University for EPMA, Dr. Tsuyoshi Nakajima of Kyoto University for ESCA and Mr. Seiji Terada of the Kawasaki Heavy Industries, Ltd. for SEM, EDX and EPMA.

This work was carried out under support from a Grant-in-Aid from the Japanese Ministry of Education, Science and Culture.

REFERENCES

1. R. S. Nicholson and I. Shain, Anal. Chem., **36**, 706(1964).
2. T. Berzins and P. Delahay, J. Amer. Chem. Soc., **5**, 4205(1953).
3. G. Picard, F. Seon and B. Tremillon, J. Electrochem. Soc., **129**, 1450(1982).
4. Y. Ito, H. Yabe, T. Nakai, K. Ema and J. Oishi, Electrochim. Acta, **31**, 1579(1986).
5. S. Senderoff and G. W. Mellors, J. Electrochem. Soc., **114**, 586(1967).
6. S. Senderoff and G. W. Mellors, Science, **153**, 1475(1966).
7. L. Meites, E. Banks and C. W. Fleischmann, Anal. Chem., **44**, 1133(1972).
8. J. M. Gomes and M. M. Wong, U.S. Bur. Mines Rep. Invest., 7247(1969).
9. K. H. Stern and S. T. Gadomski, J. Electrochem. Soc., **130**, 300(1983).
10. K. H. Stern and I. L. Singer, Thin Solid Films, **108**, 9(1983).
11. K. H. Stern and M. L. Deanhardt, J. Electrochem. Soc., **132**, 1891(1985).
12. K. Ema, Y. Ito, T. Takenaka and J. Oishi, J. Chem. Soc., Japan, to be published

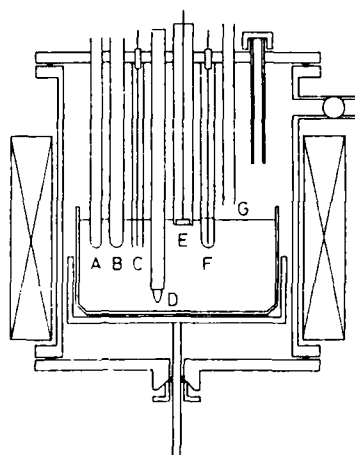


Fig.1 Experimental Apparatus.
 A: Thermocouple, B: Zirconia Electrode, C: M/M^+
 ($M:Li, K$) Electrode, D: Counter Electrode (Anode),
 E: Working Electrode (Cathode), F: Reference
 Electrode, G: Gas Inlet

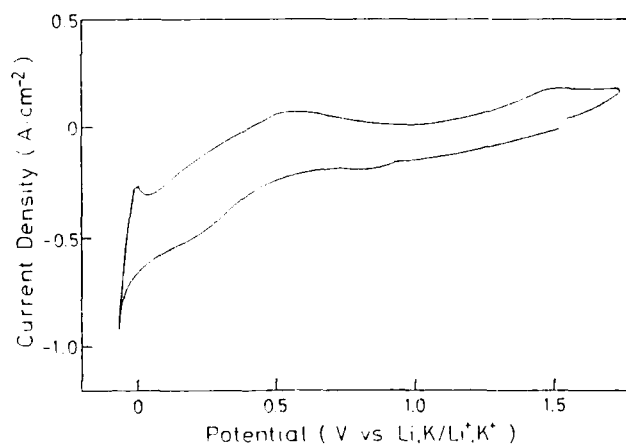


Fig.2 Typical Voltammogram of Molten LiF-KF
 Containing 0.1mol% of K_2WO_4 . (973K, Scan Rate
 (.3V/sec)

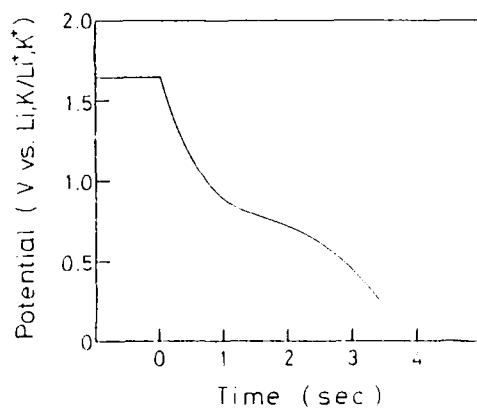


Fig.3 Typical Chronopotentiogram of Molten LiF-KF Containing 0.1mol% of K_2WO_4 . (973K, Current Density $100mA/cm^2$)

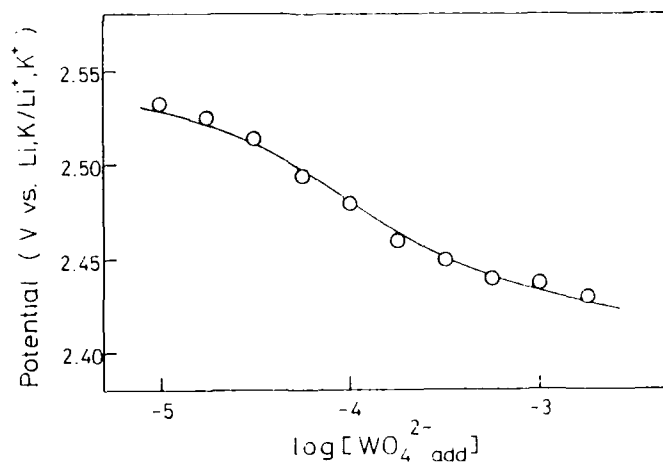


Fig.4 Potential- $\log[WO_4^{2-} \text{ add}]$ Curve of Molten LiF-KF. ($K=5 \times 10^{-12}$, $[O^{2-} \text{ initial}] = 1.3 \times 10^{-4}$ mole fraction, Zirconia Constants: $E_0 = 2.17V$, $K' = 0$, 973K)

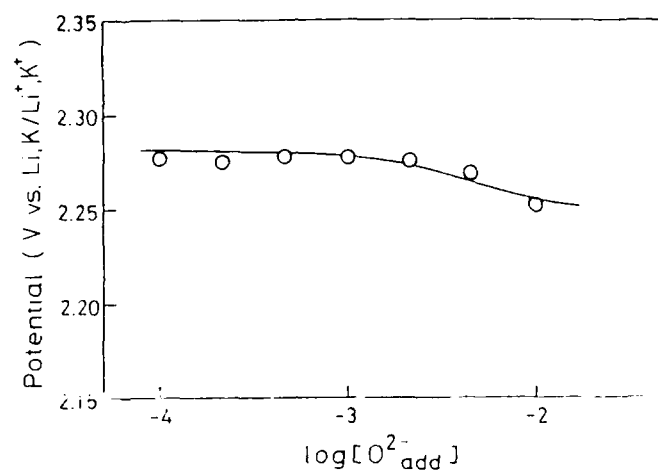


Fig.5 Potential- $\log[O^{2-}_{add}]$ Curve of Molten LiF-KF. ($K=6 \times 10^{-12}$, $[WO_4^{2-}_{add(initial)}]=1.78 \times 10^{-3}$ mole fraction, $[O^{2-}_{initial}]=4.0 \times 10^{-4}$ mole fraction, Zirconia Constants: $E_0=2.00V$, $K'=350$, 973K)

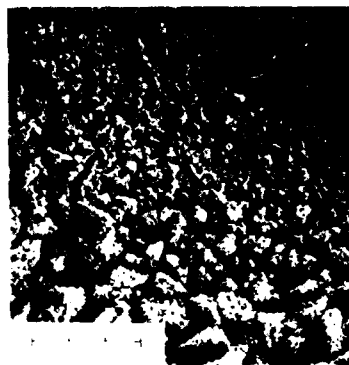


Fig.6 Scanning Electron Micrograph of Tungsten. (LiF-KF, $K_2WO_4:1.0mol\%$, Current Density $50mA/cm^2$, 973K)

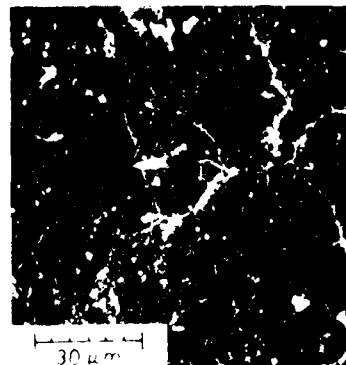


Fig.7 Scanning Electron Micrograph of Tungsten Carbide. (LiF-KF, $K_2WO_4:1.0mol\%$, $K_2CO_3:2.0mol\%$, Current Density $48.2mA/cm^2$, 973K)

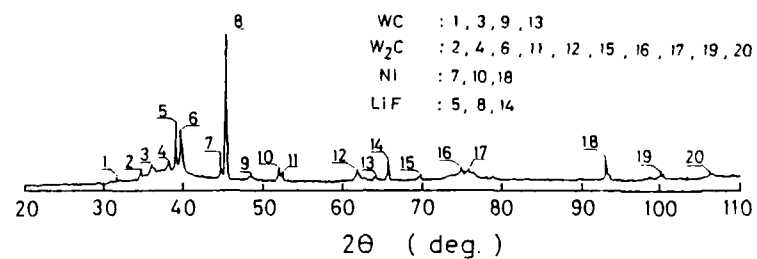


Fig.8 X-ray Diffraction Pattern (Cu K- α) of Tungsten Carbide Sample (Fig.7).

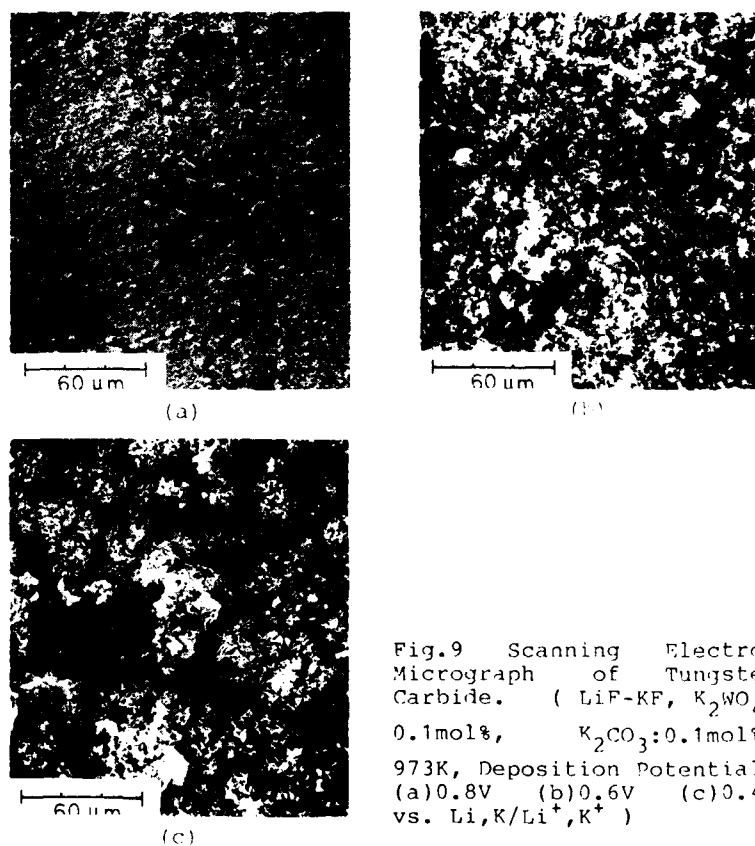


Fig.9 Scanning Electron Micrograph of Tungsten Carbide. (LiF-KF, K_2WO_4 : 0.1mol%, K_2CO_3 :0.1mol%, 973K, Deposition Potential: (a)0.8V (b)0.6V (c)0.4V vs. Li,K/Li $^+$,K $^+$)

ELECTRODEPOSITION OF TUNGSTEN FROM
ZnBr₂-NaBr MELTS

H.Hayashi^o, N.Hayashi, K.Uno and Z.Takehara
Department of Industrial Chemistry, Faculty of Engineering
Kyoto University, Kyoto 606, JAPAN

A.Katagiri
Department of Chemistry, College of Liberal Arts
Kyoto University, Kyoto 606, JAPAN

ABSTRACT

The possibility of tungsten electrodeposition from ZnBr₂-NaBr melts at 350-450 °C was examined mainly by means of constant potential method and pulse potential method. The morphology and quality of the deposits were closely related to the acidity of the melt. In basic melts, the deposits were thick and coarse, while in the acidic melts, the deposits were fine but thin. These results are interpreted based on the stability of a possible tungsten cluster species.

INTRODUCTION

For many years, a lot of useful refractory metals have been produced by means of molten salt electrolysis (1-5). Most of them are obtained by the electrolysis of molten fluoride systems, where the working temperature is relatively high (700-850°C, approximately), and therefore the corrosion of container materials and electrode materials is serious.

The authors have tried to find alternative solvent materials for electrowinning of refractory metals and mainly have been studying the molten ZnBr₂-NaBr systems. These melts exhibit so-called Lewis acidity and have a concentration dependent acid-base character as in the case of sodium chloroaluminate melts. The acid is defined as bromide ion acceptor, while the base is defined as a bromide ion donor. The acidity is indicated by using pBr⁻ value, which is equal to $-\log[aBr^-]$. So called "basic" melts are melts where the NaBr mole fraction is larger than 0.5 and vice-versa for "acidic" melts.

^opresent address: Department of Synthetic Chemistry,
Faculty of Engineering, Okayama University, 700, Okayama, JAPAN

So, "neutral" means that NaBr and ZnBr_2 are equimolar. In acidic melts, some kinds of oxyanions or complex ions that have an unusual oxidation state can be stable (6), because the concentration of "free" halide ion is very low (7-9). Therefore it is possible to obtain some metallic elements by the electroreduction of these unusual oxidation state ions. In the bromide systems, metal-halogen bond increases their covalent character compared with chloride systems, so the acidity of the bromide system is higher than that of the chloride system with same cation ratio.

The liquidus temperature of ZnBr_2 -NaBr system is about 300°C for compositions ranging from 30% NaBr (acidic melts) to 70% NaBr (basic melts). Although the working temperature of electrolysis should be higher by 100-150 degrees than that of aluminum containing melts, it is very interesting to investigate these melts as potential solvents in refractory metal deposition and to study the chemistry of most refractory metal species in this melt. From this point of view, we have studied the electrodeposition of tungsten in ZnBr_2 -NaBr melts.

EXPERIMENTAL

A nickel plate (square shape 2.0cm^2) was used as the substrate for tungsten electrodeposition. It was electropolished in a mixed solution of sulfuric acid and phosphoric acid for 1 minute before use. A tungsten spiral was used as the counter electrode. In the case of cyclic voltammetry, a zinc wire was used as the reference electrode which was separated from the bulk electrolyte by a glass frit. The zinc wire (99.99% Rare Metallic) was dipped in a dilute hydrochloric acid solution in order to remove oxide films on the surface. All chemicals used were of reagent grade quality. Zinc bromide (Wako Chemical) and sodium bromide (Wako Chemical) were dried individually at 300°C for more than 24 hours under vacuum. Tungsten trioxide (Wako Chemical) and tungsten(V) bromide (Alfa Product) were used without any purification. The electrolysis was performed by means of constant potential method and constant potential pulse method. During the electrolysis, dry argon gas was bubbled through the melt for stirring. After electrodeposition, the substrate was taken out from the cell, washed by distilled water then dried in vacuo. The electrode surface was examined by SEM and EPMA. X-ray diffraction pattern was also obtained for the identification of deposits.

RESULTS

Fig.1 shows an example of cyclic voltammogram at a platinum micro electrode in ZnBr_2 -NaBr plus WO_3 solute. In the case of cathodic scan, the cathodic current starts to flow at the potential of 0.1V vs. Zn/Zn^{2+} . A cathodic current peak is observed at the potential of 50mV, which is considered to correspond to tungsten deposition. Therefore, potentials from 0 to 100mV were employed in subsequent controlled potential experiments. The peaks around 1.35V correspond to the bromine evolution and its reduction.

Photo 1 shows the morphology of the deposits obtained in a controlled potential electrolysis at 50mV in neutral ZnBr_2 -NaBr (NaBr 50 mol %) with WO_3 solute. The deposits were composed of small particles of different sizes. Many cracks between the particles were observed. Although some amount of tungsten species was detected by EPMA, the existence of metallic tungsten was not confirmed by the X-ray diffraction pattern. In order to obtain metallic tungsten, pulse electrolysis at constant potentials was tried. The pulse wave described in Fig.2 was used for electrolysis. Photos 2-4 show the morphology of deposits in cases of basic (NaBr 60 mol %), neutral (NaBr 50 mol %) and acidic (NaBr 40 mol %) compositions, respectively. X-ray diffraction pattern and EPMA chart for each sample are also described in Figs.3-5, which clearly indicate that the deposition of metallic tungsten occurred. By changing the ZnBr_2 -NaBr melt condition from basic to acidic, the size of deposited particles decreases and the deposits become compact. In basic composition, it is clear from Fig.3 that the deposited tungsten film is relatively thick. On the other hand in neutral and acidic compositions, the deposited film is thin.

The solubility of WO_3 in ZnBr_2 -NaBr melt is very small, although it is easy to handle WO_3 as a solute. Therefore, WO_3 was replaced by WBr_5 as a solute. Photos 5 and 6 show the morphology of deposits by using WBr_5 solute in basic and acidic melts, respectively. The morphology and the quality of deposits are also dependent on the melt composition, as in the case of WO_3 solute. Photo 7 shows the morphology of tungsten deposit obtained by constant current method at 450°C. The deposited particles are cubic shaped and the deposited film is rather thick.

DISCUSSION

As described above, the acidity of the melt, i.e. its composition affects the morphology and quality of the tungsten deposits. The deposited particle is fundamentally cubic shaped (Photo 7). Going from acidic to basic the deposited particle increases its size and becomes coarse. The following explanation can be given to the effect of melt acidity. Thus, in basic composition, the deposit grows faster in the direction perpendicular to the electrode surface and most of the overvoltage component is used for crystal growth. In acidic melt, the overvoltage component is used for crystal nucleation and a lot of fine particles are formed on the electrode surface, although the thickness is small.

As pointed out by Mamantov et. al.(10), some refractory metal halogen clusters exist in acidic melts, for example, $W_6Cl_8^{4+}$ species in $AlCl_3$ -NaCl. According to the study on electroplating of chromium from fluoride melts(11), chromium metal is not formed directly from Cr^{3+} but from Cr^{2+} intermediate species. This intermediate species is insoluble below $850^{\circ}C$ but becomes soluble at temperatures higher than $893^{\circ}C$. By taking into account the above results, some tungsten cluster species may exist in $ZnBr_2$ -NaBr melts during the tungsten deposition process. In acidic melts, the tungsten cluster species may be stable in the melt, so that the rate determining step may be its reduction process. Therefore, fine but thin deposits can be obtained. In basic melts, the cluster species may not be stable, then the growth rate of the crystal may be large. By increasing the working temperature, also the stability of the cluster species seems to decrease. This explains that relatively thick deposits were obtained at $450^{\circ}C$ even in acidic melts.

REFERENCES

1. S.Senderoff, G.W.Mellors and W.J.Reinhart, J.Electrochem.Soc., **112**, 840 (1965)
2. G.W.Mellors and S.Senderoff, ibid., **113**, 60 (1966)
3. G.W.Mellors and S.Senderoff, ibid., **118**, 220 (1971)
4. S.Senderoff and G.W.Mellors, ibid., **113**, 66 (1966)
5. S.Senderoff and G.W.Mellors, ibid., **114**, 556 (1967)
6. G.Mamantov and R.A.Osteryoung, "Characterization of Solutes in Nonaqueous Solvents", chap. 11, p.223, Plenum Press, New York and London (1978)
7. G.Torsi and G.Mamantov, Inorg. Chem., **10**, 1900 (1971)
8. A.A.Fannin, L.A.King and D.W.Seegmiller, J.Electrochem.Soc., **119**, 801 (1972)
9. L.G.Boxall, H.L.Jones and R.A.Osteryoung, ibid., **120**, 223 (1973)
10. A.G.Cavinato, G.Mamantov and X.B.Cox III, J.Electrochem.Soc., **132**, 1136 (1985)
11. T.Yoko and R.A.Bailey, ibid., **131**, 2590 (1984)

$\text{ZnBr}_2:\text{NaBr}=50:50$
 $\text{WO}_3 = 0.05 \text{ mol/kg}$
 350°C

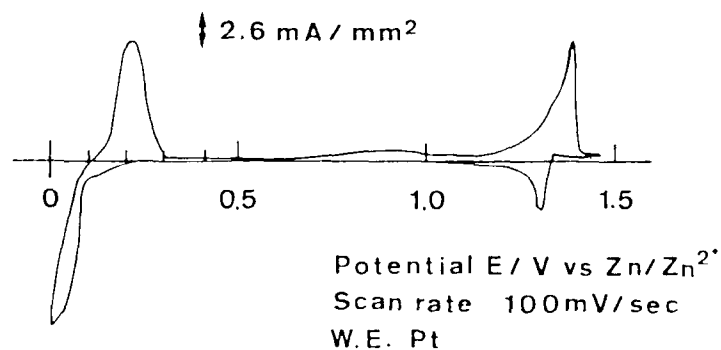


Fig.1 Cyclic voltammogram of tungsten species in the ZnBr_2 -NaBr melts

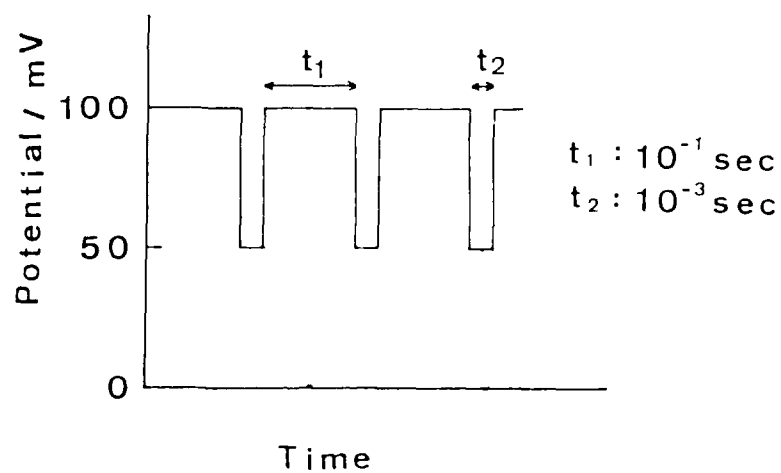


Fig.2 Pulse shape used in the pulse electrolysis

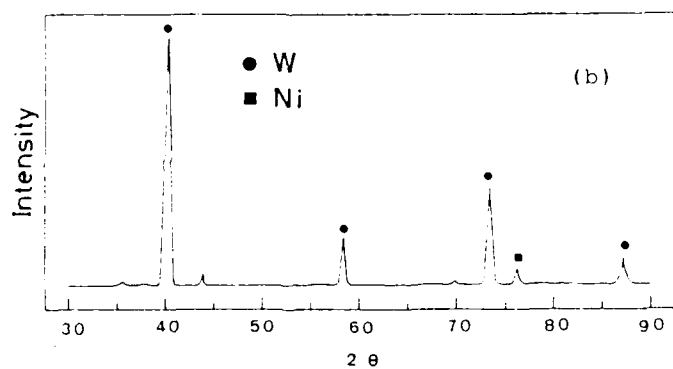
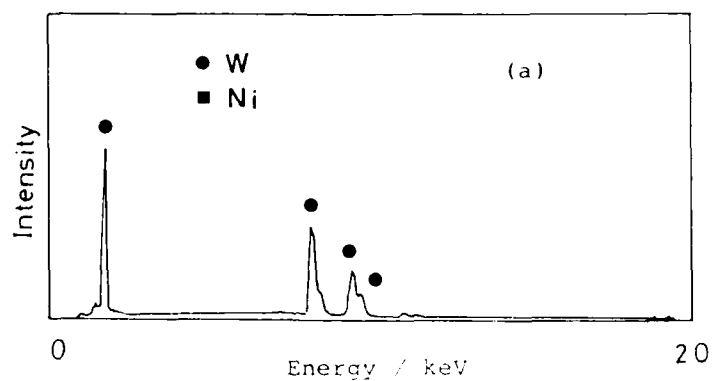


Fig.3 EPMA chart (a) and X-ray diffraction pattern (b) of the deposits; WO_3 solute in basic composition ($\text{ZnBr}_2:\text{NaBr}=40.1:59.9$) pulse potential method (cf.Photo 2)

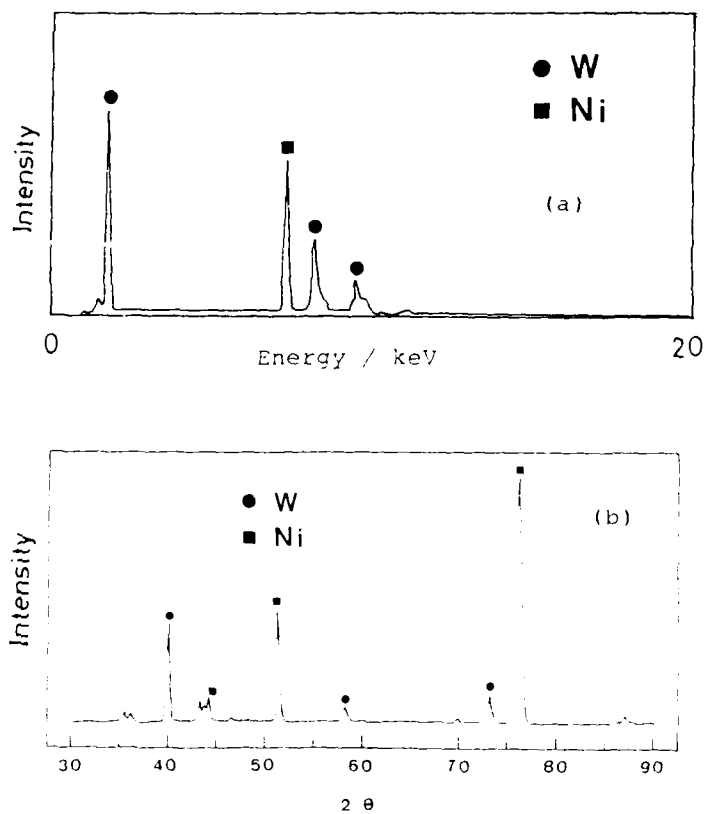


Fig.4 EPMA chart (a) and X-ray diffraction pattern (b) of the deposits; WO_3 solute in neutral composition ($\text{ZnBr}_2:\text{NaBr}=50.1:49.9$) pulse potential method (cf.Photo 3)

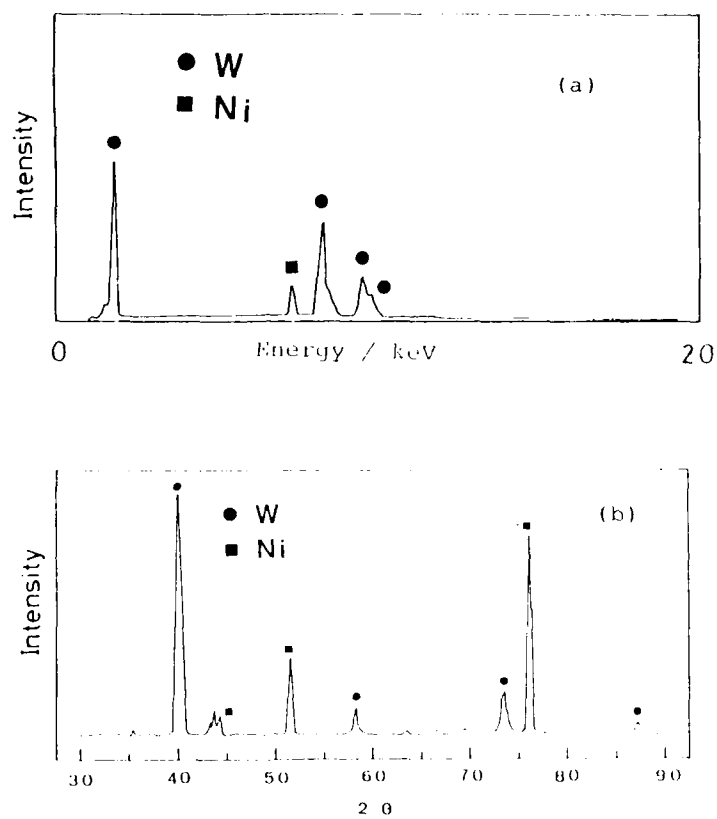


Fig.5 EPMA chart (a) and X-ray diffraction pattern (b) of the deposits; WO_3 solute in acidic composition ($\text{ZnBr}_2:\text{NaBr}=59.8:40.2$) pulse potential method (cf. Photo 4)

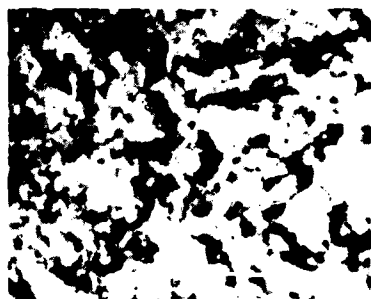


Photo 1

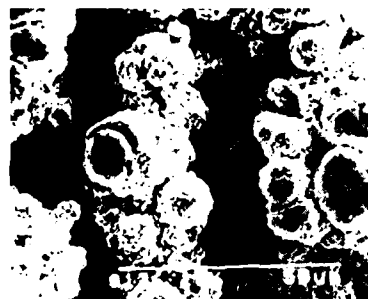


Photo 2

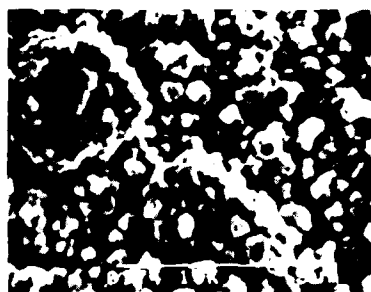


Photo 3

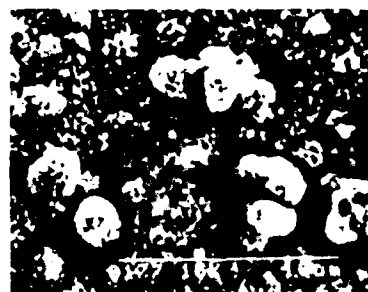


Photo 4

Photo 1-4 SEM picture of electrodeposits obtained by constant potential method(1) and pulse potential method(2-4) with WO_3 solute at $350^\circ C$

melt composition	1 --	50.5:49.5
($ZnBr_2:NaBr$)	2 --	40.1:59.9
	3 --	50.1:49.9
	4 --	59.9:40.2



Photo 5



Photo 6



Photo 7

Photo 5-7 SEM picture of electrodeposits obtained by pulse potential method(5-6) and constant current method at 450°C(7) with WBr_5 solute

melt composition	5 --	40.4:59.6
(ZnBr_2 :NaBr)	6 --	60.0:40.0
	7 --	40.3:59.7

ELECTROCHEMICAL REACTION OF WO_4^{2-} ION
IN LiCl-KCl EUTECTIC MELT

Yasuhiko Ito, Takashi Shimada, Hideki Yabe and Jun Oishi

Department of Nuclear Engineering
Faculty of Engineering
Kyoto University
Sakyo-ku, Kyoto 606, Japan

ABSTRACT

The electrochemical reduction of WO_4^{2-} ion to tungsten metal in LiCl-KCl eutectic melt has been studied, in order to find the optimum electrolytic condition to obtain desirable tungsten metal film on the cathode. Tungsten metal was actually obtained on the nickel substrate and its surface state depends on the electrolytic condition. In some condition it is flower-like and in the other condition it is scale-like. High pure cubic tungsten crystal could be obtained when the electrolyte contained very small amount of silver ion.

Tungsten ion was reduced to metallic tungsten through several steps, which include not only electrode reactions but also disproportionation reactions. In order to obtain good and adherent tungsten film, deposition by disproportionation reaction should be avoided. For this purpose it seems desirable to supply HCl gas into the melt after dissolving tungstate ion and to keep potential more negative than 0.5V (vs. $\text{Li,K/Li}^+, \text{K}^+$)

INTRODUCTION

Tungsten metal is a useful high temperature material which has superior properties concerned with corrosion resistance and electric conductivity, etc., and tungsten carbide is used as a super hard material. In order to obtain these materials by electrodeposition from molten halide system, a series of electrochemical studies has been conducted by the authors(1). This work has been done as a part of them and has been conducted to clarify electrochemical reduction of WO_4^{2-} ion to tungsten metal in LiCl-KCl eutectic melt.

The tungsten film obtained by this reaction has various surface states depending on electrolytic conditions, such as concentration of tungstate ion, temperature, potential and current density, etc. Adherence between tungsten film and substrate is also to be taken into consideration.

Thus, in order to find the optimum electrolytic condition to obtain desirable tungsten metal film on the cathode, relation between surface state and electrolytic condition, effect of a small amount of additives on the crystal structure as well as reduction mechanism of tungstate ion have been investigated.

EXPERIMENTAL

Experimental apparatus is shown in Fig.1. As an electrolyte, LiCl-KCl eutectic system was used, which was contained in a high purity alumina or quartz glass crucible. All chemicals were reagent grade (Wako Chemicals Co., Ltd.). In order to remove contaminated water, it was dried under vacuum at 200 °C for three days. Then, after it was melted, HCl-Ar gas mixture was bubbled into the melt for an hour. Finally, Ar gas was bubbled to remove HCl entirely. Insides of both experimental apparatus and glove box were kept under argon atmosphere at 823-973K.

As a reference electrode (Fig.1-E), an Ag/AgCl electrode was used, for which silver wire was dipped into the eutectic salt containing silver chloride in pyrex glass tube whose tip was very thin. For potential calibration, alkali metal electrode Li/E/Li⁺, K⁺ (Fig.1-B) was used, for which alkali metal was electrodeposited on the nickel wire in the molten electrolyte. The electrode thus prepared showed good reproducibility. As an anode (Fig.1-B), glassy carbon was used, and as a cathode (Fig.1-D), nickel, gold, platinum and glassy carbon were used. After melting the salt, potassium tungstate of 0.01-1.0 mol% was added, and electrodeposition was conducted on the nickel substrate that was placed inside the alumina tube.

For analyses of the electrodeposited samples, SEM, EPMA, EDX and X-ray diffraction were used.

In order to observe how the electrodeposition was going on, transparent electric furnace (Ishikawa Sangyo Co., Ltd.) was used.

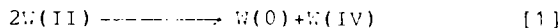
RESULTS AND DISCUSSION

1. Electrodeposition of tungsten

Fig.2 and 3 show SEM of tungsten electrodeposited at 823K by a potential of 0.5V and 0.8V (against $\text{Li,K/Li}^+,\text{K}$), respectively, in LiCl-KCl containing 1.0 mol% of potassium tungstate. The figure of the electrodeposit is flower-like in Fig.2 and scale-like in Fig.3, respectively. Fig.4 shows SEM of tungsten electrodeposited at 973K by a current density of 100 mA/cm^2 in LiCl-KCl containing 1.0 mol% of potassium tungstate, when a very small amount of silver ion was added in the melt. Cubic crystal could be obtained. By X-ray diffraction (Fig.5) and EDX (Fig.6), it was concluded to be high purity tungsten crystal. Thus, surface state of an electrodeposited tungsten film is strongly dependent on the electrolytic condition.

2. Direct observation of the electrodeposition reaction

Fig.7 shows schematic illustration of the electrodeposition reaction observed by using transparent electric furnace. As the cathodic current flowed, small particles appeared in the electrolyte near the electrode, which then deposited on it. These particles almost fell down from the substrate as soon as the current was cut-off. But they could be recovered as powders. By X-ray diffraction, they were proved to be metallic tungsten. So, tungsten is reduced not only by electrode reaction but also by disproportionation in the electrolyte due to the reaction of, for example, Eq.[1].



3. Voltammetric studies

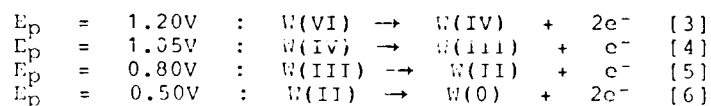
Fig.8 shows voltammograms obtained with the use of gold, platinum, glassy carbon and nickel, at 823K in LiCl-KCl by potential sweep method. Among them, as seen in the figure, the most negative potentials can be reached with nickel. Then nickel was used as a working electrode in the following experiments.

Fig.9 shows a typical voltammogram obtained at 823K in LiCl-KCl containing 0.4 mol% of potassium tungstate. The peak indicating the reduction of tungsten ion can be seen at about 1.2V and 0.5V against the alkali metal electrode, respectively. That is, tungstate ion is reduced to metallic tungsten through two steps. Number of electrons n at each step calculated using Nicholson's equation (2):

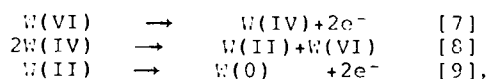
$$n = -2.20 \times (RT/F) / (E_p - E_p/2) \quad [2]$$

both are nearly equal to 2.

When HCl gas was supplied to the melt after the dissolution of potassium tungstate, (We call it W-Cl system), drastic change of voltammogram has been observed as shown in Fig.10. That is, current peaks can be seen at about 1.2V, 1.05V, 0.8V and 0.5V, respectively. Thus, by supplying HCl into the melt, the peaks newly appear at 1.05V and 0.8V. Number of electrons n of the reduction corresponding to each peak can be calculated from Eq.[2], to be 2, 1, 1 and 2, respectively. Then the reaction at each peak can be assigned as Eq.[3]-[6], respectively.

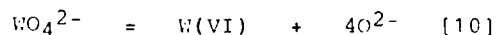


Taking into consideration that the reduction of tungsten ion can proceed not only by electrode reaction but also by disproportionation reaction, the difference of number of peaks between W-O system (the system into which HCl was not supplied) and W-Cl system can be understood by assuming that disproportionation occurs more easily in W-O system than in W-Cl system. That is, in W-O system, the possible reactions are Eq.[7]-[9]



and only two peaks, concerned with the reactions of Eq.[7] and [9], appear in the voltammogram. On the other hand, in W-Cl system, four peaks concerned with the reactions of Eq.[3]-[6] are to be observed.

Sometimes, also in W-O system, four peaks appear depending on the experimental condition. This can be explained by the shift of the dissociation equilibrium :



to the right hand side due to the very small concentration of oxide ion in LiCl-KCl by some reasons. In this case, the ligands of tungstate ion are changed from oxide ion to chloride ion, and the disproportionation reaction may no longer occur.

CONCLUSIONS

The electrodeposition of tungsten in LiCl-KCl eutectic system was investigated. The results are summarized as follows:

1. Tungsten metal was obtained on the nickel substrate by electrodeposition from LiCl-KCl eutectic system containing tungstate ion.
2. Surface state of the electrodeposited tungsten depends on the electrolytic condition. Some of them are flower-like and some are scale-like. High purity cubic tungsten crystal could be obtained by electrodeposition from the electrolyte which contained very small amount of silver ion.
3. Tungstate ion in LiCl-KCl was reduced to metallic tungsten through several steps, which include not only electrode reactions but also disproportionation reactions.
4. Disproportionation reaction occurs more easily in W-O system. Tungsten obtained by disproportionation is powder. In order to obtain good and adherent tungsten film by electrodeposition in LiCl-KCl eutectic system containing tungstate ion, deposition by disproportionation should be avoided. The most desirable way to obtain good and adherent tungsten film is to supply HCl gas into the melt after dissolving tungstate ion, and to keep potential more negative than 0.5V (vs. Li,K/Li⁺,K⁺).

ACKNOWLEDGEMENTS

We would like to thank Mr. Teruyoshi Unezaki of the Kyoto University for EPMA and Mr. Seiji Terada of the Kawasaki Heavy Industries, Ltd. for SEM, EDX and EPMA.

This work was carried out under support from a Grant-in-Aid from the Japanese Ministry of Education, Science and Culture.

REFERENCES

1. H. Yabe, Y. Ito, K. Ema and J. Oishi, to be published.
2. R. S. Nicholson and I. Shain, Anal. Chem., **36**, 704 (1964).



Fig. 1 Experimental Apparatus
 A: Thermocouple
 B: Li/P/Li⁺ Electrode
 C: Counter Electrode (Anode)
 D: Working Electrode (Cathode)
 E: Reference Electrode

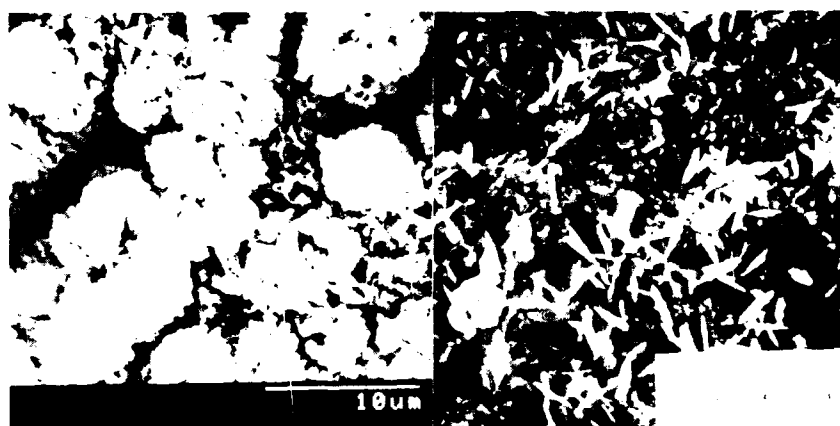


Fig. 2 SEM of Carbon
 (1) 1000x magnification
 (2) 1000x magnification
 (3) 1000x magnification
 (4) 1000x magnification
 (5) 1000x magnification

Fig. 3 SEM of Carbon
 (1) 1000x magnification
 (2) 1000x magnification
 (3) 1000x magnification
 (4) 1000x magnification
 (5) 1000x magnification



Fig.4 SEM of Tungsten
(LiCl-KCl, 973K,
K₂NO₄: 1.0 mol%,
Small Amount of Ag⁺,
Current Density:
100 mA/cm²)

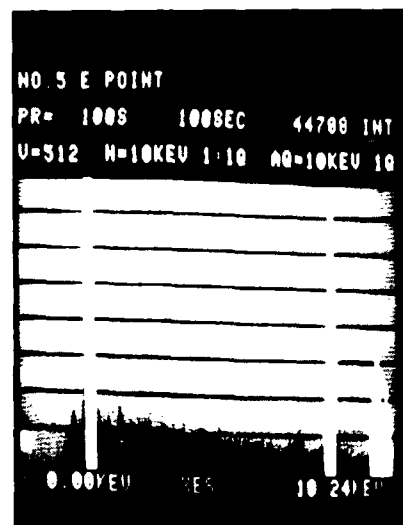


Fig.6 EDX Spectrum of
Tungsten Sample (Fig.4)
(Three white peaks
indicate tungsten)

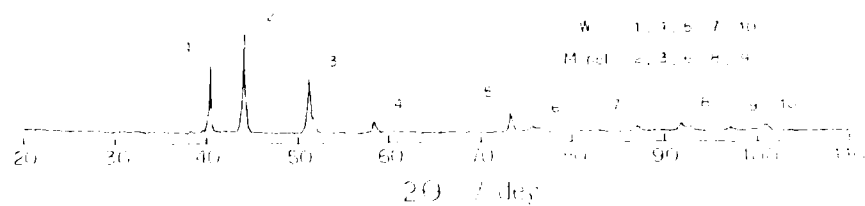
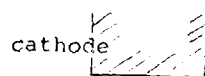


Fig.5 X-ray Diffraction Pattern (Cu K- α)
of Tungsten Sample (Fig.4)

(1) Before electrolysis



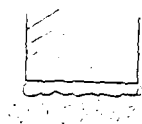
Transparent dark blue solution

(2) Beginning of electrolysis



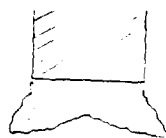
Colloidal powders appear
in the electrolyte

(3) During electrolysis



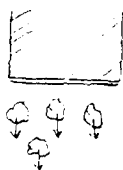
Powders deposit on the cathode
to form thick layer

(4) End of electrolysis



Very thick deposit layer

(5) After electrolysis



Falling off of the deposit layer
leaving thin surface film

Fig.7 Schematic Illustration of The
Electrodeposition Reaction

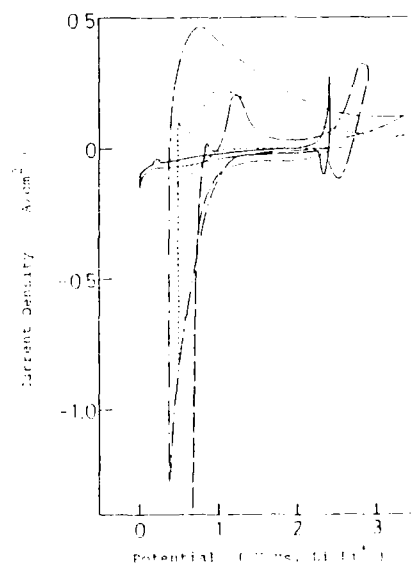


Fig.8 Voltammogram
 LiCl-KCl (823K)
 Scan Rate 0.1 V/sec
 — : Ni
 --- : Glassy Carbon
 - · - : Pt
 : Au

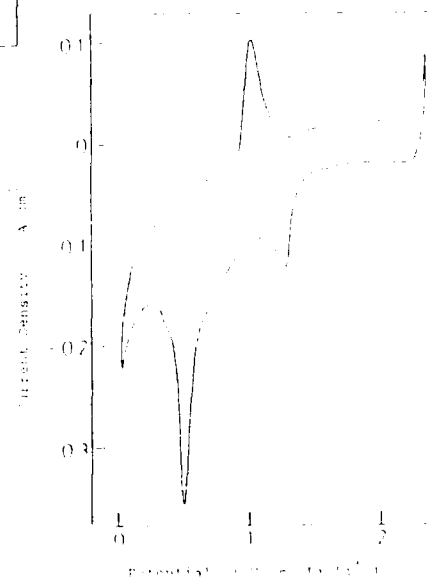


Fig.9 Voltammogram
 LiCl-KCl (823K)
 K₂WO₄ 0.4 mol%
 Scan Rate 0.1 V/sec
 HCl gas was not supplied.

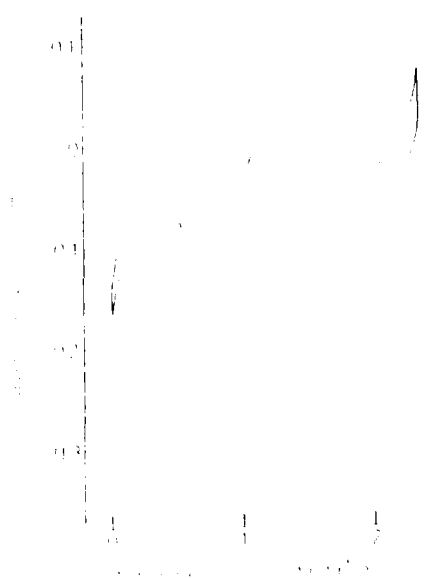


Fig.10 Voltammogram
 LiCl-HCl (823K)
 H_2WO_4 0.1 mol%
 Scan Rate 0.1 V/sec
 HCl gas was supplied.

**PREPARATION OF NEODYMIUM-IRON MASTER
ALLOYS FROM NEODYMIUM (III) SALTS AND
METALLIC IRON IN MOLTEN CHLORIDE -
FLUORIDE MIXTURES**

Francine M. SLOV,
Rhodie-POLSKO

Centre de Recherche d'Albervilliers,
14, rue des Gardinoux,
F-93308 Albervilliers Cedex, France

ABSTRACT

Over the last few years, the need for neodymium has increased because of the development of neodymium-iron-boron magnets with very high magnetic properties. Today, metallic or alloyed neodymium is mainly manufactured using the electrothermic reduction technique. Here, the results are presented of our laboratory investigations on a new route for obtaining low melting point master neodymium alloys, which are obtained from NdCl_3 by electroreduction in molten chlorides. A comparison between this method and the electrothermic preparation is given.

INTRODUCTION

The first permanent magnets, those containing iron-nickel alloys, were developed in the 1930's. About 10 years later, ferrites (compounds of iron and barium or strontium oxide) appeared on the market. These two kinds of magnets have a maximum energy product (Prmax) of about 0.5 M J/m³ (density 4.720 g/cm³). More than twenty years later, in the 1950's, rare earth and cobalt magnets made their appearance. Their strength is four times higher than Al-Ni and ferrites, and they have a Curie temperature in the range of 700-900°C (1). In 1963, General Motors and DuPont reported (2) that they revealed the new possibilities offered by neodymium-iron-boron (Nd-Fe-B) magnets, which have very high Prmax (4.5 M J/m³) and a low Curie temperature (about 300°C) (3,4).

The need for metallic neodymium, which was only a few hundred tons in 1963, increased up to 60 t last year and is forecasted to pass 1100 t by 1990, a figure that could double by 2000.

Today, metallic or alloyed neodymium is mainly produced by using the electrothermic reduction route (5,6). The purpose of this paper is to report the results of our laboratory investigations on a new route for obtaining low melting point master neodymium alloys, whose compositions are close to the eutectic point, Fe-20%Nd (7,8) (See Fig. 1). This technique is based on the electroreduction of NdCl_3 containing salts using consumable iron cathodes. A comparison of these two routes indicates that the electrolytic process is a very promising preparation technique.

EXPERIMENTAL

Reagents

The compounds used for the electroreduction experiments were:

are grouped in Table 1, where suppliers and purity of the compounds are summarized. $\text{NdCl}_3 \cdot 6\text{H}_2\text{O}$, $\text{CaCl}_2 \cdot 2\text{H}_2\text{O}$ and lithium halides were dehydrated and dried by heating under reduced pressure. Their maximum water content was ~ 1 wt %. Other products were used in their commercially available form.

Electrolysis operating procedure.

The experiments were carried out in either alumina or glassy carbon crucibles placed in an Inconel-made reactor. Heating was carried out by means of an electric furnace. Two types of electrodes, vertical or horizontal, were investigated, as shown in Fig. 2. The anode was a graphite rod, and the consumable cathodes were iron rods. The anode-cathode distance depended on the runs. The electrolytic bath was made up of a mixture of the neodymium chloride to be electrolyzed and alkaline halides.

Values of the cathodic current density (ccd) were $100 - 250 \text{ A.dm}^{-2}$, and the voltage was 4 - 10 volts. For each electrolysis operation, the metal produced was recovered after hot pouring into a cast iron ingot mold.

Calciothermic reduction operating procedure.

Iron chips, calcium grains, neodymium fluoride and anhydrous calcium chloride to constitute the loading were intimately mixed together.

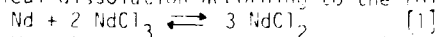
The amount of CaCl_2 added was adjusted so as to obtain, after reduction, a $\text{CaCl}_2\text{-CaF}_2$ molten slag. The amount of the reducing metal (Ca) was above the stoichiometric quantity, and the amount of iron depended on the desired composition of the alloy to be produced.

The mixture described above was introduced into a tantalum crucible (whose capacity was approximately one liter) placed at the bottom of an Inconel-made reactor, itself placed in an electric-resistance furnace. After reducing pressure (1 cm Hg), the temperature was raised to $1000-1100^\circ\text{C}$. Then the reaction was conducted at this temperature, under atmospheric pressure in an inert gas atmosphere (argon) maintained throughout the reduction. During heating, two phases were formed in the reaction medium: a metallic phase constituted by the rare earth - iron alloy, on top of which floated a $\text{CaCl}_2\text{-CaF}_2$ slag. After a reaction time ranging from 30 min to 2 hours, the alloy was separated from the slag by hot pouring into a cast iron ingot mold.

RESULTS AND DISCUSSION

Solubility of metallic neodymium in various molten alkaline halide + neodymium (III) chloride mixtures.

The solubility of neodymium in chloride melts is a complex process involving both physical dissolution as a metal fog, and chemical dissolution according to the following equilibrium:



We take into account the overall solubility by defining it as the weight loss of a metal sample occurring when it is immersed in the melt.

Effect of NdCl_3 content and temperature in pure chloride melts.

It is first to be noted that neodymium "dissolves" in a melt which does not contain NdCl_3 because of a metal dispersion phenomenon

(e.g. after 3 hours, we observed that 2 wt % metal dissolves in a BaCl_2 (78 wt %) - NaCl bath at 940°C). Metal solubility strongly depends on NdCl_3 content in the melt. At 800°C , for example, solubility equal to 7 wt % in a melt containing 30 wt % NdCl_3 is at least tripled when NdCl_3 content reaches 80 wt %. Moreover, temperature has a great influence on solubility: solubility (7 wt % at 800°C) becomes unacceptable (~ 22 wt %) beyond 1000°C , which is close to neodymium's melting point. These results explain why Kurita (14) obtained only yields lower or equal to 20 % for the electrowinning of neodymium from a NdCl_3 - KCl bath.

Benefit due to the presence of alkaline fluorides and lithium salts. Our experiments have shown that solubility is always lower in chloride-fluoride media than in pure chloride melts when temperature is less than 1000°C . For example, solubility is equal to 4 wt % at 800°C in a chloride-fluoride bath containing 30 wt % NdCl_3 , that is, twice lower than in pure chloride melts (7 wt %). This effect of fluoride salts may be explained by their complexing role, causing the oxidation state + III of neodymium to stabilize. This, in turn, leads to the disproportionation of neodymium (II) (displacement of equilibrium [1] to the left), thus decreasing the "chemical" solubility.

We also observed that lithium salts give a similar effect: compared with melts without lithium, solubility is always lower in melts containing LiCl or LiF . The major impact of lithium salts will be seen in electrolysis yields.

Impact on the choice of electrolytic bath composition. Our experimental results described above can be summarized as follows: (i) metal solubility strongly depends on neodymium (III) content of the bath; (ii) whatever the bath composition, neodymium solubility steeply increases when temperature reaches 1000°C ; (iii) for a given neodymium (III) content of the bath, solubility is higher in pure chloride melts than in chloride-fluoride melts. Thus, for the electrowinning of neodymium - iron alloys, chloride-fluoride baths containing lithium salts with a low amount of neodymium chloride are preferable to pure chloride melts in order to minimize the yield loss due to metal solubilization.

Neodymium - iron alloy electrowinning on consumable iron cathodes.

The master alloy under study was the eutectic neodymium - iron composition (88 wt % Nd - 12 wt % Fe), which melts at 640°C (see Fig. 1); it can be electrolyzed at a low enough temperature for neodymium solubility to remain sufficiently low.

Effect of several operating parameters on metal yield. In the following, the metal yield R_M designates the ratio of the neodymium obtained with respect to the neodymium in the NdCl_3 introduced in the electrolytic bath. In addition, the duration of electrolysis t is given with respect to t_0 , which is the time theoretically required for reduction of all the NdCl_3 at 100% current efficiency R_F .

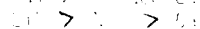
Fig. 3a indicates the effect of temperature on the metal yield of alloys electrowon on consumable vertical cathodes in a melt containing 25 wt % NdCl_3 , and Fig. 3b gives the corresponding neodymium content of these alloys. It is observed that the metal yield reaches 75 %

at 850°C, R_M becomes very low ($\approx 10^{-3}$) for temperatures close to 1000°C, at which metal solubility is predominant. In the temperature range from 800 to 1000°C, the electrolyzer metal composition can be deduced from the Nd/Fe phase diagram (Fig. 1). On the contrary, when temperature is lower than 800°C, a Nd-Fe alloy is difficult to obtain because of the decreasing of the diffusion rate of neodymium into iron.

The influence electrolyzing time on metal yield and current efficiency has been studied by electrolyzing neodymium chloride at 850°C on horizontal iron cathodes in the molten desiccant above. Values of η and R_M have been respectively 70 to 75% and 70. Depending on the time, the recovered nodules titrated 65 to 68 wt % neodymium. An analysis of Fig. 4, which specifically gives the metal yield, current efficiency, electrolysis time relationship, shows that aiming at high productivity (high metal yield) leads to weak current efficiency. In order to optimize the batch operating conditions, by reaching a compromise between productivity and energy consumption, we have considered the cumulative yield R_M , defined as the product of R_M and η . As we can see from Fig. 4 that R_M presents a maximum for an electrolyzing time $t = 1.5$ h. For this set of experiments a metal yield of 70% and a current efficiency of 50% are obtained.

Concerning the electrolyzing time, it has been found that LiCl-Li₂O bath at 850°C with an electrolyzing time of 1.5 h, we have observed that there is practically no dependence of the metal yield when the anode-cathode distance is within 10 to 15 cm.

It has been considered desirable to obtain a molten salt bath for neodymium from electrolyzing neodymium chloride in a LiCl-Li₂O bath with $x = 0.01$. This bath has been used in a neodymium-iron cathode compositions have been chosen containing 25 wt % of neodymium chloride. Electrolysis has been carried out at a constant voltage of 2.5 V, with a ccd of 100 A/cm². Their electrolyzing time was varied from 1 to 10 h. Fig. 5 positively shows that replacement of LiCl by Li₂O is unfavorable as metal yield falls when the amount of LiCl in the bath decreases. R_M , which is equal to 70% with a salt containing LiCl only, falls to 28% with a LiCl-Li₂O containing bath. However, it is preferable to replace LiCl completely with Li₂O rather than LiCl, as the metal yield is almost twice as high (Fig. 6). The electrolyzing time of 1 h, the salt used is 100 g of neodymium chloride, and the anode is graphite. It is shown that metal yield decreases as follows:



Electrolysis carried out on horizontal cathodes at 850°C with LiCl-Li₂O-Li₂CO₃ bath containing a varying amount of Li₂CO₃ (from 250 to 750 g A/cm²; $x = 2/3$) unequivocally demonstrated (Fig. 6) that metal yield falls when Li₂CO₃ content increases. On the contrary, R_M has a nearly constant value of 40 to 41%.

Comparison of the electrolytic process and calcium reduction to obtain neodymium-iron alloys.

Typical example of a calciothermic reduction of NdFe₃ in the presence of iron chips. We carried out the following experiment: 100 g of iron chips, 101.0 g of calcium, 281.4 g of Fe₂O₃ and 100 g of anhydrous

CaCl_2 . 188.0 g of neodymium-iron alloy has been recovered with a composition of 87.4 wt % Nd, 12 wt % Fe and almost 0.6 wt % Ca, with a metal yield equal to 81 % (15). In general, metal yields were always better than 80 %.

Electrolysis compared with chemical reduction.

Both preparation methods make it possible to produce the desired master alloy, with a good purity level, as is seen in Table 2. Here, the main impurities are different in each case. Electrolytic alloys generally contain 0.2 wt % Al (due to a slight corrosion of the crucible) and 0.2 wt % Cl. Calciothermic alloys have an average calcium level of 0.4 wt %. This can, however, be decreased to 200 ppm by distillation in a HF furnace at 1300 °C under reduced pressure. Metal yields are quite similar (> 80 %).

CONCLUSION

Operating conditions for optimum efficiency are now known for both processes. In particular, the calciothermic percentage of conversion (or yield) is virtually the same in both cases, and contamination of the alloy by the crucible is slight. In conclusion, the respective features and advantages of the two processes have been compared. (Calcium reduction of neodymium fluoride is a good technique because, if the required procedure is followed, slag separation is easily accomplished (15). Although available for an industrial process, calcium (which has to be used in excess) is a costly reductant. Virtually the calciothermic preparation is a batch process, while electrolysis of neodymium chloride is a continuous method. The master alloy is produced at the bottom of the electrolytic cell where it can be drained off (16). In addition, electrowinning offers great flexibility with respect to the amount of metal to be produced and potential low cost in the preparation of master iron-neodymium alloys to be used in obtaining the desired composition (30-37 wt % Nd, 1-7 % Al, Fe) for permanent magnets.

REFERENCES

1. P. Falconnet, Commission of the European Communities, Proceedings of the workshop on rare earth permanent magnets held in Brussels, (1984) p.15, edited by I.V. Mitchell, CRC.
2. M. Sagawa, S. Fujimura, H. Yamamoto, Y. Matsuda and K. Hirada, IEEE Transactions on magnetics, Mag. 20, 1584 (1984).
3. K.A. Gschneidner Jr., J. Less. Common Metals, 100, 1 (1984).
4. J.J. Croat, European patent 6108474 (1984).
5. A.L. Robinson, Science, 223, 920 (1984).
6. J.J. Croat, Appl. Phys. Lett., 34, 357 (1981).
7. F. Trombe, Ann. de Chim., 6, 24 (1936).
8. F. Trombe, Chimie et Industrie, 77, 277 (1957).
9. K.A. Gschneidner Jr., Science and Technology of Rare Earth Materials, (1980) p.25, Academic Press, NY.
10. I.K.S. Murphy and C.K. Gupta, Science and Technology of Rare Earth Materials, (1980) p.17 and 27, Academic Press, NY.

11. B.J. Beaudry and K.A. Gschneidner Jr., Handbook of the Physics and Chemistry of Rare Earths, (1978) p. 173, North Holland Publish. Cie.
12. J.L. Morarty Jr., J. Metals, 41 (1968).
13. V.F. Terekhova, E.V. Maslova, Ye.M. Savitskiy, Russ. Metallurgy (Metally) 3, 50 (1965).
14. T. Kurita, Denki Kagaku, 35, 7, 496 (1967).
15. F. Seon and B. Boudot, French Patent 2548687 (1985), U.S. Patent 4636253 (1987).
16. F. Seon and G. Barthole, European Patent 184515 (1986).

Table 1 : Suppliers and purity level of the main reagents used.

Products	Suppliers	Purity
Rare earth halides and oxides	Rhone-Poulenc La Rochelle Plant	Halides (*) : 96 % Oxides (*) : 99.0 or 99.9 %
Metallic Calcium	China Nuclear Energy Industry Corporation	Ca grains > 99.5 % main impurities { Al : 0.01 % Mg : 0.02 %
Calcium chloride	Rhone-Poulenc (Prolabo)	CaCl ₂ · 2 H ₂ O RP (further dehydrated under reduced pressure).
Iron	Höganäs	Iron chips > 99 % main impurities Si : 0.2 % C, P, S each ~ 0.01 %
Lithium halides	Parker	LiCl : 99.3 % LiF : 99.5 %

(*) Ratio of neodymium/rare earth.

Table 2 : Average analyses (wt %) of typical alloys resulting from either a calciothermic reduction or an electrolysis.

Elements	Calciothermic reduction	Electrolysis production
Nd	86.0	88.2
Fe	13.0	11.7
Ca	0.4	0.002
Li	-	0.02
Mg	0.02	0.01
Al	0.001	0.20 (*)
Si	0.05	0.01
C	0.06	< 0.02
Mn	0.07	0.03
Cr	-	0.02 (*)
F	≤ 0.02	0.04
Cl	< 0.01	0.2
O ₂	0.04	0.08
N ₂	≤ 0.01	0.004

(*) Crucible corrosion

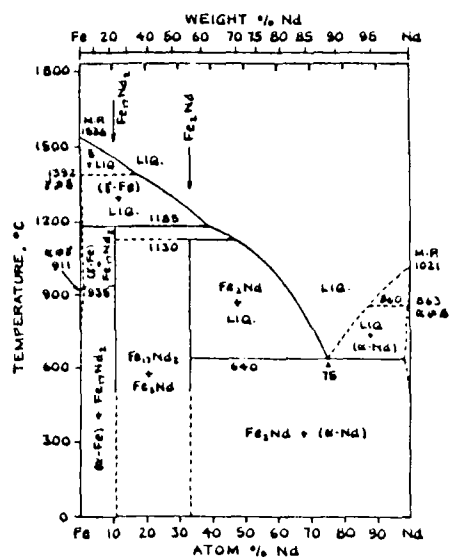


Figure 1 : Binary phase diagram Nd/Fe [after (13)].

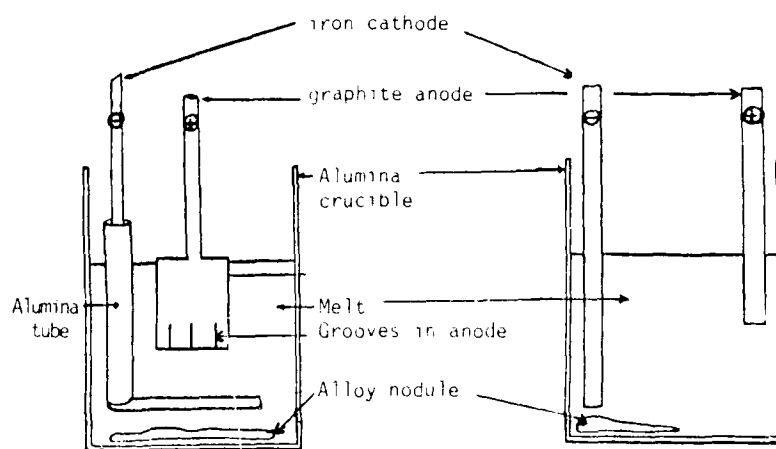


Figure 2 : Electrochemical cell

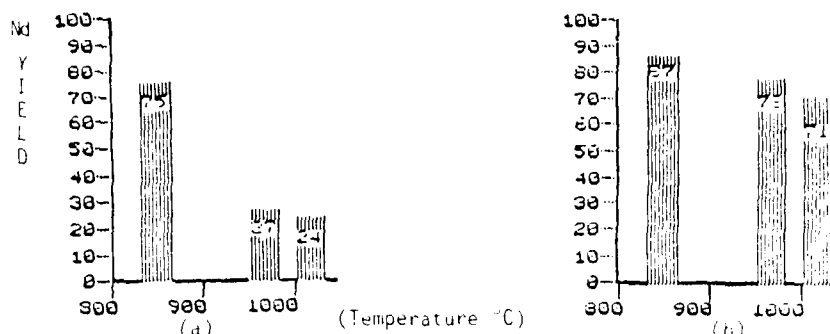


Figure 3 : Nd/Fe electrowinning on consumable iron cathode.
Effect of temperature on :
a) metal yield
b) neodymium content of resulting alloys
(NdCl_3 25 wt % - LiCl - LiF ; ccd 200 to 250 $\text{A} \cdot \text{dm}^{-2}$;
electrolysis time $t = 1.5 t_0$).

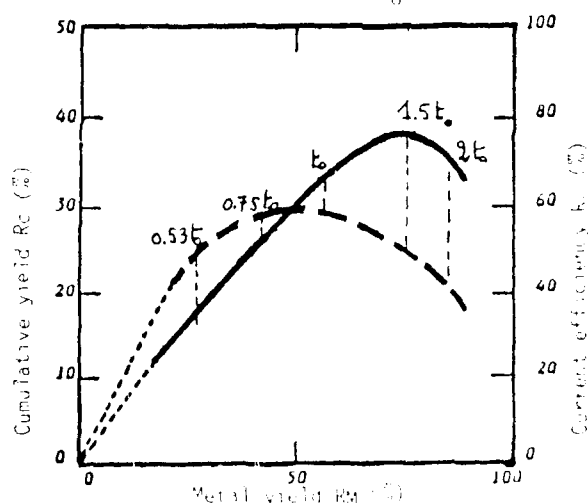


Figure 4 : Nd/Fe electrowinning on horizontal iron cathode.
Relationships between metal yield R_M , current efficiency R_F , cumulative yield ($R_M \times R_F$) and electrolysis time (given with respect to t_0).
(NdCl_3 25 wt % - LiCl - LiF ; $T = 850^\circ \text{C}$; ccd = 200 to 250 $\text{A} \cdot \text{dm}^{-2}$).
- - - : current efficiency
— : cumulative yield
... : metal yield

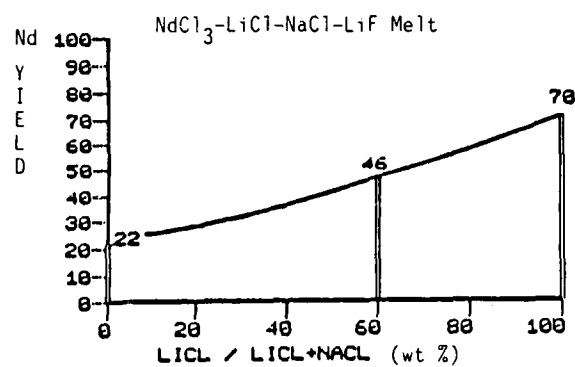


Figure 5 : Variation of metal yield as a function of melt composition. Replacement of LiCl by NaCl.

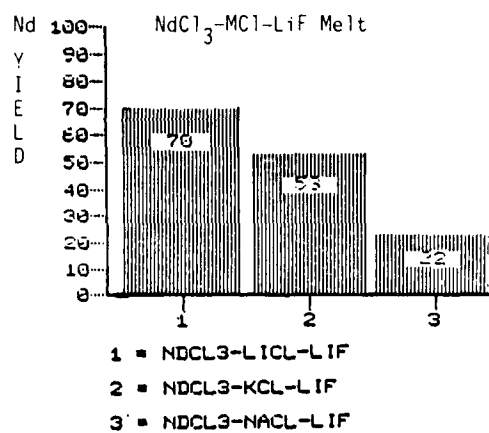


Figure 6 : Variation of metal yield as a function of melt composition - complete replacement of LiCl by NaCl or KCl.

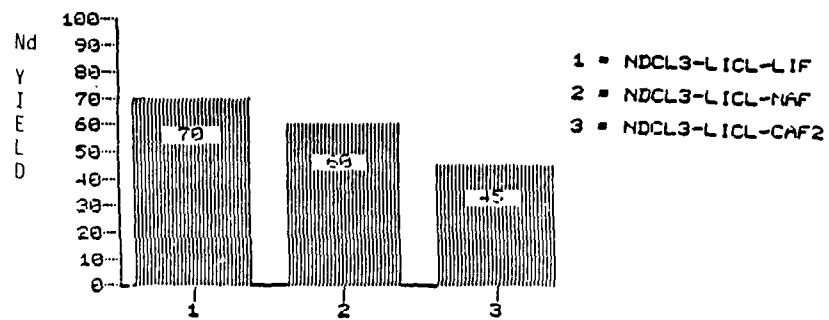


Figure 7 : Variation of metal yield as a function of melt composition.

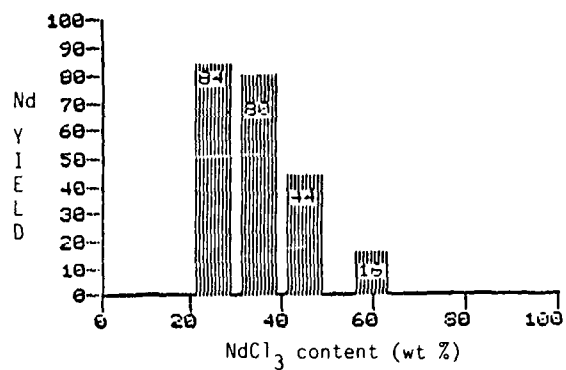


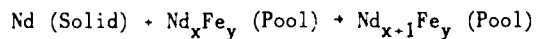
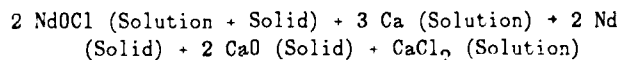
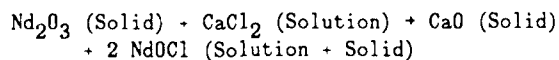
Figure 8 : Evidence of a limiting NdCl_3 content in electrolytic melt.

METALLOTHERMIC REDUCTION OF Nd_2O_3 WITH
Ca IN CaCl_2 -NaCl MELTS

R. A. Sharma and R. N. Seefurth
General Motors Research Laboratories
Warren, MI 48090-9055

ABSTRACT

Neodymium metal was produced by metallothermic reduction of Nd_2O_3 with calcium in a CaCl_2 -NaCl melt by the overall reaction $\text{Nd}_2\text{O}_3 + 3 \text{Ca} + 3 \text{CaO} + 2 \text{Nd}$ at temperatures between 983 and 1063 K. Neodymium was recovered from the salt melt by dissolution in a molten metal pool of either Nd-Zn or Nd-Fe. The reduction process was observed to proceed through the following reactions



To obtain good yields it was necessary to keep the concentration of CaCl_2 in the molten salt phase at least 70 w/o.

The yield (percentage of neodymium oxide recovered as metal) was ~95% in the case of a Nd-Zn extraction pool. Neodymium metal, freed of zinc by vacuum distillation, was of high purity (>99% Nd). The yield was also ~95% for the case of a Nd-Fe extraction pool. The Nd-Fe alloy produced was of high quality and can be directly used in producing MAGNEQUENCH alloy for permanent magnets.

INTRODUCTION

General Motors has developed a process known as MAGNEQUENCHTM* (1,2) for producing Nd-Fe-B alloys for permanent magnets. To make MAGNEQUENCHTM more cost-effective, a systematic study was undertaken to develop a process for producing low-cost neodymium metal. First of all, most of the existing methods of production were critically evaluated and a new method of production was proposed (3). Experimental work was initiated on the new process (4). In this process, neodymium oxide powder suspended in a CaCl_2 based salt medium is reduced by calcium, and the neodymium metal produced is extracted by dissolution in a neodymium-zinc or neodymium-iron metallic pool of approximately eutectic composition at ≈ 1025 K. The new process of chemical reduction and extraction is different from existing neodymium production processes in that it is a combination of both production and refining processes.

THEORETICAL BACKGROUND

The metallothermic reduction of Nd_2O_3 by calcium is represented by the following reaction

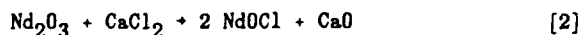


The standard free energy change of this reaction, ΔG° , is negative at all temperatures of interest (Figure 1). To separate Nd from CaO and also to keep CaO from interfering with the reaction, the reduction is carried out in CaCl_2 -NaCl melts. The phase diagram of the CaCl_2 -NaCl system (6) shows a broad liquid range suitable for conducting the reaction of interest. The standard free energies of formation of CaCl_2 (7), NaCl (7), NdCl_3 (8), and NdCl_2^{**} are shown in Figure 2. The standard free energies of formation of both CaCl_2 and NaCl are far more negative than those of NdCl_2 and NdCl_3 . Thus, CaCl_2 and NaCl should not react with Nd to form neodymium chloride.

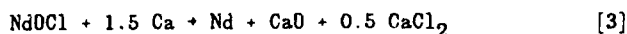
However, in the presence of CaCl_2 based salt media, neodymium oxychloride should form by the reaction

* MAGNEQUENCH is a trademark of General Motors.

**The values of ΔG° for NdCl_2 were calculated using the enthalpy of formation at 298 K, $\Delta H_{298}^\circ = -168.93 \pm 1$ kcal per mole (9) and the entropy of formation at 298 K, $\Delta S_{298}^\circ = -40.29 \pm 1.5$ eu. The ΔS_{298}° was calculated using S_{298} for $\text{NdCl}_2 = 30.1$ eu calculated by Latimer's method (10), S_{298} for Nd = 17.1 eu (11) and S_{298} for $\text{Cl}_2 = 53.29$ eu (11).



The standard free energy change of this reaction is negative at all temperatures of interest (Figure 1). The neodymium oxychloride so formed is subsequently reduced to neodymium metal by the reaction



The standard free energy change of this reaction is also negative as shown in Figure 1. Therefore, reaction [1] represents the overall reduction in the presence of CaCl_2 based salt media.

It is believed that the reduction of Nd_2O_3 is effected by calcium dissolved in the molten salt phase. The fact that calcium metal is appreciably soluble (12) in CaCl_2 -NaCl melts is critical to the kinetics of the process.

The next step in achieving complete separation of neodymium metal from the salt phases is to dissolve it in a liquid metallic pool of Nd-Zn or Nd-Fe, the composition of which can be selected using the corresponding phase diagrams (5). The density of the metallic pool will be about 7 g/cc (13), that of salt ~1.9 g/cc (14) and that of CaO ~3.0 g/cc (13). This suggests that there should be no difficulty in separating the metallic pool from the molten salt. Neodymium which melts at 1294 K (5) can be separated from zinc which boils at 1180 K (11) by vacuum distillation at ~1325 K. The vapor pressure of neodymium at the temperature required for distillation is negligible (2.5×10^{-6} mm Hg, (15)). In the case of a Nd-Fe pool, the alloy produced can be directly used in making MAGNEQUENCHTM alloys.

EXPERIMENTAL

Materials

Random cuttings of neodymium metal (99% purity) and zinc metal sticks of 99.9+% purity were used to make the Nd-Zn extraction pools. Neodymium-iron alloy pieces of eutectic (88.1 w/o rare earth) composition (99% purity) and iron metal of 99% purity were used to make the Nd-Fe alloy extraction pools.

Sodium chloride of 99+% purity, calcium fluoride of 99.9+% purity and anhydrous calcium chloride of 99.9+% purity were used to prepare the various salt baths. Prior to use, each salt was oven baked for ~2 h at 773 K to remove moisture. Calcium metal granules of 99.5% purity and sodium metal of 99.9+% purity were used as the reductants, and neodymium

oxide (Nd_2O_3) powder of at least 95% purity (up to 5% praseodymium oxide) was used as the source of neodymium. Before reduction, the oxide was oven dried for ~2 h at 1273 K to remove moisture.

Apparatus

All experimental procedures were carried out in a helium-atmosphere (typically less than 1 ppm O_2 , N_2 , or H_2O) drybox having a 12.7 cm ID by 54.6 cm deep furnace well extending beneath its floor. The furnace well was heated by means of a tubular three-zone clamshell heating element furnace, 13.3 cm ID by 45.7 cm long.

A schematic diagram of the apparatus is shown in Figure 3. The reduction reaction was carried out in a tantalum crucible 10.2 cm OD by 12.7 cm deep having a 0.15 cm thick wall. Experiments were also conducted in mild steel reaction vessels (10.2 cm I.D. x 17.8 cm deep x 0.15 cm wall), and in some instances, mild steel stirrers were used.

Procedures

The molten alloy pool (enough to make ~300 g of eutectic alloy) for recovery of reduced neodymium metal from the molten salt was prepared by fusing the zinc and neodymium metals together in the preweighed tantalum reaction vessel. The iron-rich molten alloy pool was prepared by fusing the neodymium-iron eutectic ingot and iron metal together in the preweighed mild steel reaction vessel. Then the preweighed salt components were added into the cup and allowed to fuse.

A preweighed amount of Nd_2O_3 was added to the molten salt bath. The stirrer was immersed and used to enhance mixing of the oxide into the melt. Predetermined weights of the reductants were added to the melt. With baffle-splash guard assembly in place, the salt bath and its contents were fast-stirred for an assigned time interval and then slow-stirred for an additional period of time.

After stirring, the stirrer blade was carefully removed from the melt, and the reaction vessel pulled from the furnace well and quenched. The cool cup was removed from the drybox and radiographs were taken. The salts were washed out of the cup with warm-running water. After oven drying, the cup and alloy product were weighed and the recovered neodymium was determined by the differences in weights. Core samples of the neodymium-iron alloy product were sent for chemical analyses. The yields were obtained from the weight gain of the metallic pool divided by the theoretical amount of Nd available from the oxide.

RESULTS AND DISCUSSION

The experimental parameters, such as container material, temperature, extraction pool, reductant, reactants and stirring details, are given in Table 1 while the results are presented in the subsequent tables and in the following two sections. The first section describes the results obtained using Nd-Zn extraction pools and the second section describes the results obtained using Nd-Fe extraction pools. All experiments started with 233.3g of Nd_2O_3 to produce 200g of Nd metal, except as noted below.

Nd-Zn Extraction Pool

The results of Nd_2O_3 reduction with Ca at ~1000 K are given in Table 2. Low recovery of Nd in Expts. 1 and 2 was observed. In the first experiment Ca was added in increments to observe the completion of the reduction reaction which was presumed to be indicated by the floating of excess Ca-Na melt on the CaCl_2 -NaCl melt. This did not happen because most of the Ca was consumed by the reaction $\text{Ca} + 2\text{NaCl} \rightarrow \text{CaCl}_2 + 2\text{Na}$ (7) to generate sodium which evaporated. In the second experiment, Nd metal recovery was low because of entrainment as nodules in the salt phase. The good recovery of Nd in three of the next four experiments was achieved by increasing the amount of salt and stirring the metallic pool at a speed of 60 rpm for one hour at the end of the four hour reduction period. The recovery was greater than 96% in these experiments. This recovery was achieved using a Nd-Zn pool and a salt phase containing greater than 70 w/o CaCl_2 . The recovery dropped drastically when a salt melt containing less than 70 w/o CaCl_2 was used (Figure 4). Two factors, i.e., slow stirring of the metallic pool at the end and a salt phase having greater than 70 w/o CaCl_2 appear to be essential for good Nd recovery.

Rinck reports that calcium-sodium melts of higher calcium concentration (>86 w/o Ca) can coexist only with CaCl_2 -NaCl melts of ≥ 70 w/o CaCl_2 (16). Therefore a CaCl_2 -NaCl melt of 70 w/o CaCl_2 is required to maintain a Ca-Na melt of high Ca concentration which appears essential for carrying out the reductions at acceptable rates and obtaining good yields.

The chemical analysis of the representative samples of the solidified metallic pool of each experiment indicated the impurity level in each case to be very low. Chemical analysis of Nd after removing zinc by vacuum distillation showed Ca = 0.01 w/o and Zn = 0.002 w/o which are satisfactory for magnetic applications. A scanning electron microscope

photograph of a sample from the solidified melt of experiment 4 showed no inclusion of any kind. This has also been observed in the case of samples from the solidified melts from the other experiments.

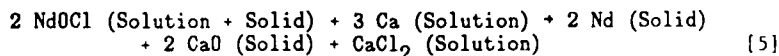
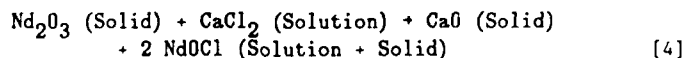
Nd-Fe Extraction Pool

The results of Nd_2O_3 reduction with calcium using a Nd-Fe extraction pool are given in Table 3. Most of the experimental conditions are given in Table 1. Neodymium yields reaching 95% were achieved in one hour at a stirring rate of 600 rpm. However, it appears the salt ratio (grams of salt per gram of Nd available in the original oxide) must be greater than 4 to obtain yields greater than 90%, and once again the salt phase must have greater than 70 w/o CaCl_2 for good Nd recovery. The yields in these experiments were essentially as good as those achieved using a Nd-Zn extraction pool. However, to obtain high yields when using a Nd-Zn pool, the experimental conditions are less stringent (e.g., 300 rpm for the case of Nd-Zn pools and 600 rpm for the case of Nd-Fe pools).

Clear separation between the salt phase and alloy pool was observed from the radiographs of the solidified products. The clear separation of the alloy from the salt phase was also indicated from the surface of the solidified alloy after the salt was washed away. Examination by optical microscope and by a scanning electron microscope of the samples taken from the solidified metallic pools did not reveal any salt inclusions. Chemical analyses of the solidified metallic pools showed the high quality of the Nd-Fe alloys produced. These alloys contain from 85.5 to 87.5 w/o Nd, from 11 to 13.7 w/o Fe and less than 0.3 w/o Ca. The concentrations of the other impurities are also very low.

It appears that the yield increases with increase in agitation rate (Table 3: 2 and 3), and temperature (Table 3: 8, 11 and 12). Data (Table 3: 5, 7-10) also indicate that the yield increased with an increase in the ratio of salt to neodymium produced. Duration of reduction time improved separation and also increased yield in the alloy pool (Table 3: 1-4). The salt phase in experiments 1, 2, and 3 contained 525 g of 67 w/o CaCl_2 , 28 w/o NaCl and 5 w/o CaF_2 , while for experiment 4 it was 500 g of 70 w/o CaCl_2 and 30 w/o NaCl. In experiments 1, 2, and 3, the salt was melted prior to adding the alloy pool materials (86.8 w/o Nd and 18.2 w/o Fe) and they were two step reductions with Fe-metal added between steps, while for experiment 4, the alloy pool (~425 g of 83.2 w/o Nd and 16.8 w/o Fe alloy) was prepared prior to adding salt and the reduction was completed in a single step.

As pointed out earlier, neodymium oxychloride forms by the reaction of Nd_2O_3 with CaCl_2 in the salt phase by reaction [2]. The presence of NdOCl was confirmed by an x-ray analysis of the salt sample from one of the experiments and comparison with data reported in the literature (17). In such experiments, immediately upon addition of Nd_2O_3 , the melt viscosity increased and the melt turned gray. This means the reaction of Nd_2O_3 with CaCl_2 to form NdOCl is very fast, and Nd_2O_3 mostly gets converted into NdOCl before its reduction with Ca. Calcium metal being lighter floats on the salt phase. The NdOCl formed settles on the top of the metallic pool so reduction of NdOCl should take place by the Ca dissolved in the CaCl_2 -NaCl melt. On the basis of these observations the following reaction scheme is proposed for the reduction of Nd_2O_3 with Ca in CaCl_2 -NaCl melts



In the above reaction scheme, one of the products is always leached out so the reduction reaction will not be hampered by formation of a solid product coating on any of the reactants. Nd_2O_3 will be converted into NdOCl which will be on the metallic pool in the salt phase and so will be easily reduced by calcium dissolved in the salt phase. The metallic pool will not be contaminated with Nd_2O_3 because of its conversion into NdOCl , and the Nd produced should be free from oxygen typically found as Nd_2O_3 inclusions in the metallic phase.

ACKNOWLEDGMENTS

The authors wish to thank Bud Verrier, Dick Murie and Noel Potter of GMR for their assistance in completing the work and to John Dunning of GMR, Tom Bradley of Delco-Remy Division and Don Sadoway of MIT for useful discussions and suggestions.

REFERENCES

1. J. J. Croat, J. F. Herbst, and F. E. Pinkerton, J. Appl. Phys. 55, 2078 (1984).
2. J. F. Herbst, R. W. Lee and F. E. Pinkerton, to be published in the Annual Review of Mat. Science.
3. R. A. Sharma, "Processes for Neodymium Production," to be published in the Journal of Metals.

4. R. A. Sharma, "Metallothermic Reduction of Rare Earth Oxides," U.S. Patent No. 4,578,242, March 25, 1986.
5. W. G. Moffatt, "The Handbook of Binary Phase Diagrams," General Electric Co., 120 Erie Boulevard, Schenectady, NY 12305.
6. E. M. Levin, C. R. Robbins, and H. F. McMurdie, "Phase Diagrams for Ceramists; 1969 Supplement," The American Ceramic Society, 4055 N. High St., Columbus, Ohio 43214.
7. JANAF Thermochemical Tables, 2nd Edition, NSRDS-NBS, June 1971-1978.
8. I. Barin, O. Knacke, and O. Kubaschewski, "Thermochemical Properties of Inorganic Substances," Supplement, Springer-Verlag Berlin, Heidelberg, New York, 1977.
9. L. R. Morss and M. C. McCue, J. Inorg. Chem., 14, 1624 (1975).
10. W. M. Latimer, J. Amer. Chem. Soc. 73, 1480 (1951).
11. O. Kubaschewski and C. B. Alcock, "Metallurgical Thermochemistry," 5th Edition, Pergamon Press, New York, 1979.
12. R. A. Sharma, J. Phys. Chem. 74, 3896 (1970).
13. "Lange's Handbook of Chemistry," Twelfth Edition, Edited by John A. Dean, McGraw-Hill Book Co., New York, 1979.
14. G. J. Janz, R. P. T. Tomkins, C. B. Allen, J. R. Downey, Jr., G. L. Garner, U. Krebs, and S. K. Singer, "Molten Salts: Vol. 4, Part 2, Chlorides and Moisture; Electrical Conductance, Density, Viscosity, and Surface Tension Data," Molten Salt Data Center, Dept. of Chem., Rensselaer Polytechnic Inst., Troy, NY 12181, p. 970.
15. J. F. Nachman, C. E. Lundin, and A. S. Yamamoto, "Vapor Pressure of Praseodymium and Neodymium," Proc. Second Conf. Rare Earth Research, Sept. 24-27, 1961, Gordon and Breach, NY, p. 163.
16. E. Rinck, "Solidification Diagram of Ca-Na Alloys," Compt. Rendu, 191, 1378-81 (1931).
17. H. E. Swanson, N. T. Gilfrich, M. I. Cook, R. Stinchfield, and P. C. Parks, NBS Circular 539, 8 (1959).

Table 1. Operating Parameters of the Experiments Described in Tables 2, and 3

Parameter	Table 2	Table 3
Container	1a	mild steel with fins
Temperature, K	1000	1020 except 980 for expt. 11 and 1060 for expt. 12
Extraction pool	~300 g of 88.2 w/o Nd* 11.8 w/o Zn	400-500 g of ~83.5 w/o Nd* 16.5 w/o Fe
Reductant	91.8 g Ca (10% excess) + ~20 g Na*	91.8 g Ca (10% excess) - ~20 g Na
Stirrer	Tantalum	--
Stirring Rates	300 rpm for 4 h 60 rpm for 1 h	--

* Some exceptions noted elsewhere in tables or text.

Table 2. Description of the Experiments of Nd_2O_3 Reduction With Ca Using a Nd-Zn Extraction Pool

Expt.	Salt Phase			Nd Recovery	
	Initial Amount (g)	Initial Composition		Amount (g)	Yield (w/o)
		w/o CaCl_2	w/o NaCl		
1	740	65.5	34.5	65.3	65.3
2	785	90	10	170.5	85.3
3	1178	90	10	195.7	97.9
	(1219)*				
4	1116	75	25	194.9	97.5
		(71.1)	(28.9)		
5	1066	60	40	99.1	49.6
		(68.5)	(31.5)		
6	1098	70	30	192.2	96.0

() Indicates final amount or composition of the salt phase.

* Additional NaCl added in an attempt to liquify the melt.

Table 3. Description of the Experiments of Nd_2O_3 Reduction with Ca Using a Nd-Fe Extraction Pool

Expt.	Amount (g)	Salt Phase			Salt Ratio	Variables			Nd Recovery		
		Initial Composition				Stirring Times			Total (g)	In Pool (%)	
		w/o CaCl_2	w/a NaCl	w/o CaF_2		Fast (m)	Slow (m)	Total (m)			
1	525	67	28	5	2.6	65 ^a	55 ^b	120	96.8	48.4	48.4
2	525	67	28	5	2.6	285 ^a	60 ^b	345	150.1	75.0	67.3
3	525	67	28	5	2.6	245	60	305	177.6	88.8	88.6
4	500	70	30	-	2.5	60	60	120	163.0	81.5	77.6
5	500	70	30	-	2.5	60	60	120	174.4	87.2	78.0
6	500 ^c	70	30	-	2.5	120	0	120	178.8	89.4	81.0
7	600	70	30	-	3	60	0	60	178.0	89.0	83.0
8	800	70	30	-	4	55	5	60	189.5	94.8	90.7
9	1000	70	30	-	5	55	5	60	189.4	94.7	93.8
10	1200	70	30	-	6	52	8	60	190.8	95.4	92.5
11	800	70	30	-	4	50	10	60	184.7	92.4	86.4
12	800	70	30	-	4	53	7	60	191.7	95.9	90.7

^a Fast stirring rate = 300 rpm; otherwise 600 rpm.

^b Slow stirring rate = 60 rpm; otherwise 125 rpm.

^c Initiated use of Ta-stirrer.

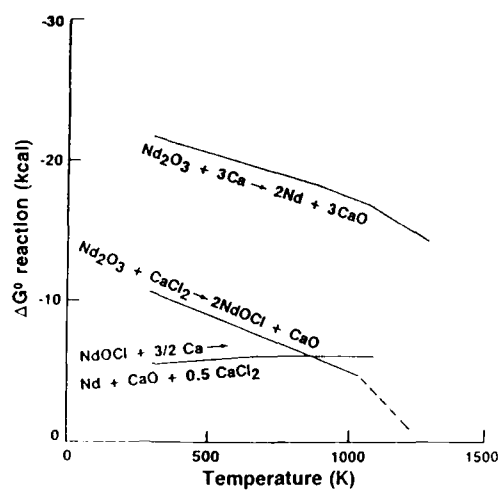


Figure 1. Standard free energy change, ΔG° , of the reduction reactions as a function of temperature (7,8).

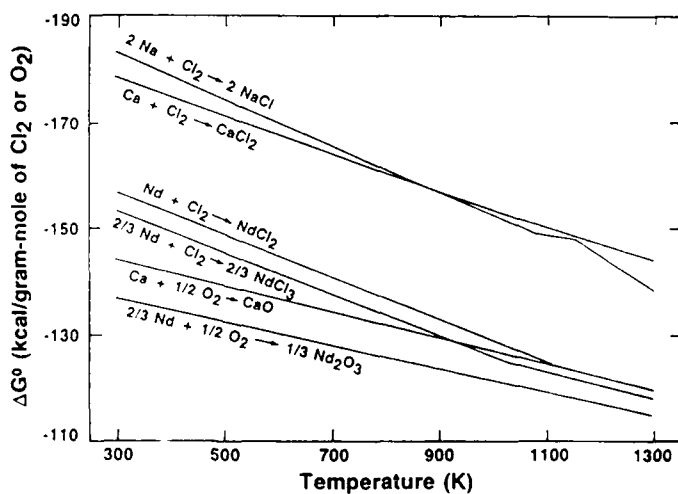


Figure 2. Standard free energy of formation, ΔG° , of the compounds of interest as a function of temperature.

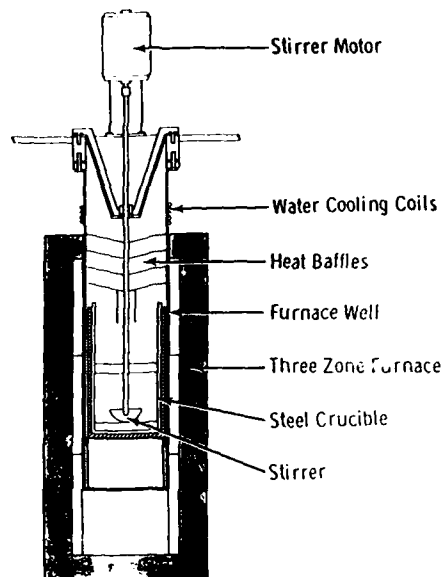


Figure 3. Schematic diagram of the reduction apparatus.

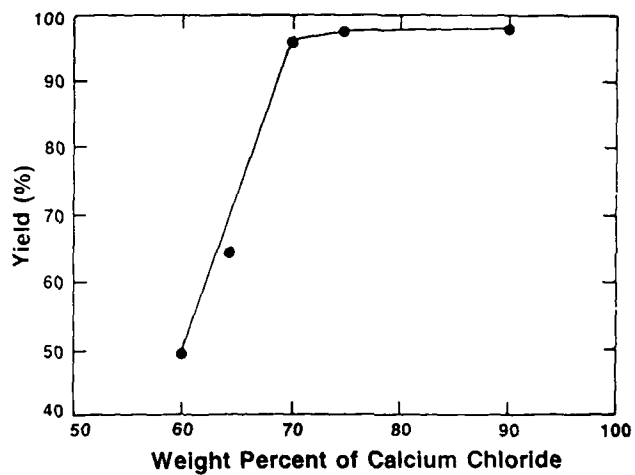


Figure 4. Yield versus CaCl_2 content of the salt phase.

THE STUDY ON THE DISSOLVING LOSS OF RARE
EARTH METALS IN THE RECl_3 -KCl- CaF_2 MELT

Xu Xiuzhi; Wei Xujun; Chen Yong

Northeast University of Technology,
Shenyang, China

ABSTRACT

The dissolving loss of the mixed rare earth metals (RE) in the RECl_3 -KCl melt was investigated under laboratory conditions with CaF_2 as an additive. The effects of both the CaF_2 content and the melt temperature on the dissolving loss were discussed. The results show that the addition of CaF_2 to the RECl_3 -KCl melt can reduce the dissolving loss of RE, and that the minimum dissolving loss occurs at about 4% in weight of CaF_2 within the studied range.

1. INTRODUCTION

During the electrolysis process in molten salts, it is commonly found that the electrolyte colour in the vicinity of cathode turns dark, viscosity increases, transparency decreases and current efficiency is lowered. This is because of the dissolution of the metals which are the cathode products in the molten salts. The metals dissolving loss in the electrolyte is one of the major reasons which cause the current efficiency to be low.

According to a previous report⁽¹⁾, the solubility of rare earth metals in molten salts is pretty high. Therefore, in order to raise the current efficiency during rare earth electrolysis in molten salts, it is necessary to try to explore and create such conditions under which only minimum dissolving loss occurs.

On the basis of previous work,⁽²⁾⁽³⁾ in the present study we chose the RECl_3 -KCl system, which is now commonly used in industry; with CaF_2 as an additive, we studied the pattern of RE dissolving loss in the RECl_3 -KCl- CaF_2 melt, so that it will provide useful information for the determination of the optimum process conditions of rare earth electrolysis in molten salts.

11. EXPERIMENTAL

1. Materials and Reagents

The mixed rare earth was bought from Shanghai Yuelong Plant of Chemical Engineering, with purity of 99%. The mixed rare earth chlorides were prepared and dehydrated in vacuum. KCl , ^{40}Cl and CaF_2 are all of analytical grade. Argon is of 99.99% purity and was further purified.

2. Experimental method and apparatus

The experimental apparatus was described previously⁽²⁾. The sample of the mixed rare earth metals ($2.2 \pm 0.2g$) together with the mixed salts of 25g was put in a molybdenum crucible which was in an air-tight stainless steel container. Under the protection of argon, the container was maintained at a constant temperature for 1 hour, then cooled naturally. The loss amount was obtained by weighing the sample before and after the above procedure.

3. Experimental design and data processing

In this paper, the research plan was arranged by adopted combinatorial design with orthogonal regression. According to the literature⁽¹⁾ and the practice in industry, the KCl_3 contents of 40 wt% was chosen. Variation ranges of the two experimental factors are 2-6 wt% for CaF_2 and 820-900°C for temperature.

The experimental data are given in table 1. Having

Table 1. RE lost amount under different conditions.

Order	Design matrix		RE lost amount in 25g mixed melts (g)			Average \bar{m}
	X_1^*	X_2^{**}	m_1	m_2	m_3	
1	-1	-1	0.7938	0.8732	0.8083	0.8251
2	0	-1	0.8686	0.8669	0.9132	0.8829
3	1	-1	1.2505	1.2476	—	1.2491
4	-1	0	0.6149	0.7393	0.7275	0.7039
5	0	0	0.6372	0.6629	0.6052	0.6351
6	1	0	0.9976	1.0232	—	1.0104
7	-1	1	0.6942	0.7519	—	0.7231
8	0	1	0.7826	0.7401	0.7960	0.7729
9	1	1	1.1025	0.9813	0.9395	1.0078

* X_1 is temperature (820-900°C)

** X_2 is CaF_2 content (2-6 wt%)

processed the experimental data, we obtain the following regression equation:

$$y = 68.4529 - 0.1620t + 0.0825C - 1.3500 \times 10^{-4} Ct + 9.7687 \times 10^{-5} t^2 + 3.1725 \times 10^{-2} C^2$$

where y is the lost weight and C is the CaF_2 content in the mixed melt of 25g, and t is temperature ($^{\circ}\text{C}$).

In order to examine the applicability of the regression equation within the experimented range, the contrast tests were made. The comparison between the values of measured and calculated is given in table 2. It is known from table 2, that the maximum error of such many factory affected dissolving loss is less than 5.3%, which is satisfactory.

Table 2. Contrast test results

Order	CaF_2 (wt%)	t ($^{\circ}\text{C}$)	Measured RE loss		Measured average \bar{m} (g)	Calculated value y (g)	Error (%)
			m_1 (g)	m_2 (g)			
1	3	820	0.7330	0.7689	0.7510	0.7606	-1.26
2	5	840	0.6648	0.6633	0.6640	0.6795	-2.27
3	5	880	0.8093	0.7095	0.7894	0.8333	-5.27

By partially differentiating the above equation, we obtain the minimum RE dissolving loss at CaF_2 content of 4.45% and temperature of 839 $^{\circ}\text{C}$.

III. RESULTS AND DISCUSSION

1. Effect of temperature on RE dissolving loss

The relationship between temperature and RE dissolving loss is shown in Fig. 1. That is, temperature t is quadratically related to RE dissolving loss y . From Fig 1, we can apparently see: the minimum RE dissolving loss occurs at temperature of 835-845 $^{\circ}\text{C}$. At lower temperature, raising temperature makes RE dissolving loss decrease a little, while at higher temperature, raising temperature makes RE dissolving loss increase apparently. This is mainly because: At higher temperature, the diffusion coefficient is larger, which hence hastens the dissolving rate of metals.

2. Effect of CaF_2 content on RE dissolving loss

The relationship between RE dissolving loss and CaF_2

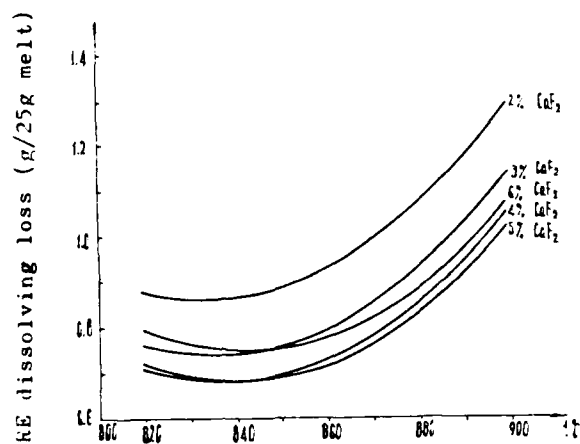


Fig 1. Relationship between RE dissolving loss and temperature

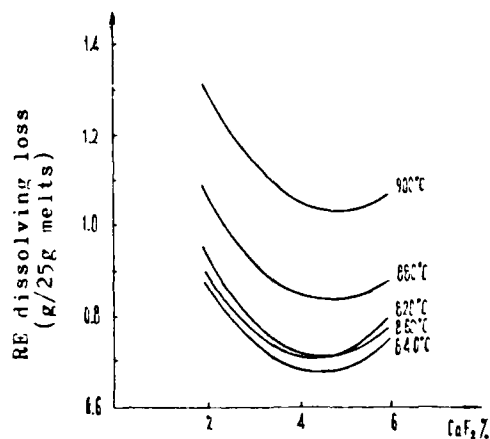


Fig 2. Relationship between RE dissolving loss and CaF₂ content

content is shown in Fig. 2, from which one can see: At certain temperatures, when CaF₂ is smaller than 4%, RE dissolving loss decreases gradually with increasing CaF₂ content. At CaF₂ content 4-5%, RE dissolving loss is

minimum at given temperatures. The minimum value is at temperature of 840°C and CaF_2 of 4.5%. When CaF_2 content is larger than 5%, HF dissolving loss tends to increase.

IV. CONCLUSION

1. The addition of CaF_2 into the $\text{RECl}_3\text{-KCl}$ melt apparently reduces the RE dissolving loss in the melt. Under the experimented conditions and within the studied range, the minimum RE loss occurs at CaF_2 of 4.5% and temperature of 840°C.

2. A regression equation of RE dissolving loss in the melt is obtained, which is applicable within 820-900°C for temperature and 2-6% for CaF_2 content.

REFERENCES

- (1) Rare Earth Editorial Board, Rare Earth, Vol. 2, 102, (1978).
- (2) Xu Xiuzhi et al, Xi Tu, (3), 18, (1985)
- (3) Xu Xiuzhi et al, Xiyou Jinshu, (5), 362, (1986)

THE ROLE OF OXIDE SOLUBILITY IN THE ELECTROCHEMICAL
EXTRACTION OF RARE EARTH ELEMENTS FROM FUSED FLUORIDES

A. Mitchell and B. Thomas
Department of Metals and Materials Engineering
The University of British Columbia
Vancouver, B.C., V6T 1W5, Canada

ABSTRACT

The major problems of operation in oxide/fluoride cells for the production of rare-earth elements have been those of balancing the low deposition rates necessitated by low oxide solubility against the cell heat balance. Unlike the Hall-Heroult electrolyte, the suitable electrolytes for rare-earth deposition have a very limited solubility for the oxides. We have used an electrical conductivity technique to analyse the oxide solubility as a function of temperature for CeO_2 , La_2O_3 and Nd_2O_3 in the appropriate fluoride solvents. The saturation solubility in all cases is in the range of 1-2 wt% oxide over the temperature range of interest. However the effect of oxide solution on the fluoride conductivity is great enough to permit the device we have used to be employed as a process monitor controlling oxide additions. We are thus able to avoid both over-feeding and anode-effect difficulties in the cell operation. The implications of this technique in the overall cell operation, particularly in the thermal regime, are discussed.

INTRODUCTION

The operation of commercial fused-salt electro-extraction processes usually involves either electrolysis of an anhydrous chloride, with or without a carrier electrolyte, or alternatively the electrolysis of an oxide dissolved in a suitable fluoride solvent. Although the former case has been practised for many years in rare-earth metal extraction, there are obvious economic gains to be made in developing an oxide-based process.

The rare-earth elements have many similarities to aluminum and we might anticipate that such a process would operate in a manner akin to the Hall cell. The fundamental chemical reasons for the success of this cell are strongly connected to the fact that cryolite will dissolve a substantial amount of alumina at a reasonable operating temperature. This fact in turn permits cell operation at economic temperatures within the oxide concentration limiting ranges defined by oversaturation and anode effect. In addition, the penalty for oversaturating the cell in oxide by miscalculation of the alumina feed-rate is not severe since the excess alumina floats ($\rho = 1.56$) on cryolite ($\rho = 2.10$) rather than falling to the salt/cathode interface and open-circuiting the cell. This sequence of fortunate chemical circumstances is met within only a very few other element systems, and

although a parallel for the Hall cell has been sought for Mg, Ca, Ti and Zr, none has yet been developed.

The rare-earths have been prepared by using oxide/fluoride cells. Gray¹ used an externally-heated carbon cell with a graphite anode and a molybdenum cathode and succeeded in producing Ce metal from CeO₂ dissolved in an electrolyte of CeF₃ + LiF + BaF₂. This work was also the first application of electrolysis under an inert (argon) atmosphere for rare-earth preparation. Similar cells² have been operated more recently but on a small scale, making up to 350 g/hr of Ce metal at a current efficiency of up to 90%. Attempts to operate such cells for the protracted periods necessary in commercial production have highlighted several fundamental problems. The most important of these is that any addition of oxide in excess of the solubility limit in the fluoride solvent will cause a "sludge" to form in the cell on top of the liquid Ce cathode. This "sludge" then causes irregular deposition of Ce, reduces the current efficiency, changes the cell heat balance and ultimately stops the cell operation. The composition of the deposit is variable, but appears to consist³ of cerium sesquioxide, cerium oxy-fluoride and cerium metal. It does not form when the cerium oxide content of the electrolyte is less than the solubility limit.

Gray¹, Morrice et al² and Porter³ all made indirect estimates of the solubility of CeO₂ in the electrolyte they used (73 wt% CeF₃, 12 wt% BaF₂, 15 wt% LiF) using oxygen analysis of quenched samples to determine the oxide content. Their values were also linked to visual observations of the solution rate of further oxide additions. The values found range from 2-3 wt% at 800°C to 2-5 wt% at 850°C. Whilst there may be inaccuracy in these determinations, the results highlight the important fact that cerium oxides are relatively insoluble in fluorides as compared with Al₂O₃ in cryolite. It is clear that an unrealistically-high cell operating temperature would be required to reproduce the Hall cell conditions and therefore that we must have a precise knowledge of oxide solubility in order to operate the cell successfully. The objective of the present work is to define the oxide solubility and to indicate how it may be controlled.

EXPERIMENTAL

Solubility Determinations

The starting materials used are listed in Table I and were dried under argon at the indicated temperature. Any subsequent exposure to air was kept to a minimum and the experimental cell was held under argon during all operations involving oxide or fluorides.

The electrolyte composition used in earlier work had not been defined and as a preliminary investigation we attempted to define an electrolyte composition as having the maximum CeF_3 content and the minimum melting temperature. Differential thermal analysis on a range of CeF_3 -rich $\text{CeF}_3 + \text{BaF}_2 + \text{LiF}$ ternary compositions confirmed that the composition 73 wt% $\text{CeF}_3 + 12 \text{ wt% BaF}_2 + 15 \text{ wt% LiF}$ was the optimum composition for this definition.

TABLE I
Composition and Sources of Materials

			Drying Temp.
CeO_2	99.9%	Unocal Inc.	850°C (24h)
CeF_3	99.9%		400°C (24h)
BaF_2	99.5%	Alfa Chemicals	400°C (24h)
LiF	99.5%	Lithium Corp. of America Inc.	400°C (24h)

Chemical analysis of quenched samples of this electrolyte after fusion failed to reveal any Ce^{4+} content above the limits of analysis (0.1 wt% Ce^{4+}). The determination method chosen was that of electrical conductivity.

The experimental apparatus (Fig. 1) consists of a 50mm diameter by 80mm high graphite crucible which is placed in a vertical tube furnace. The furnace consists of a 54mm diameter stainless steel pipe which is surrounded by two 650 watt chromel elements. The elements are insulated with approximately 100mm of fiberfax insulation. The pipe is sealed at both top and bottom with water cooled copper plates which are held in place by tube clamps. Argon is fed in through the bottom of the furnace to maintain an inert atmosphere. A 25mm diameter fused quartz tube extends vertically from the furnace. The conductivity probe rests in this tube when not in use. A 15mm diameter fused quartz tube is attached horizontally to the vertical tube. This is used as the feeding port for the cerium oxide. The conductivity probe (Fig.2) consist of a 1mm diameter molybdenum wire as one electrode and a 16mm diameter concentric molybdenum tube as the other electrode. A Hewlett Packard 4328A milliohmmeter is used to measure the resistance between the electrodes.

A four lead probe consisting of separate leads for current and voltage measurements is used. Two of the leads are used to impose an alternating current between the electrodes, and two separate leads are used to measure the voltage drop of the imposed current.

This enables the voltmeter to have a very high internal resistance, and thus eliminates errors due to lead resistance and contact resistance.

This milliohmmeter uses a high frequency (1KHz) low amperage current (5mA). This ensures that there are no measurement errors due to electrolytic polarization and capacitance effects. A concentric tube conductivity cell is used instead of the usual parallel plate cell to prevent interference from parallel electrical paths through the fused salt bath⁴.

The cylindrical geometry of the conductivity cell results in a cell constant that is independent of the crucible geometry or the cell-crucible distance. The cell constant is dependent solely on a reproducible immersion depth. This method is more precise and easier to operate than a parallel plate cell. A platinum-platinum 10% rhodium thermocouple was used to measure the salt temperature.

EXPERIMENTAL RESULTS

The saturation solubility of cerium oxide in a $\text{CeF}_3\text{-LiF-BaF}_2$ melt was determined by noting the point at which additional amounts of cerium oxide did not decrease the conductivity of the melt. Figure 3 shows the relationship between conductivity and amount of cerium oxide added. From this figure the saturation solubilities were obtained. Thus, the amount of cerium oxide in the cell can be controlled by monitoring the conductivity of the bath. At 800°C , the saturation solubility occurs at a conductivity of $2.15 \pm 0.05 \text{ ohm}^{-1} \text{ cm}^{-1}$. The oxide content of an electrolytic cell could be controlled by keeping the conductivity between 2.20 and 2.40 $\text{ohm}^{-1} \text{ cm}^{-1}$.

The influence of the composition with respect to fluoride, was also determined by varying the bath composition. It was observed that when the cerium fluoride content is increased there is a small increase in the solubility of approximately 0.1 wt% for a bath containing 80% CeF_3 .

At the oxygen potential in equilibrium with solid graphite, we would not expect a significant reduction of Ce^{4+} to Ce^{3+} . However, to examine the influence of this factor, a series of experiments parallel to the above was carried out with cerium metal added to the crucible. We did not observe any detectable change in the solubility behaviour. The oxide precipitated on freezing in both cases was identified as Ce_2O_3 as would be expected from the ratio of $\text{Ce}^{4+}/\text{Ce}^{3+}$ in the electrolyte.

Determinations of the saturation solubility of La_2O_3 and Nd_2O_3 have been carried out, using the equivalent salt solutions in temperature ranges appropriate for electrolytic cell operation.

As will be seen from Figs. 4 & 5, the solution behaviour is similar, but with a more restricted solubility range.

DISCUSSION

It is seen from the above results that the solubility range of rare-earth oxides in appropriate fluoride electrolytes is very small. We may readily see why the problem of overfeeding has been so persistent in these electrolytic cells. The small potential operating range between the onset of anode effect and oversaturation, combined with the severe problem of heat balance control implies that cell operation will be possible only with very good on-line controls of oxide concentration and oxide temperature. To this end we would propose to operate such a cell with an on-line predictive heat balance to control temperature and an immersion resistance device similar to that of Fig. 2 to control oxide content. These operating structures have been constructed and have been shown to operate satisfactorily at the laboratory scale.

REFERENCES

1. R.M.J. Gray: Trans. Inst. Min. Met. (Lond.) 61, 141, 1951.
2. E. Morrice and B. Porter: U.S. Bureau of Mines, RI 5868, 1961.
3. B. Porter and E.A. Brown: U.S. Bureau of Mines, RI 5878, 1961.
4. A. Mitchell and J. Cameron: Metallurgical Transactions 2, 3361, 1971.

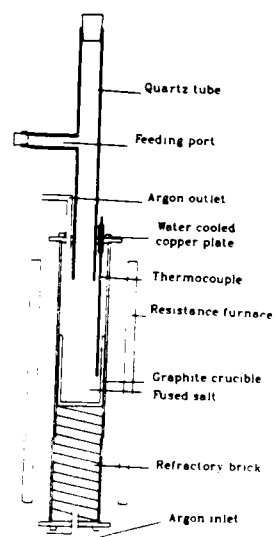


Fig 1. Conductivity Measuring Apparatus

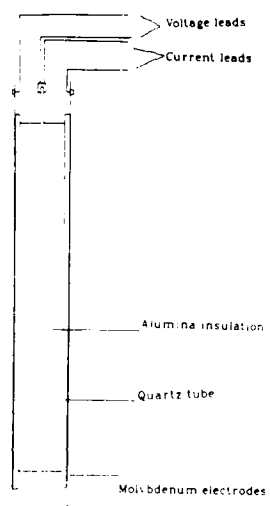


Fig 2. Conductivity Probe Detail

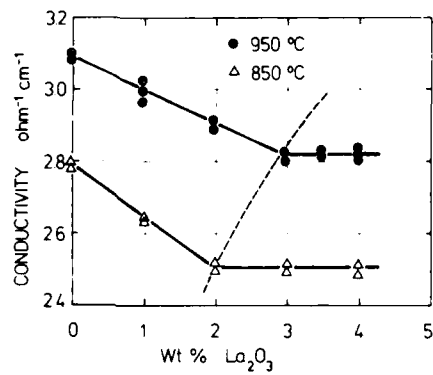


Fig 3. Conductivity of " CeO_3 "
Solutions in liquid
Fluoride Eutectic.

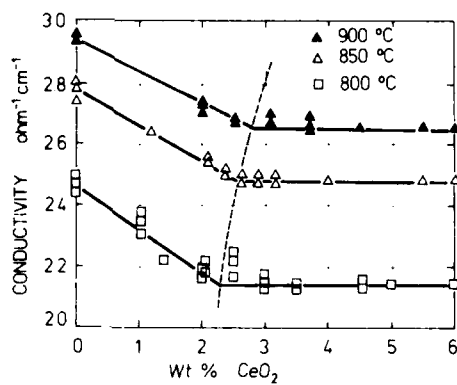


Fig 4. Conductivity of La_2O_3
Solutions in liquid
Fluoride Eutectic

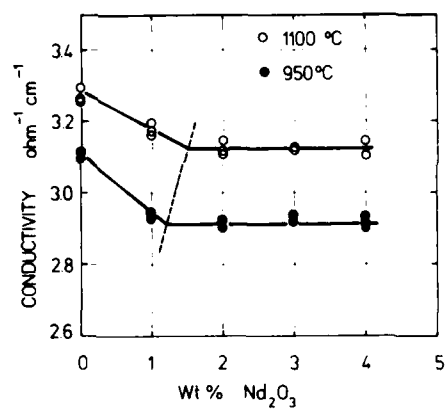


Fig 5. Conductivity of Nd_2O_3
Solutions in liquid
Fluoride Eutectic

APPLICATIONS OF MOLTEN SALTS IN PLUTONIUM PROCESSING

D. F. Bowersox, D. C. Christensen, and J. D. Williams
Los Alamos National Laboratory, Los Alamos, NM 87545

ABSTRACT

Plutonium is efficiently recovered from scrap at Los Alamos by a series of chemical reactions and separations conducted at temperatures ranging from 700° to 900°C. These processes usually employ a molten salt or salt eutectic as a heat sink and/or reaction medium. Salts for these operations were selected early in the development cycle. The selection criteria are being reevaluated. In this article we describe the processes now in use at Los Alamos and our studies of alternate salts and eutectics.

INTRODUCTION

Pyrochemical processes are defined as nonaqueous operations conducted at elevated temperatures. Records indicate that crude methods for producing some metals existed as early as 3000 BC. Copper, silver, tin, lead, gold, iron, and steel were made pyrochemically by 1000 BC. Pyrometallurgy is still employed to make iron, copper, zinc, and nickel; however, the modern application most similar to the plutonium process is that used to produce aluminum.

Reductions of uranium and plutonium tetrafluoride to metal were developed by R. D. Baker and co-workers during the Manhattan Project.^{1,2} However, most recovery of plutonium has been by aqueous methods developed after World War II. In the 1950s, proposals to build metal-fueled fast reactors led to studies of pyroprocessing spent fuels. In such cases, uranium and plutonium could be purified without altering their metallic states. With adoption of the concept of oxide fuels, development of pyrochemical reprocessing was no longer emphasized. However, the results from these earlier studies were adapted into our pyrochemical scrap recovery program. The recent proposal by Argonne National Laboratory of the Integrated Fast Reactor, which utilizes a metallic fuel, includes pyrochemical processing of spent fuels and the spent blanket.³

At Los Alamos, high purity plutonium metal is prepared from process residues by the flow diagram shown in Fig. 1. The two major process steps to produce metal (usually still impure) are direct reduction of plutonium dioxide and conversion of oxide to fluoride by hydrofluorination followed by reduction. If the americium content is high, either step is followed by molten salt extraction. The impure metal is then vacuum cast to shape and converted to high purity metal by electrorefining. The complexity of the process is increased because residues and wastes must be treated to recover all of the plutonium.

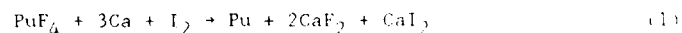
The pyrochemical research and development section at Los Alamos was formed to demonstrate an integrated scrap recovery process and, as a result of this demonstration, to provide high purity metal for other programs. In our studies, we also study methods to:

- Develop and demonstrate improved pyrochemical processes.
- Decrease waste generation while increasing productivity.
- Establish and maintain an expertise in plutonium chemistry and in pyrochemical operations, and
- Transfer applicable technology to others in the nuclear community.

In this report, the four major steps in processing plutonium by our methods will be described. Salts and eutectics in use and promising alternatives will be discussed.

MAJOR PROCESSES

Hydrofluorination and Plutonium Tetrafluoride Reduction. In the hydrofluorination and plutonium tetrafluoride reduction process, plutonium peroxide, oxalate, or low-fired (under 800°C) oxide is converted to the tetrafluoride by hydrogen fluoride gas. Plutonium metal is produced at high pressure by the high temperature reaction between the fluoride and calcium metal. A booster, such as iodine, initiates the reaction



at about 600°C. While the slag residue remains molten, the more dense plutonium sinks to the bottom of the crucible, and, upon cooling, the metal solidifies into a button.

The waste streams from this process are a calcium iodide-calcium fluoride slag, the reaction crucible, and magnesia sand (which is reused). Any plutonium remaining in the slag or crucible is recovered by aqueous processing. Off-gases from the fluorination are scrubbed and discarded.

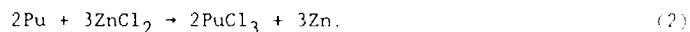
The relatively small volume of residue and waste constitutes a major advantage of this process. Little or no purification occurs during the processing. On the other hand, no impurities are introduced from the process. Therefore, if the feed material is sufficiently pure, the product metal is satisfactory for high purity applications. Yields are usually high, varying from 97 to 99%.

The high neutron radiation field generated by the (alpha, neutron) reaction is a major disadvantage in the process because it constitutes a hazard for the personnel. The high pressure system, the high temperatures of reaction, and the highly corrosive gas are also potential hazards. Finally, high-fired, refractory oxide does not hydrofluorinate and cannot be reduced to metal by this process.

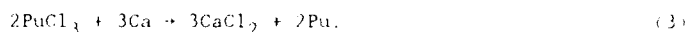
From a long-range view, a major change in this process would be replacement by a method employing plutonium trichloride as the intermediate reactant. Such a process might use controlled potential for metal separation by deposition rather than by chemical reductant. The new process would yield high-purity metal and eliminate the high radiation field.

In work at Hanford in the early sixties, the trichloride was produced and tested as an alternate processing route. However, corrosion problems and difficulty in obtaining high yields with refractory oxides led to adoption of a nitrate, aqueous system.⁴ We have produced plutonium trichloride from oxide on a 100 g scale and reduced the product to metal with calcium under several conditions.⁵

In the pyroreodox process,⁶ plutonium trichloride is produced in a potassium chloride melt by the reaction of zinc chloride with impure plutonium metal. The reaction is



The zinc button, which contains the less reactive impurities, is mechanically separated from the salt and transferred to waste. The salt is then contacted with calcium to produce metal:



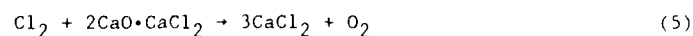
The salt, which contains the impurities more reactive than calcium, is discarded or recycled. The impure metal, which contains significant amounts of calcium, is further treated and electrorefined to produce high purity plutonium. This process would be applicable to lean plutonium streams; at present, it is used for recovering plutonium from spent anodes produced by electrorefining.

Direct Oxide Reduction. Most scrap containing plutonium can be converted to oxide by burning in air at an elevated temperature. In the direct oxide reduction process (DOR), this oxidation is carried out at 800°C to ensure removal of carbon and organic impurities. This produces high-fired oxide which cannot be hydrofluorinated. However, the oxide can be reduced to metal in a solvent salt system by the addition of a strong reducing agent.⁷ In the DOR, the reaction is



The reaction begins at about 825°C in a large excess of molten calcium chloride salt. The salt melt provides both a heat sink and a solvent for the calcium oxide produced as a by-product. As shown by the phase diagram, Fig. 2, the oxide is soluble up to about 20 mol percent CaO .⁸ The metal button, containing 97-99% of the feed plutonium, is mechanically separated from the salt.

The fused salt block is counted to ensure a low plutonium content and discarded as low level waste. The metal button is transferred to the next processing step. The volume of spent salt is the largest residue formed in the integrated process. Studies have been shown that it can be regenerated to calcium chloride and recycled. The chloride-oxide mixture is melted and maintained at 850°C while chlorine is bubbled through the liquid melt. Under our operating conditions, the reaction:



proceeds until the salt contains less than 0.1% oxygen.⁹ Approximately 5 kg of spent salt is converted to usable chloride in less than two hours. The regenerated melt is purged with argon, transferred and cast for recycle.

Plutonium metal produced with the regenerated salt is comparable to that produced with first-pass salt. By recycling, very little plutonium is discarded in spent salt and residue volumes are significantly decreased. Salt has been cycled up to ten times with no detectable buildup of impurities. Yields averaged 98%. Potential waste reductions of 80% are calculated by utilizing regeneration and recycle.

The standard DOR process produces an impure button containing magnesium, which may be caused by the reaction of the magnesia crucible wall with calcium in the melt:

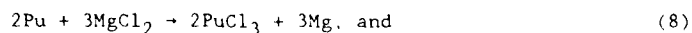
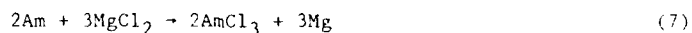


This reaction can be minimized by adjusting the process parameters such as stirring rate, excess calcium, and operating temperature. Tests employing boron nitride crucibles have also been promising.

The calcium chloride salt was initially chosen, along with calcium as the reductant, because the oxide by-product is soluble in the salt. Similar solubility has been reported in the lower melting calcium chloride-calcium fluoride eutectic. We are currently comparing data such as yields from experiments employing either regenerated calcium chloride or a

fluoride eutectic with the results of the reference DOR utilized in the integrated processes. Metal has been produced in the fluoride eutectic system at temperatures below the melting point of calcium. At these temperatures reaction with the crucible wall is minimized and thus magnesium metal generation is reduced.¹⁰ The lower temperature should also increase furnace life. The salt/metal interface is also very well delineated and salt occlusion in the metallic phase has not been observed. Additional data are being collected.

Molten Salt Extraction. The more reactive elements such as americium, the rare earths, alkali metals and alkaline earth metals can be separated from plutonium by the molten salt extraction process (MSE). A ternary salt composed of a calculated quantity of an oxidizing agent and a eutectic salt is contacted with impure metal.¹¹ The more reactive elements, such as americium, along with some of the plutonium, are oxidized into the salt phase. Most of the plutonium remains in the heavier metal phase, and upon cooling forms a metal button. At Los Alamos, the MSE process is employed when the americium would not be sufficiently reduced by electrolysis [generally greater than 1000 parts per million (ppm)]. Magnesium chloride is used as the oxidizing agent in a sodium chloride-potassium chloride eutectic. The major reactions are



The americium and plutonium concentrations in the salt are dependent on the amount of oxidant added, the concentrations of the elements in the impure metal feed, the operating temperature, the number of contacting stages and the mode of operation. Under our operating conditions, 90% of the americium and 1-3% of the plutonium are transferred into the salt.¹² This plutonium must be recovered before the salt is discarded to waste. The relatively high americium content of the salt is a radiation hazard. The

americium is potentially valuable, and, if it were recovered, the salt could be recycled.

In extractions where plutonium trichloride was substituted for magnesium chloride as the oxidizing agent, more americium was extracted.¹² In addition, magnesium was not introduced by the process. The reaction is

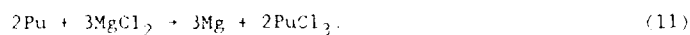


The black salt formed during the extraction has been reported as containing divalent americium.^{12,13} We plan to calculate the distribution constant for this reaction as a function of concentration and temperature. The americium and plutonium in the salt will be recovered either by aqueous or pyrochemical methods; for example, by controlled potential deposition.

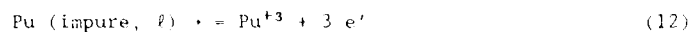
Casting. Impure metal buttons from DOR or MSE are collected, placed in a tantalum pour crucible, and vacuum cast to fit into the anode compartment of our electrorefining cell.¹³ The buttons are heated inductively under vacuum until liquid and then bottom poured into a graphite mold. Under the operating conditions, metallic impurities such as sodium, calcium and magnesium are partially volatilized. Additional magnesium and calcium evaporate and form a dark coating on the container walls during casting. Thorium, americium, alkali metals, alkaline earth and rare earth metals oxidize preferentially and remain in the pour crucible. Insoluble impurities, such as oxides, carbides and some metals, float on the melt surface and also remain in the crucible as residue. These residues are burned in air and cycled back into the recovery stream.

Experiments will test the feasibility of replacing the casting operation with either a salt extraction or distillation separation step. The extraction would be conducted in a vessel with a diameter suitable for forming a right cylinder of metal to fit in the anode cup of the electrorefining cell. Calcium chloride and various salt eutectics are being tested in extraction experiments and results, to date, are quite encouraging.

Electrorefining. At Los Alamos, electrorefining is the major process for converting impure plutonium metal to a high purity product.¹⁴ Impure metal is placed in the anode compartment within an electrorefining cell (Fig. 3), and a sodium chloride-potassium chloride eutectic containing magnesium chloride is added. The cell is assembled, placed under argon, and heated. The salt eutectic serves as an electrolyte for transport of ionic species. The magnesium chloride provides plutonium ion in the electrolyte prior to electrolysis by the reaction



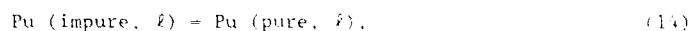
Current is passed through the cell and plutonium is oxidized in the anode compartment:



The positive ions are transported through the molten eutectic to the cathode, where reduction occurs:



The overall reaction is



and pure liquid plutonium metal collects directly below the cathode shield in the annulus between the outer cell walls and the walls of the anode compartment. The elements less active than plutonium remain in the anode compartment, combining with residual plutonium to form a solid anode heel. This spent anode must be further processed to recover plutonium.

In electrorefining, the elements more reactive than plutonium concentrate in the salt, along with trivalent plutonium and plutonium shot (believed to be small uncoalesced metal product). This salt residue is heated to 800°C with calcium present as a reducing agent. The resulting plutonium-americiu-m-calcium button is recycled into the production stream and the spent salt is discarded.

The purity of electrorefined buttons under our operating conditions is typically greater than 99.95%, and one-pass yields range from 75-80%. The yield depends on the purity of the anode metal. The process has been used to produce high purity metal for a number of years.¹⁵

Our research has been concentrated on developing a solvent anode such as cadmium, bismuth or lead in which the plutonium in the anode dissolves and is oxidized to depletion.¹⁶ Experiments have been quite successful with little or no plutonium remaining in the spent anode. However, at temperatures above the melting point of the sodium chloride-potassium chloride eutectic the cadmium in the anode is volatilized. Some of this metal condenses in the product, and additional cadmium is lost to the walls of the reaction vessel. In addition to experiments with lead and bismuth solvent anodes, substitutions of lower melting eutectics, such as lithium chloride-potassium chloride, are being evaluated. Operating temperatures can then be dropped into the 675-700°C range.

Magnesium chloride is used to provide trivalent plutonium in the electrolyte upon initiation of electrorefining. This eliminates some, but not all, of the generation of sodium and potassium during electrolysis. However, this step adds magnesium to the anode, which is an impurity that may interfere with the maintenance of a liquid anode. Tests show that plutonium trichloride is a suitable substitute for magnesium chloride in the cell.

Residues would be reduced by recycling the spent anode (if it is a solvent anode) and the eutectic salt. Impurities would probably build up with recycle, and a regeneration step should be evaluated. Since the cost of storage of discards and residues is escalating, such a recycle could be quite beneficial.

SUMMARY AND CONCLUSIONS

The present integrated pyrochemical process for producing high purity metal from plutonium scrap has been used quite successfully at Los Alamos. Yields from a one-pass system are about 65-75%, and the residual plutonium is efficiently recovered by a series of secondary operations. However, yields can be significantly increased and residue generation reduced by altering the operating conditions. Many of these changes are related to the salts employed in the operations.

Considerations of other molten salts and eutectics are particularly interesting and potentially useful in the DOR process. The addition of calcium fluoride to the present calcium chloride system to form a lower melting eutectic produces a metal button that does not adhere to the salt. The reaction can apparently be carried out at lower temperatures, thus, possibly, reducing calcium reaction with the crucible wall. Further study of reaction parameters is underway.

A second area of concerted study in the DOR system is regeneration of the spent salt followed by recycle. Development tests are complete, and a demonstration has been initiated.

Further changes in casting could evolve from the present study of the DOR process. If DOR were combined, or followed by a salt extraction step or distillation process to remove magnesium and excess calcium from the impure metal button, casting might become unnecessary. This is particularly valid if a solvent anode operation, with no dimension requirements for the anode materials, is adopted.

Lithium chloride-potassium chloride has been substituted for sodium chloride-potassium chloride in electrorefining, and plutonium trichloride has been used in place of magnesium chloride. Results have been encouraging, but more study will be needed.

Recycle of both the solvent anode and the salt in electrorefining, and plutonium trichloride has been used in place of magnesium chloride. Results have been encouraging, but more study will be needed.

Recycle of both the solvent anode and the salt in electrorefining is feasible, and tests are planned. As impurities build up in both salt and the anode, some method of regeneration or purification, perhaps distillation, will be needed. Semicontinuous operation and remote control

of processing are also areas of interest. Finally, nondestructive, in-line assay would be very useful in these systems and work has been initiated in this field.

On-going research and development programs in pyrochemistry at Los Alamos have been described in this report. As data are collected and evaluated, areas of concern, and concepts of the processes, will change. We are presently emphasizing development, but we are also interested in reaction mechanisms, salt purification and equipment design. We hope to learn more through interaction with the scientific community through related studies, and we plan to continue to report upon our programs.

REFERENCES

1. R. D. Baker, et al., "Preparation of Uranium Metal by The Bomb Method," Los Alamos Scientific Laboratory document LA-DC-3012 (1946).
2. R. D. Baker, "Preparation of Plutonium Metal by The Bomb Method," Los Alamos Scientific Laboratory report LA-493 (1946).
3. L. Burris, M. Steindler, and W. Miller, "A Proposed Pyrometallurgical Process for the Rapid Recycle of Discharged Fuel Materials From The Integral Fast Reactor," Proc. Fuel Reprocessing and Waste Management, Vol. 2, p. 257, Jackson, WY (August 26-29, 1984) American Nuclear Society, La Grange Park, Illinois (1984).
4. M. J. Rasmussen and H. H. Hopkins, Jr., "Preparing Plutonium Metal via The Chloride Process," Industrial and Eng. Chem. 53(6), 453 (1961).
5. M. H. West, M. D. Ferran, and K. W. Fife, "Synthesis of Plutonium Trichloride and Utilization in the Bomb Reduction Process," Los Alamos National Laboratory document LA-UR-86-3255 (1986).
6. J. A. McNeese, D. F. Bowersox, and D. C. Christensen, "The Recovery of Plutonium by Pyroreodox Processing," Los Alamos National Laboratory report LA-10457-MS (1985).
7. J. A. Leary and L. J. Mullins, "Practical Applications of Thermodynamics to Plutonium Process Reactions at High Temperature," in Thermodynamics, Vol. 1, pp. 459-471, International Atomic Energy Agency, Vienna (1966).
8. D. A. Wenz, I. Johnson, and R. D. Wolson, "CaCl₂ - Rich Region of the CaCl₂-CaF₂-CaO System," J. Chem. Eng. Data 11(2), pp. 250-252 (1969).
9. K. W. Fife, D. F. Bowersox, C. C. Davis, and E. D. McCormick, "Direct Oxide Reduction Solvent Salt Recycle in Pyrochemical Plutonium Recovery Operations," Los Alamos National Laboratory report LA-10891-MS (1987).
10. G. D. Bird, C. Thorn, V. D. Dole, A. Vargas, B. Miller, "DOR Comparisons in Demonstration Experiments," Los Alamos National Laboratory report (in preparation).
11. J. B. Knighton, R. G. Auge, J. W. Berry, and P. C. Frachini, "Molten Salt Extraction of Americium from Molten Plutonium Metal," Rocky Flats Plant report RFP-2365 (1976).
12. L. J. Mullins, A. J. Beaumont, and J. A. Leary, J. Inorg. Nucl. Chem. 30, 147 (1968).
13. R. D. Baybarz, L. B. Asprey, C. E. Strouse, and E. Fukushima, J. Inorg. Nucl. Chem. 34, 3427 (1972).

14. L. J. Mullins, A. N. Morgan, S. A. Apgar III, and D. C. Christensen, "Six-Kilogram Scale Electrorefining of Plutonium Metal." Los Alamos National Laboratory report LA-9469-MS (1982).
15. L. J. Mullins and A. N. Morgan, "A Review of Operating Experience at the Los Alamos Plutonium Electrorefining Facility, 1963-1977," Los Alamos National Laboratory report LA-8943-MS (1981).
16. D. F. Bowersox, K. W. Fife, and D. C. Christensen, "A Solvent Anode for Plutonium Purification," Chemical Separation, Vol. II, Applications, C. J. King and J. D. Navratel (eds.), Litarvan Literature, Denver, CO (1986), pp. 411-436.

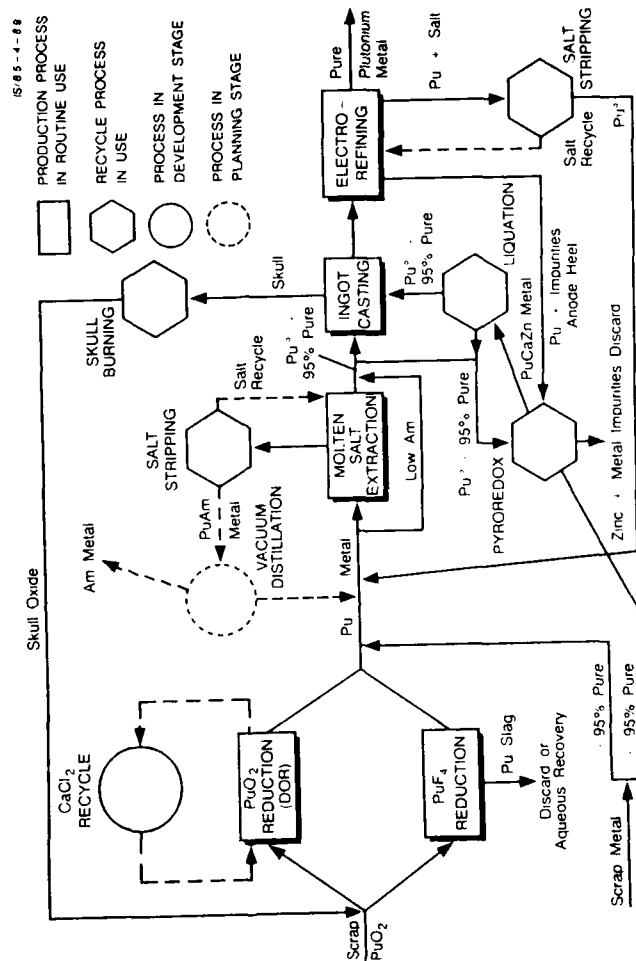


Fig 1. Pyrochemical Processing Flowsheet.

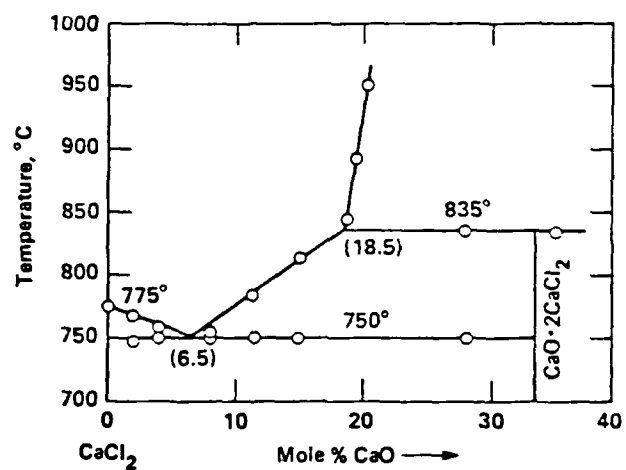


Fig. 2. CaCl_2 - CaO Phase Diagram.

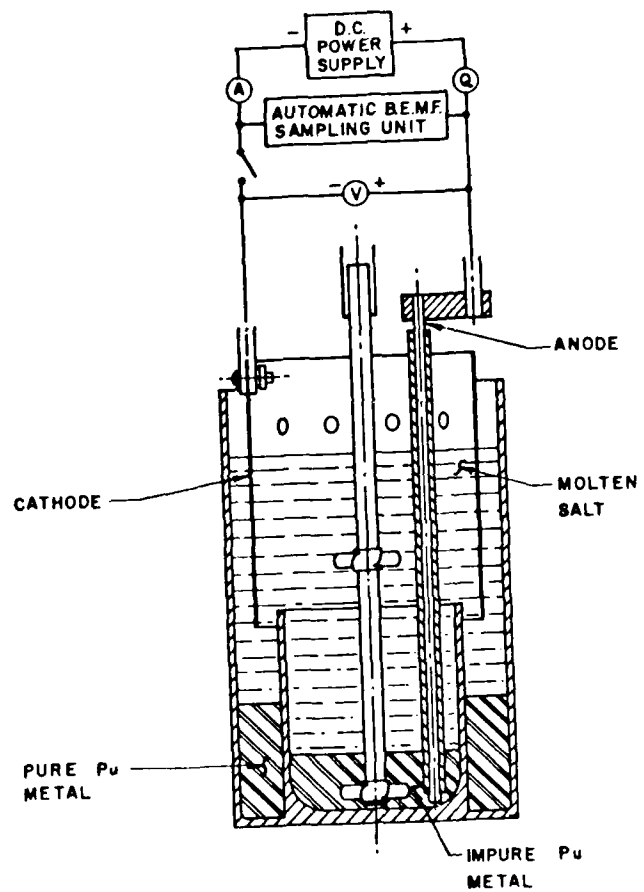


Fig. 3. Electrorefining Cell.

STATUS OF PLUTONIUM PURIFICATION BY BISMUTH SOLVENT ANODE ELECTROREFINING

Keith W. Fife, David F. Bowersox, Lynn E. McCurry,
Peter C. Lopez, and Cecil Brown

Los Alamos National Laboratory, Los Alamos, NM 87545

ABSTRACT

Recent investigations into plutonium purification by electrorefining from a molten secondary-metal solvent anode pool (metal solvent: $\text{Pu} \geq 1$) have concentrated on bismuth and bismuth-gallium solvents contained in shallow tantalum crucibles. Electrorefining is reversed from our standard LAMEX cell design and occurs via plutonium oxidation from a high-surface-area anode, using either molten $\text{NaCl} \cdot \text{KCl}$ or $\text{LiCl} \cdot \text{KCl}$ electrolytes and reduction on a cylindrical tungsten cathode. We are recovering high-purity plutonium from electrorefining anode residue and from PuO_2 reduction product. Recently, we have been recycling the spent solvent and are achieving overall plutonium recoveries similar to those obtained from conventional electrorefining.

INTRODUCTION

Impure plutonium metal is currently purified at Los Alamos by molten salt electrorefining (1-3). The procedure involves plutonium oxidation from an impure ($> 95\%$ Pu) molten plutonium anode, transport through an equimolar $\text{NaCl} \cdot \text{KCl}$ electrolyte, and reduction at a tungsten cathode. Overall plutonium recovery from the process ranges between 70% and 75%, considering all types of process feed. The technique is effective for producing pure plutonium metal ($> 99.95\%$). Overall plutonium recoveries, however, are directly related to the purity of the feed material. High-purity feed exhibits high oxidation and reduction (collection) efficiencies resulting in high overall recovery. With impure feed, high-melting plutonium alloys tend to form as plutonium is depleted from the anode and the impurities concentrate. The formation of these high-melting alloys reduces plutonium oxidation and diffusion rates, prohibits good mixing in the anode compartment, and effectively terminates the run leaving significant quantities of plutonium in the spent anode.

To reprocess this rich residue, a variation of molten salt electrorefining is being developed. Solvent anode electrorefining incorporates a secondary-metal solvent added to the plutonium (solvent metal: $\text{Pu} \geq 1$) in sufficient concentrations to keep the resulting

mixture liquid throughout all anticipated plutonium concentration ranges. With the anode remaining liquid throughout the process, the opportunity for increased oxidation efficiencies and, therefore, increased overall recoveries is possible from electrorefining. By extending the solvent anode concept to rich residue treatment, these conventional spent electrorefining anodes can be treated by a single-step solvent anode electrorefining process.

Initial experiments were conducted with cadmium as the solvent (4), but suffered from cadmium contamination of the product caused by the high vapor pressure of cadmium at cell temperatures of 690-720°C (cadmium boils at 765°C). Overall product recovery for the cadmium experiments was 65% to 75%, depending on the origin of the feed.

In addition to cadmium, we have investigated other solvents and now have some experience with bismuth and lead. With all solvents in their pure form, the amounts necessary to form a sustained liquid throughout all plutonium concentrations of interest are normally greater than 2:1. By adding small amounts of gallium to the system, however, the liquid range has been extended down to 1:1 ratios.

EQUIPMENT AND PROCEDURE

Initial experiments were performed in the standard Los Alamos or LAMEX electrorefining cell (Fig. 1). This cell is constructed of vitrified magnesia, and the general procedure consists of placing an ingot of impure plutonium metal (< 6 kg) in the inner cup, then loading equimolar NaCl-KCl with approximately 100 g MgCl₂ into the cell. When the system is molten at about 750°C, the stirrer, anode rod, and cathode are lowered into position and stirring is begun. Stirring is necessary to insure reaction of the MgCl₂ with the plutonium and to charge the electrolyte with Pu³⁺ before electrolysis begins. Once initiated, electrolysis continues until the static cell potential (back-emf) increases to a preset value. Back-emf is automatically measured throughout the run by interrupting the d.c. power and measuring the instantaneous cell potential. This cell potential increases as impurities concentrate in the anode during electrolysis and is used as a qualitative tool to monitor production runs. Terminating the run at a predetermined value insures that the quality of the product metal will be high although the quantity may be variable. By ignoring back-emf, we can extend the process to maximize plutonium oxidation but then create the possibility of co-oxidizing impurities and contaminating the product metal.

Solvent anode experiments performed in the LAMEX cells used electrically insulated tantalum stirrers and followed standard electrorefining operating guidelines. The limited anode compartment volume of the LAMEX cell presented a scale-up problem, so we designed a modified cell with a large-volume anode compartment (Fig. 2). This

modified cell is also constructed primarily of vitrified MgO but without an attached anode compartment. The anode pool is located at the bottom of the cell and is contained in a shallow tantalum vessel to eliminate MgO crucible breakage by solvent expansion during furnace heat-up or cool-down. The plutonium product collection cup is also magnesia and is contained in a stainless steel or tantalum basket assembly suspended in the molten salt. A cylindrical tungsten cathode is suspended above the collection cup and insulated from accidentally touching the basket with a magnesia sleeve.

We felt this radical change in cell design was necessary to accommodate larger-scale solvent anode runs and also to facilitate a semicontinuous mode of operation. In the modified cell, all hardware (stirrer, thermocouple, anode rod, and cathode/product assembly) is suspended in the melt. When the anode pool is depleted of plutonium, the hardware can be removed, the product cooled and collected, hardware replaced as necessary, and additional plutonium feed charged to the solvent without having to shut the furnace down.

Back-emf control is more complicated for solvent anode runs than for the conventional electrorefining process. The addition of large amounts of solvent metal and the change in cell design have caused us to re-examine back-emf behavior during electrolysis. Although we still use back-emf to terminate solvent anode experiments, we have not been able to rely on back-emf for consistent electrorefining performance.

EXPERIMENTAL RESULTS WITH BISMUTH

Bismuth was selected as a solvent because of its large liquid range. It melts at 271°C and boils at 1560°C. With plutonium, bismuth forms high-melting compounds (Fig. 3) that apparently can be suppressed by the addition of small amounts of gallium. The melting point of all bismuth-gallium mixtures is sufficiently low (Fig. 4) to apparently exert a synergistic effect on both the Pu-Bi and Pu-Ga (Fig. 5) systems and reduce or eliminate the formation of high-melting plutonium compounds. By adding gallium, we have been able to electrorefine at solvent-to-plutonium ratios approaching 1. With pure bismuth, however, a ratio > 2.0 (at 70 mol% Bi) was used to maintain a two-phase anode through the plutonium concentrations of interest.

Initial experiments with bismuth were discouraging because of crucible failure during the run. We suspect that bismuth was expanding anisotropically during heat-up or cool-down, resulting in a broken anode cup in the LAMEX cell. In contrast to the LAMEX cell, the product compartment in the modified cell is unaffected in the event of a broken anode vessel. With tantalum liners, both LAMEX and modified cell experiments have been completed without crucible breakage from bismuth expansion.

Table 1 summarizes our solvent anode experiments with bismuth and bismuth-gallium mixtures with both spent conventional electrorefining anodes (PMA) and PuO_2 reduction product (XOP). The PMA feed had gallium added for criticality control before the original electrorefining. The XOP feed was the product from reduction of high-purity PuO_2 with densities between 17.5 and 18.0 g/cc (pure α phase plutonium has a density of approximately 19.7). Table 1 illustrates variable oxidation and reduction (collection) efficiencies caused by changes in cell design and operation. In all cases, however, product purity was high (Table 2) but not as high as conventional electrorefined plutonium ($> 99.95\%$ pure). We are contaminating our product metal with magnesium and to some extent, with bismuth, tungsten, and other metals. The source of the magnesium is our feed (PMA and XOP) and the MgCl_2 we use to initially charge the electrolyte with Pu^{4+} . The redox potential of magnesium is very similar to that of plutonium in both LiCl-KCl and NaCl-KCl systems and tends to follow plutonium to the cathode. Final separation of magnesium from the plutonium should be straightforward because of their vapor pressure differences. At 800°C , magnesium has a vapor pressure about nine orders of magnitude greater than that of plutonium and should be effectively removed by vacuum distillation or vacuum casting (7).

The erratic presence of other impurities in the product may be a result of any combination of the following:

- unfavorable cell current distribution,
- metallic hardware participating in or introducing electrochemical side reactions in the melt,
- potential for occasional cell operation at large negative voltages,
- an unfavorable cathode/anode surface area ratio in the modified cell.

In addition to continued experimentation with the modified cell, we are beginning to reuse solvent metal in multiple runs. Our approach has been to keep the solvent and electrolyte molten, remove the head assembly in a circulating argon glovebox, replace the affected hardware (basket assembly and cathode), add new feed to the molten system, equilibrate, and restart electrolysis. We have completed several experiments using recycled solvent and XOP feed. In this situation, it appears that solvent recycle is not adversely affecting operation, overall recovery, or product quality. Analyses, however, to determine product purity and impurity build-up in the solvent are not yet available.

FUTURE DIRECTION

In solvent anode electrorefining, we plan to continue studying

- cell design and operation to achieve consistency in our performance,
- back-emf behavior in different solvent plutonium systems,
- lead and cadmium in addition to bismuth as solvents,
- use of gallium in the solvent,
- potential of solvent metal recycle, and
- different electrolyte compositions and the potential for electrolyte recycle.

We are confident that solvent anode electrorefining can be developed and demonstrated as a technique for recovering plutonium from many types of rich residues. Once developed, this procedure may supplement the conventional electrorefining process and provide recycle of plutonium with lower generation of residues and waste.

REFERENCES

1. L. J. Mullins and J. A. Leary, I&EC Process Design and Development 4, pp. 394-400 (October 1965).
2. L. J. Mullins and A. N. Morgan, "A Review of Operating Experience at the Los Alamos Plutonium Electrorefining Facility, 1963-1977," Los Alamos National Laboratory report LA-8943 (December 1981).
3. L. J. Mullins, A. N. Morgan, S. A. Apgar, III, and D. C. Christensen, "Six-Kilogram Scale Electrorefining of Plutonium Metal," Los Alamos National Laboratory report LA-9469-MS (September 1982).
4. D. F. Bowersox, K. W. Fife, and D. C. Christensen, "A Solvent Anode for Plutonium Purification," in Applications from Proceedings of the First International Conference on Separations Science and Technology II, C. J. King and J. D. Navratil (eds.), Litarvan Literature, Denver, pp. 411-426 (1986).
5. F. H. Ellinger, W. H. Miner, D. R. O'Boyle, and F. W. Schonfeld, "Constitution of Plutonium Alloys," Los Alamos Scientific Laboratory report LA-3870 (December 1968).
6. R. P. Elliott, Constitution of Binary Alloys, First Supplement, McGraw-Hill, New York, p. 182 (1965).
7. R. Hultgren, P. O. Desai, D. T. Hawkins, M. Gleisner, K. K. Kelley, and D. D. Wagman, Selected Values of the Thermodynamics Properties of the Elements, American Society for Metals, Metals Park, Ohio (1973).

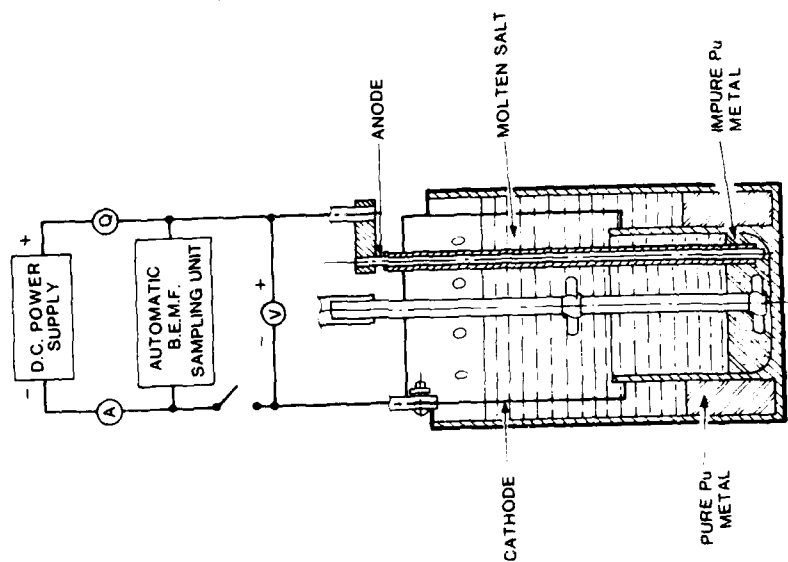


Fig. 1. Los Alamos Electrowinning Cell.

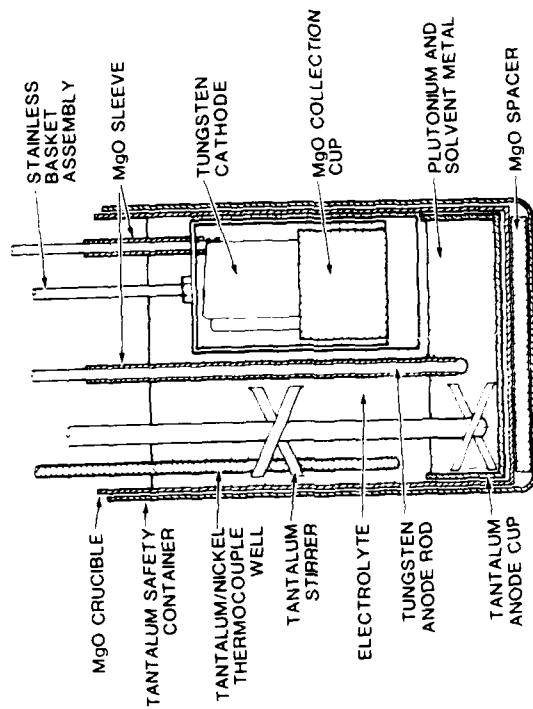


Fig. 2. Modified Solvent Anode Electrowinning Cell.

Table 1. Bismuth Solvent Anode Electrorefining from Modified Cell

Run	Feed Type ^a	Plutonium Feed (gPu)	Bi/Pu Ratio (g/g)	Temp (°C)	Electrolyte ^b	Oxidation Efficiency ^c (%)	Reduction Efficiency ^d (%)	Product Purity (%)
ER56	PMA	931	2.2	850	NaCl-KCl	67.6	47.9	81.1
ER57	PMA	947	2.1	850	NaCl-KCl	84.3	69.7	78.4
ER71	XOP	943	1.1	850	NaCl-KCl	99.6	54.3	81.1
ER74	XOP	944	1.1	880	NaCl-KCl	87.0	75.0	80.4
ER76	XOP	895	1.4	880	NaCl-KCl	93.0	83.0	80.4
ER79	XOP	1210	0.95	885	LiCl-KCl	99.3	89.5	88.9
ER80	XOP	1321	0.90	860	LiCl-KCl	87.5	79.5	82.9

^a PMA is a spent conventional electrorefining anode. XOP is Pu₂O₃ reduced product.

^b Equimolar NaCl-KCl, LiCl-40 m/o KCl, 100 g MgCl₂ added to each run.

^c Calculated from (initial Pu in Bi - final Pu in Bi)/(initial Pu in Bi).

^d Calculated from (Pu in product)/(initial Pu in Bi - final Pu in Bi).

^e Early modified cell had a hemispherical anode container and an offset stirrer which resulted in poor mixing.

Table 2. Bismuth Solvent Anode Electrorefining Product Purity Results

Run	Product Density (g/cc)	Product Purity (%Pu)	Product Impurities (ppm)										
			Al	Bi	Cr	Fe	Ga	Mg	Mn	Ni	Si	Ta	W
ER56	19.7	99.94	60	150	15	40	<100	300-3000	100	6	7	41	1
ER57	19.5	99.99	50	300-3000	9	<20	<100	300-3000	100	<5	25	<10	1
ER71	19.6	--	40	300	<5	--	45	50	8	<5	15	<10	1
ER74	19.3	99.86	<5	300	90	270	104	300-3000	40	20	20	<10	8-10
ER76	19.2	99.83	210	100	65	150	245	300	20	55	50	<1	1
ER79	19.4	99.86	55	80	25	70	450	300	50	15	10	<10	1
ER80	19.1	99.83	<5	35	<5	<20	33	300-3000	10	<5	20	<10	1

COMPACT MOLTEN-SALT FISSION POWER STATIONS (FUJI-series) AND THEIR DEVELOPMENTAL PROGRAM

Kazuo Furukawa, Kazuyoshi Minami*, Kohshi Mitachi** and Yoshio Katoh***

Institute of Research & Development, Tokai Univ., Hiratsuka, Kanagawa,
Japan 259-12

* Science System Develop. Dept., Fujitsu Ltd., Shinkamata, Tokyo, Japan 144

** Dept. of Engineering, Toyohashi Univ. of Tech., Toyohashi, Japan 440

*** Fuel Develop. Div., Japan Atomic Energy Research Inst., Tokai, Ibaraki,
Japan 319-11

ABSTRACT

The design studies of Compact Molten-Salt Power Stations (Th-²³³U fueled molten-fluoride fission converters) were presented in the two directions: [class I] (50~300MWe) and [class II] (2~30MWe). Both have several advantages on safety, simplicity, easy operation & maintenance, trans-U elements and nuclear proliferation resistance, due to the non-exchange of core elements and the non-continuous chemical processing. In class I, very high conversion ratio more than 95% might be expected in low fissile inventory. In class II, very small but high performance could be achieved in small fissile supply. Their inherent safety, simplicity and smaller capacity would be useful for developing countries, ship-propulsion, and generating electricity on ships etc., improving the world environment.

INTRODUCTION

Considering the environmental impact from fossil fuel burning all over the world, a rational nuclear energy system should be established for the next century in the following ways (1):

- [A] thorium resources utilization,
 - [B] simple and practical breeding fuel cycle integration,
 - [C] separation of fissile producing breeders (process plants) and fission power stations (utility facilities),
 - [D] fissile producing breeders development till the next century (2)(3),
 - [E] smaller fission power stations development among this century.
- The last [E] is a main problem to be discussed, and the thorium containing molten fluorides are technological key-materials in here.

All proven-type solid fuel nuclear reactors are principally favoring the larger size, even though keeping some potentials toward minimizing in size (4). These reactors have potential problems, such as the safety aspects and nuclear proliferation issues. It has been clarified by the recent reactor design study that the Compact Molten-Salt Fission Power Stations might be helpful for improvement of all the above, and recommendable for further reactor development. A brief review will be given including a developmental program.

DESIGN PRINCIPLE OF COMPACT MOLTEN-SALT POWER STATIONS (FUJI-series) AND THEIR MAIN BENEFITS

The design study and technological development of molten fluoride fueled fission reactors were intensely and comprehensively performed by the **Molten-Salt Reactor Program** (1960~1976) in ORNL, USA. They presented remarkable results on the development of fission breeder, MSBR (Molten-Salt Breeder Reactor) (5). The large fission converter, MSCR, also examined (6). However, they had focused only on the 1000MWe class reactors but not on the small reactors, and their excellent proposal was not pursued due to the non-nuclear proliferation policy of former President Carter, not due to any technological reason (7).

Four years ago, the design study of Compact Molten-Salt Power Stations was started by us principally following a similar direction as MSRP of ORNL; the essential reactor feature was clarified in the following two classes of power size :

[class I] : 50~300 MWe,

[class II] : 2~30 MWe.

The reactors of both classes have essentially the same design principles explained below. Therefore, they are named "FUJI-series" in all. The real examples are "FUJI-I" (compact high conversion type) and "FUJI-II" (fuel self-sufficient type) of 155 MWe size in class I, and "mini-FUJI-I" of 4.2 MWe and "miniFUJI-II" of 7 MWe in the class II.

The main design principle chosen for FUJI-series (Compact Molten-Salt Fission Power Stations) is as follows:

- 1) single-fluid multi-region type, graphite moderated, and molten fluoride fueled fission converter.
- 2) reactor inlet and outlet temperatures : 560~580°C and 700~725°C.
- 3) thorium contained in a fluoride mixture:
- 4) **graphite core: no exchange** thus a weld-sealed reactor vessel (simple tank without big flanges, can be used which has:
 - a) low power density of about 10kWth/liter in core and blanket regions, and of flat distribution. [possibly 15~20 kWth/liter in miniFUJI].
 - b) 99% removal of fission gases (Xe, Kr), and **no continuous chemical processing**, which is one of the most difficult R & D items.
 - c) **high conversion ratio** and low fissile inventory.

From the above design principles, the following significant advantages might be expected:

(A) **Excellent Safety Aspects:** low pressure; no chemical reaction of reactor materials (no gas generation); no core melt-down; and no fear of re-criticality accident due to the automatic isolation of leaked-fuel and moderator (graphite).

(B) **Simple Structure, and Easy Operation and Maintenance:** no fuel assembly fabrication and handling; short graphite size; few control rods due to the low excess-reactivity in fluid fuel reactors in general; self-controllable, load-following and easy restarting characteristics; and no continuous chemical processing facility.

(C) **High Reactor Performance:** high conversion ratio inherent in Th-²³³U cycled thermal reactors but unusual in small converters; and high thermal efficiency (42-46%) by (ultra-) ultra-super critical steam cycle.

(D) **Advantage in Resource Problem, thorium utilization:** non-localized and 3~4 times more abundant than uranium.

(E) **Trans-U elements (Pu, Am, Cm) burnup:** essentially no production can burnup trans U elements from other reactors.

(F) **High Nuclear Proliferation Resistance:** intense hard- γ radiation from impurities (²³²U) inherently produced with ²³³U; very few supply (transportation) of fissile materials due to the high conversion ratio.

(G) **Finally Excellent Economy:** originated from all of the above items, and from the feasibility of simple rational fuel-cycle system in future.

MAIN FEATURE AND PERFORMANCE OF SOME EXAMPLES OF COMPACT MOLTEN-SALT POWER STATIONS (FUJI-series)

For the neutronic core calculation, the two-dimensional diffusion-burn-up code, CITATION, was used applying 9 group reactor constants produced by ORNL (8,9). The calculations were performed by FACOM M-380 machine. The neutron irradiation limit of core graphite will be 3×10^{23} nvt (>50 keV), following MSBR design criteria (5,10). Therefore, the maximum core flux should be less than 3×10^{13} n/cm²sec in 30 year life and 50% load (as local power stations). Graphite volume fractions (G) are chosen 93-85% in core-zone, 65-75% in blanket-zone and 99% in reflector-zone. The low power density will allow to choose a high G value such as 93%. This is a big advantage for intensifying neutron-moderation, which is followed by an improved fuel conversion ratio. The reflector thickness was determined by the neutron irradiation limit in modified Hastelloy N of reactor vessel, which is 1.2×10^{21} n/cm²sec (>0.8 MeV), and 6.5×10^{20} n/cm²sec (<0.18 eV) at temperatures less than 650°C.

A lot of model calculations have been performed. Among them the following four cases are shown as significantly interesting examples. Their main characteristics are presented in Table 1, with MSBR and MSRE (Molten-Salt Reactor Experiment Operated in 1965~1969) of ORNL.

FUJI-I [155MWe: Compact High Conversion type]

This reactor has two-core zone arrangement of maximum diameters: 1.4 and 3.4m, and of G: 93 and 90% (cf. Table 1). This was highly effective for achieving a flat power distribution in core/blanket region, a comparatively compact size, a lower fuel inventory and a higher conversion ratio 0.98 after 1000 days burn according to the calculations.

The maximum salt flow velocity is about 0.8m/sec only. The net thermal efficiency for generation of electricity is kept in very high 44.3% by ultra supercritical steam cycle, which will be improved more to 46% by ultra-ultra supercritical cycle only changing the fuel inlet/outlet temperature to 585/725°C. The conceptual model of FUJI-I was shown in Fig. 1, and the primary system is accommodated in the high-temperature containment (500°C) of 12m in diameter, as shown in Fig. 2.

The initial fissile inventory is 304 kg, and additional supply of ^{233}U in early transient stage is about 43kg. This reactor could be continuously operated by adding ^{233}U 16g/day (=5.8kg/year) and Th 400g/day only. The total demand of ^{233}U in full life will be 444kg, of which 322 Kg will be recovered. Semi-annual transport of 2.9kg of fissile materials will not be enough even for one nuclear weapon owing to the dirty isotope mixture. More detailed description will be found in ref. (4).

FUJI-IUI [155MWe: Fuel Self-Sufficient type--"near-breeder"--]

The blanket thickness and G of FUJI-I were modified for the improvement of conversion ratio resulting in a slightly bigger size and a fissile inventory as shown in Table 1. After about 500 days of operation, the conversion ratio settled to 1.002 from initial 1.044, and essentially no fissile transport is required, which is significantly safer in terms of reactivity and resistance to nuclear proliferation.

This reactor would be an ideal small power station, and one of the best partners for fissile breeding facilities such as AMSB (Accelerator Molten-Salt Breeder) or IFMSB (Impact Fusion Molten-Salt Breeder) due to the surprisingly small demand (392 Kg) of fissile materials in full life (1,2,3). More details are given in ref. (4).

It will be possible that the above mentioned reactor performances are weakened after the detailed design is developed. However, the conversion ratio might be kept higher than 0.95, which will be still an ambitious value.

miniFUJI-I [4.2 MWe:mini-size type]

Initially this was studied as a pilot-plant for developing the Compact M.S. Power Stations [FUJI-series]. The design result was surprisingly good and useful for practical mini-size power stations. In mini-FUJI-I, the core is a single zone, keeping a more flat power density distribution. The total volume of core/blanket zones is 1m^3 , and the reactor size is 1.7m in diameter, 2m in height and 4.5m^3 in volume.

The conceptual model of this reactor was shown in Figs. 3 and 4. The horizontal cross sections of graphite moderators are shown in Fig. 5. In the center of the reactor core, 2~3 control rods are inserted, and 1~2 rods of the center area are able to be used for materials-irradiation tests, as required. This is nearly the same as for MSRE, which was successfully operated in 1965~1969 without any severe troubles. The high-temperature containment of the primary system will be only 3.5m in inner diameter, fairly smaller than 5.8m of MSRE. The wall-thickness of the reactor vessel is about 8cm (15cm in MSRE). The total weight of the reactor vessel is about 10 ton, except for 1 ton of salt.

The consumption of fertile Th is about 13 g/day corresponding to 4.7kg/year. This reactor has a conversion ratio of 0.55 due to its very small size. However, this is nearly the same as LWR (Light Water Reactors) of 250 times larger power capacity, and ^{233}U supply is only about 2.1 kg/year, which is not enough for one nuclear weapon.

miniFUJI-II [7 MWe : super compact mini-size type]

The above miniFUJI-I has an average density of 9.8MWth/liter, which is nearly the same as for FUJI-I and -II, and suitable for a pilot-plant. However, its neutron flux is about half of FUJI-I; nearly two times larger power capacity (7MWe) could be achieved without changing the size of any reactor component except for the reflector whose thickness should be increased by about 5cm. If this miniFUJI-II development had been pursued, it would have been attractive for ship-propulsion engines or for generating electricity on ships.

DEVELOPMENTAL PROGRAM FOR FUJI-series REACTORS

As shown in the above preliminary design study of FUJI-series reactors, the complete shift from U-Pu solid to Th-U fluid fuel cycle will be attractive since it improves the economy, safety, trans-U elements burnup and non-nuclear proliferation.

As the total demand of ^{233}U is not big and less than 400Kg for 10 years in our program, its supply could be satisfied by irradiation of Th in LWR, for example, as MSRE. In the future, the dry chemical processing (molten fluoride) method originated by the French and now being developed at Demitrovgrad, USSR, will be more attractive (12). Until the beginning of the next century, some useful breeders such as AMSR or IFMSB would be developed establishing the Molten-Salt Nuclear Energy Synergetics (1)(13).

Already the basic R & D has been comprehensively established by ORNL except for the data base of modified-Hastelloy N, which specification has been settled. The pilot-plant program could accept immeasurable contributions from MSRE. The bigger components and high temperature molten material technologies could greatly benefit from the recent Na-cooled reactor development. The general ideas in our program will be presented below suggesting the bigger test rigs (cf. Table 2) :

A. General R & D

Fuel-salt chemistry loop (impurity monitor, F.B.behav., mass transfer)
Coolant-salt chemistry loop (imp.monitor, tritium behav., mass transfer)
Integral steam generator test loop (material test, electric generation)
Materials development (Hastelloy N, Graphite and the others)
Salt preparation, chemical analysis, and batch chemical processing.

B. Pilot-plant (miniFUJI-I) Program

Reactor mock-up test loop (pump, heat exchanger, instrumentations, etc.)
Reactor remote maintenance mock-up
Reactor : 1) long term endurance test, 2) materials test,
3) F.P. (tritium) behavior test, 4) power-up for miniFUJI-II project.

C. Compact Molten-Salt Power Station (FUJI-I) Program

Full size small reactor engineering development (2 MWe loop)
Long term endurance test of the reactor

- D. Medium-, and Large-Molten-Salt Power Stations Program
- E. Fissile Producing Breeder Development (AMSB or IFMSB etc.)
- F. Establishment of Molten-Salt Nuclear Energy Synergetics

The time schedule in general was shown in Table 2, and the personnel plan for the initial 7 years (A+B+C) was shown in Table 3. The total cost for the initial 7 years would be about \$100~150 millions.

CONCLUSIONS

Compact Molten-Salt Power Stations with excellent performances were successfully designed promising a wider social applicability of Th-U fuel cycled fission reactors by miniaturization. These small reactors would not compete with inherently larger sized solid-fuel power reactors, and could end several useful applications in developing countries and isolated areas, and especially for ship-propulsion engines or generating electricity on ships, improving the world environment.

Now we have to start the developmental program of FUJI-series reactors, and should establish the rational Th molten-salt breeding fuel cycle (**Molten-Salt Nuclear Energy Synergetics**) for the next century.

ACKNOWLEDGEMENTS

The authors are very much indebted to Dr.J.R.Engel of ORNL for providing the nine group reactor constants for the molten-salt reactors. They also acknowledge Dr.T.Oosawa of Kyushu Univ. and the members of MSR working group in MSTT (the society of molten-salt thermal technology).

REFERENCES

- (1) K.Furukawa, Proc. 7th Miami Int. Conf. Alt. Energy Sources (Decem. 1985)
- (2) K.Furukawa, K.Tsukada and Y.Nakahara: J. Nucl. Sci. Tech. 18 79 (1981); K.Furukawa: Atomkern./Kerntechn. 44 42 (1984)
- (3) K. Ikuta, and K.Furukawa: another report presenting in this Sympo.
- (4) K.Furukawa, K.Minami, T.Oosawa, M.Ohta, N.Nakamura, K.Mitachi, Y.Katoh: 4th Int. Conf. Emerging Nucl. Energy Sys. (June/July 1986, Madrid) p 233
- (5) M.W.Rosenthal, P.N.Haubenreich and R.B.Briggs: ORNL-4812 (1972)
- (6) A.M.Perry: Ann. Nuclear Energy 2 809 (1975)
- (7) H.G.MacPherson: Nuclear Science & Eng. 90 374 (1985)
- (8) R.J.Engel, W.R.Grimes, H.F.Bauman, E.H.McCoy, J.F.Dearing, and W.A.Rhoades: ORNL/TM-7207 (1980)
- (9) T.Oosawa, H.Matsuoka, M.Ohta and K.Kudo: Memoirs Fac. Eng. Kyushu Univ. 43 193 (1983)
- (10) R.C.Robertson ed.: ORNL-4541 (1970)
- (11) D.E.Lilienthal: "Atomic Energy: A New Start", Harper & Row, 1981 [trans. to Japanese by K.Furukawa, pub. Japan Productivity Center, 1982]
- (12) MacLachlan: Nuclear Fuel 14 14 June 4, 1984
- (13) A.A.Harms & M.Heindler: "Nuclear Energy Synergetics", plenum, 1982 [translated to Japanese by us, pub. Baifuu-kan, 1986]

Table 1. Important characteristics of several molten-salt reactors including our FUJI-series Reactors, and MSBR(Molten-Salt Breeder Reactor) and MSRE (Molten-Salt Reactor Experiment) of ORNL, USA.

	MSBR-ORNL	FUJI-I	FUJI-II	miniFUJI-I	miniFUJI-II	MSRE-ORNL
thermal capacity (MWth)	2250	350	"	10	16.7	7.3
net electric generation (MWe)	1000	155, 161 [#]	"	4.2	7.0	—
thermal efficiency (%)	44.4	44.3, 46 [#]	"	42.5	42	—
Reactor Vessel:	(super. cr.) (vol. s.) (vol. s.)	(vol. s.) (vol. s.)	(vol. s.) (vol. s.)	(vol. s.) (vol. s.)	(vol. s.) (vol. s.)	(vol. s.) (vol. s.)
inner diameter X height (m)	6.8 X 6.1	5.4 X 4.0	5.5 X 4.1	1.7 X 2.0	1.8 X 2.1	1.45 X 2.2
Core maximum diameter (m)	4.4	1.4, 3.4*	"	0.6	0.6	1.41
Graphite fraction (vol%)	87	93, 90*	"	90	90	77.5
Blanket thickness (cm)	40	30	35	20	20	—
Graphite fraction (vol%)	63	68	65	70	70	—
Reflector thickness (cm)	75	68	68	35	40	77
Core/Blanket power density:						
average—peak (kWth/liter)	22.4—70.4	10.4—23.5	9.5—17.5	9.8—14.9	16.4—24.9	2.9—6.6
n flux: max. thermal (n/cm ² sec)	8.3 x 10 ¹⁴	1.9 x 10 ¹⁴	2.4 x 10 ¹⁴	0.35 x 10 ¹⁴	0.58 x 10 ¹⁴	0.5 x 10 ¹⁴
max. Graphite damage (50KWe)	3.5 x 10 ¹⁴	0.8 x 10 ¹⁴	0.8 x 10 ¹⁴	0.45 x 10 ¹⁴	0.75 x 10 ¹⁴	0.3 x 10 ¹⁴
Fuel Salt:						
23Uf4 concentration (mol%)	0.3+1	0.217+1	0.22+1	0.47+1	"	0.14+2
volume: reactor (m ³)	30.4	8.1	9.7	0.29	0.30	0.54
: primary (sum) (m ³)	48.7	12.1	13.7	0.44	0.45	2.1
flow rate (m ³ /min)	213.	33.2	"	0.95	1.59	4.5
inlet—outlet temperature (°C)	565—704	560—700	"	"	"	632—654
Fuel conversion ratio	1.06+3	(0.40)	(1.00?)	(0.55)	(0.55)	—
inventory:						
23Uf4 : (per 1000MWe) (ton)	1.79	0.32; (2.1)	0.37; (2.4)	0.027; (6.3)	0.027; (6.4)	0.032; (—)
232Th (ton)	70.7	17.7	20.1	0.64	0.65	—
Graphite (ton)	304.	158.3	161.6	7.4	8.8	3.7

*1 : 7/1 if Ref 2—thf 4—23Uf4; (72-X)—16—12—X mol%.

*2 : 7/1 if Ref 2—thf 4—thf 4; 64.5—30.2—5.2—0.15 mol%.

*3 : continuous chemical processing.

: ultra-ultra supercritical steam turbine cycle (593°C, 317 atm)

* : second core zone

Table 2. Developmental Program of Molten-Salt Fission Power System
(==> construction; ----> operation)

	1991	1994	1997	2000
A. General R & D..				
Fuel-salt loop	==>----->-----			
Coolant-salt loop	==>----->-----			
Electric generating test loops	==>----->----->----->-----			
	(200KWe)		(2 MWe)	
Hastelloy N	----->----->			
Graphite, etc.	mechanical data			
B. Pilot-plant (miniFUJI-I) Program				
Reactor design	==>----->			
Reactor mock-up	==>----->			
Reactor remote mainte.	==>----->-----operation			
Reactor const.& ope.	----->-----const. crit.-----miniFUJI-II test			
C. Compact Molten-Salt Power Station (FUJI-I) Program				
Reactor design	----->----->			
Reactor mock-up	----->----->			
Reactor remote mainte.	----->----->-----operation			
Reactor const.& ope.	----->----->-----const. crit.-----			
D. Medium-, and Large-Molten-Salt Power Stations Program				
E. Fissile Producing Breeder Development (AMSB or IFMSB etc.)				
Prelimi. R & D	----->-----			
Integral exp. fac.	----->----->-----design const. low power ope.-->high power ope.			
Prototype fac.	----->----->-----design study design const. ope.			
F. Establishment of Molten-Salt Nuclear Energy Synergetics				
System design study	----->-----			

Table 3. Personnel Plan for Compact Molten-Salt Power Station
(FUJI-series) Development Program (among initial 7 years)

administration	4	chem. processing dev.	5
reactor design study	7	chemistry	10
heat transfer	3	analytical chem. dev.	5
components & system dev.	14		
instruments & control	4	operation	30
physics	3		
materials	15		
		<u>in total</u>	<u>100</u>

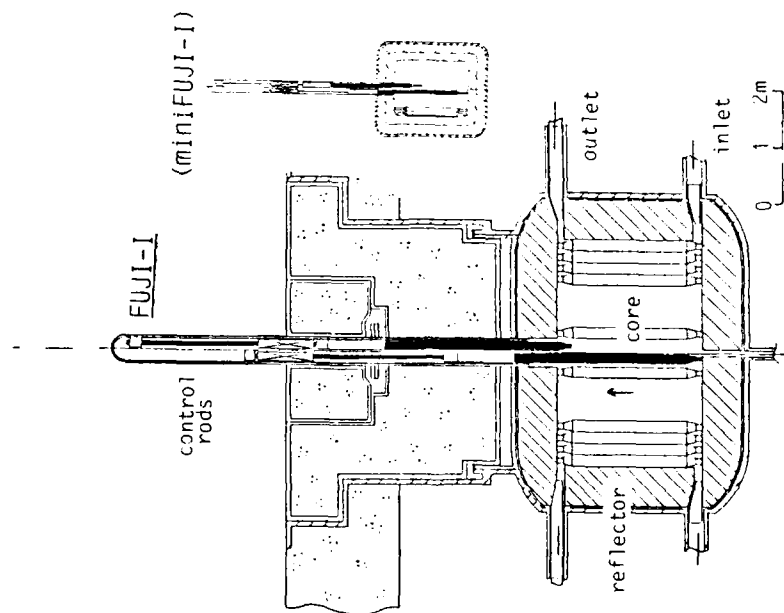


Fig.1. Horizontal cross section of the reactor vessel of FUJI-I. (reactor contour of miniFUJI-I is shown in same scale)

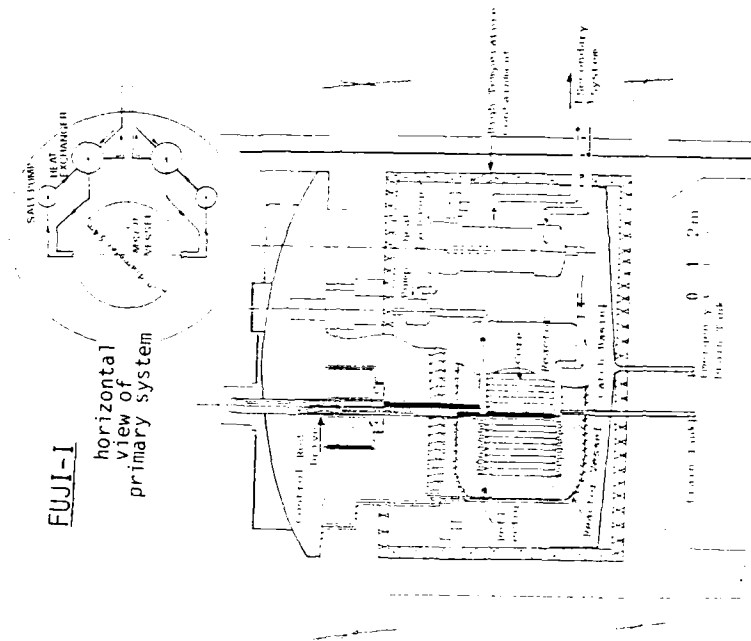


Fig.2. Conceptual model of the primary system of FUJI-I arranged in the high-temperature containment (500°C).

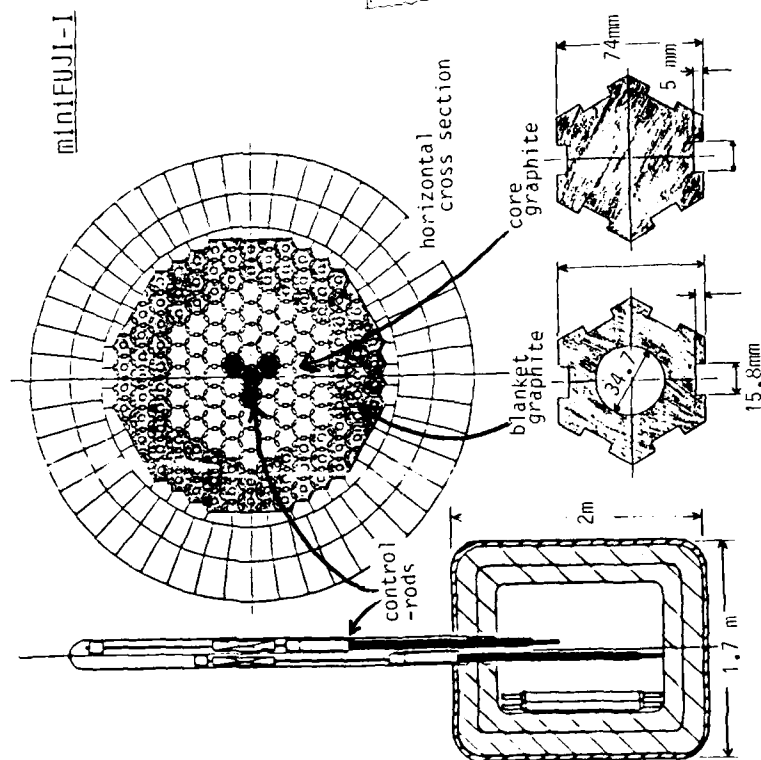


Fig. 3. Reactor vessel of miniFUJI-1 and its horizontal cross section.

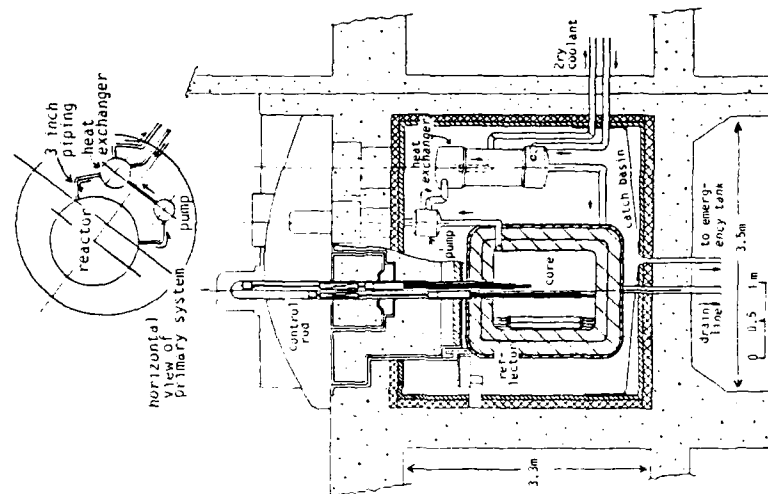


Fig. 4. Conceptual model of the primary system of miniFUJI-1 in its horizontal view.

**IMPACT-FUSION MOLTEN-SALT BREEDER (IFMSB)
USING SHAPED-PROJECTILE AND AXIALLY SYMMETRIC MASS DRIVER**

Kazunari Ikuta and Kazuo Furukawa*

Nagoya University, Institute of Plasma Physics,
Chikusa, Nagoya, Japan 464

*Tokai University, Institute of Research & Development,
Hiratsuka, Kanagawa, Japan 259-12

ABSTRACT

A new design concept for fissile material production breeder is proposed. The key technologies are (1) a shaped-projectile, which has a built-in imploding mechanism with a DT fuel-pellet eliminating a fuel target injection in fine alignment, (2) an axially symmetric mass driver, which is based on a rapid Z-pinch discharge between the cylindrical electrodes expecting positionally stable acceleration of the projectile, and (3) a molten-salt target/blanket technology, which is similar to that of Accelerator Molten-Salt Breeder having a big salt bath with deep vortex but now adding He bubbles. The target salt including ^{235}U prepared in IFMSB could be supplied to Molten-Salt Fission Power Stations, integrally constituting an idealistic molten salt fuel cycle system.

INTRODUCTION

In the rational, economical and safer nuclear fission energy system, the power stations of several sizes (utility facilities) and the fissile-fuel breeders (process plants) should be separated and coupled by a simple molten-fluoride fuel cycle. Already Accelerator(Spallation) Molten-Salt Breeder(AMSB) and Inertial-confined Fusion Molten-Salt Breeder(IFMSB) were proposed (1)(2), and now another idea will be presented.

Impact fusion (3) is one of the approaches to produce controlled thermonuclear power using hypervelocity impact of a target made of deuterium-tritium (DT) ice. This concept is as follows: Small projectiles with a mass of 0.1g designed by appropriate materials are accelerated to a velocity of $V \sim 10^8$ cm/sec. They collide with a DT target, and their kinetic energy is abruptly converted into thermal energy (~ 10 keV per nucleon, temperature $\sim 10^8$ K) which is inertially-confined in the shocked region. To achieve a uniform acceleration α of a small projectile, a non-relativistic accelerator will have a length

$$x = v^2 / 2\alpha. \quad [1]$$

The differential or tidal stresses caused by an accelerating force F acting on a projectile with characteristics of size L are in the order of $\sim F/L^2$. If these stresses are not to exceed the yield stress S of the projectile, the minimum length of the accelerator must be

$x_{\min} \sim \rho L V^2 / S$ [2]
for a projectile of density ρ and mass ρL^3 , because the relation between S and α is

$$\rho L \alpha = S. \quad [3]$$

The criterion (3) for a net gain in impact fusion is approximately $L \rho \sim 0.1 \text{ g/cm}^2$. With a reasonable value for the yield stress of $S \sim 10^{10} \text{ dyne/cm}^2$, it is found that the minimum accelerator length is $x_{\min} \sim 1 \text{ km}$. This result is generally acceptable and applicable to any kind of accelerators. A shorter accelerator would require a material with a larger yield stress S .

In order for impact fusion to have a reasonable hope of practical application, the maximum length of the accelerator should be of the order of 10 m. This can be achieved by adopting shaped-targets, as proposed in the literature (4). In this case, the necessary velocity of the small projectiles is $V \sim 10^7 \text{ cm/sec}$, which gives an accelerator length x_{\min} described by [2] as

$$x_{\min} \approx 10 \text{ m}, \quad [4]$$

even taking a standard value of the yield stress,

$$S \sim 10^{10} \text{ dyne/cm}^2.$$

In this report, the following three key technologies are applied for the breeding of ^{233}U utilizing neutrons generated from the impact fusion.

[I] The first is the choice of the shaped-projectile (5) instead of the shaped-target (4). It has a built-in imploding mechanism with a fuel-pellet, and now a fuel target pellet injection in fine alignment is not necessary.

[II] The next is the development of the mass driver system. By the choice of the shaped-projectile the aspect ratio d/h , of the shaped-projectile must be as small as possible in order to reduce the mass of the projectile. In this case, the positional stability of the projectile becomes an important problem in the course of accelerating the projectile. This means that the position of accelerating disk-like projectile should be stabilized by its spinning motion and that the accelerator must be axially symmetric in order to minimize the perturbation to the spinning disc. We are thus naturally lead to the investigation of the totally axial-symmetric accelerator system developed by one of the authors (K.I.) (6).

[III] The third is the application of the molten-salt target/blanket technology, which is similar to that of the Accelerator (Spallation) Molten-Salt Breeder (AMSB), which was developed by one of the authors

(K.F.)(1). A big molten-salt bath including Thorium fluoride will effectively work for the several purposes such as

- (a) non-destructive permanent target system,
- (b) collision- and reaction-heat removal system,
- (c) blanket material for fissile ^{233}U production by the neutron absorption of ^{232}Th in salt, and
- (d) chemical processing medium.

In **chap. II** we review the accelerator system. In **chap. III** the functions of the components composing the breeding system including the shaped-projectile are analyzed in order to decide the breeder parameters. The necessary data base for the impact fusion breeder will be discussed in **chap. IV**.

A REVIEW OF THE AXIALLY SYMMETRIC ABLATION MASS DRIVER

The electro-magnetic acceleration of projectile in axially symmetric geometry is thoroughly described in the literature (7). The mechanism for accelerating the projectile is based on a rapid Z-pinch discharge between the cylindrical electrodes shown in **Fig. 1**.

Consider a Z-pinch between a pair of long hollow electrodes whose axes of symmetry are on a common straight line. We can expect a plasma column between the electrodes like that in an ordinary Z-pinch in a plane electrode geometry. In the case of a Z-pinch in the hollow electrode geometry, however, a pair of plasma disks are formed at both ends of the plasma column which propagate along the cylinder axis, down to both ends of the cylindrical electrodes because of the force unbalance across the plasma disk, where the disk plasma is called the "plasma brim". If the projectile with an ablator is loaded in a cylindrical electrode in front of a plasma brim, as shown in **Fig. 1**, the projectile will be accelerated by the interaction of the current through the disk with the self-magnetic field.

The equation of motion of the projectile in the barrel is

$$\frac{d}{dt} \left(M \frac{dz}{dt} \right) = \frac{\mu_0 I^2}{2\pi} g, \quad [5]$$

where I is the total current in the plasma brim, M is the mass of the projectile including ablator and the plasma brim, and g is a constant of the order unity, depending on the current distribution in the plasma brim. The quantity μ_0 is the magnetic permeability of the vacuum.

The acceleration of projectiles to hypervelocity in a single pair of long cylindrical electrodes is questionable from various view points, such as the stability of the long plasma column, the energy dissipation by the resistive loss in the long cylindrical electrode, etc.. These problems are reduced if the accelerator is formed by many short cylindrical electrodes. A schematic diagram of the accelerator system with a

segmented electrode is shown in Fig.2. An important point for mentioning in this case is that it may not be necessary to use switches to close the circuit because the switching is automatically provided by the plasma brim following the projectile.

The two-stage accelerator was built to test this accelerator concept at Texas Tech University in 1986 (8), and it was confirmed that the automatic switching mechanism worked.

The advantages of this axial-symmetric accelerator compared with the standard rail gun are as follows: In the axial-symmetric case, (a) the plasma spilling over the nose of the projectile is inhibited because there is no gap for the plasma to penetrate past the projectile in the cylindrical electrode arrangement, (b) there is another acceleration force by the rocket effect from the flowing-out plasma through the field-null-line of the azimuthal magnetic field in the direction opposite to the projectile acceleration, and (c) the break-down voltage along the insulator surface between the electrodes does not depend on the size of the projectile, although the diameter of the projectile is the distance of the rails in the case of rail gun so that the small projectile is rather hard to accelerate by the rail gun because of the low flash-over voltage along the short insulator surface.

In the next section we consider the Impact Fusion Molten-Salt Breeder (IFMSB) under the assumptions that every stage of the Z-pinches, except the first one, is triggered automatically by Z-pinch following after the projectile, and that the velocity of the projectile is attained over a value required for the impact fusion to be triggered by the hypervelocity impact of the shaped-projectile.

IMPACT FUSION MOLTEN-SALT BREEDER (IFMSB) WITH A SHAPED-PROJECTILE

In order to trigger the thermonuclear fusion based on the hypervelocity impact of the shaped-projectile with the molten salt, the structure of the shaped-projectile should have a built-in imploding mechanism as schematically shown in Fig.3.

Once the velocity of the projectile becomes over 200 km/sec, the implosion of thermonuclear fuel-pellet in the cavity could be expected by black body radiation generated by the hypervelocity impact of a thin and high-atomic-weight material covering in front of the cavity with the liquid(molten salt) target.

The schematic drawing of the Impact Fusion Molten-Salt Breeder (IFMSB) is shown in Fig.4 with a shaped projectile made of the frozen salt and thorium metal. The hypervelocity shaped-projectile is injected into the center of vortex of molten salt target/blanket bath, and the generated neutrons by the thermonuclear fusion penetrate deep in the

target salt to produce ^{233}U from ^{232}Th (or ^{239}Pu from ^{238}U).

This molten-salt system is essentially similar to AMSB (1) except the addition of He bubbler, which is not clear about suitable length yet. He bubbles will be helpful for the relaxation of mechanical and thermal shock by injection and reaction (cf. Fig. 4). The size of target salt bath is about 4 m in diameter and 10 m in depth. Inside of the reactor vessel made by Hastelloy N (Ni-Mo-Cr alloy) is covered by thick graphite blocks for neutron reflection. The target salt is circulated in flow-rate of about $5 \text{ m}^3/\text{sec}$ by a free-surface type centrifugal pump. The inlet and outlet temperatures of salt in reactor vessel will be 560 and 680 °C. The generated heat is transferred to the coolant salt NaF-NaBF₄ through the intermediate heat exchanger from target salt circuit, and is used for electric power generation applying essentially same technology, which is developed for Molten-Salt Breeder Reactor by ORNL USA (9), except the improvement of the electric conversion efficiency to 46% or more by the application of recent ultra-supercritical steam turbine technology.

The composition of target/blanket salt is chosen from the several candidates of Th or U containing fluoride salts, as presented in the papers of AMSB or IHMSB (1) (2). At moment one of the most interesting composition will be

$\text{LiF}-\text{BeF}_2-\text{ThF}_4-^{233}\text{UF}_4$ (64-18-17.5-0.5 mol%), [6]
which has the melting point of about 540 °C.

The shaped-projectile is composed of frozen glassy salt such as
 $\text{LiF}-\text{BeF}_2-\text{ThF}_4$ (64-18-18 mol%) [7]
cluded by Th metal. The DT fuel-pellet accommodated in it will be a Th metal sphere of inner diameter 8 mm.

ESTIMATION OF IFMSB PERFORMANCE

We are not understanding yet the detailed phenomena in impact fusion in practice. However, the following scenario will be predicted: The fuel-pellet of about 10 g including 67 mg DT will be injected into target salt once in every 2.5 sec. The electric power required for projectile acceleration will become about 820 MWe, assuming the conversion efficiency of about 10 %.

Assuming the thermonuclear reaction efficiency of 10 %, the annual yield of neutron is about 33,800 mol/year. If the isotope composition of Li in target salt of composition [7] is chosen as about 40 % ^6Li , the production of tritium will become self-sufficient for continuous reaction operation, and the production of ^{233}U will be about 3.0 ton/year, by the estimation from the neutronic calculation results in the case of IHMSB (2). However, if the salt composition is changed to the composition shown in [6], the ^{233}U production will become about 4.4 ton/year increasing about 50 % [cf.(1)].

The heat generations in target salt are (1) thermalization of kinetic energy of projectile : about 82 MW corresponding to 10 % of electric power consumed for acceleration is and (2) thermonuclear reaction heat: 1820 MW produced from 10 % burning. The total 1902 Mwth will reproduce the electric power of 874 MWe, which will be able to compensate the consumed electric power.

DISCUSSIONS

Already the three ideas on the fissile breeder facilities have been proposed:

- [A] **AMSB** : Accelerator(Spallation) Molten-Salt Breeder (1)(2),
- [B] **IHMSB** : Inertial-confined Fusion Hybrid Molten-Salt Breeder (2),
- [C] **IFMSB** : Impact Fusion Molten-Salt Breeder.

A is the most reliable concept depending on the sound theoretical bases. However, we have to widely search the alternative methods. B is more ambitious but not clear on technological feasibility. Many injection holes are necessary, which will introduce several engineering difficulties. C has only one injection hole as same as A, and is based on further ambitious, simple but crude technologies. Their technical parameters were chosen in some conservative side as shown in previous chapter, expecting the higher performances of IFMSB from the following reasons.

(1) Many Molten-Salt Fission Power Stations will be operated by the direct supply of the target salt including ^{233}U from IFMSB. Careful design of Molten-Salt Converter Reactors(MSCR) could guarantee its self-sufficient operation, that means the no fissile consumption in stationary operation except the initial stage (10) (11). For example, even the small 155 MWe MSCR (named FUS-1, -II) has the conversion ratio of about 95 % or more. The possible shortage of electric power for acceleration will be solved by the electric power from these power stations.

(2) The recovery of electric power from the electric loss of about 737 MWe in the accelerator should be expected in the amount of 150~250 MWe.

(3) The separation technology of tritium from molten-fluoride system was experimentally established by ORNL. This is depending on the tritium trapping by the water content of secondary coolant salt after permeating through the tube wall of intermediate heat exchanger. However, the total tritium amount handling in reactor system is huge such as 2.3 kg/day. IFMSB is connected with the accelerator vacuum through the injection hole. To minimize the tritium inventory in IFMSB, the improvement of tritium burning efficiency is essential, and the production participation in outside of breeder will be preferable. IFMSB can choose the lower isotope concentration of ^6Li , and the partial tritium production will be performed in the other closed MSCRs consuming ^{233}U (or ^{239}Pu) (12), in which ^6Li composition is increased than the ordinary MSCR, and the tritium permeation to atmosphere will be perfectly protec-

ted by Mo or oxide plating of vessel and components.

(4) The Th content in the projectile is useful for compensation of Th consumed in target salt, and the excess Th tips will be collected by strainer. IFMSB has not any fine structures feasible for blockage.

(5) The engineering of injection port is one of the most ambiguous problems. However, the number of injection port is only one as same as AMSB and might be closed among the interruption of injection.

CONCLUSIONS

The concept of the Impact Fusion Molten-Salt Breeder (IFMSB) is outlined. The key technology of IFMSB is to develop highly efficient accelerators, one of which is being developed by one of the authors(K.I.). Once the required velocity is attained, the molten salt target/blanket concept developed by modification of that of the Accelerator Molten-Salt Breeder (AMSB) will provide an ideal technology for breeding ^{233}U or other fissile materials.

Many unknown phenomena exist in this concept, and the estimation of several important technical parameters is in low reliability still. However, if these points are solved in sound basis, IFMSB might be expected to become one of the most powerful fissile breeder, which target salt would be supplied as the fuel salt of Molten-Salt Fission Power Stations, integrally constituting one of the most idealistic energy systems for the next century.

References

- (1) K.Furukawa, K.Tsukada and Y.Nakahara : J.Nucl.Sci.Tech. 18 79 (1981); K.Furukawa et al.: Proc.First Int.Sympo. Molten Salt Chem. Tech. (April 20-22, 1983, Kyoto, Japan) P.399, 405, 409, 497.
- (2) K.Furukawa: Atomkernene.Kerntech. 44 42 (1984).
- (3) E. R. Harrison : Phys. Rev. Lett. 11 535(1963)
- (4) F. Winterberg : Nature 286 364(1980)
- (5) K. Ikuta : Jpn. J. Appl. Phys. 25 L587(1986)
- (6) K. Ikuta : Jpn. J. Appl. Phys. 24 862(1985)
- (7) K. Ikuta, M. Kristiansen and M. F. Rose : J. Appl. Phys. 59 3397 (1986)
- (8) K. Ikuta : unpublished
- (9) M. W. Rosenthal, P.N. Haubenreich, and R.B. Briggs : ORNL-4812 (1972).
- (10) K. Furukawa, K.Minami, T.Oosawa, M.Ohta, N.Nakamura, K.Mitachi, and Y.Katoh: 4th Int.Conf. Emerging Nucl.Energy sys. (June/July 1986, Madrid). P.235(1987)World Sci.
- (11) K. Furukawa, K.Mitachi, K.Minami and Y.Katoh : another report presenting in this Symposium.
- (12) K. Furukawa : unpublished.

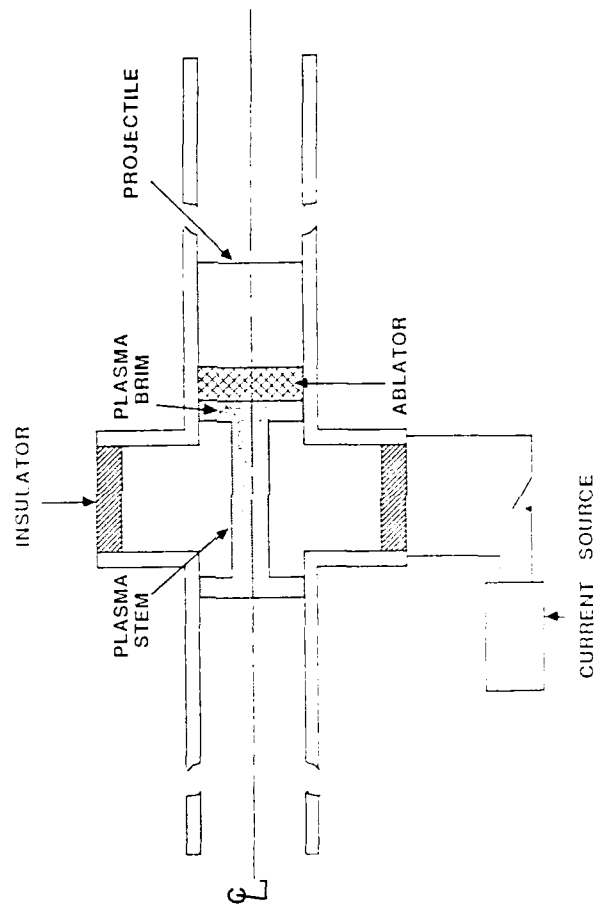


Fig. 1. Mechanism of the electromagnetic acceleration of a projectile in a cylindrical electrode. The interaction between the plasma brim and the self-magnetic field gives the forward thrust to the projectile.

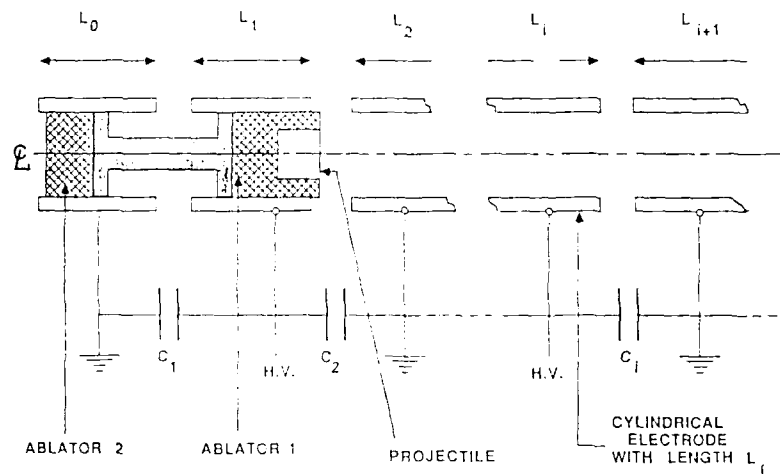


Fig.2. Schematic drawing of the ablation mass driver system. In order to give the initial velocity to the projectile without the use of an additional injection system, the second ablator, i.e. ablator 2, is loaded in the first electrode with length L_0 .

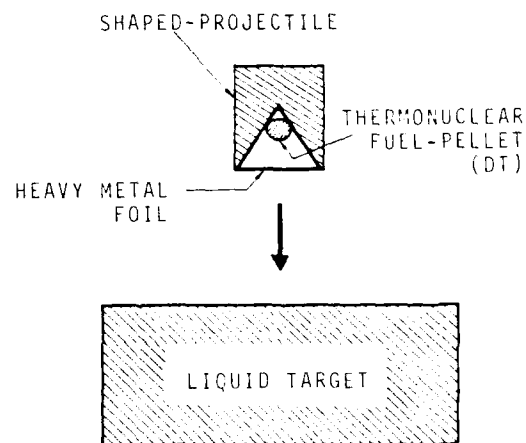


Fig.3. A shaped projectile with built-in thermonuclear pellet and the liquid target. Heavy metal foil is a thin and high-atomic weight material covering the cavity.

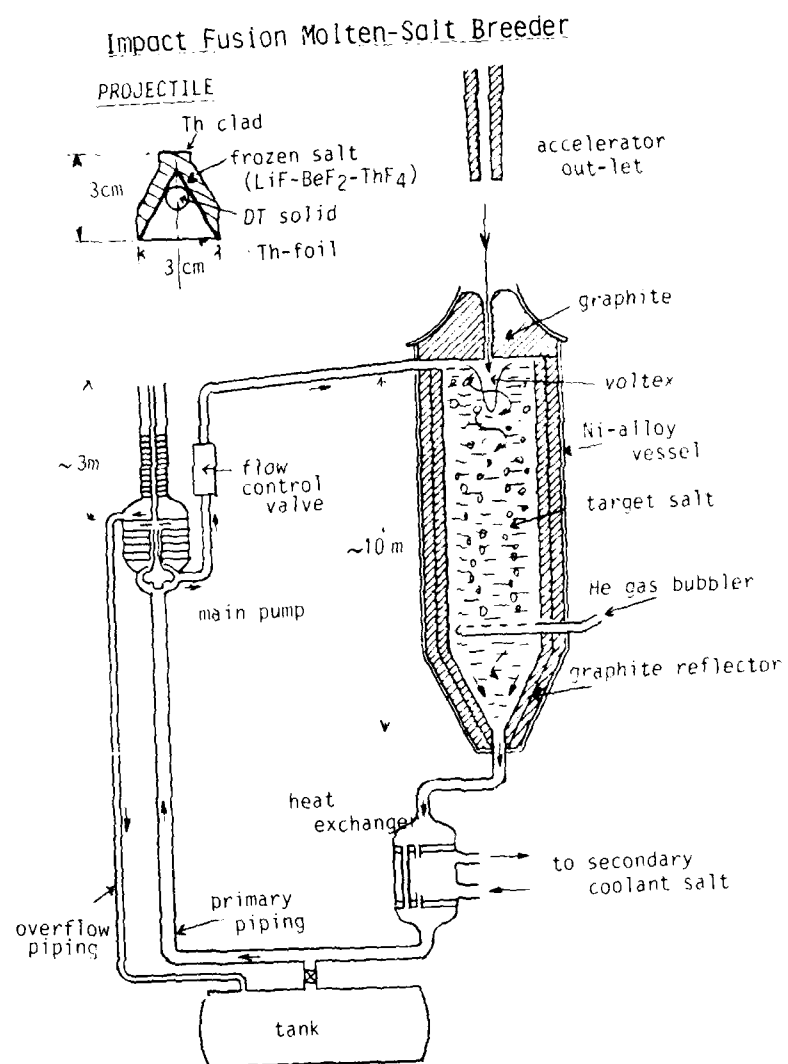


Fig.4. Impact Fusion Molten-Salt Breeder system with a projectile made of frozen salt.

SUBMERGED ARC FLUX WELDING WITH $\text{CaF}_2\text{-CaO-SiO}_2$ FLUXES:
POSSIBLE ELECTROCHEMICAL EFFECTS ON WELD METAL

S. Shah,* M. Blander, and J. E. Indacochea*
Argonne National Laboratory
Chemical Technology Division/
Materials Science and Technology Program
Argonne, Illinois 60439

*University of Illinois/Chicago
CEMM Department
Chicago, Illinois 60680

ABSTRACT

Compositional changes of weld metal from welds made by submerged arc flux welding of steel using $\text{CaF}_2\text{-CaO-SiO}_2$ fluxes are consistent with an electrochemical mechanism in which the filler wire is anodically oxidized to form oxides and fluorides, and metals are cathodically deposited at the weld pool-flux interface. This speculative mechanism, if proven by further detailed studies, could make it possible to predict fluxes which will improve the quality of welds.

BACKGROUND

The control of the chemistry of weld metal is important for producing high quality welds. An understanding of the mechanisms which alter the compositions of weld metal would be a primary aid in such control. Much prior work has focused primarily on kinetically limited thermodynamically driven reaction mechanisms. Such a pyrometallurgical approach has proven to be useful in analyzing some data on weld metal chemistry. However, such analyses have not yet led to methods for predicting the chemistry of weld metal. In this paper, we consider the possible importance of electrochemical effects on the chemistry of weld metal produced in submerged arc welding (SAW) with $\text{CaF}_2\text{-CaO-SiO}_2$ fluxes.

Thermodynamic models have been proposed to predict the final composition of submerged arc welds (1-3). In view of the very high temperatures involved and small molten volumes, some investigators (1) assume that equilibrium is attained. Davis and Bailey (1) propose that the transfer of elements between the slag and

the weld metal depends on the oxide activities in the slag, which are directly connected to the basicity index (B.I.) of the slags. Limited measurements have indicated that the higher the basicity indexes, the lower the oxygen content of the weld metal. However, it is probable that equilibrium is not attained and that kinetic factors are important. For example, Thier and Dring (2) proposed a diffusional model to predict the final content of elements in the weld metal. Thier and Dring concluded that the slag composition where an element was not transferred to the metal, the neutral point, is affected only by the current, but not by the voltage changes and that the neutral point is characteristic for a specific type of flux.

Ekstron and Olson (4) reported that the change in Si in weld metal is influenced by the basicity of the slag and that this influence is higher when the basicity index is less than two. Dallam *et al.* (5) found that while the Si level in the weld metal was correlated with the basicity index, the Mn content of the weld depends on the amount of MnO in the slag. Indacochea *et al.* (6) showed qualitatively the same correlation between flux and weld metal composition.

Despite qualitative agreement among researchers regarding the flux type and direction of elemental transfer, there is no precise determination of a "neutral point," even though very similar types of fluxes were used in several of these studies. These discrepancies may be attributed to the different welding parameters used, as well as to wire and flux compositions. Consideration of such parameters, primarily current and voltage, could lead to a better understanding of the elemental transfer.

It is clear that essentially all prior studies have been relatively narrowly defined. A more comprehensive approach is needed in which the diverse kinetic and thermodynamic factors involved in SAW (6,7) are examined and which also explores the possibility of mechanistic factors which have not been considered. Such an approach is made difficult by the complexity of the processes in SAW. The D.C. voltages and currents are very high (e.g., 30 V, 400 A) and lead to a system containing the four principal phases, a weld wire, a molten flux, a plasma arc and a weld pool with five interfaces among them. Most of the current is transported by electrons in the plasma from the generally cathodic weld pool to the generally anodic weld wire (or filler wire). The electrons heat the continuously fed wire to melt it and form droplets which fall through the molten flux and the plasma. In addition, not only are the temperatures high, but there are also large temperature gradients, as well as, large temporal changes in temperature as the weld wire position is moved along the weld. An attack on such a complicated problem requires some simplification.

One way to simplify the approach to such a complex system is to isolate the different parts of the problems. For example, in this paper we chose to examine electrochemical effects, which have not been considered before. All welding fluxes when molten are, at least in part, ionic and the number of coulombs passed per

mole of metal is very large. If even a small fraction of the total current (≤ 0.01) is involved in a Faradaic process, electrochemical effects at metal-flux interfaces could be a major factor controlling the chemistry of weld metal (8). In addition, because the very hot plasma is essentially electrically neutral and in contact with the relatively volatile fluxes, there have to be at least as many positive ions as there are electrons. In addition, there could be stable negative ions formed from flux evaporates. Thus, there could also be electrochemical reactions at the plasma-metal interfaces (8).

In this paper, we examine the possibility that the changes in chemistries of weld metal with changes in the composition of CaF_2 containing fluxes might be related to an electrochemical mechanism.

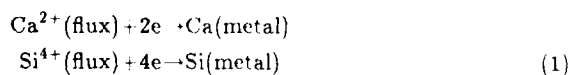
EXPERIMENTAL WORK

Experimental reagent-grade fused fluxes at differing compositions of the CaF_2 - CaO - SiO_2 system were used. The different fluxes used are summarized in Table 1. The base metal and filler metal compositions and the welding process parameters are summarized in Tables 2 and 3, respectively. All the welds were automatically programmed in a microprocessor-controlled welding apparatus. The welds were single-pass bead-on-plate. The chemistries of the welds and base plate were measured by x-ray spectrometry and those of the filler weld wires were measured by an atomic absorption method. The contents of silicon, manganese, and oxygen in weld metal are given in Figures 1-3 for measurements on these different mixtures.

ELECTROCHEMICAL MECHANISMS

In SAW, the filler wire is generally anodic and the weld pool is cathodic. Current is carried between these metals by the plasma-arc and by the molten flux with the plasma-arc carrying most of the current.

At the interface between the flux and the cathodic weld pool, the metals in the flux tend to deposit by reactions such as



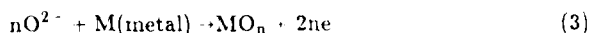
The products, which are formed metastably at the interface, tend to simultaneously diffuse into the metal and back react with the slag components by reactions such as



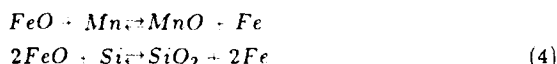
Thus, the balance between the different elements, which might be deposited is controlled by the relative kinetics of the electrodeposition process, of the back

reactions (or volatilities), and of the diffusive processes which carry the interfacial materials away from the interface. Because of the high volatility of Ca and its relative insolubility in steel, Ca is likely to vaporize through the flux and to partly react according to Eq. (2).

The most important anodic reaction is



where M is a metal at the weld wire-flux interface and $2n$ is the valence of the metal in the oxide. Fluoride is probably also involved in an anodic reaction, but forms relatively volatile products, which need not be considered here. Because of large overpotentials, all of the metals at the interface, principally Fe, will oxidize. The less noble metals in the alloy, such as Mn and Si, will diffuse towards the interface and react with the FeO by reactions such as



In addition, some oxides will diffuse into the metal and some will dissolve in the flux. The overall effect is to greatly increase the oxygen content of the weld wire tip and to decrease the less noble metals, such as Mn and Si somewhat. When heated sufficiently, the tip forms a droplet, which will have a high oxide content near the surface and which will tend to lose some of its less noble metals to the flux. Measurements of such droplets by Lau *et al.* (9,10) in CaO-Al₂O₃ based fluxes have demonstrated their very high oxygen contents.

When these oxide rich droplets fall into the weld pool, the oxides can react with the more active metals, including those which have been electrodeposited. In the measurements of Lau *et al.* (9,10), a large fraction of the oxide associated with the droplets is removed before being incorporated in the weld, probably by back reactions with the most active metals in the weld, such as Ca or Si (or Al in their measurements).

An understanding of the electrochemistry of the plasma is limited by the sparsity of information on plasma species. Most of the current is carried by electrons. However, because of the constraint of electroneutrality of the dense plasma, the number of positive ions is at least as large as the number of electrons and these ions can carry a small, but significant, fraction of the current. Metals such as Fe, Ca, and Mn are relatively volatile and are probably ionized to form positive ions. Oxygen can be present as O⁺ and possibly as O⁻ and the presence of some oxyions derived from SiO, SiO₂, FeO, or MnO vapor molecules is likely, but there is no information on the numbers or distributions of such positively and negatively charged ions. All of these ions can participate in Faradaic processes, which will, to a first approximation, parallel the Faradaic processes involving the slag.

INTERPRETATION OF THE EXPERIMENTS

As can be seen in Fig. 1, the silicon contents of the weld metals are generally higher than the nominal values expected from simple mixing of roughly equal amounts of the base metal and filler wire and increases with an increase in the SiO_2 content of the CaF_2 - CaO - SiO_2 mixtures, but decreases with an increase in the current density. Since the silica in the fluxes tends to form anionic species (chain silicates or fluosilicates), it is probably that the kinetics of direct electrochemical deposition of silicon is not as favorable as that for the deposition of the volatile Ca. Consequently, a small amount of Si would be directly formed electrochemically, but more is likely to form by the evaporation of Ca, which would then reduce SiO_2 in the flux to Si. Back reactions of the Si with the oxides on weld wire droplets would reduce the total amount of metallic Si produced by this mechanism. The higher the ratio of CaO to CaF_2 in the melt, the greater the amount of oxide which is produced at the weld wire tip and the greater the amount of Si which would be reoxidized and redissolve in the flux. Of course, one also expects that the amount of metallic Si produced would be larger the greater the SiO_2 content of the flux. This is consistent with the results in Fig. 1. The increase of Si content in weld metal with an increase of current could be understood by any one of a number of possible mechanisms, which are too numerous to discuss here. Further work on the effect of current is needed to completely define the mechanism.

As can be seen from Fig. 2, the manganese content of the weld metal is fairly close to that expected for mixtures of weld wire and base plate metal for the lowest contents of SiO_2 in the flux. With an increase in the concentration of SiO_2 , one would expect an increased amount of oxide produced at the anode and a larger loss of Mn from the filler wire, which contains the majority of the Mn expected in the weld. This can thus lead to the observed decrease in Mn with increased SiO_2 in the flux.

The compositional changes of most concern are those related to oxygen. The physical properties and quality of welds is strongly influenced by the amount of oxygen. Fig. 3 exhibits the changes in oxygen content for the different flux compositions. It is obvious that the concentration of oxygen in the weld decreased with a decrease in the amount of silica in the flux. For the lowest concentrations of silica, the concentration of oxygen differs little from that of the original metals (~ 200 ppm). This difference is consistent with the electrochemical mechanism we propose.

DISCUSSION

The measurements we present are consistent with the speculation that an electrochemical mechanism is important in altering the chemistry of weld metal in SAW. In prior work (8), examination of the effects of this mechanism on weld metal compositions measured by Indacocha *et al.* (6) have indicated that the

contents of Mn, Si, O, and other elements in welds produced from $\text{SiO}_2\text{-FeO-MnO}$ fluxes were also consistent with an electrochemical mechanism. However, a thermodynamically-driven kinetically-constrained mechanism may also be possible if the slag-metal interface is at very high temperatures ($> 2200\text{ K}$). Heat flow considerations make this high a temperature unlikely. A test of the correctness of our speculations will ultimately require much more detailed measurements. One set of such measurements has been made by Lau *et al.* (9,10) who have shown that metal droplets from the filler wire are very high in oxygen, which is largely present as FeO , MnO , and SiO_2 containing inclusions in the metal (10); these could not have been formed by a thermodynamic mechanism. We are planning measurements of analogous microscopic compositional details to test the validity of our speculations.

The long term goal of our work is to integrate our finding on this electrochemical mechanism with a comprehensive analysis of the important thermodynamic (6) and kinetic (7) factors. Although consideration of these factors and of all the welding parameters (currents, voltages, wire-feed rate, welding speed) simultaneously is very difficult and too complex for quantitative predictions, our results to date have led to useful qualitative predictions on flux compositions which should improve the properties of welds. If an electrochemical mechanism can be shown to be important, the deduction of methods for predicting weld chemistry would be greatly simplified.

ACKNOWLEDGMENTS

This work was performed under the research support of the Office of Naval Research at Argonne National Laboratories under Navy Order No. N00014-87-F-0064.

REFERENCES

1. M. L. E. Davis and N. Bailey, "How Submerged-Arc Flux Composition Influences Element Transfer," Weld Pool Chemistry and Metallurgy Conference, pp. 289-302, The Welding Institute, Cambridge (1980).
2. H. Thier and Dring, "Metallurgical Reactions in SAW," Weld Pool Chemistry and Metallurgy Conference, pp. 271-278, The Welding Institute, Cambridge (1980).
3. C. S. Chai and T. W. Eagar, "Slag-Metal Equilibrium During SAW," Metallurgical Transactions B, V. **16-B**, pp. 539-547 (1985).
4. V. Ekström and K. Olson, "The Influence of Ferrite and Oxygen Contents on Weld Metal Mechanical Properties of Submerged Arc Welded Stainless

- Steel," Weld Pool Chemistry and Metallurgy Conference, pp. 323-332, The Welding Institute, Cambridge (1980).
5. C. B. Dallam, S. Liu, and D. L. Olson, "Flux Composition Dependence of Microstructure and Toughness of Submerged Arc HSLA Weldments," *Welding Journal*, V. **64**, pp. 140s-151s (1985).
 6. J. E. Indacochea, M. Blander, N. Christensen, and D. L. Olson, "Chemical Reactions During SAW With FeO-MnO-SiO₂ Fluxes," *Metall. Trans.*, V. **16B**, pp. 237-245 (1985).
 7. M. Blander and D. L. Olson, "Thermodynamic and Kinetic Factors in the Pyrochemistry of Submerged Arc Flux Welding of Iron Based Alloys," in *Second International Symposium on Metallurgical Slags and Fluxes*, eds. A. Fine and D. R. Gaskell, TMS-AIME, Warrendale, PA, pp. 271-277 (1984).
 8. M. Blander and D. L. Olson, "Electrochemical Effects on Weld Pool Chemistry in Submerged Arc and D.C. Electroslag Welding," *Proceedings International Conference on Trends in Welding Research (Advances in Welding Science and Technology)*, pp. 363-366, Gatlinburg, TN, May 18-22, 1986.
 9. T. Lau, G. C. Weatherly, and A. McLean, "The Sources of Oxygen and Nitrogen Contamination in Submerged Arc Welding Using CaO-Al₂O₃ Based Fluxes," *Welding Journal* **64**(12), pp. 343s-347s (1985).
 10. T. Lau, G. C. Weatherly, and A. McLean, "Gas Metal Slag Reactions in Submerged Arc Welding Using CaO-Al₂O₃ Based Fluxes," *Welding Journal* **65**(2), pp. 31s-38s (1986).

Table 1. Nominal Flux Compositions w/o

SiO ₂	CaF ₂	CaO
40	10	50
40	20	40
40	30	30
40	40	20
30	30	40
30	40	30
30	50	20
30	60	10
20	40	40
20	50	30
20	60	20
20	70	10

Table 2. Base Metal and Filler Metal Compositions (w/o)

Material	C	Mn	P	S	Si	Ti	Al	0 ppm
Base Metal	0.04	0.37	0.012	0.022	0.03	0.003	0.001	220
Filler Metal	0.09	1.18	0.007	0.013	0.58	0.002	<0.008	195

Table 3. Welding Process Parameters

Voltage	33 volts	31 volts
Current	600 amps	330 amps
Travel Speed	12.2 in/min	12.2 in/min
Wire Speed	75 in/min	40 in/min
Heat Input	97.4 kJ/in	50.3 kJ/in
	3.83 kJ/mm	1.98 kJ/mm

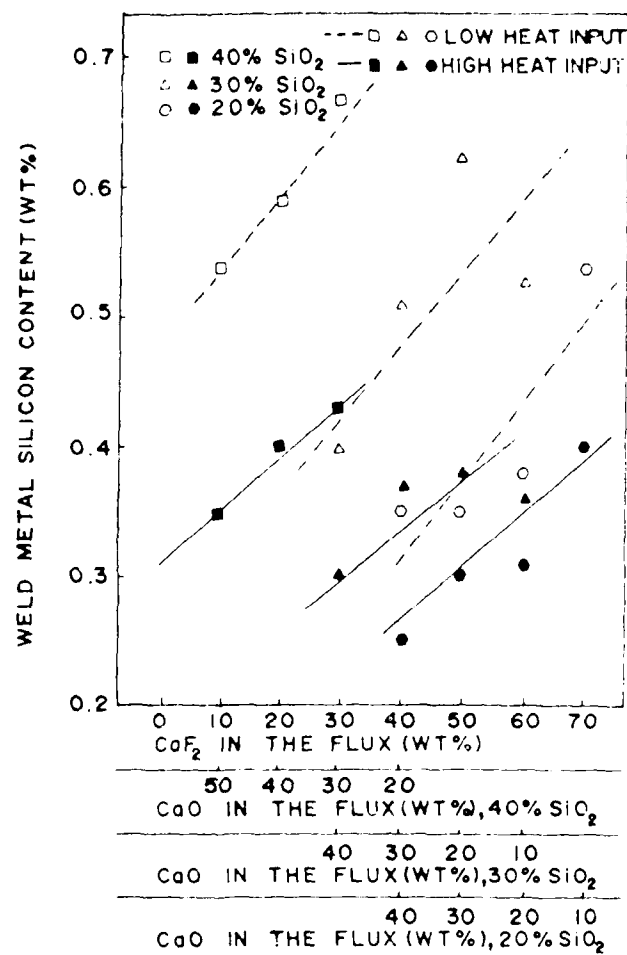


Fig. 1. Silicon Content in the Welds Produced with the SiO₂-CaO-CaF₂ Submerged Arc Welding Fluxes for Two Heat Inputs.

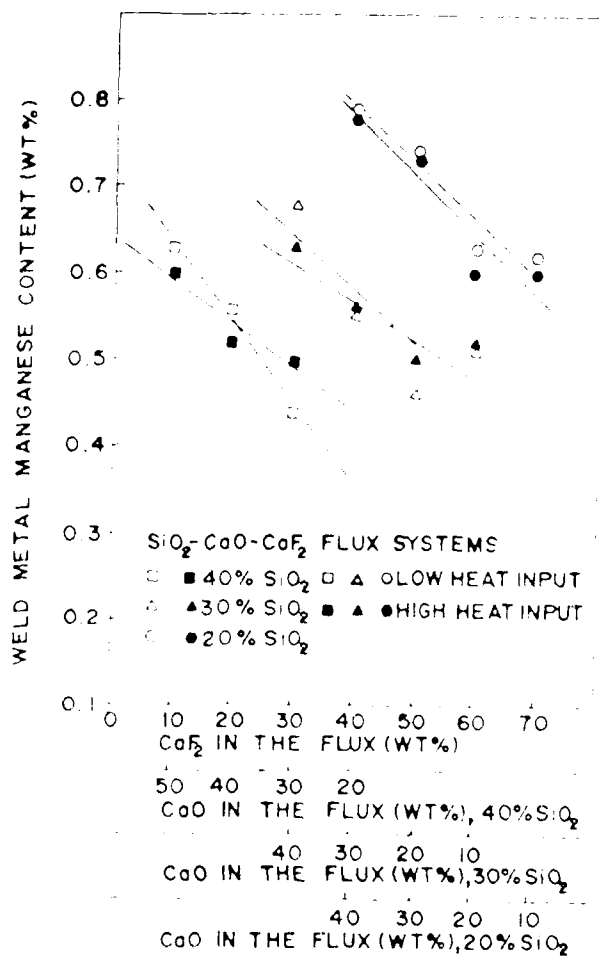


Fig. 2. Manganese Content in the Welds Produced with the SiO₂-CaO-CaF₂ System and Low-Heat Fluxes for Two Heat Inputs.

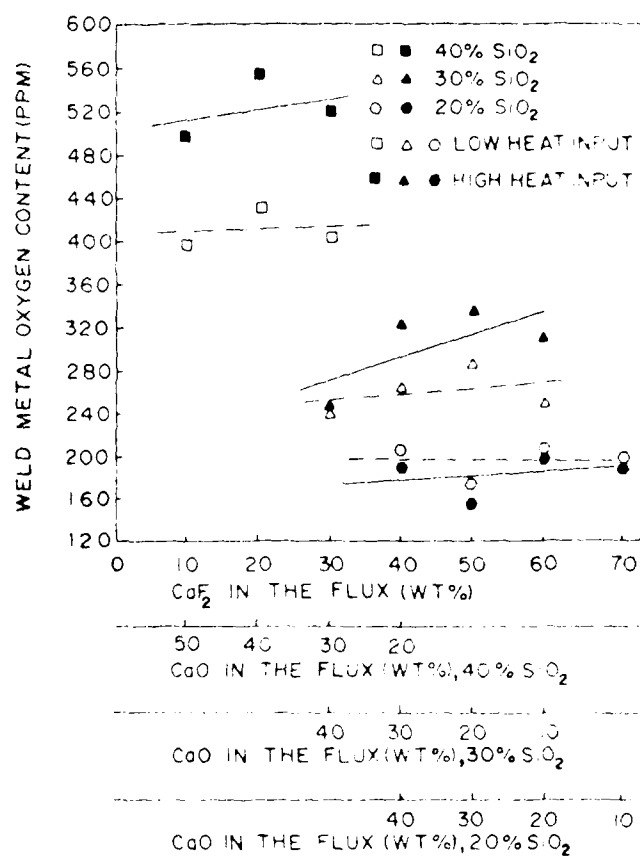


Fig. 3. Oxygen Content in the Welds Produced with the SiO₂-CaO-CaF₂ Submerged Arc Welding Fluxes for Two Heat Inputs.

ELECTROCHEMICAL REACTIONS AT THE ELECTRODE IN SUBMERGED ARC WELDING

J. H. Kim, R. H. Frost, D. L. Olson, and M. Blander*

Center for Welding Research
Department of Metallurgical Engineering
Colorado School of Mines
Golden, Colorado 80401

*Argonne National Laboratory
Chemical Technology Division
Materials Science and Technology Program
Argonne, Illinois 60439-4837

ABSTRACT

The submerged arc welding process uses a D.C. arc under a protective slag cover to melt a consumable wire electrode. The purpose of this work is to investigate the relative influence of electrochemical and thermochemical reactions at the surface of the electrode of the composition on the liquid metal droplet. Chemical analyses were carried out on the melted wire electrode tips and on the detached droplets for both reverse polarity (wire is anodic) and straight polarity (wire is cathodic) polarities. The results suggest that both thermochemical and electrochemical reactions are important in altering the composition of the detached droplet.

INTRODUCTION

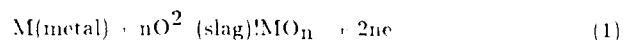
The submerged arc welding process consists of a consumable electrode, an electrically conducting slag and a work piece. Figure 1 shows a schematic drawing of the submerged arc welding process, which is complex and characterized by large currents, large gradients of temperature, and four complex phases. The flux is fed to the plate surface ahead of the weld, and the arc and weld pool are protected from the atmosphere by a molten flux layer. The welding current is carried largely by the submerged arc and to some extent by conduction in the molten flux layer. The overall composition of the weld is controlled by the composition of the metal droplets which enter the weld pool, by the amount of dilution of the weld pool by the parent plate, and by electrochemical and thermochemical reactions at the weld pool/slag and electrode/slag interfaces before solidification takes place. Three chemical reaction sites and two generic reaction mechanisms are available

for modification of the weld metal composition by reaction with the slag. Both thermochemical and electrochemical reactions are expected to occur at the electrode tip. The electrochemical reactions would result from ionic conduction of a portion of the welding current through the molten slag layer. Only thermochemical reactions are expected to occur at the surface of the detached droplets since the droplets are no longer carrying current. The molten metal in the weld pool is influenced by both electrochemical and thermochemical reactions with the slag before solidification occurs.

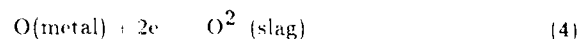
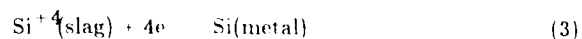
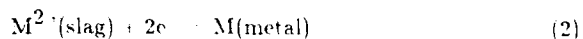
The most important chemical considerations for submerged arc welding include the control of oxygen, oxidation losses of alloy elements, and the pickup of undesirable elements from the slag. The objective of this work was to understand the nature and extent of electrochemical and thermochemical reactions at the electrode tip and in the detached droplets.

A number of investigations have been made concerning the nature of chemical reactions at the electrode tip and in the detached droplets. These include work by Pokhodnya and Kostenko (1), Potapov and Lyubauskii (2), Norin and Malyshev (3), Grong and Christensen (4), Mitra (5), and Lau et al. (6). However, few investigators have considered the electrochemical reactions that occur when direct current is used in welding. Frost et al. (7) considered the different chemical effects at the anode and cathode in electrosag welding. Blander and Olson (8) postulated an electrochemical mechanism for the alteration of weld metal chemistry in submerged arc welding. The purpose of this research is to investigate the importance of electrochemical reactions in controlling the chemistry of weld metal in submerged arc welding.

The possible anodic reactions include the oxidation of iron and alloy elements, and the discharge and pickup of oxygen anions from the flux



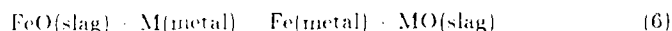
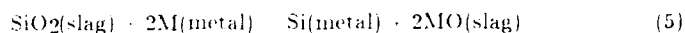
where M is iron or an alloy element at the electrode tip slag interface. The possible cathodic reactions include the reduction of metal ions from the flux, and, to some extent, the refining of nonmetallic elements such as oxygen and sulfur



where M and Si represent electrodeposited metals at the interface.

The thermochemical reactions at the electrode tip are rapid because of the high temperatures in the vicinity of 1800 to 2000[°]C. These include deoxidation

reactions, such as those encountered in steel making, and reactions which lead to a closer approach to equilibrium between the flux and metal phase. Examples of such reactions would be silicon pickup from a high silica flux or the oxidation loss of transition elements through a deoxidation reaction



where M can be Al or Ca in reactions (5) and (6) and Mn in reaction (6) for the flux system used in this research. Once the molten droplet separates from the electrode, the electrochemical reactions stop, and compositional changes occur only by thermochemical reactions. The objectives of this research are to evaluate the nature and relative extent of the electrochemical and thermochemical reactions which occur at the electrode and in the molten droplets in the submerged arc welding process.

EXPERIMENTAL PROCEDURE

Straight (cathodic electrode wire) and reverse (anodic electrode wire) polarity submerged arc "welds" were made with a commercial low-carbon steel welding wire (2.38 mm) on a pure copper plate. The compositions of the welding wire and the commercial flux are given in Table I.

The welding process was operated in both straight and reverse polarity at a constant welding current of 585 amperes and a constant potential of 28.5 volts. The constant current was obtained by adjustment of the wire electrode velocity which was 170 inches/minute for the anodic wire and 235 inches/minute for the cathodic wire. The electrode tips were collected by stopping the welding process and pulling the electrode away from the weld pool. The separated droplets were collected by magnetic separation after running the weld at a high velocity over a water cooled copper plate so that the droplets remained suspended in the molten flux.

Chemical analyses of the alloy elements in the electrode tips were carried out by rolling the tips to produce flat specimens and analyzing with an emission spectrograph. The compositions used for comparison are averages of the compositions for several electrode tips. The separated droplets were analyzed using the wave length dispersive analyzer on a JEOL scanning electron microscope. The reported analyses are an average of the compositions for several droplets. Analyses for oxygen were carried out using a LECO interstitial analyzer.

RESULTS AND DISCUSSION

The purpose of this investigation was to consider the relative influence of thermochemical and electrochemical reactions on the composition of the liquid metal droplet. Electrochemical reactions are expected because of the high current densities, and thermochemical reactions are expected because of the high temperatures and the generally large and temperature dependent differences in chemical potentials of the various reactants and products in the flux and metal phases. An examination of the metal and flux compositions in Table I shows that the electrode has very low silicon and oxygen concentrations, and a relatively high manganese concentration, while the flux has a high silica activity and a relatively very low manganese oxide-iron oxide ratio, which is far from equilibrium with the wire. Thus, the manganese content of the metal would be expected to drop through thermochemical oxidation losses to the flux, and the silicon and oxygen content in the metal would be expected to increase through reaction with the flux.

Figure 2 shows a plot of the average oxygen contents of the wire, the electrode tip, and the separated droplets for both straight (cathodic wire electrode) and reverse (anodic wire electrode) polarity welds. The data show a very low oxygen content in the electrode (20 ppm) and very significant oxygen pickup in the electrode tip from both thermochemical and electrochemical reactions. The influence of electrochemical reactions is shown by the fact that the oxygen content of the anode tip in the reverse polarity power mode (591 ppm) is over twice that of the cathode in the straight polarity power mode (277 ppm). The real difference is somewhat less since more wire is fed and melted at the cathode for a fixed current, thus diluting the total electrochemical and thermochemical effect at the cathode. The influence of thermochemical oxygen pickup is shown by the fact that significant oxygen pickup is observed in both electrode positive and electrode negative configurations. Since the electrode tip is, on the average, halfway to becoming a droplet, the droplets should start with, very roughly, twice the oxygen content of the tip.

If the electrochemical and thermochemical reactions were considered as separate steps, the average electrode tip oxygen concentration for the two polarities could be considered to crudely represent the thermochemical contribution, and the separation of the two concentrations from this mean would represent the electrochemical effects. However, the different wire feed rates cloud this interpretation. The average oxygen concentration for the two electrode tips is 434. This can only crudely represent the substantial thermochemical pickup above the 20 ppm oxygen present in the initial electrode.

Figure 3 shows the silicon contents in the initial electrode, the electrode tip, and the separated droplet. The analyses suggest significant contributions from both thermochemical and electrochemical reactions. The wire electrode has a

very low oxygen content of around 0.002 wt %, while the flux has a SiO₂ content of about 11.22 wt %. This causes the thermochemical pickup of around 0.19 wt % silicon from the flux. The electrochemical influence is significant, as is indicated by the fact that the cathodic tip silicon content is about 0.06 wt % higher than that of the anodic tip and by the fact that the cathode feed rate is higher than the anode feed rate which means that the total amount of Si in the cathodic tips and droplets is relatively much higher than is indicated in Figure 3. The change in the silicon concentration from the electrode tip to the detached droplet is mostly thermochemical. With silicon, however, there is a decrease rather than the expected increase in silicon content of the droplet compared to the electrode tip indicating that a large fraction of the silicon in the droplet has back reacted with more noble metal oxides in the flux (e.g., Fe₂O₃). One of the possible driving forces for this reaction is related to the probability that the droplet is at a lower temperature and has a higher oxygen content than the tip.

Figure 4 shows similar behavior for the manganese contents in the electrode, the electrode tip, and the detached droplet. Both thermochemical and electrochemical reactions are indicated; however, the high manganese content in the electrode and low MnO iron oxide ratio in the flux lead to a thermochemical manganese loss at the electrode tip. The average manganese content is further decreased by thermochemical reactions with more noble metal oxides in the flux in going from the electrode tip to the separated droplet, which falls through and reacts with the flux.

Figure 5 compares the droplet compositions for the various alloy elements to the initial electrode contents. Significant electrochemical reactions are present for most of the alloy elements. Silicon, aluminum, and manganese show higher concentrations in the cathodic droplets than in the anodic droplets. This is largely caused by oxidation losses to the flux at the anode, and electrochemical reduction from the flux at the cathode. The differences for nickel, titanium, and chromium are of the order of the analytical uncertainties and are thus inconclusive. Molybdenum shows the opposite trend. That is, the concentration in the anode is higher than that of the cathode. This behavior may be caused by the fact that molybdenum is more noble than iron, and the apparent concentration changes are the result of iron oxidation losses at the anode and reduction from the flux at the cathode. Figure 5 suggests significant thermochemical contributions only in the cases of silicon, aluminum, and manganese.

CONCLUSIONS

1. Composition changes at the electrode tip and in the separated droplets in submerged arc welding appear to be the result of both thermochemical and electrochemical reactions.

2. The thermochemical reactions are caused by expected reactions between the flux and metal. The electrochemical reactions at the anode include oxidation losses of alloy elements to the flux and the discharge and pickup of oxygen anions from the flux. The electrochemical reactions at the cathode include the reduction of metal ions from the flux and the refining of oxygen.
3. Composition changes in the droplets after separation from the submerged arc electrode are primarily thermochemical in nature.

Further experiments with synthetic fluxes, which are chosen to minimize thermochemical reactions, are planned and should help to better define the relative importance of electrochemical reactions.

ACKNOWLEDGMENTS

Three authors (J.H.K., R.H.F., and D.L.O.) wish to acknowledge the support of the U.S. Army Research Office at the Colorado School of Mines and M.B. acknowledges the support of the Office of Naval Research at Argonne National Laboratory under Navy Order No. N00014-85-F-0097.

REFERENCES

1. Pokhodnya, I. K., and Kostenko, B. A., "Fusion of Electrode Metal and Its Interaction with the Slag During Submerged Arc Welding," *Automatic Welding*, No. 10, pp. 16-22 (1965).
2. Potapov, N. N. and Lyubauskii, K. V., "Interaction between the Metal and Slag in the Reaction Zone During Submerged Arc Welding," *Automatic Welding*, No. 7, pp. 9-11 (1971).
3. Norin, P. A. and Malyshev, N. I., "Losses of Manganese from Electrode Droplets in Arc Welding in Air," *Automatic Welding* No. 2, pp. 21-12 (1982).
4. Grong, O. and Christensen, N., "Factors Controlling Weld Metal Chemistry," final Report Contract No. DAJA 376-81-C-0309, European Research Office of the U.S. Army.
5. Mita, U., "Kinetics of Slag Metal Reactions During Submerged Arc Welding of Steel," Sc. D. Thesis, Massachusetts Institute of Technology (1984).
6. Lau, T., Weatherly, G. C., and McLean, A., "The Sources of Oxygen and Nitrogen Contamination in Submerged Arc Welding Using CaO-Al₂O₃ Based Fluxes," *Welding Journal Research Supplement*, pp. 343-347s (Dec. 1985).

7. Frost, R. H., Olson, D. L., and Edwards, G. R., "Influence of Electrochemical Reactions on the Chemistry of the Electroslag Welding Process", Proc. Modeling Cast. Weld. Process., Hemiker, N. H., Eng. Found., New York (1983) p147.
8. Blander, M. and Olson, D. L., "Electrochemical Effects on Weld Pool Chemistry in Submerged Arc and D.C. Electroslag Welding," Proceedings International Conference on Trends in Welding Research (Advances in Welding Science and Technology), pp. 363-366, Gatlinburg, TN, May 18-22, 1986.

Table I. Compositions of Weld Wire and Welding Flux (wt %)

Weld Wire		Welding Flux	
C	0.06	SiO ₂	11.22
Mn	1.38	Al ₂ O ₃	18.14
Si	0.05	MgO	33.23
Mo	0.33	CaF ₂	25.26
Cr	0.07	CaO	6.92
Ni	0.11	MnO	1.15
Al	0.02	TiO ₂	0.90
Cu	0.77	Na ₂ O	0.82
Ti	0.03	Fe ₂ O ₃	1.99
P	0.012	C	0.37
S	0.015		
O	0.002		
N	0.004		

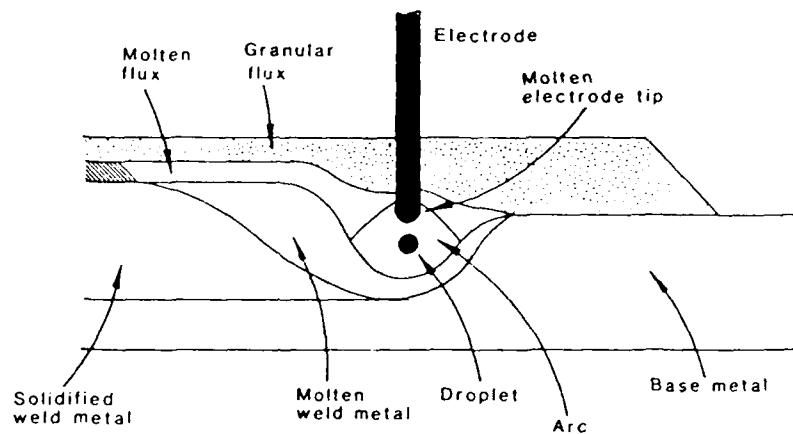


Fig. 1. Schematic of the submerged arc flux welding process.

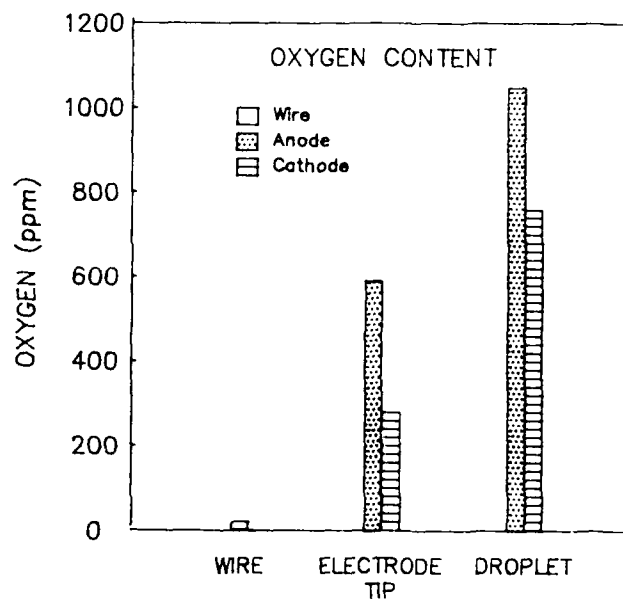


Fig. 2. Average oxygen contents of the initial weld wires, the electrode tips, and the separated droplets for both straight (cathodic wire) and reverse (anodic wire) polarities.

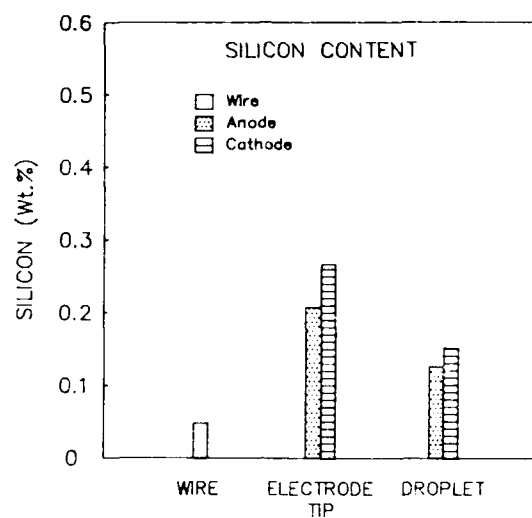


Fig. 3. Average silicon contents in the initial weld wires, electrode tips, and the separated droplets for both straight and reverse polarities.

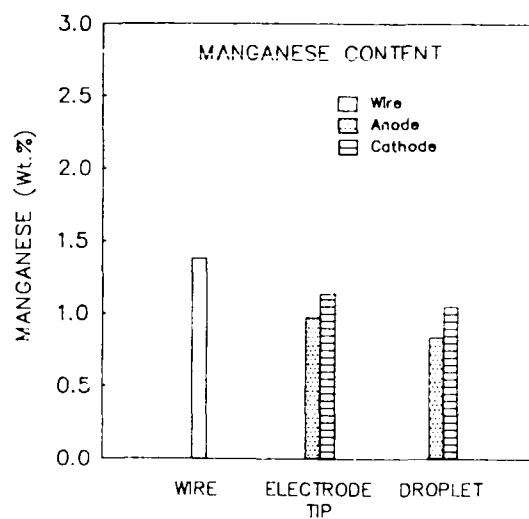


Fig. 4. Average manganese contents in the initial weld wires, electrode tips, and the separated droplets for both straight and reverse polarities.

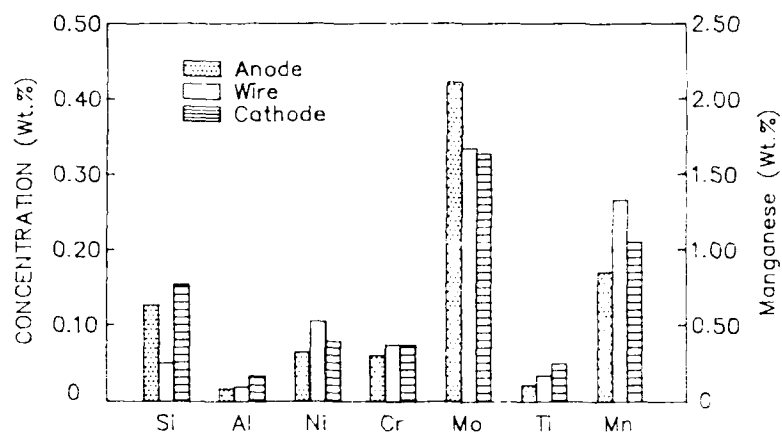


Fig. 5. Average droplet compositions for Si, Al, Ni, Cr, Mo, Ti, and Mn for straight and reverse polarities compared with the initial weld wire compositions.

A METHOD FOR CONTINUOUS MONOLAYER SEPARATION
UTILIZING MELTEN SALT ELECTROLYSIS

Kenzo Sato, Hiroaki Iai, Kazuo Sineshita, Hiroaki Saitoh,
Masaru Itami, Hiroaki Ouchi and Yoshifumi Yamanaka

Kamatetsu Electronic Metals Co., Ltd.
2-12 Shimizu-cho, Hatahara
Kanagawa, Japan 114

ABSTRACT

We investigated and developed a practical and efficient
production of monolayers which yielded monolayers on a molten
molten salt bath containing electrolyte. The electrolyte
generation in molten salt bath was controlled by the
the molten salt bath. The molten salt bath was
which attached at the anode surface and at the cathode.
This liquid current caused by the molten salt bath
efficiency degradation. We were able to control the
this current by using the molten salt bath. The
layer electrolytically and by growing of the layer of the
molten salt bath electrolysis. When the electrolysis was
performed at 1.0 A, the molten salt bath electrolysis
showed a high yield and a good quality of monolayers
of 10% and 10%, respectively.

INTRODUCTION

The voltage electric power generation has been a subject of
than as a source of electric energy. The silicon monolayers
silicon monolayers, which are used in the production of
crystal silicon cells, have been used in the production of
the production. For this reason, the molten salt bath
heat energy. The molten salt bath electrolysis is a
part of the electrolysis, this process was used in the
production of monolayers. The molten salt bath electrolysis
silicon films. The molten salt bath electrolysis is a
electrolysis was proposed by M. Saitoh, et al. (1) and
and M. Saitoh, et al. (2). The molten salt bath electrolysis
was not successful.

When the molten salt bath electrolysis was performed, the
the electrolysis of the molten salt bath electrolysis was
the molten salt bath electrolysis was performed.

in Figure 1. Each of three reactions requiring a molten salt bath takes place in a sealed molten salt vessel. The main feature of the present investigation is that the reactions take place continuously and in parallel (5). As compared to the work carried out by past investigators, the present process and apparatus possess many advantageous features such as: safety when equipment is broken or fails functionally, ability to handle pressure variations, reliable material transport, and ease of start-up and or maintaining operation. This project was supported by the Sunshine Project since 1980 as a commercialization research effort.

This commercialization research was carried out with the closed cycle apparatus, consisting of a monosilane generation apparatus shown in Figure 2, plus a silicon chlorinator, a silicon tetrachloride separation and recovery unit, and a monosilane purifier. The initial design had a problem with a valve operation in transporting the molten salt. This problem was solved by employing an overflow transport method and a simple pump with no moving parts actuated by gas pressure. This modification made it possible to reliably run the hydrogenation and monosilane generation reaction, and it clearly exposed the electrolysis problems.

When the electrolysis is performed at 2000 to 3000 A, the current efficiencies of electrolysis and of monosilane generation were 90 and 80%, respectively. These are essentially satisfactory numbers for production of metals by molten salt electrolysis in general. However, there were signs which gave doubts about long-term operability, such as erosion of the anode, a sudden drop of the anode chamber pressure, accumulation of Li on the salt bath surface, etc.

We discovered that, as shown in Figure 3(Left), a bypass current is generated through the anode chamber caused by Li in the Li collector and by Li attached on the diaphragm. In the case of the anode chamber which is separated and electrically isolated from the rest, another bypass current is generated caused by Li attached on the anode chamber as shown in Figure 3(Right). And the bypass current causes electrolysis between the anode chamber and the anode, depositing Li on the inside surface of the anode chamber wall. Thus, if the bypass current is eliminated, we believe that the various problems preventing commercialization will be solved and that the current efficiencies would approach the theoretical values.

THE EXPERIMENT

In order to eliminate the bypass current in the apparatus shown in Figure 2, the following steps were attempted:

(a) By raising the voltage potential of the anode chamber and the diaphragm with respect to the cathode and by means of dissolution and deposition of the attached Li, the Li can be transferred to the cathode and to other surfaces.

(b) Some Li, which moves to places other than the cathode by the above process, may float on the molten salt and may reattach itself to the anode chamber. In order to prevent this phenomenon from happening, the Li is eliminated by injecting chlorine and forming LiCl.

In order to carry out the above corrective measures, the following revisions to the apparatus were made:

(a) The anode chamber equipped with the diaphragm was separated from the collector and electrically isolated from the rest.

(b) A "Li transport power source" was installed between the anode chamber equipped with the diaphragm and the cathode.

(c) A chlorine blow-in tube was installed below the molten salt surface at a place between the anode chamber and the closest equipment to it, which are the outer jackets covering three cathode leader rods. This location is expected to be the main Li transfer point.

(d) A chlorine recovery chamber was added which is electrically isolated and which surrounds the anode chamber and the cathode leader rod outer jackets. This addition is a safety measure to prevent the outside of the reaction chambers from filling with reactive chlorine.

Figure 4 shows the cross-sectional view of the monosilane generation test set-up after the modifications.

The following steps are used to run the test apparatus. First, introduce the raw material, salt, into the molten salt vessel. Cover the vessel with a simple lid, dry the material, melt and dehydrate. Next, replace the lid with the one from which all equipment is hung, and then start the electrolysis. As Li begins to appear at the cathode, it will float as droplets, be collected in the collector, and be transferred via a transfer tube to the hydrogenator. The hydrogenator is filled with hydrogen, and the hydrogen is added as it is consumed to maintain the hydrogenator pressure. Moreover, the molten salt is fed at a constant rate from the molten salt vessel by a overflow mechanism. Li, which enters the hydrogenator, is hydrogenized to form LiH, is immediately dissolved in the molten salt and is fed to the silane generation chamber. Since an excess amount of SiCl_4 is continually fed into the chamber, the LiH which flows in will react to produce SiCl_4 and LiCl. The latter will flow out to the molten salt vessel dissolved in the salt. Thus, the Li cycle is completed and it is possible to operate the electrolysis continuously for a long period of time.

The following test parameters were employed:

The electrolysis current was automatically controlled at 1100 A.

The maximum voltage potential at the anode chamber was set at

2.6 V above the cathode potential. This voltage was applied at the start of the electrolysis. This potential takes into account the 0.5 V margin against the apparatus corrosion, and the figure was computed in the following way. Also, when the Li transport current exceeded its maximum value of 100 A, the voltage was adjusted to keep the current at around 100 A.

$$V_{\max} = \{V_t - I \times (R_a + R_c) - E_0\} \times (R_1/R_2) + (E_0 - E_1) - V_p$$

Where,

V_t : Applied electrolysis voltage

R_a, R_c : Anode and cathode resistance

I : Electrolytic current

E_0 : Decomposition Voltage of LiCl at 400°C

E_1 : Electrolytic potential of Ni/NiCl₂ against C/Cl₂ at 400°C

R_1 : Molten salt resistance between the cathode and the diaphragm

R_2 : Molten salt resistance between the anode and the cathode

V_p : Voltage margin for corrosion prevention. (Voltage drop due to the anode chamber and the cathode leader rods, etc.)

From the start of the electrolysis, chlorine was blown in through three nozzles at the rate of 0.5 l/min. Chlorine was diluted with twice the volume of argon. This volume is about one tenth of chlorine generated at the anode during electrolysis.

Main dimensions in the electrolysis area are: the anode: 30cm OD by 60cm long; the cathode: 42cm ID by 60cm long (crown shaped); the diaphragm: 35cm ID by 65cm long (10 mesh screen made of Ni). The salt bath temperature was maintained at 400°C in the molten salt vessel and at 570°C in the hydrogenator.

Since it is difficult to directly measure the bypass current, the effect was compared by computing the electrolysis efficiency and the monosilane production efficiency and also by observing the test apparatus during and after the operation. The efficiencies were computed by the following definitions.

$$\text{The current efficiency of electrolysis} = \frac{\text{Li (mol) calculated from H}_2 \text{ consumed}}{\text{Theoretical Li (mol) Value based on the electrolysis current}}$$

$$\text{The current efficiency of monosilane production} = \frac{\text{SiH}_4 \text{ (mol) actually collected}}{\text{Theoretical SiH}_4 \text{ (mol) production based on the electrolysis current}}$$

RESULTS AND DISCUSSION

Test operations were made at a constant electrolysis current of 1100 A. The Li transport power source was turned on and chlorine was

injected to minimize the bypass current. Test results are given in Table 1. Observation of the electrolysis section was made after test runs with the Li transport power source (total electrical consumption was 1.1×10^9 coul.). There was no corrosion on the anode surface near the salt level which normally is the most susceptible to corrosion. Even tool marks were still visible. The diaphragm and the anode chamber were also quite healthy.

For a comparison, tests were conducted without the Li transport power source and without chlorine injection. Results are given in Table 2. These test results have not changed much from those obtained in the past with a similar set-up. On the other hand, table 1 shows that there were no phenomena observed which preclude commercialization and that the electrolysis efficiency increased substantially and approached that of the theoretical values. Thus, we believe that these improvements are due to minimization of the bypass current and are not due to hardware or its arrangement.

The same conclusion can be reached by observing the voltages (the cathode as the base) vs. elapsed time at key equipment. When the bypass current is present, a large drop in electrolysis voltage is observed (Fig. 6) in the early stage of the electrolysis when the electrolysis current is kept constant. On the other hand, when the bypass current is eliminated by the use of the Li transport power source and the chlorine injection, the electrolysis voltage stays constant throughout as shown in Fig. 5. Also, when the bypass current was present, the voltage at the anode chamber decreased and the Li collector increased. Since these voltage values approach the short circuit values when the electrical pass is from the anode chamber to the Li collector via the salt bath surface, the main bypass current is thought to be flowing from Anode - Anode Chamber - Li Collector - Cathode (the bypass current II) rather than from Anode - Anode Chamber - Diaphragm - Cathode (the bypass current I).

The reason for the above is that the bypass current I is constant because it is only created by attaching around the diaphragm of a portion of Li freed from the cathode during electrolysis. On the other hand, the bypass current II is created mainly by Li attached on the exterior surface of the anode chamber. In other words, during electrolysis between the anode and anode chamber due to the bypass current I, Li is freed which is transferred out to the molten salt bath. The Li then floats on the surface of the bath and is attached to the anode chamber. The bypass current II does not flow until this happens. This floating Li causes an undesirable process cycle. Namely, it will create the bypass current II and the Li moves to attach itself to the nearest equipment. Since the floating Li is replenished continually, the attached Li will refloat and reattach to the anode chamber creating more bypass current II. This cycle is repeated. The bypass current deposits Li on the inside surface of the anode chamber, which subsequently increases the floating Li, and which further increases the bypass current II. This vicious cycle continues and the

bypass current increases until the limit is reached which is determined by the resistance of the molten salt and the voltage of electrolysis. The result is that during a long-term operation, a large amount of Li is accumulated on the molten salt surface.

Figure 7 and 8 show the relationship between the current consumption for Li transport during operation and the relative voltage potential of the anode chamber(diaphragm) or of the Li collector. The anode chamber voltage and the resistance to Li transport vary depending on the location and amount of Li attached. However, in comparison with the early stage of operation, the current drops and the voltage stabilizes toward the end of the run. The early fluctuation may be due to the floating Li left over from the earlier run.

Table 3 shows the current and power consumed for transporting Li. This indicates that about 2% of the total Li was attracted to the anode chamber in the normal operation. The maximum current used to transport Li in the test was 100 A. So, the objective was accomplished below one-tenth of the electrolysis current. When a Ni-made apparatus shown in Figure 4 is used to perform electrolysis at 5000 A, the electrolysis voltage will be 8.5 V, and the maximum voltage and current required to transport Li would be about 5.5 V and 500 A, respectively.

CONCLUSION

Tests were conducted to commercialize a new monosilane production method which utilizes electrolysis of a molten salt. The main objective of the investigation were to remove undesirable phenomena during electrolysis and to improve the efficiency by eliminating the cause of the problems, i.e., by minimizing the bypass current flowing through the anode chamber.

It was possible to sufficiently remove the bypass current by the following method: raise the voltage potential of the anode chamber and the diaphragm with respect to the cathode, transport Li from the diaphragm to the cathode, and attract Li at the anode chamber to the nearest equipment and then blow in chlorine to remove Li as LiCl. A further finding is that the anode chamber can be protected from corrosion by selecting the proper voltage potential.

The overall effect of the elimination of the bypass current was that the current efficiency of electrolysis increased from 90% to 97.5%. Also, it became possible to make a long-duration run while maintaining high efficiency. Moreover, we found that there is no danger of floating Li after shutdown and that it is easy to maintain the equipment.

REFERENCES

1. B.D.P. 1,092,890
2. U.S.P. 3,163,590
3. W. Sundermeyer and L.M.Litz; Chemi-Ing.-Techn. 37,14(1965)
4. K.Seto et al.; Molten Salt 25,63(1981)
5. J.P. 1,229,057

TABLE 1. Test Run Data with Li Transport Power Source and Chlorine Injection.

Electrolytic Current (A avg.).....	1104
Quantity of Electricity(10^6 Coul.).....	23.8
Hydrogen Consumed (mol.).....	120.4
Monosilane Produced (mol.).....	56.6
Current Efficiency of	
Electrolysis(%).....	97.5
Monosilane Production(%).....	91.8
Li Accumulation on the Bath.....	NO
Sudden Pressure Drop in the Anode Chamber.....	NO

TABLE 2. Test Run Data without Li Transport Power Source and Chlorine Injection, before and after Modifications. (Conventional Electrolysis)

	Apparatus Used	
	Fig.2	Fig.4
Electrolytic Current (A avg.).....	2104	2000
Quantity of Electricity(10^6 Coul.).....	468.5	215.4
Hydrogen Consumed (mol.).....	2230	1019
Monosilane Produced (mol.).....	1027	455
Current Efficiency of		
Electrolysis(%).....	91.8	91.3
Monosilane Production(%).....	83.8	81.5
Li Accumulation on the Bath.....	YES	YES
Sudden Pressure Drop in the Anode Chamber.....	YES	YES

TABLE 3. Electric Current and Power Consumption in Transporting Li.

		Mean Current (A)	Current Ratio (%)	Power Ratio (%)
electrolysis		1104	100	100
Li Transport	1st half	53.1	4.8	2.3
	2nd half	25.1	2.3	1.1
	Mean	41.4	3.7	1.8

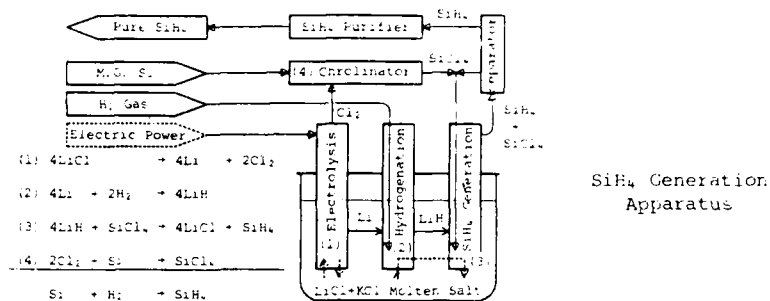


Figure 1. Principle of our Monosilane Generation Method.

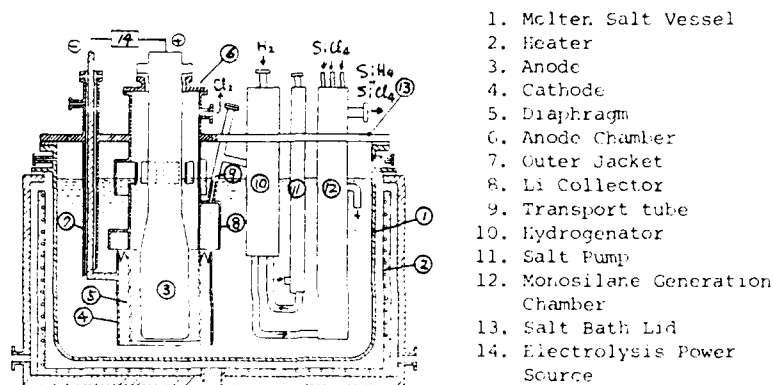


Figure 2. The Original Monosilane Production Apparatus Design Used in This Investigation. (Cross-sectional View)

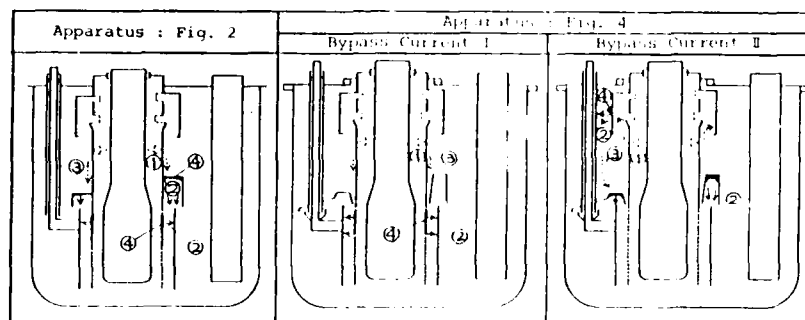


Figure 3. Main Passages of Bypass Current and Mechanisms of Current Generation. (1 = LiCl electrolysis, 2 = Movement of Li by dissolving and Depositing, 3 = Current Path through Metal, 4 = Li - Cause of Bypass Current Generation.)

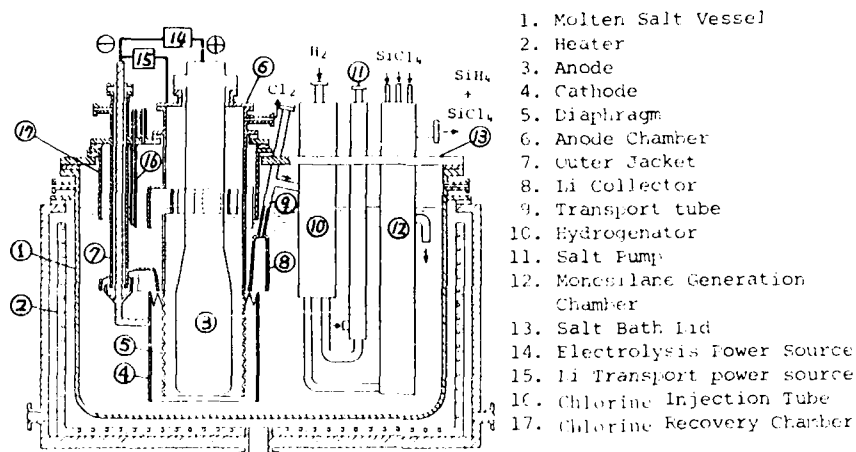


Figure 4. Revised Monosilane Production Apparatus to Prevent Bypass Current (Cross-Sectional View).

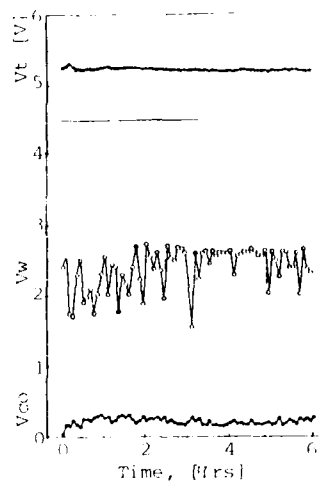


Figure 5. Voltages of each parts during the Test Run to prevent the Bypass Current.

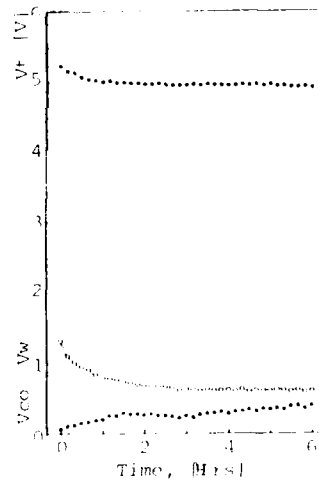


Figure 6. Voltages of each parts during a Conventional Run with the Apparatus shown in Figure 4.

Voltage of the electrolysis (V_t), Anode chamber voltage (V_w) and Collector voltage (V_{co}) are given with respect to the Cathode.

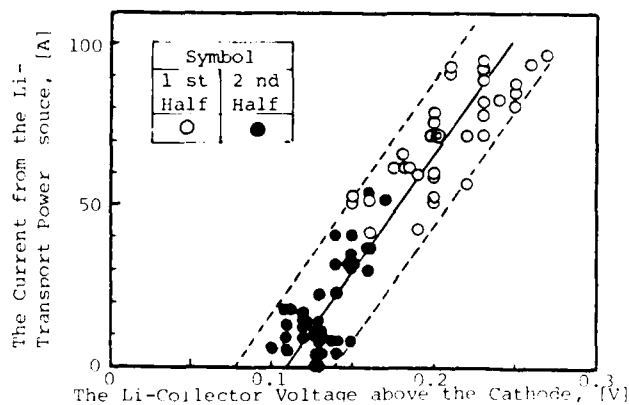


Figure 7. Relationship between the Current for Li Transport and the Li Collector Voltage above the Cathode.

The current readings are the maximum and the minimum over time. The proportional relationship is maintained only at the stable minimum current for a short duration as the current drop. It appears that the main Li transport comes from Li attached around the diaphragm.

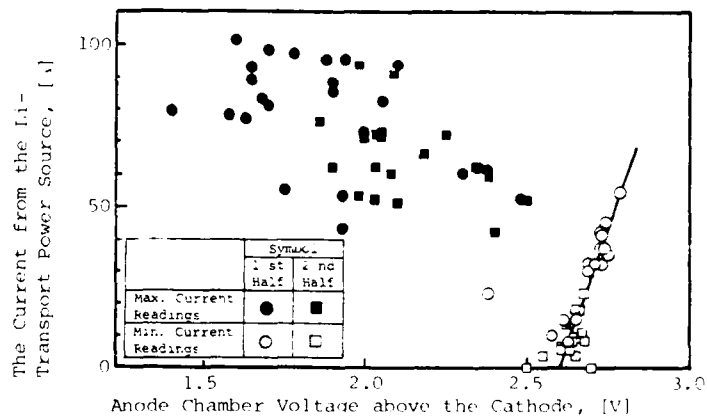


Figure 8. Relationship between the Current for Li Transport and the Anode Chamber Voltage above the Cathode.

The current readings are the maximum and the minimum over time. Since the proportional I-V relationship is maintained, it is believed that the large current is due to the movement of Li attached around the anode chamber. The main current is believed to be flowing in the bypass current II path.

EFFECT OF METAL COMPLEX ION ADDED INTO A MOLTEN $\text{NH}_4\text{F} \cdot 2\text{HF}$
ON THE CURRENT EFFICIENCY OF NF_3 -FORMATION⁴

Akimasa TASAKA, Hiroshi KOBAYASHI and Masahiko HORI

Doshisha University, Department of Applied Chemistry
Imadegawa, Karasuma, Kamigyo-ku, Kyoto 602 JAPAN

Hidetoshi NAKAYAMA

Showa Denko Co. Ltd., Chemical Research Laboratory
Oogi-machi 5-1, Kawasaki-ku, Kawasaki 210 JAPAN

ABSTRACT

The anodic reaction on nickel electrode was carried out at 1.0°C in the molten $\text{NH}_4\text{F} \cdot 2\text{HF}$ by a few kinds of electrochemical methods. AlF_3 , NH_4NiF_3 and $(\text{NH}_4)_3\text{FeF}_6$ containing a small amount of $(\text{NH}_4)_4\text{FeF}_6$ were added into the melt in order to investigate the effects of these additives on the current efficiency of NF_3 -formation and the anodic dissolution of Ni electrode. A Pt-rod was used as the reference electrode. The anode gas was quantitatively analyzed by both gas chromatography and infrared spectroscopy. With nickel anode, the passivation didn't occur and the amount of anodic dissolution was about 4%. In electrolysis under the controlled current, the anode gas was composed of N_2 , O_2 , NF_3 , N_2O , N_2F_4 and so on. The current efficiency was calculated from the flow rate of anode gas and its composition. The maximum current efficiency of NF_3 on Ni anode reached at 66% and then the anodic dissolution of Ni was only 3%. In the case of the addition of 0.1 mol% NH_4NiF_3 into the melt, the anodic dissolution of Ni electrode was about 1% and then the decrease in the current efficiency of NF_3 was only 6%. The greatest decrease in the current efficiency of NF_3 occurred in the melt added $(\text{NH}_4)_3\text{FeF}_6$. The addition of AlF_3 was not effective for the prevention of anodic dissolution of Ni. These results indicate that the addition of 0.1 mol% NH_4NiF_3 is favorable for the electrolytic production of NF_3 .

INTRODUCTION

Nitrogen trifluoride (NF_3) is a stable gas at room temperature and has a strong oxidising action at higher temperature (1). Therefore, it has been already used as an oxidising agent for rocket fuels and a stable fluorinating agent (2~8). It may be also used as a welding agent for metals and a gas filler in order to increase the life and the brightness of lamps (9). Recently, a few researches have been attempted to develop the use of NF_3 as a laser gas (10~12), an etchant gas for a dry etching process (13~16) and a cleaner gas for apparatus used

in the CVD technique (17).

Some processes for the preparation of NF_3 have been proposed up to date, and the electrochemical process is better than the chemical process in the view point of the purity of NF_3 , especially, free of CF_4 (18-21).

In earlier papers, we have reported on the electrolytic production of NF_3 from ammonium fluoride, urea and amides dissolved in a molten KHF_2 with a carbon electrode, and clarified the mechanism of electrochemical fluorination in this melt. But, in this procedure, NF_3 is contaminated with CF_4 , because of the decomposition of $(\text{CF})_n$ and/or $(\text{CxF})_n$ ($x \leq 2$) film formed on the carbon electrode. On the contrary, nickel was the best material for the anode from the view point of both the production of NF_3 free of CF_4 and the anodic dissolution. However, even a small amount of the loss of Ni anode increases the cost of the production of NF_3 and hence it is very important to prevent the anodic dissolution of Ni for the industrial production of NF_3 . The addition of a metal fluoride or ammonium metal fluorides into the melt was attempted in order to prevent the anodic dissolution of Ni, and then the effect of additives on the current efficiency of NF_3 -formation and the anodic dissolution of Ni was also investigated.

EXPERIMENTAL

One electrolytic cell of 1.5 dm³ in capacity was made of copper as shown in earlier papers (21,23) and another electrolytic cell of 0.4 dm³ in capacity made of polytetrafluoroethylene resin (teflon) as shown in Fig. 1. The rod of nickel with the surface area of 1.97 cm² was used as the anode for determination of polarization curves by the cyclic voltammetry and the anodic dissolution by the galvanostatic method. The plate nickel with the surface area of 10 or 60 cm² were also used for determination of the anodic dissolution of Ni and for the electrofluorination, respectively. The inside wall of the cell made of copper and a platinum wire were used as the cathode and the reference electrode, respectively. The inside wall of cell bottom was masked by teflon and the anode compartment of the cell was separated from the cathode compartment by a skirt of copper or teflon welded to the gas cover. The anode gas was passed through the absorption tube of gaseous HF filled with tablets of sodium fluoride (NaF) and then led to a gas-sampler. The sample gas was fractionated by gas chromatography and the fractionated samples, each corresponding to a distinct peak on the gas chromatogram, were identified by infrared spectroscopy.

The electrolyte was pre-electrolyzed at a low current density until NF_3 was detected, and then anodic polarization curves were determined by the cyclic voltammetry.

RESULTS AND DISCUSSION

The cyclic voltammograms on nickel in the molten $\text{NH}_4\text{F} \cdot 2\text{HF}$ were shown in Fig. 2. Two current peaks at about 0 V were observed on the anodic polarization curve. At the potential range between 0 and 6 V, the current density was very small. And then it increased again at the potential over 6 V. But the cathodic current peak was not observed at the potential below 3.0 V and the anodic current at potentials over 5 V increased with the number of cyclic scanning. From this result, it is concluded that nickel difluoride (NiF_2) formed on nickel dissolves in the electrolyte to form complex ions, for example, NiF_6^{n-} ($n = 3$ or 4) and/or $\text{Ni}(\text{NH}_3)_6^{m+}$ ($m = 2$ or 3) and no atomic fluorine adsorbs on nickel and/or nickel difluoride.

Figs. 3 and 4 showed the effects of added AlF_3 and NH_4NiF_3 on the anodic polarization curves on nickel in the molten $\text{NH}_4\text{F} \cdot 2\text{HF}$, respectively. In the addition of AlF_3 , the change in the shape of wave was not observed. On the contrary, the addition of NH_4NiF_3 changed drastically the shape of wave; i.e., the first current peak at about +0.3 V disappeared on the anodic polarization curve after the addition of NH_4NiF_3 , while the second current peak at about 0 V increased with increasing the concentration of the additive. These results indicate that nickel anode would be dissolved at the first peak to form Ni^{2+} and that the formed Ni^{2+} would be further oxidized at the second peak to form Ni^{3+} .

Fig. 5 showed the anodic polarization curves obtained by scanning the potential to the lower side from 9 V. The anodic current at the potential range between 5 and 8 V increased with increasing the concentration of NH_4NiF_3 .

Fig. 6 showed the effect of the additive on the weight loss of Ni anode. In no additive, the same behavior as that in the addition of AlF_3 was observed. The effect of the NH_4NiF_3 -concentration added into the melt on the weight loss of Ni anode during electrolysis was given in Table 1. From the figure and the table, it was found that the addition of only 0.1 mol % NH_4NiF_3 was effective enough for the prevention of anodic dissolution of Ni and that the ratio of quantity of electricity dissipated by anodic dissolution of Ni electrode to total quantity of electricity (Q_a/Q_t) decreased from 3.1 to only 1.3 by the addition of 0.1 mol % NH_4NiF_3 .

Fig. 7 showed the change of anode gas composition in electrolysis at the current density of $15 \text{ mA} \cdot \text{cm}^{-2}$ as a function of time. NF_3 was already detected in the anode gas after electrolysis for only 7 hours and its composition ratio of anode gas, i.e. yield, increased with the lapse of time and reached the constant value of about 65%.

The flow rates of cathode gas composed of hydrogen only and anode gas composed of N_2 , O_2 , NF_3 , N_2O , N_2F_4 , and an unknown substance (N_2F_4) during electrolysis at the current density of $15 \text{ mA} \cdot \text{cm}^{-2}$ were shown in

Figs. 8 and 9, respectively. Both flow rates didn't decrease in the addition of AlF_3 , while they decreased in the addition of NH_4NiF_3 and $(\text{NH}_4)_3\text{FeF}_6$ containing a small amount of $(\text{NH}_4)_4\text{FeF}_6$. This fact indicates that the ions with the higher valence metal such as Ni^{3+} or Fe^{3+} would be reduced on the cathode to form the ions with the lower valence metal such as Ni^{2+} or Fe^{2+} and that the formed ions would be oxidized on the anode to form the original ions.

Table 2 showed the effect of NH_4NiF_3 -concentration on the yield of each product in the anode gas. This table revealed that the addition of NH_4NiF_3 decreased the yield of NF_3 . It is concluded, therefore, that the concentration lower than 0.1 mol% NH_4NiF_3 is favorable for the electrolytic production of NF_3 in the view point of both the increment of the yield of NF_3 and the prevention of anodic dissolution of Ni.

REFERENCE

1. C.E. Colburn, "Advances in Fluorine Chemistry", Vol. 3, Butterworths, London, 1963, p. 92.
2. H.H. Rogers, Ind. Engng. Chem., **51**, 309 (1959).
3. C.J. Hoffman and R.G. Neville, Chem. Rev., **62**, 1 (1962).
4. M. Schmeiser and P. Sartori, Chem. Ing. Techn., **36**, 9 (1964).
5. O. Glemser, U. Bierman, J. Knaak and A. Haas, Chem. Ber., **98**, 446 (1965).
6. O. Glemser and U. Bierman, Chem. Ber., **100**, 1184 (1967).
7. O. Glemser, J. Wegener and R. Mews, Chem. Ber., **100**, 2474 (1967).
8. O. Glemser and U. Bierman, Chem. Ber., **100**, 2484 (1967).
9. Chem. Eng. News, **43** (No. 6), 47 (1965).
10. J.L. Lyman and R.J. Jensen, Chem. Phys. Letters, **13**, 421 (1972).
11. J.L. Lyman and R.J. Jensen, J. Phys. Chem., **77**, 883 (1973).
12. D. Padrick and M.A. Gusinow, Chem. Phys. Letters, **24**, 270 (1974).
13. S. Nakayama, K. Tsuneto, A. Tasaka, T. Ohachi, D. Naito and I. Taniguchi, "Proc. 2nd Symposium on Dry-process", Tokyo, Oct., 1980, p. 115.
14. N.J. Ianno, K.E. Greenberg and J.T. Verdeyen, J. Electrochem. Soc., **128**, 2174 (1981).
15. K.M. Eisele, J. Electrochem. Soc., **128**, 123 (1981).
16. A. Kawamura, K. Tsuneto, T. Ohachi, T. Fujii and I. Taniguchi, "Proc. 4th Symposium on Dry-process", Tokyo, Oct., 1982, p. 39.
17. Nikkei Microdevices, p. 113 (1985).
18. A. Tasaka and N. Watanabe, Z. anorg. allg. Chem., **385**, 156 (1971).
19. O. Ruff, J. Fisher and F. Luft, Z. anorg. allg. Chem., **172**, 417 (1928).
20. O. Glemser, J. Schröder and J. Knaak, Chem. Ber., **99**, 371 (1966).
21. N. Watanabe, A. Tasaka and K. Nakanishi, Denki Kagaku, **36**, 685 (1968).
22. A. Tasaka, M. Oguchi, M. Kawaguchi and K. Yoshie, Nippon Kagaku Kaishi, **1982**, 1082.
23. A. Tasaka, H. Sakaguchi, R. Aki, H. Ihara, K. Saka and T. Yamamoto, J. Fluorine Chem., **27**, 23 (1985).

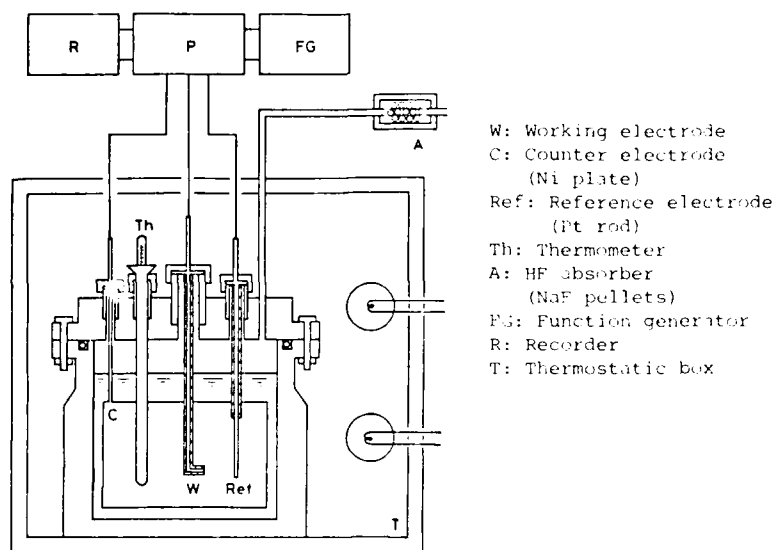


Fig. 1 Experimental apparatus for determination of anode polarization curve

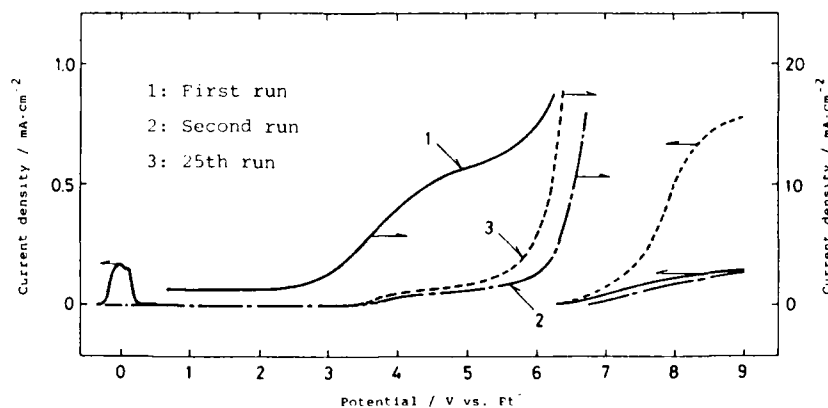


Fig. 2 Anodic polarization curves on nickel electrode at 120°C in $\text{NH}_4\text{F} \cdot 2\text{HF}$ by potential sweep method with sweep rate of $0.2 \text{ V} \cdot \text{s}^{-1}$

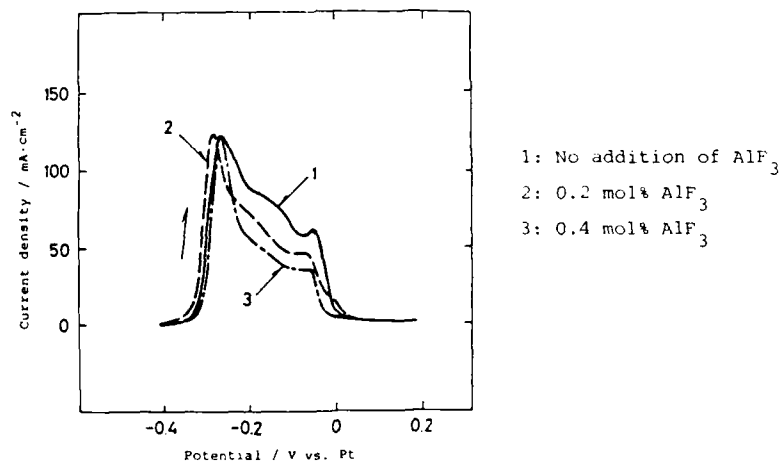


Fig. 3 Anodic polarization curves on nickel electrode in electrolyte of $\text{NH}_4\text{F} \cdot 2\text{HF} + \text{AlF}_3$ at 120°C by potential sweep method with sweep rate of $20 \text{ mV} \cdot \text{s}^{-1}$ (First run)

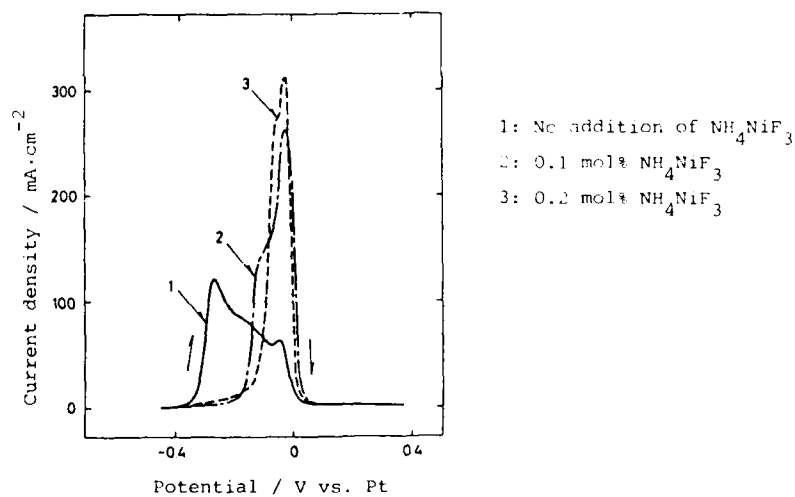


Fig. 4 Anodic polarization curves on nickel electrode in electrolyte of $\text{NH}_4\text{F} \cdot 2\text{HF} + \text{NH}_4\text{NiF}_3$ at 120°C by potential sweep method with sweep rate of $20 \text{ mV} \cdot \text{s}^{-1}$ (First run)

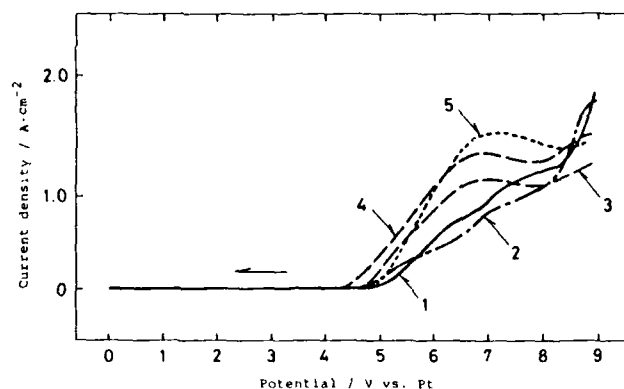


Fig. 5 Effect of added AlF_3 , NH_4NiF_3 or $(\text{NH}_4)_3\text{FeF}_6$ on anodic polarization curves on nickel electrode at 120°C in $\text{NH}_4\text{F} \cdot 2\text{HF}$ by potential sweep method with sweep rate of $0.2 \text{ V} \cdot \text{s}^{-1}$ (30th run)

1: No additive, 2: 0.8 mol% AlF_3 , 3: 0.4 mol% NH_4NiF_3 ,
4: 0.8 mol% NH_4NiF_3 , 5: 0.06 mol% $(\text{NH}_4)_3\text{FeF}_6$.

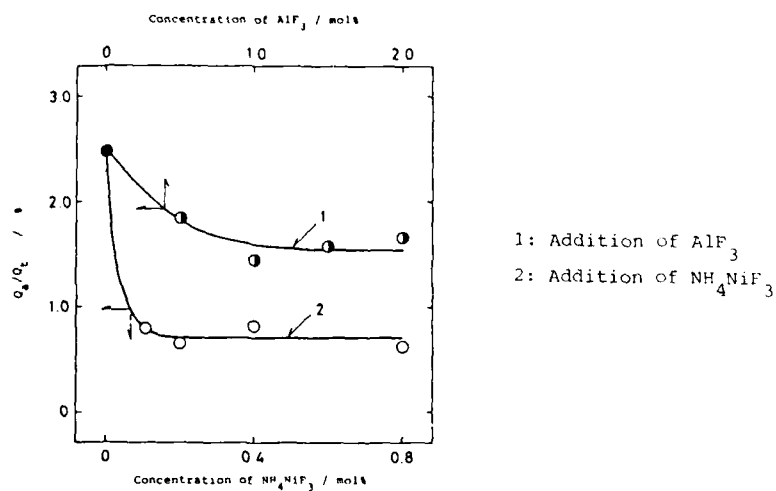


Fig. 6 Relationship between ratio of quantity of electricity dissipated by anodic dissolution of nickel electrode to total quantity of electricity (Q_a/Q_t) at 120°C and current density of $25 \text{ mA} \cdot \text{cm}^{-2}$ and concentration of AlF_3 or NH_4NiF_3 in $\text{NH}_4\text{F} \cdot 2\text{HF}$

Table 1 Effect of added NH_4NiF_3 -molar concentration on weight loss of nickel anode in electrolysis

NH_4NiF_3 (mol%)	C.D. ($\text{mA}\cdot\text{cm}^{-2}$)	E.D. (hrs.)	Potential (V vs. Pt)	number of electron
0	25	97	4.4 ~ 5.1	2 3
0.1	25	74	4.2 ~ 6.9	2 3
0.2	25	76	5.0 ~ 5.5	2 3
0.4	25	74	5.2 ~ 5.9	2 3
0.8	25	50	5.2 ~ 5.9	2 3

Calculation weight loss of anode (g)	Observed weight loss of anode (g)	R.D. (%)
26.161	0.7330	2.80
17.387	0.7330	4.20
20.260	0.1636	0.81
13.507	0.1636	1.21
20.990	0.1391	0.66
13.993	0.1391	0.99
20.594	0.1693	0.82
13.729	0.1693	1.23
18.860	0.1180	0.63
12.573	0.1180	0.94

Headings; C.D.: Current density, D.E.: Duration of electrolysis,
R.D.: Ratio of quantity of electricity dissipated by anodic
dissolution of nickel electrode to total quantity of
electricity (Q_a/Q_t)

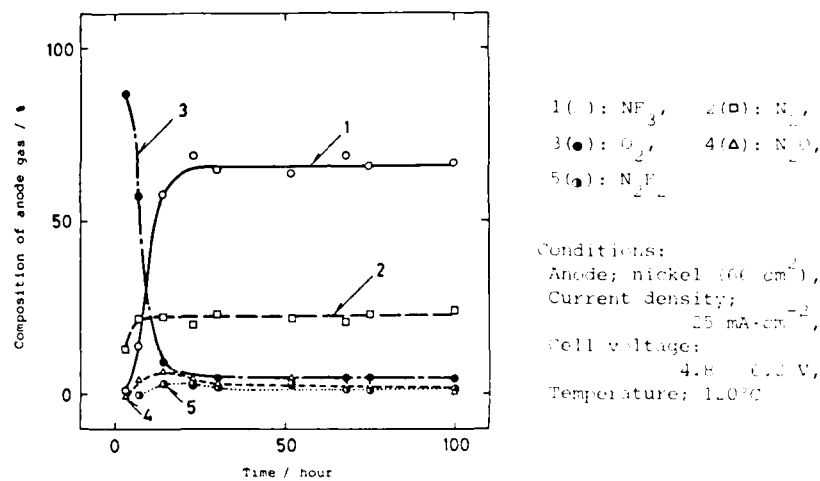


Fig. 7 Change of anode gas composition in electrolyte of $\text{NH}_4\text{F}\cdot 2\text{HF}$ as a function of time

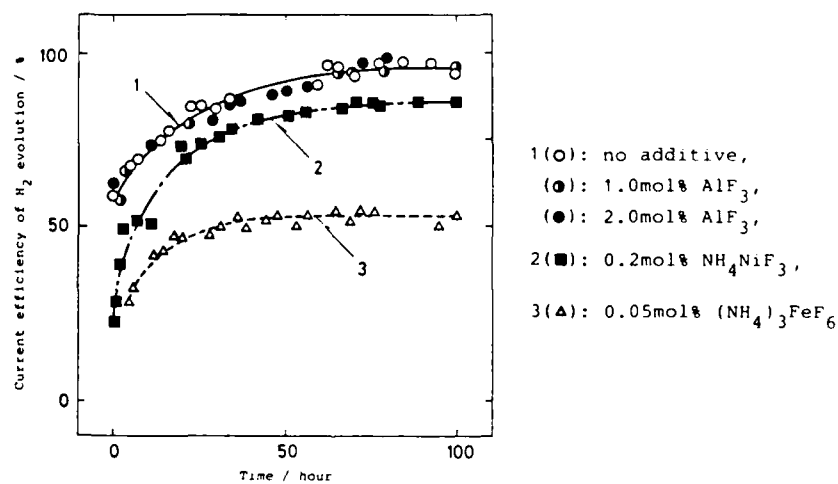


Fig. 8 Change of current efficiency of H_2 evolution in electrolyte of $\text{NH}_4\text{F}\cdot 2\text{HF}$ containing added AlF_3 , NH_4NiF_3 or $(\text{NH}_4)_3\text{FeF}_6$ as a function of time

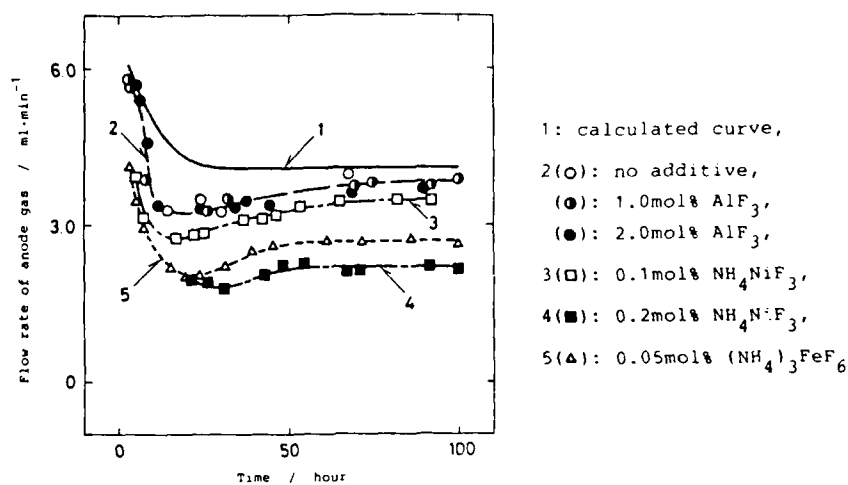


Fig. 9 Change of flow rate of anode gas in $\text{NH}_4\text{F} \cdot 2\text{HF}$ containing added AlF_3 , NH_4NiF_3 or $(\text{NH}_4)_3\text{FeF}_6$

Table 2 Effect of AlF_3 , NH_4NiF_3 and $(\text{NH}_4)_3\text{FeF}_6$ -molar concentration on each current efficiency of anode gas products

Additive	mol%	Current efficiency of anode gas products(%)						
		NF_3	N_2	O_2	N_2O	N_2F_2	$\text{X}(\text{N}_2\text{F}_4?)$	Total
-	-	65.5	20.1	3.3	3.5	2.9	0.8	96
AlF_3	1.0	68.3	22.2	0.3	1.4	3.2	1.1	97
AlF_3	2.0	66.7	21.8	0.2	2.9	4.1	1.0	97
NH_4NiF_3	0.1	59.8	20.9	3.8	1.0	3.1	0.9	90
NH_4NiF_3	0.2	36.0	17.0	5.8	1.0	1.6	0.7	62
$(\text{NH}_4)_3\text{FeF}_6$	0.05	49.8	15.3	2.9	0.5	2.9	1.2	73

Conditions: Anode; nickel(66cm^2), Current density; $25\text{mA} \cdot \text{cm}^{-2}$,
 Temperature; 120°C

A REVIEW OF THE CHEMICAL AND PHYSICAL PROPERTIES OF MOLTEN ALKALI
NITRATE SALTS AND THEIR EFFECT ON MATERIALS USED
FOR SOLAR CENTRAL RECEIVERS

R. W. Bradshaw and R. W. Carling

Sandia National Laboratories
Livermore, CA 94550

ABSTRACT

Sandia National Laboratories, Livermore (SNLL), has been responsible for developing thermal energy collection and storage technologies for solar central receiver (SCR) applications as the lead laboratory designated by the U. S. Department of Energy. The focus of one of these efforts has been the evaluation of the properties of a mixture of sodium nitrate and potassium nitrate as a single-phase working fluid for SCR systems. This paper summarizes the results of a comprehensive research program that was established by SNLL to address issues relevant to the use of molten nitrates at temperatures up to 600°C. It was concluded that molten nitrate salt is technically feasible as a working fluid for advanced SCR and offers a number of advantages compared to alternative fluids.

Introduction

The selection of a molten salt, consisting of a mixture of sodium nitrate and potassium nitrate, as a heat transfer fluid for high-temperature solar central receivers (SCR) was initially derived from a systematic screening process which identified several favorable characteristics, such as a low melting point (222°C), the availability of large quantities at low cost, and the minimal hazards associated with its use [1,2]. Low cost is particularly important if the fluid is to serve as the thermal energy storage media as well as the receiver coolant [3]. Although molten nitrate salts have been used extensively for heat transfer in industrial processes [4] and compilations of some of their properties are available [5], the maximum temperature intended for SCR systems is 600°C, which is significantly higher than previous applications. For this reason, a research program was undertaken to establish a data base describing the properties of a molten mixture of NaNO_3 and KNO_3 over the complete range of temperatures relevant to advanced SCRs.

The majority of the research efforts were conducted at SNLL, although several industrial, university, and national laboratories participated as well. The program included studies of chemical stability, physical properties, corrosion of metallic materials, environmental effects on the mechanical properties of alloys, and compatibility of non-metallic materials with the molten salt. A comprehensive group of studies has been completed and this review

*This work supported by U.S. Dept. of Energy contract DE-AC04-76DP00789.

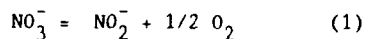
summarizes those research activities and the results obtained. The technical issues which motivated the studies in each area are described and their impact on engineering concerns are discussed. This review includes results obtained during the operation of large-scale demonstration experiments.

Chemical Properties

The important issues concerning the chemical properties of molten nitrate salt mixtures were choosing the composition, verifying chemical stability at high temperature, determining the effects of cover gas composition and atmospheric contamination on the melt and assessing any hazards which might arise when using molten salt in an SCR.

The liquidus line in the phase diagram reported in a previous study does not indicate a eutectic, but rather a broad band of low-melting mixtures surrounding the minimum melting point of 222°C at 50 NaNO₃-50 KNO₃ (mol. %, 46-54 wt. %) [5]. The phase diagram was re-examined using differential scanning calorimetry (DSC) and its important features were confirmed [6]. The data suggested that a mixture enriched in NaNO₃ relative to KNO₃ would be desirable since the significant reduction in cost would easily offset the disadvantages of a slightly increased melting point. The composition 44 NaNO₃-56 KNO₃ (mol. %, 60-40 wt. %), which melts at 238°C, was chosen for advanced SCR applications and was successfully used in several engineering projects [7-9].

A key consideration in qualifying this molten salt mixture for long-term use was chemical stability, since molten nitrate salts may undergo a variety of reactions depending on the temperature and the composition of the cover gas. The primary reaction is the decomposition of nitrate to nitrite and oxygen.



Experimental investigations of the equilibrium of reaction (1), at temperatures up to 600°C, determined the equilibrium constant [10,11] and the enthalpy change (23.03 Kcal/mol [10]). Figure 1 compares the equilibrium constant of the mixed salt, as a function of temperature, with published results for the pure components. The concentration of nitrite in melts in equilibrium with air is about 3 wt.% at 565°C and 7% at 600°C. The equilibrium data have been used to calculate the amount of nitrite expected to form in either open or closed systems covered with a variety of gases [11]. It was concluded that air at atmospheric pressure is more than adequate to minimize nitrite formation.

Thermochemical equilibrium calculations were used to predict the behavior of nitrate melts over a wide range of conditions. The thermodynamic model included reactions of nitrate and nitrite which yield alkali oxides and gases, such as oxygen, nitrogen and NO_x. The result of these studies was the construction of the phase stability diagram of the Na-O-N system at various temperatures [12]. The study determined that the concentration of oxide ions was negligible at SCR

temperatures, but increased rapidly above 600°C. This is an important finding because oxide ions are known to be very corrosive (a later section discusses rapid corrosion above 600°C). A comparison of the oxide ion concentrations measured in equilibrium melts with predictions of the thermodynamic calculations suggested that oxide ions behave non-ideally in nitrate melts [13].

The stability of the melt with respect to the major constituents of air is an obvious benefit for an SCR system. However, a concern that atmospheric carbon dioxide and water vapor might cause the salt to deteriorate during long-term use was also addressed. The interactions of CO₂ and H₂O with nitrate melts were studied using electrochemical and chemical techniques [14]. It was found that CO₂ can cause minor chemical changes by reacting to form carbonate. Although DSC studies showed that the solubilities of alkali carbonates in the nitrate salt were large [1], the carbonates of metallic impurities might precipitate in the coolest sections of heat exchangers. However, problems related to carbonate precipitation are not expected because the availability of CO₂ is very limited. The solubility of water vapor was found to be completely reversible up to 600°C and no hydrolysis was observed [14]. Procedures are available for removing anionic contaminants, such as nitrite and carbonate, if needed [11,15]. No adverse effects on the molten salt were observed during approximately 1000 hours of testing of a one-megawatt SCR electric power generating system at the Central Receiver Test Facility in Albuquerque, NM [9].

Two reports were prepared which discuss loading, operating and maintaining SCR systems that contain large quantities of salt [15,16]. Hazards management related to the use of molten nitrate salt has also been discussed, although in an SCR the necessary precautions are those associated with any hot fluid, since oxidizable materials will not be present [15,16]. A comprehensive review of the hazards associated with molten salts has been published by Allen and Janz [17].

Physical Properties

A knowledge of the physical properties of the working fluid in a SCR is essential for design calculations involving heat transfer and fluid flow in such components as receivers, heat exchangers, pumps, and thermal energy storage subsystems. Although data on most of the important properties (for example, viscosity, density, thermal conductivity and heat capacity) are available in the literature for single alkali nitrate salts [5], the properties of the SCR mixture were not available over the operating temperature range. Experimental measurements of these properties were made at temperatures which significantly extended the range of existing data. The measured values are presented in Figure 2.

Viscosity, density and surface tension (not shown) were determined from 250°C to 600°C using a single apparatus [18]. Viscosity decreased from about 5 gm/cm²/sec at 250°C to 1 at 600°C, while density decreased moderately with temperature and was nominally 1.8 gm/cm³. These data

agree with literature values at lower temperatures where comparisons can be made. Thermal conductivity was found to be weakly dependent on temperature from 250°C to 400°C and the measured values were nominally $0.5 \text{ W m}^{-1} \text{ K}^{-1}$ [19]. Minor additions of NaNO_2 and/or Na_2CO_3 to the melt had a negligible effect. The heat capacity of the molten mixture was determined by differential scanning calorimetry and found to be about $140 \text{ J K}^{-1} \text{ mol}^{-1}$ [20,21]. Difficulty in containing the salt in the thermal conductivity and heat capacity apparatus limited the accessible temperature range. The equations expressing the temperature dependence of each property are available in the above references.

Corrosion of Metallic Materials

It was necessary to resolve two issues before selecting suitable alloys and metals for containment of the molten salt. These were the corrosion rates at operational temperatures and the solubility of metallic oxides in the molten salt. Although the corrosion behavior of various metals and alloys has been reported previously, the data have been derived from short-term tests and were not considered adequate for engineering design. The concern with regard to solubility behavior was that dissolved corrosion products might precipitate in the coldest parts of the flow system and foul or plug them, a phenomena called thermal-gradient mass transfer.

Corrosion and mass transfer behavior were investigated using thermal convection loops, which operated at temperatures spanning the range of a SCR, 300°C to 600°C [22]. The alloys tested were Alloy 800, 304SS and 316SS. The rates of metal loss of these alloys were 5-12 micron/year at 600°C [23-26]. Measurements of metal losses by chemical descaling revealed that the majority of metal consumption was due to oxidation [26]. Chemical analyses of the salt in the loops established that chromium was soluble, whereas iron and nickel were negligibly soluble. The solubility of chromium, as chromate ion, in molten nitrates is quite large; accordingly, thermal-gradient mass transfer was not observed.

Corrosion data for a wide variety of alloys and metals were obtained from long-term experiments in isothermal crucibles. Materials for the complete range of operating temperature environments were tested, including stainless steels (austenitic and ferritic), chromium-molybdenum steels, carbon steel, aluminum diffusion-coated steels, nickel, aluminum and titanium. Representative results from these studies are summarized in Table 1. In general, alloys with at least 9% chromium were quite corrosion resistant up to 600°C [27]. A nickel-base alloy, IN600, was somewhat more corrosion resistant than Alloy 800, although it underwent internal oxidation, which the iron-base alloy did not. Cr-Mo steels with 1 to 5% Cr experienced metal loss rates as high as 100 micron/year over a restricted temperature range [28]. Aluminized Cr-Mo steels were very resistant at 600°C [29]. Similarly, aluminum was negligibly affected at 565°C. Titanium oxidized more rapidly than ferrous alloys, but formed an adherent surface oxide layer, while nickel experienced severe intergranular corrosion [30].

A better understanding of corrosion mechanisms was obtained by studies of the kinetics of oxidation and depletion in crucible tests. The rate laws for both processes in most Cr-containing alloys were parabolic up to 600°C [27,32]. At these temperatures, the corrosion products were spinels of iron and chromium and Fe_2O_3 . Above 615°C, sodium ferrite was formed [31], corrosion rates increased markedly, and kinetics were observed that indicated the formation of a non-protective surface film [32], as shown by the plot of Cr depletion from Alloy 800 in Figure 3. The relatively rapid oxidation of Cr-Mo steels was associated with the formation of $\psi\text{-Fe}_2\text{O}_3$ [28]. Electrochemical polarization studies of Alloy 800 confirmed the passivation of Alloy 800 in the melt [33] and the suppression of galvanic corrosion of Alloy 800/mild steel couples by surface films [1]. Some of the chemical and electrochemical factors relevant to corrosion in molten nitrates, including the inadvisability of cathodic protection, have been discussed by Smryl [34].

Since the oxide scales on high-temperature alloys were very adherent, no thermal cycling tests were done. Examination of scale layers on the inside surface of Alloy 800 receiver tubes, that had operated for about 1000 hours in a cyclic solar radiation environment, revealed adherent oxides that grew somewhat faster than isothermally-grown scales [35]. Operation of a forced-convection loop did not reveal any obvious erosion damage to surface scales [11].

Environmental Effects on the Mechanical Properties of Alloys

The receiver tubes of SCRs present unusual problems in materials selection and design because of the stresses which arise from one-sided heating, as well as from the thermal cycling inherent in solar receiver operation [36]. A key concern was whether the molten salt, in conjunction with the thermomechanical environment, would promote cracking of alloys used for receiver tubes and other components or otherwise degrade their mechanical properties. The complexity of mechanical testing in a molten salt environment limited studies to the most favored alloys, Alloy 800, 316SS and HT-9 (receiver tubes) and 2-1/4Cr-1Mo steel (steam generator tubes).

Slow strain rate tests and creep tests in the molten salt at 600°C established that neither environmentally-induced cracking nor significant acceleration of oxidation due to deformation occurred in Alloy 800 [37,38]. Figure 4 shows the insensitivity of the ductility of Alloy 800 to strain rate during prolonged immersion in the molten salt, as compared to air. Slow strain rate tests showed that the strength and ductility of 316SS were unaffected, but a measurable loss of the ductility of HT-9 was observed [39]. No significant reduction in lifetime was found during fatigue and creep-fatigue tests of Alloy 800 in molten salt at 650°C when compared to tests in air [40]. 2-1/4Cr-1Mo steel experienced a loss in ductility at temperatures up to 525°C, due to the acceleration of oxidation by deformation over a range of strain rates [41]. However, this does not preclude its use in heat exchangers at lower temperature.

Compatibility of Non-metallic Materials

Other compatibility questions which were investigated concerned the selection of non-metallic materials for several important functions, including fluid seals for valves, thrust bearings in pumps, and internal insulation and solid ballast for thermal energy storage.

A comprehensive study was conducted to evaluate materials for valve stem seals in flow control valves [42]. Compression packings were emphasized because this type of seal offers economic advantages in large valves. Below 300°C, good compatibility was observed with polytetrafluoroethylene (PTFE) and graphite. Other materials commonly used to fabricate packings for high temperature, including asbestos, borosilicate glass, aramid fiber and perfluoroelastomers, were not suitable. PTFE is not mechanically acceptable at higher temperature, and graphite began to oxidize rapidly above 400°C, as shown in the thermogravimetric analysis plot in Figure 5. Thus, valve designs must limit the temperature of the packing to 300°C.

Compatibility tests were conducted with a variety of ceramics. Silicon carbide, proposed as an thrust bearing in pumps, displayed good resistance to the molten salt, resulting in a corrosion rate of 7 micron/year at 565°C, due to dissolution of SiC as silica or silicate [30]. Boron nitride was relatively inert in the melt below 300°C [42], while dense alumina was unaffected up to 630°C [32]. Many refractory insulating materials were evaluated as internal insulation for large salt storage tanks, where wetting by the molten salt at 565°C would be necessary [43]. Dissolution of the silica phases in these materials caused unacceptable deterioration. Experiments were also conducted with materials which would be useful as inexpensive ballast for thermal energy storage. Taconite pellets (mainly iron oxide) were relatively stable in contact with the salt at 565°C, but granite was not [44].

Conclusions

A comprehensive data base on the properties of molten nitrate salts has been established that allows SCR systems to be designed with confidence in their performance. The data base includes information on the chemical and physical properties of molten mixtures of NaNO_3 and KNO_3 and the effects of the molten salt on many metallic and non-metallic materials commonly used in high-temperature applications.

Molten nitrate salt was shown to be chemically stable in air at temperatures up to 600°C, the upper design limit. Higher temperatures should be avoided because decomposition yields high concentrations of nitrite and alkali oxides. The effects of atmospheric CO_2 and H_2O on the melt appeared to be minimal as a practical matter. The important physical properties of the melt were determined and are available to designers. Although values of thermal conductivity and heat capacity at maximum temperatures would be desirable, extrapolations of available data are suitable for design purposes.

Materials are available to fabricate all the components needed for an SCR system. Good corrosion resistance was demonstrated by Alloy 800, 300-series stainless steels, and 9Cr-1Mo at 600°C during long-term tests. Corrosion rates of ferrous alloys increased rapidly at higher temperatures and these temperatures should be avoided. Chromium was slowly leached from some alloys by the salt, but thermal gradient mass transfer was not observed. The oxide layers on high-temperature alloys were adherent, although oxidation was somewhat faster during the thermal cycling experienced in receiver demonstration tests. Corrosion allowances of up to 100 micron/year may be necessary for 2-1/4Cr-1Mo at 460°C. The molten salt did not cause cracking of receiver tube alloys. Among non-metallic materials, graphite and PTFE were resistant at 300°C, but silica-containing refractories deteriorated at 565°C.

The fundamental conclusion of this research program is that the use of molten nitrate salts for energy collection, transfer and storage in SCR systems is technically feasible. This conclusion is supported by demonstrations in multi-megawatt receiver tests and electric power generation experiments.

References

1. R. W. Carling, et al, "Molten Nitrate Salt Technology Development Status Report," SNLL, SAND80-8052, March 1981.
2. T. T. Bramlette, et al, "Survey of High Temperature Thermal Energy Storage," SNLL, SAND75-8063, March 1976.
3. J. D. Fish, et al, *Chem. Eng. Prog.*, p. 48, Jan. 1983.
4. R. W. Carling and R. W. Mar, "Industrial Use of Molten Nitrate/Nitrite Salts," SNLL, SAND81-8020, December 1981.
5. G. J. Janz, et al, "Physical Properties Data Compilation Relevant to Energy Storage. Vol. II. Molten Salts," National Bureau of Standards, NSRDS-NBS 61, part II, April 1979.
6. C. M. Kramer and C. J. Wilson, "The Phase Diagram of $\text{NaNO}_3\text{-KNO}_3$," SNLL, SAND80-8052, April 1980.
7. "Advanced Central Receiver, Phase 2, Final Report", Martin-Marietta Corp., MCR-81-1707, Sandia Contract 18-6879C, Vol. 2, May 1981.
8. J. T. Holmes, Proc. 19th Intersociety Energy Conversion Engineering Conf., p. 1700, Amer. Nucl. Soc., 1984.
9. "Molten Salt Electric Experiment (MSEE) - Phase I", Martin-Marietta Corp., MCR-84-548-2, Sandia Contract 81-7469, Sept. 1984.
10. D. A. Nissen and D. E. Meeker, *Inorg. Chem.*, 22, 716 (1983).
11. Op. cit., Ref. 7, Vol. 3 - Materials.
12. R. W. Mar and C. M. Kramer, *Solar Energy Matls.*, 5, 71 (1981).
13. A. S. Nagelberg and R. W. Mar, "Thermochemistry of Nitrate Salts," SNLL, SAND81-8879, January 1982.
14. S. H. White and U. M. Twardoch, "A Study of the Interactions of Molten Sodium Nitrate-Potassium Nitrate 50 Mol % Mixture with Water Vapor and Carbon Dioxide in the Air," EIC Laboratories, Inc., Sandia Contract 20-2991, SAND80-8182, Sept. 1981.
15. L. C. Fiorucci and S. L. Goldstein, "Manufacture, Distribution, and Handling of Nitrate Salts for Solar Thermal Applications," Olin Corp., SNLL Contractor Report, SAND81-8186, November 1982.

16. "Design, Handling, Operation and Maintenance Procedures for Hitec Molten Salt", Badger Energy, Inc., SNLL Contractor Report, SAND80-8179, Jan. 1981.
17. C. B. Allen and G. J. Janz, *J. Hazardous Matls.*, 4, 145 (1980).
18. D. A. Nissen, *J. Chem. Eng. Data*, 27, 269 (1982).
19. T. Foosnaes, et al., "Thermal Conductivity of Nitrate Mixtures," University of Trondheim (Norway), Sandia Contract 20-2992, 1982.
20. R. W. Carling, "Heat Capacities of NaNO_3 , KNO_3 , and $(\text{Na,K})\text{NO}_3$," *Proc. Third Intl. Symp. on Molten Salts*, p. 385, The Electrochemical Society, 1981.
21. D. A. Nissen and R. W. Carling, "Viscous Flow and Structure in Alkali Metal Nitrates", SNLL, SAND82-8669, April, 1982.
22. W. S. Winters, R. W. Bradshaw and P. W. Hart, "Design and Operation of Thermal Convection Loops for Corrosion Testing in Molten NaNO_3 - KNO_3 ", SAND80-8212, June, 1980.
23. R. W. Bradshaw, "Corrosion of 304SS by Molten NaNO_3 - KNO_3 in a Thermal Convection Loop," SNLL, SAND80-8856, December 1980.
24. R. W. Bradshaw, "Thermal Convection Loop Corrosion Tests of 316SS and IN800 in Molten Nitrate Salts," SNLL, SAND81-8210, Feb. 1982.
25. P. F. Tortorelli and J. H. DeVan, "Thermal Convection Loop Study of the Corrosion of Fe-Ni-Cr Alloys by Molten NaNO_3 - KNO_3 ," Oak Ridge National Laboratory, ORNL TM-8298, December 1982.
26. R. W. Bradshaw, "A Thermal Convection Loop Study of Corrosion of Alloy 800 in Molten NaNO_3 - KNO_3 ," SNLL, SAND82-8911, January 1983.
27. R. W. Bradshaw, "Kinetics of Oxidation and Elemental Depletion of Austenitic and Ferritic Steels in Molten Nitrate Salt", SNLL, SAND87-8011, 1987.
28. R. W. Bradshaw, "Oxidation of Chromium-Molybdenum Steels by Molten Sodium Nitrate - Potassium Nitrate," SNLL, SAND87-8012, 1987.
29. R. W. Carling, R. W. Bradshaw, and R. W. Mar, *J. Matl. Energy Sys.*, 4, 229 (1983).
30. R. W. Bradshaw, SNLL, unpublished data.
31. D. R. Boehme and R. W. Bradshaw, *High Temp. Sci.*, 18, 39 (1984).
32. R. W. Bradshaw, "Oxidation and Chromium Depletion of Alloy 800 and 316SS in Molten NaNO_3 - KNO_3 at Temperatures above 600°C," SNLL, SAND86-9009, Jan. 1987.
33. R. A. Osteryoung and H. Fernandez, "Corrosion of Alloys in Molten Nitrates", Univ. of Buffalo Foundation, SAND80-8181, Sept. 1982.
34. W. H. Smyrl, "Corrosion in Molten Salts Used for Solar Thermal Storage Applications", SNLA, SAND78-0246C, Dec. 1978.
35. J. J. Stephens, R. E. Semarge and R. W. Bradshaw, in *Microbeam Analysis-1986*, A. D. Romig and W. F. Chambers, eds., Microbeam Analysis Society, 1986.
36. R. W. Mar and J. C. Swearingen, *Solar Energy Matls.*, 5, 37 (1981).
37. S. H. Goods, *J. Matl. Energy Sys.*, 3, 43 (1981).
38. S. H. Goods, *J. Matl. Energy Sys.*, 5, 28 (1983).
39. S. H. Goods, *High Temperature Corrosion in Energy Systems*, p. 643, M. F. Rothman, ed., The Metallurgical Society, 1985.
40. J. L. Kaae, "Final Report on Low-Cycle Fatigue and Creep-Fatigue Testing of Salt-Filled Alloy 800 Specimens," General Atomic Co., Sandia Contract 82-8182, May 1982.
41. S. H. Goods, *Metall. Trans. A*, 16, 1031 (1985).

42. R. W. Bradshaw, "An Evaluation of Valve Packing Materials for Long-Term Use in Molten Nitrate Salt," SNLL, SAND86-8207, March 1986.
43. "Internally Insulated Thermal Storage System Development Program", Martin-Marietta Corp., MCR-79-1369, Sandia Contract 83-3638, Dec. 1979.
44. V. P. Burolla and J. J. Bartel, "The High Temperature Compatibility of Nitrate Salts, Granite Rock and Pelletized Iron Ore," SNLL, SAND79-8634, August 1979.

Table 1. Corrosion rates of selected alloys and metals in molten $\text{NaNO}_3\text{-KNO}_3$.

Alloy	Temp. ($^{\circ}\text{C}$)	Corrosion rate (microns/year)	Reference
Alloy 800	565	5	24,25
	600	6-10	25,26
	630	75	32
316SS	600	7-10	24,25
	630	106	32
304SS	600	12	23,27
IN600	600	24	30
	630	60	30
12Cr steel	600	22	27
9Cr1Mo	550	6	28
	600	23	27
2-1/4Cr1Mo	460	101	28
	500	26	28
carbon steel	460	120	30
nickel	565	>500	30
titanium	565	40	30
aluminum	565	<4	30
aluminized Cr-Mo steel	600	<4	29

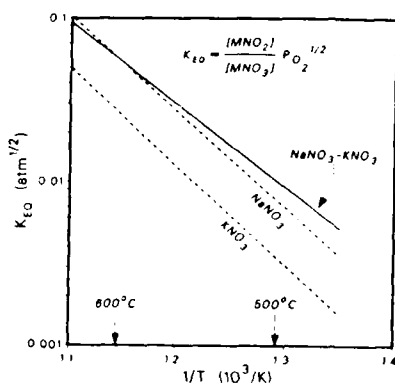


Figure 1 Arrhenius plot of the equilibrium constants for the decomposition of an equimolar mixture of NaNO_3 and KNO_3 and the pure salts.

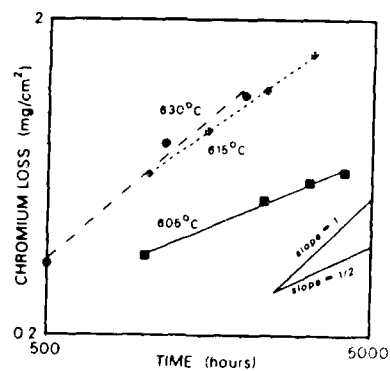


Figure 3. Kinetics of the loss of soluble chromium oxidation products from Alloy 800 immersed in the molten salt.

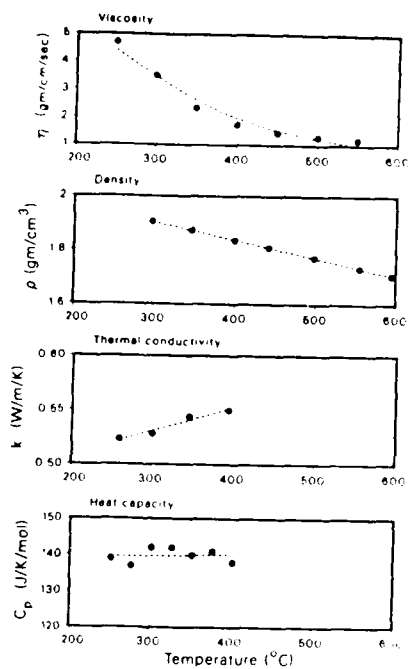


Figure 2. Experimental values of viscosity, density, thermal conductivity and heat capacity of a molten nitrate salt mixture at temperatures up to 600°C .

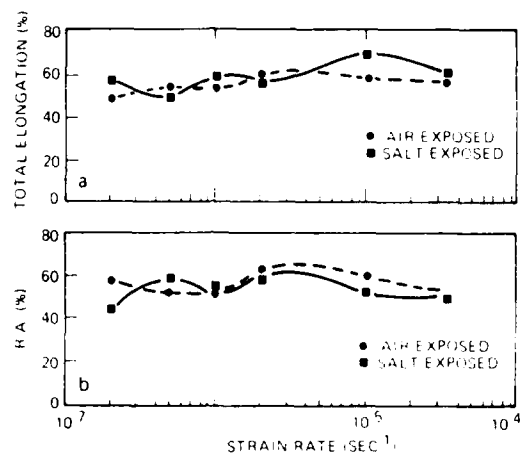


Figure 4. The effect of strain rate on the ductility of Alloy 800 exposed to molten nitrate salt at 600°C.
a) total elongation (strain to fracture)
b) reduction in area (R.A.)

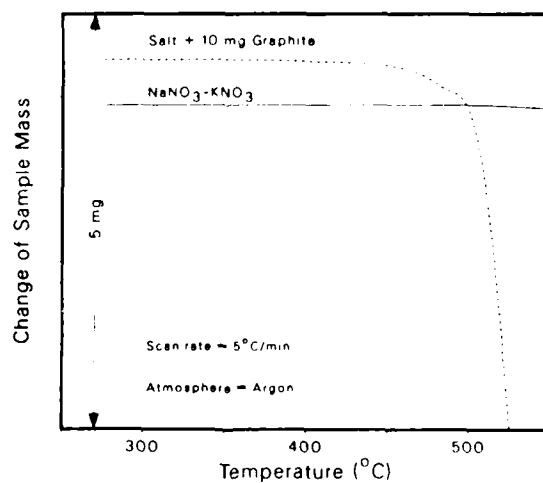


Figure 5. Thermogravimetric analysis of the oxidation of graphite by molten nitrate salt.

MOLTEN SALT CHLORINATION OF A BRAZILIAN TITANIUM ORE

Richard Louis Combes*, and Arnaud Jacques Albert Soirat*,
Mário Jardim Paixão**, and José Machado Paixão**

*Laboratoire d'Etudes et de Projets Industriels
Ecole Nationale Supérieure de Chimie de Paris
11, rue P. et M. Curie ; 75231 Paris, France

**Superintendencia de Tecnologia
Companhia Vale do Rio Doce
351, rua Sao Paulo ; 30.000 Belo Horizonte, Brazil

ABSTRACT

In the frame of the beneficiation program of an anatase titanium ore, a carbo-chlorination process of very fine particles of high TiO_2 content (80%) in molten NaCl at 880°C has been developed at a kilogram pilot scale. Titanium tetrachloride, 99% pure, has been obtained with yields as high as 98% and a mean velocity of $1000 \text{ mol.m}^{-2}\text{h}^{-1}$. Mass balance-sheets, performed on melt, residue and gas samples, have demonstrated the following facts:
-the stoichiometry is two C and two Cl_2 for one Ti,
-the alkaline-earth and rare-earth impurities contained in the ore are completely chlorinated (>99%) and dissolve in the melt enabling a subsequent recuperation.

INTRODUCTION

Anatase, an allotropic variety of rutile, can be found in "Minas Gerais" state in the center of Brazil under the form of huge and high TiO_2 content deposits (reserves over 10^9t with a 25% average content), and are being beneficiated by the top Brazilian mining company "CVRD", through a wide program called "Projeto Titânio".

In the present phase, this program is mainly aimed toward a $4 \times 10^5\text{t/y}$ production of a 90% TiO_2 concentrate for the chlorine route pigment industries. An original up-grading process has been developed by CVRD (1) in order to take into account the specificity of this world unique titanium ore deposit, and a 15000 t/y pilot plant has been running for 3 years producing a concentrate with the characteristics collected in table 1-A. In this process, quantities, as high as 4 times the production, are evolved as sub-product under the form of fine particles (>400 mesh) of high titanium oxide content, as shown in table 1-B.

These particles, which are much too small to be used in the fluidized bed chlorine process for pigment production (2), are, on the contrary, an excellent material for reactions in molten salt media due to the high specific surface of exchange (3,4).

The work presented here describes the batch production of titanium tetrachloride at a kilogram pilot scale by chlorination of these anatase fine particles, and the subsequent recuperation of rare-earth impurities of much higher financial interest.

CHOICE OF PARAMETERS

Though chlorination of titanium oxide ores be widely described (5), few processes have been developed in molten salts (6 to 17) and none for the anatase variety. Consequently, parameters such as temperature, medium and chlorinating agent have been chosen as undermentioned.

-Temperature : for kinetics reasons, most of reactions described in molten salts have been undertaken at temperatures higher than 700°C, even with lower melting point melts, as it has been shown that below this temperature the rate of reaction drops sharply (11,18).

-Melt : for the above mentioned kinetics reasons, as well as for economical ones, molten sodium chloride has been used as solvent at a temperature ranging 10° around 880°C.

-Chlorinating agent : as shown in table 2, chlorination by Cl₂ or by HCl is thermodynamically impossible for the major part of the oxides present in the anatase concentrate at 1150K (19). At this temperature, the most efficient chlorinating mixture, carbon and chlorine, has been used, the former being obtained from charcoal in-situ decomposition during the heating step of the whole charge. In fact, thermogravimetric studies have shown that carbon is obtained with a yield of 90%, while 9 to 9.5% volatile compounds are expelled around 300°C, the balance being obtained with ashes.

-Granulometry : though this parameter be settled at less than 400 mesh by the fabrication process, attempts to evaluate its influence on kinetics have been made by sintering fine particles up to 3 mesh and chlorinating them respectively.

EQUIPMENT

The pilot unit is composed by four main parts, such as heating device, reactor, condensation set, and scrubbing device, as represented in fig.1.

-The heating device is a 13 kw furnace composed by two hemi-cylindrical parts separable by moving them along a rail track. It is thermoregulated in three different regions.

-The reactor is a silica vessel, 2.8m high and 0.1m in diameter, composed of a jacket thermoregulated top, a central body in which is introduced a tube with a porous silica disk, and a bottom containing a crucible for collecting the molten salt after operation. The whole set is operated as in the pictogram represented in fig. 2.

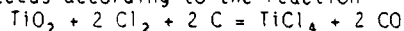
-The condensation set is composed of two vessels. The first one, filled with NaCl, is maintained at 200°C in order to trap NbCl₅ and FeCl₃ in the form of liquid chloride complex. The second vessel is cooled down in order to condense the evolved titanium tetrachloride.

-The destruction of excess chlorine is obtained by scrubbing outlet gases with a concentrated soda shower, recirculated from a 100l. tank.

RESULTS AND DISCUSSION

The function analysis of the whole process is as represented in fig. 3 and gave the following results:

-Chlorination proceeds according to the reaction



as the mean values of C/Ti and Cl₂/Ti ratios for 12 runs at 880°C have been found equal to 2.0 with an uncertainty of 0.1 respectively. This result is in agreement with previous works in the same temperature range (4,9).

-The maximum chlorination yield for titanium di-oxide has been found around 98% at 880°C, which is in good agreement with the results of Baikova in molten carnalite at 900°C (6), and significantly higher than in a classical process (2).

-The rate of chlorination was found respectively equal to 10⁴, 1.3x10³, 7.5x10², and 4x10² mol.m⁻²h⁻¹, for 400, 32, 9, and 3 mesh feed material granulometry. These values are higher than those available in literature, probably thanks to anatase high reactivity and low granulometry. For example, Sultanova and col.(16) obtained rates in the range 3 to 6x10⁻² mol.m⁻²h⁻¹, at temperatures around 700°C in molten carnalite. Another result, claimed in a Japanese patent(9), is 0.25 mol.h⁻¹, for a 0.45 kg NaCl melt at 900°C, which, assuming a reasonable cylindrical shape, would correspond to a rate of about 100 mol.m⁻²h⁻¹. A velocity of 0.13 mol.h⁻¹, is given in the example of a French chlorination patent(17) in a 10 kg reactor, which, with the same assumptions as above, would lead to a chlorination rate of 20 mol.m⁻²h⁻¹, a value that can be explained by the low temperature used (470°C) and the granulometry (100 mesh).

-The chemical analysis of TiCl₄ obtained for two different yields are reported in table 3 and demonstrate that the purity is over 99%, while the one obtained by the fluidized bed process is around 98.5% (20,21). This can be explained by a trapping and filtering effect of the molten salt bath.

-The impurities contained in the feed material (see table 1) are chlorinated more or less according to the order of ΔG indicated in table 2. Non-volatile ones, such as alkaline-earth and rare-earth, are completely dissolved in the melt, as shown in table 4. Their recuperation under the form of chloride compounds is possible by reversing the chlorine flow and filtering the melt through the porous silica disk.

CONCLUSION

The set of results obtained on a dozen runs of this pilot unit demonstrated the feasibility of production of high-grade titanium tetrachloride by molten salt chlorination. The advantages of this process with respect to the fluidized-bed one are, on one side, the use of a sub-product that is too fine and too rich in compounds which give clogging non-volatile chlorides, and on the other side, the purity of the obtained product and the possible recuperation of high-value rare-earth compounds.

For these reasons, a prototype plant of 1000 t/y capacity is to be built at CVRD's for early 1988, by "Extramet", a French company specialized in molten salts process engineering.

REFERENCES

- 1- Industrial Minerals, January (1984), p. 45.
- 2- Kirk Othmer, Encyclopedia of Chemical Technology, 23, (1983).
- 3- S. Zezyanov and V. Il'ichev, Zh. Prikl. Khim., 39, 2179, (1966).
- 4- A. Bezukladnikov, Zh. Prikl. Khim., 40, 31, (1967).
- 5- P. Pascal, "Traité de Chimie Minérale", Masson ed., Paris (1963).
- 6- A. Serebryakova and V. Efremkin, Akad. Nauk SSSR Inst. Met., 2, 78, (1959).
- 7- A. Bezukladnikov, Zh. Prikl. Khim., 36, 451, (1963).
- 8- A. Bezukladnikov, Akad. Nauk SSSR Inst. Met., 5, 135, (1961).
- 9- Seiji Sawada and Koichi Fuji, Japan patent 264, (1956).
- 10- A. Bezukladnikov, Zh. Prikl. Khim., 35, 2380, (1962).
- 11- Meng Ring Kim and B. Menlent'ev, Akad. Nauk SSSR Inst. Met., 5, 120, (1961).
- 12- S. Zezyanov and V. Il'ichev, Zh. Prikl. Khim., 39, 2174, (1966).
- 13- G. Seryakov, Zh. Prikl. Khim., 45, 9, (1972).
- 14- V. Resnichenko and V. Solomakha, Protsesty Proizvod. Titana Ego Dvukisi, 131, (1973).
- 15- G. Seryakov, Kinet. Katal. 15, 1125, (1974).
- 16- Z. Sultanova, Zh. Prikl. Khim., 52, 245, (1979).
- 17- F. Seon, G. Picard, B. Tremillon and Y. Bertaud, French patent 1825, (1981).
- 18- A. Bezukladnikov and Ya. Vil'nyanskii, Zhur. Priklad. Khim., 34, 49, (1961).
- 19- I. Barin and O. Knacke, "Thermochemical Properties of Inorganic Substances", Springer Verlag, Berlin, New-York, (1973).
- 20- R. A. Wood, The Titanium Industry in the Mid-1970's, Battelle Report MCIC-75-26, Battelle Memorial Institute, Columbus, Ohio, June 1975.
- 21- W.W. Minkler and E.F. Baroch, The Production of Titanium, Zirconium and Hafnium, 1981.

Table 1: Chemical analysis of concentrated anatase ore (1-A) and anatase fines (1-B), in weight percent.

Oxide	Concentrate A	Fines B
TiO ₂	89.20	82.01
Fe ₂ O ₃	4.80	3.77
Al ₂ O ₃	1.40	2.33
SiO ₂	3.50	0.83
P ₂ O ₅	1.22	3.66
Nb ₂ O ₅	0.56	0.78
CaO	0.20	0.85
BaO	0.10	0.15
MgO	0.10	0.07
CeO ₂	0.39	1.45
La ₂ O ₃	0.16	0.92
Y ₂ O ₃	0.01	0.09

Table 2: Free energy values (kcal/mol) for chlorination reactions at 1150 K, according to (19).

Oxide	TiO ₂	Fe ₂ O ₃	Al ₂ O ₃	SiO ₂	P ₂ O ₅	CaO	BaO	MgO
ΔG for Cl ₂	24.38	17.70	66.17	47.44	55.29	-29.30	-56.51	2.46
ΔG for HCl	31.57	28.49	76.96	54.63	66.07	-25.71	-52.90	6.05
ΔG for Cl ₂ /C	-75.61	-132.2	-83.82	-52.51	-94.60	-79.32	-106.50	-47.52

Table 3: TiCl_4 chemical analysis (weight %) for anatase fines chlorination yields of 97.5 and 70.0 % respectively.

Chlorination yield	97.5	70.0
TiCl_4	99.39	99.32
FeCl_3	0.08	0.04
AlCl_3	0.18	0.28
SiCl_4	0.07	0.05
POCl_3	0.01	0.04
NbCl_5	0.05	0.05
CaCl_2	0.02	0.01
BaCl_2	0.02	0.02
MgCl_2	0.01	0.008
CeCl_3	0.15	0.15
LaCl_3	0.02	0.02
YCl_3	0.008	0.006

Table 4: Chlorination yields and mass percentages of remaining elements in the melt at 880° C.

Element	Ti	Fe	Al	Si	P	Nb	Ca	Ba	Mg	Ce	La	C
Chlorination yield	97.5	99.5	86.5	79.0	89.0	96.5	99.5	99.5	96.0	99.5	99.9	94.0
% in melt	6.0	33.0	74.5	95.0	39.0	6.5	100	100	100	90.0	99.2	-

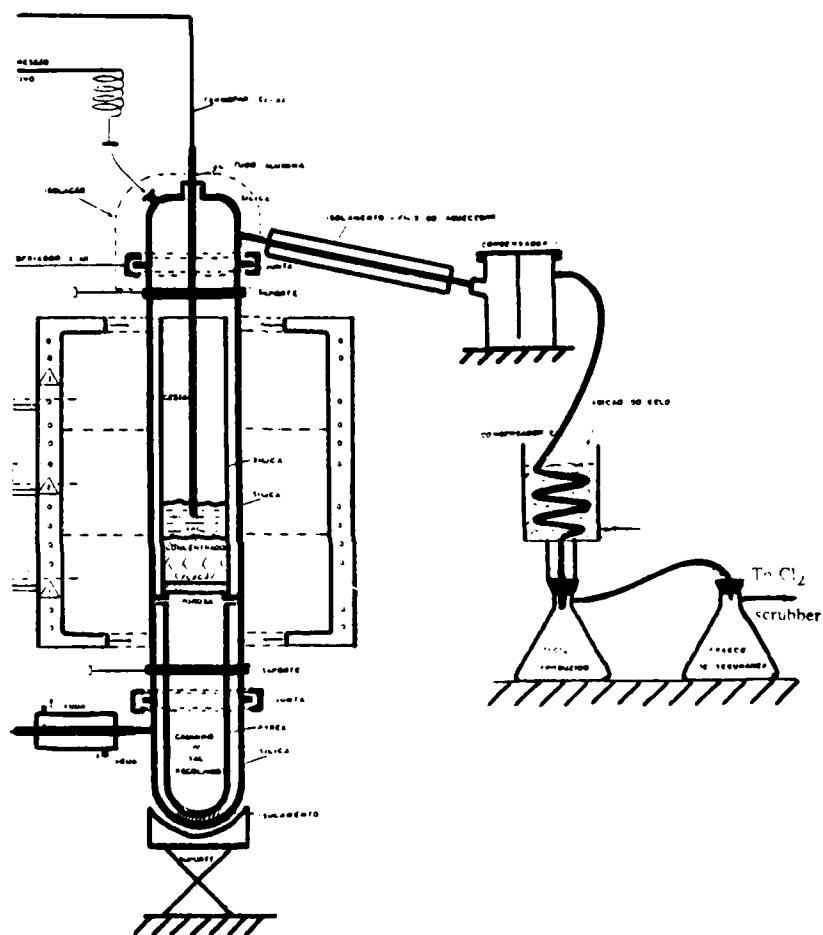


Figure 1: Pilot unit for batch kilogram scale chlorination of anatase in molten salt.

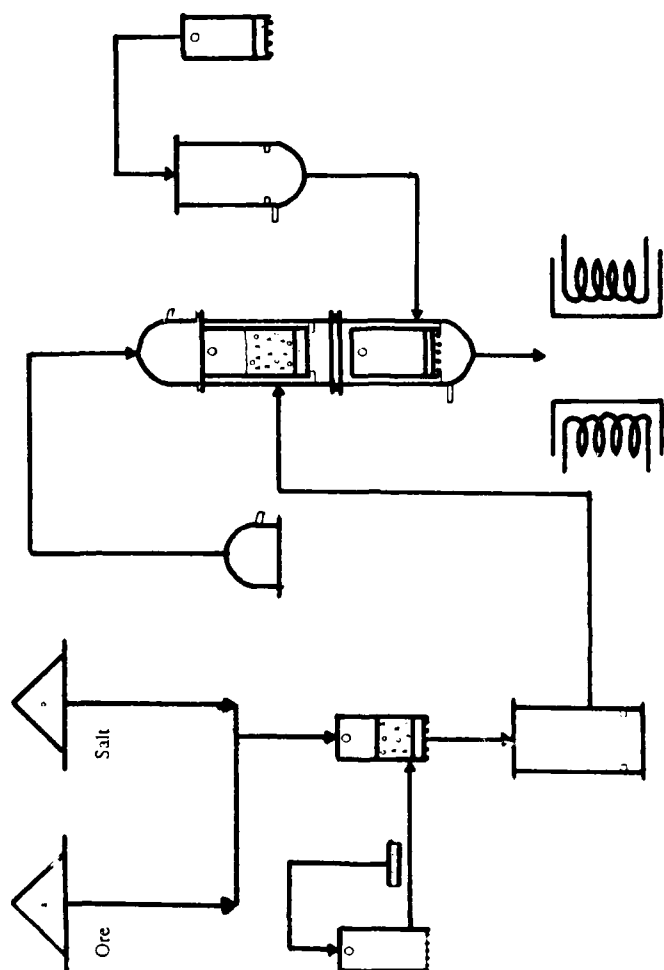
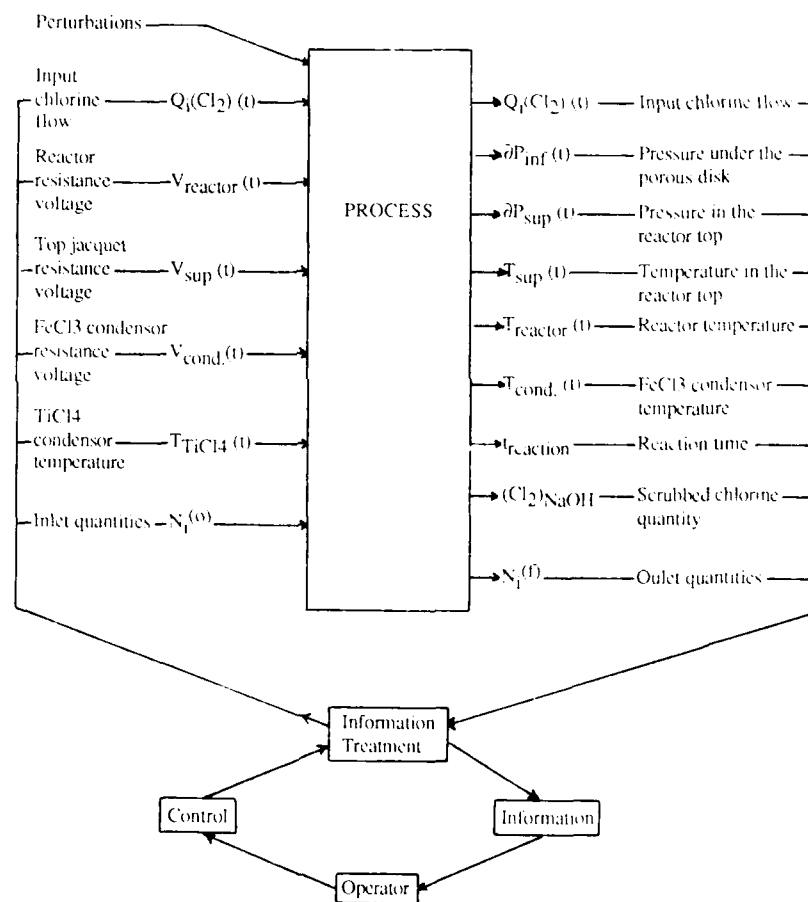


Figure 2: Procedure pictogram for the chlorination of anatase in molten salt.

Figure 3: Fonction analysis of the chlorination process of anatase in molten salt.



CATALYSIS AND REACTIVITY OF ELECTROPHILIC REACTIONS IN ROOM TEMPERATURE CHLOROALUMINATE MOLTEN SALTS

Jeffrey A. Boon, Stephen W. Lander, Jr., Joseph A. Levisky,
J. Lloyd Pflug, Lisa M. Skrzynecki-Cooke, and John S. Wilkes

The Frank J. Seiler Research Laboratory
United States Air Force Academy
Colorado Springs, CO 80840-6528

ABSTRACT

The molten salt composed of 1-methyl-3-ethylimidazolium chloride and aluminum chloride may be used as a medium for several types of electrophilic aromatic substitution reactions. The melt is liquid at room temperature and its acidity may be readily adjusted. The types of reactions found to be catalyzed by the melt were Friedel-Crafts alkylations and acylations, chlorinations and nitrations. In some cases, the reactive electrophile intermediate could be isolated from the melt.

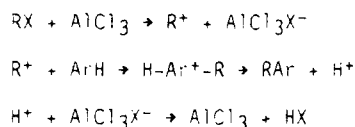
INTRODUCTION

Organic reactions in molten salts have a long but not particularly extensive history. Reactions of organic solutes in general (1) and chloroaluminate molten salts in particular (2) have been reviewed. A very thorough treatment of organic chemistry in molten salts up to 1986 has been provided by Pagni (3). Organic solvents are justifiably the medium of choice for most reactions involving organic reactants and products. However, in some cases molten salts offer advantages of faster reaction, improved yield and easier product recovery. For example, some interesting redox properties of SbCl_3 -based molten salts were exploited by Smith *et al.* to facilitate some hydrogen transfer reactions that would be highly unusual in normal organic solvents (4).

Chloroaluminates are an interesting class of molten salts, due to their relatively low melting points and rich acid-base chemistry. NaCl-AlCl_3 has a eutectic at 107°C , and may be a basic medium (in a Lewis sense) when NaCl is in excess or it may be an acidic medium when AlCl_3 is in excess. More recently, chloroaluminates composed of 1-methyl-3-ethylimidazolium chloride and aluminum chloride (MEIC-AlCl_3) have demonstrated similar acid-base properties, but are liquid at room temperature (5, 6). The below room temperature melting points for the MEIC-AlCl_3 salts and their ability to readily dissolve many organic compounds perhaps justifies considering them more as non-aqueous solvents rather than molten salts.

MEIC- AlCl_3 mixtures with excess AlCl_3 provide a medium that is very acidic but are rather easily prepared and handled. The composition is denoted as the apparent mole fraction of AlCl_3 , N . For $N \approx 0.5$, the melts are acidic, and the species responsible for the acidity is Al_2Cl_7^- . In very acidic melts ($N \approx 0.75$) there is mounting evidence that Al_2Cl_6 and $\text{Al}_3\text{Cl}_{10}^-$ may be important. It is important to emphasize the nature of the species in the acidic melts because the naive reader may be tempted to interpret the results of the organic reactions described below as simply due to dissolved AlCl_3 .

These very acidic, and of course non-aqueous, media are quite attractive for certain types of organic reactions. The key to their great utility is that they have catalytic activity similar to AlCl_3 in more conventional media, but the catalytic activity may be readily controlled through the Al_2Cl_7^- concentration, which is determined by the melt composition, N . In general the type of organic reaction promoted by acidic conditions are those where electrophilic intermediates are generated. The most notable of these are electrophilic aromatic substitutions (EAS), which includes the broad category known as Friedel-Crafts reactions. Scheme 1 shows a general



Scheme 1. Mechanism of Electrophilic Aromatic Substitution

mechanism for EAS, in this case catalyzed by AlCl_3 . The "R", "X", "Ar" and " AlCl_3 " are variables that may be selected by the chemist. "R" is not necessarily alkyl, "X" is not necessarily a halide, and " AlCl_3 " is not necessarily as simple as it appears. In this report we will describe the utility of the room temperature organic chloroaluminate melts as media for EAS. In particular, we will show that a variety of "RX" reactants may be used in the melts, and that some of the "R⁺" intermediates are surprisingly stable. We will also summarize some earlier work regarding the true participation of " AlCl_3 " for organic reactions in the MEIC- AlCl_3 ionic liquids.

EXPERIMENTAL

MATERIALS

The 1-methyl-3-ethylimidazolium chloride, aluminum chloride and the melts derived from these materials were prepared and/or purified as described earlier (5). Acetonitrile, dichloromethane, carbon tetrachloride and chloroform were dried by refluxing over P_2O_5 for two days and distilled into oven-dried bottles. The mono-acyl chlorides (acetyl, propanoyl and butanoyl) were refluxed over P_2O_5 , then vacuum distilled. The di-acyl chlorides (malonyl, succinyl,

glutaryl and adipyl) were used as received (Fluka purum grade).

INSTRUMENTAL METHODS

Melts were prepared and reaction vessels were loaded in He-filled glove boxes maintained at less than 10ppm combined O₂ and H₂O. Infrared spectra were obtained on an IBM model 32 FTIR spectrophotometer. Nuclear magnetic resonance spectra were obtained on either a JEOL model FX-90Q or IBM model NR-80 spectrometer. GC/MS analysis of the reaction products was performed on a Hewlett-Packard model 5985 GC/MS using a 3 ft column packed with 2% OV-101.

ACYLIUM INTERMEDIATES

The solid crystalline reactive intermediates were all prepared in a similar manner. The acetylum intermediate is described as an example. Acetyl chloride (19.35 g) was added slowly to an N=0.67 MEIC-AlCl₃ melt (100 g), and the mixture was allowed to stand for 12-24 hrs. White needle crystals formed during the reaction. The mixture was vacuum filtered through a fritted glass filter, washed with 1/1 (v/v) chloroform/carbon tetrachloride, dried, then stored under dry He.

GENERAL PROCEDURE FOR CHLORINATION REACTIONS

Benzene (1 mL) was added to 5.0 g of melt (N=0.33 or 0.55). Chlorine gas was slowly bubbled into the mixture for 1 hr in an inert atmosphere. A 1 mL aliquot was removed, hydrolyzed, and extracted into 3 mL of ether. The ether was dried over MgSO₄ and analyzed by GC/MS.

GENERAL PROCEDURE FOR NITRATION REACTIONS

Acidic melt (N=0.67, 1.5 mmol) was placed in an oven dried 50 mL flask, capped with a septum, and removed from the glove box. The aromatic reactant (1.0 mmol) was added via syringe. The mixture was stirred with a magnetic stir bar. The dry nitrating agent (1.5 mmol) was added very slowly. The mixture typically changed to a reddish color upon addition of the nitrating agent and the solid did not completely dissolve. The reaction was allowed to continue at room temperature for up to 3 hr. The reaction was quenched with water (10 mL), extracted with ether and analyzed by GC/MS as described above for chlorination reactions.

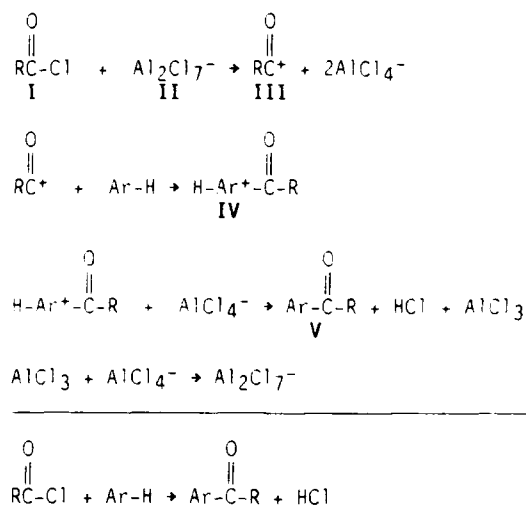
RESULTS AND DISCUSSION

ALKYLATIONS AND ACYLATIONS

The alkylation and acylation of aromatic compounds catalyzed by AlCl₃ are the archetypal Friedel-Crafts reactions. In an earlier report (7) we showed that numerous chloroalkanes will very rapidly alkylate the aromatic ring of a variety of compounds in acidic MEIC-AlCl₃ melts. The acylation of aromatic compounds by acetyl chloride also occurred in the same media, although at a slower rate. In these reactions the molten salt was acting as both the solvent (benzene is

soluble in the melts up to about 50 weight %) and the catalyst. An important feature of the use of the MEIC- AlCl_3 melts as reaction media was the ability to control easily the catalytic activity of the solvent, and thus the rate of reaction.

The earlier work also revealed some details about the mechanism of the electrophilic reactions in the room temperature melts. The reaction rate for acylation of benzene correlated precisely with the Al_2Cl_7^- concentration in the melt, which was varied by varying the proportions of MEIC and AlCl_3 . Thus, in melts with $N < 0.5$ there was no reaction, while for $N > 0.5$ the initial rate increased as N increased. Nuclear magnetic resonance (NMR) spectra of the protons in acetyl chloride in the acidic melts indicated a reaction between CH_3COCl and Al_2Cl_7^- with a 1:1 stoichiometry. The mechanism in Scheme 2 was proposed.

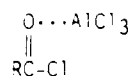


Scheme 2. Mechanism for acylation in chloroaluminate melt.

More recently some electrochemical experiments have been completed that show details about some of the reactants, intermediates and products proposed in Scheme 2. The experiments took advantage of the fact that neutral MEIC- AlCl_3 melt has an extraordinarily wide electrochemical window (8). As long as Al_2Cl_7^- was present in relatively low concentration, it was possible to observe the reduction of I, II, III and V by cyclic voltammetry. First, cyclic voltammetry of acetophenone (product V in Scheme 2, where $\text{R}=\text{CH}_3$) showed an irreversible reduction at about -0.52V in a slightly acidic melt, and an irreversible reduction at -1.80V in a slightly basic melt. In the acidic melt the reversible reduction of Al_2Cl_7^- at

-0.040V disappeared as the V was added. If excess Al_2Cl_7^- was present, both a reversible Al(III)/Al peak and an irreversible reduction of V were seen. These experiments simply show that ketones complex Lewis acids, which is well known in chloroaluminate melts (9).

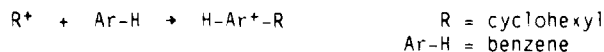
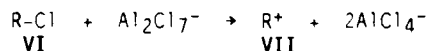
A similar set of experiments proved that acetyl chloride (I) does in fact react with Al_2Cl_7^- as proposed in Scheme 2. Figure 1 shows that when I is added to a slightly acidic melt, the reversible couple due to II disappears and a broad irreversible wave appears at about -0.60V. A control experiment of I in neutral melt showed that unreacted acetyl chloride is irreversibly reduced at -2.08V. Unfortunately, both III and V have broad irreversible reduction waves close to each other, however, the conversion of III to V can be seen in Figure 1 as benzene is added. Note that after complete reaction of III, Al_2Cl_7^- does not reappear. This is almost certainly due to the complexation of the Al_2Cl_7^- by the ketone. Electrochemistry does not provide structural information, so III may have a structure such as

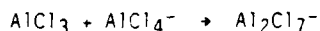


which should have a similar reactivity.

Cyclic voltammetry performed before, during and after alkylation of benzene by chlorocyclohexane also showed some interesting details. A mechanism for that reaction analogous to Scheme 2 is shown in Scheme 3.

Scheme 3 is something of a simplification, since GC/MS analysis of the products proved that di- and tri-cyclohexylbenzene were also formed. The cyclic voltammograms in Figure 2 show that the intermediate VII is seen during the reaction of VI with benzene in slightly acidic MEIC-AlCl_3 melt. The alkylation is different than the acylation in that after the reaction is complete, the regeneration of Al_2Cl_7^- is clearly shown. This is undoubtedly due to the lack of keto groups present to complex with the Al_2Cl_7^- . Neither the reactant VI nor the product VIII are electroactive, so they are not seen in Figure 2.





Scheme 3. Alkylation in Chloroaluminate Melts

ISOLATION OF ACYLIUM INTERMEDIATES

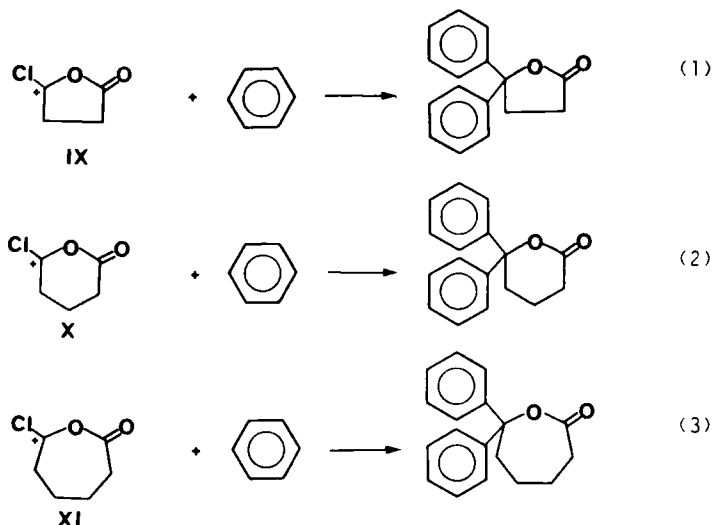
During the course of the study of acylation reactions, we observed that sometimes a solid product would form in the acidic MEIC-AlCl_3 melt before the addition of an aromatic substrate. For example, acetyl chloride was added to an $N=0.67$ MEIC-AlCl_3 melt so that it was equimolar with the Al_2Cl_7^- present. Over a period of several hours a mass of large needle crystals formed, which could be filtered and isolated free of melt. These crystals are apparently the $\text{R-CO}^+\text{AlCl}_4^-$ formed in the first step shown in Scheme 2, where R is CH_3 . There was no aromatic reactant present to consume the R-CO^+ and the tetrachloroaluminate salt was sufficiently insoluble in the melt to allow its isolation.

It is difficult to prove that the crystalline material is actually $\text{R-CO}^+\text{AlCl}_4^-$. While the crystals are stable for a long period, they are very reactive. Traces of moisture produce acetic acid and the material reacts with many organic solvents. The $\text{R-CO}^+\text{AlCl}_4^-$ crystals react very rapidly with aromatic compounds to produce the acetylated product, as expected if the crystals are in fact an isolated form of the reactive intermediate in Scheme 2. The elemental analysis is consistent with $\text{R-CO}^+\text{AlCl}_4^-$, although the Cl analysis is expectedly off from the theoretical value. Infrared and NMR analysis of solutions of the crystals were ambiguous due to suspected reaction with the solvents. Solid state IR gave the C-O stretching frequency reported for the R-CO^+ ion (10). Determination of the crystal structure by X-ray diffraction is now in progress. There is precedent for compounds of the type $\text{R-CO}^+\text{AlCl}_4^-$ (11), although their properties are not well described.

Propanoyl and butanoyl chlorides did not produce crystals when added to the acidic MEIC-AlCl_3 melt, however in both cases a second phase separated as an oil. We were unsuccessful in crystallizing the oils. Both of the oils were very reactive and gave products expected from material with the composition $\text{R-CO}^+\text{AlCl}_4^-$, where R is ethyl or propyl.

The acyl chlorides derived from diacids also sometimes produce a solid isolatable material from the melts in the absence of an aromatic reactant. Succinyl chloride, $\text{ClCOCH}_2\text{CH}_2\text{COCl}$, and adipoyl chloride $\text{ClCOCH}_2\text{CH}_2\text{CH}_2\text{CH}_2\text{COCl}$, produced solid crystalline materials IX and X from acidic melt. Glutaryl chloride, $\text{ClCOCH}_2\text{CH}_2\text{CH}_2\text{COCl}$, gave an isolatable material XI as an oil phase. The materials derived from the diacid chlorides have not been completely characterized, but their products of reaction with benzene suggest

that they are not the simple tetrachloroaluminate salts. The products of the reactions shown in Equations 1, 2 and 3 suggest that rearranged cyclic electrophiles are formed.



CHLORINATION REACTIONS

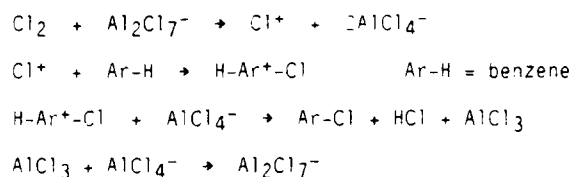
Chlorination of organic compounds can occur via electrophilic, nucleophilic and free-radical mechanisms. We have observed what we believe to be electrophilic chlorination reactions in the MEIC- AlCl_3 melts, although these reactions are not as well characterized as the alkylations and acylations described above. The possibility that the chlorinations described below proceed by free-radical mechanisms have not been rigorously excluded; however, control reactions done in the dark mitigate that mechanism.

We previously reported that chlorine gas will cause the substitution of the hydrogens at the 4 and 5 positions on the imidazolium ring of the 1-methyl-3-ethylimidazolium cation of the melt itself (12). The chlorination proceeds in both acidic and basic melts, but not in the pure molten MEIC. This suggests that chloroaluminate ions are required, but the details must be different in the acidic versus the basic composition melts.

We report here for the first time that benzene is chlorinated by chlorine in both acidic and basic melts. Figure 3 shows the result of the reaction of chlorine with benzene in basic and acidic melts. In both reactions the principal product is chlorobenzene (retention time 3.2 min). In acidic melt substantial amounts of at least two dichlorobenzene isomers are formed (4.3 and 4.5 min) and some

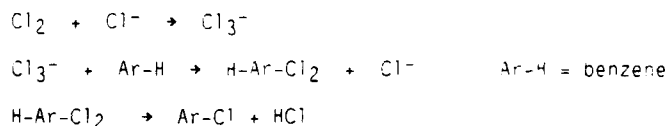
trichlorobenzene products are seen. In basic melt no polychlorobenzenes are observed, but substantial formation of tetrachlorocyclohexene isomers (6-7 min) and hexachlorocyclohexene isomers (7.5-8.5 min) occurs.

Electrophilic reactions could be occurring in both basic and acidic media. In the acidic melts, clearly a very reactive electrophile is formed, as shown by the extensive polychlorination. In a process analogous to the formation of the electrophile in the Friedel-Crafts reactions discussed above, it is reasonable to suggest the mechanism depicted in Scheme 4.



Scheme 4. Chlorination in Acidic Chloroaluminate Melts

It is more difficult to imagine electrophilic chlorination in the basic melts because the base would inevitably destroy the electrophile. The explanation lies in the fact that chlorine reacts with Cl^- (the base in basic MEIC- AlCl_3 melt) to form the trichloride ion (Cl_3^-) (13). This in effect neutralizes the melt, and the trichloride could conceivably act as an electrophile. A mechanism is proposed in Scheme 5.



Scheme 5. Chlorination in Basic Chloroaluminate Melts

The melt itself does not catalyze the chlorination in basic melts, and the reaction should proceed only while there is excess chlorine available. In fact, the reactions in basic melt were run with chlorine gas bubbling through the reaction mixture.

The mechanisms proposed in Schemes 4 and 5 are largely speculative, and there is little hard proof for either one. They do explain the

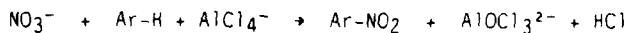
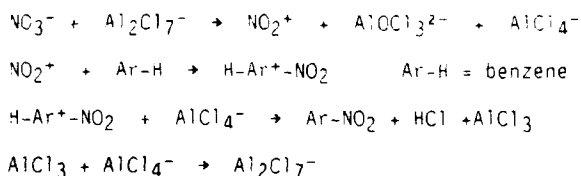
relative rates of chlorination and the fact that chlorination can occur at all in basic melts.

NITRATION REACTIONS

The nitration of aromatic compounds is the classic textbook example of EAS. The reaction is usually run in very strong mineral acid, with HNO_3 as the source of the putative NO_2^+ electrophile. The high Lewis acidity available in the MEIC-AlCl_3 melts suggested that nitration reactions may be possible in the room temperature melts. Nitric acid was rejected as the source of the electrophile, since we wished to avoid the introduction of protons into the medium. There is mention in the literature (14) that nitrate can act as a nitrating agent for aromatic compounds, although NO_3^- itself cannot be the electrophile responsible.

When benzene is placed in an acidic ($N=0.67$) melt containing KNO_3 (1.5:1), nitrobenzene (55%) results. Toluene gives an expected increased yield (77%), while nitrobenzene showed no reaction. The amount of melt was carefully measured to have at least a 1.5:1 molar excess of Al_2Cl_7^- , since this Lewis acid species must react with KNO_3 to produce an NO_2^+ equivalent. Unfortunately, since oxide is scavenged from the KNO_3 by the Al_2Cl_7^- , the melt is a reagent, and not a catalyst as it was in the alkylation reactions. Further studies are being performed to find a catalytic nitration system. Other ionic nitrating agents tested to date include NH_4NO_3 and NO_2BF_4 . These gave reduced yields with benzene (about 10%).

As for the other electrophilic reactions described in this report, we propose a mechanism to aid in the visualization of the reactions. Scheme 6 shows a mechanism for nitration from nitrate in acidic melts.



Scheme 6. Nitration in Acidic Chloroaluminate Melts

The crucial step in Scheme 6 is the formation of the NO_2^+ electrophile from the nitrate ion; the first step shown above. A similar extraction of oxide by the Al_2Cl_7^- in acidic chloroaluminate melt is known for carbonate. The AlOCl_3^{2-} product may not be the true aluminum oxychloride species, since oxide is known to take many forms in chloroaluminate melts.

SUMMARY

Several electrophilic reactions in acidic room temperature chloroaluminate molten salts have been described. They all have in common the rapid formation of an electrophile by the melt itself. The use of the room temperature molten salts as reaction medium for these organic reactions has several attractive features. First, the melts have surprisingly good solvent properties for organic compounds. Second, the reactions are entirely homogeneous, unlike most similar reactions catalyzed by suspended $AlCl_3$. Third, the rates are very rapid, and may be controlled easily by adjusting the melt composition. Fourth, the isolation of the products is fast and easy, since the melt can be hydrolyzed and the organic products extracted from the aqueous phase. One feature of the molten salt solvents not examined here is the temperature effect. The melts are liquid at very low temperatures, yet can also be raised to high temperatures without significant vapor pressure or decomposition.

REFERENCES

1. W. Sundermeyer, Angew. Chem. Int. Ed., **4**, 222 (1965).
2. H. L. Jones and R. A. Osteryoung in Advances in Molten Salt Chemistry, J. Braunstein, G. Mamantov and G. P. Smith, eds., Plenum Press, 1971.
3. R. Pagni, Advances in Molten Salt Chemistry, in press.
4. S. P. Zingg, A. S. Dworkin, Morten Sørli, D. M. Chapman, A. C. Buchanan, III, and G. Pedro Smith, J. Electrochem. Soc., **131**, 1602 (1984).
5. J. S. Wilkes, J. A. Levisky, R. A. Wilson, and C. L. Hussey, Inorg. Chem., **21**, 1263 (1982).
6. A. A. Fannin, Jr., D. A. Floreani, L. A. King, J. S. Landers, B. J. Piersma, D. J. Stech, R. L. Vaughn, J. S. Wilkes, and J. L. Williams, J. Phys. Chem., **88**, 2614 (1984).
7. J. A. Boon, J. A. Levisky, J. L. Pflug and J. S. Wilkes, J. Org. Chem., **51**, 480 (1986).
8. M. Lipsztajn and R. A. Osteryoung, J. Electrochem. Soc., **130**, 1968 (1983).
9. G. T. Cheek and R. A. Osteryoung, J. Electrochem. Soc., **129**, 2488 (1982).

10. G. Olah, A. Germain and A. M. White, in Carbonium Ions, Vol. 1, G. A. Olah and P. von R. Schleyer, eds., Interscience, 1968, p. 2077.
11. J.-M. LeCarpentier and R. Weiss, Acta Cryst., B28, 1421 (1972).
12. F. M. Donahue, J. A. Levisky, G. F. Reynolds and J. S. Wilkes, Proc. 5th Intl. Symp. Molten Salts, The Electrochemical Society, 1986, p. 332.
13. Z. Karpinski and R. A. Osteryoung, Inorg. Chem., 24, 2259 (1985).
14. G. A. Olah and S. J. Kuhn, in Friedel-Crafts and Related Reactions, G. A. Olah, ed., Interscience, 1964, p. 1395.

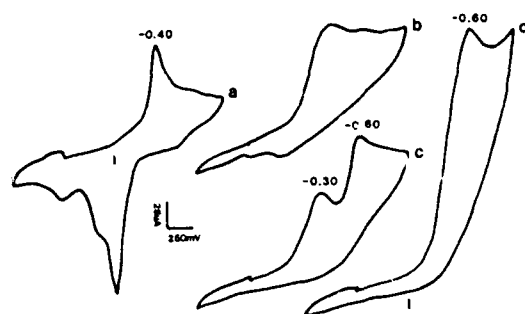


Figure 1. Cyclic voltammetry of acylation reaction. a: slightly acidic melt before addition of reactants. b: acetyl chloride in slightly acidic melt. c: immediately after addition of benzene to b. d: 10 min. after addition of benzene.

Figure 2. Cyclic voltammetry of alkylation reaction. a: slightly acidic melt with benzene added. b: immediately after addition of chlorocyclohexane. c: 20 hours after addition of chlorocyclohexane.

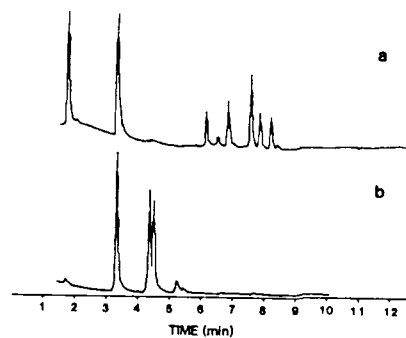
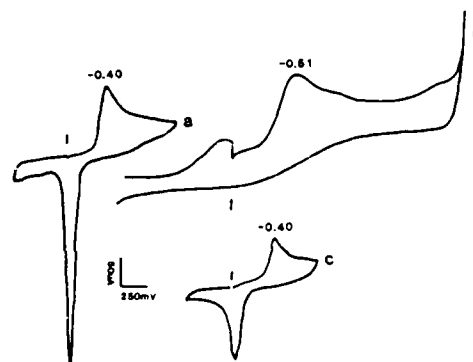


Figure 3. Total ion chromatograms of products of chlorination of benzene. a: basic melt ($N=0.33$). b: acidic melt ($N=0.55$).

THE ACYLATION OF COAL AND MODEL COAL COMPOUNDS
IN ROOM TEMPERATURE MOLTEN SALTS

David S. Newman, Thomas H. Kinstle and Gnanaraja Thanoo
Department of Chemistry
Bowling Green State University
Bowling Green, OH 43403

ABSTRACT

An ambient temperature molten salt, 2:1 pyridinium chloride-aluminum chloride, was used as the reaction medium and catalyst for the Friedel-Crafts acylation of coals and model coal compounds. The solubilities of the acylated coals were increased substantially over the solubilities of the unreacted coals, but with relatively little modification of the sub-units of the coal macromolecule. Acylated coal was then oxy-alkylated and the oxy-acylated coal's solubility was substantially greater than that of the acylated coal. Both acylation and oxy-acylation show great promise as techniques for modifying coal prior to liquifaction or desulfurization.

INTRODUCTION

It has become apparent that gaseous byproducts of the combustion of coal are a major contributor to acid rain. Because a gradual change from a primarily petroleum based economy to a coal based economy is virtually inevitable, cleaning, liquifying, gasifying, and generally modifying coal have become major goals of chemistry and chemical engineering. Ideally, the way to modify coal is to devise chemical scission reactions which remove designated portions of the coal or alter specific chemical bonds in a known way. Unfortunately, coal is extremely complex and very heterogeneous. With the possible exception of Illinois #6, no individual coal's structure is even remotely well enough understood to begin to devise coal-specific scission reactions. Nevertheless, there are several reactions that show promise for modifying many coals in a

known way, and may, in fact, be quite general. Among these are Friedel-Crafts (F-C) alkylations and acylations (1,2,3) and Oxyalkylations (4,6).

In an earlier investigation, we F-C alkylated PSOC 244 high sulfur coal [C:55.8%, H:7.5%, N:0.95%, S:7.5% (total), ash:19.5%, O:12% (by difference)] with 2-propanol in an ambient temperature molten salt, 2:1 aluminum chloride-pyridinium chloride (pyrCl-AlCl₃) (3). We found that this alkylated coal's solubility in 3:1 benzene-methanol was approximately 28%, a five-fold increase over that of the untreated coal. The increased solubility is most likely due to the breaking of methylene chains holding the sub-units of the coal macromolecule together. The molten salt served as both catalyst and solvent for the reaction.

Liotta and coworkers found that oxy-alkylating several coals, including Illinois #6, caused a four to five-fold increase in the coal's solubility in a variety of solvents. The reason for the increased solubility seems to be that the alkyl group replaces a labile hydrogen on an hydroxyl group thereby preventing hydrogen bonding and causing the coal to "denature", as it were. The denatured coal is more easily solvated or liquified than the untreated coal.

F-C alkylation alters the coal's primary structure and oxy-alkylation alters its secondary structure making it potentially more susceptible to further modification, but with minimum damage to the sub-units of the coal macromolecule. F-C acylation of coal is expected to have a similar effect to that of alkylation, but because of the acid-base equilibrium

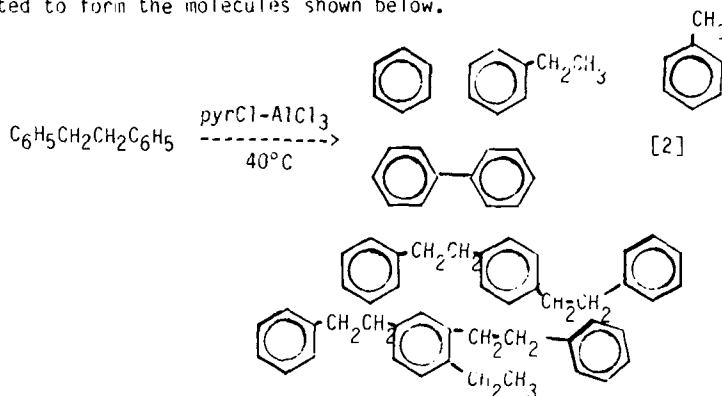


may be a more efficient process if acetyl chloride is the acylating agent. The chloride is easily removed forming the very reactive 1-oxoethyl cation (vide infra). Therefore, in the present investigation, we initially acylated several coals and model coal compounds in pyrCl-AlCl melt. We then combined F-C chemistry with oxy-alkylation chemistry by oxy-alkylating previously acylated coals. The reactions were monitored by noting changes in the coal's solubility in 3:1 benzene-methanol (benz-meth) and by various instrumental and analytical techniques.

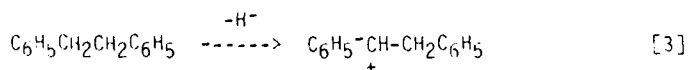
RESULTS AND DISCUSSION

F-C Acylation of Model Coal Compounds

The model coal compounds 1,2-diphenylethane (bibenzyl) and benzophenone were separately introduced into the pyrCl-AlCl_3 melt and allowed to react at 40°C for four hours under a nitrogen atmosphere. This was done to test the extent of auto-alkylation. Bibenzyl reacted to form the molecules shown below.



Each of these species was identified by GC/MS or by HPLC or by HNMR. In addition, a polymeric material of indeterminate structure was formed. Benzophenone did not react with itself and could be recovered from the melt. Acetyl chloride did not polymerize in the melt. These data indicate the initial step in the autoalkylation reaction is the removal of a H^- ion from the bibenzyl to form the carbonium ion:

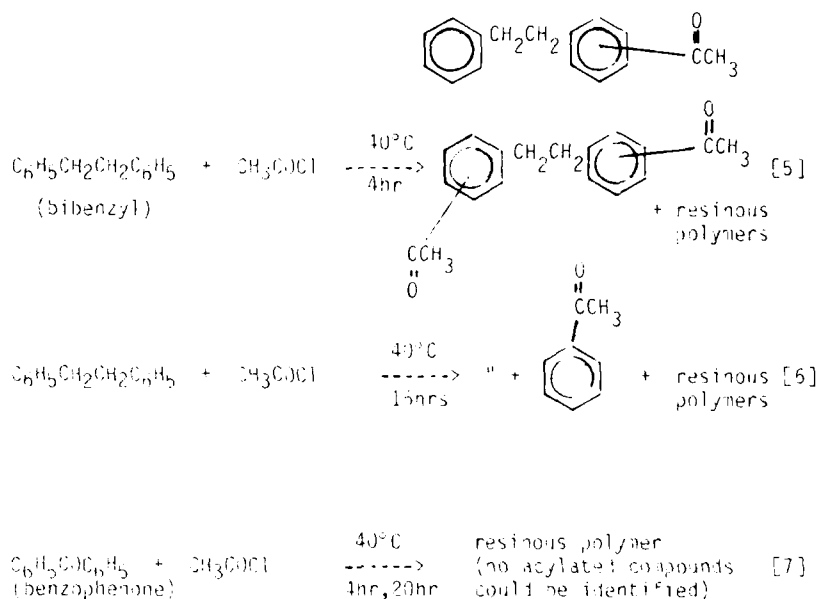


Another bibenzyl then attacks the carbonium ion and eventually forms the identified products via the "transalkylation" mechanism described by Roberts and coworkers (6). The benzophenone does not readily eliminate a hydride ion to form a carbonium ion and consequently does not polymerize. Acetyl chloride probably reacts with the heptachloroaluminate to form the 1-oxoethylum ion (7):



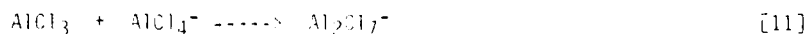
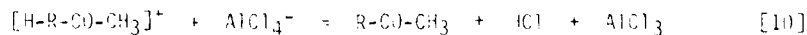
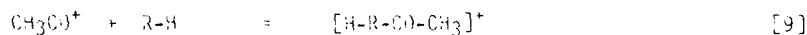
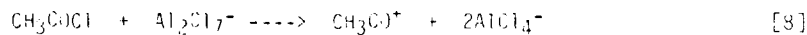
but the pyridinium ion is too inert and positively charged, and there is no other substrate for the cation to attack, so no further reaction occurs.

Bibenzyl and benzophenone were then acylated in the pyrCl-AlCl_3 melts to give the products shown below:

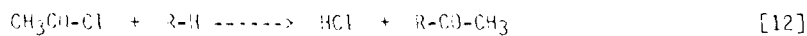


Curiously enough, identified products of the acylation reaction of bibenzyl never contained more than one acyl group per benzene ring. This is the same result Wilkes and coworkers found for the acylation of benzene in acidic 1-methyl-3-ethylimidazolium chloride-aluminum chloride (MEICl-AlCl_3) ambient temperature molten salt (7).

The mechanism for the acylation is probably



The net reaction being



with the first and last steps in the above mechanism being very rapid (7).

F-C Acylation of Coal

The coals used in this study were Illinois #6 and PSOC-1103. Their chemical analyses before and after demineralization are listed in Table I.

TABLE I
% Composition of Coals

	IL #6		PSOC-1103	
	Raw	Demineralized	Raw	Demineralized
C	58.7	58.57	76.8	79.5
H	4.1	4.91	5.2	5.4
N	1.1	1.36	1.4	1.64
S	4.47	5.22	2.18	1.89
Ash	5.58	3.78	4.9	1.64
O	15.78	16.19	9.52	9.44

Both coals are bituminous with the PSOC-1103 being of higher rank than the IL #6. All of the subsequent coal chemistry was done with HF/HCl demineralized samples (vide infra).

The coals were slurried in the melt for 16 hours at 40°C with no acylating agent present and their solubilities in 3:1 benz-neth were compared with their original solubilities. The PSOC-1103 had an initial solubility of 4.92 wt% and a final solubility of 6.83 wt%. The IL #6 had an initial solubility of 2.65 wt% and a final solubility of 2.60 wt%. These data indicate that the coals were not reacting with the melt to any significant extent. This was further verified by comparing the FT-IR spectra of each of the coals before and after contact with the melt.

The effects of time, temperature and acylating agent on each of the coals' solubility in 3:1 benz-neth were measured. Table II shows the results of varying the acylating agent, but keeping temperature and time constant, on both solubility and weight increase.

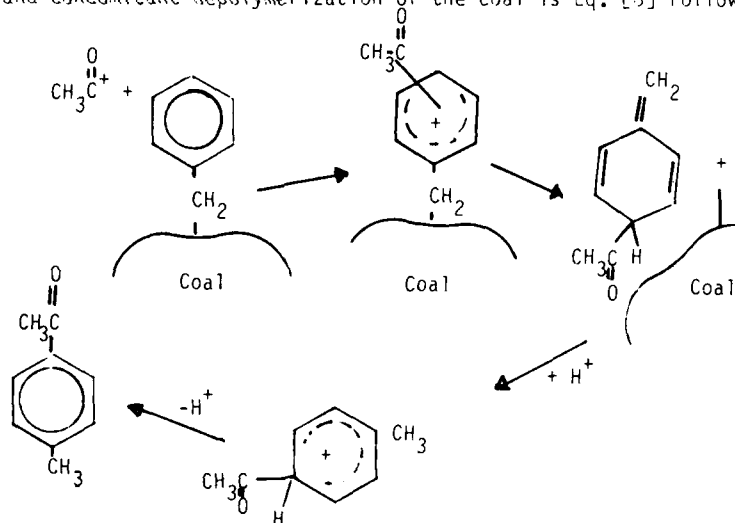
TABLE II

The Effect of Acylating Agent on Solubility and Weight Increase

Acylating Agent	PSOC-1103 (4hr, 40°C)		IL #6 (15hr, 40°C)	
	% weight increase	% solubility	% weight increase	% solubility
Acetyl Chloride	12.11	14.28	14.63	16.46
Acetic Anhydride	8.20	12.10	12.18	11.16
Propionic Anhydride	9.18	12.90	12.16	14.08

These data indicate a rough correlation between weight increase and solubility increase, which is not unexpected because acyl groups are replacing hydrogens on the coal macromolecule. The data also indicate that acetyl chloride is the most efficient acylating agent.

The first step of the probable mechanism for the F-C acylation and concomitant depolymerization of the coal is Eq. [3] followed by:



The final step is the formation of the acylated depolymerized coal and HCl.

The effect of temperature on weight increase and solubility is shown in Table III

TABLE III

The Effect of Temperature on Weight Increase and Solubility

Coal	Reaction Time (hrs)	40°C		60°C	
		% weight	% solubility	% weight	% solubility
PSOC-1103	4	12.11	14.28	11.98	14.50
	8	8.60	11.20	9.29	13.90
IL #6	15	14.63	16.46	14.80	15.15
	30	13.83	14.76	14.10	14.20

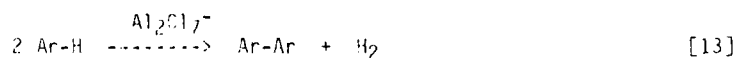
These data indicate there is little or no advantage to acylating at higher temperatures. In the case of the 30 hr IL #6 experiment, there might even be a slight disadvantage because Scholl reactions may polymerize the coal faster than the acylation depolymerizes it (8). However, the experimental errors involved are such that the temperature dependent differences in solubilities shown in Table III may be insignificant. Since we were interested in finding the mildest conditions possible for coal modification, the lower temperature was used in most reactions. The data also indicate PSOC coal gains less weight after reacting for 8 hrs than it gains after reacting for 4 hrs. Why this occurs is not clear, but it happens at both 40°C and 60°C.

TABLE IV

Effect of Reaction Time on Solubility

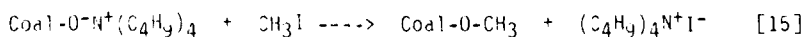
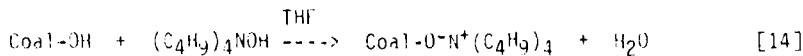
Reaction Time (hr)	PSUC-1103 Solubility	IL #6 Solubility
4	14.28	4.10
8	11.20	6.90
15	11.48	16.46
30	10.21	14.76

The data in Table IV strikingly illustrate the differences found between coals ostensibly treated in identical fashion. The solubility of PSUC-1103 coal reaches a maximum after reacting between 4 and 5 hrs, whereas the solubility of IL #6 is maximized after reacting between 15 and 16 hrs. The increase in weight of each coal follows the same pattern. A possible reason for this is that the aryl sites used for acylation are near the surface of the PSUC coal macromolecule, but are buried in the interior of the IL #6 coal so that the acylating agent has to slowly diffuse through the coal to the appropriate site to react. The PSUC system seems to reach a steady state in about 7-8 hrs and then neither increases in weight nor decreases in solubility significantly. IL #6 takes approximately 16 hrs to reach a steady state. The decrease in the coals solubility is probably caused by Scholl type reactions repolymerizing the coal.



Oxy-Alkylation of Acylated Coal

PSUC-1103 and IL #6 coal were oxy-alkylated in tetrahydrofuran (THF) by a method similar to that used by Liotta (4,5) and the solubilities of the oxy-alkylated product measured. The method is summarized by the equations:



Since the alkylammonium hydroxide quantitatively attacks oxygens

with acidic hydrogens, oxy-alkylation should not be directly affected by a prior acylation. In other words, the F-C alkylation should break methylene chains and the oxy-alkylation should break hydrogen bonds. We therefore oxy-alkylated F-C acylated coals and measured their solubilities. The results of the oxy-alkylation experiments are summarized in Table V. It is immediately obvious from these data that oxy-alkylation alone is at least as efficient

TABLE V

% Solubility of Oxy-alkylated Coal

Coal	O-alkylated	Acylated	Acylated + O-alkylated	O-alkylated + acylated
PSOC-1103	16.1	14.28	20.52	11.62
IL #6	17.4	16.46	22.25	16.81

a coal solubilizing technique as is F-C acylation. It is also apparent that oxy-alkylating and then acylating is ineffective. In the latter case, the ether and ester linkages formed during oxy-alkylation of the coal are converted to alcohols, acids, and methyl chloride, in the acidic melts, and hydrogen bonding occurs all over again. Acylation, followed by oxy-alkylation, is substantially better at solubilizing the coals than is either technique alone, but not as efficient as the two methods should be if they functioned together as well as each did separately. A plausible reason for this apparent negative synergism is that we have not optimized conditions for oxy-alkylating acylated coal and these conditions are considerably different than for raw coal. Our oxy-alkylating solubilities were always 15-20% lower than those reported by Liotta using the same coal in the same solvent, which is not unusual in coal research. This means our oxy-alkylation technique is effectively "calibrated" for unreacted coals. Alternatively the coal is somehow polymerized during the oxy-alkylation. Why this would occur is not clear at this point.

CONCLUSION

The 2:1 pyridinium chloride-aluminum chloride ambient temperature molten salt is an extremely good medium for F-C acylations and alkylations of coal and model coal compounds.

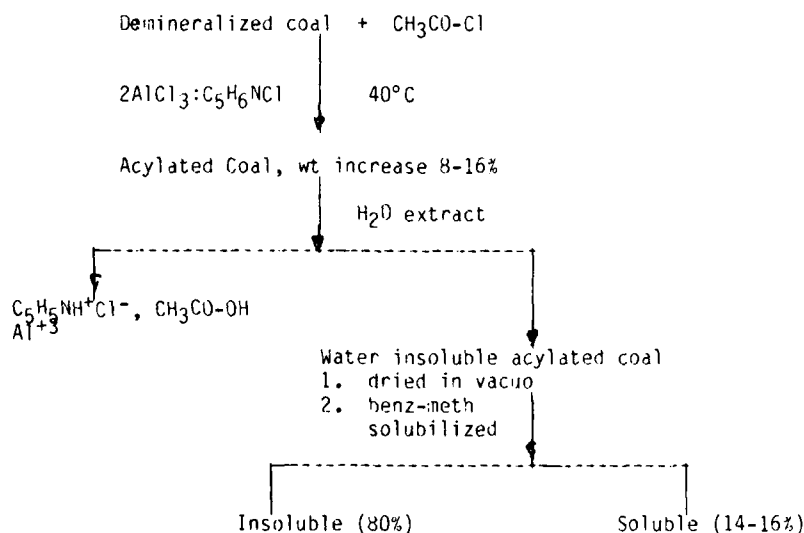
Modification of the coal's primary structure (F-C reactions) and secondary structure (oxy-alkylations) are possibly important

first steps in designing scission reactions to solubilize coal and remove undesirable moieties from the coal macromolecule. For example, demineralization followed by acylation, followed by oxy-acylation might substantially improve the coals desulfurizability.

EXPERIMENTAL DETAILS

Each coal was ground in a shatter box for 15 minutes and then demineralized using an aqueous HF/HCl solution (see ref 3 for details). Reagent grade AlCl_3 (Cerac 99.999%) and pyridinium chloride which had been distilled at 219°C were used to form the 2:1 melt which was stored in a dry box and not purified further. Weighed amounts of coal, acylating agents, model compounds, etc., were added to the melt which had been poured into a reaction vessel. The vessel was removed from the dry box, placed in a constant temperature bath and the reaction mixture stirred with a magnetic stirrer and maintained under a nitrogen atmosphere.

After the requisite amount of time had elapsed, the reaction was carefully quenched by first cooling the closed reaction vessel and then dropping small pieces of ice into the reaction vessel so as not to raise the temperature substantially. After all of the AlCl_3 had reacted with water, the aqueous slurry was filtered, and the reacted coal dried and weighed. These operations are summarized schematically below. For more experimental detail see ref. 2,3.



LIST OF REFERENCES

1. J.W. Larsen, W.F. Kuemmerle, *Fuel*, 55, 162 (1979).
2. D.S. Newman, R.E. Winans, "Proceedings of the Third International Symposium on Molten Salts", G. Mainantov, M. Blander, G.P. Smith, Editors, The Electrochemical Society Softbound Series, p. 425. Pennington, N.J., 1981.
3. D.S. Newman, R.E. Winans, R.L. McBeth, *J. Electrochem. Soc.* 131, 1079 (1984).
4. R. Liotta, *Fuel*, 58, 724 (1979).
5. R. Liotta, K. Rose, E. Hippo, *J. Org. Chem.*, 46, 277 (1981).
6. R.M. Roberts, S. Roengsumran, *ibid*, 46, 3689 (1981).
7. J.A. Boon, J.A. Levisky, J.L. Pflug, J.S. Wilkes, *ibid*, 51, 480 (1986).
8. A.T. Balaban and C.D. Nenitzescu, in "Friedel-Crafts and Related Reactions", Vol. II, Interscience. New York (1965).

SOME AROMATIC REACTIONS USING AlCl_3 -RICH MELTEN SALTS

E. Ota

College of Technology, Gunma University
Tiryu, Gunma 376 Japan

ABSTRACT Alkylation, acylation, condensation, and allyl- and aryl-migration were studied using two acidic molten salts with compositions of $[\text{AlCl}_3\text{-KCl-NaCl}]$ (MS-A) and $[\text{AlCl}_3\text{-N-ethylpyridinium bromide}]$ (MS-B). In MS-A, 1-methylnaphthalene was methylated with MeI and Me_2SO , yielding mixtures of 1,2-, 2,6-, and 1,5-dimethylnaphthalenes, particularly in a high yield of the 1,5-isomer with Me_2SO . 1- and 2-naphthyls both gave perylene as the main product when heated in MS-A. Benzoylation and acetylation of naphthalene in MS-A resulted in a very high β -selectivity of 97 and 98%, respectively. At high temperatures, 1-benzoylnaphthalene was proved to isomerize to the 2-isomer through intermolecular mechanism. Anthraquinone was successfully reduced from benzene and phthalic anhydride in a yield of 94% by a one pot synthesis involving Friedel-Crafts' acylation and successive intramolecular condensation in MS-A. MS-A is an acid catalyst and a dehydration agent.

Friedel-Crafts' and related aromatic reactions were conveniently studied using two kinds of acidic AlCl_3 -rich molten salts shown below as MS-A and MS-B.

$[\text{AlCl}_3\text{-60-50(15.7- NaCl 26.5 mol \%), mp 95 }^\circ\text{C} \dots \text{MS-A (1)}$

$[\text{AlCl}_3\text{-66.7- N-ethylpyridinium bromide 33.3 mol \%}],$
liquid at room temperature.....MS-B (2)

1. ISOMER DISTRIBUTION IN METHYLATION OF 1-METHYLNAPHTHALENE USING MS-A

In connection with our earlier study (5) on isomerization and other reactions of methylnaphthalenes in MS-A, a supplementary study was carried out on methylation of 1-methylnaphthalene with interest of orientation scheme 1.

EXPERIMENTAL

A mixture of 0.01 mol of α -methylnaphthalene and 0.01 mol of MeI or 0.005 mol of Me_2SO was added all at once to MS-A, containing 0.6 mol of AlCl_3 , at 100°C in an air stream. After given periods of time specimens of the mixture were taken out, poured into an ice-HCl mixture, extracted with benzene, and subjected to analysis of the products by gas chromatography.

RESULTS AND DISCUSSION

In both reactions quick isomerization of the starting α -methylnaphthalene to the β -isomer was observed and the amounts of both isomers decreased quickly within the first 5 min and then gradually. The methylating agents, especially MeI, seemed to be lost partially by evaporation. The main products were 1,2-, 2,6-, and 1,5-dimethylnaphthalenes, commonly in both reactions, but the isomer distribution was different from each other as shown in Fig. 1. The higher yield of 1,5-dimethylnaphthalene in the reaction with Me_2SO is remarkable.

It is known that α - and β -methylnaphthalenes isomerize very fast to each other reaching to the equilibrium ratio = 4.4) and 1,4-dimethylnaphthalene similarly isomerized to the 1,5-isomer, both within 2 min under the same reaction conditions as employed in the present experiments. (3) From these facts and general rules of orientation of methylnaphthalenes shown in Scheme 2, the reaction path should be as shown in Scheme 3.

According to the orientation rules, such a large amount of the 1,5-compound as observed cannot be produced by direct substitution of both methylnaphthalenes. Formation of the 1,5-isomer from the 1,2- and 2,6-isomers is possible but it is by slow intermolecular rearrangement. Therefore, the major part of the 1,5-compound must be produced by fast intramolecular rearrangement of the 1,4-isomer compound, which can be directly formed from α -methylnaphthalene. This indicates that the higher yield of the 1,5-isomer in the reaction with Me_2SO than in the reaction with MeI is attributable to the larger formation of the 1,4-compound in the former reaction than in the latter. This difference should be ascribed to the characteristics of the methylating agents and/or the molten salt used.

2. FORMATION OF PERYLENE FROM BINAPHTHYLS IN MS-A

In connection of our earlier work (1) on condensation of naphthalene as a new way leading aromatics to pitch and carbon, the reaction of binaphthyls was studied. Binaphthyls are the first condensation products from naphthalene and, therefore, their reaction is just the key step in a series of complicated reactions.

EXPERIMENTAL

A tenth m mol of binaphthyl was added to 0.05 mol of MS-A, kept at 100°C in a test tube, and the mixture was stirred well. After a given reaction time (1 and 10 min) the test tube was immersed into an ice bath to quench the reaction by solidification of the mixture. Then the mixture was dissolved in an ice-HCl mixture and extracted with chloroform. The extract was subjected to analysis of the products by HPLC and UV.

RESULTS AND DISCUSSION

From the results shown in Table 1 it is obvious that perylene was formed from both binaphthyls as the main product after the 10-min reaction and that a very quick isomerization of 1,1'-binaphthyl to the 2,2'-isomer took place. These facts are, of course, important for the purpose of this study mentioned above, and also interesting from view point of aromatic reaction mechanism.

If a working hypothesis that the perylene observed was produced only through the intramolecular condensation of 1,1'-binaphthyl is acceptable, the formation of perylene from 2,2'-binaphthyl demands the reversed isomerization of 2,2'-binaphthyl to the 1,1'-isomer. The absence of 1,1'-isomer among the products from 2,2'-binaphthyl can be explained by assuming that the change of 1,1'-binaphthyl to perylene is faster than its formation from 2,2'-binaphthyl. Based on these facts and consideration, the reaction path should be given as shown in Scheme 4.

5. ISOMER DISTRIBUTION IN ACYLATION OF AROMATIC COMPOUNDS AND RELATED REARRANGEMENT IN MS-B (5)

Some aromatic compounds were acylated with acid chlorides in MS-B with interest of isomer distribution and related isomerization. Solvent effect on isomer distribution is an unsolved problem in Friedel-Crafts' acylation.

EXPERIMENTAL

To a solution of an aromatic compound in MS-B, kept in a flask at a given temperature, an equimolar amount of acylating agent was added dropwise. After planned periods of time, specimens were taken out, poured into an ice-HCl mixture, and extracted with benzene. The extracts were subjected to analysis of the products by G.L.C. Some of the results were given in Table 2.

RESULTS AND DISCUSSION

The results of the reactions of naphthalene are noticeable because of the very high selectivity of substitution to the α -position. According to Gore (4), the Friedel-Crafts acylation in organic solvents shows a widely ranging α -selectivity depending on the nature of solvent; i.e., 38-96% in benzooylation and 25-91% in acetylation. Compared with these values, the α -selectivity of 97 and 98% observed here presents newly the highest ones.

In contrast to naphthalene, phenanthrene showed a fairly dispersed isomer proportion. This is also interesting since phenanthrene usually shows a similar reactivity to naphthalene in substitution reaction. This difference shall be studied in relation to the characteristics of MS-B.

The α/β -isomer ratio in benzooylation of naphthalene did not change at reaction temperatures between -15 and 20°C, while α -benzoylnaphthalene was found to isomerize to the β -isomer at temperatures above ca. 150°C. To examine the mode of this isomerization an equimolar mixture of the α -isomer with phenanthrene was heated at 170°C in MS-B and as a result, at least, three isomeric benzoylphenanthrenes were detected as the cross-rearrangement products as shown in Fig. 2. This indicates that the isomerization proceeds through intermolecular mechanism. In Fig. 2 formation of benzanthrones is also shown, which must be produced from α -benzoylnaphthalene and benzoylphenanthrenes by the Scholl peri-condensation. This is under investigation now.

4. ONE-POT SYNTHESIS OF ANTHRAQUINONE IN MS-B (6)

Among others there is a commercial preparation method of anthraquinone which consists of two steps of reaction; i.e., preparation of *o*-benzoylbenzoic acid from benzene and phthalic anhydride by usual Friedel-Crafts' reaction and its condensation to anthraquinone in sulfuric acid. Here an improved one-pot process (Scheme 5) shall be reported.

EXPERIMENTAL

First, phthalic anhydride (0.11-0.2 mol) was dissolved in MS-B at room temperature and then 0.1 mol of benzene were added dropwise under well-stirring. The mixture was heated up to a given temperature in 1 h and kept there for another 1 h. The mixture was poured into an ice-HCl mixture and the resulting precipitate was filtered and washed. The filtercake was treated with a Na_2CO_3 solution to separate into alkali-soluble and -insoluble matters. The former contained mainly the intermediate o-benzoylbenzoic acid and the latter the final product anthraquinone.

RESULTS AND DISCUSSION

As shown in Table 3, anthraquinone was obtained in fairly good yields. The success of this one-pot synthesis is attributable to the dehydrating ability of MS-B in the second step of the reactions. Another point of this process is in the sequence of adding the raw materials to MS-A. When benzene was first added and then phthalic anhydride, the main product was o-dibenzoylbenzene, which rarely changed to anthraquinone even after a prolonged reaction time.

REFERENCES

1. a) E. Ota and S. Otani, *Chemistry Lett.*, 1973, 241.
b) E. Ota, S. Inoue, M. Horiguchi, and S. Otani, *Bull. Chem. Soc. Japan*, **52**, 3499 (1979).
2. P. A. Osteryoung, *J. Amer. Chem. Soc.*, **98**, 5217 (1976).
3. E. Ota, S. Inoue, M. Dornae, and S. Otani, *Nippon Kagaku Kaishi*, 1979, 1210.
4. P. H. Gore, *Chemical Reviews*, **55**, 229 (1955).
5. Partly reported in Reference 6.
6. E. Ota, S. Hagiwara, K. Ishizaki, and O. Shibasaki, *The 50th Annual Meeting of Chem. Soc. Japan, Abstract Vol. 2*, 1228 (1985), Tokyo.

Table 1. Naphthalene Dimers* in the Products from Biphenyls

Binaphthyls	Reaction Time(min)	Yields of Dimers(mol%)		
		1,1'-	2,2'-	Perylene
1,1'-	1	55.0	59.0	6.0
	10	0.0	2.1	44.0
2,2'-	1	0.0	94.0	5.5
	10	0.0	1.7	38.0

*Other products were mainly polymers of naphthalene.

Table 2. Isomer Distribution in Acylation*

Aromatics	Acylation agent	Reaction Conditions		Isomer Ratio (mol%)
		Temp.(°C)	Time(h)	
Toluene	Ph-COCl	30	0.5	o- 1, m- 1, p- 95
Naphthalene	Ac-COCl	20	0.5	o- 98, p- 2
Naphthalene	Ph-COCl	20	0.5	o- 97, p- 3
Phenanthrene	Ac-COCl	20	0.5	1- 20, 2- 9, 3- 27, 4- Trace, 9- 44
α -Benzoyl-naphthalene	Ph-COCl	100	5	1,5- 67, 1,8(2)- 8, 1,6(2)- 25

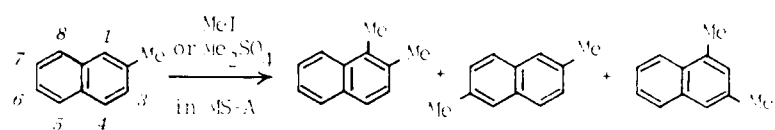
*The yields were usually high or almost quantitative.

Table 3. One-pot Synthesis of Anthraquinone using MS-B

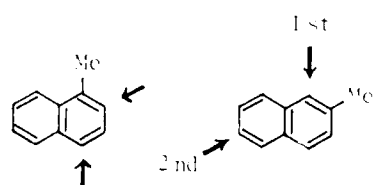
Raw Materials		Reaction Conditions			Anthraquinone	
Benzene (mol)	Phthalic Anhydride (mol)	MS-B (unit*)	Temp. (°C)	Time (h)	Yield (%)	mp** (°C)
0.1	0.2	5	160	1	88	285-4
0.1	0.11	5	160	1	53	285-4
0.1	0.11	5	170	5	91	279-80

*One "unit" means an amount of MS-B consisting of 0.1 mol of ethylpyridinium bromide and 0.2 mol of AlCl₃.

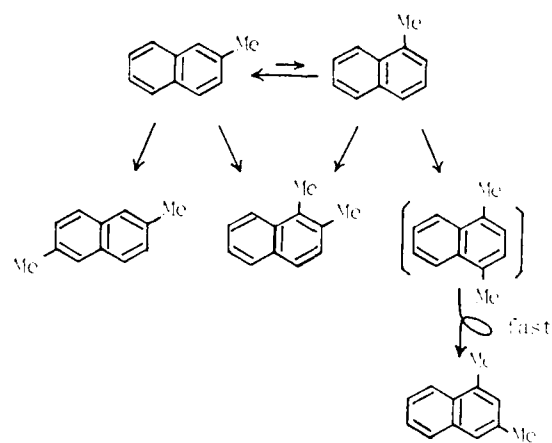
**Pure anthraquinone melts at 286°C.



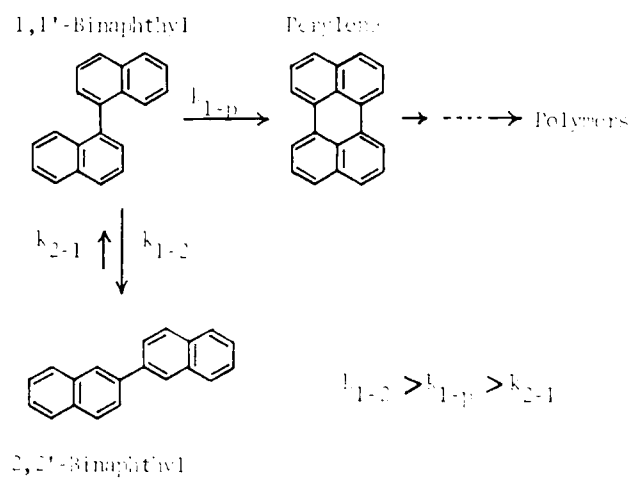
Scheme 1



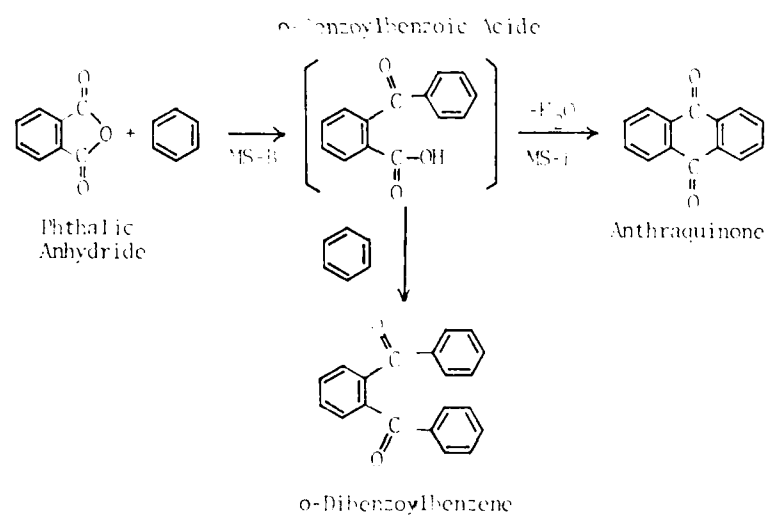
Scheme 2



Scheme 3



Scheme 4



Scheme 5

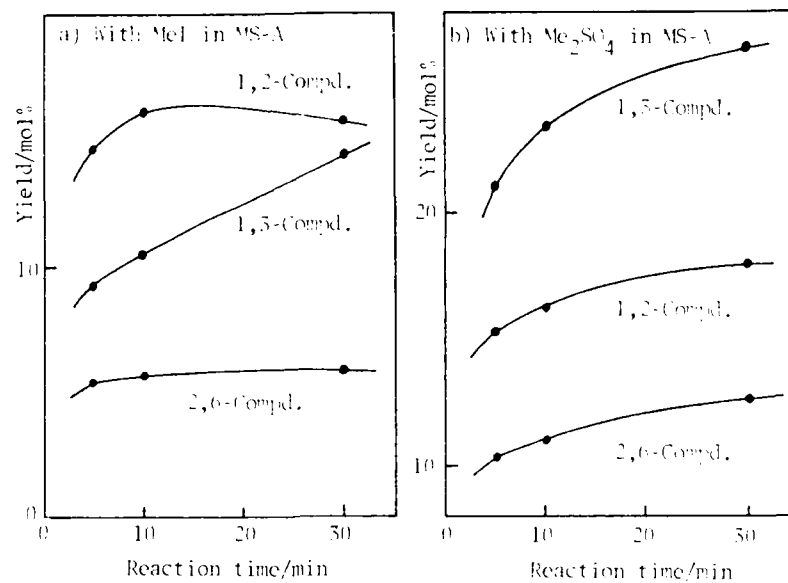


Fig.1 Product distribution in Methylation of 1-Methylnaphthalene

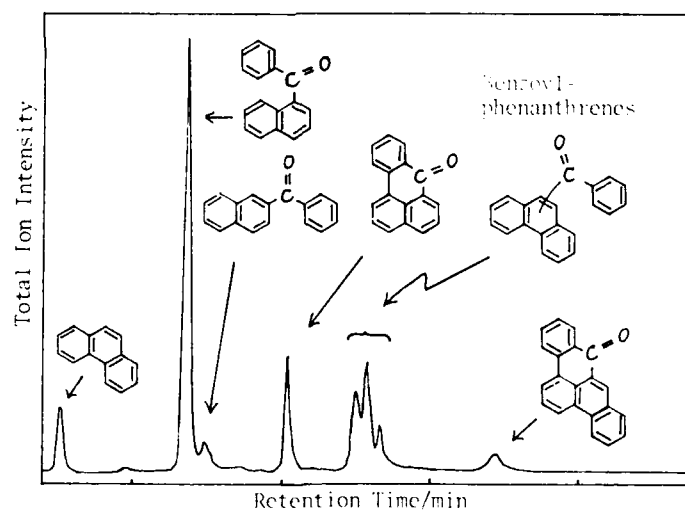


Fig.2 GC-MS Chromatogram of the Products of Reaction of a Mixture of 1-Benzoylnaphthalene and Phenanthrene in MS-A

SPECTROSCOPIC AND ELECTROCHEMICAL STUDIES OF MOLTEN SALT ELECTROLYSIS OF ALUMINUM AND MAGNESIUM

Seok-Yeol Yoon and Donald R. Sadoway
Department of Materials Science and Engineering,
Massachusetts Institute of Technology,
Cambridge, Massachusetts 02139.

ABSTRACT

Chloride based electrolytes employed in the electrolytic production of aluminum and magnesium have been investigated by laser Raman spectroscopy and cyclic voltammetry. In solutions of composition approximating industrial conditions, aluminum and magnesium exist as tetrahedrally coordinated chloro-complexes, AlCl_4^- and MgCl_4^{2-} , respectively. For both elements the electrodeposition of liquid metal was found to be quasi-reversible.

INTRODUCTION

The extraction of light metals is achieved for the most part by molten salt electrolysis, a very energy-intensive process. The production of primary aluminum and magnesium is estimated to have consumed 2.1% of total generated electric power in the United States during the year 1985 (1).

The characteristics of laboratory-scale aluminum and magnesium cells were investigated by spectroscopic and electrochemical techniques. The electrolytes were constituted to be representative of industrial conditions. Aluminum cells operated at a temperature of 900°C with an electrolyte of composition 5 wt % AlCl_3 , 42 wt % LiCl , and 53 wt % NaCl . Magnesium cells operated at a temperature of 750°C with an electrolyte of composition 11 wt % MgCl_2 , 65 wt % NaCl , 18 wt % KCl , and 6 wt % CaCl_2 . The maximum current density was 2 A cm^{-2} .

As part of a study of the causes of poor power efficiency, Raman spectra of laboratory-scale aluminum chloride and magnesium chloride electrolysis cells were measured. Commercially available laser Raman scattering instrumentation was adapted to permit *in situ* real-time investigation of melt chemistry and to establish the basis for "fast Raman" spectroelectrochemistry in this and other melt systems (2). The results of the Raman work were combined with those of cyclic voltammetry in an attempt to reveal the mechanisms and kinetic pathways that decrease power efficiency in aluminum and magnesium cells and also to understand the nature of such phenomena as metal fog, streamers, and melt coloration, all of which were observed in these laboratory-scale cells.

LITERATURE

Reasons for the loss of current efficiency in aluminum cells (3,4) and magnesium cells (5,6) have been discussed in the literature.

Raman spectra of pure MgCl_2 and solutions of MgCl_2 in alkali chlorides have been measured (2,7-13). In contrast, in the analogous aluminum chloride systems spectra have been taken of AlCl_3 only in solution in alkali chlorides as pure AlCl_3 sublimes without melting under an applied pressure of 1 atmosphere (14-18).

Over the years, magnesium electrodeposition has rarely been the topic of electrochemical analysis. In the last decade there have been only two reports, one by Tunold (19) and one by Duan, Dudley, and Inman (20). As for aluminum chloride, it has been found primarily as a constituent of supporting electrolytes for use in electrochemical studies of other ions, particularly those of refractory metals (Groups 4,5, and 6). However, there have been some studies of the electrodeposition of aluminum in chloride melts (21-23).

EXPERIMENTAL

A detailed description of the Raman instrumentation and the laboratory-scale electrolysis cell can be found in previous reports (2,12,24).

Cyclic voltammetry was conducted in a fused quartz cell, 52 mm ϕ . The stainless steel cap had 7 fittings, 2 gas ports, and one 3/8" O.D. tube which accessed the cell by means of a 3/8" valve. The fittings were used for a thermocouple, a reference electrode, cathode and anode for pre-electrolysis, and for voltammetry a counter electrode and two working electrodes. The valved tube allowed melt composition to be regulated and sampled as well as the introduction of a new electrode, all without interruption of the experiment.

The preparation of anhydrous salts for electrolyte formulation has been described previously (12).

In a typical experiment, the cell was charged with salt and assembled with the cap and electrodes in the glove box. The charged cell was placed in an electrical resistance furnace with windows (12), and the salt was melted under high purity argon.

For pre-electrolysis, a platinum plate, 4 mm x 8 mm, and a glassy carbon rod, 1/8" ϕ , served as cathode and anode, respectively. For the working electrode, each of silver, gold, glassy carbon, tungsten, titanium diboride, and platinum was employed. The reference

electrode was a silver wire immersed in a solution of AgCl (5 weight percent) in the appropriate supporting electrolyte: for magnesium electrolysis, CaCl_2 -KCl-NaCl in the ratio of 6:18:65 by weight, and for aluminum electrolysis, NaCl-LiCl in the ratio of 50:40 by weight.

Cyclic voltammetry was conducted with an EG&G PARC Model 173 potentiostat/galvanostat and Model 175 universal programmer. Slow scan responses were recorded on an X-Y recorder, while fast scan responses were recorded on a digital computer.

RESULTS AND DISCUSSION

Figure 1 shows the Raman spectrum of aluminum chloride in its supporting electrolyte at a temperature of 700°C. Excitation was caused by radiation of wavelength, $\lambda = 514.5 \text{ nm}$. Four distinct peaks have been identified: 125 cm^{-1} , 183 cm^{-1} , 349 cm^{-1} , and 483 cm^{-1} . The peak at 349 cm^{-1} is polarized; the others are depolarized. Such a pattern of peaks is indicative of tetrahedral coordination and suggests the presence of the tetrachloroaluminate complex, AlCl_4^- .

Figure 2 shows the Raman spectrum of magnesium chloride in its supporting electrolyte at a temperature of 750°C. Excitation was caused by radiation of wavelength, $\lambda = 514.5 \text{ nm}$. Four distinct peaks have been identified: 107 cm^{-1} , 142 cm^{-1} , 249 cm^{-1} , and 351 cm^{-1} . The peak at 249 cm^{-1} is polarized; the others are depolarized. As was the case above with the aluminum chloride system, such a pattern is indicative of tetrahedral coordination and suggests the presence of the tetrachloromagnesate complex, MgCl_4^{2-} .

Figure 3 shows a cyclic voltammogram for the deposition of aluminum on gold at 700°C from a melt containing 1.5 wt % AlCl_3 in NaCl-LiCl in the ratio of 50:40 by weight. The reference electrode was silver wire immersed in a melt of AgCl-NaCl-LiCl (5:53:42 by weight). The counter electrode was glassy carbon. The area of the working electrode was 0.173 cm^2 . The scan rate was 0.05 V s^{-1} . In Figure 3 the reduction and oxidation peaks are clearly evident and are separated by 56 mV which is close to the theoretical value of 62 mV for a simple reversible 3-electron reduction process (25). However, the ratio of the anodic peak current to the cathodic peak current is much greater than unity, so the process cannot be considered strictly reversible. The peak potentials did not change with scan rate. Thus, the reduction process of aluminum on gold appears to be quasi-reversible.

Figure 4 shows a cyclic voltammogram for the deposition of magnesium on silver at 800°C from a melt containing 2 wt % MgCl_2 in CaCl_2 -KCl-NaCl in the ratio of 6:18:65 by weight. The scan rate was 0.4 V s^{-1} , and the area of the working electrode was 0.08 cm^2 . The well defined trace shows clearly the reduction and oxidation processes. The residual current was extremely low and did not decrease with

pre-electrolysis. The value of the potential difference between peak potentials for the cathodic and reoxidation processes is greater than would be expected for a simple reversible process (25). The scan rate had essentially no effect on the peak potential: if anything, both peaks seem to shift very slightly in the cathodic direction as scan rate increases.

For both the aluminum and the magnesium studies the cathodic peak current is linear in the square root of scan rate: over the range of experiments conducted in the present cell configuration, the current was mass transfer controlled by diffusion.

ACKNOWLEDGEMENT

This material was prepared with the support of the U.S. Department of Energy (DOE) Grant No. DE-FC07-82-CE40545. However, any opinions, findings, conclusions, or recommendations expressed herein are those of the authors and do not necessarily reflect the views of DOE.

REFERENCES

1. E. Spore and B.V. Tilak, *J. Electrochem. Soc.*, **134**(1987), 179C-219C.
2. S.-Y. Yoon, J.H. Flint, G.J. Kipouros, and D.R. Sadoway, "Raman Scattering Studies of Magnesium Electrolysis," in Light Metals 1986, R.E. Miller, ed., (Warrendale PA: TMS-AIME, 1986), 1009-12.
3. N. Jarrett, W.B. Frank, and R. Keller, "Advances in the Smelting of Aluminum," in Metallurgical Treatises, J.K. Tien and J.F. Elliott, eds., (Warrendale PA: TMS-AIME, 1981), 127-57.
4. K. Grjotheim and B.J. Welch, Aluminium Smelter Technology, (Dusseldorf: Aluminium-Verlag, 1980), 81-96.
5. G.J. Kipouros and D.R. Sadoway, "The Chemistry and Electrochemistry of Magnesium Production," in Advances in Molten Salt Chemistry, Vol. 6, G. Mamantov and J. Braumanstein, eds., (Amsterdam: Elsevier, in press).
6. Kh.L. Strelets, Electrolytic Production of Magnesium, trans. by J. Schworak (Jerusalem: Keter Publishing House, Jerusalem Ltd, 1977).
7. K. Balasubrahmanyam, *J. Chem. Phys.*, **44**(3) (1966), 3270-3.
8. C.H. Huang and M.H. Brooker, *Chem. Phys. Letters*, **43**(1976), 180-2.
9. M.H. Brooker, *J. Chem. Phys.*, **63**(7)(1975), 3054-60.
10. M.H. Brooker and C.H. Huang, *Can. J. Chem.*, **58**(1980), 168-79.
11. V.A. Maroni, *J. Chem. Phys.*, **55**(10)(1971), 1789-92.
12. S.-Y. Yoon, J.H. Flint, G.J. Kipouros, and D.R. Sadoway, "Raman Scattering Studies of Molten Salt Electrolysis of Light Metals," in Energy Reduction Techniques in Metal Electrochemical

- Processes, R.G. Bautista and R. Wesely, eds., (Warrendale PA: TMS-AIME, 1985), 479-90.
13. S.-Y. Yoon and D.R. Sadoway, "Spectroelectrochemical Study of Magnesium Electrolysis," in Light Metals 1987, R.D. Zabreznik, ed., (Warrendale PA: TMS-AIME, 1987), 851-9.
 14. G. Torsi, G. Mamantov, and G.M. Begun, *Inorg. Nucl. Chem. Letters*, 6(1970), 553-65.
 15. H. Gerding and H. Houtgraaf, *Rec. Trav. Chem.*, 72(1953), 21-38.
 16. K. Balasubrahmanyam and L. Nanis, *J. Chem. Phys.*, 42(2)(1965), 676-80.
 17. H.A. Øye, E. Rytter, P. Klæboe, and S.J. Cyvin, *Acta Chem. Scand.*, 25(1971), 559-76.
 18. R. Fehrmann, J.H. von Barner, N.J. Bjerrum, and O.P. Nielsen, *Inorg. Chem.*, 20(1981), 1712-8.
 19. R. Tunold, "The Cathode Reaction in Magnesium Electrolysis," in Light Metals 1980, C.J. McMinn, editor (Warrendale PA: TMS-AIME, 1980), 949-57.
 20. S. Duan, P.G. Dudley, and D. Inman, "Voltammetric Studies of Magnesium in Chloride melts," in Proceedings of the Fifth International Symposium on Molten Salts, M.-L. Saboungi, K. Johnson, D.S. Newman, and D. Inman, eds., (Pennington NJ: The Electrochemical Society, Inc., 1986), 248-61.
 21. S. Takahashi and N. Koura, *Denki Kagaku*, 50(10)(1982), 852-3.
 22. Yu.K. Delimarsky, V.F. Makogon, and O.P. Gritsenko, *Sov. Prog. Chem.*, 46(2)(1980), 1-4.
 23. R. Tunold, Y.J. Zhang, and R. Ødegard, "Kinetics of the deposition of aluminium from chloride melts," in Proceedings of the Fifth International Symposium on Molten Salts, M.-L. Saboungi, K. Johnson, D.S. Newman, and D. Inman, eds., (Pennington NJ: The Electrochemical Society, Inc., 1986), 408-44.
 24. G.J. Kipouros, J.H. Flint, and D.R. Sadoway, *Inorg. Chem.*, 24(11)(1985), 3881-4.
 25. R.S. Nicholson and I. Shain, *Anal. Chem.*, 36(4)(1964), 707-21.



Figure 1. Raman spectrum of 10 wt % AlCl_3 - 40 wt % LiCl - 50 wt % NaCl . $T = 700^\circ\text{C}$. $\lambda = 514.5 \text{ nm}$.

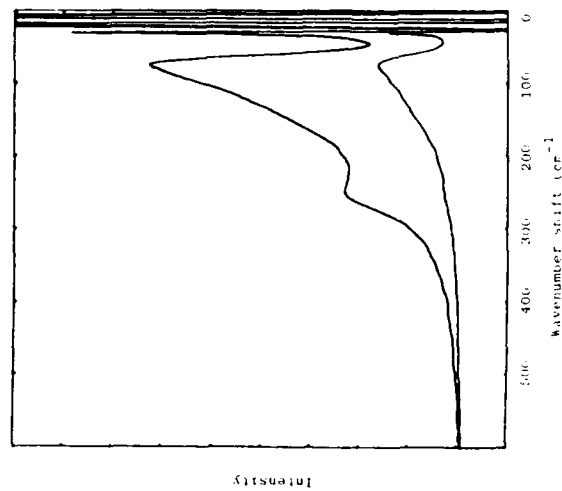


Figure 2. Raman spectrum of 11 wt % MgCl_2 - 6 wt % CaCl_2 - 18 wt % KCl - 65 wt % NaCl . $T = 760^\circ\text{C}$. $\lambda = 514.5 \text{ nm}$.

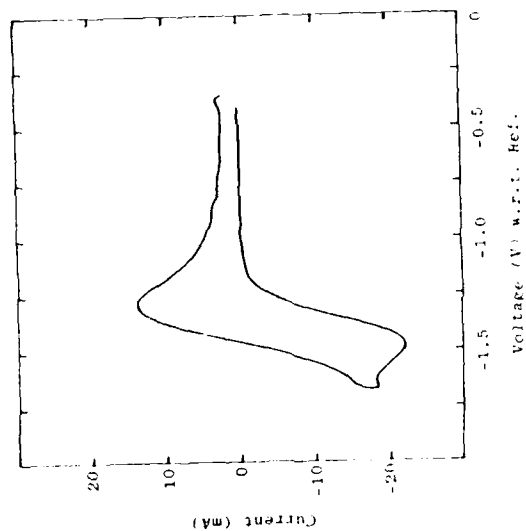


Figure 4. Cyclic voltammogram of 2.2 wt % MgCl_2 in $\text{CaCl}_2 - \text{KCl} - \text{NaCl}$ in a weight ratio 6:18:65, working electrode: silver, Area: 0.08 cm^2 , $T = 750^\circ\text{C}$, Scan rate: 0.4 V s^{-1} .

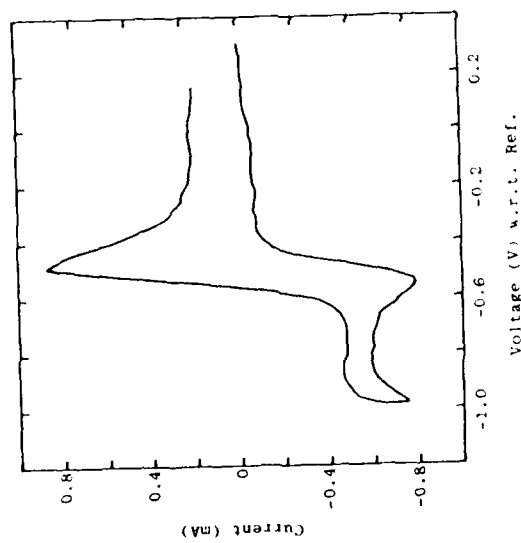


Figure 3. Cyclic voltammogram of 1.5 wt % AlCl_3 in $\text{LiCl} - \text{NaCl}$ in a weight ratio 40:50, Working electrode: gold, Area: 0.173 cm^2 , $T = 700^\circ\text{C}$, Scan rate: 0.05 V s^{-1} .

ELECTRODEPOSITION OF MICROCRYSTALLINE CHROMIUM FROM FUSED SALTS

T. Vargas, R. Varma, and A. Brown

Chemical Technology Division
Argonne National Laboratory
Argonne, IL 60439

ABSTRACT

Chromium can be conveniently electroplated from fused chloride electrolytes. The deposition from LiCl-KCl (eutectic)- CrCl_2 melts is known to produce large crystal grains. Large grain size and other problems encountered in the electrodeposition of microcrystalline chromium from fused salt are discussed. The results indicate that combined use of forced electrolyte convection and a nucleating pulse in conjunction with a periodic reverse pulse produces fine-grained deposits.

INTRODUCTION

Chromium metal has been shown to offer good corrosion resistance in sulfur/polysulfide environments and, therefore, constitutes a suitable material for use as a protective coating in sodium/sulfur batteries (1). The protective action of chromium can be fully utilized only if such coatings are coherent, have good adhesion, and provide a thorough coverage of the substrate. Chromium electrodeposition from aqueous solutions produces deposits which may have microcracks and incorporate hydrogen during plating. Hence, coatings thusly derived have not fully utilized the protective action of chromium (2).

In principle, the use of molten salt electrolytes (e.g., chlorides, fluorides) represents an attractive alternative for the production of chromium electrodeposits. Such electrolytes are oxygen-free, hydrogen-free, highly conductive media by which it is possible to deposit the pure metal at high current efficiencies. The electrodeposition of chromium from fluorides has received some attention, and the production of coherent, well-adhered deposits has been successfully demonstrated (3-6). However, the disadvantage of fluorides is that the systems are generally considered to be toxic and corrosive, and their utilization implies the use of relatively high temperatures (800-1000°C) (4). Chloride melts are a more suitable alternative for the following reasons: they can be operated

at relatively low temperatures (400-600°C), they offer high conductivity, and they are not considered too toxic or corrosive. In this work chromium was electrodeposited from (LiCl-KCl)eutectic-CrCl₂ melts. This melt is an adequate refining media for chromium, which can be obtained with total impurity contents of less than 70 ppm at average current efficiencies of 96% (7). Under single galvanostatic/potentiostatic conditions, the electrodeposition of chromium from (LiCl-KCl)eutectic-CrCl₂ melts usually resulted in the production of highly dendritic or crystallized noncoherent coatings (8). Clearly, a different approach was needed.

APPROACH

A notable improvement in the morphology of chromium electrodeposits obtained from these melts has been achieved by introducing an initial nucleation pulse (8) followed by periodic reverse current. These steps enable the production of coherent, crack-free, well-adhered, and fine-grained deposits. Further work related to the characterization and understanding of the chromium electrocrystallization mechanism was undertaken, and the result was better control of the grain size of the deposits.

EXPERIMENTAL

The experiments were conducted in a helium-purified glove box (Sherman Reynolds Model B5935) which has two cylindrical furnace wells (each with a 7-cm dia and a 40-cm length). The furnace wells, which are provided with removable sealed tops, can be evacuated by a Duo Seal Vacuum Pump Model 1397. The electrochemical cell is placed in one of the wells. The heat is provided by a Marshall tubular furnace, and the temperature is controlled by a West S.C.R. stepless control unit. The melt is contained in a 80-mL Pyrex beaker that is placed within a 6.5-cm-dia by 17-cm-long stainless steel protective container resting on the bottom of the well. The cell is capped by a three-inlet glass head, which provides a centered stable base for the electrodes and enables their quick interchange. The preparation and weighing of the different salt mixtures were done within the same glove box, which is equipped with a Sartorius balance.

To generate the different potential and current programs needed for the tests, a Princeton Applied Research Model 273 Potentiostat/Galvanostat and a PAR Model 175 Universal Programmer were used. The output signals (current/voltage transients) were recorded on a Tektronik Model R5103N Oscilloscope and on a Hewlett Packard 7044A X-Y Recorder or a Hewlett Packard 7100B Strip Chart Recorder. Coulometric measurements were done using the PAR Model 379 Digital Coulometer.

A conventional three-electrode system was used: the reference and the counter electrodes were made of chromium pieces (purified, carbon-free, fused) from Fisher Scientific Co. and were spot-welded to platinum wire for electrical contact. The chromium-melt contact areas were approximately 2 cm² and 0.5 cm², respectively. The working electrodes were Type 304 stainless steel (SS) coupons made of 0.5-mm thick plate spot-welded to 1.6-mm-dia Type 308 SS rods for electrical contact (1-2 cm² melt-substrate area). In some experiments, the working electrodes were held in a motor-driven stirrer, with variable speed in the range of 20-300 rpm. The SS electrodes were anodically cleaned before use in a H₂SO₄ solution (0.53 specific gravity) at 6 V for 1 min, according to a procedure recommended for improved deposit-substrate adherence (9). The morphology of surfaces and sections of the electrodeposits on steel substrate were examined by scanning electron microscopy (SEM).

The electrolyte consisted of LiCl-KCl (41.5-58.5 mol %, purified, Li contacted) eutectic from Anderson Physics Laboratories and chromium (II) chloride (98%, anhydrous) from Alfa Products. The working temperature was 450°C.

RESULTS AND DISCUSSIONS

Characterization of the System

Figure 1 shows some typical cyclic voltammograms obtained with the (LiCl-KCl)eutectic-CrCl₂ system. Two reversible waves are observed when scanning on tungsten electrode (curve a). A small pair of waves are on the anodic side at approximately +0.2 V, and a large pair are on the cathodic side at approximately -0.7 V. These potentials correspond to the reduction of Cr(III) to Cr(II) and Cr(II) to Cr(0), respectively. Studies of similar cyclic voltammograms obtained in the LiCl-KCl-CrCl₃ system at 500°C confirmed the number of electrons associated with each wave (10). The Cr(III)/Cr(0) wave does not appear in the cyclic voltammograms for tungsten or Type 304 SS (curve b). This is precluded by the early wave related to the anodic dissolution of the substrate. The waves corresponding to the Cr(II)/Cr(0) pair are observed in both substrates, and they exhibit the typical shape associated with a deposition/dissolution process on an inert substrate (11-13). Instead of increasing smoothly with the overpotential change, the current on the cathodic branch rises abruptly (curve a, Fig. 1) resulting in a sharp cathodic peak. An equally sharp fall in current occurs after the anodic peak; this is consistent with the stripping of a finite quantity of metallic deposit from the electrode surface. The rising part of the cathodic wave is cathodically displaced with respect to the equilibrium potential (E°) for Cr(II)/Cr(0). This delay in starting the cathodic process is related to the initial

resistance involved in the formation of the new chromium phase on a foreign substrate. This process requires the application of an extra overpotential related to the extra work necessary for the initial creation of critical chromium nuclei.

The chromium electrodeposition for low-concentration melts ($0.931 \text{ mol dm}^{-3}$) has been observed to be controlled by mass transfer (9). Several facts suggest that, at very high CrCl_2 concentrations, the chromium electrodeposition process in this melt is controlled, to a large extent, by ohmic resistance in the melt. Figure 2 shows cyclic voltammograms obtained on Type 304 SS at 2.12 mol dm^{-3} concentration. The rising cathodic branch shows a practically linear current-voltage relation for the case of still and rotated electrodes. The rotation of the electrode introduced only a slight increase in the current-voltage slope, indicating a slight degree of mass transfer control. Previous work on electrorefining chromium from similar melts reported a decrease of the conductivity of the electrolyte with an increase in the CrCl_2 concentration (7).

Chromium Electrodeposits

Chromium deposits were obtained by different controlled-potential techniques at various CrCl_2 concentrations. The most-frequent deposition technique used at this stage is the initial nucleation pulse (INP) technique, shown in Fig. 3. In this technique, the deposition process is started with a high, short overpotential pulse, where a large number of isolated chromium nuclei are formed to secure a thorough initial coverage of the substrate. The deposit is then grown at a low overpotential, precluding the growth of dendrites and ensuring the development of a coherent morphology.¹⁴

Figures 4 and 5 show the dramatic influence of CrCl_2 concentration on the morphology of chromic electrodeposits produced by the INP technique. At the highest concentration 2.12 mol dm^{-3} , Fig. 4), the deposit consists of large crystals that have not merged into a continuous layer, leaving large spaces between them. Between the large crystals, a lower layer of small crystals were formed during the initial nucleation stage these do not fully cover the substrate. At the low concentration (1.5 mol dm^{-3} , Fig. 5), the deposits obtained show a noticeable decrease of the grain size and a very compact structure (deposits of this kind already show some metallic shine on their surface). The coatings were found to be well adhered to surface, as shown by optical microscopy of the chromium-substrate interface. Also, no microcracks were observed.

The observed morphological changes with CrCl_2 concentration can be explained mainly based on the cyclic voltammograms. With the CrCl_2 concentration variation from high to low, there is a

displacement in the electrodeposition-controlling mechanism from ohmic control in the melt toward mass-transfer control given by the diffusion of active species toward the electrode surface. This effect is also shown (Fig. 6) by the observed I vs. ω plots for tungsten electrodes that were rotated at two different speeds. When the electrogrowth occurs under ohmic control, the formation and growth of nuclei involve the simultaneous development of large deactivating zones around each nuclei. These originate in the potential drop arising in the melt around growing centers¹⁹ and preclude the formation of a large number of nuclei and the development of a compact structure. This effect explains the morphological characteristics observed in deposits obtained at very high concentrations. The decrease in $CrCl_3$ concentration reduces the effect of the ohmic control. This results in the initial formation of larger nuclei numbers and development of compact structures, provided that the development of dendritic structures is precluded by growing at overpotentials sufficiently low.

The application of both higher rotational speeds and a continuous potentiostatic pulse contributes to further reduction of the grain size. The results are shown in Fig. 7.

CONCLUSIONS

The electrodeposition of chromium from (100-1000) molar $CrCl_3$ melts using the INP technique enabled the production of coherent well-adhered as chromium coatings on Type 304 SS probes. The resultant morphology in the deposits seems to be the product of a delicate balance between the different mechanisms that control the electrocrystallization mechanism at different stages. These mechanisms are very dependent on the $CrCl_3$ concentration present in the melt. The choice of very high $CrCl_3$ concentrations, which would be, in principle, desirable with regard to the use of higher deposition currents, is restricted in practice by the decrease in the melt conductivity, which has deleterious effects on the electrogrowth process. On the other hand, the choice of very low $CrCl_3$ concentrations is also not very desirable since the overpotentials then become too important, resulting in the crystallization of very crystalline deposits and a consequent loss of adhesion. The experimental results obtained in this work indicate a low $CrCl_3$ concentration working range.

The current density at the cathode used to produce a coating of chromium plated Type 304 SS probes. A melt with 1.8 molar $CrCl_3$ concentration produced the most adherent deposits of small grain size.

Further work will focus on the electrodeposition of chromium using forced mass-transfer conditions and more-complex pulsing current/voltage regimes and will be reported later. The desired result is to reach a more accurate control on the grain size distribution and morphology of the deposit.

ACKNOWLEDGMENT

This work was supported by the U.S. Department of Energy, Office of Energy Storage under contract number W-31-109-ENG-38.

REFERENCES

1. A. Brown and J. E. Battles, Argonne National Laboratory, personal communication (1986).
2. Electric Power Research Institute, "Corrosion of Chromium Coated Steel in Sodium Polysulfide Environments," Report EPRIEM-2948 (1983).
3. R. A. Bailey and T. Yoko, in Proceedings of the First International Symposium on Molten Salts Chemistry and Technology, Kyoto, Japan, p. 115 (1983).
4. J. F. Smith, *Thin Solid Films*, **95**, 151 (1982).
5. U. Cohen, *J. Electrochem. Soc.*, **128**, 731 (1981).
6. S. Senderoff, G. W. Mollers, et al., *J. Electrochem. Soc.*, **112**, 841 (1965).
7. K. P. V. Lei, J. M. Hiegel, and T. A. Sullivan, *J. Less-Common Metals*, **27**, 353 (1972).
8. T. Vargas, Ph.D. Thesis, University of London (1984).
9. F. M. Dorey, *Ind. Eng. Chem.*, **20**, 1644 (1928).
10. S. Levy and W. Reinhardt, *J. Electrochem. Soc.*, **122**, 200 (1975).
11. W. K. Behl, *J. Electrochem. Soc.*, **118**, 869 (1971).
12. G. J. Hills, D. J. Scullifrin and J. Thompson, *Electrochimica Acta*, **1**, 657 (1974).

13. G. Gunawardena, G. Hills, and I. Montenegro, *J. Electroanal. Chem.*, **138**, 241 (1982).
14. D. Inman, T. Vargas, S. Duan, and P. Dudley, in Proceedings Fourth International Symposium on Molten Salts, The Electrochemical Society, Inc., New Jersey (1982).
15. I. Markov, A. Boynov, and S. Toshev, *Electrochimica Acta*, **18**, 377 (1973).

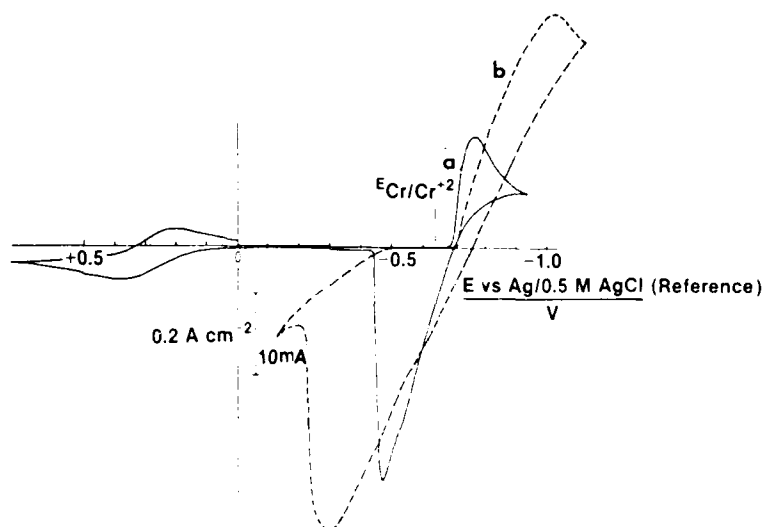


Figure 1. Cyclic Voltammogram for the (LiCl-KCl) eut- CrCl_2 System. $C: 0.931 \text{ mol dm}^{-3}$, $V: 0.1 \text{ s}^{-1}$. a: on Tungsten, b: on 304 SS.

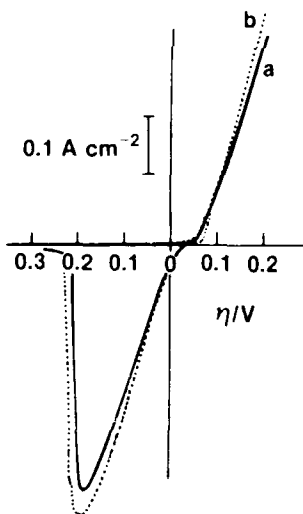


Figure 2. Cyclic Voltammogram for the CrCl_2 on 304 SS. $C: 2.12 \text{ mol dm}^{-3}$, $v: 0.1 \text{ V s}^{-1}$. a: Still Electrode, b: Rotated Electrode (24 rpm).

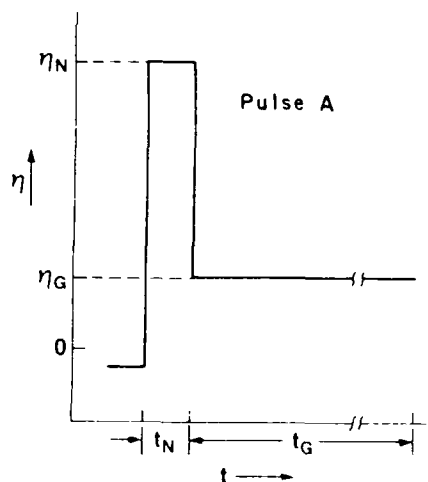


Figure 3. Initial Nucleation Pulse Method; η_N : Nucleation Over-Potential, η_G : Growth Over-Potential, t_N : Nucleation Pulse Width, t_G : Growth Time.

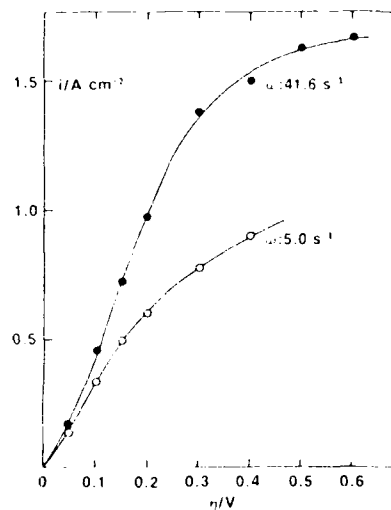


Figure 4. SEM of Chromium Electrodeposit on 304 SS. $C: 2.12 \text{ mol dm}^{-3}$, $\eta_N: -0.6 \text{ V}$, $t_N: 2 \text{ s}$, $\eta_G: -0.05 \text{ V}$, $i_G: 0.025 \text{ A cm}^{-2}$, $l: \sim 40 \text{ μm}$.



Figure 5. SEM of Chromium Electrodeposit on 304 SS. $C: 1.5 \text{ mol dm}^{-3}$, $\eta_N: -1.0 \text{ V}$, $t_N: 1 \text{ s}$, $\eta_G: -0.09 \text{ V}$, $i_G: 0.07 \text{ A cm}^{-2}$, $l: \sim 25 \text{ μm}$.

Figure 6. i vs. η Plot for Chromium Deposition at Different Rotation Rates for Tungsten Disc Electrode (Area = 0.0707 cm^2 , $C = 1.0 \text{ M/cm}^3$).





A



B



C

Figure 7. SEM of Chromium Electrodeposit on Substrate of type 304 SS. $C=1.0 \text{ M/dm}^3$, 3-mm-dia Rod Electrode, Total Area 1 cm^2 (disc area 0.0707 cm^2), 2500 rpm; Pulse B; $\eta_N=-0.9 \text{ V}$, $t_N=20 \text{ ms}$, $\eta_G=-0.1 \text{ V}$, $t_G=25 \text{ s}$, $T_R=20 \text{ s}$; Surface (A) and Cross Sections [(B) and (C)] Etched for Different Times.

USE OF IMPEDANCE MEASUREMENTS FOR STUDYING
THE EFFECT OF ACIDITY ON THE CORROSION OF IRON
IN THE MOLTEN EQUIMOLAR NaNO_3 - NaNO_2 MIXTURE

Gerard S. Picard, Herve M. Lefebvre* and Bernard L. Tremillon
Laboratoire d'Electrochimie Analytique et Appliquee
associe au CNRS (U.A. 216)
E.N.S.C.P., 11 rue Pierre et Marie Curie
75231-Paris Cedex 05-FRANCE

ABSTRACT

The iron corrosion process in the molten equimolar NaNO_3 - NaNO_2 mixture was studied as a function of melt acidity. A reaction model has been proposed from analysis of impedance spectra and was compared with earlier thermodynamic and kinetic results. This model which accounts for experimental data has allowed us to show the importance of the diffusion phenomena through the various iron oxide layers constituting the corrosion products. Besides, the acidity dependence of impedance spectra and more precisely of charge transfer resistances has revealed the existence of a narrow range of acidity (relative to NaFeO_2 stability) for which iron corrosion is minimized.

INTRODUCTION

Corrosion of iron and iron alloys in molten nitrate-nitrite mixtures has been studied primarily because of the application of these salts as both a heat transfer fluid and a thermal energy storage medium. Results in the literature for salts without contaminants indicate the formation of iron oxides (1-11). It has been observed that the corrosion products are $\text{Fe}_2\text{O}_3(\text{s})$, which forms the external layer in contact with the salt, and $\text{Fe}_3\text{O}_4(\text{s})$, the internal layer in contact with the metal. For temperatures greater than 600°C , it has been shown that a highly basic species of iron(III), the sodium ferrate, NaFeO_2 , appears in the external layer (8). Studies on steel behavior in molten sodium-potassium nitrate-nitrite mixtures at 450°C reported by Spiteri (6) indicate that there

*present address: S.A.F.T./GTA, rue Georges Leclanche,
86009 Poitiers-FRANCE

are different corrosion rates depending on the (oxo)acidity level [defined by $pO^{2-} = -\log m(O^{2-})$]. In particular, a decrease in the corrosion rate has been observed in moderately basic media, jointly with the formation of sodium ferrate as one corrosion product. A similar result has been observed by Baraka *et al.* (1) in sodium-potassium nitrate for temperatures between 250°C and 400°C.

In previous work (9,10) we have demonstrated the relationship between the nature of iron oxide species and the oxide anion content in the melt. Stability constants of iron oxides have been determined by means of potentiometric titrations and equilibrium potential- pO^{2-} diagrams have been deduced from them in the temperature range from 420 to 500°C. The main result of this thermodynamic study is that different compounds of iron(III) may be formed according to the acidity of the nitrate-nitrite mixtures. In strongly basic media, $Fe_2O_5^{4-}$ or $Na_4Fe_2O_5(s)$ are stable in contact with the melt. In moderately basic media, the stable iron oxide species are FeO_2^- or $NaFeO_2(s)$, and in acidic media $Fe_2O_3(s)$.

From the previously quoted authors' works and ours, we can assert that the iron corrosion in molten nitrate-nitrite mixtures leads to the formation of a multilayered product. The outer layer in contact with the melt is constituted by iron(III) oxides whose surface composition depends on the melt acidity, and the deepest layer consisting of $Fe_3O_4(s)$ [and perhaps $FeO(s)$] in contact with metallic iron. Moreover, knowing after Spiteri (6) that alkali ions are contained in the iron(III) oxide layer, suggests penetration of melt inside the outer layer, we can predict for the latter a structure formed by several secondary layers constituted by iron(III) compounds all the more acidic the deeper they are because of the oxide ion concentration gradient in the layer (Fig. 1).

The purpose of this paper is to study the iron corrosion process in the molten equimolar nitrate-nitrite mixture from a kinetic point of view, thus completing our work on the stability of iron(III) oxides. This was undertaken by using chronopotentiometry and especially A.C. impedance techniques. The latter allow us to obtain *in situ* information on the mechanism and kinetics of the steps involved. This electrochemical technique has been successfully used in aqueous solutions (12-14). However, relatively few studies have been carried out in media where corrosion leads to the formation of insoluble products adhering to the metal surface (15-17).

EXPERIMENTAL RESULTS AND DISCUSSION

Technical.

Preparation of the melt, procedure, and apparatus have been described in detail in previous papers (18-20). For each experiment,

100g of an equimolar sodium nitrate-nitrite mixture were introduced into a platinum crucible. pO^{2-} was imposed by using the buffer couple $H_2O(g)/OH^-$ whose acidity constant, given by $K_d = P(H_2O) \cdot m(O^{2-}) / m(OH^-)^2$, takes the value $10^{-3.1}$ at $420^\circ C$ (20). [concentrations m of the dissolved species are given in the molality scale and partial pressure of water $P(H_2O)$ is given in atm].

The working electrode was a high purity iron wire (1 mm diam.) supplied by Johnson-Matthey, with a dipped surface area in the melt of $60 mm^2$. The platinum crucible was used as a counter electrode. The reference electrode is described elsewhere (20).

The chronopotentiograms were recorded with the help of a three pen Y/T Servofram SRM recorder (Sefram).

Impedance measurements have been performed over the frequency range 100 kHz-10MHz using the Z computer system (Tacussel) composed of a Tacussel electronic unit and of a Hewlett-Packard 9826 microcomputer. Measurements have been carried out under linear conditions using a small amplitude sine wave signal of 10mV. In order to avoid external perturbations on the electrical measurements, the cell was surrounded with a ground connected Faraday cage, and screened wires were used for connecting electrodes with the electronic unit. Fifteen minutes are necessary to perform measurements over the whole frequency range considered. Data were stored on standard 5 1/4 inch flexible disks and further analyzed by means of the HP 9826 microcomputer and HP 7470 A plotter.

Chronopotentiometric evidence for a first transient phase followed by a quasi steady-state second phase in iron corrosion.

The potential of an iron electrode under open circuit conditions was followed as a function of time for different values of pO^{2-} (Fig.2). In all cases, the iron electrode potential increases at the beginning of corrosion, involving the formation of iron oxides. This transient phase was observed until the potential reaches a steady-state value depending on melt acidity, which corresponds to the potential of the NO_3^-/NO_2^- redox couple as indicated by comparison with the potential of an inert platinum electrode (Fig. 2). The stabilization of the iron electrode potential does not exceed 2 hours and is shorter at lower pO^{2-} values. Impedance measurements were performed at the stabilized rest potential of the iron working electrode.

A.C. Impedance studies of the second phase of the iron corrosion process.

Variation of impedance spectra as a function of oxide ion bulk concentration at a given immersion time ($t = 3.5$ h). Fig. 3 gives in the complex plane typical impedance spectra obtained in the

molten equimolar NaNO_3 - NaNO_2 mixture at 420°C , for four pO^{2-} values: 1.4 and 2.9 corresponding to basic media where the stable iron(III) oxide is $\text{Na}_4\text{FeO}_2\text{O}_5$, $\text{pO}^{2-} = 4.3$ which is the value for which the latter ferrate transforms into NaFeO_2 (moderately basic media) and the last, $\text{pO}^{2-} = 5.2$, which corresponds to the transformation of NaFeO_2 into Fe_2O_3 (acidic media).

These spectra are constituted, whatever the pO^{2-} values, by two composite capacitive loops. They show (i) that the different phenomena involved during iron corrosion have time constants close to each other, resulting in a convolution of capacitive loops and (ii) that the effect of pO^{2-} is characterized by a frequency shift of the capacitive phenomenon (Fig. 5) and by a maximum of impedance (and so a minimum in the corrosion rate) for a pO^{2-} value equal to 4.3, which corresponds to the formation of the ferrate, NaFeO_2 .

Variation of impedance spectra as a function of immersion time at a given oxide anion bulk concentration. Two values of pO^{2-} were considered: 1.4 and 4.3 for which a maximum impedance was observed. Analysis of Fig. 4 clearly shows the opposite corrosion behavior of iron for the two media considered. In the first case ($\text{pO}^{2-} = 1.4$), impedance decreases when immersion time increases, to reach a low value indicating a fairly constant corrosion rate. On the contrary, for $\text{pO}^{2-} = 4.3$, impedance increases with immersion time indicating the formation of a passivating film. Iron corrosion is then strongly limited.

Somewhat different behavior, depending on melt acidity, is observed for impedance spectra toward the low frequency region. Contrary to that which is observed for a pO^{2-} value equal to 4.3, experimental data obtained at $\text{pO}^{2-} = 1.4$ present a large scattering for frequencies lower than 1 Hz (Fig. 5). This fact suggests that iron corrosion products can flake off the metal for this melt acidity.

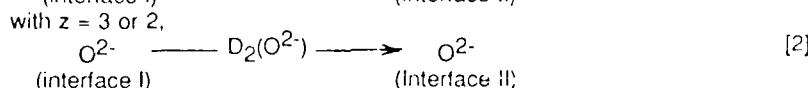
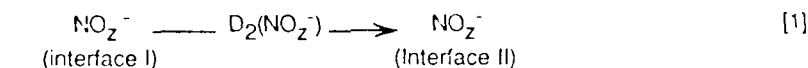
MODELLING OF THE IRON CORROSION PROCESS

Thermodynamic and kinetic experimental studies have shown that after the transient phase of iron corrosion (during which NO_3^- and/or NO_2^- oxidize the metallic iron which is quickly recovered by an oxide layer), corroded iron can be schematically represented as follows: metallic iron is coated by a layer of magnetite, which is itself covered by a layer of iron(III) oxides (whose surface is in contact with the melt), thus defining four zones and three interfaces as indicated in Fig. 6. It should be noticed here that the sequence $\text{Fe}/\text{Fe}_3\text{O}_4/\text{Fe}_2\text{O}_3$ has been reported as the thermodynamically most stable system (21) and is often referred as the passive film on iron in aqueous solutions (21,22).

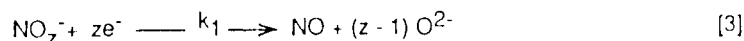
Proposed reaction mechanism.

The iron corrosion process in the molten equimolar $\text{NaNO}_3\text{-NaNO}_2$ mixture can be described by the following steps:

(i) diffusion of the oxidizing species (NO_3^- and/or NO_2^-) and O^{2-} anions through the outer iron (III) oxide layer from its interface I melt to the interface II (Fig. 6):

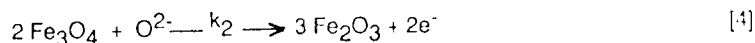


(ii) the occurrence of two electrochemical reactions at the interface II: the NO_z^- species, which have diffused, can be reduced when they contact the magnetite [which is known to have excellent semi-conductive properties (23,24)] with the production of oxide ions:

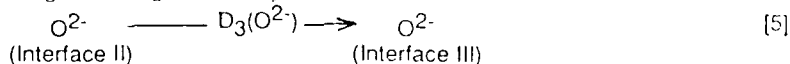


(diffusion of NO has been assumed to be sufficiently fast so as not to be a limiting step).

The oxidation of Fe_3O_4 to Fe_2O_3 , which consumes a part of both O^{2-} produced by reaction [3] and O^{2-} coming from the melt by diffusion [2], according to:

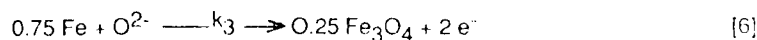


(iii) diffusion of the oxide anions not consumed by reaction [4] through the magnetite layer:



and finally,

(iv) oxidation of metallic iron into magnetite (Interface III):



We can state here that nitriding is a result of isolating the surface of the metallic iron from the melt by oxide layers. Metallic iron is in fact in contact with nitrogen monoxide under a very low partial pressure of oxygen; conditions are favorable for further nitriding (10,11).

Determination of the faradaic impedance.

In order to test the reaction model, we have calculated the corresponding impedance Z_f by the classical method. The details of the calculation of Z_f have been given elsewhere (25). The following expression for the faradaic impedance was obtained:

$$Z_f = \frac{R_1 R_2 R_3 (1+a)(1+b)(1+c)}{R_1 R_2 (1+a) + R_1 R_3 (1+a)(1+c) + R_2 R_3 (1-0.33b)(1+c)} \quad [7]$$

where: R_i = charge transfer resistance of the i th electrochemical reaction:

$$\begin{aligned} R_1 &= [3FS k_1 b_1 m_{II}(\text{NO}_3^-)]^{-1} \text{ for [3]}, \\ R_2 &= [2FS k_2 b_2 m_{II}(\text{O}^{2-})]^{-1} \text{ for [4]}, \text{ and} \\ R_3 &= [2FS k_3 b_3 m_{II}(\text{O}^{2-})]^{-1} \text{ for [6]} \end{aligned}$$

$$F = 9.6487 \cdot 10^4 \text{ C mol}^{-1}$$

S = surface area of the iron electrode (0.6 cm^2)

k_i = rate constant for the i th electrochemical reaction =

$$k_i^0 \exp(-b_i \eta)$$

(k_i^0 = intrinsic rate constant; b_i = Tafel slope; η = overpotential).

$m_{II}(\text{NO}_3^-)$ and $m_{II}(\text{O}^{2-})$ are the concentrations of NO_3^- and O^{2-} at the interface II, respectively.

$$\begin{aligned} a &= k_1 \tanh \left[\frac{\delta_2 \sqrt{j\omega / D_2(\text{NO}_3^-)}}{\sqrt{j\omega D_2(\text{NO}_3^-)}} \right] \\ b &= k_2 \tanh \left[\frac{\delta_2 \sqrt{j\omega / D_2(\text{O}^{2-})}}{\sqrt{j\omega D_2(\text{O}^{2-})}} \right] \\ c &= k_3 \tanh \left[\frac{\delta_3 \sqrt{j\omega / D_3(\text{O}^{2-})}}{\sqrt{j\omega D_3(\text{O}^{2-})}} \right] \end{aligned}$$

where: δ_2 and δ_3 are the thicknesses of the iron(III) oxide layer and that of the magnetite layer, respectively; $D_2(\text{NO}_3^-)$ and $D_2(\text{O}^{2-})$ are the diffusion coefficients of NO_3^- and O^{2-} in the iron(III) oxide layer, respectively, and $D_3(\text{O}^{2-})$ is the diffusion coefficient of O^{2-} in the magnetite layer.

The overall impedance was obtained by taking into account the contribution of electrolyte resistance R_e and double layer capacitance C_d , as well as, the resistance R and the capacitance C of the iron(III) oxide layer, which appears as indicated in the equivalent electrical circuit represented in Fig. 7. Such a circuit has been successfully used in aqueous solution to describe the corrosion of iron(26) and mild steel(27) coated with organic compounds. The overall impedance Z is given by the following expression:

$$Z = R_e + z [1 + j\omega Cz]^{-1} \quad [8]$$

with:

$$z = R + Z_f [1 + j\omega CdZ_f]^{-1} \quad [9]$$

Testing of the proposed reaction mechanism

Impedance spectra have been simulated from the expression of the overall impedance (Eq.[8]). A good fit has been observed (Fig. 8) with the values of the considered parameters collected in Tables 1 and 2. This confirms that the proposed reaction model accounts well for all the experimental data.

Moreover, information about the electrical properties of the iron(III) oxide layer and the charge transfer resistances were also obtained. In particular, the charge transfer resistances determined at $pO_2^- = 4.3$ are quite obviously higher (low corrosion rate) than those determined at $pO_2^- = 1.4$. This is consistent with the fact that the product RC has a constant value for $pO_2^- = 4.3$ (Table 2) thus indicating a poor porous film, which is not the case for $pO_2^- = 1.4$ (Table 1).

CONCLUSION

Iron corrosion in the molten equimolar $NaNO_3$ - $NaNO_2$ mixture involves complex processes in which diffusion phenomena play an important role. A reaction model accounting for impedance measurements has been proposed and has led to the acquisition of electrical parameters characterizing the outer iron(III) oxide layer, which is one of the corrosion products. The composition of this layer depends on melt acidity. Only $NaFeO_2$, formed in the very narrow domain ranging from $pO_2^- = 4.3$ to 5.2 has passivating properties.

ACKNOWLEDGMENT

We are grateful to Electricite de France Company for the financial support of this study. We express thanks especially to P. Saint-Paul, P. Spiteri, and J. M. Gras of this Company for their interest in this work.

REFERENCES

1. A. Baraka, A. I. Abdel Rohman and A. A. EL Hosary, Br. Corros. J., **11**, 44(1976).
2. Sandia National Laboratories Report, Sandia Report 78-8256, Albuquerque, NM (Feb. 1979).
3. Sandia National Laboratories Report, Sandia Report 80-8062, Albuquerque, NM (March 1981).
4. Sandia National Laboratories Report, Sandia Report 81-8210, Albuquerque, NM (Feb. 1982).
5. H. V. Venkasetty and D. J. Saathoff, in "Molten Salts", P. Femsler, J. Braunstein, D. R. Morris, K. Nobe and M. E. Richards, Editors, p. 329, The Electrochemical Society Softbound Proceedings, Princeton, N.J. (1976).
6. P. Spiteri, Electricite de France, E.D.F. Report D 554 MAT 140 (June 1984).
7. J. W. Slusser, J. B. Titcomb, M. T. Heffelfinger and B. R. Dunbobbin, J. Metals, **24** (1985).
8. D. R. Boehme and R. W. Bradshaw, High Temperature Sci., **18**, 39(1984).
9. G. Picard, H. Lefebvre and B. Tremillon, Proc. of the 5th Intl. Symp. on Molten Salts (held in Las Vegas), the Electrochemical Society, vol. 86-1 (1986), p. 428.
10. G. Picard, H. Lefebvre and B. Tremillon, J. Electrochem. Soc., **134**, 52 (1987).
11. P. Spiteri, P. Saint-Paul, G. Picard, H. Lefebvre and B. Tremillon, in Proc. Intl. Symp. on High Temp. Corr. (held in Marseille, France, July 7-12, 1986), CEFRACOR, in press.
12. J. Epelboin and M. Keddam, J. Electrochem. Soc., **117**, 1052 (1970).
13. J. Habrecht and A. Verbeeken, J. Electrochem. Soc., **132**, 2386 (1985).
14. M. Duprat, M. C. Latent, F. Dabosi and F. Moran, Electrochim. Acta, **30**, 553 (1985).

15. M. G. S. Ferreira and J. L. Dawson, J. Electrochem. Soc., **132**, 760 (1985).
16. A. Bonnel, F. Dabosi, C. Deslouis, M. Duprat, M. Keddam and B. Tribollet, J. Electrochem. Soc., **130**, 753 (1983).
17. R. D. Armstrong and A. C. Coates, J. Electroanal. Chem., **50**, 303 (1974).
18. G. Picard, T. Flament and B. Tremillon, in Proc. of the 1st Intl. Symp. on Molten Salt Chem. and Tech., Kyoto, Japan, April 1983. The Electrochemical Soc. of Japan, ed., (1983), p. 85.
19. G. Picard, T. Flament and B. Tremillon, in Proc. of the 4th Int. Symp. on Molten Salts (held in San Francisco), the Electrochemical Society, vol. 84-2 (1984), p. 649.
20. G. Picard, T. Flament and B. Tremillon, J. Electrochem. Soc., **132**, 863 (1985).
21. V. Brusic, in "Oxides and Oxide Films", John W. Diggle, ed., Marcel Dekker (1972), vol. 1, p. 42.
22. K. J. Vetter, in "Electrochemical Kinetics", S. Brukenstein and B. Howard, translation ed., Academic Press, New York, London (1967), pp. 749-789.
23. R. T. Shuey, in "Semiconducting Ore Minerals", Elsevier Publishing Company, Amsterdam, Oxford, New York (1975), pp. 357 and 371.
24. P. Pascal, "Nouveau Traite de Chimie Minerale", tome XVII, p. 625.
25. H. Lefebvre, Thesis, Paris, France (1987).
26. L. Beaunier, I. Epelboin, J. C. Lestrade and M. Takenouti, Surf. Technol., **4**, 237 (1976).
27. M. M. Musiani, C. Pagura and G. Mengoli, Electrochim. Acta, **30**, 501 (1985).

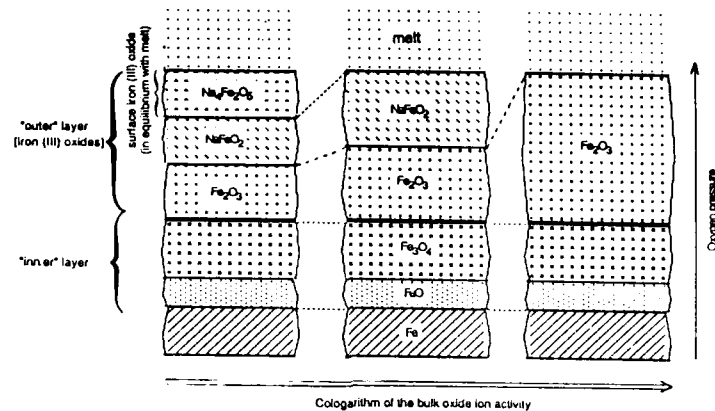


Figure 1: Predicted compositions of iron corrosion products as a function of the bulk oxide ion activity in the molten equimolar $\text{NaNO}_3\text{-NaNO}_2$ mixture.

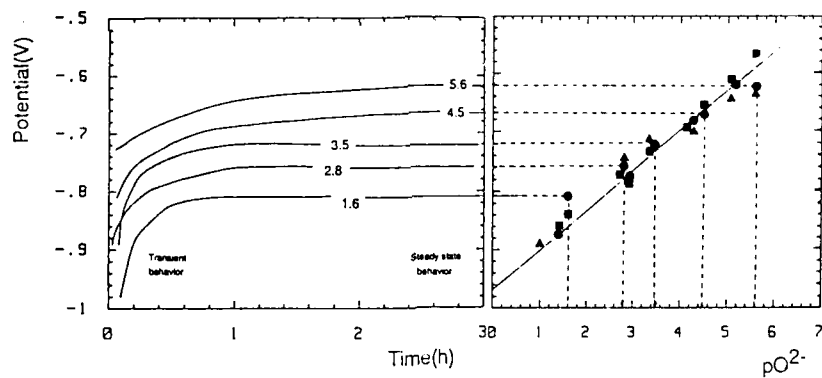


Figure 2: Chronopotentiometric study of iron corrosion in the molten equimolar $\text{NaNO}_3\text{-NaNO}_2$ mixture at 420°C for given values of $p\text{O}_2^-$, cologarithm of the bulk oxide ion activity [(Δ) iron electrode; (\bullet) platinum electrode]

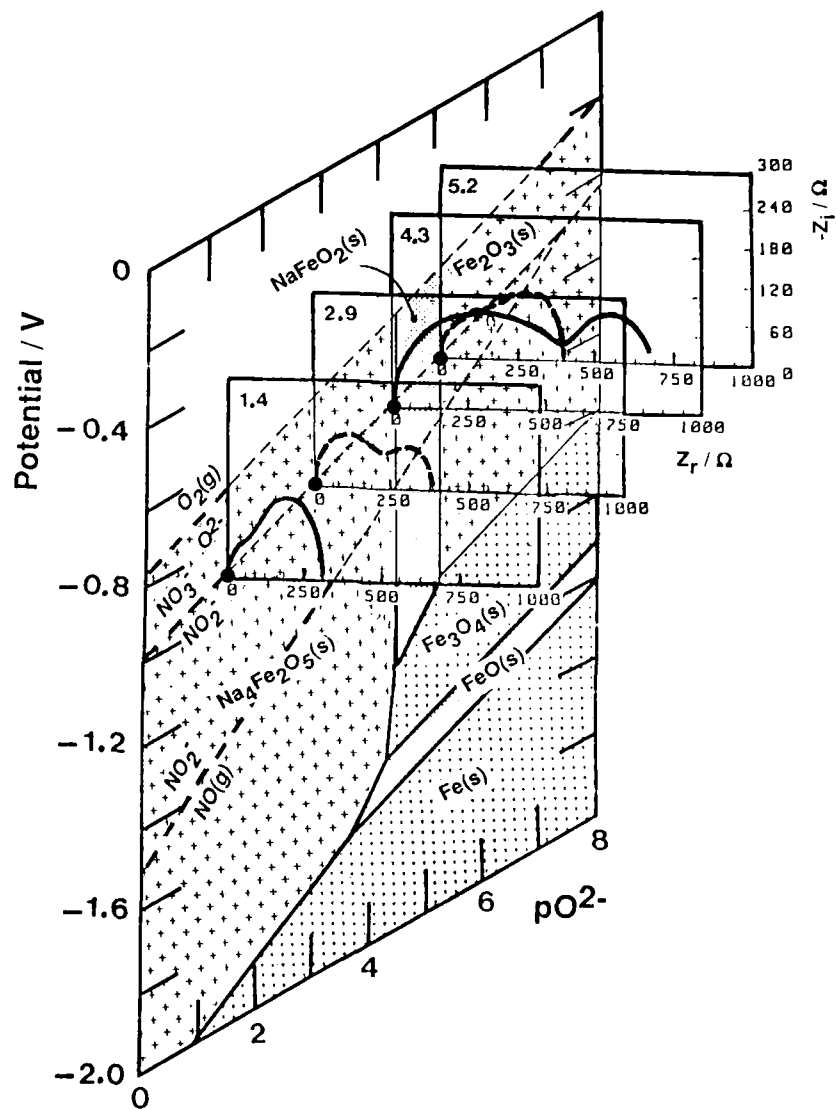


Figure 3: Potential-acidity diagram of iron and Nyquist plots obtained at given pO_2^- values in the molten equimolar NaNO_3 - NaNO_2 mixture at 420°C .

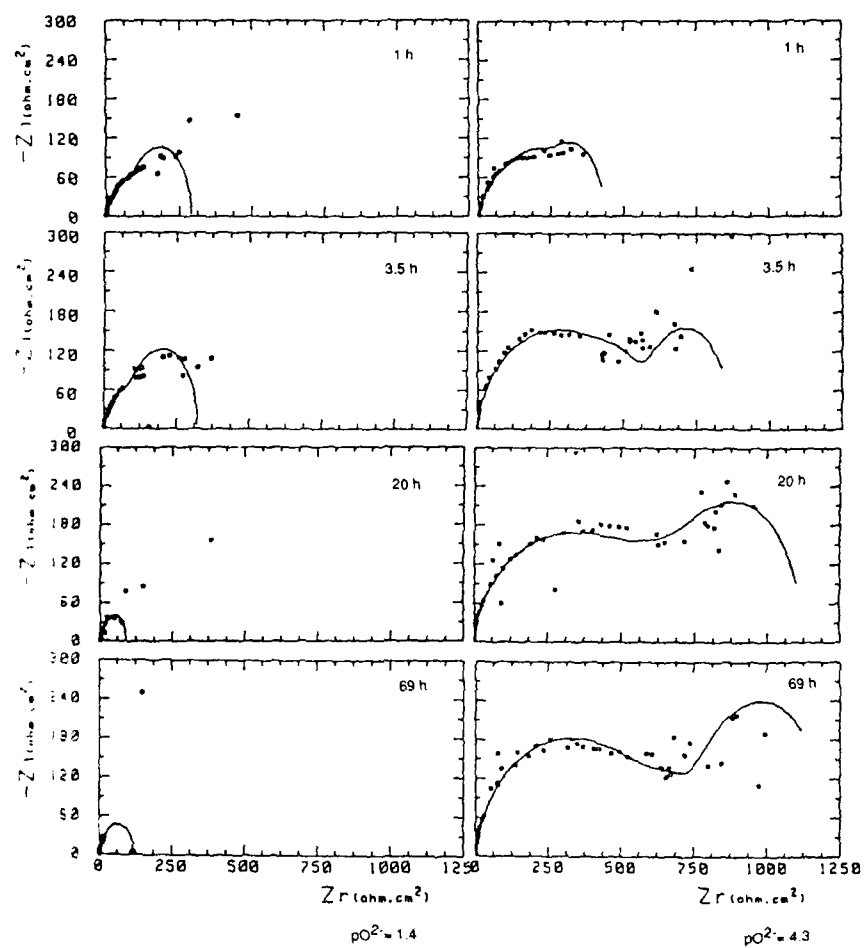


Figure 4: Immersion time dependence of impedance spectra for two values of melt acidity : $pO_2^- = 1.4$ and $pO_2^- = 4.3$ [equimolar $NaNO_3$ - $NaNO_2$ mixture at $420^\circ C$].

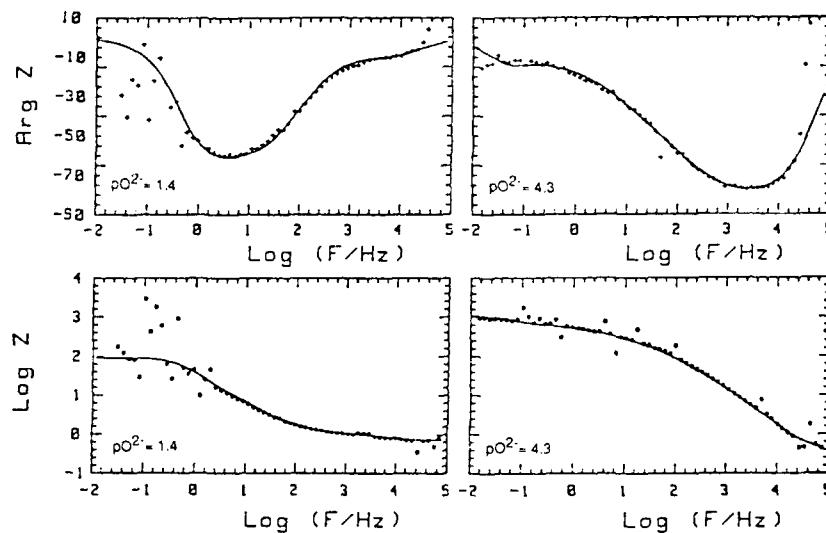


Figure 5: Bode phase plots and Bode amplitude plots for iron corrosion in the molten equimolar NaNO_3 - NaNO_2 mixture at 420°C , obtained with an iron electrode immersion time of 20 hours at two given $p\text{O}_2^-$ values: showing experimental data scattering for frequencies lower than 1 Hz when $p\text{O}_2^- = 1.4$ (strongly basic medium).

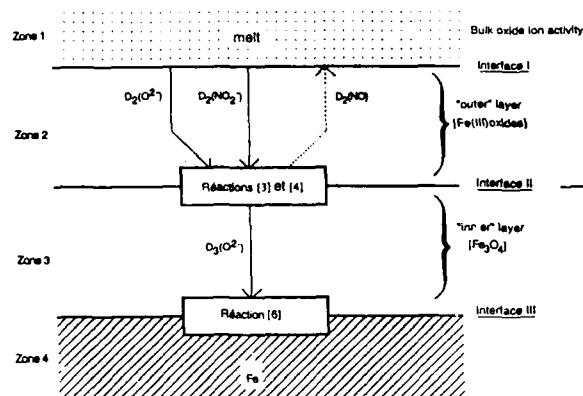


Figure 6: Schematic representation of the proposed reaction mechanism for iron corrosion in the molten equimolar NaNO_3 - NaNO_2 mixture.

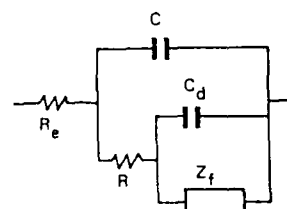


Figure 7: Equivalent circuit of the overall impedance relative to iron corrosion in the molten equimolar NaNO_3 - NaNO_2 mixture.

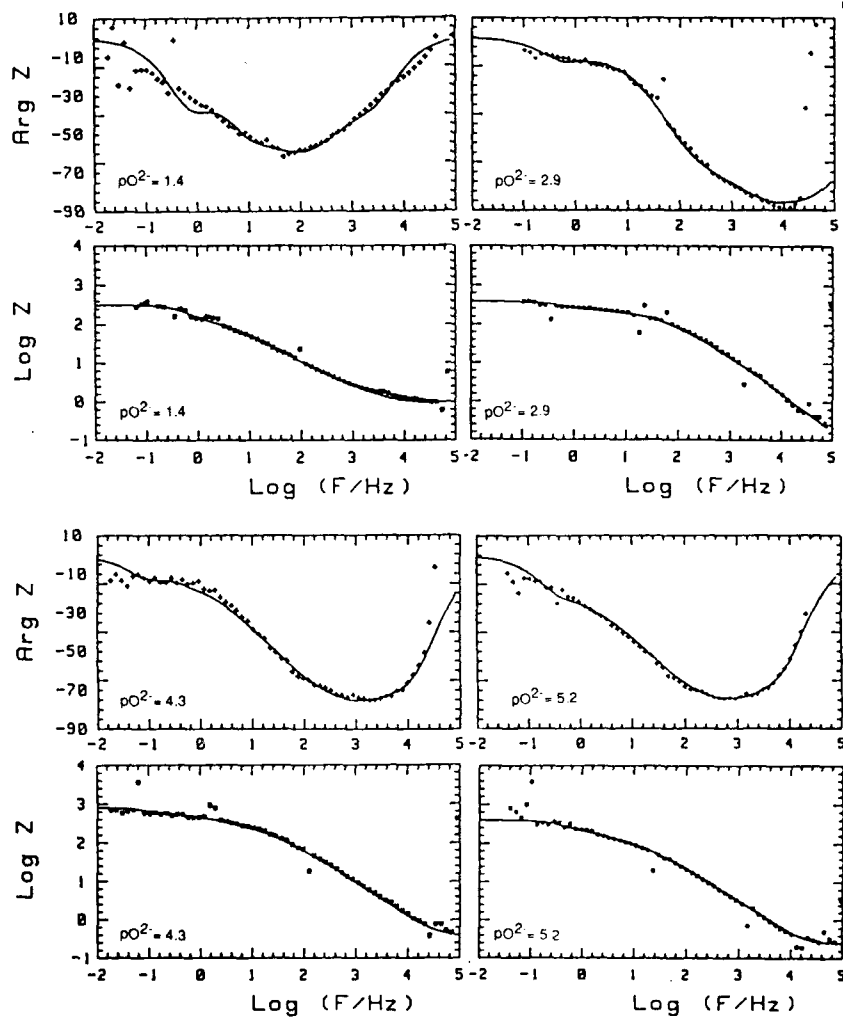


Figure 8: Comparison of the Bode phase plots and Bode amplitude plots calculated from Eq [8] (solid lines) and experimental data (points) for iron corrosion in the molten equimolar $\text{NaNO}_3\text{-NaNO}_2$ mixture at 420°C and for an immersion time equal to 3.5 h showing the consistency of the reaction mechanism proposed.

Table 1 : Immersion time dependence of impedance model parameters for iron corrosion in the molten equimolar $\text{NaNO}_3\text{-NaNO}_2$ mixture at $p\text{O}^{2-} = 1.4$ and $T = 420^\circ\text{C}$.

t	1,25	3,5	23	69
R_e	1,1	1	0,7	0,5
R	1,8	3	0,2	0,8
C	25	50	66	16
C_d	30	60	100	55
R_1	200	280	100	100
R_2	400	200	3	3
$k_2/\sqrt{2D_2(O^{2-})}$	2	2,25	26	26
$\delta_2\sqrt{2/D_2(O^{2-})}$	1	1,2	1,2	1,2
R_3	1	1	0,1	0,2
$k_3/\sqrt{2D_3(O^{2-})}$	400	400	100	150
$\delta_3\sqrt{2/D_3(O^{2-})}$	0,4	0,4	0,8	0,8

Table 2 : Immersion time dependence of impedance model parameters for iron corrosion in the molten equimolar $\text{NaNO}_3\text{-NaNO}_2$ mixture at $p\text{O}^{2-} = 4.3$ and $T = 420^\circ\text{C}$.

t	1	3,5	20,5	44	69
R_e	1	0,4	0,4	0,4	0,4
R	9	11	17	18	20
C	27	13	9	8,5	7,5
C_d	15	4,5	2	3	2,5
R_1	350	700	750	750	780
R_2	2000	3000	4000	4000	5000
$k_2/\sqrt{2D_2(O^{2-})}$	0,4	0,15	0,15	0,1	0,1
$\delta_2\sqrt{2/D_2(O^{2-})}$	1,7	3	4	6	6
R_3	5	20	20	20	20
$k_3/\sqrt{2D_3(O^{2-})}$	160	110	125	160	160
$\delta_3\sqrt{2/D_3(O^{2-})}$	1	2	3	4	3

[In Table 1 and Table 2, all parameters have their usual units].

AUTHOR INDEX

- | | |
|-----------------------------------|------------------------|
| Asahina, T., 717 | Fife, K. W., 888 |
| Asako, K.-i., 557 | Flengas, S. N., 28, 52 |
| Baluja, S., 295 | Flowers, P. A., 437 |
| Bardet, J.-P., 428 | Freyland, W., 200 |
| Barnard, P. A., 445 | Frost, R. H., 928 |
| Berchiesi, G., 333 | Fukui, M., 105 |
| Berg, R. W., 657 | Funaki, J., 424 |
| Bert, J., 340 | Fung, Y. S., 647 |
| Bjerrum, N. J., 657 | Funke, K., 256 |
| Blander, M., 1, 72, 156, 916, 928 | Furukawa, K., 896, 906 |
| Bohn, M. S., 317 | Gale, R. J., 591 |
| Boon, J. A., 979 | Garbade, K., 200 |
| Bowersox, D. F., 872, 888 | Glibert, J., 373 |
| Bradshaw, R. W., 959 | Grau, A. E., 28 |
| Brown, A., 1018 | Guang-sen, C., 507 |
| Brown, C., 888 | Guion, J., 130 |
| Brunet, C., 753 | Haarberg, G. M., 235 |
| Carling, R. W., 959 | Hacetoglu, A., 52 |
| Chabrier, G., 210, 222 | Haibara, T., 275 |
| Chemla, M., 546 | Haiming, X., 744, 751 |
| Chen, B., 156 | Haruyama, S., 557 |
| Chen, S. G., 491 | Hasebe, M., 317 |
| Christensen, D. C., 872 | Hashida, H., 786 |
| Claes, P., 373 | Hashimoto, Y., 795 |
| Combes, R. L., 970 | Hayashi, H., 814 |
| Curtiss, L. A., 185 | Hayashi, N., 814 |
| Dai, N., 939 | Heimer, N. E., 414 |
| Darendelioglu, H. S., 139 | Henry, D., 340 |
| Deki, S., 105 | Hermeling, J., 256 |
| Devilliers, D., 546 | Hjuler, H. A., 657 |
| Dieter, K. M., 414 | Hori, M., 949 |
| Dittrich, A., 111 | Hosokawa, K., 669 |
| Dupuy, J., 244, 340 | Hussey, C. L., 93, 445 |
| Dymek, Jr., C. J., 93, 414 | Igarashi, K., 165, 175 |
| Egan, J. J., 235 | Iida, T., 146 |
| Einarsrud, M.-A., 391 | Ikuta, K., 906 |
| Ejima, T., 317, 324 | Indacochea, J. E., 916 |
| Elias, A. M., 305 | Ishikawa, T., 734 |
| Elias, M. E., 305 | Itatsu, M., 939 |
| Ema, K., 581, 804 | Ito, K., 723 |
| Emons, H.-H., 111 | Ito, Y., 581, 804, 825 |
| Endoh, A., 295 | Jaffrin, A., 130 |
| Erikson, U., 602 | Jal, J. F., 244 |
| Ferry, D. M., 517 | Janz, G. J., 317 |
| | Johnson, K. E., 613 |

Kajinami, A., 105
 Kanaji, Y., 105
 Kaneko, Y., 786
 Katagiri, A., 814
 Katoh, Y., 896
 Kaun, T. D., 621
 Kawabe, M., 723
 Kawakami, M., 723
 Kawamura, K., 485
 Kawasaki, T., 557
 Kim, J. H., 928
 Kinoshita, K., 939
 Kinstle, T. H., 991
 Kobayashi, H., 949
 Kojima, H., 786
 Konda, S., 734
 Kosaka, M., 717
 Koyama, K., 795
 Lander, Jr., S. W., 979
 Laugt, M., 130
 Lefebvre, H. M., 1028
 Levisky, J. A., 979
 Li, S. X., 491
 Lobbia, G. G., 333
 Longyu, L., 744
 Lopez, P. C., 888
 Lu, Q. T., 491
 Mamantov, G., 437
 Matsunaga, M., 669
 Matthieu, C., 244
 McCurry, L. E., 888
 Mellon, H., 340
 Mergault, P., 428, 753
 Minami, K., 896
 Minh, N. Q., 677
 Mitachi, K., 896
 Mitchell, A., 863
 Mizobuchi, T., 146
 Mochinaga, J., 165, 175
 Momma, A., 557
 Morita, Z., 146
 Nakajima, T., 527, 537
 Nakamura, T., 382
 Nakamura, Y., 424
 Nakayama, H., 949

Nanjo, M., 267
 Narita, T., 734
 Natesan, K., 72
 Newman, D. S., 991
 Nishina, T., 571
 Nishio, T., 717
 Nomura, M., 275
 Numata, H., 557
 O'Donnell, T. A., 363
 Odawara, O., 275, 285
 Ogawa, T., 537
 Ohta, H., 353
 Oishi, J., 581, 804, 825
 Okada, I., 275, 285, 295
 Okamoto, M., 275
 Okamoto, Y., 165, 175
 Oki, T., 507, 765
 Okido, M., 507
 Okuyama, M., 723
 Olson, D. L., 928
 Osen, K. S., 235
 Osteryoung, R. A., 406
 Ota, E., 1002
 Oye, H. A., 93
 Paixao, J. M., 970
 Paixao, M. J., 970
 Peeters, G., 373
 Pelton, A. D., 12
 Pfeiffer, E., 200
 Pflug, J. L., 979
 Picard, G. S., 517, 1028
 Plowiec, R., 333
 Prengle, Jr., H. W., 83
 Qingfu, L., 758
 Rabenau, A., 637
 Rapp, R. A., 707
 Reddy, R. G., 156
 Redey, L., 631
 Rolland, W., 775
 Rovang, J. W., 414
 Rovere, M., 195
 Rytter, E., 391
 Sadoway, D. R., 1011
 Saotome, N., 939
 Sato, N., 267

Sato, Y., 317	Waseda, Y., 353
Schoch, B., 637	Watanabe, N., 527, 537
Schoebrechts, J.-P., 437	Weppner, W., 637
Seefurth, R. N., 846	Wicelinski, S. P., 591
Seon, F. M., 836	Wilkes, J. S., 93, 414, 979
Seto, K., 939	Williams, J. D., 872
Shah, S., 916	von Winbush, S., 657
Shah, S. P., 83	Xiuzhi, X., 858
Sharma, R. A., 846	Xujun, W., 858
Shimada, T., 825	Xuiiang, L., 498
Shimizu, M., 485	Yabe, H., 804, 825
Shimokawa, S., 424	Yamamura, T., 317, 324
Shiyang, S., 498	Yanagase, T., 382
Sinha, S. P., 458	Yang, C.-C., 285
Sinha, S., 72	Yatsurugi, Y., 939
Skryznecki-Cooke, L. M., 979	Yerhoff, F. W., 613
Soirat, A. J. A., 970	Yexiang, L., 744, 751
Stern, K. H., 469	Yokokawa, T., 485
Sterten, A., 775	Yong, C., 858
Sun, I.-W., 445	Yoon, S.-Y., 1011
Suzuki, H., 939	Yu, R. L., 491
Tajiri, K., 717	Yueqiang, Z., 758
Takahashi, M., 571	Zawodzinski, Jr., T. A., 406
Takehara, Z., 814	Zhang, Y. S., 707
Takenaka, T., 581	Zhu, K., 324
Tamai, K., 317	
Tasaka, A., 949	
Teisseire, M., 130	
Thambo, G., 991	
Thomas, B., 863	
Thonstad, J., 775	
Tosi, M. P., 195	
Tremillon, B. L., 517, 689, 1028	
Tunold, R., 602	
Uchida, I., 571	
Ueda, Y., 382	
Uno, K., 814	
Valognes, J.-C., 428	
Vargas, T., 1018	
Varma, R., 1018	
Vitali, G., 333	
Voigt, W., 111	
Ward, E. H., 445	

SUBJECT INDEX

A.C. Impedance Studies	520
Ab Initio Molecular Orbital Investigation	185
Ablation Mass Driver	908
Accelerated Oxidation	723
Acetyl Chloride	993
Acid-Base Chemistry Na_2SO_4	707
Acid-Base Reactions	613
Acid/Base Dependent Reactions	368
Acidity-Basicity in Molten Alkali Nitrates	689
Acidity, Lewis	93
Activity, CaO in Silicates	43
Activity, CoO in Silicates	41
Activity, FeO	39
Activity, Lanthana	44
Activity, MnO in Silicates	42
Activity, Na_2O in Na_2SO_4	707
Activity, Na in NaCl	238
Activity, PbO	40, 54, 56
Activity, PbO-PbCl_2 system	52, 56
Activity, SnO in Silicates	44
Alkali Metals-Alkali Halides Mixtures	210
Aluminum Underpotential Deposition	595
Aluminum Cell	1011
Aluminum Chloride, Automatic Feed	738
Aluminum Electrolysis	744
Aluminum-Nickel Sulfide Batteries	657
Anatase (Rutile)	970
Anhydrous Hydrogen Fluoride	363
Anion Chemla Effect	295
Anode Effect	428, 527, 537, 602
Anode with Dopants	745
Anodic Dissolution of Nickel	950
Anodic Filler Wire	918
Anodic Insulating Coverage	754
Anodic Micro-Plasmas	428
Anodic Ohmic Impedance	753
Anthraquinone	1002
Arrhenius Activation Energy	307

Assymetric Combining Rule (Toop)	16
Average Electron Density	382
Barclay-Butler Rule	107
Basicity, Absolute	377
Basicity Index	917
Basicity Scale	385
Basicity Scale, Oxides	46
Basicity, Silicates	487
Basis Sets	186
o-Benzoylbenzoic Acid	1006
Benzophenone	993
Benzoylphenanthrene	1005
Bibenzyl	993
Binaphthyls	1002
Bipolar Electrode	734
Boiling Point Method	94
Bond Equilibria in Silicates	31
Bridging Structure	186
Brillouin Scattering	325
Bubble Formation	605
Bulk Viscosity	326
Bypass Current	942
CaCl ₂ -H ₂ O System	110
CaF ₂ -CaO-SiO ₂ Fluxes	916
CaO-CaCl ₂ System	385
Cahn-Hilliard Theory	146, 148
Calcium Chloride Hexahydrate	133
Carbon Anode	529
Carbonates, Molten	571, 718
Carbonates, Viscosity	317
Cathode Dissolution	679
Cathode Materials	777
Cathodic Reduction of Oxygen in Carbonate	561
Cathodic Weld Pool	918
Cell Efficiency	741
Charge-Discharge Behavior	671
Charge/Discharge Imbalance	636
Chemical Transport Method in Molten Salts	770
Chemistry Of Coal Combustion and Gasification	72
Chemla Effect	278, 285, 295
Chlorination, Electrophilic	979
Chlorination, Titanium Oxide Ores	972
Chlorine Evolution	780
Chlorine Injection	943
Chloro Complex Stability	198

Chloroaluminate Melts	406, 414, 437, 657, 670, 1002, 1013 363
Chloroaluminate Melts, Cationic Species	
Chloroaluminate Melts, Electrochemical Properties	460
Chloroaluminate Melts, Room Temperature	447, 458, 591
Chromium Carbide Film	767
Chromous Chloride	1019
Chronoabsorptometry	448
Chronoamperometry	448, 519, 574
Chronopotentiometry	519, 550, 806, 1029
Collective Modes	222
Complex Conductivity	258
Complex Permittivity	258
Complex Plane Plot (Cole-Cole Plot)	562, 573
Complexation	613
Compressibility, Isentropic	146
Compressibility, Isothermal	146
Computer Simulation of i-E Curves	485
Computerized Thermodynamic Analyses	12
Concentration Cell	498
Conductivity Cell	866
Conductivity Probe	865
Conformal Ionic Solution Theory	5, 12, 19
Consumable Iron Cathodes	836
Contact Angle	528
Conversion Ratio	896
Cooperative Process	335
Coordination of M^{+2} in MCl_2 - $AlCl_3$ Melts	397
Correlation Functions	166, 176
Correlation Length	215
Corrosion, Iron by Molten Nitrates	696
Corrosion Product, Multilayered	1029
Corrosion, Silicon Nitride	717
Corrosion Rate	719, 1030
Corrosion Resistant Cathodes	1018
Coulometric Titration	640
Countercurrent Electromigration	286
Critical Current Density	529
Critical Potential	649
Cryoscopy	333
Crystal Growth	780
Crystal Orientation, Carbide Films	769
Current Density, Exchange	574
Current Efficiency	780, 837, 858, 943
Current Efficiency, NF_3	951

Cyclic Voltammetry	439, 623, 788, 1013
Cycling Efficiency	650
Data Base, Solution Properties	21
Decomposition Voltage	639
Defect Model, NaX-Na Mixtures	236
Degradation of Electrocatalyst	749
Demineralization	1000
Deposition, Electrochemical	920
Desulfurizability	1000
Dielectric Relaxation	335
Diffusion Phenomena	1033
Diffusion Treatment	765
Diffusive Processes	919
Direct Oxide Reduction, Plutonium Oxides	875
Disproportionation	825
Disproportionation Mechanism	766
Disproportionation Reaction	765
Dissolution of Neodymium in Molten Neodymium Trichloride	491
Double Layer Capacitance	520, 574, 1033
Double Pulse Method	558
Dynamic Conductivity	256
EDX Spectrum, Tungsten	827
EMF, Nd-NdCl ₃ Concentration Cell	492
EOS-Perturbation Expansion	214
ESCA Spectra	527
Effective Screening	197
Einstein's Compressibility Formula	146
Electrical Conductivity	305
Electrocatalytic Activity Of Carbon Anode	747
Electrolysis	779
Electrolysis, Magnesium	758
Electrolysis, PbO-PbCl ₂	62
Electromigration Flow	276
Electron Gas	213
Electronic Conductivity	237
Electronic Screening	227
Electrowinning Cell	734
Energy Density	669
Energy Storage	130
Energy Storage Cycle, Sulfates, Low Melting	83
Enrichment of ⁶ Li	278
Enthalpies of Mixing, Silicates	34
Enthalpy of Vaporization	107, 109
Entropy of Vaporization	107
Equation of State	205

Equivalent Circuit, Oxygen Electrode	563
Equivalent Ion Fractions	13
Excess Gibbs Energy	12
Excess Gibbs Energy Per Equivalent	14
Exchange Energy, Isotropic Interaction	140
Exchange Integral Magnetic Modes	141
Extraction, Electrochemical	863
Extraction Pool, Nd-Fe	851
Extraction Pool, Nd-Zn	850
F-Center	204
FeS ₂	632
FeS ₂ Electrode	622
Ferrates (III)	696, 1028
Ferrosilicon-Graphite Composite Film	767
Fiber Optic Spectrophotometer	445
Fissile-Fuel Breeders	906
FLINAK, Molten	469
Fluorescence	459
Fluoride Melt	469, 527
Fluoride Melts, Extraction from	863
Fluorination, Electrochemical	949
Fluorine Evolution	527, 537, 546
Fluorine Intercalation	530, 537
Freezing Point Model	86
Friedel-Crafts Acylation	979, 992, 1002
Friedel-Crafts Alkylation	979, 992, 1002
Fuel Cell	677
GaCl ₃ Complex	594
Gallium Anodization	593
Gallium Electrochemistry	591
Gallium(I) Potentiometry	592
Galvanostatic Transient Technique	641
Geometry Optimization	187
Glass Formation	305
Glass Transition Temperature	307
Grain Size Control	1021
Graphite Core, Irradiation Limit	898
Graphite Fluoride	527, 537, 546
Graphite Moderator	899
Graphite Oxide	529, 539
Graphitization Degree	529
Guinier Behavior	203
HF Cathodic Behavior	581
HF-KF Melts	546
HF/H ₂ Gas Electrode in LiF-KF	583
Halide Polarizability	188

Hammett Acidity Function	363
Hard Sphere Model	148
Hastelloy N	898
Heat Resistant Alloys	723
High-Frequency Measurements	257
High-Sulfur Coal	72
Hitec Mixture	690
Homopolyatomic Cations of Halogens and Chalcogens	363
Hot Corrosion	723
Hydrodynamics Theory	222
Hydrofluorination	873
Hydrous Melt	105
Hydroxide-Water Acid-Base System in Molten Nitrates	692
Illinois #6 Coal	995
Immersion Time	1031
Impact Fusion	906
Impedance Analysis	509
Impedance, Faraday	573, 1032
Impedance Method	572
Impedance Method, Nernst Electrode	559
Impedance Spectra	1030
Impedance Study	564
Infrared Detection of Thermal Conductivity	353
Infrared Reflection Spectra, $AlCl_3 - MCl_2$	391
Intensity Function	176
Intercalation Compound	673
Interdiffusion Coefficient	344
Interionic Distances	167, 177
Internal Cation Mobility	275, 285
Internal Pressure	205
Internal Reforming	681
Inversion Barrier	188
Ion-Electron Interaction	212
Ion-Water Interaction	116
Ionic Hamiltonian	211
Ionic Interactions	414
Iron Boride Film	769
Iron Oxides	1028
Isomerization	1002
Jump-Relaxation Model	260
KCl-NaCl System	507
KF-Borate-Molybdate Melts	795
Kinematic Viscosity	305
Kinetically-Constrained Mechanism	921

Klemm Method	286
LAMEX	889
Laplace's Equation	754
Laser-Flash Method	353
Lead Oxide, Properties in Silicates	38
Li_2FeS_2	643
$\text{Li}_3\text{Fe}_2\text{S}_4$	643
Li, K/Li, K Electrode	826
Li-Alloy/Metal Disulfide Cells	621, 631
LiAl Anode	647
LiCl-LiBr-KBr Electrolyte	621
LiF-BeF ₂	724
Lifetime, Doped Carbon Anodes	748
Ligand-Exchange Process	115
Limiting Current Density, Mg Electrolysis	758
Lindemann's Melting Formula Modification	146
Linear Sweep Voltammetry	485
Low Ionicity Limit	196
Low Oxidation States	366
M-Cluster	204
Magnequench	847
Magnesium Cell	1011
Magnesium Chloride Hydrates	111
Magnetic Alloys	847
Mechanism Of Oxygen Evolution	752
Metal Dispersion	836
Metal Rich Mixtures	224
Metal-Flux Interfaces	918
Metallic Conduction Regime	246
Metallic-Nonmetallic Transition, Potassium-	
Potassium Chloride	200
Metallurgical Reduction	846
1-Methyl-3-Ethylimidazolium Chloride Melts	406, 414, 459, 994
MgO Adsorption	759
Microgravity	341
Miscibility Gap-Excess Volume of Mixing	214
Mixed Alkali Effect	289
MnCl_2 - AlCl_3 System	393
Model Coal Compounds	992
Molar Volume	204
Molecular Dynamics Simulation	295
Molten Carbonate Fuel Cells	677
Molten Hydroxides/Acids-Basicity	373
Molten-Fission Power Stations	896, 911
Molten-Fission Target/Blanket	906
Molybdenum Coatings	797

Molybdenum Deposition	795
Monosilane Generation	939
Multicomponent Cation-Ion Systems	17
Multicomponent Systems, General	
Solution Properties	20
Na ₂ O-SiO ₂ Melts	156
Na ₂ SO ₄ -NaVO ₃ Solutions	709
NaBF ₄ -NaF	724
Naphthalene	1002
Nearest-Neighbor Interaction	143
Neel Point, Fourier Method	139
Neodymium Oxide Reduction	850
Neodymium Oxychloride	848
Neodymium Production	846
Neodymium-Iron Eutectic	837
Nernst-Einstein Equation	261
Neutron Scattering Experiments, Alkali Metal	
-Alkali Halides	247
Ni/Ni(II) Reference Electrode	471
NiS	632
Nitrate-Nitrite Mixtures	689
Nitrates	614, 689
Nitration, Electrophilic	979
Nitriding	1032
Nitrites	614, 689
Nitrogen Electrochemical System	
in Molten Nitrates	691
Nitrogen Trifluoride	949
Normal Pulse Voltammetry	439
Nuclear Magnetic Resonance	406
Nuclear Spin Relaxation, ¹ Hs	424
Nucleation	779
Nucleation Polarization	650
Nucleation Pulse	1018
¹⁷ O NMR	407
Optical Basicity	159, 382
Overcharge Protection	631
Overcharge Reactions	631
Overcharge Tolerance	633
Overdamping, Sound Waves	226
Overpotential, KF ₂ HF	528
Overpotentials	919
Oxide Impurity	437
Oxide Ion in Molten Nitrates	689
Oxides in Nitrates	614
Oxides in Chloroaluminate Melts	399

Oxochloroaluminate Melts	391
Oxyalkylation	992
Oxyanion Melts	474
Oxygen Electrochemical Systems in	
Molten Nitrates	691
Oxygen Electrode	499, 557
Oxygen Evolution on SnO_2 Anode	752
Oxygen Meniscus Electrode	569
pO_2 -Indicator Electrode	693
PVTx Results	202
Pair Correlation Function	296
Partial Molar Volume, Water	113
Partial Structure Factor Analysis, Isotopic	
Substitution Method	244
Partial Structure Factors, K-KCl	246
Passivating Properties, NaFeO_2	1034
Passivation	650
PbO Properties in Silicates	40
PbO, Enthalpies of Solution	56
PbO-PbCl System	52
Peroxide Ion in Molten Nitrates	690
Perylene	1004
Phase Change Materials	130
Phase Stability, Na-Cr-S-O System	708
Phase Stability, Na-Fe-S-O System	708
Phosphate Melt	788
Photoacoustic Spectroscopy	382
Plasma Arc	917
Plasma Brim	908
Plutonium Casting	878
Plutonium Electrowinning	879
Plutonium Extraction from Molten Salts	877
Plutonium Processing	872
Plutonium Purification	888
Plutonium Tetrafluoride Reduction	873
Polymeric Melts	157
Potential Step Amperometry	778
Potential-Step Method	572
Potential- pO_2 -Diagrams in Molten Nitrates	691
Potentiometric Studies, Molten Fluorides	469
Power-Law Behavior	259
Protonic Superacids	363
Pyridinium Chloride	991
Pyrochemical Processes	872
Pyroredox Process	874
Quasichemical Theory	3

Radial Distribution Function	166, 176
Raman Spectra, Aluminum Chloride Electrolysis Cell	1011
Raman Spectra, Magnesium Chloride Electrolysis Cell	1011
Rare Earth Extraction	863
Rare Earth Loss	859
Rare Earth Loss, Influence of CaF_2	860
Rare Earth Loss, Influence of Temperature	860
Rare Earth Metals, Dissolution	858
Rare Earth Metals, Electrolysis	858
Rare Earth Metals, Solubility	858
Reaction Mechanism, Iron Corrosion	1031
Rechargeable Batteries	657, 669
Reciprocal System	2
Reciprocal Ternary System	18
Recycle, Solvent Metal	892
Reduced Intensities	177
Relaxation Time	328
Reorientational Relaxation Time	260
Reticulated Vitreous Carbon Optically Transparent Electrode	445
Reverse Salt Effect	379
Rigid Background Model	223
SEM, Tungsten	827
Salt Rich Mixtures	225
Scholl Reaction	998
Scission Reactions	991
Screening Lengths	217
Self Diffusion Coefficient	299
Self-Exchange Velocity	289, 295
Separation Coefficient	343
Silicate Melts, Quasichemical Model	28
Silicate Solution Properties	33
Silicates	156
Silicon Nitride	719
Single Electron Screening Theory	244
Slags	156
Sludge in Rare Earth Extraction	864
Small Angle X-Ray Scattering Experiment (SAXS)	201
Smooth Electrodeposits	795
SnCl_2 - AlCl_3 System	394
SnO_2 -Based Inert Anodes	751
Sodium/Molten Chloroaluminate Battery	669
Solar Central Receivers	959

Solubility, Oxides in Na_2SO_4	707
Solubility, Cerium Oxide	709, 866
Solubility, Cr_2O_3	708
Solubility, Fe_2O_3	708
Solubility, Fe_3O_4	708
Solubility, Lanthanum Oxide	866
Solubility, Neodymium Oxide	866
Solubility, Rare Earth Oxides	863
Solubility, SiO_2	708
Solution Interaction Parameter	3
Sound Velocity	326
Space Thermal Diffusion Experiment	340
Specific Electrical Conductivity Isotherms	269
Specific Electrical Conductivity of Pseudo Binary NbCl_5 - NaCl - KCl	267
Spectroelectrochemistry, Room Temperature Haloaluminates	445
Spectropotentiostatic Technique	449
Spin-Lattice Relaxation Time	424
Stabilized Zirconia Electrode	470
Structural Parameters in Mixtures	171
Structural Relaxation	257
Sulfide Capacities	156
Sulfide Equilibria	157
Supercooling	333
Superoxide Ion in Molten Nitrates	690
Surface Free Energy	528
Symmetric Combining Rule (Kohler)	15
Tantalum Carbide Film	767
Ternary Molten Fluoride Phase Diagram	2
Tetrahalogallates	591
Tetravalent Selenium Cathode	669
Thermal Decomposition of CF_x	552
Thermodynamic Data Base	13
Thermodynamically-Driven Mechanism	921
Thermodynamics of 1-Methyl-3-Ethylimidazolium Chloride/Aluminum Chloride Mixtures	93
Thermoelectric Power	345
Thermogravimetric Measurements	724
Thermonuclear Reaction Efficiency	910
Thorium	896
Titanium Boride Film	769
Titanium Carbide Film	767
Titanium Electrodeposition	775
Titanium Fluorides	507
Transalkylation	993

Transfer Resistance	562
Transition-Metal Disulfides	632
Transpiration Method	106
Transport Number of Electrons	237
Tritium	911
Tungsten Crystals	829
Tungsten Hexachloride	437
Tungsten Nucleation Cluster Species	817
Tungsten and Tungsten Carbide	
Electrodeposition	804
Tungsten, Electrodeposition	814, 825
Ultrasonic Relaxation	334
Ultrasonic Spectroscopy	324
Underpotential Deposition	595
Vanadium Boride Film	769
Vanadium Bronze	786
Vanadium Bronze Crystals	789
Vanadium Carbide Film	767
Vanadyl Phosphate and Vanadate Electrolysis	787
Vapor Pressure, Apparatus for Measuring	108
Vapor Pressure, Hydrous Melts	108
Vapor Pressure Method	93
Velocity Autocorrelation Function	261
Viscoelastic Relaxation	334
Voltabsorptometry	448
Voltammetry	448, 777, 806, 827
Voltammograms, Linear Voltage Scan	759
WO_4^{2-} , Reduction of	825
Wagner Polarization Technique	235
Warburg Impedance	564
Water Content	530
Water Impurity	407
Weld Droplet Compositions	931
Weld Wire Compositions	931
Welding Parameters	921
Welding, Electrochemical Reactions in	929
Welding, Flux	928
Welding, Submerged Arc	928
Welding, Thermochemical Reactions in	929
Wetting, Visual Observations	605
X-Ray Diffraction, $\text{CaCl}_2\text{-KCl}$	175
X-Ray Diffraction, Tungsten Carbide	808
X-Ray Diffraction, LiF-KCl , KF-KBr , KF-KI	165
Ytria-Stabilized Zirconia	471

Zirconia Membrane Electrode	693
Zirconia-Air Electrode	805
Zirconium Boride Film	769
Zirconium Carbide Film	767
ZnBr ₂ -NaBr Melts	814
ZnCl ₂ -AlCl ₃ System	394
ZnCl ₂ -H ₂ O System	110